

TABLE OF CONTENTS

INVITED TALKS

OPENING PLENARY SESSION (OPS)

OPS-001-I	New Initiatives for Fostering Open Innovation Campus	1
	<u>Jean-Charles Guibert</u>	
OPS-002-I	Origami Fabrication using Single Layer Photolithography and Capillary Folding	3
	Derosh George, Edwin A. Peraza Hernandez and <u>Marc J. Madou</u>	
OPS-003-I	A Place in the Sun for Artificial Photosynthesis	9
	<u>Lionel Vayssieres</u>	

FUNDAMENTALS OF NANOTECHNOLOGY (FON)

FON-002-I	2019 Fuel Cell Technologies: Modelling and Controlling	13
	<u>Majid Monajjemi</u> , Chien Mau Dang	
FON-003-I	National French Hydrogen Program is launched	25
	<u>Valérie Nguyen</u> , François Le Naour	
FON-004-I	Design of Isostructural Metal-Insulator Transition in VO₂	27
	<u>Jaichan Lee</u> , B. Jung, D.-S. Lee, C.-B. Eom, and S.-Y. Choi	
FON-005-I	Langmuir-Type Mechanism for In-Situ Co-Doping of Boron and Carbon in CVD Silicon-Germanium Epitaxial Growth	29
	<u>Junichi Murota</u> and Hiromu Ishii	
FON-006-I	Designing Functional Materials via Atomic-Resolution Microscopy and Spectroscopy	35
	<u>Stephen J. Pennycook</u> , Xiaoxu Zhao, Jiong Lu, Wenjie Zang, Haijun Wu, Changjian Li, A. Ariando, T. Venkatesan and John Wang	
FON-019-I	Current Status of Research and Applications of Carbon Nanomaterial	39
	Bui Hung Thang, Tran Van Hau, Nguyen Trong Tam, To Anh Duc, Mai Thi Phuong, Pham Van Trinh, Nguyen Van Chuc, Cao Thi Thanh, Nguyen Huu Hong, Nguyen Tuan Hong, Phan Ngoc Hong, Phan Hong Khoi and <u>Phan Ngoc Minh</u>	

NANOFABRICATION TECHNIQUES (NFT)

NFT-002-I	Road to the Development of Mechanical Sensors using Piezoresistive Effect	41
	<u>Susumu Sugiyama</u>	

NFT-003-I	Fabrication of Mn-(Bi,Ga) based Hard Magnetic Nanocomposites	47
	<u>Huy Dan Nguyen</u> , Jung-Goo Lee, Thi Thanh Pham, Mau Lam Nguyen, Huy Ngoc Nguyen, Thi Kim Oanh Dinh, Hai Yen Nguyen and Dang Thanh Tran	
NFT-004-I	Plasmonic Interconnects for Global Wires in Integrated Circuits	55
	<u>Chua SJ</u> , Liu Yan, Lu Ding, Aaron Thean, Ting Mei and Christian A. Nijhuis	
NFT-005-I	One-Photon Absorption based Direct Laser Writing for fabrication of Multi-Dimensional Photonic and Plasmonic Nanostructures	59
	Thi Huong Au, Mai Trang Do, Qinggele Li, Mai Hoang Luong, Fei Mao, Dam Thuy Trang Nguyen, Amber Perry, Thi Nhung Pham, Quang Cong Tong and <u>Ngoc Diep Lai</u>	
NFT-006-I	Solar-driven Cu-based Photocatalysts	63
	Le Van Hoang, Thu Loan Nguyen, Thi Dieu Thuy Ung, Tran Dinh Phong, <u>Nguyen Quang Liem</u>	
NFT-007-I	Sputtering of Two Dimensional Metal Sulphide Films	65
	<u>Tomas Nyberg</u>	
NFT-008-I	Chemical Functionalization of Carbon Nanotubes using DNA Binding Peptides	69
	<u>Jung Heon Lee</u>	
NFT-010-I	The Reactive Nano Silicate (RNS) as a Precursor for Reinforcement of Rubber using Reactive Graphene	71
	<u>Khe. NC</u> , Linh V. H	
<i>NANOMATERIALS AND NANODEVICES (NMD)</i>		
NMD-001-I	Development of New Biodegradable Alloys for Medical Purposes	77
	Zuzana Molčanová, Beata Balloková, Juraj Ďurišin, Slávka Martinková, Dagmara Varcholová , Štefan Michalik, Robert Tang-Kong, Logan Ward, Apurva Mehta, Katarína Šuľová, Michaela Šulíková, Miloš Fejerečák, Andrea Lachová , Róbert Džunda and <u>Karel Saks</u>	
NMD-002-I	Development of Nanomaterials-Based Chemiresistive Gas Sensors for Detection of Hazardous Gases	83
	Hyoun Woo Kim and <u>Sang Sub Kim</u>	
NMD-003-I	MEMS-Approaches for Controlling Infrared Thermal Energy in Light Source and Detector	85
	<u>Minoru Sasaki</u>	
NMD-004-I	Low-Dimensional (0D, 1D, 2D) Devices for Future Electronics	89
	<u>Shunri Oda</u> , Takamasa Kawanago and Hitoshi Wakabayashi	
NMD-005-I	Quai-2 Dimension Optoelectronic Devices	95
	<u>Sunkook Kim</u>	
NMD-006-I	Fine Chemical Composition Analysis of Silicon Particles for Soft Circular Recycling in PV Solar Cells	97
	V. Brizé, A. Benayad, H. Hajjaji, F. Coustier, M. Benmansour, <u>Amal Chabli</u>	

NMD-007-I	Synthesis and Optical Properties of Rare-Earth Doped Persistent Nanophosphors	99
	Zhengfa Dai, Vitalli Boiko and <u>Dariusz Hreniak</u>	
NMD-008-I	Supported Lipid Monolayers as Innovative Sensing and Selective Layers for Sensors	101
	V. Kilinc, T. Nguy, A. Kenaan, S. Lamant, C. Henry-de-Villeneuve, G. Monier, M. Petit, Y. Wakayama, A. Charrier, <u>J. M. Raimundo</u>	
NMD-009-I	Changes in the Conventional and Persistent Luminescence Induced by Sintering Pressure in Garnet and Aluminate Ceramics	103
	<u>Paweł Głuchowski</u> , Mika Lastusaari, Adrian Patej, Kamila Rajfur, Simona Veltri, Robert Tomala, Wiesław Stręk	
NMD-010-I	Structured-Catalyst Material for Direct Conversion of Biofuel to Power	107
	Phuc Hoan Tu, Diep Ngoc Le, Tin Chanh Duc Doan, Mau Chien Dang and <u>Yusuke Shiratori</u>	
NMD-011-I	Application of Surface and Interface Characterization of Materials in Back-End-Of-Line Interconnect	113
	<u>Quoc Toan Le</u> , E. Kesters, E. Altamirano Sanchez, and F. Holsteyns	
NMD-012-I	Multifunctional Magnetic Nanoparticles and Applications in Biomedicine	115
	Nguyen Hoang Nam and <u>Nguyen Hoang Luong</u>	
NMD-013-I	Thermoelectric Properties of Lead Halide Perovskites Single Crystals	123
	Thi-Mai Huong Duong, Ryo Saeki, Kotaro Matsuyama, Satria Rusdiputra and <u>Hirokazu Tada</u>	
NMD-014-I	Upconversion Nanoparticles Linked Gold Nanorod Theranostic Nanocomposites for Oral Cancer Cells	125
	Duc Tu Vu, Quoc Minh Le, Churng-Ren Chris Wang, Lai-Kwan Chau, Tzyy-Schiuan Yang, Michael W.Y. Chan, Cheng-I Lee, Chu-Chi Ting, Jiunn-Yuan Lin, Hung-Chih Kan, and <u>Chia-Chen Hsu</u>	
NMD-015-I	Silver Nanowires for Flexible Electronics	127
	<u>Byungkwon Lim</u>	
NMD-016-I	Single Molecular Transistor Based on Nanogap Electrodes	129
	Yutaka Majima and <u>Phan Trong Tue</u>	
NMD-017-I	From Micro to Quantum Electronics	133
	<u>Christophe Wyon</u>	
NMD-020-I	Wafer Scale Fabrication and Modification of Silicon Nano-Pillar Arrays for Nanoelectronics, Nanofluidics and Beyond	135
	Yasser Pordeli, Bernhard van der Wel, Lucas Kooijman, Dirk Jonker, Erwin Berenschot, Bjorn Borgelink, Hai Le The, Meint de Boer, Jan Eijkel, Ray Hueting, Roald Tiggelaar, Han Gardeniers, <u>Niels Tas</u>	
NMD-021-I	Low-Cost Printable TFT-Driven PZT Actuator Array Towards Single-Cell Analysis	141
	<u>Phan Trong Tue</u> , Tatsuya Shimoda and Yuzuru Takamura	

NMD-023-I	Stable Viscous Liquid Threads Inside Microchannels	145
	<u>Cees J.M. van Rijn</u>	

**APPLICATION OF MICRO-NANOTECHNOLOGY
(AMN)**

AMN-002-I	The use of High Viscous Ink for Fine Inkjet Printing and the Printed Electronics Applications	147
	<u>Kye-Si Kwon</u> , Seong-jun Kim, Md. Khalilur Rahman and Phung Thanh Huy	
AMN-003-I	Peptide Arrays and Easy-To-Operate Optical Sensor for Wide Spectrum Sensing of Pathogenic Bacteria	153
	Éric Pardoux, Agnès Roux, Raphaël Mathey, Didier Boturyn, <u>Yoann Roupioz</u>	
AMN-004-I	Bioactive Nanoglasses and Graphene-Based Nanocomposites for Medical Applications	155
	<u>Anna Lukowiak</u> , Yuriy Gerasymchuk, Leili Tahershamsi, Katarzyna Halubek-Gluchowska, Anna Wedzynska, Wieslaw Strek, Dominika Piatek, Anna Kedziora, Gabriela Bugla-Ploskonska, Beata Borak, Justyna Krzak	
AMN-005-I	3D Hierarchical Nanostructures to Elaborate Supercapacitors for Electrochemical Energy Storage	159
	<u>G. Bidan</u> , D. Aradilla and S. Sadki	
AMN-006-I	Enhancing Luminescence Intensity of Nanostructured Phosphor Containing Rare Earth Elements	161
	<u>Le Quoc Minh</u>	
AMN-007-I	Solar Energy: From Materials to Applications Situation in the World, Vietnam & Binh Thuan: Challenges and Solutions	163
	<u>Tran Quoc Tuan</u>	
AMN-008-I	Laser Induced White Emission in Re Doped Nanocrystals	165
	<u>Wieslaw Strek</u> , Robert Tomala, Mariusz Stefanski, Paweł Gluchowski and Bartłomiej Cichy	
AMN-009-I	Micropatterning of Electret by Thermal Imprinting Method and Its Application to Electret Based Rotary Energy Harvester	171
	<u>Masato Suzuki</u> , Yuki Onishi, Tomokazu Takahashi and Seiji Aoyagi	
AMN-010-I	High Performance MEMS Sensors: Research and Applications	175
	<u>Dzung Dao</u> and Toan Dinh	
AMN-012-I	Vacuum-Sealed Resonant Microelectromechanical Resonant Sensors for Noninvasive Detection of Health	179
	<u>Takahito Ono</u>	
AMN-013-I	Photonics and MEMS Sensors for the Digital Olfaction	181
	<u>Thierry Livache</u> and Cyril Herrier	
AMN-014-I	Surfaces for Water Harvesting	
	Youngjin Kim, Céline Ternon, Michel Langlet and <u>David Riasset</u>	185

- AMN-016-I Lensfree Microscopy: a New Framework for the Imaging of Viruses, Bacteria, Cells and Tissue** 187
C.P. Allier, S. Vinjimore Kesavan, Y. Hennequin O. Cioni, F. Momey, T. Bordy, L. Hervé, J.-G. Coutard, S. Morel, A. Berdeu, F. Navarro, J.-M. Dinten, R. Campagnolo
- AMN-028-I Ferroelectric Perovskites: From Inorganic to Hybrid Materials** 193
Pham Duc Thang and Nguyen Huy Tiep
- AMN-031-I High Energy Storage Density of Antiferroelectric PbZrO₃ Thin-Film Capacitors fabricated by Sol-Gel Process** 195
Trang T. Trinh, Ha T. Dang, Chi T.Q. Nguyen, Thanh N. Nguyen, Minh D. Nguyen and Hung N. Vu

ORAL SESSIONS

FUNDAMENTALS OF NANOTECHNOLOGY (FON)

- FON-008-O Design and Simulation of Polymeric Microfluidic Cantilever-Based Biosensor with Integrated Piezo-Resistor** 201
Le Van Tam and Mai Anh Tuan
- FON-010-O Nano-Bio-Lipid Bilayers as Variable Capacitors Resonate with Helical Myelin Proteins: a Nano Approach** 205
Majid Monajjemi, Azadeh Shekarabi, Maryam Otadi, Azam Ghadami, Afshar Alihosseini, Thu Thi Pham, Fatemeh Mollaamin
- FON-011-O Impacts of Copper-Containing Precursors used in Thermal Shock Method on the Photocatalytic Activity of Cu-Modified ZnO Nanoparticles** 211
The Luan Nguyen, Tien Khoa Le, Torben Lund, Huu Khanh Hung Nguyen and Thi Kieu Xuan Huynh
- FON-018-O Study on Simulation of Silicon Piezoresistive Strain Sensor Sensitive to Uniaxial Strain** 215
Nguyen Chi Cuong, Lam Minh Thinh, Trinh Xuan Thang, Le Quoc Cuong, Ngo Vo Ke Thanh, Maxime Projetti and Susumu Sugiyama

NANOFABRICATION TECHNIQUES (NFT)

- NFT-012-O Study on the Preparation of Selenium Nanoparticles by Gamma Co-60 Method and Investigate the Stability** 219
Ngoc Duy Nguyen, Van Phu Dang, Anh Quoc Le, T. Kim Lan Nguyen, Quoc Hien Nguyen and T. Thu Ngan Tran
- NFT-013-O One-Step Synthesis of Gold Nanostar by using Chitosan as Protecting Agent** 223
Quoc Khuong Vo, Quynh Nhu Vo Nguyen and Phuong Phong Nguyen

- NFT-014-O Optimized - Polymer - Coated Magnetic Nanoparticles Preparation for use as an Enhanced Oil Recovery Agent** 227
Thi-Lieu Nguyen, Duy-Khanh Pham, Xuan-Truong Mai, Anh-Quan Hoang and Phuong-Tung Nguyen
- NFT-015-O Phosmet Pesticide Detection using 2d-Arrays of Au Nanoparticles** 237
Do Nhu Quynh, Tran Duc Tien, Lo Van Giap, Do Danh Bich Do, Ung Thi Dieu Thuy and Nguyen Quang Liem
- NFT-017-O Gold Nanoparticle Synthesis by AC Glow Discharge on Liquid and the Effect of pH value in the Size of Synthesized Nanoparticle** 241
Phuoc Van Thai, Shinnosuke Abe, Kenichiro Kosugi, Nobuo Saito, Kazumasa Takahashi, Toru Sasaki and Takashi Kikuchi
- NFT-018-O Synthesis of Cu₂O Nano/Diatomite using Hydrazine as Reducing Agent and Its Antibacterial Activity** 245
T. Thuy Nhung Dang, T. Ai Trinh Nguyen, T. Thu Huyen Pham, Dinh Tuan Phan, Ngoc Duy Nguyen, Van Phu Dang, Quoc Hien Nguyen

NANOMATERIALS AND NANODEVICES (NMD)

- NMD-018-O AlGa_N/Ga_N Two-Dimensional Electron Gas for Sensing Applications** 249
Hong-Quan Nguyen, Toan Dinh, H. Amini Moghadam, Hoang-Phuong Phan, Tuan-Khoa Nguyen, Jisheng Han, Sima Dimitrijevic, Nam-Trung Nguyen and Dzung Viet Dao
- NMD-025-O Effect of TiO₂ Morphology on its Performance in the Photocatalytic Degradation of Cinnamic Acid Solution** 253
Dien Trung Nguyen, Cam Anh Ha, Tri Nguyen, Tien Cuong Hoang, Thuc Nhi Thi Vo and Cam Loc Luu
- NMD-026-O The Effect of Electron Density Fluctuation on the Microstructures of Polymer Electrolyte Membranes for Fuel Cell Application** 257
La Ly Nguyen, Lam Hoang Hao, Le Viet Hai, Nguyen Tien Cuong, Huynh Truc Phuong and Tran Duy Tap
- NMD-027-O Effect of Calcination Temperature on Optical Properties of Gd₃PO₇:Eu³⁺ Nanophosphors Synthesized by Combustion Method** 261
Khac Khong Minh Ngo, Thi Kieu Giang Lam, Manh Tien Dinh, Thi Khuyen Hoang, Van Do Phan, Dariusz Hreniak, Mariusz Stefanski, Karina Grzeszkiewicz and Vu Nguyen
- NMD-029-O High Performance Core/Shell Multi-Colour and Multifunctional Colloidal Quantum Dots for Advanced Hybrid Nanosystems** 269
Tien Hoa Nguyen, A. Broussier, S. Jradi, R. Bachelot and Xuan Quyen Dinh
- NMD-030-O Development of Aluminum-Based Metal-Organic Frameworks for Water Adsorption** 273
Thuy Thi Dieu Ung, Loan Thu Nguyen and Liem Quang Nguyen
- NMD-031-O Photocatalytic Properties of Nanostructure and Nanocomposites Based on Anatase TiO₂ Synthesized by Themolysis** 277
Duong Ngoc Huyen, Mai Van Tuan and Mai Xuan Dung

NMD-040-O	Morphology and Optical Properties of CePO₄:Tb³⁺ Hollow Spheres	281
	<u>Chinh Dung Trinh</u> , <u>Phuong Hau Thi Pham</u> , <u>Dung My Thi Dang</u> and <u>Chien Mau Dang</u>	
NMD-054-O	Fabrication of Graphene by Thermal Reduction-Exfoliation of Graphite Oxide	287
	<u>Danh Phuong Bui</u> , <u>Duong Thuy Vo</u> , <u>Diep Ngoc Le</u> , <u>Oanh Kim Thi Nguyen</u> , <u>Dung Trung Dao</u> and <u>Chien Mau Dang</u>	
NMD-056-O	The Synthesis and Electrochemical Behavior of Pt_xSn_y Nanoparticles	291
	<u>Do Thi Dieu Ai</u> , <u>Le My Loan Phung</u> , <u>Vu Thi Hong Phuong</u> , <u>Tran Van Man</u>	
NMD-068-O	Comparison of Structural and Morphology Properties of Multiferroic Materials Synthesized by Various Methods	295
	<u>Robert Tomala</u> , <u>Pawel Gluchowski</u> , <u>Anna Lukowiak</u> , <u>Yuriy Gerasymchuk</u> , <u>Tatsiana Shulha</u> , <u>Maria Serdechnova</u> , <u>Mikhail Zhedkevich</u> and <u>Wieslaw Strek</u>	
NMD-069-O	Microfluidic Paper-Based Devices for Detecting Human Chorionic Gonadotropin	299
	<u>Ngan Nguyen Le</u> , <u>Hue Cam Thi Phan</u> , <u>Huong Kim Tran</u> , <u>Dung My Thi Dang</u> and <u>Chien Mau Dang</u>	

APPLICATION OF MICRO-NANOTECHNOLOGY (AMN)

AMN-019-O	Development of Flood Monitoring System in Ho Chi Minh City using Piezoresistive Pressure Sensor Fabricated by SHTP Labs	303
	<u>Xuan Thang Trinh</u> , <u>Nguyen Tuan Khoa</u> , <u>Tran Duy Hoai</u> , <u>Nguyen Thanh Phuong</u> , <u>Vu Le Thanh Long</u> , <u>Truong Huu Ly</u> , <u>Nguyen Chi Cuong</u> , <u>Hoang Ba Cuong</u> , <u>Ngo Vo Ke Thanh</u> , <u>Le Quoc Cuong</u> and <u>Susumu Sugiyama</u>	
AMN-020-O	Preparation and Cell Labeling Evaluation of Antibody conjugated CdSe/MSA Quantum Dots	307
	<u>Khanh Thien Le</u> , <u>Hong Diep Thi Tran</u> , <u>Ngoc Thuy Thi Vo</u> and <u>Hieu Tran Van</u>	
AMN-023-O	Towards Highly-Sensitive Massively-Parallel Temperature Sensing with Printed PTC Elements	311
	<u>Philipp Rinklin</u> , <u>Nouran Adly</u> , <u>Leroy Grob</u> , <u>Korkut Terkan</u> , <u>Lennart Weiss</u> , <u>Sabine Zips</u> and <u>Bernhard Wolfrum</u>	
AMN-024-O	A Study on Electrical Parameters of Interdigitated Array Electrodes (Ideas) Sensor for Concentration Measurement of Phosphate-Buffered Saline	315
	<u>Tuan Vu Quoc</u> , <u>Tung Bui Thanh</u> and <u>Trinh Chu Duc</u>	
AMN-026-O	The Hepatoprotective Effects Activity in Mice of Gold Nanoparticles/B-Glucan Prepared by Gamma Co-60 Irradiation	319
	<u>Nguyen Trong Nghia</u> , <u>Do Thi Phuong Linh</u> , <u>Nguyen Thanh Vu</u> , <u>Nguyen Thi Ngoc Anh</u> , <u>Nguyen Hong Thoai Vy</u> , <u>Le Quang Luan</u>	

- AMN-027-O** **Application of AgNPs/PVA Prepared by Gamma Rays Irradiation for Increasing Survival Rate of Tra Catfish Inoculated with Edwardsiella ictaluri** 323
Le Quang Luan, Lam Vy Nguyen Hang Khanh Linh and Duong Hoa Xo
- AMN-030-O** **Development of a Flow Focusing Droplet Generation Microfluidic System Based on Rapid Prototyping Technique** 327
Loc Do Quang, Tuan Vu Quoc, Cuong Nguyen Nhu, Hang Nguyen Thu, Hang Tran Thanh, Tung Thanh Bui and Trinh Chu Duc

POSTER SESSION

FUNDAMENTALS OF NANOTECHNOLOGY (FON)

- FON-012-P** **Evolution of Hexagonal Boron Nitride Nanoribbon using Molecular Dynamic Simulation: Free-Standing Model and Hybrid Graphene/Hexagonal Boron Nitride Model** 331
Nguyen Thi Thuy Hang
- FON-013-P** **Size Effects on Melting Process of 2D Glassy Monatomic Solids** 335
Duong Thi Nhu Tranh, Le Nguyen Tue Minh, Vo Van Hoang

NANOFABRICATION TECHNIQUES (NFT)

- NFT-020-P** **Synthesis of Two-Dimensional MoS₂ Crystals by a Two-Steps Chemical Vapor Deposition Process** 339
Dao Xuan Duong, Tran D. Phong and Nguyen Tran Thuat
- NFT-021-P** **La_{1-x}Sr_xMnO₃ Nanoparticles: Synthesized by Ultrasound Wave and High Annealing Temperature** 345
Phan Van Cuong and Nguyen Quang Trung
- NFT-022-P** **A Novel Cathodic Composite in Lithium Ion Battery (LIBTs) Based on LiNi_{0.7}Co_{0.3}O₂, Li₂MnO₃, and LiCoO₂ Combination: Synthesis and Characterization** 349
Thu Thi Pham, Majid Monajjemi, Fatemeh Mollaamin, Azam Ghadami and Chien Mau Dang
- NFT-023-P** **A Straightforward Route to Nano Gold From Gold Metal and Molecular Chlorine for Biomedical Applications** 355
Xuan-Truong Mai, Hong-Nhung Nguyen T., Anh-Quan Hoang and Phuong-Tung Nguyen
- NFT-024-P** **Fabrication of Gold Nanostructures on Copper Foil for use as SERS Substrates** 359
Cao Tuan Anh, Luong Truc Quynh Ngan, Dao Tran Cao and Kieu Ngoc Minh and Nguyen Anh Vu

- NFT-025-P** **Facile Fabrication of Gold Nanoparticles by Sputtering Methods** 363
Thi Ha Tran, Thi Huyen Trang Nguyen, Thanh Cong Bach, Nguyen Hai Pham, Cong Doanh Sai, Quang Hoa Nguyen, Trong Tam Nguyen, Khac Hieu Ho and Viet Tuyen Nguyen

NANOMATERIALS AND NANODEVICES (NMD)

- NMD-019-P** **Temperature Dependent Properties of L1₀ FePd Magnetic Nanoparticles** 367
Nguyen Hoang Nam, Truong Thanh Trung, Tran Thi Hong, Luu Manh Kien, Nguyen Hoang Luong
- NMD-022-P** **Synthesis and Adsorption Properties of Odered Mesoporous Carbon Material using MCF Silica as Hard Template** 371
Hoa T.H.Nguyen, Hy G. Le and Phuong T.Dang
- NMD-028-P** **Effect of Additional Nanoparticles on Magnetic Properties of Sintered Nd-Fe-B Magnets** 375
Huy Dan Nguyen, Thi Thanh Pham, Van Duong Nguyen, Huy Ngoc Nguyen, Thi Kim Oanh Dinh, Hai Yen Nguyen, Dang Thanh Tran
- NMD-032-P** **Simple Design of Co-Polarization Broadband Metamaterial Absorber for C-Band Appications** 381
Tran Sy Tuan, Nguyen Thi Kim Thu, Nguyen Thi Minh, Lam Quang Hieu, Nguyen Hong Quang, Duong Ngoc Huyen, Hugo Nguyen, Nguyen T. Q. Hoa
- NMD-033-P** **Numerical Study of an Efficient Broadband Metamaterial Absorber in Visible Light Region** 385
Tran Sy Tuan, Nguyen Thi Kim Thu, Nguyen Thi Minh, Lam Quang Hieu, Nguyen Hong Quang, Duong Ngoc Huyen, Hugo Nguyen, Nguyen T. Q. Hoa
- NMD-034-P** **Effect of Support on Performance of Ni-Based Nanocatalysts and Kinetics of Methane Dry Reforming** 389
Phan Hong Phuong, Luu Cam Loc, Nguyen Tri, Nguyen Xuan Linh, Pham Minh Tai, Nguyen Phung Anh, Nguyen Thi Thuy Van
- NMD-035-P** **Study and Synthesis of Fe₃O₄@Poly(Glycidyl Methacrylate) Nanocomposite Materials Applied for Removal of Pb (II) Ions From Aqueous Systems** 395
NT Hoang, DLM Phuong, NLH Phuong, LH Phuc, LK Vinh, NQ Hien, NM Tuan
- NMD-037-P** **Synthesis of Various Functional Luminescent Nanoparticles Based on Zinc** 399
Thanh Thao Bui, Van Khiem Nguyen, Duy Khanh Pham, Ngoc Tinh Cao, Thanh Mien Nguyen, Jin-Woo Oh, Bich Thi Luong
- NMD-038-P** **The Effect of Different Concentrations of Nitric Acid Solution on the Characteristics of MWCNTs Functionalized by a Mixture of HNO₃/ H₂SO₄** 405
Hoa Mai Thi Le, Dam Duy Le, Cuong Kim Thi Phu, Thu Thi Pham and Chien Mau Dang

NMD-041-P	Morphology and Optical Properties of CePO₄:Tb³⁺ Nanoparticles Fabricated by Chemical Method	409
	<u>Phuong Hau Thi Pham</u> , Chinh Dung Trinh, Dung My Thi Dang and Chien Mau Dang	
NMD-042-P	Ex-Situ and In-Situ Synthesis of Fe-Doped TiO₂ Nanorod Arrays with Enhanced Photoelectrochemical Activity	415
	Pham Thi Minh Huong, Ngo Thi Hien Thao, Nguyen Thi Minh Thuc, Nguyen Tan Lam and <u>Tran Nam Trung</u>	
NMD-043-P	Combustion Synthesis and Characterization of Eu³⁺-Doped GdVO₄ Nanoparticle Phosphors	419
	<u>Thai Thi Dieu Hien</u> , Pham Đức Roan, Ngo Khac Khong Minh and Nguyen Vu	
NMD-045-P	Structure and Magnetic Properties of Nd-Fe-B Based Nanocomposite Magnets Prepared by Spark Plasma Sintering	425
	<u>Duong Dinh Thang</u> , Pham Thi Thanh, Nguyen Mau Lam, Nguyen Hai Yen, Pham Van Hao, Nguyen Huy Ngoc, Tran Dang Thanh and Nguyen Huy Dan	
NMD-047-P	Carbon Support Magnetic Fe₃O₄, Fe₂MnO₄, Fe₂NiO₄ Nanoparticles as Fenton-Like Catalysts for Removal of Organic Pollutant (Methyl Orange) in Water	429
	Nguyen Thi Dung, <u>Tran Boi An</u> and Do Manh Huy	
NMD-048-P	Preparation of Nanocomposite PaNi@GO-HT via Directly Polymerization From Aniline	435
	<u>Boi An Tran</u> , Thanh Thao Phan and Xuan Hang To Thi	
NMD-049-P	First-Principle Study of the Adsorbed Hydrogen on the Two-Dimensional Confined Germanene	441
	<u>Tran Thi Thu Hanh</u> , Nguyen Minh Phi, Nguyen Van Hoa, Nguyen Hoang Giang, Nguyen Ngoc Thien and Dong Cao Hieu	
NMD-050-P	The Interaction of Hydrogen Atoms on the Missing Row Pt(110)-(1X2) Surface	445
	<u>Tran Thi Thu Hanh</u> , Nguyen Van Hoa, Nguyen Minh Phi	
NMD-057-P	Investigation of Nano-Structure of Olivine LiMn_xFe_{1-x}PO₄ by Rietveld Refinement	449
	<u>Le Thanh Nguyen Huynh</u> , Viet Dung Trinh and Van Man Tran	
NMD-059-P	Hierarchical Structures in Graft-Type Polymer Electrolyte Membranes for Fuel Cell Vehicles using Ultra Small Angle X-Ray Scattering Method	453
	Tran Duy Tap, <u>La Ly Nguyen</u> , Nguyen Nhat Kim Ngan, Tran Thanh Danh, Tran Mai Kieu, Dang Van Hoa, Lam Hoang Hao, Huynh Truc Phuong, Le Quang Luan, Tran Thanh Hien, Hoang Thi Lan, Tran Hoang Long, Nguyen Thi Hoai My and Phan Thi Quynh Nga	
NMD-061-P	Study on the Electrochemical Properties of Gelled Electrolytes using Nano Fumed Silica in the Presence of Some Other Organics Additives	457
	<u>Thi Binh Phan</u> , Thi Van Anh Nguyen, Thi Thanh Thuy Mai and Thi Xuan Mai	

- NMD-062-P Sensitive Electrochemical Measurement of as (III) using Nafion Modified Platinum Electrode via Anode Stripping Voltammetry** 461
Tung Son Vinh Nguyen, Tien Minh Huynh, Linh Duy Nguyen, Tin Chanh Duc Doan, Chien Mau Dang
- NMD-066-P Preparation of Silver Nanoparticles Ink for Inkjet Printing Technology** 467
Huong Kim Tran, Ngan Nguyen Le, Dung My Thi Dang and Chien Mau Dang
- NMD-070-P Fabrication of Graphene Thin Films on Flat Substrate by Spin-Coating Method Combined with Corona Plasma Treatment** 471
Tien Minh Huynh, Tung T. V. Nguyen, Chien Mau Dang, Tung Thanh Bui
- NMD-071-P Surface Characterization of Corona Plasma-Treated Silicon Surface with Deposited Reduced Graphene Oxide Sheets for Solar Cell Applications** 475
Tung Thanh Bui, Tien Minh Huynh, Tung T. V. Nguyen and Chien Mau Dang
- NMD-072-P Silver Nanoparticles-Assembled Graphene Oxide Sheets on TiO₂ Nanotubes: Synthesis, Characterization and Photocatalytic Activity Investigation** 481
Loan Thuy Thi Pham, Khang Duy Vu Nguyen, Anh Phuong Thi Nguyen and Khoa Dang Nguyen Vo

APPLICATION OF MICRO-NANOTECHNOLOGY (AMN)

- AMN-032-P Solvothermal Synthesis of Undoped and Ni-Doped FeS₂ Nanoparticles and Its Composite with Reduced Graphene Oxide for Photocatalysis Application** 487
Ho Dinh Quang, Phan Thi Hong Tuyet, Nguyen Hong Quang, Lam Quang Hieu, Duong Ngoc Huyen, and Nguyen Thi Quynh Hoa
- AMN-033-P Enhancing Bioavailability of Silymarin using Redox Nanoparticle for the Treatment of Inflammation** 491
Nguyen Thi Thu Ha, Tran Ngoc Han, Mai Huu Phuong, Trinh Nhu Thuy, Vong Binh Long, Nagasaki Yukio
- AMN-035-P Fabrication of Paper-Based Microchannel by Electrohydrodynamic Inkjet Printing of Ethylene Glycol Solvent-Based Ink** 495
Ngan Nguyen Le, Hue Cam Thi Phan, Huong Kim Tran, Dung My Thi Dang and Chien Mau Dang
- AMN-038-P Study on the Antifungal Efficiency Against *Rhizoctonia solani* Cause Collar Root Rot Disease on *Brassica integrifolia* of LDH Nanoparticles Immobilized Organic Salicylate** 499
Nguyen Xuan Tuan, Tran Duc Trong, Tran Le Truc Ha, Duong Hoa Xo, Le Quang Luan
- AMN-040-P High Effective Adsorption of Uranium From Aqueous Solution by Reduced Graphene Oxide - Zinc/Nickel Ferrite - Porous Polyaniline Nanocomposite** 505
Tran Quang Dat, Nguyen Vu Tung, Nguyen Tran Ha and Pham Van Thi

- AMN-042-P Antifungal Activity of Silver Nanoparticles Against *Neoscytalidium dimidiatum* Causes Black Rot on Dragon Fruit Tree *Hylocereus undatus*** 513
Anh Van Thi Le, Dung My Thi Dang and Chien Mau Dang
- AMN-044-P Surface Enhance Raman Scattering of Methylene Blue Adsorbed on Gold Nanoparticles** 517
Thi Ha Tran, Thi Huyen Trang Nguyen, Thanh Cong Bach, Nguyen Hai Pham, Cong Doanh Sai, Quang Hoa Nguyen, Trong Tam Nguyen, Khac Hieu Ho and Viet Tuyen Nguyen
- AMN-045-P High Packaging Efficiency and Color Performance of White LEDs by Hemisphere Dome of Yellow Phosphor Packaging** 521
Quang-Khoi Nguyen, Shih-Kang Lin, Mai Van Tan, Vu Thi Ngoc Nuong, Vo Tran Khoa Nguyen, Trinh Thi Ngoc Huyen, Ton Nu Quynh Trang, Nguyen Van Hieu, Lam Quang Vinh, Vu Thi Hanh Thu, and Ching-Cherng Sun
- AMN-046-P Reducing the Influence of Backward Scattering in White LEDs Packaging with using Remote Yellow Phosphor Structure** 525
Quang-Khoi Nguyen, Shih-Kang Lin, Mai Van Tan, Vu Thi Ngoc Nuong, Vo Tran Khoa Nguyen, Trinh Thi Ngoc Huyen, Ton Nu Quynh Trang, Nguyen Van Hieu, Lam Quang Vinh, Vu Thi Hanh Thu and Ching-Cherng Sun
- AMN-047-P Effects of Silver Nanoparticles to the Growth of White Leg Shrimp (*Litopenaeus Vannamei*)** 529
Thanh Chi Nguyen, Thinh Huu Nguyen, Phuong Hong Lam, Mai Thi Le, Dung My Thi Dang Tin Chanh Duc Doan, and Chien Mau Dang
- AMN-048-P Efficient Antitumor Effect of Sorafenib-Loaded Silica Containing Redox Nanoparticle** 533
Tran Ngoc Han, Nguyen Trinh Quynh Nhu, Vong Binh Long, Nagasaki Yukio
- AMN-049-P Nickel Nanoparticles Loaded on Ceria Oxide Spheres as Catalyst for Dry Reforming of Methane** 537
Diep Ngoc Le, Phuc Hoan Tu, Dung Trung Dao Tin Chanh Duc Doan, and Chien Mau Dang

INVITED TALKS

OPENING PLENARY SESSION
(OPS)

NEW INITIATIVES FOR FOSTERING OPEN INNOVATION CAMPUS

Jean-Charles Guibert

CEA, MINATEC, 17 Avenue des Martyrs, 38054 Grenoble, France

Email: jcguibert@cea.fr

ABSTRACT

Research activities are covered both by public institutions, including universities and by industrial teams and a closer collaboration between both have to be developed. Different issues have to be overcome, including not invented here problem, multiple geographical sites, difference of salary, stress related management, long term vision vs. shorter term one,...

In order to facilitate these interactions, and to progress within an open innovation scheme, a common implantation on one unique site is a solution which was implanted in Grenoble / France on MINATEC innovation campus.

Different countries generated similar initiatives and we will present three projects in Asia, mainly in China (Zhangjiang Lab in Shanghai and Huairou science city in Beijing) and Thailand (Eastern Economic Corridor for Innovation).

Keywords: innovation, technology transfer



BIOGRAPHY

Jean-Charles Guibert

CEA

Senior advisor to the CEO for innovation,

Chairman of MINATEC®

Jean-Charles Guibert graduated in 1981 from Languedoc University “Institut des Sciences de l’Ingénieur de Montpellier” in Materials science and then in 1983 from Strasbourg University “Ecole d’Application des Hauts Polymères” in Polymer science.

In the 80’s and 90’s, Jean-Charles Guibert was actively involved in managing the development of lithographic activities and microelectronics program at CEA-Leti, the Europe’s largest microelectronics research center.

In 2000, as deputy manager of CEA-Leti in charge of strategic marketing and international partnership development, he took an active role in the development of the MINATEC, one of the largest world-wide innovation campus in Micro-Nano-Bio Technologies.

In October 2004, Jean-Charles Guibert was appointed Director for the Technology Transfer activities of CEA, a leading Research Technological Organisation in Europe (15.000 staff, 3.3 B€ annual budget), ranked as N°1 RTO worldwide from Thomson Reuters. This responsibility until 2016 covered different activities, ie strategic marketing, contracts, intellectual property and start-up creation. From January 2017, Jean-Charles Guibert is senior advisor to the CEO of CEA for innovation at international.

In addition, Jean-Charles Guibert was elected as Chairman of MINATEC in June 2008 by the steering committee. His on-going mission is to foster cross-exchanges between the different institutions within Minatec and to develop an international vision and recognition.

Jean-Charles Guibert is an expert for the European commission and multiple national authorities for innovation activities in the field of new technologies. He is a permanent member of the commission in charge to evaluate French innovation policies.

He is also at the board of different companies and non-profit organisations related to technology transfer activities.

Jean-Charles Guibert is Doctor Honoris Causa of INRS - Université of Quebec / Canada.

ORIGAMI FABRICATION USING SINGLE LAYER PHOTOLITHOGRAPHY AND CAPILLARY FOLDING

Derosh George ¹, Edwin A. Peraza Hernandez ¹ and Marc J. Madou ¹

¹Mechanical and Aerospace Engineering, University of California, Irvine, Irvine, CA, 92697-3975
Email: mmadou@uci.edu

ABSTRACT

Polymer and carbon origami structures are fabricated by first producing patterned sheets with less cross-linked compliant folds and more cross-linked stiff faces through differential UV exposure. The obtained patterned sheets are heated to further raise their compliance by increasing polymer chain mobility. These softened sheets with designated compliant fold regions are then folded to their target polyhedral shape using capillary forces induced by droplets placed on top of them. By cooling the three-dimensional shapes to room temperature and subsequently completing their cross-linking by an additional UV exposure step, the shape of the sheets is locked in the folded position. The obtained polymer origami structures are converted into isometrically shrunken carbon structures through pyrolysis. This capability of making three-dimensional carbon polyhedra could open new ways to fabricate complex structures of different material and surface properties through techniques such as electroplating and electroless deposition.

Keywords: Origami, three-dimensional carbon structures, elastocapillarity, cross-linking, photolithography

INTRODUCTION

Microparticles are used in multiple timely applications including drug delivery [1], bioimaging [2] and diagnostics [3]. Recent studies have quantified how the physical parameters of microparticles such as size, shape, strength, and deformability contribute to their functionality [2], [4]. Several naturally existing particles, such as living cells, possess shape-based advantage. For instance, the shape of viruses and bacteria aids them in preventing immune response on the host. Findings on the effect of shape on the properties/behavior of microparticles have led to more research on the subject. However, studies were majorly confined to the shapes that are derivative of spheres, since they are easy to fabricate using microfluidic techniques [5], [6]. A folding-based fabrication technique, origami, can overcome this limitation [7], [8].

Various conventional fabrication techniques are adopted to make origami shapes. Differential thermal expansion, melting of folding hinges, and application of pre-strain are some of the techniques that have been explored to fold patterned two-dimensional sheets into three-dimensional shapes [9]–[11]. However, these methods demand multilayer photolithography. Alternatively, an elastocapillary-based folding

using droplets can be used to make three-dimensional shapes by folding a single layer polymer material utilizing surface tension [12]. Although this method enables the use of a single layer polymer sheets for the fabrication of three-dimensional shapes, the folded particles return to their original flat configuration once the droplet evaporates. This reversibility is because the method often uses sheets made of elastomers. Also, for the fabrication of accurate three-dimensional shapes, folds and faces of the origami should have different properties, with folds being relatively soft, to get sharp bending at these locations; and faces should be stiff, to resist the bending. Attaining this contrast in material properties is challenging when a single material is used for elastocapillary-based folding. Moreover, elastocapillary-based folding generally is demonstrated on polydimethylsiloxane, which is challenging to be patterned into the desired two-dimensional sheets.

Here, we present an elastocapillary-based folding of photo-patternable materials to fabricate three-dimensional shapes using lithography involving only a single layer of polymer. The use of a photopolymer enables facile fabrication of two-dimensional unfolded shapes. It also allows for the patterning of faces

of the shapes with ease. Moreover, distinct material properties are introduced for folds (compliant) and faces (stiff) by controlling the level of cross-linking and the temperature of the sheets.

EXPERIMENTAL PROCEDURE

The planar sheets used for the fabrication of origami polyhedra are created using photolithography as illustrated in Fig. 1(a). A thin film of SU8-2050 (MicroChem) is spin-coated on a silicon wafer at 1500 rpm. Soft baking for 15 minutes at 85°C is performed to remove the solvent from the SU8 film. This soft baking duration and temperature are lower than the recommended values (20 minutes and 95°C), ensuring a weak adhesion between the SU8 film and the wafer, enabling the later release of the finalized patterned sheets from the wafer. After soft bake, a photo mask that completely exposes the origami sheets, including folds and faces (but not the holes patterned in the faces), is used to irradiate such regions for 40 seconds using a 2 mW/cm² UV light source (Fig. 1(a)). Following the first exposure, a mask that exposes only the face regions, but not the folds or the patterned holes in the faces, is aligned on top of the first mask to exclusively irradiate the faces for another 40 seconds. The maximum exposure duration (80 seconds) used here is less than the recommended

period (120 seconds) for the photolithography process. This reduced exposure duration allows for a straightforward release of the sheets from the wafer. The period of the post-exposure bake (PEB) is also reduced from 10 minutes (recommended period) to 5 minutes for the same reason. The sheets are released from the silicon substrate after the PEB by developing using acetone or SU8 developer. The released patterned sheets are later separated from the developer by carefully draining the developer, cleaning them with isopropyl alcohol (IPA), and then drying.

The patterned SU8 sheets are folded inside a silicone oil bath as shown in Fig. 1(b). A water droplet is placed on top of the sheet, and then the oil bath is heated up to 105°C, causing the sheets to become more compliant. These softened sheets are consequently folded by capillary forces induced by the droplet. The initial volume of the deposited droplets is at least 1.5 times larger than the volume of the target polyhedral shape to ensure that the droplets enter in contact with all the faces of the sheet during capillary folding. At this point, the polyhedral shape is partially open. Heating continues until the excess liquid is evaporated, forming a fully closed polyhedral structure. The silicone oil bath is then cooled to room temperature to lock the sheet in its folded polyhedral shape.

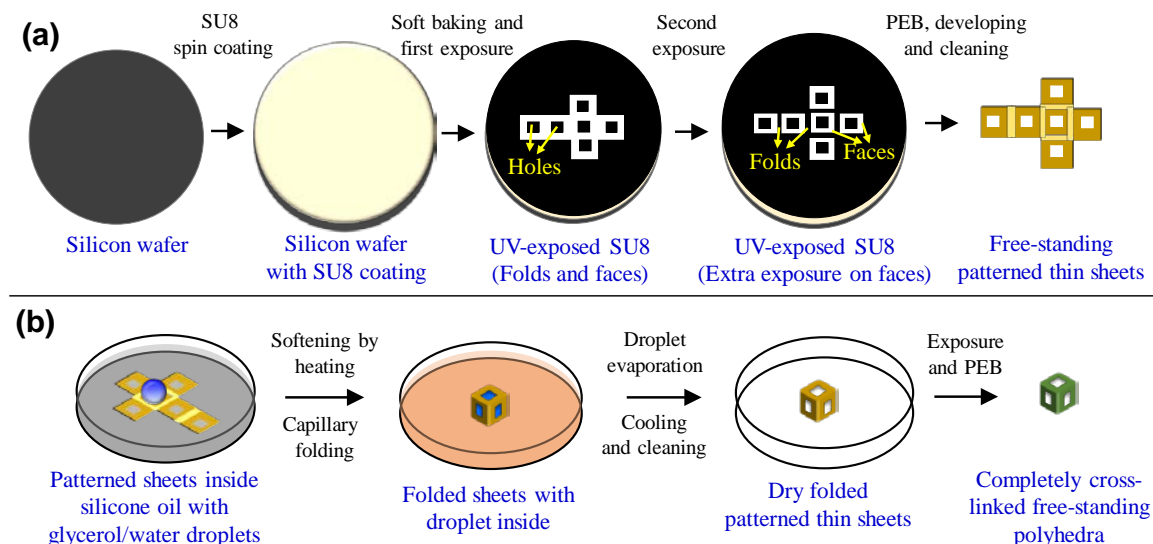


Figure 1 (a) Steps to fabricate patterned origami sheets with patterned holes at the faces using photolithography. (b) Capillary folding of the patterned sheets into three-dimensional shapes.

SU8 strips (2.5 mm × 25 mm × 0.053 mm) are characterized using dynamic mechanical analysis (DMA) to find the effect of exposure energy and

the temperature of the sheets on their elastic properties. A tensile preload of 0.001 N is applied to prevent compressive buckling of the

specimens. The characterization is performed by applying a sinusoidal force. The temperature of the specimen is changed from 40°C to 90°C at a temperature ramp of 3°C/min.

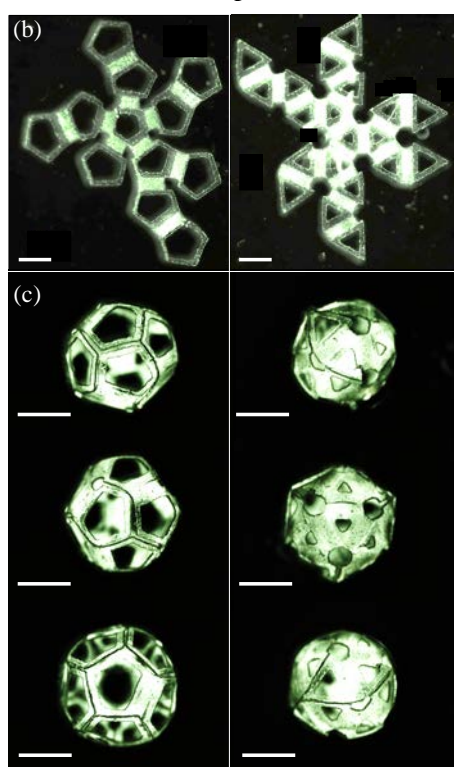
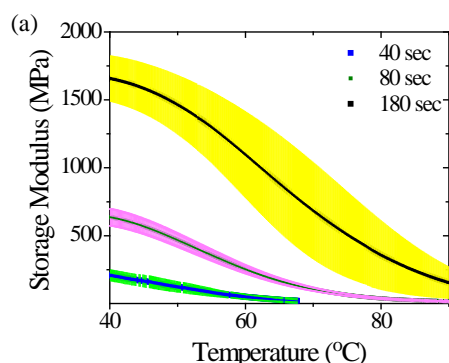


Figure 2 (a) Storage modulus vs. temperature for sheets made by exposing SU8 film for 40 sec, 80 sec, and 180 sec. (b) Unfolded sheets for dodecahedron and icosahedron with faces having patterned holes. (c) Folded dodecahedron and icosahedron from different views. The scale bar is 1.5 mm long.

RESULTS AND DISCUSSION

SU8, the photopolymer used in this study, undergoes cross-linking when it is irradiated with UV light. The level of cross-linking can be adjusted by controlling the exposure duration. Here, the faces of the target polyhedral shapes are exposed for a longer duration than the folds. The

difference in total exposure time leads to dissimilar levels of cross-linking at the folds and faces. Additionally, holes of different shapes can be patterned on the faces by not exposing selected regions within them (Fig 1(a)). When thermally treated, the SU8 sheets are softened, with the less-cross linked fold regions softening more than the more-cross linked face regions (Fig. 2(a)). The characterization study performed with dynamic mechanical analysis showed that the storage modulus (the dynamic modulus that represents the elastic behavior of the material) correlates directly with the exposure density (Fig. 2(a)). This correlation indicates a direct relationship between the exposure energy and the degree of crosslinking.

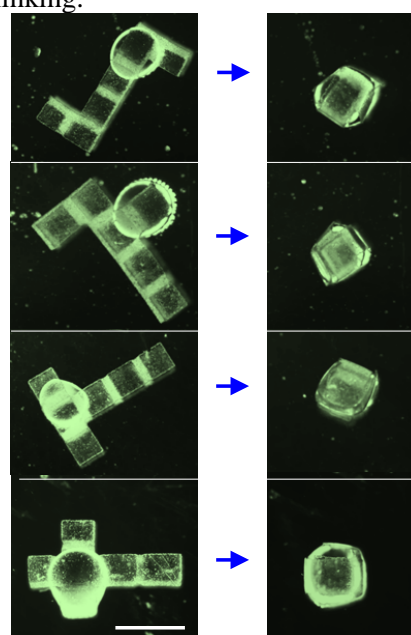


Figure 3 Folding of a cube from different unfolded configurations (nets). The scale bar is 2 mm long.

The compliant patterned sheet is folded when a liquid droplet is placed on it. This folding occurs by the minimization of the total energy of the droplet-sheet system. That is, the addition of the surface energy of the droplet and the elastic strain energy of the sheet. Depending on the original sheet pattern, different final polyhedral shapes can be achieved (Fig. 2(b) and (c)). The difference in the modulus along the platform ensures a folding response in good agreement with theoretical assumptions. Such assumptions require the folds to be highly flexible (less cross-linked) and the faces to be stiff (more cross-linked). The contrast in the material properties at the folds and the faces also enable the folding of the same final polyhedral shape from its multiple

unfolded configurations, as shown in Fig. 3. The shapes that are made of polymers with carbon-rich back bones can be converted to an isometrically shrunken carbon through pyrolysis, as shown in Fig. 4.

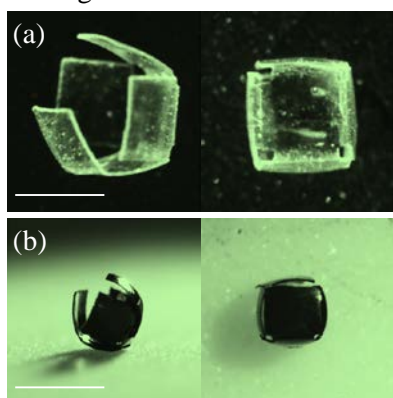


Figure 4 (a) Images of open and closed polymer cubes. (b) Images of the open and closed cubes of (a) converted into carbon. The scale bars are 1 mm long.

CONCLUSION

Fabrication of three-dimensional polymer and carbon shapes was achieved by adjusting the material properties of photopolymer films along their planform and utilizing the enhanced surface tension effect at small length scales. Complex geometries with patterned walls were fabricated by implementing capillary folding on a photopatternable material. Pyrolysis was used to make carbon structures from the folded patterned sheets. This fabrication method for carbon and polymer origami could potentially contribute to many fields, including drug delivery and biosensing.

Acknowledgment

This work was funded in part by the National Science Foundation (NSF) grant #1449397. The authors thank the UCI Laser Spectroscopy labs for access to their Raman spectroscopy equipment. DMA analysis was performed at the UC Irvine Materials Research Institute (IMRI). D.G. is partially funded by the Science and Engineering Research Board (SERB), India. E.P.H. acknowledges the start-up support from the Department of Mechanical and Aerospace Engineering at the University of California, Irvine.

References

- [1] D. C. Hyun, P. Lu, S. Il Choi, U. Jeong, and Y. Xia, *Microscale polymer bottles corked with a phase-change material for temperature-controlled release*, *Angew. Chemie - Int. Ed.* 52(2013), no. 40, pp. 10468–10471.
- [2] D. A. Canelas, K. P. Herlihy, and J. M. Desimone, *Top-down particle fabrication: control of size and shape for diagnostic imaging and drug delivery*, *Adv. Rev.*1(2009), pp. 391–404.
- [3] X. Xie *et al.*, *Microfluidic Fabrication of Colloidal Nanomaterials-Encapsulated Microcapsules for Biomolecular Sensing*, *Nano Lett.* 17(2017), no. 3, pp. 2015–2020.
- [4] J. A. Champion, Y. K. Katare, and S. Mitragotri, *Particle shape: A new design parameter for micro- and nanoscale drug delivery carriers*, *J. Control. Release* 121(2007), no. 1–2, pp. 3–9.
- [5] T. Nisisako, T. Ando, and T. Hatsuzawa, *Capillary-assisted fabrication of biconcave polymeric microlenses from microfluidic ternary emulsion droplets*, *Small.* 10(2014), no. 24, pp. 5116–5125.
- [6] J. Chen, N. E. Clay, N. Park, and H. Kong, *Non-spherical particles for targeted drug delivery*, *Chem. Eng. Sci.* (2015), vol. 125, pp. 20–24.
- [7] E. A. Peraza-Hernandez, D. J. Hartl, and D. C. Lagoudas, *Active Origami: modeling, design, and applications*. Springer, 2018.
- [8] E. A. Peraza-Hernandez, D. J. Hartl, R. J. Malak, and D. C. Lagoudas, *Origami-inspired active structures: A synthesis and review*, *Smart Mater. Struct.* 23(2014), no. 9., pp. 1-28.
- [9] M. Boncheva and G. M. Whitesides, *Templated self-assembly: Formation of folded structures by relaxation of pre-stressed, planar tapes*, *Adv. Mater.*17(2005), no. 5, pp. 553–557.
- [10] J. Cui, S. Yao, Q. Huang, J. G. M. Adams, and Y. Zhu, *Controlling the self-folding of a polymer sheet using a local heater: The effect of the polymer-heater interface*, *Soft Matter* 13(2017), no. 21, pp. 3863–3870.
- [11] P. Tyagi, N. Bassik, T. G. Leong, J. Cho, B. R. Benson, and D. H. Gracias, *Self-assembly based on chromium / copper bilayers*, *J. Microelectromechanical Syst.* 18(2009), pp. 784–791.
- [12] C. Py, P. Reverdy, L. Doppler, J. Bico, B. Roman, and C. N. Baroud, *Capillary origami: Spontaneous wrapping of a droplet with an elastic sheet*, *Phys. Rev. Lett.* 98 (2007) no. 15, pp. 2–5.

BIOGRAPHY



Derosh George is currently pursuing a Ph.D. degree in Mechanical and Aerospace Engineering at the University of California, Irvine. He received his Bachelor's and Master's degrees in Mechanical Engineering from the Indian Institute of Technology (IIT) Madras. Afterwards, he joined General Electric (GE), where he was a part of the Edison Engineering Development Program (EEDP) in the Gas Turbine—New Product Introduction team until 2015. Following this stint at GE, he worked as a research fellow at IIT Madras for over a year. His current research interest is in the development of novel fabrication techniques for carbon origami and carbon nanowires.



Edwin A. Peraza Hernandez is an Assistant Professor of Mechanical and Aerospace Engineering at the University of California, Irvine. He obtained his Ph.D. and B.S. degrees in Aerospace Engineering from Texas A&M University in 2016 and 2012, respectively. His research integrates structural mechanics, design optimization, active materials, and principles of origami and tensegrity. He is the author of one book and more than 38 technical publications in archival journals and conference proceedings. The overarching goal of Hernandez's research is the development of aerospace structures with optimal properties such as minimal mass, minimal energy usage, and tailorable stiffness.



Marc Madou was the Vice President of Advanced Technology with Nanogen, San Diego, CA, USA, before joining the University of California at Irvine as the Chancellor's Professor of Mechanical and Aerospace Engineering. He specializes in the application of miniaturization technology to chemical and biological problems (BIO-MEMS). He has authored several books in this burgeoning field and has helped pioneer both in academia and industry. He founded several micromachining companies and has been on the board of many more. He was the Founder of the Department of Microsensor, SRI International, Menlo Park, CA; the Founder and President of Teknekron Sensor Development Corporation, Menlo Park; a Visiting Miller Professor with the University of California at Berkeley, Berkeley, CA; and is the Endowed Chair with Ohio State University (Professor of Chemistry and Materials Science and Engineering), Columbus, OH, USA.

A PLACE IN THE SUN FOR ARTIFICIAL PHOTOSYNTHESIS

Lionel Vayssieres¹

¹ International Research Center for Renewable Energy (IRCRES), School of Energy & Power Engineering, Xi'an Jiaotong University, China
Email: lionelv@xjtu.edu.cn

ABSTRACT

The transition from hydrocarbons energy sources to clean renewable ones has become a top priority worldwide due to the catastrophic effects of pollution on public health and the environment. A hydrogen-based energy economy would be ideal as it would produce no carbon emission (only water). Yet, most of the hydrogen produced nowadays still comes from nonrenewable sources, made by steam reforming of methane which produces carbon oxides. The cleanest way to sustainably produce hydrogen at large scale is by splitting water. Consequently, a significant increase in research during the last decade has been conducted to identify new and ideal systems both from a performance and stability viewpoints.

An overview of decades of research on semiconductors and water splitting as well as the latest advances in controlled fabrication of highly ordered hybrids consisting of a visible light active semiconductor and molecular co-catalysts, the atomic-scale origin of performance and stability of GaN-based nanorod-arrays for overall water splitting in neutral and simulated seawater and the latest development in industry-friendly highly efficient devices for solar hydrogen generation will be presented.

Keywords: Solar hydrogen generation, photocatalytic water splitting, quantum-confined structures, industry-friendly devices

INTRODUCTION

The demand of low-cost and highly efficient materials has become a major challenge scientists are facing to answer crucial contemporary issues such as clean alternative energy resources for a safer and cleaner environment. One of the promising alternatives for the transition of fossil fuel-based energy to a clean and renewable one relies on the widespread implementation of solar energy systems [1], yet the high cost of energy production and low-energy of currently used material combinations pose an intrinsic limitation. In this context, new materials development is required to achieve the necessary crucial increase in power generation and conversion efficiency. The necessity of materials development which is not limited to materials that can achieve their theoretical limits, but makes it possible to raise these limits by changing the fundamental underlying physics and chemistry is critical. Low cost purpose-built materials with optimized structure and properties combined with inexpensive large scale manufacturing methods will play a decisive role in the success of renewable energy

systems. However, fabricating large areas of such materials is a daunting challenge.

Novel smarter and cheaper fabrication techniques and, just as important, better fundamental knowledge and comprehensive understanding of their properties using nanoscale phenomena such as quantum confinements to create multi-functional structures and devices is the key to success.

RESULTS AND DISCUSSION

Such concepts can be achieved and demonstrated by the thermodynamic modeling, low-cost aqueous design and fabrication of highly oriented crystalline arrays of metal oxide quantum dots and rods-based structures and devices with controlled orientation, size and shape onto various substrates designed at multiple scales by aqueous chemical growth at low-temperature [2] along with the in-depth study of their electronic structure and quantum confinement effects performed at synchrotron radiation facilities [3] as well as their electrical [4] and photoelectrochemical applications for sustainable solar energy conversion such as solar fuels [1].

CONCLUSION

Low-cost strategies are now available to produce large-area commercially-sound highly-efficient clean and sustainable photo(electro)chemical solar hydrogen generation devices which our environment, health and societies are in critical needs for a clean, safe and sustainable future [1].

Acknowledgment

The author thank the National Science Foundation of China (NSFC), the one-thousand talent program, the State Key Laboratory for Multiphase Flow in Power Engineering and the School of Energy & Power Engineering at Xi'an Jiaotong University, china for their support.

References

- [1] Y. Wei et al. Something new under the sun for ultra low-cost single-junction photoanodes for highly efficient photocatalytic water splitting”, *Sol. Energy Mater. Sol. Cells* **2019**, 201, 110083; X. Guan et al. Making of an industry-friendly artificial photosynthesis device, *ACS Energy Lett.* **2018**, 3, 2230; Efficient unassisted overall photocatalytic seawater splitting on GaN-based nanowire arrays, *J. Phys. Chem. C* **2018**, 122, 13797; J. Su et al. Stability and performance of sulfide-, nitride-, and phosphide-based electrodes for photocatalytic solar water splitting, *J. Phys. Chem. Lett.* **2017**, 8, 5228; A place in the sun for artificial photosynthesis? *ACS Energy Lett.* **2016**, 1, 121; Y. Tachibana et al. Artificial photosynthesis for solar water splitting, *Nat. Photon.* **2012**, 6, 511; C.X. Kronawitter et al. A perspective on solar-driven water splitting with all-oxide heteronanostructures, *Energy Environ. Sci.* **2011**, 4, 3889; On Solar Hydrogen & Nanotechnology, L.Vayssieres ed., Wiley **2010**, pp 1-704.
- [2] L.Vayssieres, Growth of arrayed nanorods and nanowires of ZnO from aqueous solutions, *Adv. Mater.* **2003**, 15, 464; On the design of advanced metal oxide nanomaterials, *Int. J. Nanotechnol.* **2004**, 1, 1; On the thermodynamic stability of metal oxide nanoparticles in aqueous solutions, *Int. J. Nanotechnol.* **2005**, 2, 411; On the effect of nanoparticle size on water-oxide interfacial chemistry, *J. Phys. Chem. C* **2009**, 113, 4733; Y.Weil et al. Spontaneous photoelectric field-enhancement effect prompts the low cost hierarchical growth of highly ordered heteronanostructures for solar water splitting, *Nano Res.* **2016**, 9, 1561.
- [3] L.Vayssieres et al. Size effect on the conduction band orbital character of Anatase TiO₂ nanocrystals, *Appl. Phys. Lett.* **2011** 99, 183101; 1D quantum-confinement effect in α -Fe₂O₃ ultrafine nanorod arrays, *Adv. Mater.*, **2005**, 17, 2320; C.X. Kronawitter et al. TiO₂-SnO₂:F interfacial electronic structure investigated by soft x-ray absorption spectroscopy, *Phys. Rev. B* **2012**, 85, 125109; Titanium incorporation into hematite photoelectrodes: Theoretical considerations and experimental observations, *Energy Environ. Sci.* **2014**, 7, 3100; Electron enrichment in 3d transition metal oxide hetero-nanostructures, *Nano Lett.* **2011**, 11, 3855; On the interfacial electronic structure origin of efficiency enhancement in hematite photoanodes, *J. Phys. Chem. C* **2012**, 116, 22780; On the orbital anisotropy in hematite nanorod-based photoanodes, *PhysChemChemPhys* **2013**, 15, 13483; M.G. Kibria et al. Atomic-scale origin of long-term stability and high performance of p-GaN nanowire arrays for photocatalytic overall pure water splitting, *Adv. Mater.* **2016**, 28, 8388; K. Nie et al. Atomic-scale understanding of the electronic structure-crystal facets synergy of nanopyramidal CoPi/BiVO₄ hybrid photocatalyst for efficient solar water oxidation, *Nano Energy* **2018**, 53, 493; C.L. Dong et al. In Situ/Operando X-ray spectroscopies for advanced investigation of energy materials, *Chem. Eur. J.* **2018**, 24, 18356.
- [4] J. Wang et al. On the Theoretical and Experimental Control of Defect Chemistry and Electrical and Photoelectrochemical Properties of Hematite Nanostructures”, *ACS Appl. Mater. Interfaces* **2019**, 11, 2031; J. Engel et al. In-situ electrical characterization of Anatase TiO₂ quantum dots, *Adv. Func. Mater.* **2014**, 24, 4952; I. Rodriguez et al. Photoelectrochemical water oxidation at FTO/WO₃@CuWO₄ and FTO/WO₃@CuWO₄/BiVO₄ heterojunction systems: An IMPS analysis, *Electrochim. Acta* **2019**, 308, 317

BIOGRAPHY



Born in 1968, [Dr. Lionel Vayssieres](#) obtained his High School Diploma in Mathematics & Life Sciences in 1986, a BSc. and MSc. in Physical Chemistry in 1989 and 1990, respectively and a Ph.D. in Inorganic Chemistry in November 1995 (after his 1994 military duty as a scientist for the French Navy) from the Université Pierre et Marie Curie, Paris, France for his research work on the Interfacial & thermodynamic growth control of metal oxide nanoparticles in aqueous solutions. Thereafter, he joined Uppsala University, Sweden as a postdoctoral researcher for the Swedish Materials Consortium on Clusters and Ultrafine Particles to extend his concepts and develop purpose-built metal oxide nanomaterials for photoelectrochemical applications as well as to characterize their

electronic structure by x-ray spectroscopies at synchrotron radiation facilities. He has been invited as a visiting scientist at: the University of Texas at Austin, USA; the UNESCO Centre for Macromolecules & Materials, Stellenbosch University, and iThemba LABS, South Africa; the Glenn T. Seaborg Center, Chemical Sciences Division, at Lawrence Berkeley National Laboratory (LBNL), CA, USA; The Texas Materials Institute, USA; The Ecole Polytechnique Fédérale de Lausanne (EPFL), Switzerland; the University of Queensland, Australia, and Nanyang Technological University (NTU), Singapore. He was also an independent scientist at the National Institute for Materials Science (NIMS), Tsukuba, Japan for 8 years.

He has (co-)authored over 100 publications in major international journals, proceedings, and book series which have generated over 12800+ citations since the year 2000 (5200+ since 2014, Google Scholar); Top 1% Scientists in Materials Science (Thomson Reuters). Essential Science Indicators (March 2014) shows 232 citations per paper for Materials Science and 89 citations per paper for All Fields; All time 8 ESI highly cited papers (5 as first and corresponding author) in Materials Science, Chemistry, Physics, and Environment/Ecology. A single-author 2003 paper No. 1 in the Top 10 hot papers in Chemistry (Jul-Aug 05), No. 2 (Sep-Dec 05) and No. 3 (May-June 05) in the Top 3 hot papers in Materials Science and highest cited paper for the country of Sweden for the last 10 years (Essential Science Indicators). He has been interviewed by In-Cites and by Science Watch in 2006 for this single authored 2003 paper cited now over 3000 times and another time in 2010 for a 2004 highly cited paper in Chemistry cited now over 300 times. Two other first-and-corresponding author 2001 original research papers have already been cited over 1100 times each. A 2012 and a 2006 articles highly cited in Physics and Material Science, respectively have already been cited over 1100 and 700 times each respectively.

He has given over 400 talks in over 30 countries including the prestigious MRS Spring Symposium X Lecture (2015) as well as seminars at universities, governmental and/or industrial research institutes. He also acted as an organizer, chairman, executive program committee, and/or advisory member for major international conferences (MRS, E-MRS, SPIE, ACERS, IEEE, TCM...) and for various projects worldwide (UNESCO, IUPAC...). He is, since 2003, the founding editor-in-chief of the *International Journal of Nanotechnology* and a referee for 100+ SCI journals (Nature, Nature Photonics, Energy Environ. Sci., JACS, Angew. Chemie, Adv. Mater....) as well as for major funding agencies worldwide.

He is currently a full professor, foreign expert, chief scientist, co-founder, and scientific director of the IRCRE-International Research Center for Renewable Energy (525+ research articles, 16000+ citations, H index = 60, 24 ESI Highly Cited papers, <https://ircre.org/research.html>), School of Energy & Power Engineering at Xi'an Jiaotong University, in Xi'an (Shaanxi Province), China. He's also the recipient of the 2014 Sanqin and the 2016 National Chinese Government Friendship awards as well as one of the most cited researcher in China in the field of Materials Science in 2014, 2015, 2016, 2017 and 2018 (Elsevier/Scopus) and one of the 2016 American Ceramic Society (ACerS) Global Ambassador award for "*his outstanding contributions and leadership to many Society conferences and professional outreach activities towards the global scientific community.*"

INVITED TALKS

***FUNDAMENTALS OF
NANOTECHNOLOGY
(FON)***

2019 FUEL CELL TECHNOLOGIES: MODELLING AND CONTROLLING

Majid Monajjemi^{1, 2}, Chien Mau Dang¹

¹Institute for Nanotechnology (INT), Vietnam National University - Ho Chi Minh City (VNUHCM), Ho Chi Minh City, Vietnam

²Department of chemical engineering, Central Tehran Branch, Islamic Azad University, Tehran, Iran

*Email: Maj.Monajjemi@iauctb.ac.ir; dmchien@vnuhcm.edu.vn

ABSTRACT

In recent years, the fuel cells technologies have been incorporated to the Research & Development plans of several major key companies in the automotive, stationary power and portable electronic instruments. Not only fuel cells are clean energy for environment, but also they can also have more than two times the efficiency of traditional combustion technologies. However, despite current developments, these kind technologies are not mature enough to be significantly into the energy market replacing with petroleum. Hydrogen is an important energy carrier and a strong candidate for energy storage. It will be a useful tool for storing intermittent energy sources such as sun. Hydrogen is a versatile energy carrier that can be used to power nearly every end-use energy need. By this work, modeling and controlling of ion transport rate efficiency in proton exchange membrane (PEMFC), alkaline (AFC), direct methanol (DMFC), phosphoric acid (PAFC), direct forming acid (DFAFC), direct carbon fuel cell (DCFC) and molten carbonate fuel cells (MCFC) have been investigated and compared together. Thermodynamic equations have been investigated for those fuel cells in viewpoint of voltage output data. Effects of operating data including temperature (T), pressure (P), proton exchange membrane water content (λ), and proton exchange membrane thickness (d_{mem}) on the optimal performance of the irreversible fuel cells have been studied. Performance of fuel cells was analyzed via simulating polarization and power curves for a fuel cell operating at various conditions with current densities.

Keywords: Proton exchange membrane (PEMFC), Alkaline fuel cells, (AFC), Direct methanol (DMFC), Phosphoric acid (PAFC), Direct forming acid (DFAFC), Direct carbon fuel cell (DCFC), Molten carbonate fuel cells (MCFC), Solid oxide fuel cells (SOFC).

INTRODUCTION

Fuel cells, already used widely throughout the economy, offer; (1)-small power units in the ranges between hundreds of watts to milli-watts, providing energies for extended operating systems, such as portable computers, vehicle's devices, video, cameras, mobile equipment, and or in industrial applications such as signaling and controlling devices. (2)- Higher efficiency in the utilization of natural fuels. (3)-A proportional decrease in the exhaust of combustion products. (4)-Improving operation of power level through loading and leveling with large-scale systems for temporary powering storage. (5)-A widely developed level of decentralized, silent, local power supply or as a combined power. (6)-Using an emergency power supply and controlled systems in individual installations such as research centers and hospitals. (7)-Traction power around tens of kilowatts for large-scale

application for electric cars, leading for cleaning the ecological situation in grand cities and populated area. (8)- Power supplying to spacecraft, submarines, offshore and other underwater structures for supplying drinking water. Based on these reasons, investigation of fuel cells has been considered by the end of 2019. By the end of the twentieth century, interest in fuel cells appears more common and global due to the dwindling world resources of oil and more serious ecological matters in big cities were recognized. Today, numerous and various fuel cells have been operated successfully, on a scale among tens of megawatts and tens or hundreds of kilowatts. Fuel cells are already making a high percentage contribution for solving economic and ecological matters facing mankind that without any doubt this contribution will continue to increase time by time. Recently, R&D attempts concerning the investigating, developing and application of fuel cells are guided in many

countries, in national laboratories, in science research centers, universities, and in industrial portions [1-4]. Fuel cells are categorized based on species of their electrolytes and also by the difference in startup time ranging between around one second for PEMFC [4] to ten minutes for solid oxide fuel cells (SOFC) with maximum efficiency in range of 45% to 60%. In the fuel cell of a solid acid electrolyte, H^+ conducting oxyanion salt (solid acid) consists of a solid supported within the membrane which is saturated with H_2O for any further ions transporting. Anode reaction is: $H_2 \rightarrow 2H^+ + 2e^-$ and Cathode reaction is: $1/2 O_2 + 2e^- + 2H^+ \rightarrow H_2O$ and the overall reaction is: $H_2 + 1/2 O_2 \rightarrow H_2O$. In viewpoint of mechanism, at the anode, H_2 first comes into contact with a nickel catalyst and break apart, bonding to the nickel surface forming weak H-Ni bonds consequently the oxidation reaction can proceed (Fig.1).

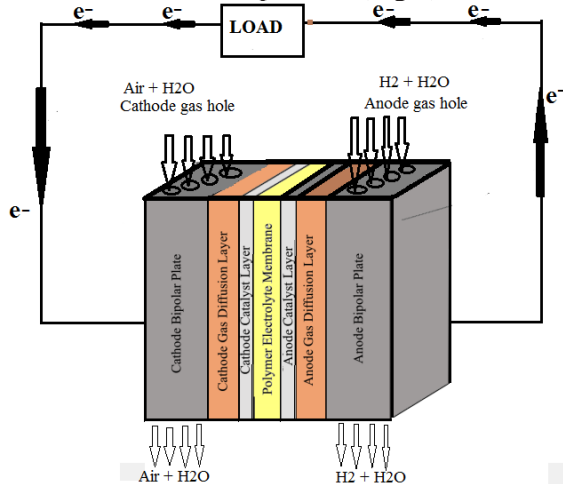


Figure 1. One unit of PEM fuel cell structure

Each H_2 releases its electron which moves around the external circuit to the cathode which is the electrical current. Then, the H^+ bonds with H_2O on the membrane surface for forming H_3O^+ that moves through the membrane to the cathode electrode, leaving the nickel catalyst for the next H_2 . At the cathode, O_2 comes into contact with a nickel catalyst on the electrode surface and break apart bonding to the nickel sheet forming weak O-Ni bonds, enabling the reduction reaction to proceed. O_2 then leaves the nickel catalyst site, combining with two electrons that move in external circuit and two protons which have moved through the membrane for forming H_2O . Increasing the H_2 storage is a major section for the transition more and more hydrogen molecules in a fuel cell [4, 5]. Direct methanol fuel cell (DMFC) is a subcategory of PEMFC in

which methanol is used as the fuel (Fig.2). The advantages which can be considered are the energy-dense, easiness of transport and reasonably stable liquid at all environmental situations and mean- while its disadvantages is low efficiency (around 10%), so they are targeted especially to portable applications, which power densities are more important than the efficiencies [6].

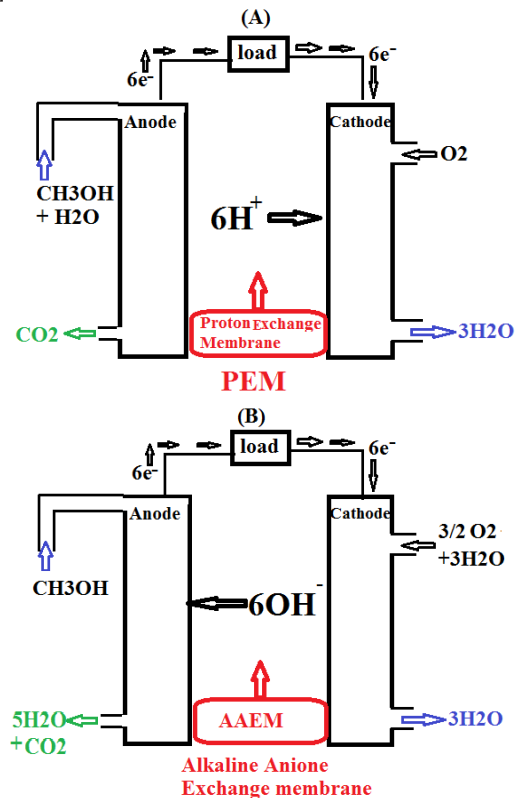


Figure 2. Direct methanol fuel cell (DMFC) with two kind electrolytes A: PEM and B: AAEM

In contrast to indirect fuel cells, which CH_3OH molecules are reacted to H_2 molecules via a steam improving, direct form use a CH_3OH solution for transporting the reactant into the cells; common operating temperature is in the range $55-115^\circ C$, which high temperature is generally pressurized [6,7]. Direct methanol fuel cell, itself is more efficient at top temperature and pressure, but these situations finally creating so many problem in whole of system that the advantage windswept, so atmospheric-pressure forms are yet preferred and applied [7, 8]. Due to the CH_3OH "cross-over" phenomena or diffusion via the membrane (without reacting), CH_3OH is unsuitable as a solvent that decreases the performance of fuel cells considerably, since this phenomenon, directly reacts with air (in cathode), consequently reduction of the cell voltage

accomplishes, therefore "cross-over" phenomenon is a main problem in inefficiency of direct methanol fuel cells [9]. This matter can be reduced through improving membranes, developing catalyst layers, reclaiming the structure of gas layers and optimizing the design of the electrodes (such as management of carbon dioxide at the anode) in viewpoint of current densities distribution [10]. The DMFC has restricted the PT factor (power*time) which means they can produce the small quantity of power in a lengthy period of time. Of course, those are suitable for large vehicles. The half-reactions of DMFC are in anode (oxidation): $CH_3OH + H_2O \rightarrow 6H^+ + 6e^- + CO_2$ and in cathode (reduction) the half-reaction: $\frac{3}{2}O_2 + 6H^+ + 6e^- \rightarrow 3H_2O$ while the overall reaction is: $CH_3OH + \frac{3}{2}O_2 \rightarrow 2H_2O + CO_2$ (Fig.2a). The CH_3OH oxidation over the catalyst layers produces CO_2 and H_2O is consumed at the anode and is again produced at the cathode [9, 10].

From each reaction, 6-proton is transported through the PEM which usually is made of Nafion [2, 7] (sulfonated tetra-fluoro-ethylene based fluoro- copolymer). Although Pt as a Nano particle might be suitable catalyst for both anode and cathode, it is very expensive and during oxidation, the number of available sites in Pt will be occupied by CO which is produced in oxidation of methanol, consequently the efficiency of the cell will decrease. An alloy of platinum with suitable percentage of Au, Ru and Cu can remove this problem. Storage of formic acid materials (HCOOH) are secure, safe, and confident compared to H_2 , as it is a non-flammable liquid and also does not cross over the polymer membrane, so its performance can be higher than that of methanol. DFAFC converts HCOOH and O_2 into CO_2 and H_2O to produce energy. The half-reactions of DFAFC are anode: $HCOOH \rightarrow CO_2 + 2H^+ + 2e^-$ and in cathode: $\frac{1}{2}O_2 + 2H^+ + 2e^- \rightarrow H_2O$ and total reaction is $HCOOH + \frac{1}{2}O_2 \rightarrow CO_2 + H_2O$ [11]. The alkaline fuel cell (Bacon) is one of the most important fuel cells with high performance that NASA has applied (Fig.2b), in Apollo-series missions and on the space shuttles. The half-reactions of DFAFC are anode: $H_2 + 2OH^- \rightarrow 2H_2O + 2e^-$. And in cathode: $O_2 + 2H_2O + 4e^- \rightarrow 4OH^-$. In AFC, two electrodes are divided through a porous materials filled with an alkaline

solvent, such as KOH, NaOH or NH_4OH . One of the important advantages of these kind fuel cells is that alkaline solutions can react with CO_2 to produce conversion K_2CO_3 . Environmentally, AFC is suitable to clean out as much of the CO_2 due to operate (even in high temperature) on pure oxygen, or at least purified air. Since, O_2 reduction reaction (ORR) at the cathode is easier than in acidic cells, AFCs in the systems can be operated up to 90 °C with higher performance than acidic electrolyte, such as PEMFC.

Other Fuel Cell Technologies:

DBFC (direct borohydride fuel cell) is a subclass of AFC which is straightly feeds via sodium or potassium borohydride as a fuel and H_2O_2 peroxide as the oxidant. It is a novel type of fuel cell which is currently in the developing situation and is attractive because of its high operating potential compared to other kind of fuel cells [12-14]. DBFCs can be fabricated cheaply than the traditional due to unnecessary expensive [Pt]-catalysts. Moreover, it has a higher power density to achieve a desired rated voltage and thus reduces the stack costs considerably [14]. Sodium borohydride can be used in more conventional hydrogen fuel cell systems and hydrogen can be reproduced for a fuel cell via catalytic decomposition of the borohydride: $NaBH_4 + 2H_2O \rightarrow NaBO_2 + 4H_2$ including anodic and cathode reactions as Cathode: $2O_2 + 4H_2O + 8e^- \rightarrow 8OH^-$ ($E^0 = +0.4V$) and Anode: $NaBH_4 + 8OH^- \rightarrow NaBO_2 + 6H_2O + 8e^-$ ($E^0 = -1.24 V$) with total reaction as $NaBH_4 + 2O_2 \rightarrow NaBO_2 + 2H_2O + 1.64V$.

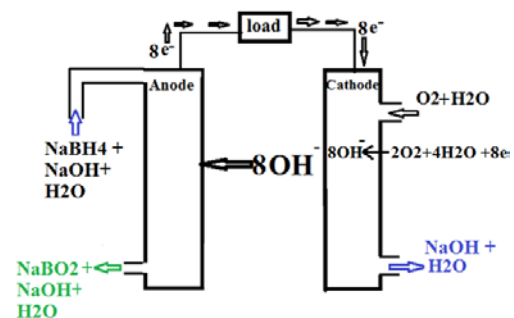


Figure 3. A schematic of direct borohydride fuel cell

In viewpoint of disadvantages, DBFC produces H_2 from a side reaction of $NaBH_4$ with water heated that H_2 molecule can either be piped out to the exhaust or piped to a conventional hydrogen fuel cell, in addition, the process of creating electricity is not easily reversible (Fig.3).

DFAFC: A formic acid fuel cell is a subclass of PEMFC which is not remade, but fed directly to the fuel cell. The advantages are including portable electronics such as phones and laptop computers as well as larger fixed power applications such as vehicles. Similar to CH_3OH , the formic acid is a small molecule that fed directly into the fuel cell, without needing a catalytic reforming and easy storing which is safer than compared to H_2 at high pressures and low temperatures. Formic acid does not cross over the polymer membrane, so its efficiency can be higher than that of methanol. It converts formic acid and O_2 to CO_2 and H_2O for producing energies in anodic and cathode sides as; Anode: $\text{HCOOH} \rightarrow \text{CO}_2 + 2\text{H}^+ + 2\text{e}^-$ Cathode: $1/2\text{O}_2 + 2\text{H}^+ + 2\text{e}^- \rightarrow \text{H}_2\text{O}$ Net reaction: $\text{HCOOH} + 1/2\text{O}_2 \rightarrow \text{CO}_2 + \text{H}_2\text{O}$. In 2018, a paper about DFAFC was published addressing the issue of requiring a high over-potential by way of golden single-atom-site platinum catalysts [15] (Fig.4).

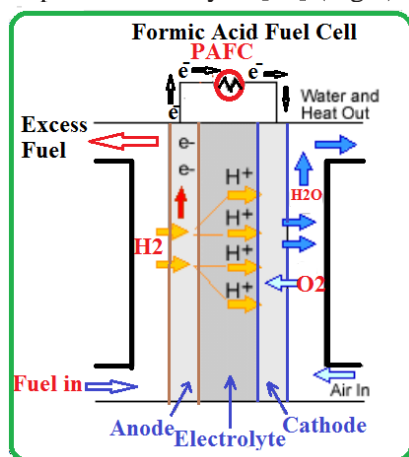


Figure 4. A schematic of phosphoric acid fuel cell

MHFC: A metal hydride fuel cell is a subclass of AFC in both research and developing processing with its ability to store H_2 within the cell, same as direct borohydride fuel cells. There are numerous of interesting characteristics including the rechargeable ability with electrical energies same as NiMH batteries, low operating temperatures, quick kinetics, extended shelf life and quick cold start properties [16-19].

EGFC: A Electro/galvanic fuel cell is an electrical system, one form of which is generally applied for measuring the concentration of O_2 in scuba diving and medical devices. The chemical reactions occur when the KOH in the cell comes into contact with O_2 that creates electrical currents among the lead anode and the gold-plated cathode via

loading resistance. This current appears due to the concentration of O_2 present. They are used in oxygen analyzers in technical diving to display the proportion of O_2 in a N_2 before a dive. The partial pressure of oxygen in diving chambers and surface supplied breathing gas mixtures can also be monitored using these cells. This can either be done by placing the cell directly in the hyperbaric environment, wired through the hull to the monitor, or indirectly, by bleeding off gas from the hyperbaric environment or diver gas supply and analyzing at atmospheric pressure, then calculating the partial pressure in the hyperbaric environment. This is frequently required in saturation diving and surface oriented surface supplied mixed gas commercial diving. EGFC has a limited lifetime that is reduced via exposure to high concentrations of O_2 [20-22].

MFC: microbial fuel cell, is a bio-electrochemical system where drives the electrical currents via using bacteria and mimicking bacterial interactions found in nature. MFC can be collected into two general classes including mediated and unmediated. Mediated category is based on a chemical that transfers electrons from the bacteria in the cell to the anode. In unmediated category, a bacterium generally has electrochemically active redox proteins such as cytochromes on their outer membrane that can transfer electrons directly to the anode. In the 21st century, MFCs started to find a commercial use in wastewater treatment [23-25]. Microbial fuel cell is noteworthy due to power generation applications which needs only low energy, such as wireless sensor networks or remote monitoring [26, 27]. The stronger power generation can be manufactured with a biofilm-covered graphite anode. Microbial fuel cell use energy more efficiently than standard internal combustion engines, which are limited by the Carnot Cycle. Microbial fuel cell operates well in biological temperature and pH (around 7) [26-29]. Recently, microbial fuel cell for environmental sensor has been considered that would be able to provide power for longer periods and enable the collection and retrieval of undersea data without a wired infrastructure. The energy created by these kinds of fuel cells is enough for sustaining the sensors after an initial startup time. In soil-based MFC principles, the soil acts as the nutrient-rich anodic media, the inoculum and the PEMFC. The anode is located in an especial depth within the soil, while

the cathode rests on the top of soil. Soil-based MFC is becoming a common educational tool for science teaching [30-33].

RFC (regenerative or revers fuel cell) is a fuel cell run in reversible situation, that uses electricity and chemical molecules (1) to chemical molecules (2). The main item is that, the process of fuel cell must be reversible. Although a given system is usually minimized for operating in one step, may not be built in such a way that it can be operated backwards. The mechanism of reverse fuel cell is based on H₂ fueled proton exchange membrane fuel cell. As instance, it is used H₂ and O₂ to produce electricity with H₂O; a regenerative hydrogen fuel cell is used electricity and water for producing H₂ and O₂. During the operating in reverse step, the anode for the electricity level becomes the cathode in the H₂ generation, which means reverse fuel cell mode, and vice versa. When an external voltage is used, H₂O at the cathode side will undergo electrolysis to produce H⁺ and O²⁻ ions; O²⁻ will be transported via the electrolyte towards anode where it can be oxidized to form O₂. In this reverse level, the polarity of the cell is opposite to that for the fuel cell. At cathode: H₂O + 2e⁻ → H₂ + O²⁻ At anode: O²⁻ → 1/2O₂ + 2e⁻ Overall: H₂O → 1/2O₂ + H₂ (Fig.5) [34-37].

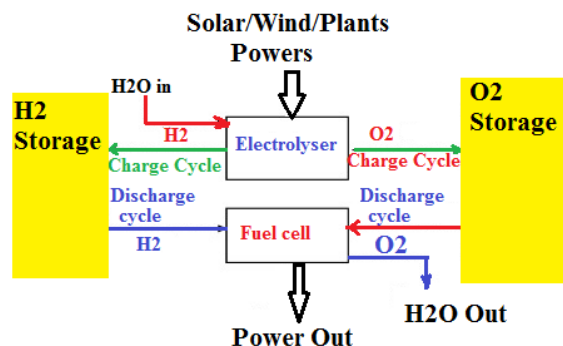


Figure 5. A schematic of regenerative fuel cell

SORFC (Solid oxide regenerative fuel cell) is a subgroup of RFC with solid oxide regenerative fuel cell. SORFC operates at high temperature with high efficiency and it is a suitable system for high temperature electrolysis. Less electricity is required for electrolysis process in SORFC due to high temperature. Although the electrolyte can be oxygen ion or hydrogen ion conducting, for oxygen ion conducting yttria stabilized zirconia (YSZ) based SORFC using Ni-YSZ as the H₂ electrode and LSM-YSZ as the oxygen electrode has been investigated [38]. Dönitz and coworkers reported on the mechanism of YSZ electrolyte

cell by current density of 0.3 A cm⁻² and 100% Faraday efficiency at only 1.05 V [39]. In one research, it has been exhibited that ceria-based composite electrolytes, where both proton and oxide ion conduction exist, produce high current output for fuel cell operation and high hydrogen output for electrolysis operation [40]. A few doped atoms such as Zr with Sc and ceria (10ScCeSZ) are also investigated as potential electrolytes in SORFC for H₂ production at 550-750 °C. It is reported that 10Sc1CeSZ exhibits suitable properties with high current densities [41]. Generally used/tested electrodes are Ni/Zr cermet (Ni/YSZ) and La-substituted Sr and Ti composite for SORFC cathode, and La-Sr-Mn (LSM) for SORFC anode. Other anode materials can be La-Sr-Fe (LSF), La-Sr-Cu-Fe and La-Sr-Co-Fe (LSCoF). Studies exhibit that Ni/YSZ electrode was less active in reverse fuel cell operation than in fuel cell operation, and this can be attributed to a diffusion-limited process in the electrolysis direction, or its susceptibility to aging in a high-steam environment, primarily due to coarsening of nickel particles [42]. Therefore, alternative materials such as the Ti/ceria composite (La_{0.35}Sr_{0.65}TiO₃-Ce_{0.5}La_{0.5}O₂) or (La_{0.75}Sr_{0.25}) and (0.95Mn_{0.5}Cr_{0.5}O₃) (LSCM) have been proposed electrolysis cathodes. Both LSF and LSM/YSZ are reported as suitable anode candidates for electrolysis mode [43, 44].

DEFC (direct-ethanol fuel cell) is a system of fuel cell in which ethanol is fed directly into the cell. It has been used as a system to investigate a range of fuel cell mechanism including the use of PEM [45]. DEFC uses C₂H₅OH in the fuel cell instead of the more toxic CH₃OH. C₂H₅OH is a hydrogen-rich liquid and it has a higher specific energy compared to CH₃OH. The use of C₂H₅OH would also overcome both the storage and infrastructure challenge of H₂ in fuel cell applications [46]. The DEFC, similar to the DMFC, relies upon the oxidation of ethanol on a catalyst layer to form carbon dioxide. Water is consumed at the anode and is produced at the cathode.

Protons (H⁺) are transported across the proton exchange membrane to the cathode where they react with O₂ to produce water. Electrons are transported through an external circuit from anode to cathode, providing power to connected devices. Anode: C₂H₅OH + 3H₂O → 12H⁺ + 12e⁻ + 2CO₂, cathode: 3O₂ + 12H⁺ + 12e⁻ → 6H₂O. SOFC (solid oxide fuel cell) is a system that produces electricity directly from oxidizing of

a fuel consist of a solid oxide. The most important advantage of this category equipment are a combination of heat and power efficiency, long-term stability, fuel flexibility, low emissions, and relatively low cost. The largest disadvantage is a high operating temperature [47]. Generally, SOFC consist of four layers which three of them are ceramics and single cell consisting of these four layers stacked together is basically only a few millimeters thick. A few hundreds of these unit cells are then connected in series for forming SOFC stack. The ceramics used in SOFC do not become active until they reach very high temperature and as a result, the stacks have to run at temperatures ranging from 500 to 1,000 °C. Reduction of oxygen into oxygen ions occurs at the cathode. These ions can then diffuse through the solid oxide electrolyte to the anode where they can electrochemically oxidize the fuel. In this reaction, a water byproduct is given off as well as two electrons. These electrons then flow through an external circuit where they can do work. The cycle then repeats as those electrons enter the cathode material again [48].

DISCUSSION

The details of the above fuel cells are summarized in table 1. The enthalpy of hydrogen combustion reaction or hydrogen heating amount for one mole of hydrogen can be calculated via $\Delta H = \Delta H_f^0(H_2O) - \Delta H_f^0(H_2) - \frac{1}{2}\Delta H_f^0(O_2) = -286.31 \text{ Kj/mol}$. Hydrogen heating amounts are used as a measure of energies input for the fuel cells and this is the maximum value of thermal energy which can be extracted from hydrogen. In addition Gibbs free energy is given by the following equation: $\Delta G = \Delta H - T\Delta S$. which the difference between entropies of products and reactants can be calculated as $\Delta S = \Delta S_f^0(H_2O) - \Delta S_f^0(H_2) - \frac{1}{2}\Delta S_f^0(O_2)$. The maximum electrical work is: $W_{max} = -n(emf)F = -\Delta G$ where F is Faraday's constant and "emf" is the ideal electro motor force or potential of the cell. Therefore the theoretical hydrogen/oxygen fuel cell potential or maximum voltage of fuel cells is: $emf = E = \frac{-\Delta G}{nF} = \frac{237.342 \text{ J mol}^{-1}}{2 \cdot 98486.5 \text{ Coulomb}} = 1.231 \text{ Volt}$. The thermal efficiency is defined based on amount of useful energy released when a fuel is reacted with an oxidant (ΔG), relative to the change in stored chemical energy (ΔH) therefore the maximum

theoretical yields in a fuel cell is $\eta = \frac{\Delta G}{\Delta H} = \frac{237.342}{-286.31} = \%82.9$. Based on Nernst equation a function of temperature and pressure can be applied for any fuel cells as; $emf = E_{(T,P)} = -\left(\frac{\Delta H}{nF} - \frac{T\Delta S}{nF}\right) + \frac{RT}{nF} \ln \left[\frac{P_{H_2} P_{O_2}^{0.5}}{P_{H_2O}}\right]$, (1). For both Phosphoric acid fuel cells (PAFC) and polymer electrolyte membrane fuel cells (PEMFC), the hydrogen molecules splitting at the anode into hydrogen ions are transport across the electrolyte to the cathode. For a PEMFC of static electrolyte with 25cm^2 active area, $50\mu\text{m}$ thickness and $9 \cdot 10^{-7} \text{cm}^2 \cdot \text{s}^{-1}$ diffusion coefficient of H^+ ions [25-28], current density obtained for applied potential difference between 0.5-1.0V at 75°C exhibited in Fig.6

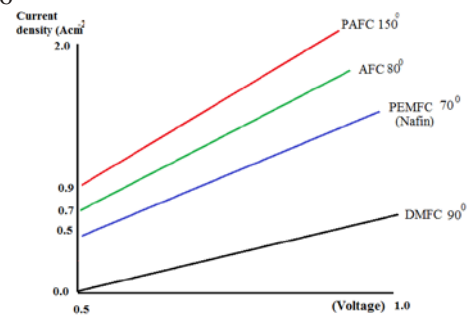


Figure 6. Current densities versus potential

Although PEMFC has lower current than PAFC, due to its lower operating temperature allowing fast startup and can be applied in automotive power applications. Another advantage of PEMFC is that its electrolyte is a solid material and is less expensive to manufacture than the liquid electrolyte $\eta(T, P) = \left(\frac{\Delta H - T\Delta S}{nF}\right) + RT \ln \left(\frac{P_{H_2} P_{O_2}^{0.5}}{P_{H_2O}}\right)$. It is notable that, the maximum electrical energies and the potential differences are achieved when the fuel cells are operating under the thermodynamically reversible condition. Practically, an open circuit potential is considerably lower than the theory due to three main losses which are, first concentration polarization V_{concen} second activation polarization V_{act} , and third ohmic polarization V_{ohmic} . The irreversible voltage loss V_{irrev} is a summation of these three parameters, $V_{irrev} = V_{act} + V_{ohmic} + V_{concen}$. Based on Butler-Volmer equation, a specific potential is needed for overcoming to the energies barriers which called activation polarization $i = I_c + I_A = i_0 \left[-\exp\left(-\frac{\alpha_c n F \eta}{RT}\right) + \exp\left(\frac{\alpha_a n F \eta}{RT}\right)\right]$ where I_A and I_c are anode and cathode current densities,

respectively and i_0 is the reaction exchange currents densities. Meanwhile α_A and α_C are the charge transfer coefficients at the anode and cathode and n is the number of exchange protons per mole of reactant. Here η is the activation over potential term or $\Delta V_{act} = \eta = -\frac{RT}{n\alpha_c F} \ln \frac{i}{i_0}$. For a fuel cell operating with a transfer coefficient of 0.45 activation losses versus current density are shown in Fig.7.

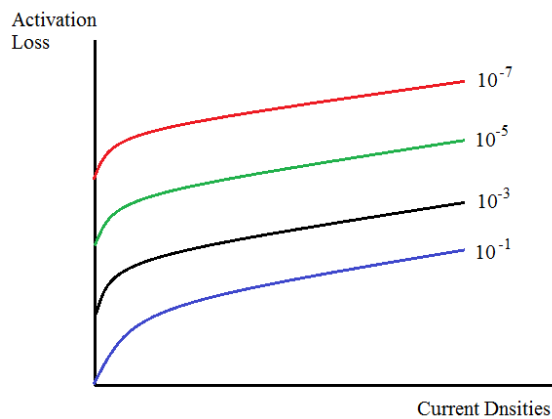


Figure 7. Activation loss as a function of current densities

With an exchange current density of 10^{-3} Acm^{-2} activation losses for different transfer coefficients are shown in (Fig.8) which indicate that for large exchange current densities, fuel cell has insignificant activation over potential. This is a measure of the system abilities for delivering a net current with significant energies loss. When the transfer's coefficients are low, the activation over potentials is large for any specific current. If the transfer's coefficients are large, the fuel cell will provide large current with small activation over potential. The electrolytes have an intrinsic resistance to prevent the charge flow due to ohmic polarization including $R_{electronic}$ and R_{ionic} . Fuel cell resistances can be written as: $V_{ohmic} = iR_{ohmic} = i(R_{electronic} + R_{ionic})$. R_{ionic} Indicates the ionic resistance and $R_{electronic}$ consist of the total electrical resistance of all components concluding bipolar plates, cell interconnects and all connection path.

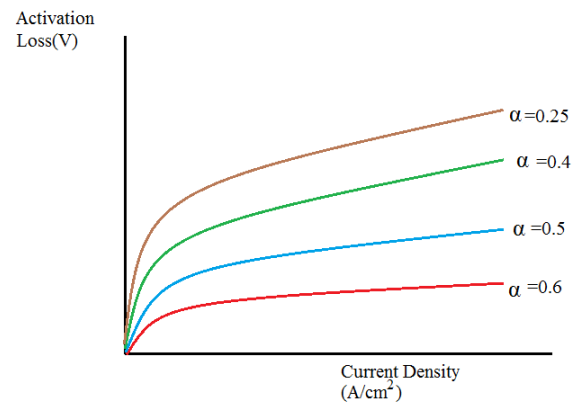


Figure 8. Activation loss versus transfer coefficient

The big amount of ohmic loss appears during the transport of ions through the membrane which depends to membrane water or membrane relative humidity (ϕ_m) parameter as a function of $\lambda = C_0 + C_1\phi_m + C_2\phi_m^2 + C_3\phi_m^3 + C_4\phi_m^4 + \dots$ where C_n are coefficients. It is notable that the resistance of the membrane changes with water because of water uptake results in membrane swelling, which changes the membrane thickness along with its conductivity. The ionic resistance can be written as: $R_{electronic} = \frac{2l_d}{\sigma_d}$ where l_d and σ_d are diffusion layers of thickness and electronic conductivities, respectively. The concentration over potential is due to the mass transfer of H_2 and O_2 . When the PEMFC cathode (O_2) and the anode (H_2) gases interact as an electrochemical process, the concentration of the H_2 and O_2 at the two electrodes will be consumed, that are lower than the initial concentration, and the irreversible loss caused by this concentration gradient is called the concentration over potential. The concentration over potential can be expressed as $V_{conc} = C \ln(\frac{i_L}{i_L - i})$. Where i_L indicates that the PEMFC can reach the limiting current density during operation and c indicates the concentration loss constant.

Table 1. Summarized information of various fuel cells

Fuel cell type	Abbreviation	General Electrolyte	~C ⁰	Size KW	~R%	Application
Proton exchange membrane fuel cell	PEMFC	Polymer membrane	80	1-100	60	R & D
Alkaline fuel cell	AFC	Diluted KOH	90	10-100	60	R & D
Phosphoric acid fuel cell	PAFC	H3PO4	150-200	100-400	40	R & D
Molten Carbonate fuel cell	MCFC	Solution of alkaline metal	600-700	300-3000	40-50	R & D
Solid Oxide fuel Cell	SOFC	Yttria Stabilized Zirconia	700-1000	1-2000	60	R & D
Metal hydride fuel cell	MHFC	Aqueous alkaline solution	> -20	1-100	50	R & D
Electro-galvanic fuel cell	EGFC	Aqueous alkaline solution	<40	1-10	40	R & D
Direct formic acid fuel cell	DFAFC	Polymer membrane	<40	< 50 W	50	R & D
Microbial-fuel cell	MFC	Polymer membrane	<40	< 50 W	30	R
Regenerative-fuel cell	RFC	Polymer membrane				R & D
Solid oxide regenerative fuel	SORFC	Polymer membrane	550-750			R & D
Direct borohydride fuel cell	DBFC	Aqueous alkaline solution				R & D
Direct-methanol fuel cell	DMFC	Polymer membrane				R & D
Direct-ethanol fuel cell	DEFC	Polymer membrane				R & D
solid oxide fuel cell	SOFC	O ²⁻ -conducting ceramic oxide	500-1000			R & D
Protonic ceramic fuel cell	PCFC	H ⁺ -conducting ceramic oxide				R & D
Direct carbon fuel cell	DCFC	Several different				R
Magnesium-Air Fuel Cell	MAFC	Salt water				R

References

- [1] Schmidt-Rohr, K., *J. Chem. Educ.* **2018**, 95, 1801- 1810
- [2] Ciureanu, M.; *Journal of Applied Electrochemistry*, **2004**, 34 (7), 705-714.
- [3] Cruz-Manzo, S.; Chen, R.; Rama, P., *International Journal of Hydrogen Energy*, **2013**; 38(3):1702-1713.
- [4] de Bruijn, F.A.; Dam, V.A.T.; Janssen GJM., *Fuel Cells*, **2008**, 8(3), 22.
- [5] Wang, J.Y., *International Journal of Hydrogen Energy*, **2008**, 33 (21): 6339–6350.
- [6] Dohle, H.; Mergel, J.; Stolten, D., *Journal of Power Sources*, **2002**, 111, 268-282.
- [7] Wei, Yongsheng; et al., *International Journal of Hydrogen Energy*, **2012**, 37 (2): 1857–1864.
- [8] Saif, M.; Liu, H., *Electrochimica Acta*, **2010**, 56 (1): 600–606.
- [9] Saif, A.; Liu, H., *Journal of Power Sources*, **2014**, 246: 899–905,
- [10] Motoo, S.; Watanabe, M., *Electrochemistry and Interfacial Electrochemistry*, **1975**, 60, 267–273.
- [11] Ha, S.; Larsen, R.; Masel R. I., *Journal of Power Sources*, **2005**, 144: 28–34.
- [12] Amendola S.C., Onnerud P., Kelly M., Petillo P., Sharp-Goldman S. L and Binder M., *J. Power Sources*, **1999**, 84, 130–133.
- [13] Choudhury, N.A.; Raman, R.K.; Sampath, S.; Shukla, A.K., *J. Power Sources*, **2005**, 143, 1-8.
- [14] Wang, Zhongyang; Parrondo, Javier; He, Cheng; Sankarasubramanian, Shrihari; Ramani, *Nature Energy*, **2019**, 4 (4): 281–289.
- [15] Zhang, Peng; Zheng, Nanfeng; Jiang, De-en; Chen, Shaowei; Almarhoon, Zainab; Aldalbahi, Ali; Regier, Tom; Yuan, Jun; Zhao, Xiaojing; Fung, Victor; Deming, Christopher P.; Li, Z. Y.; Duchesne, Paul N., *Nature Materials*. **17** (11): 1033–1039.
- [16] Appleby, John; C. Wang; F. Little, *The Electrochemical Society*, 2003.
- [17] Wang, X.H.; et al., *Journal of Alloys and Compounds*, **1999**, 293-295, 833–837.
- [18] Lee, S-M.; J.-H. Kim; H.-H. Lee; P S. Lee; J.-Y. Lee, *Journal of the Electrochemical Society*, **2002**, 149 (5): A603–A606.
- [19] Tanaka, H.; N. Kaneki; H. Hara; K. Shimada; T. Takeuchi, *Canadian Journal of Chemical Engineering*, **1986**, 64 (2): 267–271.
- [20] Lang, M.A. (2001). DAN Nitrox Workshop Proceedings. Durham, NC: Divers Alert Network. p. 197. Retrieved 2009-03-20.
- [21] Goble, Steve, *South Pacific Underwater Medicine Society Journal*, **2003**, 33 (2): 98–102. Retrieved 2009-03-20.
- [22] Vann RD, Pollock NW, Denoble PJ (2007). NW Pollock, JM Godfrey, eds. American Academy of Underwater Sciences (Twenty-sixth annual Scientific Diving Symposium). ISBN 0-9800423-1-3. Retrieved 2009-03-20.
- [23] Subhas C Mukhopadhyay; Joe-Air Jiang, Springer, **2013**, 3, 151–178.
- [24] Wang, Victor Bochuan; Chua, Song-Lin; Cai, Zhao; Sivakumar, Krishnakumar; Zhang, Qichun; Kjelleberg, Staffan; Cao, Bin; Loo, Say Chye Joachim; Yang, Liang, *Bioresource Technology*, **2014**, 155: 71–6.
- [25] Wang, Victor Bochuan; Chua, Song-Lin; Cao, Bin; Seviour, Thomas; Nesatyy, Victor J; Marsili, Enrico; Kjelleberg, Staffan; Givskov, Michael; Tolker-Nielsen, Tim; Song, Hao; Loo, Joachim Say Chye; Yang, Liang, *PLoS ONE*, **2013**, 8 (5): e63129
- [26] Venkata Mohan, S; Mohanakrishna, G; Srikanth, S; Sarma, P.N., *Fuel*, **2008**, 87 (12): 2667– 76.
- [27] Venkata Mohan, S; Mohanakrishna, G; Reddy, B. Purushotham; Saravanan, R; Sarma, P.N., *Biochemical Engineering Journal*, **2008**, 39: 121–30.
- [28] Mohan, S. Venkata; Veer Raghavulu, S.; Srikanth, S.; Sarma, P.N., *Current Science*, **2007**, 92 (12): 1720–6. .
- [29] Venkata Mohan, S; Saravanan, R; Raghavulu, S. Veer; Mohanakrishna, G; Sarma, P.N., *Bioresource Technology*, **2008**, 99 (3): 596–603.
- [30] Venkata Mohan, S; Veer Raghavulu, S; Sarma, P.N., *Biosensors and Bioelectronics*, **2008**, 23 (9): 1326–32.
- [31] Venkata Mohan, S; Veer Raghavulu, S; Sarma, P.N., *Biosensors and Bioelectronics*, **2008**, 24 (1): 41–7.
- [32] Choi, Y.; Jung, S.; Kim, S. (2000). "Development of Microbial Fuel Cells Using *Proteus Vulgaris* Bulletin of the Korean Chemical Society". **21** (1): 44–8.

- [33] Chen, T.; Barton, S.C.; Binyamin, G.; Gao, Z.; Zhang, Y.; Kim, H.-H.; Heller, A., *J. Am Chem Soc.*, **2001**, 123 (35): 8630–1.
- [34] Reversible fuel cell learning kit". Ecosoul.org. Archived from the original on May 11, 2008. Retrieved 2009-09-24.
- [35] Microsoft Word - E-14264 Layout.doc" (PDF). Archived from the original (PDF) on 2009-06-29. Retrieved 2009-09-24.
- [36] Electrolyzer and Reversible Fuel Cell". Nfrcr.uci.edu. Archived from the original on 2009-06-18. Retrieved 2009-09-24.
- [37] "6th Framework Programme, Research – STREP program GenHyPEM n° 019802 and Global Energy". Whec2008.com. 2008-06-19. Retrieved 2009-09-24.
- [38] Laguna-Bercero, M. A.; Campana, R.; Larrea, A.; Kilner, J. A.; Orera, V. M., *Fuel Cells*, **2010**, 11: 116–123.
- [39] Dönitz, W.; Erdle, E., *International Journal of Hydrogen Energy*, **1985**, 10(5): 291–295.
- [40] zhu, Bin; Ingvar Albinsson; Camilla Andersson; Karin Borsand; Monika Nilsson; Bengt-Erik Mellander, **2006**, 8 (3): 495–498.
- [41] Laguna-Bercero, M.A; S.J. Skinnera; J.A. Kilner, *Journal of Power Sources*, **2009**, 192 (1): 126–131.
- [42] Marina, O. A.; Pederson, L. R.; Williams, M. C.; Coffey, G. W.; Meinhardt, K. D.; Nguyen, C. D.; Thomsen, E. C., *Journal of the Electrochemical Society*, **2007**, 154 (5): B452.
- [43] Laguna-Bercero, M.A.; J.A. Kilner; S.J. Skinner, *Solid State Ionics*, **2011**, 192: 501–504.
- [44] Hauch, A.; S. H. Jensen; S. Ramousse; M. Mogensen., *Journal of the Electrochemical Society*, **2006**, 153(9): A1741.
- [45] Badwal, S.P.S.; Giddey, S.; Kulkarni, A.; Goel, J.; Basu, S., *Applied Energy*, **2015**, 145: 80–103.
- [46] Badwal, S.P.S.; Giddey, S.; Kulkarni, A.; Goel, J.; Basu, S., *Applied Energy*, **2015**, 145: 80–103.
- [47] Badwal, SPS. *Journal of the Australian Ceramics Society*. **50** (1). Archived from the original on 29 November 2014.
- [48] Badwal, *Journal of the Australian Ceramics Society*. **50** (1). Archived from the original on 29 November 20..

BIOGRAPHY



Majid Monajjemi

He was born in 21 of March 1957 in Mashhad, a big city in the north eastern of Iran. He received his B. Sc. in Chemistry from Kharazemi University in Tehran in 1981 and his Ph.D. from Islamic Azad University of Tehran in 1994. He was the dean of science faculty in Islamic Azad University of Tehran from 2000 to 2006 and director of Interdisciplinary Science and Research Center from 2006 to 2008.

He has been collaborating with several universities worldwide; including his collaborations with Professor Arkonites (Karplus's research group) in Department of Physics, University of Cyprus, (working on Regulation of Glycogen metabolism and oxidative repair of DNA using CHARMM software program), Professor James.

E. Boggs in the Institute of Theoretical Chemistry in University of Texas Austin, Texas, USA (working on molecular modeling and computational calculations of nano-molecules), and so on.

He is a professor in the field of Computational Chemistry in Science and Research Branch of Islamic Azad University in Tehran. His research interests are in the area of interdisciplinary sciences, mainly in molecular modeling and QM/MM calculations of macro-biomolecules, electronic structure calculations of nano-biomolecules, non-bonded electronic structure of B_nN_n rings, NMR contour maps, and quantum investigations of non-bonded interactions. He designed a nano- molecular motor structure which can be used for detecting the biological molecules.

He is focusing for understanding the root of some human behaviors for instance the role of microtubules in the human's conscious or what is the biophysical chemistry role in the telepathy which is interdisciplinary subjects among chemistry, biology, quantum theory and calculations.

Currently, he started collaboration with INT center in Vietnam, Ho Chi Minh City on the Lithium Ion Batteries (LIBTs) both theoretically and experimentally with Professor Chien Mau Dang and his groups.

Selected publication:

- [1]. Monajjemi, M. Biophysical Chemistry. 2015 Cell membrane causes the lipid bilayers to behave as variable capacitors: A resonance with self-induction of helical proteins, 207, 114–127
- [2]. Monajjemi M, Boggs JE (2013) a New Generation of B_nN_n Rings as a Supplement to Boron Nitride Tubes and Cages. *J Phys Chem A* (117): 1670-1684. doi.org/10.1021/jp312073q
- [3]. Monajjemi M (2013) none bonded interaction between B_nN_n (stator) and image (rotor) systems: A quantum rotation in IR region. *Chemical physics* (425): 29-45
- [4]. Monajjemi M, Khaleghian M (2011) EPR Study of Electronic Structure of $[CoF_6]$ and $B_{18}N_{18}$ Nano Ring Field Effects on Octahedral Complex. *J Clust Sci* (22):673–692
- [5]. Monajjemi M (2012) Quantum investigation of non-bonded interaction between the $B_{15}N_{15}$ ring and BH_2NBH_2 (radical, cation, and anion) systems: a nano molecular motor, *Struct. Chem.* (23): 551
- [6]. Monajjemi M et al (2010) Theoretical Description of Electromagnetic Nonbonded Interactions of Radical, Cationic, and Anionic $NH_2BHNBNH_2$ Inside of the $B_{18}N_{18}$ Nanoring *J. Phys.Chem C* 2010, 114, 15315–15330
- [7]. Monajjemi M, Wayne R.J, Boggs JE, NMR (2014) Contour maps as a new parameter of carboxyl's OH groups in amino acids recognition. *Chemical physics* (433) 1-11
- [8]. Monajjemi M, (2014) Metal-doped graphene layers composed with boron nitride–graphene as an insulator: a nano-capacitor" *Journal of Molecular Modeling*, Volume 20, Issue 11
- [9]. Chien Mau Dang, Dung My Thi Dang, and Majid Monajjemi, Lithium Ion Battery Modification via Interaction between "Graphite Oxide// h-BN" Capacitor with Anodic Material *Journal of Computational and Theoretical Nanoscience* Vol. 14, 2368–2382, 2017

NATIONAL FRENCH HYDROGEN PROGRAM IS LAUNCHED

Valérie Nguyen, François Le Naour

Commissariat à l’Energie Atomique et aux Energies Alternatives (CEA), 17 av. des Martyrs F-38054

Grenoble France

Email : vnguyen@cea.fr

ABSTRACT

In 2018, France has announced the launch of its national hydrogen program. CEA and the major French academic and industrial players contribute actively to this program. This presentation aims at giving an overview of the Hydrogen state of the art research and academic eco-system located in the Grenoble area in France.

Keywords: Hydrogen, Energy 4.0, France, nanocaraterization

BIOGRAPHY



Valérie NGUYEN

CEAtech

VP Strategic Industrial Partnerships

As VP of Strategic Industrial Partnerships for Ceatech, Dr. Valérie Nguyen is skilled in understanding market needs and creating valuable innovation opportunities thanks to micro –nanotechnologies & systems, renewable energy disruptive technologies, new materials and Artificial Intelligence.

Prior to joining CeaTech in 2007, she spent more than 15 years in the imaging industry, serving as worldwide sales and marketing and imaging Manager for e2v, Atmel and Thales. Her marketing activity focused on identifying business opportunities and building the roadmaps for new product introductions based on visible & infrared imaging technologies to address space, scientific, medical and industrial markets.

She holds a PhD. degree in x-ray wide-field-of-view imagers from INPG of Grenoble France.

DESIGN OF ISOSTRUCTURAL METAL-INSULATOR TRANSITION IN VO₂

Jaichan Lee¹, Bongwook Jung¹, Dae-Su Lee², Chang-Beom Eom², and Si-Young Choi³

¹School of Advanced Materials Science and Engineering, Sungkyunkwan University, Korea;

²Department of Materials Science and Engineering, University of Wisconsin, Madison, USA;

³Department of Materials Science and Engineering, Pohang University of Science and Technology, Korea

Email: jclee@skku.edu

ABSTRACT

In correlated materials, electron and lattice distortion is coupled, therefore metal-insulator transition (MIT) of correlated materials accompanies the structural phase transition (SPT). We focused on the near room temperature phase transition process, i.e. insulating monoclinic to metallic rutile phase transition of the vanadium dioxide (VO₂), a representative correlated materials. By the first principles calculation, we designed the rutile/monoclinic heterogeneous interface that electron-electron interaction of monoclinic VO₂ region is successfully reduced without crystal structure changing [1]. This interface design can stabilize unstable metallic monoclinic phase. The MIT without SPT of VO₂ is also confirmed by combination with experimental approaches like thin-film growth, structural and electrical characterizations. Our results clarify the long-time controversy about origin of phase transition in VO₂ and will be applied by the high speed functional devices which are based on phase transition.

Keywords: metal-insulator transition, VO₂

References

[1] Dae-su Lee et al., Science 362, 1037 (2018)

BIOGRAPHY



Professor Jaichan Lee

School of Advanced Materials Science & Engineering
Sungkyunkwan University, Suwon, 16419, South Korea
Office: (031) 290-7397
Fax: (031) 290-7410
E-mail: jclee@skku.edu

Jaichan Lee obtained his B.S. (1983), at Department of Metallurgical Engineering, Seoul National University, M.S. (1985), at Department of Materials Science and Engineering, Korea Advanced Institute of Science and Technology (KAIST), and Ph.D. (1993) at Department of Ceramic Science and Engineering, Rutgers, The State University of New Jersey in School of Chemical and Biological Engineering from Seoul National University, South Korea. After Ph.D, he worked on ferroelectric memory at Bell Communication Research (Bellcore), USA. He joined Sungkyunkwan University as an Assistant Professor in 1995, and became Professor in 2004. His current research interest includes computational materials design, atomic scale materials synthesis.

Education

- 1993 Ph.D. Rutgers, The State University of New Jersey, New Brunswick, NJ, USA
- 1985 M.S. Korea Advanced Institute of Science and Technology (KAIST), Seoul, Korea
- 1998 B.S. Seoul National University, Metallurgical Engineering, Seoul, Korea

Research and Professional Experience

- 1995 – Present: Professor, Associate Professor, Assistant Professor
Advanced Materials Science & Engineering, Sungkyunkwan University
- 2007 – 2007: Samsung Electronics, DMC Research Center
Technology Consulting Professor
- 2009 – 2010: Visiting Professor
Department of Physics, University of California, Davis, USA
- 1993 – 1994 Member of Technical Staff
Bellcore Communication Research (Bellcore), USA
- 1985 – 1989 Member of Research Staff
Samsung Electro-Mechanics, Samsung Adv. Inst. of Tech., Korea

LANGMUIR-TYPE MECHANISM FOR IN-SITU CO-DOPING OF BORON AND CARBON IN CVD SILICON-GERMANIUM EPITAXIAL GROWTH

Junichi Murota¹ and Hiromu Ishii²

¹Micro System Integration Center, Tohoku Univ., 519-1176 Aramaki Aza Aoba, Aoba-ku, Sendai 980-0845, Japan;

²Toyohashi Univ. of Technology, 1-1 Hibarigaoka, Tempaku, Toyohashi 441-8580, Japan
Email: murota@riec.tohoku.ac.jp

ABSTRACT

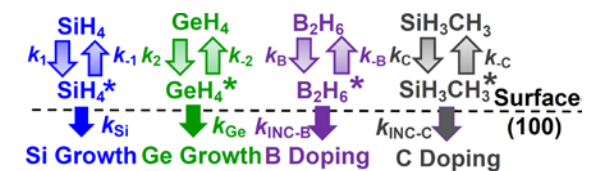
High performance Si-based devices require atomically ordered interface of heterostructures and doping profiles as well as strain engineering, which is obtained by the introduction of Ge and C into Si. In this work, in-situ co-doping process of B and C in $\text{Si}_{1-x}\text{Ge}_x$ epitaxial growth on Si (100) substrates using SiH_4 - GeH_4 - B_2H_6 - SiH_3CH_3 - H_2 gas mixtures at 550°C is explained by the modified Langmuir-type mechanism. It is proposed that the increase of growth rate by B_2H_6 addition for heavy B doping is caused by reactions of SiH_4 , GeH_4 and B_2H_6 at the B-occupied sites where B_2H_6 molecules have been adsorbed at Si-Si, Si-Ge and Ge-Ge pair sites and that the decrease of growth rate by SiH_3CH_3 addition for higher GeH_4 partial pressure is caused mainly by the increase of inactive site density for both the SiH_4 and GeH_4 due to the adsorption of SiH_3CH_3 at Ge-Ge pair sites. It is also proposed that the C doping is influenced by reaction of SiH_3CH_3 at the B-occupied sites. Fairly good agreement is obtained between all the experimental data and the calculated values using the modified Langmuir-type mechanism.

Keywords: Si, Ge, Co-doping, CVD, Langmuir

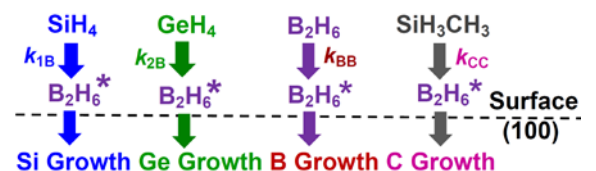
INTRODUCTION

For the fabrication of Si-based ultra-small devices, atomically ordered interface of heterostructures and doping profiles as well as strain engineering due to introduction of Ge and C into Si are required. Our interest is the generalization of atomic-order surface reaction processes for group IV semiconductors [1-6]. The growth rate of Si, $\text{Si}_{1-x}\text{Ge}_x$, the Ge fraction x and the dopant concentration in $\text{Si}_{1-x}\text{Ge}_x$ (100) were related to the growth conditions using the Langmuir-type mechanism although there were the disagreements of fitting [5]. Recently, it was found that the incorporation rate constants of B into the grown film and adsorption rate constant of the B_2H_6 molecule are obtained from the depth profile of dopant in the grown layer during in-situ doping [7]. For lower B_2H_6 partial pressure, growth rate, Ge fraction and B concentration in the films are explained by a Langmuir-type mechanism [8]. For higher B_2H_6 gas partial pressure, it was proposed that SiH_4 , GeH_4 and B_2H_6 molecules are absorbed and react partially at the B-occupied sites where B_2H_6 molecules have been adsorbed on (100) surface. In this work, in-situ co-doping process

of B and C in $\text{Si}_{1-x}\text{Ge}_x$ epitaxial growth on Si (100) substrates is explained by the Langmuir-type mechanism shown in Fig.1 using the experimental data [9, 10].



(a) Adsorption/reactions of SiH_4 and GeH_4 and co-doping of B and C at $\text{Si}_{1-x}\text{Ge}_x$ (100) surface.



(b) Adsorption/reactions of SiH_4 and GeH_4 and co-growth of B and C at B-occupied site.

Figure 1. Reactant gas adsorption/reactions for co-doping of B and C in $\text{Si}_{1-x}\text{Ge}_x$ (100) epitaxial growth.

EXPERIMENTAL

The in-situ co-doping of B and C in $\text{Si}_{1-x}\text{Ge}_x$ epitaxial growth on Si (100) substrates at 550°C in a $\text{SiH}_4\text{-GeH}_4\text{-H}_2\text{-B}_2\text{H}_6\text{-SiH}_3\text{CH}_3$ gas mixture has been performed [10] by using an ultraclean hot-wall low-pressure CVD system shown in Fig.2 [5]. Details of the epitaxial growth and surface treatment conditions were described elsewhere [10, 5].

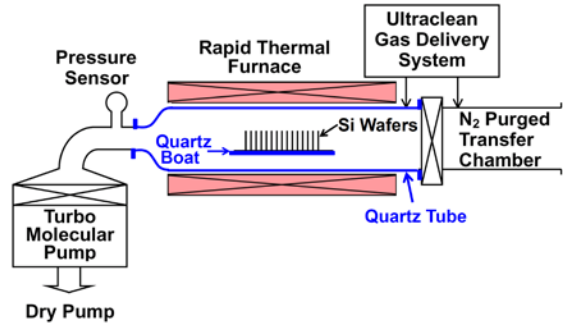


Figure 2. Schematic diagram of an ultraclean hot-wall low-pressure CVD.

RESULTS AND DISCUSSION

Langmuir-type formulation for in-situ co-doping

By the formulation based on the Langmuir-type adsorption and reaction mechanism shown in Table 1, in-situ doping characteristics of dopant (B or C) in $\text{Si}_{1-x}\text{Ge}_x$ epitaxial growth can be explained, assuming that:

- 1) One dopant molecule (B_2H_6 or SiH_3CH_3) occupies one free surface site according to Langmuir's adsorption isotherm, independently of SiH_4 or GeH_4 partial pressure [3], as shown by eqs. (1), (2) and (4) in Table I,
- 2) The B-occupied site where B_2H_6 molecule has been adsorbed becomes active for the SiH_4 , GeH_4 and B_2H_6 adsorption /reactions on the surface [8], as shown by eqs. (3) - (7), and (9). In the present work, it is also proposed that the B-occupied site becomes active for the SiH_3CH_3 adsorption/reaction on the surface, as shown by eqs. (2), (8) and (10).
- 3) The dopant occupancy is different at the Si-Si, Si-Ge, and Ge-Ge pair sites on the surface [3],
- 4) B and C incorporation rate constants into the epitaxial grown film are given by eqs. (1) - (10).

Table 1. Equations in the modified Langmuir-type mechanism for formulating growth rate, Ge fraction, B and C concentration in the epitaxial growth on the (100) surface. $i = 1, 2$ and 3 correspond to the Si-Si, Si-Ge, and Ge-Ge pair sites, respectively.

Total adsorption site density n_i at each pair site

$$n_i = Q_{\text{Si}} + Q_{\text{Bi}} + Q_{\text{Ci}} \quad (1)$$

Q_{Si} : free site density for B_2H_6 and SiH_3CH_3 , Q_{Bi} and Q_{Ci} : B_2H_6 and SiH_3CH_3 adsorption site density, respectively.

Q_{Bi} , Q_{Ci} and Q_{Si} in steady state

$$Q_{\text{Bi}} = [k_{\text{Bi}} P_{\text{B}} / (k_{-\text{Bi}} + k_{\text{INC-Bi}})] Q_{\text{Si}},$$

$$Q_{\text{Ci}} = [k_{\text{Ci}} P_{\text{C}} / (k_{-\text{Ci}} + k_{\text{INC-Ci}})] Q_{\text{Si}},$$

$$Q_{\text{Si}} = n_i / [1 + k_{\text{B}} P_{\text{B}} / (k_{-\text{B}} + k_{\text{INC-B}}) + k_{\text{C}} P_{\text{C}} / (k_{-\text{C}} + k_{\text{INC-C}})] \quad (2)$$

k_{Bi} , $k_{-\text{Bi}}$, k_{Ci} , $k_{-\text{Ci}}$, $k_{\text{INC-Bi}}$ and $k_{\text{INC-Ci}}$: adsorption, desorption and incorporation rate constants shown in Fig. 1(a). P_{B} and P_{C} : partial pressure of B_2H_6 and SiH_3CH_3 gas.

B precipitation amount Q_{BB} by reaction of B_2H_6 gas at B-occupied sites

$$Q_{\text{BB}} = k_{\text{BB}} P_{\text{B}} \sum_{i=1}^3 (c_i Q_{\text{Bi}}), \quad (3)$$

k_{BB} : B precipitation rate constant shown in Fig. 1(b).

$\text{Si}_{1-x}\text{Ge}_x$ growth rate R_0 at free site

$$R_0 = (k_1 n_0 P_{\text{SiH}_4} + k_2 n_0 P_{\text{GeH}_4}) / [1 + (k_1/k_{\text{Si}}) P_{\text{SiH}_4}], \quad (4)$$

$$\text{with } k_a n_0 = \sum_{i=1}^3 k_{\text{ai}} n_i c_i (Q_{\text{Si}}/n_i)$$

$$a=1, 2, \text{Si}; c_1=(1-x)^2, c_2=2x(1-x), c_3=x^2,$$

k_1, k_2, k_{Si} : adsorption and reaction rate constant shown in Fig.1(a). P_{SiH_4} , P_{GeH_4} : partial pressure of SiH_4 and GeH_4 gas.

$\text{Si}_{1-x}\text{Ge}_x$ and B growth rate R_{B} at B-occupied sites

$$R_{\text{B}} = (k_{1\text{B}} n_0 P_{\text{SiH}_4} + k_{2\text{B}} n_0 P_{\text{GeH}_4}) \sum_{i=1}^3 (c_i Q_{\text{Bi}}(t)/n_i) + Q_{\text{BB}} / (1.16 \times 10^{23}), \text{ with } n_0 = \sum_{i=1}^3 (c_i n_i), \quad (5)$$

$k_{1\text{B}}, k_{2\text{B}}$: growth rate constant shown in Fig. 1(b).

Total growth rate R

$$R = R_0 + R_{\text{B}}. \quad (6)$$

Ge Fraction x in the grown film

$$x = \{k_2 n_0 P_{\text{GeH}_4} / [1 + (k_1/k_{\text{Si}}) P_{\text{SiH}_4}] + k_{2\text{B}} P_{\text{GeH}_4} \sum_{i=1}^3 (c_i Q_{\text{Bi}})\} / (R_0 + R_{\text{B}}). \quad (7)$$

C precipitation amount Q_{CC} by reaction of SiH_3CH_3 gas at B-occupied sites

$$Q_{\text{CC}} = k_{\text{CC}} P_{\text{C}} \sum_{i=1}^3 (c_i Q_{\text{Bi}}), \quad (8)$$

k_{CC} : C precipitation shown in Fig. 1(b).

B concentration C_{B} in the grown film

$$C_{\text{B}} = [\sum_{i=1}^3 (c_i k_{\text{INC-Bi}} Q_{\text{Bi}}) + Q_{\text{BB}}] / R. \quad (9)$$

C concentration C_{C} in the grown film

$$C_C = \frac{\sum_{i=1}^3 (C_i k_{INC-C_i} Q_{C_i}) + Q_{CC}}{R}. \quad (10)$$

In Table 1, the values of k_{1i} , k_{2i} , k_{Si} and k_{Bi} , k_{Bi} , k_{BB} are shown in ref. [5] and [8], respectively. The values of k_{Ci} , k_{-Ci} and k_{INC-C_i} in Table I are shown in Table II, determined by fitting the experimental data [9] of C doping without B_2H_6 addition to equations in Table I. Therefore, by the determination of k_{CC} shown in **Table II**, the comparison between the co-doping data and the mechanism shown in Table I are performed.

Table 2. The fitting parameters k_{Ci} , k_{-Ci} , k_{INC-C_i} and k_{CC} on the (100) surface at 550°C, calculated from equations in Table I using the fitting parameters shown in ref. [8], the experimental data in ref. [5] and in Fig. 3.

i		1	2	3
		Si-Si	Si-Ge	Ge-Ge
k_{Ci}	($\text{min}^{-1}\text{Pa}^{-1}$)	1.6	10	200
k_{-Ci}	(min^{-1})	-	-	-
k_{INC-C_i}	(min^{-1})	2	0.5	30
k_{CC}	(min^{-1})	400		

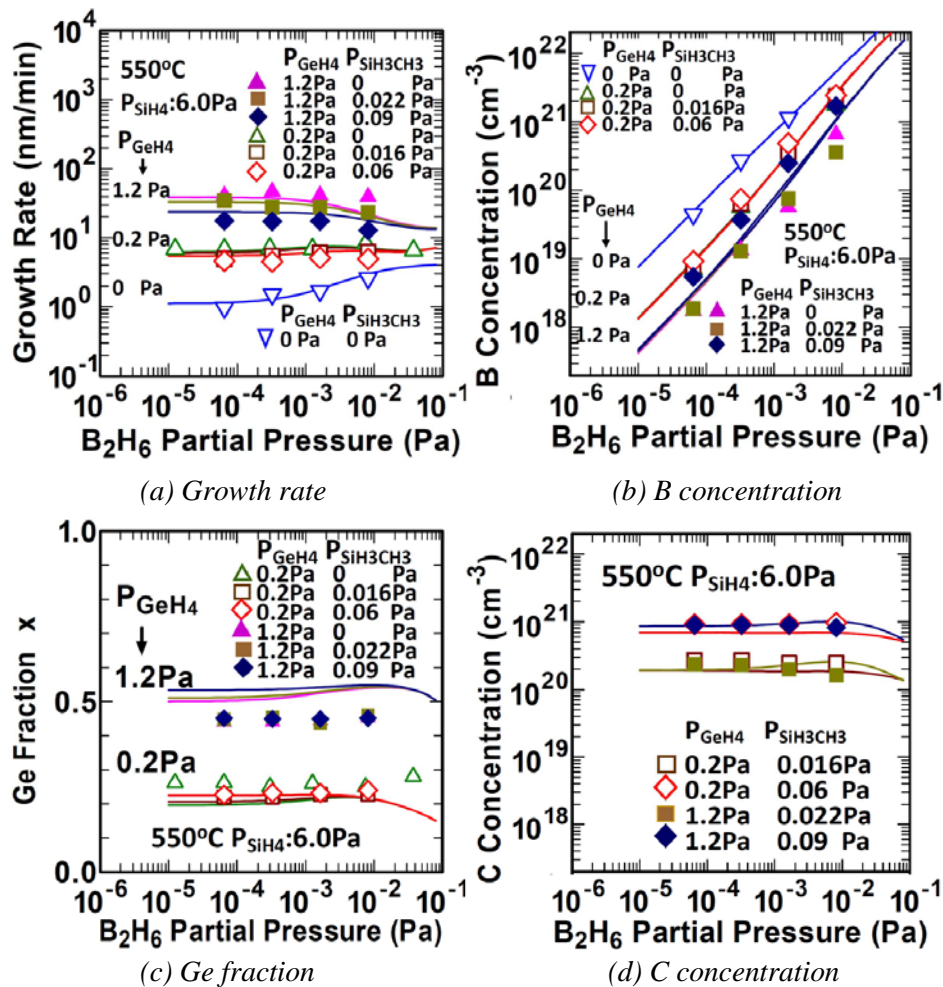


Figure 3. Dependences of the (a) growth rate, (b) B concentration, (c) Ge fraction and (d) C concentration in $Si_{1-x}Ge_x$ on the B_2H_6 partial pressures. The solid lines are calculated from equations in Table I using the fitting parameters in Table II and in ref. [8]. The total pressure and the SiH_4 partial pressure are 30 Pa and 6.0 Pa, respectively. The deposition temperature is 550°C

In-situ co-doping of B and C in $Si_{1-x}Ge_x$ epitaxial growth

Figure 3 shows the dependences of growth rate, B concentration, Ge fraction and C concentration for co-doping of B and C in $Si_{1-x}Ge_x$.

xGe_x epitaxial growth at 550°C on Si (100). The growth rate at lower P_{GeH_4} increases with increasing $P_{B_2H_6}$. But that at higher P_{GeH_4} decreases with increasing $P_{B_2H_6}$ (Fig. 3(a)). With SiH_3CH_3 addition, the growth rate scarcely changes at lower P_{GeH_4} and decreases at higher P_{GeH_4} , corresponding the calculated lines. This

means that the decrease of the growth rate is caused mainly by the increase of inactive site density for both the SiH₄ and GeH₄ due to the adsorption of SiH₃CH₃ at Ge-Ge pair sites. The calculated values of B concentration correspond to the experimental data expect for the samples grown at $P_{\text{GeH}_4}=1.2$ Pa and $P_{\text{SiH}_3\text{CH}_3}=0.09$ Pa. For those samples (Ge fraction>0.44 and C concentration> 8×10^{20} cm⁻³) as shown in Fig. 3(b). It was suggested that the B and C atoms exist at interstitial site [8]. Therefore, for the samples, it is considered that the value of $k_{\text{INC-Bi}}$ is mainly different from that of the other samples. The calculated values of the Ge fraction and C concentration correspond the experimental data shown in Fig. (c) and (d). It should be noted that the calculated C concentration, which is almost independent of B concentration, results from C precipitation by reaction of SiH₃CH₃ gas at B-occupied sites shown in eq. (8).

SUMMARY

The in-situ co-doping process of B and C in Si_{1-x}Ge_x epitaxial growth on Si (100) substrates using SiH₄ - GeH₄ - B₂H₆ - SiH₃CH₃ - H₂ gas mixtures at 550°C is explained by the modified Langmuir-type mechanism. In the calculation of growth rate, B concentration, Ge Fraction and C concentration in the grown film using Table I, the values of k_{li} , k_{2i} and k_{Si} are used in ref. [5] for undoped Si_{1-x}Ge_x epitaxial growth and k_{Bi} , k_{BB} in ref. [8] for B doped Si_{1-x}Ge_x epitaxial growth. The values of k_{Ci} , $k_{\text{-Ci}}$ and $k_{\text{INC-Ci}}$ are determined by fitting the experimental data [9] for C doped Si_{1-x}Ge_x epitaxial growth to equations in Table I. Therefore, for the present co-doping, only k_{CC} as a fitting parameter is obtained. By such fitting, it is proposed that the increase of growth rate at lower P_{GeH_4} by B₂H₆ addition for heavy B doping (Fig.3(a)) is caused by reactions of SiH₄, GeH₄ and B₂H₆ at the B-occupied sites where B₂H₆ molecules have been adsorbed at Si-Si, Si-Ge and Ge-Ge pair sites [8]. As shown in Fig. 3(a), it is proposed that the decrease of growth rate by SiH₃CH₃ addition for higher P_{GeH_4} is caused mainly by the increase of inactive site density for both the SiH₄ and GeH₄ due to the adsorption of SiH₃CH₃ at Ge-Ge pair sites. It is also proposed that the C concentration shown in Fig. 3(d) is influenced by reaction of SiH₃CH₃ at the B-occupied sites. Fairly good agreement is

obtained between all experimental data shown in Fig. 3 and the calculated values using the modified Langmuir-type mechanism.

These results open the way for generalization of atomically controlled surface reaction process in group IV semiconductors by CVD.

Acknowledgment

The authors wish Prof. M. Sakuraba of Tohoku University, Prof. B. Tillack of IHP/Berlin Institute of Technology and Dr. Yamamoto of IHP for encouragement and stimulating discussion in executing this study and also their thank to staffs, students and visiting researchers for contributions for the research works at Tohoku University.

References

- [1] J. Murota: The Electrochemical Society Extended Abstracts, Fall Meeting, Detroit, Oct.17-21, 1982, Abs.No.226, p.363.
- [2] H. Ishii, Y. Takahashi and J. Murota: Appl. Phys. Lett. **47**, 863 (1985).
- [3] J. Murota and S. Ono: *Jpn. J. Appl. Phys.*, **33**, 2290 (1994).
- [4] B. Tillack, B. Heinemann, D. Knoll: *Thin Solid Films*, **369**, 189 (2000).
- [5] J. Murota, M. Sakuraba and B. Tillack: *Jpn. J. Appl. Phys.*, **45**, 6767 (2006).
- [6] B. Tillack, Y. Yamamoto, D. Bolze, B. Heinemann, H. Rücker, D. Knoll, J. Murota and W. Mehr: *Thin Solid Films*, **508**, 279 (2006).
- [7] J. Murota, Y. Yamamoto, I. Costina, B. Tillack, V. Le Thanh, R. Loo and M. Caymax: *ECS J. Solid State Sci. Technol.*, **7**(6), P305 (2018).
- [8] J. Murota: *ECS Trans.*, **90**(1), 43 (2019).
- [9] A. Ichikawa, Y. Hirose, T. Ikeda, T. Noda, M. Fujiu, T. Takatsuka, A. Moriya, M. Sakuraba, T. Matsuura and J. Murota: *Thin Solid Films*, **369**(1-2), 167 (2000).
- [10] T. Noda, D. Lee, H. Shim, M. Sakuraba, T. Matsuura and J. Murota: *Thin Solid Films*. **380**, 57 (2000).

BIOGRAPHY



Junichi Murota

Professor Emeritus, Micro System Integration Center, Tohoku University,
519-1176 Aramaki aza Aoba, Aoba-ku, Sendai, 980-0845, Japan.
+81 (0)22 217 3913 murota@riec.tohoku.ac.jp

Personal Details

Family name: Murota

First name: Junichi

Birth date : January 13, 1948

Birth place: Hakodate, Hokkaido, Japan,

Nationality: Japan

Education

B.E. (1970.3), M.E. (1972.3) and Ph.D (1985.3) in electronic engineering, Hokkaido University, Japan.

Professional Experience

- 1972.4-1985.3 Researcher at the Musashino and Atsugi Electrical Communication Laboratories, Nippon Telegraph and Telephone Public Corporation (NTT), Tokyo, Japan.
- 1985.3-1995.1 Associate Professor in the Laboratory for Microelectronics of Research Institute of Electrical Communication (RIEC), Tohoku University.
- 1995.2-2012.3 Professor of Atomically Controlled Processing in RIEC.
- 2008.3-2008.6 Invited Professor, Center of Interdisciplinary Nanoscience of Marseille (CINaM-CNRS) and University of Aix Marseille.
- 2008.4-2013.3 Chairperson of 154th Committee on Semiconductor Interfaces and Their Applications in the University-Industry Cooperative Research Committees of the Japan Society for the Promotion of Science.
- 2012.4- Professor Emeritus, Tohoku University.

Main Research Fields

- Atomically Controlled Processing for Group IV Semiconductors – CVD epitaxial growth
- High-Quality Process Technologies - impurity diffusion and Si-based heterostructure preparation

Award

- The 3rd Yamazaki-Teiichi Prize Award(2003.11)
- JSAP (Japan Society of Applied Physics) Fellow (2009.9)
- The Commendation for Science and Technology by the MEXT-Japan for 2010: The Prizes for Science and Technology in Research Category (2010.4) : “Study on Atomically Controlled CVD Processing of Group IV Semiconductors for Ultralarge Scale Integrations”
- ECS (The Electrochemical Society) Fellow (2012.10)

Selection of Publications

- [1] “Low-Temperature Epitaxial Growth of Si/Si_{1-x}Ge_x/Si Heterostructure by Chemical Vapor Deposition” (Review Paper), J. Murota and S. Ono, Jpn. J. Appl. Phys., Vol.33, No.4B, pp.2290-2299 (1994).
- [2] “Atomically Controlled Processing for Group IV Semiconductors by Chemical Vapor Deposition” (Invited Review Paper), J. Murota, M. Sakuraba and B. Tillack, Jpn. J. Appl. Phys., Vol.45, No.9A, pp.6767-6785 (2006).
- [3] “Atomically Controlled Processing for Dopant Segregation in CVD Si and Ge Epitaxial Growth”, J. Murota, Y. Yamamoto, I. Costina, B. Tillack, V. Le Thanh, R. Loo and M. Caymax, ECS J. Solid State Sci. and Technol., Vol.7, No.5, pp.P305-P310 (2018).
- [4] “Langmuir-Type Mechanism for In-Situ Doping in CVD Silicon-Germanium Epitaxial Growth”, J. Murota, ECS Trans. Vol.90, No.1, pp.43-53 (2019).

DESIGNING FUNCTIONAL MATERIALS VIA ATOMIC-RESOLUTION MICROSCOPY AND SPECTROSCOPY

Stephen J. Pennycook^{1,2,3,4*}, Xiaoxu Zhao¹, Jiong Lu⁵, Wenjie Zang¹, Haijun Wu¹, Changjian Li, A. Ariando⁴, T. Venkatesan⁴ and John Wang^{1,2}

¹. Department of Materials Science and Engineering, National University of Singapore, 117575, Singapore.

². NUS Graduate School for Integrative Sciences and Engineering, Centre for Life Sciences, 117456, Singapore.

³. Centre for Advanced 2D Materials, National University of Singapore, 117546, Singapore.

⁴. NUSNNI-Nanocore, National University of Singapore, Singapore 117411, Singapore.

⁵. Department of Chemistry, National University of Singapore, 117543, Singapore.

Email: msepsj@nus.edu.sg

ABSTRACT

In recent years, our sensitivity for imaging and spectroscopy has dramatically improved due to aberration correction, greatly assisting the correlation of atomic-scale structure and bonding to materials' properties. Trial and error materials' development is increasingly being replaced by atomic scale engineering, informed by the powerful combination of microscopy and theoretical calculations. Here we present some recent applications of this approach to catalysts, batteries, piezoelectrics, thermoelectrics and complex oxide device structures.

Keywords: Scanning transmission electron microscopy, catalysts, piezoelectrics, thermoelectrics, complex oxides

INTRODUCTION

With aberration-corrected scanning transmission electron microscopy it is possible to form probes smaller than atomic dimensions, allowing an unprecedented view of microstructural details. It is also possible to perform spectroscopy with such a probe, providing atomic-level information on composition and electronic structure. With such tools, coupled with theoretical calculations, it is becoming increasingly feasible to design and tune functional materials based on sound understanding of the fundamental atomistic origin of their structure-property relations.

EXPERIMENTAL

All experimental data presented here were obtained in a JEOL ARM200F microscope at the National University of Singapore, which is equipped with an ASCOR probe corrector, cold field emission gun, UHR pole piece, Gatan Quantum ER spectrometer, OneView camera and Oxford Aztec EDS system. Results were obtained at 200 kV accelerating voltage, although 40, 60 and 80 kV are also available for beam sensitive materials.

RESULTS AND DISCUSSION

We present illustrative results from several classes of functional materials, ranging from catalysts through piezoelectrics and thermoelectrics to complex oxide device structures.

The first direct observation that active catalyst clusters could be as small as dimers or even single atoms was in 1996.[1] Today, after aberration correction, it has become almost routine to image single atoms and probe their coordination by spectroscopy, greatly aiding the development of single atom catalysts (SACs). Their unique coordination can impart exceptional activity and selectivity, and much effort is ongoing to replace platinum group metals by cheaper, earth abundant metals such as cobalt or nickel. However, SACs must be sufficiently anchored on a support to avoid coalescence into nanoparticles. One such example is the synthesis of graphene-supported cobalt SACs with a tunable high loading using atomic layer deposition.[2] These SACs show exceptional activity and selectivity for the hydrogenation of nitroarenes to azoxy aromatic compounds. Figure

1 shows a high-angle annular dark field (HAADF) Z-contrast image where single Co atoms are visible. The electron energy loss (EEL) spectra show that whenever Co is detected, so

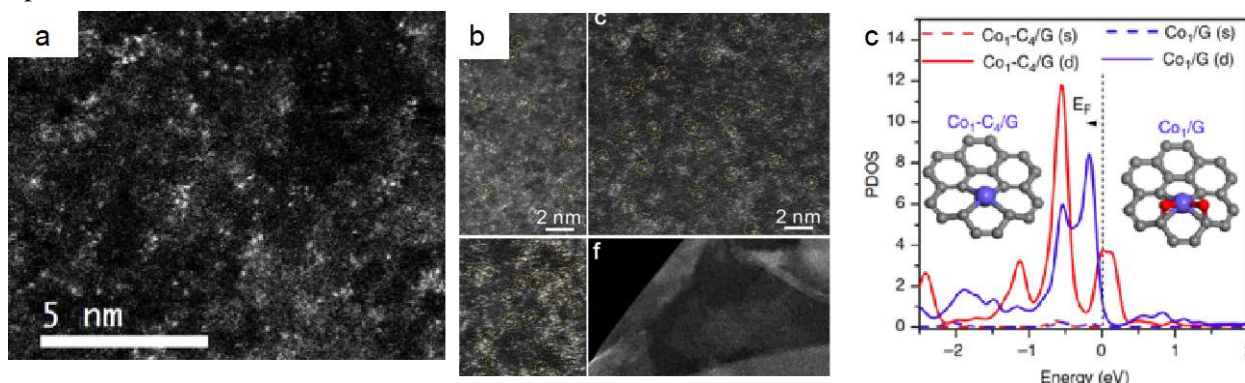


Figure 1. (a) Z-contrast image of Co SAC. (b) EELS showing O associated with the Co atoms. (c) Theoretical simulation of a Co atom (blue ball) with and without O (red balls), showing their respective partial density of states (blue and red curves). The presence of O uncovers the Co d orbitals at the Fermi energy. [2]

Another example of a Co-SAC is using porous nitrogen-doped carbon nanoflake arrays, which are synthesized from a Co-metal-organic-framework (MOF) precursor, followed by acid leaching to remove Co nanoparticles and create extra porosity and active surface area.[3] Interestingly, these SACs show a lower oxygen evolution reaction (OER) over potential and higher oxygen reduction reaction (ORR) saturation current than the Co nanoparticle catalysts and have been used as the air cathode in a solid-state Zn-air battery.[3]

Piezoelectric materials translate electrical energy into mechanical strain, and vice versa, finding broad application as electronic and electro-mechanical devices. Most materials in current use contain lead, so the development of suitable lead-free alternatives is urgently required. It is well known that giant responses occur near structural phase boundaries, but the atomistic understanding of the origin of the response has been lacking. By employing atomic-resolution polarization mapping we can uncover the general structural origin of the giant response, a coexistence of ferroelectric phases inside nanodomains allowing gradual polarization rotation between them in response to the applied field. Combined with systematic density functional calculations, we have significantly enhanced the properties of (K,Na)NbO₃ and BaTiO₃ based lead-free piezoceramics.[4-6]

Thermoelectric materials translate electrical energy into thermal energy, and vice versa, and

also is O; it is these proximal O atoms that expose partially-filled Co-d orbitals, resulting in the excellent catalytic activity.

hold promise for solid-state refrigeration and harvesting electric power from waste heat. Structural defects have a major influence on thermal and electrical transport properties. [7] Nanostructuring has been widely used to enhance thermoelectric properties, however, atomic-scale defects have been difficult to quantify via traditional methods. The improved sensitivity of aberration-corrected STEM has now allowed the direct observation of intrinsic Pb vacancies and extrinsic Cu interstitials in PbTe thermoelectric (Fig. 2), revealing the critical roles of Cu for the simultaneous optimization of phonon and carrier transport. [8]

Similar structural origins are proposed for the new-generation “phonon glass, electron crystal” materials such as SnSe and CoSb₃. Recently, we have shown that doping S into Se sites in SnSe markedly improves performance, representing an important step toward low-cost, earth-abundant, and environmentally friendly thermoelectrics. [9]

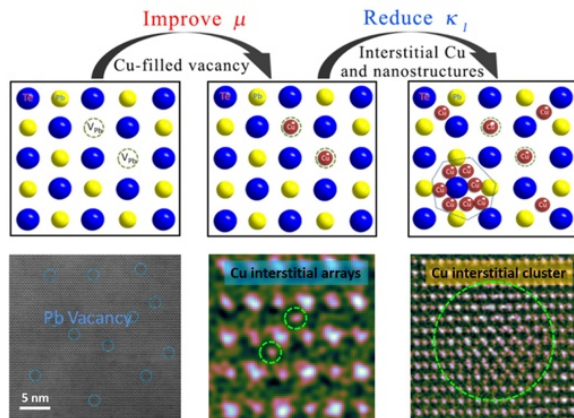


Figure 2. Top: Schematic showing the roles of Cu in PbTe, filling the intrinsic Pb vacancies to enhance carrier mobility and reduce the lattice thermal conductivity through scattering all-wavelength phonons via forming interstitials, clusters and precipitates. Bottom, direct imaging of the defects.[8].

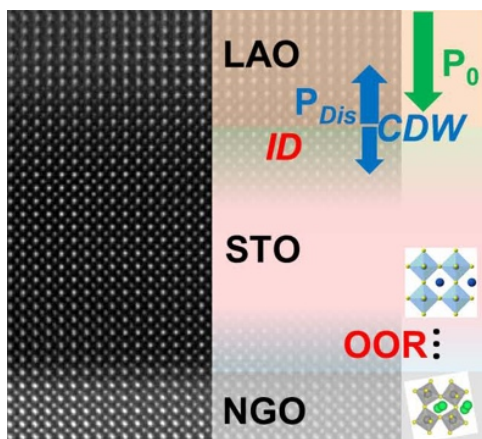


Figure 3. By scanning transmission electron microscopy and electron energy loss spectroscopy, tail-to-tail charged domain walls (CDW), are revealed in $\text{LaAlO}_3/\text{SrTiO}_3/\text{NdGaO}_3$ heterostructures. The strong correlation between the domain wall and interface interdiffusion (ID), plus oxygen octahedral rotation (OOR) determine the complicated SrTiO_3 thickness dependent transport properties. [11]

Finally, complex oxides offer new functionality through the interplay of charge, spin, orbital, and lattice degrees of freedom, as well as oxygen vacancies, and represents the key to boosting device performance. The microscope can track key parameters unit cell by unit cell, including vacancy concentration, valence, oxygen octahedral rotations, and ferroelectric

displacements, enabling these complex phenomena to be unraveled unambiguously and revealing the underlying physics. Examples will include generation of an ultrathin ferromagnetic insulator at a $\text{LaMnO}_3/\text{SrTiO}_3$ interface,[10] and the emergence of charged domain walls in $\text{LaAlO}_3/\text{SrTiO}_3/\text{NdGaO}_3$ heterostructures (Fig. 3).[11]

CONCLUSION

A wide variety of materials are now able to be studied at their atomic level to provide fundamental insight into the origin of their structure-property relations and revealing new opportunities to engineer their properties towards improved functionality.

Acknowledgment

The authors acknowledge funding from the Ministry of Education, Singapore, under Tier 2 grants 2017 (R-143-000-A06-112), MOE2015-T2-2-094, MOE2017-T2-1-129, MOE2017-T2-2-139 and Singapore National Research Foundation under the Competitive Research Programs (CRP Awards No. NRF-CRP15-2015-01).

References

- [1] P Nellist and S Pennycook, *Science* 274, (1996) 413-415.
- [2] H Yan et al., *Nature Communications* DOI: 10.1038/s41467-018-05754-9 (2018).
- [3] W Zang et al., *ACS Catal*, 8, (2018) 8961-8969.
- [4] T. Zheng, H. Wu, et al., *Energy Environmental Science*, 10, (2017) 528–537.
- [5] B. Wu, H. Wu, et al., *Journal of the American Chemical Society*, 138, (2016) 15459–15464.
- [6] C. Zhao, H. Wu, et al., *J. Am. Chem. Soc.* 140, (2018) 15252–15260.
- [7] X. Zhang, D. Wang, H. Wu, et al., *Energy and Environmental Science*, 10, (2017) 2420-2431.
- [8] Y. Xiao, H. Wu, et al., *Journal of the American Chemical Society*, 139, (2017) 18732.
- [9] W. He et al., *Science*, accepted (2019).
- [10] M. Li, et al., *Adv Mater*, 6, 1901386–8(2019).
- [11] M. Li, et al., *Adv Mater*, DOI: 10.1002/adfm.201906655 (2019).

BIOGRAPHY



Stephen J. Pennycook is a Professor in the Materials Science and Engineering Dept., National University of Singapore, an Adjunct Professor in the University of Tennessee and Adjoin Professor in Vanderbilt University, USA. Previously, he was Corporate Fellow in the Materials Science and Technology Division of Oak Ridge National Laboratory and leader of the Scanning Transmission Electron Microscopy Group. He completed his PhD in physics at the Cavendish Laboratory, University of Cambridge in 1978. Since then he has been actively pursuing the development and materials applications of atomic resolution Z-contrast microscopy and electron energy loss spectroscopy. Pennycook is a Fellow of the American Physical Society, the American Association for the Advancement of Science, the Microscopy Society of America, the Institute of Physics and the Materials Research Society. He has received the Microbeam Analysis Society Heinrich Award, the Materials Research Society Medal, the Institute of Physics Thomas J. Young Medal and, the Materials Research Society Innovation in Characterization Award and the Microscopy Society (Singapore) Antonie van Leeuwenhoek Award. He has 38 books and book chapters, over 600 publications in refereed journals and has given over 290 invited presentations. His latest book is “Scanning Transmission Electron Microscopy.”

CURRENT STATUS OF RESEARCH AND APPLICATIONS OF CARBON NANOMATERIAL

Bui Hung Thang¹, Tran Van Hau^{1,5}, Nguyen Trong Tam², To Anh Duc^{2,4,5}, Mai Thi Phuong¹, Pham Van Trinh¹, Nguyen Van Chuc¹, Cao Thi Thanh¹, Nguyen Huu Hong³, Nguyen Tuan Hong³, Phan Ngoc Hong³, Phan Hong Khoi³, and Phan Ngoc Minh^{1,2,3}

¹ Institute of Materials Science, Vietnam Academy of Science and Technology,
18 Hoang Quoc Viet Str., Cau Giay District, Hanoi, Vietnam

² Graduate University of Science and Technology, Vietnam Academy of Science and Technology,
18 Hoang Quoc Viet Str., Cau Giay District, Hanoi, Vietnam

³ Center for High Technology Development, Vietnam Academy of Science and Technology,
18 Hoang Quoc Viet Str., Cau Giay District, Hanoi, Vietnam

⁴ Vietnam National Space Center, Vietnam Academy of Science and Technology,
18 Hoang Quoc Viet Street, Cau Giay District, Hanoi, Vietnam

⁵ University of Engineering and Technology, Vietnam National University - Hanoi
144 Xuan Thuy Str., Cau Giay District, Hanoi, Vietnam

Email: pnminh@vast.vn

ABSTRACT

In this presentation, we try to review the current status of research and applications of carbon nanomaterials in various fields such as environment, medicine, construction, metallurgy, agriculture, etc. We also focus on the obtained results of our group at Vietnam Academy of Science and Technology in these fields. Detail results of our research in nanofluids for high power electronic devices such as CPU of the computer, LED street lighting, marine vessel, solar powered stirling engines for electric generation, electrodeposition ... will be presented.

Keywords: Graphene, carbon nanotubes, nanofluids, electrodeposition

BIOGRAPHY



Prof. Dr. Phan Ngoc Minh completed his PhD of solid state physics at Institute of Physic, Vietnam Academy of Science and Technology (VAST) in 1996; PhD in Engineering at Tohoku University, Japan in 2001.

From 2001-2004 he worked as a Post-Doctoral and then Assistant Professor at Tohoku University, Japan in the field of Nanotechnology. He became Associate Professor and Professor of Physics of VAST in 2007 and 2016, respectively.

Now, he is now Vice President of Vietnam Academy of Science and Technology, President of the University Council - University of Science and Technology of Hanoi (USTH, VAST). He is a Professor and Senior Researcher at Laboratory of Carbon nanomaterials, Center of Applications & Development of Technology, Institute of Materials Science; Center of Advanced Materials, Center of High Technology Development of the Academy. He is also a Editorial Board Member of the Journal of Advances in Natural Sciences: Nanoscience and Nanotechnology, VAST.

INVITED TALKS

NANOFABRICATION TECHNIQUES
(NFT)

ROAD TO THE DEVELOPMENT OF MECHANICAL SENSORS USING PIEZORESISTIVE EFFECT

Susumu Sugiyama

Research Organization of Science and Technology, Ritsumeikan University
1-1-1, Nojihigashi, Kusatsu City, Shiga Pref. 525-8577, Japan
Email: sugiyama@fc.ritsumei.ac.jp

ABSTRACT

The road to the development of mechanical sensors using semiconductor piezoresistive effect began with the theoretical grounds and experimental results on resistors of Ge and Si single crystals in 1954. After that, it progressed to practical application research of pressure sensor, accelerometer, force sensor, tactile sensor and so on. At present, the basic type of widely used Si pressure sensor has been used diffused lead type on Si planar technology presented in 1970. A sensitivity temperature compensation method has been developed by using the constant current drive method. It has been achieved good temperature compensation of $\pm 0.01\%/^{\circ}\text{C}$. With the adoption of semiconductor pressure sensors for automobiles with severe environment of use, made progress in practical development of various mechanical and physical sensors. As other sensor developments applying the piezoresistive effect that I have been involved with, a seat pressure sensor, a micro diaphragm pressure sensor of square diaphragm of $80\ \mu\text{m}$, a full integrated pressure sensor, a pressure image sensor array of 32×32 (1024) and a 6-degree-of-freedom force/moment sensor are explained.

INTRODUCTION

When talking about the path of development of piezoresistive semiconductor mechanical sensors, we must go back to the birth of semiconductor strain gauges. In 1954 C.S. Smith presented theoretical and experimental results on the piezoresistance of Ge and Si [1]. Application of these results to the development of strain gauges was promoted [2] [3]. The origin of the piezoresistive semiconductor pressure sensor is the Ge semiconductor strain gauge adhesive pressure sensor announced by Igarashi et al. in 1964 [4]. This concept became the starting point, and pressure sensors and acceleration sensors were developed. Furthermore, it has come to be developed as a pressure sensor for medical diagnosis and measurement. Currently, the basic type of semiconductor pressure sensor widely used is a diffused type using Si planar technology pressure sensor developed by Sugiyama et al. in 1970 [5]. Ten years later, in 1981, a semiconductor intake pressure sensor was successfully installed in a car as a semiconductor sensor for automobiles. Used in the electronic fuel injection (EFI) system of Toyota Motor Corporation, which cleared exhaust gas regulations in 1978 in Japan. This track record of mounting semiconductor

pressure sensors in automobiles has given us confidence in industrial applications of piezoresistive mechanical sensors, and we have come to this day through many technological innovations with high reliability.

In this paper, I would like to look back on the development of piezoresistive mechanical sensors and help create new technologies in the future.

SILICON PRESSURE SENSOR

Diffused type pressure sensor: By applying Si planar technology, a pressure sensor was developed in which four p-type piezoresistive elements were formed on an n-type Si substrate by impurity diffusion in 1970 [5]. Since no organic adhesive is used, creep characteristics and temperature hysteresis characteristics have been dramatically improved, and stable characteristics can be exhibited. In addition, mounting became easier and variations in mass productivity and performance were improved. Since the pressure medium is in direct contact with the pressure receiving diaphragm, the electrical components must be electrically isolated from the pressure medium. In response to this requirement, a diffusion lead structure was devised in 1975 [6]. The upper surface of the pressure receiving part was covered with a

chemically stable SiO₂ film, and a diffusion resistance piezoresistive element and a low resistance diffusion lead connecting the electrodes were provided thereunder. A structure with no Al wiring was realized in the mechanical strain generator (Fig. 1). By using this structure, differential pressure can be measured. Furthermore, by adopting diffusion leads, thermal hysteresis was improved and stable temperature characteristics could be obtained. The diffusion lead structure is now widely used as a basic structure of a sensor having a movable part such as an acceleration sensor as well as a pressure sensor.

Sensitivity temperature compensation:

The sensitivity of the piezoresistor that is the detection element of the pressure sensor, that is, the temperature characteristic of the piezoresistive effect has a relatively large negative temperature coefficient of several thousand ppm. On the other hand, the resistance value has a positive temperature coefficient. By using this relationship, a decrease in sensitivity due to a temperature increase can be compensated by an increase in the voltage applied to the bridge by constant current driving. It was found that the surface impurity (Boron) concentration of p-type piezoresistive element was about $3 \times 10^{20} \text{ cm}^{-3}$. In 1976 good sensitivity temperature compensation of $\pm 0.01\% / ^\circ\text{C}$ was realized in the temperature range of -20°C to 80°C [7]. This constant-current self-sensitivity temperature compensation method is widely used as the basic type of silicon pressure sensor, similar to the diffusion lead structure described above (Fig. 2).

In 1981, the semiconductor intake pressure sensor succeeded in mounting the automobile, it was adopted in the electronic fuel injection (EFI) system, and it could clear the exhaust gas regulation [8]. With the adoption of semiconductor pressure sensors for automobiles with severe environment of use, Si piezoresistive pressure sensors became the basic form and made progress in practical development of various mechanical sensors. Figure 3 shows the measurement items of the mechanical and physical sensors installed in the latest automobile with reference.

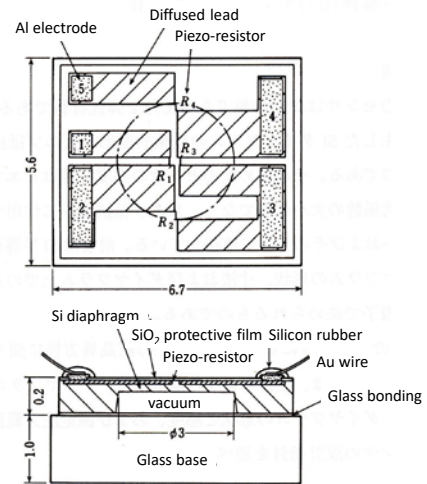


Figure 1. Basic type Si pressure sensor using Si planar technology.

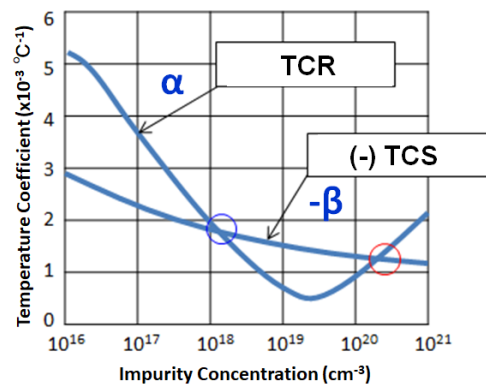


Figure 2. Negative temperature coefficient of sensitivity of the piezoresistive element can be canceled by using positive temperature coefficient of resistance.

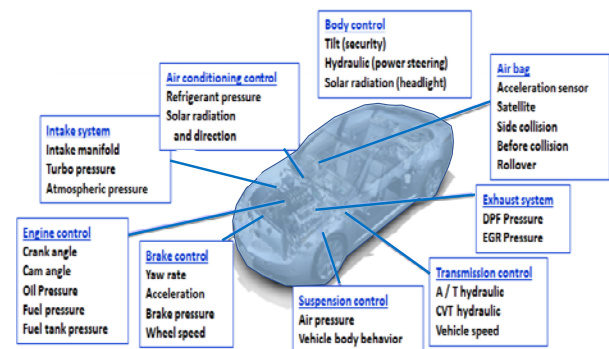


Figure 3. Measurement items of the mechanical and physical sensors installed in a latest automobile

MICRONIZATION

Micro diaphragm pressure sensor: A micro-diaphragm pressure sensor that can be manufactured by single-sided processing was developed 1986 (Fig. 4) [9]. In the center of the chip, a square diaphragm is formed with a 40

μm to $80 \mu\text{m}$ square Si_3N_4 film with a thickness of $2 \mu\text{m}$. As a pressure reference chamber, a pyramidal cavity is formed by anisotropic etching. The etching hole provided in the periphery of the diaphragm is an absolute pressure type that is finally sealed by plasma CVD. Four polysilicon piezoresistive elements are arranged on the diaphragm to form a full bridge. The output sensitivity was 1 mV/V at a pressure of 500 kPa .

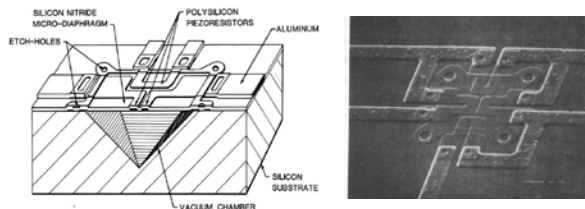


Figure 4. Micro diaphragm pressure sensor fabricated by single side processing. A square Si_3N_4 diaphragm of $80 \mu\text{m}$ is formed. A pyramidal cavity is formed by anisotropic etching.

Surface micro diaphragm pressure sensor: A micro pressure sensor by surface micro-machining using sacrificial layer etching was also devised and prototyped in 1987 (Fig. 5) [10]. The difference from the micro-diaphragm pressure sensor is that the pressure reference chamber is formed by polysilicon sacrificial layer etching with a thickness of $2 \mu\text{m}$ and vacuum sealing is performed at the center. The circular diaphragm has no stress concentration and can reduce the amount of leakage in vacuum sealing. A diaphragm with a diameter of $100 \mu\text{m}$ or less was stably formed.

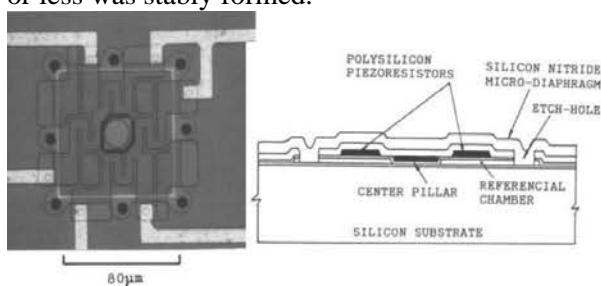


Figure 5. Surface micro diaphragm pressure sensor

INTEGRATION

Integrated pressure sensor with amplifier: In the 1980s, a series of monolithic temperature compensation circuits and amplifiers were announced. In 1983, an integrated pressure sensor with both analog and digital (frequency output) outputs was developed, which included a

frequency converter IC in addition to a bipolar amplifier circuit [11].

Pressure imager: A pressure image sensor that can measure the two-dimensional distribution of pressure by arranging sensor elements with the same characteristics in a 32×32 (1024) array was developed in 1987 (Fig. 6) [10]. A $100 \mu\text{m}$ square micro diaphragm is formed in each detection unit by single-sided processing technology. Four polysilicon piezoresistive elements are bridged on the micro diaphragm. Each detection unit includes a CMOS logic circuit. The detection units are arranged and configured at intervals of $250 \mu\text{m}$, and a CMOS signal processing circuit is formed around the array. The pressure sensitivity was about $100 \text{ mV} / (\text{g}/\text{mm}^2)$, and the readout speed was $16 \text{ ms} / \text{frame}$ at a clock frequency of 4 MHz .

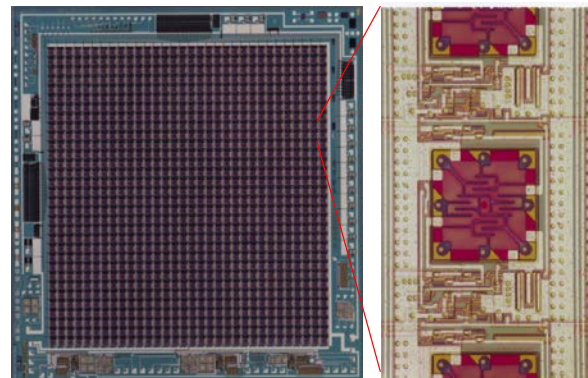


Figure 6. Pressure imager has been developed by arranging sensor elements in an array of 32×32 (1024). Micro diaphragms of $100 \mu\text{m}$ square were formed with CMOS signal processing LSI.

One-chip integrated pressure sensor: A complete one-chip pressure sensor was developed in 1989 with a diffusion lead type, bipolar amplifier, and SiCr thin film trimming resistor, which are the basic types of silicon pressure sensors (Fig. 7) [12]. For sensitivity temperature compensation, the impurity diffusion concentration of two types of diffusion resistors is optimally adjusted, and a wide range of sensitivity compensation is performed by constant voltage drive. This technology has been developed for mass production and used in automotive products.

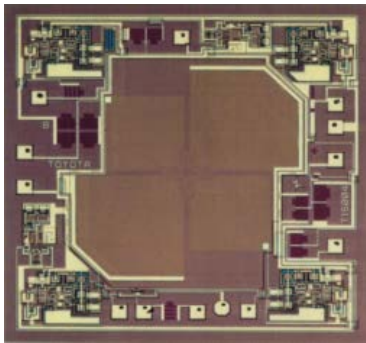


Figure 7. One-chip integrated pressure sensor with amplifiers, a temperature compensator and offset trimming resistors of IC

Force/moment sensor: A six-degree-of-freedom force/moment sensor measuring three-directional forces and three-axis moments by forming cross-shaped beams fixed at the center of the chip and forming 20 piezoresistive elements on the crossed beam has been developed. This sensor is applied to the robot's fingertip force control and fluid flow analysis (Fig. 8) [13].

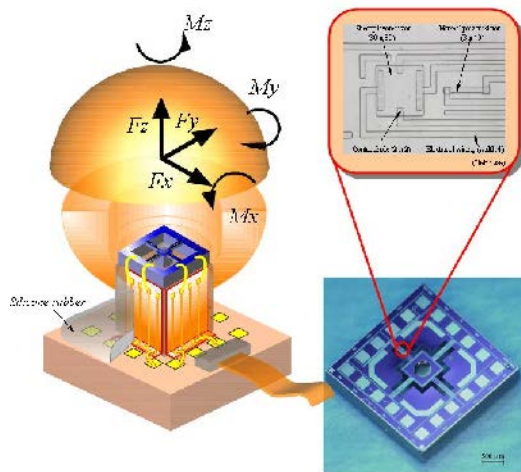


Figure 8. Six-degree-of-freedom force/moment sensor formed a cross-shaped beam fixed at the center of the chip at both ends with 20 piezoresistive elements on the crossed beam has been developed.

CONCLUSION

The road to technological progress of piezoresistive semiconductor mechanical sensors was observed. It has a history of 50 years. The driving force for technological development can be said that the first is innovation in semiconductor manufacturing technology and the second is the development of micromachining. Today, the world's production volume of semiconductor sensors reaches

several billions a year. In the future, we must face many global issues to realize a sustainable society. Sensors will occupy an increasingly important position as key devices.

References

- [1]. C.S. Smith, Piezoresistive effect in germanium and silicon, Phys. Rev. 94 p42 (1954)
- [2]. F. Miyamoto and I. Igarashi: "Elastic Deformation and Variation of Conductivity in Germanium at Room Temperature", Research Reports of Kogakuin University, No.3, pp.1-5 (1956) (in Japanese)
- [3]. I. Igarashi: "Strain Gauges Utilizing the Piezoresistive Effect", Journal of JSNDI, Vol.9, No.5, pp.259-263 (1960) (in Japanese)
- [4]. T. Chiku and I. Igarashi: "Semi-Conductor Strain Gage Elements Applied to Some Measurements", Journal of Society of Automotive Engineers of Japan, Vol.18, No.9, pp.706-711(1964) (in Japanese)
- [5]. S. Sugiyama, K. Hayakawa and H. Nakamura: "Diffused Type Pressure Sensors", Proceedings of The13rd Automatic Control Union Conference, pp. 333-334 (1970) (in Japanese)
- [6]. H. Nakamura, S. Sugiyama, K. Hayakawa and I. Igarashi: "A Pressure Transducer Using Silicon Piezoresistive Effect", Technical Report of The Institute of Electronics and Communication Engineers, SSD 75-54, pp.57-66 (1975) (in Japanese)
- [7]. K. Hayakawa, H. Nakamura, S. Sugiyama and I. Igarashi: "A Self Temperature Compensated Semiconductor Pressure Sensor", Journal of JSNDI, Vol.25, No.2, pp.132-133(1976) (in Japanese)
- [8]. TOYOTA CARELECTRONICS, Press Information July (1991) (in Japanese)
- [9]. S. Sugiyama, T. Suzuki, K. Kawahata, K. Shimaoka, M. Takigawa & I. Igarashi, "Micro-Diaphragm Pressure Sensor", Proc. of the Int. Electron Devices Meeting (IEDM'86), Los Angeles, pp.184-187 (1986).
- [10]. S. Sugiyama, K. Kawahata, M. Abe, H. Funabashi & I. Igarashi, "High-Resolution Silicon Pressure Imager with CMOS Processing Circuits", Tech. Digest of the 4th Int. Conf. on Solid-State Sensors and Actuators (Transducers'87), pp.444-447, June 2-5 (1987)

- [11]. S. Sugiyama, M. Takigawa, I. Igarashi:
“Integrated Piezoresistive Pressure Sensor
With Both Voltage and Frequency Output”,
Sensors and Actuators, Vol. 4 pp. 113-
120(1983)
- [12]. S. Sugiyama, S. Yamashita, H.
Funabashi, K. Shimaoka, M. Takigawa & I.
Igarashi, “One-Chip Integrated Pressure
Sensor”, Trans. IEE of Japan, Vol.109-C,
No.12, pp.855-861 (1989) (in Japanese).
- [13]. Dao Viet Dzung, Toshiyuki Toriyama,
John Wells and Susumu Sugiyama, “Design
of a Micro Multi-Axis Force-Moment
Sensor”, Trans. IEE of Japan, Vol.122-E,
No.1, pp.35-41 (2002).

BIOGRAPHY



Susumu SUGIYAMA, Dr. Eng

Affiliation 1: Ritsumeikan University, JAPAN

Position: Professor Emeritus

Senior Researcher, Research Organization of Science and Technology

Affiliation 2: Support Organization for Research on Industrial Science and Technology

Position: Representative Director

Affiliation 3: Research Labs, Saigon Hi-Tech Park, VIETNAM

Position: Scientific Director.

Research Interests: MEMS, Micro/Nano Fabrication, Micro Sensor

Email: sugiyama@fc.ritsumei.ac.jp

Website: <http://www.ritsumei.ac.jp/se/~sugiyama/member/sugiyama2e.html>

Prof. S. Sugiyama was born in Nagoya, Japan in 1946. He received the B. S. Degree in Electrical Engineering from Meijo University, Nagoya, Japan, in 1970, and the Dr. Eng. Degree from Tokyo Institute of Technology, Tokyo, Japan, in 1994. From 1965 to 1995 he has been with Toyota Central Research & Development Laboratories, Inc., Aichi, Japan, where he served as the Chief of Silicon Devices Lab. (1992-1993), Head of Device Development Section (1993-1995). Since 1995 he has been with Ritsumeikan University, Shiga, Japa, where he served as a Prof. of College of Science & Engineering (1995-2007), Vice Director of Synchrotron Radiation Center (1998-2002), Director of Research Institute for Micro System Technology (2000-2010), Project Leader of 21st Century COE Program, MEXT- Japan (2002-2007), Prof. of Ritsumeikan Global Innovation Research Organization (2007-2015), Chair Prof. of Research Organization of Science and Technology (2015-2017). He had served a Director Executive, Japan Institute of Electronics Packaging (2007-2011), President of Sensors and Micro Machine Society, The Institute of Electrical Engineers of Japan (2008-2010), JICA Expert / Dispatch Researcher of Science and Technology of JSPS, Sri Lanka Institute for Nano Tech. (2009-2011), Chief Research Scientist, BEANS Research Association (NEDO, Japan) (2010-2011), Executive Principal Research Scientist, NMEMS Technology Research Organization (NEDO, Japan) (2011-2013), Project Researcher, Information and Robot Technology Research Initiative, The University of Tokyo (2015-2019). He had served as Editor-in Chief of the International Journal "Sensors and Materials" (1995-2012). Since 2013 he has become the Representative Director, Support Organization for Research on Industrial Science and Technology. Since 2017, he has become the scientific director of the Research Labs of Saigon Hi-Tech Park, Ho Chi Minh City, Vietnam.

MEMBER:

Fellow of The Institute of Electrical Engineers of Japan (IEEJ)

Japan Society of Applied Physics (JSAP)

The Japan Society of Mechanical Engineers (JSME)

SELECTED AWARDS

- [1] Kyoto Governor's Appreciation Letter "Small and Medium-sized Enterprises Special Technical Guidance", 2012
- [2] The Honorable Achievement Award, The Institute of Electrical Engineers of Japan, 2012.
- [3] The Research Distinguished Person Prize, Minister of Education, Culture, Sports, Science and Technology, Japan, 2004.
- [4] The Best Teacher Award, Ritsumeikan University, 2003.
- [5] The Excellent Technical Activity Special Prize, The Institute of Electrical Engineers of Japan, 2000.

FABRICATION OF Mn-(Bi,Ga) BASED HARD MAGNETIC NANOCOMPOSITES

Huy Dan Nguyen^{1,2,*}, Jung-Goo Lee³, Thi Thanh Pham^{1,2}, Mau Lam Nguyen⁴, Huy Ngoc Nguyen¹, Thi Kim Oanh Dinh², Hai Yen Nguyen^{1,2}, Dang Thanh Tran^{1,2}

¹Institute of Materials Science, Vietnam Academy of Science and Technology, 18 Hoang Quoc Viet, Cau Giay, Hanoi, Vietnam;

²Graduate University of Science and Technology, Vietnam Academy of Science and Technology, 18 Hoang Quoc Viet, Cau Giay, Ha Noi, Vietnam;

³Korea Institute of Materials Science, 797 Changwondaero, Seongsan-gu, Changwon, Gyeongnam, 51508, Republic of Korea;

⁴Hanoi Pedagogical University No.2, Xuan Hoa, Vinh Phuc, Vietnam

*Email: danh@ims.vast.ac.vn

ABSTRACT

The hard and soft magnetic nanoparticles of Mn-(Bi,Ga) and Fe-Co, respectively, were prepared by using a high energy ball milling method. These nanoparticles were then mixed together with different ratios and subsequently annealed in various conditions of temperature and time to make nanocomposite magnets. The coercivity H_c and maximum energy product $(BH)_{max}$ of these magnets depend on the nanoparticle size and the ratio of the hard/soft magnetic phases. The annealing process plays an important role for exchange-coupling between the hard and soft magnetic phases. With size in a range of 40 - 60 nm, the Mn-(Bi,Ga) nanoparticles reveal high coercivity ($H_c > 12$ kOe) to be a potential rare-earth-free hard magnetic phase for producing nanocomposite magnets. Quite high coercivities, $H_c > 4$ kOe, and maximum energy products, $(BH)_{max} > 4$ MGOe, have been achieved for this kind of rare-earth-free nanocomposite magnets.

Keywords: Magnetic nanoparticles, nanocomposite magnets, rare-earth-free magnets, high coercivity, high energy ball milling method.

INTRODUCTION

In fact, the hard magnetic nanocomposites are widely applied because of their mechanical, physical and chemical properties, which are different from bulk materials with the large particle sizes. Besides, the exchange-spring interaction effect between the hard and soft magnetic phases is combined by the values of the high saturation M_s of the soft magnetic phase and the large coercivity H_c of the hard magnetic phase to create new materials, which exhibit the high value of the maximum energy product $(BH)_{max}$ [1].

It is well known that the physical properties of the materials are strongly decided by their microstructure. Meanwhile, the technological conditions such as the ratio of magnetic phases, annealing process greatly influence on the structure and the magnetic interactions between the phases. Therefore, the investigations of the technological factors to create the hard magnetic nanocomposites with high performance has

always been interested [2-4]. It is also known that rare earth hard magnetic materials such as Nd-Fe-B and Sm-Co alloys exhibit the large coercivity H_c and high maximum energy product $(BH)_{max}$. However, the rare earth elements are expensive and limited resources. Thus, it is necessary to research and develop the rare-earth-free hard magnetic materials.

In this work, the Mn-(Bi,Ga) based hard magnetic phases have been selected to create the magnetic nanocomposite. For Mn-Bi alloy, theoretically, it has a quite large maximum energy product $(BH)_{max}$ of 18 MGOe and a high value of coercivity H_c due to the large magnetocrystalline anisotropy ($1,6 \times 10^6$ J/m³) [6]. A high coercivity of 18 kOe has been observed at 550 K based on the MnBi melt-spun ribbons, which is very useful for high temperature applications [7]. According to Yang *et al.* [8], the coercivity of MnBi alloy rapidly increases with temperature in a range of 150 - 400 K, and coercivity larger than 20 kOe can be expected at higher temperature. For examples,

Rao *et al.* [9] observed $H_c = 26$ kOe at 550 K for MnBi ribbons.

Another Mn based alloy, Mn-Ga system, it exhibits complicated binary phase diagram and is also suggested that MnGa and Mn₃Ga alloys have potential for permanent magnets. According to Hyh *et al.* [10], magnetic properties of Mn_xGa ribbons are assigned to the competing ferromagnetic coupling between Mn moments in the regular L1₀-MnGa lattice sites and antiferromagnetic coupling with excess Mn occupying Ga sites. Unfortunately, the L1₀ phase is a metastable one. Sawada *et al.* [12] reported that the hard magnetic properties of Mn₃Ga with the D0₂₂ structure (a modified of the L1₀ structure) can be improved by an addition of a small amount of Cu, Al, Cr, Fe... Accordingly, the coercivity of materials will be increased to over 20 kOe.

Recently, the Fe₆₅Co₃₅ nanoparticles have attracted the attention of the materials scientists. Previous reports have shown that they exhibit some excellent soft magnetic properties such as high Curie temperature and high value of the saturation ($M_s \sim 240$ emu/g) [13]. Besides, the Fe₆₅Co₃₅ nanoparticles can be easily fabricated by several methods such as high energy ball milling [14], wet chemical processes [15, 16], which is convenient to make a composite of the hard/soft magnetic phases. Therefore, in this work, the Fe₆₅Co₃₅ nanoparticles have been used as a soft magnetic material to combine with one of the hard magnetic materials of Mn-(Bi,Ga) based nanoparticles, namely Mn₅₀Bi₅₀ and Mn₆₅Ga₂₀Al₁₅. The wt% ratio of the hard/soft magnetic phase will be changed to find out the good hard magnetic nanocomposites. Our purpose is that the rare-earth-free magnets can be produced by cost-effective and sustainable manufacturing processes, useful for high temperature applications.

EXPERIMENTAL

The alloy ingots of Mn₅₀Bi₅₀, Mn₆₅Ga₂₀Al₁₅ and Fe₆₅Co₃₅ were prepared from high purity (99.9%) metals of Mn, Bi, Ga, Al, Fe and Co by an arc-melting method in argon gas. Herein, Mn is a strongly evaporating element during melting process. The weight of Mn metal was thus increased 15% before arc-melting. These alloy ingots were then used as the starting materials for high energy ball milling on the SPEX 8000D equipment with the different milling times (t_m). Accordingly, we obtained the nanopowders of

Mn₅₀Bi₅₀, Mn₆₅Ga₂₀Al₁₅ and Fe₆₅Co₃₅. The nanopowders of Mn₅₀Bi₅₀ and Mn₆₅Ga₂₀Al₁₅ were divided into two parts, one was as-milled, and the rest was annealed in argon gas at 250°C in 2 h for Mn₅₀Bi₅₀ and at 650°C in 0.25 h for Mn₆₅Ga₂₀Al₁₅. Both of them were then mixed well with the Fe₆₅Co₃₅ nanopowder with different wt% to create the nanocomposites. Finally, these nanocomposites were annealed in argon at 250°C in 2 h for Mn₅₀Bi₅₀/Fe₆₅Co₃₅ and at 650°C in 0.25 h for Mn₆₅Ga₂₀Al₁₅/Fe₆₅Co₃₅. For convenience, these samples are denoted according to Table 1.

Table 1. Denoted samples and their annealing process.

Samples	Components	Technology conditions
MB-AM	Mn ₅₀ Bi ₅₀	As-milled
MB-A	Mn ₅₀ Bi ₅₀	Annealed 250°C/2h
MG-AM	Mn ₆₅ Ga ₂₀ Al ₁₅	As-milled
MG-A	Mn ₆₅ Ga ₂₀ Al ₁₅	Annealed 650°C/0.25h
FC	Fe ₆₅ Co ₃₅	As-milled
MB-AM/FC	Mn ₅₀ Bi ₅₀ /Fe ₆₅ Co ₃₅	wt% FC = 2, 4, 6, 8%
MB-A/FC	Mn ₅₀ Bi ₅₀ /Fe ₆₅ Co ₃₅	Annealed 250°C/2h
MG-AM/FC	Mn ₆₅ Ga ₂₀ Al ₁₅ /Fe ₆₅ Co ₃₅	wt% FC = 5, 10, 15, 20%
MG-A/FC	Mn ₆₅ Ga ₂₀ Al ₁₅ /Fe ₆₅ Co ₃₅	Annealed 650°C/0.25h

The crystalline structure of all the samples was checked by an X-ray diffractometer (Equinox 5000 - Thermo Scientific) with the Cu-K_α radiation source ($\lambda = 1.5406$ Å). A field-emission scanning electron microscope (FESEM, S4800 - Hitachi) technique has been used to analyze the size and shape of the nanoparticles. The magnetic properties of the samples were investigated via the magnetization measurements on a vibrating sample magnetometer (VSM) with $H_{max} = \pm 12$ kOe and a pulsed field magnetometer (PFM) with $H_{max} = \pm 90$ kOe at room temperature.

RESULTS AND DISCUSSION

The X-ray diffraction (XRD) patterns of the separate hard and soft magnetic phases are presented in Fig.1. We found that the annealing process strongly influences on the crystallization and the formation of the desired phase. With the optimal conditions, characteristic XRD peaks of

the hard magnetic phases are appeared. Herein Mn-Ga-Al phase appears in MG-A sample in two types of the structure, $D0_{22}$ - Mn_3Ga and $D0_{19}$ - Mn_3Ga , Fig. 1(b). According to Liu *et al.* [17], the magnetic properties of $D0_{19}$ - Mn_3Ga structure is lower than that of $D0_{22}$ - Mn_3Ga one.

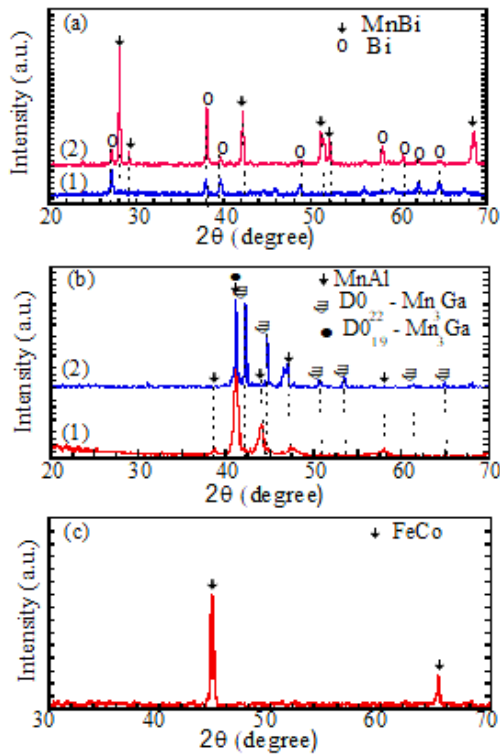


Figure 1. XRD patterns of the hard and soft magnetic phases: a) MB-AM (1) and MB-A (2); b) MG-AM (1) and MG-A (2); and c) FC samples.

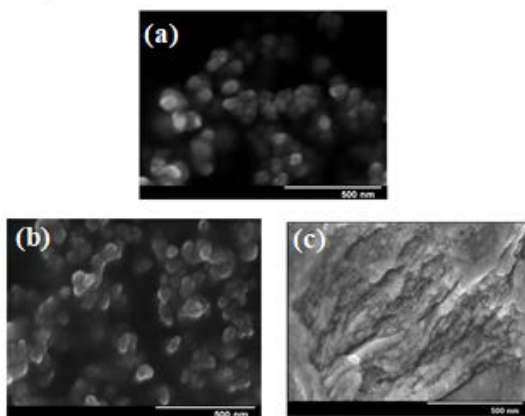


Figure 2. FESEM images of (a) MB-AM, (b) MG-AM, and (c) FC samples.

In this work, we thus believe that the magnetic properties of the hard magnetic phases are significantly enhanced after annealing. Fig. 1(c) shows the XRD pattern of FC sample.

There are two XRD peaks corresponding to $Fe_{65}Co_{35}$ phase, no the characteristic peaks of secondary phase. It means that FC sample is a single phase of $Fe_{65}Co_{35}$. Fig. 2 shows the representative FESEM images of the MB-AM, MG-AM, and FC samples. We can see all samples are nanoparticles. Their shape is spherical or pseudo-spherical. The size of particles is about 40 - 60 nm for MB-AM and MG-AM samples, Figs. 2(a) and 2(b). For FC sample, particles are smaller than that of MB-AM and MG-AM samples, and creating to clusters. However, we predict they are about 10 - 30 nm. The particle size of composite samples is almost unchanged. Thus, they are not shown here.

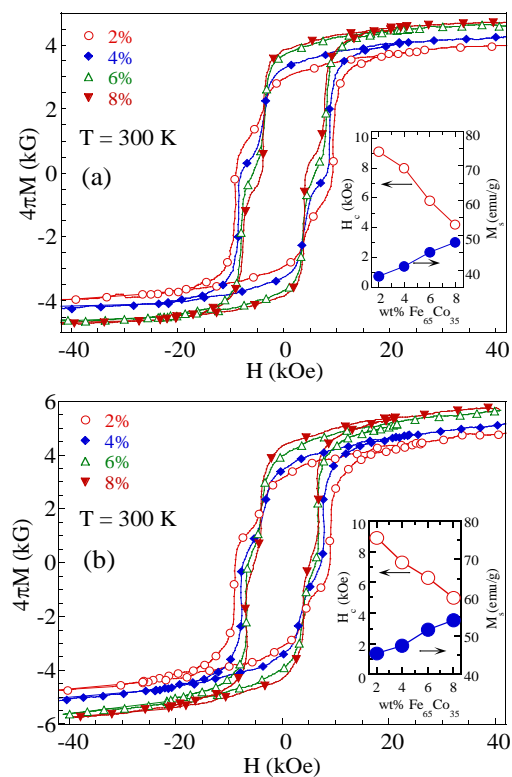


Figure 3. Hysteresis loops measured at 300 K of $Mn_{50}Bi_{50}/Fe_{65}Co_{35}$ nanocomposites with different $Fe_{65}Co_{35}$ concentrations. The insets present the change of H_c and M_s with wt% of $Fe_{65}Co_{35}$. (a) MB-AM/FC and (b) MG-AM/FC.

Figs. 3 and 4 show hysteresis loops of $Mn_{50}Bi_{50}/Fe_{65}Co_{35}$ and $Mn_{65}Ga_{20}Al_{15}/Fe_{65}Co_{35}$ nanocomposites, respectively, with different $Fe_{65}Co_{35}$ concentrations measured at 300 K. Clearly, these samples exhibit the hard magnetic characters. For each system, the value of M_s increases with an increasing of $Fe_{65}Co_{35}$ concentration, while the value of H_c decreases. This is related to the change in the ratio of the

hard/soft magnetic phases. It is completely understandable because the hard magnetic phases ($Mn_{50}Bi_{50}$ and $Mn_{65}Ga_{20}Al_{15}$) have the large values of H_c but low M_s , while the soft magnetic phase ($Fe_{65}Co_{35}$) has very small value of H_c but quite high M_s . The change of M_s and H_c with $Fe_{65}Co_{35}$ concentration in these systems has been determined and plotted in the insets of Figs. 3 and 4. Accordingly, H_c value decreases rapidly from 9 to 4 kOe, while M_s value increases from 38 to 48 emu/g when the soft magnetic phase concentration increased from 2 to 8% in MB-AM/FC samples, Fig. 3(a). For MB-A/FC samples, their tendency of changing in H_c is quite similar to MB-AM/FC samples ($H_c = 5 - 8.9$ kOe) but the value of M_s is higher than that of MB-AM/FC samples. The maximum M_s value of MB-A/FC samples is found to be 55 emu/g for 8% of $Fe_{65}Co_{35}$, Fig. 3(b).

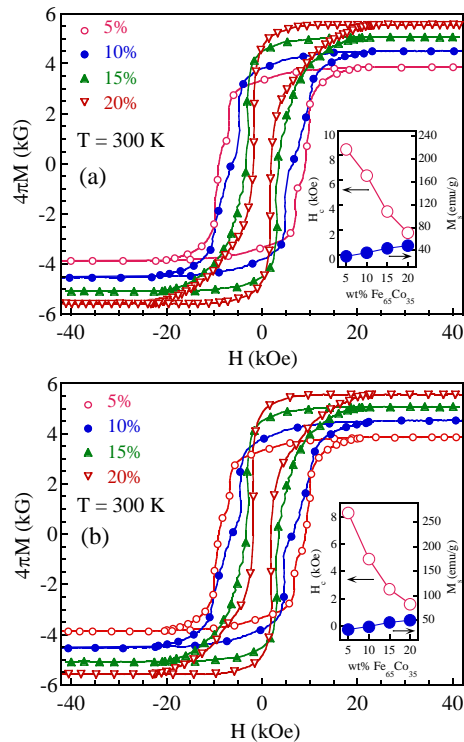


Figure 4. Hysteresis loops measured at 300 K of $Mn_{65}Ga_{20}Al_{15}/Fe_{65}Co_{35}$ nanocomposites with different $Fe_{65}Co_{35}$ concentrations. The insets present the change of H_c and M_s with wt% of $Fe_{65}Co_{35}$. (a) MG-AM/FC and (b) MG-A/FC.

Additionally, the hysteresis loops of samples exhibit the waists, which are related to the coexistence and competition of the hard and soft magnetic phases in the samples. The sunken level in these hysteresis loops increases with increasing the concentration of the soft magnetic

phase. According to theoretical models proposed by Skomski-Coey and Kneller-Hawig [18, 19], for magnetic nanocomposites, to achieve the excellent interactions between two hard and soft magnetic phases, the optimal particle size should be about 10 nm. Unfortunately, in this work, the particle size in our samples prepared by the high energy ball milling method is rather greater (they are about 40 - 60 nm). It means the size of the hard and soft magnetic particles is not optimal. Therefore, a part of the hard and soft magnetic particles has no interaction between them but exists independently.

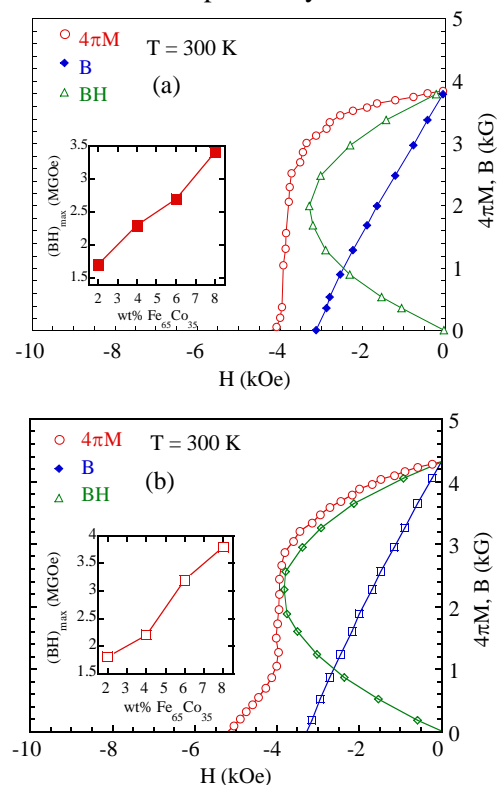


Figure 5. Magnetic characteristic curves obtained at 300 K of $Mn_{50}Bi_{50}/Fe_{65}Co_{35}$ nanocomposites with 8% $Fe_{65}Co_{35}$. The insets show the change of the maximum energy product $(BH)_{max}$ with various fractions of $Fe_{65}Co_{35}$.

(a) MB-AM/FC and (b) MB-A/FC.

Based on the hysteresis loops of the nanocomposites obtained above, we have determined their maximum energy product $(BH)_{max}$. Figs. 5 and 6 perform the representative magnetic characteristic curves of the nanocomposites with the highest content of the soft magnetic phase, 8 and 20 wt% $Fe_{65}Co_{35}$ for $Mn_{50}Bi_{50}/Fe_{65}Co_{35}$ and $Mn_{65}Ga_{20}Al_{15}/Fe_{65}Co_{35}$, respectively. Herein, the dependences of $(BH)_{max}$ on $Fe_{65}Co_{35}$ content

for both systems are plotted in the insets. Clearly, the maximum energy product $(BH)_{\max}$ strongly depends on the ratio of the hard/soft magnetic phases and technological conditions.

The highest values of the maximum energy product $(BH)_{\max}$ are 3.4 and 3.8 MGOe corresponding to MB-AM/FC and MB-A/FC samples with 8% $Fe_{65}Co_{35}$ in $Mn_{50}Bi_{50}/Fe_{65}Co_{35}$ system; 4.8 and 4.2 MGOe corresponding to MG-AM/FC and MG-A/FC samples with 20% $Fe_{65}Co_{35}$ in $Mn_{65}Ga_{20}Al_{15}/Fe_{65}Co_{35}$ system. These values are moderate in compared with other rare earth free hard magnetic materials. However, they but they have an advantage of quite high H_c value (4-9 kOe). To enhance the value of $(BH)_{\max}$, the optimal particle size of the magnetic phases should be reduced to make the best exchange-spring interactions for the material. It thus will become a potential material for high temperature applications.

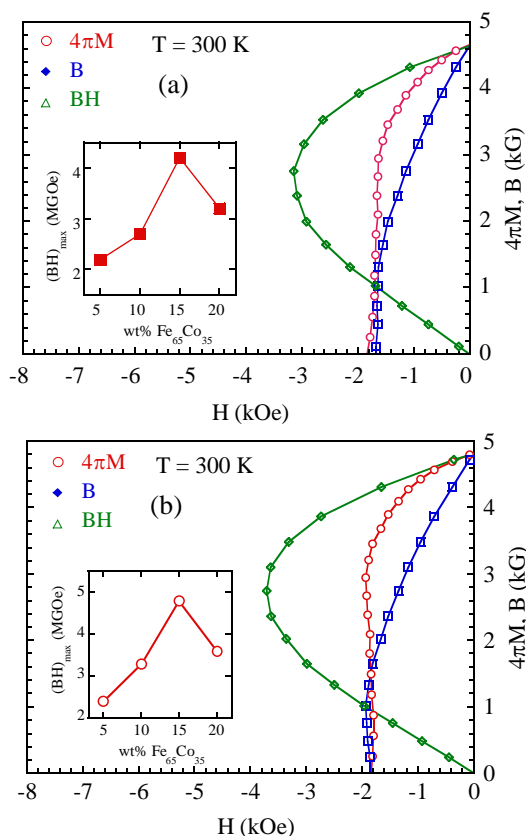


Figure 6. Magnetic characteristic curves obtained at 300 K of $Mn_{65}Ga_{20}Al_{15}/Fe_{65}Co_{35}$ nanocomposites with 20% $Fe_{65}Co_{35}$. The insets show the change of the maximum energy product $(BH)_{\max}$ with various fractions of $Fe_{65}Co_{35}$: (a) MG-AM/FC and (b) MG-A/FC.

CONCLUSIONS

In summary, we have successfully prepared two nanocomposite systems of $Mn_{50}Bi_{50}/Fe_{65}Co_{35}$ and $Mn_{65}Ga_{20}Al_{15}/Fe_{65}Co_{35}$ based on the hard and soft magnetic phases by using the combination of arc-melting and high energy ball milling methods. We pointed that the magnetic properties, including the maximum energy product $(BH)_{\max}$ of systems strongly depend on the content of the phases and technological conditions. Two good hard magnetic nanocomposites are found to be MB-A/FC and MG-AM/FC samples, corresponding to 8 and 20 wt% of $Fe_{65}Co_{35}$. With quite high hard magnetic quality ($H_c > 4$ kOe and $(BH)_{\max} \sim 4$ MGOe), these materials are useful for high temperature applications.

Acknowledgment

This research is supported by the collaborative project “Development of permanent magnetic materials” between Korea Institute of Materials Science (KIMS) and Institute of Materials Science (IMS), VAST, and the National Foundation for Science and Technology Development (NAFOSTED) of Viet Nam under grant number of 103.02-2018.339. A part of the work was done in the Key Laboratory for Electronic Materials and Devices, IMS-VAST.

References

- [1]. R. Coehoorn, D. B. de Mooij, J. P. W. B. Duchateau and K. H. J. Buchow, *Novel permanent magnetic materials made by rapid quenching*, Journal de Physique **49** (1988) 669-670.
- [2]. N. Pang, F. Ye, Y. Jiang, *Cryogenic ball milling synthesis of L_{10} - $Mn_{55}Ga_{45}/FeCo$ composites with effective exchange coupling and enhanced maximum energy products*, Mater. Lett. **231** (2018) 167-170.
- [3]. Y. Q. Li, M. Yue, T. Wang, Q. Wu, D. T. Zhang, Y. Gao, *Investigation of magnetic properties of $MnBi/Co$ and $MnBi/Fe_{65}Co_{35}$ nanocomposite permanent magnets by micro-magnetic simulation*, J Magn. Magn. Mate. **393** (2015) 484-489.
- [4]. W. Lu, Z. Luo, Z. Xiang, X. Wang, F. Pan, W. Tian, Y. Yan, *Synthesis and magnetic properties of LTP- $Mn_{55}Bi_{45}/Fe_{7}Co_3$ and LTP- $Mn_{55}Bi_{45}/Co$*

- magnetic nanocomposites with enhanced energy product*, Mater. Lett. **236** (2019) 514-516.
- [5]. Y. Yan, J. Guo, J. Li, R. Li, *Magnetically exchange coupled MnBi/FeCo thin film composites with enhanced maximum energy products*, Mater. Lett. **184** (2016) 13-16.
- [6]. E. Adams, W. M. Hubbard, and A. M. Syeles, *A new permanent magnet from powdered manganese bismuthide*, J Appl. Phys. **23** (1952) 1207-1211.
- [7]. X. Guo, X. Chen, Z. Altounian, and J.O. Strom-Olsen, *Magnetic properties of MnBi prepared by rapid solidification*, Phys. Rev. B **46** (1992) 14578-14582.
- [8]. J. B. Yang, W. B. Yelon, W. J. James, Q. Cai, S. Roy, and N. Ali, *Structure and magnetic properties of the MnBi low temperature phase*, J Appl. Phys. **91** (2002) 7866-7868.
- [9]. N. V. R. Rao, A. M. Gabay, and G. C. Hadjipanayis, *Anisotropic fully dense MnBi permanent magnet with high energy product and high coercivity at elevated temperatures*, J Phys. D: Appl. Phys. **46** (2013) 062001.
- [10]. Y. Huh, P. Kharel, V. R. Shah, X. Z. Li, R. Skomski, and D. J. Sellmyer, *Magnetism and electron transport of Mn_yGa ($1 < y < 2$) nanostructures*, J Appl. Phys. **114** (2013) 013906.
- [11]. J. J. Wyslocki, P. Pawlik, A. Przybyl, *Magnetic properties of the non-oriented ϵ -phase in Mn-Al-C permanent magnet*, Mater. Chem. Phys. **60** (1999) 211-213.
- [12]. R. Sawada, T. Yamamoto, K. Minakuchi, M. Nagasako, Y. Hayasaka, K. Niitsu, Y. Cho, R. Kainuma, Y. Murakami, *Cellular microstructures superposed on martensite plates in $Mn_{55.2}Ga_{19.0}Cu_{25.8}$ alloy showing large coercivity*, Scr. Mater. **135** (2017) 33-36.
- [13]. N. M Lam, T. M. Thi, P. T. Thanh, N. H. Yen, and N. H. Dan, *Structure and magnetic properties of Fe-Co nanoparticles prepared by polyol method*, Physica B **532** (2018) 71-75.
- [14]. Y. D. Kim, J. Y. Chung, J. Kim, H. Jeon, *Formation of nanocrystalline Fe-Co powders produced by mechanical alloying*, Mater. Sci. Eng. **A291** (2000) 17-21.
- [15]. S. J. Shin, Y. H. Kim, C. W. Kim, H. Gil Cha, Y. J. Kim, and Y. S. Kang, *Preparation of magnetic FeCo nanoparticles by coprecipitation route*, Curr. Appl. Phys. **7** (2007) 404-408.
- [16]. R. Kuchi, K. Lee, Y. Lee, C. H. Luong, K. Lee, B. Park, and J. Jeong, *Synthesis of highly magnetic FeCo nanoparticles through a one pot polyol process using all metal chlorides precursors with precise composition tunability*, Nanosci. Nanotechnol. Lett. **7** (2015) 734-737.
- [17]. Z. Liu, K. Su, Y. Cheng, and R. V. Ramanujan, *Structure and properties evolutions for hard magnetic MnAl and MnGa based alloys prepared by melt spinning or mechanical milling*, Mater. Sci. Eng. Adv. Res. **1** (2015) 12-19.
- [18]. R. Skomski and J. M. D. Coey, *Giant energy product in nanostructured two-phase magnets*, Phys. Rev. B **48** (1993) 15812-15816.
- [19]. E. F. Kneller and R. Hawig, *The exchange-spring magnet: a new material principle for permanent magnets*, IEEE Trans. Magn. **27** (1991) 3588 - 3560.



BIOGRAPHY

Professor Nguyen Huy Dan is Director of Key Laboratory for Electronic Materials and Devices, where he leads the group working in the fields of magnetic nanocomposites, hard magnetic materials, energy conversion materials, magnetic refrigeration, magnetic and electric properties of nanocrystalline and Heusler alloys, shape memory alloys. He has a lot of experience in preparation and characterization for both the electronic ceramic and metallic materials. At present, he is the PI of a national project involved in permanent magnets for applications in motors and generators. He is the co-author of more than 200 scientific papers, and is the supervisor for about 10 PhD. and 40 Msc. students within electronic materials.

PLASMONIC INTERCONNECTS FOR GLOBAL WIRES IN INTEGRATED CIRCUITS

Chua SJ^{1,3,4,6}, Liu Yan¹, Lu Ding,² Aaron Thean,³ Ting Mei,⁴ Christian A. Nijhuis^{1,5}

¹NUSNNI-Nanocore, National University of Singapore, 5A Engineering Drive 1, #11-00, Singapore 117411, Singapore

²Institute of Materials Research and Engineering, A*STAR (Agency for Science, Technology and Research) 117602 Singapore, Singapore.

³Department of Electrical and Computer Engineering, 4 Engineering Drive 3, National University of Singapore, Singapore 117576, Singapore

⁴Key Laboratory of Space Applied Physics and Chemistry, Ministry of Education; and Shaanxi Key Laboratory of Optical Information Technology, School of Science, Northwestern Polytechnical University, Xi'an 710072, China

⁵Department of Chemistry, National University of Singapore, 3 Science Drive 3, Singapore 117543, Singapore

⁶LEES Program, Singapore-MIT Alliance for Research & Technology (SMART), Singapore 138602, Singapore

INTRODUCTION

The history of the Integrated Circuits has always followed the trend towards smaller dimensions of the chip to serve the need of increasing the speed for internal intrachip communication and to increase the packing density. The latter allows for more transistors per chip and hence offer greater functionality for new applications. This trend of doubling the transistor density every year in the 60s and 70s, famously described by Moore's law, has more lately seen a decline to every two years due to the complexity of resolving the multiple issues. The increasing demand of data rates requires novel interconnect technologies to replace classical electronic wires, particularly in terms of signal latency, energy dissipation per bit, wire throughput, crosstalk effect and higher integration. In the prevailing 10 nm technology from Intel [1], it is seen that the global wires (top metals) with pitch of $\sim 11 \mu\text{m}$ for asynchronous communication occupy a large footprint both in the vertical and lateral directions. It has been suggested that plasmonics, working at optical frequencies, has the potential to replace the metallization wires to enhance the processing speed at reduced physical dimensions of future integrated circuits. In the proposed scheme, signals are not transmitted by electrons in wires as in typical ICs with speeds limited to only $2.2 \times 10^6 \text{ m/s}$, but by surface plasmon polaritons (SPP) propagating along plasmonic waveguides with much higher speed in excess of 10^7 m/s . The

main attraction is that they work at optical frequencies but operate at wavelengths much smaller than the optical wavelength and thus are able to interface naturally with the small dimension of electronic devices.

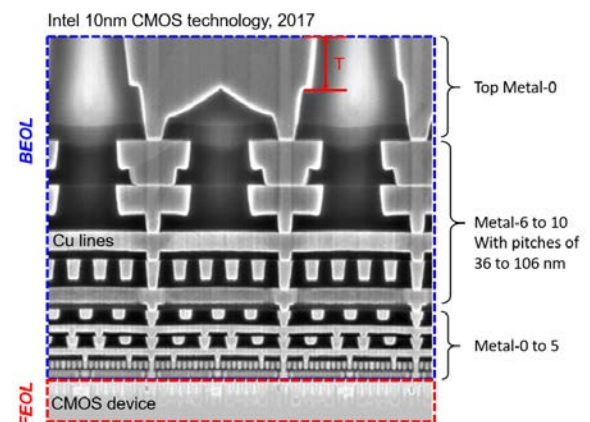


Figure 1. The metal wires used in conventional integrated circuits is $6 \mu\text{m}$ thick at the global level (metal-0 and metal-1). Plasmonics waveguides replacing the global wires can be only 40 nm thick. The smaller dimension of plasmonic waveguides means that higher integration can be achieved.

The local wires (Metal 0 to Metal 5) and intermediate wires (Metal 6 to Metal 10) in 10 nm CMOS technology, shown in Fig 1, have pitches in the range of 36 to 160 nm, which can implement the good feature of a small RC delay, low noise and high speed data transport. However,

in the level of asynchronous communication between blocks, the global wires (top metal layers) are thicker (thickness, $T \sim 6 \mu\text{m}$) and with a wider pitch (~ 1 to $11 \mu\text{m}$) to accommodate for the larger bandwidth for data transport. Thus, the footprint and data transport efficiency of global wires will increasingly impede the pursuit of chip scaling beyond the 10 nm node. With plasmonic interconnects, the thickness can be as small as 40 nm with pitches on the order of 500 to 1000 nm. To be successful in the scheme of using plasmonic interconnects, a source and a detector of plasmons are necessary and progress in these areas has been made in utilizing tunnel junctions for both purposes [2].

SIMULATION AND EXPERIMENTAL VERIFICATION OF SPP PERFORMANCE

A plasmonic waveguide is typically formed by a metal strip or metal-like strip sandwiched between two dielectrics such as SiO_2 or Si_3N_4 referred to as the I-M-I structure. The SPPs are electron waves formed by the oscillations of electron densities formed at the interfaces between the metal and the dielectrics. The electrons therefore do not move from one end of the wire to the other. These waves are Transverse Magnetic waves supported by the negative value of the dielectric constant of the metal. Thus any metal-like materials with negative dielectric constant such as TiN can also be used. To study the properties of these waves, a Au metal layer 50 nm thick is deposited on top of a thin layer of native oxide on Si. The upper surface is bounded by air. This configuration is used so as to compare with the results obtained from experiment where such a structure facilitates the measurement of the SPP fields using a scanning SNOM. The simulation is carried out with the finite-element method (FEM) using the commercial software COMSOLTM. Two optical frequencies are used in the simulation, one corresponding to that of the He-Ne at wavelength 633 nm for verification with the experiment which uses the laser for SPP excitation and the other at the communication wavelength of 1550 nm to be used in the actual ICs.

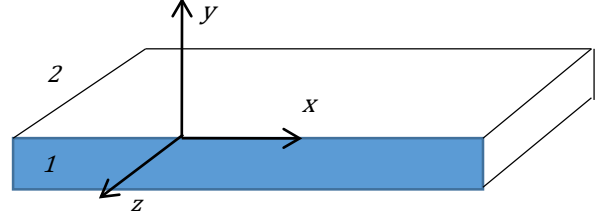


Figure 2. The axes used in the simulation.

The TM wave field components are given by

$$\begin{aligned} H_z &= A_2 e^{i\beta x} e^{-k_2 y} \\ E_x &= \frac{ik_2}{\omega \epsilon_0 \epsilon_{r2}} A_2 e^{i\beta x} e^{-k_2 y} \\ E_y &= -\frac{\beta}{\omega \epsilon_0 \epsilon_{r2}} A_2 e^{i\beta x} e^{-k_2 y} \end{aligned}$$

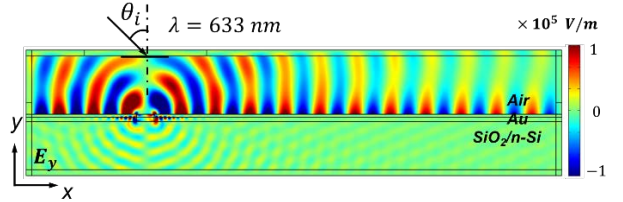


Figure 3. The simulated field E_y in the air. At the location $x = 0$ where the SPP is generated by the coupling of the HeNe beam of wavelength 633 nm, it can be seen another wave at the lower interface which propagates a short distance. Total length of guide is 9000 nm.

Fig 2 shows the axes used in the simulation and the field components that are present in layer 2 in the air. Layer 1 is the metal. β is the propagation constant and $k_2 = \sqrt{\beta^2 - k_0^2 \epsilon_{r2}}$. A similar set of equations exist in the metal. For a thin metal, the two SPP modes existing at the metal/air interface and at the metal/Si interface are hybridized to form the Long Range Surface Plasmon Resonance (LR-SPR) concentrated in the upper interface and the Short Range Surface Plasmon Resonance (SR-SPR) in the lower interface. It can just be seen in Fig. 3 that the SR-SPP propagates a short distance from $x = 0$ where the beam is coupled to the waveguide by a grating. The field that is seen in air in the simulation is to be measured by Scanning Near-field Optical Microscopy (s-SNOM). s-SNOM operates as a tapping AFM tip which scans simultaneously both the topology and the near field optical signal of the sample surface. The tip, of 20 nm radius of curvature, is made of Si and coated with PtIr. An AFM tip is used because the

spatial resolution, determined by the radius of the apex of the tip, far exceeds optical resolution. A p-polarized 633 nm laser is focused on the sample at an incident angle $\theta_i = 60^\circ$.

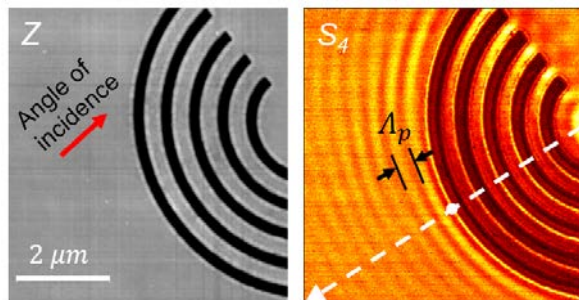


Figure 4. Nanostructured Au semi-ring slits on *n*-Si substrate (with 1~2 nm native SiO₂). The left picture shows the SEM image of the semi-ring grating. The right picture shows the detected optical amplitude *S*₄ of an interference pattern with the period $\Lambda_p = 320$ nm.

To facilitate the excitation of the SPP in the Au film with a HeNe laser, a semi-ring structure is used as shown in Fig 4. The signal *S*₄ is obtained at the 4th order tapping frequency (~1.2 MHz) where it is most sensitive to the near-field. The scattered light at the edge of the slits generates a spectrum of in-plane wave-vectors, one of which compensates the momentum mismatch between the in-plane component of light in free space and the SPP wave (k_{spp}). Due to the reflection-mode in sSNOM measurement, the SPP wave cannot be detected directly on the surface of Au film. The excited SPP wave on the surface of Au film interferes with the back-reflected in-plane wave and forms the interference fringes. The (k_{spp}) is obtained from the following equation, where Λ_p is the period of the interference pattern which value is measured from the picture

$$k_{spp} \pm k_0 \sin \theta = 2\pi/\Lambda_p$$

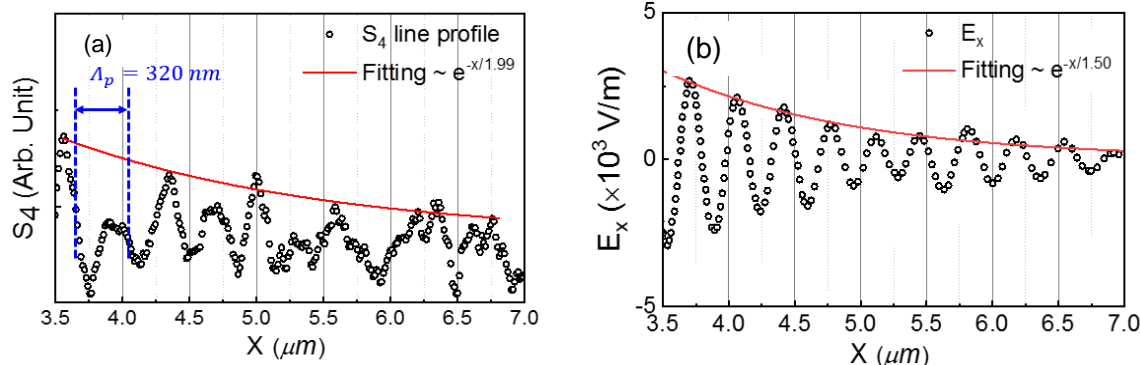


Fig 5. (a) The propagation length ($1.99 \pm 0.5 \mu\text{m}$) of SPP wave is obtained by curve fitting the oscillations obtained from the experiment. (b) Results of numerical simulation showing the magnitude E_x of hybridized SPP wave, with a propagation length of $1.5 \mu\text{m}$ obtained by curve fitting. The incident angle $\theta = 60^\circ$ of the excitation beam is determined from the experimental set-up and $k_0 = 2\pi/633\text{nm}$.

A comparison of the results obtained from simulation and experiment is tabulated below:

Characteristics	Simulation	Experiment
SPP propagation length (μm)	1.5	1.9 ± 0.5
SPP wavelength (nm)	604	607

The propagation lengths compare reasonably well between values obtained from simulation and experiment. For the air-Au-Si waveguide the propagation length is about $\sim 1.7 \mu\text{m}$.

I-M-I STRUCTURE FOR SPP WAVEGUIDE.

With the experimental results confirming the simulation results, the design of an I-M-I SPP waveguide is undertaken. The results of the propagation lengths of the SPP at the frequency of light at the communication wavelength of $1.55 \mu\text{m}$ is shown in Fig.6. The propagation length is the length where the signal has decayed by $1/e$ of its initial value.

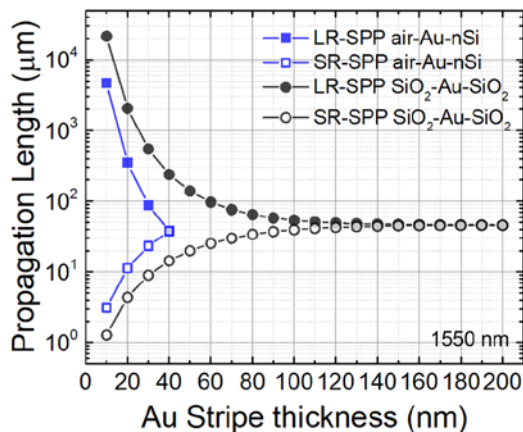


Figure 6 The propagation lengths of asymmetric (air-Au-nSi) and symmetric (SiO₂-Au-SiO₂) structure at 1550 nm for a thin Au film of thickness varying from 10 nm to 200 nm. For 50nm thick Au, the LR-SPP for the symmetric structure has a propagation length of 100μm. For 633 nm, LR-SPP of the 50 nm thick Au for the asymmetric structure was shown earlier in Fig. 5 to be only about 1.5 μm.

For the symmetric SiO₂-Au-SiO₂, Fig 6 shows that the LR-SPP can reach a propagation length of 100 μm for a Au thickness of 50 nm and can reach even longer lengths for thinner Au layers due to the fact that more of the energy is residing in the oxide. Such long lengths are sufficient for use as intrachip interconnects in ICs. Au is not a material compatible with Si foundry processes and thus alternative materials such as Cu and TiN have been explored. The results from these plasmonic waveguides using

these materials will be reported in a separate paper.

CONCLUSION

Surface plasmons polariton has the potential of fulfilling the role as the next generation of metal interconnects for intrachip communication at the global level. Metal lines as thin as 40 nm can have propagation lengths as large as 100 μm. It has a small footprint compatible with the small dimension down to the 10 nm node and having a large bandwidth commensurate with optical frequencies.

Acknowledgements

This research is supported by the National Research Foundation Singapore project on Integration of Electrically Driven Plasmonic Components in High Speed (NRF2016_CRP001_111). We thank Dr. Arseniy from the Institute of Materials Research and Engineering (IMRE, A*STAR) who has kindly consented the use of the s-SNOM for this work

Reference

- [1]. Chao-Wei Chen, Yu-Han Chen, Cheng-Hsing Chen, Cheng-Huang Yang, Bang-Hao Huang, and Shih-Hsin Chang, "10 nm vs 10 nm technology node comparison", MSSCORPS CO., LTD, Hsinchu, Taiwan, Feb 2018.
- [2]. W. Du, T. Wang, H.-S. Chu, L. Wu, R. Liu, S. Sun, L. Wang, N. Tomczak, C. A. Nijhuis, Nat. Photon. 10, 274 – 280, (2016).

BIOGRAPHY



Prof. Soo-Jin Chua graduated with a B.Eng (Hons) from the University of Singapore in 1974 and his PhD from the University of Wales, United Kingdom in 1977. In 1978, he worked for the Standard Telecommunications Labs, Harlow, UK, as a research scientist. In 1981, he spent a year at the Fraunhofer Institute of Semiconductor Technology, Munich under a German Exchange Scholarship (DAAD). He was a Visiting Fellow of Japan Society for the Promotion of Science in 1988 and of the British Council in 1990. Currently, he is Professor in the Department of Electrical Engineering, National University of Singapore, Principal Scientist in the Institute of Materials Research and Engineering (IMRE) and Principal Investigator in SMART. He was Deputy Director of the Singapore-MIT Alliance (SMA) from 1999 – 2014, Executive

Deputy Director, IMRE from 2004- 2010, Assistant Director of the Institute of Microelectronics from 1991-1995, and Director of the Centre for Optoelectronics, Department of Electrical and Computer Engineering, NUS from 1990 - 2010

ONE-PHOTON ABSORPTION BASED DIRECT LASER WRITING FOR FABRICATION OF MULTI-DIMENSIONAL PHOTONIC AND PLASMONIC NANOSTRUCTURES

Thi Huong Au¹, Mai Trang Do¹, Qingge Li¹, Mai Hoang Luong¹, Fei Mao¹, Dam Thuy Trang Nguyen¹, Amber Perry¹, Thi Nhung Pham¹, Quang Cong Tong², and Ngoc Diep Lai¹

¹Laboratoire de Photonique Quantique et Moléculaire, UMR 8537, École Normale Supérieure Paris-Saclay, Centrale Supélec, CNRS, Université Paris-Saclay, 61 avenue du Président Wilson, 94230 Cachan, France

²Institute of Materials Science, Vietnam Academy of Science and Technology, 18 Hoang Quoc Viet, Cau Giay, Hanoi 100000, Vietnam
Email: ngoc-diep.lai@ens-paris-saclay.fr

ABSTRACT

We present a simple and low-cost fabrication technique, based on low one-photon absorption (LOPA) phenomena in a weakly absorbing photoresist (532 nm laser versus SU8 or S18 photoresist). This novel approach enables production of submicrometer 2D and 3D photonic structures on demand using a very modest laser power. We also demonstrate that the LOPA based direct laser writing allows realization of plasmonic (gold, silver) and magneto-photonic (Fe_3O_4) nanostructures. Different applications of these fabricated structures could be envisioned, and partially realized, such as tuneable photonic devices, data storage, bright single photon source, quantum information, plasmonic data storage, and color nanoprinter. Keywords: Direc Laser Writing, LOPA, Plasmonics, Photonic Crystals, Quantum Optics

INTRODUCTION

Recently, Direct laser writing (DLW) becomes a common and powerful technique for fabrication of arbitrary shapes micro and submicro-structures. In this technique, a laser beam is tightly focused, by using a high numerical aperture (NA) objective lens (OL), into a photosensitive material, which locally induces a chemical or physical change of such material. In order to realize a thick structure or a three-dimensional (3D) structure, a two-photon absorption (TPA) method is usually employed. For that, a femto-second laser source and a complicated optical system are required in order to achieve a nonlinear absorption at the focusing spot. This technique is therefore expensive and bulky. Recently, by using the one-photon absorption (OPA) technique at very low absorption regime, called as LOPA method [1,2], any desired 2D and 3D structures have been also demonstrated. In such method, a combination of a very low absorption effect and a very high excitation intensity allows one to achieve a complete polymerization only within the focusing spot of the OL. Therefore, the LOPA-based DLW enables 3D

submicrostructures fabrication, similar to the case of TPA-based DLW. The advantage of this technique is that it is very simple and low-cost. The OPA-based DLW has also applied to obtain desired structures in different materials, such as magnetic [3], metallic [4,5], etc. Moreover, the use of a simple continuous-wave (cw) laser at 532 nm - wavelength allows us to realize different photonic structures containing as desired a single active nanoparticle, resulting in strong enhancement of the optical properties of the nanoparticle [6-9].

EXPERIMENTAL

Figure 1 shows the experimental set up of the LOPA-based DLW system. A cw laser beam emitting at 532 nm is focused into a sample (photoresist, metallic, magnetic thin films) via an OL (NA=1.3, oil immersion). The sample is moved in three dimensions by using a piezoelectric translator. This setup is used for both fabrication of desired 2D and 3D photonic structures (PS) and characterization of active nanoparticles (NP), which are embedded (or not) in PSs.

To fabricate PSs, we have used both a negative photoresist SU-8 [1] and a positive

photoresist, S18 [2]. The desired 1D, 2D, and 3D PSs could be fabricated by moving the photoresist sample following a pre-design. The laser power is only about few milliwatt, a very modest one. A magneto PS has been also demonstrated, by mixing magnetic Fe_3O_4 nanoparticles with SU-8 photoresist [3].

To fabricate plasmonic nanostructures, the laser power was increased to few dozen milliwatts. The laser beam was focused into a metallic film (gold, silver) having a thickness of few nanometers. Thanks to the optically induced local thermal effect, metallic nanoparticles have been created via the dewetting effect [4]. By moving the focusing spot, any 1D and 2D plasmonic nanostructure can be obtained [5].

Furthermore, we have demonstrated that the LOPA technique enables the coupling of any active NP into polymeric PS by a double step process. The first step consists of determining the position of the NP via the fluorescent mapping by using only few microatts of the 532 nm laser. Once the NP position is known, the PS can be fabricated, which contains the NP at desired position, by increasing the 532 nm laser to few milliwatts. Figure 2 illustrates a possibility of coupling a single active NP (plasmonic, nonlinear, or fluorescent) [6-9] into a PS, by using the LOPA-based DLW technique.

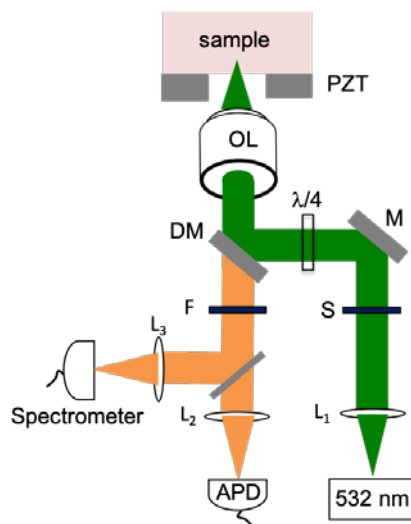


Figure 1. Experimental setup of the LOPA-based DLW technique. PZT: piezoelectric translator; OL: oil immersion microscope objective; DM: dichroic mirror; M: mirror; $\lambda/4$: quarter-wave plate; S: electronic shutter; F: long-pass filter; APD: silicon avalanche photodiode; L_i ($i=1,2,3$): lenses.

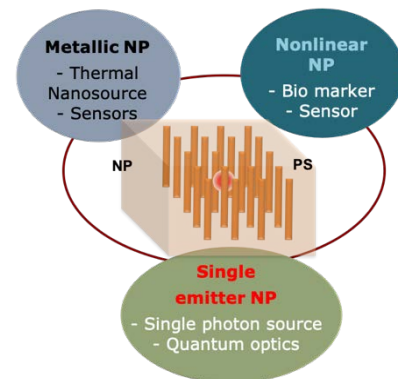


Figure 2. Illustration of different possibilities of coupling a single nanoparticle into a photonic structure by the use of the LOPA-based DLW method.

RESULTS AND DISCUSSION

Figure 3 shows the scanning microscope images of several 2D and 3D PSs realized by the LOPA-based DLW technique. The 3D spiral PS is obtained by a pure SU-8 photoresist. The microfish is made by a magnetic nanocomposite $\text{Fe}_3\text{O}_4/\text{SU-8}$. The last structure is a 3D membrane containing a single KTP nanocrystal at the center.

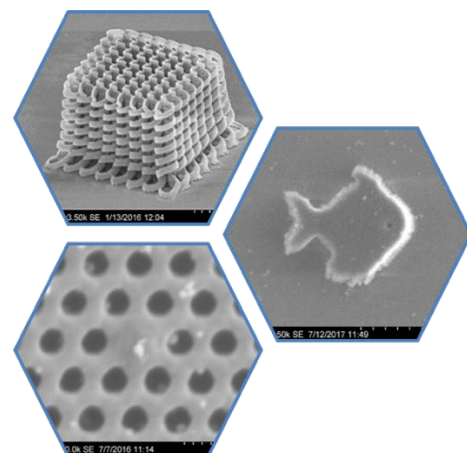


Figure 3. Scanning microscope images of few examples of 2D and 3D photonic and/or magnetic structures, with and without single nanoparticles, realized by the LOPA-based DLW technique.

The fabricated PSs could be used directly as photonic crystals, even the refractive index is low, thanks to the optimum design of the PS. These structures can be also transferred to other materials for other applications, such as laser, nonlinear optic, plasmonic, etc. In particular, the PS containing a single active NP, could enhance the optical properties of those NPs. Strong enhancement of second-harmonic generation

[7], or of the single photon generation [8,9] have been successfully demonstrated.

CONCLUSION

We have demonstrated a simple and low-cost technique, based on one-photon absorption (OPA) phenomena, to realize on demand photonic, magneto-photonic, as well as plasmonic nanostructures. In particular, at very low absorption regime (LOPA), this approach enabled production of any 2D and 3D submicrometer structures using a very modest laser power. We then demonstrated that the LOPA-based DLW technique also enables incorporation of a single nanoparticle (nonlinear, metallic, or fluorescent) into photonic structures, at any desired position. Different applications of these fabricated structures could be envisioned, and were partially realized, such as polymer-based photonic crystals, waveguide grating resonant, enhanced second-harmonic generation, as well as controlled bright single photon source.

Acknowledgment

This work is supported by two public grants overseen by the French National Research Agency (ANR), as part of the “Investissements d’Avenir” program (Labex NanoSaclay, reference: ANR-10-LABX-0035), and of the GRATEOM project (ANR-17-CE09-0047-01). This research is also supported by a public grant of Ministry of Science and Technology of Vietnam (project: ĐTĐLCN.01/2017).

References

- [1]. M. T. Do, T. T. N. Nguyen, Q. Li, H. Benisty, I. Ledoux-Rak, and N. D. Lai, *Opt. Express* 21, 20964 (2013).
- [2]. Q. C. Tong, M. T. Do, M. H. Luong, B. Journet, I. Ledoux-Rak, and N. D. Lai, *Appl. Phys. Lett.* 108, 183104 (2016).
- [3]. T. H. Au, D. T. Trinh, Q. C. Tong, D. B. Do, D. P. Nguyen, M. H. Phan, and N. D. Lai, *Nanomaterials* 7, 105 (2017).
- [4]. Q. C. Tong, M. H. Luong, J. Remmel, M. T. Do, D. T. T. Nguyen, and N. D. Lai, *Opt. Lett.* 42, 2382 (2017).
- [5]. F. Mao, A. Davis, Q. C. Tong, M. H. Luong, C. T. Nguyen, I. Ledoux-Rak, and N. D. Lai, *Plasmonics* 13, 2285–2291 (2018).
- [6]. M. T. Do, D. T. T. Nguyen, H. M. Ngo, I. Ledoux-Rak, and N. D. Lai, *Nanotechnology* 26, 105301 (2015)
- [7]. D. T. T. Nguyen and N. D. Lai, *Crystals* 9, 365 (2019)
- [8]. T. H. Au, S. Buil, X. Quelin, J.-P. Hermier and N. D. Lai, *Nanoscale Adv.* 1, 3225-3231 (2019).
- [9]. T. H. Au, S. Buil, X. Quelin, J.-P. Hermier and N. D. Lai, *ACS Photonics* (2019): DOI 10.1021/acsp Photonics.9b01358

BIOGRAPHY



Ngoc Diep Lai obtained a Ph.D. degree in laser physics at the University of Rennes 1 (France) in 2003. He spent 4 years at the National Chung Cheng University (Taiwan) for his first Postdoctoral Research. His work focused on studies of nonlinear properties of polymer materials and nanotechnologies for fabrication of polymer-based photonic crystals. In 2007, he joined the Quantum Photonics and Molecular Laboratory of the École Normale Supérieure Paris-Saclay (ENS Paris-Saclay), France. He worked towards the optimization of single photons source, coherent manipulation of single-electron spin associated to color center in diamond, and super-resolution imaging techniques. He is hired in 2009 at ENS

Paris-Saclay as an Assistant Professor and he became an Associate Professor in 2013. His expertise includes single-photon source and electron spin resonance; micro and nanofabrication; interference and direct laser writing; photonics crystals and super-resolution imaging; quasi-phase matching and nonlinear photonic crystals; two-frequency laser, Lidar-radar, and THz generation. His current research focuses on optical coupling of nanoparticles (single quantum center, metallic and nonlinear particles) into photonic systems and also on optical nanotechnology for imaging and fabrication of desired photonic, magnetic and plasmonic structures at nanometer scale.

SOLAR-DRIVEN Cu-BASED PHOTOCATALYSTS

Le Van Hoang, Thu Loan Nguyen, Thi Dieu Thuy Ung, Tran Dinh Phong, Nguyen Quang Liem*

Institute of Materials Science, Vietnam Academy of Science and Technology,

18 Hoang Quoc Viet, Cau Giay, Hanoi, Vietnam

*Email: liemng@vast.vn

ABSTRACT

Photocatalysts made from earth-abundant elements represent attractive candidates to harvest photon energy in the sun light to drive the photocatalytic activities for the H₂ fuel generation and the organic pollutants degradation processes. In this talk, we present our recent progress in engineering Cu-based photocatalysts, namely Cu₂O, CuO, Cu₂S, Cu_{2-x}Se etc., to enhance their photocatalytic activity and robustness. Indeed, these p-type semiconductors have narrow band gap of 1.2 – 2.0 eV which are suitable to harvest the visible light of the solar spectrum. However, they suffer from the photocorrosion that leads to a quick degradation of catalytic performance over operation time. To address this issue, we investigate various strategies to “push” the corrosive agents, namely the photogenerated electron and hole, out of the Cu-based light harvesters. Onto the Cu₂S [1, 2] or the CuO [3] core, a shell made of large band gap n-type semiconductor like ZnS or TiO₂ is introduced. As such, a pn heterojunction Cu₂S/ZnS or CuO/TiO₂ is created that enhances the charge separation within Cu₂S, CuO light harvesters therefore to enhance the photocatalytic activity. Furthermore, with this core/shell design, the photogenerated electron is quickly migrated to the ZnS or TiO₂ shell to lose its reducing action to Cu ions that helps to enhance the stability of the Cu₂S and CuO light harvesters. With the same engineering concept, a n-type Cu₂O shell is introduced onto the p-type Cu₂O core to create an pn homojunction [4]. Thus, the photo-generated electron within the p-type Cu₂O core is quickly quenched by the n-type Cu₂O shell that enhances both the catalytic H₂-evolving activity and the stability against the reductive photocorrosion. In another approach, we apply a protective layer made of thermal sputtered gold [4] or graphene sheets [5] onto the Cu₂O light harvester surface. In this cases, a Schottky junction is formed that also significantly enhances the charge separation within the Cu₂O light harvester. Furthermore, the decorated gold nanoparticles also act as an efficient H₂-evolving catalyst that promotes the catalytic H₂ generation on Cu₂O photocatalyst. We emphasise that our developed engineering strategies, mainly based on a solution process, could be applied for other photocatalysts but not only the Cu-based ones as described here.

References

- [1]. Ung Thi Dieu Thuy, Nguyen Quang Liem, Christopher M.A. Parlett, GeorgiM. Lalev, KarenWilson, *Catalysis Communications* **44** (2014) 62–67.
- [2]. Ung Thi Dieu Thuy, Irena Borisova, Olya Stoilova, Iliya Rashkov, Nguyen Quang Liem, *Catalysis Letters* **148** (2018) 2756–2764.
- [3]. Thi Hiep Nguyen, Thu Loan Nguyen, Thi Dieu Thuy Ung, Quang Liem Nguyen, *Adv. Nat. Sci.: Nanosci. Nanotechnol.*, **4** (2013) 025002.
- [4]. Le Van Hoang, Tran Dinh Phong, Mai Van Huy, Ung Thi Dieu Thuy, Nguyen Quang Liem, *International Journal of Hydrogen Energy* **43** (2018) 21209-21218.
- [5]. Le Van Hoang, Le Thi Ly, Tran Dinh Phong, Jong-San Chang, Ung Thi Dieu Thuy, Nguyen Quang Liem, *International Journal of Hydrogen Energy* **44** (2019) 14635-14641.

BIOGRAPHY

Full name: Nguyen Quang Liem

Sex: Male

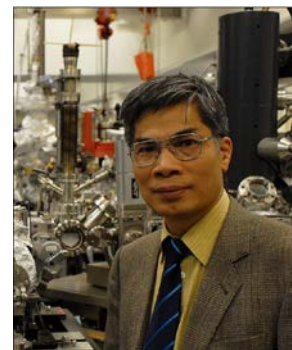
Nationality: Vietnamese

Affiliation: Institute of Materials Science (IMS),
Vietnam Academy of Science and Technology (VAST)

Tel: +84-4-37912835; HP: +84904282217

Fax: +84-4-38360705

E-mail: liemnq@vast.vn; liemnqvast@gmail.com



Education, titles and positions

- 1995 PhD, Inst of Physics, National Centre for Natural Science and Technology
- 2001 Principal researcher, VAST
- 2002 Associate Professor in Physics
- 2005 Vice-Director, VAST/IMS
- 2009 Senior researcher, Director, VAST/IMS (till 10/2017)
- 2011 Full Professor in Physics, Vice-President VAST Council for MS Direction

Working Experiences

Visiting scientist at CEA/ Grenoble, France (2004-2007, 1-3 months/year); Visiting scientist at Osaka University, Osaka, Japan (6/2003, 8/2004); Visiting scientist at LADIR/CNRS France (1999-2002, 3 months/year); Visiting scientist at KAIST, Daejeon, Korea (5-11/1998); PostDoc at KRISS, Korea (1996); Visiting scientist at Ecole Centrale Paris, France (3-6/1994); Visiting scientist at Florence University, Italy (1988-1989).

Society

- + Vice-President of the Vietnam Physical Society VPS (2013-2023)
- + Member of the Association of Asia Pacific Physical Societies (AAPPS) Council
- + Editor-in-Chief of *Adv. Nat. Sci.: Nanosci. Nanotechnol.* (IOP Publishing), Editorial board member of *Heliyon* (Elsevier), and of *Journal of Science: Advanced Materials and Devices* (Elsevier).
- + Focal point of Vietnam/Chairman of the Sub-Committee on Materials Science and Tech (SCMST), ASEAN Committee of Science and Technology (ASEAN COST), 2009-2017.

Research interests

- Optoelectronic materials (bulk, film and quantum dots/nanocrystals based on II-VI, III-V, and I-III-VI semiconductors) and devices (luminescent materials for LEDs and for biolabeling/sensors, photocatalysts for photo-reactivity and for photoreactor, H₂ generator).
- Development of scientific instruments and spectroscopic measuring techniques, especially some related ones like Raman scattering and photoluminescence spectroscopy enhanced with surface plasmon resonance for fast/non-destructive and sensitive analysis/detection of residual pesticides, chemical radicals etc.
- Characterizations of the ancient art/cultural products (potteries, bricks, bronzes etc.)

Publications

- (i) More than 150 journal papers and conference proceedings
- (ii) 1 Book, 1 book chapter, and 3 patents

SPUTTERING OF TWO DIMENSIONAL METAL SULPHIDE FILMS

Tomas Nyberg

Division of Solid State Electronics, Angstrom Laboratory, Uppsala University, Box 534, SE-751 21
Uppsala, Sweden

Email: tomas.nyberg@angstrom.uu.se

ABSTRACT

It is challenging to sputter deposit layered two dimensional metal sulphide films since the energetic bombardment associated with the sputtering process typically exceeds the level needed to break the chemical bonds and consequently destroy the material and deteriorate its properties. Another problem is the fact that the formation of the layered structure occurs at relatively high temperatures. At these elevated temperatures, the sulphur has a tendency to evaporate resulting in a substoichiometric film.

We have studied sputtering of WS₂ films from a WS₂ target in H₂S as well as in pure Ar. Highly (001)-textured layered, slightly substoichiometric, WS₂ films have been deposited. XRD reveals only (002), (004), (006) and (008) peaks and Raman spectroscopy shows peaks at 355 cm⁻¹ and 419 cm⁻¹ which is characteristic for layered WS₂ material. Further, TEM images show distinguishable layers in the deposited film. Raman indicates that it is possible to deposit few monolayers end close to one monolayer of WS₂ material. Further, it has been shown that WS₂ can be mixed with SnS₂ to deposit a mixed multi-metal high quality 2D-film. The challenges of obtaining an epitaxial film is pointed out and suggestions on how to obtain growth conditions for this is presented.

Keywords: WS₂, 2D materials, sputtering, sulphides

INTRODUCTION

Two-dimensional (2D) materials, such as MoS₂, WS₂, and graphene, have recently received a great deal of attention in the scientific community. The reason for this is their unique properties giving them enormous potential in a variety of applications in fields such as electronics, photovoltaics, and as tribological coatings. One example of such application is the recently presented single layer MoS₂ transistor.[1] However, the MoS₂ layer in that work was not deposited by a thin film process but was the result of exfoliation of a single-layer MoS₂ and subsequently transferred to a silicon substrate. In this work, we propose to develop a sputter-deposition process that is compatible with the sensitive layered sulphide materials. Sputter deposition is a commonly used process and the ability of using it in conjunction with 2D materials would constitute an enormous advantage for the possibility of incorporating such materials into electronics and sensor applications. This has however not been accomplished yet. One reason for this is the energetic particle bombardment associated with conventional sputtering which will easily break the weak bonds in these materials. [2,3] The

sputtering process normally involves significant energetic particle flux onto the growing film. Such flux is usually beneficial for the film quality but may be detrimental during sputtering of sensitive materials such as the two-dimensional sulphide materials. By sputtering at high pressures, the energetic particles may be thermalized and a sputtering process with low energetic particle flux, which is compatible with sputter deposition of sensitive materials, can be obtained.

EXPERIMENTAL

All coatings were deposited by pulsed DC magnetron sputtering in a turbo pumped high vacuum von Ardenne system with a cylindrical chamber with a diameter of 50 cm and a height of 28 cm. The base pressure for all depositions was below $7 \cdot 10^{-4}$ Pa. Two 4-inch WS₂ and SnS₂ sputter targets, with purity >99.9%, were used. Ar and H₂S were employed as sputtering gases. Si and SiO₂ were used as substrates. Substrate could be heated up to 700°C. The total gas flow (Ar+H₂S) was kept at 20 sccm and the pressure was 50 mTorr. Target power was kept at 200 W.

RESULTS AND DISCUSSION

Fig 1 shows TEM images of films deposited in only Ar as well as only H₂S. Others have previously sputtered tungsten sulphide films in Ar/H₂S mixtures but only from a metallic W-target.[4] Films sputtered from such target were reported to be substoichiometric due to the reducing effect of hydrogen radicals produced from H₂S in the plasma.[4] It is therefore a good idea to sputter from a sulphide target which may serve as another source of Sulphur and thereby increase the Sulphur content in the films.

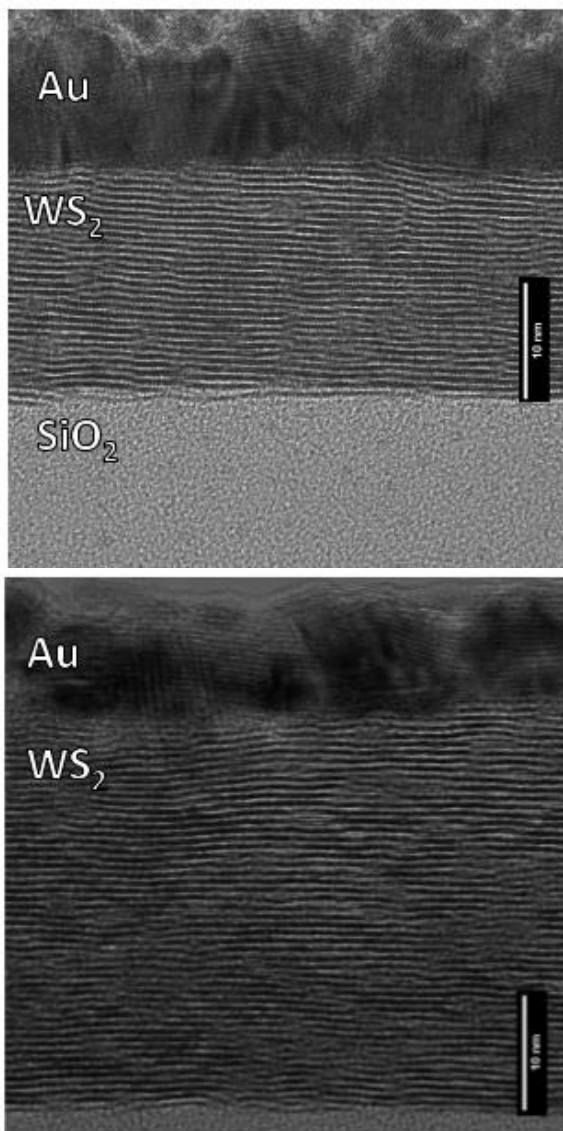


Figure 1. TEM images of WS₂ films deposited in 100 % Ar (top) and 100 % H₂S (bottom)

It can be concluded from Fig. 1 that the quality of the films is rather similar. The different thicknesses are due to different deposition times and different sputtering yields for Ar and H₂S. The comparable quality between the films is

further corroborated in Fig. 2, which shows X-Ray Diffraction from the two films.

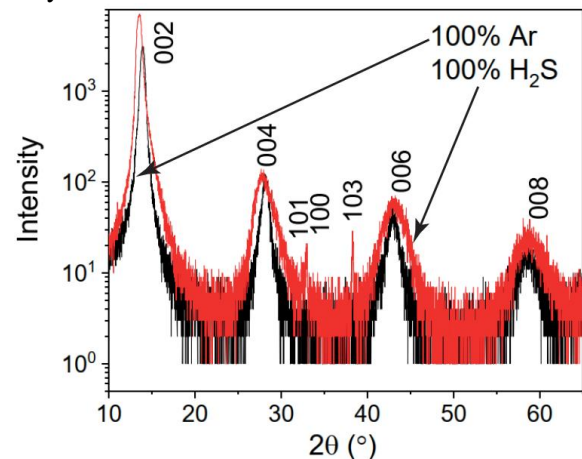


Figure 2. XRD (θ - 2θ scan) of WS₂ films sputter deposited in 100 % Ar and 100 % H₂S

It can be seen in Fig. 2 that the films sputtered in Ar has a somewhat smaller Full Width Half Maximum (FWHM) compared to the film sputtered in H₂S. This is believed to be due to incorporation of hydrogen in the latter films. However, the hydrogen content in the films has so far not been measured.

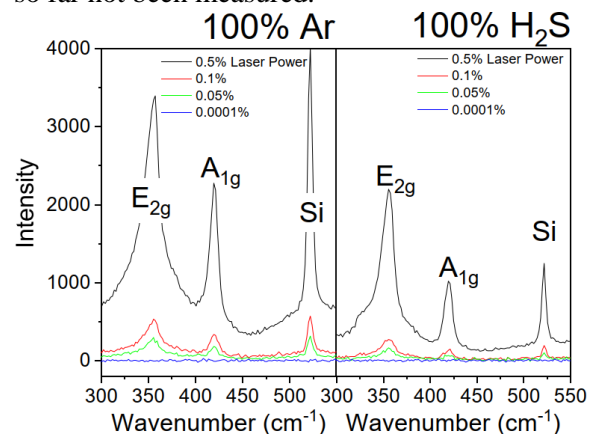


Figure 3. Raman from WS₂ films sputtered in 100 % Ar and 100 % H₂S (different laser powers)

The Raman spectroscopy in Fig. 3 shows peaks at 355 cm⁻¹ and 419 cm⁻¹ which is characteristic for two dimensional WS₂ films. Other results from Raman have indicated very uniform thin sputtered WS₂ film.

With respect to the film composition, results from RBS has indicated somewhat inconclusive results so far. Stoichiometric films cannot however be excluded. Further compositional analysis will be carried out. Also electrical characterization will be conducted in detail.

Very recent results from co-sputtering of WS₂ and SnS₂ targets in pure Ar has indicated that the

crystalline quality may be equally good in such composite films as in the sputtered WS₂ films.

CONCLUSION

It is possible to deposit very high quality two dimensional WS₂ films by sputtering from a WS₂ target in either Ar or H₂S. Moreover, it is possible to obtain very thin films of high quality which are uniform over large areas. It is further possible to get high quality two dimensional WS₂/SnS₂ films from co-sputtering in Ar.

Acknowledgment

This work was supported by the FLAG-ERA grant LaMeS, by Swedish Research Council contract 2017-06816.

References

- [1] B. Radisavljevic, A. Radenovic, J. Brivio, V. Giacometti, A. Kis, *Single-layer MoS₂ transistors*, Nature Nanotechnology **6** (2011), 147–150
- [2] F.O.L. Johansson, P. Ahlberg, U. Jansson, S.-L. Zhang, A. Lindblad, T. Nyberg, *Minimizing sputter-induced damage during deposition of WS₂ onto graphene*, Appl. Phys. Lett. **110** (2017), 091601
- [3] P. Ahlberg, F. O. L. Johansson, Z.-B. Zhang, U. Jansson, S.-L. Zhang, A. Lindblad, T. Nyberg, *Defect formation in graphene during lowenergy ion bombardment*, APL Mater. **4** (2016), 046104
- [4] V. Weiß, S. Seeger, K. Ellmer, R. Mientus, *Reactive magnetron sputtering of tungsten disulfide (WS_{2-x}) films: Influence of deposition parameters on texture, microstructure, and stoichiometry*, Journ. of Appl. Phys. **101** (2007), 103502



BIOGRAPHY

Tomas Nyberg took his PhD in Electronics at the Angstrom Laboratory, Uppsala University in Sweden in 1998. Primary research focus is on experimental studies and modelling of the sputtering and reactive sputtering deposition process. He is an Associate Professor at Uppsala University and works with research and lecturing. Further, he has published more than 70 articles in international journals and written several chapters in textbooks on reactive sputtering and ion assisted thin film growth.

**CHEMICAL FUNCTIONALIZATION OF CARBON NANOTUBES
USING DNA BINDING PEPTIDES**

Jung Heon Lee

School of Advanced Materials Science & Engineering, SKKU Advanced Institute of Nanotechnology (SAINT), Advanced Materials Technology Research Center, Sungkyunkwan University (SKKU), Suwon 16419, Rep. of Korea
Email: jhlee7@skku.edu

ABSTRACT

Although carbon nanotubes (CNTs) are remarkable materials with exceptional physical, optical, electrical, thermal, and mechanical properties, their poor chemical functionality limits their various potential applications. In this work, I present a novel strategy to functionalize CNTs with any functional group without degrading their intrinsic structure using a DNA-binding peptide (DBP) anchor. Using a DBP tagged with a certain functional group, such as thiol, biotin, and carboxyl acid, it is possible to introduce the functional group with controlled density on DNA-wrapped CNT. Multiple types of functional groups can be introduced on a CNT as well using DBP molecules tagged with different functional groups at the same time. This method can be used to construct multifunctional CNT nanocomposites containing different types of nanoparticles (NPs), such as gold (AuNPs), magnetic (MNPs), and quantum dots (QDs), using different conjugation chemistries. The CNT nanocomposites decorated with these nanoparticles not only have efficient catalase activity, due to the synergistic catalytic effects of multiple nanomaterials, but also are reusable multiple times after separation with magnets. We believe this method can be a novel chemistry platform to construct new functional CNTs suitable for diverse applications.

Keywords: carbon nanotube, DNA binding peptide, heterogeneous, multi-functionalization, nanocomposites

BIOGRAPHY



Prof. Lee got his B.S. in Metallurgical Engineering from Yonsei University, M.S in Materials Science and Engineering from Seoul National University, and Ph.D in Materials Science and Engineering from the University of Illinois at Urbana-Champaign. After post-doctoral training at Northwestern University, he became a faculty of Materials Science and Engineering at Sungkyunkwan University since 2012. Prof. Lee's research interest is on developing nanoscale materials or devices which can be applied to diverse levels of biological systems for diagnostics or therapeutics. He is also investigating opportunities to adapt programmable and readily modifiable properties of biomolecules in the fabrication of smart materials or advanced nanoscale devices.

THE REACTIVE NANO SILICATE (RNS) AS A PRECURSOR FOR REINFORCEMENT OF RUBBER USING REACTIVE GRAPHENE

Khe. NC*, Linh V. H.*

*HK Invent Technology Lab

HK Invent Inc, Hiep Phuoc Industry Park, Long Thoi, Nha Be, Ho Chi Minh City, Vietnam

Email: Kng33228196@aol.com

ABSTRACT

Graphene had been known as tough material and is expected to offer reasonable reinforcement of rubber. However, in reality, there is no reports about significant reinforcement of rubber (natural rubber and synthetic rubber) with graphene, which can satisfy industrial demands of low portion of filler in tire for light weight and low cost.

Recently, molecularly disturbing of (silica/acid composite) (SAC, USP Application 20180099905) with electron acceptor derivative such as fumed silica rendered it into reactive nano silicate (RNS). RNS is self- reactive forming rigid film exhibiting interesting properties over raw materials; such as **fire flame retardant** (anti fire), **water proofing**, **heat resistant**, **anti UV** and provides protection of materials against **weather changes**.

RNS is reactive with rubber and hydroxylated graphene hybrid composite (GHC, US9460827 B2_1, USP Application 20190202701) and becomes the chemical bridge connecting GHC with rubber and thus exhibiting significant reinforcement effect of GHC in rubber.

Overall, RNS is precursor to overcome the limit of graphene for mechanical and thermal properties applications.

INTRODUCTION

Graphene and related materials such as pristine graphene, graphene oxide (GO), reduced graphene oxide, graphene nano platelet (GNP) and recently disclosed graphene hybrid composite had been known tough materials and they are expected to offer good contribution to the reinforcement of rubber . In reality, not thing seriously happened when graphene is simply mixed into rubber as filler indicating that graphene is not effective for rubber reinforcement.

On the other hand, in the rubber tire compounding technology, complicated additive components including silica had been added to balance elastomeric force but not reinforcement.

SILICA/ACID COMPOSITE (SAC)

U.S. Patent Publication 20180099905 [1](the “‘905 Publication”) disclosed a composite formed from liquid glass with specific carboxylic acid. In the ‘905 Publication, liquid glass is extracted from paddy husk, which husk originated in Vietnam. The product can be called a silica/acid composite (“SAC”), which exhibits a primary particle size in the range of

approximately 5 nm. These primary particles can stick to each other to form a translucent white gel. However the translucent white gel did not form a film upon drying and show no effect of water proofing even dried SAC particles exhibits excellent waterfastness. Thus when SAC was mixed with colorant in attempt to form waterproof for house paint, it is not capable of fully shielding colorant of the house-painting product from water attack.

In another study, SAC was added onto rubber latex as nano filler. The mixture was uniform due to relatively good compatibility between SAC and rubber latex. However, upon being dried, the rubber comprising SAC did not show any significant improvement in physical properties.

Based upon these tests, it was concluded that SAC is relatively inert and non-reactive. The SAC showed smaller particle sizes than other gels but was not found to be robust enough to cause any significant enhancement in material durability.

REACTIVE NANO SILICATE (RNS)

In an attempt to change the nature of SAC, we are successfully incorporate into the network of SAC a disturber, which can convert the non-reactive SAC into reactive species named as Reactive Nano Silicate (RNS), which is more interactive with other materials. The SAC disturbing molecule can be SAC family but not exactly the same physical structure. Example of the SAC disturber is metal oxide such as but not limited Fe_2O_3 , TiO_2 , Xe_2O , SnO_2 , Al_2O_3 , SiO_2 , TiO_2 , V_2O_5 , In_2O_3 , rare earth oxide such as La_2O_3 , cerium oxide, neodymium oxide, samarium oxide, and the like. RNS is self-reactive and forms film upon being dried. The dried film of RNS exhibiting water proofing properties.

Fig.1 is a photograph of a water drop on a dry surface coated with RNS. The photograph shows that the dried film of RNS repels water.

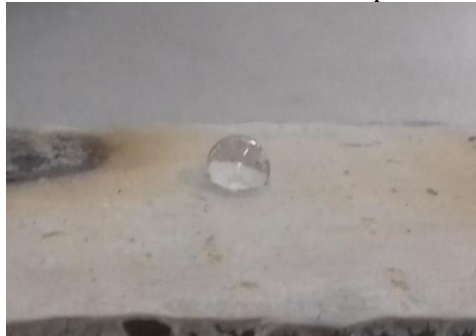


Figure 1. Photograph of a water drop on a dry surface coated with RNS.

Fig. 2 illustrates a TEM image of SAC (shown on left) and RNS (shown on right) (the image scale is 200nm). One can recognize that

SAC appears as individual particle while RNS shows a particle connected into cloudy membrane. Thus, this is evidence that SAC and RNS are different species.

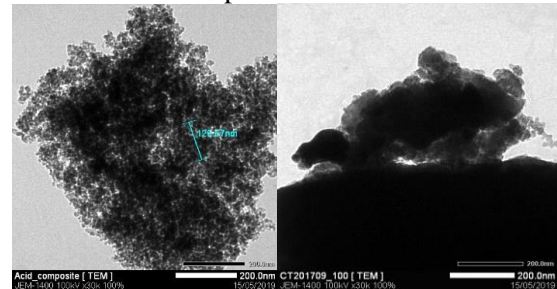


Figure 2. Illustrates a TEM image of SAC (shown on left) and an RNS (shown on right) (the image scale is 200nm).

Now, it can be suggested that the stranger molecule added on the solution of SAC, somehow, had successfully disturbed the structure of SAC and converted the non-reactive nature of SAC into reactive species, which is RNS. RNS can be strongly intramolecular interaction to form film.

Next , water reactive GHC (as disclosed in United States Patent 9460827 and U.S. Patent Publication 20190202701 [2] [3]) was added into synthetic rubber SBR emulsion (KRL341 SBR obtained from Kumho, a company of South Korea) with different levels into in the presence of RNS. The mixture was baked at approximately 85 oC for approximately 72 hours then exposed to TGA test. The data is illustrated in Fig.3. One can recognize the heat resistance of SBR increased with increased concentration of (GHC/RNS).

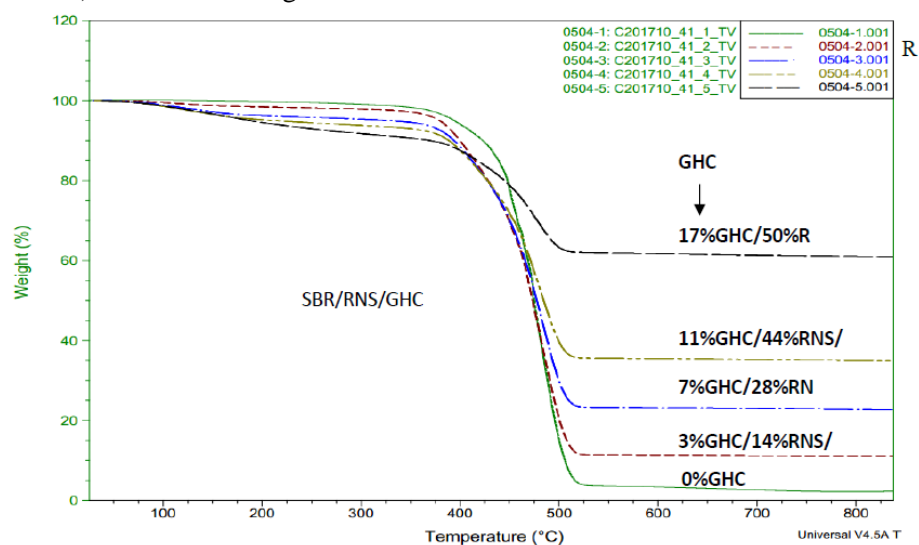


Figure 3. TGA data of SBR doped with GHC in the presence of RNS.

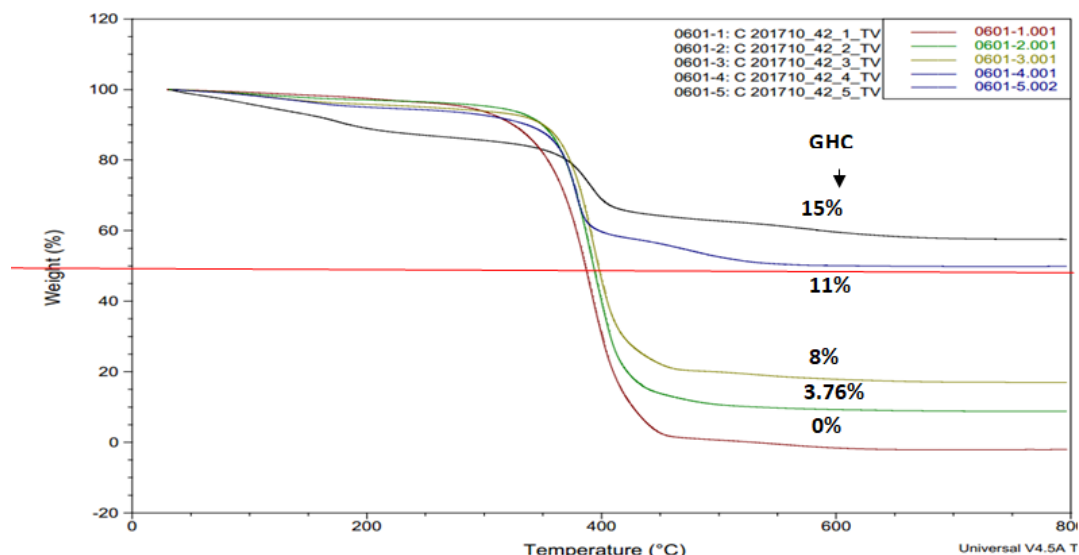


Figure 4. TGA data of NR doped with GHC in the presence of RNS

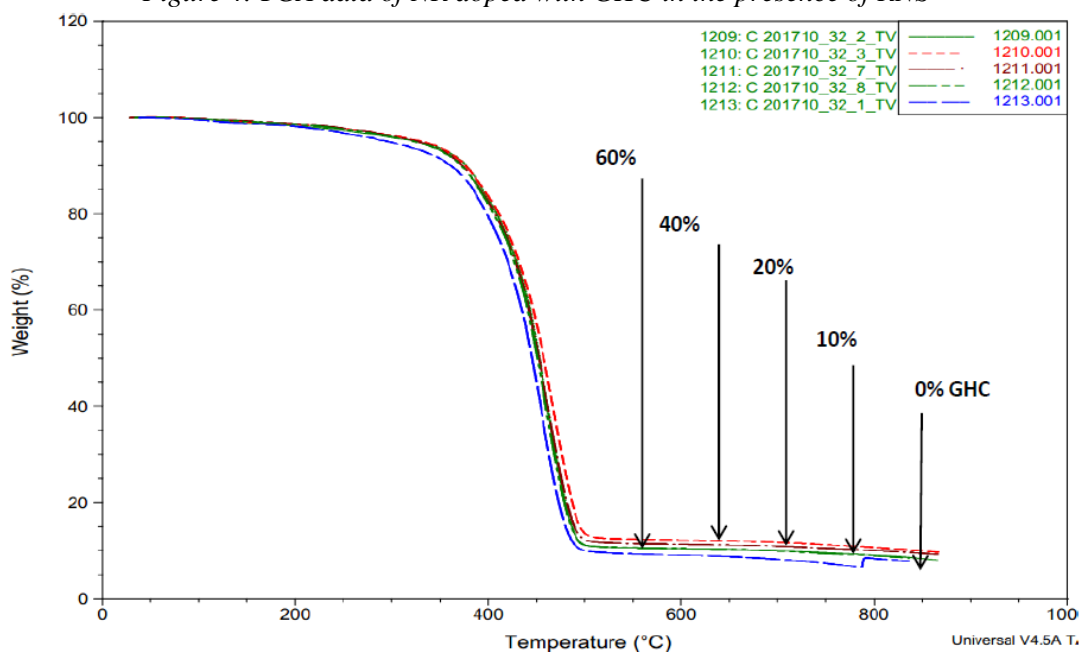


Figure 5. TGA data of rubber doped with GHC only (no RNS)

Fig.4 is a graph of TGA data of Natural Rubber (“NR”) doped with (GHC/RNS) composite. A similar reinforcement effect was observed. For further confirmation of the role of RNS, GHC alone was added into the SBR or Natural rubber, The TGA data of (GHC/rubber) composite was shown in Fig.5. One can observe that nothing change with no matter what GHC was added. It is suggested from this result that RNS is reactive; RNS can react with both rubber and GHC and (GHC/RNS) composite enables chemical bonding of GHC into rubber. Without RNS, GHC is substantially inert relative to any kinds of rubber. The chemical bonding of GHC

with rubber can cause reinforcement of rubber with GHC.

Overall, the present study provides a reactive nano silicate, which can comprise a silica/acid composite comprising reactive functional groups activated by an intramolecular disturber. The reactive functional groups can comprise -SiH, -SiOH, silazane, durazane, polysilazane, and spiro silazane.

The mechanism of causing increased reactivity of SAC by disturber molecule is not clear at this point in time. However, the specific disturber molecule somehow molecularly connected to SAC and successfully transfer electron from SAC into disturber causing

electron starving SAC and increase SAC reactivity as illustrated in Fig.6 as a band gap model of electron transfer between SAC and disturber. According to this model, SAC should be more electrically conductive than disturber. The thermal electron from conduction band of

SAC can be transferred into conduction band of disturber. Thus, disturber is relatively more electron acceptor than SAC. The disturber can be found in the group of oxide such as but not limited to Fe_2O_3 , Xe_2O , SnO_2 , Al_2O_3 , SiO_2 , TiO_2 , or a rare earth element oxide.

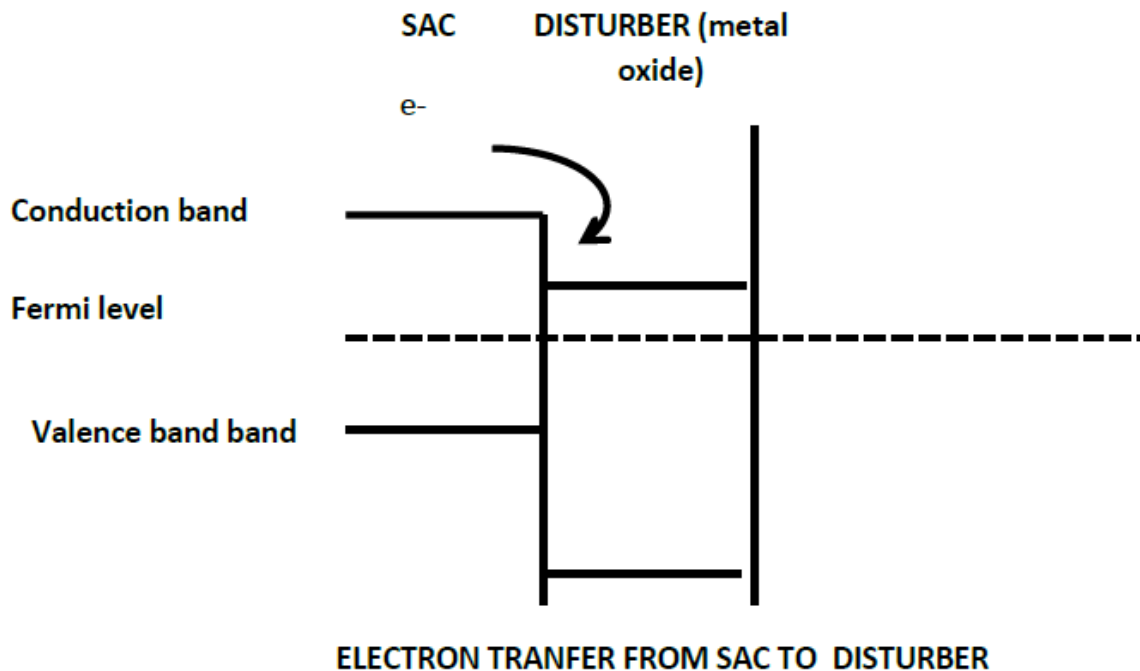


Figure 6. Electron transfer from SAC into Disturber

CONCLUSION

The RNS can exhibit intramolecular interaction caused by the reactive functional groups. The RNS can exhibit:

- Film forming properties;
- Water proofing properties;
- Flame retardant properties;
- Heat resistant properties;
- Ultraviolet energy (“UV”) blocking properties; and/or
- Weather resistant properties, etc.

The RNS can be reactive with:

- Rubber
- A hydroxylated material; and/or a hydroxylated nano carbon, such as a hydroxylated nano carbon that comprises at least one of a surface modified carbon black, carbon nano tube, fullerene, thin film graphene, graphene oxide, reduced graphene oxide, graphene nano platelet, graphene

hybrid composite, and/or a water soluble GHC, etc.

The RNS can be used as a precursor to:

- Provide a reinforcement capability of graphene in rubber;
- Enhance thermal conductivity of graphene in media;
- Enhance thermal conductivity of graphene in boron nitride; and/or Enhance thermal conductivity of graphene in aluminium nitride, etc.

References

- [1] Waterfastness, smearfastness, wear resistance, toughness and overall material durability enhancing nano additive U.S. Patent Publication 20180099905

[2] Physically functionalized graphene hybrid composite (GHC) and its applications United States Patent 9460827

[3] Systems, Devices, and/or Methods for Reactive Graphene and its Applications U.S. Patent Publication 20190202701

BIOGRAPHY



PROF. NGUYEN CHANH KHE

- PhD in 1982, Tokyo, Institute of Technology, Japan, Material Science
- Joined Dainippon Ink company in Tokyo, Japan 1982-1985)
- Join Eastman Kodak Research Laboratories, Rochester, NY, USA (1985_1989) (Electronic Printing)
- Joined Ricoh Corporation of USA in San Jose, California, USA (Electronic Printing) (1989 -1990)
- Joined Hewlett-Packard Lab in Palo Alto, California, USA (Printing Department) (1991 -2000)
- Joined APTOS, Milpitas, CA, USA (Semiconductor) (2000)
- Joined IC Sensor., Milpitas, CA, USA (Semiconductor) (2001)
- Saigon Hi Tech Park, SHTP Lab, Lab Head (2002 -2012)
- HK INVENT, CEO & CHAIRMAN (2014 until now)
- Dr Khe owns more than 40 US Patents in the field of electronic printing, electronic materials and nanotechnology.

INVITED TALKS

***NANOMATERIALS AND
NANODEVICES
(NMD)***

DEVELOPMENT OF NEW BIODEGRADABLE ALLOYS FOR MEDICAL PURPOSES

Zuzana Molčanová¹, Beata Balloková¹, Juraj Ďurišín², Slávka Martinková³, Dagmara Varcholová^{1,4}, Štefan Michalik⁵, Robert Tang-Kong⁶, Logan Ward⁷, Apurva Mehta⁸, Katarína Šul'ová^{1,4}, Michaela Šulíková³, Miloš Fejerčák^{1,3}, Andrea Lachová³, Róbert Džunda¹ and Karel Saks^{1,3}

¹Institute of Materials Research, Slovak Academy of Sciences, Watsonova 47, 040 01 Košice, Slovakia;

²Department of Technologies in Electronics, Faculty of Electrical Engineering and Informatics, Technical University of Košice, Letná 9, 042 00 Košice, Slovakia;

³Faculty of Science, Institute of Physics, Pavol Jozef Šafárik University in Košice, Košice 041 80, Slovakia;

⁴Faculty of Materials Metallurgy and Recycling, Technical University of Košice, Letná 9, 042 00 Košice, Slovakia;

⁵Diamond Light Source Ltd., Harwell Science and Innovation Campus, Didcot, Oxfordshire OX11 0DE, UK;

⁶Stanford University, 450 Serra Mall, Stanford, CA 94305, USA;

⁷Argonne National Laboratory, 9700 S. Cass Avenue, Lemont, IL 60439, USA;

⁸Stanford Synchrotron Radiation Lightsource, SLAC National Accelerator Laboratory, Menlo Park, CA 94025, USA

Email: ksaks@saske.sk

ABSTRACT

In surgery, besides the joint replacements that need permanent prosthesis implantation in the human body, there are many other clinical cases, such as bone fracture, cardiovascular diseases, in which the temporary implant materials are needed. The fixation or mechanical support are temporarily needed during the healing process of the injured or pathological tissue, and after that, the implants accomplish their mission and will no longer function in human body. In this case, biodegradable materials are the optimal choice as these materials do their job while healing and new tissue forming occur and degrade in the human body thereafter. Amorphous magnesium-zinc based alloys are nowadays a very promising group of metallic glasses. Unfortunately, the brittleness of Mg-Zn MGs and poor glass forming ability have hindered their further application. We have developed composition series of completely new (not published) ternary Mg-Zn-Sr biodegradable alloys with attractive properties in terms of possible future applications (density comparable to human bones, wide supercooled liquid region etc.). These ternary alloys will serve as precursors for design of future highly alloyed systems with tuned dissociation rate in human body.

Keywords: Biodegradable, alloys, X-ray diffraction, nanoindentation

INTRODUCTION

In the field of surgical orthopaedics, an important aspect is the suppression of inflammatory reaction at the site of contact of metal implants with human tissue. Materials considered to be bio-inert such as titanium, stainless steel and cobalt and chromium-based alloys are widely used joint replacement materials such as ribs and knees [1]. The human defence (immune) mechanism naturally defends itself against foreign objects and there is a risk of implant rejection. The human body tends to reject titanium, and in addition, abrasion may result in

the release of toxic ions into the surrounding tissue [2]. For these reasons, stainless steel, which exhibits higher compatibility is more commonly used, but its drawback is a significantly higher density compared to bones. A breakthrough class in the field of the use of metal implants is the so-called biodegradable metals (BMs) [1]. They do not need to be surgically removed after fulfilling their function and thus cause further discomfort to the patient in the form of re-operation. These materials dissolve in a controlled manner, in addition to assisting in healing (since they nourish the surrounding tissue) because they are

made up of elements inherently existing in the human body.

Mg alloys with excellent biocompatibility have become one of the most revolutionary research topics as bio-implant materials [3]. However, the clinic applications are limited with the current developed Mg alloys due to their high corrosion rate and hydrogen release rate. Mg-Zn-Ca based bulk metallic glasses (BMG) have received considerable attention because of their much lower corrosion rate and good mechanical properties. Unfortunately, the brittleness of Mg-Zn-Ca MGs and poor glass forming ability (GFA) have hindered their further application [4]. Thus, it is desirable to develop new Mg-based MGs with superior GFA and mechanical properties. Strontium, a bone-seeking element, has been reported to be capable of stimulating bone-cells replication and protein synthesis, depressing bone resorption, and increasing bone mass and strength [5]. Other studies have shown that strontium can inhibit bone resorption and stimulate bone formation [6]. Sr-based drug treatments can reduce the risk of fracture in patients after one year of treatment and inhibit osteoclast activity and stimulate osteoblast proliferation [7].

This work reports our development of a brand new fully biocompatible bulk metallic glass based on Mg, Zn and Sr. Our alloys development is based on machine learning prediction described in the article [8].

EXPERIMENTAL

The alloys selection was based on the condition that the elements that will be used are exclusively biocompatible. The choice of the chemical composition of alloys that could form metallic glass is based on the new machine learning prediction approach described in the article F. Ren et al. [8]. The result of this prediction is shown on the Mg-Ca-Sr ternary alloy as probabilistic color map where the most probable compositions to form metallic glass are in red color, see Figure 1. We decided to experimentally verify compositions laying on concentration of Sr up to 8 at.%. Our selections are marked in the figure by squares and circles. The Mg-Zn-Sr alloys of different compositions were fabricated by induction melting of the pure constituent elements (Mg 99.98 wt.% Zn 99.9% wt.% and Sr 99 wt.%) in a BN coated quartz tube under a high vacuum (better than 3.0×10^{-3} Pa) at 1000 °C. Ribbons of maximum thickness of 40

μm, width ~4 mm and length below 70 mm were prepared by the single-roller melt-spinning method.

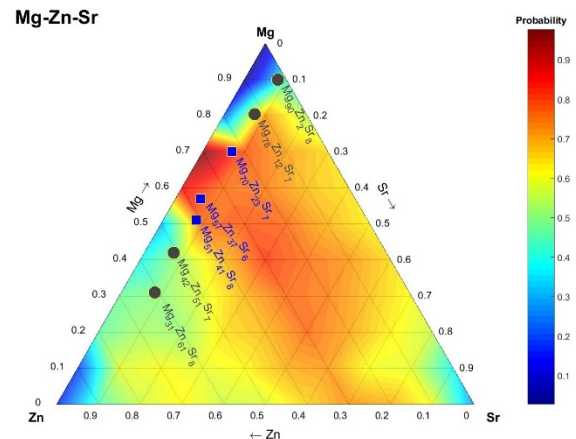


Figure 1. Mg-Ca-Sr ternary diagram showing in colormap prediction of glass forming probability calculated by machine learning algorithm, the alloys which were tested experimentally are marked by squares and circles.

The densities of the alloys were measured at room temperature using a gas pycnometer (Micromeritics, AccuPyc II 1340) with helium as the displacing fluid. The density measurements were performed 40 times and the measurement values were averaged.

Elastic modulus of the alloys was determined by nanoindentation experiment conducted using the NHT, CSM nanoindenter instruments calibrated on pure fused silica. The indenter tip was a diamond Berkovich indenter (three sided pyramid) and the results were evaluated using the Oliver-Pharr method. Indentation was performed in single load mode as high as 25 mN using the loading rate 1 mN/s, with dwell time 10 s.

Thermal stability of the alloys was ascertained by Perkin Elmer power-compensated differential scanning calorimeter (DSC 8000) at the scanning rate of 10 K.min⁻¹. Measurement was carried out in graphite sample pans under pure argon atmosphere. Each measurement was followed by a second run to determine baseline of the measurement.

To determine phase composition of crystalline samples the laboratory X-ray diffractometer Philips X'Pert PRO using Cu K α radiation was applied. For the amorphous alloys the hard X-ray diffraction experiment was performed at the beamline P21.1 located at the PETRA III (electron storage ring operating at an energy of 6 GeV with beam current ~100mA

operating in top-up mode). During the experiment the following setup was used: transmission (Debye-Scherrer) geometry; monochromatized high energy X-ray beam of photon energy 103.06 keV ($\lambda = 0.01203$ nm) to obtain high quality diffraction patterns up to large magnitude of the scattering vector $Q_{max}=4\pi \sin(\theta)/\lambda=18 \text{ \AA}^{-1}$; beam cross-section on the sample was $\sim 1 \text{ mm} \times 1 \text{ mm}$ (h x v); fast 2D image plate detector Perkin Elmer XRD1621 (2048 pixels \times 2048 pixels, size of a pixel: 200 $\mu\text{m} \times 200 \mu\text{m}$) to record diffracted X-rays.

RESULTS AND DISCUSSION

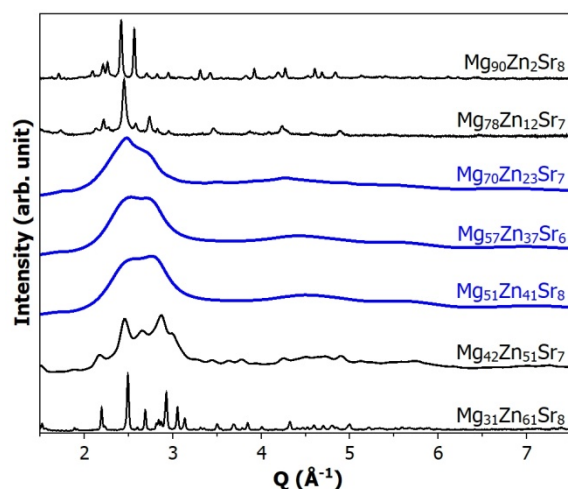


Figure 2. X-ray diffraction patterns of the Mg-Zn-Sr alloys prepared by rapid solidification method – melt spinning. XRD patterns of the amorphous alloys are in blue, while the partially or fully crystalline alloys are black.

Figure 2 shows X-ray diffraction patterns of the Mg-Zn-Sr alloys. From this figure it is evident that the alloys of the composition $\text{Mg}_{90}\text{Zn}_2\text{Sr}_8$, $\text{Mg}_{78}\text{Zn}_{12}\text{Sr}_7$ and $\text{Mg}_{31}\text{Zn}_{61}\text{Sr}_8$ are fully crystalline, (marked by grey circles on the Figure 1), while the $\text{Mg}_{70}\text{Zn}_{23}\text{Sr}_7$, $\text{Mg}_{57}\text{Zn}_{37}\text{Sr}_6$ and $\text{Mg}_{51}\text{Zn}_{41}\text{Sr}_8$ were prepared in fully amorphous state (blue squares). The $\text{Mg}_{42}\text{Zn}_{51}\text{Sr}_7$ alloy is only a partially crystalline. The DSC signal from this alloy, not shown here, exhibits glass transition followed by crystallization exothermic peak, features characteristic for metallic glasses.

Chemical composition determined by the EDX analysis, phase composition, elastic

modulus, nano-hardness as well as the characteristic phase transformation temperatures of the Mg-Zn-Sr alloys are listed in Table 1. By comparing the results we can formulate the following conclusions:

- By change of magnesium to zinc ratio, the modulus of elasticity E_{IT} of the alloys does not change, and its value is approximately twice that of the modulus of cortical bone (~ 20 GPa). The highest value 61 ± 6 GPa shows the alloy $\text{Mg}_{31}\text{Zn}_{61}\text{Sr}_8$.
- Nano-hardness H_{IT} of the alloys are for all the alloys the same within the experimental error.
- Super-cooled liquid region (important technological parameter for thermoplastic forming of the material) is in the case of the $\text{Mg}_{57}\text{Zn}_{37}\text{Sr}_6$ extraordinarily wide 79°C . This parameter also confirms that the $\text{Mg}_{57}\text{Zn}_{37}\text{Sr}_6$ composition is close to deep eutectic of this ternary system. Such observation is in good agreement with the machine learning prediction, see amorphous phase probability map in Figure 1.
- As expected, the alloy density increases with increasing Zn content at the expense of Mg. The lowest measured density $2.103 \text{ g}\cdot\text{cm}^{-3}$ is close the value reported for of non-porous cortical bones $1.9 \text{ g}\cdot\text{cm}^{-3}$.

CONCLUSION

In this paper we report our development of a brand new fully biocompatible bulk metallic glass based on Mg, Zn and Sr elements. Design of the alloys was based on machine learning prediction described in the work of F. Ren et al. [8]. In the range of strontium concentrations from 6 to 8 at.% we have identified compositional areas that can be prepared to fully amorphous state by rapid quenching method with critical cooling rate $\sim 10^5 \text{ K}^{-1}$, see Figure 1. The alloys except of the $\text{Mg}_{31}\text{Zn}_{61}\text{Sr}_8$ have elastic modulus ~ 45 GPa, and indentation nanohardness ~ 4 GPa. The alloy $\text{Mg}_{57}\text{Zn}_{37}\text{Sr}_6$ exhibits extraordinarily wide 79°C super-cooled liquid region, indicating that this alloys composition is close to deep eutectic point of the Mg-Zn-Sr system.

Table 1. Properties of the Mg-Zn-Sr alloys, from left to right EDX determined chemical composition, phase composition (A - amorphous C – crystalline phase, A/C - mixed state), E_{IT} - elastic modulus, H_{IT} – hardness, T_g – glass transition temperature, T_{x1} onset – onset of the 1th crystallization temperature, ΔT – supercooled liquid region and ρ – density.

Alloy	Phase	E_{IT} [GPa]	H_{IT} [GPa]	T_g [°C]	T_{x1} onset [°C]	ΔT [°C]	ρ [g.cm ⁻³]
Mg ₉₀ Zn ₂ Sr ₈	C	46±4	4.4±0.8				2.106
Mg ₇₈ Zn ₁₂ Sr ₇	C	46±5	5.0±0.9				2.484
Mg ₇₀ Zn ₂₃ Sr ₇	A	44±3	3.9±0.3	96	130	34	2.807
Mg ₅₇ Zn ₃₇ Sr ₆	A	45±4	3.4±0.7	96	175	79	3.291
Mg ₅₁ Zn ₄₁ Sr ₈	A	46±4	4.4±0.8	147	214	67	3.663
Mg ₄₂ Zn ₅₁ Sr ₇	A/C	46±3	4.4±0.7	179	243	64	4.291
Mg ₃₁ Zn ₆₁ Sr ₈	C	61±6	4.7±0.7				4.985

Acknowledgment

This work was realized within the framework of the project „Research Centre of Advanced Materials and Technologies for Recent and Future Applications „PROMATECH“, ITMS 26220220186, supported by the Operational Program “Research and Development” financed through the European Regional Development Fund. This work was supported by the Slovak Research and Development Agency under contract No. APVV-17-0008 and APVV-15-0202. Zuzana Molčanová, Beata Balloková, Juraj Ďurišin, Dagmara Varcholová, Katarína Šul'ová, Michaela Šulíková, Miloš Fejercák and Karel Saksl are grateful to the Scientific Grant Agency of the Ministry of Education, Science, Research and Sport of the Slovak Republic and the Slovak Academy of Sciences (VEGA projects No. 2/0013/19, 2/0080/17 and 1/0776/14). This work was carried out with the support of the PETRA III (proposal I-20190621 EC). We thank Dr. Oleh Ivashko for assistance in using beamline P21.1.

References

[1]. Y.F. Zheng, X.N. Gu, F. Witte, *Biodegradable metals*, Materials Science and Engineering R 77 (2014) 1-34
 [2]. M. P. Staiger, A. M. Pietak, J. Huadmai, G. Dias, *Magnesium and its alloys as orthopedic*

biomaterials: a review, Biomaterials 27 (2005) 1728-1734

[3]. S.Y. Cho, S.W. Chae, K.W. Choi, H.K. Seok, Y.C. Kim, J.Y. Jung, et al., *Biocompatibility and strength retention of biodegradable Mg-Ca-Zn alloy bone implants*, Journal of Biomedical Materials Research Part B: Applied Biomaterials 101 (2013) 201–212.
 [4]. Q.F. Li, H.R. Weng, Z.Y. Suo, Y.L. Ren, X.G. Yuan, K.Q. Qiu, *Microstructure and mechanical properties of bulk Mg-Zn-Ca amorphous alloys and amorphous matrix composites*, Materials Science and Engineering: A 487 (2008) 301–308.
 [5]. Y. Li, C. Wen, D. Mushahary, R. Sravanthi, N. Harishankar, G. Pande, et al., *Mg–Zr–Sr alloys as biodegradable implant materials*, Acta Biomaterialia 8 (2012) 3177–3188.
 [6]. P. Marie, P. Ammann, G. Boivin, C. Rey, *Mechanisms of action and therapeutic potential of strontium in bone*, Calcified Tissue International 69 (2001) 121–129.
 [7]. P. Marie, *Strontium ranelate: a physiological approach for optimizing bone formation and resorption*, Bone 38 (2006) 10–14.
 [8]. F. Ren, L. Ward, T. Williams, K.J. Laws, Ch. Wolverton, J.H.-Simpers, A. Mehta, *Accelerated discovery of metallic glasses through iteration of machine learning and high-throughput experiments*, Science Advances 13 (2018) EAAQ1566



BIOGRAPHY

Family name, First name: **SAKSL, Karel**
Researcher unique identifier(s): Scopus Author Identifier 6602635254
Date of birth: 27th May 1974
Nationality: Slovak

• EDUCATION

2010 DrSc, Technical University of Košice, Slovakia
2000 PhD, Faculty of Mechanical Engineering, Technical University of Košice, Slovakia
1997 Master, Faculty of Metallurgy, Technical University of Košice, Letná 9, Košice, Slovakia

• CURRENT POSITION(S)

2007 – Current leading scientist
Institute of Materials Research, Slovak Academy of Sciences, Košice, Slovakia

• PREVIOUS POSITIONS

2002 – 2007 Postdoctoral researcher
DESY, Notkestr.85, D–226 03 Hamburg, Germany
2001 – 2001 Postdoctoral researcher
Department of Physics, Technical University of Denmark, Lyngby, Denmark

• FELLOWSHIPS AND AWARDS

2009 Honorable Mention - Scientist of the Year 2009 contest for the scientific work "Turning solid aluminum transparent by intense soft X-ray photoionization", published in NATURE PHYSICS, Slovakia
2008 Honorable Mention - Scientist of the Year 2008 contest for the scientific work "How Metallic Fe Controls of its Native Oxide", published in one of the world's most prestigious magazines devoted to solid state physics "PHYSICAL REVIEW LETTERS", Slovakia
2007 Honorable Mention - Scientist of the Year 2007 contest for the scientific work "Atomic structure of glassy Mg₆₀Cu₃₀Y₁₀ investigated with EXAFS, X-ray and neutron diffraction, and reverse Monte Carlo simulations", published in one of the world's most prestigious magazines devoted to solid state physics "PHYSICAL REVIEW B", Slovakia

• SUPERVISION OF GRADUATE STUDENTS AND POSTDOCTORAL FELLOWS

2007 – 2019 Number of PhD: 8, finished 5, current 3
Faculty of Metallurgy, Technical University of Košice, Košice, Slovakia
Faculty of Science, Pavol Jozef Šafárik University in Košice, Košice, Slovakia

• TEACHING ACTIVITIES

2014 – Current Teacher – Structural analysis methods, Faculty of Science, Pavol Jozef Šafárik University in Košice, Košice, Slovakia

• ORGANISATION OF SCIENTIFIC MEETINGS

2014-2019 Head of organization committee of the School of XFEL and Synchrotron Radiation Users, Slovakia

• INSTITUTIONAL RESPONSIBILITIES

2010 - Current Deputy Director for science, Institute of Materials Research SAS, Slovakia
2016 – Current Head of Scientific Division - Metallic systems, (28 members), Institute of Materials Research SAS, Slovakia

- **REVIEWING ACTIVITIES**

2009- 2013 Member of Scientific Advisory Committee of the European XFEL, Hamburg Germany
2007 – Current Scientific Advisory Board, Institute of Materials Research SAS, Slovakia

- **MAJOR COLLABORATIONS**

2010 – Current Representative of the Slovak Republic in the Council of the European XFEL project.
2014 – Current Representative of the Slovak Republic in User consortia “Serial Femtosecond Crystallography” and “XFEL Biology Infrastructure”.
2009 Member of the scientific team involved in the discovery of saturable absorption in aluminum using record intensities over 10^{16} W cm⁻² at photon energy of 92 eV, never observed before in core-electron transitions.

DEVELOPMENT OF NANOMATERIALS-BASED CHEMIRESENSITIVE GAS SENSORS FOR DETECTION OF HAZARDOUS GASES

Hyoun Woo Kim¹ and Sang Sub Kim²

¹ Division of Materials Science and Engineering, Hanyang University, Seoul 04763, Republic of Korea;

² Department of Materials Science and Engineering, Inha University, Incheon 22212, Republic of Korea

Email: sangsub@inha.ac.kr

ABSTRACT

Over the past decades, the reliable and early-stage detection of hazardous gases has become gradually important in various areas of modern industrialized, mobile-networked society. The purpose includes safety both in industry and at home, health care, defense of terror and chemical warfare, and environment monitoring. Stimulated by the great demand, significant efforts have been made to realize highly sensitive and selective chemical gas sensors not only by the creative design of new materials but also by innovation in sensor structure and architecture. It is widely accepted that improving the sensing capability is to use nanomaterials. In this talk, an overview on the current status of nanomaterials-based chemiresistive gas sensors and their prospect will be presented. In addition, various approaches to obtain better sensing properties of nanomaterials will be discussed.

Keywords: Nanomaterials, Chemiresistive sensor, Gas sensor, Environment monitoring

BIOGRAPHY



Sang Sub Kim joined the Department of Materials Science and Engineering, Inha University, in 2007 as a full professor. He received his B.S. degree from Seoul National University and his M.S and Ph.D. degrees from Pohang University of Science and Technology (POSTECH) in Material Science and Engineering in 1987, 1990, and 1994, respectively. He was a visiting researcher at the National Research in Inorganic Materials (currently NIMS), Japan for 2 years each in 1995 and in 2000. In 2006, he was a visiting professor at Department of Chemistry, University of Alberta, Canada. In 2010, he also served as a cooperative professor at Nagaoka University of Technology, Japan. His research interests include the synthesis and applications of nanomaterials such as nanowires and nanofibers, functional thin films, and surface and interfacial characterizations. Currently, he is serving as Editorial Board Members for the following journals: Scientific Reports, Sensors, Applied Sciences, Journal of Sensors, Metals and Materials International, and Electronic Materials Letters.

MEMS-APPROACHES FOR CONTROLLING INFRARED THERMAL ENERGY IN LIGHT SOURCE AND DETECTOR

Minoru Sasaki

Toyota Technological Institute,
2-12-1 Hisakata, Tenpaku-ku, Nagoya, 468-8511, Japan
Email: mnr-sasaki@toyota-ti.ac.jp

ABSTRACT

The thermal devices can work without cooling. This is different from the quantum devices based on the semiconductor bandgap which suffers from the thermal noise especially for the infrared (IR) application. For saving the operation power for cooling the device, the thermal devices become attractive to many applications. Here, (1) a light source and (2) a detector are described. The basic MEMS advantage is the low thermal conduction loss keeping the thermal energy at the specific position. (1) A microheater for the wavelength selective IR emitter shows the enhanced emission peak for CO₂ gas sensing using to the surface plasmon polariton. Figure 1 shows the schematic drawing of the emitter. The thermal isolation is obtained using 2 μm-thick Si membrane having 5.4mm outer diameter realized by the structure with the ring reinforcement. Figure 2 shows the photo of the microheater observed from the front and the back sides. Figure 3 show the emission spectra. The underlying gold grating is designed to have 4.3 μm pitch. The emission at the wavelength of the absorption band of CO₂ gas is enhanced. Against input power, the intensity at the peak wavelength shows the steeper increase than the background intensity. The peak at 4.3 μm has the width of about 400 nm and CO₂ absorption band is inside. (2) A temperature-sensitive electrostatic resonator is realized. Figure 4 shows the resonator at (a) the initial and (b) the heated conditions. The resonator consists of two layers. The base layer is the tensile (600 MPa) poly-Si. The larger thermal expansion of the top Al layer bends the structure, making the torsion bar slant. This increases the torsional spring constant. From the frequency change, the incident infrared can be measured. Figure 5 shows one fabricated device. The twisting resonant frequency increases from 112 kHz at the rate of 426 Hz/K. The ratio is +3790 ppm/K. This is more than 10-times larger in magnitude and opposite in direction compared to the temperature dependence of the material used indicating the high sensitivity. The temperature dependence of the transverse elastic moduli of Al and Si will give the ratio of -285 and -30 ppm/K, respectively. Figure 6 shows the response when the resonator is irradiated by the infrared spot. Keywords: Optical MEMS, Infrared Emitter, Surface Plasmon Polariton, Infrared Detector, Resonator

Acknowledgment

Part of this research is supported by Subsidy to Private Institution of Higher Education.

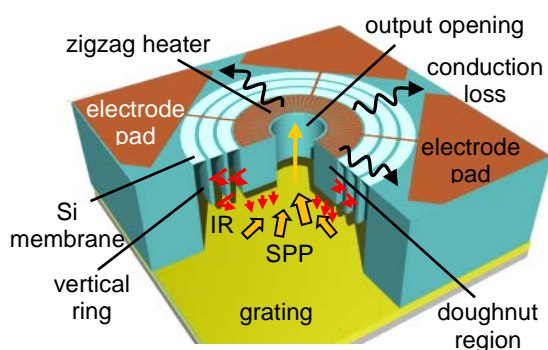


Figure 1. Schematic drawing of the indirect wavelength selective thermal emitter and the energy flows of the microheater on the grating.

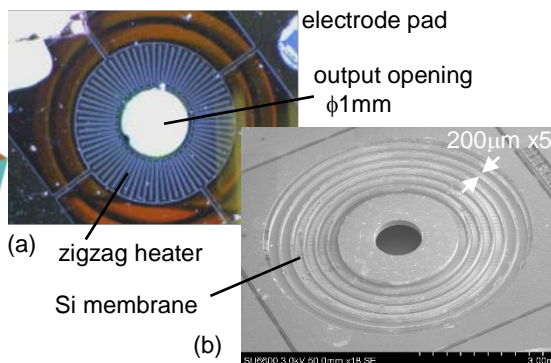


Figure 2. (a) Photo of the microheater. The current flows between electrodes at the opposite corners. (b) SEM image of the microheater observed from backside. The membrane outer diameter is 5.4mm.

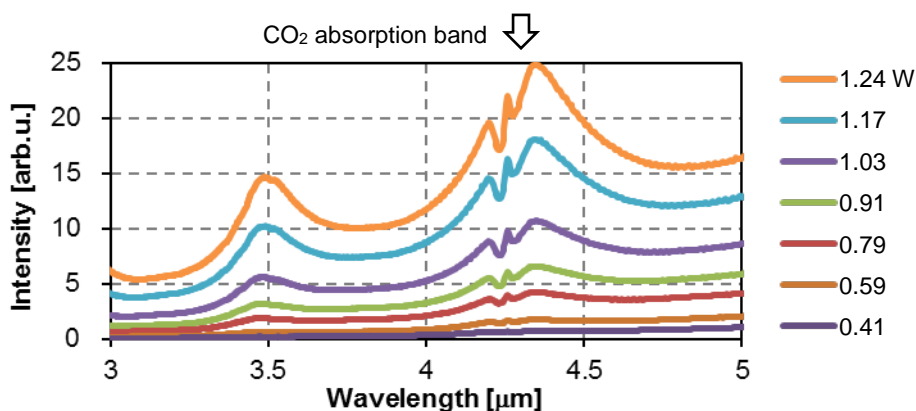


Figure 3. FT-IR spectra of the emission. With the aimed peak at $4.3\mu\text{m}$, other peaks at 2.9 and $3.5\mu\text{m}$ are also observed. This can be attributed to the insufficient grating profile control at present.

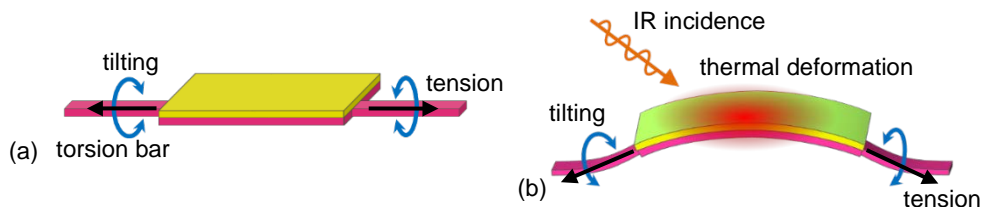


Figure 4. Principle of increasing the natural frequency of the torsional resonator showing (a) the initial and (b) the heated conditions.

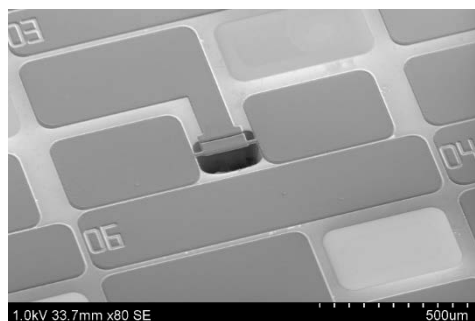


Figure 5. One fabricated device. The tensile poly-Si is obtained by crystallizing LPCVD grown amorphous Si.

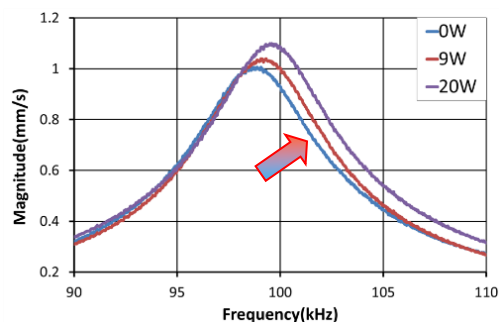


Figure 6. Resonant frequency shift of the resonator being irradiated by the infrared light spot at the different source power.

BIOGRAPHY



Minoru Sasaki received the M. S. and Dr. Eng. degrees from Nagoya University in 1993 and 1995, respectively. In 1995, he is a Research Fellow of the Japan Society for the Promotion of Science. Since 1996, he has been a member of the Department of Mechatronics and Precision Engineering, Tohoku University. Since 2007, he has been a professor in the Department of Advanced Science and Technology, Toyota Technological Institute, Nagoya, Japan. He is the responsibility of Toyota Technological Institute in MEXT nanotechnology platform project, Japan. His research interests include micro/nano-fabrication technique especially realizing 3D structures, MEMS devices including the human and the environment monitoring.

LOW-DIMENSIONAL (0D, 1D, 2D) DEVICES FOR FUTURE ELECTRONICS

Shunri Oda¹, **Takamasa Kawanago**¹ and **Hitoshi Wakabayashi**²

¹Tokyo Institute of Technology, Ookayama, Meguro-ku, Tokyo 152-8552, Japan;

²Tokyo Institute of Technology, Nagatsuta, Midori-ku, Yokohama 226-8503, Japan

Email: soda@pe.titech.ac.jp

ABSTRACT

One of the major application targets for future electronics is wearable communication tools with low-power consumption. Tunnel field-effect-transistors (TFET) are promising since extremely low-voltage operation of switching beyond the limitation of CMOS devices would be possible. 2D materials and 1D nanowires attract attention not only because these materials would be suitable for the fabrication of TFETs, but also various novel application such as sensors, displays would be possible. Quantum computing is no longer a future technology. Recent advances in D-Wave computers based on quantum annealing and superconducting devices, and the demonstration of long spin decoherence times in isotopically-enriched Si qubits, have accelerated the research and development of this technology. The remaining challenge is large scale integration of qubits. Physically-defined coupled quantum dots (QDs) on silicon-on-insulator substrates are promising for multiple scaled qubits. In this paper, we discuss recent progress of 0D (quantum dots), 1D (nanowires) and 2D atomic-layer materials devices.

Keywords: Quantum dot, Si nanowire, 2D atomic layer devices

INTRODUCTION

One of the major application targets for future electronics is zero-power (without the need of recharging battery) wearable communication tools [1]. Combination of low-power consumption devices and energy harvesting devices are necessary. Tunnel field-effect-transistors (TFET) are promising since extremely low-voltage operation of switching beyond the limitation of CMOS devices would be possible [2]. 2D materials and 1D nanowires attract attention not only because these materials would be suitable for the fabrication of TFETs, but also various novel application such as sensors, displays would be possible [3].

On the other hand, quantum computing is no longer a future technology. Recent advances in D-Wave computers based on quantum annealing [4] and superconducting devices, and the demonstration of long spin decoherence times in isotopically-enriched Si qubits [5], have accelerated the research and development of this technology. The remaining challenge is large scale integration of qubits. Physically-defined coupled quantum dots (QDs) on silicon-on-insulator substrates represent potential multiple scaled qubits.

In this paper, we discuss recent progress of quantum dot (0D), nanowire (1D) and 2D atomic-layer material devices

COUPLED QUANTUM DOTS FOR SILICON QUBITS

A. Device Fabrication

Physically-defined double quantum dots connected to source/drain electrodes, five side gate electrode to control the number of electrons in QDs and interaction between QDs and electrodes, are fabricated on SOI (silicon-on-insulator) substrates by electron-beam lithography and reactive ion etching [6].

B. Pauli Spin Blockade

Electron transport was measured at 250 mK. Current counter plot as functions of two control gate electrodes showed honeycomb-like structure, which suggests quantum interaction between two quantum dots. We also observed current rectification in coupled QDs due to Pauli spin blockade, which is a valuable tool for the initialization and readout of spin states during the operation of spin qubits [6, 7].

C. A Few Electron Regime

To implement quantum logic gates based on electron spin, it is necessary to reduce the number of electrons in individual QDs to only a few or even to a single electron, so as to create spin states that are energetically well defined and separate from other states. We prepared integrated charge sensors (CSs) composed of QDs in order to determine the absolute number of electrons in the individual QDs.

We have successfully determined the number of electrons in each QD and controlled a few electron regimes in coupled QDs as shown in Fig. 1; essential steps for qubit operation [7,8]. Recently, single-qubit gate fidelities exceeding 99.9% have been observed on an electron spin confined in a $^{28}\text{Si}/\text{SiGe}$ quantum dot [9]. This is quite promising for the realization of fault-tolerant universal quantum computation.

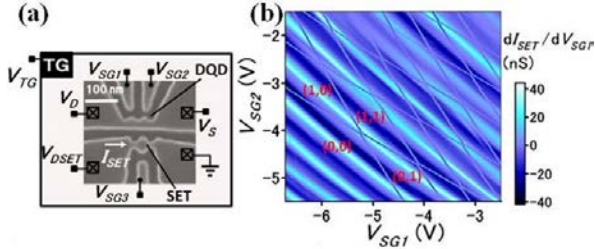


Figure 1. (a) SEM image of a double-quantum dot (DQD) device and a schematic of the measurement setup. The DQD device was fabricated by the same process used to make the single QD device and measurements were performed at a base temperature of 300 mK. (b) Plots of the SET transconductance, dI_{SET}/dV_{SG1} , as functions of V_{SG1} and V_{SG2} in a DQD; $V_{TG} = 5.8$ V and $V_{SG3} = 0$ V, $V_D = V_S = 0.9$ V, and $V_{DSET} = 3$ mV. A charge stability diagram of the few electron regimes in the DQD is clearly obtained. [7]

Ge/Si CORE/SHELL NANOWIRES

For the implementation of zero-power devices, energy harvesting systems from light, thermal, vibration, and RF energy are investigated. We propose thermoelectric devices using the temperature difference between human skin and ambient based on Ge/Si core/shell nanowires are promising for wearable power generators.

The figure of merit ZT of the thermoelectric system is described as

$$ZT = \frac{\sigma S^2}{\kappa} T \quad (1)$$

where κ is the thermal conductivity, σ is the electrical conductivity, S is the Seebeck coefficient, and T is the absolute temperature.

Because of the unique density of states distribution of one-dimensionally quantized structure of nanowires, high Seebeck coefficient is expected. Since Ge core region is confined by Si potential well, high hole concentration is obtained even in undoped Ge, that results in high electrical conductivity. Surface phonon scattering of Si shell region suppresses thermal conductivity. All these effects result in large value of the figure of merit for thermoelectric energy conversion.

We have prepared high crystalline quality and narrow Si and Ge nanowires by vapor-liquid-solid chemical vapor deposition [10-12]. We have also fabricated Ge/Si core/shell nanowires. The problem we encountered was the formation of branch structure due to migrated Au particles on the surface of Ge nanowires. We solved the problem by suppressing Au migration using two step growth methods [13]. We have obtained very high quality interface between Ge core and Si shell, as shown in Fig. 2, and measured electron transport in core/shell structures [14]. We also prepared thermoelectric devices based on Ge/Si core/shell nanowires. The preliminary measurements show very promising properties for energy harvesting devices for zero-power wearable devices.

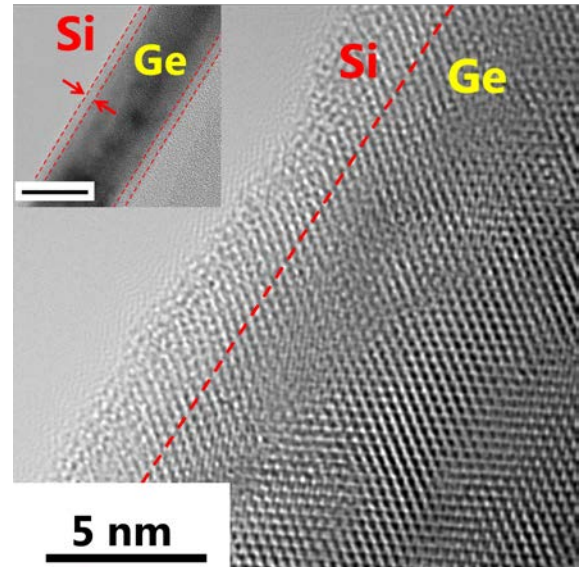


Figure 2. TEM image of a Ge/Si core/shell nanowire. The inset shows the whole Ge/Si NW with a 20 nm scale bar. [14]

TWO DIMENSIONAL ATOMIC LAYER TRANSISTORS

Two-dimensional atomic layer materials are promising for wearable device application, because of high-electric and thermal conductivity, low-power consumption, flexibility and transparency [15]. Particularly, MoS₂ transistors are promising, because of low interface defect density due to free of dangling bonds, scalability to sub-5-nm region due to ultra-thin uniform layer and relatively large bandgap [16, 17].

A self-assembled monolayer (SAM), an organic molecular film that spontaneously forms on the surface of a substrate exactly one molecule thick, has ideal characteristics for gate dielectrics in FETs because of insulating properties at a very thin layer and easy fabrication process. We applied n-octadecylphosphonic acid (ODPA) and AlO_x dual layer as gate dielectrics for MoS₂ transistors. The electrical properties are excellent with very steep subthreshold slope of 69 mV/dec and no hysteresis, which means free of interface defects [18]. A SAM layer is also used as a self-alignment mask to simplify the device fabrication process [19, 20]. Adhesion lithography using SAM has been applied to various material systems including organic semiconductors [21]. We also improved gate characteristics using transfer printing technology as shown in Fig. 3 [22]. Normally-off characteristics are achieved by controlling threshold voltage using proper gate metals [23].

Wafer scale MoS₂ films are commonly prepared by chemical vapor deposition. However, sometimes triangular structure deteriorates the uniformness of CVD grown films. In order to circumvent this problem, we deposited MoS₂ films by RF sputtering [24]. We clarified that surface flatness of the substrate is essential for high quality films [25]. To reduce the number of sulfur defects, annealing in the forming gas [26], H₂S [27] and sulfur vapor [28] was effective and low carrier density MoS₂ films were obtained. Normally-off nMISFET characteristics were observed from sputtered MoS₂ with MoSi₂ contacts by sulfur powder annealing [29]. High Hall-effect mobility of 1,250 cm²/Vs was obtained from atomic-layered ZrS₂ films using sputtering and annealing [30]. These processing technologies are important

steps towards future high-performance wearable devices.

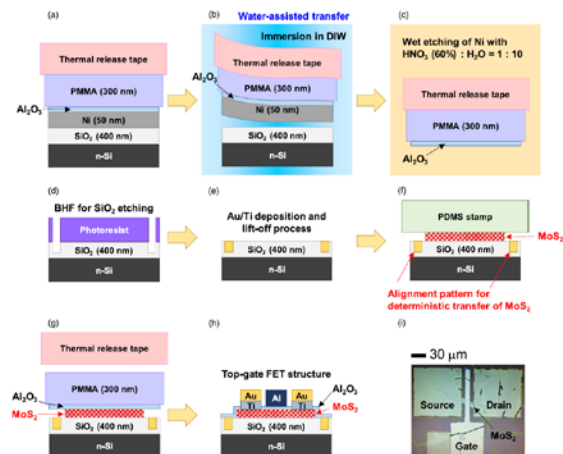


Figure 3. Schematic illustrations of transfer printing of Al₂O₃ gate dielectric and fabrication process for top-gate MoS₂ FET. (a) Deposition of Ni on SiO₂/Si substrate, ALD of Al₂O₃ gate dielectric on Ni, spin-coating of PMMA on Al₂O₃, and attachment of thermal release tape onto PMMA. (b) Immersion of entire substrate in DIW and separation of laminated structure from SiO₂ surface. (c) Wet etching of Ni with dilute HNO₃. (d) Formation of trench by photolithography and BHF etching. (e) Deposition and lift-off of Au/Ti to form alignment mark. (f) Deterministic transfer of MoS₂ flakes on the receiver substrate. (g) Transfer printing of Al₂O₃ gate dielectric on MoS₂ through a thermal release process. (h) Deposition and lift-off of Al and Au/Ti for gate and source/drain, respectively. (i) Optical image of top-gate MoS₂ FET. [22]

CONCLUSION

Low-dimensional materials are emerging. Novel properties, self-assembled fabrication are promising for next generation wearable devices and new architecture computations.

Acknowledgment

This work was supported in part by JST-CREST and JSPS KAKENHI Grant No. 26249048. The authors thank Tetsuo Kodera, Tomohiro Noguchi, Marolop Simanullang and Kousuke Horibe for discussion and performing experiments.

References

- [1] A. M. Ionescu, IEDM 2017, 1.2.
- [2] A. M. Ionescu and H. Riel, Nature, **479**, pp. 329-337, 2011.
- [3] D. Sarkar et al., Nature, **526**, pp. 91-95, 2015.

- [4] M.W. Johnson et al., *Nature*, **473**, 194-198 2011.
- [6] G. Yamahata, T. Kodera, H. O. H. Churchill, K. Uchida, C. M. Marcus, and S. Oda, *Phys. Rev. B*, **86**, 115322, 2012.
- [7] S. Oda, G. Yamahata, K. Horibe and T. Kodera, *IEDM 2016*, 13.3.
- [8] K. Horibe, T. Kodera and S. Oda, *Appl. Phys. Lett.* **106**, 083111, 2015.
- [9] J. Yoneda et al., *Nature Nanotechnology*, **13**, pp. 102-106, 2017.
- [10] S. Akhtar, K. Usami, Y. Tsuchiya, H. Mizuta, and S. Oda, *Appl. Phys. Express*, **1**, 014003, 2008.
- [11] C. B. Li, K. Usami, T. Muraki, H. Mizuta, and S. Oda, *Appl. Phys. Lett.* **93**, 041917, 2008.
- [12] M. Simanullang, K. Usami, T. Kodera, K. Uchida, and S. Oda, *J. Nanosci. Nanotechnol.* **11**, 8163, 2011.
- [13] T. Noguchi, Marolop Simanullang, Z. Y. Xu, K. Usami, T. Kodera and S. Oda, *Appl. Phys. Express*, **9**, 055504, 2016.
- [14] T. Noguchi et al., *Phys. Status Solidi A*, **212**, 1578, 2015.
- [15] P. Ajayan, P. Kim, and K. Banerjee, *Physics Today*, **69**, 38-44, 2016
- [16] W. Cao, J. Kang, D. Sarkar, W. Liu, and K. Banerjee, *IEEE Trans. Electron Dev.*, **62**, pp. 3459–3469, Nov. 2015.
- [17] A. Pal, W. Cao, J. Kang, and K. Banerjee, *IEDM 2017*, 31.3.
- [18] T. Kawanago and S. Oda, *Applied Physics Letters*, **108**, 041605, 2016.
- [19] T. Kawanago, R. Ikoma, W.J. Du and S. Oda, *IEEE ESSDERC 2016*, pp. 251-254.
- [20] W.J. Du, T. Kawanago and S. Oda, *Japanese Journal of Applied Physics*, **56**, 04CP10, 2017.
- [21] J. Semple et al., *npj Flexible Electronics (online)*, **2**, 18, 2018.
- [22] T. Kawanago, T. Oba and S. Oda, *Applied Physics Express*, **12**, 026501, 2019
- [23] T. Kawanago and S. Oda, *Applied Physics Letters*, **110**, 133507, 2017.
- [24] T. Ohashi, et al., *Japanese Journal of Applied Physics*. **54**, 04DN08, 2015.
- [25] T. Ohashi et al., *Appl. Phys. Express*, **10**, 041202, 2017.
- [26] J. Shimizu et al., *Japanese Journal of Applied Physics*, **56**, 04CP06, 2017.
- [27] J. Shimizu et al., *Electron Devices Technology and Manufacturing Conference (EDTM) 2017*, P-22.
- [5] M. Veldhorst et al., *Nature Nanotech.* **9**, 981, 2014.
- [28] K. Matsuura et al., *Journal of Electronic Materials*, **47**, pp. 3947 - 3501, 2018.
- [29] K. Matsuura et al., 19th International Workshop on Junction Technology (IWJT) 2019, S1-3.
- [30] M. Hamada et al., *IEEE J. EDS*, 2019 Published Online. DOI: [10.1109/JEDS.2019.2943609](https://doi.org/10.1109/JEDS.2019.2943609).

BIOGRAPHY



Shunri Oda received the B. Sc degree in physics, the M. Eng. and Dr. Eng. degree from Tokyo Institute of Technology in 1974, 1976 and 1979, respectively.

He joined faculty of Tokyo Institute of Technology in 1979 and now is a Professor Emeritus. His research interests include fabrication of silicon quantum dots by pulsed plasma processes, single electron tunneling devices based on nanocrystalline silicon, ballistic transport in silicon nanodevices, silicon based quantum information devices, and NEMS hybrid devices. He was a Research Leader of MEXT Center of Innovation program. He has authored more than 700 technical papers in international journals and conferences including 200 invited papers. He edited books (with D. Ferry) “Silicon Nanoelectronics” (CRC Press, 2006) and “Nanoscale Silicon Devices” (CRC Press, 2015).

Prof. Oda is a Fellow of IEEE and Japan Society for Applied Physics, and a member of Electrochemical Society and Materials Research Society. He is a Distinguished Lecturer of IEEE Electron Devices Society.

QUAI-2 DIMENSION OPTOELECTRONIC DEVICES

Sunkook Kim

Multifunctional Nano BioElectronics Lab, Department of Advanced Materials and Science Engineering,
Sungkyunkwan University (SKKU), Suwon, South Korea.
Email: seonkuk@skku.edu

ABSTRACT

Low dimensional materials such as nanowire, graphene, transition metal dichalcogenides (TMDs) has significantly attracted in future optoelectronic materials due to high performance electrical and optical behaviors, mechanical stability, and tunable bandgap with respect to the structure of nanomaterial. However, Nanowires have their limitation of device-to-device deviation and uniform film for a channel of device. In this regards, 2D materials was suggested as an alternative solution to integrate them into a large-area circuit. Unlike graphene, the existence of bandgap (1~2.1 eV) in TMDs, especially MoS₂, MoSe₂, WS₂, and WSe₂, combined with a large area growth, would be a strong candidate for future optoelectronic materials. In this talk, I will introduce High-mobility and low-power 2D semiconducting transistor¹, giant photoamplification in multilayer MoS₂ phototransistor with local-bottom gate structures², and high-detectivity MoS₂ phototransistor with wideband spectral response³.

Keywords: transition metal dichalcogenides, phototransistor, flexible, electronics, photodiode.



BIOGRAPHY

Sunkook Kim received his Ph.D. degree from the Department of Electrical and Computer Engineering of Purdue University in Indiana, IN, USA in 2009. He had worked at Intel in 2009 and Samsung Advanced Institute of Tehcnology until 2012. He has been a professor at the School of Advanced Materials Science & Engineering of Sungkunkwan University in Suwon, South Korea since 2017.

FINE CHEMICAL COMPOSITION ANALYSIS OF SILICON PARTICLES FOR SOFT CIRCULAR RECYCLING IN PV SOLAR CELLS

Virginie Brizé, Anass Benayad, Hamza Hajjaji[†], Fabrice Coustier, Malek Benmansour, Amal Chabli,
Univ. Grenoble ALPES, CEA, LITEN, INES, 50 avenue du Lac Léman, F-73375 Le Bourget-du-Lac,
France
Email: amal.chabli@cea.fr

ABSTRACT

The recycling of the silicon particles issued from silicon wafer production for electronic applications such as photovoltaics has great energy value and environmental benefits. This paper deals with the contamination management of these particles to allow an efficient circular recycling. An accurate elemental chemical analysis of the particles as function of the cutting parameters of the silicon ingot into wafers shows that the light elements contamination –oxygen, carbon and sulfur–strongly depends on the cutting fluid composition. A fine characterization of the surface chemical-bonds of the Si particles through photo-emission spectroscopy and infra-red spectrophotometry using appropriate analysis configurations reveal that a significant part of the light elements concentration is located at the surface of the powder in the form of adsorbed elements [1]. In addition, the study of the different potential sources of contamination shows that the metallic contamination is mainly induced by the tools used for the wafers production such as the cutting wire and the ingot holder. The Si-particles characterization methodology reported in the present work is a powerful tool towards a controlled process for the recycling of the Si particles without heavy chemical etching steps.

Keywords: Si particles, XPS, ATR-FTIR, Mass spectrometry, recycling

References

[1]. Benayad, H. Hajjaji, F. Coustier, M. Benmansour and A. Chabli, *J. Appl. Phys.*, 2016, 120, 235308.

[†] Present address: Areva NP, Olkiluoto, 27160 Eurajoki, Finland.

BIOGRAPHY



Amal Chabli joined the CEA in 1983. She received her Ph.D. in Electrochemistry from Grenoble Institute of Technology in 1982. Since then, she has worked at LETI, the electronic and information institute of CEA. Mainly involved in physical and chemical characterization of materials for the micro and nanotechnology programs, she has been the leader of the MINATEC nano-characterization project. In January 2009, she has been awarded the title of Director of Research in Material Characterization for CEA. She has managed several research programs in that field including the “*Recherche Technologique de Base*” French programme that supports the investment and R&D projects on the MINATEC Nano-Characterization Centre of CEA. Since 2014 she has joined LITEN, the research institute of CEA on the development of the sustainable energy technologies of the future. Hence she extended her research activity to the characterization of materials for photovoltaic applications. She has authored and co-authored more than 90 scientific papers. She is used to give courses about nano-characterization at international workshops, and she has organized several international conferences.

SYNTHESIS AND OPTICAL PROPERTIES OF RARE-EARTH DOPED PERSISTENT NANOPHOSPHORS

Zhengfa Dai ¹, Vitalli Boiko ¹ and Dariusz Hreniak ²

¹ Institute of Low Temperature and Structure Research, Polish Academy of Sciences
ul. Okólna 2, PL-50-422 Wrocław, Poland
Email: d.hreniak@intibs.pl

ABSTRACT

Red or near infrared (NIR) persistent phosphors, emitting red or near infrared luminescence for a long time after removal of the excitation source, have recently gained great interest and play more important role in many areas, especially in vivo bio-imaging system [1, 2]. In this work, Y₃(Al,Ga)₅O₁₂ co-doped with Cr³⁺ and rare-earth ions (YAGG:Cr³⁺, RE³⁺) persistent phosphors, emitting red and NIR persistent luminescence, were synthesized by the co-precipitation method. Structure and morphology of nano-powders were characterized by X-Ray Powder Diffraction (XRPD), Brunauere-Emmette-Teller method (BET), Infrared Spectroscopy (FT-IR) and Transmission Electron Microscopy (TEM). The average crystallite sizes and particle sizes were calculated from the Rietveld refinement data and TEM images, respectively. The emission and excitation spectra were measured in order to study the optical properties of the YAGG:Cr³⁺, RE³⁺ persistent phosphors. In addition, the energy transfer efficiency between dopants was also calculated based on the luminescence decay curves. For developing the optical quality, the influence of annealing temperature of phosphors on their optical properties was also determined.

Keywords: Nano-phosphors, NIR persistent luminescence, Rare earths

References

- [1]. J. Ueda, P. Dorenbos, A. J. J. Bos, K. Kuroishi, S. Tanabe, M. Suzuki, J. Mater. Chem. C, 3 (2015) 5642.
- [2]. Z. Dai, V. Boiko, M. Markowska, A. Gerus, K. Grzeszkiewicz, J. Holsa, M. L. Saladino, D. Hreniak, J. Rare. Earth (2019), [org/10.1016/j.jre.2019.04.006](https://doi.org/10.1016/j.jre.2019.04.006).

<The 7th International Workshop on Nanotechnology and Application (IWNA 2019)>

Invited Speaker's CV

	Full Name	Dariusz Grzegorz HRENIAK
	Education	2011 Post-doctoral degree (dr hab.) in Chemical Sciences, Institute of Low Temperature and Structure Research of the Polish Academy of Sciences in Wrocław; 2005 PhD (Chemical Sciences) 2000 Master degree, the Faculty of Fundamental Problems of Technology, (specialisation: Materials Engineering), Wrocław University of Technology
Working Experience	<p>Research activities are laser spectroscopy, nanocrystals syntheses, sol-gel materials, rare-earth elements, luminescent markers, nanoceramic processing and characterization and luminescence properties of the rare-earth ions in glasses, nanoceramics and nanocomposites.</p> <p>Author and co-author of over 160 scientific publications created as a result of R&D projects implementation (JCR list) >2900 citations (>2250 without auto-citations) h-index=30, 04.10.2019, Scopus. Co-author of six patents and 17 patent applications.</p> <p>CEO in spin-off type companies: Nanovectors Sp. z o.o. (since 2011-2017, optical securing of valuable objects), Ipanterm Sp. z o.o. (since 2013-2019, new fire-proof insulating materials).</p>	

SUPPORTED LIPID MONOLAYERS AS INNOVATIVE SENSING AND SELECTIVE LAYERS FOR SENSORS

V. Kilinc¹, T. Nguy², A. Kenaan¹, S. Lamant¹, C. Henry-de-Villeneuve³, G. Monier⁴,
M. Petit¹, Y. Wakayama², A. Charrier¹, J. M. Raimundo^{1*}

¹CINaM, Aix-Marseille Université, CNRS, Marseille, France

²NIMS, Tsukuba, Japan

³PMC, Ecole Polytechnique, Palaiseau, France

⁴Institut Pascal, Aubière, France

Email: jean-manuel.raimundo@univ-amu.fr

ABSTRACT

We present an original platform constituted of an engineered lipid monolayer, which is used as the active sensitive layer and as ultra-thin gate dielectric in field effect transistor sensors. Supported lipid layers, with thicknesses of a few nanometers indeed constitute good candidates. In living cells lipid membranes are known to constitute natural insulators which play an efficient role as barrier to both ionic and electronic transport across the membrane, associated with an electrical resistance of the order of several giga-Ohms in magnitude. However, despite excellent insulating properties, lipid bilayers and even more lipid monolayers have been poorly exploited in devices due to their inherent instability under application of an electric field, leading to damages caused mainly by an electroporation process occurring at low electric field. Furthermore a lack of mechanical stability is often observed.

We show that the mechanical and chemical stability of lipid layers as well as their dielectric performances can be improved by changing the molecular structure of the lipids and by achieving intra-chain reticulations within the layer, and that surprisingly both these properties are correlated. In fact such reticulated layers with a thickness of 2.5 nm only present low leakage current even at high electric field, and a direct dielectric breakdown occurring at ~ 30 MV/cm, i.e. much higher than for a silicon oxide layer of similar thickness or other high-K dielectrics.

We show that once the lipid monolayer on the transistor channel the specificity of the sensor given by the grafting of probes to the lipids can be tuned using simple procedure making our sensor extremely versatile. As a proof of concept, we present here different sensors that were developed for the detection of Fe^{3+} , Cu^{2+} and Cs^+ ions using different materials, inorganic transistors with silicon channel and organic transistors with a Poly(3-hethyl)thiophene as channel, and different types of probes. Our sensors present good specificities with exceptional low limit of detection down to the sub-femtomolar range, high sensitivity and a linear response over several decades.

Keywords: lipid monolayers, mechanical and dielectric properties, ISFET sensors



BIOGRAPHY

Jean-Manuel Raimundo is Professor at Aix-Marseille Université. He is the head of the Molecular Engineering and Functional Materials department at CINaM UMR 7325 (Interdisciplinary Center of Nanoscience of Marseille) His research activity is devoted to the (supra) molecular engineering of π -conjugated chromophores for optoelectronic, biomedical, surface engineering and sensor applications.

CHANGES IN THE CONVENTIONAL AND PERSISTENT LUMINESCENCE INDUCED BY SINTERING PRESSURE IN GARNET AND ALUMINATE CERAMICS

Pawel Gluchowski¹, **Mika Lastusaari**^{2,3}, **Adrian Patej**⁴, **Kamila Rajfur**⁵, **Simona Veltri**¹, **Robert Tomala**¹, **Wieslaw Stręk**¹

¹Institute of Low Temperature and Structural Research PAS, PL-50422 Wrocław, Poland

²Department of Chemistry, University of Turku, FI-20014 Turku, Finland

³Turku University Centre for Materials and Surfaces (MatSurf), Turku, Finland

⁴Wrocław University, 50-383 Wrocław, Poland

⁵Wrocław University of Technology, 50-370 Wrocław, Poland

Email: p.gluchowski@intibs.pl

ABSTRACT

In this paper, the impact of sintering on the conventional and persistent luminescence in the ceramics is presented. Spectroscopic properties were characterized by the photoluminescence, excitation spectra and kinetics of luminescence. It was found that sintering pressure decreases the grain size, forms new traps, change the color of conventional and prolongs persistent luminescence. Mechanism of persistent luminescence in the ceramics is proposed.

Keywords: Rare-earth ions, aluminates, garnets, persistent luminescence, ceramics

INTRODUCTION

Persistent luminescence materials are able to emit light a few seconds, minutes, or even hours after ceasing the irradiation [1]. This phenomenon results from the storage of the excitation energy in traps and its subsequent release induced by the thermal energy available at room temperature. Materials exhibiting persistent luminescence have been widely studied because of their potential applications such as emergency signalization, defect indicators, solar energy harvesting or bio imaging [2, 3].

The advantages of aluminate and garnet based persistent phosphors over the previous sulfide-based ones are as follows: longer persistence time, higher luminescence intensity, non-toxicity, stable crystal structures as well as good physical and chemical stability. The blue $\text{CaAl}_2\text{O}_4:\text{Eu}^{2+},\text{Dy}^{3+}$ and green $\text{SrAl}_2\text{O}_4:\text{Eu}^{2+},\text{Dy}^{3+}$ phosphors are a well-known persistent luminescence materials. Less known but also often studied are persistent phosphors from the garnet group such as $\text{Gd}_3\text{Ga}_3\text{Al}_2\text{O}_{15}:\text{Ce}^{3+}$ or $\text{Gd}_3\text{Ga}_3\text{Al}_2\text{O}_{15}:\text{Pr}^{3+}$.

There are a lot of publications about persistent luminescence properties of powders but only few describing ceramics. Most of them, however, do not deal with the impact of the

preparation process on the properties of the ceramics. For such reason we prepared series of powders and ceramics made of them. The impact of sintering on the conventional and persistent luminescence in the ceramics was presented. Spectroscopic properties were characterized by the photoluminescence and kinetic of the process. The difference between powders and ceramics was. It was found that sintering pressure decreases the grain size, forms new traps, and prolongs the filling and bleaching of the traps. In garnets also change of the crystal field was observed and discussed.

EXPERIMENTAL

The powders were obtained by a self-combustion method. Stoichiometric amounts of reagents (nitrate form) were placed in a quartz crucible and appropriate amounts of urea (reducer) were added. The mixture was heated on an electric hot plate to evaporate water to about 30 % of the original volume. Then crucible was placed in a furnace with temperature of 650 °C for 5 minutes until spontaneous ignition. The duration of the combustion was about 30 seconds and, after cooling, a foam-like product was obtained. The foam was ground with an agate mortar to obtain fine powder. The ceramics were fabricated with

a one minute reaction time from the respective phosphors by a low temperature (450 °C) - high pressure (8 GPa) technique described earlier by us [4].

Emission and excitation spectra were measured using FLS980 fluorescence spectrometer from Edinburgh Instrument equipped with a 450W xenon lamp as an excitation source and a Hamamatsu 928 PMT detector and a USB 2000 Ocean Optics CCD camera (0.3 nm resolution).

RESULTS AND DISCUSSION

The emission spectra were recorded for ceramics sintered at different pressures and from powders prepared at different temperatures. It can be seen that for ceramics made from smallest grains (calcined at lowest temperature) emission band is shifted to the red (Fig.1). With increase of grain size (increase of calcining temperature) band is shifted to the blue. This behavior is related to the change of crystal field that was observed also for YAG/YGG matrix [5], where crystal field strength was changed by increase of Ga content in the matrix. The decrease of crystal field lead to red shift of the emission band and decreasing of the luminescence intensity. In case of GGAG:Ce³⁺ ceramics applied pressure leads to increase of 5d levels splitting and in consequence recombination of electrons with conductance band and decreasing emission intensity.

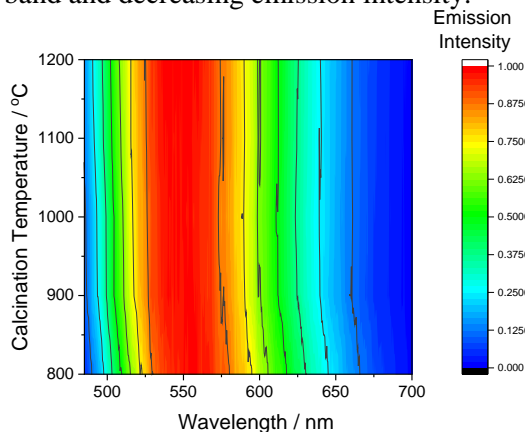


Figure 1. Changes of the position of the Ce³⁺ emission band after applying the pressure measured for the GGAG ceramics prepared from powders calcined at different temperatures.

The red shift is also observed for the ceramics sintered at highest pressure. Since in our previous paper we showed that with increasing the pressure the size of grains

decrease [6] red shift of the emission may be directly linked to the change of crystal field strength.

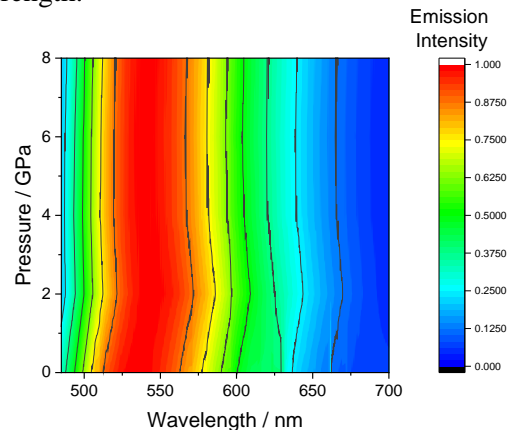


Figure 2. Impact of the applied pressure on the position of the Ce³⁺ emission band in GGAG:Ce³⁺

After ceasing the UV radiation, emission intensity decay is observed due to the release of the energy from the traps (Fig. 3). In the materials where more traps are predicted, decay time should be longer. In the present case, an increase in the decay time observed for ceramic samples suggest formation of the new traps after sintering process. This assumption is confirmed by the calculation of the fading time of the persistent luminescence. The decay time was ca. 60 – 80 % longer after sintering of powders. This shows that the sintering process induce the formation of new traps leading to longer persistent luminescence.

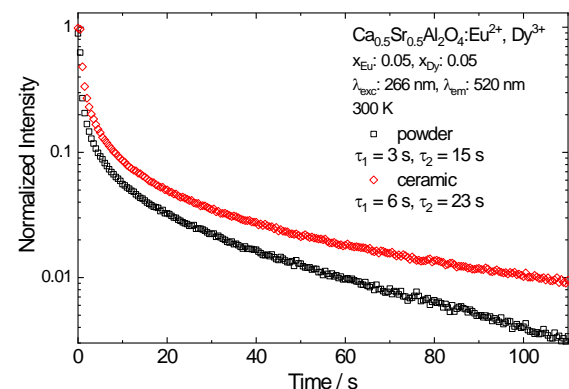


Figure 3. Fading times of persistent luminescence of Ca_{0.5}Sr_{0.5}Al₂O₄:Eu²⁺, Dy³⁺ (bottom) powders and ceramics measured after ceasing 266 nm excitation.

CONCLUSION

For all ceramics prepared from respective powders it was observed that pressure applied

during sintering change persistent luminescence properties of the materials. In case of garnet structures it was found relation between crystal field strength and resulting from this splitting and size of the crystals. After sintering process the crystal field decrease and lead to the red shift of the emission band. The biggest changes are observed for the ceramics composed of smallest grains. It was also observed that the fading time of the persistent luminescence observed in the aluminate ceramics were longer than in the powders because of presence of additional traps induced by the sintering process.

Acknowledgment

This work was supported by the National Science Centre, Poland under SONATA 13 project, grant number - 2017/26/D/ST5/00904.

References

- [1] J. Hölsä, *Persistent luminescence beats the afterglow: 400 years of persistent luminescence*, ECS Interface **18** (2009) 42
- [2] X. Wang and D. Jia, *Long Persistent Phosphors, Practical Applications of Phosphors*, CRC Press, Boca Raton, FL USA, 2006.
- [3] Y. Li, M. Gecevicius, J. R. Qiu, *Long persistent phosphors—from fundamentals to applications*, Chemical Society Review **45** (2016) 2090.
- [4] P. Gluchowski, W. Streck, *Luminescence and excitation spectra of Cr^{3+} : $MgAl_2O_4$ nanoceramics*, Materials Chemistry and Physics **140** (2013) 222e227
- [5] L. Chen, X. Chen, F. Liu, H. Chen, H. Wang, E. Zhao, Y. Jiang, T.-S. Chan, C.-H. Wang, W. Zhang, Y. Wang, S. Chen, *Charge deformation and orbital hybridization: intrinsic mechanisms on tunable chromaticity of $Y_3Al_5O_{12}:Ce^{3+}$ luminescence by doping Gd^{3+} for warm white LEDs*, Sci. Rep. **5** (2015) 11514,
- [6] P. Gluchowski, W. Streck, *Studies of upconversion emission of $Yb^{3+},Er^{3+}:Lu_2O_3$ nanoceramics*, Optical Materials **35** (2013) 731–734

BIOGRAPHY



Dr. Eng. Pawel Gluchowski, Associate professor in Institute of Low Temperature and Structural Research of the Polish Academy of Sciences and CEO of Nanoceramics Inc. Graduate of the Wrocław University of Technology (Master of Science in Material Engineering), Institute of Low Temperature and Structural Research of the Polish Academy of Sciences (PhD in Physics) and the University of Economics in Wrocław (post-graduate studies Project Management). After PhD, he spend 1-year in Turku University, Finland (postdoc position) where he work on persistent luminescence materials. Leader of three national projects and main contractor in seven national and two international projects (FP 7, H2020), in which he dealt with both research into innovative materials and project management. Author of 62 publications on an international scale, 1 monograph, 4 international patents (and 4 patent applications). Beneficiary of 3 international travel grants, author of 2 lecture on invitation and 8 oral communications and several scientific stays, which resulted in international cooperation and development of a new class of optical and magnetic materials. The main direction of his research are rare earth doped luminescent and magnetic nanostructures (powders, glasses, and ceramics). He work also on the commercialization of discovered and patented innovative materials.

STRUCTURED-CATALYST MATERIAL FOR DIRECT CONVERSION OF BIOFUEL TO POWER

Phuc Hoan Tu ¹, Diep Ngoc Le ², Tin Chanh Duc Doan ², Mau Chien Dang ² and Yusuke Shiratori^{3,4}

¹ Department of Hydrogen Energy Systems, Graduate School of Engineering, Kyushu University, Motooka 744, Nishi-ku, Fukuoka 819-0395, Japan;

² Institute for Nanotechnology, Vietnam National University-Ho Chi Minh City, Community 6, Linh Trung Ward, Thu Duc District, Ho Chi Minh City, Vietnam;

³ International Research Center for Hydrogen Energy, Kyushu University, Motooka 744, Nishi-ku, Fukuoka 819-0395, Japan;

⁴ Department of Mechanical Engineering, Faculty of Engineering, Kyushu University, Motooka 744, Nishi-ku, Fukuoka 819-0395, Japan

Email: shiratori.yusuke.500@m.kyushu-u.ac.jp

ABSTRACT

Paper-structured catalyst (PSC) for the application to direct internal reforming (DIR) SOFC is studied. Different oxide supports, (Mg,Al)O derived from hydrotalcite (HT), (Ce,Zr)O₂ (CZ) and flowerlike CeO₂ (Ce(F)) were dispersed into the ceramic fiber network to have three types of Ni-loaded PSCs, (a) Ni/HT-PSC, (b) Ni/CZ-PSC and (c) Ni/Ce(F)-PSC, respectively. Catalytic activities of these PSCs for the dry reforming of methane (DRM) were evaluated at the operating temperature of 750°C. Ni/Ce(F)-PSC exhibited the highest and most stable methane conversion, and coking hardly occurred after 15h of DRM, which may be due to the unique morphology of Ce(F).

Keywords: paper-structured catalyst, flowerlike structure, dry reforming of methane, solid oxide fuel cell.

INTRODUCTION

Dry reforming of methane (DRM) ($\text{CH}_4 + \text{CO}_2 \rightarrow 2\text{CO} + 2\text{H}_2$) is the endothermic reaction ($\Delta H_{298}^0 = 248 \text{ kJ.mol}^{-1}$). It not only produces syngas but also reduces CH₄ and CO₂ emission. Our group make efforts to promote this reaction right next to the fuel electrode (anode) of solid oxide fuel cell to realize direct internal reforming (DIR) operation of solid oxide fuel cell (SOFC) [1,2]. Catalysts for DRM, precious metal (Pt, Ru, Pd...) and non-precious metal (Ni, Co, Cu...) [3,4], have been widely studied. Among them, Ni-based catalysts were used because of its satisfactory catalytic activity and lower price, but prone to coking [5] and sintering [6,7]. To improve the catalytic properties of nickel for DRM, various oxide supports had been synthesized and applied [8, 9, 10]. In this study, three types of oxides, (Mg,Al)O derived from hydrotalcite (HT), (Ce,Zr)O₂ (CZ) and flowerlike CeO₂ (Ce(F)) were synthesized, and dispersed into the ceramic fiber network as the Ni supports to form Ni-loaded paper-structured catalyst (PSC) which will be applied on the SOFC anode to realize DIRSOFC.

EXPERIMENTAL

Preparation of PSCs

Ni/HT-PSC was prepared by the paper making process, as described elsewhere [9]. Ni/CZ-PSC was prepared from the precipitate of Ni(NO₃)₂.6H₂O, Ce(NO₃)₃.6H₂O and ZrO(NO₃)₂ with NaOH and NaBH₄ during the paper making process [10]. For Ni/Ce(F)-PSC, first of all Ce(F) was prepared. 0.0075 mol Ce(NO₃)₃.6H₂O, 0.015 mol glucose and 0.03 mol acrylic acid were dissolved in 130 mL of deionized water (DI) under magnetic stirring. After that, 6.6 mL of 25 wt% ammonia solution was added in 20 mL DI water, and the diluted ammonia solution was supplied dropwise to the above mixture. The solution was stirred at 30°C for 5 h to form a deep brown solution and transferred into a Teflon-lined autoclave (150 mL), sealed and kept at 180°C for 72 h, and naturally cooled down to room temperature. The resulting orange suspension was washed with water and alcohol for several times, and then dried at 80°C overnight. By the subsequent calcination at 600°C for 6 h in air, the Ce(F) were

obtained. The NiO/Ce(F) catalyst powder was prepared by the impregnation method. 2 g of Ce(F) was added into 4 mL of 0.5 M Ni(NO₃)₂ solution with polyvinylpyrrolidone (5 wt%), and kept for 5 h, then dried at 80°C for 8 h. The green powder was calcined at 600°C for 6 h to obtain NiO/Ce(F) powder. 1.21 g of ceramic fiber (Al₂O₃: 48 wt%, SiO₂: 52 wt%) and 0.012 g of cotton fiber were mixed in 100 mL of DI water. After adding 2 g of NiO/Ce(F) (with Ni/Ce(F) weight ratio of 6/94) and 0.6 mL of 2 wt% cationic polymer solution (polydiallyldimethylammonium chloride), the suspension underwent ultrasonic treatment for 15 min followed by magnetic stirring for 1 h. Then, 0.6 mL of 2 wt% anionic polymer solution (acrylamide-co-acrylic acid) was added with continuous magnetic stirring for 15 minutes. After 1 h stabilization, the suspension was mixed again just before filtration to obtain a wet-state sheet with a diameter of 6.6 cm, which was pressed and dried at 80°C overnight. Finally, 3 wt% Ni-loaded Ce(F)-dispersed PSC (Ni/Ce(F)-PSC) was obtained by heat treatment at 600°C for 5 h with subsequent reduction treatment.

Characterization and Analyses

The microstructure of PSCs was characterized by a field emission scanning electron microscope (FE-SEM-SU8010, Hitachi, Japan) and the nickel loading on PSCs was quantified in percentage by Inductively Coupled Plasma (Plasma Atomic Emission Spectrometer, Shimadzu ICPE-9000). The crystal structure was analyzed by an X-ray Diffractometer (Rint-Ultima III diffractometer, Rigaku, Japan) at 40 kV and 40 mA of CuK α radiation. The specific surface area of the samples was measured by N₂ adsorption using a Belsorp-mini II analyzer (Microtra BEL Corp., Japan).

RESULTS AND DISCUSSION

Figure 1 shows the dispersion of Ni/oxide supports into the fiber network. In the case of Ni/HT-PSC, HT powder was added in the water suspension for paper-making process, leading to large Ni/(Mg,Al)O clusters (Fig 1a). In the case of Ni/CZ-PSC, CZ was prepared by on-paper synthesis using co-precipitation method, therefore Ni/CZ was well dispersed in the fiber network (Fig 1b). Figure 1c shows the dispersion of Ni/Ce(F) in the fiber network.

Table 1. Specific surface area (S_{BET}) and Ni loading of the prepared PSCs

Sample	S_{BET} (m ² g ⁻¹)	Ni loading (%)
Ni/HT-PSC	20	8.6
Ni/CZ-PSC	24	6.1
Ni/Ce(F)-PSC	32	3

As listed in Table 1, Specific surface area of Ni/HT-PSC, Ni/CZ-PSC and Ni/Ce(F)-PSC were 20, 24, 32 m² g⁻¹ with Ni loading of 8.6, 6.1 and 3 %, respectively. The crystal structure of Ni and oxide supports were evaluated by XRD (see Fig 2). The (Ni,Mg,Al)O solid solution [9], cubic Ni with tetragonal (Ce,Zr)O₂ [10] and cubic Ni with cubic CeO₂ were detected in Ni/HT-PSC, Ni/CZ-PSC and Ni/Ce(F)-PSC, respectively.

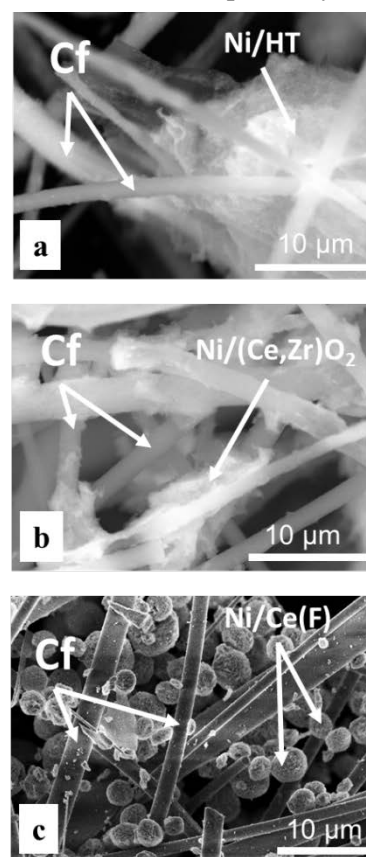


Figure 1. Morphology of (a) Ni/HT-PSC, (b) Ni/CZ-PSC and (c) Ni/Ce(F)-PSC.

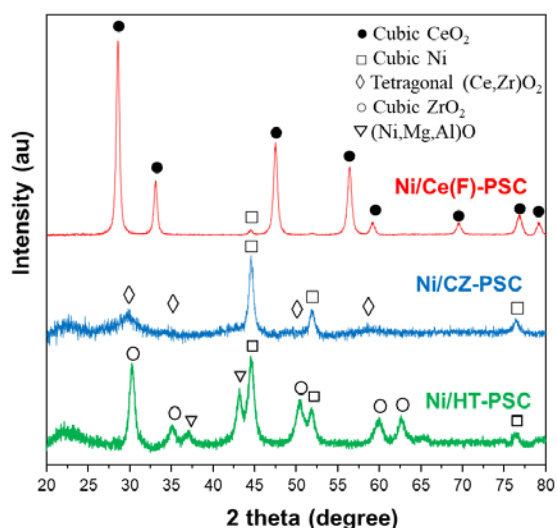


Figure 2. XRD patterns of PSCs after reduction treatment at 600°C for 5 h in the flow of 5 % H₂-N₂.

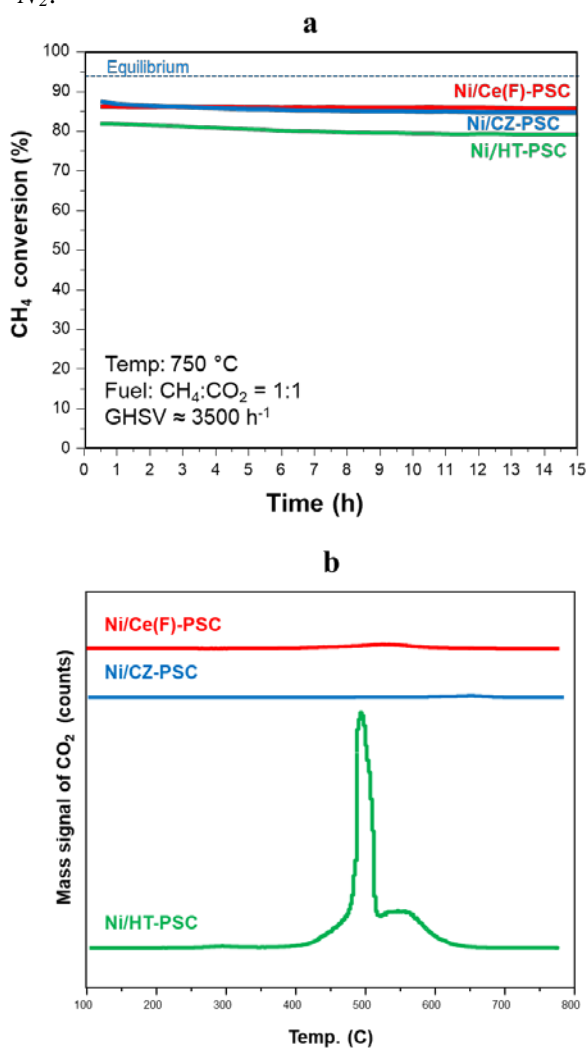


Figure 3. (a) CH₄ conversion measured during 15 h DRM test at 750°C and (b) TPO profiles after 15 h DRM.

Figure 3a shows CH₄ conversion measured during 15 h DRM test at 750°C. For the dispersion of (Mg,Al)O (Ni/HT-PSC), initial CH₄ conversion within 15 h was 81%. For the dispersion of CZ having high oxygen storage capacity (OSC), that was 87.5%. In the case of Ce(F) dispersion, despite the lower OSC than that of CZ, that was 86.1%, and most stable. These results indicate that catalytic function (especially anti-coking property) of CeO₂-based oxide particles derived from OSC can be further enhanced by controlling geometry of the particles.

TPO profiles (CO₂ signal) for the PSCs after 15 h DRM test at 750°C are shown in Figure 3b. Appearance of CO₂ signal in TPO means the burning of carbon deposited in PSCs during the DRM test. The large peak of CO₂ signal for the Ni/HT-PSC indicates the occurrence of severe coking during the DRM test. By the dispersion of Ce(F) and CZ, coking was considerably suppressed, due to the unique geometry of the Ce(F) and high OSC of CZ well-dispersed in the fiber network (16), respectively.

CONCLUSION

Ni-loaded paper-structured catalyst (PSC) with the dispersion of flowerlike ceria (Ce(F)), Ni/Ce(F)-PSC, exhibited the higher and more stable methane conversion for the dry reforming of methane (DRM) at 750°C compared to the PSCs with the dispersion of (Mg,Al)O and (Ce,Zr)O₂ (CZ), Ni/HT-PSC and Ni/CZ-PSC, respectively. After 15 h DRM, in the case of Ni/Ce(F)-PSC, coking was considerably suppressed in spite of lower Ni-loading than the other PSCs. The unique morphology of Ce(F) was found to be promising as an oxide support of Ni catalyst for DRM, and further enhancement of catalytic activity is expected if the flowerlike (Ce,Zr)O₂ can be prepared.

Acknowledgment

This research was supported by the Science and Technology Research Partnership for Sustainable Development (SATREPS) program of the Japan Science and Technology Agency (JST) and Japan International Cooperation Agency (JICA), Grant Number JPMJSA1402, and Vietnam National University - Ho Chi Minh City (VNUHCM) under grant number B2017-32-01.

References

- [1]. Y. Shiratori, T. Ogura, H. Nakajima, M. Sakamoto, Y. Takahashi, Y. Wakita, T. Kitaoka, K. Sasaki, *Study on paper-structured catalyst for direct internal reforming SOFC fuelled by the mixture of CH₄ and CO₂*, International Journal of Hydrogen Energy **38** (2013) 10542-10551.
- [2]. T.G.H. Nguyen, M. Sakamoto, T. Uchida, D.C.T. Doan, M.C. Dang, P.H. Tu, K. Sasaki, Y. Shiratori, *Development of paper-structured catalyst for application to direct internal reforming solid oxide fuel cell fuelled by biogas*, International Journal of Hydrogen Energy **44** (2019) 10484-10497.
- [3]. N. A. K. Aramouni, J. G. Touma, B. A. Tarboush, J. Zeaiter and M. N. Ahmad, *Catalyst design for dry reforming of methane: analysis review*, Renewable and Sustainable Energy Reviews **82** (2018) 2570-2585.
- [4]. D. Pakhare, J. Spivey, *A review of dry (CO₂) reforming of methane over noble metal catalysts*, Chemical Society Reviews **43**(22) (2014) 7813-7837.
- [5]. J. M. Ginsburg, J. Piña, T. El Solh, & H. I. De Lasa, *Coke formation over a nickel catalyst under methane dry reforming conditions: thermodynamic and kinetic models*, Industrial & engineering chemistry research **44**(14) (2005) 4846-4854.
- [6]. T. W. Hansen, A. T. DeLaRiva, S. R. Challa, & A. K. Datye, *Sintering of catalytic nanoparticles: particle migration or Ostwald ripening?*, Accounts of chemical research **46**(8) (2013) 1720-1730.
- [7]. Z. Bian, S. Das, M. H. Wai, P. Hongmanorom, & S. Kawi, *A review on bimetallic nickel based catalysts for CO₂ reforming of methane*, ChemPhysChem **18**(22) (2017) 3117-3134.
- [8]. P. H. Tu, T. G. H. Nguyen, M. Sakamoto, T. Uchida, T. C. D Doan, M. C. Dang, & Y. Shiratori, *Performance Enhancement of Ni-Loaded Paper-Structured Catalyst for Dry Reforming of Methane by the Dispersion of Ceria-Based Oxides*. ECS Transactions **91**(1) (2019) 1661-1670.
- [9]. Y. Shiratori, M. Sakamoto, *Performance improvement of direct internal reforming solid oxide fuel cell fuelled by H₂S-contaminated biogas with paper-structured catalyst technology*, Journal of Power Sources **332** (2016) 170-179.
- [10]. T. G. H. Nguyen, D. L. Tran, M. Sakamoto, T. Uchida, K. Sasaki, T. D. To, & Y. Shiratori, *Ni-loaded (Ce, Zr)O_{2-δ}-dispersed paper-structured catalyst for dry reforming of methane*, International Journal of Hydrogen Energy **43**(10) (2018) 4951-4960.

BIOGRAPHY



Yusuke Shiratori earned his Ph.D. in the field of electrochemistry (Modeling and Performance Simulation of Solid Oxide Fuel Cell (SOFC)) at Tokyo Institute of Technology in 2002. He, then, engaged in the development of electrolyte material for SOFC at Forschungszentrum Jülich (Germany) as a postdoctoral fellow. After his stay in Germany, he has been working for Department of Mechanical Engineering, Faculty of Engineering, Kyushu University as an Assistant Professor to study fuel cell anodes with enhanced catalytic activity for hydrocarbon reforming. In 2011, he became an Associate Professor of this department, and his research created a novel structured-catalyst material to realize direct internal reforming SOFC. From 2015, he started Vietnam-Japan international joint research project as a leader of Japan side to develop and demonstrate a fuel cell-incorporated energy circulation system using regional biomasses as energy resources to contribute to the sustainable development of Mekong Delta region.

APPLICATION OF SURFACE AND INTERFACE CHARACTERIZATION OF MATERIALS IN BACK-END-OF-LINE INTERCONNECT

Quoc Toan Le, E. Kesters, E. Altamirano Sanchez, and F. Holsteys

IMEC, 75 Kapeldreef, 3001 Leuven, Belgium

Email: QuocToan.Le@imec.be

ABSTRACT

The fabrication of advanced CMOS devices consists of numerous processing steps including deposition, oxidation, photolithography, etching, implantation, planarization, and surface preparation. These steps are repeated throughout the whole process. The surface preparation and cleaning represent more than 20% of the total process steps in the fabrication [1]. For such multi-layer structures, the surface properties of materials play a key role in determining the extent of adhesion and the properties of the interface formed with a deposited layer. This presentation gives a number of examples of the characterization of materials used in back-end of line (BEOL) using common characterization methods such as X-ray photoelectron spectroscopy (XPS), time of flight secondary ion mass spectrometry (ToF-SIMS), atomic force microscopy (AFM), transmission electron microscopy (TEM), and attenuated total reflection Fourier transform infrared spectroscopy (ATR-FTIR).

Porous dielectrics and copper have been used in back-end of line interconnect since the past decades. The dielectric layer is typically patterned by plasma etching through metal hard mask using fluorocarbon-containing plasmas, followed by electroplating of Cu inside the etched patterns. Porous dielectrics are extremely sensitive to plasma processes, and the extent of the damaged layer strongly depends on the porosity of the dielectrics [2]. In addition, fluorocarbon polymers are formed during the dielectric etch to ensure etching anisotropy and profile control of the patterned structure. The “polymers” (post-etch residues - PER) deposited on the created dielectric sidewalls and the metal surface must be removed (Figure 1) prior to the deposition of subsequent materials (barrier layer, metal) to achieve good adhesion and coverage of materials deposited in the etched features. Etching a TiN hard mask-on-porous low-k damascene stack using fluorocarbon-based plasma mainly resulted in two types of etch residues. XPS characterization showed the presence of both Ti-containing residues and polymer-type residues CF_x [3,4]. The XPS spectra collected at different take-off angles clearly indicate that the CF_x residues are detected on all the exposed surface, i.e. TiN hard mask, trench sidewall and bottom.

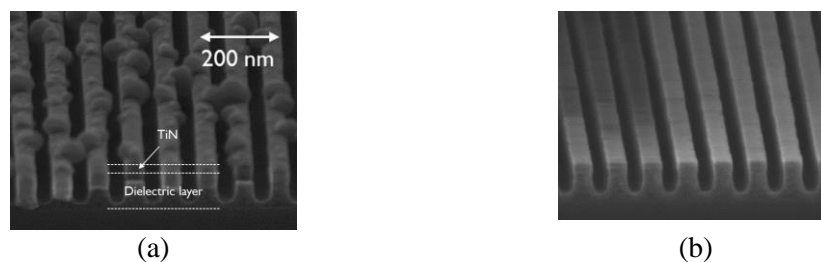


Figure 1. Cross-section SEM images of a single damascene TiN/porous dielectric test structure, (a) before and (b) after TiN removal and surface cleaning.

The surface cleaning becomes even more challenging as the spacing between interconnect lines decreases, together with an increase in aspect ratio. For instance, for dielectric lines with width of ~10.5-12 nm (critical dimension or CD), the structures become more prone to pattern collapsing. Several parameters affect pattern collapse, such as CD variations due to variations in the patterning process, the aspect ratio, the surface chemistry of the dielectric sidewall, the wet clean chemistry and the rinse-dry process. During wet processing, the capillary forces acting on the structures during the rinse-dry process

cause deflection of the lines, leading to pattern collapse (Figure 2a). The capillary forces can be reduced by changing the surface chemistry of the outermost surface layer of the dielectrics, which in turn modifies the surface energy of the sidewall. Figure 2b gives an example of surface modification using silane, which changes the surface of the dielectrics from hydrophilic to hydrophobic surface. As a result, the presence of these hydrophobic (methyl) groups at the surface suppresses capillary forces and interaction forces between the dielectric lines, which in turn mitigate the pattern collapse during wet treatment of the structure.

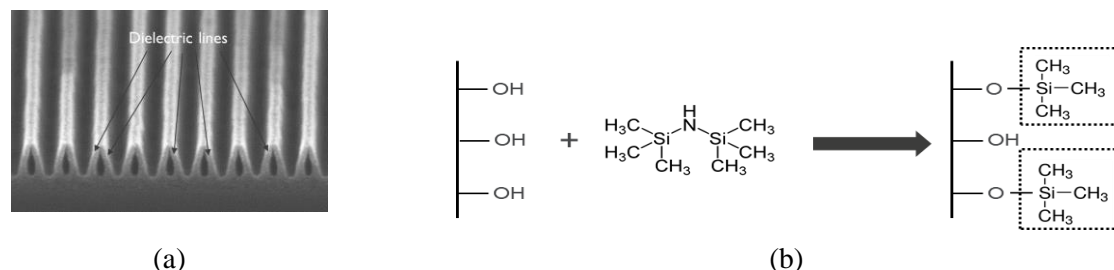


Figure 2. (a) Cross-section SEM image showing the deformation of the dielectric lines (pattern collapse) after being processed in a chemical solution followed by a rinse in deionized water and (b) a scheme describing a surface modification process using silane.

Copper has been used for more than 20 years as the metal of choice for BEOL interconnection [5]. However, as the interconnect dimensions continue to shrink, alternative metals need to be introduced to replace copper. Despite having higher bulk resistivities with respect to that of copper, alternative metal candidates for interconnects, such as cobalt and ruthenium, are believed to have lower size effects. In particular, Ru is a noble metal, which has been widely used for microelectronic applications. For interconnect application, Ru may not need a diffusion barrier layer [6], which may result in lower line resistance compared to Cu of the same dimensions. This presentation highlights the importance of the surface (and interface) properties of these metals after different process steps in the device performance. Keywords: Surface modification, Silylation, XPS, TEM, AFM

References

- [1] A. Busnaina, *Nanomanufacturing Handbook*, CRC Press, Francis & Taylor Group, LLC (2007).
- [2] F. Iacopi, M. Stucchi, O. Richard, and K. Maex, *Electrochem. Solid-St. Lett.*, **7**, G79-G82 (2004).
- [3] T. Mukherjee, et al., *ECS Solid-St. Lett.*, **2**, N11 (2013).
- [4] Q. T. Le, E. Kesters, and F. Holsteys, *ECS J. Solid State Sci. Technol.* **7**, P602 (2018).
- [5] <https://www.ibm.com/ibm/history/ibm100/us/en/icons/copperchip/>
- [6] D. C. Edelstein, *IEEE IEDM 2017*; J. Kelly et al., *IEEE IITC/AMC 2016*.

BIOGRAPHY



Quoc Toan Le received his B.S. in chemistry (1988, University of Namur) and in polymer science (1989, Université Catholique de Louvain, Belgium). After working for 3 years in two successive European Programs (EURAM and BRITE) as a researcher at the University of Namur, he started the doctoral study in 1992 and received his PhD in Material and Surface Science from the same university (1996). He then joined the Institut National Polytechnique de Grenoble (INPG, France) as a postdoctoral fellow, focusing on the synthesis and characterization of carbon fibres. In 1997, he joined the Department of Physics and Astronomy, University of Rochester, New York, as a research associate, where he studied the surface and interface phenomena in organic light-emitting diodes devices for optimization of the device performance. He is currently a senior scientist in the Surface and Interface Processing group, Imec (Interuniversity Microelectronics Center) in Leuven, Belgium, where he has been since 2000. His current research interests focus on the surface preparation and characterization of dielectric materials and metal surface and wet processing of metals. Quoc Toan Le is the author and coauthor of over 100 scientific publications and 8 patents.

MULTIFUNCTIONAL MAGNETIC NANOPARTICLES AND APPLICATIONS IN BIOMEDICINE

Nguyen Hoang Nam^{1,2,3} and Nguyen Hoang Luong^{2,3}

¹Faculty of Physics, VNU University of Science, Vietnam National University, Hanoi,
334 Nguyen Trai, Hanoi, Vietnam;

²Nano and Energy Center, VNU University of Science, Vietnam National University, Hanoi,
334 Nguyen Trai, Hanoi, Vietnam;

³Nanotechnology Program, Vietnam Japan University, Vietnam National University, Hanoi,
My Dinh Campus, Nam Tu Liem, Hanoi, Vietnam.
Email: namnh@hus.edu.vn, luongnh@hus.edu.vn

ABSTRACT

Multifunctional magnetic nanoparticles have attracted researchers due to their applications and potential applications, especially in biomedicine. Magnetic nanoparticles show special effects such as high surface area, superparamagnetism and biocompatibility. The organic as well as inorganic functionalizations of magnetic nanoparticles give them more applicable in biomedicine, including multifunctional applications. This work reports the synthesis, functionalization and applications of multifunctional magnetic nanoparticles. The applications of multifunctional magnetic nanoparticles include detection of pathogenic viruses, separation and detection of CD34+ stem cells, etc. In conclusion, some promising perspectives are also pointed out.

Keywords: Magnetic nanoparticles, multifunctionalization, biomedicine applications.

INTRODUCTION

Magnetic nanoparticles have been widely developed for their applications and potential applications due to their particular properties [1-4]. In general, magnetic materials are classified according to their susceptibility to external field effects [4]. Ferromagnetic materials exhibit magnetic properties even without external magnetic field due to strong exchange interactions between magnetic moments. When the size of ferromagnetic materials reduces to a limit of single-domain size, all magnetic moments in a particle align in the same direction and the total magnetic moment can be seen as one giant magnetic moment which composes of all the individual magnetic moments in the particle. These materials are called superparamagnetic nanoparticles, which show paramagnetic behavior even below Curie temperature T_C with high magnetization under low external magnetic field. Furthermore, magnetic nanoparticles have high surface area and their nanosizes are comparable to those of target entities, such as the sizes of a cell, virus, and

protein are in range of 10 – 100 μm , 20 – 450 nm and 5 – 50 nm, respectively. Based on described properties, magnetic nanoparticles are highly applicable in biomedicine. The magnetic nanoparticles can be effected by an external magnetic field, then, can be applied as drug deliverer [5], bio-entity tagger [6] or act as separation agent [3,7]. They also can be resonantly excited, which allows the heat transfer to the surrounding tissues for hyperthermia application [8,9]. Furthermore, they can be applied for magnetic resonance imaging (MRI) as contrast agents due to their short relaxation time [10,11].

Magnetic nanoparticles have been synthesized by various methods, which can be divided into physical methods, biological methods and chemical methods [12]. Physical methods, such as power ball milling, gas phase deposition, electronbeam lithography, pulsed laser ablation and laser induced pyrolysis, provide magnetic nanoparticles with well controlled composition and crystallites, however difficult in controlling size distribution. Biological methods, such as plant mediated,

fungi mediated, bacteria mediated and microbial incubation, are of good reproducibility, scalability, and low cost, however, slow and laborious. Chemical methods, such as sol-gel, oxidation, chemical coprecipitation, hydrothermal, thermal deposition, etc... are simple, tractable and efficient, in which the composition, size and shape of nanoparticles can be controlled [12]. Among them, coprecipitation method is the most commonly used to synthesize magnetite Fe_3O_4 superparamagnetic nanoparticles by the coprecipitation of Fe^{2+} and Fe^{3+} with controlling pH at around 9-14 by adding base to an aqueous mixture of these ions chloride at 1:2 molar ratio. In our studies, the base was aqueous ammonia solution [13]. Figure 1 shows the TEM, X-ray analysis and magnetization curve of prepared magnetic nanoparticles. The magnetic properties of nanoparticles show high saturation magnetization as can be seen in the figure. The synthesized nanoparticles are usually coated by a surfactant to prevent the oxidation and agglomeration, which caused by the large surface-volume ratio and to reduce surface

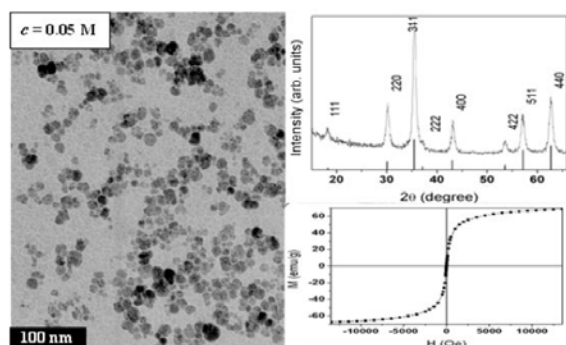


Figure 1. TEM image, XRD result and magnetization curve of the magnetite nanoparticles [13].

energy. The coating may aim for the function of biocompatibility, as well as targeting to certain applications. Especially, the functionalization can be achieved by adding the functions of metallic and semiconductor nanoparticles. Finally the applications of multifunctional magnetic nanoparticles in biomedicine will be reviewed with some perspectives.

MULTIFUNCTIONALIZATION OF MAGNETIC NANOPARTICLES

The surface modification or functionalization

prevent the magnetic loss due to the oxidation in air and the agglomeration, make them hydrophilic for water dispersible, nontoxic or biocompatible and also provide abilities for certain application aims. The simplest functionalization of magnetic nanoparticles is coating by a silica layer [14]. The coating was carried out by using hydrolysis of tetraethylorthosilicate (TEOS) with water. The coating thickness of around 2-5 nm is controlled by the concentration of ammonium base and the ratio of TEOS to water. Silica layer protect as-prepared magnetic nanoparticles against the oxidation by oxygen, or erosion by acid, or base. The additional functionalization of silica layer, such as amino groups, is also possible due to the biocompatibility of silica [15].

To improve the stability, biocompatibility and functionality for bio-applications, the development in synthesis procedure of silica coating was carried out by the assist of ultrasonic wave with various molar ratios of TEOS to Fe_3O_4 nanoparticles and various ultrasonical times [16]. The optimization time is observed as the result of saturation behavior observed in amount of coated silica with the ultrasonical time over 30 min. As can be seen in Fig. 2, Fig. 2A-a-c shows the dependence of weight (calculated by mass measurements) of silica coated Fe_3O_4 nanoparticles ($\text{Fe}_3\text{O}_4@ \text{SiO}_2$ NPs) on the time of ultrasonic treatment at a TEOS: Fe_3O_4 NPs molar ratios of 17.8, 8.9 and 1. Fig. 2A-d-f shows the dependence of the prepared $\text{Fe}_3\text{O}_4@ \text{SiO}_2$ NPs' average particle size on the time of ultrasonic treatment at a TEOS: Fe_3O_4 NPs molar ratio of 17.8, 8.9 and 1. The increase of the average size of the particles due to the increasing of ultrasonic time and TEOS: Fe_3O_4 NPs molar ratio observed from the TEM results can be seen in Fig. 2A-d-f. The dependence of the $\text{SiO}_2:\text{Fe}_3\text{O}_4$ weight ratio on the time of the ultrasonic treatment calculated from saturation magnetization (Fig. 2B) shows the saturate tendency of the coating. This saturate behavior is almost the same as that of the magnetic properties and together they indicate that the coating did not increase after 30 min of ultrasonic treatment.

Further studies also carried out on the effect of pH in the coating procedure by manipulating ammonia concentration [17]. The results show

that the saturation magnetization of coated nanoparticles decreases with increasing pH

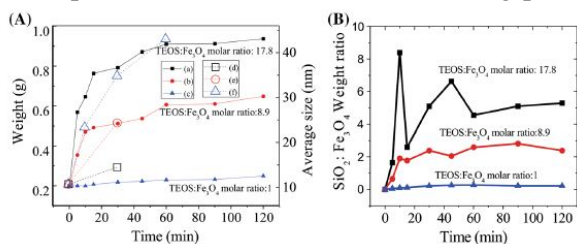


Figure 2. (A)-(a), (b), (c) The dependence of weight Fe₃O₄@SiO₂ NPs on the duration of the ultrasonic treatment from mass measurements at TEOS:Fe₃O₄ NPs molar ratios of 17.8, 8.9 and 1; (A)-(d), (e), (f) The dependence of the prepared Fe₃O₄@SiO₂ NPs's average particle size on duration of ultrasonic treatment at TEOS:Fe₃O₄ NPs molar ratio of 17.8, 8.9 and 1; (B) The dependence of SiO₂:Fe₃O₄ weight ratio on the duration of the ultrasonic treatment calculated from saturation magnetization [16].

from 8.7 to 13.2 due to the increase of the coating layer. The additional functionalizations of coated silica layer were carried out depending on the applications. For example, amino groups were functionalized on the silica layer using silanol reaction of 3-aminopropyltriethoxysilane H₂N(CH₂)₃-Si(OC₂H₅)₃ (APTS) in a mixed solution containing silica coated magnetic nanoparticles and ammonia [15]. The amino-functionalized nanoparticles are ready for further functionalization to conjugation with bio entities.

According to the aim of applications, especially in biomedicine, the magnetic nanoparticles can be functionalized with certain polymer or bio-groups. Besides, the development of multifunctional nanoparticles, which combine the properties of magnetic nanoparticles with properties inorganic nanoparticles such as metallic or semiconductor ones, have attracted many interests [1]. There are many composites structures, including core-shell, matrix dispersed, etc... with various preparation methods. In our studies, the simple preparations were developed to combine the properties of individual nanoparticles in various forms of multifunctional magnetic nanoparticles.

The combination of the individual nanoparticles can be formed by embedding the individual nanoparticles in a matrix. Since the

silica matrix is a good candidate for the matrix due to the easy preparation and the biocompatibility then was used to embed magnetic nanoparticles with silver nanoparticles by inversed microemulsion method [18,19]. Silver nanoparticles were synthesized by wet chemical reduction method using NaBH₄ with the presence of surface activator polyvinylpyrrolidone (PVP), then was coated by 4-Aminothiophenol (4-ATP) to form Ag-4ATP nanoparticles. Under sonic bath, different mass rates of Ag-4ATP/Fe₃O₄ were moderated for 2 h before TEOS was added to react with water in solution to form SiO₂ coat that covered both types of particles. The TEM images of Ag-4ATP, magnetic and combined nanoparticles are showed in Fig. 3. The model of the combined nanoparticles was also proposed. The good magnetic properties and the Surface Enhanced Raman Scattering results, as shown in Fig. 4, indicated that the coated nanoparticles can act simultaneously as individual magnetic and silver nanoparticles.

This method of silica coating also was used to prepare ZnS:Mn-Fe₃O₄ bifunctional nanoparticles which show both the magnetic and photoluminescence properties, which are applicable in biomedicine [20]. The multifunctional composites were also successfully synthesized using ultrasound assisted chemical method [15]. Firstly, magnetic nanoparticles were prepared by coprecipitation method then coated by a silica layer. Silver ions were absorbed on the surface of APTS functionalized silica-coated magnetic NPs, then they were reduced by sodium borohydride under the influence of a 200 W ultrasonic wave for 60 min. The schematic

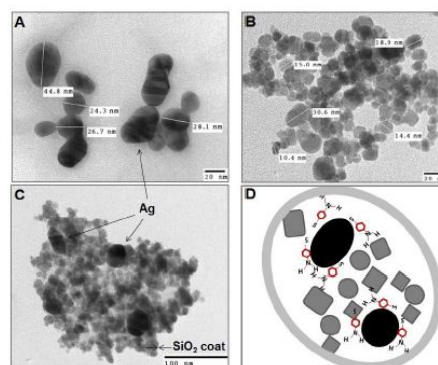


Figure 3. TEM image of Ag-4ATP nanoparticles (A), Fe₃O₄ magnetic nanoparticles (B), as-prepared complex

nanocolloids (C) and schematic graph of the colloid (D) [19].

illustration of the synthesis process can be seen in Fig. 5.

The relative intensity of diffraction peaks of silver crystals in all nanoparticles increased when the atomic ratio of silver:iron increasing from 0.208 to 0.455 and saturation magnetization decreasing from 44.68 emu/g to 34.74 emu/g. The superparamagnetic properties and strong surface plasmon absorption at 420 nm make these particles promising for biomedical applications.

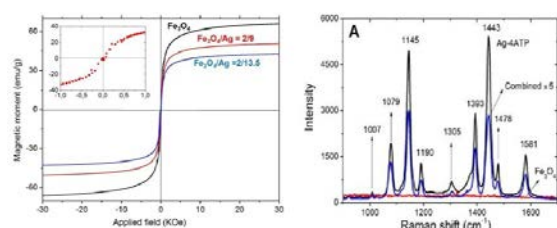


Figure 4. Magnetic properties (left) and Raman spectra (right) of Fe_3O_4 , Ag-4ATP and multifunctional Fe_3O_4/Ag nanoparticles [19].

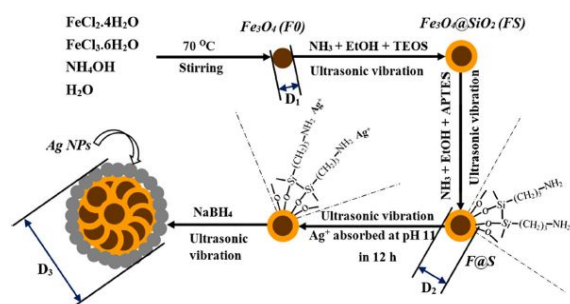


Figure 5. Schematic illustration of multifunctional nanoparticles synthesis [15].

Magnetic nanoparticles can be directly functionalized with amino group without coating by silica layer [21]. By this way, Fe_3O_4 -ZnO multifunctional nanoparticles were successfully prepared in aqueous solution by ultrasound assisted thermolysis. Fe_3O_4 magnetic NPs were prepared by co-precipitation method then were modified by APTS to have free amine ($-NH_2$) groups on their surface. Zn^{2+} ions then were added and stirred to adsorb onto the surface of Fe_3O_4 - NH_2 NPs in alkaline solution at pH of 11. The solution was decomposed through thermolysis in ultrasound bath. The results show that photoluminescence of Fe_3O_4 -ZnO

multifunctional NPs was enhanced in visible light at wavelength of 565 nm to allow detection, labeling, diagnosis, and therapy in biomedicine. Moreover, they exhibit superparamagnetic properties of Fe_3O_4 with high saturation magnetization, which can be used for separation application in biomedicine under an external magnetic field.

Another way of combining the properties of the individual nanoparticles is using them in some special complex structures. For instant, the fast DNA diagnostics was successfully developed using fluorescent ZnS:Mn nanoparticles and NH_2 -functionalized SiO_2 coated Fe_3O_4 nanoparticles in a sandwich structure [22]. In one end of the sandwich structure, NH_2 -modified SiO_2 coated Fe_3O_4 nanoparticles were employed as a docking matrix. A so-called capture probe oligonucleotide chain, that specifically identifies the target DNA, linked to the docking magnetic particles. In the other end, other oligonucleotide chain – named detector probe – contacted with the semiconductor particles. The complementary hybridization of the detector probe – target – capture probe formed the sandwich configuration that attached the fluorescent particles to the docking matrix. This configuration was used to detect DNA of Epstein-Bar virus (EBV) and as the result, a fine affinity between the luminescent intensity at 586 nm of ZnS:Mn nanoparticles appeared with the initially added DNA target concentration, which could detect the presence of target DNA within 2×10^6 copies/ml (~ 0.3 fM). This methodology promised an attractive applicability for designing a DNA detecting fast KIT.

APPLICATION OF NANOPARTICLES

Multifunctional magnetic nanoparticles have many applications in biomedicine. Due to the strong response with external field, the separation is the most common application. The magnetic purifications using silica coated Fe_3O_4 nanoparticles were performed to purify DNA of Hepatitis virus type B (HBV) and Epstein-Barr viruses (EBV) [14]. The results showed that $Fe_3O_4@SiO_2$ nanoparticles and the optimized buffer could successfully enrich DNA from solution and that the purified DNA was qualified for further PCR-based detection of HBV at a sensitivity of 4×10^2 copies/ml.

The results obtained in isolating DNA of HBV in six real serum samples showed good agreement with those confirmed by the hospital where the samples were collected. Furthermore, the results also show that $\text{Fe}_3\text{O}_4@\text{SiO}_2$ nanoparticles may be more efficient than Dynabeads Myone silane (short name: Dynabeads), Life Technologies Company, in DNA isolation of HBV from serum. Similarly, $\text{Fe}_3\text{O}_4@\text{SiO}_2$ nanoparticles and the buffers were then used to separate DNA of EBV in real serum samples, in comparison to Dynabeads [14]. The results indicate that the DNA separation efficiency of EBV by $\text{Fe}_3\text{O}_4@\text{SiO}_2$ nanoparticles was higher than that using Dynabeads. The higher concentrations of EBV (copies/ml) were measured with using $\text{Fe}_3\text{O}_4@\text{SiO}_2$ nanoparticles to purify DNA compared to those with using Dynabeads. The increase in DNA isolation efficiency by $\text{Fe}_3\text{O}_4@\text{SiO}_2$ nanoparticles is may due to a larger total surface of silica-coated magnetic nanoparticles. Furthermore, during the process of DNA isolation, the time required for magnets to attract completely the Dynabeads from solution was much longer, about 2 – 3 min, compared to 15 – 20 s for $\text{Fe}_3\text{O}_4@\text{SiO}_2$ nanoparticles, which is probably also due to the fact that $\text{Fe}_3\text{O}_4@\text{SiO}_2$ nanoparticles have a larger total surface area compared to that of the Dynabeads.

The silica coated magnetic nanoparticles using ultrasound-assisted method were applied for DNA extraction from formalin-fixed, paraffin-embedded (FFPE) human cancer tissues [16]. $\text{Fe}_3\text{O}_4@\text{SiO}_2$ NPs allowed extraction of DNAs from 10 mg FFPE tissues of nasopharyngeal carcinoma patients with the highest recovery of about 100–500 ng/ μl and good purity (A260/A280: 1.8–1.9). The extracted DNAs could be used as templates for downstream amplification of 252-bp sequencing specifically for the Braf cancer biomarker gene using polymerase chain reaction (PCR), as well as detection of EBV and the human papilloma-virus (HPV) using real-time PCR. DNA extraction recoveries of both EBV and HPV using $\text{Fe}_3\text{O}_4@\text{SiO}_2$ NPs were significantly better than those using commercialized $\text{Fe}_3\text{O}_4@\text{SiO}_2$ microbeads, as indicated by lower threshold cycles of all fluorescent signals including fluorescein amidite (FAM) dye representative for EBV infection, hexachlorofluorescein (HEX) dye

representative for b-globin (internal control), and SYBR Green dye representative for HPV infection in tested clinical samples from patients with nasopharyngeal carcinoma (NPC).

$\text{Fe}_3\text{O}_4/\text{Ag}$ nanoparticles were functionalized with the free amino (NH_2) functional groups ($\text{Fe}_3\text{O}_4/\text{Ag-NH}_2$), then were conjugated with fluorescent electron coupled dye (ECD)-antiCD34 antibody using the 1-ethyl-3-(3'-dimethyl-aminopropyl) carbodiimide (EDC) catalyst (ECD – Electron Coupled Dye or R Phycoerythrin-Texas Red is a fluorescent organic dye attached to the antibody). The characteristic fluorescence of ECD in the antibody was used to estimate the percentage of the antibodies that were successfully conjugated with the nanoparticles. The conjugation efficiency was found to increase depending on the volumes ratio x of the nanoparticle solution (concentration of 50 ppm) and the as-purchased antibody solution. The conjugation efficiency rapidly increased from approximately 18% to approximately 70% when x was increased from 2:1 to 100:1, and it gradually reached the saturated state as the $x = 300:1$ at an efficiency of 95%. To isolate the CD34+ stem cells from the bone marrow samples, the solution containing the $\text{Fe}_3\text{O}_4/\text{Ag-antiCD34}$ nanoparticles was added to the bone marrow samples, including the CD34+ stem cells and the CD45+ leukemia cells. At that time, the $\text{Fe}_3\text{O}_4/\text{Ag-antiCD34}$ nanoparticles specifically bound to the CD34+ stem cells due to antigen-antibody interactions between the antiCD34 antibody and the CD34+ stem cells, but they did not bind to the CD45+ leukemia cells. By applying the external permanent magnet, one can collect the magnetic nanoparticle-CD34+ cell complexes, i.e., isolate the CD34+ stem cells from the bone marrow samples.

CONCLUSION

This work reviewed a developing of magnetic nanoparticles and multifunctional nanoparticles synthesis and characterization for applications in biomedicine. By coating with silica or functionalizing with appropriate groups, the nanoparticles are suitable for various applications. Further investigation in order to fully control the size, shape and the uniformity is required. In addition, the developing of multifunctional nanoparticles synthesis is a promising research trend because many

structures and features can be designed. The applications can be improved and broaden using synthesized nanoparticles.

Acknowledgments

This work was supported by the Grant No. ĐTĐL.CN-02/18. Authors would like to thank Prof. Nguyen Ngoc Long, Prof. Nguyen Thi Van Anh, Mr. Luu Manh Quynh, Mr. Nguyen Minh Hieu and Mr Chu Tien Dung for their support and effective cooperation.

References

- [1] W. Wu, Z. Wu, T. Yu, C. Jiang, and W.S. Kim, *Recent progress on magnetic iron oxide nanoparticles: synthesis, surface functional strategies and biomedical applications*, Sci. Technol. Adv. Mater. **16** (2015) 023501 (43pp).
- [2] F. Fathi, M.S. Sadjadi, and M.G. Cherati, *Systematic review: Superparamagnetic Iron Oxide nanoparticles as contrast agents in diagnosis of multiple sclerosis*, Int. J. Nano Dimens. **7** (2016) 270-277.
- [3] N.H. Luong, N.H. Nam, N.H. Hai, L.M. Quynh, and N.M. Hieu, *Nanoparticles: synthesis and applications in life science and environmental technology*, Adv. Nat. Sci.: Nanosci. Nanotechnol. **6** (2015) 015008 (9pp).
- [4] Q.A. Pankhurst, J. Connolly, S.K. Jones, and J. Dobson, *Applications of magnetic nanoparticles in biomedicine*, J. Phys. D: Appl. Phys. **36** (2003) R167–R181.
- [5] Wahajuddin and S. Arora, *Superparamagnetic iron oxide nanoparticles: magnetic nanoplatforms as drug carriers*, Int. J. Nanomed. **7** (2012) 3445-3471.
- [6] X. Peng, H. Chen, J. Huang, H. Mao, and D.M. Shin, *Targeted magnetic iron oxide nanoparticles for tumor imaging and therapy*, Biomedical Engineering - From Theory to Applications, Rijeka: InTech, 2011, Chapter 9.
- [7] D.D. Shao, K.K. Xu, X.J. Song, J.H. Hu, W.L. Yang, and C.C. Wang, *Effective adsorption and separation of lysozyme with PAA-modified Fe₃O₄@silica core/shell microspheres*, J. Colloid Interface Sci. **336** (2009) 526-532.
- [8] K. O'Grady, *Progress in applications of magnetic nanoparticles in biomedicine*, J. Phys. D: Appl. Phys. **42** (2009) 220301.
- [9] A.G. Roca, R. Costo, A.F. Rebolledo, S. Veintemillas-Verdaguer, P. Tartaj, T. Gonzalez-Carreno, M.P. Morales, and C.J. Serna, *Progress in the preparation of magnetic nanoparticles for applications in biomedicine*, J. Phys. D: Appl. Phys. **42** (2009) 224002.
- [10] X.H. Peng, X.M. Qian, H. Mao, A.Y. Wang, Z. Chen, S.M. Nie, and D.M. Shin, *Targeted magnetic iron oxide nanoparticles for tumor imaging and therapy*, Int. J. Nanomed. **3** (2008) 311.
- [11] Y.J. Chen, J.A. Tao, F. Xiong, J.B. Zhu, N. Gu, Y.H. Zhang, Y. Ding, and L.A. Ge, *Synthesis, self-assembly, and characterization of PEG-coated iron oxide nanoparticles as potential MRI contrast agent*, Drug Dev. Ind. Pharm. **36** (2010) 1235.
- [12] A. Ali, H. Zafar, M. Zia, I. Haq, A. R. Phull, J.S. Ali, and A. Hussain, *Synthesis, characterization, applications, and challenges of iron oxide nanoparticles*, Nanotech., Sci. and Appl. **9** (2016) 49–67.
- [13] N.H. Hai, N.Chau, N.H. Luong, N.T.V. Anh, P.T. Nghia, *Applications of Magnetite Nanoparticles for Water Treatment and for DNA and Cell Separation*, J. Kor. Phys. Soc. **53** (2008) 1601-1606.
- [14] D.V. Quy, N.M. Hieu, P.T. Tra, N. H. Nam, N.H. Hai, N.T. Son, P.T. Nghia, N.T.V. Anh, T.T. Hong and N. H. Luong, *Synthesis of silica-coated magnetic nanoparticles and application in the detection of pathogenic viruses*, J. Nanomater. **2013** (2013) 603940, 6 pages.
- [15] C.T. Dung, S.C. Doanh, L.M. Quynh, T.T. Hong, T.D. Quach, D.H. Kim, and N.H. Nam, *Synthesis of bifunctional Fe₃O₄@SiO₂-Ag magnetic-plasmonic nanoparticles by an ultrasound assisted chemical method*, J. Electro. Mater. **46** (2017) 3646-3653.
- [16] N.M. Hieu, N.H. Nam, N.T. Huyen, N.T.V. Anh, P.T. Nghia, N.B. Khoa, N.L. Toan, and N.H. Luong, *Synthesis of SiO₂-coated Fe₃O₄ nanoparticles using ultrasound and its application in DNA extraction from formalin-fixed, paraffin-embedded human cancer tissues*, J. Electro. Mater. **46** (2017) 3738-3747.
- [17] N.M. Hieu, J. Coignot, N.H. Nam, and N.H. Luong, *Effect of pH on magnetic properties of SiO₂-coated Fe₃O₄ nanoparticles*, Proceedings of IWNA 2017, 8-11 November 2017, Phan Thiet, Vietnam, pp. 531-533.
- [18] L.M. Quynh, C.T. Dung, B.T. Mai, H.V. Huy, N.Q. Loc, N.Q. Hoa, P.T. Thach, B.V. Anh, C.T. Thao, N.H. Nam, H.T.M. Nhung, N.N. Long and L.V.Vu, *Development of Fe₃O₄/Ag core/shell-based multifunctional immunomagnetic nanoparticles for isolation and detection of CD34+ stem cells*, J. Immu. **39** (2018) 308-322.
- [19] C.T. Dung, N.Q. Loc, P.T. Huong, D.T.T. Duong, T.T. Hong, L.M. Quynh, and N.H. Nam, *Combination of 4-ATP coated silver nanoparticles and magnetic Fe₃O₄ nanoparticles by inverse emulsion method*, VNU Journal of Science: Mathematics – Physics **30** (2014) 1-9.
- [20] C.T. Dung, L.M. Quynh, N.P. Linh, N.H. Nam, and N.H. Luong, *Synthesis of ZnS:MnFe₃O₄ bifunctional nanoparticles by inverse microemulsion method*, J. Sci. Adv. Mater. Devices **1** (2016) 200-203.
- [21] C.T. Dung, L.M. Quynh, T.T. Hong, and N.H. Nam, *Synthesis, Magnetic Properties and Enhanced Photoluminescence of Fe₃O₄-ZnO Heterostructure Multifunctional Nanoparticles*, VNU Journal of Science: Mathematics – Physics **33** (2017) 16-23.
- [22] L.M. Quynh, N.M. Hieu, and N.H. Nam, *Fast DNA diagnostic using Fe₃O₄ magnetic nanoparticles and light emitting ZnS/Mn nanoparticles*, VNU Journal of Science: Mathematics – Physics **30** (2014) 1-11.

BIOGRAPHY



Associate Professor Nguyen Hoang Nam got PhD in Osaka University, Japan. He is senior lecturer in Faculty of Physics, VNU University of Science, Vietnam National University, Hanoi from 2009. He is focusing on the synthesis of nanomaterials and their application in life science, especially in biomedicine.



Professor Nguyen Hoang Luong graduated from the Physics Department of Kishinev State University in 1977. He received his PhD degree in Solid State Physics at the University of Hanoi in 1984, the degree of Doctor of Habilitation at University of Mining and Metallurgy (AGH University of Science and Technology), Krakow, Poland, in 1999.

He is now the Director of Nano and Energy Center, VNU University of Science, Vietnam National University, Hanoi. He is the author/co-author of over 70 publications in international journals. His current research interests include synthesis, characterization and application of nanomaterials.

THERMOELECTRIC PROPERTIES OF LEAD HALIDE PEROVSKITES SINGLE CRYSTALS

Thi-Mai Huong Duong, Ryo Saeki, Kotaro Matsuyama, Satria Rusdiputra and Hirokazu Tada

Division of Frontier Materials Science, Graduate School of Engineering Science, Osaka University

1-3 Machikaneyama, Toyonaka 560-8531, Japan

Email: tada@molelectronics.jp

ABSTRACT

Considerable attention has long been paid to thermoelectric materials for energy conversion from heat to electricity. The efficiency of thermoelectric conversion is estimated using dimensionless figure of merit, $ZT (= S^2\sigma T\kappa^{-1})$. Here, T is temperature, S is Seebeck coefficient, σ is electrical conductivity and κ is thermal conductivity. It has been demonstrated that organic-inorganic hybrid perovskites show the potentials for thermoelectric device, that is, they show high S , high σ and low κ [1,2]. The hybrid perovskite is abbreviated as ABX_3 where A is an organic cation including $CH_3NH_3^+$, B is a metal cation such as Pb^{2+} and Sn^{2+} , and X is a halogen anion (Cl^- , Br^- or I^-). When $CH_3NH_3^+$ is replaced by larger molecules such as pyridine and its derivatives, perovskites form low dimensional crystals (2D, 1D, and 0D) [3] as shown in Fig. 1.

In the present work, we inserted various organic molecules into the perovskite frameworks to have 2D and 1D single crystals. It was found that thermoelectric properties, S , σ and κ varied depending upon the molecules inserted. Electrical conductivity was measured by a four-probe method. We examined a replacement of B^{2+} by Bi^{3+} and Eu^{2+} , and found that the carrier density increased on the basis of the Hall effect measurement. Seebeck coefficient was measured in vacuum by applying the temperature gradient at both end of the crystal. It was found that the 2D crystals with 4-methyl pyridine showed rather large S values of a few hundred $\mu V K^{-1}$. Thermal conductivity was measured in the wide temperature range from 4 K to 350 K, from which we discussed the scattering mechanism of phonons.

Keywords: Organic inorganic hybrid perovskite, Thermoelectric property, Thermal conductivity, Seebeck coefficient

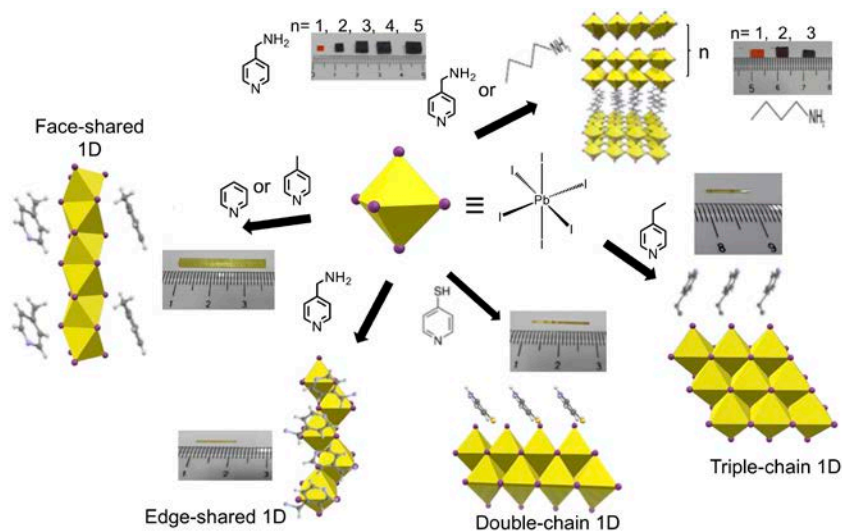


Figure 1. Crystal structures of hybrid perovskites with various organic

References

- [1] X. Mettan et al., J. Phys. Chem. C 119, 11506 (2015).
- [2] T. Ye et al., J. Mater. Chem. C 5, 1255 (2017).
- [3] T. M. H. Duong et al., APEX 11, 115562 (2018).

BIOGRAPHY



Professor Hirokazu Tada

Division of Future Materials,
Graduate School of Engineering Science, Osaka University

Education

- May 1993: PhD., The University of Tokyo
April 1988-May 1989: PhD Course, Department of Chemistry, Graduate School of Science, The University of Tokyo
April 1986-March 1988: Master Course, Department of Chemistry, Graduate School of Science, The University of Tokyo
April 1982-March 1986: Undergraduate Course, Department of Chemistry, School of Science, The University of Tokyo

Professional Positions

- April 2005-Present: Professor, Graduate School of Engineering Science, Osaka University
April 2000-March 2005: Associate Professor, Institute for Molecular Science, Okazaki National Institutes of Science
September 1996-March 2000: Lecturer, Department of Electronic Engineering Science, Graduate School of Engineering, Kyoto University
October 1993-August 1996: Senior Researcher, Communications Research laboratory, Ministry of Posts and Telecommunications
May 1989-September 1993: Assistant Professor, Department of Chemistry, School of Science, The University of Tokyo

UPCONVERSION NANOPARTICLES LINKED GOLD NANOROD THERANOSTIC NANOCOMPOSITES FOR ORAL CANCER CELLS

Duc Tu Vu,^{a,b} Quoc Minh Le,^{b,c} Churng-Ren Chris Wang,^d Lai-Kwan Chau,^d Tzyy-Schiuan Yang,^d Michael W.Y. Chan,^e Cheng-I Lee,^e Chu-Chi Ting,^f Jiunn-Yuan Lin,^a Hung-Chih Kan,^a and Chia-Chen Hsu^{*,a}.

^aDepartment of Physics, National Chung Cheng University, Ming-Hsiung, Chia-Yi 621, Taiwan

^bInstitute of Materials Science, VAST of Vietnam, Hanoi, 100000, Vietnam

^cDuy Tan University, Danang, 550000, Vietnam

^dDepartment of Chemistry and Biochemistry, National Chung Cheng University, Ming-Hsiung, Chia-Yi 621, Taiwan

^eDepartment of Biomedical Sciences, National Chung Cheng University, Min-Hsiung, Chia-Yi, Taiwan

^fGraduate Institute of Opto-Mechatronics, National Chung Cheng University, Ming-Hsiung, Chia-Yi 621, Taiwan

Email: phycch@ccu.edu.tw

ABSTRACT

In this work, multifunctional hybrid nanocomposites were prepared by linking NaYF₄:Yb³⁺,Er³⁺ upconversion nanoparticles (UCNPs) with gold nanorods (AuNR) to serve as theranostic agents for oral cancer cells. The hybrid nanocomposites exhibited superior upconversion luminescence (UCL) labeling, local temperature sensing and photothermal functions simultaneously with a single NIR laser excitation. The hybrid nanocomposites displayed better photothermal properties compared with pure AuNRs or a blend of AuNRs and NaYF₄:Yb³⁺,Er³⁺ UCNPs. The temperature-dependent UCL property was applied to determine local temperature at the hybrid nanocomposites, which is useful for selecting appropriate irradiation dosage for photothermal therapy (PTT). The therapeutic performance of the hybrid nanocomposites in PTT for OML-1 oral cancer cells was determined. For specific cell targeting, we successfully labeled streptavidin-linked nanocomposites on the surface of OML-1 oral cancer using anti-human epidermal growth factor receptor 2 (anti-Her2) antibody. Finally, this nanocomposite caused exceptional destruction of cancer cells up to 70% dead cells under 976 nm laser irradiation for only one min at 0.3 W/cm² which is below the maximal permissible exposure of human skin.

Keywords: Upconversion nanoparticles, gold nanorods, theranostic agents, phototheraml therapy, oral cancer cells.

BIOGRAPHY



Chia Chen Hsu

Department of Physics, National Chung Cheng University (CCU)
168 University Road, Ming-Hsiung, Chia-Yi County, 62102 Taiwan
Phone : 886-5-2720411-66305, Fax :886-5-2720587,
Email :phycch@ccu.edu.tw

Education

Ph.D., Physics, University of Arizona, 1991.

Master, Optical Sciences, National Central University 1984.

B.S., Physics, National Central University, 1981.

Work Experience

Distinguished Professor, Department of Physics, CCU, Taiwan, 2016/01-present.

Professor, Department of Physics, CCU, Taiwan, 2001/08-2015/12.

Invited Professor, Laboratoire de photonique quantique et moléculaire, École normale supérieure de Cachan, France, 2015/09-2016/01.

Dean, College of Science, CCU, Taiwan, 2009/08-2012/07.

Visiting Professor, Department of Physics and Astronomy, University of British Columbia, Canada, 2006/05-2006/08.

Director, Graduate Institute of Opto-Mechatronics, CCU, Taiwan, 2002/08-2005/07.

Associate Professor, Department of Physics, CCU, Taiwan, 1991/08-2001/07.

Awards

2009, Outstanding research award, National Chung Cheng University

2016, Distinguished Professor, National Chung Cheng University

Research Interests

Nanophotonics, Nonlinear Optics, Organic Electronics, Polymer Optics

Selected publications

- [1]. D. T. Vu, H. W. Chiu, R. Nababan, Q. M. Le, S. W. Kuo, L. K. Chau, C. C. Ting, H. C. Kan, and **C. C. Hsu***, 2018 “Enhancing upconversion luminescence emission of rare earth nanophosphors in aqueous solution with thousands fold enhancement factor by low refractive index resonant waveguide grating” *ACS Photonics*, **5**, 3263.
- [2]. A. T. Nguyen, W. C. Lai, B. D. To, D. D. Nguyen, Y. P. Hsieh, M. Hofmann, H. C. Kan, and **C. C. Hsu***, 2017 “Layer control of tubular graphene for corrosion inhibition of nickel wires” *ACS Applied Materials and Interfaces*, **9**, 22911.
- [3]. J. H. Lin, H. Y. Liou, C. D. Wang, C. Y. Tseng, C. T. Lee, C. C. Ting, H. C. Kan*, and **C. C. Hsu***, 2015.” Giant enhancement of upconversion fluorescence NaYF₄:Yb³⁺,Tm³⁺ nanocrystals with resonant waveguide grating substrate”, *ACS Photonics*, **2**, 530.
- [4]. J. H. Lin, C. Y. Tseng, C. T. Lee, J. F. Young, H. C. Kan, **C. C. Hsu***, 2014. “Strong guided mode resonant local field enhanced visible harmonic generation in an azo-polymer resonant waveguide grating” *Optics Express*, **22**, 2790.
- [5]. J. H. Lin, C. Y. Tseng, C. T. Lee, H. C. Kan, **C. C. Hsu***, 2013. “Guided-mode resonance enhanced excitation and extraction of two-photon photoluminescence in a resonant waveguide grating” *Optics Express*, **21**, 24318.

SILVER NANOWIRES FOR FLEXIBLE ELECTRONICS

Byungkwon Lim

School of Advanced Materials Science & Engineering, Sungkyunkwan University (SKKU), Suwon
16419, Republic of Korea
Email: blim@skku.edu

ABSTRACT

Silver (Ag) nanowires (NWs) are promising building blocks for fabrication of flexible transparent electrodes, but their poor adhesion to polymeric substrates causes delamination of NWs from a substrate during repeated deformation, which leads to degradation in electrical performance. We developed a new and simple approach to dramatically improve mechanical, chemical, and thermal stability of a Ag NW electrode by hybridizing a NW network film with an organic molecular nanoadhesive layer without sacrificing inherent excellent optoelectrical properties of a NW film. In this work, we discovered, for the first time, that some of pyridine derivatives can be solution-processed and annealed to form a transparent continuous film with high adhesion to a polymeric substrate such as poly(ethylene terephthalate). In addition to high optical transparency and electrical conductivity, the NW-nanoadhesive hybrid film exhibited low surface roughness, reduced optical haze, excellent adhesion to the substrate without delamination against tape and bending tests, and good air-oxidation and thermal stability. Because of these synergistic properties, hybrid electrodes showed good performance in applications for flexible touch panel and thin film heater. Our work opens a promising route to fabrication of high-performance, exceptionally durable NW electrodes, and also a great opportunity for exploring novel organic molecular nanoadhesives for application in flexible transparent electronics.

Keywords: silver nanowires; transparent electrodes; molecular nanoadhesives; touch panel; thin film heater

BIOGRAPHY



Byungkwon Lim obtained his B.S. (1998), M.S. (2000), and Ph.D. (2004) in School of Chemical and Biological Engineering from Seoul National University, South Korea. He then worked on the synthesis and structural analysis of polymers for three years in the R&D Center of LG Chem, South Korea. He joined the Younan Xia group (University of Washington at Seattle and then Washington University in St. Louis) as a postdoctoral fellow in 2007, started as an Assistant Professor at Sungkyunkwan University in 2010, and became Associate Professor in 2014. His current research interests include the synthesis of nanostructured materials, catalysis, self-assembly, and the fabrication of flexible devices.

SINGLE MOLECULAR TRANSISTOR BASED ON NANOGAP ELECTRODES

Yutaka Majima¹ and Phan Trong Tue¹

¹Laboratory for Materials and Structures, Tokyo Institute of Technology
4259 Nagatsuta-cho, Midori-ku, Yokohama, Japan
Email: majima@msl.titech.ac.jp

ABSTRACT

Single molecular transistor is one of the candidates of next-generation 3 nm scale three-terminal devices due to small size, unique structure, and high-speed operation. Stable operations of single molecular transistor have been the challenge in the research field of molecular electronics. However, a stable operation could not be obtained ever. Here, we demonstrate operations of single molecular transistors. We have established the fabrication processes of electroless Au plated (ELGP) nanogap electrodes with the gap separation equal to the size of the molecule. We introduce π -conjugated molecule between the gap. The key to obtain stable operation on single molecular transistors will be discussed.

Keywords: Nanogap electrodes, electron beam lithography, electroless Au plating, molecular transistor, single-electron transistor

INTRODUCTION

Nanogap electrodes with gate electrodes are the fundamental elements for fabricating bottom-up nanoscale transistors such as single-electron transistors (SETs) and molecular transistors. To realize such transistors, many fabrication methods for nanogap electrodes, have been developed. However, these methods have fabrication problems such as lack of reproducibility, poor gap separation control, improper preparation of gate electrodes, and reduction in the linewidth of nanogap electrodes. Among the available fabrication methods, electron-beam lithography (EBL) is considered as a robust fabrication method for nanogap electrodes with gate electrodes. We have reported the fabrication of electroless Au-plated (ELGP) Au-based nanogap electrodes with two-side gate electrodes and a 3-nm gap separation at a 90% yield by using the combination of EBL and electroless Au plating. The use of electroless Au plating for fabricating Au-based nanogap electrodes ensures that the gap separation is kept below the 3-nm scale by using a self-termination mechanism or molecular ruler. By using the ELGP Au-based nanogap electrodes with two-side gate electrodes, we have demonstrated the stable logic gate operation of chemically assembled multigate SETs at 9 K.

Single molecular transistor is one of the candidates of next-generation a few nm scale

three-terminal devices. Stable operations of single molecular transistor have been the challenge in the research field of molecular electronics. However, a stable operation could not be obtained ever.

Here, we demonstrate operations of single molecular transistors. We have established the fabrication processes of electroless Au plated (ELGP) nanogap electrodes with the gap separation equal to the size of the molecule. We introduced π -conjugated molecule between the gap. The key to obtain stable operation on single molecular transistors will be discussed.

EXPERIMENTAL

The single molecular transistors were fabricated through a combination of top-down and bottom-up methods based on previous studies. Electrode patterns were designed by EBL (Elionix, ELS-7500EX, Japan) on a SiO₂ (50 nm)/Si substrate, and electrode materials were evaporated onto the substrate by electron-beam evaporation equipment under high vacuum conditions. At this point, the average gap separation is approximately 10 nm. Probing electrodes were then added by photolithography, and an iodine ELGP solution was used to reduce the size of the nanogaps to less than 3 nm via a self-termination mechanism. A π -conjugated molecule was then chemisorbed between the nanogap electrodes from the solution.

The electron transport properties of single molecular transistors were measured using a mechanical refrigerator-type probe (Nagase, GRAIL10-LOGOS01S, Nihonbashi, Japan) and a semiconductor device analyzer (B1500, Agilent, Santa Rosa, CA, USA). The measurement temperature was 9 K. All measurements were conducted under the same conditions as in previous studies [21–23].

RESULTS AND DISCUSSION

Gate voltage (V_g) dependence of drain current (I_d) - drain voltage (V_d) characteristics on single molecular transistor is shown in Figure 1. Coulomb staircase with no current V_d region depended on V_g . Based on these results, this single molecular transistor operation is attributed to single-electron transistor.

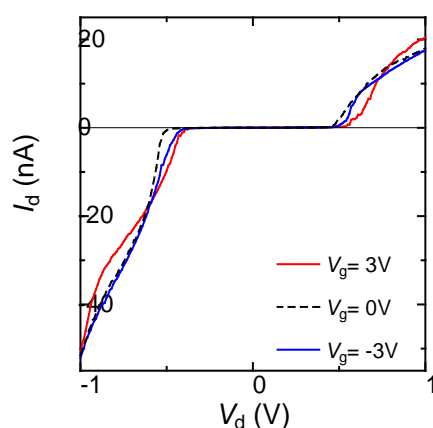


Figure 1 V_g dependence on $I_d - V_d$ characteristics on single molecular transistor

CONCLUSION

We have demonstrated typical single molecular transistor operation by introducing π -conjugated molecule between the gap. The operation mechanism of the single molecular transistor is attributed to the single-electron transistor. These results will open the era for molecular electronics.

Acknowledgment

This study was partially supported by MEXT Elements Strategy Initiative to Form Core Research Center; and the BK Plus program, Basic Science Research program (NRF-2014R1A6A1030419).

References

[1] Y. Yasutake, K. Kono, M. Kanehara, T. Teranishi, M. R. Buitelaar, C. G. Smith, Y. Majima, *Simultaneous fabrication of*

nanogap gold electrodes by electroless gold plating using a common medical liquid. Appl. Phys. Lett. **91** (2007) 203107.

[2] V. M. Serdio, Y. Azuma, S. Takeshita, T. Muraki, T. Teranishi, Y. Majima, *Robust nanogap electrodes by self-terminating electroless gold plating.* Nanoscale **4** (2012) 7161.

[3] V. M. Serdio, Y. Azuma, S. Takeshita, T. Muraki, T. Teranishi, Y. Majima, *Gap separation-controlled nanogap electrodes by molecular ruler electroless gold plating.* RSC Adv. **5** (2015) 22160.

[4] Y. Y. Choi, T. Teranishi, Y. Majima, *Robust Pt-based nanogap electrodes with 10 nm scale ultrafine linewidth,* Appl. Phys. Express **12** (2019) 025002.

[5] Y. Azuma, Y. Yasutake, K. Kono, M. Kanehara, T. Teranishi, Y. Majima, *Single-electron transistor fabricated by two bottom-up processes of electroless Au plating and chemisorption of Au nanoparticle,* Jpn. J. Appl. Phys. **49** (2010) 090206.

[6] N. Okabayashi, K. Maeda, T. Muraki, D. Tanaka, M. Sakamoto, T. Teranishi, Y. Majima, *Uniform charging energy of single-electron transistors by using size-controlled Au nanoparticles,* Appl. Phys. Lett. **100** (2012) 033101.

[7] K. Maeda, N. Okabayashi, S. Kano, S. Takeshita, D. Tanaka, M. Sakamoto, T. Teranishi, Y. Majima, *Logic operations of chemically assembled single-electron transistor,* ACS Nano **6** (2012) 2798.

[8] Y. Azuma, Y. Onuma, M. Sakamoto, T. Teranishi, Y. Majima, *Rhombic Coulomb diamonds in a single-electron transistor based on an Au nanoparticle chemically anchored at both ends,* Nanoscale **8** (2016) 4720.

[9] Y. Majima, G. Hackenberger, Y. Azuma, S. Kano, K. Matsuzaki, T. Susaki, M. Sakamoto, T. Teranishi, *Three-input gate logic circuits on chemically assembled single-electron transistors with organic and inorganic hybrid passivation layers,* Sci. Technol. Adv. Mater. **18** (2017) 374.

[10] C. Ouyang, K. Hashimoto, H. Tsuji, E. Nakamura, Y. Majima, *Coherent Resonant Electron Tunneling at 9 and 300 K through a 4.5 nm Long, Rigid, Planar Organic Molecular Wire,* ACS Omega **3** (2018) 5125.

BIOGRAPHY



Yutaka Majima received B.S. and Dr. of Engineering degrees in the department of electrical and electronic engineering from Tokyo Institute of Technology (Tokyo Tech), Japan, in 1987 and 1992, respectively. In 1992, he joined Toshiba Corporation, and became a Research Scientist in 1996. In 1996, he moved to Tokyo Tech as an Assistant Professor. He became an Associate Professor of the department of Physical Electronics, Tokyo Tech in 1998. He is a full Professor of Laboratory for Materials and Structures, Tokyo Tech from 2009. He is also a Chief Adjunct Professor, Department of Printed Electronics Engineering, Sunchon National University from 2009. His research covers nanofabrication, molecular devices, organic electronics, and scanning probe microscope.

FROM MICRO TO QUANTUM ELECTRONICS

Christophe Wyon

Université Grenoble Alpes, 38000 Grenoble, France
CEA, LETI, MINATEC Campus, 38054 Grenoble, France
E-mail: cwyon@cea.fr

ABSTRACT

This paper will present the evolution of silicon-based microelectronics for the last decades and will survey the future roadmap for the next logic integrated circuits (IC). It will mainly focus on the technologies used for achieving high performance IC such as the introduction of EUV lithography, of high-k and low-k materials, as well as the introduction of new transistor architectures (FinFET, FDSOI). This paper will also deal with the introduction of new concepts for the next-generation of IC such as the nanowire and the nanosheet-based transistors, the neuromorphic circuits and the logic circuits that will afford quantum computing.

Keywords: Silicon, Microelectronics, Field Effect transistor, Integrated Circuits

BIOGRAPHY



Christophe Wyon received an Engineer degree (1980) and a PhD (1984) as well as the habilitation to manage research (2009) in Physics and Chemistry of Materials from the Grenoble Polytechnique National Institute. He managed several laboratories in LETI involving the crystal growth of laser, scintillator and semiconductor materials, the thermal and cleaning processes for advanced transistors and Flash memories, and the development of OLED micro-displays. He managed the physical characterization and failure analysis of advanced IC within ST. He also worked during 8 years for the French Ministry of Industry for promoting the microelectronics industry in France. He is now the LETI representative in Brussels in order to promote the nanoelectronics industry inside the Europe.

WAFER SCALE FABRICATION AND MODIFICATION OF SILICON NANO-PILLAR ARRAYS FOR NANOELECTRONICS, NANOFUIDICS AND BEYOND

Yasser Pordeli¹, Bernhard van der Wel², Lucas Kooijman³, Dirk Jonker¹, Erwin Berenschot¹, Bjorn Borgelink¹, Hai Le The⁴, Meint de Boer⁵, Jan Eijkel⁶, Ray Hueting², Roald Tiggelaar⁵, Han Gardeniers¹, Niels Tas¹

¹MCS group, Faculty of Science and Technology

²IDS group, Faculty of Electrical Engineering, Mathematics and Computer Science

³AMBER group, Faculty of Electrical Engineering, Mathematics and Computer Science

⁴POF group, Faculty of Science and Technology

⁵NanoLab

⁶BIOS Lab-on-a-Chip group, Faculty of Electrical Engineering, Mathematics and Computer Science
All with MESA+ Institute, University of Twente, P.O. Box 217, 7500 AE Enschede, The Netherlands.

Email: n.r.tas@utwente.nl

ABSTRACT

We report here on a top-down nanofabrication platform for massive parallel silicon nano-pillar based devices. Through different device examples we illustrate the pillar array formation, the embedding of the pillar array in an insulating membrane, the nanoscale modification of the pillars, as well as the sacrificial removal of the pillars to form arrays of well-defined nano-pores. This platform is expected to find application in many different device domains, including nanofluidics, (3D)-nanoelectronics, as well as nanophotonics.

Keywords: 3D nanofabrication, 3D electronics, nanofluidics, nanoelectronics

INTRODUCTION

Silicon vertical nanowires, here referred to as silicon nano-pillars, are already known as key building blocks for ultrahigh density electronic integrated circuits, making use of the 3rd dimension to stretch the limits in areal density. An example is the implementation of high areal density memory chips (3D-NAND technology) [1, 2]. This technology typically consists of a multilevel integrated thin-film transistor (TFT) arrangement based on relatively deep (~2.5 μ m) polycrystalline silicon nanopillars, in which each transistor includes a silicon-oxide-nitride-oxide-silicon (SONOS) multilayer structure that facilitates non-volatile charge-trapping.

We have introduced an alternative fabrication route for high density single crystalline silicon nano-pillar devices, based on the combination of advanced interference lithography, nanoscale reactive ion etching (RIE), and a novel approach for filling the space between the pillars by an insulating ceramic material (so far typically silicon nitride) that can be deposited through low pressure chemical vapor deposition (LPCVD) [3].

An intriguing aspect of the resulting configuration is that free standing ceramic membranes can be obtained, in which the silicon nano-pillar arrays are embedded. This enables the direct access to the nano-pillars from both sides (top and bottom), paving the road towards novel electronic configurations, as well as nanofluidic device configurations in which typically the nano-pillars are sacrificed to create arrays of well-controlled nano-pores.

Furthermore, as the nano-pillars are composed of single crystalline silicon, they can be machined by a combination of anisotropic etching and self-aligned nano-patterning techniques such as corner lithography [4, 5]. This combination we refer to as crystallographic nano-lithography [6].

By introducing four examples of novel device concepts, based on the nano-pillar array fabrication, we will discuss the different innovative aspects of this new platform. Further opportunities will be discussed during the presentation.

FABRICATION OF HIGH DENSITY ARRAYS OF NANO-PILLARS: FIELD EMITTER ELECTRODES

High-density nano field emitter arrays contribute to important applications in *e.g.* vacuum electronics, display technology, and multibeam electron lithography. A new method has been developed to fabricate a large area of field emitters (LAFE), by a hybrid process that merges displacement Talbot lithography (DTL) nanoscale pattern with an i-line photoresist microscale pattern, yielding a combined photoresist pattern in a high-throughput fashion [7]. The combined pattern is transferred into a silicon substrate by mixed mode RIE in an SF₆ and C₄F₈ plasma (PlasmaPro 100 Estrelas, Oxford Instruments), as is illustrated in fig. 1. As fig. 2 shows, pattern transfer is successful close the mask transition edge and mid-field.

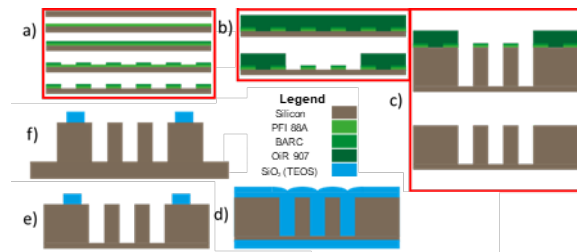


Figure 1. Schematic cross sections of the LAFE production process. The red boxes indicate a) nanopatterning, b) micropatterning, and c) combined result. d) TEOS CVD, e) spacer layer, and f) pulsed mode RIE of plateau [7].

Electrical characterization of the fabricated devices was performed by (I, V) measurements in air (2410, Keithley). The counter electrode was pressed against a 500 nm SiO₂ spacer layer using a vertically suspended stainless steel rod connected to a strain gauge (LSM250, Futek) and a piezo element (P-603.3S1, PI). The Fowler-Nordheim (FN) plots are displayed in fig. 3. The near-linear behavior in the FN plots indicate that field emission was indeed observed.

FABRICATION AND TESTING OF NANO-PILLAR BASED DIODES

Mainly in the context of power handling and for “rectenna” energy harvesting systems, we are developing diodes which can function efficiently for high voltage applications (up to ~200V) or at high frequencies (GHz or above), respectively.

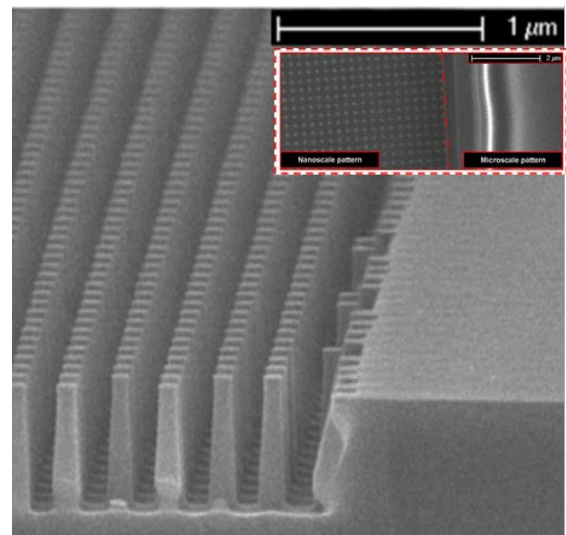


Figure 2. Cross-sectional scanning electron micrograph of the silicon nanowires at the micropattern edge (scale bar: 1 μm). The top-right inset shows a top-view of the combined resist pattern (scale bar: 2 μm) [7].

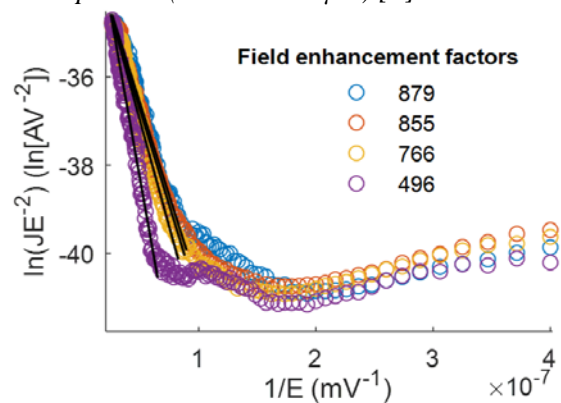


Figure 3. Measurement data obtained by electrical characterization (I, V) of field emitter devices. The data is plotted in a characteristic Fowler Nordheim-plot while the legend contains apparent field enhancement factors [7].

Two concepts are being explored: Nanopillar Schottky diodes [8] and “curved” metal – insulator – semiconductor (cMIS) tunnel diodes [9]. In the following, the latter concept is discussed in more detail.

A schematic overview of the fabrication process of the cMIS tunneling junctions is shown in fig. 4. Wafer-scale nanopillars were fabricated by combining DTL with inductively coupled plasma - reactive ion etching (ICP-RIE) [9], steps 1-3. After locally protecting pillars by silicon nitride, followed by a local oxidation of silicon (LOCOS) step, pillars in selected regions can be “de-activated”, as to avoid edge effects in final devices (steps 4-5). After accessing the

tops of the pillars (step 6), inverted pyramids were etched into the pillars by a TMAH solution (step 7). In steps 8 and 9 corner lithography [4, 5] was applied to define the window for tunnel barrier formation, and a thin (2.5 nm) silicon oxide was formed by rapid thermal oxidation (step 9). In step 10, finally, Aluminum was deposited by evaporation to complete the curved MIS junction array. Details of all steps can be found in [9].

Fig. 5 shows the measured normalized (I , V)-curves for cMIS devices with varying active device areas, where the total current is divided by the estimated amount (N) of cMIS junctions in parallel. In our technology, the tunneling current density of a planar reference junction at a bias potential of 0.5 V is $(2.5 \pm 0.2) \times 10^{-4}$ A/cm², which corresponds with earlier reported values for a 2.5 nm (planar) oxide barrier [9]. Assuming a tunneling window area of 100 nm² for one cMIS junction, we find a tunneling current density of $(3.0 \pm 0.6) \times 10^{-3}$ A/cm² at 0.5 V. This is in reasonable correspondence, given the uncertainty in exact window area and oxide thickness near the apex [9].

FABRICATION AND TESTING OF MASSIVE PARALLEL NANO-PORE BASED EOF-PUMP

Based on sacrificial nano-pillar moulding, a process was developed for manufacturing massively parallel ($\sim 6 \times 10^6$ nanopores) electro-osmotic flow (EOF) pumps in silicon nitride (SiN) (Fig. 6). The technique enables a high pore density and well-controlled pore dimensions resulting in a high-throughput pump at low actuation voltages. Fig. 7 summarizes and illustrates the fabrication process.

For testing, a 1 cm² chip with 37 square 100 μ m membranes containing a total of 5.92 million pores of 455 nm length and 83 nm diameter, was placed between two reservoirs with electrodes and measurement tubes. Preliminary tests with a buffered potassium phosphate solution (pH \sim 8) at 117 mV cross-membrane voltage showed a maximum flow around 13 μ l/min or 0.11 ml/(min \cdot V), and a calculated maximum back-pressure of 14 kPa or 120 kPa/V. These values were 35% of the initially calculated values; the 117 mV cross-membrane voltage is a calculated value based on the applied constant 20 mA current, the conductivity of the solution and membrane geometry.

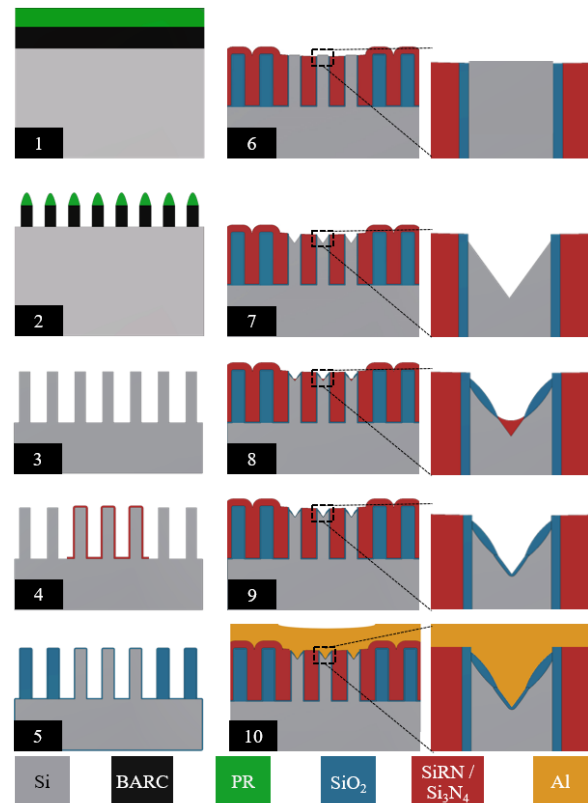


Figure 4. Schematic illustration of the main fabrication steps [9].

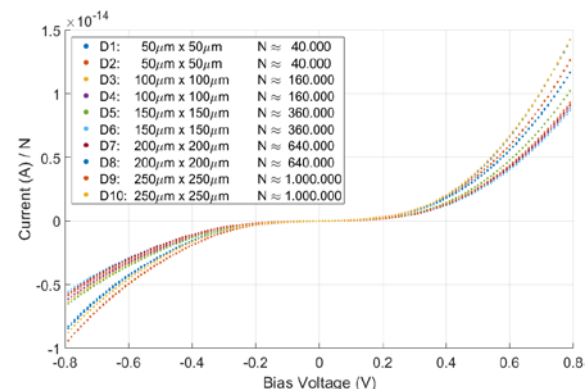


Figure 5. Normalized (I , V)-curves of the cMIS junctions. The caption indicates the device name, the device area and the calculated amount of pillars N of cMIS devices in parallel, respectively [9].

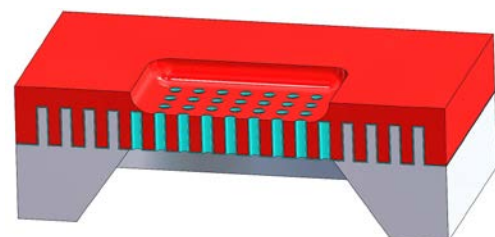


Figure 6. Illustration of the EOF membrane. Red: SiN. Green: SiO₂. Grey: Silicon [10].

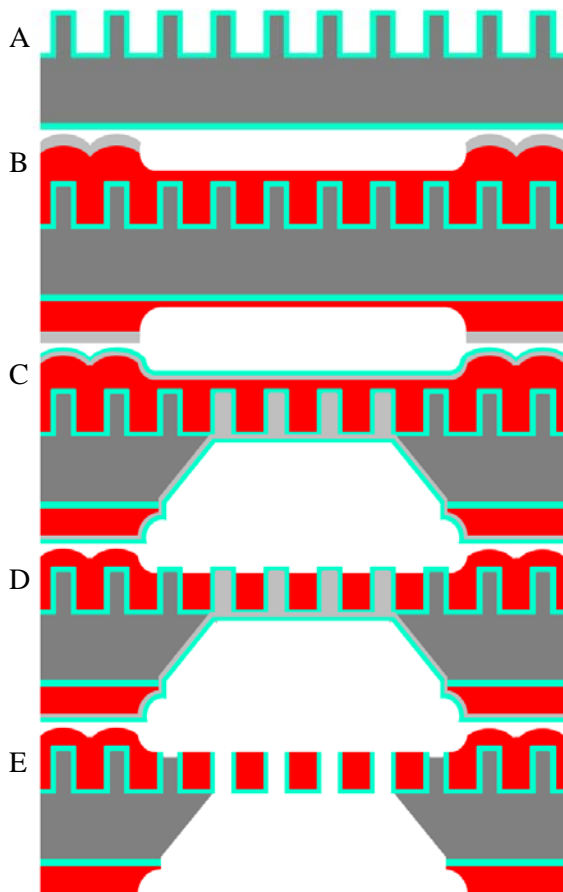


Figure 7. Summarised process flow. Red: SiN. Green: SiO₂. Dark grey: <100> silicon. Light grey: Poly-silicon. Yellow: Resist. A: Oxidised nanopillars. B: Etched SiN with poly-silicon hard-mask. C: Single sided etching of the sacrificial mould with protective poly-silicon deposition and oxidation. D: Single sided etching of the top SiN down to the pillar tops. E: Finished membrane [10].

CONCLUSION

We have introduced silicon nano-pillar arrays fabricated by a combination of advanced interference lithography and RIE. Nano-pillars can be embedded in an insulating ceramic membrane, which can be made free-standing to access both sides of the pillars. The versatility of the platform is illustrated by a number of device implementations in the nanoelectronic and nanofluidic domains. The combination with crystallographic nanolithography for detailed shaping and functionalization of the pillars is

expected to further increase the opportunities offered by this platform.

Acknowledgment

The authors gratefully acknowledge the extensive support by the MESA+ NanoLab staff.

References

- [1]. S.-H Chen *et al.*, *A Highly Scalable 8-layer Vertical Gate 3D NAND with Split-page Bit Line Layout and Efficient Binary-sum MiLC (Minimal Incremental Layer Cost) Staircase Contacts*, IEEE Int. Electron Devices Meeting (IEDM), San Francisco-2012, 21-24.
- [2]. A. Nitayama, H. Aochi, *Vertical 3D NAND Flash Memory Technology*, ECS Transactions **41.7** (2011) 15-25.
- [3]. J. W. Berenschot *et al.*, *Wafer-scale nanostructure formation inside vertical nano-pores*, NEMS'12, Los Angeles-2017, 57-60.
- [4]. E. Berenschot *et al.*, *3D nanofabrication of fluidic components by corner lithography*, Small **8.24** (2012) 3823-3831.
- [5]. N. Burouni *et al.*, *Wafer-scale fabrication of nanoapertures using corner lithography*, Nanotechnology **24.28** (2013) 285303.
- [6]. J. W. Berenschot *et al.*, *crystallographic nanolithography at convex corners*, manuscript in preparation.
- [7]. D. Jonker *et al.*, *High-throughput DTL/optical-hybrid lithography for fabricating high-density silicon nanopillar arrays for field emission*, presented at MNE 45, Rhodes-2019.
- [8]. B.Y van der Wel, *Miniaturizing the Trench MOS Barrier Schottky (TMBS) rectifier*, SAFE, Delft-2019, 778-781.
- [9]. Y. Pordeli *et al.*, *Wafer-Scale Self-Aligned Fabrication of Nanometric Curved Tunnelling Junctions*, TRANSDUCERS 2019 & EUROSENSORS 33, Berlin-2019, 2376-2379.
- [10]. L. J. Kooijman *et al.*, *High-Performance Ceramic EOF Pump Realized by Massively Parallel Sacrificial Silicon Nano-Pillar Moulding*, MicroTAS 23, Basel-2019.

BIOGRAPHY



Niels Tas received his Ph.D. degree from the University of Twente (UT) in April 2000. His Thesis dealt with the design and realization of MEMS linear electrostatic motors, employing walking motion and mechanical leverage. The main results of the thesis work include the invention of the electrostatic “shuffle motor” and modelling and characterization of sliding friction in adhesive rough contacts. From 2000 – 2004 he was a post-doctoral fellow in the BIOS lab-on-a-chip group, UT, working on surface tension effects in nanochannels, like capillary negative pressure and directional bubble injection (“bubble pump”). Also he contributed to the invention of the UT nano-fountain pen. In 2004 he was appointed as assistant professor at the Transducers Science and Technology group. In 2008 Niels Tas was awarded a Vidi-grant which he used to further develop new 3D-nanofabrication techniques for application in advanced scanning probe microscopy and beyond. In 2010 he was appointed associate professor. Since 2014, he is working in the Mesoscale

Chemical Systems group at the University of Twente, headed by Prof. Dr. Han Gardeniers. In close collaboration with Erwin Berenschot B.Sc., he is working on a broad range of applications of innovative 3D-nanofabrication techniques in the fields of nanofluidics, NEMS, nano-electronics and photovoltaics.

LOW-COST PRINTABLE TFT-DRIVEN PZT ACTUATOR ARRAY TOWARDS SINGLE-CELL ANALYSIS

Phan Trong Tue^{1,*}, Tatsuya Shimoda¹ and Yuzuru Takamura¹

¹ School of Materials Science, Japan Advanced Institute of Science and Technology, 1-1 Asahidai, Nomi, Ishikawa 923-1292, Japan;

* Present address: Laboratory for Materials and Structures, Institute of Innovative Research, Tokyo Institute of Technology, 4259 R3-5 Nagatsuta-cho, Midori-ku, Yokohama 226-8503, Japan
Email: phan.t.ac@m.titech.ac.jp

ABSTRACT

This paper reports a novel thermal ultraviolet/ozone (UV/O₃) assisted annealing method for fabrication of solution-processed piezoelectric PZT film at a low-temperature (<450 °C) compatible with CMOS technology, which allows, for the first time, an integration of a PZT actuator array on an active-matrix oxide TFT. The actuation of the PZT actuator array electrically driven by the active-matrix TFT, was confirmed. Fluidic control in microchannel by the PZT/TFT micropump array was successfully demonstrated as well.

Keywords: PZT, Oxide-TFT, Solution process, Piezoactuator, Single-cell analysis

INTRODUCTION

The integration of a piezoelectric PZT actuator with a controlling element such as thin-film transistor (TFT) has attracted many practical interests for totally integrated smart devices such as integrated electronics, microfluidics, sensors and actuators. However, the integration remains challenging due to a required high annealing temperature of the device-quality PZT film (> 600°C), at which other integrated components cannot tolerate. In this paper, we report the first successful integration of PZT actuator array on an active-matrix oxide TFT using the low-temperature solution-process for micropump application.

EXPERIMENTAL

A schematic fabrication process of the oxide-TFT is given in Fig. 1 (step 1-6) [1-4]. In this process, all TFT components such as gate insulator (La-Zr-O), semiconducting channel (In-Zn-O), etch stopper (SiO₂), and passivation layers (La-Zr-O) were fabricated by a chemical solution deposition technique. The maximum process temperature was below 550°C. The integration of PZT actuator on the fabricated TFT array is described by step 7-10 (Fig. 1). Here, a novel thermal UV/O₃ assisted annealing process was applied for a gel state of PZT film [5]. In short, the dried PZT gel film was placed on a heated stage (200°C) and exposed to UV

irradiation under ozone ambient, followed by a post-annealing at 450°C for crystallization. An optical microscope image of the fabricated PZT/TFT array is presented in Fig. 2.

RESULTS AND DISCUSSION

Cross-sectional SEM image of the fabricated PZT actuator array revealed the successful fabrication of the device. XRD diffraction patterns of PZT films prepared by the low-temperature process (450°C) with and without the thermal UV/O₃ treatment, and the conventional ones (600°C) as a reference were also examined. Pure perovskite diffraction patterns of PZT were observed for the UV/O₃ treated film indicating its good crystallinity. A squared-hysteresis loop was obtained for the film with the UV/O₃ treatment, which is comparable to the conventional PZT film (Fig. 3). Figure 4 demonstrates operation of the fabricated oxide-TFT with a large “on/off” current ratio, a high electron mobility, a small subthreshold swing factor, and a small hysteresis loop. Performance of the PZT actuator, which was electrically controlled by the fabricated oxide-TFT, is given in Fig. 5. Dependence of the actuator displacement on the applied voltage and frequency was observed. A maximum displacement of approximately 180 nm was achieved, which agrees with simulation results. The displacement was confirmed to get

decreased less than 10% when an external pressure of 1000 hPa was applied indicating that the actuator is able to generate ideal driving force for micropump. A demonstration of microfluidic control in microchannel by the PZT/TFT pump array was performed. The demonstrated system is promising for future smart devices such as piezoMEMS, microfluidics, sensors and actuators.

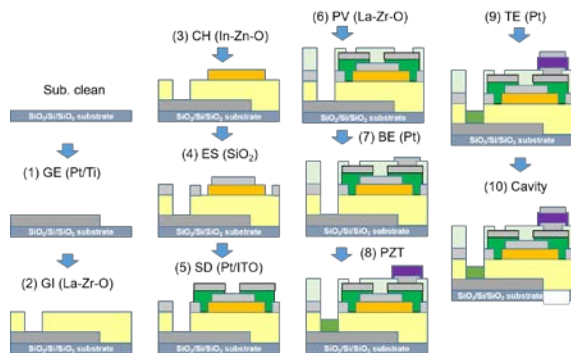


Figure 1. Fabrication process of a PZT actuator array integrated on an active-matrix oxide-TFT.

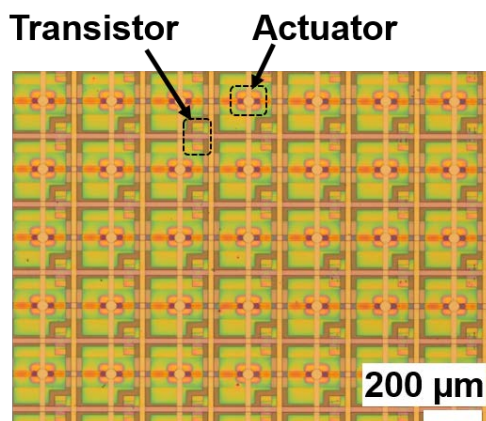


Figure 2. Optical microscope image of the fabricated PZT/TFT array.

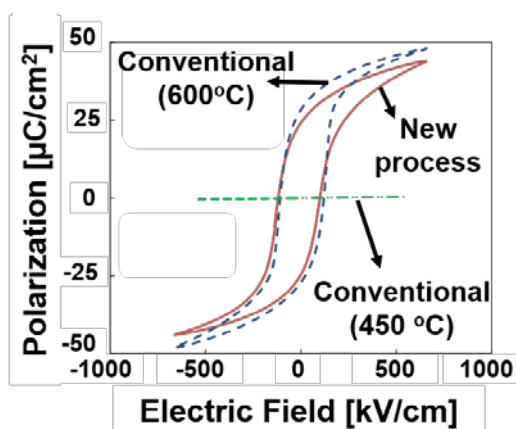


Figure 3. Hysteresis characteristics of PZT films prepared by different methods.

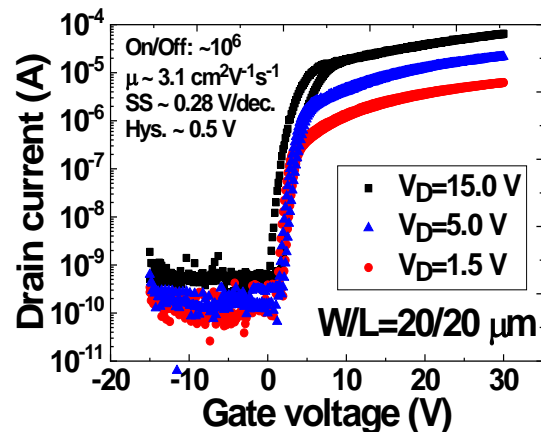


Figure 4. Transfer characteristics of the fabricated oxide TFT.

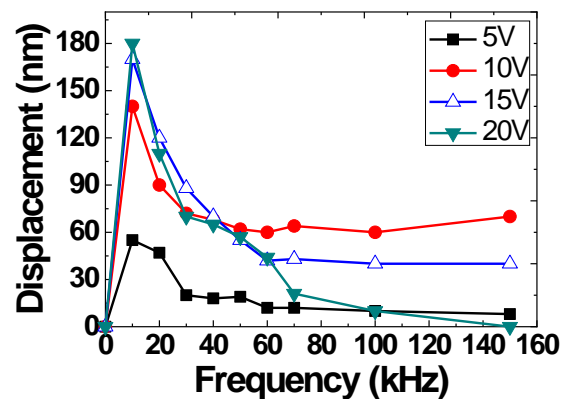


Figure 5. Actuating response of the fabricated PZT actuator.

CONCLUSION

A piezoelectric actuator array electrically driven by an active-matrix oxide-TFT has been successfully developed using a low-temperature solution-processed PZT film. The demonstrated system is promising for future smart integrated devices such as piezoMEMS, microfluidics, sensors and actuators.

Acknowledgment

This work was financially supported by the Japan Science and Technology Agency (JST), CREST project.

References

- [1]. P. T. Tue et al., *Low-temperature all solution-derived amorphous oxide thin film transistors*, IEEE Electron Device Letters **32** (2013) 1536-1538.
- [2]. P. T. Tue et al., *High-Performance Solution-Processed ZrInZnO Thin-Film Transistors*,

- IEEE Transaction on Electron Devices **60**
(2013) 320-326.
- [3]. S. Inoue, P. T. Tue et al., *Electrophoretic displays driven by all-oxide thin-film transistor backplanes fabricated using a solution process*, Phys. Status Solidi A **212** (2015) 2133–2140.
- [4]. P. T. Tue et al., *Direct integration of piezoactuator array with active-matrix oxide thin-film transistors using a low-temperature solution process*, Sensors and Actuators A: Physical **295** (2019) 125-132.
- [5]. R. Shimura, P. T. Tue et al., *Solution-based process with thermal UV treatment for fabrication of piezoelectric PZT films for an actuator array at temperatures under 450 °C*, Sensors and Actuators A: Physical **267** (2017) 287-292.

BIOGRAPHY



Dr. Phan is currently an Assistant Professor at the Laboratory for Materials and Structures, Institute of Innovative Research, Tokyo Institute of Technology, Japan. He received MSc. in Faculty of Physics, Hanoi University of Science, Vietnam in 2008, and Ph.D in School of Materials Science, JAIST in 2011. During 2011-2014, he worked as Post-doctoral researcher at the JST-ERATO Shimoda Nano-Liquid Process Project and Green Devices Research Center, JAIST. From 2015 till March 2019, he joined the Department of Bioscience and Biotechnology, JAIST as an Assistant Professor. His research focuses on development of novel functional inks and precise printing technology for printed bio/nano-electronics using a micro/nano liquid process. He has published more than 50 papers in ISI journals, 06 patents, and was a principal investigator for several projects. Dr. Phan received several awards including Young Scientist Award (MRS Spring 2014), Outstanding Poster Presentation Award (IDW 2014), and Best Poster Presentation Award (EM-NANO 2015).

STABLE VISCOUS LIQUID THREADS INSIDE MICROCHANNELS

Cees J.M. van Rijn

Institute of Physics, Soft Matter group, University of Amsterdam,
Science Park 904, 1098XH Amsterdam, The Netherlands
Email: c.j.m.vanrijn@uva.nl

ABSTRACT

Forming droplets are often accompanied with an interconnecting liquid thread. Postulated is that this phenomenon can only exist as long as a pressure gradient exists within the thread, for instance when a viscous liquid is conveyed via the liquid thread to the forming droplet. We show from the experimental results that the thread starts to show unstable behavior as soon as these capillary effects come into play. We show how to predict the thread length at which the capillary instability sets in for any liquid thread system. It is found that the predicted maximum dimensionless thread length is given by the capillary number.

Keywords: Viscous Liquid Threads, Surface Tension, Stability, Breakup, Microchannels

INTRODUCTION

In many liquid thread and droplet formation processes a general pattern is observed: droplets appear and coupled liquid threads quickly disappear. Fluid threads seem to be intrinsically unstable and under influence of the interfacial tension force they tend to be readily transformed into droplets [1, 2]. One might anticipate that any sufficiently extended fluid element will always break up and converted into droplets. However, experiments and calculations have shown that this is not always the case [3, 5]. For example, Eggers has derived that a strongly stretched viscous element will never break up, as long as inertial forces can be neglected⁶. Anomalous breakup processes with unexpectedly slender and stable viscous threads have also been reported [5, 6].

In recent years, microfluidic devices [7] are progressively used to form droplets from liquid threads with techniques based on flow focusing, co-flow, cross-flow, and microchannels [7, 8]. In most of these devices a liquid thread is created to transport liquid towards a forming droplet enabling growth of the droplet, until a maximum is reached followed by pinching, and next the droplet formation process restarts. The breakup of the liquid thread normally appears downstream at a point close to the droplet. Liquid threads can be stabilized by regulating the inner fluid flow [8].

EXPERIMENTAL

We used an inner fluid of silicone oil ($\eta = 373$ mPa·s, $\rho = 972$ kg/m³) in aqueous 1% tween20 (interfacial tension $\gamma = 5.0$ mN/m) for use in a microfluidic device (10 x 10 x 120 mm), tilted 0°, 7° & 20° from horizontal position. Inner fluid flows from a nozzle in the stationary outer fluid from the bottom of the device. The generated droplet floats to the tilted ceiling still attached to the nozzle connected by a liquid thread.

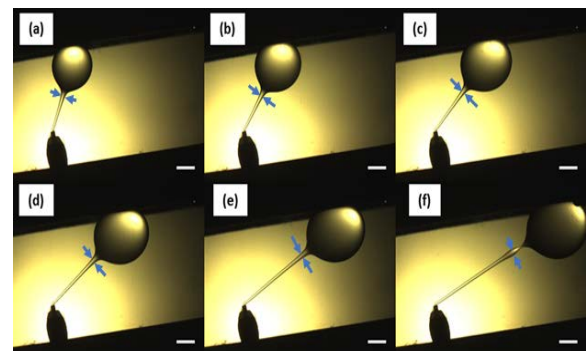


Figure 1. Snapshots taken at times 24.90, 20.00, 14.90, 9.90, 4.90 and 0.1 s before breakup of a liquid thread developing in time. (a) The droplet touches the ceiling and starts to shift along it under influence of buoyancy. (b-e) Both thread length and droplet volume grow in time. (f) Eventually, an instability occurs leading to breakup close to the droplet. Arrows indicate the location where the initial liquid thread radius has doubled in size and defines the length L of the liquid thread as measured from the nozzle exit. Scale bars are 2000 μm .

RESULTS AND DISCUSSION

Detailed experimental analysis showed that the liquid flowing inside the liquid thread is subject to a pressure gradient, denoted by Q . The forces contributing to Q may comprise: (i) the pressure difference between nozzle exit and droplet, (ii) the buoyancy force experienced by the droplet, and (iii) the friction force exerted by the surrounding fluid on the thread interface.

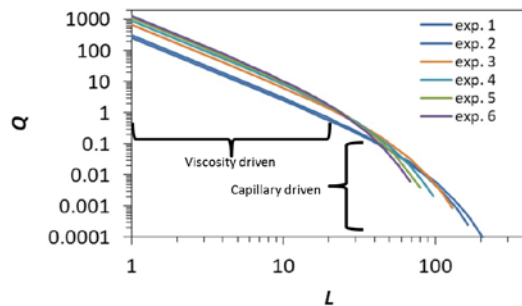


Figure 2. Dimensionless pressure gradient $Q^* \equiv QR_o/pv_o^2$ as a function of dimensionless thread length $L^* \equiv L/R_o$ for in total 6 different experiments.

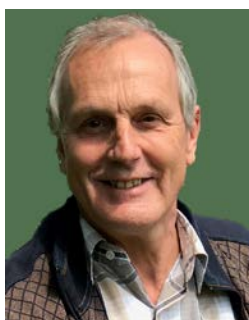
For short threads the curves are straight lines with height fully determined by the dimensionless Reynolds number, so by viscosity. For longer L values the curves tend to bend downwards, due to the increasing influence of surface tension effects, represented by the Weber number. After bending the shape of the curves is nearly completely determined by the quotient Re/We , i.e., the capillary number Ca . From the analysis of the experiments we learn that the liquid thread becomes unstable when the value Q decreases to a value where it enters

the capillary driven regime and find $L_{max} \approx 12Re/We$.

References

- [1] Rayleigh, L., *On the instability of jets*, Proc. London Math. Soc. s1-10, 1878, 4-13.
- [2] Eggers, J., *Universal pinching of 3D axisymmetric free-surface flow*, Phys. Rev. Lett. 71, 1993, 3458.
- [3] Stone, H. A., *Dynamics of drop deformation and breakup in viscous fluids*, Annu. Rev. Fluid Mech. 26, 1994, 65-102.
- [4] Stone, H. A. and Leal, L. G., *Relaxation and breakup of an initially extended drop in an otherwise quiescent fluid*, J. Fluid Mech. 198, 1989, 399-427.
- [5] Gunawan, A. Y., Molenaar, J. and van de Ven, A. A. F., *Break-up of a set of liquid threads under influence of surface tension*, J. Eng. Math. 50, 2004, 25-49.
- [6] Eggers, J. and Fontelos, M. A., *Isolated inertialess drops cannot break up*, J. Fluid Mech. 530, 2005, 177-180.
- [7] van Rijn, C. J. M., *Nano and Micro Engineered Membrane Technology*, (Elsevier Publishers, 2004), pp. 1-384.
- [8] van Rijn, C.J.M., van Heugten, W.G.N., *Droplet Formation by Confined Liquid Threads inside Microchannels*, Langmuir, 33 (38), 2017, 10035-10040.

BIOGRAPHY



Prof. Dr. Cees van Rijn graduated from the Free University of Amsterdam in 1982 on Condensed Matter Physics and is currently appointed at University of Amsterdam. He received PhD degree from the University of Leiden. He has worked at Philips Eindhoven and is founding father of www.aquamarijn.nl in 1995, www.medspray.com in 2001, www.nanomi.com in 2004, www.nanosens.nl in 2006, www.vycap.com in 2011, www.viatarctcsolutions.com in 2012 and www.surfix.nl in 2013. He is author and co-author of more than 125 publications and inventor of more than 35 patents. His current interest is in the field of atomization processes, in particular monodisperse sprays, and is supervisor of a PhD (3) program on this subject.

INVITED TALKS

***APPLICATIONS OF MICRO-
NANOTECHNOLOGY
(AMN)***

THE USE OF HIGH VISCOUS INK FOR FINE INKJET PRINTING AND THE PRINTED ELECTRONICS APPLICATIONS

Kye-Si Kwon¹, Seong-jun Kim², Md. Khalilur Rahman³ and Phung Thanh Huy³

¹ Department of Mechanical Engineering, Soonchunhyang University 22, Soonchunhyang-Ro, Shinchang, Asan, Chungnam, 336-745, South Korea;

² Global Technology Center, Samsung Electronics Co. Ltd, Suwon, South Korea;

³ Department of Electronic Materials and Devices Engineering, Soonchunhyang University, 22, Soonchunhyang-Ro, Shinchang, Asan, Chungnam, 336-745, South Korea

Email: kswon@sch.ac.kr

ABSTRACT

Inkjet printing method has been of main interests for printed electronics applications because it can easily be scaled up for mass production. However, there have been demands for fine pattern printing using highly viscous jetting material, which are beyond the capability of conventional piezo inkjet head. In order to overcome the previous shortcomings, we will discuss an alternative method in order to meet industry requirements. The required pattern width in display industry could be less than 5 μm since the pattern could be invisible by human naked eye. To achieve very fine line printing, electrohydrodynamic (EHD) jet printing method has been drawn attention. However, EHD drop on demand printing normally uses low viscous ink less than 100 cP, which could often result in non-conductive lines due to thin thickness of printed patterns (less than 100 nm). In order to ensure sufficiently low resistance of fine printed lines by achieving high aspect ratio, the use of high viscous ink has been required in printing methods. For this purpose, we proposed the use of near-field electrospinning (NFES) method for fine pattern printing. NFES is a continuous jet type of EHD method, which can use highly viscous ink more than 1000 cP. Finally, we will discuss industrial applications of the proposed method.

Keywords: Near-field electrospinning, inkjet printing, fine patterning, printed electronics

INTRODUCTION

Inkjet printing technology has advantages over conventional photolithographic manufacturing process since the manufacturing costs could be significantly reduced via its additive manufacturing features. However, recent printed electronics requires to print fine patterns using high viscous ink. For example, display electronics often requires patterns width ($<5 \mu\text{m}$) for conductive lines, which can be invisible to the human naked eye. However, in practice the printed dot sizes less than 30 μm are difficult to achieve via conventional inkjet without proper surface treatment of a substrate [1]. To achieve very small printed dots using inkjet method, attention has been drawn to the electrohydrodynamic (EHD) jet printing method. The EHD uses electrostatic forces to pull down the jet from the nozzle tip rather than apply thermal or acoustic energy to push the droplet out of nozzle.

EHD has an advantage of producing very fine dots. However, there have been two limitations: 1) low printing speed of DOD (Drop on demand) printing and 2) low viscosity of ink. Recently, high speed DOD printing has been proposed by changing the ink properties, but considering the nozzle size, the viscosity of the ink should be used less than 100 cP [2]. Nonetheless, the viscosity of ink should increase further as the solid loading needs to be increased for practical applications. In such case, the nozzle inner diameter should be increased in order to push the highly viscous ink through the nozzle for printing. Here, the nozzle with larger inner diameter often result in patterns with large dimension. However, unlike the conventional dispenser, EHD jetting uses electrical field to form cone jet. As a result, the deposited jet size could be significantly smaller than the nozzle inner diameter. For stable continuous jet printing, high molecular weight polymer is added to functional ink. For printing purpose, the stand-off distance is set to a few millimeters and printing

speed should be more than 100 mm/s [3]. By using these features, printing lines could be aligned with respect to printing direction and the method is often referred to as near-field electrospinning (NFES) [4] in contrast with electrospinning [5]. The NFES is based on continuous printing and on-off printing is not yet reported. Therefore, to obtain the print on-off patterns using continuous jet printing, the masking layer needs to be employed. For example, non-printed area can be covered by thin masking layer to remove the unnecessary patterns after printing.

In this presentation, we will discuss two industry applications for NFES: i) bridge electrodes for touch screen and ii) printing wires for connecting electrodes on both sides of glass substrate without via holes.

i. BRIDGE ELECTRODE PRINTING FOR TOUCH SCREEN

A capacitive touch panel uses two axial conducting patterns (sensing electrodes and driving electrodes) on a substrate [6] as shown in Fig.1. In order to reduce the cost and complexity, we propose the implementation method for touch screen using one sheet of driving (sensing) electrodes by printing the sensing (driving) electrodes over the insulator as shown in Fig.2. The connected line over the insulator in the intersection is called as bridge electrode.

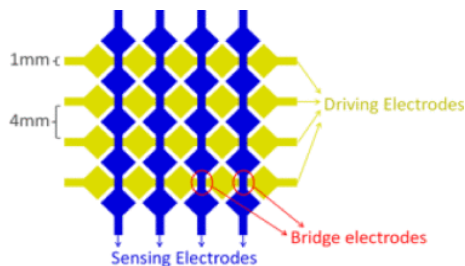


Figure 1. Electrodes for conventional touch screen [6].

For implementation of the invisible bridge electrode by using direct printing, the line width should be reduced to about 5 μm . In this presentation, we will discuss how we can use NFES method to implement invisible conductive lines for touch screen applications.

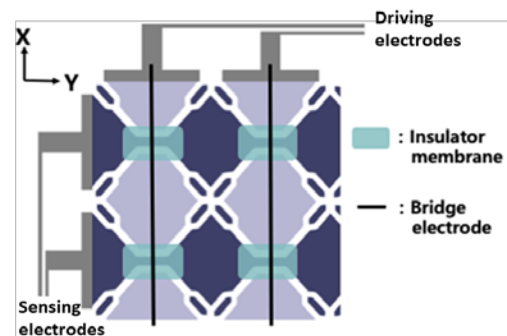


Figure 2. Proposed method for printing bridge patterns for touch screen.

ii. PRINTING FOR DOUBLE SIDED CONNECTION

As another industrial application of NFES, the method for connecting of electrodes on the other side will be presented. Recently, glass substrate has been widely used for display applications. However, unlike the printed circuit board (PCB), via hole is difficult to make due to the brittle nature of the glass. In this presentation, we propose the direct printing method for connecting electrodes on the opposite side of glass as shown in Fig. 3. This method does not require via hole for connecting electrodes on opposite sides.

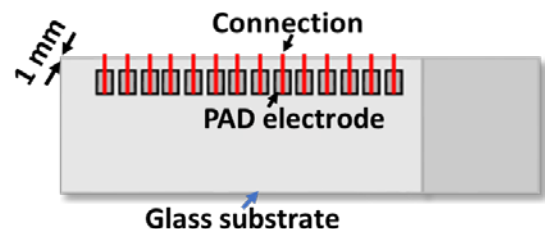


Figure 3. Layout for double sided connection of glass substrate by direct printing method.

EXPERIMENTAL

For NFES ink, high viscous (viscosity = 11,200 cPs) Ag paste ink (ES-INK, NPK, South Korea) mixed with high molecular weight polymer ($M_v = 400000$) solution was fed (1.5 $\mu\text{L}/\text{min}$) to the nozzle (100~200 μm inner diameter) to implement NEFS printing. To obtain continuous jet from the nozzle, we used high voltage (1 -1.5 kV) supply to pull the charged ink to the substrate.

By using NFES printing, patterns are aligned with respect to printing direction as shown in Fig. 4. Here, the printed line should pass over the insulating part to connect two ITO batters over the insulator. After printing, the printed lines was

sintered via laser light irradiation in order to obtain the proper conductivity.

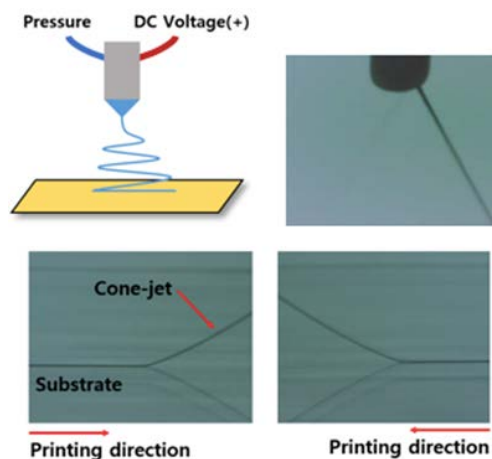


Figure 4. NFES for printing fine patterns.

On the other hand, to print connecting lines between two pads on the opposite sides, we modified substrate holder as shown in Fig. 5. To obtain continuous jet stream and to hold the glass substrate in the vertical direction we used two conducting blocks.

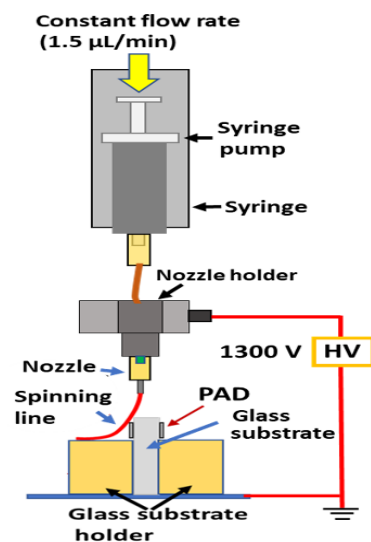


Figure 5. Schematic of NFES for connecting electrodes over the edge of glass substrate.

Due to the continuous jet stream, the printing from one side of the glass through top surface to the other side pad can be possible by using relative movement of nozzle to the substrate.

RESULTS AND DISCUSSION

TRANSPARENT TOUCH SCREEN PRINTING ON PET FILM

By alignment of printing direction, the line was printed on the desired location as shown in

Fig. 6. The printed line width is ranging from 4~6 μm depending on the printing conditions. After sintering, the line has resistance of $9.6 \Omega/\text{mm}$ and the printed bridge electrodes can be used as a capacitive touch sensor.

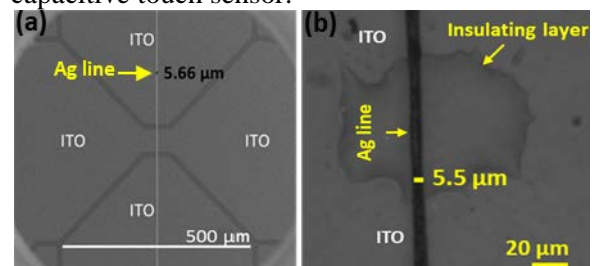


Figure 6. Scanning electron and optical microscopy images of printed line

DOUBLE-SIDED CONNECTION OF GLASS SUBSTRATE

Figure 7 shows our typical printing results to connect both electrodes on the opposite surface. The printed line width is about $40 \mu\text{m}$ and obtained pad spacing is $400 \mu\text{m}$, which satisfies the industry requirement. To increase the reliability of conductive lines, we printed multiple wiring (three times) over the same location and the printing accuracy is limited to about $120 \mu\text{m}$. After printing, to obtain the desired conductivity we used two steps of thermal sintering process. Firstly, printed lines were pre-sintered in convection oven at $150 \text{ }^\circ\text{C}/30 \text{ min}$. Then, in hot plate at $350 \text{ }^\circ\text{C}/5 \text{ min}$. After completing the two steps of sintering process, we obtained the average line resistance is $0.94 \Omega/\text{mm}$ which meet most industry requirement.

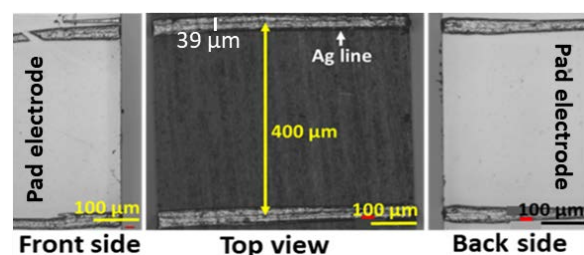


Figure 7. Typical two-sided printing results.

CONCLUSION

We discuss the two industrial applications of NFES printing to print very fine patterns for bridge electrodes and double-sided connection. The high viscous ink with high molecular weight polymer was shown to effective on connecting electrodes on non-flat surfaces as well as on flexible substrate.

Acknowledgement

This work is supported by Samsung electronics and the Basic Science Research Program through the National Research Foundation (NRF) of Korea, funded by the Ministry of Education (2016R1D1A1B01006801).

References

- [1]. K. Barton, S. Mishra, A. Alleyne, P. Ferreira, J. Rogers, *Control of high-resolution electrohydrodynamic jet printing*, *Control Engineering Practice* **19** (2011) 1266–1273
- [2]. T. H. Phung, S. Kim, K.-S. Kwon, *A high speed electrohydrodynamic (EHD) jet printing method for line printing*, *Journal of Micromechanics and Microengineering*, **27** (2017) 095003
- [3]. T. H. Phung, S.B. Oh, K.-S. Kwon, *High-resolution Patterning Using Two Modes of Electrohydrodynamic Jet: Drop on Demand and Near-field Electrospinning*, *JoVE* **e57846** (2018) 1-12
- [4]. X.-X. He, J. Zheng, G.-F. Yu, M.-H. You, M. Yu, X. Ning, Y.-Z. Long, *Near-Field Electrospinning: Progress and Applications*. *The Journal of Physical Chemistry C*, **121** (2017) 8663–8678
- [5]. A. Greiner, J.H. Wendorff, *Electrospinning: A Fascinating Method for the Preparation of Ultrathin Fibers*, *Angewandte Chemie* **46** (2007) 5670.
- [6]. J. Lee, M. T. Cole, J. C. S. Lai, A. Nathan, *An Analysis of Electrode Patterns in Capacitive Touch Screen Panels*, *Journal of display technology* **10** (2014) 362-366

BIOGRAPHY



Kye-Si Kwon (권계시) is a professor at Soonchunhyang University in South Korea in the department of mechanical engineering (website: inkjet.sch.ac.kr). After his PhD, obtained from KAIST, South Korea, in 1999, he was a member of research staffs in companies such as Samsung and LG electronics. He joined Soonchunhyang University in 2006 where his teaching and research is centered on inkjet-related measurement methods and system developments. In 2012, he spent one year at Palo Alto Research Center (PARC) in Palo Alto, California, as a visiting researcher. In 2013, Prof. Kwon established a start-up company of PS. Co. In 2019, he is spending his sabbatical leave at University of California, San Diego (UCSD) as a visiting scholar.

PEPTIDE ARRAYS AND EASY-TO-OPERATE OPTICAL SENSOR FOR WIDE SPECTRUM SENSING OF PATHOGENIC BACTERIA

Éric Pardoux^{a,b}, Agnès Roux^a, Raphaël Mathey^a, Didier Boturyn^b, Yoann Roupioz^{a,*}

^aUniv. Grenoble Alpes, CNRS, CEA, INAC-SyMMES, 38000 Grenoble, France

^bUniv. Grenoble Alpes, CNRS, DCM, 38000 Grenoble, France

*Corresponding author: yoann.roupioz@cea.fr

ABSTRACT

Fast detection of bacteria in samples presumed to be un-contaminated, such as blood, is of great importance. Indeed, rapid diagnosis allows the set-up of appropriate antibiotic treatment. Besides clinical issues, there are many other domains, such as food processing or drug manufacturing, where the strict absence of any bacteria has to be assessed. Because the bacterial load found in most contaminated samples is often below the limit of detection for currently validated assays, a preliminary enrichment step is required to allow bacterial multiplication before proceeding to the analysis step, whatever it might be – cultural, immunological or molecular methods. In this presentation, I will describe the use of a biosensor, consisting in a peptide microarray, for single-step bacteria detection.

The whole analysis is performed in less than 20 hours, during the growth phase of the micro-organisms, using an array of antimicrobial peptides (AMPs) coupled with a surface plasmon resonance imager (SPRI). A wide range of bacterial strains are assayed, showing differentiated affinity patterns with the immobilized peptides, which are confirmed by multivariate analysis. This approach has been first validated in model culture media, and then extended and validated in 'real' samples like human plasma and human blood.

This work establishes the evidence that antimicrobial peptides, mostly used so far in the antibiotic drug industry, are suited for the wide-spectrum detection of unknown bacteria in samples, even at very low initial loads. Moreover, the small set of AMPs that were assayed provided a specific affinity profile for each pathogen, as confirmed by multivariate analyses. Furthermore, this work opens up the possibility of applying this method in more complex and relevant samples such as foodstuff, urine or blood.

BIOGRAPHY



Yoann Roupioz is developing micro-arrays and new technologies for Health at the SyMMES lab in Grenoble, France, since 2005. In 2012, he co-founded the Prestodiag Company, based near Paris, which developed micro-arrays and dedicated instruments for the detection of bacterial pathogens in food. Since 2014, he is also Deputy Head of the SyMMES lab, and co-founded the French network for Surface Bio-engineering (GDR B2I). In 2016, he was promoted CNRS Research Director, and became member of the Nanobiose Company Scientific Board. His research projects are currently split into three different topics: 1) SPR-based detection of pathogenic bacteria; 2) DNA engineering for biosensing and nanotechnologies; 3) biochip design and operation for cellular studies.

BIOACTIVE NANOGLASSES AND GRAPHENE-BASED NANOCOMPOSITES FOR MEDICAL APPLICATIONS

Anna Lukowiak¹, **Yuriy Gerasymchuk**¹, **Leili Tahershamsi**¹, **Katarzyna Halubek-Gluchowska**¹, **Anna Wedzyska**¹, **Wieslaw Strek**¹, **Dominika Piatek**², **Anna Kedziora**³, **Gabriela Bugla-Ploskonska**³, **Beata Borak**⁴, **Justyna Krzak**⁴

¹ Institute of Low Temperature and Structure Research, PAS, ul. Okolna 2, 50-422 Wroclaw, Poland

² Medical University of Lublin, al. Raclawickie 1, 20-059 Lublin, Poland

³ Institute of Genetics and Microbiology, Faculty of Biological Sciences, University of Wroclaw, ul. Przybyszewskiego 63/77, 51-148 Wroclaw, Poland

⁴ Department of Mechanics, Materials Science and Engineering, Wroclaw University of Science and Technology, ul. Smoluchowskiego 25, 50-370 Wroclaw, Poland

Email: A.Lukowiak@intibs.pl

ABSTRACT

Two kinds of optically active nanomaterials, that might be very useful for medicine due to their biological properties, are presented. One of them are spherical nanoparticles of bioactive glass based on the silica-calcia system doped with lanthanide ions (Er^{3+}) and obtained by the sol-gel route. The second group is graphite-oxide-based composite with zirconium phthalocyanine complex activated by light to generate reactive oxygen species. For both systems, the photoluminescent characteristics were examined. In the case of glass particles, the introduction of erbium ions allowed to obtain optically active materials that could be used in regenerative medicine for monitoring structural changes of the glass during mineralization or to control a drug release from the particles used as carriers. Photoactivation of the phthalocyanine complex loaded on GO caused singlet oxygen generation. These properties allow the samples to be used as photosensitizers in photodynamic therapy.

Keywords: silica-calcia, graphite oxide, photoluminescence, photoactivation, ROS generation

INTRODUCTION

Various types of nanomaterials play currently more and more important role in different fields of medicine. For example, silica-calcia amorphous systems are well-known basic composition of bioactive glass that are used in regenerative medicine showing higher activity than similar microsized particles [1]. On the other hand, carbon nanostructures are intensively studied for their potential as biocompatible materials. So far they have been recognized as worthy of attention for, among others, biocompatible coatings, bioimaging, antimicrobial or theranostic agents [2]. Application of both materials forming nanocomposites is even broader.

Optically passive $\text{SiO}_2\text{-CaO}$ glass may be doped with active lanthanide ions leading to photoluminescent materials. Nanofoms of such system can be obtained by the sol-gel method as it is presented in this paper.

Graphen-based structures already possess some luminescent properties but they can be

much more useful when they are additionally activated, for example, with organic or metal-organic compounds. For this purpose, zirconium (IV) phthalocyanine was here proposed to be bonded to graphite oxide (GO) particles.

EXPERIMENTAL

The syntheses procedures were previously developed to fabricate the materials studied here. Two step sol-gel procedure (acid-base catalyzed reactions) [3] was used to prepare $80\text{SiO}_2\text{-}20\text{CaO}$ (in wt.%) particles doped with erbium ions. The glass was annealed at different temperatures (600–1100 °C).

Graphite oxide flakes were intercalated with a derivative of zirconium(IV) phthalocyanine, viz. bis(11-aminoundecannato)ZrPc, according to the procedure described in [4].

RESULTS AND DISCUSSION

Silica-calcia system can be successfully prepared as nano- or submicro-sized particles when the sol-gel method is applied for the synthesis. During glass preparation, lanthanide

ions can be introduced in the solution and then, in the matrix, resulting in luminescent properties of the material.

Here, the particles of average diameter of about 100 nm were obtained (Fig. 1). Silicon, calcium and erbium content were confirmed by the EDS analysis. The presence of Er^{3+} is also verified by the luminescence spectra measurements. Emission in the visible range was registered when samples were excited at 514 nm (Fig. 2) showing two bands in the visible range at around 550 nm and 655 nm. Moreover, what can be seen looking at the shape of the spectra, are the structural changes in the glass during annealing. Higher intensity and better resolved Stark components in the spectral lines for samples heat-treated above 900 °C demonstrate partial crystallization of the amorphous matrix.

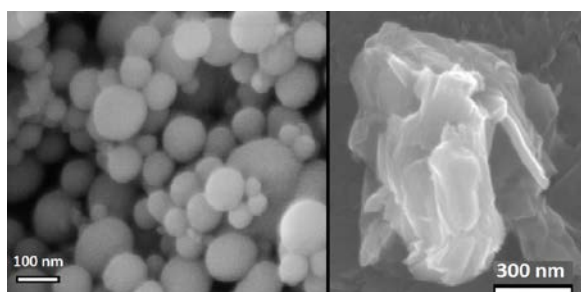


Figure 1. SEM images of $\text{SiO}_2\text{-CaO}$ glass and graphene oxide particles.

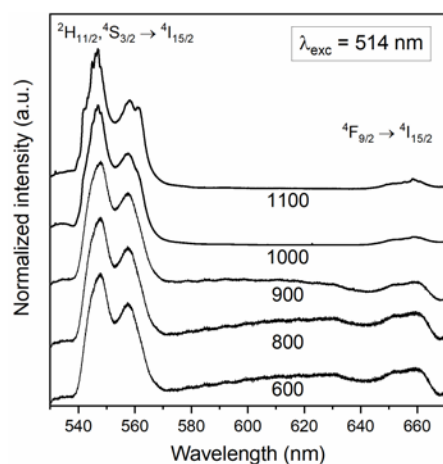


Figure 2. Luminescence spectra of Er^{3+} -doped $\text{SiO}_2\text{-CaO}$ glass nanoparticles annealed at different temperatures (600–1100 °C).

The luminescent properties of this highly biocompatible and bioactive material can be used for monitoring structural changes of the glass in biological fluids (dissolution and remineralization of the system). Other possible

utility is in bioimaging or monitoring drugs delivery when particles are used as drug carriers.

Graphite oxide flakes with few nanometer thickness and few microns width (Fig. 1) possess weak luminescence characterized by band shift depending on the excitation wavelength. Much better emission can be seen when GO is activated with organic luminescent dyes such as complexes of phthalocyanines with metals. Phthalocyanines have very high molar extinction coefficient and absorption cross section that makes them also good phosphors. But what is particularly interesting, is the ability to generate singlet oxygen molecules (highly reactive species) during irradiation that is used in photodynamic therapy to kill selected cells or microorganisms [5].

Emission spectrum of bis(11-aminoundecannato) ZrPc show characteristic emission band in the range of 650–820 nm (Fig. 3). Broad absorption bands in the UV and red-near-infrared range (data not shown here) allow to excite the molecules in both these regions as is shown in Figure 3. All excitation wavelengths chosen in the experiment (350, 400, and 620 nm) emission was observed although, with different intensity. The red light is particularly interesting and is usually applied to activate the molecules for singlet oxygen generation.

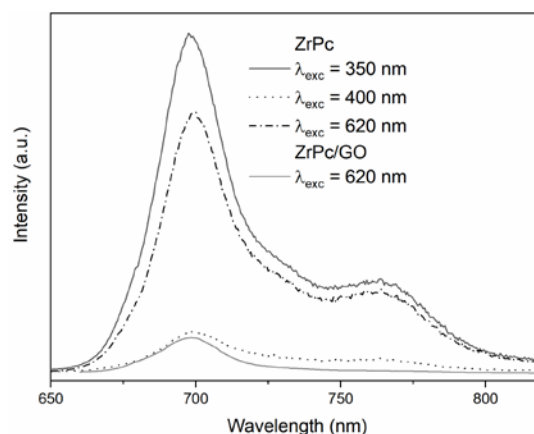


Figure. 3 Luminescence spectra of phthalocyanine (bis(11-aminoundecannato)-ZrPc) under different excitation wavelengths and GO intercalated with phthalocyanine and excited in red. Measured in DMSO.

Luminescence of GO particles with ZrPc was also observed (Fig. 3). Its intensity was lower than for ZrPc but the concentration of the dye was much lower in the composite in comparison to the measured solution. What is

important, is the activity of the GO-based system that was maintained after immobilization – singlet oxygen was still generated under red-near-infrared light exposition as was lately reported [6].

CONCLUSION

Biocompatible materials such as glasses or graphene oxide structures can be activated by luminescent ions or molecules. In this way, the modified properties of the systems allow them to find broader application in biology and medicine. Especially, when they are optically active in the range of the first, second or third biological windows.

Acknowledgment

This research was performed in the framework of the National Science Centre research grants Nos. 2016/22/E/ST5/00530 and 2016/23/B/ST5/024830.

References

- [1] S.K. Misra, D. Mohn, T.J. Brunner, W.J. Stark, S.E. Philip, I. Roy, V. Salih, J.C. Knowles, A.R. Boccaccini, *Comparison of nanoscale and microscale bioactive glass on the properties of P(3HB)/Bioglass composites*, *Biomaterials*, **29** (2008) 1750-1761
- [2] V.B. Mohan, K. Lau, D. Hui, D. Bhattacharyya, *Graphene-based materials and their composites: A review on production, applications and product limitations*, *Composites B* **142** (2018) 200-220
- [3] A. Lukowiak, J. Lao, J. Lacroix, J.M. Nedelec, *Bioactive glass nanoparticles obtained through sol-gel chemistry*, *Chem. Comm.* **49** (2013) 6620-6622
- [4] Y. Gerasymchuk, A. Lukowiak, A. Wedzynska, A. Kedziora, G. Bugla-Ploskonska, D. Piatek, T. Bachanek, V. Chernii, L. Tomachynski, W. Streck, *New photosensitive nanometric graphite oxide composites as antimicrobial material with prolonged action*, *J. Inorg. Biochem.* **159** (2016) 142-148
- [5] B.W. Henderson, T.J. Doougherty, *How does photodynamic therapy work?* *Photochem. Photobiol.* **55** (1992) 145-147
- [6] A. Lukowiak, Y. Gerasymchuk, A. Wedzynska, L. Tahershamsi, R. Tomala et al. *Light activated zirconium(IV) phthalocyanine derivatives linked to graphite oxide flakes and discussion on their antibacterial activity*, *Appl. Sci.* (2019) in press.

BIOGRAPHY



Anna Lukowiak received her PhD in chemistry from Wroclaw University of Technology (Poland) and post-doctoral degree in chemistry from the Institute of Low Temperature and Structure Research PAS. She has been an assistant professor at ILTSR PAS since 2008. In 2011–2013 she worked in postdoc positions in France and Italy. Her current research activity concerns mainly synthesis and physicochemical analysis of sol–gel-derived optical materials, lanthanide-doped nanocrystals, graphene oxide composites, and biomaterials.

3D HIERARCHICAL NANOSTRUCTURES TO ELABORATE SUPERCAPACITORS FOR ELECTROCHEMICAL ENERGY STORAGE

G. Bidan¹, D. Aradilla³, S. Sadki^{1,2}

¹University Grenoble Alpes, CEA, CNRS, Institute of Interdisciplinary Research of Grenoble,

²Department of the Interfaces for Energy, Health and Environment, F-38000 Grenoble, France

³University of Goettingen, Institute of Inorganic Chemistry, Tammannstrasse 4, 37077 Goettingen, Germany.

Email: gerard.bidan@cea.fr

ABSTRACT

In addition to the need to store electricity to compensate for the intermittency of renewable energies, two other strong societal requirements are driving development of more and more efficient electrical storage devices. This is about the growth of fully or plug-in hybrid electrically powered vehicles market, and the increasing role of mobile electronics and wireless tools including the strong emergence of the Internet of Things. Presently, batteries (mainly Li-ion) and capacitors, dominate opposite ends of the energy spectrum, the former exhibit high energy and restricted power, while the latter possess constrained energy and high power. **Electrochemical double layer capacitors or supercapacitors, SCaps**, bridge the gap by exhibiting moderate energy density and high power density and are categorized based on their energy storage mechanism.

Recently, we have developed μ -SCaps electrodes based on silicon nanowires (SiNWs), compatible with Si-based microelectronics integration process, which exhibit very interesting capacitive properties in terms of pulse power capabilities and long cycle life [1].

In order to improve their electrical performances in terms of specific capacitance, power and energy density, conformal electrodepositions of different conducting polymers, CPs, nano-films were successfully performed on silicon nanostructures (Fig. 1).

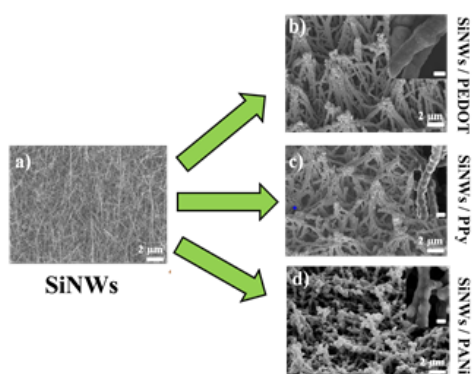


Fig.1 SEM image of b) PEDOT; c) polypyrrole; d) Polyaniline coated a) silicon nanowires after electrodeposition in ionic liquids.

In this lecture, I will describe the various steps which has enabled us to reach several hundred thousand charge/discharge cycles. In particular, I will focus on: the use of stable CPs such as PEDOT; the transition from aqueous or organic electrolytes to ionic liquids [2]. The synthesis of hybrid and nanostructured materials [2] and recently, the decisive role of interactions at the molecular level at the interface between the CP and the electrode substrate [3, 4]

These latest results show that at least 90% of the capacitance is retained after 500,000 [4] cycles, and, this in a somewhat surprising way, even in aqueous electrolytic medium. These remarkable advances thus pave the way for genuine industrial use, targeting micro-supercapacitors.

Keywords: Supercapacitors, silicon nanowires, conducting polymers, Electrochemical energy storage

References

- [1]. D. Aradilla, G. Bidan, P. Gentile, P. Weathers, F. Thissandier, V. Ruiz, P. Gómez-Romero, T. J. S. Schubert, H. Sahin and S. Sadki, *RSC Adv.*, 4 (2014) 26462.
- [2]. D. Aradilla, S. Sadki, G. Bidan, *Synth. Met.*, 247 (2019) 131.
- [3]. S. Acharya, L. M. Santino, Y. Lu, H. Anandarajah, A. Wayne and J. M. D'Arcy, *Sustainable Energy Fuels*, 1 (2017), 482.
- [4]. A. Valero, A. Mery, D. Gaboriau, P. Gentile and S. Sadki, *ACS Appl. Energ. Mater.* 2 (2019) 436.

BIOGRAPHY



Personnal details: BIDAN Gérard

Personal address:

3, rue des Trois Epis,
38100 Grenoble, France

Family status:

68 year old; Nationality: French;
Married, 2 children,
Phone (mob): + 33 (0)6 87 98 45 93
E-mail: bidan.gerard@gmail.com

Professional addresses

CEA-Grenoble, IRIG/DIR,
17, rue des Martyrs,
39054 Grenoble cedex 09, France



<http://www.cea.fr/drf/irig/english>

Phone (work): + 33 (0)4 38 78 48 41,

E-mail: gerard.bidan@cea.fr

Present status:

Scientific Advisor « Emeritus » (previously Director of Research) at CEA (French Atomic and Alternative Energies Commission).

Project manager « Electrochemical Energy Storage » at CEA/IRIG (Interdisciplinary Research Institute of Grenoble; previously INAC, Institute Nanosciences & Cryogenics).

Professional history at CEA:

- 2017-present: Projects manager for “Electrochemical Energy Storage” at IRIG (previously INAC), CEA-Grenoble.
- 2005-2016: Projects manager for “Chemistry for Nanosciences” and from 2010 in charge of the “Energy axis” for INAC.
- 1996-2004: Deputy Head of the SI3M research Unit at DRFMC, CEA-Grenoble;
- 1985-2000: Head of the research laboratory “Molecular Electrochemistry & Structures at the Interfaces” (EMSI).

Research interests, an overview:

- During the years 1981-2000, Dr. BIDAN developed pioneering researches on pi-conjugated systems. **Electrodeposition of Conducting Polymers (CPs) films** at the surface of an electrode has opened a field at the convergence between two rich domains: (i), **electrochemistry of modified electrodes for (bio)sensing and (ii), conjugated architectures for electronics and/or photonics.**
- From 1993 to 2005, Dr. BIDAN’s EMSI laboratory was a pioneer in **interfacing of CPs with biology**, and opened the route to the development of biosensors based on polypyrrole coatings such as **DNA chips.**
- Around 1996, EMSI laboratory also started **molecular engineering on CPs** to build up new conjugated architectures for organic photovoltaics and molecular electronics.
- **Dr. BIDAN participated in 2005 to the implementation of “Chemtronics”** (chemistry for nano-electronics), an innovative CEA transverse programme.
- From 2009, Dr. BIDAN was in charge of electrochemical energy storage at the Institute. Presently, Dr. BIDAN is personally involved in the development of **3D hierarchized silicon or graphene nanostructures for super-capacitors and Li-ion batteries.** These researches have been supported by national and European contracts (coordination of NEST (Nanowire for Energy Storage), FET EU project, 2012-2016). The functionalization of these nanostructures with electroactive CP coatings has contributed to the **renewal of CPs for electrochemical energy storage applications.**

Summary of the work achievements:

H-index 40; 157 articles with referees, 17 patents.

Award:

- 2006 (May): **Hood fellowships grant award** from Auckland University, New Zealand, as a visiting scientist at PERC (Polymer Electronic Research Centre).
- 2017: appointed as **«Distinguished Member» of the SCF** (French Chemical Society)

ENHANCING LUMINESCENCE INTENSITY OF NANOSTRUCTURED PHOSPHOR CONTAINING RARE EARTH ELEMENTS

Le Quoc Minh

Institute of Materials Science, Graduate University of Science and Technology,
Vietnam Academy of Science and Technology (VAST)
18 Hoang Quoc Viet, Cau Giay Hanoi, Vietnam
Phone: (+84) 903432070; Email: lequocminhvn@gmail.com

ABSTRACT

Rare Earth Nanostructured Phosphor (RENP) have become main trend not only in basic research and also for deployment in different branch of industry, agriculture, environment, biology and medicine. RENPs exhibit unique emission properties, including a large Stokes shift, a sharp band width of luminescence, high resistance to optical blinking, and photo bleaching. Indeed RENP show also very weak inherent fluorescence intensity due to the low absorption cross section and quenching radiation relaxation. In the last decade it has been many efforts in investigation for improving or so far enhancing the output emission intensity of RENP. Among them, it can be summarized some approaches such as the energy transfer, defect passivation, surface engineering, interaction of emission center and Plasmon and wave guide resonance between in- or out- light beam and a photonic crystal structure on surface. In this review it presented the last results of our research group in using the Tb to Eu energy transfer, the decreasing defect content by annealing, coating Eu complex to surface of Au nanoparticles (Plasmon), core/shell structuration of NaYF₄:Er,Yb by an inert layer and wave guide resonance of a Bragg-grating with up conversion luminescent nanoparticles NaYF₄:Tm,Yb; all for enhancing the output intensity of RENP emission. In this talk I will discuss recent advances' in the broad utility of RENP for multifunctional bio imaging, bio detection and also security technology, digital display and photonics.

BIOGRAPHY



Prof. Dr. Le Quoc Minh

Institute of Materials Science, Graduated University of Science and Technology, Director of IMAG Corporation, Vietnamese Academy of Science and Technology (VAST),

Vice President and Secretary General of Vietnamese Materials Research Society (V-MRS), and Senior Researcher and Lecturer at Duy Tan University (DTU).

250 Publications, 3 Books, and Sponsorship 8 Ph.D. These, Coordinator of over 12 International and State Research and Development Projects. Organize Committee Members of Conferences ICCE, IWAMSN, SPSM and IWNA

Interests include Optoelectronic Materials, Rare Earth Phosphores, Nano Materials and NanoTechnology, Digital Imaging, Composite for Infrastructure and Application for Biology, Medicine.

SOLAR ENERGY: FROM MATERIALS TO APPLICATIONS SITUATION IN THE WORLD, VIETNAM & BINH THUAN: CHALLENGES AND SOLUTIONS

Tran Quoc-Tuan

CEA/Liten – INES (National Institute for Solar Energy), France
INSTN-Paris Saclay University & Grenoble-Alpes University
tranqtuan@yahoo.com

ABSTRACT

Since 2017, the annual installed capacity of the Solar Energy has surpassed all other energy sources and doubled that of Wind power. In 2018 in the world, the annual installed capacity of the PV Solar Energy solar energy is about 115 GW in comparison with 53.9 GW for wind power. In Vietnam, until now more than 26 GW of projects are registered, and more than 12 GW are approved. The total average capacity and daily output of these plants at the end of June 2019 reached 4.463 MW and 16.4 million KWh/day, accounting for 8.3% and 2.3% of the national electricity system. The solar energy could be the world's largest source of electricity by 2050, ahead of fossil fuels, wind, hydro and nuclear, according to a pair of reports issued today by the International Energy Agency (IEA).

Increasing integration of renewables, in particular solar PV integration along with the electrification and decarbonisation challenges the existing grid infrastructures due to their intermittent characteristics with high levels of uncertainty and complexity. Several impacts on the grid operation include voltage variations, frequency variation, voltage unbalance, stability, protection and challenges for managing... These impacts are even more complicated for islanded or weak grid areas. In Vietnam solar power projects have been heavily invested, especially in localities such as Ninh Thuan, Binh Thuan, Khanh Hoa ... causing overload on transmission lines.

A better knowledge, analysis and evaluation methods of the induced constraints become necessary in order to determine the hosting capacity, to assess impacts of renewable generation on distribution network and to assess technical and economic opportunities provided by renewable generation.

This presentation presents experiences of CEA-INES (French National Institute for Solar Energy) for energy solar from materials to applications, in particular for analysing impacts provided by PV integration into grid, solutions by intelligent control and energy management in order to reduce these impacts, to maximize the ancillary services contributed by PV installations and to maintain the grid stability are discussed, solutions associated with energy storage and development of micro-grid technologies will be presented to address mentioned grid challenges.

BIOGRAPHY



Prof. Tran Quoc-Tuan received his PhD degree in Electrical Engineering and his “Habilitation à Diriger des Recherches” degree (Dr. Habil) from the Grenoble Institute of Technology (Grenoble-INP), France, in 1993 and 2000, respectively. He is actually Professor at the INSTN (National Institute for Science and Technology of Nuclear - Paris Saclay University) and International Expert at the CEA (Atomic Energy and Alternative Energies Commission), Scientific Manager for Smart Grids at the CEA/INES (National Institute for Solar Energy) and Teacher at the INSTN and the Grenoble Polytechnic Institute. His research interests are in the fields of smart-grid, microgrid, power system, renewable energy, and energy management and control. He holds 7 patents, is (co-)author of five books, and author of more than 200 publications in journals and conference proceedings. He has supervised more than 40 PhD students. He has realized and piloted more than 50 projects. He is senior member IEEE and Member of executive committee of Smart Grid Institute.

LASER INDUCED WHITE EMISSION IN RE DOPED NANOCRYSTALS

Wiesław Strek, Robert Tomala, Mariusz Stefanski, Paweł Gluchowski, Bartłomiej Cichy
Institute of Low Temperatures and Structure Research, Polish Academy of Sciences Wrocław, Poland
Email: w.strek@intibs.pl

ABSTRACT

The laser induced white emission (LIWE) generated from different materials under strict conditions is reported. The studied broad emission band fully covers the entire visible range, which is an extremely desirable feature of new generation light sources. The compounds were synthesized by various wet chemistry routes. Investigations of such phenomenon show that in both power and pressure dependencies the threshold behavior are clearly observed regardless of the investigated sample or infrared laser diode excitation. Moreover the LIWE generation is assisted by efficient photocurrent.

Keywords: Nanocrystals, white luminescence, threshold behavior, avalanche effect, photocurrent

INTRODUCTION

Nowadays, the quality of white light emitted by commercially available optical devices plays an extremely important role. Currently, white light sources such as light-emitting diodes based on organic or inorganic composites with reduced demand for electricity are very popular. The principle of their operation is to combine several colors to obtain white luminescence. Most often, these diodes use few phosphors to emit three different colors - RGB (i.e., red, green, blue) or a mixture of yellow and blue light provided from yttrium-aluminum garnet doped with cerium(III) ions excited with a blue electroluminescent diode based on gallium nitride. Unfortunately, in the sources of white light commercially available, the balance between the colors is not maintained. It has been found that this affects the human body in a negative way. In response to the growing demand for broadband white light emitters, work has begun to find a healthy light source. The first research in this field was published in 2010 [1]. Wang and Tanner received broadband white luminescence from lanthanide oxides excited with a concentrated infrared CW laser beam under reduced pressure conditions. Since then, intensive research has begun to develop this technology. As a result, a generation of laser induced white emission (LIWE) from many different materials was obtained [2–8] as well as several models explaining the studied phenomenon were proposed [1,9–13].

EXPERIMENTAL

The nanocrystals presented in this paper were prepared using wet chemistry methods such as solvothermal [14], Pechini [15], sol-gel [16,17], co-precipitation [18]. All details related with synthesis procedures can be found in appropriate references.

Structure of the investigated samples was evaluated by X-ray powder diffraction. X-ray powder diffraction patterns were collected by a XPERT PRO PANalytical diffractometer. The anti-Stokes emission spectra were measured using focused continuous wave (CW) laser diodes (808, 975 or 1064 nm) as the excitation sources and AVS-USB2000 Spectrometer (Avantes) as a detector. The rise and decay times of the emission intensity were recorded using a LeCroy WaveSurfer 400 oscilloscope with a mechanical chopper under excitation of a focused beam of a CW laser diodes mentioned before. All measurements were performed in low pressure conditions using a vacuum cell supplied with a Turbomolecular Drag Pump TMH071 P and an electronic drive unit TC 600 (Pfeiffer).

RESULTS AND DISCUSSION

In order to perform the measurements of anti-Stokes white emission of all investigated samples correctly, their powders were transformed to pellets on the hand press. The first stage of the spectroscopic characteristic of studied compounds assumed to record the power dependence of emitted luminescence as a function of increasing excitation power density

(Fig. 1). All of the samples presented similar behavior related with the excitation threshold typical for photon avalanche effect [19]. It can be observed that the intensity of the luminescence is stable until it reaches the appropriate threshold. After that it increased rapidly regardless of the both analyzed sample and infrared diode. Such behavior can be easily explained by following equation $I \propto P^N$ where I is an emission intensity, P is the infrared excitation power and N usually means photons included in the absorption, but recent research exhibit that it must be treated more carefully [13]. It was turned out that commonly the N factor is smaller when the sample is excited by a laser diode with a lower wavelength. However, converting the obtained values into energy leads to similar results [13,15,20]. Our last research shown that N parameter can be affected by average grain size of investigated material [21]. This behavior is related with the fact that samples characterized by lower sizes exhibit lower thermal conductivity, and consequently higher values of N factor. Additionally, it was found that the position of the threshold depends on the excitation wavelength. It is related with the different absorption cross section of infrared laser diodes used. Usually an excitation source characterized by a shorter wavelength needs more energy to generate white luminescence.

The second stage of the spectroscopic characteristic included measurements of pressure dependence of emitted luminescence as a function of increasing pressure in measurement system (Fig. 2). It was found that similar to the power dependence results, all samples presented the threshold behavior [5,15,17,18,21,22]. The emission intensity was stable until it reaches the appropriate threshold. Subsequently, it decreased significantly regardless of the both analyzed sample and infrared laser diode. Such phenomenon is associated to the fact that under low pressure conditions the amount of gas molecules are very limited, and consequently energy from excitation source is transferred directly to the sample.

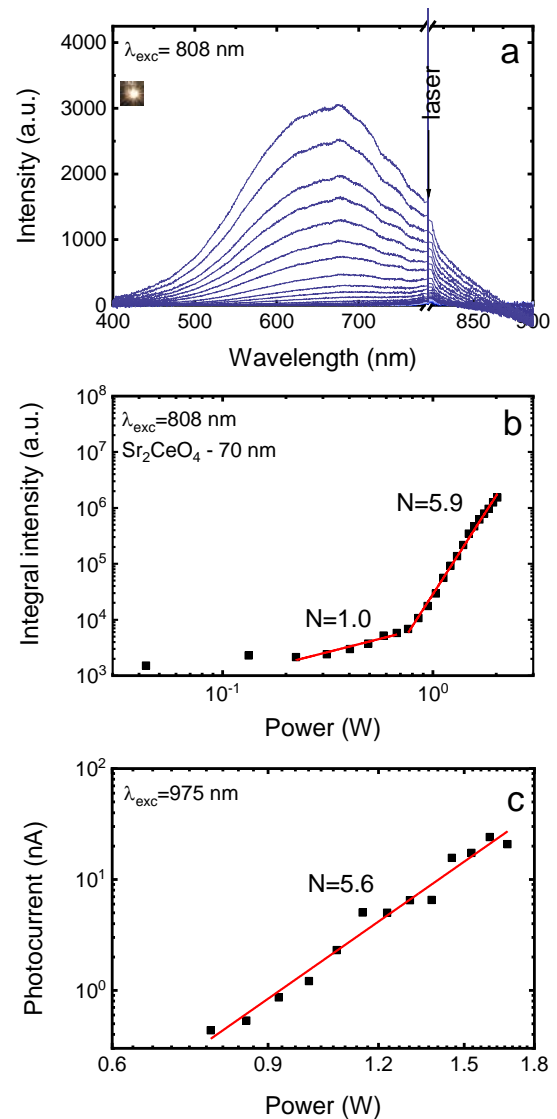


Figure 1. Representative power dependence of emission (a,b) and the power dependence of photocurrent (c) recorded for Sr_2CeO_4 nanocrystals,

In result its temperature increases as well as their emission intensity. In case of atmospheric pressure conditions there is opposite situation. The energy from laser diode is distracted by air molecules before it reaches the sample. This behavior is well explained by the thermal dissipation model represents by the following equation $I_{em} = I_0 \cdot \exp(-p/p_0)$ where I_0 is the emission intensity and p_0 is the critical magnitude of pressure [23]. It is worth to note, that other factors can affect the values of p_0 parameters such as rare earth dopant content [21], gas atmosphere [1], density of excitation beam or average gran size [14].

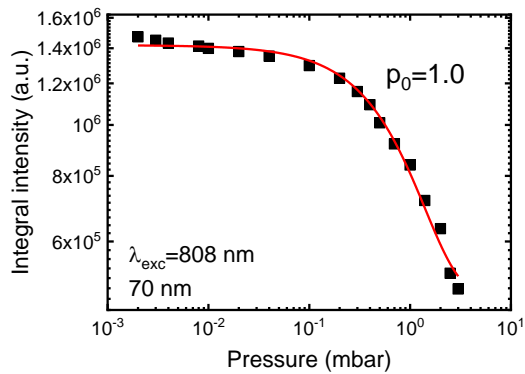


Figure 2. Representative pressure dependence recorded for Sr_2CeO_4 nanocrystals.

The characteristic of the LIWE generated from different compounds involved also the measurements of the luminescence kinetics depending on different excitation power density of infrared laser diode. In most cases of the rise times measurements, the samples under low power excitation show relatively long rise times which is shortening with increasing excitation power density. These measurements determine the time needed to transfer an electron from the valence band to the conduction band. It was found that pumping more energy to the sample results in shortening this time. Similar tendency was observed by us in different host lattices [18,20,21].

It is also interesting to note, that above excitation power threshold of the white luminescence generation, the investigated phenomenon is accompanied by photoconductivity which below the threshold is not observed. It was found that the conductivity increases with excitation power density by up to several orders of magnitude [13,20,21]. Unlike other spectroscopic measurements, no effect of average grain size on photoconductivity results was noted [14]. Conductance effect is probably related with the mechanism of hopping electron conductivity [24].

The mechanism responsible for generation of LIWE in RE doped nanocrystallite compounds were proposed. The first one predicts that broadband white luminescence is related with black body radiation. However the sample temperature during generation of LIWE was too low to confirm such hypothesis [1,13]. The authors of the second hypothesis assume ionization of the material caused by its irradiation by focused infrared laser diodes. Consequently, free electrons are created and recombined with RE^{3+} to form RE^{2+} , responsible

for generating LIWE [9,16]. The third one considering illumination of the compounds with a concentrated infrared laser beam which leads to thermal effects resulting in the formation of oxygen vacancies. As a result of the tunneling process electrons are trapped in oxygen gaps and then relaxed to the valence band [10,11]. Last hypothesis concerns creation of $RE^{n+}-RE^{m+}$ ionic pairs (where n and m present various degrees of oxidation states) as a consequence of irradiation of the host with a focused infrared laser. In result white luminescence is obtained via IVCT (intervalance charge transfer) transitions [13].

CONCLUSION

The RE nanocrystals prepared with different wet chemistry methods were synthesized. The X-ray diffraction patterns confirmed phase purity of obtained samples. The laser induced white emission observed from all studied compounds was assisted by efficient photocurrent. It was found that both the white emission intensity and photoconductivity demonstrated similar dependence on excitation laser power case of power and pressure dependencies all Furthermore, the rise time measurements show that high excitation power density reduces the time needed to transfer an electron from the valence band to the conduction band regardless of the tested material. In order to explain the mechanism of LIWE phenomenon in RE nanocrystals the further studies are in progress.

References

- [1] J. Wang, P.A. Tanner, *Upconversion for White Light Generation by a Single Compound*, J. Am. Chem. Soc. **132** (2010) 947–949.
- [2] M. Erdem, B. Sitt, *Up conversion based white light emission from sol-gel derived α - $Y_2Si_2O_7$ nanoparticles activated with Yb^{3+} , Er^{3+} ions*, Opt. Mater. **46** (2015) 260–264.
- [3] G. Bilir, J. Liguori, *Laser diode induced white light emission of γ - Al_2O_3 nanopowders*, J. Lumin. **153** (2014) 350–355.
- [4] G. Ozen, J. Collins, M. Cesaria, B. Di Bartolo, *Unconventional Production of Bright White Light Emission by Nd-Doped and Nominally Un-Doped Y_2O_3 Nanopowders*, IEEE Photonics Journal **6** (2014) 8200518.
- [5] W. Streck, L. Marciniak, P. Gluchowski, D. Hreniak, *Infrared laser stimulated broadband white emission of Yb^{3+} :YAG*

- nanoceramics, *Opt. Mater.* **35** (2013) 2013–2017.
- [6] Y. Zhu, S. Cui, M. Liu, X. Liu, C. Lu, X. Xu, W. Xu, *Observation of upconversion white light and ultrabroad infrared emission in YbAG:Ln³⁺ (Ln=Nd, Sm, Tb, Er)*, *Appl. Phys. Express.* **8** (2015) 072602.
- [7] J. Wang, J.H. Hao, P. A. Tanner, *Persistent luminescence upconversion for Er₂O₃ under 975nm excitation in vacuum*, *J. Lumin.* **164** (2015) 116–122.
- [8] A. Olejniczak, R. Tomala, B. Cichy, P. Gluchowski, M. Jakimow, A. Zieba, L. Kępiński, O. Ignatenko, W. Strek, *Laser-driven proliferation of sp²-sp³ changes during anti-Stokes white light emission of μ -diamonds*, *Carbon* **146** (2019) 438–446.
- [9] S. Zhu, C. Wang, Z. Li, W. Jiang, Y. Wang, H. Yin, L. Wu, Z. Chen, G. Zhang, *High-efficiency broadband anti-Stokes emission from Yb³⁺-doped bulk crystals*, *Opt. Lett.* **41** (2016) 2141–2144.
- [10] C. Miao, T. Liu, Y. Zhu, Q. Dai, W. Xu, L. Xu, S. Xu, Y. Zhao, H. Song, *Super-intense white upconversion emission of Yb₂O₃ polycrystals and its application on luminescence converter of dye-sensitized solar cells*, *Opt. Lett.* **38** (2013) 3340–3343.
- [11] X. Chen, W. Xu, Y. Zhu, P. Zhou, S. Cui, L. Tao, L. Xu, H. Song, *Nd₂O₃/Au nanocomposites: Upconversion broadband emission and enhancement under near-infrared light excitation*, *J. Mater. Chem. C* **2** (2014) 5857–5863.
- [12] W. Strek, B. Cichy, L. Radosinski, P. Gluchowski, L. Marciniak, M. Lukaszewicz, D. Hreniak, *Laser-induced white-light emission from graphene ceramics—opening a band gap in graphene*, *Light Sci. Appl.* **4** (2015) e237.
- [13] W. Strek, R. Tomala, L. Marciniak, M. Lukaszewicz, B. Cichy, M. Stefanski, D. Hreniak, A. Kedzierski, M. Krosnicki, L. Seijo, *Broadband anti-Stokes white emission of Sr₂CeO₄ nanocrystals induced by laser irradiation*, *Phys. Chem. Chem. Phys.* **18** (2016) 27921–27927.
- [14] M. Stefanski, M. Lukaszewicz, D. Hreniak, W. Strek, *Impact of the synthesis procedure on the spectroscopic properties of anti-Stokes white emission obtained from Sr₂CeO₄ phosphor*, *J. Photochem. Photobiol. A Chem.* **382** (2019) 111855.
- [15] M. Stefanski, D. Hreniak, W. Strek, *Broadband white emission from Yb³⁺ doped Sr₂CeO₄ nanocrystals*, *Opt. Mater.* **65** (2017) 95–98.
- [16] W. Strek, L. Marciniak, D. Hreniak, A. Lukowiak, *Anti-Stokes bright yellowish emission of NdAlO₃ nanocrystals*, *J. Appl. Phys.* **111** (2012) 024305.
- [17] R. Tomala, D. Hreniak, W. Strek, *Influence concentration of Nd³⁺ ion on the laser induced white emission of Y₂Si₂O₇:Nd³⁺*, *Opt. Mater.* **74** (2017) 135–138.
- [18] L. Marciniak, R. Tomala, M. Stefanski, D. Hreniak, W. Strek, *Laser induced broad band anti-Stokes white emission from LiYbF₄ nanocrystals*, *J. Rare Earths.* **34** (2016) 227–234.
- [19] M. Joubert, *Photon avalanche upconversion in rare earth laser materials*, *Opt. Mater.* **11** (1999) 181–203.
- [20] M. Stefanski, M. Lukaszewicz, D. Hreniak, W. Strek, *Laser induced white emission generated by infrared excitation from Eu³⁺:Sr₂CeO₄ nanocrystals*, *J. Chem. Phys.* **146** (2017) 104705. doi:10.1063/1.4978237.
- [21] M. Stefanski, M. Lukaszewicz, D. Hreniak, W. Strek, *Broadband laser induced white emission observed from Nd³⁺ doped Sr₂CeO₄ nanocrystals*, *J. Lumin.* **192** (2017) 243–249.
- [22] W. Strek, L. Marciniak, A. Bednarkiewicz, A. Lukowiak, R. Wiglusz, D. Hreniak, *White emission of lithium ytterbium tetrakisphosphate nanocrystals*, *Opt. Express.* **19** (2011) 14083–14092.
- [23] J. Wang, J.H. Hao, P.A. Tanner, *Upconversion luminescence of an insulator involving a band to band multiphoton excitation process*, *Opt. Express.* **19** (2011) 11753–11758.
- [24] J.J. Plata, A.M. Marquez, J.F. Sanz, *Electron Mobility via Polaron Hopping in Bulk Ceria: A First-Principles Study*, *J. Phys. Chem. C* **117** (2013) 14502–14509.

BIOGRAPHY



Professor at Institute of Low Temperatures and Structure Research, Polish Academy of Sciences Wrocław, Poland. His research activity cover luminescence properties of rare earth and transition metal ions in crystal, glasses and nanostructures; laser spectroscopy; optical sensors; laser materials; technologies of luminescent materials, transparent ceramics, porous thermo-isolation materials, nanoceramic materials for fuel cells; cryotherapy; photodynamic phenomena of therapy and diagnostic; laser therapy; laser induced white lighting in rare earth systems and graphene, graphene for hydrogen generation. In the last 10 years he participated in 16 national and international research projects, and in 9 projects he held managerial functions. Author and co-author of 550 scientific publications, 7700 citations, Hirsch index: 41 (Web of Sciences), i 45 (Google Scholar). Supervisor of 12 doctoral thesis. He has completed scientific internships in Denmark many times; multiple research stays in Brazil, France, Finland, Israel, Germany, Italy, Russia, USA, Vietnam, China and Belarus. He lectured at numerous national and international conferences (over 100 lectures), visiting professor (Israel, Denmark, France, Brazil). Organizer and co-organizer of numerous (over 50) national and international conferences. Member of editorial boards of international scientific journals (Journal Alloys and Compounds, Rare Earth Journal, Polish Journal of Materials Sciences, Reports in Physics (Elsevier), Polish Materials Science, ISRN Spectroscopy, Acta Bio-Optica et Informatica Medica.) and editor of many conference publications and monographs. He got many prizes in area of science, inventiveness and business ; Prize of Scientific Secretary of Polish Academy of Sciences (PAS), Warsaw, 1979, 1984; Individual Prize of Scientific Secretary of PAS, Warsaw, 1983; Scientific Secretary of Spectroscopy Committee of PAS (1984-90); Member of Steering Committee European Rare Earth Society (1982-1990); Gold medals at the International Innovation Exhibition "Eureka" Brussels (1999, 2000, 2002, 2004, 2006, 2008, 2009); Knight's Cross of the Order Inventiveness of the Kingdom Belgium 2003; Officer's Cross of the Order Inventiveness of the Kingdom Belgium 2006; Member of European Academy of Sciences Arts and Literature, Commander's Cross of the Order Inventiveness of the Kingdom Belgium 2010; Knight's Cross of the Order of Polonia Restituta 2018. Co-creator more than 60 patents and patent applications in cryomedicine, laser therapy, photodynamic therapy (PDT), security, nanotechnology, sol-gel technology, thermal insulation porous, graphene technologies, luminescent materials, lighting, co-founder of the Polish Cryogenic Chamber. He has participated in the implementation of new technologies in companies such as: Medical Center for Laser Techniques Laser Secura Systems, Haemato, Nano-Tech, Medical Cryogenics, Nanovectors Ipanterm, Nanoceramics, Graphene Project, Graphene Light Project.

MICROPATTERNING OF ELECTRET BY THERMAL IMPRINTING METHOD AND ITS APPLICATION TO ELECTRET BASED ROTARY ENERGY HARVESTER

Masato Suzuki¹, Yuki Onishi¹, Tomokazu Takahashi¹, and Seiji Aoyagi¹

¹ Faculty of Engineering Science, Kansai University, 3-3-35 Yamate-cho, Suita, Osaka, 564-8680, Japan.
Email: m.suzuki@kansai-u.ac.jp

ABSTRACT

In this study, we proposed and developed a method of patterning electret using thermal imprinting method. Electric charge was uniformly injected to the unpatterned electret film made of a fluoropolymer. Then, a glass mold, on which linear protrusions are arranged at regular intervals, was pressed against the electret film after being heated. As a result, electric charge was disappeared from parts of the electret where the heated protrusions were pressed. The surface potential of the electret was decreased by the thermal imprinting from approximately -1000V to -400 V when temperature of the glass mold is 130°C. A rotary energy harvester was developed using the thermal imprinted electret pattern. The number of electrode poles is 25. The gap between upper and lower electrodes is about 0.5 mm. The electric power of 6.0 μ W was output when the energy harvester was rotated at 10 Hz.

Keywords: Energy harvester, Electret, Micro patterning (less than 5 keywords)

INTRODUCTION

Recently, as an energy source suitable for wireless sensor systems, an energy harvester that converts low-density energy existing in the environment into electric energy attracts attention [1]-[2]. The studies about a Rotary Energy Harvester (REH) have been reported, which is a kind of energy harvester that generates electric energy using the rotary motion. Three advantages of REH are as follows. 1) The REH can be connected directly to the rotor to generate electric energy with high efficiency. 2) The REH can generate electricity from vibration energy when it was used together with a rotating weight. The RHE can generate electrical energy both from rotation and vibration with wide frequency.

Many small REHs have been reported which generate electricity using electrostatic force. Figure 1 is a schematic diagram showing the energy generation principle of the electrostatic type small REH. It consists of two circular substrate facing each other. Radial electrodes are formed on each substrate. A capacitance C is formed between the two facing electrodes. A film-shaped electret is formed on one electrode on one side of the substrate. The electrons (negative charge) are semi-permanently trapped in the electret. The trapped charge keeps the potential V of electret constant. This potential V

induces a charge on the electrode without the electret. Here, Q is expressed by the equation $Q=CV$. When one substrate is rotated and the other electrode is fixed, C changes and Q also changes accordingly. This change in Q generates electrical energy.

The energy generation efficiency of REH is improved by increasing the surface potential of the electret V or the division number of electrode N . Ideally, the electrical energy generated by REH is proportional to N and V^2 , respectively [3]. However, when charges are injected into an electret using the corona discharge method, which is the most common method of injecting charges, V decreases with increasing N [4]. Namely, N and V are in the trade-off relation, and both cannot be made large at the same time as long as the traditional corona discharge method is used for injecting charges. Charge injection using soft X-rays and removal of unnecessary charges using an excimer laser solve this trade-off problem [5]-[6]. However, these solutions have the disadvantage that the necessary equipment is very expensive.

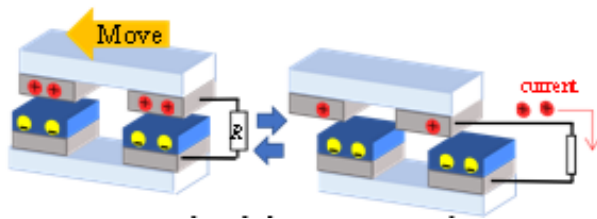


Figure 1. Principle of electrostatic induction.

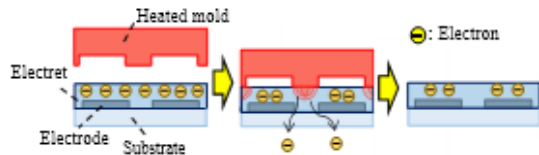


Figure 2. Principle of patterning method of electret using thermal imprinting.

In this study, fine patterned electret was formed by the thermal imprinting method, and the surface potential of the patterned electret was measured to verify the effectiveness of the proposed method. The REH was fabricated using the electret patterned by a thermal imprinting method, and the amount of power generated using the REH was measured.

METHOD FOR MANUFACTURING REH DEVICE AND METHOD FOR PATTERNING ELECTRET BY THERMAL IMPRINTING METHOD

First, radial-shaped electrodes were fabricated by depositing an Al film ($\approx 0.5 \mu\text{m}$) using a sputtering method, patterning the electrodes using a photolithography method, and etching the Al film using a special etching agent. The substrate is made of a glass plates (Made by Corning, model name: Eagle XG, size: $\approx 0.7 \text{ mm} \times 50 \text{ mm} \times 50 \text{ mm}$). After the forming of electrode, an electret film ($\approx 5.4 \mu\text{m}$) was formed on it. The electret is made of CYTOP[®] (made by Asahi Glass Co., Ltd., Model name: CTL -809 M). The outer diameter and inner diameter of the radial-shaped electrodes are 40 mm and 20 mm, respectively. The division number of the electret is 25. Al electrodes having the same radial shape were formed on a circular glass substrate. The diameter of the circular substrate is 50 mm. There is no electret film of the electret on the circular substrate. The fabricated two electrodes device is shown in Fig. 3.

Next, a pressing mold for thermal imprinting was prepared. A Cr film ($\approx 0.5 \mu\text{m}$) was formed on a glass plate by a sputtering method, followed by a patterning of Cr to radial shaped pattern. Shape of the Cr pattern is the same as the above-mentioned electrodes on the REH

device. The glass plate was etched by a hydrofluoric acid solution. In this case, the glass just under the Cr pattern is not etched because the Cr pattern acts as an etching mask. The photograph of the fabricated mold is shown in Fig. 4.

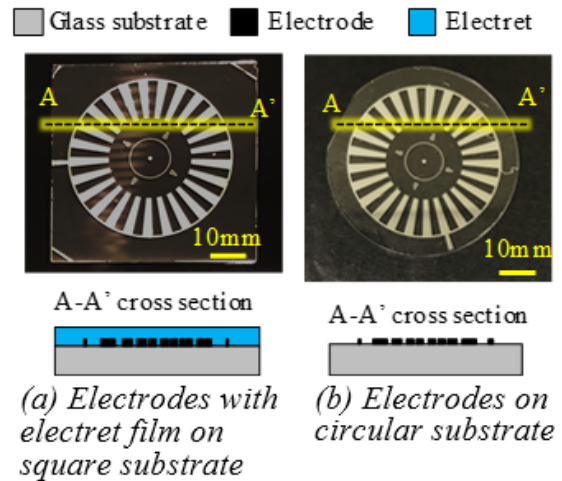


Figure 3. Photographs of fabricated REH device.

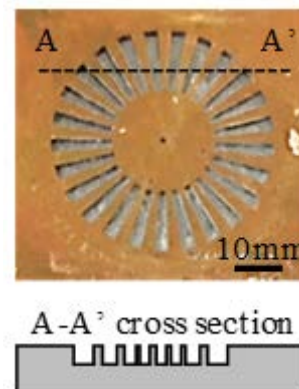
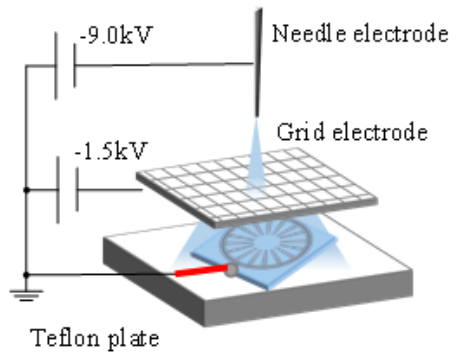


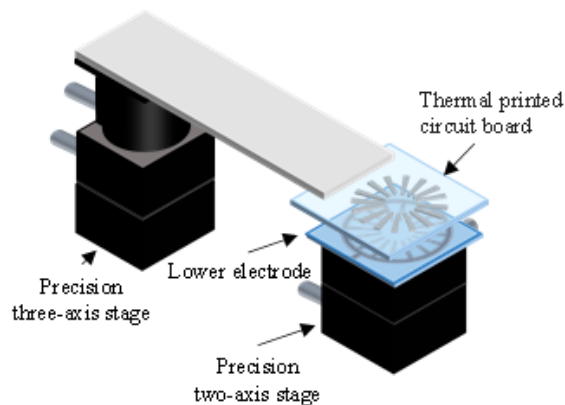
Figure 4. Photograph of mold for thermal imprinting.

Next, an electric charge was injected into the electret, followed by the thermal imprinting to remove the charge trapped in an unnecessary region. Figure 5 (a) and (b) show schematic diagrams of the charge injection system using corona discharge method, and the thermal imprint experimental system, respectively.

The procedure for charge removal by thermal imprinting is as follows. First, the pressing mold was separated from the substrate until a gap of about 1 mm was formed between them. Next, the mold was heated to the target temperature, followed by pressing the mold to the electret film for about one second. In this process, the mold was pressed only to areas where no charge was required, that is, to the outside of the electrode.



(a) Charge implantation system



(b) Thermal imprinting system

Figure 5. Schematic of experimental systems for charge implantation and thermal imprinting for patterning of electret.

RESULTS AND DISCUSSION

Result of patterning of electret by thermal imprinting

The patterning characteristics of an electret by thermal imprinting were evaluated. First, the decrease of the electret surface potential was measured by heating an unpatterned glass plate. This is because the measurement range of the surface electrometer (Monroe, ISOPROBE 279) used in this study is approximately 2 mm, and it is impossible to accurately measure the fine contrast of surface potential. The surface potential of the electret decreased from -1000 V to -400 V when the mold was pressed at 130°C for 1 second, t.

Next, after pressing the patterned mold shown in Fig. 4 under the same conditions, the surface potential was measured after adjusting the measurement range so that the contact portion with the mold and the non-contact portion were in the same area. As a result, the

surface potential decreased from -1000 V to -650 V.

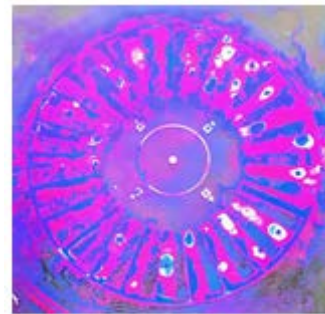


Figure 6. Visualization of surface potential contrast of electret using special toner.

On the surface of the heat-imprinted electret, a special toner was applied to visualize the charged state of the sample. The toner is a mixture of red and blue toner. Only red toner adsorbs on strongly negatively charged areas. In the region where the surface potential is close to 0 V, both red toner and blue toner adsorb and appear relatively blue. The results are shown in Fig. 6. This figure suggests that there is a contrast of the surface potential between the region in contact with the mold and the region in no contact.

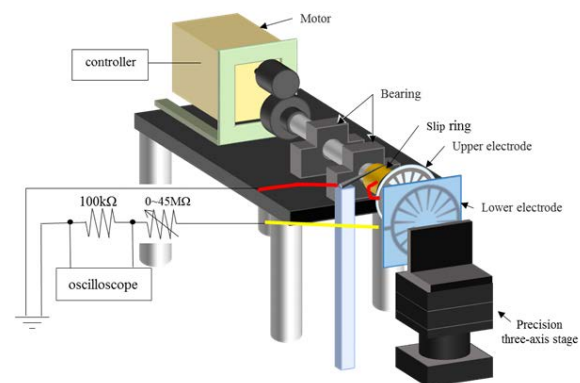


Figure 7. Setup for power generation test for fabricated REH.

Result of power generation test of REH

The fabricated two electrode devices (see Figure 3) were attached to the power generation test system shown in Fig. 7, and the test were carried out. The distance between the fixed and rotated substrate was set to 0.5 mm, and the rotational speed of the upper electrode device was 10 Hz. In this test, four types of REH devices were prepared, in which the mold temperatures at the patterning of the electret using thermal imprinting method were 110°C, 130°C, and 160°C, and the electric charge was injected after patterning the electret beforehand by etching (The electret surface potential is about -

500 V). The results of the power generation test are shown in Table 1. As a result, a maximum power generation of about 6.0 μW was obtained when the electret was patterned using the mold at 130°C.

Table 1. Result of power generation test using fabricated REHs.

Temperature of mold [°C]	110	130	170	Control*
Generated power [μW]	1.5	6.0	1.1	1.0

*Electret was formed by conventional etching process.

In the future, the optimization of the mold size and imprinting condition will be carried out to improve the efficiency of the RHE.

CONCLUSION

In this study, we proposed and developed a method of patterning electret using thermal imprinting method. Electric charge was uniformly injected to the unpatterned electret film made of a fluoropolymer. Then, a glass mold, on which linear protrusions are arranged at regular intervals, was pressed against the electret film after being heated. As a result, electric charge was disappeared from parts of the electret where the heated protrusions were pressed. The surface potential of the electret was decreased by the thermal imprinting from approximately -1000V to -400 V when temperature of the glass mold is 130°C. The

RHE developed using the thermal imprinted electret pattern. The number of electrode poles is 25. The electric power of 6.0 μW was output when the energy harvester was rotated at 10 Hz.

Acknowledgment

This work was supported in part by a grant of “Strategic Research Foundation Grant-aided Project for Private Universities”: Matching Fund Subsidy of MEXT (Ministry of Education, Culture, Sport, Science, and Technology, Japan), 2015-2019. This work was supported in part by JSPS (Japan Society for the Promotion of Science) KAKENHI (26870728).

References

- [1] C. K. Jeong, *et al.*, Nano Research, vol.10 pp.435-455, (2017).
- [2] P Basset, *et al.*, *J. Micromechanics and Microengineering*, Vol. 14, 035001, (2014).
- [3] J. Boland, *et al.*, *proc. IEEE MEMS 2003*, pp.538-541, (2003).
- [4] Y. TADA, *et al.*, *Jpn. J. Appl. Phys.*, Vol. 31, pp.846-851, (1992).
- [5] K. Hagiwara, *et al.*, *IEEE Transactions on Dielectrics and Electrical Insulation*, Vol. 19, pp.1291-1298, (2012).
- [6] M. Suzuki *et al.*, *Proceedings of Internat. Conf. IEEE MEMS 2012*, pp.1229-1232, (2012).

BIOGRAPHY



Masato Suzuki received his BE, ME, and PhD degrees in semiconductor engineering from Hiroshima University, Hiroshima, Japan, in 2002, 2004, and 2007, respectively. From 2007 to 2008, he was with the Research Center for Nanodevices and Materials at the same university as a post-doctoral fellow. He is currently an associate professor of the Mechanical Engineering Department at Kansai University, Osaka, Japan.

His current researches are microsensors and microactuators.

HIGH PERFORMANCE MEMS SENSORS: RESEARCH AND APPLICATIONS

Dzung Dao^{1,2}, Toan Dinh²

¹ School of Engineering and Built Environment, Griffith University, Queensland, Australia;

² Queensland Micro- and Nanotechnology Centre, Griffith University, Queensland, Australia

Email: d.dao@griffith.edu.au

ABSTRACT

High-performance MEMS sensors have been attracting great interests for a wide range of applications in daily life, laboratory and industrial processes. At Griffith University, we have successfully developed mechanical, thermal and optical MEMS sensors with high sensitivity, wide working range, and low cost. For example, optoelectronic coupling in a SiC/Si heterojunction exhibited an ultra-high gauge factor of up to 58,000 which is the highest gauge factor reported for semiconductor-based mechanical sensors to date. Moreover, SiC temperature sensors can work at a high temperature of up to 800 K with a high temperature coefficient of conductivity of 50,000 ppm/K. Interestingly, 3C/Si has been proven as a potential platform for highly sensitive position photodetectors. Our successful demonstration of mechanical, thermal and optical sensing concepts and devices could open a new door for the development of high-performance MEMS sensors from research point of view to a wide range of potential applications.

Keywords: Silicon carbide, mechanical sensors, thermal sensors, optical sensors, Optoelectronic, MEMS

INTRODUCTION

Silicon carbide (SiC) is a promising material for physical sensors thanks to its large energy bandgap, chemical inertness, and high Young's modulus. These properties make 3C-SiC suitable for high performance MEMS/NEMS sensors [1]. Recently, cubic SiC has been successfully grown on large silicon (Si) substrates for low cost MEMS sensors [2]. Other SiC polytypes have been also available on the market. Consequently, tremendous progress has been made to understand SiC sensing properties and the development of high performance SiC-based MEMS sensors for applications in oil/gas exploration and high-tech industries. For example, the sensing effects of 3C-SiC including piezoresistance [3] and thermoresistance [4] have been intensively investigated for mechanical, thermal and optical sensors [5, 6].

In this paper, we summarize our recent work on research and applications of SiC MEMS sensors, including high performance strain, thermal, and optical sensors. We highlight the applications of these SiC MEMS sensors toward harsh environment applications, including high temperatures.

RESULTS AND DISCUSSION

Strain sensor

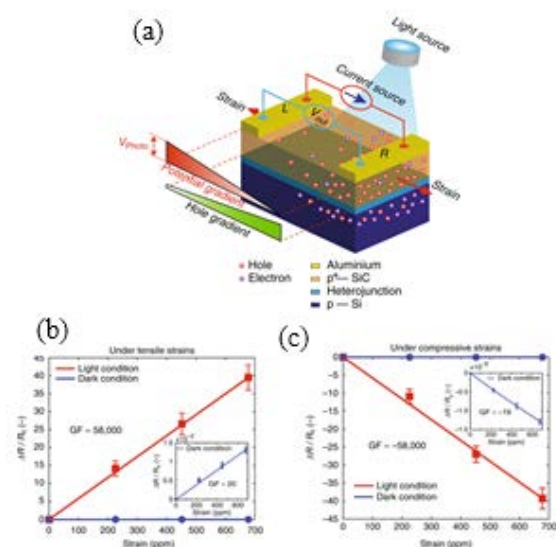


Figure 1. Ultra-sensitive strain sensors by optoelectronic coupling in a SiC/Si heterojunction [7]. (a) Concept of optoelectronic coupling, (b,c) Enhancement of the mechanical sensing effect with a GF of 58,000.

We have found that the piezoresistive effect in a semiconductor heterojunction could be significantly enhanced using optoelectronic coupling [7]. A lateral photovoltage, generated in the top material layer of a heterojunction under non-uniform illumination, can be coupled with an optimally tuned electric current to modulate the magnitude of the piezoresistive effect, Figure 1a. We demonstrated a tuneable giant piezoresistive effect in a cubic silicon carbide/silicon heterojunction, resulting in an extraordinarily high gauge factor of approximately 58,000 (Figures 1b,c), which is the highest gauge factor reported for semiconductor-based mechanical sensors to date. This gauge factor is approximately 30,000 times greater than that of commercial metal strain gauges and more than 2,000 times greater than that of cubic silicon carbide.

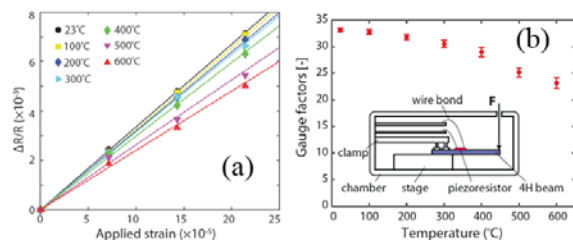


Figure 2. SiC strain sensors working at high temperatures of up to 600°C [8]. (a) Resistance change vs applied strain. (b) The stability of gauge factor at elevated temperatures.

In addition, we successfully demonstrated the use of p-type 4H-SiC for strain sensing at high temperatures of up to 600°C [8]. Firstly, a good ohmic contact was formed by the metallisation process using titanium and aluminium annealed at 1000 °C. The resistance change of SiC was found to be linear with applied strain (Figure 2a). Owing to the superior physical properties of the bulk 4H-SiC material, a high gauge factor of 23 was obtained at 600 °C, Figure 2b. The piezoresistive effect also exhibits good linearity and high stability at high temperatures. The results demonstrated the capability of p-type 4H-SiC for the development of highly sensitive sensors for hostile environments.

Temperature sensor

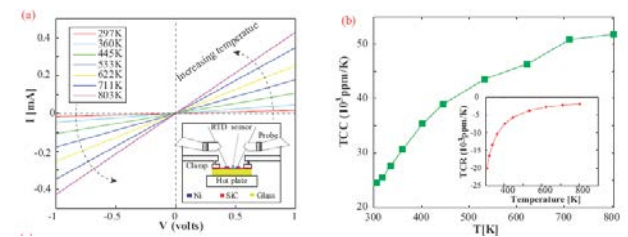
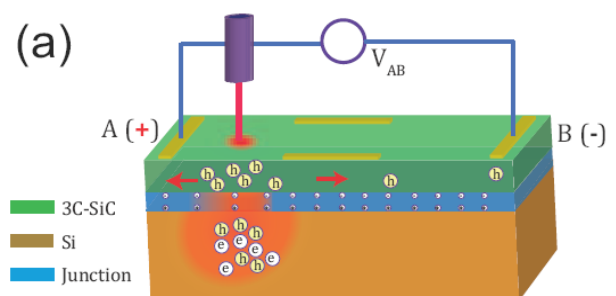


Figure 3. Sensitive SiC temperature sensors working at high temperatures of up to 800 K [4]. (a) Linearity of the current-voltage characteristics at high temperatures. (b) Temperature coefficient of conductivity (up to 50,000 ppm/K).

There is a growing interest and demand to develop temperature sensors that operate at high temperatures and a wide temperature range. We successfully demonstrated the temperature sensing properties of unintentionally doped n-type single crystalline cubic silicon carbide (3C-SiC) for high temperatures up to 800 K [4]. A highly sensitive temperature sensor was demonstrated with the linear current-voltage (I-V) characteristics at elevated temperatures, Figure 3a. The temperature sensor exhibited a large temperature coefficient of conductivity (TCC) ranging from 20,000 to 50,000 ppm/K, Figure 3b. The application of this material was successfully demonstrated as a hot film flow sensor with its high signal-to-noise response to air flow at elevated temperatures [4]. The high TCC of the single crystalline SiC film at, and above 800 K strongly revealed its potential for highly sensitive thermal sensors working at high temperatures.

Optical sensor



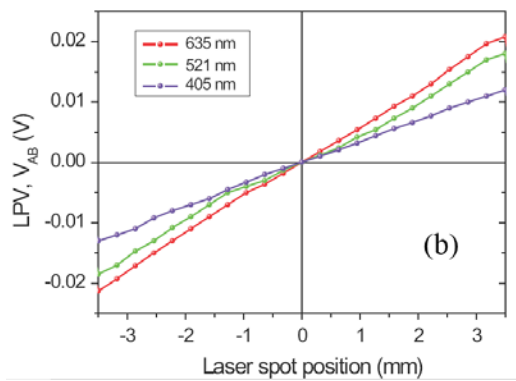


Figure 4. Position photodetector using the lateral photovoltage in 3C/Si [10]. (a) The generation of lateral photovoltage in 3C/Si. (b) The change of the lateral photovoltage V_{AB} when the laser spot moves from electrode A to B along the X-axis ($Y=0$) under 405 nm, 521 nm, and 635 nm illuminations (23 mW/cm^2).

We report another promising application of the heterostructure as a laser spot position sensitive detector based on the lateral photovoltaic effect (LPE) under nonuniform optical illuminations at zero-bias conditions, Figure 4a [10]. The LPE shows a linear dependency on spot positions and the sensitivity is found to be as high as 33 mV/mm under an illumination of 2.8 W/cm^2 (635 nm), Figure 4b [10]. The structure also exhibits a linear dependency of LPE over a large distance (7 mm) between two electrodes, which is crucial for PSDs as the region with a linear dependence of LPE is only usable for PSDs. The LPE at different spot positions and under different illumination conditions have been investigated and explained based on the energy-band analysis. The temperature dependency of the LPE and position sensitivity are also investigated. Furthermore, the 2D-mapping of the lateral photovoltages reveals the potential for utilizing the 3C-SiC/Si heterostructure to detect the laser spot position precisely on a plane [10].

CONCLUSION

We successfully demonstrated a number of MEMS sensors based on mechanical, thermal and optical sensing concepts. These sensors showed exceptional high sensitivity and ability to work in at high temperatures. Our work indicates the potential development of high-performance MEMS sensors in research and wide range of applications in laboratory and high-tech industries.

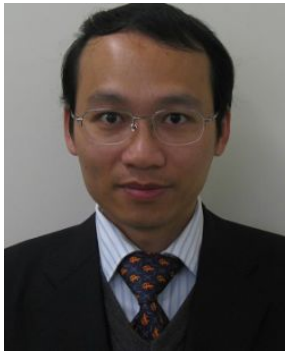
Acknowledgment

This work has been partially supported by Australian Research Council grants LP150100153 and LP160101553.

References

- [1] T. Dinh, H.-P. Phan, A. Qamar, P. Woodfield, N.-T. Nguyen, and D. V. Dao, "Thermoresistive effect for advanced thermal sensors: Fundamentals, design considerations, and applications," *Journal of Microelectromechanical Systems*, vol. 26, pp. 966-986, 2017.
- [2] L. Wang et al., "Growth of 3C-SiC on 150-mm Si (100) substrates by alternating supply epitaxy at 1000 C," *Thin solid films*, vol. 519, no. 19, pp. 6443-6446, 2011.
- [3] A. R. Md Faisal et al., "Pushing the limits of piezoresistive effect by optomechanical coupling in 3C-SiC/Si heterostructure," *ACS applied materials & interfaces*, vol. 9, no. 46, pp. 39921-39925, 2017.
- [4] T. Dinh et al., "Unintentionally doped epitaxial 3C-SiC (111) nanothin film as material for highly sensitive thermal sensors at high temperatures," *IEEE Electron Device Letters*, vol. 39, no. 4, pp. 580-583, 2018.
- [5] V. Balakrishnan, T. Dinh, H.-P. Phan, D. V. Dao, and N.-T. Nguyen, "Highly sensitive 3C-SiC on glass based thermal flow sensor realized using MEMS technology," *Sensors and Actuators A: Physical*, vol. 279, pp. 293-305, 2018.
- [6] A. Qamar et al., "The effect of device geometry and crystal orientation on the stress-dependent offset voltage of 3C-SiC (100) four terminal devices," *Journal of Materials Chemistry C*, vol. 3, no. 34, pp. 8804-8809, 2015.
- [7] T. Nguyen, T. Dinh, A. R. M. Faisal, H.-P. Phan, T.-K. Nguyen, N.-T. Nguyen, et al., "Giant piezoresistive effect by optoelectronic coupling in a heterojunction," *Nature communications*, vol. 10, pp. 1-8, 2019.
- [8] T.-K. Nguyen, H.-P. Phan, T. Dinh, A. R. M. Faisal, N.-T. Nguyen, and D. V. Dao, "High-temperature tolerance of the piezoresistive effect in p-4H-SiC for harsh environment sensing," *Journal of Materials Chemistry C*, vol. 6, pp. 8613-8617, 2018.
- [9] A. R. Md Faisal, T. Nguyen, T. K. Dinh, T.-K. Nguyen, P. Tanner, E. Streed, et al., "3C-SiC/Si heterostructure: an excellent platform for position sensitive detectors based on photovoltaic effect," *ACS Applied Materials & Interfaces*, 2019.

BIOGRAPHY



Associate Professor Dzung DAO received his BEng degree in Mechano-informatics (later renamed to Mechatronics) in 1995, and a PhD degree in Micro Electro Mechanical Systems (MEMS) from Ritsumeikan University, Japan in 2003. He then worked as a Postdoctoral Research Fellow from 2003 to 2006, a Lecturer from 2006 to 2007, and a Chair Professor from 2007 to 2011, all at Ritsumeikan University.

From 2011 A/Prof Dao joined Griffith University's School of Engineering and Built Environment, where he has been teaching in Mechatronics and Mechanical Engineering. Currently, he is the Head of Mechanical Engineering Discipline (Department) and Director of Mechatronic Engineering program.

A/Prof. Dao current research interests include advanced manufacturing, MEMS sensors & actuators, transducers for harsh environments, and mechatronics/robotics. A/Prof Dao has published over 350 papers in scientific journals and conference proceedings, and filed 17 patents.

VACUUM-SEALED RESONANT MICROELECTROMECHANICAL RESONANT SENSORS FOR NONINVASIVE DETECTION OF HEALTH

Takahito Ono

Graduate School of Engineering, Tohoku University, Aramaki Aza-Aoba 6-6-01, Aoba-ku, Sendai, Japan;

Micro System Integration Center, Tohoku University, Aramaki Aza-Aoba, Aoba-ku, Sendai, Japan;
Email: ono@nme.mech.tohoku.ac.jp

ABSTRACT

Vacuum-sealed microelectromechanical resonant sensors have been developed for the noninvasive detection of human body condition and the detection of biological substances. Micromechanical resonators based on microfabrication can be applied to ultra-sensitive sensors for magnetic field and acoustic wave detection. However, the resonators are unstable in ambient atmosphere due to molecule adsorption and contaminant adsorbed on it. In addition, in atmosphere air damping induces the acoustic energy loss, which reduce the sensitivity of the resonant sensors. Hermetic packaging of the resonators can improve the sensitivity and stability of the sensors. Three kinds of developed sensors based on Si microfabrication are presented in this talk.

First one is micromechanical resonant magnetic sensors for healthcare monitoring using biomagnetic sensing. The sensor consists of Si resonator with a small magnet and micro magnetic field concentrator. An external magnetic field creates magnetic field gradient using the micro magnetic field concentrator, which induces the resonant frequency change due to magnetic fields. It is shown that the optimized design of the sensor can achieve the detectable magnetic field smaller than pT.

The high-sensitive magnetic sensors can be applied to radical detection using magnetic resonance principle. Similarly, a silicon resonator with a magnet is hermetically sealed. Magnetic force caused by spin flip of the radical molecules induces the vibration of the resonance the Si resonator, and from the vibration amplitude, the density of the radical can be detected.

Final one is the photo-acoustic sensors. The high quality-factor of mechanical resonance can respond to external sound wave. Thus, the sensors can detect photoacoustic waves generated by adsorption of pulse laser to human body. The fundamental experiments for glucose detection are conducted, which shows a high potential ability for noninvasive detection of glucose.

Keywords: Resonant sensors, Biomagnetics, Magnetic sensors, Radical sensors, Photoacoustic sensors

BIOGRAPHY



He received the D.E. degree in mechatronics and precision engineering from Tohoku University in 1996. During 1996–1999, he has been a Research Associate in the Department of Mechatronics and Precision Engineering, Tohoku University. During 1999-2009, he has been an Associate Professor.

He is currently a Professor at Department of Mechanical Systems Engineering in Tohoku University. Also he was a professor of Department of Mechanical Engineering, Graduate School of Engineering at The University of Tokyo during 2013-2016. He was director of Micro/Nanomachining education center, Tohoku University during 2012-2014. He is the vice-director of The Micro System Integration Center, Tohoku University. Since 2017, He is the director of The Micro System Integration Center, Tohoku University. His expertise is in the area of microelectromechanical systems (MEMSs), nanoelectromechanical systems (NEMSs), ultra-sensitive sensing based on resonating device. Recent interests cover nanomaterials and their integration into the microsystems for applications of IoT sensors, environment monitoring, biomedical sensors, nano-energy, and scientific instrumentation.

PHOTONICS AND MEMS SENSORS FOR THE DIGITAL OLFACTION

Thierry Livache and Cyril Herrier

Aryballe Technologies
7 rue des Arts et Metiers,
38000 Grenoble, France

Email: thierry.livache@aryballe.com

ABSTRACT

Beyond the classical lock/key-recognition-based approach in used in the bio-analytical field, an electronic tongue or nose device (eT/eN) is an assembly of non-specific sensors. Following a long story around the imaging of biological interactions of biomolecules by Surface Plasmon Resonance Imaging, we extended this approach to the non-specific interactions studies in gas phase giving rise to a new optical-nose generation. The signals resulting from the binding of VOCs on an array of bioinspired receptors can be seen as 3D continuous dynamic images or movies. Finally, complex data obtained from odors are analyzed as simple images via a specific database. This flexible and straightforward approach allowed a down-scaling of the device and a new miniaturized portable and generic opto-nose *Neose* was recently launched. A new generation of instruments based on a MEMS approach are currently designed. The translation of a smell into an image could be seen as a first step to open up the merging of the olfactory and visual senses.

Keywords: olfaction sensor, plasmonics,

INTRODUCTION

During the last decades, microtechnologies have prompted the development of miniaturized and highly parallel devices allowing a high biological analysis throughput. The possibility to graft biomolecules on metals, opened the development of SPR imaging (Surface Plasmon Resonance) allowing the real time and label free measurement of biological interactions on a microarray format [1]. The development of this analytical instruments has opened a large panel of biological applications. Applications of SPRi cover different fields from fundamental biological researches [2] to more applied fields. Beyond the classical process of specific bio-recognition via a lock-key approach using receptors, antibodies, aptamers *etc.* the use of non-specific interactions remains the base of e-nose/tongue development [3].

In this way, a new approach of SPRi-based optical e-tongue using an assembly of non-specific combinatorial sensors was developed [5]. In this case, the information given by each sensor is complementary and the combination of all

sensors results generates a unique fingerprint. We have indeed developed a new paradigm based on a combinatorial approach to simplify greatly the preparation of sensing materials for constructing e-noses/tongues.

Instead of designing and synthesizing a large number of differential receptors, that often represents a laborious and time-consuming task, we prepared an array of combinatorial assemblies behaving as cross-reactive receptors by self-assembly of a handful of building blocks mixed in varying and controlled proportions. By combining such an array with a real-time optical detection system such as SPR imaging, the obtained eTongue is capable of generating 3D continuous evolution patterns just like vivid landscapes for each sample [4]. The extension of this approach for a SPRi-based gas sensing was not obvious. It is indeed well known that small compounds are very difficult to detect by SPR. The optical signal generated by an SPR imaging can be seen as a 2D optical balance and, in a first approach, the localized signal is roughly proportional to the mass of the compounds adsorbed on the SPR gold layer. Based on a saturated 2D assembly model, the typical mass

density of a small volatile compound to detect would be in the range of 1 to 500pg/mm². However, using a specific SPRi setup, the optical contrast generated between an adsorbed molecular layer and air is sufficient to generate an SPR signal [5]. The second point is related to the chemical sensors arrayed of the gold surface of the prism. The binding of volatile compounds must generate a reversible SPR signal. It is why the sensors are chosen among small organic molecules or biological molecules as small oligosaccharides or peptides. These molecules were arrayed on the gold prism using a x-y spotter as reported by Hou et al [4]. Starting from this point, the development was focused on the instrument miniaturization and optimization.

Aryballe first-generation instruments included an SPRimaging setup, a glass prism covered with a 50nm gold layer and the arrayed molecular sensors, a fluidic chamber and a pumping system. The analyses were carried out in few seconds, at room temperature by pumping few mL of the sample. The binding of VOCs on the sensors generates dynamic images (movie) corresponding to the association/dissociation phases of the recognition process. Following a training step, the images generated by a sample are compared to the image database and the sample can be identified and, if necessary quantified (Fig.1). A simplified result can also be given as a normalized radar chart allowing for a straightforward recognition process.



Figure 1. Optical-nose in a scheme. Left to right, binding of VOCs on the ligands arrayed on prism covered by a gold layer, interrogating the surface by SPRi, image analysis and data transfer.

This flexible and simple approach allowed a down-scaling of the device and a new miniaturized portable and generic opto-nose *Neose-pro* containing optimized optical setup and fluidic systems was recently launched (Fig.2). In this case the camera collecting the SPR images was connected by Wifi or Bluetooth to a smartphone integrated in the casing. The SPRi-based device enables to detect a wide panel of chemicals with ppmv detection thresholds for the vast majority of them. Since this approach relies on an imaging process, the number of sensors used in parallel can be easily extended from one hundred, currently used, to few hundreds if

necessary using the same optical setup paving the way of the design of new generations of generic and flexible sensors. It is also worth mentioning that this dynamic and biomimetic approach does not modify the sample and operates at room temperature, without complex concentration/desorption processes. It is why it remains fully compatible with the analysis of unstable volatile molecules. Moreover, this means that it can be easily hyphenated with orthogonal analytical systems as mass spectrometry or olfactometry generating complementary data.



Figure 2. Two generations of Neose instruments. The more recent (2017) includes a smartphone as interface. Top right, typical image generated by the sensors.

Finally, this approach is a way to translate an odor, a complex chemical signal assembly, into an image that can be analyzed by a classical image recognition process. The complex multidimensional correlated images generated by the use of mixtures of biomolecular sensors could be a way to represent the complexity of an odor. The next generation of sensors will involve a specific development a new microsystems...

References

- [1]. L. Laplatine; L. Leroy; R. Calemczuk; D. Baganizi; P. N. Marche; Y. Roupioz and T. Livache. *Spatial resolution in prism-based surface plasmon resonance microscopy*. Optics Express Vol: **22**(19), 2014.
- [2]. E. Bulard, A. Bouchet-Spinelli, P. Chaud, A. Roget, R. Calemczuk, S. Fort, and T. Livache. *Carbohydrates as New Probes for the Identification of Closely Related Escherichia coli Strains Using Surface Plasmon Resonance Imaging*. Anal. Chem. **87**, 2015
- [3]. AD. Wilson. *Review of electronic-nose technologies and algorithms to detect hazardous chemicals in the environment*. Procedia Technology **1**:453-463. 2012.
- [4]. Y. Hou, M. Genua, D. Tada Batista, R. Calemczuk, A. Buhot, P. Fornarelli, J. Koubachi, D. Bonnaffé, E. Saesen, C. Laguri, H. Lortat-Jacob and T. Livache, "Continuous evolution profiles for electronic tongue based analysis", Angew. Chem. Int. Ed., **51**, 10394, 2012.
- [5]. S Brenet A John-Herpin, FX Gallat, B Musnier, A Buhot, C Herrier, T Rousselle, T Livache, Y Hou. *Highly-Selective Optoelectronic Nose Based on Surface Plasmon Resonance Imaging for Sensing Volatile Organic Compounds*. Anal Chem. 2018 Aug 21; **90**(16):9879-9887. 2018

BIOGRAPHY
Thierry Livache



Thierry Livache, (PharmD, Hab.) is the Scientific Director (CSO) of Aryballe Technologies since sept. 2016. He had been previously a senior R&D scientist in a pharmaceutical company, CIS-bio, for 10 years (1990-2000) where he had developed microsystems for biological analyses, then “Directeur de Recherche” at CEA (French Atomic Energy Commission) and group leader in the joined unit Spram (CEA, CNRS, University of Grenoble). His expertise includes the development of micro-bioanalytical tools at the interface of physics, chemistry and biology and their clinical applications. His work in plasmonics coupled with combinatorial chemistry led to the development of a new photonic e-nose approach and to the launching of Aryballe Technologies.

He cofounded the companies Genoptics (SPR imaging now included in the Horiba Scientific Group) in 2002, PrestoDiag in 2012 (plasmonic bacteria detection), and more recently Aryballe Technologies in 2014.

He is the author of more than 100 peer-reviewed publications ~60 invited conferences and 30 families of patents.

SURFACES FOR WATER HARVESTING

Youngjin Kim, Céline Ternon, Michel Langlet and David Riassetto*

Associate Professor

Grenoble INP-PHELMA

Laboratory of Physical Engineering and Material Science (LMGP), FRANCE

ABSTRACT

Wettability is a feature of a surface that characterized his ability of being wetted or not by different kinds of liquids. This feature is synergistically dependent of both the surface chemistry and morphology. Tuning the wettability of a surface requires a fine control of these two parameters, which is still a challenging research topic, especially if one want to be able to spatially tuned the wettability of whatever kind of surface. Such kind of surface may be found in the nature. For instance, the Namib beetle's back has hydrophilic bumps surrounded by hydrophobic valleys. Water micro-droplets from fog adhere to the bumps and coalesce. When the drops become big enough, they touch the surrounding hydrophobic zone, detach and roll into the valleys for collection.

Herein, we present a simple strategy to create hydrophilic patches on superhydrophobic surfaces. The superhydrophobic feature arise from the sol-gel based fabrication of a micro/nano dual-roughness coating composed of zinc oxide nanowires (ZnO NWs). The rough ZnO NWs coating was then functionalized with a monolayer of hexadecyl trimethoxysilane (C16) to yield a superhydrophobic surface without fluorine. We confirmed that the micro/nano-roughness ZnO NW coating maintained its superhydrophobic feature of above 170o over more than a month even in the case of an underwater storage. In addition, the micro/nano-porous ZnO NW film with superhydrophobic property was also studied on anti-icing and anti-fouling abilities. The hydrophilic areas are simply made by hydrophilic microparticles spread onto the superhydrophilic coating by depositing hydrophilic microparticles using spincoating technique on a (super-) hydrophobic coating.

BIOGRAPHY



Dr. David Riassetto is an Associate professor of Material Science. He got a Master of Science degree in physics and energy with honors in 2005 at University Joseph Fourier of Grenoble and a Ph.D. at Grenoble Institute of Technology in 2009. Between 2009 and 2011 he was a postdoctoral researcher at the University of Utah. Since 2011, he is an associate professor at Grenoble Institute of Technology and doing his researches in the LMGP laboratory (Laboratory of Materials and Physical Engineering) has a member of the Thin Films, Nanomaterials and Nanostructures team, and more precisely of the Wet Chemistry & Surface Functionalization group. Currently Dr. David Riassetto's researches focus on the surface functionalization at the nanometer scale, using wet-chemistry methods (e.g. sol-gel, photochemistry ...)

LENSFREE MICROSCOPY: A NEW FRAMEWORK FOR THE IMAGING OF VIRUSES, BACTERIA, CELLS AND TISSUE

C.P. Allier, S. Vinjimore Kesavan, Y. Hennequin O. Cioni, F. Momey, T. Bordy, L. Hervé, J.-G. Coutard, S. Morel, A. Berdeu, F. Navarro, J.-M. Dinten, R. Campagnolo
CEA, LETI, MINATEC Campus, Technologies for Healthcare and Biology division, University.
Grenoble Alpes, F-38000 Grenoble, France
Email: raymond.campagnolo@cea.fr

ABSTRACT

Lens free imaging is a minimalist microscopy technique based on in-line holography as invented by Gabor in 1948. Albeit the existence of the method since decades, the recent development of digital sensors, helped the realization of its full potential. Over the recent years, innovations and improvements in CMOS imaging technology design and fabrication have allowed to decrease the pixel pitch down to $\sim 1\mu\text{m}$ and the number of pixels has dramatically increased up to 250 million of pixels. As a result, the performance of lens-free microscopy, which features a bare CMOS imager without any magnification optics, have tremendously increased while keeping the design simple, robust, and at a reasonable cost. The detection ability have improved from $10\mu\text{m}$ (cell) to $1\mu\text{m}$ (bacteria) down to 100nm beads paving the way to the detection of viruses.

Keywords: CMOS imaging technology; lens-free microscopy; bio-imaging incubator-proof. Moreover, biological samples can be imaged without staining. Our proposal can be summarized in a set of four guidelines and criteria:

INTRODUCTION

Biology is the study of living organisms, their structure, evolution and origin. Research is continuously developing imaging methods to better understand the structure and function of biological systems. Efforts during the last century to develop the methods of microscopy have pushed the boundaries in terms of resolution, sensitivity, and specificity. The introduction of the electron microscope (1930) allowed for the first time probing sub-micron objects. Photographic sensors (1970) allowed the acquisition of digital images and effective implementation of image processing. More recently the use of a fluorescent protein, GFP (1992), has introduced a new paradigm in cellular imaging. But despite our ability to peer through increasingly powerful and complex microscope, many questions are yet to be answered, e.g. in oncology and morphogenesis. Today, thanks to the new CMOS imaging technology (up to 250 million of pixels, down to $0.8\mu\text{m}$ pixel pitch) it is possible to build a new microscope, without eyepieces. In this paper we propose a new framework for bio-imaging based on lensfree microscopy which features only a bare CMOS imager without any magnification optics, and a LED illumination. By its simple design, the system is low cost, robust and

1-Multiscale: Life handles different orders of dimensions, ranging from basics units, i.e. DNA ($<10\text{nm}$), viruses ($20\text{-}500\text{nm}$), bacteria ($1\text{-}3\mu\text{m}$) and cells ($5\text{-}30\mu\text{m}$) to more complex system like tissues and small organisms. Observing one dimension only is thus restrictive as it prevents us from accounting the interactions at different scales. The new imaging modality must allow the simultaneous observation of at least two scales (e.g. tissue and cells, bacteria and viruses).

2-Large field of view: It cannot, of course, be argued that the observation of biology with a limited field of view and therefore low statistics is attractive. We do consider that the field of view must be larger than 20mm^2 . This criterion is defined by the dimension of an image featuring e.g. 10,000 cells. Further the imaging modality must allow 3D capture to embrace biology complexity. At first the ability to grab a volume of 100mm^3 will be disruptive in comparison with any other techniques.

3-Live capture: Life is about movement and action, and so the acquisition must be in real-time. Many phenomena occur in the order of minutes (e.g. cell motility, bacteria growth, etc.),

but there are many others that last much longer, in the order of hours up to weeks. As a compromise: we require the frame-rate to be smaller than 10 minutes and the movie duration to extend more than 24 hours.

4-Simple, small and low cost: We want to spread the new microscopy at a large scale. This guideline is thus a prerequisite that cannot suffer from any compromise.

Not any microscopy technique satisfactory tucks the four mentioned guidelines. Even taken separately, the guidelines strongly redefine bio imaging as we know it today. For instance, compound (lens-based) microscope is meant to observe a tiny portion of view ($<1\text{mm}^2$) featuring at most hundreds of cells within a focal plane. At large magnification, very few cells are imaged. So in order to gain additional information, microscopy makes use of multiple refinements (raster scan, fluorescence, time-lapse, super-resolution, etc.). But clearly this is at the price of higher cost and complexity and so the fourth guidelines ‘simple, small and low cost’ cannot be achieved. In this paper we demonstrate the capabilities of lens-free microscopy to fulfill most if not all of the guidelines.

DETECTION OF BACTERIA AND VIRUSES

Lensfree imaging has attracted a lot of attention for cell monitoring due to its very large field of view with microscopic resolution, compact setup (Fig. 1), easy implementation and image quality when reconstructing holographic data [1–5]. However, imaging small objects, like bacteria ($\sim 1\ \mu\text{m}$) and further viruses ($\sim 100\ \text{nm}$), has proven to be difficult, as these objects usually do not diffract enough light to be detected when immersed into aqueous buffers. We discovered in 2009 that the use of thin wetting film after the sample dry-up results into the self-assembling of microlenses that strongly amplifies the signal of micro and nano biological objects [6][7][8]. Hence creating a thin wetting film has shifted the challenge from detecting the object itself to detecting the effect of the microlenses that formed onto the objects. This allowed us to increase the signal to noise ratio of bacteria detection up to 100 and dramatically enhanced the detection efficiency up to 70% [9] (Figs. 1 and 2). Next, in collaboration with the Ozcan Group (UCLA), we achieved the detection of single viruses as

small as 100 nm, again without compromising the large field of view of 25mm^2 and overall simplicity [10]. These breakthrough paved the way for simple bacterial and viral load assays.

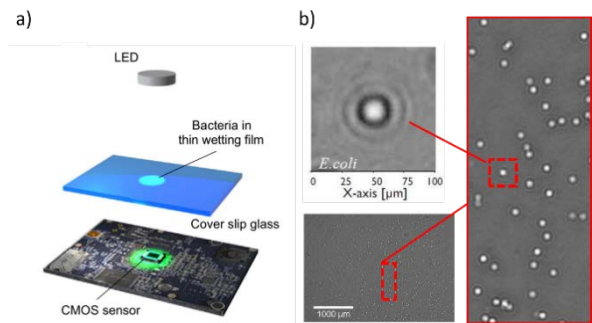


Figure 1. (a) Schematic of the thin wetting film lensfree imaging setup for the detection of bacteria. (b) Image of a sample containing *E. coli* bacteria recorded in the presence of a thin wetting film of DI water. An $11\ \mu\text{l}$ droplet has been evaporated to form a $\sim 7\text{mm}$ in diameter thin wetting film. The FOV of the CMOS sensor is $24\ \text{mm}^2$. 1700 bacteria are detected using a pattern matching algorithm.

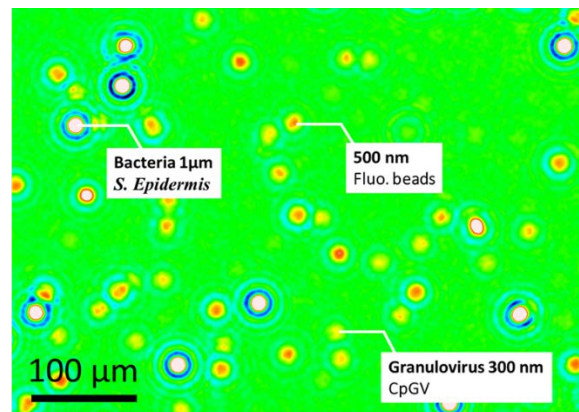


Figure 2. Detection of Granulovirus (300 nm), beads (500 nm) and bacteria ($1\ \mu\text{m}$) by means of thin wetting film lensfree microscopy

VIDEO LENSFREE MICROSCOPY OF CELL CULTURE

Majority of modern-day microscopic techniques focuses on increasing resolution which is achieved at the expense of cost, loss of compactness and simplicity, and reduction of field of view. The substantial decrease in the field of observation limits the visibility to a few single cells at best. Therefore, despite our ability to peer through the cells using increasingly powerful optical instruments, fundamental biology questions remain unanswered at

mesoscopic scales. A global view of cell population with significant statistics both in terms of cell numbers, space and time is necessary to understand the dynamics of cell biology, taking in to account the heterogeneity of the population and the cell-cell variability. By focusing on simplicity, cost, feasibility, field of view, and time-lapse in-incubator imaging, we have developed a lensfree video microscope based on digital in-line holography[11–13]

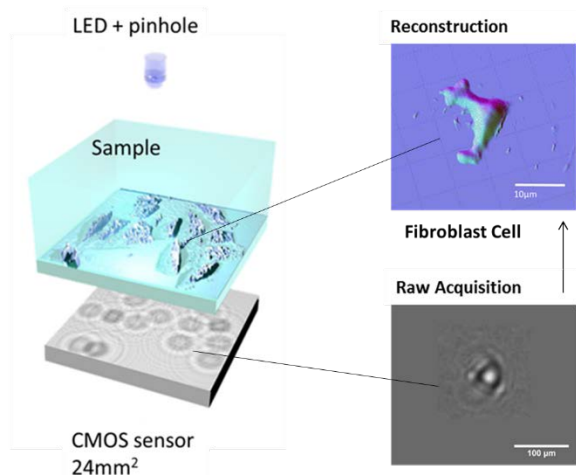


Figure 3. Experimental setup of the Lensfree video microscope. A CMOS image sensor is used for image acquisition and an LED and a $150\ \mu\text{m}$ pinhole for illumination (5 cm above the image sensor). The CMOS image sensor is put in contact with the Petri dish and records the holographic patterns resulting from the interference between the partially coherent incident light and the light scattered by the cells.

In a typical experiment, the lensfree video microscope is placed inside the cell incubator and the culture dish containing the cells is placed on top of the lensfree video microscope (Fig. 3a). This lensfree imaging setup does not acquire an image of the cell but a holographic interference pattern formed by the interference of the semi-coherent light scattered by the cell and the light passing directly from the source to the image sensor. A reconstruction algorithm is then used to recover the overall shape of every cell and their precise location from the interference holographic patterns (Fig. 3b and Fig. 4).

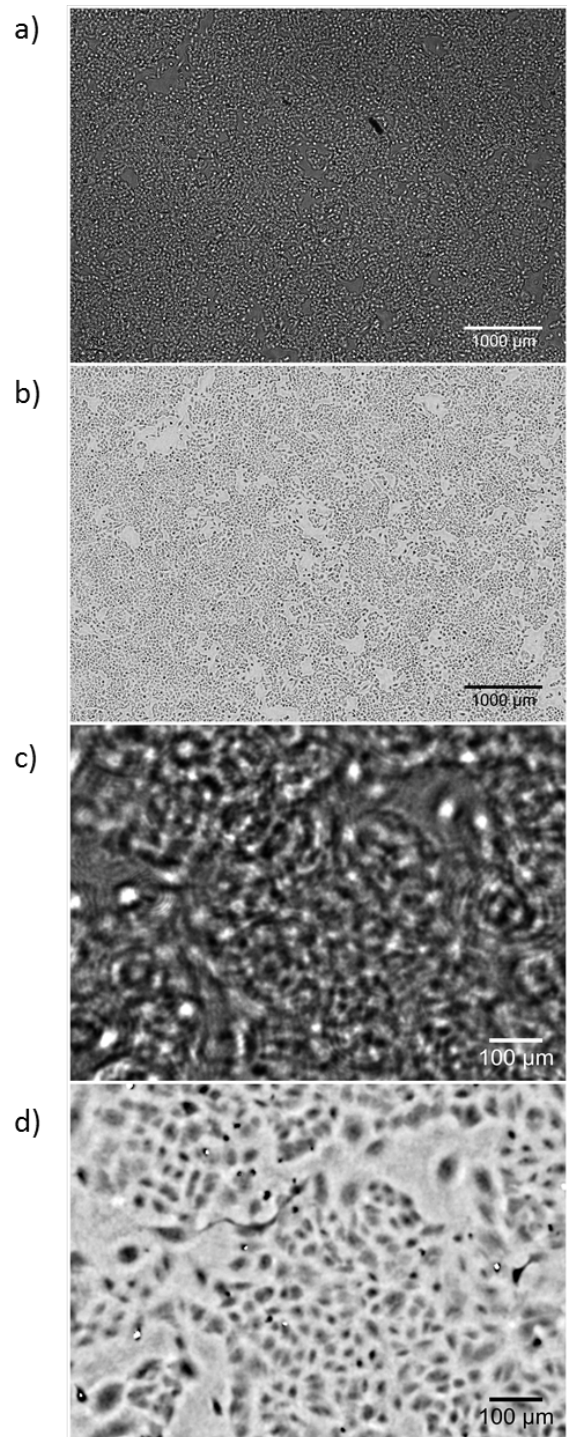


Figure 4. (a) Raw acquisition of a culture of A549 cells. The field of view is $29.4\ \text{mm}^2$ and the pixel pitch $1.67\ \mu\text{m}$. (b) Holographic reconstruction of the recorded image. (c) and (d) are cropped image taken respectively in (a) and (b). In (d), ultimately one can distinguish all single cell, their size and their density. After cell segmentation, we have determined that the number of cells recorded was approximately 21.000.

CONCLUSION

In summary, we have discussed a disruptive bio-physics imaging framework which favor statistics (10.000 cells at a glance), dynamics (video recording from days to weeks) and multiscale analysis (from cell population to single cell, observations lasting minutes to hours). Lensfree microscopy takes advantage of the ongoing innovations in the field of the CMOS imaging technology, so its performance will continue to improve drastically in a near future. And we argue that lensfree microscopy has the potential to be the new tool that will fulfill most requirements of diagnostics, drug screening and fundamental Biology applications, e.g. sound statistics, label-free measurement, cost and ease of use.

Acknowledgment

I would like to thank the entire team for the outstanding work they have done and the remarkable results achieved.

References

- [1] L. Repetto, E. Piano, and C. Pontiggia, "Lensless digital holographic microscope with light-emitting diode illumination", *Optics letters* **29** (2004) 1132–1134
- [2] S. Seo, T.-W. Su, A. Erlinger, and A. Ozcan, "Multi-color LUCAS: Lensfree On-chip Cytometry Using Tunable Monochromatic Illumination and Digital Noise Reduction", *Cellular and Molecular Bioengineering* **1** (2008) 146–156
- [3] S. Moon, H. O. Keles, A. Ozcan, A. Khademhosseini, E. Haeggstrom, D. Kuritzkes, and U. Demirci, "Integrating microfluidics and lensless imaging for point-of-care testing", *Biosensors & bioelectronics* **24** (2009) 3208–3214
- [4] D. Tseng, O. Mudanyali, C. Oztoprak, S. O. Isikman, I. Sencan, O. Yaglidere, and A. Ozcan, "Lensfree microscopy on a cellphone", *Lab on a chip* **10** (2010) 1787–1792
- [5] S. Moon, H. O. Keles, A. Ozcan, A. Khademhosseini, E. Haeggstrom, D. Kuritzkes, and U. Demirci, "Integrating microfluidics and lensless imaging for point-of-care testing" *Biosensors & bioelectronics* **24** (2009) 3208–3214
- [6] O. Mudanyali, C. Oztoprak, D. Tseng, A. Erlinger, and A. Ozcan, "Detection of waterborne parasites using field-portable and cost-effective lensfree microscopy", *Lab on a chip* **10** (2010) 2419–2423
- [7] O. Mudanyali, "Lensfree super-resolution microscopy using wetting films," *Optics express* **19** (2011) 17378-17389
- [8] Y. Hennequin, C.P. Allier et al. "Optical detection and sizing of single nanoparticles using continuous wetting films", *ACS nano* **7** (2013) 7601-7609
- [9] V. Poher, C. P. Allier, J. G. Coutard, et al. "Lensfree in-line holographic detection of bacteria", In *European Conferences on Biomedical Optics* (2011) 808619-808619
- [10] O. Mudanyali, E. McLeod, W. Luo, A. Greenbaum, et al. "Wide-field optical detection of nanoparticles using on-chip microscopy and self-assembled nanolenses", *Nature photonics* **7** (2013) 247-254.
- [11] O. S. V. Kesavan, F. Momey, O. Cioni, and N. Dubrulle, "High-throughput monitoring of major cell functions by means of lensfree video microscopy", *Scientific Reports* **4/5942** (2014) 1-11
- [12] M. E. Dolega, C. Allier, S. Vinjimore Kesavan, S. Gerbaud, F. Kermarrec, P. Marcoux, J.-M. Dinten, X. Gidrol, and P.-D. Nathalie, "Label-free analysis of prostate acini-like 3D structures by lensfree imaging" *Biosensors & bioelectronics* **49** (2013) 176–183
- [13] S. V. Kesavan, F. P. Navarro, et al., "Real-time label-free detection of dividing cells by means of lensfree video-microscopy", *Journal of Biomedical Optics* **19** (2013)

BIOGRAPHY



Raymond CAMPAGNOLO

66 years old, born on January 23rd 1953 in Sannois (Val d'Oise, France)
Married, two children.



CEA Grenoble
LETI/DTBS-DIR
17 rue des Martyrs
38054 Grenoble CEDEX 9
France

EDUCATION

In **1976, Engineer** graduated from Ecole Nationale Supérieure d'Electronique et Radio Electricité de Grenoble (France)

In **1980, Ph. D. degree of Doctor** from the Institut National Polytechnique de Grenoble (France)

POSITIONS

1980-1989: research engineer on algorithms, hardware architecture and software design for Positron Emission Tomography Scanners for medical imaging at CEA-LETI. Principal scientist in image reconstruction and test software for first and second generation PET cameras. Field maintenance engineer of the scanners.

1989 - 1994: project manager of the 3D X-Ray imaging device, MORPHOMETRE project at CEA-LETI, using cone-beam image reconstruction from digital subtracted angiograms in collaboration with General Electric Medical Systems. Head of the support team for the two prototypes of 3D cameras.

1994 - 1998: project manager of Digital X-Ray Imaging System for Mammography and Full Field general purpose Radiography at CEA-LETI, he designed and developed a full field imaging device (40 cm x 40 cm) using scintillating screen and high performance cooled CCD camera.

1998 - 2001: lab manager of the Electronic & Biology Laboratory at CEA-LETI, his team studied and developed dedicated instrumentation for fluorescent measurements in the field of DNA biochip and Lab-On-Chip using detection technologies for micro-capillaries.

2001 - 2006: associated manager of the joined team between CEA-LETI and the French company bioMérieux (World leader of microbiology bacterial identification and antimicrobial susceptibility testing system), the team applies micro-technology skills to Nucleic Acid amplification, detection and screening systems.

2006 - 2012: Program Manager in the field of Implantable Medical Devices at CEA-LETI in the **Microtechnologies for Biology and Healthcare Department (DTBS)**

2012 - 2015: Chief Scientist Officer at CEA-LETI in the **Microtechnologies for Biology and Healthcare Department (DTBS)**

2015 - 2019: Scientific Advisor at CEA-LETI in the **Microtechnologies for Biology and Healthcare Department (DTBS)** in the field of wearable medical devices

He holds 25 patents in the field of fluorescent detection technology (DNA chip and Lab-On-Chip), control of micro-systems for local drug delivery and molecular information in vivo capture.

AWARD

In 1982, he received the George Von HEVESY Prize for Nuclear Medicine for its contribution to the Time of Flight Information to Positron Tomographic Imaging.

FERROELECTRIC PEROVSKITES: FROM INORGANIC TO HYBRID MATERIALS

Pham Duc Thang, Nguyen Huy Tiep

Faculty of Engineering Physics and Nanotechnology, VNU University of Engineering and Technology,
Building E3, 144 Xuan Thuy, Cau Giay, Hanoi, Vietnam
Email: thangducpham@yahoo.com

ABSTRACT

Ferroelectric perovskites, with a general formula of AMX_3 , where A = inorganic or organic cation, M = metal cation, and X = Oxygen or halogen anion, have been widely used for fundamental research and industrial applications in microelectronic technologies. In this talk, firstly we will mention the study on some inorganic-based ferroelectric materials, such as micro-nanostructured $Pb(Zr,Ti)O_3$, $BaTiO_3$, and their composites with metals and metallic oxides. The interesting observations, such as enhancements in dielectric constant and polarization, doping induced and electrical field induced magnetization will be presented. And recently, hybrid halide perovskites have been a hot research subject due to their remarkable electronic and optical properties. Next, we will report the synthesis method of two-dimensional layered organic-based ferroelectric perovskites, containing Pb and Cu. The obtained results on their ferroelectric, piezoelectric and optical properties demonstrated that it opens a facile way to grow hybrid halide perovskite crystals for practical applications in optoelectronics.

Keywords: Ferroelectrics, perovskites, composites, hybrids

BIOGRAPHY



Pham Duc Thang received the B.Sc. degree in Physics and the M.Sc. degree in Materials Science in 1994 and 1996 from the University of Hanoi (nowadays Hanoi University of Science, Vietnam National University) and the International Training Institute for Materials Science (Ministry of Education and Training) in Hanoi, Vietnam. Then he received the Ph.D. degree in Experimental Physics in 2003 from the University of Amsterdam, The Netherlands. From 1996 to 1998 he was a lecturer at the International Training Institute for Materials Science. He was a post-doc fellow at the University of Twente, The Netherlands from 2003 to 2006. Since 2006 he has served as associate professor at Faculty of Engineering Physics and

Nanotechnology, University of Engineering and Technology, Vietnam National University in Hanoi, Vietnam, and then as the Dean of this Faculty.

His research interests include nanostructured magnetics, ferroelectrics and multiferroics, energy conversion and storage materials and systems, and their applications.

HIGH ENERGY STORAGE DENSITY OF ANTIFERROELECTRIC PbZrO₃ THIN-FILM CAPACITORS FABRICATED BY SOL-GEL PROCESS

Trang T. Trinh¹, **Ha T. Dang**^{1,3}, **Chi T.Q. Nguyen**^{1,3}, **Thanh N. Nguyen**^{1,4},
Minh D. Nguyen^{1,2} and **Hung N. Vu**^{1,*}

¹ International Training Institute for Materials Science, Hanoi University of Science and Technology,
Dai Co Viet 1, Hanoi 10000, Vietnam

² MESA+ Institute for Nanotechnology, University of Twente, P.O. Box 217, 7500AE Enschede,
The Netherlands

³ Vietnam National University of Forestry, Chuong My district, Hanoi 10000, Vietnam

⁴ Faculty of Electro-Mechatronics, Phuong Dong University, Hanoi 10000, Vietnam

Email: hung.vungoc@hust.edu.vn

ABSTRACT

In this paper, antiferroelectric PbZrO₃ (PZO) thin films were fabricated on (111)Pt/Ti/SiO₂/Si substrates by sol-gel spin-coating method. The (111)-oriented PZO thin films have a slanted double polarization hysteresis loop with a diffused antiferroelectric-ferroelectric phase transition. It is shown that the high recoverable energy storage (U_{reco}) of 19.4 J/cm³, and energy efficiency (η) of 70.8% at 1750 kV/cm. More importantly, this film shows excellent charge-discharge cycling endurance of both U_{reco} and η values after 10¹⁰ cycles. These results indicate that the sol-gel method is considered to be a promising approach towards producing low-cost antiferroelectric PZO thin films, for pulse-power energy-storage systems, operating in long-term working stability.

Keywords: Antiferroelectric, PZO thin film, energy storage, charge-discharge stability, thermal stability.

INTRODUCTION

Antiferroelectric (AFE) thin films have recently attracted considerable attention in terms of both fundamental research studies and practical applications [1-6]. Metal perovskite lead zirconate (PbZrO₃, PZO) is a simple prototype of antiferroelectric materials and is one of the most studied antiferroelectric materials due to its unique, electric field-induced, antiferroelectric-to-ferroelectric (AFE-FE) phase transition [7, 8]. This characteristic enables AFE PZO thin films to be used in capacitors for high power energy storage applications and digital displacement transducers [1, 6, 9, 10]. Fig. 1 shows a typical AFE double hysteresis (P - E) loop.

In general, the volumetric energy-storage density (U_{store}), recoverable energy-storage density (U_{reco}), energy-loss density (U_{loss}), and energy-storage efficiency (η), of a dielectric capacitor can be calculated from the polarization hysteresis loop as indicated in Fig. 1:

$$U_{store} = \int_0^{P_{max}} E dP \quad (1)$$

$$U_{reco} = \int_{P_r}^{P_{max}} E dP \quad (2)$$

$$U_{loss} = U_{store} - U_{reco} \quad (3)$$

$$\eta(\%) = 100 \times U_{reco} / U_{store} \quad (4)$$

where P_r and P_{max} are the remanent polarization and maximum polarization (polarization at the maximum applied electrical field E_{max}), respectively. As indicated in Fig. 1, the U_{reco} is presented by integrating the area between the polarization axis and the discharge curve, while the U_{loss} , caused by the domain reorientation, is calculated by integrating the area between the charge and discharge curves.

The shape of the P - E loop can benefit to the energy storage density in two aspects: (i) AFE films can sustain a high dielectric constant in relatively high electric field due to the presence of AFE-FE phase transition; (ii) P - E loop can turn back to AFE phase at low electric field and release nearly all the energy.

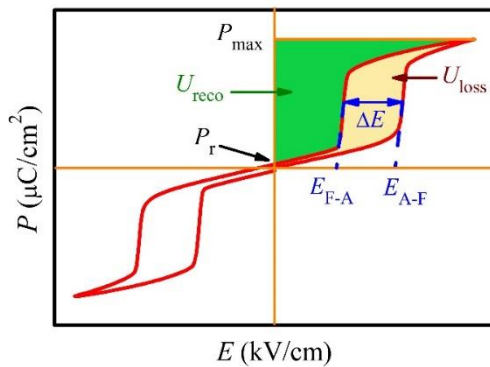


Figure 1. Schematic of electric-field-induced polarization hysteresis (P - E) loop of an antiferroelectric material.

In this work, antiferroelectric PbZrO_3 (PZO) thin films, grown on (111)Pt/Ti/SiO₂/Si (Pt/Si) substrates using the sol-gel spin-coating method is presented. Compared to the other methods, such as pulsed laser deposition (PLD), sputtering, or chemical vapor deposition, the sol-gel method is simple, cost-effective, scalable for industrial production, and moreover, it is easy to control the material composition in multi-component systems. In the present case, the polarization measurements indicate that the slanted P - E loops, with a lower AFE-FE coercive field, are obtained in the sol-gel PZO thin films (whereas, the square-double P - E loops, with a sharp AFE-FE phase transition, are observed in the PLD-PZO thin films). Due to the slanted P - E loops, the high U_{reco} and large η values are received in the sol-gel PZO thin films. Furthermore, the effect of charge-discharge cycling on the energy storage performance of PZO thin films have been also investigated. These findings could be important for the further integration of PZO thin-film capacitors onto commercial Pt/Si substrates in order to open the way to a simple route, and a cost-effective product, for pulse-power energy storage devices directly connected to electronic circuits.

EXPERIMENTAL

Sol-gel spin-coating method. PbZrO_3 (PZO) thin films were prepared using a sol-gel spin-coating process. Lead acetate trihydrate ($\text{Pb}[\text{CH}_3\text{COO}]_2 \cdot 3\text{H}_2\text{O}$), and zirconium n -propoxide ($\text{Zr}[n\text{-OPr}]_4$) were used as the starting materials. In this process, 2-methoxyethanol (MOE) was used as a solvent, while acetic acid was used in the function of a catalyzer. In order to compensate the lead loss during annealing/sintering, 15 mol% excess lead was

added into the starting solution. Lead acetate was dissolved in MOE on heating at 90°C with an acetic acid catalyst, and then refluxed at 124°C for 10 hours. Zirconium n -propoxide and MOE were refluxed at 124°C for 4 hours. After that, the complex solution was well stirred at 124°C for 3 hours to obtain a homogeneous solution. The 0.4 M PZO precursor solutions were then deposited onto Pt/Si substrates by spin-coating at 2000 rpm for 30 s, followed by pyrolysis at 400°C for 10 min. This process was repeated seven times. Finally, the films were then annealed at 650°C for 1 hour in air. The final thickness of the films was about 500 nm (the thickness of each coating layer was about 70-72 nm).

Analysis and characterization..

Crystallographic properties of the thin films were analyzed by X-ray θ - 2θ scans (XRD) using a PANalytical X-ray diffractometer (MalvernPANalytical) with $\text{Cu-K}\alpha$ radiation (wavelength: 1.5405 Å). Normal operating power was 1.8 kW (45 kV and 40 mA). Atomic force microscopy (AFM, Bruker Dimension Icon) and cross-sectional high-resolution scanning electron microscopy (HRSEM, Zeiss-1550, Carl Zeiss Microscopy GmbH), were performed to investigate the morphology, microstructure and thickness of the as-grown thin films. For the electrical measurements, Pt top-electrodes ($200 \times 200 \mu\text{m}^2$) were deposited at room temperature by DC magnetron sputtering and patterned using a lift-off technique. The polarization-electric field (P - E) hysteresis loops and switching current-electric field (I_s - E) curves, were measured with the dynamic hysteresis measurement option of the ferroelectric module of the aixACCT TF-2000 Analyzer (aixACCT Systems GmbH). The ferroelectric charge-discharge cycling fatigue measurements were performed with a bipolar switching pulse of the aixACCT TF-2000 Analyzer (aixACCT Systems GmbH).

RESULTS AND DISCUSSION

Fig. 2(a) presents the θ - 2θ XRD pattern of the PZO thin films. It exhibits a pure polycrystalline perovskite phase with strongly (111)-preferred orientation and no formation of a pyrochlore phase is observed. The cross-sectional SEM image shown in Fig. 2(b) indicates that the dense and crack-free film is obtained. The thickness of the sol-gel PZO thin films is about 496 nm.

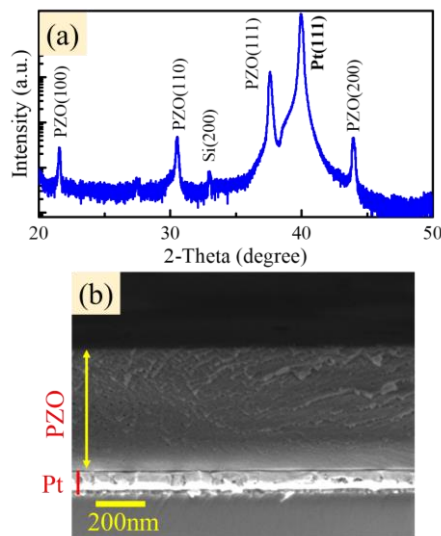


Figure 2. (a) XRD pattern and (b) cross-sectional SEM image of sol-gel PZO thin films.

The electric field-induced AFE-FE phase switching in the PZO thin films, under various applied electric fields (E_{app}), is illustrated by the P - E loops in Fig. 3(a). At low electric field (up to 350 kV/cm), the external field is not enough to switch the AFE dipoles, and therefore the P - E loops of the PZO thin films show a near-linear dependence, reminiscent of normal dielectric behavior. According to Park *et al.* [11], the alignment of randomly arranged AFE polarization occurs at low applied electric fields. At and above 450 kV/cm, the slanted double P - E hysteresis loops start to appear (Fig. 3(a)), revealing the AFE nature. In order to verify the significance of AFE behavior in the PZO thin films, the electric field dependence of the switching current curves was also investigated. Fig. 3(b) also indicates that the four switching peaks, in the switching current-electric field measurements, are detected. The first two switching current peaks of the I_{sw} - E switching curves correspond to the polarized forward phase switching field (E_{A-F} : electric field at which the AFE phase to FE phase transition occurs), and the polarized backward phase switching field (E_{F-A} : electric field which forces the FE phase to the AFE phase transition). The aligned AFE domains start to transform into the FE state at $E_{A-F} \approx 430$ kV/cm (called the critical phase transition field, under $E=450$ kV/cm) and the AFE-FE phase transition becomes more significant with additional increments of the electric field (Figs. 3(c)-3(d)). The E_{A-F} of the sol-gel PZO thin films slightly increases with increasing E_{app} , while the E_{F-A} value

is almost constant and so the ΔE ($=E_{A-F} - E_{F-A}$) value increases slightly.

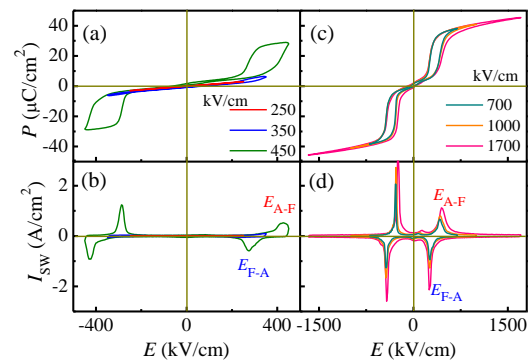


Figure 3. (a,c) P - E loops and (b,d) switching curves (I_{sw} - E) of sol-gel PZO thin films as a function of electric field.

As compared to sol-gel PZO thin films with the diffused phase transition, PLD PZO thin films have a sharp phase transition (Fig. 4). On the other hand, the change from diffused phase transition to sharp phase transition, between AFE and FE phases, can be tuned by changing the deposition method. Moreover, the diffused phase transition also leads to lower E_{A-F} and E_{F-A} values in the sol-gel PZO thin films, than that in the PLD thin films, when measured under the same conditions. Under an applied electric field of 1000 kV/cm, the obtained U_{reco} (14.1 J/cm³) value for the PLD PZO thin films is higher than that in sol-gel PZO thin films ($U_{reco}=13.3$ J/cm³). However, the energy efficiency (η) value, related to the charge/discharge speed, of sol-gel PZO thin films (73.5%) is much higher than that of PLD PZO thin films (62.4%), which can be explained from the lower ΔE value. According to a previous report on AFE materials, the slanted P - E loop is more efficient in energy storage devices than the square loop [12].

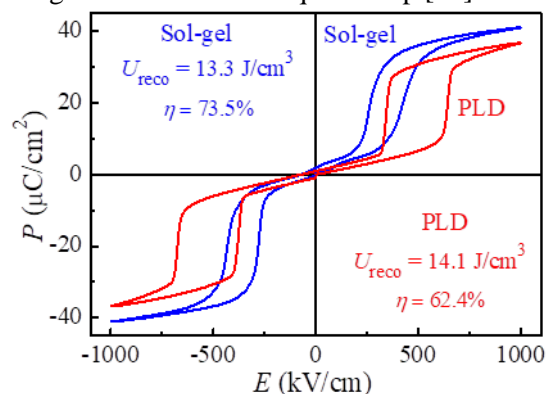


Figure 4. Compared P - E loops of PLD and sol-gel PZO thin films. The measurements were performed at 1000 kV/cm, 1 kHz and room temperature.

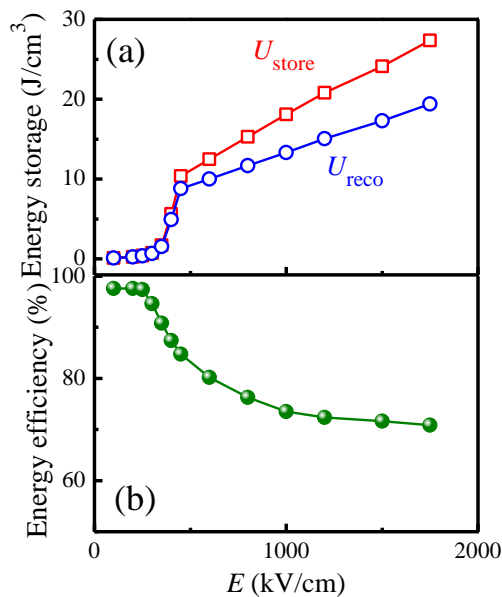


Figure 5. Electric field dependence of (a) energy storage (U_{store} & U_{reco}) and (b) energy efficiency (η), of sol-gel PZO thin films. The data were calculated from the corresponding P - E loops given in Figure 3.

The energy density and energy efficiency of the sol-gel PZO thin films, calculated from the P - E loops, measured from low electric field to the maximum electric-field, where the capacitor breaks down (called as electric breakdown strength, E_{BD}), are presented in Fig. 5. By increasing the applied electric field, both U_{store} and U_{reco} values increase slowly, at first, and then show an abrupt jump when the critical phase transition occurs (around 400-450 kV/cm), as shown in Fig. 5(a). Above the critical phase transition field, U_{store} and U_{reco} values gradually increase with further increases in the applied electric field. However, the increased rate of U_{reco} is lower than that of U_{store} , therefore the η value gradually decreases with increasing applied electric field as shown in Fig. 5(b). Below the critical phase transition field, the value of U_{reco} is close to that of U_{store} and leads to a high η value (~96-98%) due to the absence of field-induced AFE-FE transformation. At the maximum applied electric field of 1750 kV/cm, the obtained U_{reco} and η values are about 19.4 J/cm³ and 70.8%, respectively.

From a practical application point of view, the superior charge-discharge endurance for long-term stability is also very important for energy-storage devices. Here, bipolar electric field charge-discharge cycling was used, which

generally causes the most severe degradation in the polarization properties. The fatigue testing was performed by applying a bipolar electric field of 200 kV/cm (pulse-height) at a frequency of 100 kHz (or 5- μ s pulse-width). Fig. 6(a) shows the plots of P_{max} and P_r values against the number of charge-discharge cycles obtained from the P - E loops of sol-gel PZO thin films, measured at 1000 kV/cm, 1 kHz and room temperature. Both P_{max} and P_r values remain unchanged up to the maximum number of 10¹⁰ applied cycles. The charge-discharge cycling does not affect the P - E loops before and after 10¹⁰ fatigue cycles, as shown in Fig. 6(a) inset. Thus, it would be expected that both U_{store} and U_{reco} , as well as η values, also remain unchanged under these fatigue conditions (Figs. 6(b)-6(c)).

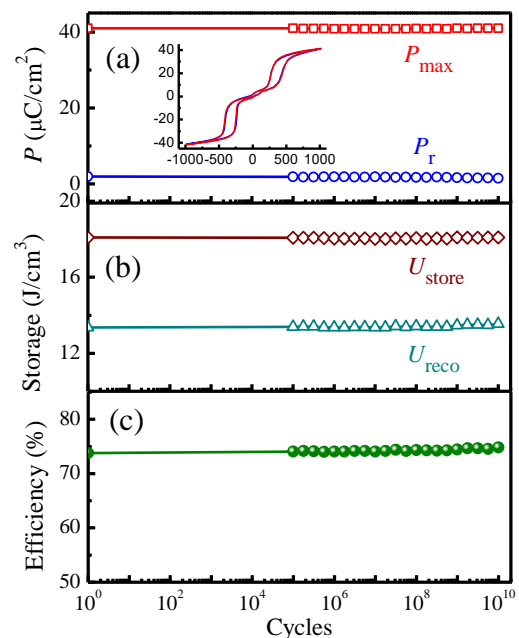


Figure 6. Dependence of charge-discharge cycling of (a) polarization (P_{max} & P_r), (b) energy storage (U_{store} & U_{reco}) and (c) energy efficiency (η), of sol-gel PZO thin films, respectively. The (a)-inset is the P - E loops at the initial stage and after 10¹⁰ cycles. The measurements were performed at 1000 kV/cm, 1 kHz and room temperature.

CONCLUSION

In this work, the antiferroelectric PZO thin films were fabricated on Pt/Si substrates by sol-gel spin-coating method and also compared with the thin films fabricated using PLD. High U_{reco} (19.4 J/cm³) and large η (70.8%) values were achieved in sol-gel PZO thin films, due to the slanted P - E loops with low ΔE value.

Meanwhile, the PLD PZO thin films had the lower efficiency due to a large difference between the E_{A-F} and E_{F-A} phase transitions obtained from the almost perfect square-double $P-E$ loops. More importantly, all the presented results indicate that sol-gel could be an effective method for developing PZO thin films with high energy storage performance and excellent charge-discharge cycling, for energy storage applications towards a low cost, scalable, and simple fabrication technique.

Acknowledgment

The authors would like to acknowledge the financial support from the National Foundation for Science and Technology Development (NAFOSTED) of Vietnam under Grant No. 103.99-2018.23.

References

- [1] A. K. Tagantsev, K. Vaideeswaran, S. B. Vakhrushev, A. V. Filimonov, R. G. Burkovsky, A. Shaganov, D. Andronikova, A. I. Rudskoy, A. Q. R. Baron, H. Uchiyama, D. Chernyshov, A. Bosak, Z. Ujma, K. Roleder, A. Majchrowski, J. H. Ko, N. Setter, *The origin of antiferroelectricity in $PbZrO_3$* , Nature Communications **4** (2013) 2229.
- [2] P. Tolédano, M. Guennou, *Theory of antiferroelectric phase transitions*, Physical Review B **94** (2016) 014107.
- [3] J. Ge, Y. Chen, X. Dong, D. Rémiens, X. Guo, F. Cao, G. Wang, *Dynamic hysteresis and scaling behavior in epitaxial antiferroelectric film*, Thin Solid Films **584** (2015) 108-111.
- [4] B. Xu, J. Íñiguez, L. Bellaiche, *Designing lead-free antiferroelectrics for energy storage*, Nature Communications **8** (2017) 15682.
- [5] X. Hao, J. Zhai, X. Yao, *Improved energy storage performance and fatigue endurance of Sr-doped $PbZrO_3$ antiferroelectric thin films*, Journal of the American Ceramic Society **92** (2009) 1133-1135.
- [6] X. Hao, J. Zhai, L. B. Kong, Z. Xu, *A comprehensive review on the progress of lead zirconate-based antiferroelectric materials*, Progress in Materials Science **63** (2014) 1-57.
- [7] G. Pilania, D. Q. Tan, Y. Cao, V. S. Venkataramani, Q. Chen, R. Ramprasad, *Ab initio study of antiferroelectric $PbZrO_3$ (001) surfaces*, Journal of Materials Science **44** (2009) 5249-5255.
- [8] X. Tan, C. Ma, J. Frederick, S. Beckman, K. G. Webber, *The Antiferroelectric \leftrightarrow ferroelectric phase rransition in lead-containing and lead-free perovskite ceramics*, Journal of the American Ceramic Society **94** (2011) 4091-4107.
- [9] W. Y. Pan, C. Q. Dam, Q. M. Zhang, L. E. Cross, *Large displacement transducers based on electric field forced phase transitions in the tetragonal $(Pb_{0.97}La_{0.02})(Ti,Zr,Sn)O_3$ family of ceramics*, Journal of Applied Physics **66** (1989) 6014-6023.
- [10] K. Uchino, *Digital displacement transducer using antiferroelectrics*, Japanese Journal of Applied Physics **24** (1985) 460-462.
- [11] S. E. Park, M. J. Pan, K. Markowski, S. Yoshikawa, L. E. Cross, *Electric field induced phase transition of antiferroelectric lead lanthanum zirconate titanate stannate ceramics*, Journal of Applied Physics **82** (1997) 1798-1803.
- [12] X. Hao, J. Zhou, S. An, *Effects of PbO content on the dielectric properties and energy storage performance of $(Pb_{0.97}La_{0.02})(Zr_{0.97}Ti_{0.03})O_3$ antiferroelectric thin films*, Journal of the American Ceramic Society **94** (2011) 1647-1650.



BIOGRAPHY

Vu Ngoc Hung received the B.S. degree in physics from Kishinev University (USSR), in 1979 and the Ph.D. degree from Hanoi University of Technology (Vietnam), in 1991. At present, he is a Professor with the International Training Institute for Materials Science (ITIMS), Hanoi University of Technology. His current research interests are in the area of MEMS inertial sensors and Piezo MEMS.

ORAL SESSIONS

***FUNDAMENTALS OF
NANOTECHNOLOGY
(FON)***

DESIGN AND SIMULATION OF POLYMERIC MICROFLUIDIC CANTILEVER-BASED BIOSENSOR WITH INTEGRATED PIEZO-RESISTOR

Le Van Tam and Mai Anh Tuan*

Microfabrication Laboratory and Pilot Plant Center
National Center for Technological Progress, Hanoi, Vietnam

*Corresponding author: tuanma@most.gov.vn

ABSTRACT

We present a design of PDMS microfluidic cantilever integrated metal piezo-resistor for biosensing based on change in surface stress induced by adsorption of biomolecules on the cantilever surface. The advantages of the design are low cost, high sensitivity, low analytics consumption and reducing size. The parameters of microfluidic cantilever are investigated by analytical calculation and simulation. The results show that the PDMS microfluidic cantilever can be alternative to silicon-based cantilever.

Keywords: microfluidic cantilever, piezo-resistive sensing, biosensor

INTRODUCTION

Micro cantilever-based biosensors have been developed as a powerful technique for detecting biomolecules. Micro cantilever sensor operates in two modes: static mode and dynamic mode. In static mode, deflection of micro cantilever is caused by surface stress change in micro cantilever when target molecules bonding with receptor molecules on micro cantilever surface [1]. In the dynamic mode, the resonant frequency of the micro cantilever changes when target molecules absorbing on micro cantilever [2]. Micro cantilever biosensor often operates in liquid medium, the sensitivity of the sensor is significantly affected by the noise from liquid medium. To solve the problem, a micro channel is integrated into micro cantilever [3]. Advantages of the solution are high sensitivity, reducing sensor size and volume of sample.

To detect the deflection and resonant frequency shift of the micro cantilever, optical readout method and piezoresistive readout method can be used. The optical readout method has high resolution, but it requires the transparent medium, large system sizes. Comparing to optical readout method, the piezoresistive readout method has more advantages, high sensitivity, simple fabrication process, small system size.

Solid-state semiconductors are conventional materials for fabrication of micro cantilever. However, the fabrication process for the solid-state semiconductors-based micro cantilever integrated micro channel is complicated and expensive [3]. In recently, polymeric micro cantilever has been studied

due to low cost, simple fabrication process and high sensitivity [4-5].

We propose a PDMS micro cantilever with integrated microfluidics for biomolecules detection. The PDMS micro cantilever sensor operates in static mode and it is integrated a gold thin film-based piezoresistive sensor. The characteristics of micro cantilever were studied by theoretical analysis and simulation.

THEORY

When a molecular bind to a cantilever surface, the molecular interaction induces the change in surface stress of the cantilever, as shown in figure 1a. The displacement of the cantilever under change in surface stress can be represented by Stoney equation [6]:

$$\Delta z = \frac{3l^2(1-\nu)}{Et^2} \quad (1)$$

The surface stress can be presented by a point load at the end of cantilever. The displacement of the cantilever under point load at the end of the cantilever is:

$$\Delta z = \frac{4Fl^3}{Ebt^3} \quad (2)$$

From two equations, we have:

$$F = \frac{3\sigma bt(1-\nu)}{4l} \quad (3)$$

To detect the change in surface stress, the piezoresistive sensor is used and connected in a Wheatstone bridge circuit, as shown in figure 1b. The

relative between change in resistance and surface stress is [7]:

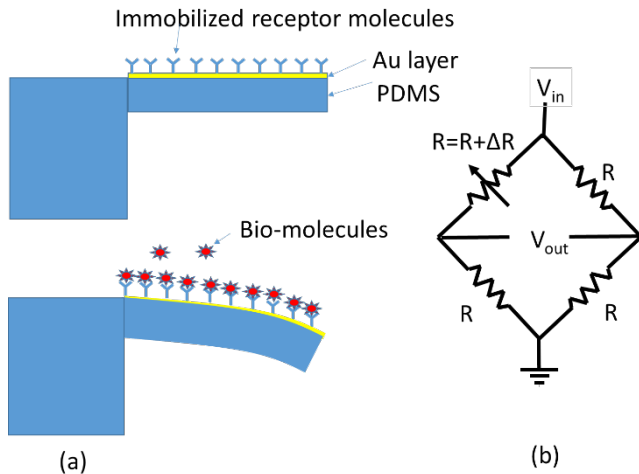


Figure 1. A schematic of simplified cantilever based bio sensor with integrated readout. Cantilever with immobilized receptor molecules (a), bending of cantilever caused target-receptor interaction (b), Wheatstone bridge circuit for detecting change in resistance.

$$\frac{\Delta R}{R} / \sigma_s = -K \frac{4}{Et} \quad (4)$$

Where K is gauge factor defined as the ratio of percent change in the resistance of the sensor to applied strain, h is the thickness of the micro cantilever, E is the Young modulus of the micro cantilever. For the PDMS micro cantilever integrated gold thin film based piezoresistive sensor, the gauge factor of gold is 4, which increases due to the distinguishing characteristic of gold thin film [4] and the Young modulus of PDMS is 0.75 MPa, the K/E is about 5.6 MPa^{-1} . In comparing with silicon-based cantilever, the gauge factor is 30, the Young modulus of single crystal silicon is 170 GPa, the K/E is about 0.18 GPa^{-1} , which is smaller 3×10^2 times than in PDMS cantilever. However, the thickness of PDMS cantilever is two orders of magnitude larger than the thickness of silicon cantilever. Therefore, the sensitivity of PDMS cantilever and silicon cantilever have the same order of magnitude.

DESIGN

The design of the micro cantilever-based biosensor is shown in figure 2. It consists of two micro cantilevers integrated microfluidics. One of the micro cantilevers is used as a reference cantilever, the other is used for detection of biomolecules. Two cantilevers are placed in the same physical conditions, so the noises from the environment can be reduced 100 times and the signal to noise is increased 25 times [8]. For electrical readout system, the Wheatstone bridge is

used to convert the change in resistance to the electrical signal.

Table 1. The parameters of the micro cantilever and the micro channel.

	Micro cantilever (μm)	Micro channel (μm)
Length	4000	3500
Width	1200	200
Thickness	75, 100, 125	25

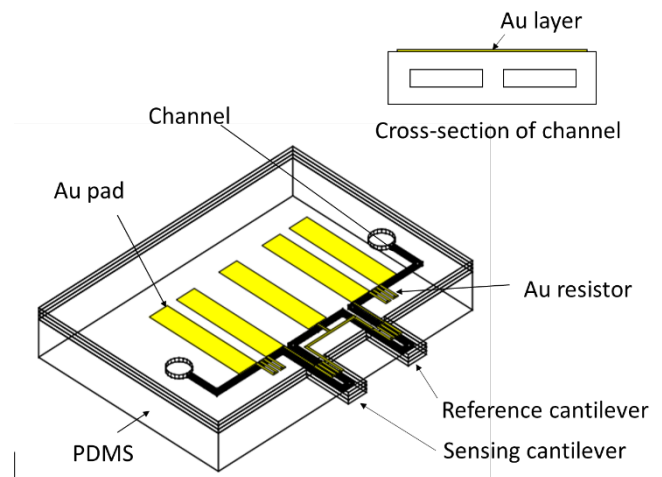


Figure 2. A schematic of micro cantilever integrated micro channel.

A thin gold film patterned on the PDMS surface is used as resistors for piezoresistive sensor. The resistors are designed as a meander structure to increase the resistance thereof. The parameters of the micro cantilever and micro channel are shown in table 1. We invest the characteristics sensor with the different thicknesses of the micro cantilever. The resistance of gold meander structure is 218Ω that is obtained from the gold resistor, the width of $50 \mu\text{m}$, the total length of $21000 \mu\text{m}$, the thickness of 50 nm , the electrical resistivity of $2.6 \times 10^{-8} \Omega/\text{m}$.

RESULTS AND DISCUSSION

From equation 4, the relative change in resistance depending on the deflection of the micro cantilever is invested and shown in figure 3. The deflection sensitivities equaling the slope of straight lines are $0.28 \times 10^{-3}/\mu\text{m}$, $0.21 \times 10^{-3}/\mu\text{m}$, $0.17 \times 10^{-3}/\mu\text{m}$, which yield different thickness, $75 \mu\text{m}$, $100 \mu\text{m}$, and $125 \mu\text{m}$, respectively.

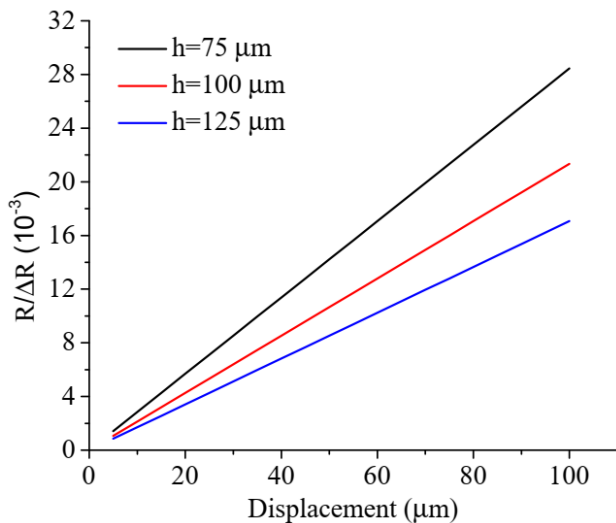


Figure 3. The relative change in resistance of gold thin film based piezoresistive sensor depends on the thickness of PDMS cantilever.

The mechanical deformation of the micro cantilever was also simulated by the finite element method. From equation 3, the surface stress change on the micro cantilever can be represented by a point load and we can simulate the deflection of the micro cantilever induced by the surface stress. Figure 4 shows the deflection of the micro cantilever under influence of surface stress of 0.9 N/m. The deflection of cantilever is normalized, the blue and red colors correspond to zero and maximum displacement, respectively. Normally, the surface stress on the cantilever is in the orders of 10^{-3} -1 N/m [6]. We invest the displacement of the micro cantilever with the change in surface stress, as shown in figure 4. With thinner cantilever has larger displacement at the same surface stress and the displacement can reach about 230 μm at surface stress of 0.1 N/m with 75 μm thick cantilever.

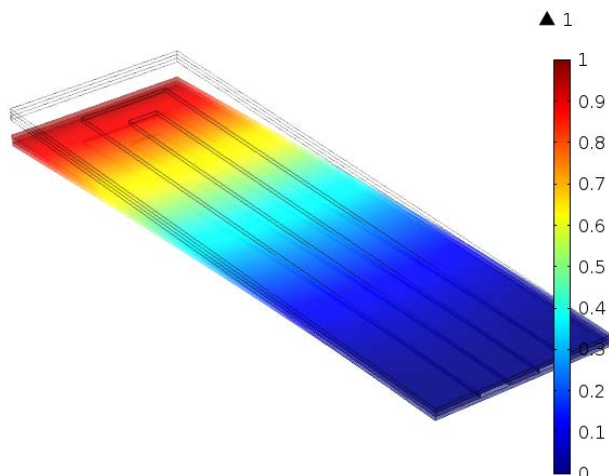


Figure 4. The deflection of the microcantilever under influence of surface stress at the microchannel.

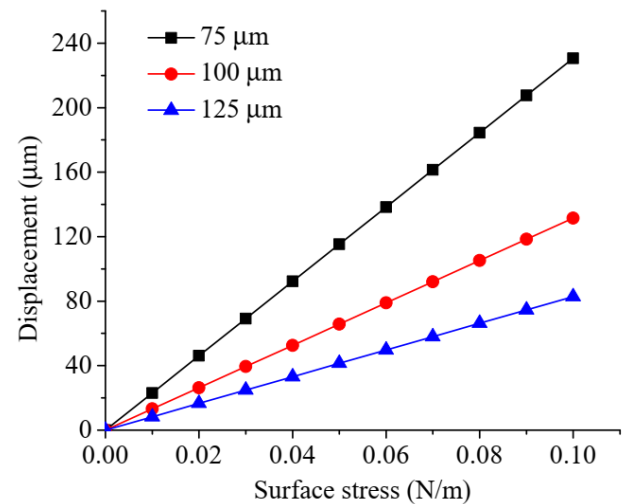


Figure 5. The displacement of the micro cantilever versus surface stress

From the simulation results, the stiffness values of 75 μm , 100 μm , and 125 μm thick cantilevers are 1.8×10^{-3} N/m, 4.2×10^{-3} N/m, 8.3×10^{-3} N/m respectively. The stiffness values are of the same order of stiffness values of commercially available micro cantilevers [9]. The sensitivity depending on the stiffness can be increased by reducing the thickness of cantilever. However, with too low stiffness, the micro cantilever can be bent due to the weight of itself.

I. CONCLUSION

A PDMS microfluidic cantilever-based biosensor with integrated piezo-resistor has been introduced and simulated in the study. The design can enhance the sensitivity and reduce the size of micro cantilever biosensor. The simulation and calculation results show that the design is suitable for biological measurements.

REFERENCES

- [1]. M. Godin et al., "Cantilever-based sensing: The origin of surface stress and optimization strategies," *Nanotechnology*, vol. **21**, no. 7, 2010.
- [2]. Y. T. Yang, C. Callegari, X. L. Feng, K. L. Ekinici, and M. L. Roukes, "Zeptogram-scale nanomechanical mass sensing," *Nano Lett.*, vol. **6**, no. 4, pp. 583–586, 2006.
- [3]. T. P. Burg et al., "Vacuum-Packaged Suspended Microchannel Resonant Mass Sensor for Biomolecular Detection," vol. **15**, no. 6, pp. 1466–1476, 2006.
- [4]. J. Thaysen, A. D. Yalçinkaya, P. Vettiger, and A. Menon, "Polymer-based stress sensor with integrated readout," *J. Phys. D. Appl. Phys.*, vol.

- 35, no. 21, pp. 2698–2703, 2002.
- [5]. H. SadAbadi and M. Packirisamy, “*Nano-Integrated Suspended Polymeric Microfluidics (SPMF) Platform for Ultra-Sensitive Bio-Molecular Recognition of Bovine Growth Hormones*,” *Sci. Rep.*, vol. **7**, no. 1, pp. 1–10, 2017.
- [6]. R. Mathew and A. Ravi Sankar, “*A Review on Surface Stress-Based Miniaturized Piezoresistive SU-8 Polymeric Cantilever Sensors*,” *Nano-Micro Lett.*, vol. **10**, no. 2, pp. 1–41, 2018.
- [7]. M. Calleja, P. A. Rasmussen, A. Johansson, and A. Boisen, “*Polymeric mechanical sensors with piezoresistive readout integrated in a microfluidic system*,” *Smart Sensors, Actuators, MEMS*, vol. **5116**, p. 314, 2003.
- [8]. J. Thaysen, A. Boisen, O. Hansen, and S. Bouwstra, “*Atomic force microscopy probe with piezoresistive read-out and a highly symmetrical Wheatstone bridge arrangement*,” pp. 47–53, 2000.
- [9]. Micromotive GmbH, “*Duo - / Octosensis Micro Cantilever Arrays*,” p. 62780, 2012.

NANO-BIO-LIPID BILAYERS AS VARIABLE CAPACITORS RESONATE WITH HELICAL MYELIN PROTEINS: A NANO APPROACH

Majid Monajjemi^{1,2}, Azadeh Shekarabi¹, Maryam Otadi¹, Azam Ghadami¹,
Afshar Alihosseini¹, Thu Thi Pham², Fatemeh Mollaamin²

¹Department of Chemical Engineering, Central Tehran Branch, Islamic Azad University, Tehran, Iran

²Institute for Nanotechnology (INT), Vietnam National University - Ho Chi Minh City (VNU-HCM), Ho Chi Minh City, Vietnam

Email: smollaamin@gmail.com

ABSTRACT

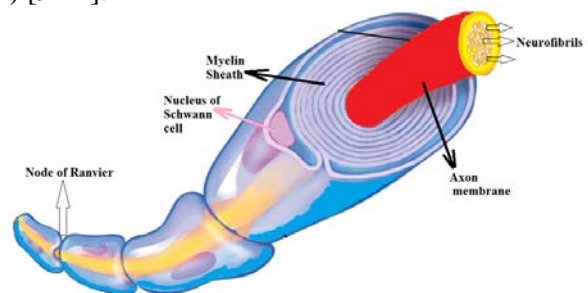
The model of this work represents electrophysiological occurrences with combination some phospholipids such as POPC and galactocerebroside lipid bilayers as variable capacitors. The quantum effects of different thicknesses in the mixed membranes of GalC/POPC, Galc/ POPE and Galc/DPPC have also been specifically investigated. It is shown that quantum effects can appear in a small region of free spaces within the membrane thickness due to the number and type of lipid's layers. In presence of the external factors such as protein transmembrane and myelin proteins as a resistance, the forces can influence the state of the membrane which results in a variable capacitance behavior. This allows introducing a capacitive susceptibility which can be resonating with self-induction of helical coils in myelin proteins, the resonance of which is the main reason for various biological pulses.

Keywords: lipid bilayers, cell membrane capacitors, GalC, POPC, DPPC, POPE, myelin-sheath.

INTRODUCTION

Myelin consists of fatty molecules (lipids) which are located in the CNC (central nervous system) and as an insulator around nerve cell axons increase the velocities information to transit from one nerve cell to another tissue [1,2] like an electrical wire (the axon) with insulating material (myelin) around it [1]. In other words, reducing axonal membrane capacitance through insulating the axon increases the action potential due to large distances between the cations on the outside of the axon and Na^+ that move through the axonal cytoplasm (axoplasm) [3]. Since the length neither of NOR (around one micron) compare to adjacent long myelinated internodes (around one millimeter) is too much shorter (1000 times), suddenly an electrical signal in a critical point between insulated myelinated towards uninsulated of unmyelinated stimulates the release of a chemical message or neurotransmitter that binds to receptors on the adjacent post-synaptic cell at specified area called synapses [4,5]. The insulating structure for myelin is important for hearing, seeing, feeling, sensation of pain and as well as perception, knowledge and memory. Therefore, multiple sclerosis which specifically affects the central nervous system is related to

disordering of myelin [6,7]. The major operation of myelin is providing acceleration to electrical impulses propagate along the myelinated fiber [8]. Although in unmyelinated fibers, electrical impulses move as continuous waves, in myelinated fibers they are propagated via saltatory conduction which is faster than continues wave. Myelin reduces the capacitor capacitance consequently enhances the electrical resistance across the axonal membrane (Scheme 1) [9-12].



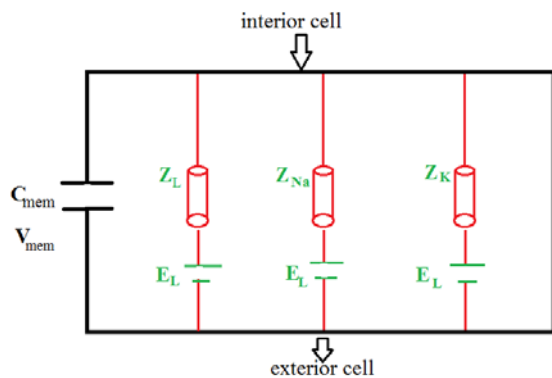
Scheme 1. A part of Neuron including myelin-sheath, Node of ranvier and Neurofibrils.

Neurons transmit information by an electrical impulse which works as action potential and has a velocity between 1 and 100 m/s. Neurons receive the pulses from dendrites and propagate the pulses with axon and connect

to other cells via synapses electrically or sometimes chemically, therefore there are various neurons in viewpoint of shapes, sizes, and electrochemical properties which generally contain a nucleus and organelles surrounded by membranes. The membranes are a combination of a lipid bilayer whose proteins are embedded inside glycolipids.

Electromechanical pulses

In an ionic exchange, the net current could be separated into 1- fast inward current carried by Na^+ ions, and 2- slow activated outward current carried by K^+ ions [13] which are results from independent permeation mechanisms for sodium and potassium ions in the membrane. This approach is known as ionic hypothesis (Scheme 2) [14]. Various ion currents contribute to the voltage signal of a neuron which 3 of them are major including sodium current, potassium current, leak current that consists (mostly chloride ions) that their flow is controlled via their respective voltage's channels in a membrane. The semipermeable membrane segregates the interior section from the exterior cell.



Scheme 2. A circuit of membranes including capacitor and ligands, sodium and potassium channels as resistance.

I_{mem} is given by:

$$I_{mem}(t) = C_{mem} \frac{dV_{mem}}{dt} + Z_{Na}(V_{mem} - E_{Na}) + Z_K(V_{mem} - E_K) + Z_{Leak}(V_{mem} - E_{Leak})$$

where E_{Na} , E_K and E_{Leak} are the Nernst potentials of different ions. It also is given by equation $E_i = \frac{RT}{zF} \ln \frac{C_{out}}{C_{in}}$ where C_{out} and C_{in} are the concentrations of ions on the inner and outer side of the cell. This equation indicates that current flows due to diffusion along the

gradients (even in the absence of other external voltages). Consequently, if the external voltage is equal to the Nernst potential, no current flows. Using Kirchhoff's laws, "cable".

Membrane contains POPC, GalC, POPE and DPPC

The cable equation of currents for potential propagation along GalC of myelinated axons yields a dynamics behavior. By this works, a small piece of cell membrane including pure GalC, POPC, DPPC, POPE and also a mixing of GalC/DPPC, GalC/POPC and GalC/POPE with 50% mol ratio of each have been simulated for our model of membrane capacitors (Fig.1).

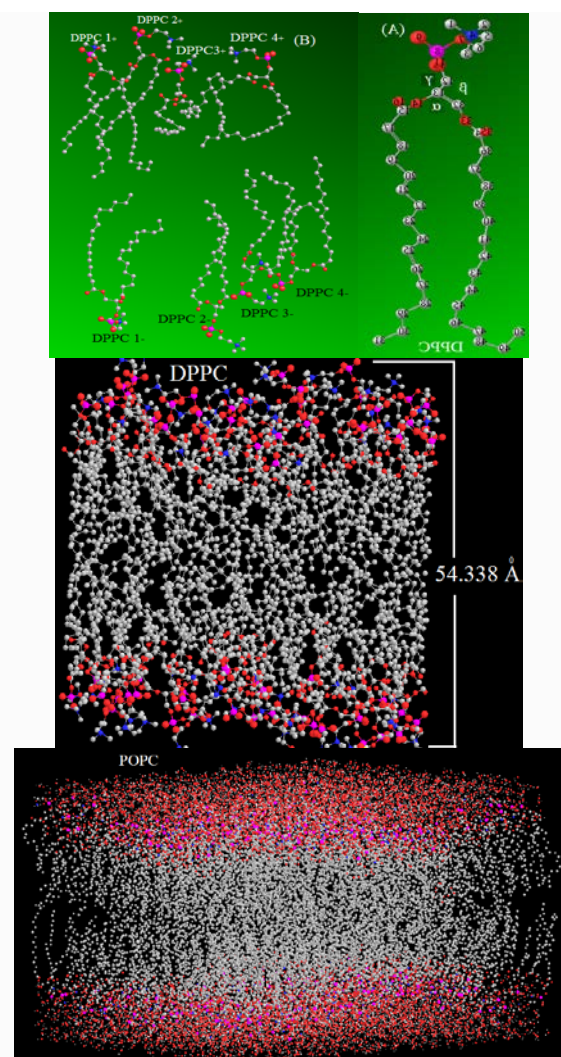
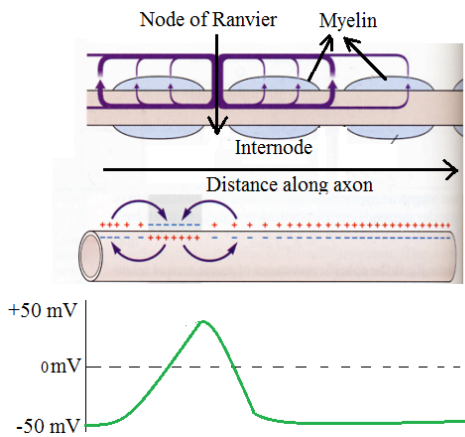


Figure 1. Monte Carlo calculation of various membranes including DPPC and POPC

Membrane capacitor model

Capacitance can be calculated from the rate and amplitude changes in the voltage responses based on voltage clamp. These ways are applied

widely to determine the total capacitance of several neurons membrane. By this work, we simulated our systems based on several membrane thicknesses in viewpoint of capacitors. In details, Glial cell wraps around axons a few times (30-150 times) this like adding 330 membranes in the series. Therefore, through myelination the diameter of axon increases and speed of conduction increased by diameter of axon. In addition, potential action is related to $\frac{1}{r_a C_{membrane}}$ (scheme 3).



Scheme 3. Voltages changing of Myelin along axon.

Generally, only two or three terms adequately describe $V_{mem}(t)$ (Fig.2). Through dividing “ I_{ext} ” to a series of the resistive terms as $R_i = \frac{V_i}{I_{ext}}$ steady state can be evaluated as the sum of these resistive terms “ $R_{in} = \frac{\Delta V_{mem}}{I_{ext}}$ ”. The time constant of the slowest exponential ($e^{-t/\tau} \rightarrow 0$) corresponds to the membrane time constant $\tau_m = r_m C_m$ [15].

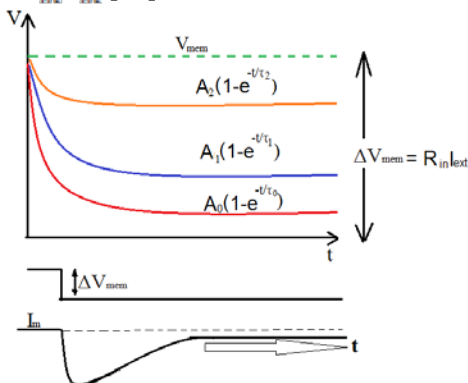


Figure 2. Schematic diagrams representing the membrane potential change, voltage-clamp step and the charge deposited on the membrane for a given “ V_{mem} ”.

It is also exhibited that the quantum effects are able for changing the membrane’s capacitances due to the external effects. In addition, it is also concluded that the electrical properties of the membranes are affected via the application of electron densities in the above mentioned membranes. In our previous works, it has been declared [36- 65] that the quantum components are a manifestation of the density of states (Dos) of the phosphate or galactose groups and their Thomas-Fermi screening lengths. Hence, the hybrid capacitance of any Nano-capacitor architecture is as follows:

$$C_{mem} = \left(\frac{1}{c_{mem}^{Qua}(\text{one hand})} + \frac{1}{c_{mem}^{geo}} + \frac{1}{c_{mem}^{Qua}(\text{opposite hand})} \right)^{-1}$$

where $c_{mem}^{Qua}(\text{top side})$ and $c_{mem}^{Qua}(\text{down side})$ are the quantum capacitances due to the finite Dos of the phosphate group’s electrodes, respectively, as illustrated in Fig. 3.

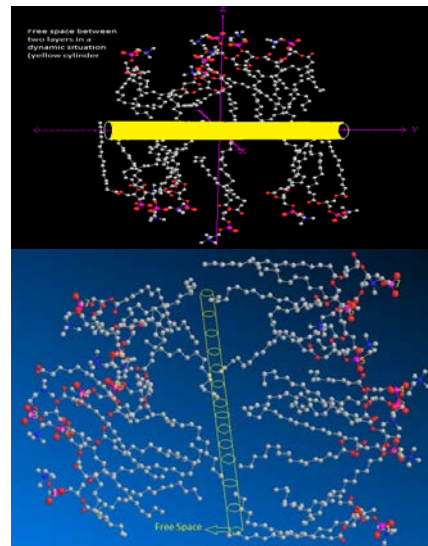


Figure 3. Free space between two layers in a dynamic situation due to tunneling coulomb blockade effect.

A change in voltage leads to a capacitive current due to the changes in the charge on the capacitor which is given by: $\frac{dQ}{dt} = \frac{d}{dt} [(C_{mem} \cdot V_{mem})] = C_{mem} \frac{dV_{mem}}{dt} + V_{mem} \frac{dC_{mem}}{dt}$ and $\frac{dC_{mem}}{dt} = f\left(\frac{dC_{mem}^{geo}}{dt}, \frac{dC_{mem}^{Qua}}{dt}\right)$.

Heimburg exhibited that the changing voltages during the nerves pulses are completely

dependent to the capacitances changing. In addition, transition voltages are able to exchange the ions. They have also exhibited how the electrical properties of the membranes are affected through the application of lateral pressure or tension in a membrane. Consequently, It can be considered that any changing in the dimension of the membrane through electrical phenomenon depends on C_{mem}^{qua} (and independent to C_{mem}^{geo}) which means tunneling effect changing due to the dynamic system in fluid mosaic model of membrane.

COMPUTATIONAL DETAILS

The final parameterization of GalC/DPPC, GalC/POPC and GalC/POPE were computed using self-consistent field calculations in order for finding the optimal pre-geometries, as well as the total and partial charges of each side of membranes. DFT or density functional theories with the van der Waals interaction were applied to model the exchange-correlation energies of DPPC monomers. All optimization of monomer molecules of each membrane were performed through Gaussian 09. The main focus in this study is to obtain the results from DFT methods such as m062x, m06-L, and m06 for the (Myelin's lipids molecules) $n \{n=1-10\}$. The m062x, m06-L and m06-HF are advanced and novel functional with a suitable correspondence in non-bonded calculations between GalC/DPPC, GalC/POPC and GalC/POPE monomers and are useful for determining the voltages in viewpoint of distance differences distance between two lateral in two sides of Myelin's lipids. For non-covalent interactions between two layers of membranes, the B3LYP method is not suitable for describing van der Waals forces via medium-range interaction.

RESULTS AND DISCUSSION

We used model descriptive structures of several membranes including GalC/DPPC, GalC/POPC and GalC/POPE with the simplest consisting of two spheres attached to the related ends of a cable, which denote a neuritis (l_{length} & $d_{diameter}$). We modeled variations in neuronal component size through changing l_{length} & $d_{diameter}$.

The fatty acid's chains layers give negative amplitude which decreases rapidly if the layers

are uniform and less rapidly if the terminal methyl groups are localized near the center, in order to give a narrow area of lower electron densities. In this work, GalC/DPPC, GalC/POPC and GalC/POPE were chosen as the mixed membranes capacitors since the alkyls groups are an excellent space filling, similar to that of biological system. Since the alkyl chains in those membranes have an ideal electrical insulator that might be polarized through applying the external electrical fields, the expected thickness of alkyl's layers between those membranes plates have been estimated, optimized and applied as an excellent model of dielectric constant for those capacitances calculations (Table 1).

Table 1. Dielectric constant, capacitance and the stability energies of various modeled membrane capacitors in various thicknesses for GalC/DPPC capacitor.

GalC/DPPC & Number of atoms	ΔE_2 (eV)	$\Delta V = \Delta(\sum V_i^{1/n})$	$\Delta Q = \Delta(\sum Q_i^{1/n})$	expectation of dielectric thickness	C_2 (F) $\times 10^{12}$	Dielectric Constant
(N=50)	0.0	-	-	-	-	-
(N=100)	+0.30	3.5	1.12	39.33	2.1	7.23
(N=200)	+1.25	3.2	1.42	38.23	4.7	7.15
(N=400)	0.95	4.9	1.63	40.31	1.2	6.13
(N=500)	+0.65	5.4	1.65	39.01	1.4	5.82
(N=600)	0.45	5.6	1.85	39.44	1.3	5.39
(N=3000)	1.45	5.75	1.90	40.25	1.3	6.29

Same as other capacitors, the an-isotropic attachment of alkyl groups allow the formation of several layered structures. Long-ranges interlayers interactions play a prevailing role in characterizing the electrical and mechanical properties of those systems and hence their efficiency in these model of capacitors. The ESP curve is drawn versus the number of lipids in where the minimum values of the ESP correspond to the odd numbers of lipids. However, as for the even numbers, the ESP values are constant, indicating that the variable capacitances in those membranes are independent of number of lipids. Which means, what make the cell membranes for acting as a model of variable capacitors do not related to the internal structures, though; they depend on the external cellular effects same as electrical situations and any other pulses. The interaction energy between two sides of membrane (P_{+30} , P_{-}

30) of the electrodes) is also calculated based on. The dielectric permittivity as a function of capacitor sizes were calculated using QM/MM methods (Table 2).

Table 2. The dielectric and capacitance C_Q = quantum capacitance, C_g = geometry capacitance, and C_{net} = net capacitance, of modeled of GalC/DPPC capacitor in various thicknesses.

GalC/DPPC & Number of atoms	$C_Q(F) \times 10^{20} = \frac{\Delta q(Q + \frac{\Delta q}{2})}{\Delta E_g}$	$C_{net}(F) \times 10^{20} = \frac{C_g C_Q}{C_g + 2C_Q}$
	ESP Mulliken	ESP Mulliken
(N=500)	1.45	1.30
	1.55	1.25
(N=600)	1.15	1.03
	1.38	0.97
(N=2000)	1.66	1.17
	1.83	1.20
(N=3000)	1.43	0.99
	1.56	0.99

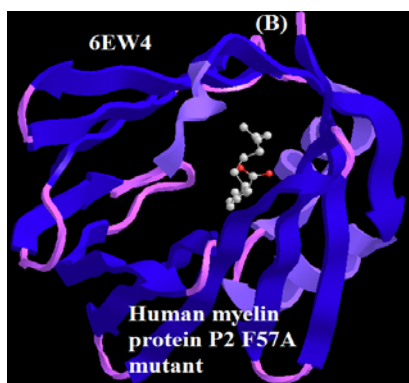
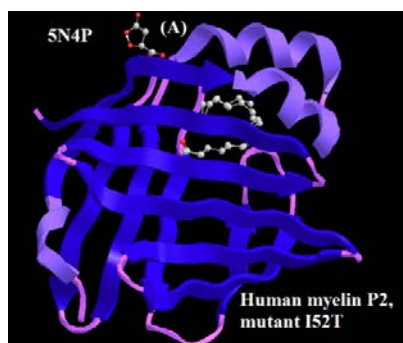


Figure 4. (A) Charcot-Marie-Tooth neuropathy linked to mutations in human myelin protein P2. (B) Structure of a human myelin protein P2, indicate opening of the beta barrel in fatty acid binding proteins

The nano-capacitances of C_g , C_Q and C_{net} for GalC/DPPC, GalC/POPC and GalC/POPE in different thickness of dielectrics are listed in

table 2. Although the dielectric strength can be deduced from the band gap of alkyl space filler, the dielectric constant is directly calculated which is much more accurate than the other ways. For large dielectric thicknesses, the classical capacitances of the " $C_g \propto \frac{1}{d}$ " is conformable. This conformability is not valid for short distances due to the quantum effect, therefore the dielectric permittivity as a function of dielectric size has been defined through,

$$C_Q(F) \times 10^{20} = \frac{\Delta q(Q + \frac{\Delta q}{2})}{\Delta E_g} \text{ and } C_{net}(F) \times 10^{20} = \frac{C_g C_Q}{C_g + 2C_Q}$$

It has been shown in this study that quantum effect has appeared in a small region of the membrane thickness due to number of lipid bilayers. In the presence of external fields via protein trace membrane or channel ions, charges employ those forces that can influence the state of the membrane in Myelin; thereby influencing the variable fields makes a variable capacitance. This effect allows one to introduce a capacitive susceptibility that resonates with self-induction effect of helical coils (Fig.4).

Acknowledgment

This research is funded by Vietnam National University – Ho Chi Minh city (VNU-HCM) under the grand number TX2019-32-01.

References

- [1]. A.I. Boullerne, The history of myelin. *Experimental Neurology*, **2016**, 283(Part B): 431–45.
- [2]. J. L. Salzer, Clustering sodium channels at the node of Ranvier: close encounters of the axon-glia kind". *Neuron*. **1997**, 18 (6): 843–846.
- [3]. M. Monajjemi, Cell membrane causes the lipid bilayers to behave as variable capacitors: A resonance with self-induction of helical proteins, *Biophysical Chemistry*, **2015**, 207, 114-127.
- [4]. M.Swire M, C. French-Constant, Seeing Is Believing: Myelin Dynamics in the Adult CNS. *Neuron*. **2018**, 98 (4): 684–686.
- [5]. R.A. Hill, A.M. Li, J.Grutzendler, Lifelong cortical myelin plasticity and age-related degeneration in the live mammalian

- brain". *Nature Neuroscience*. **2018**, 21 (5): 683–695.
- [6]. E. G. Hughes, J. L. Orthmann-Murphy, A. J. Langseth, D.E Bergles, "Myelin remodeling through experience-dependent oligodendrogenesis in the adult somatosensory cortex". *Nature Neuroscience*. **2018**, 21 (5): 696–706.
- [7]. D.K. Hartline, "What is myelin?" *Neuron Glia Biology*. **2008**, 4 (2): 153–63.
- [8]. J.L.Salzer, B. Zalc, "Myelination". *Current Biology*. **2016**, 26 (20): R971-R975.
- [9]. L. Steinman, "Multiple sclerosis: a coordinated immunological attack against myelin in the central nervous system". *Cell*. **1996**, 85 (3):299–302.
- [10]. J.M.Greer, M.B. Lees, "Myelin proteolipid protein-the first 50 years". *The International Journal of Biochemistry & Cell Biology*. **2002**, 34 (3): 211–5.
- [11]. C.S. Raine, "Characteristics of Neuroglia". In Siegel GJ, Agranoff BW, Albers RW, Fisher SK, Uhler MD (eds.). *Basic Neurochemistry: Molecular, Cellular and Medical Aspects (6th ed.)*. Philadelphia: Lippincott-Raven. **1999**
- [12]. M.R.Kaplan, M.H.Cho, E.M. Ullian, L.L.Isom, S.R.Levinson, B.A. Barres, "Differential control of clustering of the sodium channels Na(v)1.2 and Na(v)1.6 at developing CNS nodes of Ranvier". *Neuron*. **2001**, 30: 105–119.
- [13]. A.L.Hodgkin, A.F.Huxley, Currents carried by sodium and potassium ions through the membrane of the giant axon of Loligo, *J. Physiol*. **1952**, 116, 449–472.
- [14]. M.Haeusser, The Hodgkin-Huxley theory of the action potential, *Nat. Neurosci*, **2000**, 3, 1165.
- [15]. W.R.Holmes, I.Segev, W.Rall, Interpretation of time constant and electronic length estimates in multi cylinder or branched neuronal structures. *J Neurophysiol*, **1992**, 68: 1401–1420.

IMPACTS OF COPPER-CONTAINING PRECURSORS USED IN THERMAL SHOCK METHOD ON THE PHOTOCATALYTIC ACTIVITY OF Cu-MODIFIED ZnO NANOPARTICLES

The Luan Nguyen¹, Tien Khoa Le¹, Torben Lund², Huu Khanh Hung Nguyen¹, Thi Kieu Xuan Huynh¹

¹VNUHCM - University of Science, 227 Nguyen Van Cu Street, Dist.5, Ho Chi Minh City, Vietnam

²Department of Science and Environment, Roskilde University, 4000 Roskilde, Denmark

Email: htkxuan@hcmus.edu.vn

ABSTRACT

Cu-modified ZnO photocatalysts were prepared by thermal shock method with different copper-containing precursors ($\text{Cu}(\text{NO}_3)_2$, $\text{Cu}(\text{CH}_3\text{COO})_2$, CuSO_4) in order to study the impacts of thermal shock method on the photocatalytic activity of ZnO under both UVA light and visible light irradiation. The influences of copper-containing precursors on the crystal structure, morphology, surface structure and surface composition were investigated by X-ray diffraction, transmission electron microscopy and X-ray photoelectron spectroscopy. The UVA-light and visible-light-induced photocatalytic activities were evaluated through the degradation of methylene blue. According to the experimental results, ZnO catalysts modified with $\text{Cu}(\text{NO}_3)_2$ and $\text{Cu}(\text{CH}_3\text{COO})_2$ exhibited higher performance than unmodified ZnO, which may be explained by the formation of oxygen vacancies and Cu(I) species on the surface of modified oxides. However, when ZnO was modified by CuSO_4 , the absence of oxygen vacancies and the remaining of large sulfate ions on ZnO surface were supposed to be the factors decreasing its photocatalytic activity.

Keywords: ZnO; photocatalysis; surface modification; thermal shock; copper-containing precursors.

INTRODUCTION

During the past decade, doping with transition metals has been considered as one of potential methods to improve the photocatalytic activity of ZnO under UV and visible light illumination. Among different metals, various efforts were carried out to dope Cu into ZnO lattice since the radius of Cu^{2+} and Cu^+ ions are close to that of Zn^{2+} ions. It was reported that the insertion of Cu^{2+} ions and the substitution of Zn^{2+} by Cu^{2+} ions in ZnO lattice can decrease the recombination rate of electron-hole pairs [1,2], which enhances the photocatalytic performance of ZnO under UV light. However, the improvement in visible-light-induced activity by Cu-doping is still under debate. According to our best knowledge, there are very few works reporting the photocatalytic response of Cu-doped ZnO under visible light.

Recently, we have developed a new and simple method, called thermal shock method, which allows us to modify specifically the surface of ZnO photocatalyst [3]. In fact, the Ag-modified ZnO nanoparticles were successfully prepared by thermal shock method,

which created several silver species, such as Ag^0 and Ag^+ , on the surface of ZnO [3]. Nevertheless, silver and silver compounds are quite expensive, limiting the application of Ag-modified ZnO catalysts in practical waste-water treatment. Therefore, in this work, we proposed to use our thermal shock method to modify the surface of ZnO nanoparticles with copper compounds in order to improve their photocatalytic activity under UVA light and visible light. Moreover, since thermal shock is based on the short-time heat treatment, using copper-containing precursors ($\text{Cu}(\text{NO}_3)_2$, $\text{Cu}(\text{CH}_3\text{COO})_2$ or CuSO_4) with different thermal stability is expected to induce different impacts on ZnO nanoparticles.

EXPERIMENTAL

In our work, the photocatalysts were synthesized via a 2-step procedure: firstly, ZnO nanoparticles were prepared by a simple precipitation process with $\text{H}_2\text{C}_2\text{O}_4 \cdot 2\text{H}_2\text{O}$ as a precipitation agent, followed by a calcination at 500 °C during 2 h, then the products were surface-modified by thermal shock method with

different copper-containing precursors. Briefly, 0.5 g of ZnO nanoparticles were mixed with 10 mL of solution containing copper precursors ($\text{Cu}(\text{NO}_3)_2$, $\text{Cu}(\text{CH}_3\text{COO})_2$ or CuSO_4). The molar ratio of Zn to Cu of was held at 100:1. The as-obtained white suspension was dried at 150°C during 3. Next, the thermal shock was carried out by quickly depositing the samples into an electric furnace which was previously set up at 500°C and rapidly withdrawing the samples from the furnace after 5 min. Finally, the products were washed with distilled water, dried at 150°C for 1 h to obtain Cu-modified ZnO catalysts. The Cu-modified ZnO catalysts with $\text{Cu}(\text{NO}_3)_2$, $\text{Cu}(\text{CH}_3\text{COO})_2$ or CuSO_4 precursor were denoted as Cu-ZnO-ni, Cu-ZnO-ac and Cu-ZnO-su, respectively.

The catalysts were characterized by XRD, TEM, XPS techniques. Their photocatalytic activities of were studied via time-dependent degradation of methylene blue (MB) in aqueous solution under UVA/visible light irradiation. The details of chacracterization studies and photocatalytic tests can be found elsewhere [3].

RESULTS AND DISCUSSION

From Figure 1, all samples exhibit the diffraction peaks at 31.82° , 34.41° , 36.22° , 47.60° which are respectively assigned to the (100), (002), (101), (102) lines of ZnO zincite phase (space group P63mc, JCPDS file no. 36-1451).

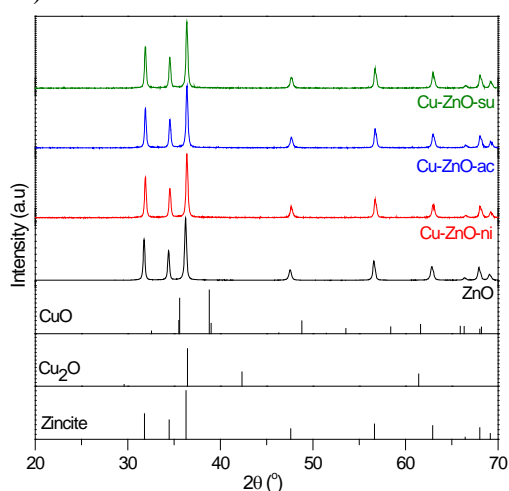


Figure 1: XRD patterns of catalysts.

These catalysts are composed of multi-dispersed particles in polyhedral shape with the particle size distribution of 20 – 80 nm (Figure 2). For Cu-ZnO-su, beside ZnO polyhedral particles, some tiny particles of 2 – 5 nm in size

appeared. Since these tiny particles were not observed in other modified ZnO samples, even in unmodified ZnO sample, their presence in Cu-ZnO-su might be attributed to the remaining of CuSO_4 nanocrystals on ZnO surface after the thermal shock process.

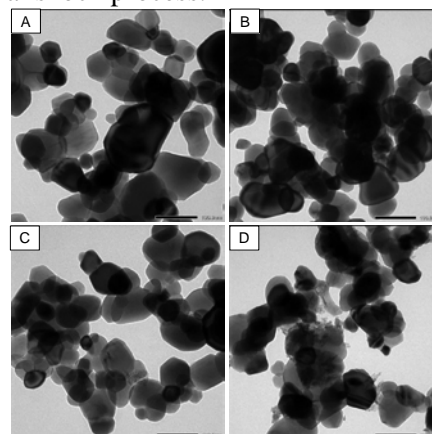


Figure 2: TEM images of (a) ZnO, Cu-ZnO-ni, (c) Cu-ZnO-ac and (d) Cu-ZnO-su.

As mentioned above, the surface composition and the chemical environment of all elements on the surface of our catalysts were characterized by X-ray photoelectron spectroscopy. Figure 3 presents the high resolution XPS spectra of Zn 2p region, taken on the surface of our catalysts.

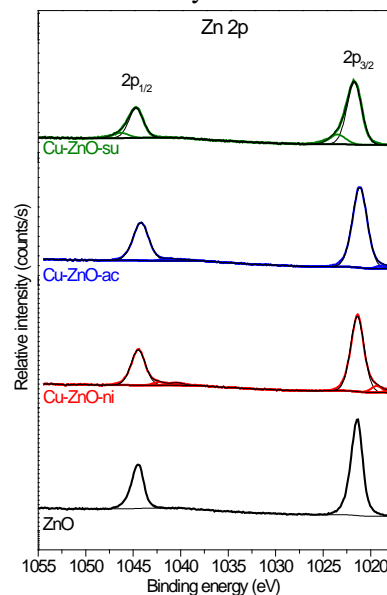


Figure 3: XPS Zn 2p spectra of catalysts.

Because of spin-orbit coupling, the Zn 2p core peaks of unmodified ZnO are composed of two components situated at 1021.4 (Zn $2p_{3/2}$) and 1044.5 eV (Zn $2p_{1/2}$), which are characteristic for the binding energies of Zn^{2+} in ZnO lattice. When ZnO was modified by $\text{Cu}(\text{NO}_3)_2$ or $\text{Cu}(\text{CH}_3\text{COO})_2$ by thermal shock

method, the main components of Zn 2p core peaks are not altered. However, beside each main component, two minor peaks are detected at lower binding energies (about 1019.3, 1017.6 eV for Zn 2p_{3/2} and 1040.4, 1042.2 eV for Zn 2p_{1/2}), which could be attributed to zinc ions in lower oxidation state or in oxygen deficient regions. However, both Zn 2p_{3/2} and Zn2p_{1/2} peaks of Cu-ZnO-su sample are found to contain two components: (i) the main spin-orbit coupling peaks at 1021.7 and 1044.7 eV are still indicative of Zn²⁺ ions in ZnO lattice, (ii) the weak spin-orbit coupling peaks at 1023.4 and 1046.3 eV are assigned to Zn²⁺ ions in ZnSO₄ environment.

Figure 4a exhibits the high resolution Cu 2p spectra of our catalysts. For Cu-ZnO-ni, Cu-ZnO-ac samples, two main spin-orbit coupling peaks are observed at 932.4 (Cu 2p_{3/2}) and 953.0 eV (Cu 2p_{1/2}), followed by their satellite peaks at 7.5 eV above the 2p_{3/2} and 2p_{1/2} peak positions. The binding energies of these peaks are representative of Cu⁺ ions [4], which indicates that the thermal shock degradation of Cu(NO₃)₂ and Cu(CH₃COO)₂ can create Cu(I) species on the surface of ZnO. In contrast, the Cu 2p spectrum of Cu-ZnO-su sample shows the main Cu 2p core peaks at 933.3 (Cu 2p_{3/2}) and 953.5 eV (Cu 2p_{1/2}), with their satellite peaks at 942.7 and 962.2 eV, respectively. From the literature, these peaks can be assigned to the Cu²⁺ ions [5].

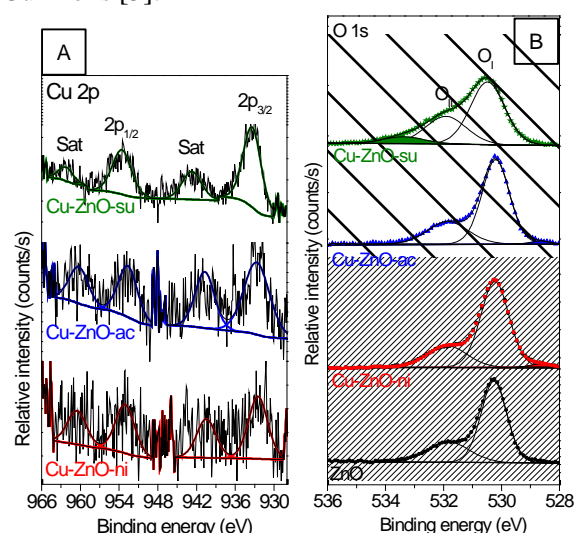


Figure 4: XPS Cu 2p (a), O 1s (b) spectra of catalysts.

The O 1s spectrum (Figure 4b) of unmodified ZnO sample shows an asymmetric peak which can be deconvoluted into two peaks: the major peak (O_I) at 530.2 eV corresponding

to O²⁻ ions in ZnO lattice and the minor peak (O_{II}) at 531.8 eV assigned to surface hydroxyl groups. For Cu-ZnO-ni and Cu-ZnO-ac, an additional peak (O_{III}) was detected at 528.6 eV, which may be attributed to the oxygen ions situated in the zinc-excessive regions. However, for Cu-ZnO-su sample, the O 1s spectrum depicts an addition peak (O_{IV}) with higher binding energy (533.3 eV) which could be assigned to water molecules adsorbed on oxide surface.

Table 1 shows the O_{I+III}/Zn and O_{II}/Zn atomic ratios calculated from corresponding XPS peak area. The unmodified ZnO presents the O_{I+III}/Zn atomic ratio of 1.00, fitting with the stoichiometric O/Zn atomic ratio in the ZnO formula. For Cu-ZnO-ni, Cu-ZnO-ac samples, both O_{I+III}/Zn and O_{II}/Zn atomic ratios decreased, which suggests the decrease of surface hydroxyl groups and the formation of oxygen vacancies on the surface of ZnO. Nevertheless, when ZnO was modified with CuSO₄, the O_{I+III}/Zn atomic ratio of this sample is identical to that of unmodified ZnO, indicating the absence of oxygen vacancies on its surface.

Table 1: Atomic ratios from XPS of catalysts

Sample	ZnO	Cu-ZnO-ni	Cu-ZnO-ac	Cu-ZnO-su
O _{I+III} /Zn	1.00	0.94	0.97	0.99
O _{II} /Zn	0.41	0.32	0.38	0.52

In this work, all our catalysts depict the MB degradation in UVA and visible light region with different pseudo-first-order rate constants (Table 3). Under UVA light and visible light illumination, the rate constants of unmodified ZnO catalyst were found to be 3.19 h⁻¹ and 0.16 h⁻¹, respectively. The photocatalytic performance was improved for Cu-ZnO-ni, Cu-ZnO-ac samples. Among them, Cu-ZnO-ni sample showed the highest rate constants for MB degradation, which are about 2.0 times (k = 6.45 h⁻¹) and 1.4 times (k = 0.22 h⁻¹) higher than those of unmodified ZnO under UVA light and visible light, respectively. However, when ZnO was modified with CuSO₄, both UVA-light-induced and visible-light-induced activities dramatically decreased.

Table 2: Rate constants of MB degradation

Sample	ZnO	Cu-ZnO-ni	Cu-ZnO-ac	Cu-ZnO-su
k_{app} under UVA (h^{-1})	3.19	6.45	5.36	1.50
k_{app} under Vis (h^{-1})	0.16	0.22	0.18	0.06

Since no modification in crystal structure and morphology was observed in our Cu-ZnO-ni, Cu-ZnO-ac and Cu-ZnO-su samples, their evolution of photoresponsive activities should be explained by surface characterization studies. Both $Cu(NO_3)_2$ and $Cu(CH_3COO)_2$ have low decomposition temperatures ($< 500^\circ C$). Hence, the thermal shock at $500^\circ C$ is able to provoke the decomposition of $Cu(NO_3)_2$ and $Cu(CH_3COO)_2$ on the surface of ZnO nanoparticles, which may induce the formation of oxygen vacancies (proved by XPS) on the surface of Cu-ZnO-ni and Cu-ZnO-ac samples. In the literature, it has been well reported that surface oxygen vacancies act as electron acceptors during the photocatalytic process, which helps to decrease the recombination rate of photo-generated charge carriers [6]. Furthermore, the formation of surface oxygen vacancies may also create new donor energy levels below the conduction band of ZnO [7], inducing the visible light absorption of ZnO. Besides, it is surprising that our XPS studies also revealed the formation of Cu(I) species on the surface of Cu-ZnO-ni and Cu-ZnO-ac, instead of Cu(II) species. The reason why Cu(I) was formed after the thermal shock of ZnO with $Cu(NO_3)_2$ and $Cu(CH_3COO)_2$ is still unclear, but its presence should induce some impacts on photocatalytic activity.

In contrast, the modification of ZnO with $CuSO_4$ by thermal shock method is not able to create the oxygen vacancies or other disturbances on the surface of ZnO. This can be explained by the high decomposition temperature of $CuSO_4$ ($> 700^\circ C$, which is superior to the thermal shock temperature used in our work. Thus, $CuSO_4$ is not decomposed during the thermal shock process, which was proved by the existence of sulfate ions on ZnO surface.

CONCLUSION

In our work, ZnO photocatalysts were modified by thermal shock method with different copper-containing precursors. The

experimental results showed that the surface modification with $Cu(CH_3COO)_2$ and $Cu(NO_3)_2$ can improve the UVA-light and visible-light induced activity of ZnO. The enhanced photocatalytic activity should be attributed to the formation of oxygen vacancies and Cu(I) species on the surface. In contrast, the photocatalytic activity dramatically decreased when ZnO was modified with $CuSO_4$ by thermal shock method, which may be related to the presence of sulfate species on the oxide surface.

Acknowledgment

This research is funded by Vietnam National Foundation for Science and Technology Development (NAFOSTED) under grant number 104.03-2016.43.

References

- [1] M. Fu, Y. Li, S. Wu, P. Lu, J. Liu, F. Dong, *Sol-gel preparation and enhanced photocatalytic performance of Cu-doped ZnO nanoparticles*, Applied Surface Science, **258** (2011) 1587–1591.
- [2] A.N. Kadam, T.G. Kim, D.S. Shin, K.M. Garadkar, J. Park, *Morphological evolution of Cu doped ZnO for enhancement of photocatalytic activity*, Journal of Alloys and Compounds, **710** (2017) 102–113.
- [3] H.T.P. Nguyen, T.M.T. Nguyen, C.N. Hoang, T.K. Le, T. Lund, H.K.H. Nguyen, T.K.X. Huynh, *Characterization and photocatalytic activity of new photocatalysts based on Ag, F-modified ZnO nanoparticles prepared by thermal shock method*, Arabian Journal of Chemistry, (2018) in press.
- [4] P. Lazcano, M. Batzill, U. Diebold, P. Haberle, *Oxygen adsorption on Cu/ZnO(0001)-Zn*, Physical Review B, **77** (2008) 035453.
- [5] B.E. Goodby, J.E. Pemberton, *XPS Characterization of a commercial Cu/ZnO/Al₂O₃ catalyst: effect of oxidation, reduction, and the steam reformation of methanol*, Applied Spectroscopy, **42** (1988) 754–760.
- [6] C. Wang, D. Wu, P. Wang, Y. Ao, J. Hou, J. Qian, *Effect of oxygen vacancy on enhanced photocatalytic activity of reduced ZnO nanorod arrays*, Applied Surface Science, **325** (2015) 112–116.
- [7] Q. Zhang, M. Xu, B. You, Q. Zhang, H. Yuan, K. Ostrikov, *Oxygen vacancmediated ZnO nanoparticle photocatalyst for degradation of methylene blue*, Applied Sciences, **8** (2018) 353 (1-12).

STUDY ON SIMULATION OF SILICON PIEZORESISTIVE STRAIN SENSOR SENSITIVE TO UNIAXIAL STRAIN

Nguyen Chi Cuong¹, Lam Minh Thinh¹, Trinh Xuan Thang¹, Le Quoc Cuong², Ngo Vo Ke Thanh¹, Maxime Progetti¹ and Susumu Sugiyama¹

¹ Research Laboratories of Saigon High-Tech-Park, Lot I3, N2 street, Saigon High-Tech-Park, District 9, Ho Chi Minh city, 700000, Vietnam;

² Department of Information and Communications, Ho Chi Minh City, Vietnam, 59 Ly Tu Trong, Ben Nghe Ward, District 1, Ho Chi Minh City, Vietnam

Email: cuong.nguyenchi@shtplabs.org; lequoccuong@tphcm.gov.vn

ABSTRACT

To improve the sensitivity of sensors, a Silicon Piezoresistive MEMS Strain Sensor is simulated and studied. A structure of micro-beam is used to amplify uniaxial stress or strain in one single direction only when a material object is subjected by a uniaxial tension loading. The studied strain sensor utilizes the piezo-resistive properties of a doped *n*-single crystal silicon sensing element to detect change of stress or strain. The 2D structure of the strain sensor is studied and simulated using Finite Element Method (FEM). Thus, the longitudinal and transverse stress or strain distributions of MEMS strain gauge are evaluated in *x* and *y* directions, respectively. Also, the stress disturbance problem is considered and discussed to obtain a homogeneous stress sensitivity of MEMS strain gauge. The results of the finite element model of this structure indicate that the longitudinal gauge factor along the strain beam will be enhanced considerably, while the transverse gauge factor along the strain beam is almost unchanged in the whole structure of MEMS strain gauge.

Keywords: MEMS strain sensor, SHMS, piezoresistive, Stress, Silicon

INTRODUCTION

The stress is one of the most important parameters to judge the health of a structure. High-performance of Micro-Electro-Mechanical-Systems (MEMS) strain sensors are highly desirable for advanced applications in the Structural Health Monitoring Systems (SHMS) [1].

Typically, the strain sensor is made by a very thin layer of metal or semiconductor materials [2]. The conventional strain sensor is made by a very thin layer of metals (such as Au [3] and Cu [4]). These conventional metal strain sensors still suffer from limited sensitivity, large temperature dependence, and high power consumption. In order to improve the sensitivity of these sensors, MEMS based piezo-resistive strain gauges with higher sensitivity can be designed and fabricated by using semiconductor materials such as silicon [5, 6]. Thus, MEMS strain sensors become more attractive due to higher sensitivity, low noise, better scaling characteristics, low cost, and less complicated conditioning circuit [7].

A key requirement of MEMS strain sensors is to design for high sensitivity to measure the stress or strain of materials in uniaxial direction to ensure higher accuracy and sensitivity of MEMS strain sensors. Hautamaki et al. [8] proposed some structures for MEMS strain gauge such as thin monofilament, cantilever beam and curved beam. Also, Cao L et al. 2000 [9] introduced a geometry of thin membrane is used to amplify the strain in thin membrane to be higher than the strain in the surrounding silicon. Mohammed et al. 2011 [10, 11] proposed trench structures etched in vicinity of sensing elements to create stress concentration regions. All sensors used a piezoresistive element to respond for uniaxial tension loading and detect for directions of strain when the device is deformed.

In this study, a new structure of micro-strain beam type of MEMS strain gauge is proposed to amplify the stress and strain on the wafer in only one direction. The sensor is proposed and verified using Finite Element Methods (FEM) in the commercial software of COMSOL Multiphysics [12]. Thus, the longitudinal and

transverse stress distributions of MEMS strain gauge are evaluated in x and y directions, respectively. Finally, the longitudinal and transverse gauge factors (GF) of MEMS strain gauge can be obtained in wide range of dimensions of strain beam. The obtained results of this work can be used to design higher sensitivity of MEMS strain gauges to detect the stress on the object materials in only one single direction.

MATERIALS AND METHODS

In this simulation, we proposed a 2D structure of MEMS strain gauge with a strain beam with the BOX (SiO_2) and device (Si) layers is completely glued on a material object with the applied tension load to measure the stress and strain distributions of a material object. A piezoresistive resistor (PZR) layer of sensing element along the $\langle 100 \rangle$ -direction for n -type of silicon of MEMS strain gauge can be implemented at the strain beam of strain gauge to measure the stress and strain distributions of a material object. For the boundary setting, one side of material object is applied by a distributed tension load (T_{input}) and an opposite side of material object is applied with a fixed boundary condition as showed in figure 1(a). The operating condition of a MEMS strain gauge is showed in table 1. For the mesh setting, a triangular mesh configuration with 48141 of the number of elements is used to refine the mesh density along the whole structure of MEMS strain gauge and the material object as showed in figure 1(b). The stress and strain distributions of MEMS strain gauge can be obtained by solving the 2D structure of MEMS strain gauge with the Stationary Solver of the Structure Mechanics model in the MEMS Modulus of the COMSOL Multiphysics [12]. The so-called gauge factor (GF) of strain gauge can be calculated as below

$$GF = \frac{1}{\varepsilon} \frac{\Delta R}{R} \quad (1)$$

Where ε is the strain ($\mu\varepsilon$), ΔR is the resistance (Ω), and R is the change in resistance (Ω).

The change in resistance (ΔR) obtain the famous form of piezoresistance effect [13]:

$$\frac{\Delta R}{R} = \pi_l \sigma_l + \pi_t \sigma_t \quad (2)$$

Where σ_l and σ_t are the longitudinal and transverse stress component, respectively. π_l and π_t are the longitudinal and transverse piezoresistive coefficients, respectively.

A numerical evaluation for the longitudinal and transverse coefficients of piezoresistance along the $\langle 100 \rangle$ -direction for n -type silicon [14] gives:

$$\begin{cases} \pi_l |_{\langle 100 \rangle} = \pi_{11} = -102.2 \times 10^{-11} / Pa \\ \pi_t |_{\langle 100 \rangle} = \pi_{12} = 53.4 \times 10^{-11} / Pa \end{cases} \quad (3)$$

Table 1. The basic geometric conditions of MEMS strain gauge used in COMSOL Multiphysics [12].

Description	Name	Value
Beam length	L_{beam}	500 μm
Beam width	W_{beam}	60 μm
Beam thickness	T_{beam}	300 μm
Device layer thickness	T_{device}	20 μm
Applied tension load	T_{input}	50 MPa
Young's modulus of Si	E_{Si}	130 GPa
Poisson's ratio of Si	ν_{Si}	0.28
Density of material of Si	ρ_{Si}	2330 kg/m^3

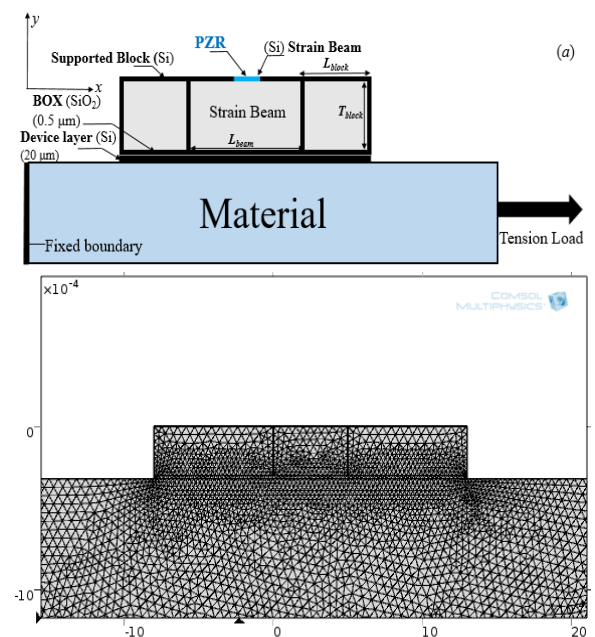


Figure 1. (a) A 2D structure of the MEMS strain gauge glued on a material; (b) Mesh setting in COMSOL Multiphysics [12].

RESULTS AND DISCUSSION

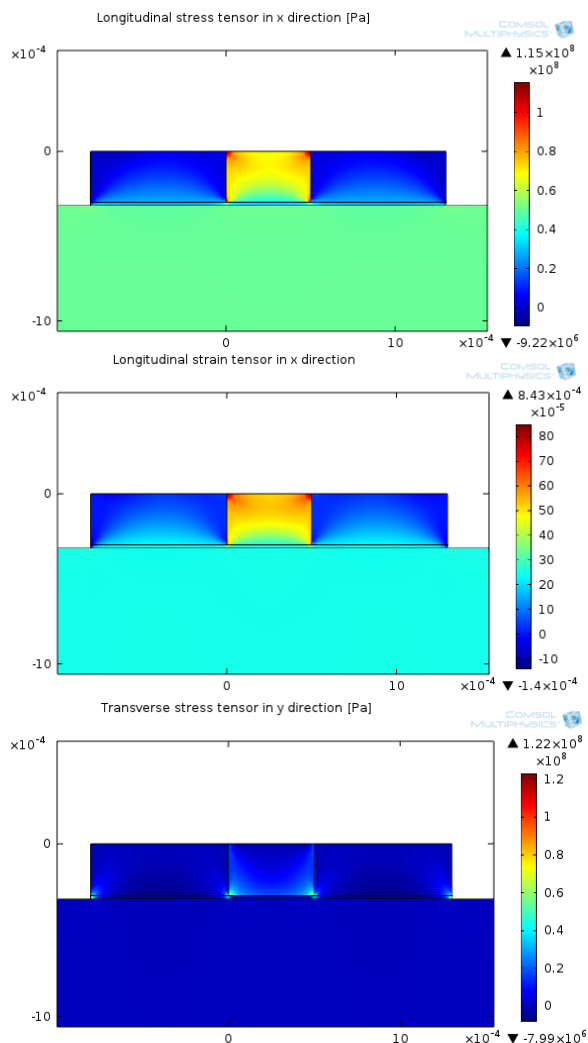


Figure 2. (a) The longitudinal stress (σ_{xx}), (b) longitudinal strain (ϵ_{xx}), and (c) transverse stress (σ_{yy}) of MEMS strain gauge plotted by 2D FEM.

In figure 2(a), the longitudinal stress (σ_{xx}) of MEMS strain gauge in x direction is plotted in the 2D FEM. The results showed that σ_{xx} of strain beam enhances significantly. In figure 2(b), the longitudinal strain (ϵ_{xx}) also enhances significantly along the strain beam of MEMS strain gauge. While, the transverse stress (σ_{yy}) in y direction is almost unchanged along the whole structure of MEMS strain gauge in figure 2(c). The inhomogeneous stress and strain sensitivities of MEMS strain gauge can be explained by the stress disturbance problem from the corners and device layer. Thus, to avoid the stress disturbance problem on MEMS strain gauge, the length (L_{beam}) must be much greater than width (W_{beam}) and thickness (T_{beam})

of strain beam ($L_{beam} \gg W_{beam} \ \& \ T_{beam}$) to reduce the stress disturbance problem from the corners and device layer.

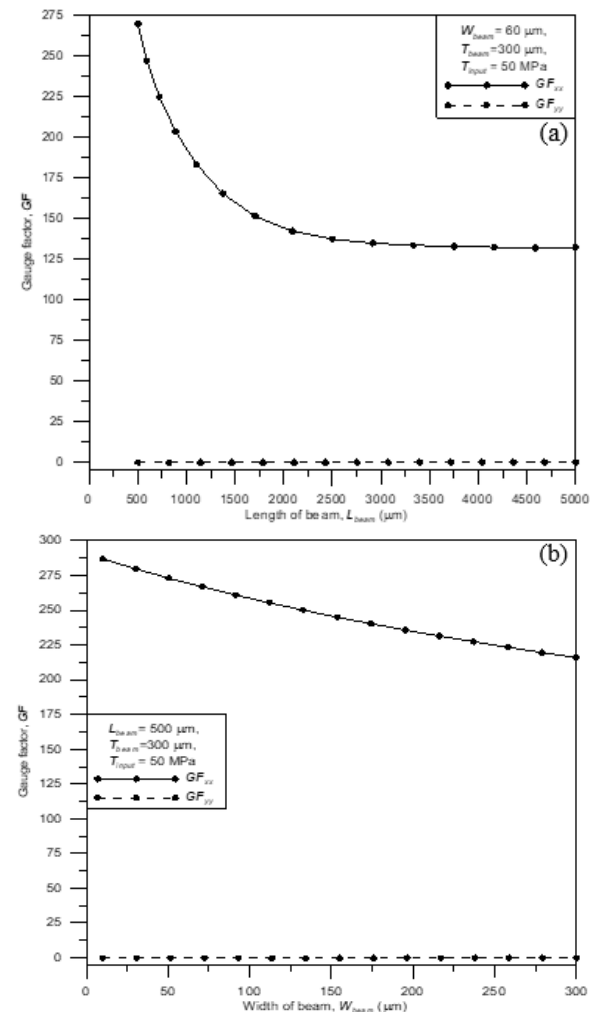


Figure 3. (a) Longitudinal and transverse Gauge factor (GF_{xx} and GF_{yy}) is plotted with different (a) length (L_{beam}), (b) width (W_{beam}) of the strain beam of MEMS strain gauge.

In figure 3, the longitudinal and transverse gauge factors (GF_{xx} and GF_{yy}) of the strain beam are plotted with the different length (L_{beam}), and width (W_{beam}) of the strain beam of MEMS strain gauge. The results showed that GF_{xx} increases significantly as L_{beam} decreases as showed in figure 3(a). GF_{xx} increases as W_{beam} decreases as showed in figure 3(b). While, GF_{yy} is almost zero in wide range of dimensions of beam (L_{beam} , and W_{beam}). Thus, the beam type structure of MEMS strain gauge can be applied to design a MEMS strain sensor to detect uniaxial stress and strain.

CONCLUSION

In this study, a new structure of micro-strain beam type of MEMS strain gauge is proposed and simulated by the 2D FEM in the COMSOL Multiphysics to detect uniaxial stress and strain on the material object. Some remarkable results are found as below:

1) The longitudinal stress and strain are significantly amplified along the strain beam. While, the transverse stress is almost unchanged along the whole structure of MEMS strain gauge.

2) The longitudinal gauge factor significantly increases in x direction, while the transverse gauge factor is almost zero in wide range of dimensions (length, width) of strain beam conditions.

Thus, the obtained results can be applied to design a higher sensitivity of MEMS strain gauge to detect uniaxial stress and strain.

Acknowledgment

This research was supported by the annual projects of The Research Laboratories of Saigon High Tech Park in 2019 according to decision No. 102/QĐ -KCNC of Management Board of Saigon High Tech Park and contract No. 01/2019/HĐNVTX-KCNC-TTRD (Project number 2).

References

- [1] H. N. Li, T. H. Yi, L. Ren, D. S. Li, L. S. Huo, *Reviews on innovations and applications in structural health monitoring for infrastructures*, Structural Monitoring and Maintenance **1** (2014) 1-45
- [2] A. Barlian, W. T. Park, J. R. Mallon, A. J. Rastegar, B. L. Pruitt, *Review: Semiconductor Piezoresistance for Microsystems*, Proc. of the IEEE 2009 513-552
- [3] K. Rajanna, S. Mohan, *Longitudinal and transverse strain sensitivity of gold film*, Journal of Materials Science Letters **6** (1987) 1027-1029
- [4] K. Rajanna, S. Mohan, *Studies of meandering path thin film strain gauge*, Sensors and Actuators A: Physical **15** (1988) 297-303
- [5] A. S. Mohammed, W. A. Moussa, E. Lou, *Mechanical Strain Measurements Using Semiconductor Piezoresistive Material*, Proc. The 2006 International Conference on MEMS, NANO and Smart Systems 2006 5-6
- [6] J. Rausch, P. Heinickel, R. Werthschuetzky, B. Koegel, K. Zogal, P. Meissner, *Experimental comparison of piezoresistive MEMS and fiber Bragg grating strain sensors*, Proc. the IEEE Sensors 2009 Conf.—SENSORS 2009, New Zealand: Christchurch 2009 1329-1333
- [7] J. Fraden, *Handbook of modern sensor: physics, designs, and applications*, AIP Press- Springer: New York 1996
- [8] Hautamaki, S. Zurn, S. C. Mantell, D. L. Polla, *Experimental evaluation of MEMS strain sensors embedded in composites*, Journal of Microelectromechanical Systems **8** (1999) 272-279
- [9] L. Cao, T. S. Kim, S. C. Mantell, D. L. Polla, *Simulation and fabrication of piezoresistive membrane type MEMS strain sensors*, Sensors and Actuators A: Physical **80** (2000) 273-279
- [10] A. S. Mohammed, W. A. Moussa, E. Lou, *High-Performance Piezoresistive MEMS Strain Sensor with Low Thermal Sensitivity*, Sensors **11** (2011), 1819-1846
- [11] A. S. Mohammed, W. A. Moussa, E. Lou, *High Sensitivity MEMS Strain Sensor: Design and Simulation*, Sensors **8** (2008) 2642-2661
- [12] COMSOL 5.4 2018 COMSOL Multiphysics <https://www.comsol.com/>. June 4, 2019
- [13] Y. Kanda, *Piezoresistance effect of silicon*, Sensors and Actuators A: Physical **28** (1991) 83-91
- [14] W. G. Pfann, R. N. Thurston, *Semiconducting Stress Transducers Utilizing the Transverse and Shear Piezoresistance Effects*, Journal of Applied Physics **32** (1961) 2008-2019

ORAL SESSIONS

NANOFABRICATION TECHNIQUES
(NFT)

STUDY ON THE PREPARATION OF SELENIUM NANOPARTICLES BY GAMMA CO-60 METHOD AND INVESTIGATE THE STABILITY

Ngoc Duy Nguyen¹, Van Phu Dang¹, Anh Quoc Le¹, T. Kim Lan Nguyen¹,
Quoc Hien Nguyen¹, T. Thu Ngan Tran²

¹Research and Development Center for Radiation Technology, 202A, Street 11, Thu Duc District, Ho Chi Minh City, Vietnam;

²University of Science, VNU-HCM, 227 Nguyen Van Cu, District 5, Ho Chi Minh City, Vietnam
Email: ngocduy158@gmail.com

ABSTRACT

Among nanoparticle materials, selenium nanoparticles (SeNPs) have attracted wide spread attention due to their excellent bioavailability, high bioactivity and low toxicity compared to other ionic selenium compounds. SeNPs with size ~ 41.75 nm were synthesized by γ -irradiation method using oligochitosan (OC) as stabilizer. The prepared SeNPs/OC were characterized by UV-Vis spectroscopy and transmission electron microscope (TEM) images. The SeNPs/OC powder was also prepared by spray drying technique and the purity was verified by energy dispersive X-ray (EDX) analysis. The results of EDX showed that SeNPs/OC solution was of high purity. The stability of SeNPs/OC solution was investigated. The results indicated that SeNPs/OC solution had good stability after 60 days of storage at 4°C. At ambient temperature, the SeNPs/OC solution was unstable and agglomerated after about 15 days. The SeNPs/OC synthesized by γ -irradiation with the advantages of environmental friendly and mass production process may be potentially promising for applications in medicines, functional food and in other fields as well.

Keywords: Selenium nanoparticles, γ -irradiation, oligochitosan

INTRODUCTION

Cancer is now the leading cause of death worldwide. According to estimation by the World Cancer Research Agency (IARC), there were 14.1 million new cancer cases and 8.2 million deaths in 2012. Radiotherapy and chemotherapy are still considered to be the most optimal measures, but they also cause many unwanted side effects such as the severely reduced number of blood cells, which can cause anemia and infection with opportunistic microorganisms caused by the weakened immune system [1]. Selenium is an important trace element, which has broad effects on biological systems, including antioxidant effect, cancer prevention and antiviral activity [8]. The necessary selenium content in the diet of adults is 50 - 200 $\mu\text{g/day}$ [2]. Compared to selenium in ionic form, SeNPs have higher bioavailability and lower toxicity [3]. Result of the previous studies showed that SeNPs have a much lower acute toxicity in mice with $\text{LD}_{50} \sim 91.2 \text{ mg Se/kg body weight}$ compared to methylselenocysteine with $\text{LD}_{50} \sim 14.6 \text{ mg Se/kg body weight}$ [4]. Recently, Zhai et al. [5] also reported that the LD_{50} for SeNPs for

Kunming mice was 258.2 mg/kg while the LD_{50} for H_2SeO_3 was 22 mg/kg. In addition, studies have shown that SeNPs were effective in treating cancer. Sonkusre et al. [6] have demonstrated that SeNPs were highly effective and specific against prostate cancer. Ali et al. found that mice supplemented SeNPs (50 - 80 nm) at a dose of 0.2 mg/kg body weight were able to fight lung cancer [7]. Faghfuri et al. [8] reported that breast tumor in mice supplemented with 200 μg SeNPs/day for 60 days was smaller than the control group that did not use SeNPs. Recently, Zhai et al. [6] also reported that the LD_{50} of SeNPs for Kunming mice was 258.2 mg/kg while the LD_{50} for H_2SeO_3 was 22 mg/kg.

Several methods have been applied to synthesize SeNPs from Se ions such as chemical reduction methods using ascorbic acid, glutathione, hydrazine hydrate, etc. as reducing agents [3, 4], biological methods. using bacterial biomass as a reducing agent [7, 8], the gamma Co-60 irradiation method used sodium dodecyl sulfate as a stabilizer and ethanol as a free radical capture agent [9, 10]. In particular, irradiation method is considered as an effective method to synthesize SeNPs with advantages

such as: (1) the reaction is performed at room temperature, (2) the efficiency of creating high SeNPs, (3) SeNPs are of high purity due to the absence of reductant residues, (4) easily adjust SeNPs particle size by changing the dose and dose rate, (5) capable of producing in large quantities [9, 10].

In this study, SeNPs were synthesized by gamma Co-60 irradiation method using OC as a stabilizer. The stability of SeNPs/OC solution during storage was investigated.

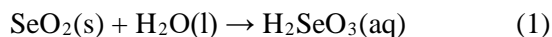
EXPERIMENTAL

Chemicals

Selenium dioxide (SeO_2) was of pure product of Merck, Germany. OC solution is a product of the Research and Development Center for Radiation Technology (VINAGAMMA) with the concentration of 3%, deacetyl $\sim 85\%$ and $M_w \sim 5000$ g/mol. Other chemicals were of pure grade. Distilled water was used throughout the experiments.

Preparation of SeNPs/OC by γ -irradiation

A required amount of SeO_2 was dissolved in 1% (w/v) OC solution to prepare selenous acid (H_2SeO_3) solution (eq. (1)) with concentration of 2.5 mM.



Irradiation of $\text{SeO}_3^{2-}/\text{OC}$ solutions to synthesize SeNPs was carried out on a Gamma Co-60 SVST at VINAGAMMA at dose of 20 kGy, with the dose rate of 1.3 kGy/h measured by a dichromate dosimetry system [10].

Characterization and stability of SeNPs/OC

The absorption spectra of OC and the resulted SeNPs/OC solutions were taken on an UV-Vis spectrophotometer model UV-2401PC

(Shimadzu, Japan). The size and size distribution of the SeNPs were characterized by TEM images on transmission electron microscope (TEM), model JEM1010 (JEOL, Japan) and statistically calculated from about 300 particles [10]. The SeNPs/OC powder was prepared by spray drying of 2.5 mM SeNPs/1% OC solution with spray dryer model ADL311 (Yamato, Japan). The content of selenium in SeNPs/OC powder was assessed by energy dispersive X-ray (EDX) spectroscopy on a JEOL 6610 LA. The stability of SeNPs/OC solution determined by changes in particle size with storage time.

RESULTS AND DISCUSSION

Characteristics of SeNPs /OC solution

Nano selenium was prepared by the gamma-Co-60 irradiation method with a dose of 20 kGy, using 2% OC as a stabilizer according to Hien et al. [10]. The UV-Vis spectra of OC, ion selenium and SeNPs/OC solutions, the color of the solution and the TEM image are shown in Figure 1. After irradiating, the color of $\text{H}_2\text{SeO}_3/\text{OC}$ solution turned from yellow orange to orange-red color that indicated the formation of SeNPs [10]. The formation of SeNPs is due to water radiolysis products (e^- , H^\bullet) to reduce Se^{4+} to Se^0 . However, the UV-Vis spectrum of SeNPs did not have typical adsorption peaks like other metallic nano such as silver ($\lambda_{\text{max}} \sim 400\text{-}500$ nm) and gold ($\lambda_{\text{max}} \sim 520\text{-}570$ nm). According to Lin and Wang [11], the SeNPs with diameter less than 100 nm do not have characteristic absorption peak (λ_{max}) in the UV-Vis region (200-800 nm). TEM images and the size distribution of SeNPs in Fig. 1 (A, a) showed that SeNPs are spherical morphology with average diameter calculated to be of 41.75 nm.

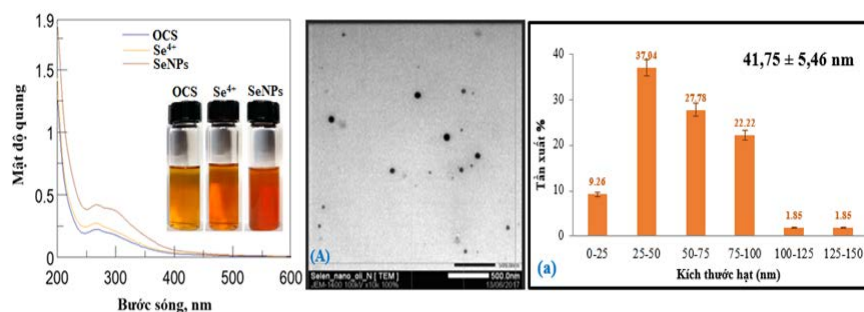


Figure 1. UV-Vis spectra of OC, ion selenium and SeNPs/OC solutions and TEM image, size distribution of SeNPs/OC solution

Stability of SeNPs/OC solution with storage time

The SeNPs after being formed will be stabilized by OC. Like other polysaccharides as alginate, dextran, gelatin, etc. OC has electron-rich functional groups such as $-NH_2$, $-OH$ groups that will stabilize SeNPs through coordinate bond and electrostatic repulsion. There are several factors that affect the stability of SeNPs solution such as H_2SeO_3 concentration, pH, stabilizer concentration, etc. [10, 11]. In particular, the temperature greatly affects the stability as well as the properties of SeNPs/OC solution. The change of color of SeNPs/OC solution during storage presented in Fig. 2. Results showed that at low temperatures ($4\text{ }^\circ\text{C}$) the color of SeNPs/OC solution remained almost unchanged over a 60-day period. Meanwhile, at 27°C , the color of the solution

changes markedly from light yellow to dark orange and coagulation happen after 25 days of storage.

TEM images and the size distribution of SeNPs/OC solution in Fig. 3 showed that SeNPs are spherical morphology with average diameter calculated to be of 41.75, 50.91, and 51.92 nm for different storage time (0, 30, and 45 days) at $4\text{ }^\circ\text{C}$, respectively. At $27\text{ }^\circ\text{C}$, SeNPs particle size increased faster than that stored at $4\text{ }^\circ\text{C}$. SeNPs particle size increased from 41.75 nm (0 days) to 115.09 and 125.75 nm, respectively, storage time of 30 days and 45 day (Fig 4). On the 45th day, the sample was coagulated and could not determine the particle size.

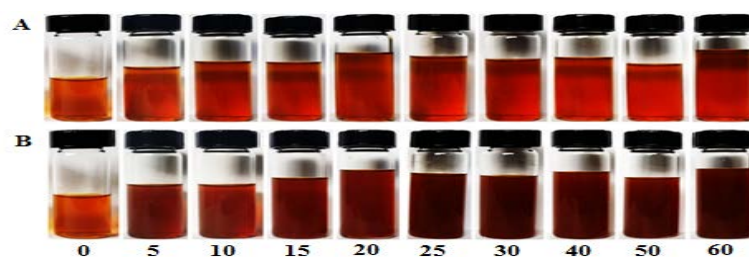


Figure 2. Color change of SeNPs / OC solution stored at 4°C (A) and 27°C (B) for 0 to 60 days

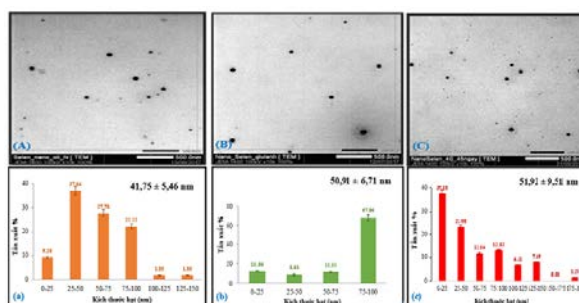


Figure 3. TEM image and size distribution of SeNPs / OC stored at 4°C at different time: 0 days (A, a); 30 days (B, b) and 45 days (C, c)

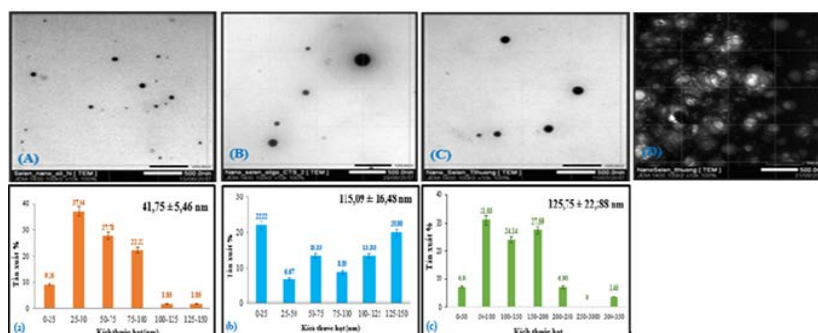


Figure 4. TEM image and size distribution of SeNPs / OC stored at 27°C at different time: 0 days (A, a); 15 days (B, b); 30 days (C, c) and 45 days (D)

The increasing size of SeNPs during storage time was also reported by Lin and Wang et al. [11]. From the above results, it can be seen that the appropriate temperature to store SeNPs/OC solution was 4°C. However, SeNPs/OC solution are not always convenient to transport. To overcome the limitation above as well as expand the scope of application, SeNPs in powder have been formed.

SeNPs/OC in powder was formed by spray drying method

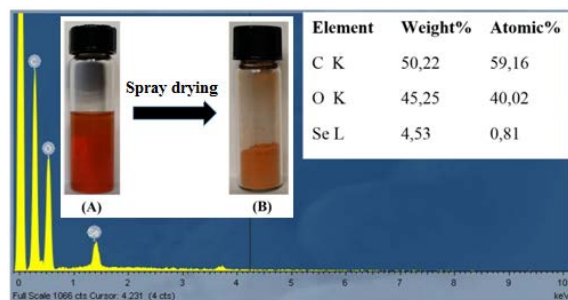


Figure 5. (A) SeNPs/OC solution, (B) SeNPs/OC powder and EDX spectrum of SeNPs/OC

The photograph and the EDX spectrum of SeNPs/OC powder prepared by spray drying technique were presented in Fig. 5. The EDX spectrum in Fig. 4 indicated that the SeNPs/OC powder contained only three elements namely selenium (2.51%), carbon (78.67%) and oxygen (18.82%). Thus, it can be deduced that SeNPs/OC powder prepared by spray drying technique from SeNPs/OC solution synthesized by gamma Co-60 ray irradiation was of high purity with composition only of SeNPs and OC.

CONCLUSION

SeNPs with concentration of 2.5 mM and diameter of ~42 nm stabilized in 2% OC solution were successfully synthesized by gamma Co-60 ray irradiation method. The appropriate temperature to store SeNPs/OC solution was 4 °C. SeNPs/OC powder with high purity was also prepared from SeNPs/dextran solution by spray drying technique. SeNPs/OC powder is potentially promising for use in injection or in oral administration for cancer therapy and for other purposes of application as well.

References

[1]. H.W. Tan, H.Y. Mo, et al., *Selenium Species: Current Status and Potentials in Cancer Prevention and Therapy*,

International Journal of Molecular Sciences **20** (2019) 1-26.

- [2]. S. Skalickova, V. Milosavljevic, et al. *Selenium nanoparticles as a nutrition supplement*, *Nutrition* **90** (2017) 83-90.
- [3]. J. Zhang, H. Wang, X. Yan, L. Zhang, *Comparison of short-term toxicity between nano-Se and selenite in mice*, *Life Sciences* **76** (2005) 1099-1109.
- [4]. J. Zhang, X. Wang, T. Xu, *Elemental selenium at nano size (nano-Se) as a potential chemopreventive agent with reduced risk of selenium toxicity: comparison with Se-methylselenocysteine in mice*, *Toxicological Sciences* **101** (2008) 22-31, 2008.
- [5]. X. Zhai, C. Zhang, G. Zhao, et al., *Antioxidant capacities of the selenium nanoparticles stabilized by chitosan*, *Journal of nanobiotechnology* **15:4** (2017).
- [6]. P. Sonkusre, R. Nanduri et al., *Improved extraction of intracellular biogenic selenium nanoparticles and their specificity for cancer chemoprevention*, *Journal of Nanomedicine & Nanotechnology* **5:2** (2014) 1000194.
- [7]. E.N. Ali, S.M. El-Sonbaty, F.M. Salem, *Evaluation of selenium nanoparticles as a potential chemopreventive agent against lung carcinoma*, *International Journal of Pharmaceutical Biological and Chemical Sciences*, **2** (2013) 38-46.
- [8]. E. Faghfuri, M.H. Yazdi, M. Mahdavi, Z. Sephezadeh, et al., *Dose-response relationship study of selenium nanoparticles as an immunostimulatory agent in cancer-bearing mice*, *Archives of medical research*, **46** (2015) 31-37.
- [9]. Y. Zhu, Y. Qian, H. Huang, M. Zhang, *Preparation of nanometer-size selenium powders of uniform particle size by γ -irradiation*, *Materials Letters*, **28** (1996) 119-122.
- [10]. N.Q. Hien, P.D. Tuan, D.V. Phu, L.A. Quoc et al., *Gamma Co-60 ray irradiation synthesis of dextran stabilized selenium nanoparticles and their antioxidant activity*, *Materials Chemistry and Physics*, **205** (2018) 29-34.
- [11]. Z.H. Lin, C.R.C. Wang, *Evidence on the size-dependent absorption spectral evolution of selenium nanoparticles*, *Material Chemistry and Physics* **92** (2005) 591-594.

ONE-STEP SYNTHESIS OF GOLD NANOSTAR BY USING CHITOSAN AS PROTECTING AGENT

Quoc Khuong Vo¹, Quynh Nhu Vo Nguyen², Phuong Phong Nguyen¹

¹Faculty of Chemistry, Ho Chi Minh City University of Science, Vietnam National University - Ho Chi Minh City, 225 Nguyen Van Cu Street, Ward 4, District 5, Ho Chi Minh City, Vietnam;

²Faculty of Materials Engineering, Ho Chi Minh City University of Technology, 268 Ly Thuong Kiet Street, Ward 14, District 10, Ho Chi Minh City, Vietnam

Email: vqkhuong@hcmus.edu.vn

ABSTRACT

In this paper, we reported a one-step synthesis procedure using chitosan and acid ascorbic for the preparation of gold nano-star. The size and shape of gold nano-star have been controlled based on changing the pH condition and the addition of chitosan. The multifunctional role of chitosan in the preparation route was also investigated to obtain the high yield (about 90 %) of gold nanostar. The particles size was ranging from 40 to 50 nm, and narrow size distribution. Gold nanostars were identified by UV-Vis spectroscopy, transmission electron microscopy (TEM), X-Ray Diffraction, dynamic light scattering (DLS) and zeta-potential. Fourier transform infrared spectroscopy (FT-IR) was used to characterize the interaction of chitosan functional group with the gold nanostars.

Keywords: gold nanostars, chitosan, one-step synthesis

INTRODUCTION

In recent years, gold nanostars have attracted great interest because of their unique optical, electronic, and catalytic properties. Star-like gold nanostructure becomes a promising candidate in various applications [1], for example, in catalysis, biosensor and cosmetic. For applying in the biological field, there are several important factors of synthesis gold nanostars should be considered: the green solvents used in the synthesis as well as the ecofriendly reducing agent and stabilizer. Although there were many reports on the controlled synthesis of gold nanostars, but to the best of our knowledge, very few studies in the one-step synthesis of star-shape gold nanostructure with natural polymer were examined. Thus, based on the understanding of the roles of composition for using in biological field purpose, we propose a new and facile preparation route of gold nanostars with a natural polymer instead of the conventional surfactants (CTAB, CTAC...) [2].

In particular, protecting agent is one of the crucial factors in controlling synthesis of gold nanostars, related to their stability in the reaction environment and the well-defined crystal

orientation properties. The specific properties of chitosan such as water solubility and nontoxicity make them feasible in a number of applications such as biomedicine and drug delivery. Furthermore, when interacted to the nanocrystal through the functional groups, chitosan exhibits its ability in preventing self-aggregation of the particles. As a natural polysaccharide, units of chitosan is composed of β -(1-4)-linked D-glucosamine (deacetylated unit) and N-acetyl-D-glucosamine (acetylated unit). Chitosan was widely known as a natural cationic biopolymer because of its excellent biocompatibility, biodegradability, and nontoxicity [3]. In this work, we have experimentally reported the synthesis of gold nanostars with the chemical reduction method by using ascorbic acid as reducing agent. In addition, the binding of natural polymer to the gold nanostars was also investigated, and the size of the AuNPs were about 55-60 nm.

EXPERIMENTAL

Materials

All reagents were of analytical grade and were used as received without purification. Tetrachloroauric (III) acid trihydrate ($\text{HAuCl}_4 \cdot 3\text{H}_2\text{O}$, 99.9%), acetic acid (CH_3COOH ,

99.5%), and ascorbic acid ($C_6H_8O_6$, 99.7%) were obtained from Merck (Darmstadt, Germany). Chitosan ($(C_{12}H_{24}N_2O_9)_n$, DD 75%) was purchased from Sigma-Aldrich (St. Louis, MO, USA).

Preparation of gold nanostars

Before synthesis, a certain amount of chitosan was dissolved in acetic acid solution 1.0 % (v/v) and stirred vigorously for 60 min at 70°C. In a typical experiment, 100 μ L of 25 mM HAuCl₄ solution was added into the mixture of chitosan acetic acid at 50°C and stirred at 700 rpm for 60 min. 0.5 mL aqueous solution of ascorbic acid 0.1 M was then added into the above mixture following by magnetically stirring at 500 rpm for 60 min. The total volume was adjusted to 10 mL by using DI water. Finally, the color of the colloidal solution changed from yellow transparent to purple pink, red, and dark-blue, predicted the formation of gold nanostars.

Characterization

The gold nanostar colloids were examined by UV-Vis absorbance spectroscopy on the UV-Vis-NIR-V670 spectrophotometer (JASCO, Japan), scanned wavelength between 300 and 800 nm with the rate of 200 nm per minute by using the 1-cm path length quartz cuvette. FTIR spectroscopy was investigated on a Tensor 27-Bruker spectrometer, the typical sample was prepared by mixing 3.00 ml colloids with KBr at ratio about 2-5%. The XRD technique was carried out by using D8 Advance-Bruker, Germany with Cu-K α radiation in the 2 θ between the 20° to 80° at 40 kV. The as-prepared gold nanostars colloids were centrifuged at the rate of 10000 rpm before dried under vacuum condition at room temperature. TEM images were obtained on a JEM-1400 (Japan) microscope operating at 200 kV. Small amount of AuNPs colloids were dropped onto the copper grids (300-mesh, Ted Pella, INC, Redding, CA, USA) and air-dried at room temperature. The TEM microphotograph was further examined statistically with the value of 200 particles to obtain the average diameter and size distribution of gold nanostars.

RESULTS AND DISCUSSION

The influence of pH condition

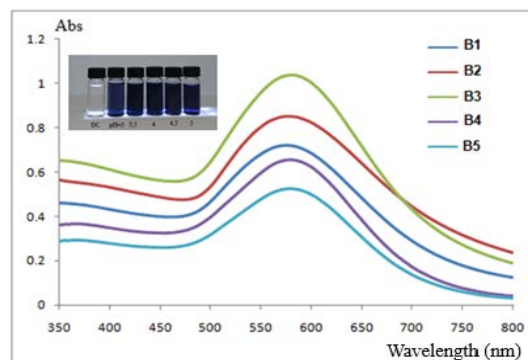


Figure 1. UV-Vis absorbance spectrum of gold nanostars synthesized by chitosan at different pH value (from 3.0 to 5.0)

Table 1. UV-Vis data of gold nanostars synthesized at different pH value from 3.0-5.0

Sample	pH value	wavelength (nm)	Intensity
B1	3.0	575	0.718
B2	3.5	576	0.851
B3	4.0	581	1.038
B4	4.5	578	0.656
B5	5.0	580	0.526

From the UV-Vis data (Fig. 1), it is revealed that the intensity of absorbance peaks at 580 nm remarkably increased when changed pH value from 3.0 to 4.0. This change indicated the growth of many star-shape particles, featured by the characteristic peaks at 581 nm. A change of absorbance wavelength from 575 to 581 nm also observed in the spectrum of gold nanoparticles, this red-shifted could be related to the formation of larger size particles [4]. Theoretically, the growth process of gold nanostars could be based on the generation and diffusion rate of growth species Au atom and the ascorbic acid form. At appropriate pH value, ascorbic acid stays at its protonate form, resulted the decrease of redox reaction rate, leading to the formation of gold nanostar.

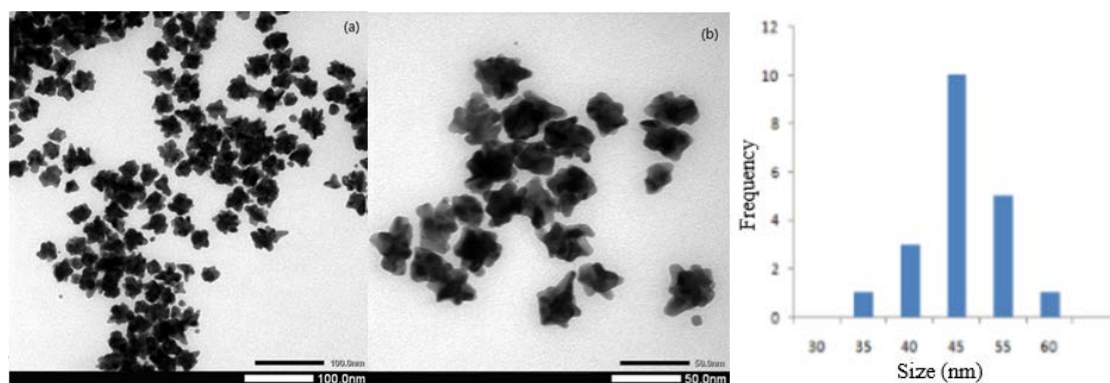


Figure 2. TEM image of gold nanostars prepared in the presence of chitosan (a) at pH 4.0 and (b) pH 5.0

In consistent with UV-Vis results, TEM images from Figure 2 showed that the formation of gold nanostars with the average size of 47.5 nm. Seemingly, the obtained star-shape particles tent to accumulate to a cluster along the polymeric chains of chitosan molecules. It was also implied that the interaction between the gold nanoparticles and the functional groups of chitosan.

X-Ray diffraction of gold nanostars

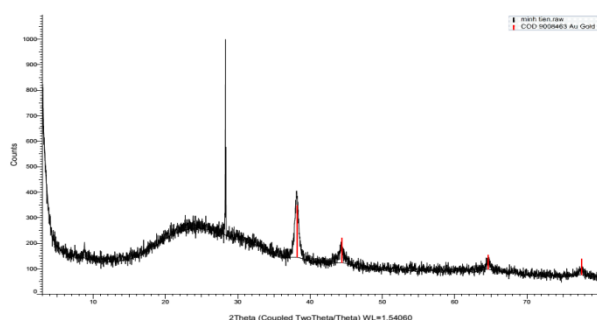


Figure 3. XRD pattern of gold nanostars stabilized at chitosan concentration of 0.045 % (w/v).

The XRD pattern of gold nanostars showed that the peaks obtained in 2- θ values of 39°, 44°, 65°, 78° (Fig. 3), featured respectively for {111}, {200}, {220}, and {311} facets of gold crystalline structure [5]. These results thus proved that the gold nanostars were made of pure gold and the broad peaks attributed to the small nanosize.

FTIR analysis of gold nanostar in the presence of chitosan

The absorbance peaks, located at the wavenumber of 3447 and 2991 cm^{-1} , assigned to the vibration of $-\text{NH}_2$, $-\text{OH}$ functional group of chitosan [6]. These peaks intensity decreased dramatically when synthesizing gold nanostars

(Fig 4.). The characteristic peaks of amine groups located at 1600 cm^{-1} , and $-\text{CONH}_2$ groups at 1657 cm^{-1} also dropped significantly in case of interaction with gold nanoparticles [6]. From the FTIR results, it is clearly demonstrated that the binding of the chitosan functional groups to the gold nanocrystal.

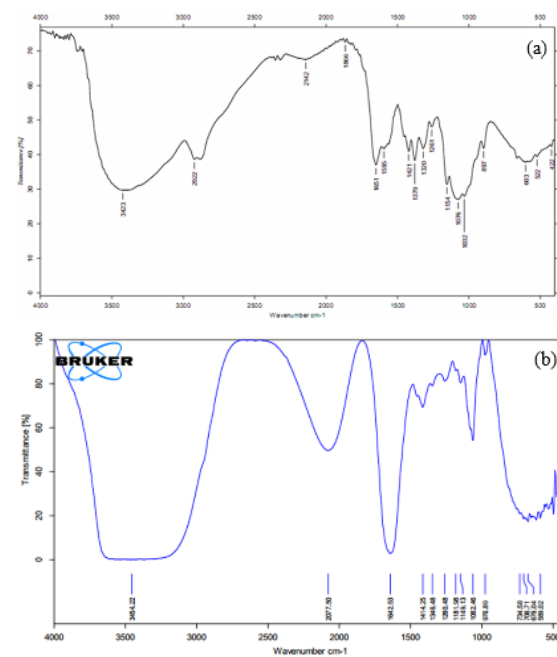


Figure 4. FTIR spectrum of (a) pure chitosan and (b) prepared gold nanostars in the presence of chitosan 0.045 %

CONCLUSION

In this work, gold nanostars were successfully synthesized by using one-pot reduction method with chitosan in adequate pH condition. The average diameter of nanostars was observed to be 55-60 nm with the SPR absorbance peaks ranging from 565-585 nm. Furthermore, the interaction of as-prepared gold nanostars with chitosan molecules has been also demonstrated.

References

- [1] Tolaymat, T.M.; Badawy, A.M.E.; Genaidy, A.; Scheckel, K.G.; Luxton, T.P.; Suidan, M. An evidence-based environmental perspective of manufactured silver nanoparticle in syntheses and applications: A systematic review and critical appraisal of peer-reviewed scientific papers, *Sci. Total Environ*, 2010, 408, 999-1006.
- [2] Ahmad, M.B.; Shameli, K.; Darroudi, M.; Yunus, W.M.Z.W.; Ibrahim, N.A. Synthesis and characterization of silver/clay/chitosan bionanocomposites by UV-irradiation method, *Am. J. Appl. Sci*, 2009, 6, 2030-2035.
- [3] Jayakumar, R.; Menon, D.; Manzoor, K.; Nair, S.V.; Tamura, H. Biomedical applications of chitin and chitosan based nanomaterials-A short review, *Carbohydrate Polymer*, 2010, 82, 227-232.
- [4] Hongtao Zhou, Han Jia, Ailing Zhang, Liping Zhang, Cunqi Jia, Liquiang Zheng, The inter-conversion between gold nanostars and gold nanodendrites controlled via temperature and concentration of sodium dodecyl sulfonate, *Journal of Molecular Liquids*, 2015, 208, 27-33.
- [5] Lehui Lu, Kelong Ai, and Yukihiro Ozaki, Environmentally Friendly Synthesis of Highly Mono-disperse Biocompatible Gold Nanoparticles with Urchin-like Shape, *Langmuir*, 2008, 24, 1058-1063.
- [6] Maragoni Venkatesham, Dasari Ayodhya, Alle Madhusudhan, Nagati Veera Babu, A novel green one-step synthesis of silver nanoparticles using chitosan; catalytic activity and antimicrobial studies, *Appl nanosci* (2012), 4: 113-119.

OPTIMIZED – POLYMER – COATED MAGNETIC NANOPARTICLES PREPARATION FOR USE AS AN ENHANCED OIL RECOVERY AGENT

^{1,2}Thi-Lieu Nguyen, ^{2,3}Duy-Khanh Pham, ³Xuan-Truong Mai, ²Anh-Quan Hoang and ^{4,2,3}Phuong-Tung Nguyen*

¹Industrial University of Hochiminh City, 12 Nguyen Van Bao, W. 4, Go Vap, Hochiminh City;

²Graduate University of Science and Technology, Vietnam Academy of Science and Technology, 1A TL 29, Dist. 12, Hochiminh City;

³Institute of Applied Materials Science, Vietnam Academy of Science and Technology, 1A TL 29, Dist. 12, Hochiminh City;

⁴Center for Interdisciplinary Research in Technology (CIRTech) -HUTECH University of Technology, 475A Dien Bien Phu, Dist. Binh Thanh, Hochiminh City
Email: phuongtungng@iams.vast.vn

ABSTRACT

Enhanced oil recovery (EOR) processes aim to recover trapped oil left in reservoirs after primary and secondary production stages. Dispersion of nanoparticles (NPs) with polymer chains grafted onto the surface (PNPs) could be an emerging injected agent due to their outstanding advantages compared with hard NPs and conventional chemical systems. The polymerization with monomers of methyl acrylate, methyl methacrylate and 2-acrylamido-2-methylpropan sulfonic acid on the ferromagnetic nanoparticles surface occurred via the free radical mechanism in microemulsion environment. The input data were optimized to give the optimized conditions. The appropriate temperature for polymerization was about 71°C and reaction time was 8 hours through calculation of orthogonal planning level 2 when with the mass percentage of co-polymer coated on MNPs surface about 12%. Characterization techniques, such as FTIR, XRD, DLS, TEM, TGA and VSM were conducted for the obtained PMNPs to confirm their surface identity, functionality, stability and morphology.

Keywords: Polymer coated magnetic nano particles, core shell structure, nanofluids, enhanced oil recovery.

INTRODUCTION

Energy is one of the determinants of the economic development and life of human society. Global energy demand was expected to increase by 2–3% annually in the coming decades and predicted to rise 50% after 20 years [1]. Fulfilling this demand for the economic development was one of most concerned problems.

So far, although many forms of renewable energy and alternative energy have been strongly invested, the majority of the energy used today and in the coming decades is fossil energy: petroleum and coal. Besides, oil and gas are an extremely important energy source for the chemical industry. Therefore, efficient and sustainable oil exploitation is always a prerequisite task of the oil and gas industry.

However, the discovery period of big and cheap oil fields is over and most of the big oil

fields in the world, especially in Vietnam, have gone through the peak period of exploitation and production has declined. With the current oil and gas exploitation techniques, after primary and secondary stages of exploitation, approximately 70% to 75% of the oil and gas deposits are left trapped in the reservoir [2,3].

Thus, the enhanced oil recovery (EOR) is an important and urgent field in the petroleum industry. There are more sophisticated approaches were needed for recovering the trapped oil from the pores and worms in reservoir solids. Therefore, the improved reservoir mapping and advanced production methods were necessary.

Nanotechnology has recently received high attention from the petroleum industry, and a decade's worth of nanotechnology development was poised to become a reality in the oil field. Specially, in EOR, it would help asymptotic to

exploit 10% more oil in place as mentioned above [4,5,6].

Magnetic nanoparticles (MNPs) surface-modified by different agents have been actively studied for biomedical applications, and investigation of their potential use in oil exploration, especially EOR has recently started. Besides the common advantages of nanoscale materials, MNPs could also be easily recovered and reused because of their magnetic responsivity. The surface of MNPs required modification to function as an EOR agent. The surrounding polymer layer enabled the particles to disperse in injected brine, to become compatible with oil and be stable at high temperatures, and resisted adsorption on the surface of the reservoir rock [7].

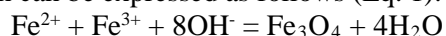
EXPERIMENTAL

Materials

Methyl methacrylate (MMA), sodium 2-acrylamido-2-methyl-propanesulfonate (AMPS), ferrous chloride tetrahydrate ($\text{FeCl}_2 \cdot 4\text{H}_2\text{O}$), Iron(III) chloride hexahydrate ($\text{FeCl}_3 \cdot 6\text{H}_2\text{O}$), oleic acid (98%), ammonium hydroxide (NH_4OH) (30%), ammonium persulfate ($(\text{NH}_4)_2\text{S}_2\text{O}_8$), Sodium dodecyl sulfate (SDS) and ethanol ($\text{C}_2\text{H}_5\text{OH}$) from Sigma Aldrich.

Synthesis of Fe_3O_4 Magnetic Nanoparticles (MNPs) and OMNPs.

MNPs were synthesized using the combined method of co-precipitation and microemulsion in the presence of SDS as surfactant. 4.75g $\text{FeCl}_3 \cdot 6\text{H}_2\text{O}$ and 1.75g $\text{FeCl}_2 \cdot 4\text{H}_2\text{O}$ (molar ratio 2:1) was dissolved in 80ml distilled water bubbled with nitrogen flow. Solution was carried in three-necked round-bottom flask and stirred in five minutes, the mixture was then heated gradually to 80°C in stirring condition (300 rpm). Subsequently, 7.5 ml of NH_4OH (30%) was added drastically into the solution. Black nanoparticles were precipitated. The reaction took place in 2h. N_2 gas is continuously bubbled during synthesis. The relevant chemical reaction can be expressed as follows (Eq. 1):



Add 1.5 ml oleic acid into the mixture and heated for 2h. The nanoparticles were isolated by centrifugation and washed with 20 ml of distilled water by magnetic decantation until the pH was neutral. Magnetic stirring speed,

temperature was maintained throughout the whole process.

Synthesis of OMNPs coated by copolymer of MMA and AMPS (PMNPs).

OMNPs (5.0950 g) were added to a three-necked round-bottom flask containing 40 ml of distilled H_2O . 0.0035 mol of 2-acrylamido-2-methylpropane sulfonic acid (AMPS) and 0.0035 mol methyl methacrylate (MMA) were fulfilled with water in 50 ml volumetric flask. Both of two flasks was stirred mildly for 30 minutes. After that, pouring the solution of 50ml volumetric flask into 250 ml three-necked round bottom flask. The mixture was sonicated and stirred with the speed of 100 rpm for 1.5 h at room temperature. Meanwhile, dissolving 1 g of ammonium persulfate ($(\text{NH}_4)_2\text{S}_2\text{O}_8$) was put into the 50 ml beaker containing 10 ml of distilled H_2O , then 0.5g SDS was added into this solution with the assistance of ultrasound for 1 h with vigorous stirring. Said solution was added dropwise with the adding speed of 0.5ml/min to three-necked round-bottom flask. The mixture was stirred, heated gradually to $T^\circ\text{C}$ with the assistance of ultrasound for t hours. Finally, the obtained mixture was decanted by using super magnet and washed 3 times with 50 ml of ethanol. The washing process stops if the color of decantation solution is transparent. The process will be repeated on the contrary to assure that the redundant polymer is eliminated fully the obtained materials. The final product was dried in an oven at 50°C overnight to yield OMNPs-MMA-co-AMPS.

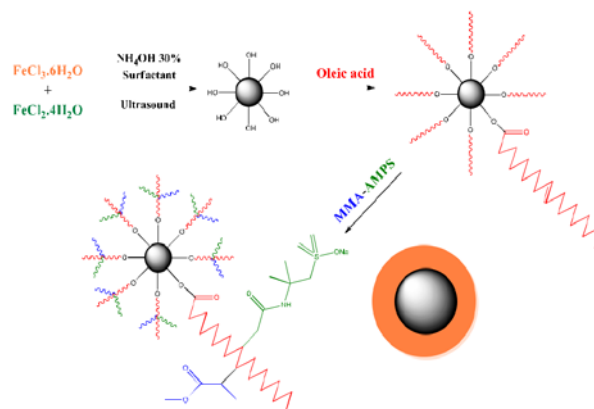


Figure 1. Synthesized procedure for OMNPs-MMA-co-AMPS [8].

Optimization of polymer coated MNPs synthesis.

There are many parameters affecting on the reaction such as the stirring speed, ultrasound time, temperature and time for polymerization but the significant parameter are temperature T and reaction time t. The polymerization is

$$\%m_{\text{copolymer coated on OMNPs}} = \%m_{\text{co-po}} = (m_{\text{PMNPs}} - m_{\text{OMNPs}}) / m_{\text{OMNPs}} \times 100\%.$$

Temperature was surveyed from 60 to 80 °C, and the time for polymerization varied from 6 to 8 hours. The different conditions according to

optimized base on the percentage of copolymer coated on OMNPs via experimental planning. And the model using in this thesis is Orthogonal planning level 2 [9].

temperature and reaction time were summarized as following table:

Table 1. The different conditions for polymerization

No.	The number of experiments	Temperature of reaction (°C)	Reaction time (hours)
1	9 experiments with varied conditions including temperature and time for reaction.	80	8
2		60	8
3		80	6
4		60	6
5		80	7
6		60	7
7		70	8
8		70	6
9		70	7
10	3 experiments at the center to calculate reappear variance s_{th} : (n)	70	7
11		70	7
12		70	7

Table 2. The parameters of orthogonal planning level 2

The number of parameters (k)	2
The number experiment at the center (n_0)	1
Find α according to k and n_0	1
The number of experiments ($2^k + 2k + n_0$)	9
The number of additional experiments at the center to calculate reappear variance s_{th} : (n)	3

Table 3. Value and variable range of affecting parameters

Value	Z_1 (°C)	Z_2 (hours)
Variable range	$60 \leq T \leq 80$	$6 \leq t \leq 8$
Average value Z_j^0	70	7
ΔZ	10	1

To facilitate for calculating experimental coefficients of mathematic model and conducting data processing, we transfer to

Therefore, we have: $x_j = \frac{Z_j - Z_j^0}{\Delta Z_j}$ with $j = 1, 2$

dimensionless coding value, with upper value and lower value of +1 and -1; average value $x_j^0 = 0$ (at the corner of coordinate).

The regression equation of experimental planning orthogonal level 2 has the general form as follows:

$$\hat{y} = b_0 + b_1x_1 + b_2x_2 + b_{12}x_1x_2 + b_{11}x_1^2 + b_{22}x_2^2$$

$$\text{Where: } x_1' = x_1^2 - \frac{4 + 2\alpha^2}{9} = x_1^2 - \frac{2}{3} \quad x_2' = x_2^2 - \frac{4 + 2\alpha^2}{9} = x_2^2 - \frac{2}{3}$$

Table 4. Matrix for orthogonal planning level 2 for polymerization

No.	Real variable		Encoding variable						Objective function, %m _{co-po}
	Z ₁ (T)	Z ₂ (t)	x ₀	x ₁	x ₂	x ₁ x ₂	x ₁ '	x ₂ '	
1	80	8	1	1	1	1	0.33	0.33	Obtained value after calculating the percentage of copolymer coated on OMNPs for every reaction.
2	60	8	1	-1	1	-1	0.33	0.33	
3	80	6	1	1	-1	-1	0.33	0.33	
4	60	6	1	-1	-1	1	0.33	0.33	
5	80	7	1	1	0	0	0.33	-0.67	
6	60	7	1	-1	0	0	0.33	-0.67	
7	70	8	1	0	1	0	-0.67	0.33	
8	70	6	1	0	-1	0	-0.67	0.33	
9	70	7	1	0	0	0	-0.67	-0.67	

After finding the optimum condition for polymerization, the reaction was carried out with

RESULTS AND DISCUSSION

The chemical structure of MNPs, OMNPs and PMNPs were characterized by using Fourier transform infrared spectroscopy (FT-IR) with a Bruker Equinox 55 spectrometer in the range of 4000–500 cm⁻¹. The crystal structure was characterized by using x-ray diffraction (XRD). The morphology and size of the obtained materials was examined by transmission electron microscopy (TEM). The Hydrodynamic size of the nanocomposite PMNPs was estimated by Dynamic light scattering (DLS). The saturation magnetization was examined by vibrating sample magnetometer (VSM). Thermo-gravimetric analysis (TGA) was conducted on both unfilled polymer and polymeric nanocomposite from 30°C to 800°C with a heating rate of 10°C/min.

FT-IR spectra

Figure 2 shows the presence of the MMA-co-AMPS copolymer on the OMNP surface which was confirmed through FT-IR. The bands at 1250 cm⁻¹, 659 cm⁻¹, 1099 cm⁻¹, and 3200–3500 cm⁻¹ from the FT-IR spectrum were assigned to S=O, S-O, C-S, and -NH-stretching vibrations, respectively, indicating that the AMPS structure compared with the -CH₃, -CH₂, and -COONa vibrations in MMA was clearly observed at 1389–2900 cm⁻¹, 1502 cm⁻¹, and 1567–1385 cm⁻¹, respectively. In addition, the absorption bands at 1747 cm⁻¹ and 1196 cm⁻¹ corresponded to carbonyl (C=O) and asymmetric C-O-C stretching vibrations,

this condition and compared with the calculated results.

respectively, indicating that oleic acid had been coated onto the MNPs' surface.

Furthermore, the band at 582 cm⁻¹ which belongs to the Fe-O bond in the Fe₃O₄ structure was still observed. Thus, the FT-IR spectrum exhibited all the component signals in the core-shell structure of the MMA-co-AMPS copolymer.

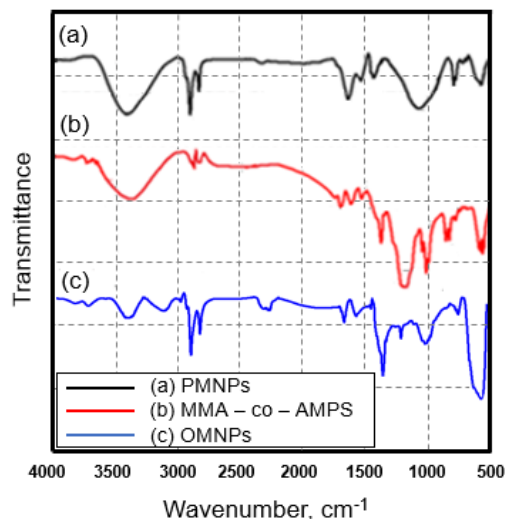


Figure 2. FT-IR spectra comparison of (a) PMNPs, (b) MMA-co-AMPS, (c) OMNPs.

X-ray diffraction

The XRD spectra analysis results of MNPs and PMNPs are shown in Figure 3. Both of them are shown that they have 6 characteristic peaks of Fe₃O₄ at 2θ = 30.1°; 35.5°; 43.3°; 53.4°; 57.2°; 62.5° correspond to crystal lattices surface that have Miller indices are (220); (311); (400);

(422); (511) and (440). It proves that after the synthesis process, PMNPs didn't change the structure of Fe_3O_4 .

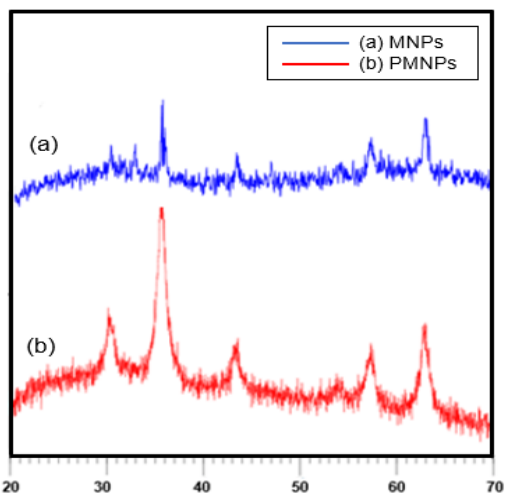


Figure 3. XRD pattern of MNPs and PMNPs

Dynamic light scattering

The average size and the polydispersity index (PI) of the PMNPs DLS results were acquired by cumulant analysis of the measured auto-correlation function and are shown in Figure 4. This result shows that the average hydrodynamic size of them is approximately 102.1 nm present the size of these particles is around nano scale and PI is about 0.13 confirming that the size distributions were monodisperse.

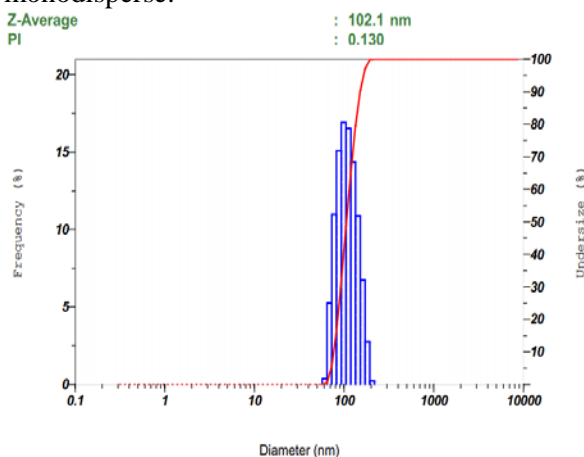


Figure 4. VSM result of MNPs and PMNPs

Transmission electron microscopy

According to the TEM images in Figure 5, the average size of MNPs was 7 nm, while the average size of PMNPs was 14 nm. This result together with FT-IR spectra showed that the copolymer MMA-AMPS coated successfully on MNPs surface. The dispersibility of PMNPs was

better than MNPs, there was no agglomeration between nanoparticles. This could be contributed by polymer AMPS that links to MNPs and change their property from inert to hydrophilic. Besides, co-polymer played roles as steric inhibition agents and created electrostatic repulsion between among PMNPs

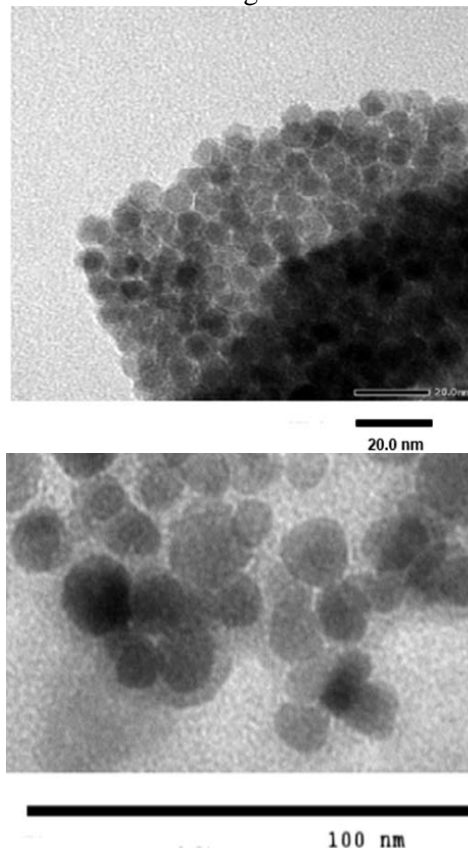


Figure 5. TEM image of MNPs and PMNPs

Vibrating sample magnetometer

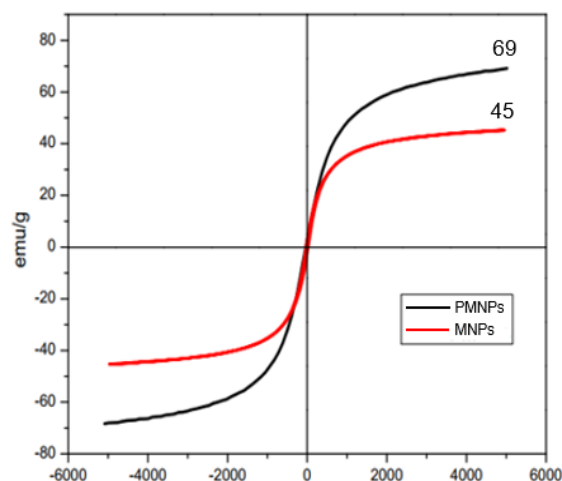


Figure 6. VSM result of MNPs and PMNPs

The saturation magnetization of MNPs and PMNPs were 69 emu/g and 45 emu/g in

respectively. This result reflected the successful of synthesizing the magnetic materials. The saturation magnetization of PMNPs was significant. Therefore, PMNPs was still keeping the good properties of magnetic materials to apply in enhanced oil recovery.

Thermo-gravimetric analysis

The thermo diagram of PMNPs in Figure 7 shown four steps. The first weight-loss process at a temperature range of 30–150°C was associated with the loss of adsorbed water that constitutes 10–15% of the weight of PMNPs. The second weight-loss process lied at the temperature range of 150–350°C that can be attributed to the loss of loosely bonded polymer matrix. This weight-loss process was influenced by the magnetite concentration used for nanocomposite preparation. The third (350–500°C) step shown the advanced thermal stability of this nanocomposite to unfilled

polymer. The fourth (600–800°C) step was related to iron oxide nanoparticles.

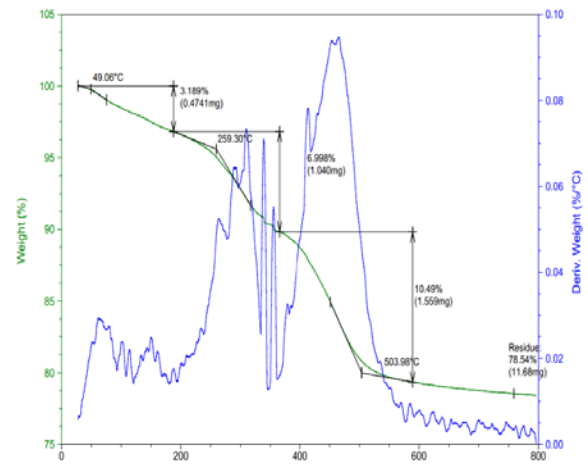


Figure 7. TGA pattern of PMNPs

Result of optimization the reaction of copolymer coated on MNPs

Table 4.1. Matrix for orthogonal planning level 2 for polymerization

No.	Real variable		Encoding variable						Objective function, % m _{copo}
	Z ₁	Z ₂	x ₀	x ₁	x ₂	x ₁ x ₂	x' ₁	x' ₂	
1	80	8	1	1	1	1	0.33	0.33	9.93
2	60	8	1	-1	1	-1	0.33	0.33	10.14
3	80	6	1	1	-1	-1	0.33	0.33	8.42
4	60	6	1	-1	-1	1	0.33	0.33	5.08
5	80	7	1	1	0	0	0.33	-0.67	7.12
6	60	7	1	-1	0	0	0.33	-0.67	6.09
7	70	8	1	0	1	0	-0.67	0.33	10.82
8	70	6	1	0	-1	0	-0.67	0.33	10.03
9	70	7	1	0	0	0	-0.67	-0.67	10.24

Reappeared variance was determined according to 3 additional experiment at the center:

$$y_{01} = 10.24\%; y_{02} = 10.32\%; y_{03} = 9.60\%$$

$$\text{We have: } \bar{y}_0 = \frac{\sum_{u=1}^3 y_{0u}}{3} = 10.05$$

$$s_{th}^2 = \frac{\sum_{u=1}^3 (y_{0u} - \bar{y}_0)^2}{3-1} = 0,16$$

The coefficients of regression equation and their error were calculated as follows:

$$b_0 = 8.65; b_1 = 0.69; b_2 = 1.23; b_{12} = -0.89; b_{11} = -2.57; b_{22} = 1.25$$

$$s_{b0} = 0.13; s_{b1} = 0.16; s_{b2} = 0.16; s_{b12} = 0.20; s_{b11} = 0.28; s_{b22} = 0.28$$

The meaning of coefficients in regression equation were verified according to Student Standard

$$t_j = \frac{|b_j|}{s_{b_j}} \quad t_0 = 65.77; t_1 = 4,3034; t_2 = 7.61; t_{12} = 4.50; t_{11} = 9.20; t_{22} = 4.49$$

Look up $t_p(f_2)$ in Microsoft Office Excel, where $f_2 = n - 1 = 3 - 1$, $p = 0.05$ was chosen. We found $t_{0,05}(2) = 4,302$

All regression coefficient was bigger than $t_{0,05}(2)$ so no coefficient was eliminated. We gained the regression equation as follows:

$$s_{du}^2 = \frac{\sum_{i=1}^N (y_i - \hat{y}_i)^2}{N - l} = \frac{\sum_{i=1}^9 (y_i - \hat{y}_i)^2}{9 - 5} = 1,10 \quad F = \frac{s_{du}^2}{s_{th}^2} = \frac{1,10}{0,16} = 7,09$$

The value of Fisher Standard looked up with level of significance $p = 0,05$ and degrees of freedom: $f_1 = N - 1 = 9 - 6 = 3$; $f_2 = n - 1 = 3 - 1 = 2$ was $F_{1-p}(f_1, f_2) = F_{1-0,05}(3, 2) = F_{0,95}(3, 2) = 19,15$ (Look up $F_{0,95}(3, 2)$ from Microsoft Office Excel)

$F < F_{1-p}(f_1, f_2)$ therefore the regression equation is compatible with experimental.

The encoding variable was shifted to real variable, where: $x_1 = \frac{T - 70}{10}$; $x_2 = \frac{t - 7}{1} = t - 7$

Therefore, regression equation with the real variables as follows:

$$\%m_{co-po} = \hat{y} = 8.65 + 0.69 \left(\frac{T - 70}{10} \right) + 1.23(t - 7) - 0.89 \left(\frac{T - 70}{10} \right) (t - 7) - 2.57 \left[\left(\frac{T - 70}{10} \right)^2 - \frac{2}{3} \right] + 1.25 \left[(t - 7)^2 - \frac{2}{3} \right]$$

From this equation, we plotted the response surface of % copolymer coated on MNPs according to temperature (**T**) and reaction time

(**t**) as Fig. 8. The graph was plotted by Matlab software with the command as follows:

```
X = [ 6  6.25  6.5  6.75  7  7.25  7.5  7.75  8 ];
Y = [ 60 62.5 65  67.5  70 72.5  75  77.5  80 ];
Z = [
    5.4  5.383125  5.5225  5.818125  6.27  6.878125  7.6425  8.563125  9.64
    6.919375  6.846875  6.930625  7.170625  7.566875  8.119375  8.828125  9.693125  10.71438
    8.1175  7.989375  8.0175  8.201875  8.5425  9.039375  9.6925  10.50188  11.4675
    8.994375  8.810625  8.783125  8.911875  9.196875  9.638125  10.23563  10.98938  11.89938
    9.55  9.310625  9.2275  9.300625  9.53  9.915625  10.4575  11.15563  12.01
    9.784375  9.489375  9.350625  9.368125  9.541875  9.871875  10.35813  11.00063  11.79938
    9.6975  9.346875  9.1525  9.114375  9.2325  9.506875  9.9375  10.52438  11.2675
    9.289375  8.883125  8.633125  8.539375  8.601875  8.820625  9.195625  9.726875  10.41438
    8.56  8.098125  7.7925  7.643125  7.65  7.813125  8.1325  8.608125  9.24
];
mesh(X, Y, Z)
grid on title ('Response surface of copolymer coated on OMNPs reaction')
xlabel('Time of reaction, h'); ylabel('Temperature of reaction, °C'); zlabel('%copolymer coated on OMNPs');
```

Notes: X presents for reaction time (t), Y presents for temperature of reaction (T) and Z

presents for the mass percentage of copolymer coated on MNPs (% m_{copo}).

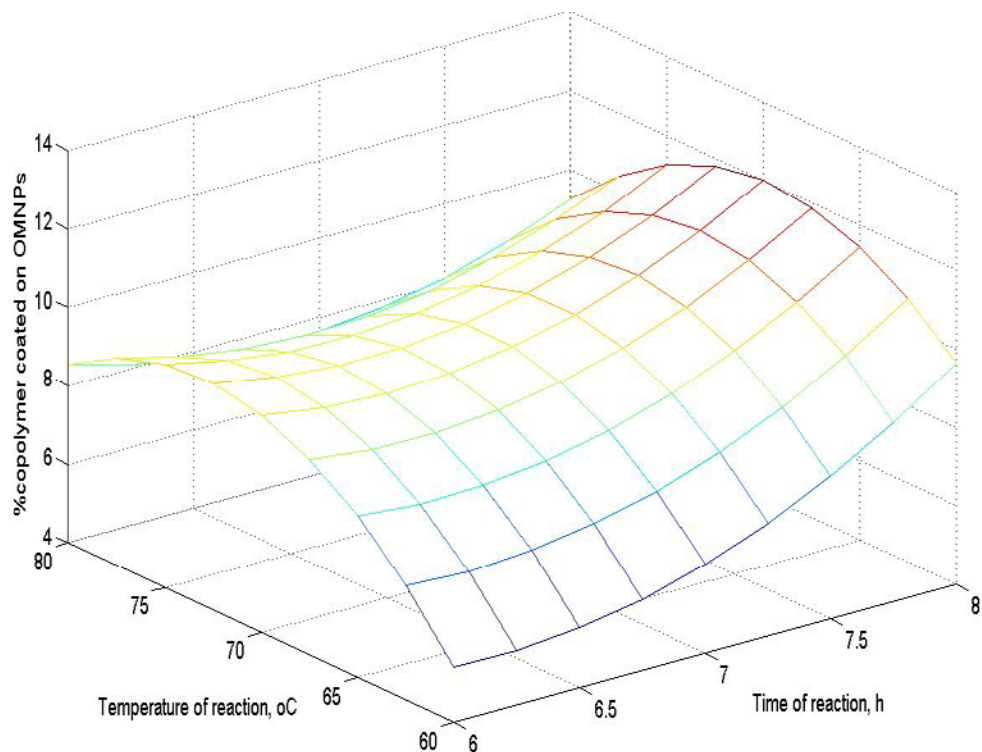


Figure 8. Response surface of mass percentage of copolymer MMA-AMPS coated on MNPs

To optimize the mass percentage of copolymer coated on MNPs, we find the maximum value of function %m_{co-po} with by

taking partial derivative and solving two equations to find T and t at the extremum position.

$$\text{We have: } \begin{cases} \frac{\partial(\% m_{co-po})}{\partial T} = 0,069 - 0,089(t - 7) - 2,57 \times 2 \frac{T - 70}{10} = 0 \\ \frac{\partial(\% m_{co-po})}{\partial t} = 1,23 - 0,089(T - 70) + 1,25 \times 2(t - 7) = 0 \end{cases} \Rightarrow \begin{cases} T = 70,22 \\ t = 6,52 \end{cases}$$

%m_{co-po}(T, t) were calculated at boundary position and extremum position as follows:

% m _{co-po} (70.22; 6.52)	= 9.25 %
% m _{co-po} (70.22; 6)	= 9.58 %
% m_{co-po} (70.22; 8)	= 12.00 %
% m _{co-po} (60; 6.52)	= 5.54 %
% m _{co-po} (80; 6.52)	= 7.77 %
% m _{co-po} (60; 6)	= 5.40 %
% m _{co-po} (60; 8)	= 9.64 %
% m _{co-po} (80; 6)	= 8.56 %
% m _{co-po} (80; 8)	= 9.24 %

From the above calculation, the optimum condition for polymerization in the surveying range was 70.22°C and the time for reaction was 8 hours. The mass percentage of copolymer coated on MNPs was 12%.

The polymerization was carried out at 71°C and 8 hours to compare with the calculated result. And the mass percentage of copolymer

coated on MNPs was 12.17 %. This result was conformity with the calculated result.

CONCLUSION

A nanocomposite of MNPs coated by copolymer 2-acrylamido-1-propane sulfonic acid (AMPS) and methyl methacrylate (MMA) has been successfully synthesized by polymerization in the presence of sodium dodecyl sulfate (SDS) surfactant and was called as PMNPs. The appropriate temperature for polymerization was about 70°C and reaction time was 8 hours through calculation of orthogonal planning level 2 when with the mass percentage of co-polymer coated on MNPs surface about 12%. The data of physical and chemical analysis such as XRD, FT-IR, DLS, TEM, SEM, TGA and VSM have confirmed the (MNPs) core- (polymer) shell structure of obtained PMNPs. The average size of MNPs and PMNPs were 7 and 14 nm.

Acknowledgment

This research is funded by Vietnam National Foundation for Science and Technology Development (NAFOSTED) under grant number 103.02-2018.333.

We also thank Vietnam Academy of Science and Technology (VAST) for providing the necessary help during the work.

References

- [1] Lake, L.W., Enhanced oil recovery. 1989: Prentice Hal
- [2] Sheng, J., Modern chemical enhanced oil recovery: theory and practice. 2010: Gulf Professional Publishing.
- [3] K k, V., et al., Application of different EOR techniques for the energy and recovery of Ashal'cha oil field Mustafa, *Journal Energy Sources, Part A: Recovery, Utilization, and Environmental Effects*, Volume 40, 2018 - Issue 6, Pages 645-653.
- [4] Koa, S., Huhb, C., Use of nanoparticles for oil production applications, *Journal of Petroleum Science and Engineering* 172 (2019) 97–114
- [5] Gbadamosi, A. O., et al., Hybrid suspension of polymer and nanoparticles for enhanced oil recovery, *Polymer Bulletin*, 2019, <https://doi.org/10.1007/s00289-019-02713-2>
- [6] Nikolov, A., et al., Historical perspective structure and stability of nanofluid films wetting solids *Advances in Colloid and Interface Science* 264 (2019) 1-10
- [7] ShamsiJazeyi, H., et al. Polymer-coated nanoparticles for enhanced oil recovery. *Applied Polymer Science*, 2014, DOI: 10.1002/APP.40576.
- [8] Nguyen, T.P., et al., Synthesis of Polymer-Coated Magnetic Nanoparticles from Red Mud Waste for Enhanced Oil Recovery in Offshore Reservoirs. *Journal of Electronic Materials*, 2016. 45(7): p. 3801-3808.
- [9] Canh, N., *Experimental planning*. 2011, Ho Chi Minh City - Vietnam National Univeristy: Viet Nam.

PHOSMET PESTICIDE DETECTION USING 2D-ARRAYS OF Au NANOPARTICLES

Do Nhu Quynh¹, Tran Duc Tien², Lo Van Giap³, Do Danh Bich Do³, Ung Thi Dieu Thuy^{1*}, and
Nguyen Quang Liem¹

¹Institute of Materials Science, Vietnam Academy of Science and Technology, 18 Hoang Quoc Viet, Cau
Giay, Hanoi, Vietnam;

²University of Science and Technology of Hanoi, Vietnam Academy of Science and Technology, 18
Hoang Quoc Viet, Hanoi, Vietnam;

³Faculty Department of Physics, Hanoi National University of Education, 136 Xuan Thuy, Hanoi,
Vietnam

Email: dieuthuy@ims.vast.ac.vn

ABSTRACT

A fast and sensitive trace analysis of phosmet pesticides was performed using the two-dimensional (2D) arrays of gold nanoparticles (AuNPs) and nanorods (AuNRs). The large 2D arrays with homogeneous and dense monolayers of AuNPs and AuNRs were prepared on ITO substrates by hybrid method based on the mixed n-alkanethiolate self-assembled monolayer. The 2D-arrays showed the surface plasmon resonance (SPR) peaking differently in the spectral range of ~530–800 nm to around 532 nm, 633 nm or 785 nm of the laser-light excitations that is very promising for surface-enhanced Raman scattering (SERS)-based sensor applications. As an example, we have used the fabricated AuNPs SERS substrate to take the Raman scattering spectra of phosmet at low concentrations ranging from 0.1 ppm to 100 ppm.

Keywords: 2D array, Au nanoparticles, hybrid method, SERS, phosmet pesticides

INTRODUCTION

Phosmet, an organophosphate pesticide, has been used on a wide range of fruit and nut crops such as pear, peach, apple, walnuts [1-3]. In Vietnam, all of these fruits and nuts are widely available everywhere, therefore, the need of developing the residual pesticides detection method in food and in the environment are a vital importance for human. Unprofessionally, this pesticide can be detected using test strips or test kits that are bought online, however, the outcome that this method provides can be widely incorrect because it needs a large amount of pesticide present in the food in order to give a positive result. Professionally, pesticides can also be detected using multiresidue methods, however, this protocol have lost some favor due to its semiquantitative nature [1,4]. Therefore, the development of rapid analytical methods to monitor the levels of phosmet in fruits and vegetables has been one of the major researches focuses in the field of food research.

Surface-enhanced Raman spectroscopy (SERS) has been shown great potential for detection of organic molecules at trace concentrations from various biological,

chemistry, medicine samples [5-8]. One of the hot areas in SERS application is rapid detection of pesticides in the skins of fruits or vegetables with short time for sample preparation [9]. Fan and co-works have shown the feasibility of applying SERS for detection of as low as 1 mg/g for phosmet in apples [10]. However, the commercial substrates are quite costly, and the sample preparation methods were complicated and time-consuming.

The purpose of this study was to investigate the possibility of phosmet analysis with SERS based on AuNPs and AuNRs. We used these SERS substrates to take the Raman scattering spectra of phosmet pesticide at very low concentrations of 0.01 ppm that is lower than the level required for food security.

EXPERIMENTAL

Chemicals: 1-Octadecanethiol, 1-dodecanethiol, 3-mercaptopropyl trimethoxysilane (MPTMS), 1,6-Hexanedithiol, chloroauric acid trihydrate, silver nitrate, trisodium citrate, hexadecyltrimethylammonium bromide (CTAB), ascorbic acid, sodium borohydride, chlorhydric

acid, were purchased from Sigma-Aldrich. All chemicals were guaranteed reagent grade and were used as received. The cleanliness of flask, beaker and stirring bars were affected to size distribution and shape monodispersity. Therefore, all the glassware and magnetic stirring bars were soaked in a fresh aqua regia solution for about an hour, followed by a rinse ten times with de-ionised water (DI), and then washed with ethanol before drying in oven. Phosmet ($\geq 99\%$, Standard, New Haven, CT, USA) was dissolved in acetonitrile (HPLC reagent, Sinopharm chemical reagent Co. Ltd., SCRC, Shanghai, China) to prepare a series of standard solutions with different concentrations (0.1 ppm, 1 ppm, 10 ppm, 100 ppm).

Synthesis of AuNPs: AuNPs were synthesized by the seed-mediated growth method, in which Au seeds were prepared following a standard citrate reduction method according to literature [11]. Briefly, a colloidal solution of Au seeds was fabricated from the reaction of 150 ml trisodium citrate solution 2.2 mM and 1 ml HAuCl₄ 0.025 M at 100 °C under stirring strongly at 1500 rpm rounds per minute. The whole system was heated under reflux. After refluxing of 30 min, the mixture solution of 1 ml trisodium citrate 60 mM and 1 ml HAuCl₄ 0.025 M were added into the above Au seeds solution, repeat this process 2 times. After 30 min, the colloidal AuNPs solution with size particle of 50 nm was obtained.

Synthesis of AuNRs: AuNRs were synthesized similarly with AuNPs by the seed-mediated growth method, in which Au seeds were prepared following a standard sodium borohydride reduction method [12]. Particularly, a colloidal Au seed solution was formed by injecting quickly 0.6 ml NaBH₄ 0.01 M into the mixture solution of 10 ml CTAB 0.1 M and 0.25 ml HAuCl₄ 0.01 M under stirring strongly for 2 min at room temperature. Then, the reaction solution was left for 2 h. This Au nano-seeds colloid was kept for further obtaining larger Au NRs by the seed-mediated growth.

The colloidal AuNRs with size of 60 nm was fabricated by adding 2ml HAuCl₄ 0.01 M to 40 ml CTAB 0.1 M at room temperature and stirred 1500 rpm. Next, the mixture solution of 0.4 ml AgNO₃ 0.01M, 0.32 ml ascorbic acid 0.1 M and 0.6 ml HCl 1M was injected into the above solution. Then, 0.096 ml Au nano-seeds colloid solution was added. Finally, the colloidal AuNRs solution with size of 60 nm was obtained.

Synthesis of AuNPs and AuNRs 2D-arrays by hybrid method: All AuNPs and AuNRs were functionalized with a mixture of octadecanethiol and dodecanethiol of 1:6 molar ratio according to our previously published method [10-15]. The ITO substrate was also functionalized with mixed alkanethiols of (3-mercaptopropyl) trimethoxysilane (MPTMS) and 1,6-Hexanedithiol [13-16]. Next, the functionalized AuNPs (or AuNRs) were arranged on the thiol-terminated ITO substrate by the electrochemical deposition method with an application of 1.0 V as bias voltage of the ITO substrate as a cathode and the carbon substrate as an anode. The electrolyte solution is a 2 ml of alkanethiol-capped Au NPs (or AuNRs) solutions in the hexane-acetone solvent (9:1 in the vol ratio). After the solvent evaporation was completed, the samples were annealed at 50 °C for 12 h to immobilize the AuNPs (or AuNRs) on the functionalized ITO substrates by substitution of thiol. Finally, washing is done in order to remove the multilayers of Au, leaving behind only the desired monolayer of AuNPs (or AuNRs).

Characterization: The morphology of as-synthesized samples was carried out by scanning electron microscopy (SEM, S-4800, Hitachi, Japan). Ultraviolet-visible (UV-vis) absorption spectra of the samples were recorded using a Jasco V670 UV-vis spectrophotometer. A Labram evolution microscopy Raman spectrometer (Horiba) equipped with a 532 nm diode laser source was utilized to collect Raman spectra. 2 μ l of phosmet standard solution was loaded onto the surface SERS substrates. During the measurement, light from a 1 mW laser power was directed and focused through a 50X objective lens onto the sample deposited on a SERS substrate. The Raman scattering signal from the sample was detected via a CCD detector. All spectra were recorded from 300 to 2000 cm⁻¹. Each spectrum was the average of three scans with exposure time of 30 s per scan.

RESULTS AND DISCUSSIONS

Fabrication 2D AuNPs and AuNRs arrays:

Fig. 1 shows the absorption spectra and SEM images of as-prepared AuNRs and AuNPs colloids.

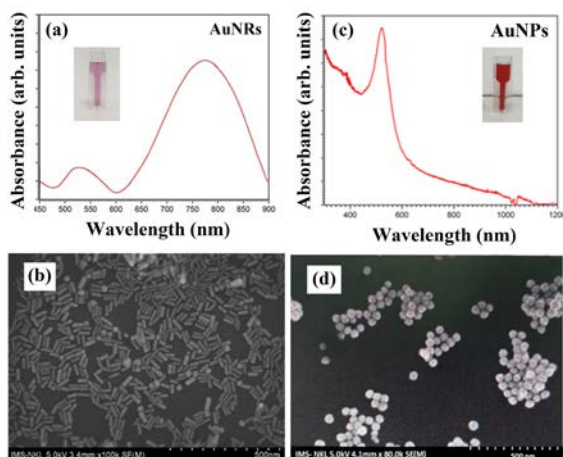


Figure 1. UV-Vis spectra SEM images of AuNRs (a, b) and AuNPs (c, d), respectively.

The UV-vis absorption spectra of AuNRs (Fig. 1a) shows clearly two absorption peaks at 520 nm and 770 nm. This phenomenon could be explained that the absorption peak at 520 nm could be originated from the spherical seeds and after growing, the spherical seeds become rods with a characteristic absorption peak at ~ 770 nm. In fact, that the efficiency during the transition of spherical seeds to AuNRs can never reach 100% and thus, both spherical seeds and AuNRs are present in the final obtained solution. This result agrees with the observation from SEM image as shown in Fig 1b. It is clearly seen that some remaining spherical NPs are obtained with AuNRs in the final as-prepared solution. From the SEM, the length and the diameter of the prepared AuNRs are ~ 60 nm and 10 nm, respectively (Fig. 1b). The absorption spectra of AuNPs show only one narrow peak at ~ 538 nm (Fig. 1c) indicating the homogenous size of synthesized AuNPs. This result is confirmed through the observation of the SEM image with a particle size of 50 ± 2.3 nm (Fig. 1d).

According to the same hybrid method to arrange the 2D-arrays of Au and Ag NPs with homogeneous and dense monolayers by functionalization of both these NPs with mixed alkanethiols (dodecanethiol:octadecanethiol = 6:1) and thiol-terminated ITO substrates [13-15], we fabricated the 2D-arrays of Au particles with different shapes. Fig. 2 shows the SEM images of the nearly close-packed and regularly ordered 2D arrays of AuNRs and AuNPs, respectively. The absorption spectra of the fabricated 2D arrays of AuNRs and AuNPs are presented in Fig.3. It can be seen that the LSPR peaks of both AuNRs and

AuNRs in 2D arrays are linearly red-shifted compared with in colloidal forms.

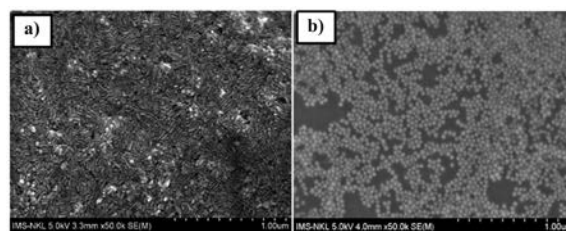


Figure 2. The SEM images of AuNRs arrays (a) and AuNPs arrays (b).

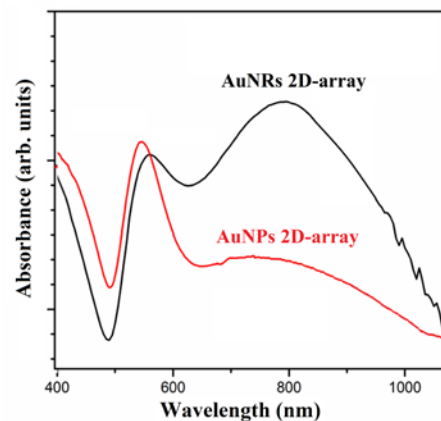


Figure 3. The UV-Vis spectra of 2D- arrays of AuNRs and AuNPs.

Detection of Phosmet pesticide by SERS substrates

The Raman spectra of phosmet pesticide with different concentrations dropped onto the fabricated AuNRs and AuNPs 2D arrays and onto the bare ITO substrates for comparison at the same experimental conditions (such as the volume of probe molecules, the wavelength and power of the excitation laser) are shown in Fig. 4. The Raman spectra show clearly the major characteristic peaks of phosmet pesticide with the vibrations of benzene rings at 714 cm^{-1} , the asymmetric stretching of P-O-C at 1017 cm^{-1} , stretching of C-O at 1772 cm^{-1} and the in-plane deformation vibrations of C=O, P=S, and C-N at 605 , 650 , and 1190 cm^{-1} , respectively. These peaks are consistent with at the standard SERS spectra of phosmet pesticide reported in the literature [10, 17, 18]. In case of AuNPs 2D array, the Raman intensity and the number of peaks are increased with increasing the concentration of phosmet pesticide (Fig. 4b); the low concentration of 0.1 ppm could be detected that is lower than the level required for food security. While the SERS substrate with AuNRs can also shows some Raman peaks of phosmet

pesticide, however, these peaks are not very clear (Fig. 4a). This is due to the fact that the LSPR peak of AuNPs is closer to the laser excitation of 532 nm. Therefore, the resonance occurs leading to stronger vibration of bonds of phosmet and thus, stronger signals are attained. For the ITO substrate without any metal NPs, the Raman scattering signals from phosmet pesticides were not clearly observed even at the high concentration of 100 ppm.

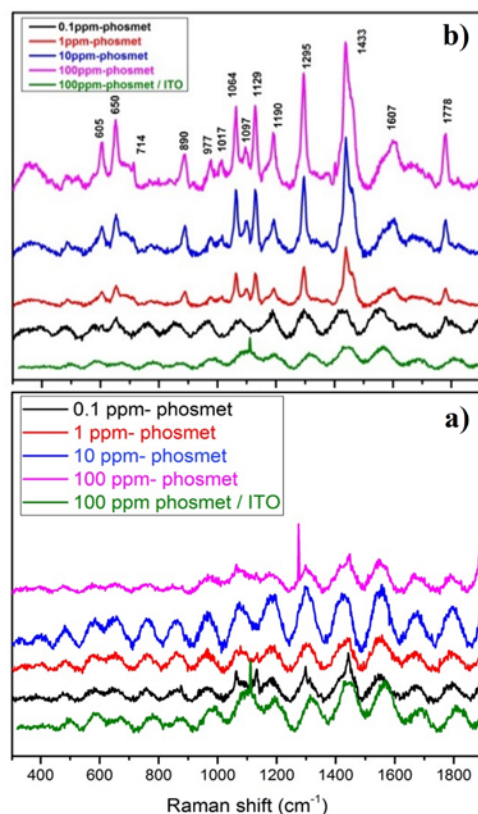


Figure 4. Raman spectra of phosmet on SERS substrate with 2D AuNRs arrays (a) and 2D AuNPs (b).

CONCLUSION

The use of seed-mediated growth as an effective approach to synthesize the monodisperse spherical Au NPs and AuNRs. The SERS substrates based on both AuNPs and AuNRs 2D-arrays with homogeneous and high coverage have been successfully fabricated by hybrid method. Both the fabricated SERS substrates showed the significant enhancement effects for the Raman scattering signals of phosmet pesticide. The AuNPs 2D-array could detect the phosmet pesticides at low concentration of 0.1 ppm which is lower than the level required for food security. The proposed method could be extended to other

pesticides for their identification and quantification in agricultural products as a rapid, highly sensitive, and reliable analyse.

Acknowledgment

This work was supported by Vietnam Academy of Science and Technology under Grant No. KHCBVL.05/18-19.

References

- [1] N. B. Valles, M. Retamal, M. Mezcuca, A. R. Fernández-Alba, *J. Chromatography* **1264** (2012) 110-116.
- [2] J. Hernández-Borges, J. C. Cabrera, M. A. Rodríguez-Delgado, E. M. Hernández-Suárez, V. G. Saúco, *Food Chemistry* **113** (2009) 313-319.
- [3] H. Bagheri, Z. Ayazi, E. Babanezhad, *Microchemical Journal* **94** (2010) 1-6.
- [4] A. Ambrus, H. P. Thier, *Pure and Applied Chemistry* **58** (1986) 1035-1062.
- [5] S. M. Nie, S. R. Emory, *Science* **275** (1997) 1102.
- [6] Zuo J, Meng G, Zhu C, Zhou Q, Li Z, Ke Y, Zhou N 2016 RSC Adv 6 26490.
- [7] U T D Thuy, N T Thuy, N T Tung, E Janssens, N Q Liem, *APL Materials* **7** (2019) 071102.
- [8] Kundan S, Kenneth S, Joseph A K, Ailing T, Yong Z, Gregory L R, Alan X W, *Adv Optical Mater* **7** (2019) 1900415.
- [9] B. Liu, G. Han, Z. Zhang, R. Liu, C. Jiang, S. Wang, *Analytical Chemistry* **84** (2012) 255-261.
- [10] Y. Fan, K. Lai, B. A. Rasco, Y. Huang, *Food Control* **37** (2014) 153-157.
- [11] N. G. Bastus, J. Comenge, V. Puntes, *Langmuir* **27** (2011) 11098-11105.
- [12] H. Chen, X. Kou, Z. Yang, W. Ni, J. Wang, *Langmuir* **24** (2008) 5233-5237.
- [13] T D T Ung, S. Kenji, S. Nishiyama, S. Yanagida, Q. L. Nguyen, K. Miki, *Langmuir* **31** (2015) 13494.
- [14] T D T Ung, T H Nguyen, Q L Nguyen, *Adv. Nat. Sci.: Nanosci. Nanotechnol.* **7** (2016) 035013.
- [15] K. Kullavadee, S. Kenji, L. Rawiwan, B. Suwussa, D. Tararaj, M. Kazushi, *RSC Adv* **7** (2017) 14099.
- [16] K. Isozaki, T. Ochiai, T. Taguchi, K. Nittoh, K. Miki, *Applied Physics Letters* **97** (2010) 221101.
- [17] J. C. S. Costa, R. A. Ando, A. C. Sant'ana, P. Corio, *Physical Chemistry Chemical Physics* **14** (2012) 15645-15651
- [18] P. Trotter, *Applied Spectroscopy* **31** (1977) 30-35.

GOLD NANOPARTICLE SYNTHESIS BY AC GLOW DISCHARGE ON LIQUID AND THE EFFECT OF PH VALUE IN THE SIZE OF SYNTHESIZED NANOPARTICLE

**Phuoc Van Thai^{1,2}, Shinnosuke Abe³, Kenichiro Kosugi⁴, Nobuo Saito⁴,
Kazumasa Takahashi³, Toru Sasaki³, and Takashi Kikuchi^{3,5}**

¹Energy and Environment Science, Nagaoka University of Technology, Nagaoka, Japan;

²Faculty of Mechanical Engineering, HCMC University of Technology and Education, Ho Chi Minh City, Vietnam;

³Department of Electrical, Electronics and Information Engineering, Nagaoka University of Technology, Nagaoka, Japan;

⁴Department of Materials Science and Technology, Nagaoka University of Technology, Nagaoka, Japan;

⁵Department of Nuclear System Safety Engineering, Nagaoka University of Technology, Nagaoka, Japan
Email: thaiphuoc.vn@gmail.com

ABSTRACT

In this work, we showed the behavior of gold nanoparticle synthesis by AC glow discharge and the effect of pH value of the precursor solution HAuCl_4 on the size of synthesized gold nanoparticles. We determined that H_2O_2 and solvated electrons generated by AC glow discharge on liquid are the main reducing species for gold nanoparticle synthesis. Our results showed that the size of synthesized gold nanoparticles was decreased due to the increase of pH value in the range of 9 to 12.

Keywords: gold nanoparticle synthesis, AC glow discharge, pH, size of gold nanoparticles

INTRODUCTION

Gold nanoparticles (AuNPs) have been employed in many fields of the application due to their unique properties of surface plasmons, high chemical stability, and antibacterial ability [1]. The practical applications of AuNPs range from sensor technique [2], catalysis [3], optical process to biomedicine [4]. Expanding applications of AuNPs have promoted continuing to improve the size-control and performance of the synthesis.

Plasma-liquid interactions (PLIs) have increasingly been attracted in nanotechnology. PLIs can directly provide electrons, radicals such as H, OH or H_2O_2 into liquid [5], which reduce metal cations into neutral molecules before aggregating to a nanoscale. This unique property of PLIs can take advantages to improve the time-consuming operation and the purity in the final product. There also have many studies investigating the process of AuNPs synthesis by PLIs, in which the process of AuNPs synthesized by the reductions of electrons, radicals from plasma and auric compounds. In these works, a direct-current (DC) power supply is used to generate on the liquid to study the

ability of particular species from plasma in the ability of AuNPs synthesis [6]. The AC glow discharge on liquid also possibly provide many radicals and electrons at same time. However, using AC glow discharge on liquid in AuNPs synthesis has still not been considered.

In this study, we have experimentally investigated the mechanism in AuNPs synthesis by AC glow discharge. We also monitored the effect of pH value in the precursor solution on the size of synthesized AuNPs.

EXPERIMENTAL

Figure 1 shows the experimental setup used in this work. The experimental setup was also used in the previous study [7-9]. The voltage and frequency of AC power supply were fixed at 18 kHz (peak to peak) and 38 kHz, respectively. Helium gas was fed into high electrode with the rate at 5 L/min. The distance between high electrode and the plasma-liquid interface is 15 mm.

The solution of chloroauric acid (1 mg Au/mL, HAuCl_4 in 1M HCl) was used as the precursor without further purification. Each sample in a glass beaker includes 1 mL of HAuCl_4 solution and 98 mL of deionized H_2O .

The solution of NaOH 1M was supplied to each sample to fix the sample at the pH of a designed value (9 – 12).

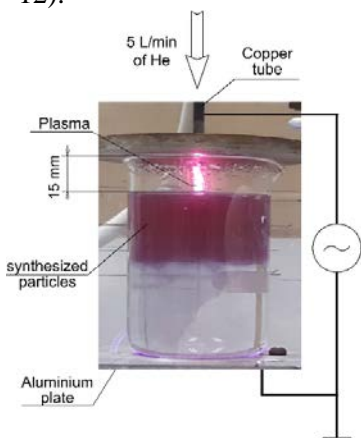


Figure 1. Schematic of experimental setup

RESULTS AND DISCUSSION

The color of the liquid below the plasma-liquid interface changed from colorless to red during the discharge as shown in Fig. 1. The thickness of this red volume increased according to time evolution and reached to the bottom of the beaker after eight minutes of the discharge.

We also analyzed synthesized particles in these solutions using a transmission electron microscopy (TEM) (HT7700, Hitachi, Tokyo, Japan) with 100 kV of accelerating voltage. Figure 2 illustrates the TEM image of the nanoparticles in the solution with pH value of 10 after 10 minutes of discharge. The energy-dispersive X-ray spectroscopy profile as shown in Fig. 2 indicates the presence of elemental gold in the nanoparticle, of which corresponding to the peaks at 2.1 and 9.7 keV. We confirmed by using EDS analysis that these particles are AuNPs.

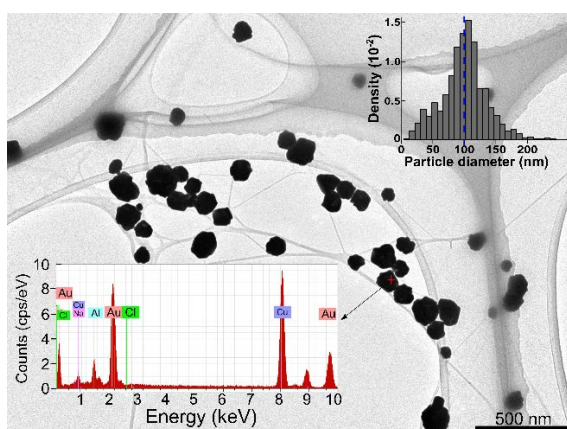
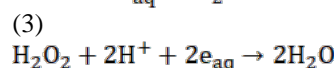
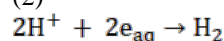
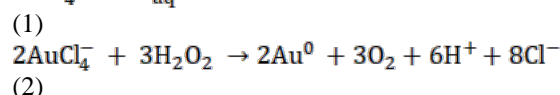
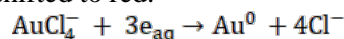


Figure 2. TEM image of AuNPs synthesized in pH 10 solution after 10 minutes of discharge.

The size of AuNPs i.e., the longest Feret diameter, synthesized in the solutions were also determined. The size of AuNPs in the solutions of pH 9 to pH 12 correspond to 120.6 ± 35.9 , 100.6 ± 36.6 , 48.7 ± 23.8 , and 36.4 ± 15.8 nm (mean \pm standard deviation), respectively. The results indicate that the pH of these solutions significantly affects the size of AuNPs synthesized by the AC glow discharge. The AuNPs in higher pH solutions of the range from 9 to 12 have a smaller size.

In the previous study [7, 9], we found that the AC glow discharge generates both of free electrons and positive ions on the liquids. Free electrons solve into the bulk liquid and become hydrated electrons (e_{aq}) in the penetration depth of 10 nm. The interaction of positive ions leads to the formation H^+ and OH radicals transforming to H_2O_2 in liquid. Therefore, AC glow discharge generates species e_{aq} , H_2O_2 , which are possible to reduce $AuCl_4^-$ into Au atoms according to reactions (1) - (2) [8]. However, the species e_{aq} and H_2O_2 also are taken by available H^+ ions in the reactions (3) - (4) [8]. Therefore, in case of solutions at high pH level (pH > 9), in which the available OH^- ions sufficiently neutralize all H^+ ions generating by positive ions from the plasma. It can be considered that all species e_{aq} , H_2O_2 only react with $AuCl_4^-$ ions to form Au^0 . This leads to the color in solutions with high pH values shifted to red.



In solutions at high pH, OH^- ions cover as a barrier around AuNPs. This barrier counteracts the Van der Waals's force between small particles and prevents these particles from aggregating to a further large size [10]. This leads to a decrease in the size of AuNPs in solutions at high pH.

CONCLUSION

In summary, we investigated the process of AuNPs synthesized by AC glow discharge on liquid and the effect of pH in $HAuCl_4$ solution

on the size of AuNPs. Our results show that AC glow discharge has the ability to generate a variety of reactive species such as e_{aq} , H_2O_2 which reduce $AuCl_4^-$ to Au atoms before growing into nanoscale. pH values of the precursor solutions affect the size of synthesized AuNPs, in which pH increases from 9 to 12, there has a decrease in the size of AuNPs.

References

- [1] Amendola, Vincenzo, Roberto Pilot, Marco Frascioni, Onofrio M. Marago, and Maria Antonia Iati. *Surface plasmon resonance in gold nanoparticles: a review*. Journal of Physics: Condensed Matter 29, no. 20 (2017): 203002.
- [2] Riboh, Jonathan C., Amanda J. Haes, Adam D. McFarland, Chanda Ranjit Yonzon, and Richard P. Van Duyne. A nanoscale optical biosensor: real-time immunoassay in physiological buffer enabled by improved nanoparticle adhesion. The Journal of Physical Chemistry B 107, no. 8 (2003): 1772-1780.
- [3] Hutchings, Graham J., and Jennifer K. Edwards. Application of gold nanoparticles in catalysis. In *Frontiers of nanoscience*, vol. 3, pp. 249-293. Elsevier, 2012.
- [4] Di Fabrizio, Enzo, Sebastian Schlücker, Jérôme Wenger, Raju Regmi, Hervé Rigneault, Giuseppe Calafiore, Melanie West et al. Roadmap on biosensing and photonics with advanced nano-optical methods. Journal of Optics 18, no. 6 (2016): 063003.
- [5] Chen, Qiang, Junshuai Li, and Yongfeng Li. A review of plasma-liquid interactions for nanomaterial synthesis. Journal of Physics D: Applied Physics 48, no. 42 (2015): 424005.
- [6] Shirai, Naoki, Satoshi Uchida, and Fumiyoshi Tochikubo. Synthesis of metal nanoparticles by dual plasma electrolysis using atmospheric dc glow discharge in contact with liquid. Japanese Journal of Applied Physics 53, no. 4 (2014): 046202.
- [7] Thai, Phuoc Van, Shinnosuke Abe, Kenichiro Kosugi, Nobuo Saito, Kazumasa Takahashi, Toru Sasaki, and Takashi Kikuchi. *Interaction and transfer of charged particles from an alternating current glow discharge in liquids: Application to silver nanoparticle synthesis*. Journal of Applied Physics 125, no. 6 (2019): 063303.
- [8] Panda, Biswa Ranjan, and Arun Chattopadhyay. *Synthesis of Au Nanoparticles at "all" pH by H₂O₂ Reduction of H₂AuCl₄*. Journal of nanoscience and nanotechnology 7, no. 6 (2007): 1911-1915.
- [9] Thai, Phuoc Van, Shinnosuke Abe, Kenichiro Kosugi, Nobuo Saito, Kazumasa Takahashi, Toru Sasaki, and Takashi Kikuchi. *Synthesis of Au Nanoparticles at "all" pH by H₂O₂ Reduction of H₂AuCl₄ Size/shape control of gold nanoparticles synthesized by alternating current glow discharge over liquid: the role of pH*. Materials Research Express 6.9 (2019): 095074.
- [10] He, Chaodong, Lanlan Liu, Zeguo Fang, Jia Li, Jinbao Guo, and Jie Wei. *Formation and characterization of silver nanoparticles in aqueous solution via ultrasonic irradiation*. Ultrasonics sonochemistry 21, no. 2 (2014): 542-548.

SYNTHESIS OF Cu₂O NANO/DIATOMITE USING HYDRAZINE AS REDUCING AGENT AND ITS ANTIBACTERIAL ACTIVITY

T. Thuy Nhung Dang¹, T. Ai Trinh Nguyen¹, T. Thu Huyen Pham¹, Dinh Tuan Phan¹, Ngoc Duy Nguyen², Van Phu Dang², Quoc Hien Nguyen²

¹Hochiminh City University of Natural Resources and Environment, 236B, Le Van Sy Street, Tan Binh District, Ho Chi Minh City, Vietnam;

²Research and Development Center for Radiation Technology, 202A, Street 11, Thu Duc District, Ho Chi Minh City, Vietnam
Email: dthnhung@hcmunre.edu.vn

ABSTRACT

Cuprous oxide nanoparticles (Cu₂O NPs) deposited on diatomite were synthesized by using hydrazine as a chemical reducing agent of copper ions (Cu²⁺) dispersed in diatomite. The obtained Cu₂O NPs/diatomite product was characterized by X-ray diffraction (XRD), UV-Vis spectroscopy, inductively coupled plasma (ICP) and dynamic laser scattering (DLS) diffraction. The UV-Vis spectrum of the Cu₂O NPs/diatomite showed the characteristic absorption peak at 430 nm. The XRD revealed the crystalline structure of Cu₂O nanoparticles with a crystallite size of 27.4 nm. The as-synthesized Cu₂O NPs/diatomite exhibited effective bactericidal activity against *E. coli*. The antibacterial efficiency could reach to 97.6% after contacting 60 min with 300 mg/L Cu₂O NPs deposited on diatomite. Thus, Cu₂O NPs/diatomite can be favorably produced on large scale and potentially used as an antimicrobial agent, especially for water treatment in aquaculture.

Keywords: Cu₂O, nanoparticles, diatomite, antibacterial activity

INTRODUCTION

Metal nanoparticles (Au, Pt, Ag) have attracted considerable attention because of their unique properties such as catalytic, magnetic, optical, biological, and electrical properties [1]. Recently, Cu nanoparticles have been expected to be a good choice of the next-generation nanoparticles (NPs) mainly because of low cost [2]. Furthermore, the progress in nanomaterial science and technology has also accelerated the development of the synthesis of cuprous oxide (Cu₂O) nano-structures due to its prospective application in antimicrobial activity [1,3-5], photocatalysts [6-8], carbon monoxide oxidation [9], solar-driven water splitting [10], solar energy conversion [11], chemical template [12] and so on. In addition, hybrid Cu₂O-based heterogeneous nanostructure possesses novel synergistic properties that arise from the integrated interaction between the disparate components [13].

Diatomite is known as diatomaceous earth, a kind of porous natural mineral, derived from the deposition of single-celled aquatic algae, consisting of a great number of diatom units

with various shapes and sizes [14,15]. Due to the high porosity, thermal resistance, chemical stability, and low cost and abundance, diatomite has been widely used as catalyst supports, filler and filter aids, insulating materials, etc. In the present study, Cu₂O NPs deposited on diatomite were synthesized using hydrazine hydrate as a reducing agent and the antibacterial activity of the obtained Cu₂O NPs/diatomite against *Escherichia coli* (*E. coli*) was also investigated.

EXPERIMENTAL

Materials and Chemicals

Diatomite (~66.3% SiO₂) was supplied by a diatomite company from Phu Yen province, Vietnam. Analytical grade CuSO₄·5H₂O, NH₄OH (25%), and hydrazine hydrate (80%) were products from China. The strain of *E. coli* ATCC 6538 was provided by the University of Medical Pharmacy, Ho Chi Minh City. The Luria-Bertani (LB) medium for *E. coli* incubation was purchased from Himedia, India. Distilled water was used in all experiments.

Synthesis of Cu₂O NPs/diatomite

10 g diatomite was mixed with 30 ml water for 30 min. Then, 10 ml Cu^{2+} solution containing 2 g $\text{CuSO}_4 \cdot 5\text{H}_2\text{O}$ was added to the above diatomite- water mixture and stirred for 30 min. pH of the mixture was adjusted to ~ 6 with NH_4OH 5%. After that, 5 ml hydrazine solution 8% was slowly added to reduce Cu^{2+} to Cu^+ (Cu_2O NPs) while stirring for 2 h [1]. A yellowish-orange colored Cu_2O NPs/diatomite was observed. Finally, the synthesized Cu_2O NPs/diatomite was filtered, washed with water, and dried at 60°C in a forced-air oven till to constant weight.

Characterization and antimicrobial activity

Cu_2O NPs/diatomite in fine powder (0.05 g) was well dispersed in 20 ml of 5% PVA solution for UV-Vis optical spectrum measurement on a UV-2401 PC, Shimadzu, Japan. X-ray diffraction (XRD) pattern was carried out on a D8 Advance, Bruker, Germany. The particle size distribution of Cu_2O NPs/diatomite was measured by dynamic laser scattering (DLS) on a particle size analyzer, LB550, HORIBA, Japan. The content of copper in Cu_2O NPs/diatomite was determined by inductively coupled plasma-atomic emission spectroscopy (ICP-AES).

Antibacterial activity (*in vitro*) of diatomite and Cu_2O NPs/diatomite against *E. coli* was carried out by culture medium toxicity method in Luria-Bertani medium following the procedure as described by Du et al. [1].

RESULTS AND DISCUSSION

The UV-Vis spectra of diatomite and Cu_2O NPs/diatomite are shown Figure 1.

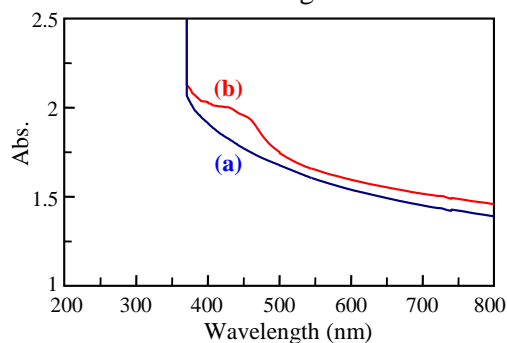


Figure 1. UV-Vis spectra of diatomite (a) and Cu_2O NPs/diatomite (b)

It is observed that the maximum optical absorption (λ_{max}) of Cu_2O NPs deposited on diatomite was at about 430 nm. Borgohain et al. [16] reported that the λ_{max} values of 448, 470,

and 584 nm corresponded to Cu_2O NPs sizes of 8, 14 and 45 nm, respectively. The longer the wavelength of the λ_{max} value, the larger the size of Cu_2O NPs. Results of Deki et al. [17] also indicated that Cu_2O NPs with a size of 6.7 nm displaying a λ_{max} at about 350 nm. Thus, Cu_2O NPs with the λ_{max} at about 430 nm deposited on diatomite was successfully synthesized.

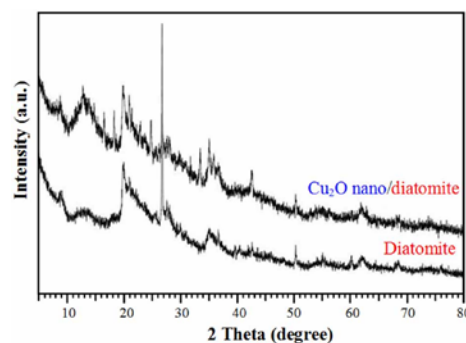


Figure 2. XRD patterns of diatomite and Cu_2O NPs/diatomite

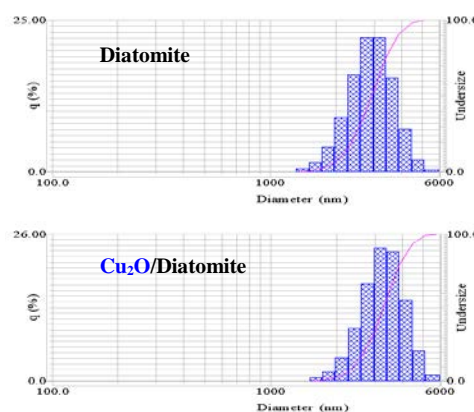


Figure 3. Dynamic laser scattering images of diatomite and Cu_2O NPs/diatomite

The XRD pattern of Cu_2O NPs/diatomite in Figure 2 showed that diffraction peaks appeared at 29.6° , 36.5° , 42.4° , 61.6° corresponding to (110), (111), (200), (220) planes of cuprite, respectively, indicated the formation of Cu_2O nanocrystals (JCPDS Card number 05-0667) [18]. The average crystalline size of Cu_2O NPs determined by taking the full width at half maximum (FWHM) of the most intense peak at 42.4° using Debye-Scherrer's formula [18] was of about 27.4 ± 4.4 nm. The crystalline size calculated from XRD patterns is usually bigger than that from TEM images [1,16]. Unfortunately, the particle size of Cu_2O NPs/diatomite synthesized in this study could not be predicted by TEM images due to the morphology of the Cu_2O NPs was not identified.

The content of Cu₂O NPs was determined by ICP-AES to be ~5.25%.

Results in Figure 3 showed the particle size of diatomite and Cu₂O NPs/diatomite measured by DLS in the range from 2.5 to 4.5 μm. Thus, the deposition of Cu₂O NPs on diatomite did almost not change the particle size of diatomite.

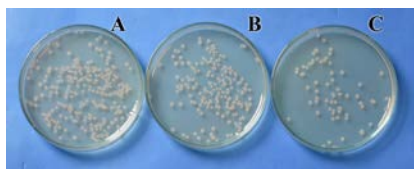


Figure 4. Photograph of the growth of *E. coli* on LB agar plates: A: control, B: diatomite, and C: Cu₂O NPs/diatomite (Cu₂O NPs: 100 ppm)

The antimicrobial efficiency (η) was calculated based on the survival number of bacteria in the control and studied samples (Figure 4) [1] to be 20.0% and 77.3% for diatomite and Cu₂O NPs/diatomite, respectively. The effect of Cu₂O NPs concentration on the antimicrobial efficiency was also investigated (see Figure 5).

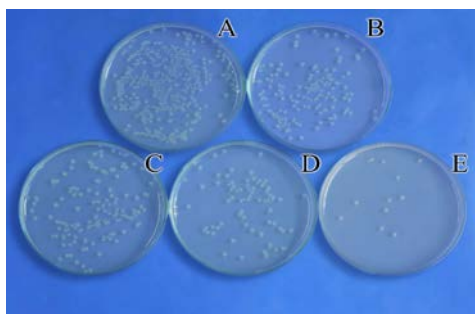


Figure 5. Photograph of the growth of *E. coli* on LB agar plates: A: control, Cu₂O NPs/diatomite B: 50, C: 100, D: 200, and E: 300 ppm calculated for Cu₂O NPs only

It was found that the η values were 67.4, 75.5, 86.9, and 97.6% for Cu₂O NPs concentration of 50, 100, 200, and 300 ppm, respectively after 1 h of contacted time of Cu₂O NPs/diatomite samples with *E. coli*. It is worth to note that Cu₂O NPs exhibited the same antibacterial activity as Cu NPs [3]. In addition, the antibacterial activity of Cu₂O NPs was still size and contacted time-dependent [1,3,5]. Recently, Yang et al. [19] reported that Cu₂O nano-composites presented powerful long-lasting antibacterial capability against *E. coli* and *S. aureus* compared to free Cu₂O NPs.

CONCLUSION

In this study, Cu₂O NPs with a crystalline size of ~27.4 nm deposited on diatomite was successfully synthesized using hydrazine hydrate as a reducing agent. Results of the antibacterial activity showed that Cu₂O NPs/diatomite exhibited highly antibacterial efficiency (η ~97.6%). The obtained Cu₂O NPs/diatomite product can be used as a bactericide especially for water treatment and agricultural application.

Acknowledgments

This work was financially supported by the Ministry of Natural Resources and Environment through the Project coded TNMT.2018.04.08.

References

- [1] B. D. Du et al., *Synthesis and investigation of antimicrobial activity of Cu₂O nano-particles/zeolite*, J. Nanopart., **2017** (2017) ID 7056864
- [2] L. Xiong et al., *Morphology-dependent antimicrobial activity of Cu/Cu_xO nanoparticles*, Ecotoxicology, **24** (2015) 2067-2072
- [3] M. Hans, *Role of copper oxides in contact killing of bacteria*, Langmuir, **29** (2013) 16160-16166
- [4] P. Li, W. Lv, S. Ai, *Green and gentle synthesis of Cu₂O nanoparticles using lignin as reducing agent and capping reagent with antibacterial properties*, J. Exp. Nanosci., **11** (2016) 18-27
- [5] L. Xiong et al., *Size controlled synthesis of nanoparticles: size effect on antibacterial activity and application as a photocatalyst for highly efficient H₂O₂ evolution*, RSC Adv., **7** (217) 51822-51830
- [6] X. Zhang et al., *Preparation and photocatalytic activity of cuprous oxide*, Solid State Sci., **12** (2010) 1215-1219
- [7] N. Li et al., *Simple synthesis of Cu₂O/Na-bentonite composites and their excellent photocatalytic properties in treating methyl orange*, Ceram. Int., **42** (2016) 5979-5984
- [8] H. Huang et al., *Preparation of cubic Cu₂O nanoparticles wrapped by reduced graphene oxide for the efficient removal of rhodamine B*, J. Alloy. Compd., **718** (2017) 112-115

- [9] B. Wei et al., *Cu₂O-CuO hollow nanospheres as a heterogeneous catalyst for synergetic oxidation of CO*, J. Phys. Chem. C, **122** (2018) 19524-19531
- [10] G. Li et al., *Highly active photocatalyst of Cu₂O/TiO₂ octahedron for hydrogen generation*, ACS Omega, **4** (2019) 3392-3397
- [11] R. Wick, S. D. Tilley, *Photovoltaic and photoelectrochemical solar energy conversion with Cu₂O*, J. Phys. Chem. C, **119** (2015) 26243-26257
- [12] S. D. Sun et al., *Formation of hierarchically polyhedral Cu₇S₄ cages from Cu₂O templates and their structure-dependent photocatalytic performances*, New J. Chem., **37** (2013) 3679-3684
- [13] S. Sun, *Recent advances in hybrid Cu₂O-based heterogeneous nanostructures*, Nanoscale, **7** (2015) 10850-10882
- [14] G. Q. Tang, A. R. Kovalick, *An experimental investigation of the effect of temperature on recovery of heavy oil from diatomite*, SPE J., **9** (2004) 163-165.
- [15] J. Seckbach, R. Gordon (eds.), *Diatoms: Fundamentals and Applications*, Scrivener Publishing LLL, 2019, 471-450
- [16] K. Borgohain, N. Murase, S. Mahamuni, *Synthesis and properties of Cu₂O quantum particles*, J. Appl. Phys., **42** (2016) 5979-5984
- [17] S. Deki et al., *Preparation and characterization of copper (I) oxide nanoparticles dispersed in a polymer matrix*, J. Mater. Chem., **8** (1998) 1865-1868
- [18] A. Khan et al., *A chemical reduction approach to the synthesis of copper nanoparticles*, Int. Nano Lett., **6** (2016) 21-26
- [19] Z. Yang et al., *Long-term antibacterial stable reduced graphene oxide nanocomposites loaded with cuprous oxide nanoparticles*, J. Colloid Interf. Sci., **533** (2019) 13-23.

ORAL SESSIONS

***NANOMATERIALS AND
NANODEVICES
(NMD)***

ALGAN/GAN TWO-DIMENSIONAL ELECTRON GAS FOR SENSING APPLICATIONS

Hong-Quan Nguyen¹, **Toan Dinh**¹, **Hamid Amini Moghadam**¹, **Hoang-Phuong Phan**¹, **Tuan-Khoa Nguyen**¹, **Jisheng Han**¹, **Sima Dimitrijević**¹, **Nam-Trung Nguyen**¹ and **Dzung Viet Dao**^{1,2}

¹ Queensland Micro- and Nanotechnology Centre, Griffith University, Queensland, Australia;

² School of Engineering and Built Environment, Griffith University, Queensland, Australia

Email: quan.nguyen@griffithuni.edu.au

ABSTRACT

The two-dimensional electron gas (2DEG) which is formed at the AlGa_N/Ga_N interface due to the difference in the spontaneous polarisation of the two adjacent AlGa_N, Ga_N layers is shown to respond very sensitively to mechanical and electrical effects. It is promising to use AlGa_N/Ga_N heterostructures in future integrated sensor devices. This work presents the design and characterisation of the stress/strain sensor and direct current (DC) sensor based AlGa_N/Ga_N 2DEG. The 2DEG based stress sensor exhibited an excellent repeatability and linearity with a significant change of the offset voltage under application of tensile and compressive strains. In particular, the sensitivity of the device to the applied strain was found to be as large as 3 (μV/V)/ppm, indicating the feasibility of using this effect for mechanical sensing applications. In addition, the 2DEG based current sensor exhibited an excellent linearity and repeatability with a high Hall voltage under the applied current ranging from -5 to 5 A. The sensitivity of the sensor was 0.26 (V/A)/A at room temperature, which are at least thirteen times greater than that of other Hall-effect based current sensors. The proposed sensor is promising for current monitoring in a wide range of operation conditions.

Keywords: AlGa_N/Ga_N 2DEG, current sensor, Hall effect sensor, stress/strain sensor.

INTRODUCTION

GaN is one of the most promising materials of group III-Nitrides (III-N) owing to its superior large energy-band gap (3.4eV) and high polarization effect. One of the advanced properties of AlGa_N/Ga_N is its capability to form two-dimensional electron gas (2DEG) [1].

By introducing external strain in the heterostructure, the change in piezoelectric polarization field leads to significant variations in 2DEG density, showing potential for developing stress/strain sensors [2]. The strain induced effect on the resistivity of two-terminal AlGa_N/Ga_N HEMT devices has been reported for pressure sensing applications with substantially high gauge factors [3]. However, for these devices, resistance-to-voltage circuit and amplifiers are normally required to convert resistance changes to output voltages and to obtain an easily detectable signal, leading to non-zero offset during operations with varying temperatures. Van der Pauw strain sensing devices (also referred to as four-terminal devices) initially presented by Kanda [4], have been proven to overcome the drawbacks of two-

terminal devices. For example, silicon and silicon carbide four-terminal devices have been demonstrated to be thermally stable as they do not rely on any external Wheatstone bridges and enable the miniaturization of such devices. Taking advantages of four-terminal configurations, several studies have recently demonstrated the strain dependence of output voltage in these devices for force and pressure sensing applications [5]. However, to the best of our knowledge, the strain dependence of AlGa_N/Ga_N based four-terminal devices on the offset voltage has not been fully understood so far. Therefore, this work aims to investigate the influence of compressive and tensile strain on the offset voltage of AlGa_N/Ga_N van der Pauw devices.

AlGa_N/Ga_N 2DEG also suitable for developing AC/DC current sensors due to its high electron mobility, wide band gap, and superior magnetic field sensitivity [6]. In this research, we demonstrated a highly sensitive current sensor based on AlGa_N/Ga_N 2DEG with a flux concentrator (magnetic core) to

concentrate the magnetic field onto the sensing area.

ALGAN/GAN 2DEG STRESS/STRAIN SENSOR

2.1 Working principal

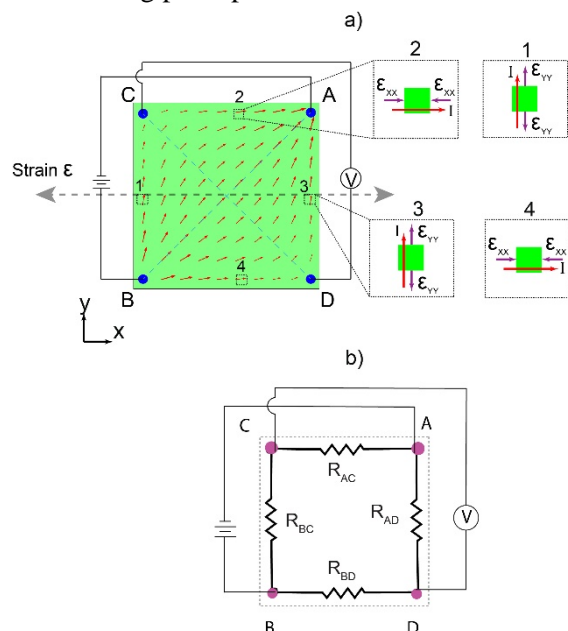


Figure 1. (a) 2D Simulation of current flux in 4 terminals device. The insets show the strain and current direction on particular cells. (b) Equivalent circuit diagram of the fabricated device.

Fig. 1(a) shows the configuration of the four-terminal strain sensor where the current was applied between terminals A, B while the output voltage was measured between terminals C, D. According to the Kanda's model [4] of a discrete constant circuit, the sensor is a square-type Wheatstone bridge circuit comprised of four resistors R_{AC} , R_{BC} , R_{BD} , and R_{AD} , Fig. 1(b). The relationship of the output signal V_{out} versus the four resistors is given by [7]

$$\frac{V_{out}}{V_{in}} = \frac{R_{BD}R_{AC} - R_{BC}R_{AD}}{(R_{BD} + R_{AD})(R_{BC} + R_{AC})} \quad (1)$$

At the strain free condition, the resistance of four sections are equal leading to a zero output voltage between terminals C and D. Upon the application of the tensile stress, the elongation of R_{AC} and R_{BD} led to a decrease in resistance, while the compression of R_{AD} and R_{BC} along the current direction caused an increase in these resistances. This asymmetric variation of the four resistors due to strain resulted in a voltage generated between terminals C and D, according to Eq. 1. Consequently, the four-terminal

configuration can be employed as a strain sensor where the induced strain can be monitored by measuring the output voltage $V_{out} = V_{CD}$.

2.2 Design and fabrication

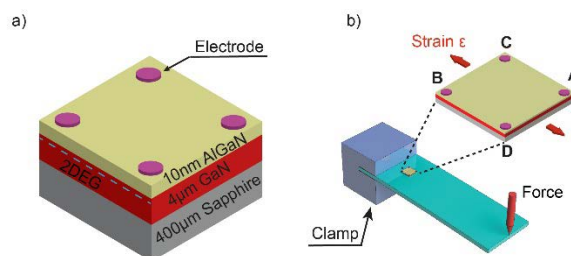


Figure 2. (a) Schematic sketch of the device structure; (b) Configuration of the experimental setup for the measurement of strain induced effect to the device.

To investigate the strain effect on four-terminal 2DEG devices, we utilize AlGaIn/GaN wafer with 10 nm AlGaIn top layer, 4 μ m GaN and 400 μ m sapphire substrate. The wafer was diced into 10 mm \times 10 mm \times 0.4 mm square strips and an Ohmic contact was formed on each corner of the device, Fig. 2(a). Finally, the square strip was bonded on a stainless-steel cantilever for the subsequent bending experiment as shown in Fig. 2(b).

The bending beam method was applied to induce strain into the sample, in which one end of a stainless-steel cantilever was fixed, while the other free end was deflected. The square-shape sample was attached to the vicinity of the fixed end of the stainless-steel beam. By pushing a force downward/upward, a tensile/compressive strain was applied to the device.

2.3 Results and discussion

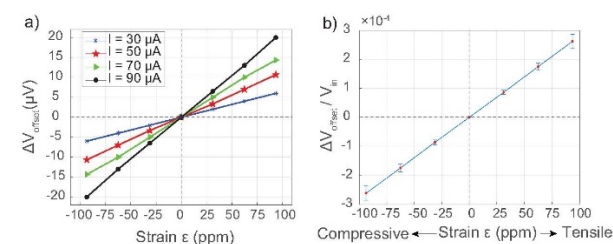


Figure 3. (a) Output voltage versus applied strains with different input currents; (b) The ratio of the output voltage to the input voltage of the device with varying strain.

Figure 3(a) shows the change in the output voltage at terminals C and D after subtracting the offset voltage under compressive and tensile strains, and under different applied currents

ranging from 30 to 90 μA . The experimental results indicated a positive value in the output voltage ΔV_{CD} under tensile strain, while a negative voltage was observed under compressive strain. The generated voltage of the device followed good linear relationships with the applied strain (varied from -90 to 90 ppm) at different applied currents, which is a preferable property for strain sensing applications. The strain sensitivity of the device can be defined as:

$$S = \left| \frac{\Delta V_{\text{offset}}}{V_{\text{in}}} \right| \times \frac{1}{\varepsilon} \quad (2)$$

It was also evident that increasing the applied current led to an increase in the change of the output voltage. Nevertheless, the sensitivity of the device to applied strain was independent of the voltage supplied through terminals C and D, Fig. 3(b). Accordingly, the strain sensitivity of the fabricated 2DEG four-terminal device was found to be as high as 3 ($\mu\text{V}/\text{V}$)/ppm which is comparable to other reported results for SiC.

ALGAN/GAN 2DEG CURRENT SENSOR

3.1 Working principal

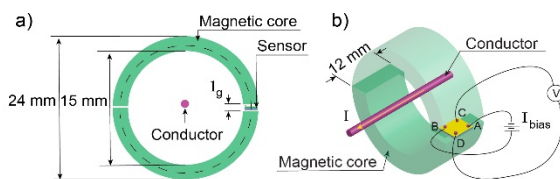


Figure 4. (a) The geometry and dimension of the magnetic core, (b) Experimental setup for characterization of the Hall current sensor

The operation of Hall effect current sensor is based on Ampere's law, where a magnetic field is generated around a current-carrying conductor. This magnetic field is converted into a voltage and detected by the Hall sensor. However, the magnetic field generated from the conductor is relatively small, consequently creating new challenges for detecting such a small signal. In addition, the magnetic field significantly depends on the distance between the sensors and the conductor [8].

As magnifying the magnetic signal would increase the Hall voltage, we utilized a magnetic flux concentrator in the form of toroidal core, as shown in Figs. 4(a) and 4(b). The nanocrystalline Vitroperm alloy was selected as core material due to its high permeability and low

remanence. The alloy contains about 82.8 % Fe, 8.8 % Si, 1.5 % B, 5.6 % Nb and 1.3 % Cu.

3.2 Design and fabrication

For device fabrication, we utilized AlGaIn/GaN wafer with 10 nm AlGaIn top layer, 4 μm GaN and 400 μm sapphire substrate. The wafer was diced into 10 mm \times 10 mm \times 0.4 mm square strips and an Ohmic contact was formed on each corner of the device, Fig. 2(a). The sensitivity of the AlGaIn/GaN 2DEG device was measured to be 77 $\text{VA}^{-1}\text{T}^{-1}$, which is greater than that of other semiconductor-based devices reported in the literature including Si, GaAs, InAs and InSb [9][10]. This result indicates the suitability of AlGaIn/GaN 2DEG for the development of sensitive current sensors. The chip was bonded on a glass film and then attached firmly to the magnetic core for the characterization of DC current sensing, as shown in Figs. 4(a) and (b).

3.3 Results and discussion

The output Hall voltage of a Hall effect device is dependent on the electron density in 2DEG and the intensity of the magnetic field:

$$V_H = G_H \frac{\gamma_H}{qN_{2\text{DEG}}} I_{\text{bias}} B \quad (3)$$

where V_H is the Hall voltage, G_H is the geometrical correction factor of Hall voltage, γ_H is the Hall factor, I_{bias} is the bias current, B is the magnetic field applied perpendicular to the plane of the device, q is the electron charge, and $N_{2\text{DEG}}$ is the sheet density.

The magnetic core converges the magnetic flux surrounding the conductor into a magnetic flux perpendicular to the chip surface. The magnetic flux density focused by the core to the sensor can be calculated as [11][12]:

$$B = \frac{\mu_0 \mu_i I}{l_m \mu_0 + l_g \mu_i} \quad (4)$$

where B is the magnetic flux density (T), μ_i is the initial permeability of the core, l_m is the mean length of core and l_g is the length of air gap.

The flux density of the magnetic field is magnified by a factor of 13 from the original field value. The measured results agree well with the simulation result. Based on the simulation result, the magnetic flux generated by the magnetic core changes only 4% due to the shifting of the conductor inside the magnetic core. Therefore, using such a core, the conductor

can be moved inside the core without significantly affecting the output voltage of the sensor.

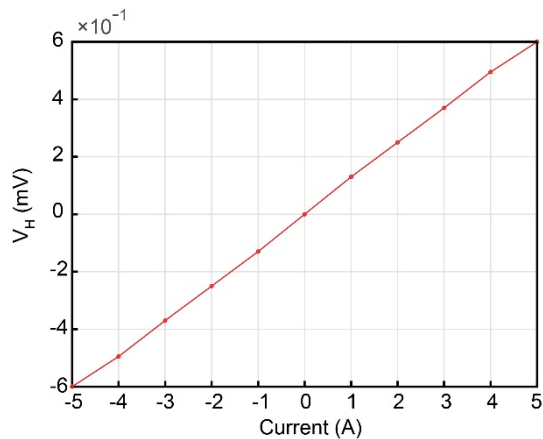


Figure 5. Hall voltage versus applied current at room temperature.

The sensitivity of the device with respect to supplied bias current can be defined as:

$$S = \frac{V_H}{I_{bias}} \times \frac{1}{I} \quad (5)$$

The current sensitivity of the fabricated 2DEG four-terminal device was found to be as high as 0.26 (V/A)/A, Fig. 5. This sensitivity is 13 times higher compared to other reported results for different current sensors [13].

CONCLUSION

The offset voltage dependence of the AlGaIn/GaN device on applied strain has been investigated for the first time. We observed that the offset voltage of the AlGaIn/GaN van der Pauw device is relatively sensitive to the applied compressive and tensile strain. This property is essential for the design of AlGaIn/GaN-based mechanical sensing devices, which can be exposed to the strain under packaging as well as operational processes. The strain sensitivity of this device has been found to be relatively high at 3(μV/V)/ppm, demonstrating its feasibility for mechanical sensors.

We also demonstrated AlGaIn/GaN heterostructure based devices for highly sensitive DC current sensing. The device exhibited a high sensitivity of 0.26 (V/A)/A, showing its feasibility for current sensing applications. The magnetic core was used to concentrate the magnetic field generated from the electric current in the conductor. By using the magnetic field concentrator, sensitivity of the Hall effect sensor increased at least 13 times compared to the case without the magnetic core.

References

- [1]. U. K. Mishra, L. Shen, T. E. Kazior, and Y. Wu, "GaN-Based RF Power Devices and Amplifiers," Proc. IEEE, vol. 96, no. 2, pp. 287-305, 2008.
- [2]. B. S. Kang et al., "Pressure-induced changes in the conductivity of AlGaIn/GaN high-electron mobility-transistor membranes," Appl. Phys. Lett., vol. 85, no. 14, pp. 2962-2964, 2004.
- [3]. J. Xie, P. Ruden, K. A. Son, Y. Liu, and H. Morko, "Effect of hydrostatic pressure on the dc characteristics of AlGaIn GaN heterojunction field effect transistors," Appl. Phys. Lett., vol. 88, no. 1, pp. 013505-013505-3, 2006.
- [4]. Y. Kanda and K. Yamamura, "Four-terminal-gauge quasi-circular and square diaphragm silicon pressure sensors," Sensors and Actuators, vol. 18, no. 3, pp. 247-257, 1989.
- [5]. H.-P. Phan, A. Qamar, D.V. Dao, T. Dinh, L. Wang, J. Han, P. Tanner, S. Dimitrijevic, and N.T. Nguyen, "Orientation dependence of the pseudo-Hall effect in p-type 3C-SiC four-terminal devices under mechanical stress," RSC Adv., 5 (69), pp.56377-56381, 2015.
- [6]. V. Cimalla, J. Pezoldt, and O. Ambacher, "Group III nitride and SiC based MEMS and NEMS: materials properties, technology and applications," J. Phys. D, vol. 40, no. 20, pp. 6386-6434, 2007.
- [7]. T.-K. Nguyen, H.-P. Phan, J. Han, T. Dinh, A. Foisal, S. Dimitrijevic "Highly sensitive p-type 4H-SiC van der Pauw sensor," RSC Adv., vol. 8, no. 6, pp. 3009-3013, 2018.
- [8]. J. Jankowski, El-Ahmar, Semir and M. Oszałdowski. "Hall Sensors for Extreme Temperatures," Sensors, vol. 11, pp. 876-885, 2011.
- [9]. S. R. int Hout and S. Middelhoek, "A 400C silicon Hall sensor," Sensors Actuators: A. Physical, vol. 60, (1), pp. 14-22, 1997. 3222-3233, 1999.
- [10]. T. Hara, M. Mihara, N. Toyoda and M. Zama, "Highly linear GaAs hall devices fabricated by ion implantation," IEEE Transactions on Electron Devices, vol. 29, (1), pp. 78-82, 1982.
- [11]. A. Bermudez, D. Gomez and P. Salgado, "Mathematical Models and Numerical Simulation in Electromagnetism," Springer, Cham, vol. 74, pp. 151-182, 2014.
- [12]. J.R. Barnes, "Robust Electronic Design Reference Book," Springer, Boston, MA, pp. 126-155, 2004.
- [13]. T. P. White, S. Shetty, E. Morgan, H. Alan and J. Gregory, "AlGaIn/GaN Micro-Hall Effect Devices for Simultaneous Current and Temperature Measurements from Line Currents," IEEE Sensors Journal, vol. 18, pp. 2944-2951, 2018.

EFFECT OF TiO₂ MORPHOLOGY ON ITS PERFORMANCE IN THE PHOTOCATALYTIC DEGRADATION OF CINNAMIC ACID SOLUTION

Dien Trung Nguyen^{2,3}, Cam Anh Ha^{1*}, Tri Nguyen⁴, Tien Cuong Hoang⁴, Thuc Nhi Thi Vo¹ and Cam Loc Luu¹

¹ Ho Chi Minh City University of Technology, VNU-HCM, 268 Ly Thuong Kiet Street, District 10, Ho Chi Minh City, Vietnam;

² School of Education, Can Tho University, 3/2 street, Ninh Kieu District, Can Tho city, Vietnam;

³ Graduate University of Science and Technology, Vietnam Academy of Science and Technology, 18 Hoang Quoc Viet street, Cay Giay district, Ha Noi city, Vietnam;

⁴ Institute of Chemical Technology, Vietnam Academy of Science and Technology, 01 Mac Dinh Chi Street, District 1, Ho Chi Minh City, Vietnam

Email: hcanh@hcmut.edu.vn

ABSTRACT

By hydrothermal method using two precursors (tetrakisopropyl titanate and titanium dioxide) at acidic and alkaline medium, TiO₂ photocatalysts with two morphologies (nanoparticles – TNPs and nanotubes – TNTs) were successfully synthesized. Characteristics of catalysts were identified by various methods including XRD, FT-IR, BET, UV-Vis, SEM, TEM, Raman, and PZC. The analysis results prove that TiO₂ nanoparticles (TNPs), containing both anatase and rutile phases, had the advantages of properties such as smaller average crystallite size (10.4 nm) related to higher BET surface area (102.9 m²g⁻¹) and band gap energy of 3.08 eV. Meanwhile, TiO₂ nanotubes were tube-shaped with a diameter of 10.7 nm and length of about 50–100 nm, contained titanate phase with the specific surface area of 137.9 m²g⁻¹ and band gap energy of 3.18 eV. The optimum conditions including photocatalyst dosage, initial pH solution, and the air flow rate in the photocatalytic degradation of cinnamic acid (CA) at 25 °C were determined. The results showed that the photocatalytic activity of TNPs was higher than that of TNTs in CA degradation. CA conversion reached at 91% on TNPs after a 40-minute reaction while it only did 52% on TNTs after 90 min in the most suitable reaction conditions.

Keywords: TiO₂ morphology, cinnamic acid, photocatalytic degradation, hydrothermal method.

INTRODUCTION

Cinnamic acid (CA) was acknowledged as a model of the persistent phenolic acids in the contaminated water. Advanced oxidation processes (AOPs) stand out as a practical technology in the stimulation of the oxidation process, helping effectively remove POPs in aqueous phase even at little concentration. In the presence of the light, photocatalysts can form highly active species including holes, electrons, hydroxyl radicals, and superoxide radicals to degrade and mineralize organic pollutants [1, 2]. The hydrothermal method has been used to produce TiO₂ with different shapes such as nanoparticles, nanorods, nanowires, and nanotubes [3]. In this work, TiO₂ catalysts were synthesized by the hydrothermal method in different shapes. The physicochemical characteristics and the photocatalytic activity of synthesized TiO₂ catalysts were determined in

more detail for the degradation of the CA solution.

EXPERIMENTAL

The preparation of TNPs was carried out by the hydrothermal method in acidic conditions as follows. 3 mL of tetrakisopropyl titanate was added dropwise to solution of 3 mL 37% hydrochloric acid in 37 mL water. The obtained homogeneous solution was hydrolyzed in the autoclave at 160 °C for 12 h. The resulting precipitate was washed with distilled water and ethanol three times and dried at 60 °C overnight.

In the same way, TNTs catalyst was synthesized by the hydrothermal method in alkaline condition. Firstly, 0.8 g of titanium dioxide powder was added to 80 mL of 10 M NaOH. Then, the obtained suspension was stirred for 1 h at room temperature and heated at 135 °C in a 100 mL autoclave for 24 h. The resulting precipitate was separated and collected

by centrifuge, followed by several washing steps with 0.1 N HCl solution and deionized water. In the final step, TNTs powder was obtained after drying at 60 °C for 12 h.

X-ray diffraction (XRD) measurements were performed on Bruker D2 Phaser X-Ray Diffractometer. UV-Vis diffuse reflectance spectroscopy (DRS) was used to examine the band gap of the catalysts and recorded on a Varian Cary 5000 UV-Vis-NIR spectrophotometer. Then, the band gap can be calculated [4] as:

$$E_g = \frac{1239.8}{\lambda}$$

where E_g is the band gap energy (eV) and λ is the edge wavelength (nm). Indeed, indirect and direct electron transitions were also supposed and calculation of the band gaps was performed by plotting $(F(R)h\nu)^{1/2}$ vs $h\nu$ (indirect method) and $(F(R)h\nu)^2$ vs $h\nu$ (direct method), according to reference [5]. Nitrogen adsorption-desorption isotherms were determined by using a Nova 2200e instrument. The morphology and surface properties of materials were investigated by a Jeol Jem 1400 transmission electron microscopy (TEM) apparatus. Fourier transform infrared (FTIR) measurements were used for the characterization of functional groups. The point of zero charge (PZC) of TiO_2 samples was determined by the salt addition method [6].

The photocatalytic activity of samples was studied by the batch method as described in [7]. The reaction mixture was stirred in the dark for 40 min to establish the adsorption/desorption equilibrium before exposing to the UV light irradiation of 36 UVA Engin LZ1-00U600 lamps ($\lambda \approx 350\text{--}400$ nm, with the maximum peak at 365 nm). The reaction solution was separated by filtration and analyzed by UV-visible spectrophotometer on UV-1800 (Shimadzu) at 272 nm.

RESULTS AND DISCUSSION

As can be seen from Figure 1, the anatase phase with main characteristic peaks at $2\theta = 25.5, 38.0, 48.2$ and 75.5° with the strongest intensity at $2\theta = 25.5^\circ$ was recognized in XRD pattern of TNPs. There are some peaks related rutile phase was observed at $27.5, 36.2, 41.4, 54.4, 62.9$ and 69.1° with the strongest intensity at $2\theta = 27.5^\circ$. Meanwhile, the XRD spectra of TNTs appeared three characteristic peaks at $2\theta = 24.1, 28.3$ and 48.0° , which have been assigned

to the diffraction of titanates such as $A_2Ti_2O_5 \cdot H_2O$, $A_2Ti_3O_7$ (where A: H or Na), and lepidocrocite titanates. Furthermore, the XRD pattern of TNTs also exhibited diffraction peak at $2\theta = 10.2^\circ$ indicating the presence of hydrogen titanates phase ($H_2Ti_3O_7$) by replacement of Na^+ by H^+ when the products were washed with water [8, 9].

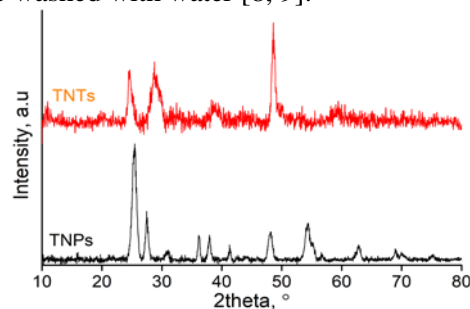


Figure 1. XRD pattern of TNPs and TNTs catalysts.

The Raman spectra of TNPs exhibited characteristic modes for anatase at $145, 399, 513$ and 639 cm^{-1} , and rutile at 210 and 445 cm^{-1} . Meanwhile, the Raman spectra of TNTs samples showed specific features at $285, 450$ and 667 cm^{-1} , attributed to Ti-O vibrating modes in titanates and Ti-O-Ti or Ti-O-Na vibrations in nanotubes structures.

On the FTIR spectra of TNPs and TNTs samples, the wide characteristic peaks at 3380 cm^{-1} , assigning to the stretching vibration of surface-absorbed H_2O molecules and peak at 1630 cm^{-1} contributing to the surface O-H bonds were observed. The new small peak at 1340 cm^{-1} in TNTs spectra is attributed to the protonation of the surface TiO_2 under acidic solution to form $TiOH_2^+$ groups that confirm the formation of titanate nanotubes.

TEM images (Figure 2) demonstrate that TNPs were nearly spherical in shape with particles' diameter ranges between 12 and 30 nm. Meanwhile, TNTs had nanotube structures with lengths up to 30–120 nm, outer diameters between 8 and 12 nm and inner diameters of 5 nm. In both cases, the nanostructures were quite a monodispersity and relatively uniform in size. The specific surface area and pore diameter of TNPs sample are $102.9\text{ m}^2\text{g}^{-1}$ and 2.72 nm, respectively (Table 1). TNT shows a higher surface area and smaller pore diameter than TNPs, being $137.9\text{ m}^2\text{g}^{-1}$ and 2.18 nm respectively. Furthermore, the PZC of TNPs and TNTs catalysts was approximately 3.11 and 3.40.

Table 1. The crystalline size (d_{cry}), the BET surface area (S_{BET}), the average pore diameter (d_{pore}), and the point of zero charge (PZC) of TNPs and TNTs catalysts

Catalyst	d_{cry} , nm	S_{BET} , m^2g^{-1}	d_{pore} , nm	PZC
TNPs	10.4	102.9	2.72	3.11
TNTs	10.7	137.9	2.18	3.40

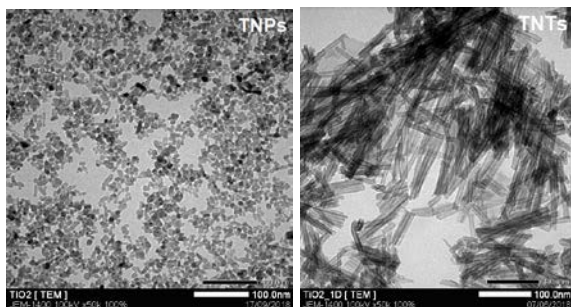


Figure 2. TEM images of TNPs and TNTs catalysts.

The data in Table 2 show that the E_g values for the indirect method (E_g^2) were in good agreement with those obtained from the absorbance method (E_g^1), while higher values E_g^3 have been obtained when the direct method was used.

Table 2. The energy band gap (E_g) values obtained from different methods for TNPs and TNTs catalysts

catalyst	E_g^1 , eV	E_g^2 , eV	E_g^3 , eV
TNPs	2.95	3.08	3.31
TNTs	3.08	3.18	3.48

¹ absorbance

² indirect allowed transitions $(\alpha h\nu)^{1/2}$

³ direct allowed transitions $(\alpha h\nu)^2$

Figure 3 shows the influences of the operational parameters on the photoactivity of TNPs catalyst in CA degradation. As it followed from Figure 3a, CA degradation was significantly affected by the catalyst dosages. When the catalyst concentration extended from 0.10 to 0.25 gL^{-1} , CA degradation extent for 40 min (X_{40}) raised from 60 to 91%. However, a further increase in the catalyst dosage (0.50 gL^{-1}) led to a decrease in CA degradation due to the turbidity of the suspension and light scattering effects [10]. As can be seen from Figure 3b, the optimum pH was found to be 3.8 and the maximum conversion of 91% was achieved within 40 min. When the initial pH of the CA solution was increased from 3.8 to 7.0,

there was a remarkable decrease in CA degradation extent from 91 to 24%. This can be explained that at pH values greater than PZC of TNPs catalyst (3.11), TiO_2 surfaces were negatively charged. At solution pH lower its pKa value (4.44), for example, pH = 3.8, CA was protonated and acted as the cation surfactant; therefore, CA favored the adsorption on the negatively charged surface lead to the activity of catalyst to be higher [11]. At pH higher 4.44, CA as well as TiO_2 surfaces were negatively charged resulting in the development of greater repulsive forces between TiO_2 surface and deprotonated CA [12]. It can be seen from Figure 3c that the conversion of CA significantly changed when increasing air flow rate from 0.2 to 0.3 $Lmin^{-1}$ the 40 min conversion of CA on TNPs catalyst increased from 79% to 91%. In the photocatalytic reaction, oxygen acts as an electron capture agent, that increased the recombination time of $e^- - h^+$ pairs and generated strong oxidative electron accepted oxygen ($O_2^{\bullet-}$), in the result the photocatalytic activity was enhanced. However, at the higher oxygen flow rate may hinder the absorbance of UV light to the photocatalyst [13].

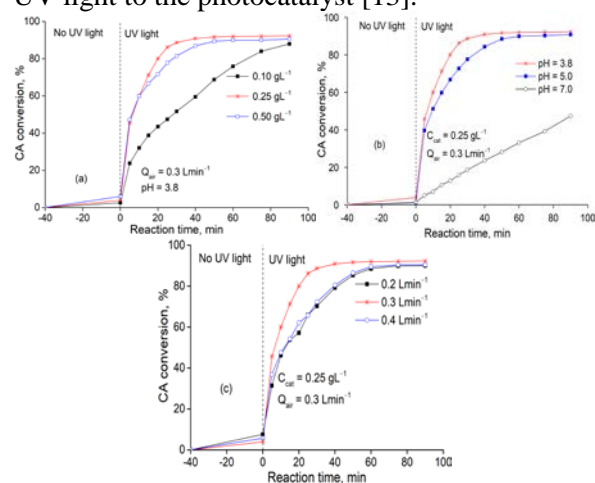


Figure 3. Effect of operational parameters: photocatalyst dosage (a), initial pH solution (b) and air flow rate (c) on the photocatalytic degradation of CA on TNPs catalyst.

The influence of the photocatalyst dosage, initial pH solution, and the air flow rate in the photocatalytic degradation of CA solution on TNTs catalyst as illustrated in Figure 4. Based on these relationships, the optimal conditions of CA photodegradation on TNPs catalyst were found as follows: catalyst dosage of 0.75 gL^{-1} , initial pH of 3.8 and an air flow of 0.5 $Lmin^{-1}$.

The conversion of cinnamic acid on TNTs sample at this condition was 52 % after 90 min.

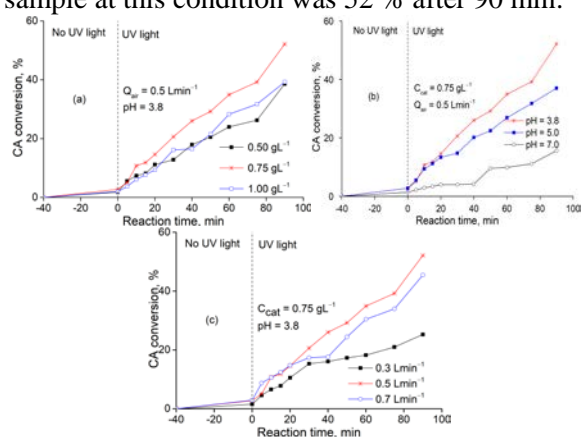


Figure 4. Effect of operational parameters: photocatalyst dosage (a), initial pH solution (b) and air flow rate (c) on the photocatalytic.

CONCLUSION

TiO₂ photocatalysts of nanoparticles and nanotubes morphologies were successfully synthesized by the hydrothermal method in acidic and alkaline conditions. TNPs TiO₂ exists in spherical crystals, size 10.4 nm including anatase and rutile phases. Besides, the TNPs catalyst also had a large specific surface area (102.9 m²g⁻¹) and a low band gap energy of 3.08 eV. TNTs catalysts were tube-shaped (length of about 50–100 nm and diameter of 10.7 nm) with a uniform structure, contained mainly titanate phase with specific surface area as high as 137.9 m²g⁻¹ and band gap energy of 3.18 eV. TNPs catalyst showed higher activity than the TNTs catalyst for the CA photodegradation.

References

- [1] G. M. Madhu, M. Raj, K. Pai and S. Rao, *Photodegradation of methylene blue dye using UV/BaTiO₃, UV/H₂O₂ and UV/H₂O₂/BaTiO₃ oxidation processes*, Indian Journal of Chemical Technology **14** (2007) 139-144.
- [2] X. Pang, W. Chang, C. Chen, H. Ji, W. Ma and J. Zhao, *Determining the TiO₂-photocatalytic aryl-ring-opening mechanism in aqueous solution using oxygen-18 labeled O₂ and H₂O*, Journal of the American Chemical Society **136** (2014) 8714-8721.
- [3] S. Y. Chae, M. K. Park, S. K. Lee, T. Y. Kim, S. K. Kim and W. I. Lee, *Preparation of size-controlled TiO₂ nanoparticles and derivation of optically transparent photocatalytic films*, Chemistry of Materials **15** (2003) 3326-3331.
- [4] A. R. Gandhe and J. B. Fernandes, *A simple method to synthesize N-doped rutile titania with enhanced photocatalytic activity in sunlight*, Journal of Solid State Chemistry **178** (2005) 2953-2957.
- [5] R. López and R. Gómez, *Band-gap energy estimation from diffuse reflectance measurements on sol-gel and commercial TiO₂: a comparative study*, Journal of Sol-Gel Science and Technology **61** (2012) 1-7.
- [6] E. N. Bakatula, D. Richard, C. M. Neculita and G. J. Zagury, *Determination of point of zero charge of natural organic materials*, Environmental science and pollution research international **25** (2018) 7823-7833.
- [7] H. C. Anh, L. C. Loc, N. Tri, N. P. Anh, N. T. N. Tot, N. T. T. Van and H. T. Cuong, *Photodegradation of cinnamic acid solution in the presence of various oxidizing agents on TiO₂ and Fe-TiO₂ catalysts*, Journal of Materials Science and Engineering A **6** (2016) 289-300.
- [8] C. C. Tsai and H. Teng, *Structural features of nanotubes synthesized from NaOH treatment on TiO₂ with different post-treatments*, Chemistry of Materials **18** (2006) 367-373.
- [9] S. Muniyappan, T. Solaiyammal, K. Sudhakar, A. Karthigeyan and P. Murugakoothan, *Conventional hydrothermal synthesis of titanate nanotubes: Systematic discussions on structural, optical, thermal and morphological properties*, Modern Electronic Materials **3** (2017) 174-178.
- [10] M. Jamil, Z. S. Khan, A. Ali and N. Iqbal, *Studies on solution processed Graphene-Nb₂O₅ nanocomposite based photoanode for dye-sensitized solar cells*, Journal of Alloys and Compounds **694** (2017) 401-407.
- [11] V. Simon, A. Thuret, L. Candy, S. Bassil, S. Duthen, C. Raynaud and A. Masseron, *Recovery of hydroxycinnamic acids from renewable resources by adsorption on zeolites*, Chemical Engineering Journal **280** (2015) 748-754.
- [12] M. Huuhtanen, R. Brahmi and R. L. Keiski, *Photocatalytic Degradation of Organic Pollutants in Wastewater*, Topics in Catalysis **58** (2015) 1085-1099.
- [13] S. M. Lam, J. C. Sin and A. R. Mohamed, *Parameter effect on photocatalytic degradation of phenol using TiO₂-P25/activated carbon (AC)*, Korean Journal of Chemical Engineering **27** (2010) 1109-1116.

THE EFFECTION OF ELECTRON DENSITY FLUCTUATION ON THE MICROSTRUCTURES OF POLYMER ELECTROLYTE MEMBRANES FOR FUEL CELL APPLICATION

La Ly Nguyen^{1,2,3,*}, **Lam Hoang Hao**², **Le Viet Hai**², **Nguyen Tien Cuong**⁵,
Huynh Truc Phuong⁴, **Tran Duy Tap**^{2,*}

¹Center for Nuclear Techniques, Vietnam Atomic Energy Institute,
217 Nguyen Trai, District 1, Ho Chi Minh City, Viet Nam.

²Faculty of Materials Science and Technology, University of Science, Viet Nam National University-Ho Chi Minh City, 227 Nguyen Van Cu, District 5, Ho Chi Minh City, Viet Nam.

³Institute for Nanotechnology, Viet Nam National University-Ho Chi Minh City, Community 6, Linh Trung Ward, Thu Duc District, Ho Chi Minh City, Viet Nam.

⁴Faculty of Physics and Engineering Physics, University of Science, Viet Nam National University-Ho Chi Minh City, 227 Nguyen Van Cu, District 5, Ho Chi Minh City, Viet Nam.

⁵Faculty of Physics, University of Science, Viet Nam National University-Ha Noi, 334 Nguyen Trai, Thanh Xuan District, Ha Noi, Viet Nam.

* Email: lalynguyen279@gmail.com; tdtap@hcmus.edu.vn

ABSTRACT

Electron density fluctuation owing to thermal motion and defects in semicrystalline polymers is present at everywhere in the small-angle X-ray scattering (SAXS) profiles but affects more strongly on the structures located in the high q-range because of its contribution more than 90% of total scattering intensity. Poly(styrenesulfonic acid)-grafted poly(ethylene-co-tetrafluoroethylene) polymer electrolyte membranes (ETFE-PEMs) possess hierarchical structures at different scale ranges including lamellar structure, interfacial boundary, and conducting layer. These structures have a close relationship with the properties of membranes such as proton conductivity, water uptake, mechanical strength, chemical strength, and thermal stability that relate strongly to the efficiency and performance of the fuel cell. In this article, we used six models such as Vonk 4, Vonk 6, Vonk 8, Ruland 2, Ruland 4, and Ruland 6 to estimate the effect of electron density fluctuation on the structures that mentioned above. The obtained results of the electron density fluctuation depend on the methods of determination and affect dramatically on the sizes of interfacial thickness and the conducting layer but not the lamellar structure.

Keywords: *ETFE-PEM, small-angle X-ray scattering (SAXS), electron density fluctuation, fuel cell.*

INTRODUCTION

Recently, poly(styrenesulfonic acid) grafted poly(ethylene-co-tetrafluoroethylene) polymer electrolyte membranes (ETFE-PEMs) prepared by the preirradiation grafting method have been exhibited as the alternative membranes for vehicle fuel cell applications. These membranes have been reported to possess the hierarchical structures including lamellar structure, interfacial boundary, and conducting layer. The small-angle X-ray scattering (SAXS) profiles of these structures have been investigated previously.^{1,2} It is well-known that the electron density fluctuation affects significantly on the microstructures located in the high q-range because the scattering due to electron density

fluctuation was reported to contribute more than 90% of total scattering intensity.³ However, there are no reports to concern this critical issue for graft-type membranes using in the fuel cell systems. Accordingly, in this study, we have investigated the affection of electron density fluctuation on the hierarchical structures of ETFE-PEMs. The hierarchical structures of ETFE-PEMs as mentioned above relate closely with the membrane properties such as proton conductivity, water uptake, mechanical strength, chemical strength, and thermal stability. Therefore, the precise determination of these higher order structures with correction of electron density fluctuation is highly desirable to improve understanding of the structure –

property relationship of the graft-type membranes for fuel cell applications.

The electron density fluctuation intensity, which is considered as scattering backgrounds ($I_{FI}(q)$ or $I_B(q)$ with q is scattering vector $q = 4\pi\sin\theta/\lambda$, where 2θ is scattering angle and λ is the wavelength of the incident radiation) is determined normally by Vonk⁴ and Ruland⁵ models as follows:

$$I_{FI}(q) = Fl + Bq^n \quad (1)$$

$$I_{FI}(q) = Fl e^{Aq^n} \quad (2)$$

where Fl is the so-called electron density fluctuation, A , B , and n (an even integer between 0 and 10) are arbitrary constants.

EXPERIMENTAL

Details on the materials, preparations and SAXS measurements were described in our previous studies.^{1,2} The ETFE-PEM membranes with grafting degree (GD) = 19%, 34%, and 59% were prepared the preirradiation grafting method and then measured by SAXS (Fig 1).

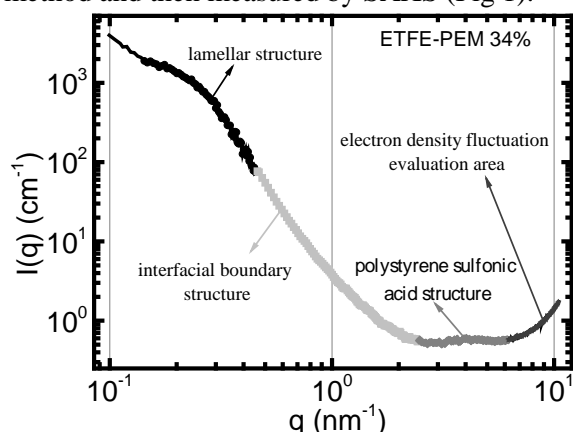


Figure 1. SAXS profile of ETFE-PEM 34% and typical structures.

RESULTS AND DISCUSSION

To estimate the intensity of electron density fluctuation $I_{FI}(q)$ and other parameters (Fl , A , B , n), the linear fitting of the plot of $I(q)$ vs q^n (for Vonk function) and $\ln(I(q))$ vs q^n (for Ruland function) were performed in the high- q region where the observed scattering intensities from the morphology and structure of polymers were negligible. In this study, we use $n = 4, 6, 8$ for Vonk models (denotes as Vonk 4, Vonk 6, Vonk 8) and $n = 2, 4, 6$ for Ruland models (denotes as

Ruland 2, Ruland 4, Ruland 6) to find out the suitable models to estimate the electron density fluctuation for original ETFE and ETFE-PEMs. Fig 2 show the detail of fitting for ETFE-PEM 19% using Vonk 6 and Ruland 4 models, and the others are conducted similarly.

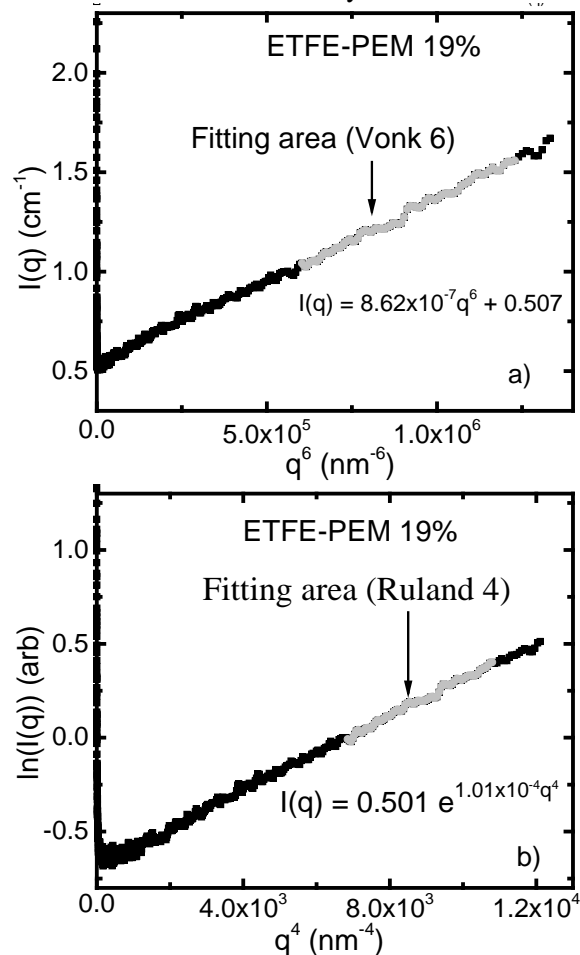


Figure 2. Background determination for ETFE-PEM 19% by Vonk 6 (a) and Ruland 4 (b).

To determine the effect of background on the whole profile, the “contribution factor (%)” = $I_{FI}(q)/I(q) \times 100\%$ was used. Fig 3 shows that models of Vonk 4 and Ruland 2 or Vonk 8 and Ruland 6 show under- or over-estimation the contribution factor, whereas Vonk 6 and Ruland 4 models seem to be suitable. It is because these models give the contribution around 100% in the q range $> 2 \text{ nm}^{-1}$, which is in good agreement with those in a previous report.³

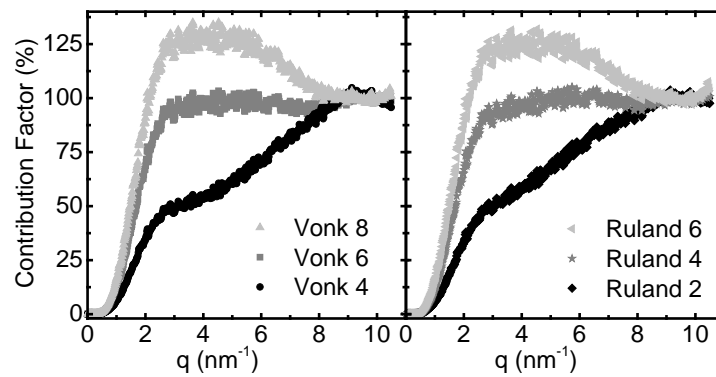


Figure 3. Contribution factor of ETFE-PEM 19% determined by Vonk and Ruland models.

Table 1. Fitting results of Vonk 6 and Ruland 4 models for ETFE and ETFE-PEMs

Sample	Vonk 6		Ruland 4	
	B	F1	A	F1
Original ETFE	$(5.26 \pm 0.12) \times 10^{-7}$	0.31 ± 0.01	$(1.08 \pm 0.03) \times 10^{-4}$	0.29 ± 0.01
ETFE-PEM 19%	$(8.62 \pm 0.08) \times 10^{-7}$	0.51 ± 0.01	$(1.01 \pm 0.02) \times 10^{-4}$	0.50 ± 0.01
ETFE-PEM 34%	$(9.90 \pm 0.48) \times 10^{-7}$	0.52 ± 0.03	$(1.18 \pm 0.11) \times 10^{-4}$	0.45 ± 0.04
ETFE-PEM 59%	$(9.83 \pm 0.05) \times 10^{-7}$	0.44 ± 0.01	$(1.30 \pm 0.05) \times 10^{-4}$	0.41 ± 0.02

In the next section, we use the fitting results of Vonk 6 and Ruland 4 models to estimate $I_{FI}(q)$. From the Porod's law for ideal two phase systems, the intensity in the q range of $0.5 - 2 \text{ nm}^{-1}$ should be proportional with q^{-4} (or slope of the plot $\log(Iq)$ vs $\log(q)$ is -4).⁶ However, the SAXS profiles of ETFE-PEMs hardly completely follow the Porod's law because the membranes possess the interfacial boundary between crystal and amorphous phase within the lamellar stacks and the high electron density fluctuation in the high q -region. Fig 4 show the SAXS profiles before and after subtraction background by both Vonk 6 and Ruland 4

methods. It is observed that the SAXS profiles were unchanged in the q range of $0.1 - 0.6 \text{ nm}^{-1}$, where the lamellar structures locate, but slightly altered in the higher q range than 0.6 nm^{-1} , where the diffuse boundary layer and proton conductance region locate (Table 2). These results clearly show that the background correction does not affect on the lamellar structure but strongly alters the SAXS profiles of the interfacial boundary structure and the ion conductance. In the other words, to determine the interfacial thickness, the electron density fluctuation must be eliminated.

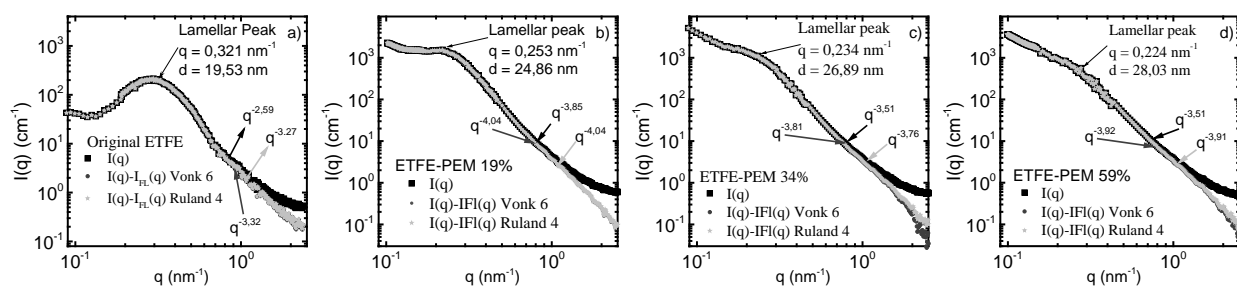


Figure 4. SAXS profiles before and after background correction in q range = $0.1 - 2.5 \text{ nm}^{-1}$.

Table 2. Slope of the $\log(Iq)$ vs $\log(q)$ plot after background correction by using Vonk 6 and Ruland 4 methods

Sample	Profile	Vonk 6	Ruland 4
Original ETFE	-2.59 ± 0.04	-3.32 ± 0.03	-3.27 ± 0.04
ETFE-PEM 19%	-3.85 ± 0.04	-4.04 ± 0.04	-4.04 ± 0.05
ETFE-PEM 34%	-3.52 ± 0.03	-3.81 ± 0.02	-3.76 ± 0.04
ETFE-PEM 59%	-3.51 ± 0.04	-3.92 ± 0.03	-3.91 ± 0.03

Next analysis is about the structure of polystyrene sulfonic acid group in the q range of $2.5 - 6 \text{ nm}^{-1}$. Before background subtraction, the SAXS profiles exhibit no peak for the original ETFE and ETFE-PEM 19% but a small, unclear, and unsymmetrical peak at around $q = 4 \text{ nm}^{-1}$ for ETFE-PEMs with GD = 34 and 59%. The peak at $q = 4 \text{ nm}^{-1}$ relates to the structure of polystyrene sulfonic acid group in the conductance layers of these electrolyte membranes. After background subtraction, the

peak at $q = 4 \text{ nm}^{-1}$ is clear, sharper, and more symmetrical (Fig 5c, 5d) for both Vonk 6 and Ruland 4 models. It should be noted here that the peak position at $q = 4 \text{ nm}^{-1}$ was not altered after background correction. In addition, the intensity of the peak is greatly reduced (about 95%) compared to those before correction $I_{F1}(q)$. The above results show that $I_{F1}(q)$ significantly affects the total scattering intensity, shape, and peak distribution of $I(q)$ at the large angle scattering vector region ($q > 2.5 \text{ nm}^{-1}$).

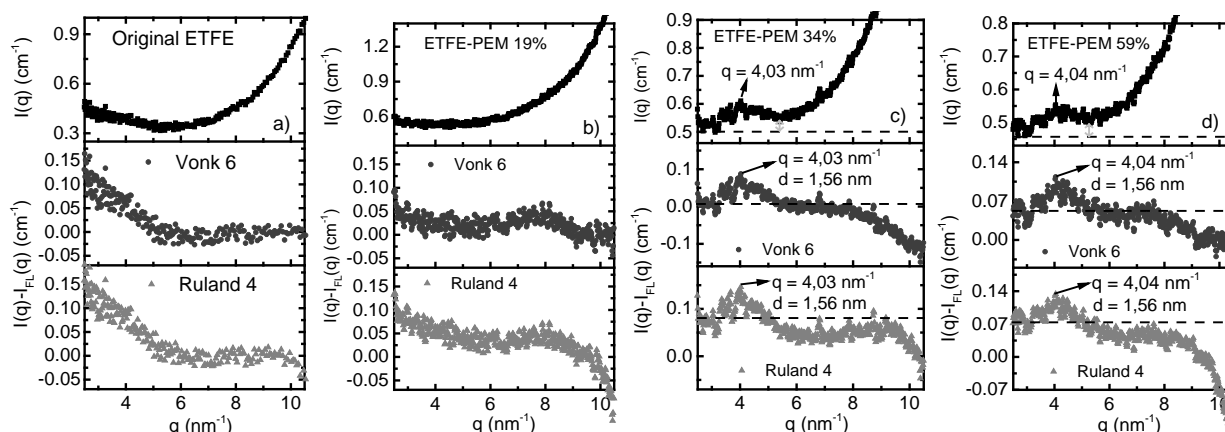


Figure 5. SAXS profiles before and after background subtraction using Vonk 6 and Ruland 4.

CONCLUSION

The obtained results of $I_{F1}(q)$ by using Vonk 6 and Ruland 4 methods indicate that the electron density fluctuation affects strongly on the SAXS profiles of interfacial thickness and the conducting layer but not the lamellar structure. The slope of the $\log(Iq)$ vs $\log(q)$ plot was altered after background correction in the higher q range than 0.6 nm^{-1} , where the diffuse boundary layer and proton conductance region locate. However, the peak position at $q = 4 \text{ nm}^{-1}$, which is related to the structure of conductance region, was not altered after background correction. Further studies are to calculate the size of interfacial thickness, the phase separation and their relationship to the mechanical properties of ETFE-PEMs.

Acknowledgment

This research is funded by Vietnam National Foundation of Science and Technology Development (NAFOSTED) under grant number 103.04-2015.61.

References

[1] T.D.Tap. S.Sawada. S.Hasegawa. Y.Katsumura. and Y.Maekawa. *Poly(ethylene-co-*

tetrafluoroethylene) (ETFE)-based graft-type polymer electrolyte membranes with different ion exchange capacities: Relative humidity dependence for fuel cell applications. *Journal of Membrane Science*. **447** (2013) 19 – 25.

- [2] T.D.Tap. S.Sawada. S.Hasegawa. K.Yoshimura. Y.Oba. M.Ohnuma. Y.Katsumura. Y.Maekawa. *Hierarchical structure-property relationships in graft-type fluorinated polymer electrolyte membranes using small- and ultrasmall-angle X-ray scattering analysis*. *Macromolecules*. **47** (2014) 2373 – 2383.
- [3] N. Striebeck. *X-ray Scattering of Soft Matter*. Springer. Berlin. 2007. 118-119.
- [4] C.G.Vonk. *Investigation of non-ideal two-phase polymer structures by small-angle X-ray scattering*, *Journal of Applied Crystallography* **6** (1973). 81 – 86.
- [5] W.Ruland. *Small-angle scattering of two-phase systems: Determination and significance of systematic deviations from Porod's law*. *Journal of Applied Crystallography*. **4** (1971) 70-77.
- [6] M.H.Kim. *Modified porod's law estimate of the transition-layer thickness between two phases: test of triangular smoothing function*. *Journal of Applied Physics*. **37** (2004) 643-651.

EFFECT OF CALCINATION TEMPERATURE ON OPTICAL PROPERTIES OF $Gd_3PO_7:Eu^{3+}$ NANOPHOSPHORS SYNTHESIZED BY COMBUSTION METHOD

Khac Khong Minh Ngo^{1,2,3}, Thi Kieu Giang Lam^{1,2}, Manh Tien Dinh¹, Thi Khuyen Hoang^{1,2}, Van Do Phan⁴, Dariusz Hreniak⁵, Mariusz Stefanski⁵, Karina Grzeszkiewicz⁵ and Vu Nguyen^{1,2,*}

¹*Institute of Materials Sciences, Vietnam Academy of Science and Technology, 18 Hoang Quoc Viet, Hanoi, Viet Nam*

²*Graduate university of Science and Technology, Vietnam Academy of Science and Technology, 18 Hoang Quoc Viet, Hanoi, Viet Nam*

³*Nam Can Tho University, Cantho, Viet Nam*

⁴*Thuyloi University, 175 Tay Son, Dong Da Dist, Hanoi, Viet Nam*

⁵*Institute of Low Temperature and Structure Research, Polish Academy of Sciences, Poland*

ABSTRACT

A red-emitting $Gd_3PO_7:1\text{mol}\%Eu^{3+}$ nanophosphors have been successfully synthesized via straightforward combustion method. Thermal behavior of the as-synthesized sample was investigated by thermogravimetric analysis (TGA) and differential thermal analysis (DTA). Besides, structures, morphologies and optical properties of $Gd_3PO_7:1\text{mol}\%Eu^{3+}$ nanophosphors were studied by X-ray diffraction (XRD), scanning electron microscopy (SEM), photoluminescent (PL) spectra, photoluminescent excitation (PLE) spectra, and decay curves. Samples were annealed at different temperatures (500, 600, 700, 800, and 900°C) for an hour. XRD analyses confirmed their monoclinic phase and the average particle size was about 20 nm. We analyzed the influence of annealing temperature on the optical properties, namely PLE, PL spectra, and decay time. Under the excitation at 252 nm, the strong red-emission at 615 nm due to the ${}^5D_0 \rightarrow {}^7F_2$ transition was observed. It also shows that Eu^{3+} ions in Gd_3PO_7 mainly occupied non-centrosymmetry sites. The maximum intensity of ${}^5D_0 \rightarrow {}^7F_2$ emission was observed corresponding to the sample annealed at 900°C. When the annealing temperature increased, the decay time increased from 1.3 to 1.5 ms, too.

INTRODUCTION

In recent years, rare earth orthophosphates have been continuously receiving a significant attention from researchers due to their special photoluminescent properties and potential applications in magnets, catalysts, biochemical probes, and medical diagnostics [1-4]. Among them, it must be mentioned $GdPO_4$ because it had extremely interesting properties. In 2018, T.T.D.Hien and co-working investigated effect of calcination temperature on phase transition of $GdPO_4:Eu^{3+}$ [5]. As a result, when the annealing temperature was from 300 to 500°C, all samples exhibited hexagonal phase (JCPDS No. 39-0232). When the reaction temperature was 600°C, the crystallinity of the nanoparticles existed in two forms: hexagonal and monoclinic. On annealing upon 800°C, monoclinic phase was observed with well formed diffraction

peaks (JCPDS No. 32-0386). Rare-doped ions were important in phosphor materials, one of them must be mentioned Eu^{3+} ions. In 2016, Yanxia Tang and co-working researched the luminescent properties of $GdPO_4:Eu^{3+}$ [6]. According to their report, the magnetic dipole transition ${}^5D_0 \rightarrow {}^7F_1$ of Eu^{3+} ions was dominant with strong orange red emission due to the symmetric site of Eu^{3+} ions in the host. Until now, there are a lot of researches on $GdPO_4:Ln^{3+}$ materials with their interesting properties. However, there was rarely reported in recently years about studying on Gd_3PO_7 doped with rare ions. In 2001, Zeng Xiao-Qing and co-working studied the luminescent properties of $Gd_3PO_7:Eu^{3+}$ [7]. It was different from Eu^{3+} -doped $GdPO_4$ that this material emitted stronger red emission corresponding ${}^5D_0 \rightarrow {}^7F_2$ transition under UV wavelength excitation. There were many ways for making materials as solid state reaction, co-

precipitation, sol-gel, combustion... In 2008, Ye Jin and co-working used a facile combustion method to synthesize $Gd_3PO_7:Eu^{3+}$ nano-spheres with an average diameter nearly 300 nm [8]. In this study, $Gd_3PO_7:Eu^{3+}$ phosphors have been synthesized via straightforward combustion method because this was an effective, low-cost method. The effect of synthesized temperature on morphology of the obtained materials and their luminescent properties were discussed.

EXPERIMENTAL

The beginning materials were gadolinium (III) oxide (Gd_2O_3 , 99.99%), europium (III) oxide (Eu_2O_3 , 99.99%). All of them were of analytical class. Besides, nitric acid (Merck), ammonia solution (Merck), phosphoric acid (Merck) and urea (Merck) were used for the experiment, too. Firstly, the preparation the rare earth nitrates, Gd_2O_3 and Eu_2O_3 were treated by concentrated nitric acid. The second step, the first solution was the mix of 0.99 mmol $Gd(NO_3)_3$ and 0.01 mmol $Eu(NO_3)_3$ solution. An appropriate amount of urea as a fuel was put into the first solution, strong stirring to a transparent solution. The second solution containing the source of phosphate was made of the mix of H_3PO_4 and ammonia solution with the mole rate of 1:2. Therein, the mole rate of PO_4^{3-} ion and Ln^{3+} ion was 1:3. The first solution was added very slowly by the second solution with a vigorously stirring for 1 hour at room temperature. Then, the mixture was heated until a white gel was formed called a precursor. These precursor samples were annealed at different temperatures (500, 600, 700, 800, and 900°C) for an hour in air.

The thermal decomposition actions of the before annealing sample was investigated by simultaneous thermo-gravimetry and differential thermal analysis (TG-DTA) on a TG-DTA/DSC (France) instruments in air with a heating rate of $10^\circ C \text{ min}^{-1}$ from room temperature to 900°C in Vietnam Academy of Science and Technology. The crystalline structure was obtained on a Advance-Bruker D8 X-ray diffractometer using Cu $K\alpha$ radiation resource ($\lambda=1,5406 \text{ \AA}$) and the scan range was set from 20 to 80 (2θ) with a step of $0,03^\circ s^{-1}$. The morphology of the final product was examined using a scanning electron microscope (SEM) (HITACHI S-4800). Excitation and emission

spectra and decay time were determined by a Cary Eclipse fluorescence spectrophotometer equipped with a 80Hz xenon lamp as the excitation source.

RESULTS AND DISCUSSION

Fig. 1 shows the XRD pattern of $Gd_3PO_7:Eu^{3+}$ phosphors particles using different annealing temperature at 500, 600, 700, 800, and 900°C. All diffraction peaks of different samples were similar, which can be indexed as the monoclinic phase of Gd_3PO_7 crystal and they were well compatible with the JCPDS card No.34-1066. The diffraction peaks were strong and sharp indicate the high crystallinity of the material. Its lattice parameters were $a=12.025\text{\AA}$, $b=15.603\text{\AA}$, and $c=13.866\text{\AA}$. Some characteristic peaks centered at $2\theta = 23.27^\circ, 28.45^\circ, 30.37^\circ, 31.41^\circ, 34.37^\circ, 41.62^\circ, 42.36^\circ, 44.88^\circ,$ and 47.25° were corresponding to (302), (321), ($\bar{4}$ 11), (331), ($\bar{4}$ 31), (224), (511), ($\bar{1}$ 73) and ($\bar{6}$ 04) planes [9-11].

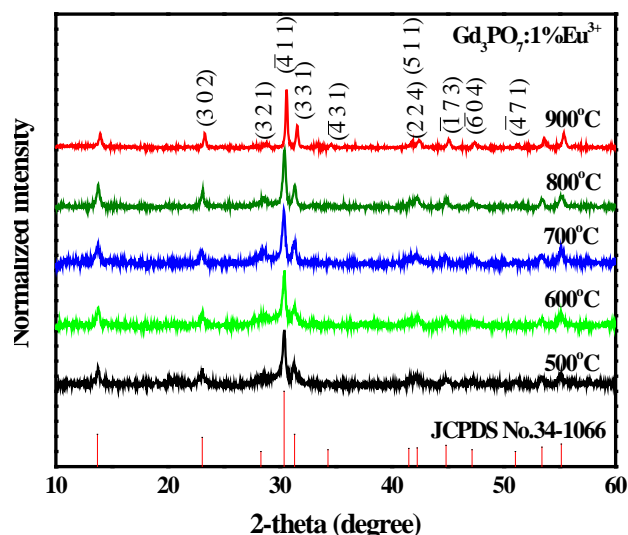


Figure 1. XRD patterns of $Gd_3PO_7:1\%Eu^{3+}$ nanoparticles annealed at different temperatures.

It suggests that, the dopant Eu^{3+} ions did not change the structure of the host matrix. As shown in Fig 1, the diffraction peaks of products became gradually narrow, sharp, and increased when the annealing temperature increased. The crystallite size (D) of $Gd_3PO_7:Eu^{3+}$ phosphors particles were calculated by Scherrer's equation: $D = \frac{0.89\lambda}{\beta \cos\theta}$. Where, D is the average crystallite size, λ is the wavelength of the Cu $K\alpha$ radiation, θ is the Bragg angle and β is the full-width at half maximum (FWHM) in radians of the peak at $2\theta = 30.37^\circ$. The

calculated nanoparticle sizes (D) of $Gd_3PO_7:Eu^{3+}$ phosphors increased as annealing temperatures increased. As experiments, the sizes were 17.8, 18.5, 18.7, 24, and 25.4 nm for annealing

temperatures of 500, 600, 700, 800, and 900°C, respectively.

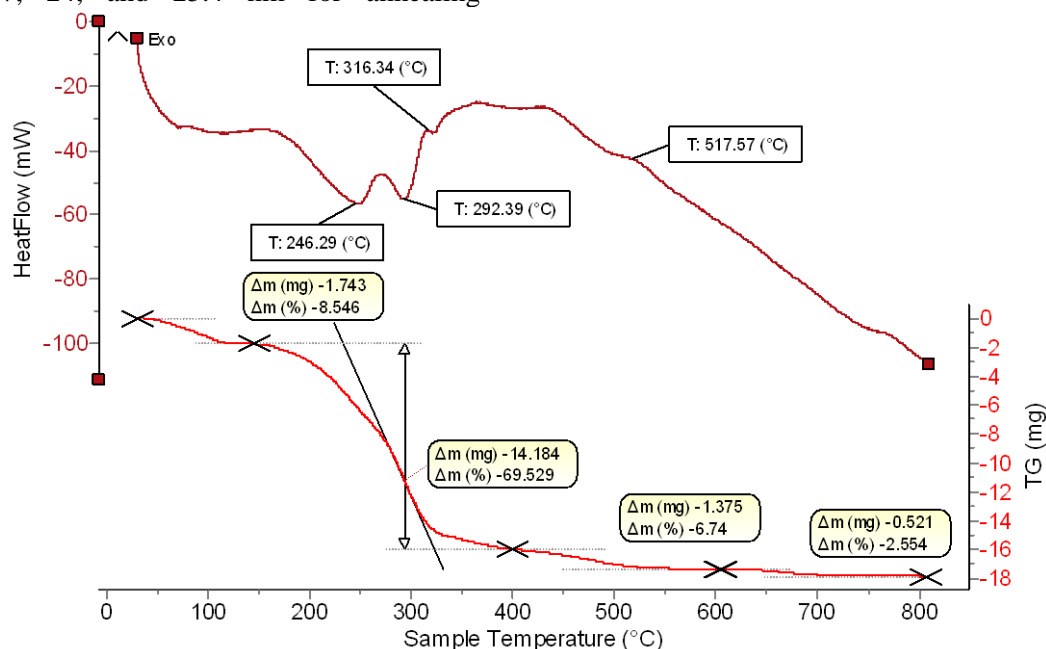


Figure 2. TG/DTA curves of as-prepared $Gd_3PO_7:1mol\%Eu^{3+}$

Fig 2 shows TG analysis and DTA curves, which were conducted simultaneously from room temperature to 800°C. Based on the TG curve, there were three main separate weight loss processes. The first stage is in the temperature range 70 – 150°C with a mass reduction of 8.5 wt% was due to the liberation of water molecules adsorbed on the product, which shows a weak endothermic peak at 100°C in the DTA curve. The second step of weight loss (69,5 wt%) occurred in the range 150 – 300°C, which can be attributed to decomposition of ammonium di-hydrogen phosphate, ammonium nitrate with two endothermic peaks occupied at

around 246,3 and 292,4°C in the corresponding DTA curve. The third stage was in the temperature range over 300 to 700 °C with a mass loss of 9.5 wt%. Besides, it can be observed that exothermic peaks were around 316, 369, and 450°C in the DTA curve. This can be explained by the burning reaction of the nitrate, $(NH_2)_2CO$ and oxygen. Above 700°C, the TG and DTA curves almost unchanged. This may be due to the absence of chemical reactions and phase transformation in the sample. The TG/DTA results are completely consistent with XRD measurements.

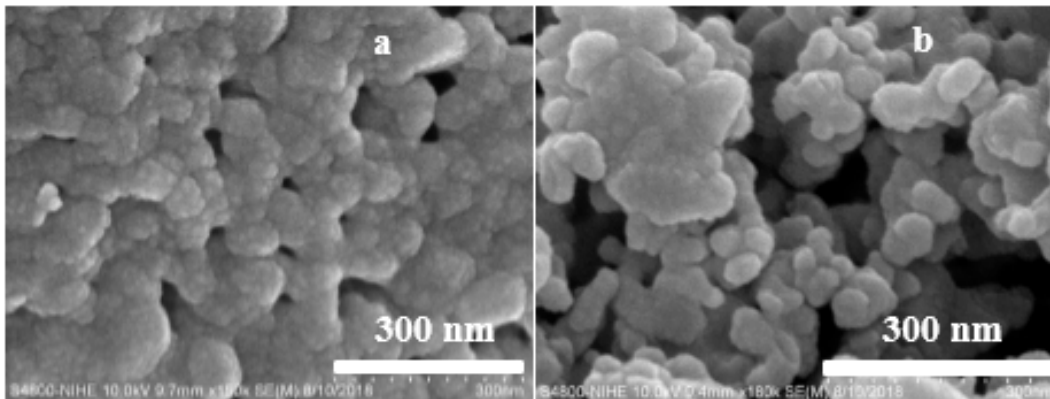


Figure 3. SEM images taken from $Gd_3PO_7:1mol\%Eu^{3+}$ nanoparticles annealed at 500°C (a) and 900°C (b).

The SEM image of $Gd_3PO_7:Eu^{3+}$ nanoparticles were shown in Fig. 2 to investigate the surface morphology of the samples annealed at 500°C (Fig. 2a) and 900°C (Fig. 2b). It can be seen that most grains have a similar spherical morphology. The average particle size of sintering temperature at 500°C was about 15-20 nm. However, when the as-prepared sample was annealed at 900°C, the average grain size was about 25-30 nm. Therefore, the grain size and level of aggregation increased as the annealing temperature increased. This was entirely consistent with XRD analysis results.

Fig. 4 showed the room temperature photoluminescence excitation (PLE) spectra of $Gd_3PO_7:1mol\%Eu^{3+}$ nanopowders annealed different temperatures. They were collected at an emission wavelength of 615 nm. All of the curves were similar characteristics. As shown in Fig. 4, the PLE spectra included three broad bands and some peaks. Therein, a broad band prolonged from 220-330 nm was well known as a charge transfer band (CTB) of Eu^{3+} . This broad band took place by electron delocalization from the filled $2p^6$ orbital of the O^{2-} to an empty $4f$ orbital of Eu^{3+} ions. Besides, the peak at around 273 nm was contributed to the $^8S_{7/2} \rightarrow ^6I_J$ transition of Gd^{3+} . Other peaks were from 300 to 450 nm due to the $f-f$ transitions of Eu^{3+} ion, namely $^7F_0 \rightarrow ^5H_3$ at 315 nm, $^7F_0 \rightarrow ^5D_4$ at 363 nm, $^7F_0 \rightarrow ^5G_4$ at 382 nm, $^7F_0 \rightarrow ^5L_6$ at 395

nm, $^7F_0 \rightarrow ^5D_3$ at 412 nm, and $^7F_0 \rightarrow ^5D_2$ at 465 nm [8, 9, 11].

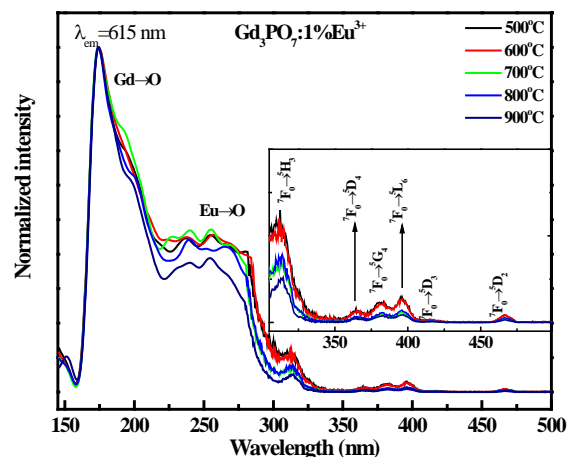


Fig. 4. Excitation spectra of $Gd_3PO_7:1mol\%Eu^{3+}$

Looking carefully to the left area of the Eu-O charge transfer band, there are three bands to consider at 151, 175 and 200 nm. The band around 151 nm is attributed to PO_4^{3-} absorption. In fact, there are two types of Gd-O bonds in Gd_3PO_7 . Therefore, two bands which located at 175 nm and around 200 nm were assigned to the absorption area of Gd-O. This result completely coincides with the study of Zeng Xiao-Qing and co-working in 2000 [7].

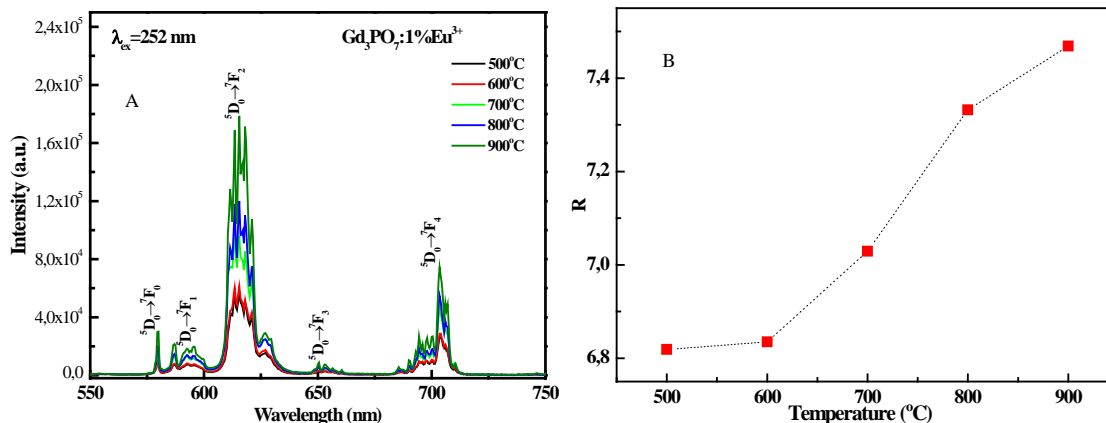


Figure 5. Emission spectra ($\lambda_{ex}=252\text{nm}$) of $\text{Gd}_3\text{PO}_7:1\text{mol}\% \text{Eu}^{3+}$ annealed at different temperature (A) and the dependence of the intensity of the ${}^5\text{D}_0 \rightarrow {}^7\text{F}_2$ transition on temperature (B).

A red emission spectrum of Eu^{3+} -doped Gd_3PO_7 under 252 nm excitation was given in Fig. 5. The peaks were corresponding to the ${}^5\text{D}_0 \rightarrow {}^7\text{F}_0$ (579 nm), ${}^5\text{D}_0 \rightarrow {}^7\text{F}_1$ (around 594 nm), ${}^5\text{D}_0 \rightarrow {}^7\text{F}_2$ (around 615 nm), ${}^5\text{D}_0 \rightarrow {}^7\text{F}_3$ (around 650 nm), and ${}^5\text{D}_0 \rightarrow {}^7\text{F}_4$ (around 703 nm). The mainly considered emissions in this study were ${}^5\text{D}_0 \rightarrow {}^7\text{F}_1$ (orange emission) and ${}^5\text{D}_0 \rightarrow {}^7\text{F}_2$ (red emission). According to Judd–Ofelt theory, the values of ratio between the intensities or integral intensities of both transitions depend mainly on the symmetry of the local environment around Eu^{3+} ion. The orange emission of the ${}^5\text{D}_0 \rightarrow {}^7\text{F}_1$ transition is a magnetic-dipole transition, whereas the red emission of the ${}^5\text{D}_0 \rightarrow {}^7\text{F}_2$ transition is an electric-dipole transition. Theoretically, If Eu^{3+} ions are in an inversion center, the magnetic-dipole transition is dominant. However, when Eu^{3+} ions occupy the non-centrosymmetric sites, the electric-dipole transition (${}^5\text{D}_0 \rightarrow {}^7\text{F}_2$) is the strongest transition [9–14]. In this report, the R asymmetric ratio was determined as the ratio of the integrated intensity of the electric dipole transition (${}^5\text{D}_0 \rightarrow {}^7\text{F}_2$) to the magnetic dipole transition (${}^5\text{D}_0 \rightarrow {}^7\text{F}_1$):

$$R = \frac{\int {}^5\text{D}_0 \rightarrow {}^7\text{F}_2}{\int {}^5\text{D}_0 \rightarrow {}^7\text{F}_1}$$

The value of R can provide structural information such as the deformity of ligand environment around the Eu^{3+} ions as well as a site symmetry. The higher the value of R indicated the lower the symmetry. In the specific case of Gd_3PO_7 , Ye Jin and co-working studied the optical

of this material in 2008 [8, 13]. They also confirmed that the dopant Eu^{3+} ions mainly occupied non-centrosymmetry sites. In this research, as in Fig. 5A, when the annealing temperature increased from 500 to 900°C, the intensity of the emission bands increased significantly. In addition, the parameter R also increased from 6.8 to 7.5 (Fig. 5B). This means that the crystal of Gd_3PO_7 nanoparticles were getting more and more perfect as the annealing temperature increased. In particular, as the value of increased, the red emission was more and more pure. The color purity has many important applications in the field of color displays, light sources, and biomedical labels...

The fluorescence decay curves for ${}^5\text{D}_0 \rightarrow {}^7\text{F}_2$ transition of $\text{Gd}_3\text{PO}_7:1\text{mol}\% \text{Eu}^{3+}$ samples annealing at different temperatures were showed in Fig. 6. The excitation and emission wavelengths were measured at 253 and 615 nm, respectively. It can be observed that all the decay curves cannot be fitted into a single exponential function but can be well fitted into a double exponential function as in the following equation:

$$I = A_1 \exp(-t/\tau_1) + A_2 \exp(-t/\tau_2)$$

Where I is the intensity at time t, τ_1 and τ_2 are the fast and slow components of the luminescence lifetimes, A_1 and A_2 are the fitting parameters [9]. Then, the average lifetime was calculated by the

$$\text{equation: } \tau = \frac{A_1 \tau_1^2 + A_2 \tau_2^2}{A_1 \tau_1 + A_2 \tau_2}$$

Annealing Temperature (°C)	500	600	700	800	900
Lifetime (τ) ($\lambda_{\text{ex}}=252\text{nm}$) (ms)	1.37	1.37	1.54	1.54	1.56
	5	5	4	7	2

It can notice that there was a monotonous increase in the emission lifetime from 1.375 to 1.562 ms when the sintering temperature was increased from 500 to 900°C. (Table 1). This is explained as the increase of annealing temperature lead to the better crystallinity of the materials thus the decay times become longer.

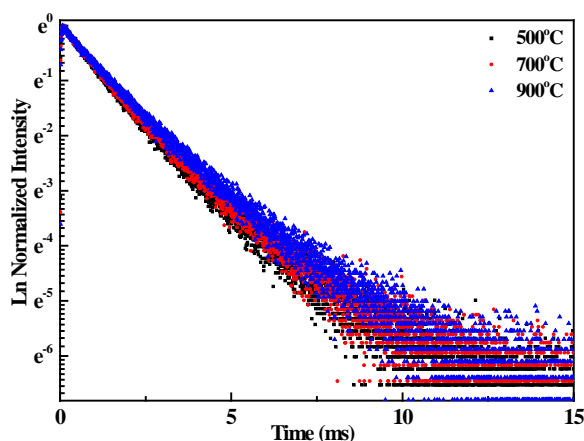


Figure 6. Luminescence decay curves of $Gd_3PO_7:1\text{mol}\%Eu^{3+}$ samples annealed at different temperatures, measured for the $^5D_0 \rightarrow ^7F_2$ transition.

CONCLUSION

In summary, $Gd_3PO_7:1 \text{ mol}\%Eu^{3+}$ nanoparticles have been successfully produced via combustion method and annealed in the temperature range from 500 to 900°C. The indexed peaks of XRD were confirmed a pure monoclinic phase and good agreement with the results of JCPDS card. When the annealing temperature increased, the average particle size increased from 17 to 25 nm. The luminescent intensity increased with annealing temperature, reaching maximum for the best crystalline samples annealed at 900°C in this study. Moreover, the ratio of the integrated intensity of $(^5D_0 \rightarrow ^7F_2) / (^5D_0 \rightarrow ^7F_1)$ reached 7.5 that demonstrated as Eu^{3+} ions occupied non-centrosymmetric sites and the red emission is pure. The lifetime of $^5D_0 \rightarrow ^7F_2$ transition increased with

the increase of sintering temperature. It implies that the crystals were more and more perfect. Finally, the optimal temperature for further studies with $Gd_3PO_7:Eu^{3+}$ material is 900°C.

Acknowledgments

This study was supported by Institute of Materials Science, Vietnamese Academy of Science and Technology (Grant No. CSCL1.01.19). A part of the work was done in the National Key Laboratory Electronic Materials and Devices.

References

- [1]. J. Shen, L-D Sun and C-H Yan. *Luminescent rare earth nanomaterials for bioprobe applications*, Dalton Trans. **42** (2008) 5678-5697.
- [2]. M. F. Dumont, C. Baligand, Y. Li, E.S. Knowles, M. W. Meisel, G. A. Walter, and D. R. Talham, *DNA Surface Modified Gadolinium Phosphate Nanoparticles as MRI Contrast Agents*, Bioconjugate Chem. **23** (2012) 951-957.
- [3]. S. Rodriguez-Liviano, A. I. Becerro, D. Alcantara, V. Grazu, J. M. de la Fuente, and M. Ocañ, *Synthesis and Properties of Multifunctional Tetragonal $Eu:GdPO_4$ Nanocubes for Optical and Magnetic Resonance Imaging Applications*, Inorg. Chem **52** (2013) 647-654.
- [4]. K. Park and M. H. Heo, *VUV Photoluminescence of $(Gd,Zn)PO_4:Tb^{3+}$ Phosphors Synthesized by Ultrasonic Spray Pyrolysis*, Metals and Materials International **17** (2011) 1027-1030.
- [5]. T.T.D Hien, P. D. Roan, N.T. Thanh, D.M. Tien and N.Vu, *Effect of calcination temperature on phase evolution and photoluminescent properties of $GdPO_4:Eu^{3+}$ nanoparticle phosphors synthesized by combustion method*, Vietnam J. Chemistry **56** (2018) 793-797.
- [6]. Y. Tang, R. Mei, S. Yang, H. Tang, W. Yin, Y. Xu, Y. Gao, *Hollow $GdPO_4:Eu^{3+}$ microspheres: Luminescent properties and applications as drug carrier*, Superlattices and Microstructures **92** (2016) 256-263.
- [7]. Z. Xiao-Qing, H. Guang-Yan, Y. Hong-Peng, W. Xue-Yan, K. Chang-Hong, P. Chong-Hong, Y. Byung-Yong, B. Hyun-Sook, P.

- Cheal-Hee, K. Il-Eok, *Luminescent Properties of $Gd_3PO_7:Eu$ in UV/VUV Region*, Chin. Phys. Lett **18** (2001) 690-691.
- [8]. Y. Jin, W. Qin, J. Zhang, X. Zhang, Y. Wang, C. Cao, *Synthesis of $Gd_3PO_7:Eu^{3+}$ nanospheres via a facile combustion method and optical properties*, Journal of Solid State Chemistry **181** (2008) 724–729.
- [9]. Y. Jin, J. Zhang, W. Qin, *Photoluminescence properties of red phosphor $Gd_3PO_7:Eu^{3+}$ for UV-pumped light-emitting diodes*, Journal of Alloys and Compounds **579** (2013) 263–266.
- [10]. A.R. Camacho, F. de J. C. Romo, A. G. Murillo, J. Oliva, C.R. García, *Sol-gel synthesis and up-conversion luminescence of $GdPO_4-Gd_3PO_7: Yb^{3+}, Ln^{3+}$ ($Ln = Er, Ho, Tm$) phosphor*, Materials Letters **226** (2018) 34–37.
- [11]. K.A. Koparkar, S.K. Omanwar, *Luminescence optimization with color purity (orange to red) by increasing Gd^{3+} ions in Eu^{3+} doped phosphate synthesized by slow evaporation method*, Journal of Luminescence **175** (2016) 176–181.
- [12]. N.K.K.Minh, L.T.K.Giang, N.T.Nghia, and N.Vu, *Properties emission of $La_3PO_7:Eu^{3+}, Bi^{3+}$ nanophosphors synthesized by combustion method*, Vietnam J. Chem. **56** (2018) 300-303.
- [13]. Y. Jin, W. Qin, J. Zhang, Y. Wang, C. Cao, J. Zhang, X. Ren, G. Wang, G. Wei, L. Wang, L. Jin, P. Zhu, *$La_3PO_7:Eu^{3+}$ nanoparticles — A novel red phosphor*, Materials Letters **62** (2008) 3146–3148.
- [14]. S. Raya, G. B. Nairb, P. Tadgea, N. Malviaa, V. Rajputa, V. Choprac, S.J. Dhoble, *Size and shape-tailored hydrothermal synthesis and characterization of nanocrystalline $LaPO_4:Eu^{3+}$ phosphor*, Journal of Luminescence **194** (2018) 64–71.

HIGH PERFORMANCE CORE/SHELL MULTI-COLOUR AND MULTI-FUNCTIONAL COLLOIDAL QUANTUM DOTS FOR ADVANCED HYBRID NANOSYSTEMS

Tien Hoa Nguyen¹, **Aurélie Broussier**², **Safi Jradi**², **Renaud Bachelot**^{2,3} and **Xuan Quyen Dinh**^{1,4}

¹ CNRS-NTU-Thales Research Alliance (CINTRA) UMI 3288, 50 Nanyang Drive, Singapore 637553

² Light, nanomaterials, nanotechnologies (L2n) Laboratory, Charles Delaunay Institute, University of Technology of Troyes, 12 rue Marie Curie, F-10004 Troyes Cedex, France

³ Sino-European School of Technology, Shanghai University, 200444, Shanghai, China

⁴ Thales Solutions Asia Pte Ltd, R&T Department, 21 Changi North Rise, Singapore 498788

Email: xddinh@ntu.edu.sg

ABSTRACT

Controlling spatial distribution of nanoemitters is still a challenge these days, especially at the nanoscale level. We report here the fabrication of a new quantum dots-containing formulation that allows precise positioning of nanoemitters via two-photon photopolymerization together with localized plasmonic modes. This hybrid structure may provide new possibilities to control emission of nanosources. The plasmonic excitation can be produced using different geometries of metal nanoparticles and structures. Our hybrid plasmonic nanoemitters are shown to be highly sensitive to the polarization of the excitation.

Keywords: 3D nanostructure, direct laser writing, quantum dots, two-photon polymerization, nanoemitter.

INTRODUCTION

Nanoplasmonics have great potential for controlling the energy transfer between nanoemitters and surface plasmons (SPs) [1]. Some nanosources rely on hybrid plasmonics that was introduced a couple of years ago [2]. Hybrid plasmonics is at the origin of the development of new light nano-emitters based on radiative and non-radiative coupling between an active medium and a metal nanoparticle (MNP) [3]. The first hybrid plasmonic lasers (where an MNP acts as a nanocavity and is coupled to a gain medium) have been proposed and developed [4-5].

Among various types of nano-emitters, quantum dots (QDs) have received immense attention for their unique optical properties suitable for light emitting hybrid plasmonic nano-system [6-9].

In this research, we report on the success of high-quality quantum dots synthesis and controlled hybrid plasmonic nanoemitter built with quantum dots, optical waveguides and/or metallic structures.

EXPERIMENTAL

Core/shell quantum dots were synthesized by mixing cadmium oxide and zinc acetate in oleic acid and octadecene. The mixture was heated at 300°C for 30 min before adding a solution of

trioctylphosphine, selenium, and sulfur. After 10 min, the quantum dots were formed, purified and collected in a centrifugation process. These synthesized quantum dots were dissolved in a polymer mixture of pentaerythritol triacrylate (PETA) and 2-(methacryloyloxy)ethyl succinate (MES). Nanoemitters were integrated by two-photon polymerization of photosensitive formulation made of 1% Irgacure and 99% PETA-grafted QDs. The photopolymerization process was achieved by using a femtosecond laser at $\lambda = 780$ nm (*Nanocribe GmbH*).

Fig. 1(a) showed photoluminescence (PL) and absorbance for different colour QDs including blue (CdZnS/ZnS), green (CdSe/ZnS), and red (CdSe/CdS/ZnS). QDs dispersed in polymers of PETA and MES were shown in Fig. 1(b). It is obvious that QDs were well dispersed in polymer after a ligand exchange process to form a homogeneous solution that suitable for a photopolymerization in our next step to produce a hybrid plasmonic nanoemitter. Due to confinement of electrons and holes and gradient compositions, our synthesized QDs exhibited a sharp absorbance, high PL intensity and a narrow bandwidth below 20 nm that is much lower compared with commercialized QDs (having 30 nm of bandwidth).

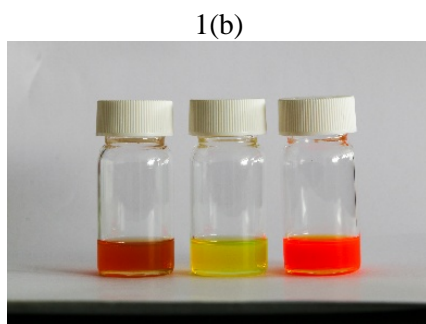
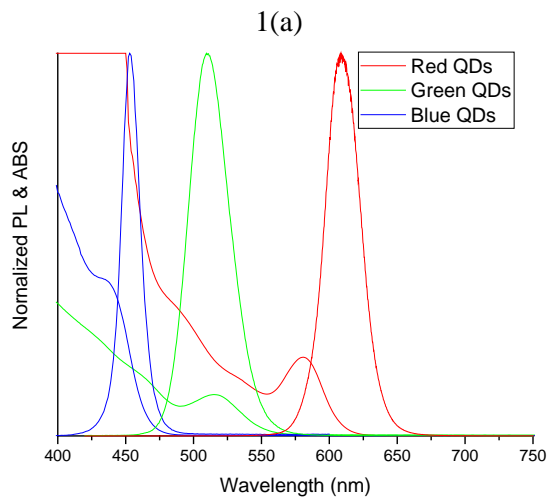


Figure 1. (a) Normalized photoluminescence and absorbance for blue, green, and red QDs. (b) Homogeneous solution of QDs dispersed in PETA and MES (Blue, Green, Red QDs from left to right).

RESULTS AND DISCUSSION

We satisfyingly photopolymerized our QDs-solution on the surface of silver nanowires (NW) and gold nanocubes. Fig. 2(a) shows the schematic of the QDs integrated with a photonic waveguide. By focusing laser light at 514 nm onto the Ag-NW end (of diameter of 130-160 nm), SPs were excited and launched, as evidenced by the green light emission spot at the other end, resulting from SPs perturbation and scattering (Fig. 2(c)-2(d)). The nanowire end geometry allowed one to couple SPs into propagating waves. No SP excitation was observed when the laser was focused on the NW body, far from its extremities.

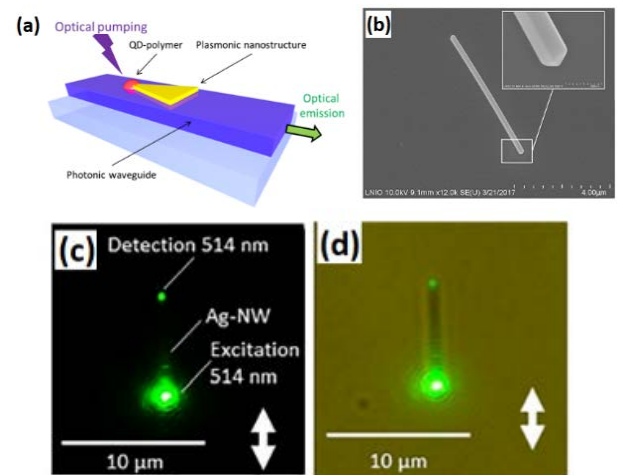


Figure 2. (a) Schematic of the QDs integrated with a photonic waveguide; (b) SEM image of Ag-NW on Si substrate and zoom in of the NW end; (c)-(d) 7 μm -long Ag-NW illuminated by a focused green laser 514 nm polarized along the wire axis.

We also integrated QDs onto other metallic structures such as gold nanocubes with QDs attached to its surface with different volume of QDs. When the volume of QDs is small enough, we might get a single emitter at the edge of the cube.

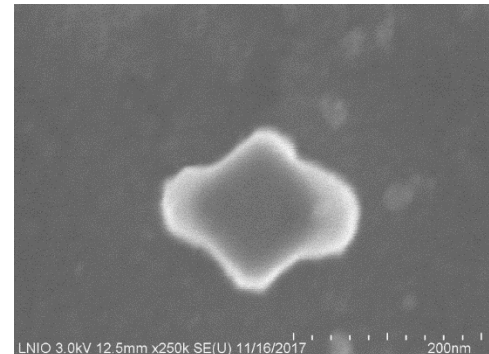


Figure 3. SEM image of the hybrid structure obtained with incident polarization along the cube diagonal.

CONCLUSION

We successfully synthesized core/shell QDs of different colours, high emission efficiency and having narrower band width than commercial QDs. Subsequently, we showed that light intensity at the waveguide extremity can be controlled by controlling the position of the launching site, through SPs propagation length. QDs were also integrated onto various metallic nanostructures (nanowire, nanocube, bow-tie,

etc.) which showed clearly potential on plasmonic enhancement. This new approach of combining plasmonic excitation and integrated optical waveguide are very promising to produce efficient acceptor-donor hybrid nano-systems by using different kinds of QD-containing photopolymerizable formulation and plasmonic structures.

Acknowledgment

This project is financially supported by the ANR (French research agency) and the NRF (Singapore Research Foundation) through the international ACTIVE-NANOPHOT (alias "MULHYN") funded project (ANR-15-CE24-0036-01 & NRF2015-NRF-ANR000-MULHYN).

References

- [1]. Hill, M. T. and Gather, M. C. *Advances in small lasers*. Nat. Photonics **8**, 908-918 (2014).
- [2]. Wang H. et al. *Nanorice: a hybrid plasmonic Nanostructure*. Nano Lett. **6**, 827 (2006).
- [3]. Viste P. et al. *Enhancement and Quenching Regimes in Metal-Semiconductor Hybrid Optical Nanosources*. ACS Nano **4**, 759 (2010).
- [4]. Stockman, M. I. *Spasers explained*. Nat. Phot. **2**, 327 (2008).
- [5]. Noginov N. A. *Demonstration of a spaser based nanolaser*. Nature **460**, 1110 (2009).
- [6]. Curto, A. G. et al. *Unidirectional Emission of a Quantum Dot Coupled to a Nanoantenna*, Science **329**, 930 (2010)
- [7]. J. Kwak et al. *Bright and efficient full-color colloidal quantum dot light-emitting diodes using an inverted device structure*. Nano Lett. **12**, 2362 (2012).
- [8]. X. Zhou et al. *Two-Color Single Hybrid Plasmonic Nanoemitters with Real Time Switchable Dominant Emission Wavelength*. Nano Lett. **15**, 7458 (2015).
- [9]. A. Broussier et al. *Hybrid plasmonic nanosystem with controlled position of nanoemitters*. Appl. Phys. Lett. **114**, 163106 (2019).

DEVELOPMENT OF ALUMINUM-BASED METAL-ORGANIC FRAMEWORKS FOR WATER ADSORPTION

Thuy Thi Dieu Ung ¹, Loan Thu Nguyen ¹ and Liem Quang Nguyen ²

¹ Institutes of Materials Science, Vietnam Academy of Science and Technology, 18 Hoang Quoc Viet, Nghia Do, Cau Giay, Hanoi, Vietnam;
Email: dieuthuy@ims.vast.ac.vn

ABSTRACT

In this work, we have synthesized two kind of Al-based metal-organic frameworks (MOFs): aluminum fumarate (Al-fumarate) and CAU-10-H involving the commercially available ligands of fumaric and isophthalic acid, respectively. The crystallinity of synthesized samples were investigated by X-ray powder diffraction while their particle morphology and crystal size were analyzed using a scanning electron microscope. The thermogravimetric analysis confirmed the stability of both as-synthesized materials. Their N₂ isotherm shows a type I, correspondent to microporous materials. Pore volume is calculated to be 0.63 cm³/g for an Al-fumarate MOF and 0.35 cm³/g for CAU-10-H. The water sorption of CAU-10H and Al-fumarate MOFs corresponding to ~25% and 35-40% were reached after 80 min. The two Al-based MOFs exhibit proven water uptake to make them eligible for water adsorption/desorption applications.

Keywords: Al-based MOFs, water adsorption, Al-fumarate MOFs, CAU-10-H MOFs

INTRODUCTION

Water adsorption in porous materials plays a crucial role in many applications such as dehumidification [1-3] or thermal batteries [4-6]. For example, microporous oxides such as zeolites are commercially employed to capture water in electric dehumidifiers [1]. More recently, water capture by porous solids is being applied for making adsorption-driven heat exchanger parts of air-conditioners in vehicles [5]. However, because of their low water uptake capacity and high regenerative temperature, these popular solid adsorbent systems are limited by the availability of heat sources [6]. It has been considered by some research groups to combine liquid and solid materials, for example, by encapsulating different salts into a porous matrix [7]. It could improve the water uptake capacity, but corrosion remains challenging, especially when the composite materials are directly applied to a metal surface [8].

Therefore, metal-organic frameworks (MOFs) have attracted many researchers' attention thanks to their high hydrothermal stability, non-toxicity and non-corrosion [9-11]. They represent a class of functional nanomaterials that are based on the condensation of metal complexes in a well-ordered structure. While physico-chemical property of MOFs can

be tuned "per demand" by changing the nature of metal ion center or of the organic ligand counterpart [12], the cavity size can be tuned by changing the spacer linker that bind the adjacent metal center [13]. The 'nearly' infinite choice of metal centers and organic linkers results in rich variety in their topology as well as chemical nature [14-16].

Aluminum is an attractive inorganic component for the construction of MOFs since its salts are non-toxic and commercially available at low-cost [17]. The low molar mass of aluminum is especially of interest for water storage applications [18-20]. The reported Al-based MOF materials exhibit remarkable thermal and chemical stabilities [21]. In this study, we have synthesized two kinds of Al-based MOFs with changing the organic ligands and investigated their characterizations as well as water adsorption properties.

EXPERIMENTAL

Synthesis of Al-fumarate MOFs

0.016 mol of Al₂(SO₄)₃·18H₂O was dissolved in 50 g of water and heated to 60 °C. The mixture solution of 0.032 mol fumaric acid, 0.095 mol sodium hydroxide and 50 g water was injected into the aluminum sulfate solution at 65 °C and strong stirring for 1h. The obtained white

suspension was filtered, then washed with 200 ml of water and 200 ml of ethanol. The filter cake was dried overnight at 100 °C in air and subsequently dried overnight again at 130 °C in a vacuum drying oven.

Synthesis of CAU-10-H MOFs

Three solutions were prepared in a typical synthesis: 0.017 mol of $\text{Al}_2(\text{SO}_4)_3 \cdot 18\text{H}_2\text{O}$ was dissolved in the mixture solvent of 33.75 g H_2O and 5.92 g ethanol (solution 1); 0.045 mol of isophthalic acid and 0.091 mol of NaOH were dissolved in 90 g of H_2O (solution 2); 0.011 mol of NaAlO_2 was dissolved in 22.5 g of H_2O (solution 3). They were mixed once in a 1 L round bottom flask and heated at 130 °C under reflux for overnight. After cooling down, the precipitate was filtered then dispersed for washing in 200 ml of H_2O by sonication and stirring. The dispersion was filtered again and washed in 200 ml of ethanol. Finally, the precipitated was dried overnight at 100 °C in air and subsequently dried overnight again at 130 °C in a vacuum drying oven.

Characterization

The crystallinity of synthesized samples were checked by X-ray powder diffraction analysis (XRD; Rigaku D/Max 2200 PC, Cu K α radiation). Thermogravimetric (TG) analysis was carried out in a thermogravimetric analyzer (TA Instruments, Universal V4.5A). Analysis was performed in dry nitrogen flow of 30cc/min. The temperature was increased from 32 to 700 °C with a heating rate of 5 °C/min. Before TG measurement, the sample was saturated by water vapor in a chamber. A scanning electron microscope (SEM, JEOL, JSM-840A) was used to study the particle morphology and crystal size. The nitrogen adsorption-desorption isotherm measurements were performed at -196 °C on a volumetric sorption analyzer (Micromeritics TriStar 3020). The samples were evacuated at 150 °C for 12 h under high vacuum (1×10^{-5} torr) before each adsorption experiment. The specific surface areas were evaluated using the Brunauer-Emmett-Teller (BET) method in the p/p_0 range 0.05-0.15. Pore size distribution curves were calculated using the adsorption branch of the isotherms by the Barrett-Joyner-Halenda (BJH) method, and pore sizes were obtained from the peak positions of the distribution curves. The pore volume was taken by a single point method at $p/p_0 = 0.99$.

RESULTS AND DISCUSSIONS

The XRD pattern of as-prepared Al-fumarate MOFs is depicted in Figure 1. The sharp diffraction peaks indicate good sample crystallinity, which can be indexed to monoclinic of Al-fumarate with the $P2_1/c$ (no. 14) space group: $a = 6.842 \text{ \AA}$, $b = 12.088 \text{ \AA}$, $c = 14.207 \text{ \AA}$, similar with that of Basolite A520 material [19]. On the other hand, the crystal structure of CAU-10-H is determined as the $I4_1/amd$ (no. 141) space group: $a = b = 21.521 \text{ \AA}$, $c = 10.321 \text{ \AA}$, which is in good agreement with the published results in literature [22].

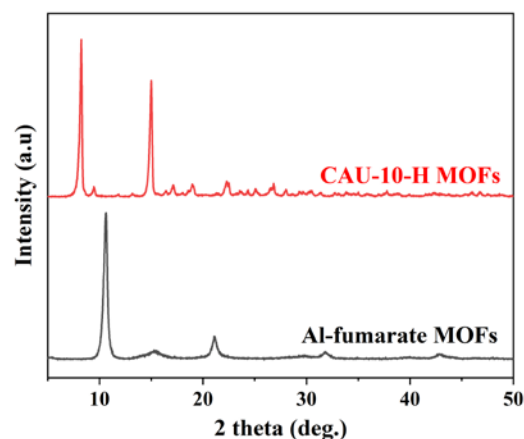


Figure 1. XRD pattern of as-prepared Al-fumarate and CAU-10-H MOFs.

Figure 2 shows the SEM images obtained for two MOFs. Both images depict similar morphology, a rough porous surface composed of irregularly shaped clusters. It was not possible to visualize individual crystals, because the crystals size is small and they are also mixed with binder used in the shaping process.

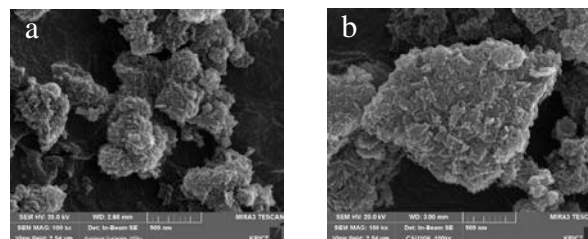


Figure 2. SEM images of as-prepared Al-fumarate MOF (a) and CAU-10-H MOF (b).

Thermogravimetric curves are illustrated in Figure 3, showing same weight loss pattern with two mass losses between 30 and 700 °C. For Al-fumarate MOFs (black line), the initial weight loss is about 30% until 100 °C, attributed to the departure of the water inside the pore. The successive major weight loss of 45% starting at

above 400 °C and extent up to 600 °C is related to the decomposition of MOF. The weight loss values are in excellent agreement with the formula deduced (Al(OH)fumarate.xH₂O (x~4)) from the structure determination and from literature [23]. Likewise, in the case of CAU-10-H MOFs, the thermogravimetric analysis showed a weight loss of 22% at about 100 °C, which also corresponded with occluded water molecules; and at 400 to 700 °C began the decomposition of the material with a 55% mass loss.

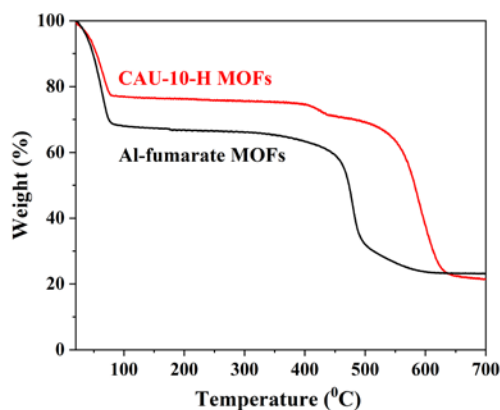


Figure 3. Thermogram of as-prepared Al-fumarate and CAU-10-H MOFs.

The nitrogen adsorption/desorption isotherms at 77 K of two MOFs are depicted in Figure 4. Both of them exhibit type I(a), a typical behavior of microporous materials with a sharp increase in the adsorbed volume at very low relative pressures followed by a nearly constant plateau up to $p/p_0 = 0.9$. The rise in the adsorbed volume at relative pressures close to 1 is indicative of the presence of mesopores and macropores.

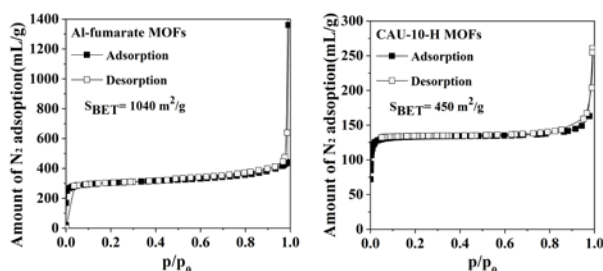


Figure 4. Nitrogen adsorption-desorption equilibrium isotherms at 77 K after degassing at 423 K on as-prepared Al-fumarate and CAU-10-H MOFs.

In the case of Al-fumarate MOFs, the surface area and average pore volume were found to be 1040 m²/g and 0.63 cm³/g, respectively. This BET surface area of 1040

m²/g is slightly higher than for Basolite A520 by about 30 m²/g [23]. This observation confirms the absence of a significant amount of inorganic impurities in our Al-fumarate sample. The estimated specific surface area of CAU-10-H MOFs was 450 m²/g with pore volume of 0.35 cm³/g, similar with that of previous report [24].

The kinetics of the mass gain during water adsorption at 30 °C under 50% and 90% relative humidity conditions are depicted in Figure 5. It can be seen the water uptake of Al-fumarate MOFs is higher than that of CAU-10-H, probably due to the larger surface area of Al-fumarate. After 20 to 30 min the CAU-10-H and Al-fumarate adsorbents are already loaded to about 50%, after 40 to 50 min they are virtually saturated. The water adsorption of CAU-10-H and Al-fumarate corresponding to ~25% and 35-40% were reached after 80 min. In this study, the water sorption kinetics for Al-fumarate MOF clearly shows the huge potential for dehumidification application.

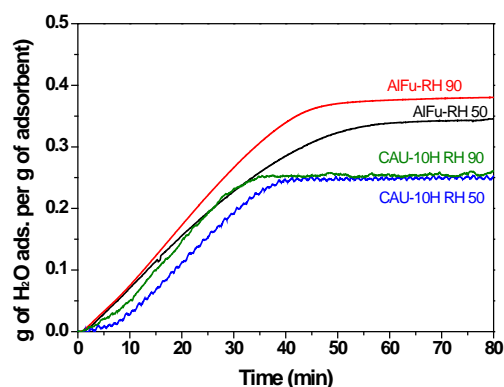


Figure 5. Thermogravimetric analysis profile of water adsorption/desorption of Al-fumarate (Al-Fu) and CAU-10-H MOFs. Test conditions: adsorption at 303 K in humid nitrogen (RH 50% and 90%) and desorption at 473 K in nitrogen.

CONCLUSION

Two kinds of Al-based MOFs were successfully synthesized and examined for water adsorption. The synthesized material was stable at up to 400 °C. The water adsorption of CAU-10-H and Al-fumarate MOF corresponding to ~25% and 35-40% were reached after 80 min. An important observation was low-temperature adsorption and desorption in both synthesized MOFs. In addition, the chemicals (fumaric and isophthalic acid) used as the organic linker were very popular and not expensive. This study

could be extended to other MOFs with a proper choice of metal.

Acknowledgment

This study was funded by Institute of Materials Science (the grant of Project numbered CSL2.02.2019) and Korea Chemical Technology Research Institute.

References

- [1]. M. N. Golubovic, H. D. M. Hettiarachchi, W. M. Worek, *Int. J. Heat Mass Transfer* **49** (2006) 2802
- [2]. S. Cui, M. Qin, A. Marandi, V. Steggles, S. Wang, X. Feng, F. Nouar, C. Serre, *Scientific Reports* **8** (2018) 15284
- [3]. Y. K. Seo, J. W. Yoon, J. S. Lee, Y. K. Hwang, C.-H. Jun, J.-S. Chang, S. Wuttke, P. Bazin, A. Vimont, M. Daturi, S. Bourrelly, P. L. Llewellyn, P. Horcajada, C. Serre, G. Férey, *Adv. Mater.* **24** (2012) 806
- [4]. F. Jeremias, D. Fröhlich, C. Janiak, S. K. Henninger, *New J. Chem.* **38** (2014) 1846
- [5]. I. Gur, K. Sawyer, R. Prasher, *Science* **335** (2012) 1454
- [6]. H. M. Henning, *Appl. Therm. Eng.* **27** (2007) 1734
- [7]. L. G. Gordeeva, Y. I. Aristov, *Int. J. Low Carbon Tech.* **7** (2012) 288
- [8]. M. M. Rafique, P. Gandhidasan, H. M. S. Bahaidarah, *Renew. Sust. Energ. Rev.* **56** (2016) 179
- [9]. X. Feng, M. Qin, S. Cui, C. Rode, *Build. Environ.* **145** (2018) 234
- [10]. N. C. Burtch, H. Jasuja, K. S. Walton, *Chem. Rev.* **114** (2014) 10575
- [11]. J. Canivet, A. Fateev, Y. Guo, B. Coasne, D. Farrusseng, *Chem. Soc. Rev.* **43** (2014) 5594
- [12]. V. V. Butova, M. A. Soldatov, A. A. Guda, K. A. Lomachenko, C. Lamberti *Russ. Chem. Rev.* **85** (2016) 280
- [13]. A. Schoedel, M. Li, D. Li, M. O’Keeffe, O. M. Yaghi, *Chem. Rev.* **116** (2016) 12466
- [14]. H. Furukawa, K. E. Cordova, M. O’Keeffe, O. M. Yaghi, *Science* **341** (2013) 1230444
- [15]. M. F. de Lange, K. J. F. M. Verouden, T. J. H. Vlugt, J. Gascon, F. Kapteijn, *Chem. Rev.* **115** (2015) 12205
- [16]. H. Furukawa, N. Ko, N. Aratani, S. Choi, E. Choi, O. Yaghi, *Science* **329** (2010) 424
- [17]. M. Gaaba, N. Trukhana, S. Maurera, R. Gummarajub, U. Müllera, *Microporous and Mesoporous Materials* **157** (2012) 131
- [18]. H. Kim, S. Yang, S R. Rao, S. Narayanan, E. A. Kapustin, H. Furukawa, A. S. Umans, O. M. Yaghi, E. N. Wang, *Science* **356** (2017) 430
- [19]. N. Tannert, C. Jansen, S. Nießing, C. Janiak, *Dalton Trans.* **48** (2019) 2967
- [20]. M. Mon, R. Bruno, J. Ferrando-Soria, D. Armentano, E. Pardo, *J. Mater. Chem. A* **6** (2018) 4912
- [21]. S. Karmakar, J. Dechnik, C. Janiak, S. De, *J. Hazard. Mater.* **303** (2016) 10
- [22]. D. Fröhlich, E. Pantatosaki, P. D. Kolokathis, K. Markey, H. Reinsch, M. Baumgartner, M. A. van der Veen, D. E. De Vos, N. Stock, G. K. Papadopoulos, S. K. Henninger, C. Janiak, *J. Mater. Chem. A*, **4** (2016) 11859
- [23]. E. Alvarez, N. Guillou, C. Martineau, B. Bueken, B. Van de Voorde, C. Le Guillouzer, P. Fabry, F. Nouar, F. Taulelle, D. de Vos, J.-S. Chang, K. H. Cho, N. Ramsahye, T. Devic, M. Daturi, G. Maurin, Christian Serre, *Angew. Chem. Int. Ed.* **54** (2015) 1
- [24]. D. Fröhlich, S. K. Henninger, C. Janiak, *Dalton Trans.* **43** (2014) 15300

PHOTOCATALYTIC PROPERTIES OF NANOSTRUCTURE AND NANO-COMPOSITES BASED ON ANATASE TiO₂ SYNTHESIZED BY THERMOLYSIS

Duong Ngoc Huyen¹, **Mai Van Tuan**^{1,2}, **Mai Xuan Dung**³

¹ School of Engineering Physics, Hanoi University of Science and Technology, No. 1, Daicoviet, Hanoi, Vietnam;

² Department of Natural Sciences, Electric Power University, 235 Hoang Quoc Viet, Hanoi, Viet Nam.

³ Department of Chemistry, Hanoi Pedagogical University 2, 32 Nguyen Van Linh, Phuc Yen, Vinh Phuc, Viet Nam

Email: huyen.duongngoc@hust.edu.vn

ABSTRACT

Titanium dioxide (TiO₂) and derivatives are considered to be among of the most promising materials for solving the environmental and energy issues due to their high photochemical activity, stability, safe and low cost. The strong photocatalysis of TiO₂ has been used and proposed for destruction of pollutants, anti-bacterial, self-cleaning, gas sensor, water photolysis and photovoltaic but its efficiency need to be further improved. Enlarge the specific surface area by using nanostructures and modify the band gap by hybrid materials to shift the photocatalysis into the visible range are being proposed as effective approaches. With respect to the viewpoints of thermodynamic considerations, the thermolysis of Ti precursors will initiate the formation of tiny anatase nanocrystalites and follow with crystal growth process. By controlling the synthesis conditions, anatase nanostructure with desirable size is achieved and can be used for improvement of photocatalytic feature. In this work, photocatalytic properties as well as formation of TiO₂ nanostructure synthesized by thermolysis is presented and discussed.

Keywords: TiO₂ anatase, photocatalysis, nanostructure, thermolysis.

INTRODUCTION

Titanium dioxide (TiO₂), a material with high refractive index, chemical stability, long durability, and nontoxicity has been widely used for many applications such as pigments, textiles, papers, cosmetics, medicines, ceramics, etc. With respect to electrochemical, TiO₂ is a n-type wide bandgap semiconductors showing strong photoactivity that involves photogenerated charge carrier reaction of adsorbed substances and photoinduced hydrophilic conversion of itself [1,2]. The feature opens to many possible applications such as photocatalyst, antibacterial purpose, self-cleaning glass, water purification,... [3, 4], convert light into electricity in dye-sensitized solar cells (DSSC), or separating hydrogen from water for fuel cells [5].

Under normal condition, TiO₂ exists in three main structures: stable rutile, metastable anatase, and brookite. For pure phases it is generally accepted that anatase exhibits a higher photocatalytic activity compared to rutile TiO₂ although the band gap is larger (3.2 eV for anatase vs. 3.0 eV for rutile). Longer lifetime for photo-excited electrons and holes in an indirect band gap TiO₂ anatase semiconductor is accounted for the feature [6]. Traditionally, TiO₂ submicron particles have been considered as poorly photocatalytic activity but in the nanostructured form, due to the

quantum confinement, it shows stronger photocatalytic activity when compared to that of the submicron [7]. The unique properties of TiO₂ nanostructures seems to be size dependent. Synthesize TiO₂ anatase nanostructures with mean size in desirable range less than 5nm then is expected to enhance the anatase photocatalys and enlarge its application.

For the synthesis of TiO₂ nanostructure, a variety of techniques based on thermolysis of Ti precursors such as hydrothermal, solvothermal, sol-gel, direct oxidation, chemical vapor deposition (CVD), electrodeposition, sonochemical, and microwave method has been used [8]. Hydrothermal method offers a simple and common route to synthesize a well-crystalline TiO₂ under the moderate reaction condition such as low temperature and short time using inexpensive precursors such as TiCl₄, TiCl₃, amorphous TiO₂, P25, etc. In addition, hydrothermal media provides an effective reaction environment for the nucleation and growth of TiO₂ nanostructure with high purity, good dispersion and controllable crystalline. It has found that thermolysis of TiCl₄ results in TiO₂ nanocrystalites in both the anatase and rutile phase. The TiO₂ anatase is mainly suspended in the aqueous solution while the TiO₂ rutile will

predominantly deposited in the sedimentation [9, 10]. Higher HCl concentration enables the agglomeration of small anatase particle forming uniform cluster and enhances the anatase to rutile transition. With respect to chemical viewpoint, a higher HCl concentration in thermolysis solution will result in a higher concentration of hydrogen ions. Then, a reduction of hydrogen ions concentration in the thermolysis aqueous solution will reduce the rutile fraction as well as size of TiO₂ anatase. Based on that consumption, this work is carried on to study the effect of pH on the formation of TiO₂ nanocrystallites by addition of basic agents such as C₂H₄OH or NH₄OH in the synthesis medium.

EXPERIMENTAL

Titanium tetrachloride (TiCl₄) of 99.9% purity (Sigma Aldrich Chemical Co.) as Ti precursor was used as received, HCl 37% solution, ethanol C₂H₄OH and NH₄OH (Merck Corp.) were used to change the pH of thermolysis medium. The TiO₂ synthesis process is straightforward as follows: TiCl₄ was added dropwise into DI water at 5C to have a given concentration of 0.4 M and was used as starting materials. In order to change the pH of the medium C₂H₄OH and NH₄OH was added to have a given value in a range from 1.0 to 10.0. The solution then was poured into test tubes and placed in an oven at 80 °C. The solution was gradually changed to opaque suspension indicating that the TiCl₄ was thermally decomposed and converted into Ti complexes [Ti(OH)_{4-n}(H₂O)_{2+n}]ⁿ⁺ (n is number of protonated OH⁻ groups) and concomitant HCl in the reaction medium [11]. After 3.0 h heating, the solution was cooled to room temperature. At a low pH range the resulting aqueous solution is transparent but remain opaque and gradually changes to opaque state and separated into opaque and milky part in the test tubes as clearly seen in Fig.1. The solution then was extracted and dried by vacuum evaporation and analyzed by XRD and TEM, SEM.

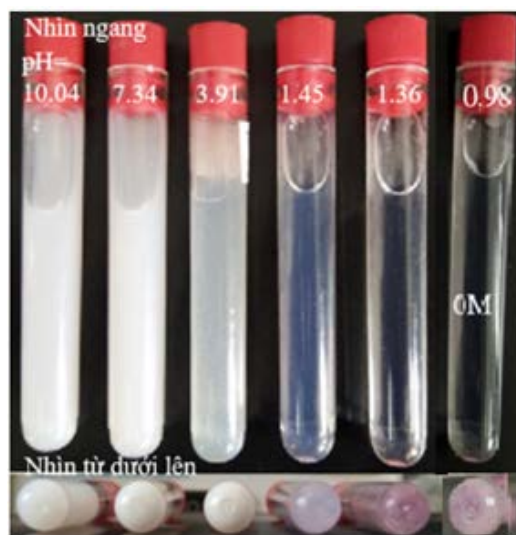


Figure 1. The appearance of TiCl₄ aqueous solution with different pH level after thermolysis at 80 °C.

XRD patterns of TiO₂ powder were conducted on a D8 Advance Bruker diffractometer using Cu K α radiation (1.54 Å wavelength). The mean size of TiO₂ nanostructures was calculated using Scherrer equation, i.e., $D = k\lambda/\beta \cos \theta$, where $k = 0.94$, $\lambda = 1.54 \text{ \AA}$ and β is full width at half maximum (FWHM) according to diffracted angle θ , namely (101) peak for anatase. Raman spectra were determined by a LabRAM HR800 (Horiba) using a 632.8 nm excitation laser at a resolution of 1.0 cm⁻¹. TEM images were obtained using a JEOL JEM-2100 Transmission Electron Microscope. The photocatalytic activity of TiO₂ nanostructures is determined by comparing the degradation of methylene blue (MB) under UV-Vis light radiation.

RESULTS AND DISCUSSION

Table 1. Anatase mean size from thermolysis of TiCl₄ in different pH medium at 80 °C.

pH	(101) peak Intensity	(101) peak FWHM	Size (nm)	Agent addition
0.93	54,75	1,82	5	No addition
1,36	24,93	1,45	6	NH ₄ OH
3,91	50,91	2,12	4	NH ₄ OH
7,34	43,54	2,55	3	NH ₄ OH
10.04	-	-	-	NH ₄ OH

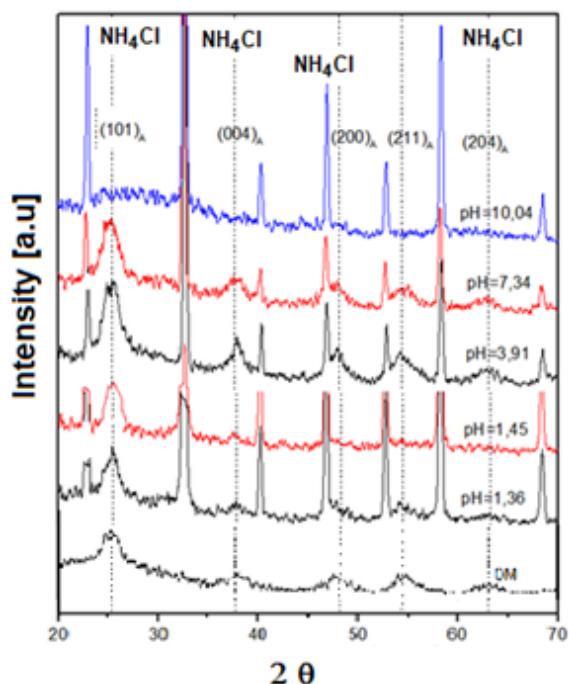


Figure 2. XRD spectra of TiO_2 resulting from thermolysis of TiCl_4 in different pH medium at 80°C .

X-ray diffraction spectra show that the resulting TiO_2 consists of anatase (JCPDS no. 00-021-1272) and rutile phase but rutile portion gradually disappears with the increasing pH level depending on $\text{C}_2\text{H}_5\text{OH}$ or NH_4OH concentration. As can be seen from Fig. 2, the prominent peak standing for anatase phase is observed at 2θ around 25.29° that assigns to (101) plane reflection and the other peaks are observed 2θ of 37.80° , 48.05° , 53.89° , and 62.68° standing for reflection at (004), (200), (105) and (204) planes, respectively. The XRD indicate that in the starting sample (no $\text{C}_2\text{H}_4\text{OH}$ and NH_4OH addition) the resulting TiO_2 is an anatase and rutile phase mixture with predominant anatase. With increasing pH level as resulting of adding more $\text{C}_2\text{H}_4\text{OH}$ or NH_4OH the trade of rutile is gradually disappeared and only the anatase present in the XRD patterns. In addition, the FWHM of (101) peak is broadening with pH level indicating a decrease in anatase particle size that is calculated by Scherrer equation and shown in Table 1.

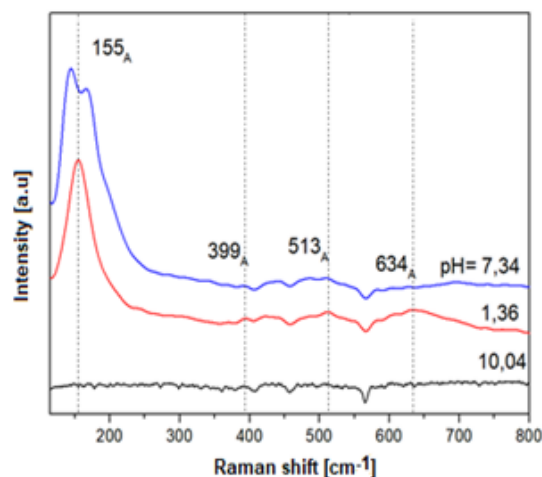


Figure 3. Raman spectra of TiO_2 resulting from thermolysis of TiCl_4 in different pH medium at 80°C .

As a complementary for XRD, Raman spectra have also shown the present of anatase in the spectra. The Raman shift peak observed at 155 cm^{-1} representing from E_g vibration mode of anatase or maybe consisting of and B_{1g} and B_{2g} modes from brookite (pH = 7,34) [12]. The blue shift in frequency and increase in FWHM of E_g vibration mode indicate an influence of the nanosize of the TiO_2 crystallites.

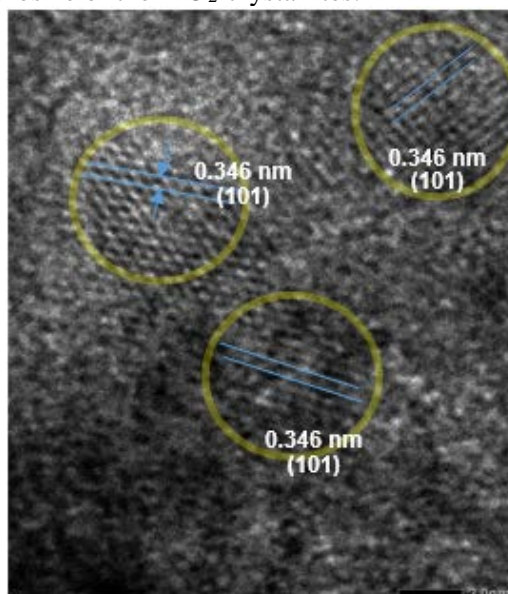


Figure 4. The appearance of anatase nanoparticle in HRTEM image.

The TiO_2 anatase nanoparticle observed through HRTEM images gives more information on the resulted anatase nanostructure. As shown in Fig. 4, the image taken from starting sample shows the appearance of TiO_2 anatase nanoparticle with size 4–5 nm, the same size as calculation from XRD pattern. For the sample having NH_4OH addition the mean grain size reduces with NH_4OH

content, i.e., decreases with the increase in pH level.

The photocatalytic activity of TiO₂ nanostructures is determined by measuring the degradation of methylene blue (MB) under UV light radiation. Typically, the UV-Vis spectrum of MB and anatase aqueous solution that is exposed to UV radiation is shown in Fig. 5. With longer UV exposure, the absorbance of MB in the UV spectrum is reduced as result of degradation of MB content in the solution. The degradation rate of MB is found to be dependent on the mean size and heat treatment,

The formation of TiO₂ nanostructures by thermolysis of TiCl₄ in aqueous medium is explained by the dissolution, recrystallization and in situ transition mechanism [13]. As a result of competition between the surface and bulk free energy, below a size limitation, the TiO₂ anatase crystallites have lower free energy than that of the rutile and will be predominant. The anatase to rutile transformation is enhanced by the appearance of concomitant HCl, that acts as chemical catalyst for the rutile formation. The addition of NH₄OH reduces the acidity of HCl, the anatase to rutile transition is depressed and the resulting anatase is intact in the synthesis medium.

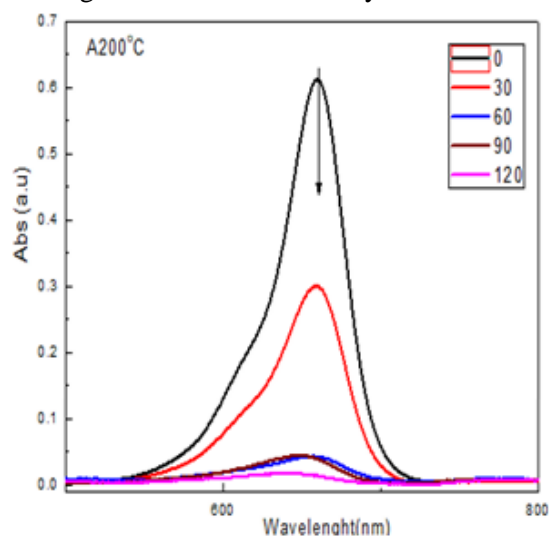


Figure 5. Degradation of methylene blue aqueous solution under UV light irradiation using anatase nanostructure as photocatalyst.

CONCLUSION

The formation of tiny anatase nanocrystalite is believed to initiate at the onset of thermal decomposition of TiCl₄ and follow with crystal

growth process. Consequence, either anatase or rutile structure is formed with assistance of concomitant HCl. By addition of basic agent to reduce the HCl acidity, it is believed that the anatase to rutile transition is depressed and the anatase nanostructures with desirable mean size to improve TiO₂ photocatalytic feature is achieved.

Acknowledgment

The authors gratefully acknowledge financial support from Research Project T2018-PC-123 provided by Hanoi University of Science and Technology (HUST), Vietnam.

References

- [1]. U. Diebold, Surf. Sci. Rep. **48**, (2003), 53-229.
- [2]. K. Hashimoto, H. Irie, and A. Fujishima, JAP **44** (12), (2005), 8269–8285.
- [3]. K. Nakata and A. Fujishima, J. Photochem. Photobiol. C **13**(3), (2012), 169–189.
- [4]. Montazer M., Seifollahzadeh S., Photochem Photobiol. **87**, (2011), 877–883.
- [5]. A. Fujishima and K. Honda, Nature **238**, (1972), 37–38.
- [6]. Liu L., Zhao H., Andino J. M. & Li Y. ACS Catal. **2**, (2012), 1817–1828.
- [7]. S. M. Gupta and M. Tripathi, Chinese Sci. Bull. **56** (16), (2011), 1639–1657.
- [8]. M. M. Byranvand, A. Nemat Kharat, L. Fatholahi, and Z. Malekshahi Beiranvand, J Nanostruct. **3**, (2013), 1-9.
- [9]. N. T. Tung, D. Ng. Huyen, J. Nanomater. **2016**, (2016).
- [10]. N. T. Tung, M. X. Dung and D. Ng. Huyen, Bull. Korean Chem. Soc., (2017).
- [11]. V. Jordan, U. Javornik, J. Plavec, A. Podgornik, A. Recnik, Sci. Rep. **6**, (2016), 24216.
- [12]. M.N. Iliev, V.G. Hadjiev, A.P. Litvinchuk, Vib. Spectroscopy **64**, (2013), 148–152.
- [13]. S. Dai, Y. Wu, T. Sakai, Z. Du, H. Sakai, and M. Abe, Nanoscale Res. Lett. **5** (11), (2010), 1829–1835,

MORPHOLOGY AND OPTICAL PROPERTIES OF CePO₄:Tb³⁺ HOLLOW SPHERES

Chinh Dung Trinh^{1,2}, Phuong Hau Thi Pham¹, Dung My Thi Dang¹ and Chien Mau Dang¹

¹ Institute for Nanotechnology, Vietnam National University, Ho Chi Minh City

² The University of Science, Vietnam National University, Ho Chi Minh City

Email: tdchinh@vnuhcm.edu.vn

ABSTRACT

There was successful synthesization of CePO₄:Tb³⁺ hollow spheres by wet chemical method and using citric acid as a structure-directing agent. The results of X-ray diffraction (XRD) showed that all samples were crystallinity which distributed to the monoclinic phase of CePO₄ host (JCPDS, No. 32-0199) and Tb³⁺ ions were doped into CePO₄ host lattice. According to the results of Field emission scanning electron microscopy (FE-SEM), the morphology of CePO₄:Tb³⁺ comprised well defined echinus-like CePO₄:Tb³⁺ hollow spheres with diameters in the range of 520 nm, rode length at ~ 110 nm and the hollow diameter at ~ 60nm. CePO₄:Tb³⁺ was determined by photoluminescence at excitation of 278 nm, showed the high intensity of green emission at 543 nm wavelength which was correspond to ⁵D₄-⁷F₅ transition of Tb³⁺.

INTRODUCTION

One-dimensional (1D) nanostructures, such as nanotubes, nanorods, nanowires, nanobelts, etc., have been the subject of intense interest because of their unique chemical, physical and optical properties, and potential applications in constructing nanoelectric and optoelectronic devices [1–6]. 1D nanostructures of various components were synthesized by various methodologies [7–11]. Hollow spheres, which have lower densities and higher surface areas, are a new kind of nano- and microstructure and have great potential applications in a variety of fields, such as drug delivery, chemical storage, battery materials and catalysis [12, 13]. Very recently, organizing 1D nanostructures into curved superstructures for high technology applications, which exhibit a unique collective property, is of great interest and attracts more attention in the areas of chemistry and materials science [14–16]. However, because the ordered nanorod-based curved superstructure remains difficult to prepare in the unsupported colloidal form, it is still a great challenge for scientists to develop a facile and effective method for constructing such a novel superstructure,

especially one composed of a unique functional species.

As we know, lanthanide compounds, as a class of multi-functional materials, have been extensively applied in phosphors, laser hosts, sensors, catalysts, photon upconversion materials, etc. [17–20]. Although a variety of 1D nanostructures, such as nanotubes, nanowires and nanorods, have already been synthesized [21–24], no method, to the best of our knowledge, has been developed for controllable fabrication of lanthanide compound hollow and core-shell spheres composed of nanoscale 1D building blocks. In this research, we successfully synthesized echinus-like CePO₄:Tb³⁺ hollow spheres using wet chemical method with citric acid (CA) as a structure-directing agent.

EXPERIMENT

Materials

Ce(NO₃)₃.6H₂O (99.8%, Aldrich), Tb(NO₃)₃.5H₂O (99.9%, Aldrich), H₃PO₄ (Aldrich) were used as starting materials. C₆H₈O (Aldrich) were used as structure-

directing agent. Sodium hydroxide (NaOH, 99%, Aldrich) was used to control pH.

Synthesis of CePO₄:Tb³⁺ hollow spheres

CePO₄:Tb³⁺ nanoparticles were synthesized by chemical method. Dissolving 1.5 mmol of Ce(NO₃)₃·6H₂O and the amount of citric acid into 15 ml DI water in 15 minutes. After that, 0.078 mmol of Tb(NO₃)₃·5H₂O and H₃PO₄ were added into the solution (Tb³⁺ doping molar concentration is 5%). The pH value of mixture was adjusted to 2 by 5M of NaOH.

Characterization

Particle size and morphology of CePO₄:Tb³⁺ is determined by Field emission scanning electron microscopy (FE-SEM). The crystallite structure of CePO₄:Tb³⁺ is analyzed by X-ray diffraction spectroscopy. The emission spectra are recorded at room temperature using a Hitachi F-4500 spectrophotometer.

RESULTS AND DISCUSSION

In all of the following experiments, molar ratio of Europium ion is fixed at 5% and pH is fixed at 2. The amount of CA is adjusted in turn at: 0; 5; 20, 40 mg.

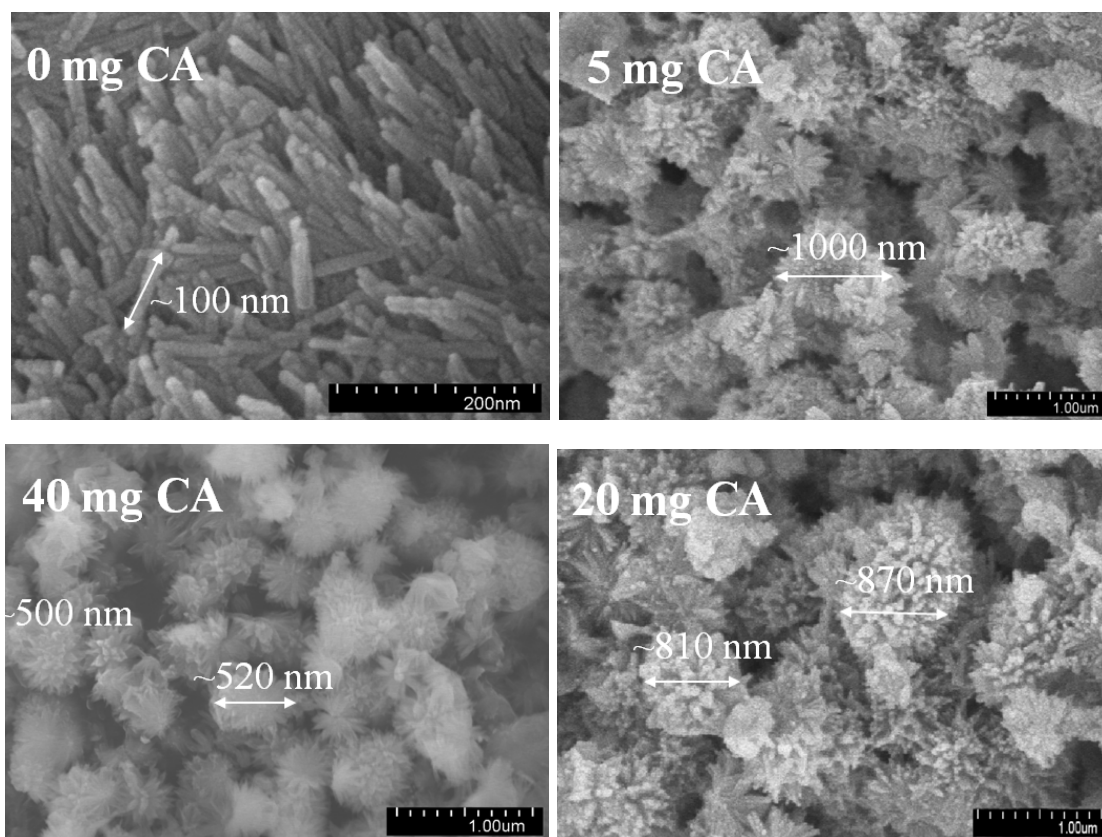


Figure 1. FE-SEM micrographs of CePO₄:Tb³⁺ synthesized with different amount of CA.

CA plays crucial roles in the formation of CePO₄:Tb³⁺ hierarchical structures. With the introduction of CA in the preparation process, 3D spherical CePO₄:Tb³⁺ can be produced, and the size of the 3D microspheres can be tuned by changing the amount of CA.

Figure 1 shows the FE-SEM micrographs of CePO₄:Tb³⁺ synthesized with different amount of CA. In the absence of CA, a large quantity of isolated nanorods with a diameter of ~15 nm and length of ~100 nm were formed, as shown in Figure 1. With only a small amount of CA (5 mg) added, 3D microspheres ~1000 nm in diameter appeared. When the amount of CA was

increased to 20 mg, the 3D microspheres were maintained, but their diameters were reduced to 800– 900 nm . A further increase in the CA amount to 40 mg, the diameters reduced to 500 nm.

Figure. 2 is FE-SEM micrographs of $\text{CePO}_4:\text{Tb}^{3+}$ synthesized with different reaction

time. In the present investigation, the formation of $\text{CePO}_4:\text{Tb}^{3+}$ hollow sphere is investigated with different reaction time, as follow: 5 minutes, 15 minutes, 30 minutes, 40 minutes. The amount of CA is 40 mg and the other conditions remain unchanged for other samples.

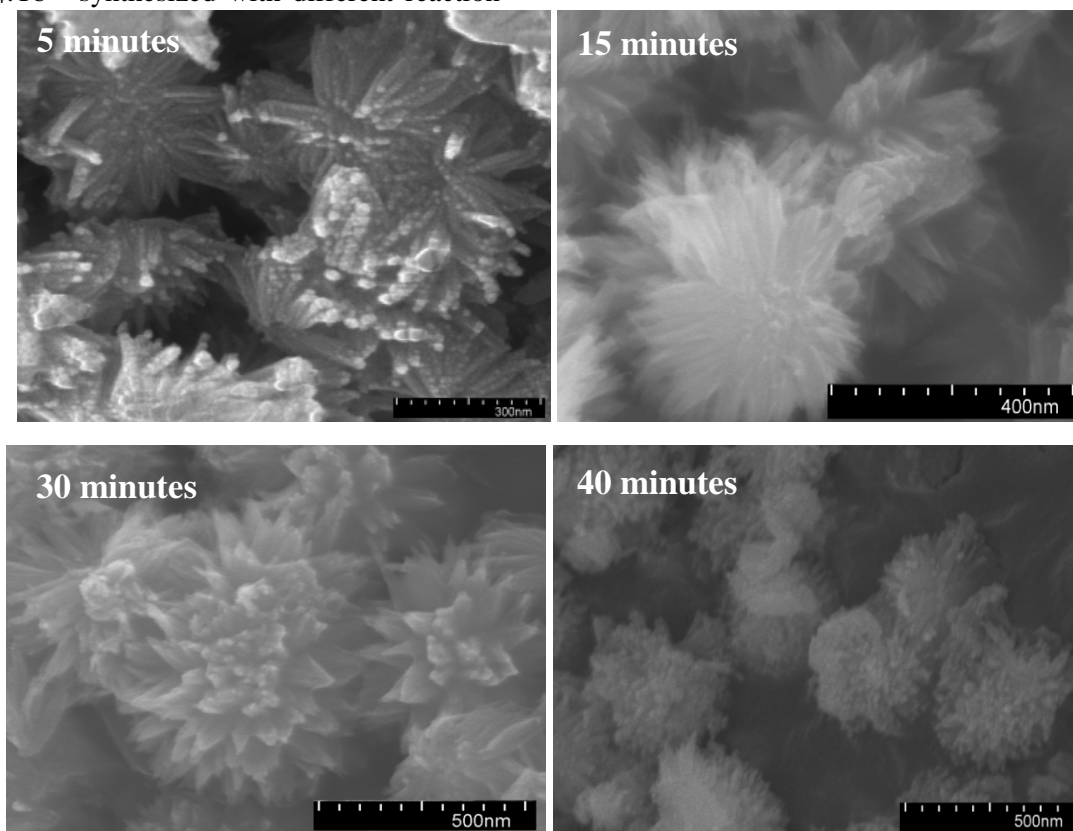
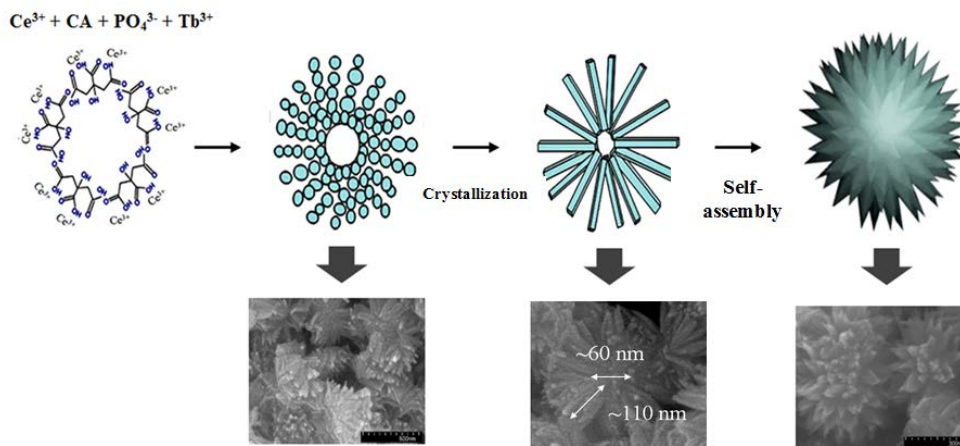


Figure 2. The FE-SEM micrographs of $\text{CePO}_4:\text{Tb}^{3+}$ synthesized with different reaction time

Time-dependent experiments were performed to understand the formation process of the $\text{CePO}_4:\text{Tb}^{3+}$ hierarchical microspheres. The morphologies of the samples with different reaction time were characterized by FE-SEM. As shown in Figure. 2, short nanorods were obtained after 5 minutes of reaction. Interestingly, nanorods assembled as hollow hemispheres after reaction for 15 minutes. As shown in Figure. 2(left corner), echinus-like hollow spheres were eventually obtained when the reaction duration was extended to 30 minutes. When the reaction time at 40 minutes,

$\text{CePO}_4:\text{Tb}^{3+}$ has no echinus-like hollow spheres morphology.

On the basis of the above experimental observations, a plausible formation mechanism for the hierarchical hollow spheres was proposed. As shown in Scheme 1, the $\text{CePO}_4:\text{Tb}^{3+}$ hollow spheres were formed through a three-step mechanism: the nucleation of $\text{CePO}_4:\text{Tb}^{3+}$ nanoparticles, the growth of nanorods through the oriented attachment of $\text{CePO}_4:\text{Tb}^{3+}$ nanoparticles, and the formation of a 3D hierarchical structure by the selfassembly of $\text{CePO}_4:\text{Tb}^{3+}$ nanorods.



Scheme 1. Formation mechanism of the echinus-like $CePO_4:Tb^{3+}$ hollow spheres.

Adding $Ce(NO_3)_3$ into water, it dissolved into Ce^{3+} and NO_3^- (Eq. (1)). The free Ce^{3+} ions can combine with citric anions (Cit^{3-}) via the chelating effect to produce a Cit-Ce complex (Eq. (2)). Hydrogen bonds were formed between the carboxyl of the CA and the hydroxyl in Cit-La and between the hydroxyls in Cit-Ce. The formed hydrogen bonds resulted in citrate agglomeration in the central region surrounded by Ce^{3+} chelating. After the addition of the

phosphorus source H_3PO_4 , an ion-exchange reaction between PO_4^{3-} and Cit^{3-} occurred under continuous stirring, leading to the formation of $CePO_4$ nanoparticles (Eq. (3)). The 3D hierarchical hollow structure formed after the ripening and growth of nanorods through the oriented attachment of $CePO_4$ nanoparticles. According to Scheme 1., echinus-like $CePO_4:Tb^{3+}$ hollow spheres has the rod length at ~ 110 nm and the hollow diameter at ~ 60 nm

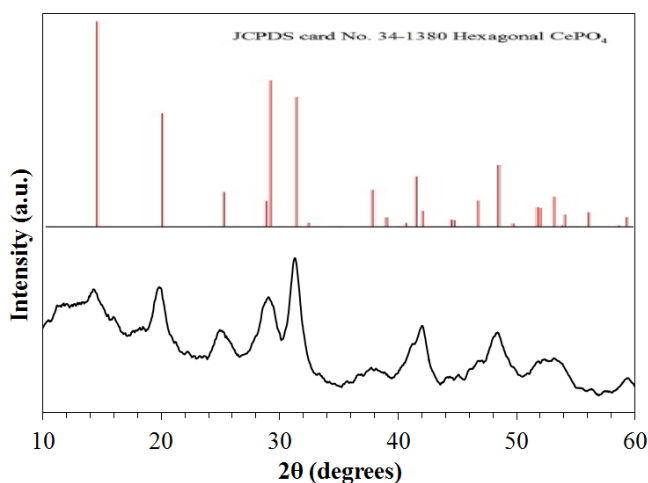
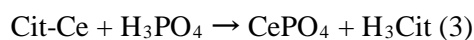
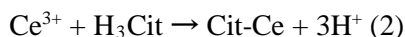


Figure 3. The XRD patterns of echinus-like $CePO_4:Tb^{3+}$ hollow spheres

Figure 3. shows the XRD patterns of echinus-like $CePO_4:Tb^{3+}$ hollow spheres synthesized

with 40 mg CA in 30 minutes reaction time. $CePO_4$ hexagonal phase (JCPDS, No. 34-1380)

attributes in all diffraction peak, indicating the existence of crystalline structure in all nanoparticles. The absence of additional peaks

for another phases indicated that Tb^{3+} ions have been effectively built into the $CePO_4$ host lattice.

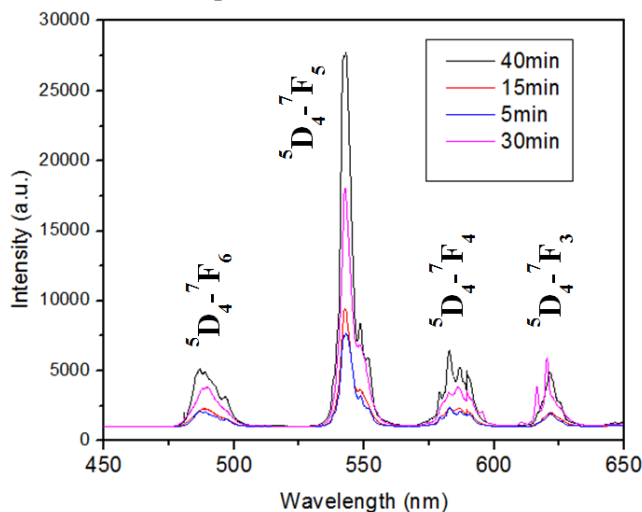


Figure 4. The photoluminescence emission spectrum of $CePO_4:Tb^{3+}$ synthesized with different reaction time

Figure 4 shows the emission spectra under excitation at 280 nm of $CePO_4:Tb^{3+}$ hollow spheres synthesized with different reaction time. The 40 min reaction time synthesized sample has highest peak intensity. The most intense line at ~ 543 nm corresponds to the transition between the 5D_4 and 7F_5 level of the Tb^{3+} ions. The more increasing of Tb^{3+} local symmetry environment cause the increase of strongest emission from $^5D_4 - ^7F_5$ transition over reaction time from 5 – 40 min.

CONCLUSION

The echinus-like $CePO_4:Tb^{3+}$ hollow spheres were synthesized by chemical method using citric acid as a structure-directing agent. The morphology of $CePO_4:Tb^{3+}$ comprised well defined echinus-like $CePO_4:Tb^{3+}$ hollow spheres with diameters in the range of 520 nm, rode length at ~ 110 nm and the hollow diameter at ~ 60 nm when the amount of CA was 20 mg and 40 min reaction time. Echinus-like $CePO_4:Tb^{3+}$ hollow spheres had hexagonal phase (JCPDS, No. 34-1380) attributes in all diffraction peaks, indicating the existence of crystalline structure in all nanoparticles. $CePO_4:Tb^{3+}$ was determined by photoluminescence at excitation of 278 nm,

showed the high intensity of green emission at 543 nm wavelength which was correspond to $^5D_4-^7F_5$ transition of Tb^{3+} .

Acknowledgment

The authors highly appreciate the financial support of the Vietnam National University - Ho Chi Minh City (VNU-HCM)

References

- [1]. Fang X S and Zhang L D 2006 *J. Mater. Sci. Technol.* **22** 1
- [2]. Hu J T, Odom T W and Lieber C M 1999 *Acc. Chem. Res.* **32** 435
- [3]. Zhu H L, Yang D R and Zhang H 2005 *J. Mater. Sci. Technol.* **21** 609
- [4]. Fang X S and Zhang L D 2006 *J. Mater. Sci. Technol.* **22** 721
- [5]. Zhang L, Deckhardt E, Weber A, Schöonenberger C and Grützmacher D 2005 *Nanotechnology* **16** 655
- [6]. Xia Y N, Yang P D, Sun Y G, Wu Y Y, Mayers B, Gates B, Yin Y D, Kim F and Yan H Q 2003 *Adv. Mater.* **15** 353
- [7]. Liu Z P, Peng S, Xie Q, Hu Z K, Yang Y, Zhang S Y and Qian Y T 2003 *Adv. Mater.* **15** 936

- [8]. Peng H Y, Pan Z W, Xu L, Fan X H, Wang N, Lee C S and Lee S T 2001 *Adv. Mater.* **13** 317
- [9]. Fang X S, Ye C H, Peng X S, Wang Y H, Wu Y C and Zhang L D 2003 *J. Mater. Chem.* **13** 3040
- [10]. Pan Z W, Dai Z R, Xu L, Lee S T and Wang Z L 2001 *J. Phys. Chem. B* **105** 2507
- [11]. Fang X S, Ye C H, Zhang L D, Wang Y H and Wu Y C 2005 *Adv. Funct. Mater.* **15** 63
- [12]. Yin Y D, Rioux R M, Erdonmez C K, Hughes S, Somorjai G A A and Alivisatos P 2004 *Science* **304** 711
- [13]. Jiang P, Bertone J F and Colvin V L 2001 *Science* **291** 453
- [14]. Vasquez Y, Sra A K and Schaak R E 2005 *J. Am. Chem. Soc.* **127** 12504
- [15]. Peng Q, Dong Y J and Li Y D 2003 *Angew. Chem. Int. Edn* **42** 3027
- [16]. Duan H W, Wang D Y, Sobal N S, Giersig M, Kurth D G and M^o ohwald H 2005 *Nano Lett.* **5** 949
- [17]. Caruso F, Caruso R A and M^o ohwald H 1998 *Science* **282** 1111
- [18]. Park S, Lim J H, Chung S W and Mirkin C A 2004 *Science* **303** 348
- [19]. Cao A M, Hu J S, Liang H P and Wang L J 2005 *Angew. Chem. Int. Edn* **44** 4391
- [20]. Liu B and Zeng H C 2004 *J. Am. Chem. Soc.* **126** 16744
- [21]. Mo M S, Yu J C, Zhang L Z and Li S K 2005 *Adv. Mater.* **17** 756
- [22]. Li Z Q, Ding Y and Xie Y 2005 *Chem. Commun.* 918
- [23]. Cheng Y, Wang Y S, Jia C and Bao F 2006 *J. Phys. Chem. B* **110** 24399
- [24]. Li B X, Rong G X, Xie Y, Huang L F and Feng C Q 2006 *Inorg. Chem.* **45** 6404

FABRICATION OF GRAPHENE BY THERMAL REDUCTION-EXFOLIATION OF GRAPHITE OXIDE

Danh Phuong Bui ^{1,2}, Duong Thuy Vo ¹, Diep Ngoc Le ¹, Oanh Kim Thi Nguyen ^{1,3}, Dung Trung Dao ¹ and Chien Mau Dang ¹

¹ Institute for Nanotechnology (INT), Vietnam National University - Ho Chi Minh City (VNUHCM), Ho Chi Minh City, Vietnam;

² Faculty of Materials Technology, Ho Chi Minh City University of Technology, Vietnam National University, 268 Ly Thuong Kiet, District 10, Ho Chi Minh City, Vietnam;

³ Ho Chi Minh City University of Education, Ho Chi Minh City, Vietnam

Email: trungdung@vnuhcm.edu.vn

ABSTRACT

In this work, the fabrication process of graphene by thermal reduction-exfoliation of graphite oxide (GO) is described. GO is prepared by oxidation of natural graphite using Hummers method. After that, dried GO powder is thermally reduced and exfoliated at 1100 °C to obtain graphene powder. The results indicate that the obtained graphene exhibits a high degree of reduction and exfoliation. With the novel properties, the obtained graphene shows promising application potential in various fields.

Keywords: Graphene, graphite oxide, thermal reduction-exfoliation

INTRODUCTION

Graphene is a single-atom-thick sheet of hexagonally arrayed sp²-bonded carbon atoms. Its large specific surface area and superior electrical, thermal, mechanical properties make graphene a grand research topic in many fields of science and engineering [1]. Graphene can be fabricated via various methods, such as, chemical vapour disposition [2], micromechanical exfoliation of graphite [3], liquid-phase exfoliation of graphite [4], or electrochemical exfoliation of graphite [5].

Methods to produce graphene from graphite oxide (GO) have been considered to be promising approaches for graphene mass production. Graphite, abundant and inexpensive, can be oxidized in great quantities into GO via simple oxidation processes. Compared to graphite, GO has greater interlayer spacing and with that, lower Van der Waals interaction force between layers. This enables the exfoliation of GO utilizing much smaller forces, which is not feasible if the precursor is graphite. For instance, the pressure between GO sheets can exfoliate the precursor into graphene [6]. Under rapid

heating condition, the functional groups of GO undergo thermal decomposition and with the sudden volumetric expansion caused by the gas products, the graphene sheets are reduced and exfoliated simultaneously. The exfoliation process is fast, solvent-free and without the need of further reducing agents. The obtained graphene is wrinkled, which prevents the sheets from restacking, and is readily functionalized with the remained oxygen-containing functional groups, so that it can be dispersed in polar organic solvents.

In this article, we describe the process of graphene fabrication by thermal reduction-exfoliation of graphite oxide as well as the characterization of the samples obtained.

EXPERIMENTAL

Natural graphite flakes, purchased from Sigma-Aldrich, was used as precursor for GO. Potassium permanganate (Merck), sulfuric acid (98%, Merck), hydrochloric acid (37%, Merck), hydrogen peroxide (30%, Acros) were also employed. All materials and chemicals were used as received.

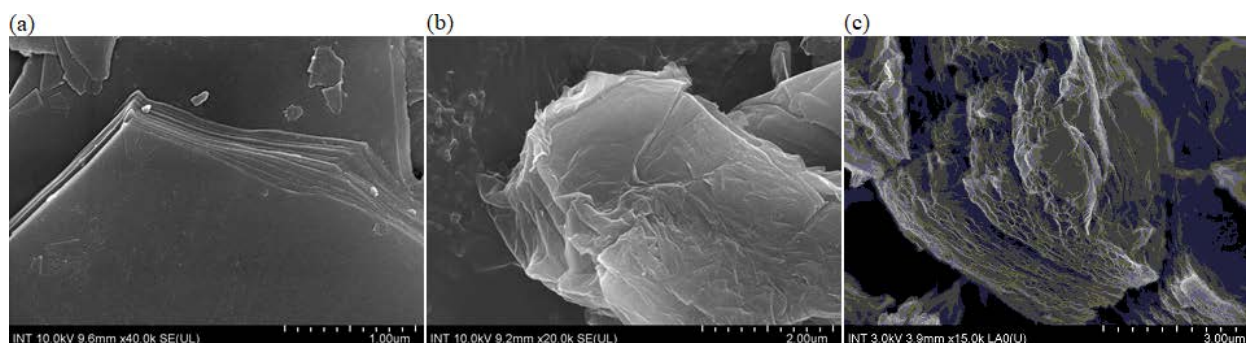


Figure 1. SEM images of natural graphite (a) and the derived graphite oxide (b) and graphene (c).

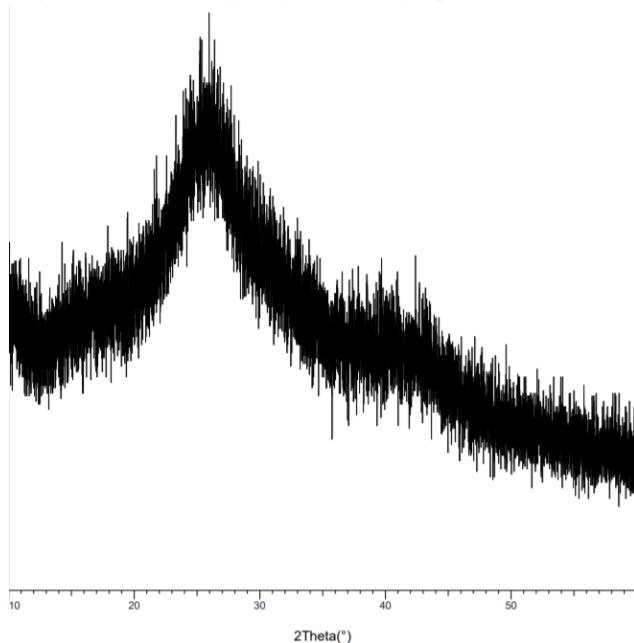


Figure 2. XRD pattern of graphene.

GO was prepared by Hummers method. The process is described as follow: Natural graphite (6g) and sulfuric acid (140 mL) were firstly mixed together in a beaker cooled by an ice bath. Potassium permanganate (20g) was then very slowly added into the mix. The mixture was maintained in vigorous stirring condition for 1 hours. After that, the temperature of the mixture was brought to 40 °C whilst the stirring was maintained for another 2 hours. The mixture gradually thickened until it became pasty. After 2 hours, 240 mL of water was slowly added into the paste, causing a sharp increase in temperature and boiling may occur. The mixture was stirred for 15 minutes then further diluted in 1.6 litres of water plus 60 mL of hydrogen peroxide. GO then settled as sediment. The liquid medium was siphoned and the sediment was further washed by 1.6 litres of water and 80 mL of chloric acid (35%) 3 times. Finally dried GO powder was obtained by drying the sediment at 60 °C.

Graphene was fabricated by rapid heating of dried GO powder. Firstly, a furnace was preheated to 1100 °C. GO powder (1g) was charged into a quartz tube, sealed and then flushed with nitrogen until an inert atmosphere was created. The tube was then inserted into the furnace and kept for 5 minutes. The tube could only be unsealed when its temperature returns to ambient temperature.

The morphology of the graphene samples was observed using a field emission scanning electron microscope (FESEM, SU8010, Hitachi). X-ray diffraction patterns of the samples were acquired with an X-ray diffractometer (D8 Advanced Eco, Burker AXS). The Brunauer-Emmett-Teller (BET, Belsorp-mini, Bell) method was employed to determine the specific surface area of the graphene powder. The weight loss caused by the increase of temperature was observed using the thermogravimetric analysis (TGA, Thermoplus EVO2, Rigaku). The Raman spectra of the samples were recorded with a Raman spectrometer (LabRAM, Jobin Yvon).

RESULTS AND DISCUSSION

SEM images of the precursory graphite flakes as well as the derived GO and graphene are shown in Fig. 1. Graphite sample shows densely packed sheets, while in GO an increase in interlayer spacing can be observed. In the graphene sample, the sheets are visibly wrinkled due to the exfoliation process. Thanks to the wrinkles, graphene sheets cannot be restacked and thus, while the sheets are still densely packed, they can be treated as multiple separated few-layer graphene sheets.

Fig. 2 shows the XRD patterns of graphene. In graphite, the characteristic interlayer diffraction peak is located at 26.4°, corresponding to an interlayer spacing d of 0.34 nm. The sharp peak shows a high degree of crystallinity of the graphite. The interlayer

diffraction peak shifts to 12.3° (corresponding to a d of 0.72 nm) and becomes slightly broader in the case of GO. This indicates an expansion of interlayer spacing in GO due to oxidation. The absence of peak 26.4° also proves that GO obtained a high degree of oxidation. In the XRD pattern of graphene there is very broad diffraction peak with low intensity at 25.9° , corresponding to a spacing of 0.34 nm. The absence of characteristic diffraction peaks proves that the graphene sample is nearly completely exfoliated. The existence of this broad peak indicates that there is a fraction of GO stack that couldn't be exfoliated, possibly due to the lack of local functional groups to generate sufficient gas pressure. Thus, these domains remained as packed graphene stacks, as shown in the SEM image in Fig. 1.

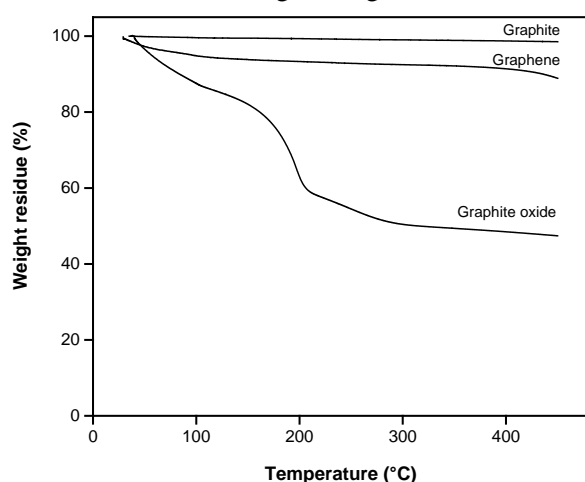


Figure 3. The TGA curves of (a) graphite, (b) graphite oxide and (c) graphene samples.

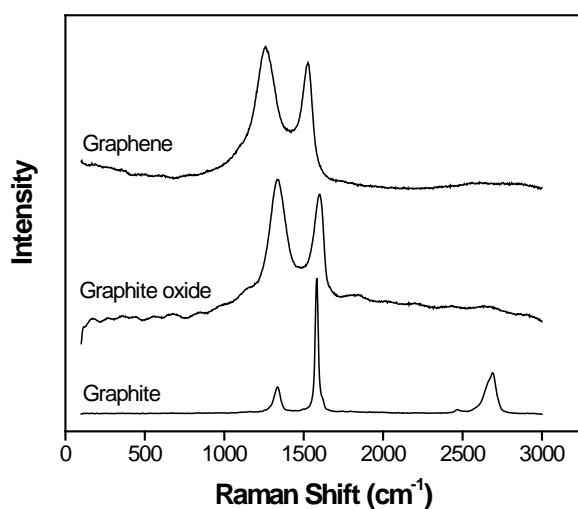


Figure 4. Raman spectra of graphite, graphite oxide and graphene.

The BET method shows that the obtained graphene have the specific surface area of $337 \text{ m}^2\text{g}^{-1}$. This value is much lower compared to the theoretical limit of $2630 \text{ m}^2\text{g}^{-1}$, but still higher than $100 \text{ m}^2\text{g}^{-1}$, which is the average surface area for graphene nanoplatelets [6-7]. Thus, the specific surface area has confirmed that the current process yields graphene with decent degree of exfoliation.

The weight loss of graphite, GO and graphene samples are presented as the TGA curves in Fig. 3. Since the graphite sample solely contains graphite lattices with little to no impurities, the TGA curve of graphite shows almost no weight loss. In GO, however, there is a major weight loss at about 100°C to 200°C . This can be attributed to the thermal decomposition of the oxygen-containing functional groups. In the TGA curve of graphene, the weight loss is negligible, indicating that the oxygen-containing functional groups were mostly removed in the thermal exfoliation process. This proves the obtained graphene has high reduction degree.

The Raman spectra of graphite, GO and graphene are shown in Fig. 4. The spectrum of natural graphite exhibits two sharp G and 2D bands at around 1580 and 2700 cm^{-1} , respectively, with a small D band at around 1350 cm^{-1} which represents a small fraction of defects found in graphite [8]. The spectrum of GO sees a significant increase in the D band intensity and a decrease in the intensity of G and 2D bands. This suggests a high degree of oxidation since the oxidation of graphite induces a great amount of defects. The spectrum of graphene is similar to that of GO. The absence of 2D band indicates that the obtained graphene contained many defects. These defects can be the residue oxygen-containing functional groups or small graphitic domains formed in the thermal exfoliation process.

CONCLUSIONS

This article described a graphene fabrication process by thermal reduction-exfoliation of graphite oxide as well as the characterization for the obtained graphene. The method is fast, dry in basis and can yield readily functionalized graphene with high degree of reduction and exfoliation.

Acknowledgments

This research is funded by Vietnam National University Ho Chi Minh City (VNU-HCM) under grant number 562-2018-32-01.

References

- [1]. K. S. Novoselov et al., *A roadmap for graphene*, Nature **490** (2012) 192–200
- [2]. C. Mattevi et al., *A review of chemical vapour deposition of graphene on copper*, Journal of Materials Chemistry **21** (2011) 3324-3334
- [3]. K. S. Novoselov, A. K. Geim, et al., *Electric Field Effect in Atomically Thin Carbon Films*, Science **306** (2004) 666–669
- [4]. M. Yi et al., *A review on mechanical exfoliation for scalable production of graphene*, Journal of Materials Chemistry A **3** (2015) 11700–11715
- [5]. N. Parveen et al., *Simple route for gram synthesis of less defective few layered graphene and its electrochemical performance*, Advances **5** (2015) 44920-44927
- [6]. J. McAllister et al., *Single Sheet Functionalized Graphene by Oxidation and Thermal Expansion of Graphite*, Chemistry of Materials **19** (2007) 4396–4404
- [7]. Kim et al., *Graphene/Polymer Nanocomposites*, Macromolecules **43** (2010) 6515–6530
- [8]. Mark Wall, *The Raman Spectroscopy of Graphene and the Determination of Layer Thickness*, Thermo Scientific Application Note AN52252

THE SYNTHESIS AND ELECTROCHEMICAL BEHAVIOR OF Pt_xSn_y NANOPARTICLES

Do Thi Dieu Ai¹, Le My Loan Phung^{1,2}, Vu Thi Hong Phuong³, Tran Van Man^{1,2}

¹Department of Physical Chemistry, Faculty of Chemistry, University of Science,
Vietnam National University – Ho Chi Minh City

²Applied Physical Chemistry Laboratory, Faculty of Chemistry, University of Science,
Vietnam National University – Ho Chi Minh City

³Ba Ria – Vung Tau University

Email: tvman@hcmus.edu.vn

ABSTRACT

EDX spectrum showed that there were both Pt and Sn in samples reduced by EG (E5, E8) and NaBH₄ (N5, N8). XDR patterns indicated the presence of Pt on carbon support. The obtained nanoparticles have the various size of 1-5 nm and 3-7 nm corresponding ethylene glycol (EG) and NaBH₄ reductant respectively. For methanol oxidation activity, EG samples exhibited the best electrochemical activities at pH 8 which is the same for NaBH₄ samples. Generally, the catalyst was reduced using EG gave better activity than NaBH₄. In addition, activity of Pt-Sn catalysts for methanol oxidation are much higher than Pt. For oxygen reduction activity, all Pt-Sn samples (both using EG and NaBH₄) except E5 (Pt-Sn catalyst synthesis by EG at pH 5) showed lower electrocatalytic activity than Pt sample for oxygen reduction reaction.

Keywords: electrocatalyst, Pt-Sn nano particles, PEMFC

INTRODUCTION

Proton exchange membrane fuel cell (PEMFC) is low-temperature (under 120°C) fuel cell that has great potential for mobile devices and electrical vehicles power source. For the commercialization of PEMFC system which composed of many membranes electrode assembly (MEA) combined in series or in parallel, the challenge is the durability of catalyst. The Pt-base catalysts are synthesized and investigated such as Pt-Pd, Pt-Ru which enhanced the stability and performance of catalyst but these metals have low abundance. Thus, in this study Pt-Sn nanoparticles on Vulcan carbon was prepared by the reduction in various pH using PtCl₆²⁻ and Sn⁴⁺ as precursors [1-3].

EXPERIMENTAL

All the chemicals were purchased from Sigma-Aldrich. Vulcan carbon was treated in 1 M HNO₃ solution for 10 hours, then ultrasonicated for 1 hour to remove the contaminants. Then it is washed several times

with water until the pH 7 and dried at 70°C for 8 hours.

For ethylene glycol reduction, the mixture of about 168.0 mg of Vulcan and 10.00 ml of EG is stirred for 16 hours. Then 1.8×10⁻⁴ mol of H₂PtCl₆, 6×10⁻⁵ mol of SnCl₄ and 4.8×10⁻⁴ mol of citric acid are added into above mixture. After adjusting pH by 0.3M NaOH solution, reactor is microwaved in 60s and constantly stirred in 3 hours. With NaBH₄ reduction, the mixture of about 168.0 mg of Vulcan and 10.00 ml of iso-propanol (iPrOH) is stirred for 16 hours. Then 1.8×10⁻⁴ mol of H₂PtCl₆, 6×10⁻⁵ mol of SnCl₄ and 4.8×10⁻⁴ mol of Citric acid are added into above mixture. Next, the solution containing 3.2×10⁻³ mol of NaBH₄ and 10.00 ml of i-PrOH is added to chloroplatinic acid-based mixture followed by adjusting pH by 0.3 M NaOH solution.

In the stage of extracting the solid product, both of the reaction suspension was centrifuged at 6000 rpm for 20 mins and then washed for three times with absolute ethanol. In the final step, the

catalyst was dried at 70°C for 16 hours to evaporate ethanol

RESULTS AND DISCUSSION

The X-ray diffraction patterns of all samples give the structure information and composition.

Peak of carbon can be seen at between 20° – 30°. All samples contain Pt element since the presence of signal at 2θ of 40°, 46°, 68° related to the (111), (200) and (220) plan. However, the positions of peaks are a bit on the right compared to the standard patterns that indicates that the lattice parameters of synthesized Pt crystals are higher than standard. The intensity of E8 is highest, which explains why it give the best electrochemical activity. Similarly, E9 and E10 didn't exhibit any signal of Pt that verified the portion of Pt is too small to record. It can explain the low electrochemical activity of these sample in CV and CA. The absence of Sn diffraction peaks at 30.7°, 32.0°, and 45.0° related to the (200), (101) and (211) plane [31] likely due to the noise caused by Vulcan carbon. Other way, Sn is probably entered in Pt structure to form alloy, so its quantity is too low to be observed by XRD, the peak shift of Pt is a strong evidence for this suggestion.

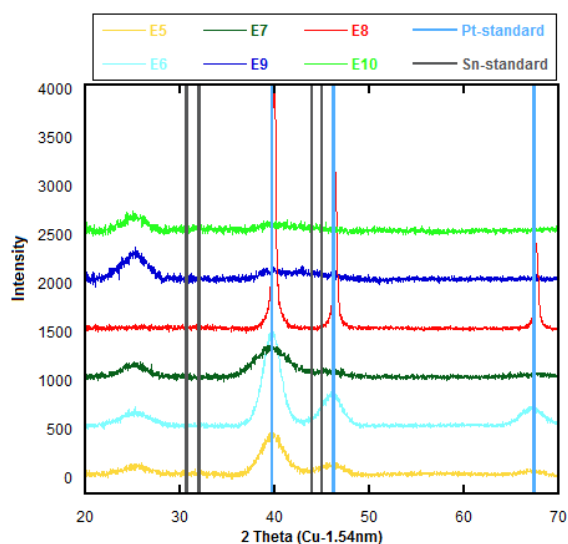


Figure 1. XRD patterns of PtSn samples

For samples reduced by EG, the composition of two samples is different. For E8, the molar ratio of Pt to Sn and the mass ratio of Vulcan to metal are close to theory ratio (3:1 and 4:1). For E5, the proportion of metal is too

low, especially Sn. It likely results from the material loss during the centrifuge process or heterogeneous material. Therefore, E8 is more homogenous than E5 and then the reduction is occurred more efficient. EDX results explained why the electrochemical of E8 is much better than E5. The presence of Sn was also verified through EDX, which confirmed the alloy structure of samples reduced by EG. For samples reduced by NaBH₄, both two analyzed samples have the composition significantly separated with theory value. The mass ratio of metal at higher pH (N8) is larger, which could conclude that reduction occurred efficiently in the alkaline medium. By comparing the composition of samples (reduced by EG and NaBH₄), the predominant electrochemical of EG samples is partially caused by the smaller particles size, the better distribution and the higher metal molar ratio, especially Pt.

As seen in TEM images (Fig. 3), the samples contain nanoparticles dispersed on the support. For samples reduced by EG, the nanoparticles were homogeneously dispersed on Vulcan carbon. Their size ranges in 1-5 nm and decrease with the pH increase.

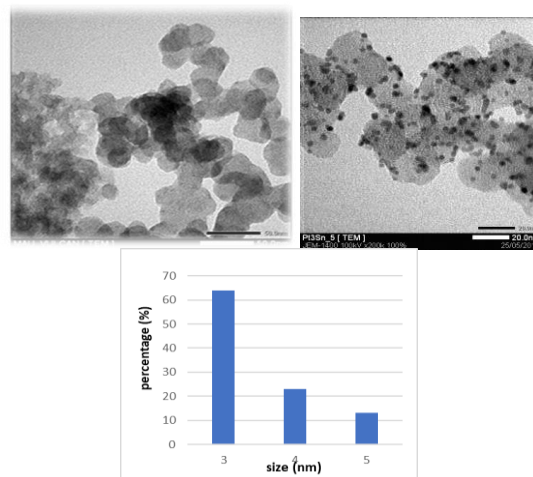


Figure 2. TEM images of Vulcan carbon (a) and E5 sample reduced by EG at pH 5 (b,c)

Although there was not any signal of Pt in E10 sample in XRD, TEM image proves the presence of Pt nanoparticles. Therefore, the disappearance of Pt signal on XRD pattern of E9 and E10 is due to low particle density and small particle sizes. For the samples reduced by NaBH₄, there is an aggregation of particles with the observation of larger dark areas. The aggregation of particle is unavoidable because NaBH₄ is added from burette to the reactor

rather than stay in reactor at first like EG. Where NaBH_4 reacts with precursor, a lot of nanoparticles immediately formed and easily gathered so that stirring cannot ideally disperse them on Vulcan carbon. Particle size range is 3-7nm which bigger than EG samples because EG played as a good capping agent in controlling of particle sizes. The uniform distribution and smaller particle size EG samples with respect to NaBH_4 samples confirmed evidently the better electrochemical activity.

The BET results show the active surface area of E8 is larger than N8 due to smaller particle size and good distribution in Vulcan carrier of E8 sample. Thus, results consistent with TEM images and the electrochemical behavior. Large surface area helps catalyst exposing to reactant better and hence creating more active site. The more active sites catalyst contains, the bigger number of substance atoms reacting in a definite time, so the higher current density obtained.

Figure 3 represents ORR polarization curve of synthesized samples. The measurement was carried out with the rotating electrode at the rate of 1600 rpm to accelerate oxygen mass transfer from solution to the electrode surface. The reduction current density was recorded in all samples with different limited current density. Generally, the oxygen reduction activity of samples containing both Sn and Pt (E7, E8, E9) is lower than samples only containing Pt (Pt-E8). It indicated that the presence of Sn in Pt catalyst eliminates the kinetics of oxygen reduction. However, E5 always generated ORR current density higher than Pt sample at the sample potential in the polarization curves. Therefore, E5 is quite different from others which requires a deeper study in structure and morphology as well as adsorption interaction.

For samples prepared by NaBH_4 , ORR activity is almost the same for all samples. Limited current density of samples involving Pt and Sn (N5, N7, N8, N9) is lower than samples involving only Pt (Pt-E8). Hence, it confirms again that Pt-Sn is not favorable for oxygen reduction.

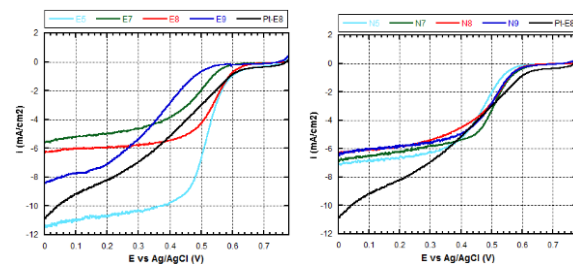


Figure 3. The CA polarization curve of synthesized samples in ORR

CONCLUSIONS

In this study, Pt-Sn nanoparticles catalyst on Vulcan carbon was successfully synthesis. The nanoparticles of the EG samples had a smaller particle sizes (1-4 nm) and better distribution on the Vulcan carbon than the NaBH_4 samples (3-7 nm), thus partially explains the predominant of their electrochemical.

For methanol oxidation activity, EG samples exhibited the best electrochemical activities at pH 8 which is the same for NaBH_4 samples. Generally, the catalyst was prepared by EG gave better activity than NaBH_4 . The activity of Pt-Sn catalysts for methanol oxidation are much higher than Pt. For oxygen reduction activity, all Pt-Sn samples (both using EG and NaBH_4) are not as good as Pt sample except E5 (Pt-Sn catalyst synthesis by EG at pH 5). Therefore, Pt-Sn catalyst is not favorable for oxygen reduction reaction

References

- [1]. N. V. Long, Y. Yang, C. Minh Thi, N. Van Minh, Y. Cao, M. Nogami, *Nano Energy*, vol. 2, no. 5, pp. 636–676, 2013.
- [2]. J. Tymoczko, F. Calle-Vallejo, W. Schuhmann, A. S. Bandarenka, *Nature Communications*, vol. 7, pp. 1–6, 2016.
- [3]. F. Kadirgan, S. Beyhan, T. Atilan, *International Journal of Hydrogen Energy*, vol. 34, no. 10, pp. 4312–4320, 2009.
- [4]. J. R. C. Salgado, F. Alcaide, G. Álvarez, L. Calvillo, M. J. Lázaro, E. Pastor, *Journal of Power Sources*, vol. 195, no. 13, pp. 4022–4029, 2010.

COMPARISON OF STRUCTURAL AND MORPHOLOGY PROPERTIES OF MULTIFERROIC MATERIALS SYNTHESIZED BY VARIOUS METHOD

Robert Tomala¹, **Pawel Gluchowski**^{1,2}, **Anna Lukowiak**¹, **Yuriy Gerasymchuk**¹, **Tatsiana Shulha**³, **Maria Serdechnova**³, **Mikhail Zhedkevich**³ and **Wieslaw Streck**²

¹ Institute of Low Temperature and Structure Research, Polish Academy of Sciences, Okolna 2, 50-422 Wroclaw, Poland;

² Nanoceramics Inc., Okolna 2, 50-422 Wroclaw, Poland

³ Helmholtz-Zentrum Geesthacht Zentrum für Material- und Küstenforschung GmbH, Max-Planck-Straße 1, 21502 Geesthacht I, Germany

Email: r.tomala@intibs.pl

ABSTRACT

The multiferroic materials are widely investigated by scientific community due to their potential for applications as actuators, switches, magnetic field sensors or new types of electronic memory devices. The changes in physical properties of these compounds become highly pronounced when characteristic crystallites size reduces down to nanoscale level. The temperature of paraelectric and magnetic transitions also depend on crystallites size. Present study shows influence of used synthesis method on structural and morphology properties of multiferroic materials LaMnO₃ doped by rare earth ions. The solid state, sol-gel, self-combustion and microemulsion methods were used to obtain this materials. The role of factors such as chemicals used to synthesis, annealing temperature and time on particle size and their distribution have been investigated.

Keywords: multiferroic, nanocrystals, self-combustion, magnetic

INTRODUCTION

Perovskite-type materials in recent years are intensively investigated in different areas of application as: optics, photovoltaics, magnetic memory elements [1–3]. LaMnO₃ system with dopants of rare earths ions and alkali metals has been extensively studied since its discovery of giants negative magnetoresistance effect in this materials [4–6].

The size of crystals, especially in nanoscale level strongly affecting on multiferroic properties of materials [7]. The structural and morphology properties of pure phase of lanthanum manganite perovskite were intensively investigated for different synthesis methods such as sol-gel [8], co-precipitation [9], self-combustion [10–13] and hydrothermal [14].

In this paper the structural and morphology properties of LaMnO₃ and LaMnO₃ doped with cobalt and samarium ions nanocrystals synthesized by self-combustion method with urea as a fuel has been presented. Especially, the role of post-synthesis heat treatment on size of nanocrystals are investigated.

EXPERIMENTAL

The LaMnO₃ and LaMnO₃ doped with samarium and cobalt ions were synthesized via self-combustion [15] and hydrothermal method [16]. Lanthanum oxide (La₂O₃, 99,999% Stanford Materials), manganese pieces (Mn, 99,9%, Alfa Aesar), cobalt powder (Co, 99,8%, Sigma Aldrich), samarium oxide (Sm₂O₃, 99,999%, Stanford Materials) and 65% nitric acid were used as raw materials. In self-combustion method Urea (98+%, Alfa Aesar) was used as a fuel. In both synthesis methods the stoichiometric amounts of lanthanum oxide, metallic manganese and for doped samples cobalt powder and samarium oxide were dissolved in nitric acid to obtain nitrates. In self-combustion method the nitrates were mixed in 30 mL of deionized water under stirring. Then, the urea was added in 5:1 ratio in relation to moles of product. The obtained solution was placed in muffle oven warmed up to 650°C in ceramic crucible and left for 30 min. The obtained crystals were graded in agate mortar and heated in 700°C to crystalize rest of amorphous phase.

In hydrothermal method the nitrates were dissolved in 60 ml of deionized water under stirring. Next, the 1 M KOH aqueous solution was added for complete co-precipitation. The hydrothermal synthesis was performed in 100 ml Teflon reactor at 200°C for 8h. The obtained nanocrystals was washed with deionized water and separate used a centrifugal.

The X-ray patterns were recorded using PANalytical X'Pert Pro powder diffractometer (Cu K α 1: 1.54060 Å). The scanning electron microscopy images were taken using a Tescan VEGA 3SB microscope.

RESULTS AND DISCUSSION

The composition of LaMnO₃ synthesized via self-combustion method in 650°C was determined by X-ray diffraction on diffractogram (Fig.1.) the peak attributed to (001) diffraction pattern of rhombohedral structure of LaMnO₃ with space group R-3c (167) was observed. Besides of crystal phase, the broadband peak associated with occurrence of amorphous phase was observed. The post-synthesis heat treatment of powder lead to high crystallization of samples. The diffractograms of samples annealed in 700-800°C for 2 h shows pure perovskite phase.

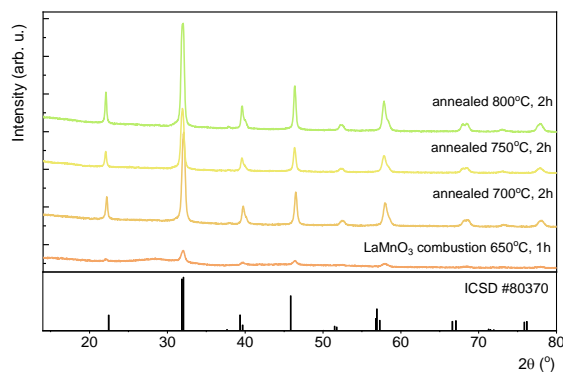


Figure 1. X-ray diffraction patterns of LaMnO₃ synthesized via self-combustion method in 650°C and annealed in 700-800°C.

Post-synthesis heat treatment of powder also causes the increasing of average grain size of nanocrystals. The average crystals size was calculated using a Rietveld conferment method, from broadening of diffraction patterns. The average crystallites size of raw powder obtained by self-combustion method is 35 nm (Table 1). The linear increasing of size with temperature was observed. For 800°C is 77 nm.

Table 1. Influence of heating temperature on average grain size of LaMnO₃ nanocrystals.

Annealing Temperature, °C	650	700	750	800
Avarage grain size, nm	35	48	63	77

To changing the magnetic properties of lanthanum manganite the compounds doped with cobalt and samarium were synthesized. These trivalent magnetic ions are substituted La-site and Mn-site for Sm³⁺ and Co³⁺ respectively, what is related with similar ionic radius of this ions. The synthesis of doped LaMnO₃ by self-combustion method with heat treatment in 700°C was performed for 1-100% concentration range for cobalt ions as well as samarium ions. For all samples pure phase of rhombohedral structure were observed. The diffractograms of samples doped with 10 mol% of cobalt and samarium are presented in Figure 2

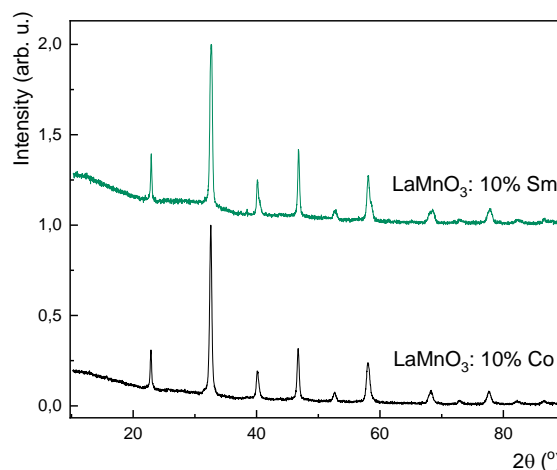


Figure 2. X-ray diffraction patterns of LaMnO₃ doped with 10 mol% of cobalt and samarium.

The morphology of obtained products were studied by Scanning Electron Microscopy method. The SEM images of LaMnO₃ and LaMnO₃:10% Co annealed in 700°C are presented in Figure 3. It was observed that obtained nanocrystals are strongly agglomerated to submicron aggregates.

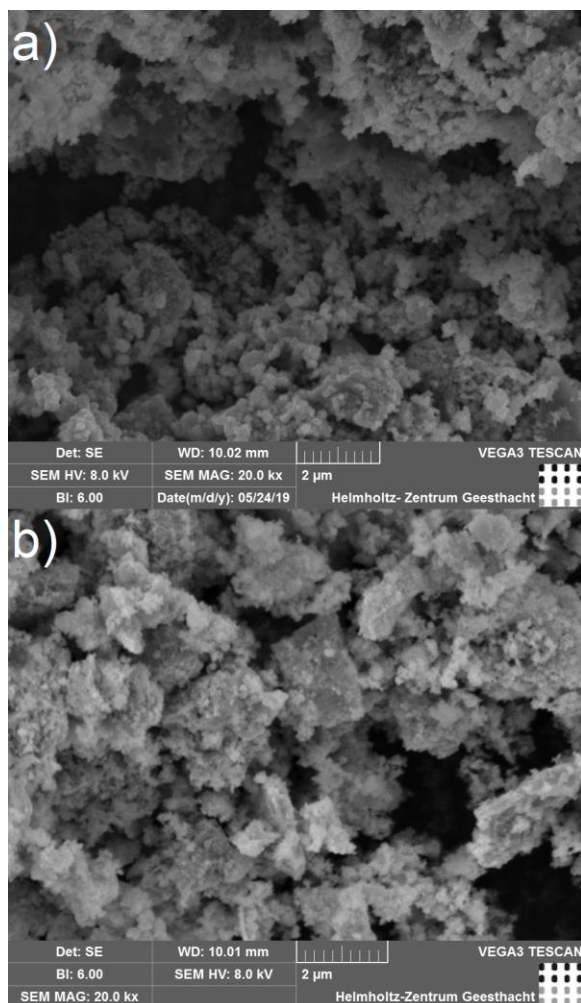


Figure 3. The scanning electron microscopy images of LaMnO_3 (a) and LaMnO_3 doped with 10 mol% of cobalt.

CONCLUSION

LaMnO_3 and LaMnO_3 doped with cobalt and samarium ions have been synthesized with self-combustion method with urea as a fuel and post-synthesis treatment. The nanocrystals size can be controlled by annealing temperature. Using this synthesis method the strongly agglomerated nanocrystals with average crystals size in 35-78 nm range were obtained

Acknowledgment

This project has received funding from the European Union's Horizon 2020 research and innovation programme under the Marie Skłodowska-Curie grant agreement No 778070—TransFerr—H2020-MSCA-RISE-2017.

References

- [1] M. Shaterian, M. Enhessari, D. Rabbani, M. Asghari, M. Salavati-Niasari, *Synthesis, characterization and photocatalytic activity of LaMnO_3 nanoparticles*, *Appl. Surf. Sci.* **318** (2014) 213–217. 7.
- [2] F. Nolting, A. Scholl, J. Stöhr, J.W. Seo, J. Fompeyrine, H. Siegwart, J.-P. Locquet, S. Anders, J. Lüning, E.E. Fullerton, M.F. Toney, M.R. Scheinfein, H.A. Padmore, *Direct observation of the alignment of ferromagnetic spins by antiferromagnetic spins*, *Nature*. **405** (2000) 767–769.
- [3] P. Głuchowski, K. Oganisian, R. Tomala, A. Łukowiak, D. Karpinsky, D. Alikin, A. Kholkin, W. Stręk, *Optical, Dielectric and Magnetic Properties of $\text{La}_{1-x}\text{Nd}_x\text{FeO}_3$ Powders and Ceramics*, *Ceramics*. **2** (2018) 1–12.
- [4] I. Troyanchuk, S. Trukhanov, D. Khalyavin, H. Szymczak, *Magnetic properties of anion deficit manganites $\text{Ln}_{0.55}\text{Ba}_{0.45}\text{MnO}_3-\gamma$ ($\text{Ln}=\text{La}, \text{Nd}, \text{Sm}, \text{Gd}, \gamma \leq 0.37$)*, *J. Magn. Magn. Mater.* **208** (2000) 217–220.
- [5] S.V. Trukhanov, V.A. Khomchenko, D.V. Karpinsky, M.V. Silibin, A.V. Trukhanov, L.S. Lobanovsky, H. Szymczak, C.E. Botez, I.O. Troyanchuk, *A-site ordered state in manganites with perovskite-like structure based on optimally doped compounds $\text{Ln}_{0.70}\text{Ba}_{0.30}\text{MnO}_3$ ($\text{Ln} = \text{Pr}, \text{Nd}$)*, *J. Rare Earths*. **37** (2019) 1242–1249.
- [6] R. von Helmolt, J. Wecker, B. Holzapfel, L. Schultz, K. Samwer, *Giant negative magnetoresistance in perovskitelike $\text{La}_{2/3}\text{Ba}_{1/3}\text{MnO}_x$ ferromagnetic films*, *Phys. Rev. Lett.* **71** (1993) 2331–2333.
- [7] S.M. Selbach, T. Tybell, M.-A. Einarsrud, T. Grande, *Size-Dependent Properties of Multiferoic BiFeO_3 Nanoparticles*, *Chem. Mater.* **19** (2007).
- [8] C. Xiulan, L.Y.-C.E. Journal, *New methods to prepare ultrafine particles of some perovskite-type oxide-s*, *Chem. Eng. Journal*, **78** (2000) 205-209 .
- [9] J. Töpfer, J.B. Goodenough, *$\text{LaMnO}_3+\delta$ Revisited*, *J. Solid State Chem.* **130** (1997) 117–128..
- [10] S.S. Manoharan, K.C. Patil, *Combustion*

- Route to Fine Particle Perovskite Oxides*, J. Solid State Chem. **102** (1993) 267.
- [11] S.. Aruna, M. Muthuraman, K.. Patil, *Studies on combustion synthesized LaMnO₃–LaCoO₃ solid solutions*, Mater. Res. Bull. **35** (2000) 289–296..
- [12] S.T. Aruna, M. Muthuraman, K.C. Patil, *Combustion synthesis and properties of strontium substituted lanthanum manganites La_{1-x}Sr_xMnO₃ (0≤x≤0.3)*, J. Mater. Chem. **7** (1997) 2499–2503.
- [13] C. Weifan, L. Fengsheng, L. Leili, L. Yang, *One-Step Synthesis of Nanocrystalline Perovskite LaMnO₃ Powders via Microwave-Induced Solution Combustion Route*, J. Rare Earths. **24** (2006) 782–787..
- [14] C.H. Feng, Q.S. Li, C.M. Liu, Y. Deng, L. Guo, *Synthesis of Perovskite-Type LaMnO₃ under Hydrothermal Conditions*, Mater. Sci. Forum. 475–479 (2005) 4051–4054.
- [15] S. Ekambaram, K.C. Patil, M. Maaza, *Synthesis of lamp phosphors: facile combustion approach*, J. Alloys Compd. **393** (2005) 81–92..
- [16] R. Pazik, D. Hreniak, W. Strek, *Microwave driven hydrothermal synthesis of Ba_{1-x}Sr_xTiO₃ nanoparticles*, Mater. Res. Bull. **42** (2007) 1188–1194.

MICROFLUIDIC PAPER-BASED DEVICES FOR DETECTING HUMAN CHORIONIC GONADOTROPIN

Ngan Nguyen Le^{1,2}, Hue Cam Thi Phan¹, Huong Kim Tran¹, Dung My Thi Dang¹ and Chien Mau Dang¹

¹ Institute for Nanotechnology, Vietnam National University-Ho Chi Minh City, Community 6, Linh Trung Ward, Thu Duc District, Ho Chi Minh City, Vietnam;

² University of Science, Vietnam National University-Ho Chi Minh City, 227 Nguyen Van Cu Street, District 5, Ho Chi Minh City, Vietnam
Email: lnngan@vnuhcm.edu.vn

ABSTRACT

In this paper, microfluidic paper-based analytical devices (μ PADs) have been developed for detecting human chorionic gonadotropin (hCG). The target was captured by two antibodies and color signal was generated after substrate reagent had come to test zone of device. All steps of this process, known as sandwich enzyme-linked immunosorbent assay (ELISA), was carried out on our small devices, 8.0 mm of width and 44.0 mm of length. There are three main parts in our devices: input leg; middle part with four minor channels; ending part with only one main channel including test zone and control zone. Paper-based channels were fabricated by inkjet printing method. Color signal was measured by ImageJ software. Results showed that hCG target can be quantitative determined with correlation coefficient (R^2) is quite good, about 0.88. Although linear regression was still not so good in this report, it is assumed that design and bio-process could be optimized for better results in the future.

Keywords: Microfluidic paper-based device, biosensor, human chorionic gonadotropin, inkjet printing

INTRODUCTION

In this paper, microfluidic paper-based analytical devices (μ PADs), which has attracted interest from many researchers in recent years [1-10], have been developed for detecting human chorionic gonadotropin (hCG). Sandwich ELISA, which can detect antigen by using two kinds of antibody (capture and detection antibody), were chosen as principle of our devices. Moreover, almost necessary steps of sandwich ELISA has been prepared on our devices before testing by end-user. Therefore, common customer just need 1 or 2 more steps to determine hCG concentration in samples.

EXPERIMENTAL

Materials

Potassium chloride (KCl), chloric acid (HCl), sodium hydroxide (NaOH), disodium hydrogenphosphate (Na_2HPO_4), casein, sucrose, boric acid and sodium dodecyl sulfate (SDS) were purchased from Wako Pure Chemical. Bovine serum albumin (BSA) was purchased from Sigma-Aldrich. Polyclonal rabbit anti-mouse immunoglobulins (anti-mouse IgG pAb) was purchased from Dako (Denmark) and anti-

human chorionic gonadotropin (anti-hCG) was purchased from Medix Biochemica (Finland). ALP-labelling kit, which was purchased from Dojindo (USA), was used to prepare alkaline phosphatase (ALP)-labelled anti-hCG (ALP-anti hCG). Antigen hCG was purchased from Rohto Pharmaceutical (Japan). 5-bromo-4-chloro-39-indolyphosphate p-toluidine salt, nitro-blue tetrazolium chloride (BCIP/NBT) substrate solution and substrate buffer were purchased from Nascalai Tesque (Japan).

Design of μ PADs for detecting hCG

Design of μ PADs is shown in figure 1. There are three main parts in this design: input leg including one main channel for leading water to entire microfluidic device; middle part including four minor channels; ending part with only one main channel including test zone and control zone. From left to right, four channels in middle parts are delayed channel, non-delayed channel, most delayed channel and delayed channel. In order to make fluid flow slower in channel, few horizontal barriers were designed on two delay channels (left and right channels) and many horizontal barriers were designed on most delayed channel. The width and length of

μ PADs are 8.0 and 44.0 millimeters. From left to right in the middle part, there are 4 spots for dropping second antibody (2^{nd} Ab), hCG sample, substrate and 2^{nd} Ab as shown in figure 1. In ending part, there are 2 spots for immobilized first antibody (1^{st} Ab) at test zone and immobilized IgG at control zone.

Figure 2 shows how our μ PADs can perform sandwich Enzyme-linked Immunosorbent assay (ELISA) to detect hCG. When dipping input leg of device into water, water flowed through main channel and split into 4 smaller channels in middle part (Step 1 in figure 2). With many horizontal barriers in most delayed channel, fluid flow slowest in this channel; thus, substrate would flow to ending part slower than hCG sample and 2^{nd} Ab. In non-delaying channel, hCG sample flowed faster and came to test zone first (step 2 and step 3 in figure 2).

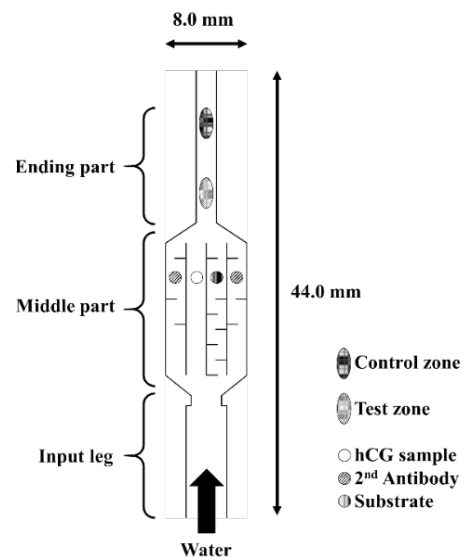


Figure 1. Design of microfluidic paper-based analytical devices for detecting human chorionic gonadotropin (hCG) including three main parts: input leg with one main channel; middle part with four channels and ending part

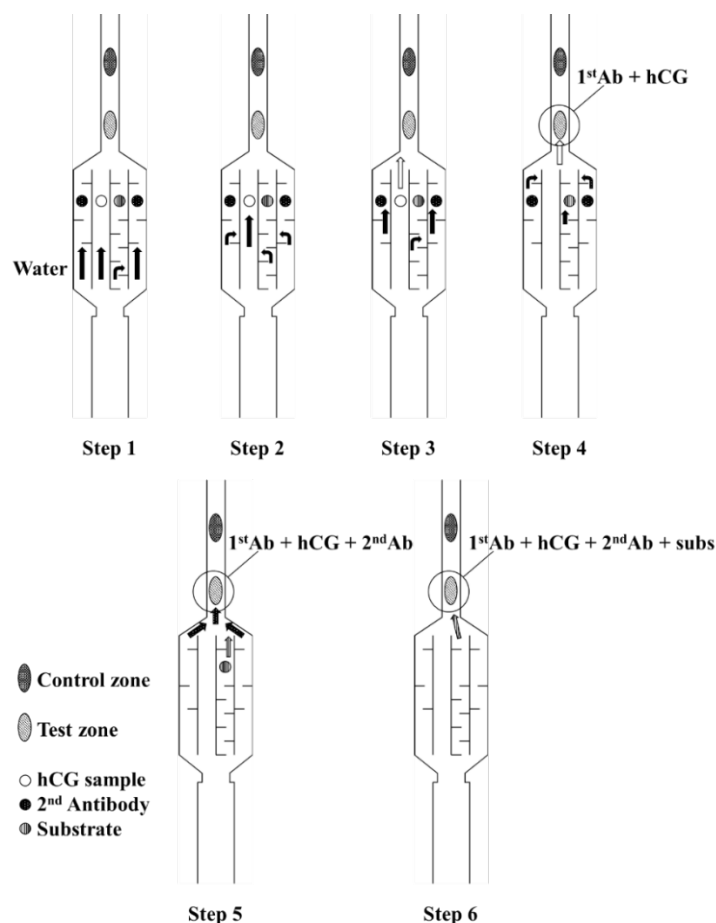


Figure 2. Schematic illustration of creating color signal in microfluidic paper-based analytical devices including 6 steps: water split into 4 channels (step 1); water flow faster in non-delaying channel (step 2); hCG sample came to test zone (step 3); hCG sample was captured by 1^{st} Ab (step 4); 2^{nd} Ab bound with hCG antigen (step 5); substrate came to test zone and create signal (step 6).

At test zone, hCG sample was captured by immobilized 1st Ab (step 4 in figure 2). After that, 2nd Ab came to test zone and bound with hCG (step 5 in figure 2). At final step, color signal was created after substrate had come to test zone (step 6 in figure 2). Color signal at control zone would be created if the test operated correctly.

Fabrication and testing of microfluidic paper-based analytical devices

Paper-based microchannels were fabricated by electrohydrodynamic (EHD) inkjet printing process. Anti-mouse IgG pAb and anti-hCG (1st antibody) were prepared at 1 mg/mL and applied to control zone and test zone, respectively. After that, devices were dried in room temperature for 1 hour. Nitrocellulose membranes were blocked by immersing into blocking solution and washed by using washing solution. The goal of this step to make sure that there are not protein adsorption in following steps as well as only IgG and 1st Ab were immobilized onto nitrocellulose

membrane. ALP-anti-hCG mAb (enzyme-second antibody or 2nd Ab) was prepared at 25 µg/mL. BCIP/NBT substrate was diluted in the substrate buffer solution with ratio of 1:10. hCG sample was prepared at many various concentration. Three bio-reagents: 2nd Ab, substrate and hCG sample were applied onto their spots in middle part of devices (figure 1). Bio-testing of µPADs was performed by dipping devices into water and waiting for color signal.

RESULTS AND DISCUSSION

Figure 3 showed fabricated µPADs and their color signals when testing with various hCG concentration from 5 to 10,000 ng/mL. Color signal was measured by using ImageJ software in two functions: histogram function and inverted function. The value of signal was calculated by taking absolute value of subtraction between signal and background color intensity.

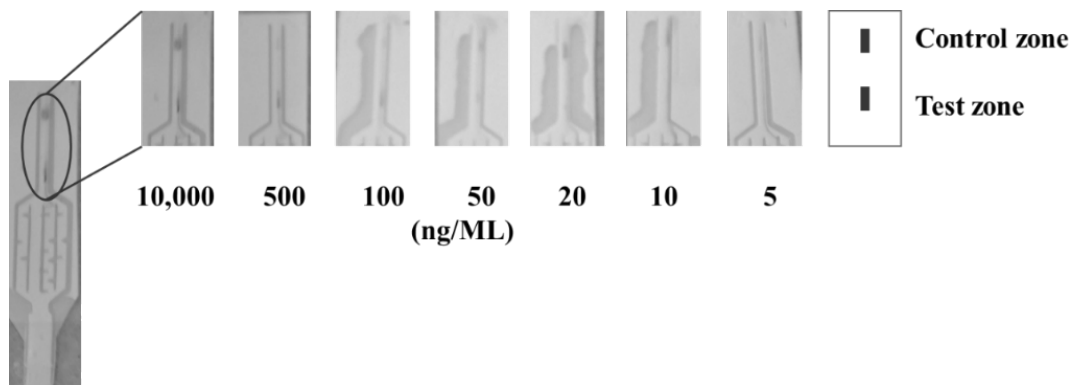


Figure 3. Color signal of µPADs when testing with various hCG concentration.

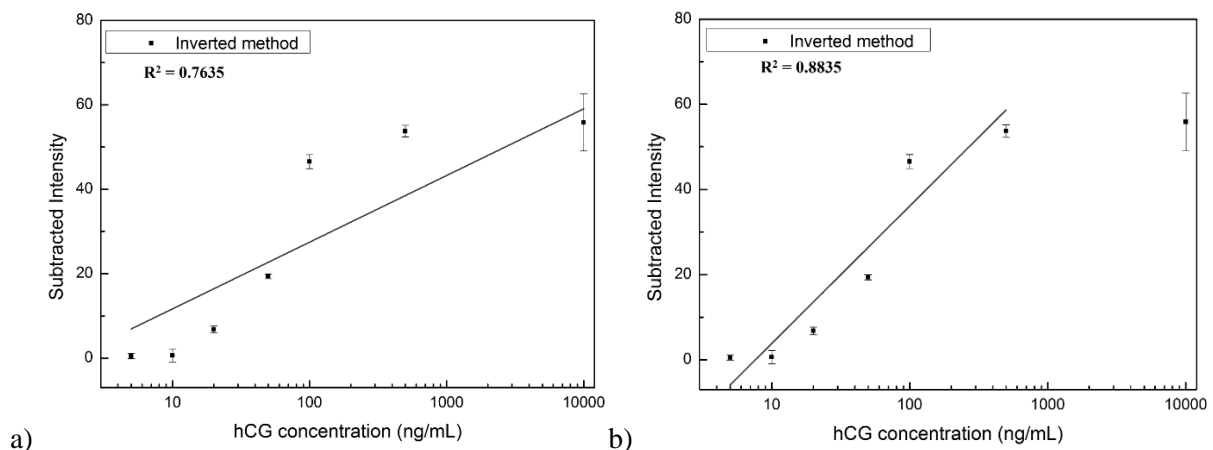


Figure 4. Influence of hCG concentration on subtracted intensity measured by inverted method and linear regression on entire range from 5 to 10,000 ng/mL (a); linear regression on smaller range from 5 to 500 ng/mL (b)

Figure 4 showed relationship between subtracted intensity measured by inverted method and hCG concentration. The linearity of intensity was not good with entire range of hCG concentration (from 5 to 10,000 ng/mL) and correlation coefficient (R^2) is just about 0.76 (figure 10a). However, the linearity was quite good with smaller range (from 5 to 500 ng/mL) and R^2 is about 0.88 (figure 10b).

Not good linearity in entire range can be explained because inverted method cannot be used to measure high color intensity. When hCG concentration was increased from 500 to 10,000 ng/mL, color intensity seemed unchanged and kept around 60. Histogram method showed better results than inverted method. Indeed, figure 5 showed quite good linear intensity and R^2 is about 0.88 in entire range of hCG concentration from 5 to 10,000 ng/mL.

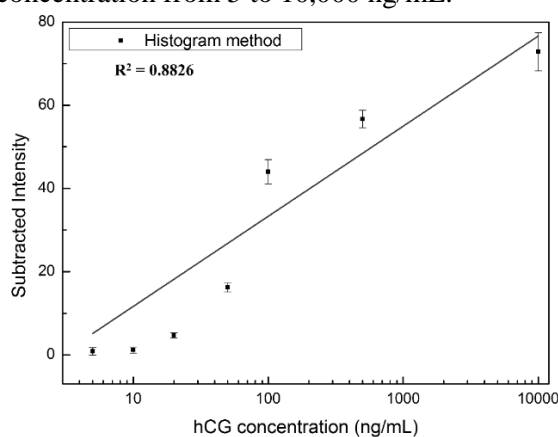


Figure 5. Influence of hCG concentration on subtracted intensity measured by histogram method and linear regression on entire range from 5 to 10,000 ng/mL

These results showed that our μ PADs can be applied for analytical biochemistry assay. Main advantages of these devices are low-cost, portable and capable of performing multi-step assay such as sandwich ELISA. Although linear regression was still not so good in this report, it is assumed that design and bio-process could be optimized for better results in the future.

CONCLUSION

In this report, we was successful in fabricating paper-based analytical devices to detect human chorionic gonadotropin (hCG). Our devices can be applied for determine hCG concentration in large range, from 5 to 10,000 ng/mL. Moreover, our devices have potential to apply for other biological targets, which can be detected by sandwich ELISA. The main

advantages of material-saving, simple process, high repeatability make our μ PADs can be applied in rural area in developing country.

Acknowledgment

The authors would like to appreciate Ministry of Science and Technology of Vietnam for funding this research under the grant number 03/2019/HĐ-SPĐP.

References

- [1] C. Xu, L. Cai, M. Zhong, S. Zheng, RSC Advances **5** (2015) 4770-4773
- [2] W. Y. Lim, B. T. Goh, S. M. Khor, Journal of Chromatography B **1060** (2017) 424-442
- [3] T. Akyazi, L. Basabe-Desmonts, F. Benito-Lopez, Analytica Chimica Acta **1001** (2018) 1-17
- [4] X. Li, J. Tian, W. Shen, Analytical and Bioanalytical Chemistry **396** (2010) 495-501
- [5] A. W. Martinez, S. T. Phillips, M. J. Butte, G. M. Whitesides, Angewandte Chemie International Edition **46** (2007) 1318-1320
- [6] A. Apilux, Y. Ukita, M. Chikae, O. Chailapakul, Y. Takamura, Lab on a Chip **13** (2013) 126-135
- [7] L. M. Fu, Y. N. Wang, Trends in Analytical Chemistry **107** (2018) 196-211
- [8] C. Liu, F. A. Gomez, Y. Miao, P. Cui, W. Lee, Talanta **194** (2019) 171-176
- [9] D. M. Cate, J. A. Adkins, J. Mettakoonpitak, C. S. Henry, Analytical Chemistry **87** (2015) 19-41
- [10] K. Yamada, T. G. Henares, K. Suzuki, D. Citterio, Angewandte Chemie International Edition **54** (2015) 5294-5310

ORAL SESSIONS

APPLICATIONS OF MICRO- NANOTECHNOLOGY (AMN)

DEVELOPMENT OF FLOOD MONITORING SYSTEM IN HO CHI MINH CITY USING PIEZORESISTIVE PRESSURE SENSOR FABRICATED BY SHTP LABS

**Xuan Thang Trinh¹, Nguyen Tuan Khoa¹, Tran Duy Hoai¹, Nguyen Thanh Phuong¹,
Vu Le Thanh Long¹, Truong Huu Ly¹, Nguyen Chi Cuong¹, Hoang Ba Cuong¹,
Ngo Vo Ke Thanh¹, Le Quoc Cuong² and Susumu Sugiyama¹**

¹Research Laboratories of Saigon High-Tech Park, Ho Chi Minh City, Vietnam (SHTP Labs), Lot I3, N2 Street, Saigon High Tech Park, District 9, Ho Chi Minh City, Vietnam

²Department of Information and Communications, Ho Chi Minh City, Vietnam

E-mail: thang.trinhxuan@shtplabs.org

ABSTRACT

Piezoresistive pressure sensors were designed and then successfully fabricated by using Silicon on Insulator (SOI) 6 inches wafer. The size of dice, thickness of diaphragm, resistance of p-type piezoresistor and the range of fabricated pressure sensor were $\sim 2.6 \text{ mm} \times 2.6 \text{ mm}$, $\sim 15 \mu\text{m}$, $\sim 1300 \Omega$ and 0-50 kPa, respectively. After packaging by using metal can package (TO-5), the pressure sensors had small offset voltage ($< 20 \text{ mV}$), high sensitivity (0.7-0.8 mV/kPa with 3V input voltage) and good linearity ($< \pm 1\%$). We have applied the pressure sensors to measure the water level on streets at several flooding locations in Ho Chi Minh City. As a result, the real-time flooding monitoring system in Ho Chi Minh City could be achieved.

Keywords: MEMS, Pressure sensor, Piezoresistive, Flood monitoring system, Smart City

INTRODUCTION

Based on several advanced properties such as low power consumption, ease of integration, low cost and fast responsibility, Micro-Electro-Mechanical Systems (MEMS) devices are considered to play an important role for the development of Internet of thing (IoT) [1]. Among MEMS devices, pressure sensor has large market and is applied in various fields such as monitoring of fuel and measurement in automobile, air plane, blood pressure measurement and other consumer applications [2]. Pressure sensor can be also used in water level monitoring system for flood control which is one of the most serious problems in Ho Chi Minh City. In this system, both sonic sensor and pressure sensor are often utilized to measure water level to ensure the accuracy of measurement. However, the climate in Ho Chi Minh City is high humidity and rainy which cause waterlogging and disturb the measured signal of sonic sensor. Thus, in this study, we only use pressure sensor in water level monitoring system in Ho Chi Minh City.

The principle of MEMS pressure sensors are often based on piezoresistive effect in which the resistances vary with applied stress. The

piezoresistive effect in Si is often larger 100-200 times to metal. In metal, the piezoresistive effect is only caused by the changing shape of the resistor. However, in semiconductor such as Si, it is mainly caused by the changing of concentration and mobility of carrier which are related to changing the lattice constant and bandgap under applied stress [3].

Piezoresistive pressure sensor often has 4 piezoresistors in Wheatstone bridge in order to cancel the effect of temperature resistivity coefficient [4]. Under applied pressure, the diaphragm will be deformed and cause stress on the diaphragm. The vary of stress leads to the vary of piezoresistance and hence, the output voltage will be change. In the piezoresistive pressure sensor, piezoresistors is often p-type Si due to its high piezoresistivity. In this sensor, the p-type piezoresistors are fabricated on n-type diaphragm to create p-n junction at the surface in order to block electronic current from top side to bottom side of the sensor which causes the noise of output signal. In p-type Si, the highest piezoresistivity is along $\langle 110 \rangle$ crystal direction and thus, the piezoresistors is often along $\langle 110 \rangle$ direction. In addition, the piezoresistive coefficient $\pi_{\ell,110}$ and $\pi_{\tau,110}$ has close value and it

will help to reduce the vary of effective piezoresistive coefficient caused by misorientaion of piezoresistors during fabrication process [4].

EXPERIMENTAL

The piezoresistive pressure sensor (range 0-50 kPa) has 4 piezoresistors along $\langle 110 \rangle$ crystal direction which are arranged symmetric in order to reduce offset voltage (Figure 1).

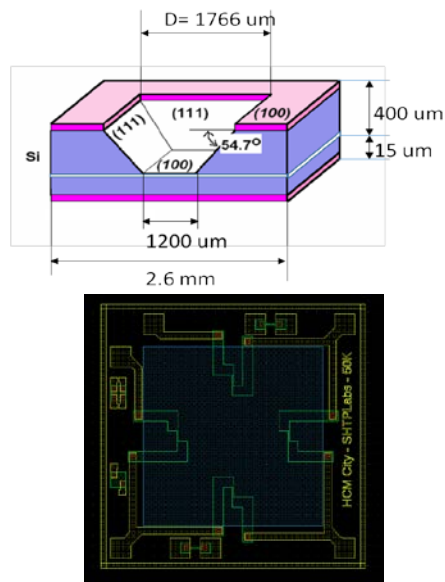


Figure 1. Design structure and top-view of pressure sensor.

Starting materials is Silicon on Insulator (SOI) 6 inches wafer (device layer: n-type, thickness 15 μm ; SiO_2 layer: thickness 0.4 μm ; and handle layer: p-type, thickness 400 μm). The pressure sensors were fabricated by using 4 – masks processes. Firstly, four piezoresistors were fabricated on the top of device layer by Boron diffusion process using the first mask (predeposition for 30 minutes at 1000 $^\circ\text{C}$, then B_2O_3 layer was removed and drive-in process was carried at 1100 $^\circ\text{C}$ for 30 minutes). After diffusion, resistance of the piezoresistor was measured by Jandel Multiposition Wafer Probe. The depth of diffusion was detected by staining method using CuSO_4 and HF [5]. Secondly, second mask was used to open contact hole. After that, 500 nm Al:Si (99% Al and 1% Si) was deposited by DC magnetron sputtering method. The third mask was used to pattern the metal. The fourth mask was utilized for etching backside using KOH solution (Figure 2). The diaphragm was created by KOH etching process (25% and at 75 $^\circ\text{C}$) in which SiO_2 layer played

as etching-stop layer in order to obtain uniform thickness of the diaphragm.

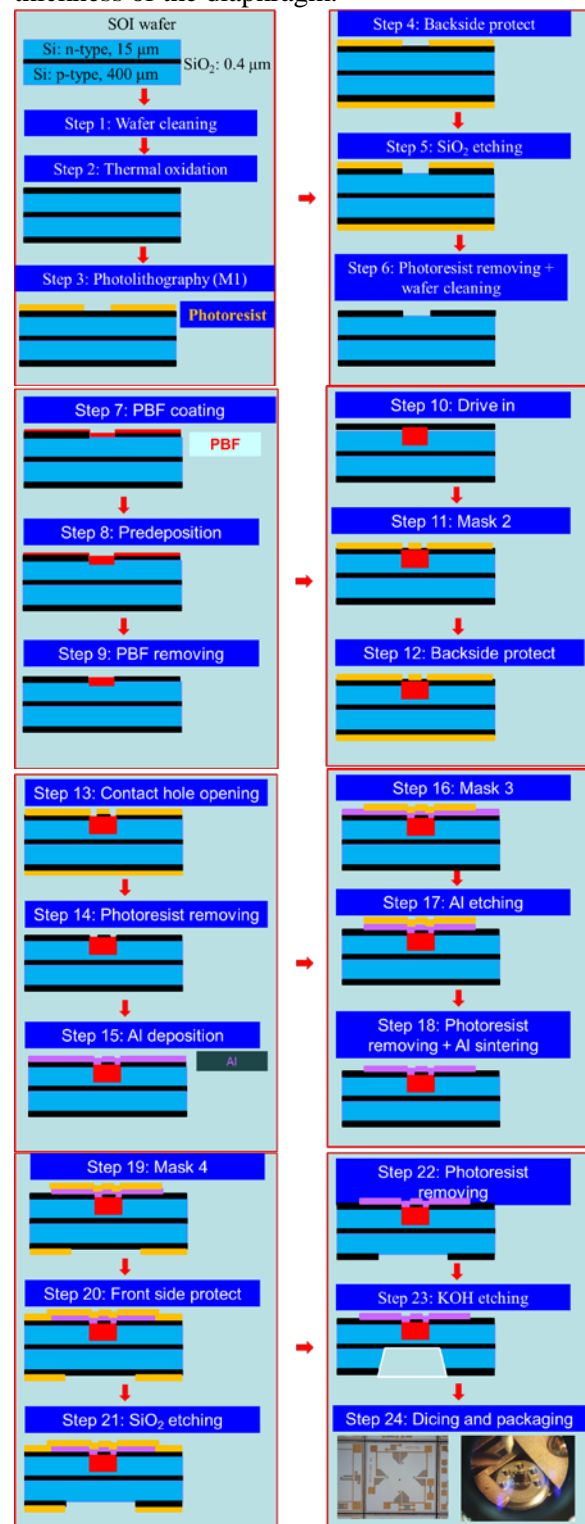


Figure 2. Fabrication processes of pressure sensors.

Finally, the wafer was dicing and the pressure sensors were packaged using metal can package (TO-5) (Figure 3). Fabricated pressure sensors were characterized by using Yokogawa

pneumatic pressure standard (model 767402) and a home-made temperature chamber. The sensors were also measured at Ho Chi Minh City Center of Standard Metrology and Quality. For reliability testing, a home-made pressure valve was used to change pressure from 0-50 kPa repeatedly for 10000 cycles. After calibration, fabricated pressure sensors were installed in water level monitoring module.



Figure 3. Fabricated pressure sensors

RESULTS AND DISCUSSION

After diffusion, resistance of the piezoresistor was about 1300Ω and the depth of diffusion $\sim 2.6 \mu\text{m}$. Using 3 V input voltage, the fabricated pressure sensors had offset voltage $< \pm 20 \text{ mV}$. The offset voltage can be attributed to the mismatch of alignment during photolithography and residual stress in packaging process.

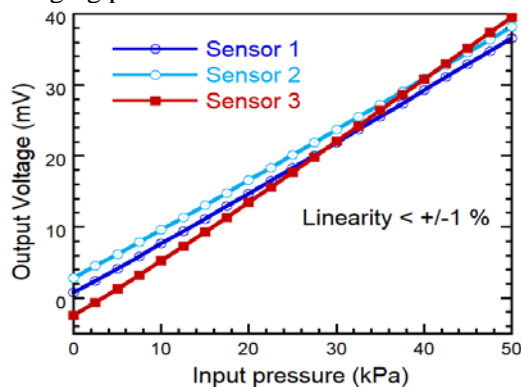


Figure 4. Output characterization at room temperature ($25 \text{ }^\circ\text{C}$) of fabricated pressure sensors

The span voltage and sensitivity of fabricated pressure sensors were $\sim 35\text{-}40 \text{ mV}$, $\sim 0.7\text{-}0.8 \text{ mV/kPa}$, respectively. From the characterization of the sensors, we obtained its linearity is smaller than $\pm 1\%$. Those parameters are similar to parameters of commercial pressure sensors. We obtained similar result from measurement of the sensors at Ho Chi Minh City

Center of Standard Metrology and Quality (Figure 4).

Temperature dependence of fabricated pressure sensors was also studied in the range of $15 - 65 \text{ }^\circ\text{C}$ (Figure 5) which is typical for outdoor temperature in Ho Chi Minh City. The offset voltage was increased with temperature while the sensitivity was decreased with temperature, which can be explained by temperature dependence of p-type Si resistivity.

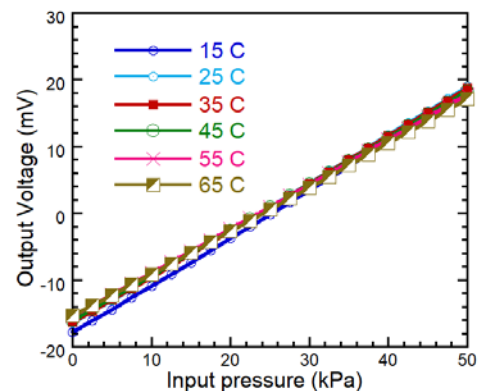


Figure 5. Temperature dependence of the output voltage of fabricated pressure sensor

For reliability testing, the properties of pressure sensors remained almost unchanged after 10000 cycles of repeated pressure from 0 to 50 kPa (Figure 6). Compare to the initial span voltage, the span voltage varied $< 1\%$ during 10000 cycles.

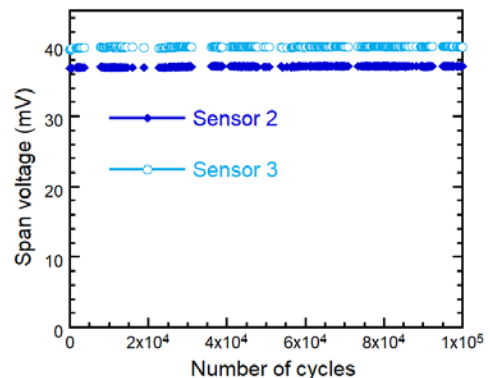


Figure 6. Repeated load characteristics of fabricated pressure sensors

We set up the water level monitoring modules using fabricated at several fooding locations in different districts of Ho Chi Minh City and compared their altitudes to the standard elevation of Vietnam. In this system, the pressure sensor detects the changing of pressure cause by the variation of water level on street. We used both lithium battery and solar cell for power supply of the system to extend lifetime of the system (Figure 7). In order to reduce the

noise, we used Kalman Filtering algorithm and the accuracy of water level measurement can be reduced to smaller than 1 cm.

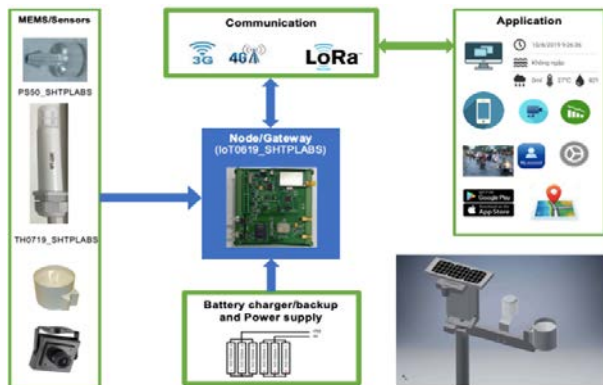


Figure 7. Block diagram of “flood monitoring system”

The real-time calculated water level was sent to data center of SHTP Labs by using 3G communication technology (Figure 8). At this moment, 15 trial nodes were installed and several other nodes would be installed in order to make real-time flood mapping for Ho Chi Minh City.

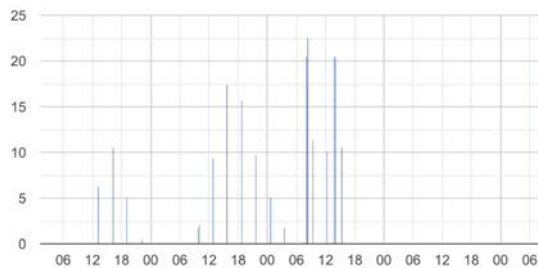


Figure 8. Real-time water level in a day (vertical axis is water level in cm; horizontal axis is time in hour) at a node of flood monitoring system

CONCLUSION

Piezoresistive pressure sensors were successfully fabricated and were characterized. We applied those sensors in flood monitoring system in Ho Chi Minh City and the real-time flooding situation in Ho Chi Minh City could be achieved.

Acknowledgment

This research was supported by the annual projects of The Research Laboratories of Saigon High Tech Park in 2019 according to decision No. 102/QĐ-KCNC of Management Board of Saigon High Tech Park and contract No. 01/2019/HĐNVTX-KCNC-TTRD and project “Research, design, fabricate and utilize flood

monitoring system at flooding places in innovative urban area in Ho Chi Minh City”

References

- [1] <http://www.yole.fr>
- [2] Les Instituts Carnot, *White Paper: Smart Networked Objects & Internet of Things*, January 2010, pp. 1–8
- [3] Charles S. Smith, *Piezoresistance effect in Germanium and Silicon*, Phys. Rev. 94 (1954), 42-49
- [4] S. Santosh Kumar, B. D. Pant, *Design principles and considerations for the ‘ideal’ silicon piezoresistive pressure sensor: a focused review*, Microsystem Technologies, Volume 20, Issue 7 (2014), 1213–1247
- [5] S. T. Ahn and W. A. Tiller, *A Staining Technique for the Study of Two-Dimensional Dopant Diffusion in Silicon*, J. Electrochem. Soc.: SOLID-STATE SCIENCE AND TECHNOLOGY, Vol. 135, No. 9 (1988), 2370-2373

PREPARATION AND CELL LABELING EVALUATION OF ANTIBODY-CONJUGATED CdSe/MSA QUANTUM DOTS

Khanh Thien Le^{1,+}, Hong Diep Thi Tran^{1,+}, Ngoc Thuy Thi Vo² and Hieu Tran Van¹

¹ Department of Molecular and Environmental Biotechnology, Faculty of Biology and Biotechnology, University of Science, Vietnam National University Ho Chi Minh City, 227 Nguyen Van Cu, Ward 4, District 5, Ho Chi Minh City, Vietnam;

² Department of Applied Physics, Faculty of Physics and Engineering Physics, University of Science, Vietnam National University Ho Chi Minh City, 227 Nguyen Van Cu, Ward 4, District 5, Ho Chi Minh City, Vietnam;

⁺ First authorship shared;

Email: thienle2603@gmail.com, tthdiep@hcmus.edu.vn, tvhieu@hcmus.edu.vn

ABSTRACT

Quantum dots (QDs) are recently used as new fluorescent nanomaterials in biological labeling applications. QDs have featured properties such as high luminous intensity, photochemical stability, and few fluorescence spectral overlap. In this study, we synthesized mercaptosuccinic acid (MSA)-coated CdSe QDs and evaluated their optical properties. The results indicated that our QDs had a broad excitation spectrum and a narrow and symmetric emission spectrum. Besides, we developed one-step synthesis of protein A/G (pA/G)-coated CdSe/MSA QDs for IgG antibody conjugation due to the affinity of pA/G with IgG antibody Fc region. The results of cell labeling assay showed that our pA/G-coated QDs could specifically label Jurkat T cells when they were conjugated to anti-CD3 IgG antibody. In conclusion, our QDs could be potential alternative fluorescent nanomaterials and could be widely used to label any biological object in general by incorporation with its specific IgG antibody.

Keywords: Quantum dots (QDs), fluorescent nanomaterials, biological labeling

INTRODUCTION

In recent years, quantum dots (QDs) are developed as new fluorescent nanoparticles. QDs contain semiconductor core which is commonly formed from the incorporation of group II-VI (CdSe, CdTe), IV-VI (PbSe), or III-V (InP, InAs, GaAs) chemical elements [1]. The role of the core is to absorb energy from excitation wavelength and to emit fluorescence. Unlike other fluorophores which are mostly excited by one single wavelength, QDs have a broad excitation spectrum. This means that QDs can be excited by many different wavelengths and easily combined with other fluorophores in multi-labeling. In contrast, QDs' emission spectrum is narrow and symmetric so QDs always emit only one wavelength. Hence, fluorescence spectral overlap can be significantly restricted in multi-labeling by using QDs. Besides, QDs also have other featured properties such as high luminous intensity, photochemical stability, and core diameter-dependent emission wavelength [2]. To protect the core as well as to prevent release of its heavy

metal ions, QDs often have a shell which is commonly ZnS or PbS layer [3]. Furthermore, QDs are frequently coated with aqueous molecules such as mercaptocarboxylic acid, silica, amphiphilic polymers, etc to increase their water-solubility so they can be easily used for labeling applications [4]. In this study, we synthesized mercaptosuccinic acid (MSA)-coated CdSe QDs and evaluated their cell labeling application when they were conjugated to IgG antibody.

Many methods were developed to conjugate antibody to nanoparticles. However, a problem that how to turn antibody Fab region outwards from nanoparticle surface to conserve antigen recognition capacity of antibody should be efficiently solved. Strategies that conjugate antibody to nanoparticles by covalent bond formation or biotin-avidin interaction cannot solve this problem because conjugated site on antibody is randomly formed. In this study, we coated our CdSe/MSA QDs with protein A/G (pA/G) as an adaptor protein in order to conjugate QDs to IgG antibody due to this

protein's affinity with IgG Fc region [5]. Therefore, the Fab region was turned outwards. QDs were coated with pA/G by stirring due to the affinity of pA/G's 6xHis tail with heavy metal ions on QDs' surface.

EXPERIMENTAL

Synthesis of CdSe/MSA QDs

At first, 0.704 g of cadmium acetate dihydrate $[(CH_3COO)_2Cd \cdot 2H_2O]$, 0.556 g of MSA, and 100 ml of distilled water were added into a three-neck flask to form Cd^{2+} precursor. The solution was stirred in nitrogen atmosphere until MSA was completely dissolved. Nitrogen gas was introduced to eliminate oxygen and acetic acid. For Se^{2-} precursor formation, 0.2 g of sodium borohydride ($NaBH_4$), 0.704 g of sodium selenite (Na_2SeO_3), and 10 ml of distilled water were mixed up for 15 minutes. After that, we rapidly injected Se^{2-} precursor solution into Cd^{2+} precursor solution at room temperature. The mixture was then stirred for 30 minutes at 1,000 rpm. Solution temperature was risen up to $90^\circ C$ without stirring. After reaction time, by injecting toluene, the solution was cooled down fast to stop development of CdSe/MSA particles.

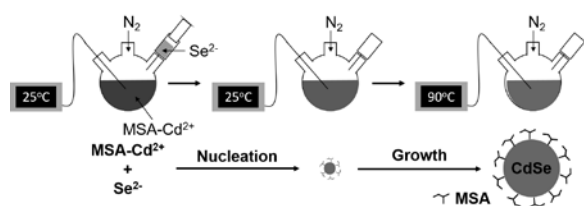


Figure 1. Schematic diagram of CdSe/MSA QDs synthesis.

Evaluation of CdSe/MSA QDs' optical properties

CdSe/MSA QDs were measured ultraviolet-visible (UV-Vis) and photoluminescence (PL) spectrum to evaluate their optical properties. Besides, we identified their PL yield by comparing their PL spectrum with the one of Rhodamine 6G which is a sensitive fluorophore commonly used for PL yield identification. The PL yield was QDs:Rhodamine 6G PL intensity ratio.

Preparation of pA/G-coated CdSe/MSA QDs and IgG-conjugated pA/G-CdSe/MSA QDs

For pA/G coating, 1 ml of CdSe/MSA QDs solution (1 mg/ml) and 1 ml of pA/G solution (1.5 mg/ml) were added into a 5 ml glass vial. The mixture was then stirred for 8 hours at room

temperature. After that, 5% (w/v) bovine serum albumin (BSA) solution was added into the vial to reach BSA's final concentration at 0.5% (w/v). The mixture was stirred overnight at room temperature to ensure that QDs' surface was completely coated with BSA.

For IgG antibody conjugation, 0.2 ml of pA/G-CdSe/MSA QDs solution and 15 μg of anti-CD3 IgG antibody, which would be used for Jurkat T cells labeling, were added into a 0.5 ml microcentrifuge tube. Phosphate buffered-saline (PBS) 1X solution was then added to reach the final volume of 0.25 ml. The tube was continuously rotated for 4 hours on end-over-end rotator at room temperature. Besides, we prepared QDs group, which was not coated with pA/G and was only coated with BSA; and QDs + IgG group, which was BSA-coated QDs mixed up with IgG antibody, by the same way as control groups for cell labeling evaluation.

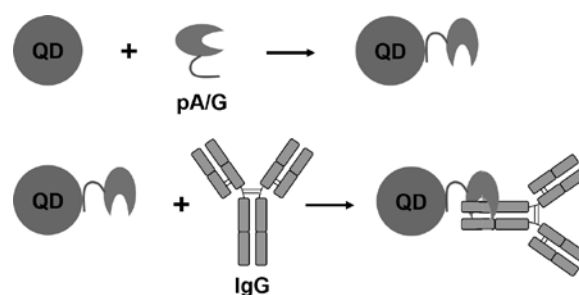


Figure 2. Conjugation of IgG antibody to QDs via pA/G.

Cell labeling assay

0.25 ml of IgG-pA/G-QDs solution and 5.10^5 Jurkat T cells in 0.75 ml RPMI 1640 medium were added into a 1.5 ml microcentrifuge tube. The tube was continuously rotated for 30 minutes on end-over-end rotator at room temperature and then centrifuged at 1,500 rpm for 5 minutes. The supernatant was discarded and the cell pellets were resuspended in 0.1 ml of RPMI 1640 medium. Finally, 20 μl of medium containing cells was spotted on a lame and the cells were observed under fluorescence microscope. The cell labeling assay was also similarly performed with control groups as indicated above.

RESULTS AND DISCUSSION

Synthesis and optical properties evaluation of CdSe/MSA QDs

CdSe/MSA QDs after synthesis in three-neck flask were derived and dissolved in PBS

1X solution. Firstly, sensory evaluation indicated that they were highly soluble in water and their color was homogeneous. Besides, no aggregation was observed in the solution (**Figure 3A**). Under excitation condition of blue light, they showed strong green luminescence (**Figure 3B**). These results basically proved that our QDs were successfully synthesized.

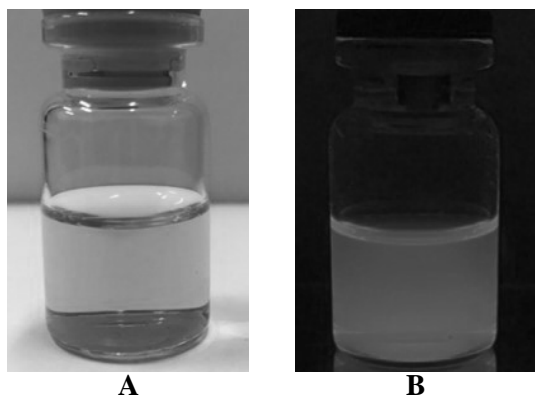


Figure 3. CdSe/MSA QDs were dissolved in PBS 1X solution (A) and emitted green fluorescent light under excitation of blue light (B).

Results of UV-Vis and PL spectrum measurement demonstrated that our CdSe/MSA QDs had featured optical properties. They could absorb a wide range of excitation wavelength from 400 to over than 500 nm and showed maximum absorbance at 501 nm wavelength (**Figure 4A**). Besides, they showed a sharp, narrow and symmetric peak in their emission spectrum. Their maximum emission wavelength was 525 nm and in line with their green fluorescence. Moreover, their surface emission was asymptotic to 0. This meant that their surface was tightly coated with MSA so surface defects and non-radiative recombination channels were significantly limited (**Figure 4B**).

Comparison between QDs and Rhodamine 6G's PL spectrum also indicated that QDs had a high luminous intensity with the PL yield reached to 80%. Although Rhodamine 6G showed a higher luminous intensity, its peak was broad and asymmetric in comparison with QDs' one (**Figure 5**). These results proved that our QDs had high quality and potentials to be used for biological labeling.

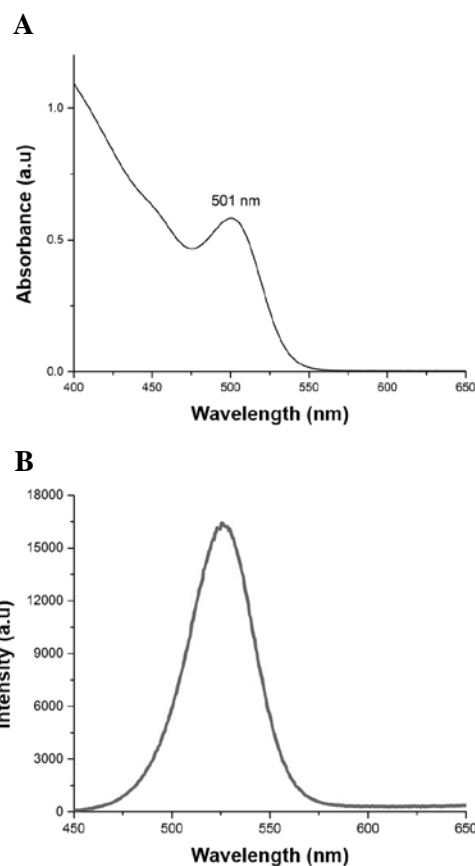


Figure 4. UV-Vis (A) and PL (B) spectrum of CdSe/MSA QDs.

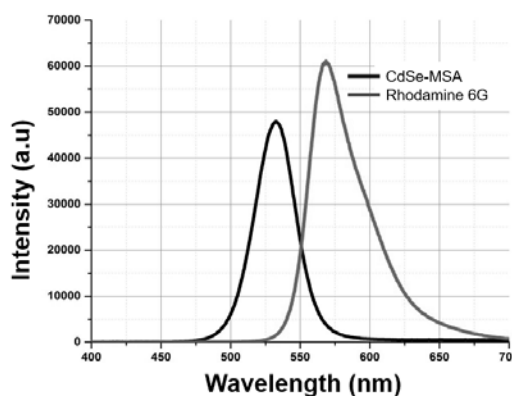


Figure 5. Comparison between CdSe/MSA QDs and Rhodamine 6G's PL spectrum.

Cell labeling evaluation

In cell labeling assay, QDs and QDs + IgG group did not show fluorescent signals on membrane of Jurkat T cells (**Figure 6A and B**). This meant that QDs' surface was completely coated with BSA so interactions between the surface and the cells were prevented and IgG antibody could not bind to QDs without the support of pA/G. In contrast, IgG-pA/G-QDs efficiently labeled the cells with high luminous

intensity (**Figure 6C**). These signals were highly specific because QDs could label the cells only when they were conjugated to specific IgG antibody. Moreover, these results verified the role of pA/G in IgG antibody conjugation to our QDs and their potentials in biological labeling.

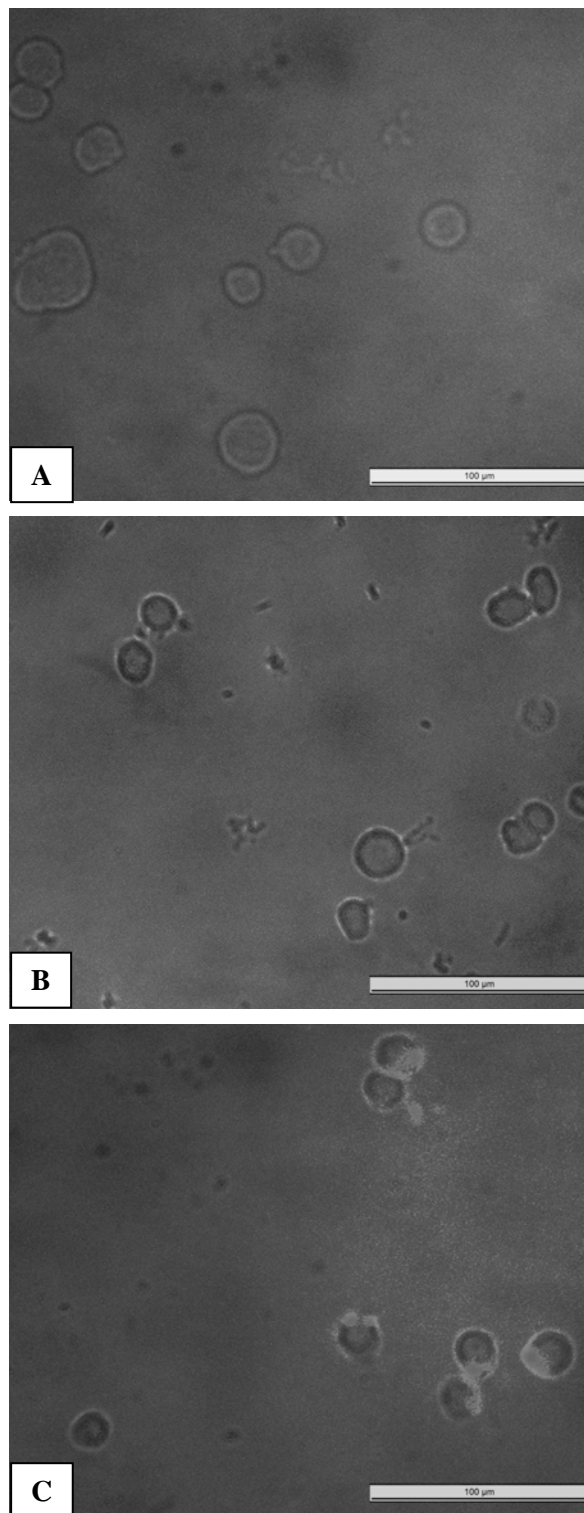


Figure 6. Cell labeling evaluation of CdSe/MSA QDs. (A) QDs; (B) QDs + IgG; and (C) IgG-pA/G-QDs.

CONCLUSION

In this study, we synthesized and characterized CdSe/MSA QDs. They showed featured optical properties as well as high quality for bio-applications. By exploiting pA/G, we successfully developed potential QDs which could effectively bind a wide range of mammal IgG antibodies. The results of cell labeling assay demonstrated that our QDs could prospectively become new fluorescent nanomaterials for biological labeling applications.

Acknowledgment

This research was supported by Ho Chi Minh City Department of Science and Technology under the research code 105/2017/HD-SKHCCN.

References

- [1] S. Jin, Y. Hu, Z. Gu, L. Liu, H.-C. Wu, *Application of Quantum Dots in Biological Imaging*, *Journal of Nanomaterials* **2011** (2011) 1-13
- [2] S. B. Rizvi, S. Ghaderi, M. Keshtgar, A. M. Seifalian, *Semiconductor quantum dots as fluorescent probes for in vitro and in vivo bio-molecular and cellular imaging*, *Nano Rev* **1** (2010)
- [3] Y. Su, Y. He, H. Lu, L. Sai, Q. Li, W. Li, L. Wang, P. Shen, Q. Huang, C. Fan, *The cytotoxicity of cadmium based, aqueous phase - synthesized, quantum dots and its modulation by surface coating*, *Biomaterials* **30** (2009) 19-25
- [4] A. S. Karakoti, R. Shukla, R. Shanker, S. Singh, *Surface functionalization of quantum dots for biological applications*, *Adv Colloid Interface Sci* **215** (2015) 28-45
- [5] W. Choe, T. A. Durgannavar, S. J. Chung, *Fc-Binding Ligands of Immunoglobulin G: An Overview of High Affinity Proteins and Peptides*, *Materials* **9** (2016)

TOWARDS HIGHLY-SENSITIVE MASSIVELY-PARALLEL TEMPERATURE SENSING WITH PRINTED PTC ELEMENTS

**Philipp Rinklin¹, Nouran Adly¹, Leroy Grob¹, Korkut Terkan¹, Lennart Weiss¹, Sabine Zips¹,
Bernhard Wolfrum¹**

¹ Neuroelectronics Group, Munich School of Bioengineering, Department of Electrical Engineering and Computer Science, Technical University of Munich
Email: philipp.rinklin@tum.de

ABSTRACT

Sensitive detection of temperature at a high throughput is of great interest in various biological and biomedical settings. However, classical methods that offer sufficient resolution to quantify e.g. cellular metabolism are slow and difficult to parallelize. Novel methods based on optical techniques are fast and parallelizable, but require a high degree of the fluorophores' physicochemical environment. Recently, highly-sensitive positive-temperature-coefficient (PTC) materials showing a several orders of magnitude change in resistance in the physiological range have been demonstrated. Here, we present a novel formulation of such materials using inkjet-compatible materials for printing-based fabrication. We synthesize and characterize the materials in a macroscopic setting and discuss preliminary results in terms of massively-parallelized sensor plates.

Keywords: positive temperature coefficient, carbon black, inkjet printing, *in vitro* temperature measurement

INTRODUCTION

In the vast majority of physico-chemical systems, temperature represents a fundamental governing parameter. Particularly in most biological systems, the regulation of temperature is tightly controlled and of vital importance. As such, being able to monitor and record temperatures with high sensitivity is of great interest to many biological and biomedical questions. Given adequate measurement techniques, such as classical microcalorimetry, it is possible to quantify the metabolism of mammalian cells¹. However, while offering excellent sensitivity, classical techniques in this context usually lack the throughput required to tackle highly parallelized studies in e.g. pharmaceutical screening. Novel fluorescent methods on the other hand are dependent on various factors other than temperature, which can cause problems in terms of reliable results². To mitigate these drawbacks, a novel type of temperature sensors using positive-temperature-coefficient (PTC) materials has recently been presented^{3,4}. These sensors show a several-orders-of-magnitude increase in resistance in the physiological regime and can be read by a simple resistance measurement. Figure 1a illustrates the principle of these sensors. The schematic shows a

polymer that is doped with a conductive filler past the percolation threshold. Thus, conduction through the material is achieved by a serial connection of low-resistance particles and high-resistance gaps through which charge transport occurs via tunneling. As a result, the overall resistivity of the material is highly dependent on temperature⁵.

Here, we present a new material formulation that show the above described characteristics, but – in contrast to previous studies – are doped with carbon nanoparticles that are compatible with inkjet processing. Using a macroscopic sensor configuration, we characterize the thermal response of the material in terms of transition temperature and sensitivity. Lastly, we present preliminary results in using these materials for highly-sensitive massively-parallelized *in vitro* temperature measurements.

EXPERIMENTAL

Synthesis of PTC materials All materials were synthesized according to a modified protocol from ^{3,4}. Briefly, octyl acrylate (OA; Sigma) butyl acrylate (BA; Sigma) were mixed to yield a total of 10 g at 70, 80, and 90 wt% OA. 10 mL of tetrahydrofuran (THF; Sigma) and 0.1 g of 2,2-dimethoxy-2-phenylacetophe-

none (DMPA; Sigma) were added, the mixture was homogenized, and exposed to 17000 flashes of UV light under N_2 atmosphere (Otoflash G171, NK Optik) and dried under vacuum. The OA/BA polymers were dissolved in 25 mL of THF at 60 °C and carbon black (Printex L, Orion Engineered Carbons) was added in a 3:1 polymer: carbon black weight ratio. The mixture was stirred for 1 h and the resulting composite material was dried under vacuum.

Sensor assembly 5 mm wide strips of copper tape were glued onto 76×52 mm² glass slides at a distance of 5 mm. 120 μm thick double-sided adhesive foil (Grace BioLabs SecureSeal, Sigma) was placed onto the copper contacts. Next, an appropriate amount of PTC material was placed into the opening and melted on a hot plate set to 100 °C before firmly pressing a 26×76 mm² onto the sensor's top side to complete the sensor assembly.

Temperature measurements and data analysis

Each sensor's base resistance was measured using a multichannel potentiostat (PalmSens 4, PalmSense BV). A precision hot plate (PZ35ET, Harry Gestigkeit) was used to control the sensor's temperature while reference measurements were taken with the thermal probe of a multimeter (80BK-A and 289, respectively, Fluke Corporation). The sensors' response was recorded by applying 10 mV to each sensor and recording the resulting current throughout the measurement.

Printed sensor arrays In order to apply our materials in printed sensor arrays, different solvent compositions were tested. Feedlines and contacts were printed onto PEN substrates (Q65HA, DuPont Teijin Films) using a silver nanoparticle ink (DGP 40LT-15C, Sigma Aldrich). Subsequently, ink candidates were printed onto the feedlines and the foils were attached to bottomless 96 well plates using double-side adhesive foil (Grace BioLabs SecureSeal, Sigma)

RESULTS AND DISCUSSION

PTC material and sensor development

The aim of the present study was to develop an inkjet-compatible positive-temperature-coefficient (PTC) material. Recently, the Someya group has presented conductively-doped acrylate co-polymers with melting points in the physiological range^{3,4}. These polymers are composed of different ratios of octadecyl

acrylate (OA) and butyl acrylate (BA) monomers. However, their work used 2-3 μm graphite particles as conductive doping elements. In the present study, we present a similar material formulation that is based on 20 nm carbon black particles as conductive agents that should allow the formulation of an inkjet-compatible ink.

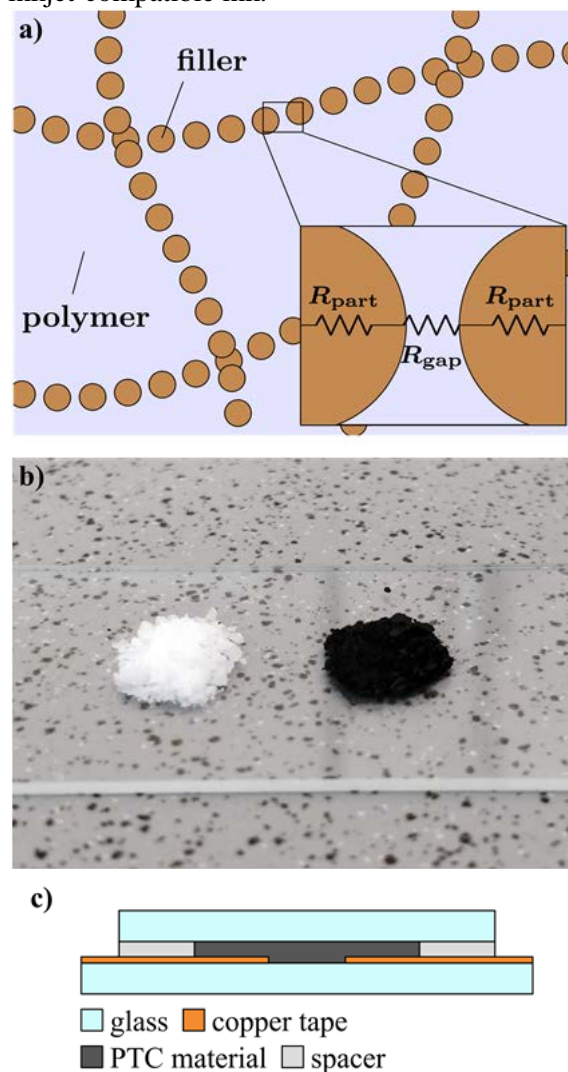


Figure 1. PTC material and sensors structure. a) In a sufficiently doped dielectric material, percolation leads to the formation of a conductive network. In this network, charge transport takes places through a serial matrix of low-resistance particles and high-resistance tunneling junctions. b) Exemplary images of OA/BA co-polymer before and after addition of carbon black filler material (left and right, respectively). c) Schematic illustration of the sensor structure.

As a first step, we synthesized acrylate co-polymers with different OA/BA ratios of 70, 80, and 90% and introduced the carbon black material by dissolving the polymer in THF and adding 25 wt% of carbon. Figure 1b shows the

resulting material before (left) and after (right) the addition of the conductive filler. As described above, the sensing mechanism of these PTC materials heavily depends on the distribution and percolation of the conductive filler. As such, we examined the as-synthesized materials' functionality in a macroscopic sensor configuration. To this end, a fast and simple layout using glass slides as substrates, conductive copper tape as contacts, and double-side adhesive foils as a spacer was developed (compare Figure 1c). By confining the PTC material with the spacer and two glass slides, a reproducible geometry and thus resistance value of the sensors was achieved.

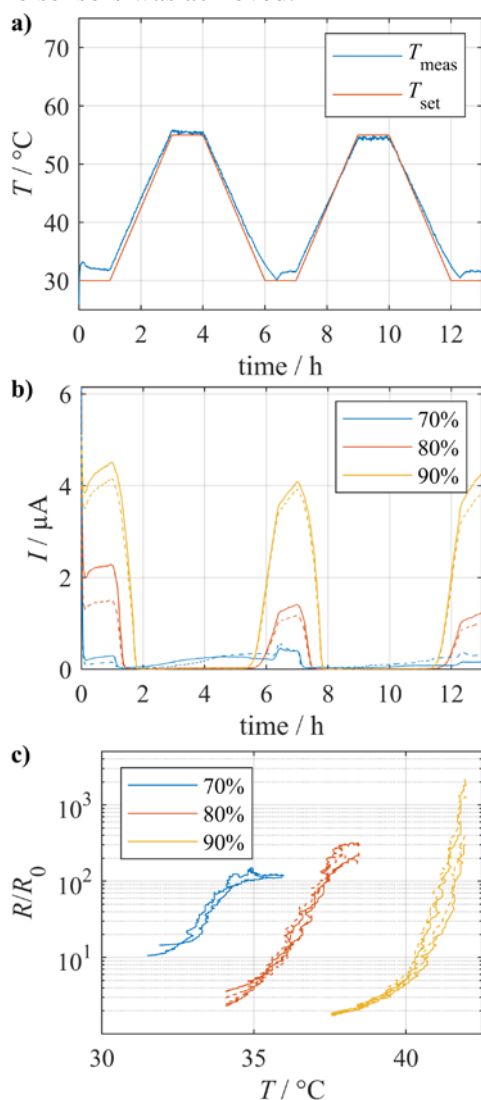


Figure 2. Temperature response of an exemplary set of sensors. a) Set temperature of the hot plate and measured temperature on the surface of the glass substrate. b) Amperometric response of 70, 80, and 90% OA/BA co-polymer. c) Temperature dependent change in resistance during the heating phase for 70, 80, and 90% OA/BA co-polymer.

Calibration and temperature measurements

In order to validate the materials' functionality, the sensors described above were exposed to a temperature profile between 30 and 55 °C. Simultaneously, in order to account for potential temperature drops over the glass substrate, the temperature at the sensor location was measured with a thermal probe. Figure 2a displays a comparison between the set and measured temperatures. While the set and measured temperature are generally in reasonable agreement, offsets during the 30 °C plateaus as well as transients caused by the thermal inertia of the system can be seen. Consequently, only the measured temperatures were used to analyze the data.

Figure 2b shows amperometric traces recorded for multiple sensors fabricated from the 70, 80, and 90% OA/BA polymers. In general, an increase in conductivity with increasing OA content can be seen. Since the carbon content is identical for all three materials, this could indicate differences in the percolation of the carbon filler caused by the different polymer composition. Comparing Figures 2a and b, a drop in current between 1 and 2 h i.e. between ~30 and ~45 °C can be seen. This drop occurs first for the 70% OA material, followed by the 80 and 90% polymers. Between 5 and 6 h, the temperature at the sensors' surface decreases again and a recovery of the current can be observed. This behavior is analogous for the second cycle.

Figure 2c shows a plot of the ratio of each sample's resistance, R , normalized by its initial resistance, R_0 , as a function of temperature during the heating phase of the experiment. The steepest points of the curves are at approx. 33.5, 36.5, and 41 °C for the 70, 80, and 90% materials, respectively, which is in good agreement with previous works^{3,4}. Comparing the resistances before and after the transition, a relative change of 10^1 - 10^3 is observed, with the higher-OA-content materials displaying a higher sensitivity. All materials display a transition within a window of approx. 2 K. This corresponds to a sensitivity of $5 \times 10^2 \text{ K}^{-1}$, compared to Pt elements, which commonly operate at $\sim 4 \times 10^{-3} \text{ K}^{-1}$. However, the sensors display a non-linear response and a notable hysteresis when exposed to temperatures notably higher than the transition temperature (data not shown). As such, while offering excellent sensitivity the operational range of the sensors is

limited and precise measurements require non-linear calibration data.

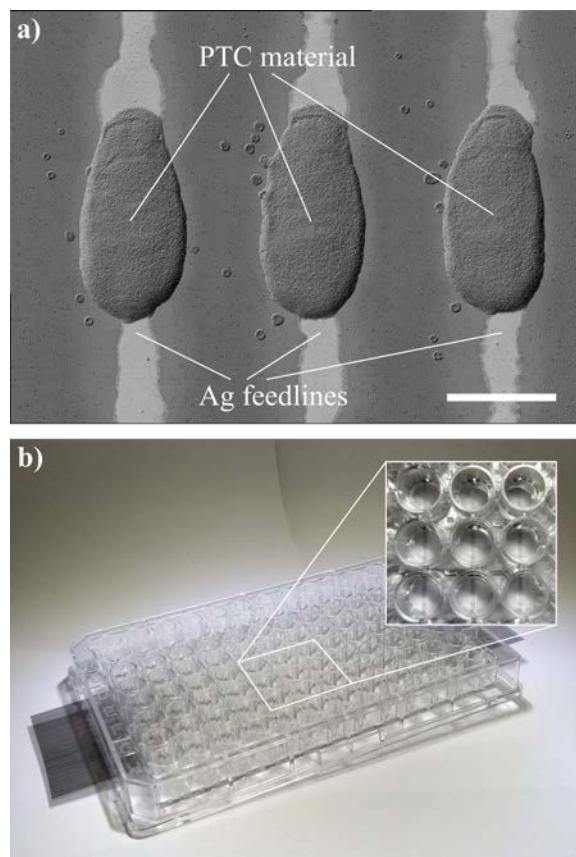


Figure 3: Preliminary images of printed structures (a, scale bar corresponds to 150 μm) and a prototype well plate (b).

Printed structures

After successfully validating the functionality of our materials, preliminary experiments towards ink formulation and high-throughput sensor plates were carried out. To this end, contacts and feedlines were printed in silver and PTC ink candidates were printed on top (compare Figure 3a). Subsequently, the printed foils were attached to bottomless well plates using double-side adhesive foil. Our approach allows the placement of 144 sensors distributed over the center 48 wells of a standard 96 well plate. However, current ink formulations lack the thermal response observed in the raw materials. As such, future studies will be directed towards suitable solvent and additive compositions that preserve the materials' functionality in the printed structures.

CONCLUSION

The present work present a novel formulation for highly-sensitive PTC materials

using only inkjet-compatible materials. To validate the materials' functionality, a macroscopic sensor setting is used and the materials are shown to exhibit excellent sensitivity, albeit with non-linear response characteristics. In order to use our materials in high-throughput sensor plates, we demonstrated an approach to assemble printed structures to bottom-less standard cell-culture well plates. Future studies will be directed at functional ink formulations and suitable passivation layers.

References

- [1] Levin, K.; Fürst, P.; Harris, R.; Hultman, E. Heat Production from Human Erythrocytes in Relation to Their Metabolism of Glucose and Amino Acids. *Scand. J. Clin. Lab. Invest.* **1974**, *34* (2), 141–148.
- [2] Baffou, G.; Rigneault, H.; Marguet, D.; Jullien, L. A Critique of Methods for Temperature Imaging in Single Cells. *Nat Meth* **2014**, *11* (9), 899–901. <https://doi.org/10.1038/nmeth.3073>.
- [3] Yokota, T.; Inoue, Y.; Terakawa, Y.; Reeder, J.; Kaltenbrunner, M.; Ware, T.; Yang, K.; Mabuchi, K.; Murakawa, T.; Sekino, M.; et al. Ultraflexible, Large-Area, Physiological Temperature Sensors for Multipoint Measurements. *PNAS* **2015**, *112* (47), 14533–14538. <https://doi.org/10.1073/pnas.1515650112>.
- [4] Nakamura, T.; Yokota, T.; Terakawa, Y.; Reeder, J.; Voit, W.; Someya, T.; Sekino, M. Development of Flexible and Wide-Range Polymer-Based Temperature Sensor for Human Bodies. In *2016 IEEE-EMBS International Conference on Biomedical and Health Informatics (BHI)*; 2016; pp 485–488. <https://doi.org/10.1109/BHI.2016.7455940>.
- [5] Strümpfer, R. Polymer Composite Thermistors for Temperature and Current Sensors. *Journal of Applied Physics* **1996**, *80* (11), 6091–6096. <https://doi.org/10.1063/1.363682>.

A STUDY ON ELECTRICAL PARAMETERS OF INTERDIGITATED ARRAY ELECTRODES (IDEAS) SENSOR FOR CONCENTRATION MEASUREMENT OF PHOSPHATE-BUFFERED SALINE

Tuan Vu Quoc^{1,2}, **Tung Bui Thanh**² and **Trinh Chu Duc**²

¹ Institute of Applied Physics and Scientific Instrument, Vietnam Academy of Science and Technology, Hanoi, Vietnam;

² VNU University of Engineering and Technology, Vietnam National University, Hanoi, Vietnam, Email: trinhcd@vnu.edu.vn

ABSTRACT

Capacitive sensors based on interdigitated array electrodes (IDAEs) integrated into microfluidic channels have been developed for many bioanalysis applications due to its advantages in comparison with electrochemical sensors. In this study, an IDEAs capacitive sensor has been proposed, fabricated and characterized. The IDEA structure is fabricated in a 100 μm -width microfluidic channel using micromachining technology. Electrical impedance spectroscopy measurements of the sensor have been carried out in a wide frequency range from 10 kHz to 1 MHz. Performance of the IDEAs sensor has been demonstrated through sensing the concentration of the phosphate buffer saline (PBS) which is fully filled in the microchannel. The obtained results show a linear relationship between the measured conductance and concentration of PBS solution, demonstrating the possibility of estimating conductance of the solution through the total impedance.

Keywords: Capacitance sensor, interdigitated array electrodes sensor, electrical impedance spectroscopy

INTRODUCTION

Capacitive sensors based on interdigitated array electrodes (IDAEs) integrated into microfluidic channels have been developed for many bioanalysis applications [1]–[4] due to its advantages in a comparison with electrochemical sensors which is based on methods of voltammetry, amperometry, and potentiometry. IDEAs is a simple structure to help avoiding problems of integrating the reference system into a microfluidic channel which is required in the electrochemical sensor [5]. Moreover, IDEAs can be easily integrated microfluidic channel for portable devices developments. For these reasons, a study of IDEAs electrical parameters is necessary to apply for developing bio-microfluidic devices.

In this study, an IDEAs capacitive sensor integrated into microfluidic channel device has been designed, fabricated and characterized to measure the properties of solution containing in the channel, for example, the concentration of phosphate-buffered saline (PBS) in the microfluidic channel. IDEA structure is made of gold and embedded in a 100 μm -width microfluidic channel filled with PBS of different concentrations. Those measurements carried out

in a wide measurement frequency range, from 10 kHz to 1MHz to find out the effective working frequency of the IDAEs sensor and then exploit electrical parameters at a certain frequency for sensing applications.

Changes in concentration of PBS solutions lead to changes in the solution conductivity which can be detected by measuring the conductance of the sensor. The resistance of solution can be estimated through the impedance measurements at high frequency. Also, thickness of the double layer formed between two layers of PBS solution and gold electrode is identified by the concentration of PBS solution. Then, the capacitance parameter of the double layer is suggested to use for detecting the change on the surface of the electrodes.

INTERDIGITATED ARRAY ELECTRODES (IDEAS) SENSOR

To investigate the IDEAs sensor working in microfluidic channel for bio applications, an IDEAs structure has been designed to integrate in the 100 μm -width microfluidic channel of a microfluidic chip. Figure 1 shows the structure design of IDEAs in microfluidic channel. The IDAEs structure is constructed by two

electrodes: one electrode with six fingers and the other with seven fingers. The width (w) and length (L) of each finger are $10\ \mu\text{m}$ and $40\ \mu\text{m}$; the gap (s) between two fingers is $10\ \mu\text{m}$. After the electrodes being fabricated on a glass substrate, the $100\ \mu\text{m}$ -width microchannel is bonded onto the glass substrate to create a microfluidic device for bio sensing application.

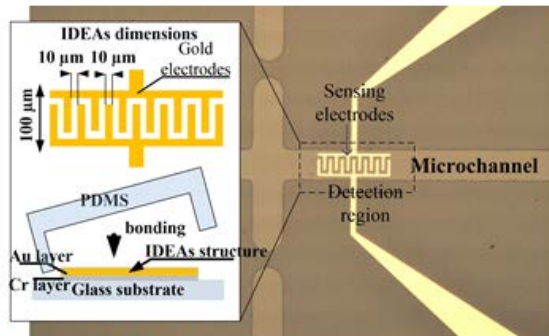


Figure 1. IDEAs sensor, structure and fabrication of the impedance IDEAs sensor integrated into microfluidic channel

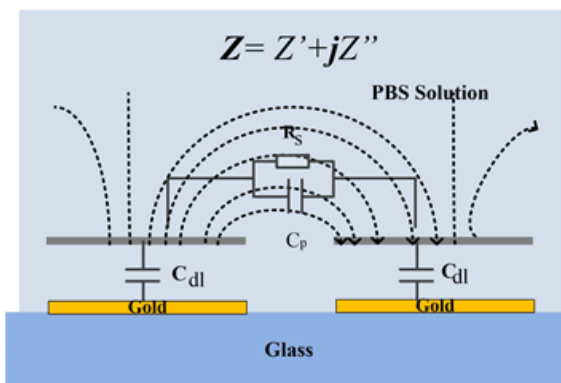


Figure 2. Model showing equivalent circuit of the impedance IDEAs sensor.

Figure 2 shows a commonly used model of the impedance IDEAs sensor. The impedance of IDEAs sensor can be separated by two parts including surface impedance and solution impedance. The surface impedance comes from the interface between gold electrodes and PBS solution which create double layer capacitances (C_{dl}). The double layer capacitance has been studied in many researches which are agreed that C_{dl} can be treated as constant phase element (CPE) [6]. The solution impedance constructs from the solution resistance (R_s) and the capacitance between two electrodes (C_p). By detecting these parameters, i.e., C_{dl} , R_s , C_p , we can sense the changes occurring on electrode surface or the changes in the medium between the electrodes.

EXPERIMENTAL RESULTS AND DISCUSSION

Performance of the IDEAs sensor has been experimentally evaluated through sensing the concentration of the phosphate buffer saline (PBS) fully filled in the microchannel. The experiments have been conducted measuring the impedance profile of IDEAs sensor in frequency range from $10\ \text{kHz}$ to $1\ \text{MHz}$ with PBS concentrations of $1\ \text{mM}$, $5\ \text{mM}$, $10\ \text{mM}$ and $20\ \text{mM}$, respectively.

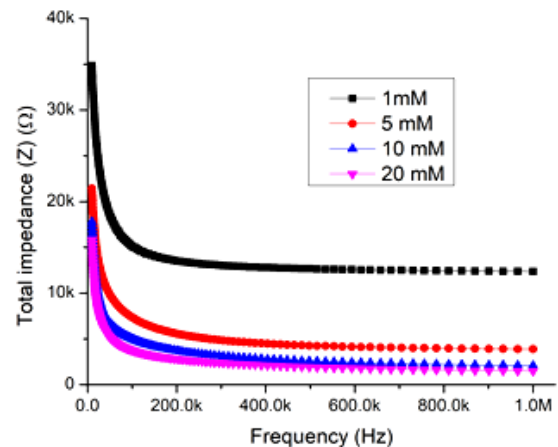
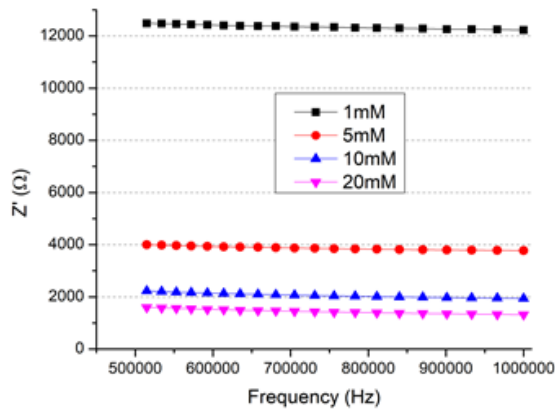
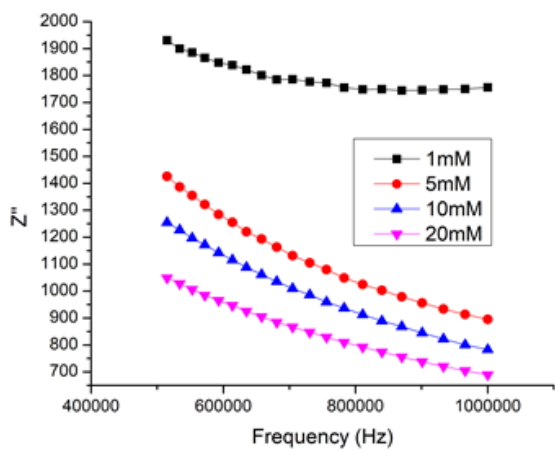


Figure 3. Electrical impedance spectroscopy measurement results of $1\ \text{mM}$, $5\ \text{mM}$, $10\ \text{mM}$ and $20\ \text{mM}$ PBS concentrations.

Figure 3 shows the impedance profiles results of the IDEAs sensor at with four PBS concentrations of $1\ \text{mM}$, $5\ \text{mM}$, $10\ \text{mM}$ and $20\ \text{mM}$. Impedance measurements were conducted in a wide frequency range, from $10\ \text{kHz}$ to $1\ \text{MHz}$. As can be seen, the impedance profiles of the four PBS concentration have the same form. The total impedance reduces significantly when the frequency increase from $10\ \text{kHz}$ to below $100\ \text{kHz}$. It means at low measurement frequency, the double layer capacitance is the main component effect to the change of the impedance. With measurement frequency in the range from $300\ \text{kHz}$ to $1\ \text{MHz}$, impedance value does not change much. At that high measurement frequencies, the total impedance reduces to R_s due to Z_{CPE} becomes small at high frequency.



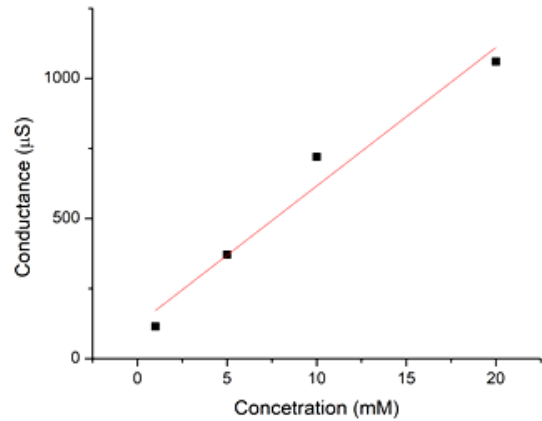
a)



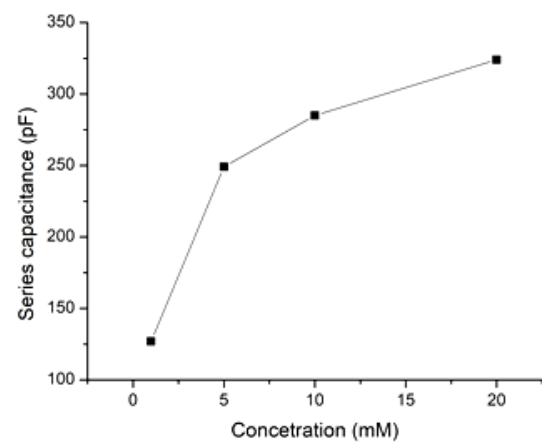
b)

Figure 4. Reality (a) and imaginary (b) part of impedance spectroscopy measurement results of 1mM, 5 mM, 10 mM and 20 mM PBS concentrations.

At high frequency, the total impedance reduces to solution resistance. Therefore, R_s can be approximated to the total impedance at high measurement frequency, i.e., at 1 MHz. The conductance then will be calculated from R_s . Figure 5a shows the calculated conductance changes corresponding to 1mM, 5 mM, 10 mM and 20 mM concentration of PBS. At measurement frequency of 1MHz, a scale factor of $74 \mu\text{S}/\text{mM}$ for the solution concentration is found. Experimental results are quasi-linearly fitted with a coefficient of 0.95 as shown in Figure 5a. From these results, we could confirm that the concentration of PBS solution can be measured by the proposed sensor.



a)



b)

Figure 5. Conductance and series capacitance of the IDAEs sensor corresponding to different PBS concentration. a) Calculated conductance b) Calculated series capacitance. The measurements were conducted at 1 MHz measurement frequency.

Besides, the concentration of PBS solution also affects to the double layer capacitance. As can be seen in the equivalent circuit, the surface impedance is mostly affected by the double layer capacitance. From the imaginary part, we could identify the series capacitance component which can be extracted by imaginary part by $C_s = (\omega \cdot Z'')^{-1}$. Figure 5b presents the measured series capacitance at 1 MHz corresponding to different concentration of PBS. As can be observed, the series capacitance also responds to the change of the solution concentration. Capacitance increases from 120 pF to 320 pF corresponding to the concentration change from 1mM to 20 mM. Then, the serial capacitance (C_s) which reflects the double layer capacitance at certain frequency can be used as a parameter

for sensing applications, such as for proteins detection [7, 8], where the medium change or bioparticles occurring inside microfluidic channel at the detection region can be detected.

CONCLUSION

The capacitive IDEAs micro-sensor integrated in the microchannel has been studied to find out the electrical parameters that is effective for the sensing purpose. The study has carried out electrical impedance spectroscopy measurement in a wide frequency range from 10 kHz to 1 MHz for measuring PBS concentrations. Experimental results demonstrate the ability to use the IDEAs sensor to detect double layer change at surface of electrodes and also the conductance change of medium between electrodes by analyzing reality and imaginary parts of total impedance of the IDEAs. This approach is high potential to be applied in biosensing applications.

References

- [1] H. Cui et al., "An AC electrokinetic impedance immunosensor for rapid detection of tuberculosis" *Analyst*, vol. **138**, no. 23, pp. 7188–7196, 2013.
- [2] M. A. Ibrahim Jasim, Zhenyu Shen, Zahar Mlaji, Nuh Yuksek, Amjed Abdullah, Jiayu Liu, Shib Dastider, Majed El-Dweik, Shuping Zhang, "An impedance biosensor for simultaneous detection of low concentration of Salmonella serogroups in poultry and fresh produce samples," *Biosensors and Bioelectronics*, vol. **126**, pp. 292–300, 2018.
- [3] G. V. Soraya et al., "An interdigitated electrode biosensor platform for rapid HLA-B*15:02 genotyping for prevention of drug hypersensitivity," *Biosensors and Bioelectronics*, vol. **111**, pp. 174–183, 2018.
- [4] Y. K. Yoo et al., "An Enhanced Platform to Analyse Low-Affinity Amyloid β Protein by Integration of Electrical Detection and Preconcentrator," *Scientific Reports*, vol. **7**, no. 1, pp. 1–8, 2017.
- [5] J. Hong, S. Yoon, K. Kim, S. Kim, S. Kim, and Y. Pak, "AC frequency characteristics of coplanar impedance sensors as design parameters," pp. 270–279, 2005.
- [6] P. Zoltowski, "On the electrical capacitance of interfaces exhibiting constant phase element behaviour," *Journal of Analytical & Bioanalytical Techniques*, pp. 149–154, 1998.
- [7] T. V. Quoc, M.-S. Wu, T. T. Bui, T. C. Duc, and C.-P. Jen, "A compact microfluidic chip with integrated impedance biosensor for protein preconcentration and detection," *Biomicrofluidics*, vol. **11**, no. 5, p. 054113, Sep. 2017.
- [8] Vu Quoc Tuan, Ngoc-Viet Nguyen, Meng-Syuan Wu, Chun-Ping Jen, Bui Thanh Tung, and Chu Duc Trinh, "Development of an Impedance Spectroscopy Measurement Circuit Board for Protein Detection," in *The International Conference on Communications and Electronics (ICCE-2018)*, Hue, Vietnam, 2018, pp. 184–188.

THE HEPATOPROTECTIVE EFFECTS ACTIVITY IN MICE OF GOLD NANOPARTICLES/ β -GLUCAN PREPARED BY GAMMA Co-60 IRRADIATION

Nguyen Trong Nghia¹, Do Thi Phuong Linh^{2,3}, Nguyen Thanh Vu¹, Nguyen Thi Ngoc Anh¹, Nguyen Hong Thoai Vy³, **Le Quang Luan^{1*}**

¹Biotechnology Center of Ho Chi Minh City, 2374, 1 Highway, Trung My Tay Ward, District 12, Ho Chi Minh City, Vietnam;

²Institute of Malarialogy Parasitology and Entomology in Ho Chi Minh City, 699 Tran Hung Dao Street, District 5, Ho Chi Minh City, Vietnam;

³Department of Biotechnology, Nong Lam University, Thu Duc District, Ho Chi Minh City, Vietnam
Email: lequangluan@gmail.com

ABSTRACT

Gold nanoparticles (AuNPs) with an average particle sizes about 13.3 nm were synthesized by γ -rays irradiation of 1.0 mM Au³⁺ solutions using low molecular weight β -glucan extracted from yeast cell wall as a stabilizer. The UV-Vis spectra and TEM images were used to analyze the optical characteristic and particle size of AuNPs. The hepatoprotective activity of AuNPs was tested in acetaminophen induced hepatotoxic mice with an average body weight of ~30 g/head by subcutaneous injection with concentrations of 0.05-0.5 mg/head. Both Alanine-aminotransferase (ALT) and Aspartate-aminotransferase (AST) indexes in blood of tested mice were found to decrease by the increase of injected concentration. In particular, the injection of above concentration decreased ALT index from 49.25 to 78.97% and AST index from 67.37 to 85.46% compared with those of the control without injection. In the group of mice injected with 0.25 mg AuNPs, the AST index in blood of tested mice was found at 47.43 U/L and decreased in 85% compared to that in blood of mice induced hepatotoxic and injected with only distilled water. The results show that AuNPs product synthesized by γ -rays irradiation may potentially be developed for application as a hepatoprotective liver agent.

Keywords: Acetaminophen, β -glucan, gold nanoparticles, γ -irradiation, hepatoprotective activity

INTRODUCTION

Nowadays, AuNPs have successfully attracted the attention and promised its effects and benefits on biosensor, bioimaging, and biomedical applications such as disease therapeutics, diagnostics, photothermal therapy, targeted delivery and cancer treatment [1]. Some studies have showed that AuNPs could absorb light and transfer it to thermal energy, so AuNPs conjugating to cancer cells can be heated by laser pulses to be used as the treatment for tumors [2]. AuNPs have been attached to EGFR antibody (Epidermal growth factor receptor) help antibody add strongly to cancer cells (higher 600 times more than normal cells) and kill cancer cells without affecting normal cells [3]. In addition, AuNPs can be used in some methods to eliminate the tumour in a short time [4]. Moreover, AuNPs have been had the ability to increase the production of hepatocytes when denatured in association with

cysteamine when added to culture medium liver cells [5].

Gamma ray irradiation is considered as an effective method due to several advantages such as: (1) the reaction can be carried out at room temperature; (2) yield of AuNPs is high; (3) AuNPs is purely prepared without contamination of excessive chemical reductant and Au³⁺ ions residue; (4) the size of AuNPs is easily controlled by varying Au³⁺ ions or seed enlargement approach [6, 7]; (5) mass production can be carried out and (6) processing is satisfied to requirement of clean production [8].

In the present study AuNPs/ β -glucan prepared by gamma ray (Co-60) irradiation was carried out and investigated its hepatoprotective activity in Swiss mice aiming to apply as a special hepatoprotective material.

EXPERIMENTAL

Materials

Hydrogen tetrachloroaurate (III) trihydrate (HAuCl₄·3H₂O) was purchased from Merck, Germany. Low molecular weight β -glucan extracted from yeast cell wall with Mw ~ 50 kDa was prepared at Bio-material and Nano Technology Department, Biotechnology Center of Ho Chi Minh City, Viet Nam. Acetaminophen (APAP) were purchased from Sigma Chemical Co. (St. Louis, MO, USA).

Synthesis of AuNPs/ β -glucan by gamma ray irradiation

The colloidal AuNPs with a concentration of 1.0 mM stabilized in 0.5% β -glucan were prepared as follow: the stock solution of 10 mM Au³⁺ was added to 2% β -glucan at an appropriate ratio with distilled water, and then adjusted pH ~ 8 by NH₄OH 2,5%. Subsequently, the above solutions were irradiated at 6 kGy by a gamma Co-60 GC-5000 sources (BRIT, India) at Biotechnology Center of Ho Chi Minh City with a dose rate of 10 kGy/h.

Characterization of AuNPs/ β -glucan

The optical characteristics and particle size of AuNPs were determined by UV-Vis spectrometry method and Transmission Electron Microscope (TEM) images, respectively [7]. The UV-Vis spectra of 0.1 mM AuNPs samples measured by a UV-Vis spectrophotometer model Genesys 10S UV-Vis (Thermo, USA). The AuNPs size and morphological characteristics were identified by a JEM 1400, JEOL (Japan) and statistically calculated from about 300 particles followed the method described by Aryal et al [9].

Determination of hepatoprotective effects of AuNPs in APAP induced hepatotoxic mice

The 4-week-old Swiss albino mice were supplied by Pasture Institute in Ho Chi Minh City and fed for 8 weeks and their average body weight was about 30 g.

In total, 144 female mice were randomly designed into two groups of 72 mice each: Normal group and APAP induced hepatotoxic group. Each group divided with eight experiments consisting of 9 mice. Each mouse was tail vein injected with 0.2 mL AuNPs/ β -glucan solution containing from 0 (only irradiated β -glucan) to 0.5 mg/head. All animals were injected three times after every 7 days. The control experiment received only water

injection. On 22nd day, mice in the “APAP induced hepatotoxic group” were injected with APAP at a dose of 500 mg/kg body weight followed by Morsy et al. [10]. The mice after intravenous injection with APAP 24 h, 0.5 mL blood from the myocardium of tested mice was collected and put into tubes containing heparin for analysis. The collected blood was then centrifuged at 4500×g for 10 min to separate the serum. The obtained serum was then used for analyzing the serum’s clinical chemistry indexes including aspartate aminotransferase (AST) and alanine aminotransferase (ALT) by a Beckman Coulter Au480 analyzer (USA).

All experiments were carried out in triplicate and data were statistically analyzed using the analysis of variance (ANOVA) test.

RESULTS AND DISCUSSION

Synthesis and characterization off AuNPs/ β -glucan

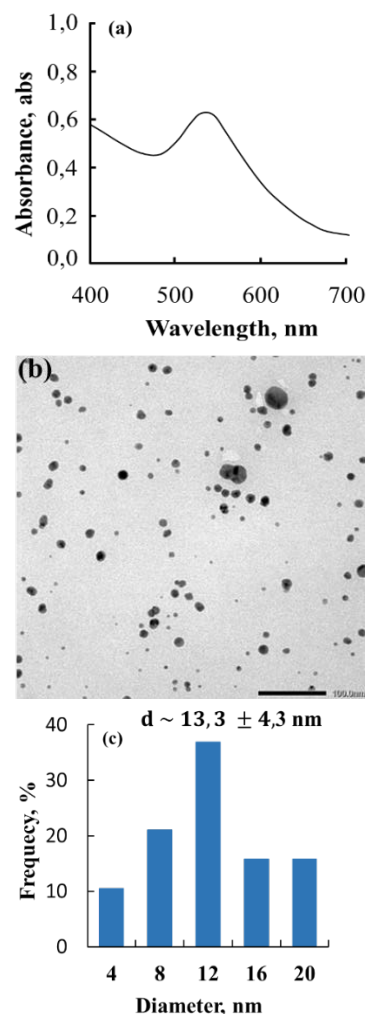


Figure 1. UV-vis spectra (a), TEM image (b) and histogram of particle size distribution (c) of AuNPs prepared by γ -rays irradiation method

The UV-Vis spectrum of AuNPs solution in Figure 1a showed the maximum absorption wavelength (λ_{max}) at 521 nm and this peak is the characteristic of the surface plasmon resonance band of AuNPs and preliminary confirmed the formation of gold nanoparticles [7,11]. The TEM image and particles size distribution are shown in figures 1b and 1c. The average diameter of AuNPs was determined to be about 13.3 nm with a fairly narrow distribution.

Effect of AuNPs/ β -glucan on AST index in mice

The hepatoprotective activity of AuNPs was tested in Swiss mice by subcutaneous injection. The results in Figure 2 show that after injecting AuNPs/ β -glucan with concentrations of 0 - 0.5 mg/head, the AST index of mice in both normal and APAP induced hepatotoxic groups of mice were decreased. Particularly, AST index in the APAP induced hepatotoxic group was found from 326.13 to 47.43 U/L and from 152.1 to 46.3 U/L in normal mice.

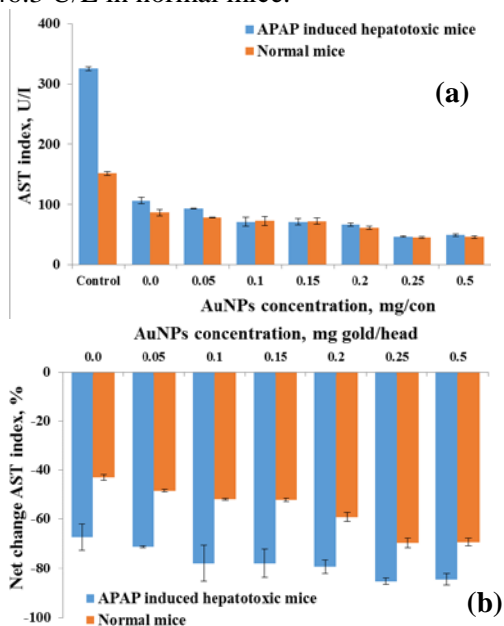


Figure 2. The reduction of AST index in the blood of APAP induced hepatotoxic and normal mice (a) and net change AST index (b) by subcutaneous injection of AuNPs at various doses

In the APAP induced hepatotoxic group (Figure 2a), the injection of 0.25 mg/head AuNPs strongly reduced the AST index to 85% and 67% compared to those in the control mice (injected with only water) and in the mice injected with irradiated β -glucan (without AuNPs), respectively. These results indicated

that AuNPs had strong effect on the decreasing AST index in APAP induced hepatotoxic mice and the dose of 0.25 mg/head was the optimum effective for reduction of AST in mice.

On the other hand, the colloidal AuNPs/ β -glucan product also showed an effect on lowering the AST index in the blood of normal mice. The injection of AuNPs with doses of 0.25 - 0.5 mg/head reduced about 69% the AST index compared to that in the control mice (Figure 2b).

Effect of AuNPs/ β -glucan on ALT index in mice

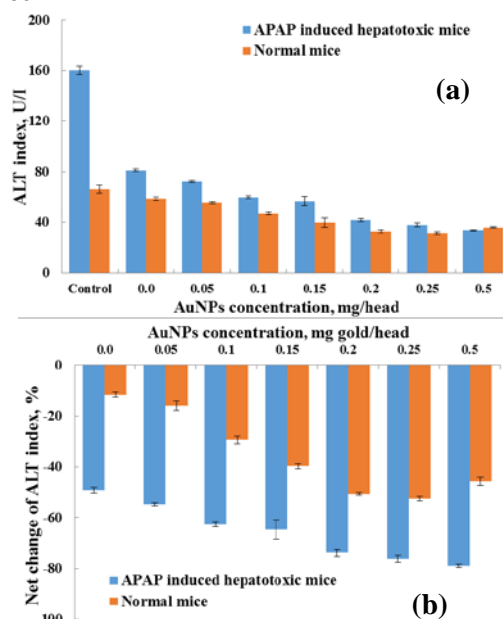


Figure 3. The reduction of ALT index in the blood of APAP induced hepatotoxic and normal mice and net change ALT index by subcutaneous injection of AuNPs at various doses

Besides AST, ALT is also a large quantities enzyme founded in the liver and this enzyme plays an important role in metabolism. ALT is usually increased in blood when liver cells were damaged. In this study, there was a big difference on ALT index between normal and APAP induced hepatotoxic mice.

The results in Figure 3a showed that in normal group, the ALT index was in range of 31.5 to 66.43 U/L and the lowest (31.5 U/L) of this value was found in blood injected with 0.25 mg/head was only

In the hepatotoxicity group, the results from Figure 3a show that the ALT index was decreased by the increase of AuNPs concentration. In particular, the ALT index in blood of mice injected with 0 - 0.5 mg/head were found at 81.33 - 33.7 U/L, respectively. In compare to the control, the injection of 0.25

mg/head was reduced 78.97% the AST value in blood of tested mice (Figure 3b).

It can be seen from the results of this study that the tail vein injection with 0.25 mg/head of AuNPs/ β -glucan preparations by gamma Co-60 strongly reduced the AST and ALT index in APAP induced hepatotoxic mice. Negahdary et al., (2015) has been also demonstrated that gold nanoparticles with a particle size of about 10 nm also had the effect of reducing the CAT and GPX index in Wistar mice [12].

CONCLUSION

AuNPs with particle sizes about 13.3 nm was successfully synthesized by γ -irradiation using β -glucan extracted from the yeast cell wall as the stabilizer. AuNPs/ β -glucan displayed a strongly reduction of ALT and AST indexes in APAP hepatotoxic mice after 21 days injecting with 0.25 mg/head. The results show that AuNPs product synthesized by γ -irradiation may potentially be developed for application as a hepatoprotective liver agent.

Acknowledgment

This research is supported by the Biotechnology Center of Ho Chi Minh City (project number NN01/17-19) and Ministry of Science and Technology (project number KC.05.16/16-20).

References

- [1] S. Bharathiraja, P. Manivasagan, N. Q. Bui, Y. O. Oh, I. G. Lim, S. Park, J. Oh, *Cytotoxic induction and photoacoustic imaging of breast cancer cells using astaxanthin-reduced gold nanoparticles*, *Nanomaterials* **6** (2016), 78.
- [2] X. Huang and M. A. El-Sayed, *Gold nanoparticles: optical properties and implementations in cancer diagnosis and photothermal therapy*, *Journal of Advanced Research* **1** (2010), 13-28.
- [3] C. R. Patra, R. Bhattacharya, D. Mukhopadhyay and P. Mukherjee, *Fabrication of gold nanoparticles for targeted therapy in pancreatic cancer*, *Advanced drug delivery reviews* **62** (2010), 346-361.
- [4] I. H. El-Sayed, X. Huang, M.A. El-Sayed, *Selective laser photo-thermal therapy of epithelial carcinoma using anti-EGFR antibody conjugated gold nanoparticles*, *Cancer Letter* **39** (2006),129-135.
- [5] H. Y. Gu, Z. Chen, R. X. Sa, S. S. Yuan, H. Y. Chen, Y. T. Ding, A. M. Yu, *The immobilization of hepatocytes on 24 nm-sized gold colloid for enhanced hepatocytes proliferation*, *Biomaterials* **25** (2004), 3445-3351.
- [6] D. T. P. Linh, N. T. Nghĩa, L. Q. Luân, *Nghiên cứu sự phân bố của vàng nano/carboxymethyl chitosan chế tạo bằng bức xạ γ -co-60 sau khi tiêm tĩnh mạch ở chuột*, *Tạp chí Công nghệ Sinh học* **16** (2018), 1-7.
- [7] L. Q. Luan, D. T. P. Linh, N. H. P. Uyen, D. V. Phu, N. Q. Hien, *Biodistribution of gold nanoparticles synthesized by γ -irradiation after intravenous administration in mice*, *Advances in Natural Sciences: Nanoscience and Nanotechnology* **5** (2014), 025009.
- [8] N. N. Duy, D. X. Du, D. V. Phu, L. A. Quoc, B. D. Du, N. Q. Hien, *Synthesis of gold nanoparticles with seed enlargement size by γ -irradiation and investigation of antioxidant activity*, *Colloids and Surfaces A: Physicochemical and engineering aspects* **436** (2013), 633-638.
- [9] S. Aryal, N. Bhattarai, H. Y. Kim, *Radical scavenger for the stabilization of gold nanoparticles*, *Materials Letters* **61** (2007), 4225-4230.
- [10] M. A. Morsy, S. A. Ibrahim, S. A. Abdelwahab, M. Z. Zedan, H. I. Elbitar, *Curative effects of hydrogen sulfide against acetaminophen-induced hepatotoxicity in mice*, *Life Sciences* **87** (2010) 692-698.
- [11] N. T. Anh, D. V. Phu, N. N. Duy, B. D. Du, Hien N. Q., *Synthesis of alginate stabilized gold nanoparticles by γ -irradiation with controllable size using different Au^{3+} concentration and seed particles enlargement*, *Radiation Physics and Chemistry* **79** (2010), 405-408.
- [12] M. Negahdary, R. Chelongar, S. K. Zadeh, M. Ajdary, *The antioxidant effects of silver, gold, and zinc oxide nanoparticles on male mice in in vivo condition*, *Advance Biomedical Research* **4**, (2015), 1-5.

APPLICATION OF AgNPs/PVA PREPARED BY GAMMA RAYS IRRADIATION FOR INCREASING SURVIVAL RATE OF TRA CATFISH INOCULATED WITH *EDWARDSIELLA ICTALURI*

Le Quang Luan, Lam Vy Nguyen Hang Khanh Linh and Duong Hoa Xo

Biotechnology Center of Ho Chi Minh City, 2374, 1 Highway, Trung My Tay Ward, District 12, Ho Chi Minh City, Vietnam

Email: lequangluan@gmail.com

ABSTRACT

The silver nanoparticles/polyvinyl alcohol (AgNPs/PVA) prepared by γ -rays irradiation of a solution containing 10 mM silver nitrate and 2% PVA at a dose of 22 kGy, had particle size of about 12.7 nm. The *in vivo* bactericidal effectiveness of AgNPs was tested in cultured ponds of fingerling Tra catfish after inoculating with *Edwardsiella ictaluri* (5H) bacteria at 105 cfu/mL. The results showed that the increase of AgNPs concentration reduced death rate of tested fishes and total bacteria number in cultivated water. At the treatment of 1 ppm AgNPs, no death fish was observed and the total bacteria number in cultivated water after culturing 30 days was quite low (about 2.300 cfu/mL for the condition without change the cultivated water and about 345 cfu/mL for the condition of the cultivated water was changed every 10 days). While the 100% fishes in the negative control inoculated with pathogenic bacteria and without treating with AgNPs were dead after 10 days of culturing and fish liver was attacked by *E. ictaluri*. It can be concluded that AgNPs/PVA synthesized by γ -rays irradiation had a high bactericidal effectiveness and showed a potential application as a safety and effective agent for killing pathogenic bacteria in water for fingerling Tra catfish culture, replacing the use of antibiotics in pangasius farming today.

Keywords: Tra catfish, bactericidal, *Edwardsiella ictaluri*, irradiation, silver nanoparticles

INTRODUCTION

Tra catfish (*Pagasianodon hypophthalmus*) is the main exporting product of Vietnamese aquaculture. It has made handsome profits for Vietnamese farmer and the Tra catfish culture area has been significantly increased for a recent few years. In the first three months of 2018, the Tra catfish industrial culture area and the yield increased by 2.1% and 5.7%, respectively, as compare with the same period last year [1]. However, the increase of the culture area can not control lead to the environment problem and the common disease. Therein, the Edwardsiellosis disease which is a specific disease catfish caused by *E. ictaluri* is the main disease lead to the high death rate of fishes (90-100%) [2]. This infectious disease may be occurred at all times during the year and fish age, especially at fingerling Tra catfish. However, farmers often treat by different antibiotics lead to bacterial resistance and decreasing effectiveness of the treatment [3]. In addition, the antibiotic residues in fish also is the obstacles to export causes serious losses of economy and the commercial competitiveness of Tra catfish on the market.

In addition, AgNPs were extensively studied and were widely used for a long time due to their unique properties such as antibacterial, fungal inhibition, odor removal, etc. at low concentration as well as safe to the human and the environment. These particles proved to have very strong bactericidal activity against both gram-positive and gram-negative bacteria [4-6]. Moreover, irradiation which gamma rays using a Co-60 source was considered as an effective method of silver nanoparticles synthesis. The advantages of irradiation method were energy, room and materials saving; environmental friendly; process can be conducted at ambient temperature and could be easily upscale to pilot production with reasonable price [7-9].

The above information suggested that the AgNPs/PVA may also be applied to inhibit several plant pathogens caused by microorganism. Therefore, this research aimed to synthesize silver nanoparticles/ Poly vinyl alcohol from natural product, safe to human and effective in Tra catfish cultivated water treatment.

EXPERIMENTAL

A. Materials

Silver nitrate (powder) and Poly vinyl alcohol were purchased from Merck (Germany). Brain Heart Infusion (BHI) Broth and Plate Count Agar were purchased from Himedia, India. *E. ictaluri* (5H) and Tra catfishes (4-months old) were provided by Biotechnology Center of Ho Chi Minh City.

B. Preparation of colloidal AgNPs

AgNPs with particle size about 12.7 nm was prepared by γ -Co 60 irradiation of the solution contained 10 mM Ag⁺ and 2% polyvinyl alcohol (PVA) at 22 kGy. The UV-Vis spectrum and TEM image of AgNPs were taken using a BioSpec-mini Shimadzu spectrophotometer (Japan) and Transmission Electron Microscope (JEM 1400, Japan).

C. In vivo antibacterial effect of AgNPs

Tra catfishes (4-month old) were divided into two groups and cultivated with the density of 20 fish/pond.

- The unchanged cultivated water condition: The Tra catfish cultivated medium was supplemented with AgNPs/PVA at concentration of 0.25, 0.5, 0.75 and 1.0 ppm and poisoned by *E. ictaluri* (10⁵ cfu.mL⁻¹).

- The changed cultivated water condition: The cultivated water was changed every 10 days and supplemented with AgNPs/PVA and Virkon (checking sample) at concentration of 1 ppm. Afterward, Tra catfishes were poisoned by *E. ictaluri* (10⁵ cfu.mL⁻¹).

After 5, 10, 15, 25 and 30 cultivation days, the fish dead rate and the total bacteria number in pond were determined. In addition, *E. ictaluri* in liver of dead fish was identified by PCR amplifications. PCR primers (IDT):

serC_F: 5'-TCTGGTTCTGGCCGAATATGGACTC-3'
serC_R:5'-CGTAATCAAACCAACACCGGGTATT-3'

The negative control Tra catfish was only poisoned by *E. ictaluri* and the control was the normal Tra catfish.

RESULTS AND DISCUSSION

A. Preparation and characterization of AgNPs/PVA

The AgNPs with particle size about 12.7 nm, stabilized by PVA were synthesized using γ -irradiation method. The results of UV-vis absorption spectrum in Figure 1 indicated that AgNPs solution showed maximum absorption wavelength (λ_{max}) at 407 nm for Ag⁺ concentration of 10 mM.

In addition, AgNPs were further analyzed by TEM analysis. TEM image and particles size distribution of AgNPs (Fig. 1) showed small sizes particles (~12.7 nm) with regular shapes and narrow Gaussian size distribution. Quantitative analysis of AuNPs size was performed by measuring the core diameter of 300 individual particles from multiple micrographs (Fig. 1) [10].

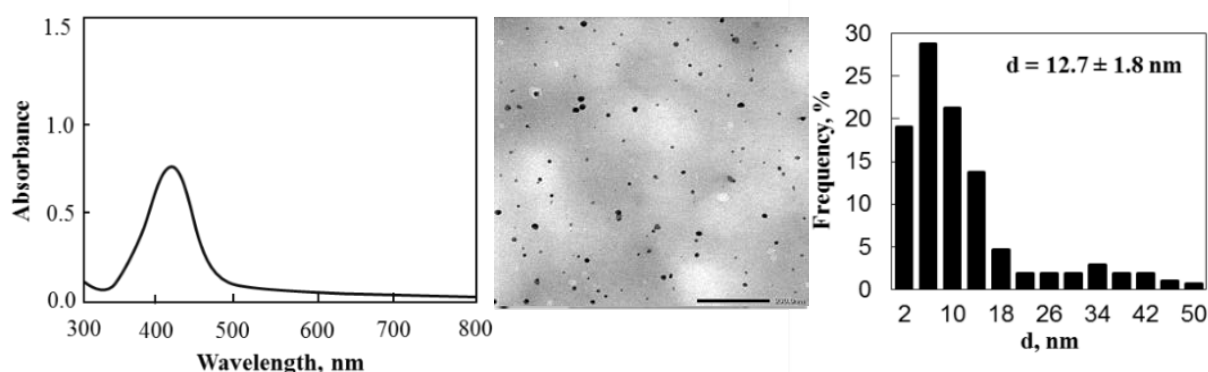


Figure 1. UV-vis spectra (left), TEM image (middle) and histogram of particle size distribution (right) of AgNPs prepared by irradiation method

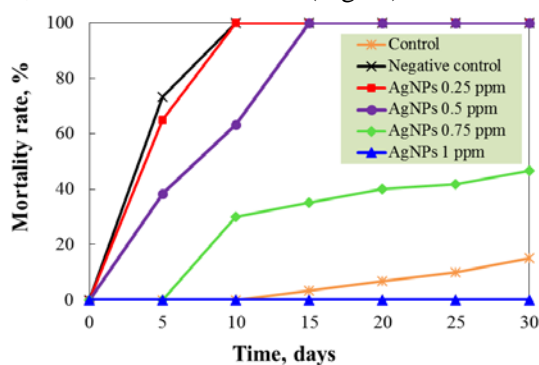
B. The in vivo antibacterial effect of AgNPs

The antibacterial activities of AgNPs/PVA at different concentrations on 4-months old Tra catfish were determined using two water-conditions.

The unchanged cultivated water condition

The results from Fig. 2 shown that the 100% fishes in the negative control and in the treatment of 0.25 ppm AgNPs were dead after 10 days cultivating. The mortality rate of fish

was significantly decreased from 63.3 to 30.0% when AgNPs concentration increased from 0.5 to 1 ppm, although the 100% fishes in the treatment of 0.5 ppm AgNPs were dead after 15 days. While the mortality rate of fish after 30 days in control group was rather low (~15%). In addition, the PCR test results (Fig. 3) showed



that *E. ictaluri* DNA appeared in all of liver of dead fishes.

Furthermore, the death fish was not observed and the total bacteria number in cultivated water after 30 days at the treatment of 1 ppm AgNPs was quiter low (~ 2300 cfu/mL).

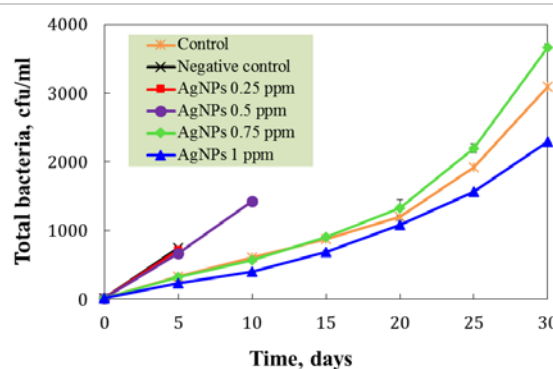


Figure 2. The dead rate of Tra catfish (left) and total bacteria in cultivated water (right) in pond treated with AgNPs and infested by *E. ictaluri*.

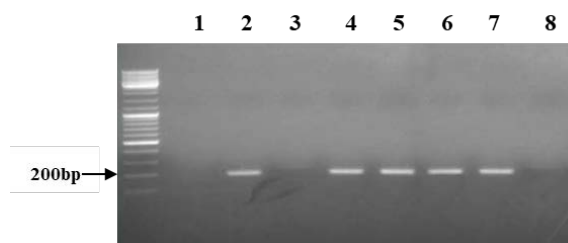


Figure 3. Genotype confirmation of *E. ictaluri* in liver of dead fish by PCR with primers *serC_F* and *serC_R* in the unchanged cultivated water condition. (1): None of *E. ictaluri* DNA, (2): *E. ictaluri* DNA, (3): Control, (4): Negative control, (5): 0.25 ppm AgNPs, (6): 0.5 ppm AgNPs, (7): 0.75 ppm AgNPs, (8): 1 ppm AgNPs

The changed cultivated water condition

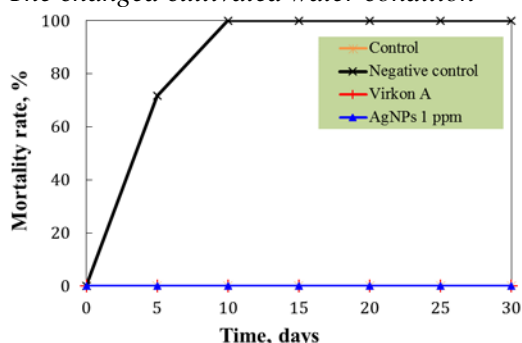


Figure 4. The cumulative mortality of Tra catfish cultured in pond treated with AgNPs (1 ppm), Virkon A (1 ppm) and infested by *E. ictaluri*

The results from Fig. 4 showed that only the negative control appeared dead fish and pathogenic symptom while the dead fish was not

observed in others. After 3-days cultivating, pathogenic symptom appeared in only the negative control. After 5-days culturing, the mortality rate of fish significantly increased to 71.7% and it enormously increased to 100% after testing 7 days. In addition, the amplification product of about 200 bps in the PCR results (Fig. 5) indicated that there is the appearance of *E. ictaluri* in the liver of dead fish sample.

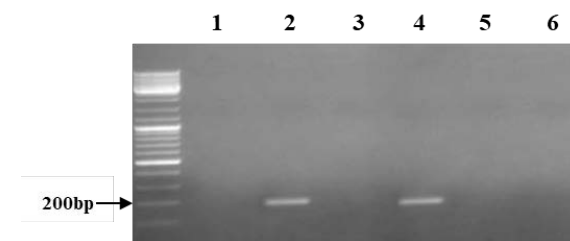


Figure 5. Genotype confirmation of *E. ictaluri* in liver of dead fish by PCR with primers *serC_F* and *serC_R* in the changed cultivated water condition. (1): None of *E. ictaluri* DNA, (2): *E. ictaluri* DNA, (3): Control, (4): Negative control, (5): Virkon A, (6): 1 ppm AgNPs

The total bacteria number in cultured water considerably changed to a low level after changing the cultivated water (Table 1). Furthermore, the total bacteria number in the Virkon A supplemented sample was the lowest (119 cfu/mL) after 30-days culturing. While these value were 345 cfu/mL and 445 cfu/mL in the supplemented with 1 ppm AgNPs and control, respectively.

Table 1: The total *b5*acteria number in pond, cfu/mL

Time, day	Control	Negative control	Virkon A	AgNPs
0	11 ± 1.2	12 ± 1.0	11 ± 2.1	11 ± 1.2
5	195 ± 11.6	747 ± 45.1	47 ± 6.7	193 ± 17.3
10	395 ± 1.0	-	118 ± 0.6	313 ± 0.6
The first change of cultivated water				
10	10 ± 0.6	-	11 ± 0.6	13 ± 2.0
15	325 ± 15.3	-	44 ± 4.0	190 ± 15.3
20	400 ± 1.5	-	121 ± 3.2	327 ± 2.1
The second change of cultivated water				
20	10 ± 0.6	-	9 ± 0.6	11 ± 2.1
25	210 ± 5.6	-	46 ± 3.8	197 ± 20.8
30	445 ± 2.1	-	119 ± 1.2	345 ± 1.5

(-): All of *Tra catfish* died

CONCLUSION

The AgNPs/PVA with size of about 12.7 nm stabilized in PVA have been successfully synthesized by gamma Co-60 irradiation method. The synthesized AgNP products showed a strongly antibacterial activity against *E. ictaluri* caused Edwardsiellosis disease on *Tra catfish*. The survival rate of fishes is extremely high by treating with a low AgNPs/PVA concentration (about 1 ppm). The AgNPs/PVA synthesized by gamma Co-60 irradiation was potentially used as an agent for killing pathogeneouse bacteria in cultural water due to the environmental-friendly production technology, highly antibacterial effect and safe use of them.

References

[1] Tổng cục thủy sản, Báo cáo sơ kết 6 tháng đầu năm 2018 của ngành Thủy sản Việt Nam, Bộ Nông nghiệp và Phát triển Nông thôn, 2018.

[2] Trần Hoàng Ngâu, Nguyễn Thị Ngọc Bích, Lại Thị Thùy Dương, Nghiên cứu phát hiện vi khuẩn *Edwardsiella ictaluri* gây bệnh gan thận mũ trên cá tra (*Pangasius Hypophthalmus*) bằng phương pháp multiplex PCR, Kỷ yếu hội thảo kỷ niệm 35 năm thành lập Trường ĐH Công nghiệp Thực phẩm TP. Hồ Chí Minh 2017, 30-37.

[3] Đặng Thị Hoàng Oanh và Nguyễn Thanh Phương, Thử nghiệm điều trị bệnh do vi khuẩn *Edwardsiella ictaluri* trên cá tra (*Pangasius Hypophthalmus*) bằng thuốc kháng sinh Erythromycin Thiocyanate, Tạp chí Khoa học **22** (2012), 146-154.

[4] Panacek, L. Kvítek, R. Prucek, M. Kolar, R. Vecerova, N. Pizúrova, V. K. Sharma, T. Nevecna, R. Zboril, *Silver colloid*

nanoparticles: Synthesis, characterization, and their antibacterial activity, The Journal of Physical Chemistry **110** (2006), 16248-16253.

[5] J. R. Morones, J. L. Elechiguerra, A. Camacho, K. Holt, J. B. Kouri, J. T. Ramirez, *The bactericidal effect of silver nanoparticles*, Nanotechnology **16** (2005), 2346-2353.

[6] L. T. A. Nhien, N. D. Luong, L. T. T. Tien and L. Q. Luan, *Radiation Synthesis of AgNPs/CTS for Controlling Leaf Fall Disease on Rubber Trees Causing by C. cassiicola*, Journal of Nanomaterials **2018** (2018), 1-9.

[7] D. Du, D. V. Phu, B. D. Cam, N. Q. Hien, *Synthesis of silver nanoparticles by γ -ray irradiation using PVA as stabilizer*, Vietnam Journal of Chemistry **45** (2007), 136-140.

[8] T. Li, H. G. Park, S. H. Choi, *γ -Irradiation-induced preparation of Ag and Au nanoparticles and their characterizations*, Materials Chemistry and Physics **105** (2007), 325-330.

[9] K. Naghavi, E. Saion, K. Rezaee, W. M. M. Yunus, *Influence of dose on particle size of colloidal silver nanoparticles synthesized by gamma radiation*, Radiation Physics and Chemistry **79** (2010), 1203-1208.

[10] L. Q. Luan and D. H. Xo, *In vitro and in vivo fungicidal effects of γ -irradiation synthesized silver nanoparticles against *Phytophthora capsici* causing the foot rot disease on pepper plant*, Journal of Plant Pathology **100** (2018), 241-248.

DEVELOPMENT OF A FLOW FOCUSING DROPLET GENERATION MICROFLUIDIC SYSTEM BASED ON RAPID PROTOTYPING TECHNIQUE

Loc Do Quang¹, Tuan Vu Quoc², Cuong Nguyen Nhu³, Hang Nguyen Thu³, Hang Tran Thanh³, Tung Thanh Bui³, Trinh Chu Duc^{3*}

¹ Faculty of Physics, VNU University of Science, Vietnam National University, Hanoi, Vietnam

² Institute of Applied Physics and Scientific Instrument, Vietnam Academy of Science and Technology, Hanoi, Vietnam

³ VNU University of Engineering and Technology, Vietnam National University, Hanoi, Vietnam
Email: trinhcd@vnu.edu.vn

ABSTRACT

Along with the rapid development of microfluidic systems and their integration into the point-of-care devices over the past decade, droplet microfluidic has emerged as an essential research area which is highly demanded in various research field such as life science research, material synthesis and drug discovery. In this paper, a microfluidic system based on microfluidic channel is developed to operate the function of generating air bubble and fluidic droplet. Droplets are generated based on the flow focusing droplet generator technique which can generate highly monodisperse droplets of varying sizes. The proposed system is fabricated using rapid prototyping techniques with PDMS molding and printed board circuit. A numerical calculation was implemented to study and analyze the operation of the proposed structure. The results from this study can be utilized as a versatile tool for widespread applications especially in synthesis of microcapsule, microparticles, and microfibers applicable to pharmaceuticals, cosmetics, foods and other lab-on-a-chip applications.

Keywords: Rapid prototyping, microfluidic, droplet generation.

INTRODUCTION

In the recent decades, the development of droplet based on microfluidics and micro-bubble has received tremendous attention from researcher. Micro-droplet emerged as a promising tool for a variety of applications in abundant field such as biology, chemistry and nanotechnology. Droplet microfluidics can be utilized to handle single or multiple cells with precise manipulation of the cell count [1] and be indispensable for cell synthetic, molecular detection and analysis. Additionally, biochemistry in microdroplet, self-droplet microcapsules [2], [3], microparticles [4], and microdroplet in microfluidic system as biochemical micro reactors are promising applications of microdroplet generation techniques. Droplet generation microfluidics has great influences on drug delivery vehicles and drug molecular [5]. The use of microdroplet in these applications has numerous advantages such as low fabrication costs, reduction of consumed reagents and waste, decrease in analysis durations, high-throughput assay with special sensitivity.

In order to generate microdroplet and air bubble in microfluidics system, two immiscible phases, i.e., fluid and gas, are manipulation in microfluidic channel. Several typical structures have been proposed to produce droplet, which consists of cross-flow, co-flow, flow-focusing, step emulsification and microchannel emulsification [6]. In flow-focusing device, two lateral channels are fed with continuous phase while the dispersed phase is injected into middle channel, after that, the two immiscible phases are focused and microdroplet are generated.

In the above-mentioned applications, controlling of quantity and qualitative of droplet and bubble in micro-scale is absolutely vital. The generation of microdroplet are expected to be predictable and well-controlled; and the highly-uniform of monodisperse droplet with varying size is essential for most of applications. In this paper, we propose a droplet generation device using flow-focusing structure integrated with microfluidic system. The proposed device is fabricated by 3D printing technology and printed circuit board (PCB) with the advantages of low fabrication cost, short fabrication time.

The numerical calculations and experiments were carried out to verify and characterize the operation of this proposed device.

FLOW FOCUSING DROPLET GENERATION MICROFLUIDIC SYSTEM

Figure 1 presents the proposed droplet generation structure for droplet formation. The proposed structure includes two sheath channels and one middle channel, which have the width of 600 μm and 100 μm , respectively. The flows from middle channel and two sheath channels meet at the break-up junction, where the liquid flows squeeze the flow into bubbles or droplets. The liquid channels are both fed by one water inlet and were designed symmetrically. Therefore, the flow rate of both liquid channels at the break-up junction are considered at the same velocity. This ensures the influence of such two channels are identical.

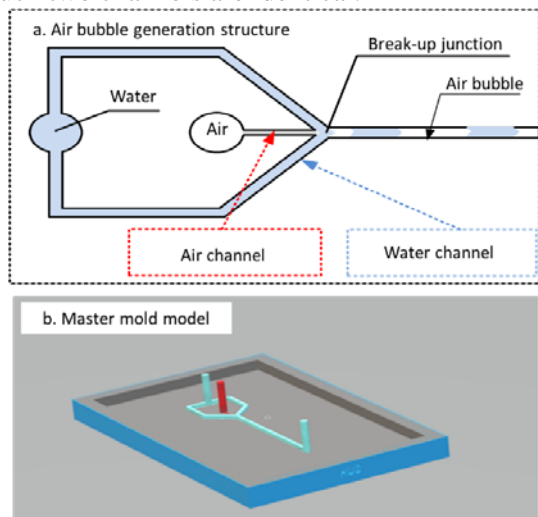


Figure 1. (a) The proposed structure and (b) The designed master mold model.

A numerical calculation was implemented to study and analyze the operation of the proposed structure. The simulation is based on phase-field method to solve the interfacial problems, i.e. the interface between the two immiscible fluids. Each fluid domain is assigned to a distinct value with a smooth change between both values in the zones where two flows meet. The meshing model and boundary conditions are shown in figure 2. Due to the symmetrical design of the microchannel structure, only one half of device is modeled and solved. The model is simulated with the inlet of air and water at the inlet 1 and inlet 2 respectively. The flowrate at the water inlet is 12 mm/s while such value at the inlet of air is 6 mm/s.

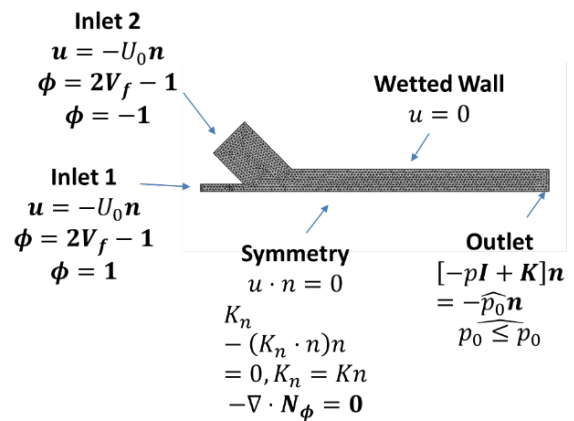


Figure 2. Simulation: Meshing model and boundary conditions.

FABRICATION

The fabrication of the devices is based on 3D printing technology for PDMS mold and the standard printed circuit board technology. The process based on 3D printing molding is shown in Figure 3.

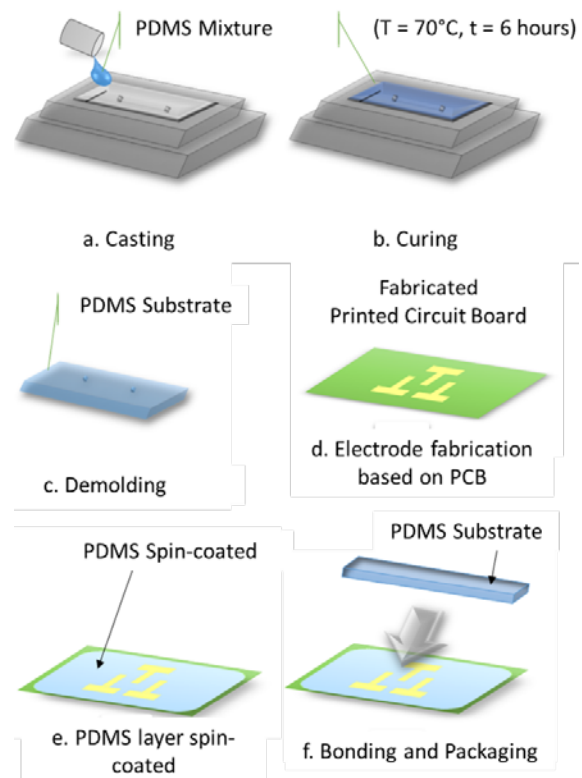


Figure 3. The fabrication process based on 3D printing mold.

A PDMS prepolymer and a curing agent (Sylgard-184 Silicone Elastomer Kit, Dow Corning, Midland, MI, USA) were first mixed at a weight ratio of 10:1, stirred thoroughly before being casting into the 3D mold (Figure 3.a). The

mixture was then cured at the temperature of 70°C for 6 hours (Figure 3.b). Once the PDMS mixture had hardened, the PDMS substrate was carefully peeled off from the mold (Figure 3.c). The master mold (Figure 1.b) patterned the microchannel shape into the PDMS bulk. The electrodes pattern of the proposed structure was fabricated using standard printed circuit board technique (Figure 3.d). The PCB substrate was spin-coated with an additional thin layer of PDMS to facilitate to bonding process between the PDMS bulk and the PCB substrate (Figure 3.e). Apart from acting as an adhesive layer for binding and preventing fluid from leakage, the proposed thin PDMS coating layer also helps protect the electrode from direct contact with the liquid in the microchannel.

RESULTS AND DISCUSSIONS

The simulations were conducted and results are obtained. The volume fraction of each material is plotted to study the generation of the droplet (Figure 4). It can be observed that the formation of the bubble includes four phases. The initial phase is the intrusion of the head of the air phase into the downstream of water (Figure 4.a). As the head of the oil phase continues to be dragged further ahead of the middle channel, it then dominates the breakup junction and block the flow path of water (Figure 4.b). Since the velocity of water flow is much higher than that of air, the interfacial tension force between two flow increases and it squeezes and breaks the tip of the air flow, this creates a bubble or droplet inside the microchannel (Figure 4.c). After the droplet is released, the process is repeated by the injection of air flow (Figure 4.d).

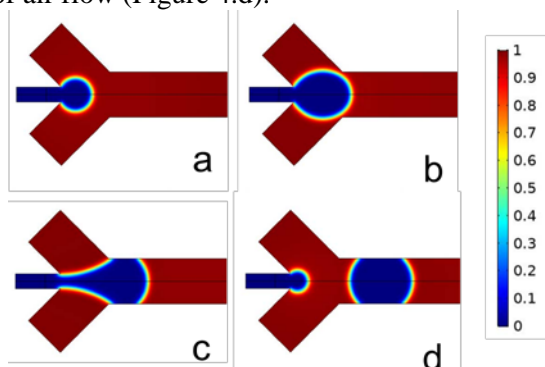


Figure 4. COMSOL simulation results of proposed droplet generation structure.

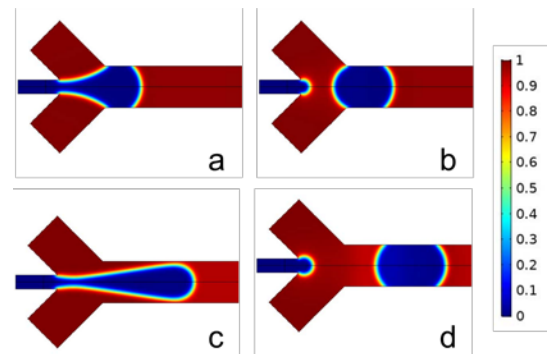


Figure 5. Volume fraction of water prior to breaking up and after breaking up with water flow rate of (a-b) 6mm/s (c-d) 12mm/s.

The simulation model was further extended to study the influence of flow velocity on the droplet formation. Figure 5 represents the results of droplet formation with the flow velocity are 12 mm/s and 6 mm/s (Figure 5. a-b) and 12mm/s and 12 mm/s (Figure 5. c-d). at the sheath channel and middle channel, respectively. The high velocity of the water flow results in the fact that the tip of the air flow is propelled further to downstream before it breaks from the main flow (Figure 5.c). In addition, it can also be inferred that the air bubbles created as a result of higher liquid flow rate are also bigger compared to one produced by lower flow rate (Figure 5.d)

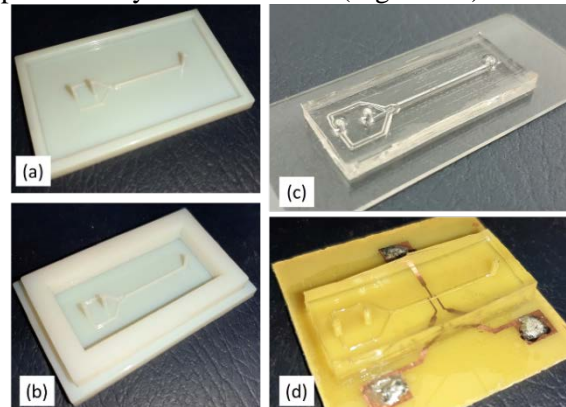


Figure 6. Image of the 3D printed mold structure (a), the PDMS mold substrate. Packaged PDMS mold (b), demolded PDMS bulk (c), and the fabricated PDMS on PCB substrate system (d).

Experiments were implemented. The PDMS mold is realized by 3D printed technology (Stratasys Objet500 Connex3). Mold fabrication results are shown in Figure 6. a-b. The mold consists of two parts, a substrate with extruded patterns to create microfluidic channels after the PDMS mixture has fully cured (Figure 6.a) and a rectangular plastic ring to form the wall hold

the PDMS mixture during curing time (Figure 6.b). This design of mold allows demolding PDMS substrate from master mold and minimizing the channel breakage while the PDMS substrate is peeling off from the mold. The demolded PDMS substrate has successfully fabricated (Figure 6.c). It was then transferred and bonded to the PCB substrate in order to package the proposed systems.

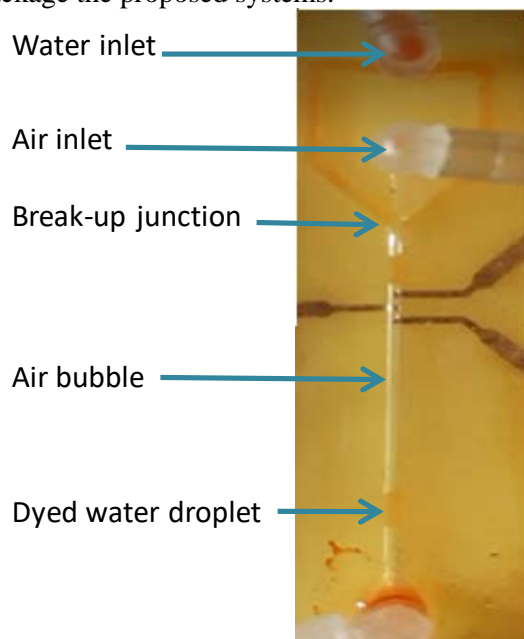


Figure 7: Experimental results of proposed structure in generating fluidic droplet

Prototypes of the droplet generation fluidic system have been realized and their performance has been characterized. The red-dyed water and air were employed to analyze the operation of fabricated proposed structure. The liquid and air flow were generated and controlled by employing pressure syringe pump. Results in Figure 7 confirm the droplet generation. The experiments were conducted by utilizing dual rate syringe pump (KD Scientific – Gemini 88). The droplet generation was implemented by driving the difference between two flow rates of air channel and water channel. It can be inferred from the results that the micro fluidic droplet is successfully generated on the proposed fabricated prototype.

CONCLUSION

A droplet generating system fabricated using rapid prototyping and printed circuit board techniques has been proposed and validated by simulation and experiments. The results from this study can be utilized as a versatile tool for

widespread applications especially in synthesis of microcapsule, microparticles, and microfibers applicable to pharmaceuticals, cosmetics, foods and other lab-on-a-chip applications.

Acknowledgment

This research is funded by the VNU University of Science under project number TN.19.04.

References

- [1] S. Mashaghi, A. Abbaspourrad, D. A. Weitz, and A. M. van Oijen, "Droplet microfluidics: A tool for biology, chemistry and nanotechnology," *TrAC - Trends Anal. Chem.*, vol. **82**, pp. 118–125, 2016.
- [2] T. Y. Lee, T. M. Choi, T. S. Shim, R. A. M. Frijns, and S. H. Kim, "Microfluidic production of multiple emulsions and functional microcapsules," *Lab Chip*, vol. **16**, no. 18, pp. 3415–3440, 2016.
- [3] S. S. Datta *et al.*, "25th anniversary article: Double emulsion templated solid microcapsules: Mechanics and controlled release," *Adv. Mater.*, vol. **26**, no. 14, pp. 2205–2218, 2014.
- [4] T. Kong, J. Wu, M. To, K. Wai Kwok Yeung, H. Cheung Shum, and L. Wang, "Droplet based microfluidic fabrication of designer microparticles for encapsulation applications," *Biomicrofluidics*, vol. **6**, no. 3, 2012.
- [5] W. Chou, P. Lee, C. Yang, and W. Huang, "Recent Advances in Applications of Droplet Microfluidics," pp. 1249–1271, 2015.
- [6] P. Zhu and L. Wang, "Passive and active droplet generation with microfluidics: a review," *Lab Chip*, vol. **17**, no. 1, pp. 34–75, 2017.

POSTER SESSIONS

***FUNDAMENTALS OF
NANOTECHNOLOGY
(FON)***

EVOLUTION OF HEXAGONAL BORON NITRIDE NANORIBBON USING MOLECULAR DYNAMIC SIMULATION: FREE-STANDING MODEL AND HYBRID GRAPHENE/HEXAGONAL BORON NITRIDE MODEL

Nguyen Thi Thuy Hang

Ho Chi Minh City University of Technology - VNU, Vietnam

Email: hangbk@hcmut.edu.vn

ABSTRACT

Different models contained hexagonal Boron Nitride nanoribbon are studied via molecular dynamics simulation. Models are heated up from room temperature to suitable melting point via Tersoff and Lennard-Jones potentials to observe the evolution of graphene layer in the models upon heating. Various thermodynamic quantities, structural characteristics, and the occurrence of liquidlike atoms are studied, such as, the total energy per atom, the heat capacity per atom, the radial distribution functions, and the appearance of liquid atoms upon heating. The phase transition exhibits the first order. The melting point of hexagonal Boron Nitride layer depends on the number of atoms in each layer. The melting process of hybrid graphene and hexagonal boron nitride satisfies the first step towards Devil's staircase type phase transition. The melting point of hexagonal Boron Nitride in hybrid graphene/h-BN model is used to compare with the free-standing one.

Keywords: Hybrid graphene/hexagonal Boron Nitride models; Layer dependence; Melting range; Liquidlike atoms; Layer dependence.

INTRODUCTION

Two-dimensional (2D) materials play an important in different fields such as electronic devices leading to many studies of different materials [1-8]. Among these materials, hexagonal Boron-Nitride (hBN) can be considered as the most analogous to graphene such as strong mechanical properties and high chemical and thermal stability [9, 10]. There are studies focusing on h-BN, h-BN nanoribbons (h-BNNRs) to observe the thermal conductivity of h-BNNRs [11, 12]. Moreover, h-BN as well as BNNRs can be considered as one of the promising dielectric materials in hybrid graphene devices [13-15]. However, there is no any study on the effect of temperature on freestanding h-BNNR such as phase transition, formation of liquid-like atoms upon heating or the atomic mechanism of the phase transition from solid to liquid states.

Related to hybrid model, 2D materials such as dichalcogenides are the best choice of transition metal devices because of some unique properties [16-18]. Moreover, the hybrid material between graphene, B, and N can create a new structure consisting of hybridized phases of h-BN and graphene (h-BNC) [19, 20]. Although there are unique properties of hBN, it

is difficult to study experimentally. Therefore, molecular dynamic simulation is one of the best choices in this case.

CALCULATION

In this study, the interactions between carbon atoms (C) described via an empirical interatomic potential which described in the modified Tersoff potential [21-23]. The interaction between boron (B) and nitride (N) atoms described via Tersoff potential which is parameterized by Albe et. al. [24]. In general, the Tersoff potential is below:

$$E_b = \frac{1}{2} \sum_{i \neq j} f_c(r_{ij}) \left[f_R(r_{ij}) + b_{ij} f_a(r_{ij}) \right],$$

In which r_{ij} represent for the distance from atom i to atom j and the sum runs over all atomic sites. The repulsive $f_R(r_{ij})$ and the attractive $f_a(r_{ij})$ terms are chosen similar to a Morse potential as proposed by Brenner [25]. The $f_c(r_{ij})$ term represents a cutoff function, which calculate the number of neighbors and makes the potential to zero outside the interaction shell.

Lennard-Jones (LJ) potential [26] is used to described the interaction between graphene and

hBN layer because of weak interlayer interaction between sheets.

$$E_b = 4\varepsilon \left[\left(\frac{\sigma}{r} \right)^{12} - \left(\frac{\sigma}{r} \right)^6 \right],$$

In which, r is the distance between two atoms, while ε is a parameter determining the depth of the potential well, σ is the diameter of the atom (a length scale parameter of the atom determining the position of the potential minimum). In LJ potential, the first term containing r^{-12} indicates attractive forces while the term of r^{-6} represents attractive forces. Parameters in LJ potential are determined by the method of Kang and Hwang [27].

The calculation is performed using the software package Large-Scale Atomic/Molecular Massively Parallel Simulator (LAMMPS) [28].

RESULTS AND DISCUSSION

To study the dependence on ribbon sizes, 10000-atom-BNNR model with different sharps (square (166Å×167Å), rectangle (131Å×212Å)) is studied in Figure 1. Total energy per atom is presented to observe the dependence on ribbon sizes (Fig. 1). In term of temperature zone, the behavior of total energy of square and rectangle sharps almost coincides (total energy of both square and rectangle sharps increases linearly at temperature below 4500K before jumping sharply at temperature around 4500K). In term of energy, the statistical noise of the rectangle sharp (circle dot in Fig. 1) is more complex in comparison with the one of square sharp (square dot in Fig. 1) because of the dangling bond at the edges. Therefore, in the range of this study, the ribbon sizes have tendency to effect on the total energy per atom.

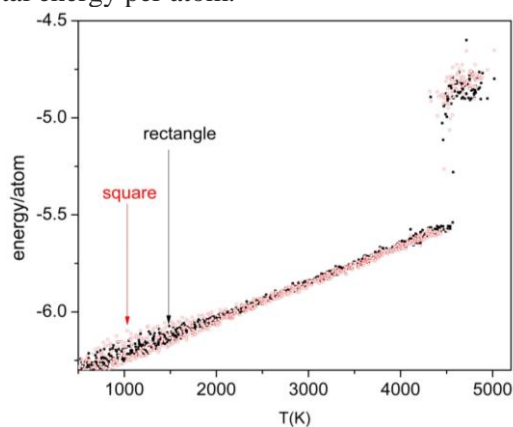


Figure 1. Dependence on ribbon sizes of melting BNNR process with 10000 atoms: square sharp – square dot, rectangle sharp – circle dot.

We present here the temperature dependence of average quantity γ_3 for 3 atoms closest to i -th atom and the evolution of liquidlike atoms.

The graph of average quantity γ_3 can be divided in three parts: below melting point, around melting point and above melting point (Fig. 3). In the first part, the graph of average quantity γ_3 of armchair BNNR fluctuates at temperature below 3630K (circle dot in Fig. 3) while the one of zigzag BNNR keeps constant at temperature below 4000K and increases slightly in the range of temperature from 4000K to 4300K (square dot in Fig. 2). Next, there is a sharp increase of average quantity γ_3 of both armchair and zigzag BNNRs (from 3630K to 3900K for armchair BNNR and from 4200K to 4400K for zigzag BNNR). In the last part, the graph of armchair BNNR fluctuates in the range of temperature higher than 3900K whereas the one of zigzag BNNR varies from 4400K and higher.

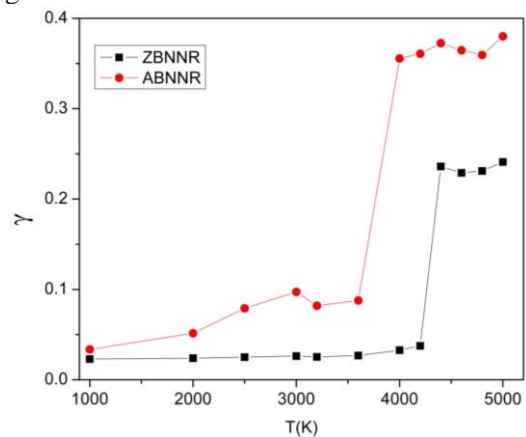


Figure 2. Dependence on temperature of average quantity: circle dot – ABNNR, square dot – ZBNNR.

The formation of liquid-like atoms upon heating of armchair BNNR (circle dot) and zigzag BNNR (square dot) can be seen in Figure 3. The liquidlike atoms of armchair BNNR fluctuate in the range of temperature below 3600K while the ones of zigzag BNNR keep constant at temperature below 4200K. After that liquidlike atoms of armchair BNNR increase significantly to 93% at 3700K whereas the ones of zigzag BNNR reach to 65% at 4400K. In conclusion, the statistical noise of armchair BNNR are more complex than the one of zigzag BNNR.

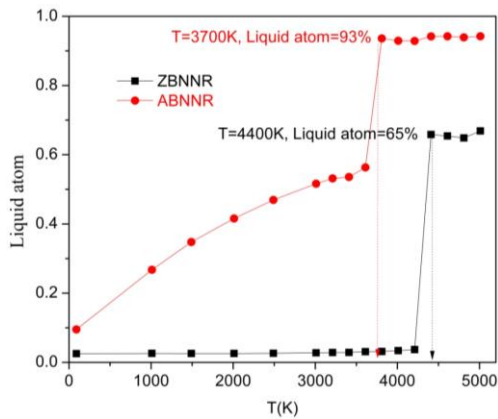


Figure 3. Dependence on temperature of liquidlike atom: circle dot – ABNNR, square dot – ZBNNR.

CONCLUSION

In conclusion, the statistical noise of armchair BNNR are more complex than the one of zigzag BNNR. In the range of this study, the ribbon sizes have tendency to effect on the total energy per atom.

Acknowledgment

This research is funded by Ho Chi Minh City University of technology – VNU-HCM under grant number T-KHUD-2018-85.

References

[1] K. Nakada, M. Fujita, G. Dresselhaus, and M.S. Dresselhaus, *Phys. Rev. B*, **54** (1996) 17954.
 [2] K.S. Novoselov, A.K. Geim, S. Morozov, D. Jiang, M. Katsnelson, I. Grigorieva, S. Dubonos, and A. Firsov, *Nature*, **438** (2005) 197.
 [3] Y.-W. Son, M.L. Cohen, and S.G. Louie, *Phys. Rev. Lett.*, **97** (2006) 216803.
 [4] Y. Zhang, Z. Jiang, J. Small, M. Purewal, Y.-W. Tan, M. Fazlollahi, J. Chudow, J. Jaszczak, H. Stormer, and P. Kim, *Phys. Rev. Lett.*, **96** (2006) 136806.
 [5] A.K. Geim and K.S. Novoselov, *Nature materials*, **6** (2007) 183.
 [6] M.Y. Han, B. Özyilmaz, Y. Zhang, and P. Kim, *Phys. Rev. Lett.*, **98** (2007) 206805.
 [7] I. Meric, M.Y. Han, A.F. Young, B. Özyilmaz, P. Kim, and K.L. Shepard, *Nat. Nanotechnol.*, **3** (2008) 654.
 [8] W.L. Wang, S. Meng, and E. Kaxiras, *Nano Lett.*, **8** (2008) 241.
 [9] D. Jin-Xiang, Z. Xiao-Kang, Y. Qian, W. Xu-Yang, C. Guang-Hua, and H. De-Yan, *Chinese Phys. B*, **18** (2009) 4013.
 [10] C. Li, Y. Bando, C. Zhi, Y. Huang, and D. Golberg, *Nanotechnology*, **20** (2009) 385707.

[11] T. Ouyang, Y. Chen, Y. Xie, K. Yang, Z. Bao, and J. Zhong, *Nanotechnology*, **21** (2010) 245701.
 [12] J. Hu, X. Ruan, and Y.P. Chen, *Nano Lett.*, **9** (2009) 2730.
 [13] D. Golberg, Y. Bando, Y. Huang, T. Terao, M. Mitome, C. Tang, and C. Zhi, *ACS nano*, **4** (2010) 2979.
 [14] M.S. Bresnehan, M.J. Hollander, M. Wetherington, M. LaBella, K.A. Trumbull, R. Cavaleiro, D.W. Snyder, and J.A. Robinson, *ACS nano*, **6** (2012) 5234.
 [15] Z. Yu, M. Hu, C. Zhang, C. He, L. Sun, and J. Zhong, *J. Phys. Chem. C*, **115** (2011) 10836.
 [16] J.-H. Chen, C. Jang, S. Adam, M. Fuhrer, E.D. Williams, and M. Ishigami, *Nature physics*, **4** (2008) 377.
 [17] J.-H. Chen, C. Jang, S. Xiao, M. Ishigami, and M.S. Fuhrer, *Nat. Nanotechnol.*, **3** (2008) 206.
 [18] C.R. Dean, A.F. Young, I. Meric, C. Lee, L. Wang, S. Sorgenfrei, K. Watanabe, T. Taniguchi, P. Kim, and K.L. Shepard, *Nat. Nanotechnol.*, **5** (2010) 722.
 [19] M. Kawaguchi, T. Kawashima, and T. Nakajima, *Chemistry of materials*, **8** (1996) 1197.
 [20] L. Ci, L. Song, C. Jin, D. Jariwala, D. Wu, Y. Li, A. Srivastava, Z. Wang, K. Storr, and L. Balicas, *Nature materials*, **9** (2010) 430.
 [21] W. Sekkal, B. Bouhafs, H. Aourag, and M. Certier, *J. Phys.: Condens. Mat.*, **10** (1998) 4975.
 [22] K. Matsunaga, C. Fisher, and H. Matsubara, *Japanese Journal of Applied Physics*, **39** (2000) L48.
 [23] M.-L. Liao, Y.-C. Wang, S.-P. Ju, T.-W. Lien, and L.-F. Huang, *J. Appl. Phys.*, **110** (2011) 054310.
 [24] K. Albe, W. Möller, and K.-H. Heinig, *Radiat. Ef. Defect. S.*, **141** (1997) 85.
 [25] D.W. Brenner, *Phys. Rev. B*, **42** (1990) 9458.
 [26] N. Yu and A.A. Polycarpou, *Journal of colloid and interface science*, **278** (2004) 428.
 [27] J.W. Kang and H.J. Hwang, *J. Phys.: Condens. Mat.*, **16** (2004) 3901.
 [28] S. Plimpton, *J. Comput. Phys.*, **117** (1995) 1.

SIZE EFFECTS ON MELTING PROCESS OF 2D GLASSY MONATOMIC SOLIDS

Dương Thi Như Tranh, Le Nguyen Tue Minh, Vo Van Hoang

Computational Physics Lab., Ho Chi Minh City University of Technology, Vietnam National University
– Ho Chi Minh City, Vietnam; 268 Ly Thuong Kiet Street, District 10, Ho Chi Minh City, Vietnam

Email: dtnttranh@hcmut.edu.vn

ABSTRACT

Size effects on melting of two-dimensional (2D) glassy monatomic solids are studied using molecular dynamics (MD) simulation with Lennard–Jones–Gauss (LJG) interaction potential. Size effects on structural and dynamical properties of the systems during heating process are analyzed and discussed via glassy transition temperature, coordination number distributions, mobility of atoms, and their clustering. Atomic mechanism of melting is also analyzed via the tendency to increase mobility and the breaking clusters of atoms upon heating. We find that glassy transition temperature T_g increases with increasing the size of the systems. Especially, this behavior can be observed clearly for small size systems (number of atoms in the system less than 4900). When the size of systems is large enough (i.e. $N \geq 4900$), glassy transition temperature T_g is not affected by the system sizes. In addition, we find that in the low temperature region, fraction of the atoms with low mobility per total atoms of the systems is slightly affected by the own sizes. In contrast, in the high temperature region, i.e. above the glassy transition temperature, this effect disappears.

Keywords: 2D glassy systems, melting process, size effect, glassy transition temperature

INTRODUCTION

The size effect is important issue in nanoscience and nanotechnology fields to apply in industry such as to fabricate mechanical structures of devices with the size less than one micron. Several simulations and experiments studied size effect on the melting process of solids [1-16]. However, information about the size effect on melting of 2D glass is still limited.

Furio Ercolessi et al. in Ref. [3] studied melting of gold particles and found that the melting process depends on the sizes of systems. The melting temperature decreases with decreasing size of the particles. In Ref. [4], authors observed the melting process of low dimensional nanocrystals (spherical particles, thin films, disc-like particles, and nanowire) and found that the melting temperature depression can be induced by both the size and the dimension. The thick films (> 4 layers), thin-films (≤ 4 layers), and monolayers exhibit different melting behaviors [10]. The solid-liquid coexistence regime decreases with the film thickness, vanishing at a critical thickness of 4 layers. The thick films start melting at grain

boundaries, and then the fluid propagates into adjacent crystal domains while the melting of the thin films begins from both grain boundaries and from within the crystalline domains.

In this study, the melting of 2D glassy monatomic systems with different sizes is studied using MD simulation. The size effect on the melting is analyzed and discussed via structural and dynamical properties such as transition temperature, coordination number distributions, mobility of atoms, and their clustering.

CALCULATION

Size effect in the melting process is studied and analyzed via 8 models with different sizes. Atoms in systems interact via Lennard–Jones–Gauss (LJG) interatomic potential form is given below [17]:

$$V(r) = \varepsilon_0 \left[\left(\frac{r_0}{r} \right)^{12} - 2 \left(\frac{r_0}{r} \right)^6 \right] - \varepsilon \exp \left[- \frac{(r - r_G)^2}{2\sigma^2} \right]$$

In this study, the parameters for LJG potential are taken as in Ref. [18]. Here, r_0 is an atomic

diameter, ε_0 is a depth of LJ part of LJG potential, r_G is a position, ε is a depth, and σ is a width of well of Gauss part one. We employ the LJ reduced units as follows [19]: energy is in units of ε_0 , length is in units of r_0 , temperature T is in units of ε_0/k_B , and time is in units of $\tau_0 = r_0(m/\varepsilon_0)^{1/2}$ where k_B is the Boltzmann constant, m is an atomic mass. If taking Ar for testing (atomic mass of Ar is $m = 0.66 \times 10^{-25} \text{ kg}$ and atomic diameter of one is $r_0 = 3.84 \text{ \AA}$), temperature T is in units of $\varepsilon_0/k_B = 118 \text{ K}$ and time is in units of $\tau_0 = r_0(m/\varepsilon_0)^{1/2} = 2.44 \text{ ps}$. The Verlet algorithm is used with the MD time step of $dt = 0.001\tau_0 = 2.44 \text{ fs}$. “NPT” ensemble is used in this MD simulation. 2D models were created under periodic boundary conditions with initially simple squared lattice structure of sizes ($S = L \times L$, L is length of simulation cell) from $S = 20r_0 \times 20r_0$ to $90r_0 \times 90r_0$ (8 sizes), corresponding total number of atoms (N) of 20^2 , 30^2 , 40^2 , 50^2 , 60^2 , 70^2 , 80^2 and 90^2 , respectively.

Initially, the atomic configuration has been relaxed at a temperature $T = 2.0$ for 2×10^6 MD steps in order to get an equilibrium liquid state. Then the system is cooled down to $T = 0.1$ at a cooling rate $\gamma = 10^6$ per MD step ($4.836 \times 10^{10} \text{ K/s}$ if taking Ar for testing) and the temperature is decreased linearly with time as $T = T_0 - \gamma \times n$ via the simple atomic velocity rescaling until reaching $T = 0.1$ [19]. Here, γ is the cooling rate and n is the number of MD steps. After cooling, the system obtained in glassy state is heated up to initial temperature at $T = 2.0$ at the same rate, $\gamma = 10^6$ per MD step via formula $T = T_0 + \gamma \times n$. In order to improve the statistics, we average results over 5 independent runs.

RESULTS AND DISCUSSION

Temperature dependence of potential energy is of great interest because from that we can infer important quantities and phenomena, such as phase transition temperature, and related phase transitions. Fig. 1 exhibits the system size

dependence of glassy transition temperature T_g .

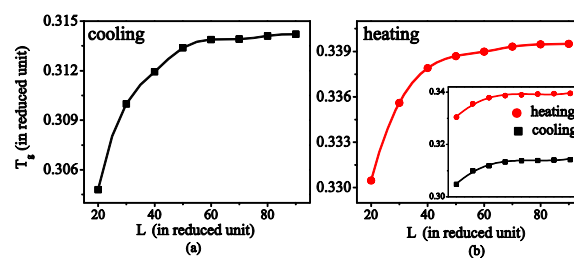


Figure 1. System size dependence of glassy transition temperature upon cooling: (a) and heating (b).

As shown in Figure 1, the glassy transition temperature T_g of the systems with size $S < 70r_0 \times 70r_0$ (corresponding to number of atoms $N < 4900$) increases with increasing the size of the systems. However, for the systems with size $S \geq 70r_0 \times 70r_0$ (i.e. $N \geq 4900$), the value T_g does not change with size. This behavior is consistent to the results obtained for the nanoparticles [16] and the thin films [4]. The inset in Figure 1b shows the size dependence of heating (circular symbol) and cooling (square symbol) processes. It can be seen that although the graphs of heating and cooling processes have the same behavior, T_g of heating process is higher than that of cooling process. It may be due to the thermal hysteresis of glass-forming systems in general (see Refs [20,21] and references therein).

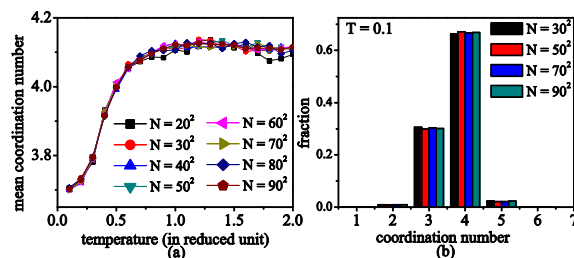


Figure 2. Temperature dependences of mean coordination number upon heating from glass (a), and (b) the coordination number distributions at $T=0.1$ of the systems with different sizes.

Information about the structure of the systems can be seen via the coordination numbers. As shown in Figure 2a, the temperature dependence curves of the mean coordination number \bar{Z} upon heating of given systems are not different in this range of study.

At $T = 0.1$, the obtained mean coordination number of the systems in the glassy state is about $\bar{Z} = 3.73$, the coordination numbers $Z = 3$ and $Z = 4$ are dominated in the model (see Figure 2b). In the temperature region of the glass-liquid transition (ranging from $T = 0.2$ to $T = 0.8$), the mean coordination numbers \bar{Z} change strongly (see Figure 2a). With increasing temperature, the mean coordination number increases due to the decreasing fraction of atoms which have $Z = 3$, $Z = 4$ and the increasing fraction of atoms which have large coordination number per total atoms. Above the melting range, \bar{Z} almost does not change with increasing temperature and fluctuates slightly around the value $\bar{Z} = 4.14$. It can be concluded that there is not existence of size effect on formed structure of the systems.

The dynamic properties of models during heating process can be seen via the analysis of the temperature dependence of the mobility of atoms (Figs. 3, 4). Models obtained by heating from the glass have been relaxed for 5000 MD steps or $5\tau_0$ at a given temperature before further spatio-temporal analysis of configurations based on the dynamics of atoms.

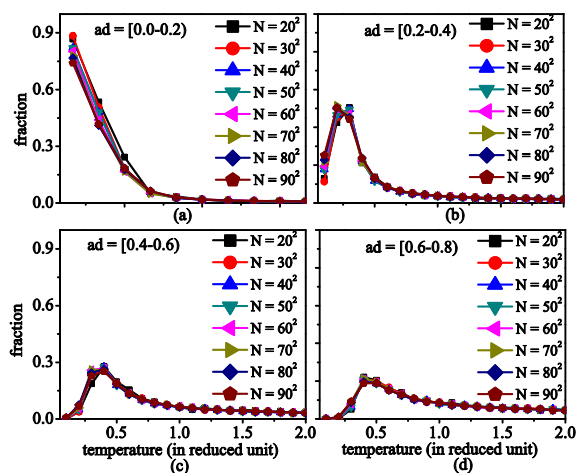


Figure 3. Temperature dependence of fraction of atoms with various atomic displacements per total number of atoms

Figure 3 exhibits temperature dependence of fraction of atoms with various atomic displacements (ad) per total number of atoms. In the low temperature region, the dependence on temperature of atoms with low mobility becomes more complicated. In glassy state at $T = 0.1$, atoms with low atomic displacement

(ad) (such as $ad = [0.0 - 0.2)$) are dominant and have a tendency to decrease rapidly with increasing temperature while atoms with different higher mobilities have tendency to increase first and then decrease at temperature about $T = 0.8$. In the high temperature region, $T \geq 0.8$, almost atoms with very low mobility are replaced by the ones with high mobility. It can be seen that temperature dependence curves of fraction of atoms with various atomic displacements per total number of atoms have the same behavior when the size of the system is changed. However, those fractions are affected by own system sizes (see Figure 4). At high temperatures ($T = 2.0$), atoms mainly have high mobility and fraction of atoms with different ad is almost the same for all system sizes. But at $T = 0.1$, atoms with $ad = [0.0 - 0.2)$ slightly decrease with increasing system sizes. Upon heating, the mobility of atoms is increased and the largest cluster of solid-like atoms is broken to many small clusters distributing in the whole model. Atoms with $ad = [0.0 - 0.2)$ decrease and the ones with $ad = [0.2 - 0.4)$ increase in the temperature region lower than the transition temperature (T_g around value 0.3). Besides, at $T = 0.3$, atoms with $ad = [0.2 - 0.4)$ clearly increase with increasing system sizes.

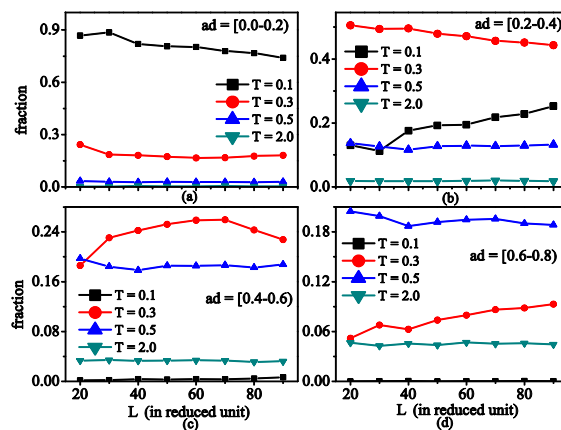


Figure 4. Size dependence of fraction of atoms with various atomic displacements per total number of atoms at given temperatures

CONCLUSION

In conclusion, we would like to mention two important points relating to dynamic and structural properties. As for dynamic properties,

glassy transition temperature T_g increases with increasing the size of the systems. When the size of systems is around $S \geq 70r_o \times 70r_o$ (i.e. $N \geq 4900$), T_g does not change indicating the critical size of system. In addition, we find that in the low temperature region, fraction of the atoms with low mobility is slightly affected by size of the system. Regarding structural properties, they are not affected by the system sizes.

Acknowledgment

This research is funded by Vietnam National Foundation for Science and Technology Development (NAFOSTED) under Grant 103.01-2017.01.

References

- [1]. K. J. Strandburg, *Two-dimensional melting*, Rev. Mod. Phys. **60** (1988) 161
- [2]. A. Hunt, *Finite-size effects on the glass transition temperature*, Sol. Stat. Comm. **90** (1994) 527
- [3]. F. Ercolessi, W. Andreoni, and E. Tosatti, *Melting of Small Gold Particles: Mechanism and Size Effects*, Phys. Rev. Lett. **66** (1991) 911
- [4]. Z Zhang, J C Li, and Q Jiang, *Modelling for size-dependent and dimension-dependent melting of nanocrystals*, J. Phys. D: Appl. Phys. **33** (2000) 2653
- [5]. K. Kim and R. Yamamoto, *Apparent finite size-effect in the dynamics of supercooled liquids*, Phys. Rev. E **61** (2000) 41
- [6]. Jae Huyn Kim, Jyongsik Jang, and Wang Cheol Zin, *Thickness dependence of the glass transition temperature in thin polymer films*, Europhys. Lett. **17** (2001) 2703
- [7]. K. Dick, T. Dhanasekaran, Z. Zhang, and D. Meisel, *Size-Dependent Melting of Silica-Encapsulated Gold Nanoparticles*, J. Am. Chem. Soc. **124** (2002) 2312
- [8]. M. Alcoutlabi and G. B. McKenna, *Effects of confinement on material behavior at the nanometer size scale*, J. Phys. Condens. Matter **17** (2005) 461
- [9]. D. Morineau, Yongde Xia, and C. Alba-Sinionesco, *Finite-size and surface effects on the glass transition of liquid toluene confined in cylindrical mesopores*, J. Chem. Phys. **117** (2002) 8966
- [10]. Y. Peng, Z. Wang, A. M. Alsayed, A. G. Yodh, and Y. Han, *Melting of Colloidal Crystal Films*, Physical Rev. Lett. **104** (2010) 205703
- [11]. A. Derzsi et al, *The metastability of the hexatic phase during the melting of two-dimensional charged particle solids*, Phys. Plasmas **21** (2014) 023706
- [12]. R. J. Larsen and C. F. Zukoski, *Effects of particle size on the glass transition*, Phys. Rev. E **83** (2011) 051504
- [13]. W. B. Zhang, J. Liu, S. H. Lu, H. Zhang, H. Wang, X. D. Wang, Q. P. Cao, D. X. Zhang, and J. Z. Jiang, *Size effect on atomic structure in low-dimensional Cu-Zr amorphous systems*, Sci. Rep. **7** (2017) 7291
- [14]. V. V. Hoang and N. N. Linh, *Finite Size Effects on Static and Dynamic Properties of Non-periodic Boundary Condition Supercooled Liquids*, J. Phys. Soc. Jpn. **76** (2007) 114602
- [15]. Q. Jiang, H.X. Shi, and J.C. Li, *Finite size effect on glass transition temperatures*, Thin Solid Films **354** (1999) 283
- [16]. Y. Z. Li, Y. T. Sun, Z. Lu, M. Z. Li, H. Y. Bai, and W. H. Wang, *Size effect on dynamics and glass transition in metallic liquids and glasses*, J. Chem. Phys. **146** (2017) 224502
- [17]. M. Engel and H-R Trebin, *Self-assembly of monatomic complex crystals and quasicrystals with a double-well interaction potential*, Phys. Rev. Lett. **98** (2007) 225505
- [18]. T. Mizuguchi and T. Odagaki, *Glass formation and crystallization of a simple monatomic liquid*, Phys. Rev. E **79** (2009) 051501
- [19]. V. V. Hoang, *New scenario of dynamical heterogeneity in supercooled liquid and glassy states of 2D monatomic system*, J. Phys. Chem. B **119** (2015) 15752
- [20]. H. Jonsson and H. C. Andersen, *Icosahedral ordering in the Lennard-Jones liquid and glass*, Phys. Rev. Lett. **60** (1988) 2295
- [21]. A. J. Kovacs and J. M. Hutchinson, *Isobaric thermal behavior of glasses during uniform cooling and heating: Dependence of the characteristic temperatures on the relative contributions of temperature and structure to the rate of recovery. II. A one-parameter model approach*, J. Polymer Sci. **17** (1979) 2031

POSTER SESSIONS

NANOFABRICATION TECHNIQUES
(NFT)

SYNTHESIS OF TWO-DIMENSIONAL MoS₂ CRYSTALS BY A TWO-STEPS CHEMICAL VAPOR DEPOSITION PROCESS

Dao Xuan Duong*¹, **Tran D. Phong**², **Nguyen Tran Thuat**³

1) Department of Fundamental Sciences, Academy of Cryptography Techniques, No 141 Chien Thang Street, Hanoi;

2) Department of Fundamental and Applied Sciences, University of Science and Technology of Hanoi, Vietnam Academy of Science, No 18 Hoang Quoc Viet Street, Hanoi;

3) Nano and Energy Center, VNU University of Science, No 334 Nguyen Trai Street, Hanoi

*E-mail: duongdx@actvn.edu.vn

ABSTRACT

Transition metal dichalcogenide two-dimensional materials, such as MoS₂, are a promising candidates for next-generation of electronic and optoelectronic devices thanks to its unique electrical and optical properties. Although MoS₂ has shown excellent properties, the construction of large size crystals or thin monolayers is difficult. In this study, we report on the synthesis of MoS₂ crystals by a two-step chemical vapor deposition process. In the first step, MoO₃ powder was reduced into MoO₂ crystals on a silicon substrate in a flow of sulfur vapor. In the second step, MoO₂ crystals were transformed subsequently into MoS₂ in another flow of sulfur vapor at higher reaction temperature. Structural and optical characterization techniques were carried out in order to confirm the crystalline properties of the resultant MoS₂ crystals. By adjusting the experimental parameters, we can control the size and the morphology of MoS₂ crystals, thereby opening an opportunity to apply MoS₂ in optoelectronics as well as in catalysis.

Key word: 2D material, catalyst, CVD

INTRODUCTION

Graphene is a two-dimensional (2D) material that was first discovered by exfoliating from large graphite crystals in 2004 [1]. Since then, specialization of two-dimensional materials has received increasing attention due to its special properties. However, graphene has a bandgap of zero [1], this presenting a number of obstacles and more works have been done in order to find new materials to overcome this problem.

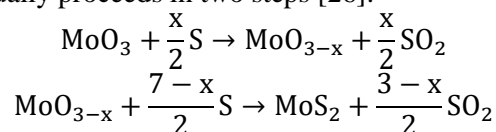
Transition metal dichalcogenides (TMDs) have been studied throughout. It has a direct band gap from 1.09 eV to 2.03 eV depending on the number of 2D layers [2]. TMDs are a large group of crystals with a generic chemical formula of MX₂ (M = transition metal, X = S, Se, or Te), about two thirds of which are known to form layered structures. TMDs are quite promising for a number of applications ranging from photovoltaics [3], photon detection [4], optoelectronics [5], to energy storage/conversion, sensing, and catalysis [6,7]. Molybdenum disulfide (MoS₂) is the most common TMDs. Monolayer MoS₂ have been implemented in field-effect transistors (FET)

with superb on/off ratios of 10⁷–10⁸ [4,8,9] in comparison to a much lower on/off ratio, typical for graphene [10], and phototransistors with fast (> 50 ms) switching times [11].

There have been many efforts in increasing the size, reducing the number of layers, increasing the quality of MoS₂ including: exfoliation [12, 13], hydrothermal synthesis [14, 15], physical vapor deposition [16, 17] and chemical vapor deposition (CVD).

Among the aforementioned methods, CVD is a method that has been used for a long time, and is considered to be simple but brings high results in size and quality of crystals. In a CVD method, there are also many precursors used to make MoS₂ as sulphurization of pre-deposited Mo thin films [18], thermolysis of (NH₄)₂MoS₄ [19], sulphurization of MoO₃ [20–24] or MoCl₅ [25].

During sulphurization of MoO₃, reaction usually proceeds in two steps [26]:



The common product of MoO_{3-x} is MoO₂. This is an uncontrolled process.

Based on the above reference, we propose a synthesis method of MoS₂ based on 2 separate steps: (i) reducing MoO₃ to MoO₂ and (ii)

turning MoO₂ into MoS₂. Both steps are done by CVD method.

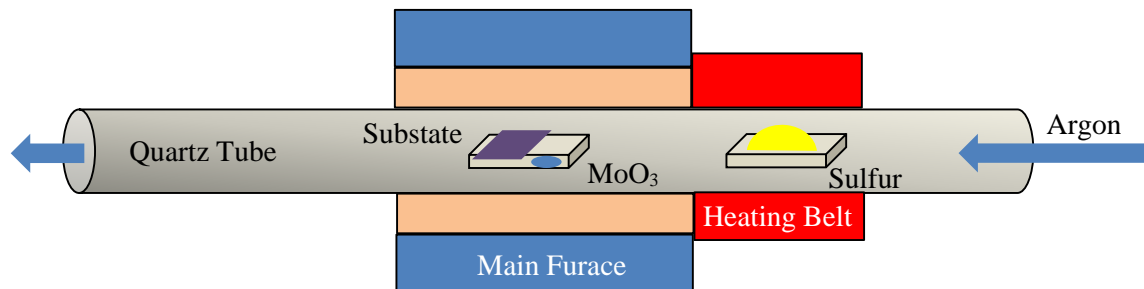


Figure 1. Schematic illustration of the MoS₂ CVD system

EXPERIMENTAL

Materials

Molybdenum (VI) oxide powder (MoO₃, 99.5%), sulfur powder (S, 99.5%) were purchased from Sigma-Aldrich. All materials were used without further purification.

Experimental setup

Sulfur powder (500mg) was located outside the main furnace and at the top of the quartz stream. This sulfur powder will be thermally controlled by heating belt.

In the center of the furnace was MoO₃ powder (10 mg) placed in a ceramic boat. Si/SiO₂ substrate, with the oxide thickness of 300 nm, was placed face down on the boat containing MoO₃. Both the system consists of sulfur and MoO₃ powder was placed in a quartz tube. The main furnace was type 1 inch of

Lindberg/Blue M. Schematic illustration of the process is shown in Figure 1.

Initially, the system was blown with pure Ar at a flowrate of 100 sccm for 30 min at room temperature in order to remove air inside the tube.

According to the reference [27] the best temperature for MoO₃ to react with S in a gaseous phase is between 800°C – 850°C. So we chose the main temperature for the reaction to take place at 800°C. All experiments were carried out in an Ar air blowing flowrate of 10 sccm and naturally cooled to room temperature.

CHARACTERIZATIONS

The room temperature Raman spectra were recorded by using Horiba LabRAM HR spectrometer with laser wavelength of 532 nm. The micrographs of samples were obtained on a conventional optical microscope.

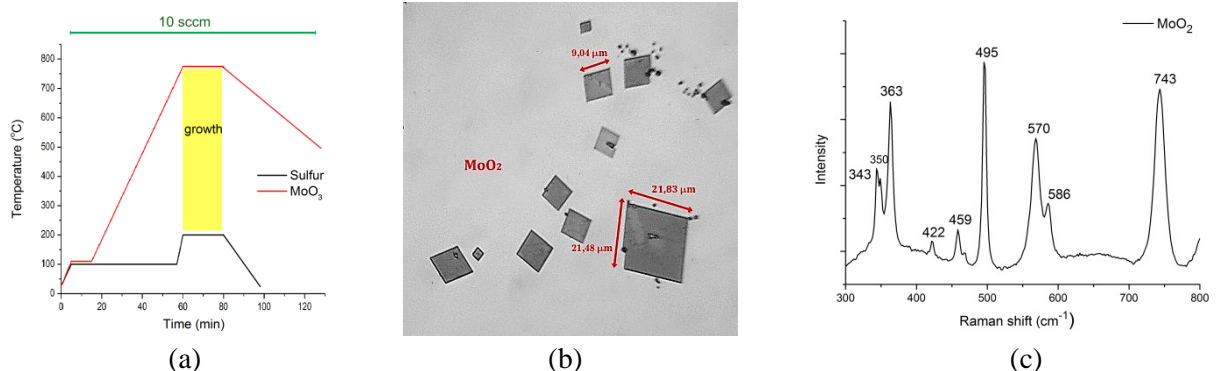


Figure 2. (a) Temperature programming process of MoO₃ and S precursors with a heating rate of 15°C/min. (b) Optical microscopy of MoO₂ on Si substrate. (c) Raman spectra of MoO₂

RESULTS AND DISCUSSION

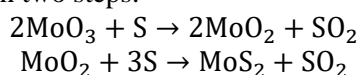
During trial experiments, when the heating rate for the precursor MoO₃ was less than 10°C

/min, from 100°C to 800°C took from 80 to 100 minutes, on Si substrates there was no deposited material. However in the downstream of the

furnace tube there was deposited material, which was probably MoO_3 . So it can be deduced that when the heating rate was small, S vapor had not been able to react with MoO_3 vapor before MoO_3 powder in the boat has completely evaporated.

After that, the heating rate is increased to $15^\circ\text{C}/\text{min}$. The diagram showing the precursor heating rate is shown in Figure 1a. On the Si substrate there was deposition of materials. Optical microscope image and Raman spectra are shown in the Figure 2b and 2c. We suggest that they are single crystals of MoO_2 [28].

Normally when reducing MoO_3 with sulfur, we obtain MoS_2 . The chemical equation of this process in two steps:



Since we did not obtain MoS_2 as a final product of reduction, the vapor phase sulfur quantity would be not enough. To confirm the above results, we conducted the following two experiments:

Firstly, a two-step heating experiment was carried out. We kept the same procedure as in above section (ex. conducting experiments with the precursor MoO_3 at 800°C , Argon was blown at a flow rate 10 sccm); and we added one more step, increasing the temperature by 50°C and blowing a new source of sulfur. The diagram of precursor temperature profile is shown in Figure 3a. An optical microscope image and a Raman spectrum are shown in Figure 3b and 3c.

On the Raman spectrum, we found that there are peaks of MoO_2 and two characteristic peaks of MoS_2 (at 381 cm^{-1} and at 406 cm^{-1}). On the optical micrograph, it can be noticed that MoS_2 crystals have been grow above MoO_2 crystals (shaped like a rhombus below). This proves that the process of forming MoS_2 crystals is ongoing but incomplete, so there exists both MoO_2 and MoS_2 .

Secondly, a two-cycle heating experiment was carried out. We took Si substrate containing monocrystalline MoO_2 (created from previous experiments, Figure 2), put it on ceramic boat, at the top of quartz tube, put ceramic boat containing 500mg sulfur. The heating process was described in schematic figure 4a. The whole process is carried out with the flow rate of Ar was 10sccm. The result when viewed under an optical microscope (Figure 4b) is a material in the form of a triangle (instead of the rhombus of a MoO_2 crystal). Raman spectrum was shown in Figure 4c. The result was that the MoO_2 crystals were completely sulfurized, converted into MoS_2 . Based on the results of Raman spectrum, we can see that the quality of MoS_2 crystal is very good, the intensity of the two characteristic peaks is large and free of impurities. In terms of size, since MoS_2 crystals grow above MoO_2 crystals, the size of MoS_2 crystals will be close to or smaller than the size of MoO_2 ; MoO_2 crystal can also be considered as the framework of MoS_2 crystal.

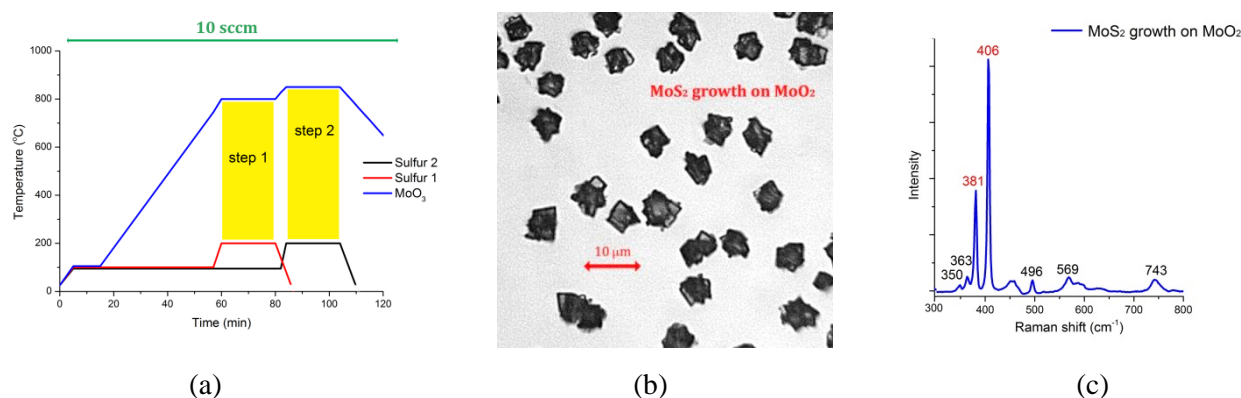


Figure 3. (a) Two-step temperature evolution of the furnace for MoO_3 precursor and S precursor (b) optical microscopy of MoS_2 crystals on top MoO_2 crystals (c) A Raman spectrum of the sample.

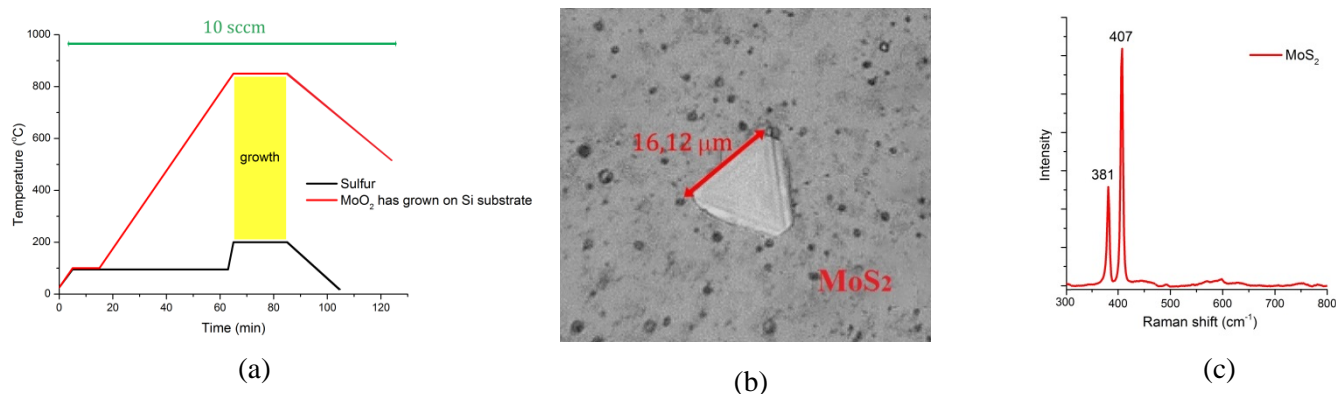


Figure 4. (a) Temperature evolution of the furnace and of S precursor for second run, (b) optical microscopy of MoS₂ on Si substrate, (c) a Raman spectrum of MoS₂

CONCLUSION

As such, we have successfully synthesized MoS₂ from the MoO₃ precursor by two steps, and also confirmed the process of forming MoS₂ from MoO₂. Thereby, if we can control the size of MoO₂ crystals, it opens up the way to control the size of MoS₂ crystals and their thickness.

Acknowledgement

We would like to thank Associate Professor Do Danh Bich (HaNoi University of Education) for Raman measurements.

References

- [1]. Novoselov KS, Geim AK, Morozov SV, Jiang D, Zhang Y, Dubonos SV, et al. *Electric field effect in atomically thin carbon films*. Science (2004)
- [2]. Julia Gusakova, Xingli Wang, Li Lynn Shiau, Anna Krivosheeva, Victor Shaposhnikov, Victor Borisenko, Vasilii Gusakov, and Beng Kang Tay. *Electronic Properties of Bulk and Monolayer TMDs: Theoretical Study Within DFT Framework (GVJ-2e Method)*, Phys. Status Solidi A (2017), 1700218
- [3]. M. Bernardi, M. Palummo, J.C. Grossman, *Extraordinary sunlight absorption and one nanometer thick photovoltaics using two-dimensional monolayer materials*, Nano Lett. 13, (2013) 3664–3670
- [4]. H.S. Lee, S.-W. Min, Y.-G. Chang, M.K. Park, T. Nam, H. Kim, J.H. Kim, S. Ryu, S. Im, *MoS₂ nanosheet phototransistors with thickness-modulated optical energy gap*, Nano Lett. 12 (2012) 3695–3700.
- [5]. Q.H. Wang, K. Kalantar-Zadeh, A. Kis, J.N. Coleman, M.S. Strano, *Electronics and optoelectronics of two-dimensional*

transition metal dichalcogenides, Nat. Nanotechnol. 7 (2012) 699–712.

- [6]. M. Chhowalla, H.S. Shin, G. Eda, L.J. Li, K.P. Loh, H. Zhang, *The chemistry of two-dimensional layered transition metal dichalcogenide nanosheets*, Nat. Chem. 5 (2013) 263–275.
- [7]. X. Chia, A.Y.S. Eng, A. Ambrosi, S.M. Tan, M. Pumera, *Electrochemistry of nanostructured layered transition-metal dichalcogenides*, Chem. Rev. (Washington, DC, US) 115 (2015) 11941–11966.
- [8]. B. Radisavljevic, A. Radenovic, J. Brivio, V. Giacometti, A. Kis, *Single-layer MoS₂ transistors*, Nat. Nanotechnol. 6 (2011) 147–150.
- [9]. H. Qiu, T. Xu, Z. Wang, W. Ren, H. Nan, Z. Ni, Q. Chen, S. Yuan, F. Miao, F. Song, G. Long, Y. Shi, L. Sun, J. Wang, X. Wang, *Hopping transport through defect-induced localized states in molybdenum disulphide*, Nat. Commun. 4 (2013) 2642.
- [10]. A. Das, S. Pisana, B. Chakraborty, S. Piscanec, S.K. Saha, U.V. Waghmare, K.S. Novoselov, H.R. Krishnamurthy, A.K. Geim, A.C. Ferrari, A.K. Sood, *Monitoring dopants by Raman scattering in an electrochemically top-gated graphene transistor*, Nat. Nanotechnol. 3 (2008) 210–215.
- [11]. Z. Yin, H. Li, H. Li, L. Jiang, Y. Shi, Y. Sun, G. Lu, Q. Zhang, X. Chen, H. Zhang, *Single-layer MoS₂ phototransistors*, ACS Nano 6 (2012) 74–80.
- [12]. Zhou K-G, Mao N-N, Wang H-X, Peng Y and Zhang H-L, *A mixed-solvent strategy for efficient exfoliation of inorganic graphene analogues* Angew. Chem. Int. Ed. Engl. 50 (2011) 10839–42

- [13]. Zeng Z, Yin Z, Huang X, Li H, He Q, Lu G, Boey F and Zhang H *Single-layer semiconducting nanosheets: high-yield preparation and device fabrication* *Angew. Chem. Int. Ed. Engl.* 50 (2011) 11093–7
- [14]. Dunne P W, Munn A S, Starkey C L and Lester E H, *The sequential continuous-flow hydrothermal synthesis of molybdenum disulphide* *Chem. Commun.* 51 (2015) 4048–50
- [15]. Rao C N R and Nag A, *Inorganic analogues of graphene* *Eur. J. Inorg. Chem.* (2010) 4244–50
- [16]. Gong C et al, *Metal contacts on physical vapor deposited monolayer MoS₂* *ACS Nano* 7 (2013) 11350–7
- [17]. Wu S, Huang C, Aivazian G, Ross J S, Cobden D H and Xu X, *Vapor–solid growth of high optical quality MoS₂ monolayers with near-unity valley polarization* *ACS Nano* 7, (2013) 2768–72
- [18]. Zhan Y, Liu Z, Najmaei S, Ajayan P M and Lou J, *Large-area vapor-phase growth and characterization of MoS₂ atomic layers on a SiO₂ substrate* *Small* 8 (2012) 966–71
- [19]. Liu K-K et al *Growth of large-area and highly crystalline MoS₂ thin layers on insulating substrates* *Nano Lett.* 12 (2012) 1538–44
- [20]. Van der Zande A M, Huang P Y, Chenet D A, Berkelbach T C, You Y, Lee G-H, Heinz T F, Reichman D R, Muller D A and Hone J C *Grains and grain boundaries in highly crystalline monolayer molybdenum disulphide* *Nat. Mater.* 12 (2013) 554–561
- [21]. Najmaei S, Liu Z, Zhou W, Zou X, Shi G, Lei S, Yakobson B I, Idrobo J-C, Ajayan P M and Lou J, *Vapour phase growth and grain boundary structure of molybdenum disulphide atomic layers* *Nat. Mater.* 12 (2013) 754–9
- [22]. Wang X, Feng H, Wu Y and Jiao L, *Controlled synthesis of highly crystalline MoS₂ flakes by chemical vapor deposition* *J. Am. Chem. Soc.* 135 (2013) 5304–7
- [23]. Ling X, Lee Y-H, Lin Y, Fang W, Yu L, Dresselhaus M S and Kong J, *Role of the seeding promoter in MoS₂ growth by chemical vapor deposition* *Nano Lett.* 14 (2014) 464–72
- [24]. Wang S, Rong Y, Fan Y, Pacios M, Bhaskaran H, He K and Warner J H, *Shape evolution of monolayer MoS₂ crystals grown by chemical vapor deposition* *Chem. Mater.* 26 (2014) 6371–9
- [25]. Yu Y, Li C, Liu Y, Su L, Zhang Y and Cao L, *Controlled scalable synthesis of uniform, high-quality monolayer and few-layer MoS₂ films* *Sci. Rep.* 3 (2013) 1866
- [26]. Perkgöz N K and Bay M, *Investigation of singlewall MoS₂ monolayer flakes grown by chemical vapor deposition* *Nano-Micro Lett.* 8 (2015) 70–9
- [27]. Wenzhao Wang, Xiangbin Zeng, Shaoxiong Wu, Yang Zeng, Yishuo Hu, Jia Ding and Sue Xu, *Effect of Mo concentration on shape and size of monolayer MoS₂ crystals by chemical vapor deposition* *J. Phys. D: Appl. Phys.* 113372.R1 (2017)
- [28]. Nataliia S Vorobeva, Alexey Lipatov, Dmitry S Muratov and Alexander Sinitskii, *Chemical vapor deposition and characterization of two-dimensional molybdenum dioxide (MoO₂) nanoplatelets* *Nanotechnol.* 29 (2018) 505707

La_{1-x}Sr_xMnO₃ NANOPARTICLES: SYNTHESIZED BY ULTRASOUND WAVE AND HIGH ANNEALING TEMPERATURE

Phan Van Cuong¹ and Nguyen Quang Trung²

¹Department of Physics, Nha Trang University, 02 Nguyen Dinh Chieu.St. Nhatrang, Vietnam;

²To Van On high school, Van Ninh, Khanh Hoa, Vietnam

Email: cuongpv@ntu.edu.vn

ABSTRACT

In this work, single-crystal Ln_{1-x}Sr_xMnO₃ (x = 0.1, 0.2, and 0.3) nanoparticles (NPs) were synthesized by ultrasound wave and post annealing temperature. The diameter of the Ln_{1-x}Sr_xMnO₃ nanoparticles are from 40 nm to 80 nm range. TEM images reveal that the surface of the NPs is very clean without any sheathed amorphous phase. The resistivity ρ depends on the temperature measured in the temperature range of 5 K - 300 K at zero field for three samples. All samples show the metal-insulator transition at the temperature T_p. The T_p increases in conjunction with the increase of the doping level clearly observed. The magnitude of resistivity ρ decreases with increasing of the doping level. The largest ρ value of sample x = 0.1 also is very low comparison with bulk materials. The insulator-metal transition temperatures T_p of our samples are 165 K, 248 K, and 264 K for x = 0.1, 0.2, and 0.3, respectively. Magnetization M as a function of temperature is measured at 0.5 T magnetic field in the temperature range of 25 K - 400 K for the La_{1-x}Sr_xMnO₃ NPs, the results show that all samples undergo a ferromagnetic transition.

Keywords: Ln_{1-x}Sr_xMnO₃, perovskite, doped manganese, nanoparticle

INTRODUCTION

Doped manganese perovskites with a formula Ln_{1-x}A_xMnO₃ (Ln: a trivalent rare-earth element; A: a divalent alkaline-earth element) have attracted considerable interest. On cooling, these compounds show a large decrease in resistivity associated with a paramagnetic to ferromagnetic transition [1]. This transition is known to give rise to a large negative magnetoresistance, the so-called colossal magnetoresistance [2, 3], near Curie temperature, T_c.

In this work, single-crystal Ln_{1-x}Sr_xMnO₃ (x = 0.1, 0.2, and 0.3) nanoparticles (NPs) were synthesized by ultrasound wave and high annealing temperature. The prepared samples were investigated by X-ray diffraction (XRD, Rigaku, Japan), field emission scanning electron microscope (FE-SEM, Hitachi S-4300, Japan), transmission electron microscopy (TEM), high-resolution transmission electron microscopy (HRTEM), and selected-area electron diffraction (SAED, Philips CM 200 STEM). The chemical compositions of samples were determined by energy-dispersive spectroscopy analysis. The temperature dependence of the resistivity of samples was measured by using four-probe

technique. The magnetic measurement was performed in a magnetic property measurement system (Quantum Design, MPMS XL 7.0).

EXPERIMENTAL

Ken Suslick [4, 5] and Detlef Lohse [6] studied about the creating the bubbles in liquid by the ultrasound. The study shows that the bubbles are low temperature and low pressure at the initial state, then grow, and collapse. The life time of each bubble is about microsecond. When the bubbles collapse, they generate the local temperature and local pressure about 5000°C and 500 atm, respectively. Figure 1 shows the schematic of the ultrasound wave creating the bubbles in liquid. From these research results we tried to apply for synthesizing the Ln_{1-x}Sr_xMnO₃ (x = 0.1, 0.2, and 0.3) nanoparticles with the post annealing to enhance the crystallinity of NPs.

High-purity KMnO₄, MnCl₂·4H₂O, La(NO₃)₃·6H₂O, Sr(NO₃)₂ were used as starting materials. KOH served as mineralizer. All chemical reagents were purchased from Sigma-Aldrich (USA) without further purification.

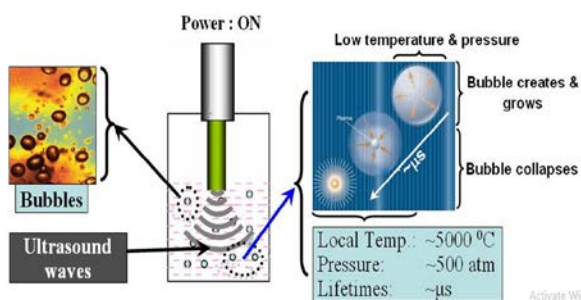


Figure 1. Schematic of the ultrasound wave create the bubbles in liquid

The synthetic procedure was as follows. All the above chemicals were dissolved in de-ionized water by stirring at room temperature. Finally, KOH was added and stirred vigorously to adjust the alkalinity. The sonication of mixed solution was carried out for 5 min in air with amplitude 45%, power 47 W using an ultrasonic probe with a 1/2 inch titanium tip (Branson Digital Sonifier, Model 450, Branson Ultrasonics Corporation, Danbury). The probe tip was kept at 1 cm from the top of the solution surface. After 5 min sonication, the solution was cooled, centrifuged, and washed several times with de-ionized water. Then the samples were dried in a vacuum oven at 70°C overnight. A black powder was finally obtained. Subsequently this powder was pressed in the same pressure to make the pellets with the size of 10mm×4mm×1mm. Then the pellets of $\text{La}_{1-x}\text{Sr}_x\text{MnO}_3$ ($x = 0.1, 0.2, \text{ and } 0.3$) NPs were finally sintered at 950°C for 10h.

RESULTS AND DISCUSSION

The chemical composition of all samples is analyzed by energy-dispersive spectroscopy measurement. The results indicate that La:Sr:Mn molar ratios of the samples ($\text{La}_{0.9}\text{Sr}_{0.1}\text{MnO}_3$, $\text{La}_{0.8}\text{Sr}_{0.2}\text{MnO}_3$, and $\text{La}_{0.7}\text{Sr}_{0.3}\text{MnO}_3$) are 0.88:0.11:1.00, 0.81:0.19:1.00, and 0.72:0.29:1.0, respectively.

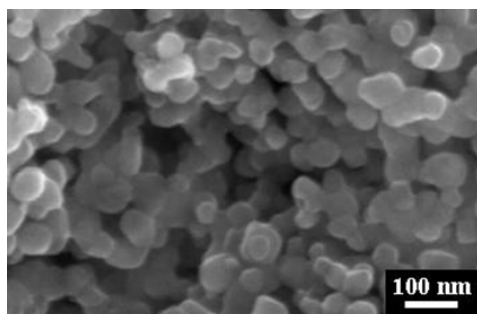


Figure 2. SEM image of $\text{La}_{0.7}\text{Sr}_{0.3}\text{MnO}_3$ nanoparticles.

In figure 2, we show the SEM image of $\text{La}_{0.7}\text{Sr}_{0.3}\text{MnO}_3$ NPs. The diameter of the LSMO NPs obtained by us varies in the 40-80 nm range. TEM and HRTEM images of $\text{La}_{0.8}\text{Sr}_{0.2}\text{MnO}_3$ NPs are shown in figure 3. The images reveal that the surface of LSMO NPs is very clean without any sheathed amorphous phase. The HRTEM image exhibits a lattice spacing of NPs of about 0.38 nm which corresponds to the (100) plane. The inset shows the corresponding SAED pattern with $[1\bar{1}0]$ zone-axis and it indicates that LSMO NPs are single crystalline. The blurred rings are the electron diffraction patterns of copper grid.

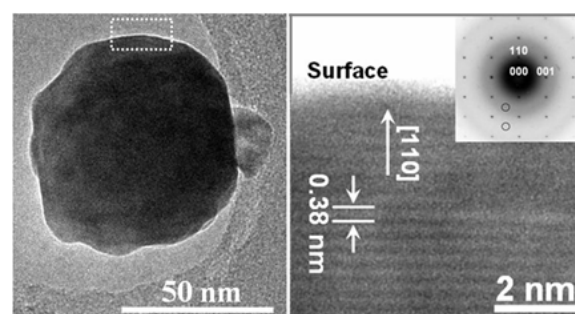


Figure 3. Typical TEM and HRTEM images of $\text{La}_{0.8}\text{Sr}_{0.2}\text{MnO}_3$ nanoparticles. The inset shows the corresponding SAED pattern, and the blurred rings are the electron diffraction patterns of copper grid.

Figure 4 shows the resistivity ρ depends on the temperature measured in the temperature range of 5 K - 300 K at zero field for three samples. All samples show the metal-insulator transition at the temperature T_p which is corresponding to the peak position of $\rho(T)$. (T_p : vertical arrow). The T_p increases in conjunction with the increase of the doping level clearly observed. The magnitude of resistivity ρ decreases with increasing of the doping level. The largest ρ value of sample $x = 0.1$ also is very low comparison with bulk materials [7]. The insulator-metal transition temperatures T_p of our samples are 165 K, 248 K, and 264 K for $x = 0.1, 0.2, \text{ and } 0.3$, respectively.

Magnetization M as a function of temperature measured at 0.5 T magnetic field in the temperature range of 25 K - 400 K for the $\text{La}_{1-x}\text{Sr}_x\text{MnO}_3$ NPs is shown in figure 5.

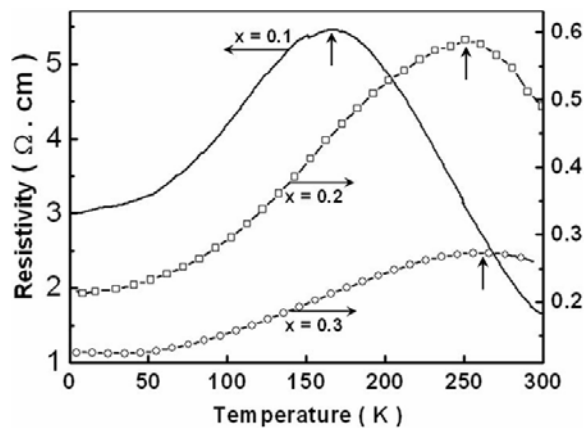


Figure 4. Electrical resistivity vs temperature for samples ($x = 0.1, 0.2,$ and 0.3).

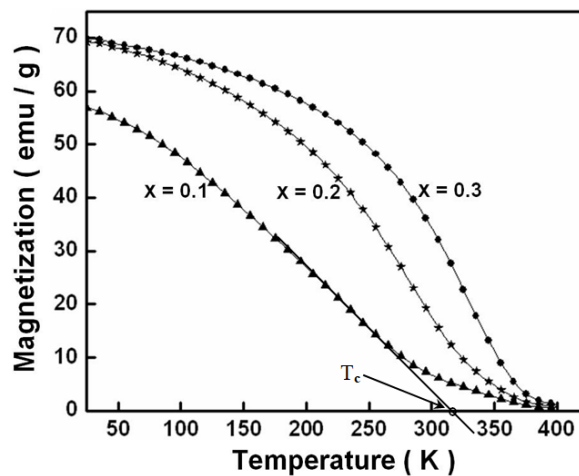


Figure 5. Magnetization M as a function of temperature measured at $0.5T$ magnetic field for three sample.

The results show that all samples undergo a ferromagnetic transition. The T_c values of samples ($x = 0.1, 0.2,$ and 0.3) are found to be $321K, 349K,$ and $377K,$ respectively. These values are higher than that of previous reports for single-crystal LSMO NPs [7-9]. It is very interesting that with increase of the doping level, the ferromagnetic transition temperature T_c is increased closely to linear. The values of magnetization M at $25K$ for the different samples ($x = 0.1, 0.2,$ and 0.3) are $56.7, 69.2,$ and 70.0 emu/g, respectively.

CONCLUSION

The single-crystal $Ln_{1-x}Sr_xMnO_3$ ($x = 0.1, 0.2,$ and 0.3) NPs were synthesized successfully by ultrasound wave and post annealing temperature. $Ln_{1-x}Sr_xMnO_3$ nanoparticles have diameters from 40 nm to 80 nm. TEM images show that NPs have clean surface without any sheathed amorphous phase. All samples show

the metal-insulator transition at the temperature T_p . The T_p increases in conjunction with the increase of the doping level. The magnitude of resistivity ρ decreases with increasing of the doping level. The largest ρ value of sample $x = 0.1$ also is very low comparison with bulk materials. Magnetization M as a function of temperature is measured at 0.5 T magnetic field in the temperature range of $25K - 400K$ for the $La_{1-x}Sr_xMnO_3$ NPs, the results show that all samples undergo a ferromagnetic transition.

Acknowledgment

This work was supported by KRF grant (No. KRF-C00536).

References

- [1] G. H. Jonker and J. H. Van Santen, *Ferromagnetic compounds of manganese with perovskite structure*, Physica **16** (1950) 337-349
- [2] S. Jin, T. H. Tiefel, M. McCormack, R. A. Fastnacht, R. Ramesh, and L. H. Chen, *Thousandfold Change in Resistivity in Magnetoresistive La-Ca-Mn-O Films*, Science **264** (1994) 413-415
- [3] R. von Helmolt, J. Wecker, B. Holzapfel, L. Schultz, and K. Samwer, *Giant negative magnetoresistance in perovskitelike $La_{2/3}Ba_{1/3}MnO_x$ ferromagnetic films*, Physical Review Letters **71** (1993) 2331-2336
- [4] K. S. Suslick, *Sonochemistry*, Science **247** (1990) 1439-1445
- [5] Y. T. Didenko and K. S. Suslick, *The energy efficiency of formation of photons, radicals and ions during single-bubble cavitation*, Nature **418** (2002) 394-397
- [6] Detlef Lohse, *Sonoluminescence: Inside a micro-reactor*, Nature **418** (2002) 381-383
- [7] A. Urushibara, Y. Moritomo, T. Arima, A. Asamitsu, G. Kido, and Y. Tokura, *Insulator-metal transition and giant magnetoresistance in $La_{1-x}Sr_xMnO_3$* , Physical Review B **51** (1995) 14103-14109
- [8] D. R. Sahu, B. K. Roul, P. Pramanik, and J.-L. Huang, *Synthesis of $La_{0.7}Sr_{0.3}MnO_3$ materials by versatile chemical technique*, Physica B: Condensed Matter **369** (2005) 209-214
- [9] R. F. C. Marques, M. Jafellicci, C. O. Paiva-Santos, R. F. Jardim, J. A. Souza, L. C. Varanda, and R. H. M. Godoi, *Nanoparticle Synthesis of $La_{1-x}Sr_xMnO_3$ (0.1, 0.2 and 0.3) Perovskites*, IEEE TRANSACTIONS ON MAGNETICS **38** (2002) 2892-2894

A NOVEL CATHODIC COMPOSITE IN LITHIUM ION BATTERY (LIBTs) BASED ON $\text{LiNi}_{0.7}\text{Co}_{0.3}\text{O}_2$, Li_2MnO_3 , AND LiCoO_2 COMBINATION: SYNTHESIS AND CHARACTERIZATION

**Thu Thi Pham^{1*}, Majid Monajjemi^{1,2*}, Fatemeh Mollaamin¹, Azam Ghadami²
and Chien Mau Dang¹**

¹ Institute for Nanotechnology, Vietnam National University-Ho Chi Minh City, Community 6, Linh Trung Ward, Thu Duc District, Ho Chi Minh City, Vietnam;

² Department of Chemical engineering, Central Tehran Branch, Islamic Azad University, Tehran, Iran
Email: Maj.monajjemi@iauctb.ac.ir

ABSTRACT

Various composites including $(1-x-y)\text{LiNi}_{0.7}\text{Co}_{0.3}\text{O}_2$, $x\text{Li}_2\text{MnO}_3$ and $y\text{LiCoO}_2$ systems were synthesized using the sol-gel method. Stoichiometric weights of the LiNO_3 , $\text{Mn}(\text{Ac})_2 \cdot 4\text{H}_2\text{O}$, $\text{Co}(\text{Ac})_2 \cdot 4\text{H}_2\text{O}$, $\text{Ni}(\text{NO}_3)_2 \cdot 6\text{H}_2\text{O}$ for preparing of 28 samples have been used. We exhibited the sample " $\text{Li}_{1.167}\text{Ni}_{0.117}\text{Co}_{0.699}\text{Al}_{0.017}\text{Mn}_{0.167}\text{O}_2$ " with Al doped is the best composition for cathode material in LIBTs. Obviously, the used weight of cobalt in this sample is lower compared to LiCoO_2 that is an advantage in view point of cost and toxic. Charge-discharge characteristics of the mentioned cathode materials were investigated by performing cycle tests in the range of 2.4 - 4.6V. Our results confirmed that these kind systems can help removing the mentioned disadvantage of cobalt with high efficiency.

Keywords: Lithium ion battery, LiCoO_2 , Li_2MnO_3 , sol-gel method.

INTRODUCTION

Transition elements of cathode materials including manganese, nickel cobalt (NMC), are especial metals for lithium ion batteries (LIBs) due to their potentials for operating in high voltages and large energy storing in a small space. Although the Ni in NMC gives a high capacity for storing energies, it is also passive and unstable, with a propensity towards destructive reactions with the electrolyte. There are both advantages and disadvantages factors for NMC of LIBTs [1-5]. A major disadvantage of cobalt is its cost and toxic and typically it is around two times more costly to manufacture than nickel. This is one important factor when considering its use in mass produced consumer items which any extra cost is a basic issue. Safety factor is also a matter of crucial importance to the lithium batteries which this problem appears in big size batteries as compared to the small size batteries i.e. batteries for electric vehicle would have more risk of catching fire as compared to batteries for cell phones. When mixed solid solution is used as cathode material, the explosion of batteries can be control, especially with doping of other elements such as Al. Moreover $(1-x-$

$y)\text{LiNi}_{0.7}\text{Co}_{0.3}\text{O}_2$ doped with Al are environment friendly as compared to isolated cathode such as LiCoO_2 [4,5].

The purpose of this study is to find a ternary solid solution of Li-based cathode material in NMC that is advantageous replacement for LiCoO_2 which is expensive and toxic. Therefore a combination of ternary composition diagram including $(1-x-y)\text{LiNi}_{0.7}\text{Co}_{0.3}\text{O}_2$, $x\text{Li}_2\text{MnO}_3$ and $y\text{LiCoO}_2$ have been considered. NMC LIBTs were the most interest among the scientist to replace with LiCoO_2 which firstly reported by Rossen et al in 1992 [6] for composition of $\text{LiNi}_{0.5}\text{Mn}_{0.5}\text{O}_2$.

Similar the work of Rossen [6], a study was reported in 1998 by Saphr et al [7] in view point of electrochemical behavior which indicate Ni as an active ion and Mn were present in "+2" and "+4" oxidation rather the "+3". They exhibited in temperature of 750 there are a large falling capacity after 25 cycle from 150mAhg^{-1} to 125mAhg^{-1} after 25 cycles and to 75mAhg^{-1} after 50 cycles. Nickel, which forms between +2 and +4 valences positions is active material in this cathode composition, meanwhile manganese is +4, which remain without Jahn-Teller distortion with the +3 valance (Mn^{+3}). Makimura and coworkers [8] presented an initial discharging

around 150.5 mAhg⁻¹ for 30 cycles at 4.35 V and again in 2003 [9] their results exhibited 200 mAhg⁻¹ of rechargeable capacity of LiNi_{0.5}Mn_{0.5}O₂ among the voltages of 2.5-4.5 V after 30 cycles [9].

Obviously, mixing proper mole fractions of various transition elements [8, 9] to get the advantageous efficiency of each led to the discovery of these kind materials. Therefore these materials are derived from Li(Ni_{1-x-y}Mn_xCo_y)O₂ categorize that were first published in 1999 and 2000 by Liu and Yoshio respectively [10, 11]. They exhibited that the enhancement of cobalt would stabilize the composition blocks the Ni from entering the lithium layers. Meanwhile nickel and manganese would provide the structural stabilities and high capacities respectively. As too much of cobalt causes decreasing capacities and large amount of nickel and manganese making problems in cation mixing and spinel structures, therefore mixing of these elements must be optimized with suitable mole fraction.

Makimura and coworkers in 2001 synthesize the layered compound of LiNi_{1/3}Mn_{1/3}Co_{1/3}O₂ [12] and exhibited that this cathode has about 205mAhg⁻¹ reversible discharge capacity in the range of 2.6-4.5 V including large rate capabilities and thermal stabilities.

For appropriate stoichiometry of Li(Ni_xCo_{1-2x}Mn_x)O₂, x = 1/3, the medium oxidation numbers must be +3 such as Mn⁺⁴, Co⁺³, and Ni⁺², with electrochemical flow in the ranges between 2.5 up to 4.4 volte versus lithium ions (through two electron transfer reaction between Co⁺³/Co⁺⁴ and Ni⁺²/Ni⁺⁴) [13]. In addition concerning of further electrochemical phenomenon some more studies of LiNi_{0.4}Mn_{0.4}Co_{0.2}O₂ [14], LiNi_{0.8}Co_{0.2}O₂ and LiNi_{0.8}Co_{0.15}Al_{0.05}O₂ cathodes [15] have been shown. Although the rate capability of this material is smaller than that of LiCoO₂, thermal stabilities are much better.

In this work we focused on various composition of binary and ternary solid solutions containing Li₂MnO₃, LiCoO₂ and (1-x-y)LiNi_{0.7}Co_{0.3}O₂ doped with Al. Currently, Li₂MnO₃ has been distinguished for its suitable capacity, better safety, without toxic and inexpensive than LiCoO₂ [16].

EXPERIMENTAL

Stoichiometric weights of the LiNO₃, Mn(Ac)₂·4H₂O, Co(Ac)₂·4H₂O,

Ni(NO₃)₂·6H₂O as starting materials of lithium, manganese, cobalt and nickel, in 28 samples of {(1-x-y)LiNi_{0.7}Co_{0.3}O₂} doped with Al. These mixtures were first dissolved in 50 ml of DI H₂O and then equivalence-molar weights of citric acid were added (the amount of citric acid was equal to the total molar of Co, Ni, and Al). The whole mixtures were heated through water bath at 90°C and during the heating process, a clear, pink solution without any precipitation formed. At last, the clear solution was slowly dried and turned into gel. This solution was continuously stirred for about 25 mins for the formation of a homogeneous mixture of gel and then is kept under a hot-plate for 12-14 hrs around 100°C so that all the distilled water gets evaporated. Usually, acetate requires two heating temperatures (low and high) for the formation of a correct phase. The beaker containing the gel is then kept in a furnace and is heated to 450°C for 3-5 hrs. The first heating is at a low temperature. Basically what happens during this stage is that all the acetates present would get burned off, but the desired phase is not formed. The heat-treated products were ground in an agate mortar to obtain powders and then the powder was calcined at 800-850°C for 10-12 hrs.

RESULTS AND DISCUSSION

This investigation is used for finding the best cathode material compositions including (1-x-y)LiNi_{0.7}Co_{0.3}O₂, xLi₂MnO₃, yLiCoO₂ systems with high initial discharge capacity, grate cyclability and inexpensive cost compared to current lithium-ion cathode materials. Therefore, initially, 28 different composition points according to using the lever rule, stoichiometric weights and mole-fractions were chosen in order to find an optimized material with good electrochemical performance. These 28 points were extracted through the triangle phase diagram of the defined system (table 1&2) and synthesis through sol-gel method.

Ni and Al amount are decreased towards down direction of triangle, meanwhile the compositions of 22, 24 have zero Ni and Al percentage. High Mn value is found at sample 22 and its content decreases at the opposite end points of the triangle. Cobalt percentage is found in a wide region in the triangle and also decreases near Li(Li_{0.33}Mn_{0.66})O₂. It is predicted which capacities and cyclability of the

compositions are directly related to the amount of Mn, Co, Ni, and Al. It is notable, specific capacity is determined as the amount of energies which can be reserve in volume or mass (Ah),

while the rate capability (which are related to their design and varies considerably between different manufactures), can be determined as the rate at which the cell is being charged.

Table 1. 28 different composition points according to using the lever rule, stoichiometric weights and mole-fractions of the triangle diagram

Sample	Composition	Al doped
1	$\text{LiNi}_{0.7}\text{Co}_{0.3}\text{O}_2$	$\text{LiNi}_{0.7}\text{Co}_{0.2}\text{Al}_{0.1}\text{O}_2$
2	$\text{Li}_{1.167}\text{Ni}_{0.583}\text{Co}_{0.25}\text{Mn}_{0.167}\text{O}_2$	$\text{Li}_{1.167}\text{Ni}_{0.583}\text{Co}_{0.167}\text{Al}_{0.083}\text{Mn}_{0.167}\text{O}_2$
3	$\text{LiNi}_{0.583}\text{Co}_{0.417}\text{O}_2$	$\text{LiNi}_{0.583}\text{Co}_{0.334}\text{Al}_{0.083}\text{O}_2$
4	$\text{Li}_{1.333}\text{Ni}_{0.467}\text{Co}_{0.203}\text{Mn}_{0.333}\text{O}_2$	$\text{Li}_{1.333}\text{Ni}_{0.467}\text{Co}_{0.133}\text{Al}_{0.067}\text{Mn}_{0.333}\text{O}_2$
5	$\text{Li}_{1.167}\text{Ni}_{0.467}\text{Co}_{0.366}\text{Mn}_{0.167}\text{O}_2$	$\text{Li}_{1.167}\text{Ni}_{0.467}\text{Co}_{0.299}\text{Al}_{0.067}\text{Mn}_{0.167}\text{O}_2$
6	$\text{LiNi}_{0.467}\text{Co}_{0.533}\text{O}_2$	$\text{LiNi}_{0.467}\text{Co}_{0.466}\text{Al}_{0.067}\text{O}_2$
7	$\text{Li}_{1.5}\text{Ni}_{0.35}\text{Co}_{0.15}\text{Mn}_{0.5}\text{O}_2$	$\text{Li}_{1.5}\text{Ni}_{0.35}\text{Co}_{0.1}\text{Al}_{0.05}\text{Mn}_{0.5}\text{O}_2$
8	$\text{Li}_{1.333}\text{Ni}_{0.35}\text{Co}_{0.317}\text{Mn}_{0.333}\text{O}_2$	$\text{Li}_{1.333}\text{Ni}_{0.35}\text{Co}_{0.267}\text{Al}_{0.05}\text{Mn}_{0.333}\text{O}_2$
9	$\text{Li}_{1.167}\text{Ni}_{0.35}\text{Co}_{0.483}\text{Mn}_{0.167}\text{O}_2$	$\text{Li}_{1.167}\text{Ni}_{0.35}\text{Co}_{0.433}\text{Al}_{0.05}\text{Mn}_{0.167}\text{O}_2$
10	$\text{LiNi}_{0.35}\text{Co}_{0.6}\text{O}_2$	$\text{LiNi}_{0.35}\text{Co}_{0.6}\text{Al}_{0.05}\text{O}_2$
11	$\text{Li}_{1.667}\text{Ni}_{0.233}\text{Co}_{0.1}\text{Mn}_{0.667}\text{O}_2$	$\text{Li}_{1.667}\text{Ni}_{0.233}\text{Co}_{0.067}\text{Al}_{0.033}\text{Mn}_{0.667}\text{O}_2$
12	$\text{Li}_{1.5}\text{Ni}_{0.233}\text{Co}_{0.267}\text{Mn}_{0.5}\text{O}_2$	$\text{Li}_{1.5}\text{Ni}_{0.233}\text{Co}_{0.234}\text{Al}_{0.033}\text{Mn}_{0.5}\text{O}_2$
13	$\text{Li}_{1.333}\text{Ni}_{0.233}\text{Co}_{0.434}\text{Mn}_{0.333}\text{O}_2$	$\text{Li}_{1.333}\text{Ni}_{0.233}\text{Co}_{0.4}\text{Al}_{0.033}\text{Mn}_{0.333}\text{O}_2$
14	$\text{Li}_{1.167}\text{Ni}_{0.233}\text{Co}_{0.6}\text{Mn}_{0.167}\text{O}_2$	$\text{Li}_{0.167}\text{Ni}_{0.233}\text{Co}_{0.567}\text{Al}_{0.033}\text{Mn}_{0.167}\text{O}_2$
15	$\text{LiNi}_{0.233}\text{Co}_{0.767}\text{O}_2$	$\text{LiNi}_{0.233}\text{Co}_{0.734}\text{Al}_{0.033}\text{O}_2$
16	$\text{Li}_{1.835}\text{Ni}_{0.116}\text{Co}_{0.049}\text{Mn}_{0.835}\text{O}_2$	$\text{Li}_{1.833}\text{Ni}_{0.117}\text{Co}_{0.033}\text{Al}_{0.017}\text{Mn}_{0.833}\text{O}_2$
17	$\text{Li}_{1.667}\text{Ni}_{0.116}\text{Co}_{0.217}\text{Mn}_{0.667}\text{O}_2$	$\text{Li}_{1.667}\text{Ni}_{0.117}\text{Co}_{0.199}\text{Al}_{0.017}\text{Mn}_{0.667}\text{O}_2$
18	$\text{Li}_{1.5}\text{Ni}_{0.116}\text{Co}_{0.384}\text{Mn}_{0.5}\text{O}_2$	$\text{Li}_{1.5}\text{Ni}_{0.117}\text{Co}_{0.366}\text{Al}_{0.017}\text{Mn}_{0.5}\text{O}_2$
19	$\text{Li}_{1.333}\text{Ni}_{0.116}\text{Co}_{0.551}\text{Mn}_{0.333}\text{O}_2$	$\text{Li}_{1.333}\text{Ni}_{0.117}\text{Co}_{0.533}\text{Al}_{0.017}\text{Mn}_{0.333}\text{O}_2$
20	$\text{Li}_{1.167}\text{Ni}_{0.116}\text{Co}_{0.717}\text{Mn}_{0.167}\text{O}_2$	$\text{Li}_{1.167}\text{Ni}_{0.117}\text{Co}_{0.699}\text{Al}_{0.017}\text{Mn}_{0.167}\text{O}_2$
21	$\text{LiNi}_{0.116}\text{Co}_{0.884}\text{O}_2$	$\text{LiNi}_{0.117}\text{Co}_{0.866}\text{Al}_{0.017}\text{O}_2$
22	Li_2MnO_2	Li_2MnO_2
23	$\text{Li}_{1.833}\text{Co}_{0.167}\text{Mn}_{0.833}\text{O}_2$	$\text{Li}_{1.833}\text{Co}_{0.167}\text{Mn}_{0.833}\text{O}_2$
24	$\text{Li}_{1.667}\text{Co}_{0.333}\text{Mn}_{0.667}\text{O}_2$	$\text{Li}_{1.667}\text{Co}_{0.333}\text{Mn}_{0.667}\text{O}_2$
25	$\text{Li}_{1.5}\text{Co}_{0.5}\text{Mn}_{0.5}\text{O}_2$	$\text{Li}_{1.5}\text{Co}_{0.5}\text{Mn}_{0.5}\text{O}_2$
26	$\text{Li}_{1.333}\text{Co}_{0.667}\text{Mn}_{0.333}\text{O}_2$	$\text{Li}_{1.333}\text{Co}_{0.667}\text{Mn}_{0.333}\text{O}_2$
27	$\text{Li}_{1.167}\text{Co}_{0.833}\text{Mn}_{0.167}\text{O}_2$	$\text{Li}_{1.167}\text{Co}_{0.833}\text{Mn}_{0.167}\text{O}_2$
28	LiCoO_2	LiCoO_2

Therefore, the C-rate is the capacity of the battery divided by the hourly charging rate. The discharge capacity curves of this work have been compared with 18650-type “C/LiCoO₂ Sony battery” result which is modified by Ehrlich [21]. Since LiCoO₂ cathode has an initial discharge capacity around 145mAhg⁻¹ [22], therefore any materials of these compositions with initial capacities more than this amount (of course with a suitable cyclability) might be considered. The samples were tested via a cyler (Arbin BT 2000 battery testing system), between 2.4 V and 4.6 V with low C-rate of C/12. The initial results indicate of a wide range and irregular of cyclability and capacities. The initial discharge capacities varied from 102 mAhg⁻¹ to 248 “mAhg⁻¹”. Both

capacity and cyclability increase from LiNi_{0.7}Co_{0.3}Al_{0.1}O₂ towards the binary composition of Li₂MnO₃ and LiCoO₂.

Although sample 20 shows high capacity of “248.1” mAhg⁻¹, it contains of a low cyclability. The sample 25 and 18 exhibit a good capacity of 201.2 and 220.2 mAhg⁻¹, respectively with high cyclability, meanwhile due to Mn⁴⁺ ion the sample 22 has a low capacity. Although these kinds of data are not sufficient for determining a suitable cathode material in view point of capacity and cyclability amount, the statistical analysis can be useful for finding the region of the best item from the data of the 28 compositions. Therefore any testing with both capacity and cyclability relation in view point of the triangle regions is needed. In this work the STATISTICA software has been used for

analyzing the data which variable (1), variable (2) and variable (3), are Li_2MnO_3 , LiCoO_2 and $\text{LiNi}_{0.7}\text{Co}_{0.2}\text{Al}_{0.1}\text{O}_2$ mole-fraction respectively while the variable (4) alternately, are the capacity and cyclability (Table 2 and Figs 1&2).

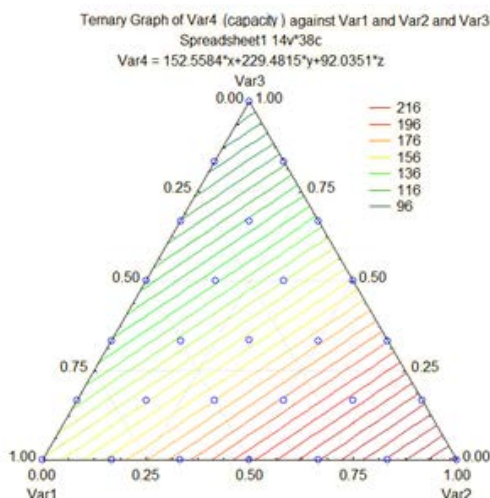


Figure 1. Ternary of capacity versus variable (1), variable (2) and variable (3) for 28 samples of $(1-x-y)\text{LiNi}_{0.7}\text{Co}_{0.2}\text{Al}_{0.1}$, $x\text{Li}_2\text{MnO}_3$, $y\text{LiCoO}_2$ composites

By this work various compositions are used for exploring the novel cathode materials with two-dimensional layered structure through the ternary composition's diagram among Iso-structural material.

Although Li_2MnO_3 or $\text{Li}[\text{Li}_{1/3}\text{Mn}_{2/3}]\text{O}_2$ has a structure similar to LiCoO_2 , there is super-lattice ordering of Mn^{4+} and Li^+ in transition layers. $\text{LiNi}_{0.7}\text{Co}_{0.2}\text{Al}_{0.1}\text{O}_2$ can be demonstrated as solid solution between LiCoO_2 and LiNiO_2 with Al doped in Co site, is a promising cathode material because of its improved stabilities and electrochemical performances. Through an analyzing among these compositions, three samples were chosen and subsequently synthesized, characterized and tested consequently with high precisionist. Via initial discharge capacity and some extra results numbers 20, 27 and 28 are indicated as the best cathode material among those structures (Figs. 3&4, table 1&2). As the number 28 is pure material (LiCoO_2) and number 27 is binary, the number 20 “ $\text{Li}_{1.167}\text{Ni}_{0.117}\text{Co}_{0.699}\text{Al}_{0.017}\text{Mn}_{0.167}\text{O}_2$ ” is suggested as the best composition for cathode material by this work. Obviously, the used weight of cobalt in these samples is lower compared with LiCoO_2 that is an advantage in view point of cost in this study.

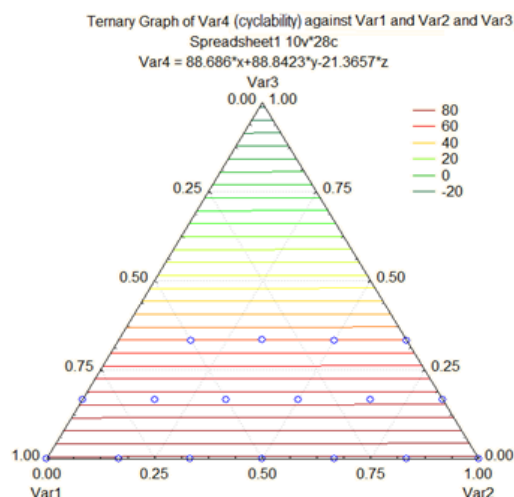


Figure 2. Ternary of cyclability versus variable (1), variable (2) and variable (3) for 28 samples of $(1-x-y)\text{LiNi}_{0.7}\text{Co}_{0.2}\text{Al}_{0.1}$, $x\text{Li}_2\text{MnO}_3$, $y\text{LiCoO}_2$ composites

The repeat of sample 20 was made into T-Cells and subjected to electrochemical testing using the original conditions and the cycling was accomplished between 2.4-4.6 V with constant C-rate of C/12 at room temperature (Fig. 5).

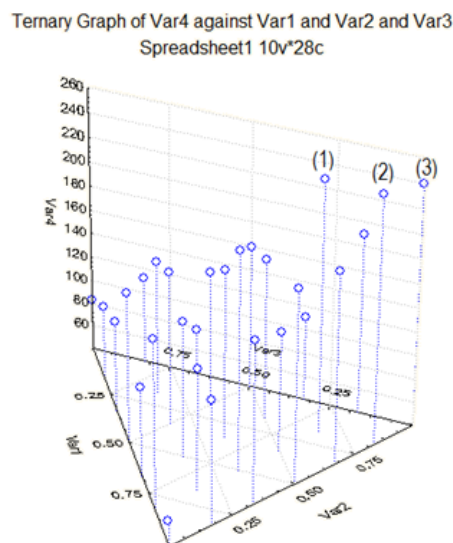


Figure 3. Three samples of $(1-x-y)\text{LiNi}_{0.7}\text{Co}_{0.2}\text{Al}_{0.1}\text{O}_2$, $x\text{Li}_2\text{MnO}_3$, $y\text{LiCoO}_2$ composites with high precisionist of capacity and cyclability versus variable (1), variable (2) and variable (3)

Table 2. Summary capacity and cyclability for 28 samples, of the system $[(1-x-y)\text{LiNi}_{0.7}\text{Co}_{0.2}\text{Al}_{0.1}]\text{O}_2$

Sample	Blend	Li_2MnO_3	LiCoO_2	$\text{LiNi}_{0.7}\text{Co}_{0.2}\text{Al}_{0.1}\text{O}_2$	Capacity	Cyclability
1	Pure	0	0	1	82.5	51
2	Binary	0.167	0	0.833	102.3	46
3	Binary	0	0.167	0.833	112.2	49
4	Binary	0.333	0	0.667	115.5	52
5	Ternary	0.167	0.167	0.667	150.5	60
6	Binary	0	0.333	0.667	78.5	80
7	Binary	0.500	0	0.500	165.5	82
8	Ternary	0.333	0.167	0.500	167.2	61
9	Ternary	0.167	0.333	0.500	153.1	81
10	Binary	0	0.500	0.500	159.2	79
11	Binary	0.667	0	0.333	114.7	99
12	Ternary	0.500	0.167	0.333	153.1	93
13	Ternary	0.333	0.333	0.333	180.1	78
14	Ternary	0.167	0.500	0.333	173.2	80
15	Binary	0	0.667	0.333	110.6	91
16	Binary	0.833	0	0.167	181.3	75
17	Ternary	0.667	0.167	0.167	141.5	95
18	Ternary	0.500	0.333	0.167	220.2	99
19	Ternary	0.333	0.5	0.167	139.3	92
20	Ternary	0.167	0.667	0.167	248.1	54
21	Binary	0	0.833	0.167	189.5	92
22	Pure	1	0	0	61.5	91
23	Binary	0.833	0.167	0	143.5	90
24	Binary	0.667	0.333	0	175.2	90
25	Binary	0.500	0.500	0	201.2	90
26	Binary	0.333	0.667	0	199.5	46
27	Binary	0.167	0.833	0	245.5	78
28	Pure	0	1	0	240.2	80

The repeat sample exhibits better charge and discharge capacities (discharge capacity of 150, mAhg^{-1}) than the original sample. This improvement in the capacities is attributed to the synthesis conditions. With the same method we used $(1-x-y)\text{LiNi}_{0.7}\text{Co}_{0.3}\text{O}_2$, $x\text{Li}_2\text{MnO}_3$ and $y\text{LiCoO}_2$ composites the sample $\text{Li}_{1.167}\text{Ni}_{0.116}\text{Co}_{0.717}\text{Mn}_{0.167}\text{O}_2$ has been tested for comparing to $\text{Li}_{1.167}\text{Ni}_{0.117}\text{Co}_{0.699}\text{Al}_{0.017}\text{Mn}_{0.167}\text{O}_2$ (Fig. 5) in viewpoints of capacity and cyclability. The repeat sample exhibits in the same mole fraction, the system with Al doped has a better charge and discharge capacities (discharge capacity of 155, mAhg^{-1}) compare to non Al doped system (discharge capacity of 144, mAhg^{-1}).

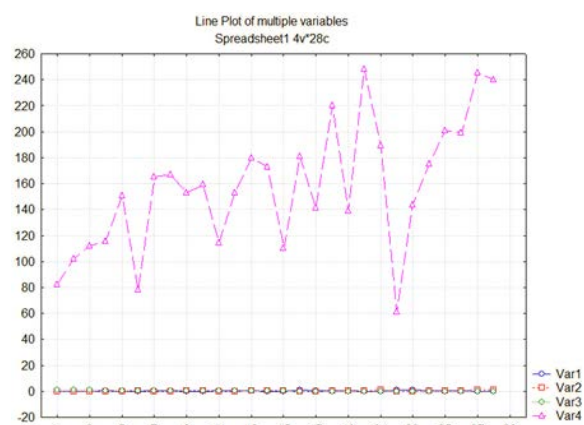


Figure 4. Multiple variable combinations of capacities and cyclability based on mole-fraction of variable (1), variable (2) and variable (3) in 28 composition

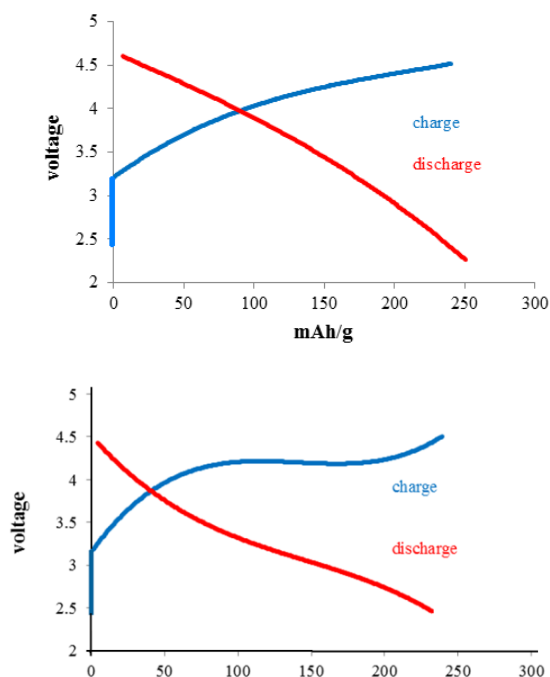


Figure 5. Charge and discharge capacity of (a): $\text{Li}_{1.167}\text{Ni}_{0.117}\text{Co}_{0.699}\text{Al}_{0.017}\text{Mn}_{0.167}\text{O}_2$ and (b): $\text{Li}_{1.167}\text{Ni}_{0.116}\text{Co}_{0.717}\text{Mn}_{0.167}\text{O}_2$

CONCLUSION

$\{[(1-x-y)\text{LiNi}_{0.7}\text{Co}_{0.3}\text{O}_2]\}$ doped with Al for cathodes materials with submicron particles have been successfully synthesized by a sol-gel method. The structural and electrochemical properties have been systemically investigated to examine the effects of charge/discharge capacities and also capacity retention. The results show that all the prepared “ $\text{Li}_{1.167}\text{Ni}_{0.117}\text{Co}_{0.699}\text{Al}_{0.017}\text{Mn}_{0.167}\text{O}_2$ ” type layered structure regardless of the nickel content and Al doped improve the capacity retention significantly. The percentage of nickel and cobalt exhibit a good performance. Although these kind systems can help for removing the disadvantage of cobalt which mainly is its cost and toxic, the performance of these kind systems is similar to LiCoO_2 cathode material. Therefore, fabrication of lithium-ion batteries using a few more transition elements such as Mn and Al are suggested for any further research.

Acknowledgment

This research is funded by Vietnam National University – Ho Chi Minh city (VNU-HCM) under the grand number TX2019-32-01.

References

- [1] D. Guerard, A. Herold, *Carbon* 13, 337-345 (1975).
- [2] M. Yoshio, R. J. Brodd, A. Kozawa, *Lithium-ion batteries* (Springer 2009).
- [3] B. Scrosati, J. Garche, *J. Pow. Sour.* 195 (9), 2419-2430 (2010).
- [4] C. Daniel, J. O. Besenhard, *Handbook of Battery Materials* (Wiley-VCH, 2011).
- [5] R. A. Meyers, *Encyclopedia of sustainability science and technology* (Springer, New York, 2012).
- [6] E. Rossen, C.D.W. Jones, J.R. Dahn, *Sol. Sta. Ion.* 57, 311-318 (1992).
- [7] M.E. Spahr, *J. Elec. Soc.* 145 (4), 1113- 1121 (1998).
- [8] T. Ohzuku, Y. Makimura, *Chem. Lett.* 30 (8), 744-745 (2001).
- [9] Y. Makimura, T. Ohzuku, *J. Pow. Sour.* 119–121, 156-160 (2003).
- [10] Z. Liu, A. Yu, J.Y. Lee, *J. Pow. Sour.* 81–82, 416-419 (1999).
- [11] Yoshio, M., et al., *J. Pow. Sour.* 90 (2), 176-181 (2000).
- [12] Ohzuku, T. and Y. Makimura, *Chem. Lett.* 30 (7), 642-643 (2001).
- [13] Belharouak, I., et al., *J. Pow. Sour.* 123 (2), 247-252 (2003).
- [14] Ngala, J.K., et al., *J. Mat. Chem.* 14 (2), 214-220 (2004).
- [15] Yoon, W.-S., et al., *Elec. Commun.* 8 (8), 1257-1262 (2006).
- [16] Ammundsen, B., et al., *J. Elec. Soci.* 149 (4), A431-A436 (2002).
- [17] Thackeray, M.M., et al., *J. Mat. Chem.*, 15 (23), 2257-2267 (2005).
- [18] Zhang, L., H. Noguchi, and M. Yoshio, *J. Pow. Sour.* 110 (1), 57-64 (2002).
- [19] Shin, S.S., Y.K. Sun, and K. Amine, *J. Pow. Sour.* 112 (2), 634-638 (2002).
- [20] Thu, T.P., Majid, M., Chien, M.D., *Int. J. Nanotechnol.*, 2018.
- [21] Thu, T.P., Majid, M., Dung, M.T.D., Fatemeh, M., Chien, M.D., *Biointerface Research in Applied Chemistry*, 1 (9), 3806 – 3811 (2019).
- [22] Thu, T.P., Majid, M., Dung, M.T.D., Fatemeh, M., A. Khakpour, Chien, M.D., *Biointerface Research in Applied Chemistry*, 2 (9), 3866 – 3873 (2019).
- [23] Thu, T.P., Majid, M., Dung, M.T.D., Fatemeh, M., Chien, M.D., *Biointerface Research in Applied Chemistry*, 2 (9), 3874 – 3883 (2019).
- [24] Hailang Zhang, *Adv. Mat. Sci. Engine.* 746341, 7 (2014).
- [25] Ehrlich, G.M., D, *Handbook of Lithium-ion batteries* (Linden, New York, 2002).
- [26] Z.-G. Yang, J.-L. Zhang, M. C. W. Kintner-Meyer, X.-C. Lu, D.-W. Choi, J. P. Lemmon, J. Liu, *Chem. Rev.* 111, 3577 (2011).

A STRAIGHTFORWARD ROUTE TO NANO GOLD FROM GOLD METAL AND MOLECULAR CHLORINE FOR BIOMEDICAL APPLICATIONS

¹Xuan-Truong Mai, ²Hong-Nhung Nguyen T., ¹Anh-Quan Hoang and ^{1,3}Phuong-Tung Nguyen*

¹Institute of Applied Materials Science-Vietnam Academy of Science and Technology, 1A TL 29, W. Thanh Loc, Dist. 12, Hochiminh City;

²Ho Chi Minh City University of Education, 280 An Duong Vuong, Dist.5, Ho Chi Minh City;

³Hutech University of Technology, 475A Dien Bien Phu, W. 25, Dist. Binh Thanh, Ho Chi Minh City

Email: phuongtungng@iams.vast.vn

ABSTRACT

Nano gold and $\text{Fe}_3\text{O}_4@Au$ core/shell nanoparticles have unique magnetic and optical properties. These nanoparticles are used for biomedical applications, such as magnetic resonance imaging, photothermal therapy, controlled drug delivery, protein separation, biosensors, DNA detection, and immunosensors. In this research, tetrachloroauric acid was prepared by using the known reaction of gold metal with chlorine gas. The straightforward procedure developed here allowed the resulting solution to be directly used for gold nanoparticle synthesis. The procedure involved bubbling chlorine gas through pure water containing the gold foils. After digestion, the given product was used to synthesize gold nanoparticles and magnetic core-shell gold nanoparticles. Depending on the specific controlled conditions, three different systems of nano Au, $\text{Fe}_x\text{O}_y@Au$ nano, $\text{Fe}_x\text{O}_y@Au$ nanostars have been synthesized. For each system, the size and shape were adjusted, allowing to tune the magneto-plasmonic properties. The impact of seed-growth method, nature of the reducing agent, seed amount, were analyzed and optimized. Nanoparticle products being characterized with TEM and UV-vis, were readily for further use in biomedical applications.

Keywords: Magnetic gold nanostar, plasmonic characteristic, seed growth.

INTRODUCTION

Research involving gold nanoparticles has increased significantly over the last two decades[1, 2], creating with it the need for high purity gold chloride (generally in the form of tetrachloroauric acid) as a starting material for the nanoparticle synthesis[3]. Many synthetic methods utilize aqueous solutions of gold(III) chloride for this purpose. Here we report a straightforward method to produce highly stable aqueous solutions of gold(III) chloride using gold metal and molecular chlorine as starting materials. After digestion, the given product was used to synthesize gold nanoparticles and magnetic core-shell gold nanoparticles[4-6].

EXPERIMENTAL

Materials

Gold metal ($Au \geq 99.99\%$), hydrochloric acid (HCl, 36%), potassium permanganate (KMnO_4 , 99%), sodium borohydride (NaBH_4 , 99%), hexadecyl trimethyl ammonium bromide (CTAB,

99%), sodium hydroxide (NaOH, 97%), ascorbic acid (AA, 99%), and sodium citrate (SC, 99%).

Synthesis of Tetrachloroauric Acid

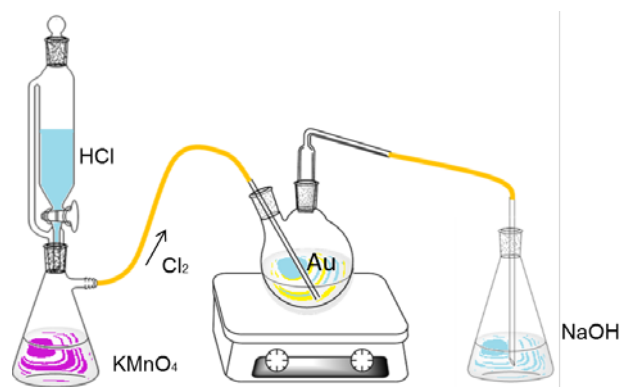


Figure 1. Apparatus for the synthesis of aqueous tetrachloroauric acid

A laboratory-scale reaction apparatus was assembled as shown in Figure 1. Hydrochloric acid (30 mL, 36%) was placed in a pressure-

equalizing dropping funnel, and slowly added drop-wise to a side-arm flask containing potassium permanganate (6.0 g). The resulting chlorine gas was passed into a two-neck round-bottom flask containing 100 mL water and one pellet of gold (~0,5g). Undissolved/unreacted chlorine gas was bubbled through a solution of NaOH. The reaction mixture was stirred at the selected temperature until all of the gold dissolved[3].

Synthesis of various Au seeds

Small GNPs with a diameter of ~5.0 nm were prepared by the following procedure: To 90 mL of deionized water, 1 mL of 1 wt % HAuCl₄.3H₂O was added, and the mixture was stirred for 1 min; then, 2 mL of 38.8 mM sodium citrate was added, and the reaction mixture was stirred for another minute. A volume of 1 mL of fresh 0.075 wt % NaBH₄ in 38.8 mM sodium citrate was added, and the reaction mixture was stirred for 5 min[1, 4].

The second step involved the preparation of Au growth solutions, as described in the paragraphs that follow. Typically, 5 mL of 0.2 M CTAB solution, 0.25 mL of 0.01 M HAuCl₄, and 4.65 mL deionized H₂O were evenly mixed in vial. Subsequently, 100 µL of the 0.04 M newly prepared AA solution was added to vial under vertical agitation. Under agitation, the color of the solution in vial changed from yellow to colorless, indicating that the Au³⁺ ions had reduced to Au⁺. The prepared growth solution should be used within a period of 1 h. The third step involved the growth of Au seeds. Typically, 25 µL of the aged seed solution in step 1 was added to growth solution 1 in vial, under agitation. This was aged for 30 min without distribution. Finally, the color of the solution appeared a wine-red shade. Subsequently, 25 µL of aged growth solution 1 in vial first was added to growth solution 2 in vial second, under agitation; finally, the color of the solution became a dark-red shade over a long period of time compared with that in the case of growth solution 1. The final Au NPs could be obtained by centrifugation of the final growth solution under various rotation speeds.

Synthesis of Fe₃O₄@Au NSs

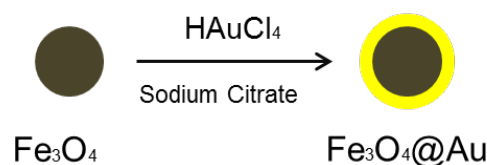


Figure 2. Synthesis of Fe₃O₄@Au core/shell nanoparticles

In a 250 mL round-bottom flask 40 ml distilled water was added to 20 mL of aqueous solution of 0.1% HAuCl₄. Then 28 mg dispersed Fe₃O₄ [7] nanoparticles in 10 ml distilled water were added into the flask. The reaction mixture was allowed to boil under reflux. Upon boiling, 4 mL of 1 wt% trisodium citrate was rapidly added into this solution under stirring resulting in color change from brown to reddish[6, 8, 9].

The solution was filtered through 0.45µm Millipore syringe filters to remove any precipitate, the pH was adjusted to 7 using dilute NaOH solution, and the filtrate was stored at room temperature.

RESULTS AND DISCUSSION

The oxidation of gold metal to form aqueous solutions of gold (III) chloride was prepared by using the bubbling chlorine gas through pure water containing the gold foils. The reaction is quantitative and no manganese-containing by-products (which may have arisen from the chlorine production process) were detected by ICP-MS. The concentration of the gold (III) chloride solutions can be reasonably accurately calculated from results of ICP-MS analysis.

To test the suitability of the gold (III) chloride solutions for direct use in nanoparticle synthesis, citrate-stabilized aqueous gold nanoparticles were synthesized. The UV-visible spectrum of the various Au seeds solution was shown in Fig 3.

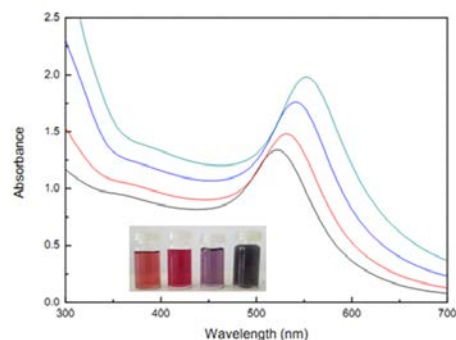


Figure 3. UV-vis spectra of nano gold.

In Figure 3, the UV-vis spectrum of the corresponding nanoflowers in dependence on wavelength λ for particle diameters between 2.5 and 100 nm were shown. The surface plasmon resonance (SPR) is clearly visible as a peak in the range between 520 and 580 nm. The peaks increase with increasing particle size.

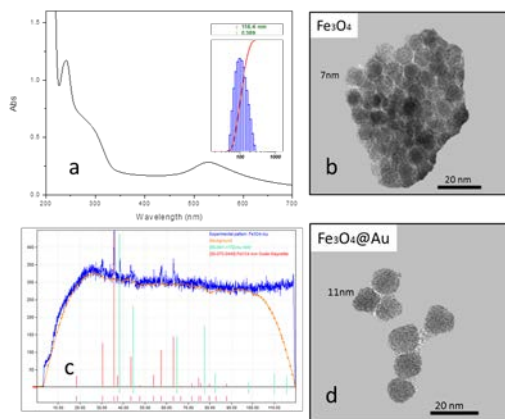


Figure 4. a) UV-vis spectra and DLS of $Fe_3O_4@Au$ c) XRD spectra of $Fe_3O_4@Au$, b,d) TEM pictures of Fe_3O_4 , $Fe_3O_4@Au$

The UV-vis spectra of the organosol were represented in Fig. 4 and characterized by broad band at 450–770 nm with maximum at 530 nm. The peak of Fig 4 relating to the absorption maximum of nano gold of Fig 3 indicated the formation of a gold shell on the surface of magnetite nanoparticles.

The XRD spectra analysis result of $Fe_3O_4@Au$ were shown in Figure 4. It was indicated that there were 6 characteristic peaks of Fe_3O_4 at $2\theta = 30.1^\circ; 35.5^\circ; 43.3^\circ; 53.4^\circ; 57.2^\circ; 62.5^\circ$. It proved that after the synthesis process, Au didn't change the structure of Fe_3O_4 . In addition, XRD spectra have a characteristic peak of Au structure at $2\theta \sim 38.1^\circ$ and another peak at $2\theta \sim 44.3^\circ; 64.5^\circ; 77.7^\circ$. It proved that Fe_3O_4 and Au have been linked together.

TEM was employed to observe the morphology and size of the Fe_3O_4 , $Fe_3O_4@Au$ (Fig. 4b–d). It was clearly seen that the NSs with Au shell coating onto the surface of Fe_3O_4 NPs possess well-defined core shell and a quite uniform size distribution. By measuring two maximal margins of the NSs, the mean diameter of Fe_3O_4 NSs was estimated to be 7 nm and $Fe_3O_4@Au$ NSs was estimated to be 11 nm. The elemental composition of Fe and Au in the $Fe_3O_4@Au$ NSs was quantified by ICP-MS, and the Fe/Au mass ratio was measured to be 2:1.6.

CONCLUSION

Here we have reported an original and simple route to synthesize nano gold particles from gold metal and molecular chlorine for biomedical applications. Aqueous solutions of gold (III) chloride of high purity and stability could reliably be obtained from gold metal and molecular chlorine via a straightforward procedure.

Gold (III) chloride solutions prepared by this method did not have any metallic gold precipitate within at least twelve months of keeping. ICP-MS analysis confirmed the absence of any manganese contamination that may have arisen from the chlorine production process, and the purity of the gold chloride solution was further demonstrated through its direct use in the synthesis of stable aqueous citrate-stabilized as well as various Au seeds.

The $Fe_3O_4@Au$ NPs were obtained using absorbed Au NPs on the surface of Fe_3O_4 . As a result, the pink colloidal solution in octane and film at the interface were shown. Characterizing by TEM, XRD and UV-vis spectroscopy it was shown that the dispersed phase of the colloidal solution contained Fe_3O_4/Au core-shell nanoparticles. The main diameter of the Fe_3O_4/Au nanoparticles was equal to 11 nm with a gold shell thickness of approximately 2 nm

Acknowledgment

This work was partly funded by the Young Science and Technology Innovation Incubator of The Youth Scientific and Technological Promotion Center (TST);

We thank Vietnam Academy of Science and Technology for providing the necessary environment for doing this research and we thank Associate Prof. Nguyen Thi Phuong Phong for the useful discussion.

References

- [1] Lévy, R., et al., *Rational and combinatorial design of peptide capping ligands for gold nanoparticles*. Journal of the American Chemical Society **126**(32) (2004) 10076-10084.
- [2] Bagheri, S., et al., *Using gold nanoparticles in diagnosis and treatment of melanoma cancer*. Artificial cells, nanomedicine, and biotechnology, **46**(sup1) (2018) 462-471.
- [3] King, S., J. Massicot, and A. McDonagh, *A straightforward route to tetrachloroauric*

- acid from gold metal and molecular chlorine for nanoparticle synthesis.* *Metals* **5**(3) (2015) 1454-1461.
- [4] Chen, M., et al., *Synthesis and optical properties of size-controlled gold nanoparticles.* *Powder technology* **311** (2017) 25-33.
- [5] Bhana, S., et al., *Near-infrared-absorbing gold nanopopcorns with iron oxide cluster core for magnetically amplified photothermal and photodynamic cancer therapy.* *ACS applied materials & interfaces* **7**(21) (2015) 11637-11647.
- [6] Nguyen, T.T., F. Mammari, and S. Ammar, *Iron oxide and gold based magneto-plasmonic nanostructures for medical applications: A review.* *Nanomaterials* **8**(3) (2018) 149.
- [7] Mohapatra, J., et al., *Surface controlled synthesis of MFe_2O_4 ($M = Mn, Fe, Co, Ni$ and Zn) nanoparticles and their magnetic characteristics.* *CrystEngComm* **15**(3) (2013) 524-532.
- [8] Karamipour, S., M. Sadjadi, and N. Farhadyar, *Fabrication and spectroscopic studies of folic acid-conjugated $Fe_3O_4@Au$ core-shell for targeted drug delivery application.* *Spectrochimica Acta Part A: Molecular and Biomolecular Spectroscopy* **148** (2015) 146-155.
- [9] Hu, Y., et al., *Multifunctional $Fe_3O_4@Au$ core/shell nanostars: a unique platform for multimode imaging and photothermal therapy of tumors.* *Scientific reports* **6** (2016) 28325.

FABRICATION OF GOLD NANOSTRUCTURES ON COPPER FOIL FOR USE AS SERS SUBSTRATES

**Cao Tuan Anh¹, Luong Truc Quynh Ngan², Dao Tran Cao² and Kieu Ngoc Minh³
and Nguyen Anh Vu⁴**

¹Tan Trao University, Trung Mon Commune, Yen Son District, Tuyen Quang Province, Vietnam;

²Institute of Materials Science, Vietnam Academy of Science and Technology, 18 Hoang Quoc Viet, Cau Giay, Hanoi, Vietnam;

³Graduate University of Science and Technology, Vietnam Academy of Science and Technology, 18 Hoang Quoc Viet, Cau Giay, Hanoi, Vietnam;

⁴Hanoi University of Pharmacy, 15 Le Thanh Tong, Hoan Kiem District Hanoi, Vietnam
Email: ctanh.iop@gmail.com

ABSTRACT

Surface-enhanced raman scattering (SERS) is being developed for use as a method for identifying molecules. The development of this analytical technique is heavily dependent on the synthesis of SERS substrates. This report presents the results of the fabrication of gold nanostructures on copper foil for use as SERS substrates. Gold nanostructures are deposited directly on copper substrates by electrochemical method in HAuCl_4 solution without using any other catalyst. The results showed that the gold nanostructures have been uniformly formed on the surface of a large area copper substrate. The morphology of gold nanostructures has been controlled by changes in fabrication parameters. On SERS substrates obtained, malachite green (MG) is used as a test agent to record SERS spectra on these substrates. Results showed that, with the most optimal SERS substrate, the SERS spectrum of MG at concentration below 0.1 ppm can be recorded. This demonstrates that the gold nanostructures on copper foil fabricated by electrochemical deposition can be used as highly active SERS substrates.

Keywords: SERS, gold nanostructures, electrodeposition, copper foil, malachite green

INTRODUCTION

Surface-enhanced Raman scattering (SERS) is increasingly being used as a method for detecting traces of contaminants in a variety of specimens. In this technique to maximize SERS's performance, the most important thing is to have highly active SERS substrates. Highly active SERS substrates are substrates capable of boosting the Raman scattering signal to several orders. In turn, this depends on how many "hot spots" there are in the substrate, i.e. the areas in which the great enhancement of the electromagnetic field exists. Normally, hot spots appear around the sharp edges or corners of the metal surface, or in the small gap (less than 10 nm) between the two metal surfaces [1].

Although it is widely known that silver has the greatest Raman enhancement potential when used as a SERS substrate, gold has the advantage of being stable, very difficult to oxidize and therefore it is also used as a substrate for SERS in many cases [2]. Currently

there are two main types of SERS substrates, namely the colloidal solution of metallic (mainly silver or gold) nanoparticles and metallic nanoparticles immobilized on a certain solid substrate (or metal structures with rugged surface at the nanoscale level). We chose to make the second type of substrates to avoid the agitation of the nanoparticles in the colloidal solution, which affects the stability and reproducibility of the Raman signal [3].

In this report we will present the fabrication of the arrays of gold nanoparticles on Cu plate (AuNPs@Cu) for use as SERS substrates and then provide an illustration of the effectiveness of this substrate. We have used electrodeposition for synthesizing AuNPs@Cu since this is a simple, powerful and convenient technique. In this method the morphology and size of the electrodeposited layer can be controlled by tuning the deposition conditions, such as the electrodeposition current density, electrodeposition time, concentration and properties of electrolyte solution [4].

EXPERIMENTAL

Pure copper foil was purchased from Sigma-Aldrich. First, each Cu plate (10 mm x 60 mm x 0.2mm) were washed in absolute ethanol (5 min), acetone (5 min), $\text{HNO}_3/\text{H}_2\text{O} = 1/1$ (10 min) and deionized water (several times). The next step Cu plate was performed an electrodeposition process to produce an array of gold nanoparticles (AuNPs) on the surface. Electrodeposition was carried out under the constant current mode with current density in the range of 0.1-2.0 mA/cm^2 for 10 min at room temperature in an aqueous solution of HAuCl_4 (0.1 mM). The electrochemical system consists of two electrodes, with a Cu plate sample serves as a cathode, while a platinum grid is the anode. After fabrication, the AuNPs@Cu samples were washed with deionized water several times and dried in air.

The surface morphology of the AuNPs@Cu substrates was investigated using the S-4800 field effect scanning electron microscope (Hitachi, Japan). X-ray diffraction measurements have also been performed on several representative samples to check whether the obtained nanoflowers are crystallized gold. This measurement was performed on a Bruker-AXS D5005 X-ray diffraction system (Siemens, Germany). SERS measurements were performed by dripping 25 μl of aqueous malachite green (MG) at various concentrations on the AuNPs@Cu substrate. The samples were then allowed to dry naturally in air at room temperature. The Raman spectra of the samples were recorded by a portable i-RamanPro spectrometer (model BWS475-785H produced by B&W Tek, Inc., USA) with a 785 nm excitation laser. The full laser power at the probe excitation position is 427 mW and the laser spot size is 105 μm (for the objective lens magnification of 20x). This spectrometer provides a Raman spectrum over the range of 65–2800 cm^{-1} with a spectral resolution of better than 3.5 cm^{-1} .

RESULTS AND DISCUSSION

Gold electrodeposition under constant current mode with different current densities was prepared. The results show that the optimal AuNPs array is obtained when the current density is 1.0 mA/cm^2 . This array is illustrated in Figure 1, at here we can see that AuNPs are fairly uniform in size in the 50-80 nm range,

with an average size of about 70 nm, the distance between AuNPs is below ten of nm. In addition, the surface of gold nanoparticles is quite rugged. To test whether the AuNPs obtained were actually gold or not, and in what form, we conducted X-ray diffraction (XRD) measurements. The results show that AuNPs are formed in crystalline form with the face centered cubic (FCC) structure.

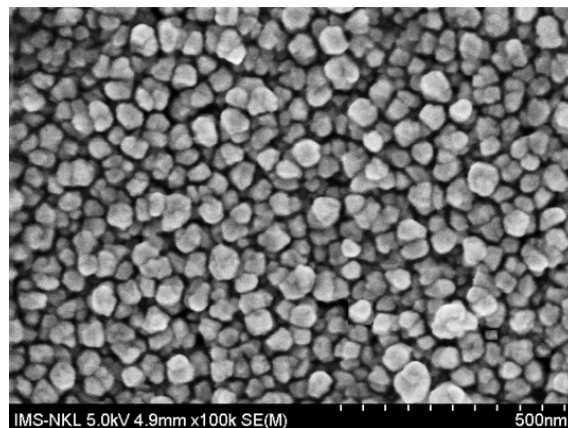


Figure 1. Plan-view SEM image of AuNPs obtained by electrodeposition with 1.0 mA/cm^2 constant current for 30 min in the solution containing 0.1 mM HAuCl_4 on the copper substrate

Given the morphology and arrangement of gold nanoparticles, we think that AuNPs array fabricated under optimal electrodeposition conditions can serve as a highly active SERS substrate. Indeed, when using such AuNPs arrays as the SERS substrates to record the Raman spectra of MG molecules, we obtained spectra with clearly distinct MG peaks in the concentration range of 10 to 0.1 ppm as shown in Figure 2. Curve (4) in Figure 2 shows the Raman spectrum of 25 μl of 10 ppm aqueous MG solution dripped on a 0.5 cm^2 AuNPs@Cu substrate. As previously reported [5], all well-separated and strong peaks in Figure 2 are the Raman peaks of the MG molecule. Especially, signals observed at 914 cm^{-1} are attributed to ring skeletal radial vibration; signals at 1171 cm^{-1} and 1294 cm^{-1} come from in-plane aromatic C–H bending vibration; signals at 1366 cm^{-1} are contributed by N–C stretch; signals at 1394 cm^{-1} come from C–C and C–H in-plane motion (aromatic) and those at 1617 cm^{-1} are assigned to N–C (bond) and C–C stretch. We also recorded SERS spectra of AuNPs array after fabrication and were washed with deionized water (Curve (1) in Figure 2), the results showed

that there were no SERS spectra of any impurities on the sample. This result will increase signal to noise ratio during SERS spectral recording.

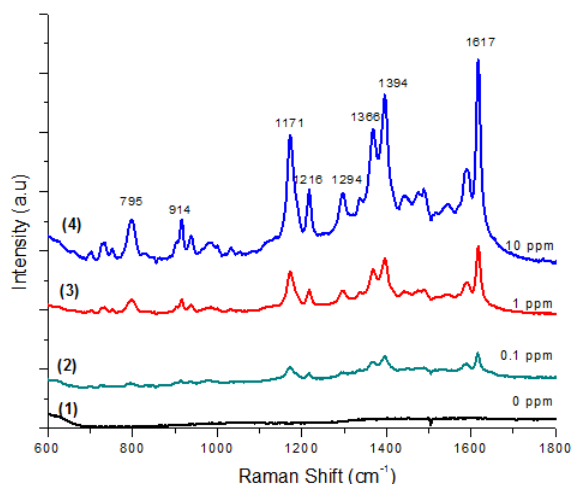


Figure 2. SERS spectra of MG at different concentrations in the region from 10 ppm to 0.1 ppm, which have been recorded using the identical AuNPs@Cu arrays electrodeposited at 1 mA/cm² constant current as SERS substrates

The next result is that the intensity of the Raman peaks decreases with decreasing of the MG concentration in the solution dropped onto the substrate. In curve (2) some peaks disappeared (due to the weak intensity), but we still can use this curve to identify MG molecule. Thus, we can conclude the detection limit for MG molecules of AuNPs@Cu substrate is as low as 0.1 ppm. This result shows that the SERS substrates made from AuNPs synthesized according to the method we have presented can be used for rapid and accurate quantitative analysis of MG.

It should be added that MG is an organic dye commonly used to test the activity of SERS substrates. In addition, it is a colorant used in the paper, textile and ceramics industries. MG recently has been reported to cause carcinogenesis, mutagenesis, chromosomal fractures and respiratory toxicity to animals exposed to it [6]. Consequently, the use of this dye in food processing is prohibited. However, at present in a series of countries it is still illegally used in food processing to produce bright green color. Due to the negative impact of MG on human health, rapid, sensitive and cost-effective detection of MG residues in food itself is valuable and necessary.

CONCLUSION

By electrodeposition method, we have successfully fabricated arrays of gold nanoparticles on copper substrate (AuNPs@Cu). The gold nanoparticles are quite rugged, and they are fairly uniform throughout the array with an average size of about 70 nm. Reproducibility of nanoparticles for different production times is quite good. Arrays of AuNPs@Cu have demonstrated the ability to work as highly active SERS substrates. Specifically, Raman spectral results with the malachite green (MG) probe have shown that these SERS substrates allow for the detection of MG at concentrations as low as 0.1 ppm.

Acknowledgment

This work was supported financially by Tan Trao University

References

- [1] H. Tang, C. Zhu, G. Meng and N. Wu 2018, *Review-Surface-Enhanced Raman Scattering Sensors for Food Safety and Environmental Monitoring*, Journal of The Electrochemical Society **165** (2018) B3098-B3118
- [2] L.T.Q. Ngan, D.T. Cao, C.T. Anh, K.N. Minh, N.N. Hai and L.V. Vu, *Electrochemical Synthesis of Flower-Like Gold Nanoparticles for SERS Application*, Journal of Electronic Materials **49** (2019) 5328-5332
- [3] H.X. Gu, L. Xue, Y.F. Zhang, D.W. Li, and Y.T. Long, *Facile Fabrication of a Silver Dendrite-Integrated Chip for Surface - Enhanced Raman Scattering*, ACS Appl. Mater. Interfaces **7** (2015) 2931-2936
- [4] D.T. Cao, L.T. Quynh-Ngan, C.T. Anh and K.N. Minh, *High-sensitive SERS detection of thiram with silver nanodendrites substrate*, Adv. Nat. Sci.: Nanosci. Nanotechnol. **10** (2019) 025012 (4pp)
- [5] L.T.Q. Ngan, C.T. Anh and D.T. Cao, *Low concentration organic molecules detection via surface enhanced Raman spectroscopy effect using Ag-nanoparticles coated silicon nanowire arrays*, Adv. Nat. Sci.: Nanosci. Nanotechnol. **4** (2013), 015018 (5pp)
- [6] E. Sudova, J. Machova, Z. Svobodova, T. Vesely, *Negative effects of malachite green and possibilities of its replacement in the treatment of fish eggs and fish: a review*, Veterinarni Medicina, **52** (2007) 527-539

FACILE FABRICATION OF GOLD NANOPARTICLES BY SPUTTERING METHODS

Thi Ha Tran^{1,2}, Thi Huyen Trang Nguyen¹, Thanh Cong Bach², Nguyen Hai Pham², Cong Doanh Sai², Quang Hoa Nguyen², Trong Tam Nguyen³, Khac Hieu Ho⁴, Viet Tuyen Nguyen^{2*}

¹Department of Physics, Faculty of Basic Science, Hanoi University of Mining and Geology, Duc Thang, Tu Liem, Hanoi;

²Vietnam National University, University of Science, 334 Nguyen Trai, Thanh Xuan, Hanoi;

³Department of Physics, Faculty of Basic –Fundamental Sciences, Vietnam Maritime University, 484 Lach Tray – Le Chan - Hai Phong;

⁴ Institute of Research and Development, Duy Tan University, 03 Quang Trung, Danang, Vietnam
Email: nguyenviettuyen@hus.edu.vn

ABSTRACT

Gold nanoparticles offer variety of applications in chemical and biological fields. Intensity and position of surface plasmon resonance (SPR) band in gold nanoparticles can be modulated by size and shape of the nanoparticles or the dielectric properties of the surrounding environment. This feature provides a convenient way to control the SPR of gold nanoparticles for surface enhance Raman scattering applications. It was popularly reported that gold nanoparticle can be synthesized favorably by chemical method but such approach also bring some limitation to applications due to surfactant often used in the synthesis process. In this report, we present the results of preparation of gold nanoparticles by combining sputtering and thermal annealing method. Size of the as-prepared gold nanoparticles, observed by scanning electron microscopy, increases monotonically with increasing sputtering time. Gold nanoparticles with size from 30 to 100 nm at high density and homogenous distribution was obtained when sputtering time is increased from 10s to 50 s. Gold thin film prepared at longer sputtering time could not be converted to gold nanoparticles as pointed out by absorption spectra. Variation of nanoparticle size results in corresponding shift of the SPR band.

Keywords: Gold nanoparticles; sputtering; thermal annealing; surface plasmon.

INTRODUCTION

Gold nanoparticles have shown its potential applications in various fields such as biomedical, electronics, photovoltaics ... due to interesting properties such as: surface plasmon resonance, biocompatibility, excellent catalytic properties, multiple surface functionalities [1–5]. These applications have fostered research related to synthesis of gold nanostructures in general and gold nanoparticles in particular. A good synthetic process should provide gold nanoparticles of controllable morphology and shapes. Since its discovery, reduction method was broadly used as an effective way to prepare gold nanoparticles from solution phase [6,7]. Further modification of reduction method offered a convenient tool to obtain gold nanostructures of various shape including nanowires, nanorods, nanoflowers, nano-urchins... and of narrow size distribution.

However the organic compounds used in the synthesis process might limit the applicability because purity is a key factor in many biological or electronic applications.

In this paper, we reported the fabrication of gold nanoparticles by a facile process with combining sputtering and thermal annealing methods. The obtained nanoparticles were characterized with different techniques such as: scanning electron microscope, diffuse reflectance spectroscopy. The results show that the products are of high quality. The major advantages of this approach are the homogeneity and uniformity of the nano products. The simple fabrication is also promising for scaling up for mass production.

EXPERIMENTAL

Sodalime glass was used as substrates for preparing gold thin films. The substrates were

first cleaned by ultrasonic bath in double distilled water, ethanol and acetone in sequences to remove any organic residue on the surface. The samples were then dried by air gun blowing. The substrates were then transferred into vacuum chamber of a DC sputtering system. The substrates were mounted onto an unheated copper plate. Thin films of gold were deposited on the prepared substrates by DC sputtering process at base pressure of 6 Pa. The used target is a gold disk (purity of 99.99%) of 2.5 inches. The current used in this research is fixed at 20 mA. The sputtering time was changed from 10s to 50s while the thickness of prepared films was estimated by using extrapolating plot provided by the sputtering system supplier.

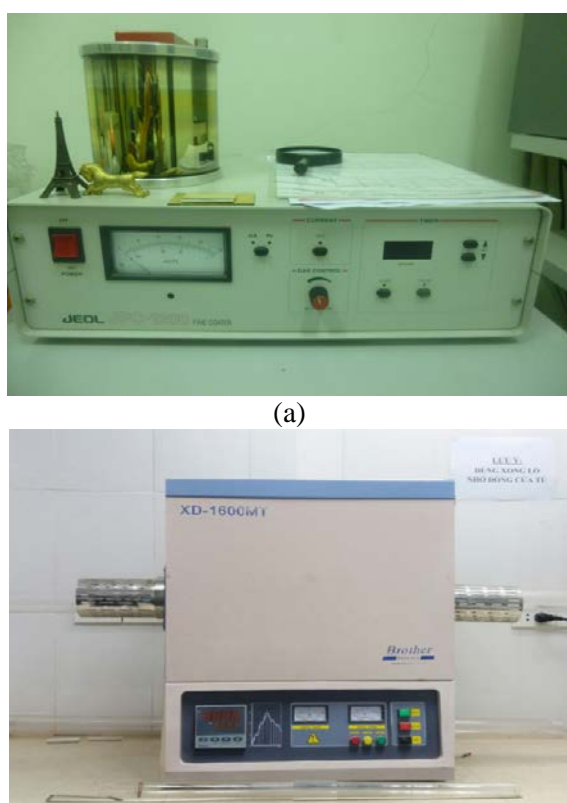


Figure 1. Image of DC sputtering system (a) and horizontal furnace (b) used to fabricate gold thin films in this research.

In order to transform gold thin films into nanoparticles, heat treatment at 300°C in 2h was applied. Morphology of the obtained nano products were then characterized with scanning electron microscope Nova Nanosem while surface plasmon property was studied by diffuse reflectance spectroscopy.

RESULTS AND DISCUSSION

Figure 2 shows SEM images of gold thin films sputtered in 10 s and 40s. The images show that the films are smooth and homogeneous. It is likely that sputtering times does not change the morphology of surface morphology of thin films except thickness.

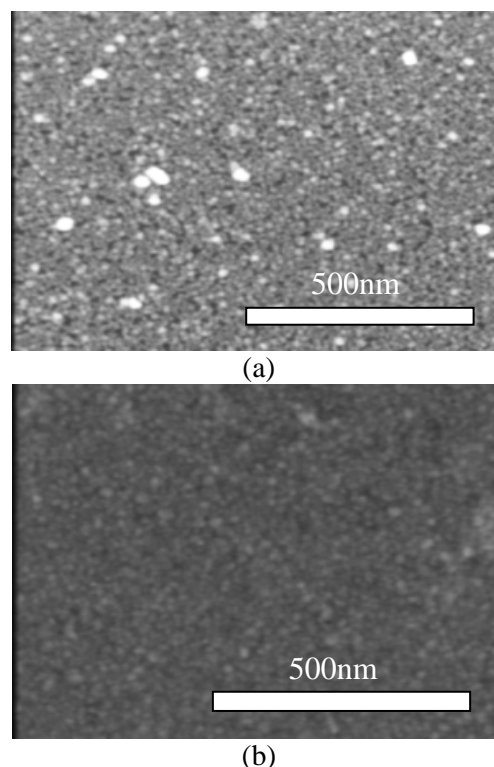


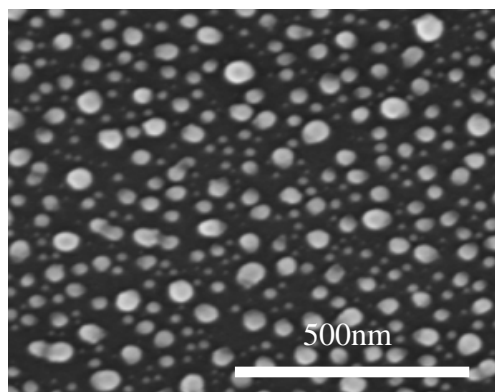
Figure 2. SEM images of gold thin films sputtered in 10s (a) and 40s (b)

After heat treatment at 300°C in 2h, the gold layer was turned into array of gold nanoparticles of quite uniform size and shape. The nanoparticles has quasi spherical shape. The images also show that particle size is in a correlation with thickness of the as-prepared thin film. As the sputtering time increasing from 10s to 50s particle size increase accordingly from 30 nm to over 100 nm. It is also noted that at long sputtering time, size distribution becomes broader.

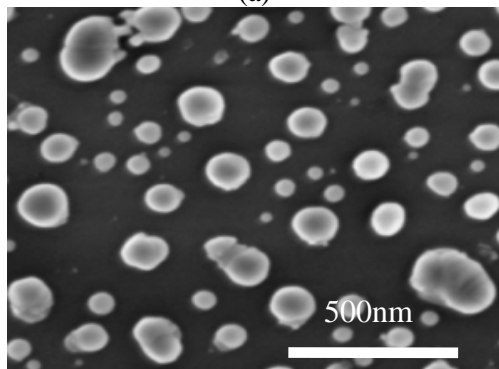
Figure 4 shows absorption spectra of the sputtered gold thin films. As can be seen that no plasmon peak was observed in the spectra which is in agreement with the fact that after sputtering gold was form as a continuous thin layer on substrates.

After heat treatment, clear plasmon peaks of gold appear in the absorption spectra. As sputtering time increasing, gold nanoparticles becomes bigger and size distribution is broader.

As a result, plasmon peak becomes broader and shifts to longer wavelengths. At sputtering time longer than 50s, plasmon peaks is faded out because of the large particle size.



(a)



(b)

Figure 3. SEM images of gold thin films sputtered in 10 s (a) and 40s (b) after being annealed at 300°C in 2h.

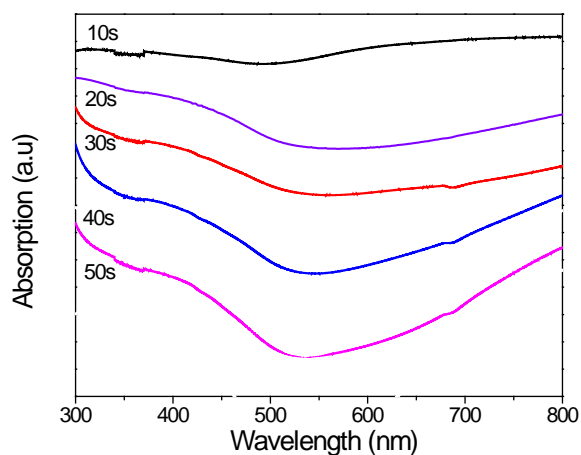


Figure 4. Absorption spectra of gold thin films prepared by sputtering method.

The results show that by controlling sputtering time, we can control the particle size, which in turn affect plasmon properties of the gold nano-particles.

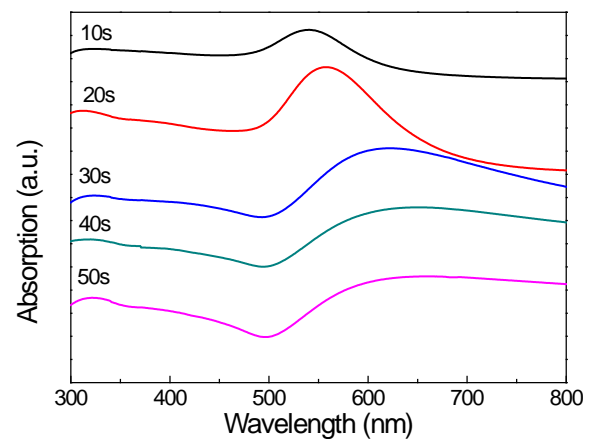


Figure 5. Absorption spectra of gold thin films prepared by sputtering method after heat treatment.

CONCLUSION

We successfully prepared gold nanoparticles on sodalime glass by combining sputtering and thermal annealing method. Particles size and surface plasmon property of gold nanoparticle can be conveniently controlled by sputtering time. The results demonstrate that combination of sputtering and annealing is a promising route to prepare gold nanoparticles array on flat substrates for various applications.

Acknowledgment

This research is funded by Vietnam National Foundation for Science and Technology Development (NAFOSTED) under grant number 103.02-2017.351. One of the author, Phd student Thi Ha Tran, would like to thank the Domestic Master/ PhD Scholarship Programme of Vingroup Innovation Foundation for supporting tuition fee.

References

- [1] B.B. Karakoçak, R. Raliya, J.T. Davis, S. Chavalmane, W.N. Wang, N. Ravi, P. Biswas, Biocompatibility of gold nanoparticles in retinal pigment epithelial cell line, *Toxicol. Vitro*. 37 (2016) 61–69. doi:10.1016/j.tiv.2016.08.013.
- [2] S. Dutta Roy, M. Ghosh, J. Chowdhury, Adsorptive parameters and influence of hot geometries on the SER(S) spectra of methylene blue molecules adsorbed on gold nanocolloidal particles, *J. Raman Spectrosc.* 46 (2015) 451–461. doi:10.1002/jrs.4675.
- [3] I. Unlu, J.W. Soares, D.M. Steeves, J.E.

- Whitten, Photocatalytic Activity and Fluorescence of Gold/Zinc Oxide Nanoparticles Formed by Dithiol Linking, *Langmuir*. 31 (2015) 8718–8725. doi:10.1021/acs.langmuir.5b01632.
- [4] G. Sinha, L.E. Depero, I. Alessandri, Recyclable SERS substrates based on Au-Coated ZnO nanorods, *ACS Appl. Mater. Interfaces*. 3 (2011) 2557–2563. doi:10.1021/am200396n.
- [5] T. Barman, A.A. Hussain, B. Sharma, A.R. Pal, Plasmonic hot hole generation by interband transition in gold-polyaniline, *Sci. Rep.* 5 (2015) 1–5. doi:10.1038/srep18276.
- [6] E. Satheeshkumar, J. Yang, Photochemical decoration of silver nanoparticles on ZnO nanowires as a three-dimensional substrate for surface-enhanced Raman scattering measurement, *J. Raman Spectrosc.* 45 (2014) 407–413. doi:10.1002/jrs.4477.
- [7] D. Wang, P. Schaaf, Nanoporous gold nanoparticles, *J. Mater. Chem.* 22 (2012) 5344–5348. doi:10.1039/c2jm15727f.

POSTER SESSIONS

***NANOMATERIALS AND
NANODEVICES
(NMD)***

TEMPERATURE DEPENDENT PROPERTIES OF L1₀ FePd MAGNETIC NANOPARTICLES

Nguyen Hoang Nam^{1,2,3}, Truong Thanh Trung², Tran Thi Hong⁴, Luu Manh Kien²,
Nguyen Hoang Luong^{2,3}

¹ Faculty of Physics, VNU University of Science, Vietnam National University, Hanoi, 334 Nguyen Trai, Hanoi, Vietnam;

² Nano and Energy Center, VNU University of Science, Vietnam National University, Hanoi, 334 Nguyen Trai, Hanoi, Vietnam;

³ Nanotechnology Program, Vietnam Japan University, Vietnam National University, Hanoi, My Dinh Campus, Nam Tu Liem, Hanoi, Vietnam;

⁴ Faculty of Environmental Sciences, VNU University of Science, Vietnam National University, Hanoi, 334 Nguyen Trai, Hanoi, Vietnam
Email: namnh@hus.edu.vn

ABSTRACT

Coercivity and magnetization of magnetic nanoparticles Fe₆₀Pd₄₀ were measured as a function of temperature from 2 K to 300 K. The nanoparticles were prepared from iron acetate and palladium acetate by sonoelectrodeposition. After annealing at various temperatures from 450°C to 700°C the nanoparticles were found to have the ordered L1₀ structure and show hard magnetic properties. Coercivity and saturation magnetization of the nanoparticles are discussed in dependence of temperature.

Keywords: FePd nanoparticles, coercivity, magnetization, sonoelectrodeposition

INTRODUCTION

FePd nanoparticles have attracted considerable attention due to their applicability in ultrahigh density magnetic recording media mainly because of their hard magnetic properties and chemical stability in the ordered face-centered tetragonal (fct) L1₀ structure [1-5]. This L1₀ ordered FePd materials are normally obtained from the disordered face-centered cubic (fcc) materials via the disorder-order transition. Recently, Van et al. [6] have studied temperature dependence of hard magnetic properties of Fe₆₀Pd₄₀ nanoparticles prepared by sono-chemistry. In this work, we report coercivity and magnetization of FePd nanoparticles prepared by sono-electrodeposition as a function of temperature.

EXPERIMENTAL

The synthesis of FePd nanoparticles was conducted by sono electro-deposition and described elsewhere [7]. The mixture of 0.15 M iron(II) acetate [Fe(C₂H₃O₂)₂], 0.1 M palladium(II) acetate [Pd(C₂H₃O₂)₂], and 0.5 M Na₂SO₄ were mixed under (Ar + 5%H₂) atmosphere in a electrolysis cell of 100 ml volume. The mixture was then sono electro-

deposited by using Sonics VCX 750 ultrasound emitter with power density of 100 W/cm², on/off current pulse of 500 ms/800 ms to form FePd nanoparticles. The samples were washed and separated from the solution by using a Hettich Universal 320 centrifuge at 5000 rpm for 30 min, and were dried in air at 70°C for 30 min. The annealing under (Ar + 5%H₂) atmosphere was carried out on as-prepared samples at various temperatures from 450°C to 700°C for 1 h.

The chemical composition of our sample is Fe₆₀Pd₄₀ as revealed from energy dispersion spectroscopy (EDS) included in scanning electron microscope (SEM, JEOL 5410LV). The results show that the composition of samples is 60:40 for Fe: Pd ratio as designed. The particle morphology was investigated by a transmission electron microscope (TEM) JEM1010, JEOL, indicating the size of as-prepared nanoparticles is around 7-10 nm and increases to around 15-20 nm after annealing. The structure of the samples was characterized by X-ray diffractometer (XRD) D5005, Bruker. The average crystallite size, d , is calculated using Scherrer's formula: $d = 0.9\lambda / (B \cos \theta)$, where λ is the wavelength of X-rays and B is the half maximum line width. Magnetic properties of samples were

investigated with a magnetic field up to 50 kOe by using Quantum Design's superconducting quantum interference device (SQUID) in the temperature range from 2 K to 300 K.

RESULTS AND DISCUSSION

Figure 1 shows the XRD patterns of the as-prepared and annealed $\text{Fe}_{60}\text{Pd}_{40}$ nanoparticles. Before annealing, the XRD pattern showed diffraction peaks at 40° , 46.5° , 68.5° which can be assigned to (111), (200) and (220) reflections, respectively. The XRD pattern of the as-prepared sample is characteristic of the chemically disordered fcc structure, showed the reflections of pure Pd structure. Meanwhile, as mentioned above, the sample exhibits the composition Fe:Pd as 60:40. For the as-prepared sample, Fe and Pd atoms appear with random probability at fcc lattice sites. This random distribution structure is called disordered structure. The reflections from Fe are very weak due to the fact that their atomic weight is much less than that of Pd which is similar to the XRD result of FePt nanoparticles prepared by sono electro-deposition [8]. From the diffraction peaks we obtained the lattice parameter $a = 3.805 \pm 0.015 \text{ \AA}$. The average crystallite size calculated by using Scherrer's formula is found to be 10 nm, in agreement with the particle size obtained from the TEM measurements. Upon annealing, the formation of the ordered L1_0 fct phase happened. The diffraction peaks were shifted to a higher position with increasing annealing temperature. This shift is due to the structure transition from fcc to fct. The as-prepared particles were not disordered FePd but may be formed by small Fe-rich- and Pd-rich domains. The ordered L1_0 fct phase of FePd was then formed after annealing by the diffusion process between the Fe-rich- and Pd-rich domains. By using Scherrer's formula, the average crystallite size is estimated to be 20.1 nm for the sample annealed at 600°C , for example, in agreement with that obtained from TEM measurements.

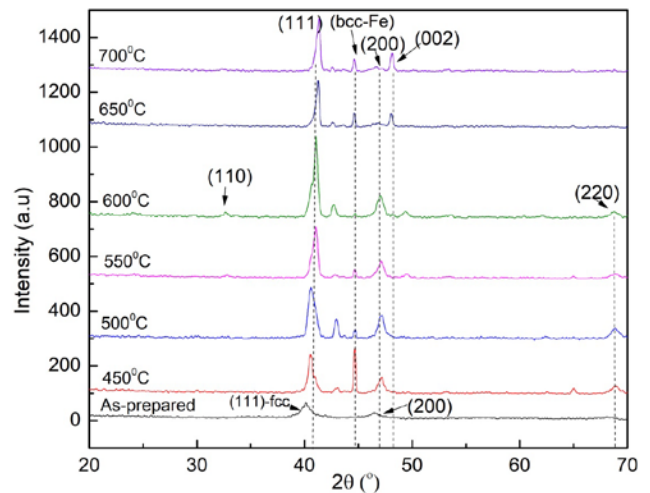


Figure 1. X-ray patterns of as-prepared and annealed $\text{Fe}_{60}\text{Pd}_{40}$ nanoparticles.

Figures 2 and 3 present the hysteresis curves of $\text{Fe}_{60}\text{Pd}_{40}$ nanoparticles annealed at various temperatures measured at 2 K and 300 K, respectively. The curves show typical hard magnetic hysteresis loops, indicating the effect of annealing. With measurements at 2 K, sample annealed at 450°C shows small coercivity H_c of 424 Oe and saturation magnetization of 79 emu/g. The coercivity then increases when the annealing temperature increases and have the

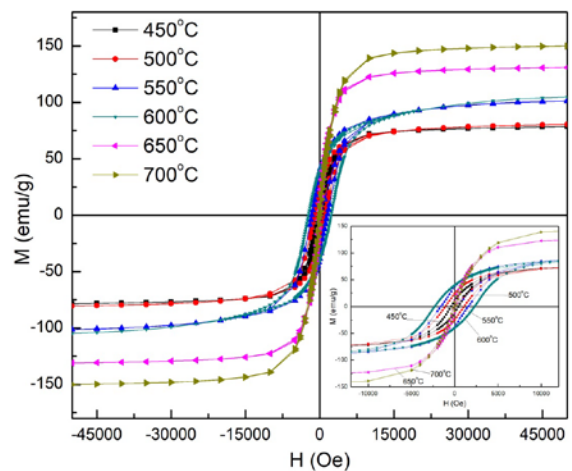


Figure 2. Hysteresis curves measured at 2 K of $\text{Fe}_{60}\text{Pd}_{40}$ nanoparticles annealed at various temperatures. Inset shows the enlarged view about origin.

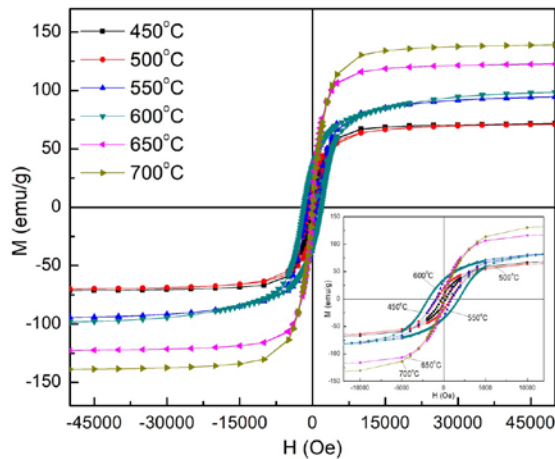


Figure 3. Hysteresis curves measured at 300 K of $Fe_{60}Pd_{40}$ nanoparticles annealed at various temperatures. Inset shows the enlarged view about origin.

maximum value of 2311 Oe at the annealing temperature of 600°C. The coercivity then dropped down to low value of 153 Oe and 158 Oe when the annealing temperature increases to 650°C and 700°C, respectively. The saturation magnetization, however, continuously increases with increasing annealing temperature and reaches around 150 emu/g at annealing temperature of 700°C. When samples were measured at 300 K, the coercivities decrease compared to those at 2 K. The sample annealed at 450°C has the coercivity of 271 Oe at 300 K. Similar as the sample measured at 2 K, the coercivity at 300 K increases with increasing annealing temperature and reaches maximum value of 1827 Oe at annealing temperature of 600°C. Similar to results measured at 2 K, the coercivity dropped down to small value of 120 Oe and 110 Oe when the annealing temperature increases to 650°C and 700°C, respectively. At 300 K, the saturation magnetization also increases with increasing annealing temperature.

The temperature dependence of the coercivity H_C of $Fe_{60}Pd_{40}$ nanoparticles annealed at various temperatures from 450°C to 700°C is shown in Figure 4. As can be clearly seen from this figure, for all annealing temperatures the coercivity of $Fe_{60}Pd_{40}$ nanoparticles increases with decreasing measuring temperature and attains a maximum value of 2311 kOe at 2 K in the sample annealed at 600°C. For the samples annealed at 650°C and 700°C the coercivity shows less pronounced dependence on measuring temperature. This is probably due to existence of a soft phase in the

samples, leading to slight increase of coercivity but strong increase of magnetization as evident in Figure 5. Watanabe et al. [5] have synthesized the $Fe_{49.2}Pd_{50.8}$ nanoparticles by the modified polyol process, i.e simultaneous reduction of palladium acetylacetonate ($Pd(acac)_2$) and thermal decomposition of iron pentacarbonyl ($Fe(CO)_5$) in a solvent.

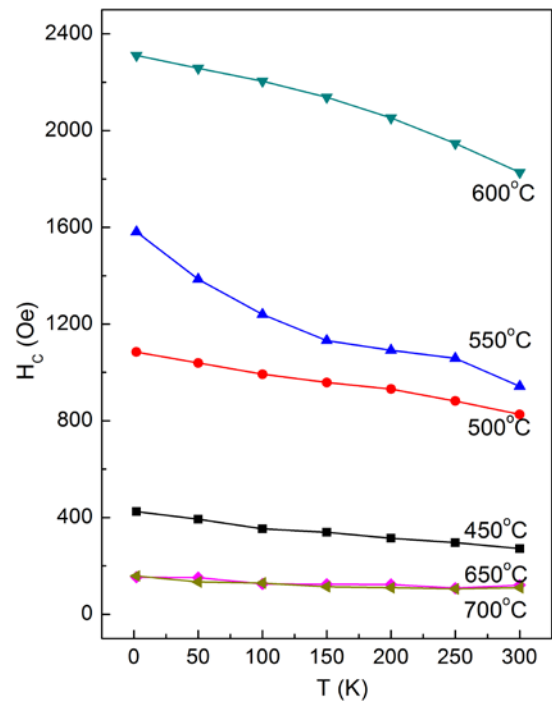


Figure 4. The temperature dependence of coercivity of $Fe_{60}Pd_{40}$ nanoparticles annealed at various temperatures.

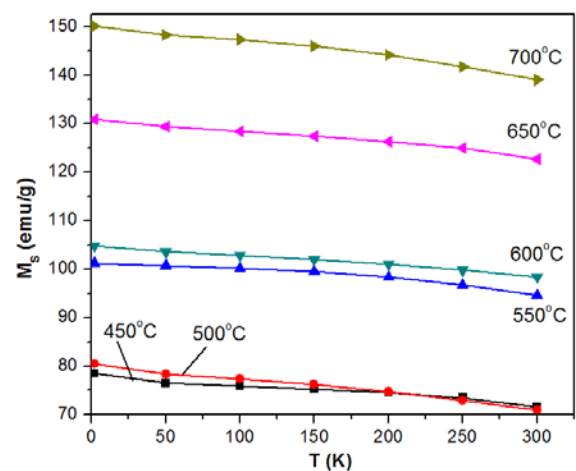


Figure 5. The temperature dependence of saturation magnetization of $Fe_{60}Pd_{40}$ nanoparticles annealed at various temperatures.

These authors obtained the coercivity value of 2.04 kOe at 5 K for the Fe_{49.2}Pd_{50.8} samples annealed at 600°C for 1 h. Van et al. [6] showed strong dependence of the coercivity of the Fe₆₀Pd₄₀ nanoparticles prepared by sonochemistry on annealing and measuring temperature. They reported that for all annealing temperatures the coercivity of the samples increases with decreasing measuring temperature and reaches a maximum value of 2.43 kOe at 2 K for the sample annealed at 550°C.

Figure 5 shows the temperature dependence of saturation magnetization M_S of Fe₆₀Pd₄₀ nanoparticles annealed at various temperatures. As can be seen from this figure, saturation magnetization of all samples increases with decreasing measuring temperature. The Fe₆₀Pd₄₀ nanoparticles annealed at 700°C exhibit the highest saturation magnetization. This behaviour is probably due to interaction between soft phase of fcc structure and hard phase of fct structure.

CONCLUSION

Upon annealing at various temperatures from 450°C to 700°C the Fe₆₀Pd₄₀ nanoparticles prepared by sonoelectrodeposition show the disorder-order transition and hard magnetic properties. Temperature dependences of coercivity and magnetization of these nanoparticles were studied. The coercivity and magnetization increase with decreasing temperature down to 2 K for all annealed samples. The Fe₆₀Pd₄₀ nanoparticles annealed at 600°C attain the highest coercivity whereas the nanoparticles annealed at 700°C exhibit the highest saturation magnetization.

Acknowledgment

This research is funded by Vietnam National Foundation for Science and Technology Development (NAFOSTED) under grant number 103.02-2017.344.

References

- [1] D. Weller, A. Moser, L. Folks, M.E. Best, W. Lee, M.F. Toney, M. Schwikert, J.U. Thiele, M.F. Doerner, *High K_U materials approach to 100 Gbits/in²*, IEEE Trans. Magn. 36 (2000) 10-15.
- [2] K. Sato, B. Bian, Y. Hirotsu, *Fabrication of oriented L1₀-FePt and FePd nanoparticles*

- with large coercivity*, J. Appl. Phys. **91** (2002) 8516-8518.
- [3] K. Sato, Y. Hirotsu, *Order-disorder transformation in L1₀-FePd nanoparticles studied by electron diffraction*, Materials Transactions **47** (2006) 59-62.
- [4] K. Sato, J.G. Wen, J.M. Zuo, *Intermetallic ordering and structure in Fe-Pd alloy nanoparticles*, J. Appl. Phys. **105** (2009) 093509.
- [5] K. Watanabe, H. Kura, T. Sato, *Transformation to L1₀ structure in FePd nanoparticles synthesized by modified polyol process*, Sci. Tech. Adv. Mater. **7** (2006) 145-149.
- [6] Nguyen Thi Thanh Van, Truong Thanh Trung, Nguyen Hoang Nam, Nguyen Hoang Luong, *Temperature dependence of hard magnetic properties of FePd nanoparticles prepared by sonochemistry*, VNU Journal of Science, Mathematics - Physics **28** (2012) 46-51.
- [7] Nguyen Hoang Luong, Truong Thanh Trung, Tran Phuong Loan, Luu Manh Kien, Tran Thi Hong, Nguyen Hoang Nam, *Magnetic properties of FePd nanoparticles prepared by sonoelectrodeposition*, Journal of Electronic Materials **45** (2016) 4309-4313.
- [8] Nguyen Hoang Nam, Nguyen Thi Thanh Van, Nguyen Dang Phu, Tran Thi Hong, Nguyen Hoang Hai, Nguyen Hoang Luong, *Magnetic properties of FePt nanoparticles prepared by sonoelectrodeposition*, J. Nanomater. 2012 (2012) 801240.

SYNTHESIS AND ADSORPTION PROPERTIES OF ORDERED MESOPOROUS CARBON MATERIAL USING MCF SILICA AS HARD TEMPLATE

Hoa T.H.Nguyen¹, Hy G. Le² and Phuong T.Dang³

1. Faculty of Chemistry, Thai Nguyen University of Sciences

Email: hoahoc@tnus.edu.vn; honghoakhtn@gmail.com

2. Institute of Biological Technology, Vietnam Academy of Science and Technology (VAST) - 18 Hoang Quoc Viet, Cau Giay, Hanoi, Vietnam

3. Institute of Chemistry, Vietnam Academy of Science and Technology (VAST) - 18 Hoang Quoc Viet, Cau Giay, Hanoi, Vietnam

ABSTRACT

Ordered mesoporous carbon materials using MCF silica as hard template (OMC(MCF)) were synthesized. The synthesized OMC(MCF) materials were characterized by different techniques such as XRD, TEM, BET. From obtained results, it revealed that the surface area, pore volume and pore size of OMC (MCF) were of 1,073 m²/g, 1.35 cm³/g and 5.7 nm, respectively. The dye adsorption experiments were carried out through a batch test to evaluate synthesized OMC(MCF) materials. Methylene blue (MB) and direct blue 71 dyes (DB71) were chosen as adsorbates. Negatively charged surfaces OMC(MCF) materials have better adsorption capacity for positively charged methylene blue than that of negatively charged direct blue 71. OMC(MCF) materials could be used as a potential adsorbent for the removal of positive charged organic dyes.

Keywords: Ordered mesoporous carbons materials, MCF template, Methylene blue, Direct blue 71, dye adsorption.

INTRODUCTION

Porous carbon materials [1, 2, 3] are of scientific and technological importance due to their unique properties (high surface area, pore size and large porosity, high adsorption capacity of bulky large molecules, high chemical and thermal stability, etc.). Therefore, porous carbon is widely used in many applications such as gas separation [4], adsorbents [5-8], gas storage [9], catalysts [10], electrochemical energy storage [11]. Most porous carbons are usually obtained via carbonization carbon precursor. Porous carbons are synthesized by hard – templating method using nanostructured silica as template to impregnate with an appropriate carbon source, followed by carbonization of the composite, and subsequent removal of the template [12].

In this paper, we report the synthesis of OMC(MCF) by hard template method using MCF as template. With our knowledge, this is first study about synthesis, characterization and MB and DB71 adsorption properties of OMC(MCF).

EXPERIMENTAL

Synthesis of OMC(MCF)

MCF silica were synthesized with a triblock copolymer, EO₂₀PO₇₀EO₂₀ (Pluronic P123, Aldrich), as the surfactant, and liquid glass as the silica source. OMC(MCF) was synthesized by calcinations of MCF impregnated with an aqueous solution of carbon sources with sulfuric acid. Typically, 1g of sucrose was mixed with 1g MCF and then added to a solution obtained by dissolving 0.14g of H₂SO₄ in 5g of H₂O. The mixture was placed in a drying oven for 6h at 100°C, and subsequently the oven temperature was increased to 160°C and maintained there for 6h. The sample turned dark brown or black during the treatment in the oven. This step was repeated at 100 and 160°C using the same oven after the addition of 1 g of carbon, 0.14 g of H₂SO₄, and 5g of H₂O. The carbonization was completed by pyrolysis with heating at typically 800°C under nitrogen flow. The carbon-silica composite obtained after pyrolysis was immersed in HF 40% solution and then washed with H₂O before being washed with a mixture of

50 vol% ethanol + 50 vol% H₂O. The final product was dried at 100°C for 3h.

Characterization.

The powder X-ray diffraction (XRD) patterns of the samples were recorded on a Shimadzu XRD-6100 analyzer with Cu K_α radiation (λ = 1.5417Å). Transmission electron microscopy (TEM) was recorded using JEOL1010 instrument operating at 80 kV with a magnification of 25,000 – 100,000. The surface area of samples was determined on Quantachrome Instruments version 3.0 at 77K and using nitrogen as an adsorbent.

Adsorption experiments.

The methylene blue (MB - C₁₆H₁₈N₃SCl) and direct blue 71 (DB71 - C₄₀H₂₃N₇Na₄O₁₃S₄) MB adsorption was performed in liquid phase at room temperature under stirring condition. Batch experiments were carried out in a set of 250mL Erlenmeyer lacks, in which a 100mL aliquot of each MB solution with initial concentrations in the range of 100–300 ppm was added. Equal masses (m) of adsorbent were added to the MB solutions (V). Adsorption capacity (Q_t) of MB is denied as follows:

$$Q_t = \frac{(C_0 - C_t) \cdot V}{m} \quad (1)$$

Where Q_t is adsorption capacity of MB or DB71; V is solution volume (V = 0.1L); m is masses of OMC (MCF); C₀ and C_t (ppm) are initial and time t MB or DB71 concentration. Equilibrium concentration of each adsorbate was determined by a UV-VIS spectrophotometer.

Adsorption isotherms

Langmuir and Freundlich isotherms models, were often used to analyze the experimental data [2]. The Langmuir equation is expressed as follows:

$$\frac{C_e}{Q_e} = \frac{1}{Q_m \cdot K_L} + \left(\frac{1}{Q_m} \right) \cdot C_e \quad (2)$$

The Freundlich equation is expressed as follows:

$$\log Q_e = \log K_F + \left(\frac{1}{n} \right) \cdot \log C_e \quad (3)$$

Where Q_m and K_L in the Langmuir equation represent the maximum adsorption capacity of adsorbents (mg/g) and Langmuir adsorption constant related to the free energy of adsorption, respectively. K_F and n are Freundlich constants

related to adsorption capacity and adsorption intensity, respectively.

RESULTS AND DISCUSSION

X-Ray Diffraction (XRD)

XRD patterns of MCF and OMC(MCF) samples are shown in figure 1. From XRD patterns of MCF and OMC(MCF) showed that OMC(MCF) had the same structure with MCF.

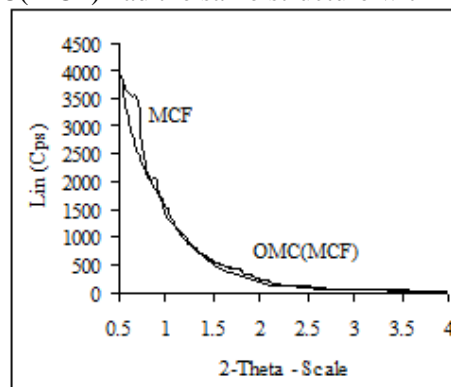


Figure 1. XRD patterns of MCF and OMC(MCF).

Transmission Electron Microscopy (TEM)

TEM images of OMC(MCF) are shown in figure 2. The ordered structures OMC(MCF) samples with hexagonal symmetry and uniform pore dimension were clearly observed.

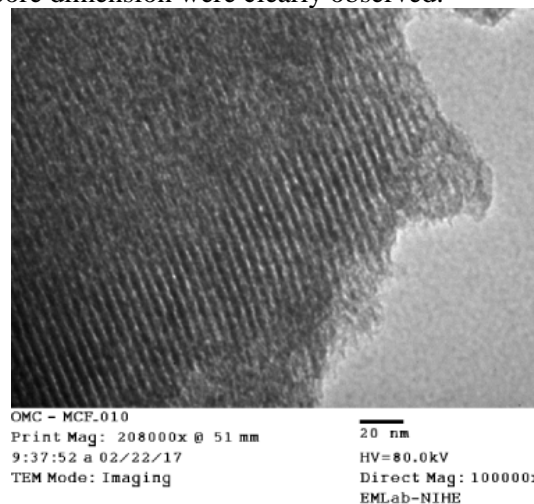


Figure 2. TEM images of OMC(MCF)

Adsorption–Desorption Isotherms (BET)

N₂ adsorption–desorption isotherms and pore-size distribution of OMC(MCF) are presented in figure 3 and figure 4. OMC(MCF) showed the isotherm curves of type IV with the hysteresis loop, characteristic for capillary condensation which is typical for mesoporous material.

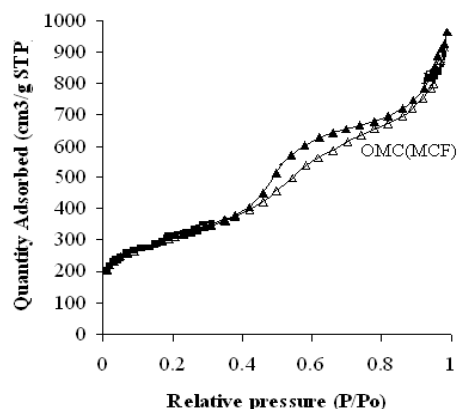


Figure 3. N_2 adsorption-desorption isotherms of OMC(MCF)

Textural properties of OMC(MCF) samples are showed in table 1. As observed in table 1, OMC (MCF) HAD high surface area of 1073 m^2/g , average pore size of 5.7 nm and pore volume of 1.35 cm^3/g .

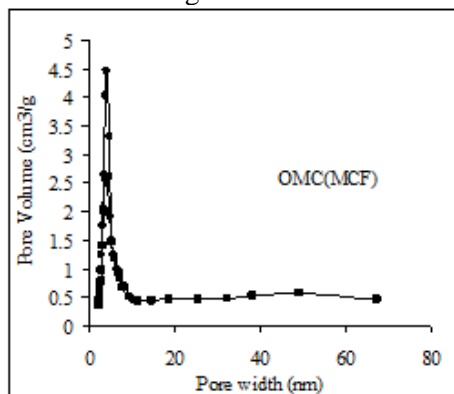


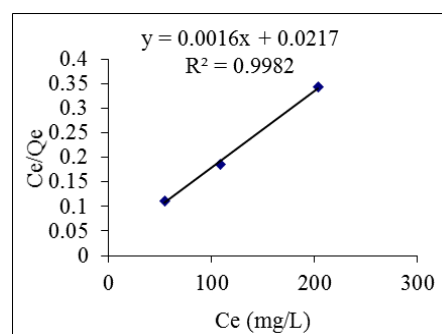
Figure 4. Pore-size distribution of OMC(MCF)

Table 1. Textural properties of OMC(MCF)

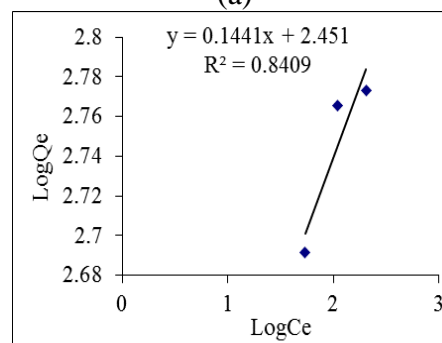
Samples	Textural properties		
	Average pore width (nm)	Pore volume (cm^3/g)	Surface area (m^2/g)
OMC(MCF)	5.7	1.35	1073

Adsorption Isotherms

MB and DB71 adsorption capacities of OMC(MCF) are given in table 2, Q_m adsorption capacities of OMC(MCF) for MB (625 mg/g) were higher than for DB71 (370 mg/g).

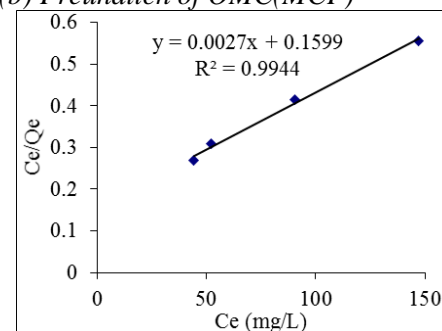


(a)

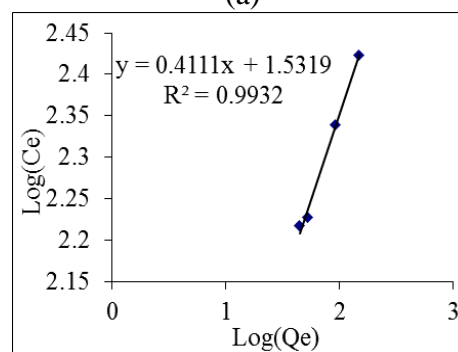


(b)

Figure 5. Experimental MB adsorption data fitted to different isotherm models (a) Langmuir and (b) Freundlich of OMC(MCF)



(a)



(b)

Figure 6. Experimental DB71 adsorption data fitted to different isotherm models (a) Langmuir and (b) Freundlich of OMC(MCF)

This can be explained that the average pore size of OMC (MCF) (5.7 nm) is greater than that of MB (1.7 nm) and DB71 (3 nm) [13]. Therefore, MB or DB71 molecules can be easily

diffuse into the pore of OMC(MCF). In water at neutral pH, OMC(MCF) with zero charged point $pH_0 = 5.5$ and DB71 are negatively charged, MB is positively charged. In addition, MB and DB71 are adsorbed on OMC(MCF) by mainly electrostatic force. This is process of multi-layered physical adsorption. That is why the adsorption capacity OMC(MCF) for MB is higher.

Table 2. Langmuir and Freundlich adsorption isotherm parameters of OMC(MCF) for MB and DB71

Langmuir and Freundlich adsorption isotherm parameters of OMC(MCF) for MB			
Langmuir isotherm		Freundlich isotherm	
Q_m (mg.g ⁻¹)	625	n	6.9
K_L (L.mg ⁻¹)	0.07	K_F (mg.g ⁻¹)	1.76
R^2	0.9982	R^2	0.8404
Langmuir and Freundlich adsorption isotherm parameters of OMC(MCF) for DB71			
Q_m (mg.g ⁻¹)	370	n	29
K_L (L.mg ⁻¹)	0.02	K_F (mg.g ⁻¹)	34
R^2	0.9944	R^2	0.9932

As observed in figure 5, figure 6 and table 2, the value of $R^2=0.9982$ and 0.9944 in the Langmuir model, $R^2=0.8404$ and 0.9932 in the Freundlich model for adsorption of MB and DB71, respectively. These results were indicating that the Langmuir model fits much better than the Freundlich model for both adsorbates.

CONCLUSION

Ordered mesoporous carbons OMC(MCF) were successful synthesized by using hard template methods using MCF silica as template. From XRD, TEM and N₂ adsorption-desorption (BET) results, it revealed that the obtained OMC(MCF) had high surface area (1073 m²/g), large pore volume and pore size (5.7 nm). MB and DB71 are adsorbed on OMC(MCF) by electrostatic forces. Thus, negatively charged surfaces OMC(MCF) have better adsorption capacity for positive charged methylene blue (625 mg/g) than that of negatively charged direct blue 71 (370 mg/g)

References

[1] Shinae Jun, Sang Hoon Joo, Ryong Ryoo, Michal Kruk, Mietek Jaroniec, Zheng Liu, Tetsu Ohsuna, Osamu Terasaki, *Synthesis of New, Nanoporous Carbon with Hexagonally Ordered Mesostucture*, J. Am. Chem. Soc. **122** (2000) 10712-10713.
 [2] Deicy Barrera, Mara Dávila, Valeria Cornette, J.C. Alexandre de Oliveira, Raúl H. López, Karim

Sapag, *Pore size distribution of ordered nanostructured carbon CMK-3 by means of experimental techniques and Monte Carlo simulations*, Microporous and Mesoporous Materials **180** (2013) 71–78.
 [3] Enterria M., F. Suárez-García, A. Martínez-Alonso, JMD Tascon, *Synthesis of ordered microporous carbons by activation of SBA-15 carbon replicas*, Microporous and Mesoporous Materials, **151** (2012) 390-396.
 [4] Farzin Nejad N, E. Shams, MK Amini, JC Bennett, *Ordered mesoporous carbon CMK-5 as a potential sorbent for fuel desulfurization: Application to the removal of dibenzothiophene and comparison with CMK-3*, Microporous and Mesoporous Materials, **168** (2013) 239- 246.
 [5] Yin Li, Bin Yuan, Jie Fu, Shuguang Deng, Xiuyang Lu, *Adsorption of alkaloids on ordered mesoporous carbon*, Journal of Colloid and Interface Science, **408** (2013) 181–190.
 [6] Jinghuan Chen, Feifei Cao, Songze Chen, Mingjiang Ni, Xiang Gao, Kefa Cen, *Adsorption kinetics of NO on ordered mesoporous carbon (OMC) and cerium-containing OMC (Ce-OMC)*, Applied Surface Science, **317** (2014) 26–34.
 [7] Zeinab Ezzeddine, Isabelle Batonneau-Gener, Yannick Pouilloux, Hussein Hamad, *Removal of methylene blue by mesoporous CMK-3: Kinetics, isotherms and thermodynamics*, Journal of Molecular Liquids **223** (2016) 763–770.
 [8] Wannes Libbrecht, An Verberckmoes, Joris W. Thybaut, Pascal Van Der Voort, Jeriffa De Clercq, *Soft templated mesoporous carbons: Tuning the porosity for the adsorption of large organic pollutants*, Carbon **116** (2017) 528-546.
 [9] Chen-Chia Huang, Yi-Hua Li, Yen-Wen Wang, Chien-Hung Chen, *Hydrogen storage in ordered mesoporous cobalt-embedded carbon*, International journal of hydrogen energy, **38** (2013) 3994-4002.
 [10] Chi-Yeong Ahn, Jae-Yeong Cheon, Sang-Hoon Joob, Junbom Kim, *Effects of ionomer content on Pt catalyst / ordered mesoporous carbon support in polymer electrolyte membrane fuel cells*, Journal of Power Sources, **222** (2013) 477 - 482
 [11] Fu Ruo-wen, Li Zheng-hui, Liang Ye-ru, Li Feng, Xu Fei, Wu Ding-cai, *Hierarchical Porous carbons: design, preparation, and performance in energy storage*, New Carbon Materials, **26** (2011) 171-179.
 [12] Ryong Ryoo, Sang Hoon Joo, Michal Kruk and Mietek Jaroniec, *Ordered Mesoporous Carbons*, Adv. Mater, **13** (2001) 677 - 681.
 [13] Motohide Hata, Yoshimasa Amano, Motoi Machida and Fumio Imazeki. *Preparation of Mesoporous Activated Carbons by Chemical Activation of Acid- and Base-Pre-treated Bamboos for Removal of Bulky Dye Molecules*. Journal of Environmental Chemistry **25**, No.2, (2015) 79 - 86.

EFFECT OF ADDITIONAL NANOPARTICLES ON MAGNETIC PROPERTIES OF SINTERED Nd-Fe-B MAGNETS

Huy Dan Nguyen^{1,2,*}, Thi Thanh Pham^{1,2}, Van Duong Nguyen³, Huy Ngoc Nguyen¹,
Thi Kim Oanh Dinh², Hai Yen Nguyen^{1,2}, Dang Thanh Tran^{1,2}

¹Institute of Materials Science, Vietnam Academy of Science and Technology, 18 Hoang Quoc Viet, Cau Giay, Hanoi, Vietnam;

²Graduate University of Science and Technology, Vietnam Academy of Science and Technology, 18 Hoang Quoc Viet, Cau Giay, Ha Noi, Vietnam;

³Hanoi Pedagogical University No.2, Xuan Hoa, Vinh Phuc, Vietnam

*Email: dannh@ims.vast.ac.vn

ABSTRACT

In this report, we present the effect of additional nanoparticles on magnetic properties of sintered Nd-Fe-B magnets. Nanoparticles of Dy-Nd-Al, Dy-Nb-Al, Nd-Cu-Al, Cu-Al... with their size of 30 - 100 nm were prepared by using high energy ball milling method. The nanoparticles were then mixed to master micro-powder of Nd-Fe-B with different concentrations and subsequently sintered in various conditions. A heat-treatment was also applied to the magnets to improve their performance. The results show that, in nanometer scale the additional particles are easier distributed homogeneously to create pinning centers and to make grain boundary more smoothly resulting in high coercivity for the magnets. The coercivity of the magnets could be enhanced by adding a small amount of the nanoparticles to boundary of Nd-Fe-B grains. The coercivity H_c and maximum energy product $(BH)_{max}$ of the Dy₄₀Nd₃₀Al₃₀-added magnets reaches a maximal value of 13 kOe and 34 MGOe, respectively. By this way, the content of heavy rare earth (Dy) can be reduced to lower cost of the high coercivity sintered Nd-Fe-B magnets.

Keywords: Nanoparticles, Sintered Nd-Fe-B magnets, Rare-earth magnets, High coercivity, High energy ball milling method.

INTRODUCTION

Nowadays, the demand for high quality permanent magnets is significantly increased by the development of modern industry. Especially, the use of sintered Nd-Fe-B magnets in electric motors, hybrid electric motors, wind power generators... is rising [1]. However, requirement of sintered Nd-Fe-B magnets in such equipment is high coercivity. A coercivity of ~ 8 kOe at ~ 200°C or ~ 25 kOe at room temperature is required to satisfy these applications [2]. One easy way to increase the coercivity is partial replacement Nd by Dy because the anisotropy field H_A of Dy₂Fe₁₄B of 278 kOe at room temperature is much higher than that of Nd₂Fe₁₄B (2:14:1), $H_A = 75$ kOe [3-6]. However, the Dy is expensive and scarce. Thus, improvement the quality of the sintered Nd-Fe-B magnets without using or using small amount of the heavy rare earth element is more and more concerned to study. Previous reports have showed that the coercivity of sintered Nd-Fe-B

magnets can be enhanced by addition of some elements other than the main components of Nd, Fe and B such as Al, Cu... or by improving technological conditions [7-9]. Recently, the addition of compounds to grain boundary not only enhances coercivity but also reduces amount of heavy rare earth [10-13]. Each additional compound with different size and elements will differently affect on the magnetic properties of the magnets. X. G. Cui *et al.* indicated that nanoparticles are probably distributed on the surface of Nd₂Fe₁₄B grains more homogeneously than microparticles [14]. According to L. Liang *et al.* [15] the coercivity of Dy_{32.5}Fe₆₂Cu_{5.5}-added Nd-Fe-B sintered magnets increases from 12.7 to 15.2 kOe by the formation of (Nd,Dy)₂Fe₁₄B shell surrounding 2:14:1 grains. On the other hand, the continuity of intergranular phase and 2:14:1 grain size were improved. By this way, amount of heavy rare earth element Dy was significantly reduced in compare to the commercial sintered (Nd,Dy)-Fe-B magnets. In another researches, smoothness of

grain boundaries, uniformity of the particles of the magnets, wettability between 2:14:1 phase and intergranular phase can be improved by adding free heavy rare earth compounds, leading to enhancing the coercivity [10, 11, 13, 16].

In this work, we investigated the effect of the additional nanoparticles with different components on magnetic properties of the sintered Nd-Fe-B magnets.

EXPERIMENTAL

The pre-alloys of $Nd_{16.5}Fe_{77}B_{6.5}$ were prepared from Nd, Fe and FeB by induction melting under Ar gas to avoid oxidation. The obtained ingots were pulverized for 8 h by ball milling method in industrial white gasoline. The addition alloys with components as in table 1 were prepared by arc-melting furnace under argon atmosphere. After that the resulted alloys were pulverized by high energy ball milling method with milling time of 4 h to obtain nanoparticles with average size of about 30 - 100 nm. The solvent/material and ball/powder weight ratios are 1/1 and 4/1, respectively. The additional nanoparticles with various weight were mixed into the Nd-Fe-B powder thoroughly. The mixed powder was pressed under a pressure of 15 MPa in an oriented magnetic field of about 20 kOe. The pressed magnets were sintered at 1080°C for 1 h. A two-stage heat treatment process was chosen and carried out using a vacuum furnace. At the first stage, the magnets were heat-treated at 820°C for 1 h and then rapidly quenched to room temperature by argon atmosphere. For the second stage, the magnets were heat-treated at 540°C for 1 h and rapidly quenched by argon atmosphere. For both the stages, the heating and quenching rates were 30°C/min and 50°C/min, respectively. The crystalline structure of all the samples was checked by an X-ray diffractometer (Equinox 5000 - Thermo Scientific) with the Cu- K_{α} radiation source ($\lambda = 1,5406 \text{ \AA}$). A field-emission scanning electron microscope (FESEM, S4800 - Hitachi) technique has been used to analyze the size and shape of the nanoparticles. The specimens of cylinders with 3 mm diameter and 3 mm height were cut to investigate magnetic properties on a pulsed high field magnetometer (PFM) with magnetic field up to 90 kOe. In order to determine the maximum energy product $(BH)_{\max}$ of the magnets, a demagnetization factor was

estimated through a semi-experimental data sheet.

Table 1. The component of addition compounds.

Samples	Components
P1	$Dy_{40}Nd_{30}Al_{30}$
P2	$Dy_{40}Nb_{30}Al_{30}$
P3	$Dy_{40}Zr_{30}Al_{30}$
P4	$Nd_{40}Cu_{30}Al_{30}$
P5	$Nb_{40}Cu_{30}Al_{30}$
P6	$Cu_{50}Al_{50}$

RESULTS AND DISCUSSION

The SEM image and XRD pattern of $Nd_{16.5}Fe_{77}B_{6.5}$ powder are presented in Fig.1. We found that the grain size of the master powder is smaller than 5 micrometer, Fig. 1a. At the same time, the sample reveals single phase of $Nd_2Fe_{14}B$ structure.

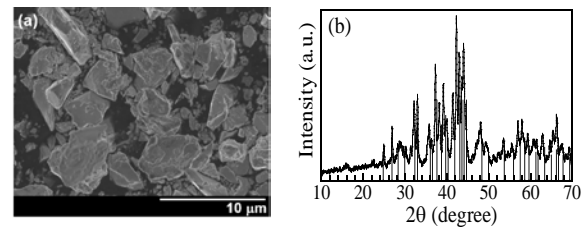


Figure 1. SEM image (a) and XRD pattern (b) of $Nd_{16.5}Fe_{77}B_{6.5}$ powder.

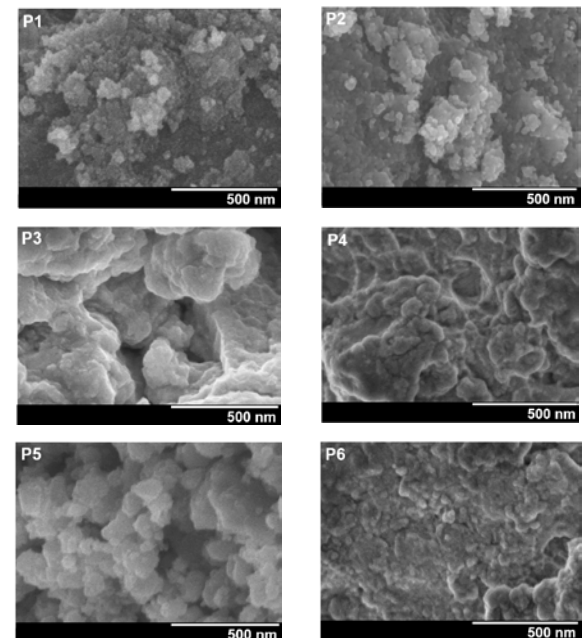


Figure 2. SEM images of the compounds powder.

Fig. 2 shows SEM images of the compounds powder. We can see all samples are nanoparticles with average size smaller than 50 nm. However, particles create to clusters,

leading to difficultly to observe individual grains.

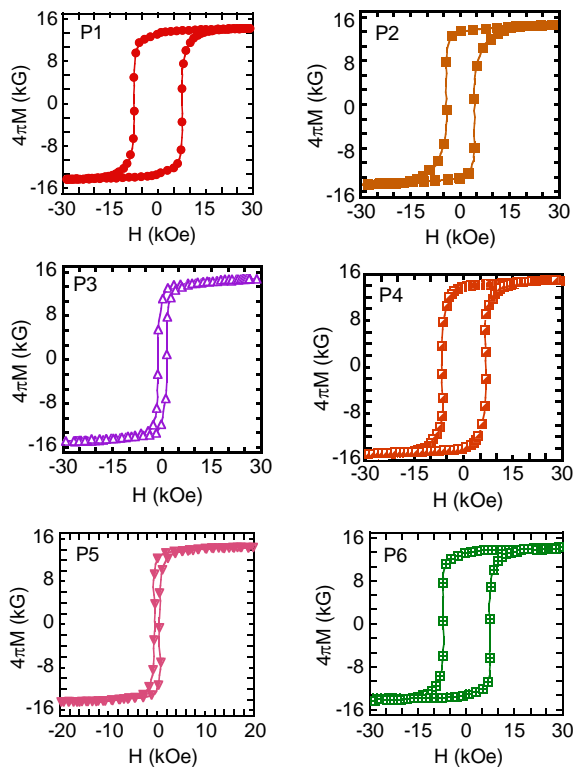


Figure 3. Hysteresis loops of the magnets added nanoparticles before heat treatment.

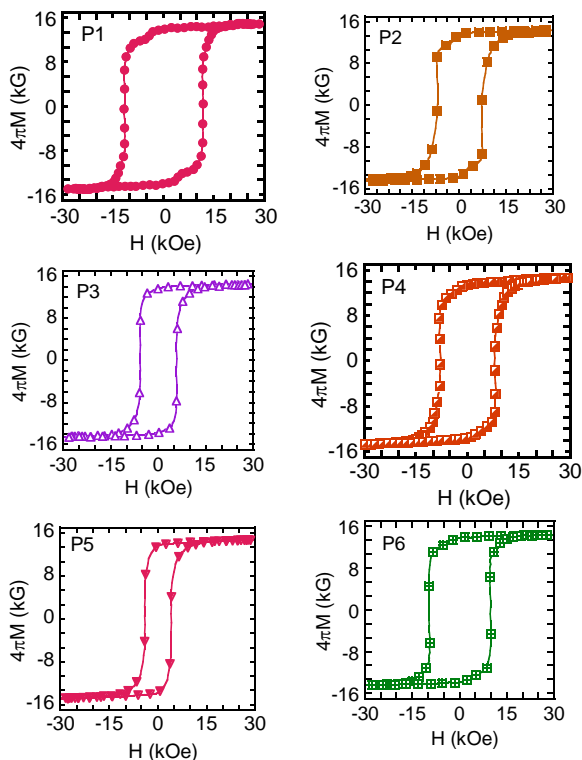


Figure 4. Hysteresis loops of the magnets added nanoparticles after heat treatment.

Figs. 3 and 4 show hysteresis loops of the magnets added nanoparticles before and after heat treatment. We can realize that, the coercivity of the magnets depends on both the nanoparticles addition and heat treatment process. Before heat treatment, the H_c of the added magnet P1, P4 and P6 was improved in comparison with that of the un-added magnet (5.3 kOe) [17]. Meanwhile, the addition of P2, P3 and P5 have reduced the coercivity (< 4 kOe). The P1-added Nd-Fe-B sintered magnets have highest coercivity ($H_c = 8$ kOe for the as-sintered magnets and $H_c = 12$ for the heat-treated magnets). The H_c and $(BH)_{max}$ of added magnets with the different additional compounds before and after heat treatment were determined and listed in Table 2.

Table 2. Coercivity H_c of the added magnets with the different additional compounds before and after heat treatment.

Condition	Compounds	H_c (kOe)	$(BH)_{max}$ (MGOe)
After heat treatment	P1	8	35.5
	P2	4.3	28
	P3	1.8	6
	P4	7.3	33.5
	P5	0.4	5.5
	P6	7	35
Before heat treatment	P1	12	37.5
	P2	7.4	32
	P3	5.5	20.5
	P4	7.9	34
	P5	4.2	24
	P6	9.8	37

The obtained results show that each addition compounds needs different optimal technological conditions. Because each additive compound have different elements which different effect on sintering temperature and time. The heat treatment step only enhances the coercivity but does not improve squareness of the hysteresis loops of the magnet. This can be explained that after heat treatment distribution of the grain size was increased. At the same time, the adding elements can change the structure and distribution of phases, leading to the inhomogeneity of demagnetization field. On the other hand, the grain boundaries are heterogeneous, leading to the formation of the soft magnetic α -Fe phase which plays a role as nucleation centre of reversal domains to cause magnetization of the magnets at lower external magnetic field [18].

After that, we change weight fractions of P1 nanoparticles from 1 to 5%. Figure 5a shows the dependences of the coercivity H_c of the magnets on various weight fractions of P1 nanoparticles before and after heat treatment. We found that the H_c depends almost linearly on the concentration of P1 (Fig. 5a). Its value increases from 6 to 10 kOe for the as-sintered magnets and from 9.5 to 13 kOe for the heat-treated magnets when weight fractions of P1 nanoparticles increases from 1 to 5%. This is agreed with the result reported by Q. Liu *et al.* [19]. The coercivity enhancement of the magnets added with P1 compounds is due to Dy diffusion from the grain boundaries to the 2:14:1 grain during sintering and heat treatment process, leading to the formation of the $(\text{Nd,Dy})_2\text{Fe}_{14}\text{B}$ shell. With higher magnetocrystalline anisotropy field of $\text{Dy}_2\text{Fe}_{14}\text{B}$, the formation $(\text{Nd,Dy})_2\text{Fe}_{14}\text{B}$ shell might make magnetic anisotropy of the outer layer higher than that of the interior.

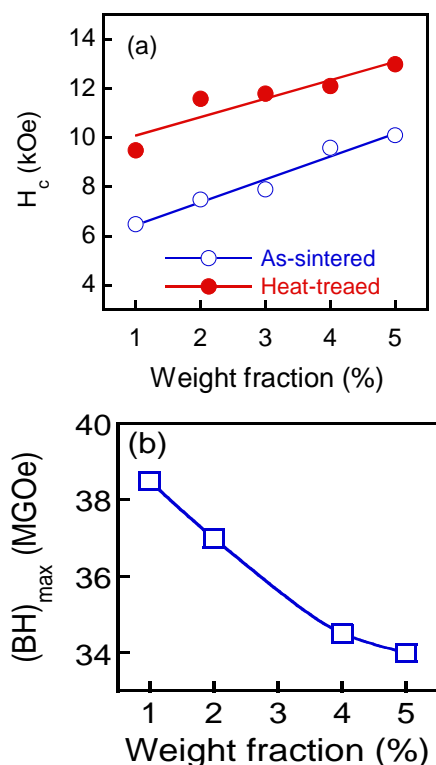


Figure 5. Dependence of coercivity H_c (a) and maximum energy product $(BH)_{max}$ (b) of magnets added with various weight fractions of P1 nanoparticles before and after heat treatment.

The dependence of maximum energy product $(BH)_{max}$ of the heat-treated magnets on various additional fractions of the P1 nanoparticles is shown in Fig. 5b. We can see

that, the $(BH)_{max}$ decreases with increasing the fraction of P1, agreeing with the results reported in [15]. The additional of non-ferromagnetic nanoparticles can be decrease saturation magnetization, leading to the reduction of the $(BH)_{max}$ in comparison to the un-added magnet ($(BH)_{max} = 40$ MGOe). Although the $(BH)_{max}$ value is still high enough (> 30 MGOe) for practical application. Especially, the enhancement of the coercivity is necessary for application with high operating temperature. On the other hand, the less use or unuse of the heavy rare earth of Dy is important for lowering the cost of the magnets.

CONCLUSIONS

In summary we have been investigated the effect of the additional nanoparticles with different components on magnetic properties of the sintered Nd-Fe-B magnets. The effect of the $\text{Dy}_{40}\text{Nd}_{30}\text{Al}_{30}$ nanoparticles on the coercivity enhancement for the magnets is stronger than that of another ones. The maximal H_c and $(BH)_{max}$ value of 13 kOe and 34 MGOe, respectively with 5 wt% of $\text{Dy}_{40}\text{Nd}_{30}\text{Al}_{30}$ nanoparticles addition. The obtained hard magnetic parameters of the magnets can be applied in practice.

Acknowledgment

This research is supported by the Ministry of Science and Technology of Viet Nam under grant number of KC.02.11/16-20 and the collaborative project “Development of Permanent Materials” between Korea Institute of Materials Science (KIMS) and Institute of Materials Science (IMS). A part of the work was done in the Key Laboratory for Electronic Materials and Devices, IMS, VAST, Viet Nam.

References

- [1]. Y. Matsuura, *Recent development of Nd-Fe-B sintered magnets and their applications*, J. Magn. Mater. **303** (2006) 344-347.
- [2]. K. Hono and H. Sepehri-Amin, *Strategy for high-coercivity Nd-Fe-B magnets*, Scr. Mater. **67** (2012) 530-535.
- [3]. S. Pandian, V. Chandrasekaran, G. Markandeyulu, K. J. L. Iyer and K. V. S. Rao Rama, *Effect of Co, Dy and Ga on the magnetic properties and the microstructure of powder metallurgically*

- processed Nd-Fe-B magnets*, J. All. Comp. **364** (2004) 295-303.
- [4]. X. B. Liu and Z. Altounian, *The partitioning of Dy and Tb in NdFeB magnets: A first-principles study*, J. Appl. Phys. **111** (2012) 07A701.
- [5]. N. J. Yu, M. X. Pan, P. Y. Zhang and H. L. Ge, *The origin of coercivity enhancement of sintered NdFeB magnets prepared by Dy addition*, J. Magn. **18** (2013) 235-239.
- [6]. H. Sepehri-Amin, Y. Une, T. Ohkubo, K. Hono and M. Sagawa, *Microstructure of fine-grained Nd-Fe-B sintered magnets with high coercivity*, Scr. Mater. **65** (2011) 396-399.
- [7]. T. Kim, S. Lee, J. Kim, Y. Kim, H. Kim, M. Lee and T. Jang, *Optimization of the post-sintering annealing condition for the high Cu content Nd-Fe-B sintered magnet*, J. Appl. Phys. **115** (2014) 17A770.
- [8]. M. Pan, P. Zhang, Q. Wu and H. Ge, *Improvement of corrosion resistance and magnetic properties of NdFeB sintered magnets with Cu and Zr Co-added*, Int. J. Electrochem. Sci. **11** (2016) 2659-2665.
- [9]. Y. L. Liu, J. Liang, Y. C. He, Y. F. Li, G. F. Wang, Q. Ma, F. Liu, Y. Zhang, and X. F. Zhang, *The effect of CuAl addition on the magnetic property, thermal stability and corrosion resistance of the sintered NdFeB magnets*, AIP Adv. **8** (2018) 056227(6).
- [10]. Y. Wang, Y. Luo, Z. Wang, G. Wu, J. Xie, W. Yan, D. Yu, *Coercivity enhancement in Nd-Fe-B magnetic powders by Nd-Cu-Al grain boundary diffusion*, J. Magn. Magn. Mater. **458** (2018) 85-89.
- [11]. K. Lu, X. Bao, M. Tang, G. Chen, X. Mu, J. Li, X. Gao, *Boundary optimization and coercivity enhancement of high (BH)_{max} Nd-Fe-B magnet by diffusing Pr-Tb-Cu-Al alloys*, Scr. Mater. **138** (2017) 83-87.
- [12]. P. Zhang, T. Ma, L. Liang, X. Liu, X. Wang, J. Jin, Y. Zhang and M. Yan, *Improved corrosion resistance of low rare-earth Nd-Fe-B sintered magnets by Nd₆Co₁₃Cu grain boundary restructuring*, J. Magn. Magn. Mater. **379** (2015) 186-191.
- [13]. X. G. Cui, M. Yan, T. Y. Ma and L. Q. Yu, *Effects of Cu nanopowders addition on magnetic properties and corrosion resistance of sintered Nd-Fe-B magnets*, Phys. B **403** (2008) 4182-4185.
- [14]. L. Liang, T. Ma, P. Zhang, J. Jin and M. Yan, *Coercivity enhancement of NdFeB sintered magnets by low melting point Dy_{32.5}Fe₆₂Cu_{5.5} alloy modification*, J. Magn. Magn. Mater. **355** (2014) 131-135.
- [15]. J. J. Ni, T. Y. Ma, Y. R. Wu and M. Yan, *Effect of post-sintering annealing on microstructure and coercivity of Al₈₅Cu₁₅-added Nd-Fe-B sintered magnets*, J. Magn. Magn. Mater. **322** (2010) 3710-3713.
- [16]. P. T. Thanh, N. V. Duong, N. H. Yen, N. H. Ngoc, N. M. Lam, K. X. Hau, D. H. Kim, S. C. Yu, *Effect of adding non-ferromagnetic nanoparticles to grain boundary on coercivity of sintered Nd-Fe-B magnet*, Curr. Appl. Phys. **18** (2018) 329-334.
- [17]. Z. Wang, X. Wang and M. Jin, *Factors affecting the squareness of hysteresis loops of sintered NdFeB magnets*, J. Rare Eart. **25** (2007) 1-4.
- [18]. Q. Liu, L. Zang, F. Xu, X. Dong, J. Wu and M. Komuro, *Dysprosium nitride-modified sintered Nd-Fe-B magnets with increased coercivity and resistivity*, Japan. J. Appl. Phys. **49** (2010) 093001.

SIMPLE DESIGN OF CO-POLARIZATION BROADBAND METAMATERIAL ABSORBER FOR C-BAND APPLICATIONS

Tran Sy Tuan,¹ Nguyen Thi Kim Thu,¹ Nguyen Thi Minh,¹ Lam Quang Hieu,¹ Nguyen Hong Quang,¹ Duong Ngoc Huyen,² Hugo Nguyen,³ Nguyen Thi Quynh Hoa^{1,*}

¹Vinh University, 182 Le Duan, Vinh City, Vietnam

²Institute of Physics Engineering, Hanoi University of Science and Technology, Vietnam

³Department of Engineering Sciences, Uppsala University, Uppsala, Sweden

Email: ntqhoa@vinh.edu.vn

ABSTRACT

A simple design of a novel co-polarization wideband metamaterial absorber (MA) for C-band applications is proposed and numerical investigated. The unit cell of the proposed MA is designed by combining the haft-moon shaped resonator (HMSR) and interior circle resonator (ICR) structures, based on FR4 substrate. The absorption performances of the proposed absorber are numerical investigated. The proposed absorber achieves the co-polarization absorptivity higher than 90% covering the entire C-band from 3.95 GHz to 8.02 GHz under normal incidence for transverse electric (TE) and transverse magnetic (TM) polarizations. Moreover, the average absorption can be maintained above 80% even for incident angles up to 60° under both TE and TM polarizations. The physical mechanism of the proposed MA is investigated by using the electric and surface current distributions, which is also supported by the retrieved constitutive electromagnetic parameters. The design in this work is a compact structure (unit cell dimension of $\sim \lambda/6.5$ and thickness of $\sim \lambda/11.8$ at the center frequency), broadband, and wide incident angle insensitivity, which can be applications in the C-band defense and stealth systems.

Keywords: Metamaterials, Single layer, Ultrathin absorber, Perfect absorption.

INTRODUCTION

Metamaterial absorber (MA) has attracted considerable interest in both fundamental research and device applications, since Landy et al. reported a thin perfect microwave MA based on electric and magnetic resonances in 2008 [1-3]. However, the realizing MA structures having a simple design, thin thickness, easy fabrication process and broadband absorption features for practical applications in microwave range such as radar cross section reduction (RSC), stealth technology and EM interference (EMI) reduction remains truly challenging. Furthermore, the design of broadband microwave MAs have been mostly focused on the frequency band above C-band, but very few design of MA for lower frequency absorption band, such as C-band, has been reported [2,4].

In this paper, we propose a simple design of a novel co-polarization wideband metamaterial absorber (MA) for C-band applications. The unit cell of the proposed MA is designed by combining the haft-moon shaped resonator (HMSR) and interior circle resonator (ICR) structures, based on FR4 substrate.

EXPERIMENTAL

Fig. 1 shows the unit cell of the proposed broadband MA. The broadband MA is formed by the periodic arrangement of the unit cells in the lateral directions and the vertical thickness consists of two metallic films separated by a dielectric layer. The metallic layers are made of copper with an electric conductivity of and thickness (t) of 0.035 mm. The dielectric layer is made of FR4 with a relative dielectric constant of 4.3, a loss - tangent of 0.025, and thickness (h) of 4.2 mm. The front layer is constituted by the combination of haft-moon shaped resonator (HMSR) and interior circle resonator (ICR) structure. The geometrical dimensions of the unit cell are $R_1=6.3$ mm, $R_2=3.35$ mm, $r=3.65$ mm, and $a=15.4$ mm. The center of the circles with radii R_1 and R_2 are $O_1(0,0)$ and $O_2(1.775,-1.175)$, respectively. For back layer of the structure, copper is used in order to block all transmission.

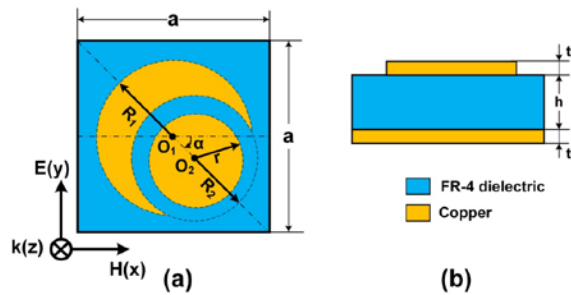


Figure 1. A unit cell geometry of the proposed MA: (a) top-view and (b) side-view.

In order to investigate the absorption performance of the proposed MA, the numerical simulation is performed by using frequency domain solver in a Computer Simulation Technology (CST) Microwave Studio. In the boundary condition set up, z-direction and x-y plane are for the direction of propagation and the E-H fields, x and y axes are fixed to the unit cell and z axis is open, the plane waves are normally incident to the structure along the z direction.

The absorption is defined by $A(\omega) = 1 - T(\omega) - R(\omega)$, where $T(\omega)$ and $R(\omega)$ are transmission and reflection, respectively. The $A(\omega)$ and $T(\omega)$ are determined from the frequency-dependent S-parameters $S_{11}(\omega)$ and $S_{21}(\omega)$, where $T(\omega) = |S_{21}(\omega)|^2$ and $R(\omega) = |S_{11}(\omega)|^2$. The reflection is calculated as $R(\omega) = |r_{yy}(\omega)|^2 + |r_{xy}(\omega)|^2$, where $r_{yy}(\omega) = |E_{yr}|^2 / |E_{yi}|^2$ and $r_{xy}(\omega) = |E_{xr}|^2 / |E_{yi}|^2$ are reflection coefficients for co-polarization and cross-polarization for y (or TE) polarized wave, respectively. In the conventional absorber model, the back layer acts as physical barrier to block the transmittance. Since $T(\omega)$ is eliminated by the ground plane, thus, the absorption is simplified to $A(\omega) = 1 - R(\omega)$.

RESULTS AND DISCUSSION

The absorption performances of the proposed absorber are numerical investigated. The proposed absorber achieves the co-polarization absorptivity higher than 90% covering the entire C-band from 3.95 GHz to 8.02 GHz under normal incidence as seen in Fig.2. Moreover, the average absorption can be maintained above 80% even for incident angles up to 60° under both TE and TM polarizations.

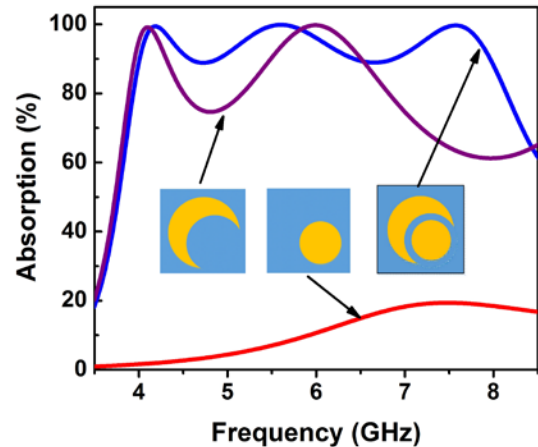


Figure 2. Absorption spectra of two components of the combined proposed MA structure.

To investigate the mechanism absorption of the proposed MA, the distributions of electric field and surface current at three resonance frequencies of 4.19 GHz, 5.63 GHz, and 7.58 GHz are performed as shown in Fig. 3.

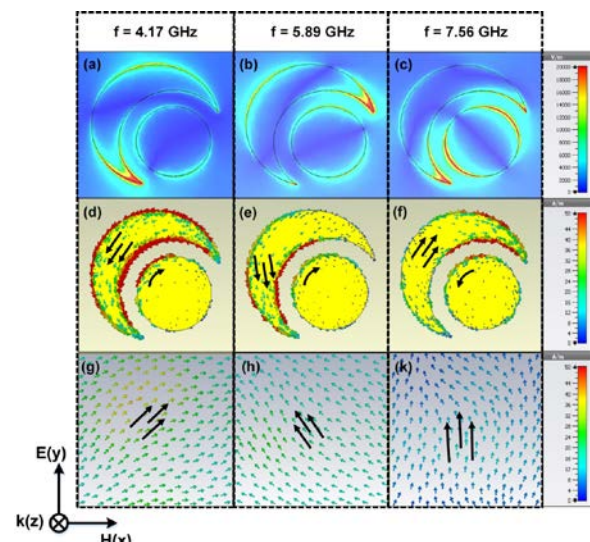


Figure 3. Distributions of (a),(b),(c) electric field, and surface current on (d),(e),(f) the front layer and (g),(h),(k) back layer of a unit cell under TE polarization with various resonant frequencies of 4.19 GHz, 5.63 GHz, and 7.58 GHz, respectively.

It can be seen from Figs. 3(a-c), the electric field with a specified frequency is concentrated at a certain part of MA. At lower frequencies of 4.19 GHz and 5.63 GHz, electric field tends to accumulate at inner top and bottom part of the HMSR, respectively. Meanwhile, at higher frequency of 7.58 GHz, the electric field is concentrated not only the outer of ICR mainly, but also in inner the top and bottom part of the

HMSR. The top and bottom surface current distributions are illustrated in Figs. 3(d-k). At the three resonance frequencies, the surface currents are mainly contributed by HMSR, while a significant amount of current flows through the ICR at higher frequency of 7.58 GHz. At the frequency of 7.58 GHz, the surface currents on the ICR and the HMSR are anti-parallel to that on the bottom layer. This means the peak at the higher frequency is not only mainly contributed by the magnetic resonance of the ICR, but also rather weak anti-parallel currents between the ICR and HMSR. However, at the lower resonance frequencies of 4.19 GHz and 5.63 GHz, the surface currents are strong coupled along the edges of HMRS. Thus, the strong induced electric field is created and it reverses to the incident electric field, which confirms the excited electric field is stronger than the incident electric field. It is clear that the electric resonance is excited at 4.19 GHz and 5.63 GHz. At the same time, the surface current distribution on the HMSR is anti-parallel with the current distribution in the ground layer, thus the circulating current is created and formed the induced magnetic field. The induced magnetic field is reverse with incident magnetic field, indicating that the strong magnetic resonance is also contributed in these resonant frequencies. Therefore, both the magnetic and the electric resonances are excited simultaneously at the lower frequencies of 4.19 GHz and 5.63 GHz.

CONCLUSION

A simple design of a novel co-polarization wideband MA based on asymmetric structure is proposed and investigated using numerical method. The unit cell of the proposed structure consists of metallic shape created by the combination of HMSR and ICR structure and ground plane separated by a dielectric layer. The effect of the structural parameters on the co-polarization absorption is thoroughly investigated. The proposed MA shows a co-polarization absorptivity of higher than 90% in wide bandwidth from 3.95 GHz to 8.02 GHz, which covers the entire C-band. The total average absorption can be retained above 75% for the wide incident angle up to 60° under both TE and TM polarizations. The electric and surface current distributions at three distinct absorption peaks are analyzed to explain the absorption mechanism. Also, the physical mechanism, which is confirmed by the retrieved

constitutive electromagnetic, is mainly contributed by the magnetic resonance. In addition, the proposed MA presents an excellent practical feasibility in term of compact structure (unit cell dimension of $\sim\lambda/6.5$ and thickness of $\sim\lambda/11.8$ at the center frequency) and wide incident angle insensitivity. The proposed MA in this work may find applications in the C-band defense and stealth systems that require only co-polarization.

Acknowledgment

This research is funded by Vietnam National Foundation for Science and Technology Development (NAFOSTED) under grant number 103.02-2017.367.

References

- [1]. N. I. Landy, S. Sajuyigbe, J. J. Mock, D. R. Smith and W. J. Padilla, Phys. Rev. Lett. **100** 207402 (2008).
- [2]. Y. Shen, J. Zhang, Y. Pang, L. Zheng, J. Wang, H. Ma and S. Qu, Sci. Rep. **8**, 4423 (2018).
- [3]. T. Beeharry, R. Yahiaoui, K. Selemani and H. H. Ouslimani, Sci. Rep. **8**, 382 (2018).
- [4]. N. T. Q. Hoa, T. S. Tuan, L. T. Hieu, B. L. Giang, Sci. Rep. **9**, pp.468 (2019).

NUMERICAL STUDY OF AN EFFICIENT BROADBAND METAMATERIAL ABSORBER IN VISIBLE LIGHT REGION

Tran Sy Tuan,¹ Nguyen Thi Kim Thu,¹ Nguyen Thi Minh,¹ Lam Quang Hieu,¹ Nguyen Hong Quang,¹ Duong Ngoc Huyen,² Hugo Nguyen,³ Nguyen Thi Quynh Hoa^{1,*}

¹Vinh University, 182 Le Duan, Vinh City, Vietnam

²Institute of Physics Engineering, Hanoi University of Science and Technology, Vietnam

³Department of Engineering Sciences, Uppsala University, Uppsala, Sweden

Email: ntqhoa@vinh.edu.vn

ABSTRACT

We report a numerical study of a broadband metamaterial absorber in visible light region by utilizing a single layer of metal-dielectric-metal configuration. The absorption bandwidth and absorption performances are tailored by varying the resonator shapes and metal materials. The absorption bandwidth of the proposed MA structure is enhanced significantly with decreasing the order of rotational symmetry of the resonator shape. Using gold configuration, the 2-fold symmetry MA structure based on the double-sized axe (DSA) shaped resonator exhibits the broadband absorption response over the entire visible light and apart of infrared spectrum range from 320 nm to 982 nm with absorptivity above 90% for both transverse electric and transverse magnetic polarizations. The physical mechanism of broadband absorption is explained by the current, electric and magnetic distributions, significantly affected by the propagating surface (PSP) and localized surface plasmon (LSP) resonances. Furthermore, the high absorber performances of the 2-fold symmetry MA structure can be obtained over entire visible light region (400 nm - 700nm) for both noble metal of gold and low-cost metal of nickel configurations, indicating the proposed absorber is a promising candidate for low-cost and large-scale fabricate device operated in visible light region.

Keywords: Metamaterials, Visible light, Perfect absorption, Absorber.

INTRODUCTION

Metamaterial absorber (MA) has been intensively studied for both theoretical research and practical applications since Landy et al. proposed the microwave MA with near-unity absorbance in 2008 [1]. Generally, the metamaterial absorbers are designed based on the metal-insulation-metal (MIM) configuration because MIM configuration can be improved the absorption intensity of the MA [2]. By the turning the shape and size of metal patch resonator, the MA was designed for different operation frequencies ranging from microwave to optics frequencies. However, the controllable design of MA to obtain a wide operation bandwidth, insensitivity to light polarization, omni-directionality, and a considerable reduction in overall thickness has remained a challenging issue. Recently, many efforts have been recently focused on the extension of absorption band and control of absorption frequency range in visible light regime for practical applications like photovoltaic device,

photo-detector, thermal emitter, and pulse generation, etc. [3,4,5,6].

In this paper, we report a numerical study of a broadband metamaterial absorber in visible light region by utilizing a single layer of metal-dielectric-metal configuration. The absorption bandwidth and absorption performances are tailored by varying the resonator shapes and metal materials. The absorption bandwidth of the proposed MA structure is enhanced significantly with decreasing the order of rotational symmetry of the resonator shape.

EXPERIMENTAL

The proposed MA is shown in the inset of Fig. 1. MA structure consists of a periodic array of various surface geometries from asymmetry to symmetry shapes (DSA to cross, square, and circle), respectively. The top and bottom layers are made of metal materials. The different metal materials are chosen to design the MA structure including noble metals (gold and silver) and common metals (nickel and aluminum). The top

metallic layer is placed directly on the surface of a homogeneous silicon dioxide substrate. Meanwhile, the backside of dielectric layer is covered the same metallic material with the top layer acting as the ground to block the transmission. Thicknesses of the layers from top to bottom are 15 nm (t_1), 55 nm (h) and 15 nm (t_2), respectively. The geometrical dimensions of the DSA unit cell are optimized using the numerical simulation based on frequency domain solver in a Computer Simulation Technology (CST) Microwave Studio. Based on the simulated results, the optimized dimensional parameters of the unit cells for designing of the broadband MA are as follows: $P = 160$ nm, $R = 50$ nm, $R_1 = R_2 = 30$ nm, and $W = 40$ nm. The centers of the circles are O ($x=0$ nm, $y=0$ nm), $O_1(x=35$ nm, $y=-35$ nm), $O_2(x=-35$ nm, $y=35$ nm). The influence of structural parameters such as different structure shapes and metallic materials on the absorption characteristics of the MA is simulated and evaluated.

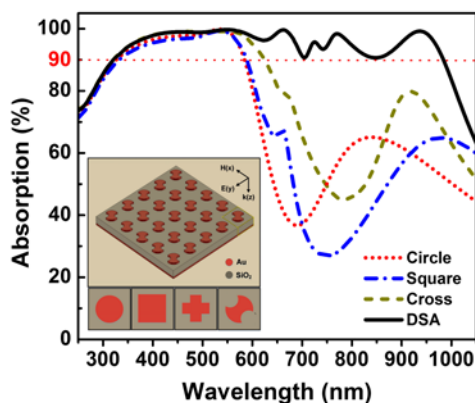


Figure 1. Absorption spectra of the proposed MA with various resonator shapes under normal incidence. The insets show the schematic of the proposed MA and top-view of various resonator shapes including circle, square, cross and double-sided axe (from left to right).

The absorption of the MA can be calculated by $A(\omega) = 1 - T(\omega) - R(\omega)$, where $A(\omega)$, $R(\omega)$ and $T(\omega)$ are the absorption, reflection, and transmission of the absorber, respectively. The transmission $T(\omega)$ and reflection $R(\omega)$ are determined from the frequency-dependent S-parameter $S_{11}(\omega)$ and $S_{21}(\omega)$, where $T(\omega) = |S_{21}(\omega)|^2$ and $R(\omega) = |S_{11}(\omega)|^2$. Because the thickness of the metal slab is thick enough to forbid the transmission of the incident wave ($T(\omega) = 0$), the absorption could be simplified to be $A(\omega) = 1 - R(\omega)$.

RESULTS AND DISCUSSION

The absorption spectra of the MAs designed with various resonator shapes under normal incidence for both transverse electric (TE) polarization are shown in Fig. 1. The absorption range of the proposed MAs can be controlled by varying the order of rotational symmetry of the resonator shapes. The largest and lowest RAB values are obtained in the MAs with DSA and circle resonator shapes, respectively. We note that the DSA shaped MA exhibits an absorption intensity higher than 90% in a wide wavelength range of 320-982 nm, covering from UV, visible to near-infrared regions and peak absorptivities of 98.97%, 99.68%, and 99.18% in UV (~450 nm), visible (~546 nm) and near-infrared regions (~938 nm), respectively. The RAB of the DSA shaped MA reaches about 102%, which indicates a good wideband property.

The physical mechanism of MA is generally based on the localized surface plasmon (LSP) resonance, the propagating surface plasmon (PSP) resonance, and the combination of both the LSP and PSP resonances. The distributions of current density, electric and magnetic fields are used to explain the absorption mechanism of the MA structure. Fig. 2 shows the current density and the distributions of electric and magnetic field of the DSA-shaped MA under the TE polarization at various resonant wavelengths of 450 nm, 546 nm and 938 nm in the YOZ plane. As seen in Figs. 2(a)-(c), the current density is mainly concentrated in the metallic resonator and on top of the metallic ground plane, which confirms the surface plasmon resonance. It was reported that the surface plasmon resonance can be attributed to the wideband absorption phenomenon. Furthermore, the electric current distributes in the top and bottom metal layers that means the origins of the energy loss in the dielectric layer which result in the broadband absorption. The electric field distribution is localized around the metal corners between the neighbor unit cells, as seen in Figs. 2(d)-(f). Furthermore, the electric field is a strong coupled in to air-slot at that resonant wavelength of 938 nm, indicating that surface plasmon polaritons (SPPs) are excited in the structure. The distributions of the magnetic field at these resonant wavelengths are shown in Figs. 2(g)-(k). The distributions of the magnetic field of the MA for various resonant wavelengths are

significantly different. It was reported that the different distributions of the magnetic field is due to different types of resonances such as LSP and PSP. At the resonant wavelength of 938 nm, the localized magnetic field within the gap between the top metallic resonator and the metallic ground plane results in LSP resonance. Meanwhile, the magnetic field is not only accumulated in the metallic resonator but also spread through the neighbor unit cells at the resonant wavelength of 450 nm, indicating that the absorption around 450 nm results from PSP resonance. Both the LSP and PSP resonances are excited at the resonant wavelength of 546 nm as evidenced by the distribution of magnetic field in Fig. 2(h). Both the LSP and PSP resonances are excited at the resonant wavelength of 546 nm as evidenced by the distribution of magnetic field in Fig. 2(h).

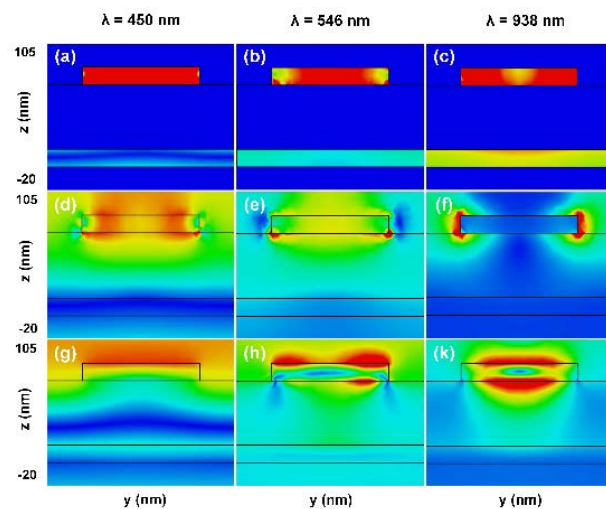


Figure 2 (a), (b), (c) Current density and distributions of (d), (e), (f) electric field and magnetic field on the YOZ plane of a unit cell at various resonant wavelengths of 450 nm, 548 nm, and 938 nm, respectively. The y-direction is taken from -80 nm to 80 nm.

Besides the order of rotational symmetry of resonator shape, the metal materials are also found to be affected on absorption performance of the MA as shown in Fig. 2. It can be observed that the variation of the metals not only influences the absorption range and bandwidth but also affects the absorption efficiency the DSA shaped MAs. Meanwhile, the absorption properties are almost unchanged for both TE and TM polarizations. The MA designed based on gold configuration shows the widest operating absorption band along with a high average absorption over both that band and visible light

range, though these highest absorbencies are obtained for nickel configuration. We note that the DSA-shaped MAs give the average absorbance higher than 90% for both noble metals (gold and silver) and common metals (nickel and aluminum), and the nearly perfect absorbance (99%) for nickel and gold in the visible light range.

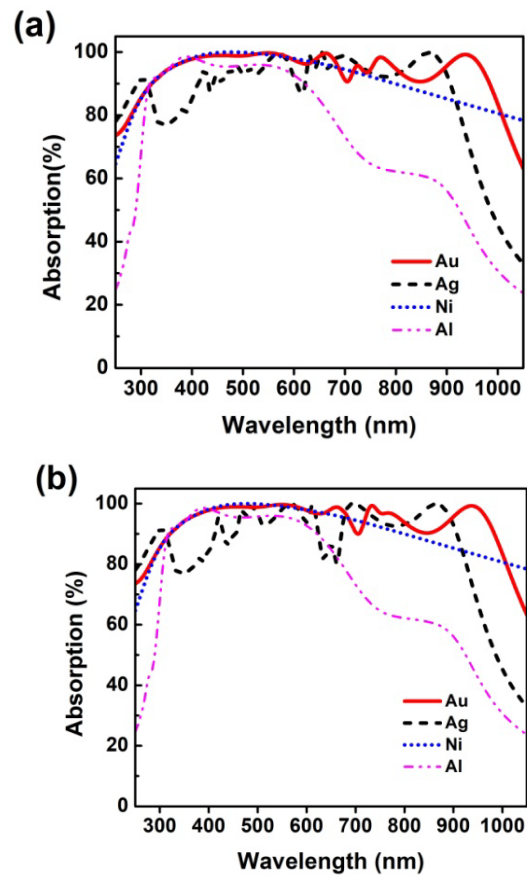


Figure 3. Absorption efficiencies of the proposed MAs designed with various metals under normal incidence for (a) TE and (b) TM polarizations.

CONCLUSION

A tailoring design of a broadband MA in visible light region based on a single layer of metal-dielectric-metal configuration was studied numerically. The absorption bandwidth and absorption performances were controlled by turning the shape and metal material of resonator shape. The absorption band was significantly increased with decreasing the order of rotational symmetry of patch resonator. Using the gold configuration, the broadband absorption response of the MA structure based on the 2-fold symmetry of the DSA shaped resonator over the entire visible light and apart of infrared

spectrum range from 320 nm to 982 nm with absorptivity above 90% for both TE and TM polarizations was obtained. The physical mechanism of broadband absorption was investigated by the current, electric and magnetic distributions, contributed by propagating surface plasmon (PSP) and localized surface plasmon (LSP) resonances. In addition, the high absorber performances of DSA shaped MA structure over entire visible light region (400 nm - 700nm) can be achieved for both noble metal of gold and low-cost metal of nickel configurations, suggesting that the proposed absorber is a promising candidate for visible light applications.

Acknowledgment

This research is funded by Vietnam National Foundation for Science and Technology Development (NAFOSTED) under grant number 103.02-2017.367.

References

- [1] N. I. Landy, S. Sajuyigbe, J. J. Mock, D. R. Smith and W. J. Padilla, *Phys. Rev. Lett.* **100** 207402 (2008).
- [2] A. Ghobadi, H. Hajian, A. R. Rashed, B. Butun, E. Ozbay, *Photonics Res.* **6**, 168 (2018).
- [3] H. A. Atwater and A. Polman, *Nat. Mater.* **9**, 205 (2010).
- [4] W. Li, J. Valentine, *Nano Lett.* **14**, 3510 (2014).
- [5] Y. Gong, Z. Wang, K. Li, L. Uggalla, J. Huang, N. Copner, Y. Zhou, D. Qiao, and J. Zhu, *Opt. Lett.* **42**, 4537 (2017).
- [6] T. S. Tuan and N. T. Q. Hoa, *IEEE Photonics Journal* **11**, 8371499 (2019).

EFFECT OF SUPPORT ON PERFORMANCE OF Ni-BASED NANOCATALYSTS AND KINETICS OF METHANE DRY REFORMING

Phan Hong Phuong¹, Luu Cam Loc^{1,2*}, Nguyen Tri², Nguyen Xuan Linh¹,
Pham Minh Tai¹, Nguyen Phung Anh², Nguyen Thi Thuy Van²

¹Ho Chi Minh City University of Technology – VNU-HCM, 268 Ly Thuong Kiet Str., Ho Chi Minh City, Vietnam

²Institute of Chemical Technology – VAST, 01 Mac Dinh Chi Street, Ho Chi Minh City, Vietnam
Email: lclloc@ict.vast.vn

ABSTRACT

Physicochemical characteristics of the nano-catalysts based on Nickel supported on α -Al₂O₃-MgO, CeO₂ and SBA-15 prepared by impregnation method were determined by N₂ physisorption measurements, powder X-ray diffraction, H₂ temperature-programmed reduction, CO₂ temperature-programmed desorption, and transmission electron microscopy. Kinetics of methane dry reforming (DRM) on catalysts was carried out in gradientless circulating micro-flow system at atmospheric pressure and temperature range of 600–750 °C. The results showed that the carriers not only changed the specific surface area of the catalyst but also changed the active state of nickel. It was shown that on Ni/Ce and Ni/SBA samples nickel exists mainly in the form of small- and medium-sized NiO particles, while on the NiMg/Al sample-in the form of the mixed metal oxide phase Mg_xNi_{1-x}O that should greatly affect the activity of the catalysts. The kinetic equation of the dry reforming of methane on three catalysts was written by fractional equation, describing the dependence of the reaction rate on the concentration of CO₂, CH₄, and reaction products. The obtained kinetics show that the reaction takes place on two different types of centers. The order in the activity, apparent rate constant as well as adsorption constants of raw materials (H₂, CO₂) was observed as follows: NiMg/Al << Ni/Ce < Ni/SBA, while the activation energy (E) is in the opposite order. The highest activity was observed on the catalyst containing 40 wt.% NiO supported on SBA-15.

Keywords: DRM, CeO₂, SBA-15, MgO- α -Al₂O₃, Ni catalyst, CH₄.

INTRODUCTION

Dry reforming of methane (DRM) is a promising way to convert greenhouse gases into valuable product, synthetic gas. Among metals, Nickel has been used frequently in researches. However, catalytic performance and stability of the Ni-based catalysts make them inapplicable commercially. So, many ways have been proposed to improve the Ni-based catalysts for reforming CH₄.

The most commonly used support for dry reforming of CH₄ is Al₂O₃ while other supports such as MgO, TiO₂, SiO₂ and La₂O₃ are also used [1]. Studies have shown that the effect of the support could be attributed to direct activation of CH₄ or CO₂ by metal oxides and differences in particle size. Both Ni/ α -Al₂O₃ and Ni/ γ -Al₂O₃ were unstable with time on feed stream for CH₄ reforming. While Ni/ α -Al₂O₃ has been reported to be unstable due to carbon formation, phase change of γ -Al₂O₃ at 973K was the reason for instability of Ni/ γ -Al₂O₃ catalyst [2]. The

excellent thermo-stability of CeO₂ and SBA-15 materials with unique properties such as flexible oxygen of CeO₂ [3] and well-ordered structure with high surface of SBA-15, are assessed as potential supports for DRM reaction.

To widely apply this process in simulation and industry, designing reactors and finding the optimal conditions for reaction, as well as the mechanism and kinetics of the process were extremely important. Kinetics research of DRM has been studied for many years. Many kinetic models were proposed, including the Power Law, Eley–Rideal and Langmuir-Hinshelwood model. Power Law model was used quite universally to calculate the kinetics for dry reforming. The main advantage of this model is the simplicity of applying and estimating parameters as the reaction order. However, it cannot fully explain the various steps in the reaction mechanism that occur on the catalyst surface [4].

Langmuir-Hinshelwood model received much attention from scientists [5] due to the

concordance between mechanisms and experimental results. For this model, both reactants were firstly adsorbed on the catalyst surface before proceeding the reaction between adsorbed species to form product. According to this mechanism, adsorption of raw substances could take place on one type or two different types of catalytic sites, resulting in the corresponding kinetic equations.

Although there have been many studies on kinetics and mechanism of DRM reaction, but no agreement on the kinetic model of this reaction has been released. Furthermore, most of studies were still focused primarily on NiO/Al₂O₃ catalyst, the kinetic studies for NiO catalyst supported on CeO₂ and SBA-15 support was limited. This study is carried out to investigate property and activity of nickel catalysts supported on different support (Al₂O₃-MgO; CeO₂ and SBA-15) as well as kinetics of DRM reaction on given samples. On these results, the effect of various supports would be clarified.

EXPERIMENTAL

CeO₂ nanorods were obtained by following procedure outlined before [6]. SBA-15 was prepared by hydrothermal method, described in detailed in our previous paper [7].

The NiO catalysts supported on CeO₂, SBA-15, and MgO + α -Al₂O₃ were prepared by impregnation method. Physicochemical properties of catalysts were determined by several methods, detailed in [7]. Activity for methane reforming of the prepared catalysts was tested in a micro-flow reactor according to our published study [7]. The kinetics of CO₂ reforming of CH₄ was studied in a gradientless flow-circulating system at 600–750°C.

RESULTS AND DISCUSSION

Physicochemical characterization

The XRD patterns of NiMg/Al, Ni/Ce and Ni/SBA samples were shown in Fig.1a. It could be seen that diffraction peaks characterizing NiO phase in Ni/Ce and Ni/SBA appear at $2\theta = 37.2^\circ$, 43.3° , 62.9° , 75.4° , and 79.6° corresponding to (101), (200), (220), (311), and (222) plans with high intensities [8]. Meanwhile, NiO diffraction peaks in NiMg/Al catalyst showed weak intensity. This would lead to differences in the active state of Nickel in these two catalyst groups, as observed in TPR analysis.

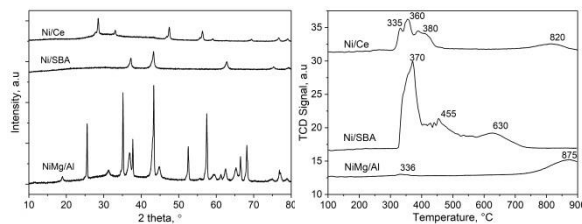


Figure 1. XRD patterns (a) and TPR patterns (b) of NiMg/Al, Ni/Ce and Ni/SBA catalysts.

H₂-TPR pattern of NiMg/Al catalysts (Fig. 1b) showed the main reduction peak with maxima at about 875 °C, corresponded to Ni²⁺ reduction in the mixed metal oxide phase (Mg_xNi_{1-x}O) and weak peak at 325 °C, assigning to the reduction of the relatively free NiO species. Meanwhile, Ni/Ce catalyst (Fig. 1b) showed the peaks in the temperature range of about 300 to 400 °C, assigning to the reduction of weakly and strongly interactive NiO species with CeO₂ supports while the peak at 450 °C is attributed to reduction of oxygen adsorbed on CeO₂ surface. The broad weak peak at around 810 °C is the reduction of lattice oxygen in bulk CeO₂. Meanwhile, H₂-TPR profile of Ni/SBA catalyst exhibited two reduction zones: T_{reduction} = 300–500°C with higher intensity and T_{max} ~ 620°C. They were ascribed to the reduction of Ni²⁺ in NiO clusters with small, medium size and reduction of NiO dispersed deeply in pores or large-sized NiO sintered. From the above analysis, it is shown that on Ni/Ce and Ni/SBA catalysts nickel exists mainly in the form of small- and medium-sized NiO particles, while on the NiMg/Al sample-in the form of the mixed metal oxide phase Mg_xNi_{1-x}O, reducing at high temperature.

Table 1. Structural properties of NiMg/Al, Ni/Ce and Ni/SBA catalysts

Catalyst	S _{BET} (m ² /g)	Pore diameter (nm)	Pore volume (cm ³ /g)
NiMg/Al	7.1	2.02	0.002
Ni/Ce	24.7	2.14	0.018
Ni/SBA	232.6	6.08	0.273

As it was followed from Tab.1, the specific surface area and the pore volume of the three catalysts are in the same decreasing order as Ni/SBA > Ni/Ce > NiMg/Al. The biggest value was attributed to Ni/SBA due to typical hexagonal structures along the channel system of SBA-15. Pore diameter of all three catalysts was ranging from 5.2 to 6.1 nm being suitable for diffusion of CH₄ and CO₂ into pores.

SEM images (not shown) indicated that the particles in Ni/Ce are uniform and have diameter

of almost 40–50 nm. Meanwhile, the small particles (50–100 nm) doped on surface of bigger lumps is observed in Ni/SBA. Agglomeration of catalyst particles is observed in the three catalysts. On the other hand, in NiMg/Al catalyst, 50–100 nm particles are attached to the surface as seen in both SEM and TEM images.

CO₂-TPD pattern of the three catalysts (not shown) reflected that there was one main desorption zone appearing at 60–250°C, corresponding to weak and mediate basic sites.

Catalytic performance for DRM

Figure 2 showed that Ni/SBA catalyst has the best activity among the three catalysts supported on different supports. While CH₄ conversion on Ni/Ce catalyst is higher than that on NiMg/Al catalyst, CO₂ conversion shows an inverted pattern. This is related to the high basicity of the catalyst promoted by MgO. The best activity of Ni/SBA catalyst could be explained by higher surface area for dispersing a bigger number of active sites and good reducibility.

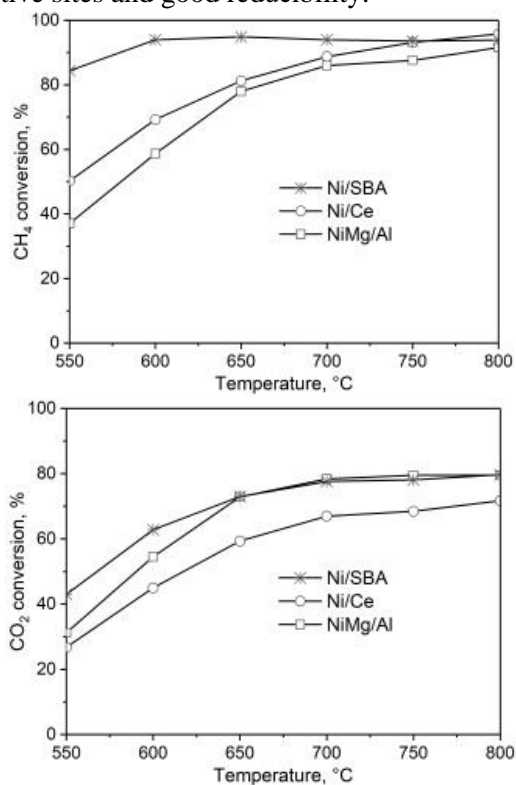


Figure 2. The conversion of a) CH₄ and b) CO₂ in DRM over NiMg/Al, Ni/Ce, Ni/SBA catalysts.

The kinetics of dry reforming of methane

The results showed that there was no effect of internal diffusion when particle size of catalyst is less than 0.75 mm. Moreover, the external diffusion did not affect the reaction when total gas flow was changed from 6 to 36 L.h⁻¹.

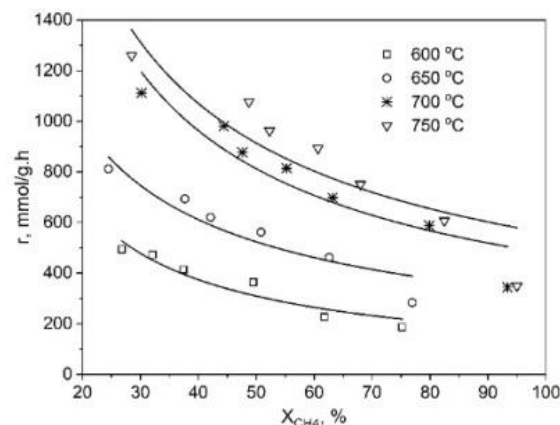


Figure 3. Variation of reaction rate (*r*) with methane conversion extent (*X*) at different reaction temperatures on Ni/SBA catalyst.

The plot of reaction rate (*r*) versus methane conversion extent (*X*) (Fig. 3) on three catalysts is in concave curve shape, implying that the reaction rate is inhibited at least by one of the products [9].

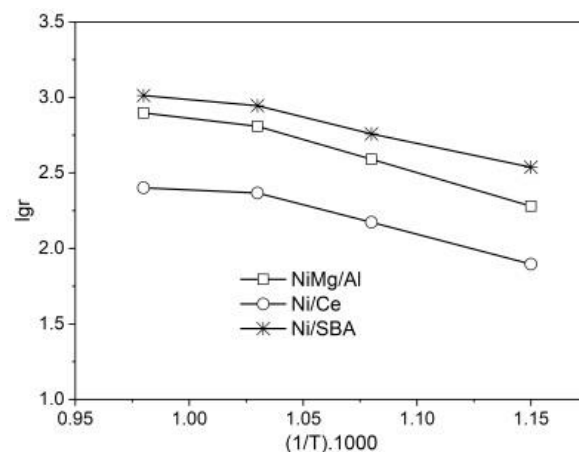


Figure 4. The dependence of logarithm of reaction rate (*lgr*) on ($1/T$) over NiMg/Al, Ni/Ce and Ni/SBA catalysts.

The temperature dependence of the rate of DRM in the Arrhenius coordinates (*lgr*– $1/T$) at a constant composition of the reaction mixture (Fig.4) was nonlinear, indicating a fractional rational rather than exponential form of the rate equation.

The partial pressure of CH₄ and CO₂ entered both the numerator and the denominator of the kinetic equation due to concave form of plot $r-P_{CH_4}$ and $r-P_{CO_2}$.

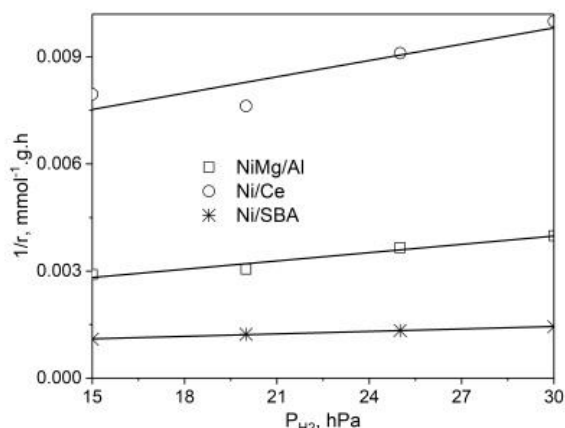


Figure 5. Variation of reversed values of reaction rate ($1/r$) with partial pressure of hydrogen (P_{H_2}) on the catalyst.

The dependence of reversed values of reaction rate ($1/r$) vs partial pressure of hydrogen (P_{H_2}) (Fig. 5) and carbon oxide (P_{CO}) (not shown) is nearly linear, that means, P_{H_2} and P_{CO} must appear in the denominator of the kinetic equation in power may be unit.

From the experimental data, it follows that, the rate of DRM on NiMg/Al and Ni/Ce catalysts is described by equation (1) and on Ni/SBA catalyst is presented in equation (2).

$$r = \frac{k P_{CH_4} \cdot P_{CO_2} \gamma}{(1 + k_1 \cdot P_{CH_4} + k_4 P_{H_2})(1 + k_2 \cdot P_{CO_2} + k_3 P_{CO})} \quad (1)$$

$$r = \frac{k P_{CH_4} \cdot P_{CO_2} \gamma}{(1 + k_1 \cdot P_{CH_4} + k_3 \cdot P_{CO} + k_4 P_{H_2})(1 + k_2 \cdot P_{CO_2})} \quad (2)$$

$$\text{Where: } \gamma = 1 - \frac{P_{CO}^2 \cdot P_{H_2}^2}{K_{Eq} \cdot P_{CH_4} \cdot P_{CO_2}} \quad (3)$$

The values of the kinetic constants in the equation (1) and (2) have been indicated in Table 2.

Table 2. Constants of Eqs. (2), (3) and the root-mean-square deviations (Δ) of calculated reaction rates from experimental values

Kinetic constants	Catalysts		
	NiMg/Al	Ni/Ce	Ni/SBA
$k, \text{mmol.g}^{-1} \cdot \text{h}^{-1} \cdot \text{hPa}^{-2}$	$1.38 \times 10^2 e^{-\frac{28000}{RT}}$	$3.82 \times 10^2 e^{-\frac{2550}{RT}}$	$5.79 \times 10^8 e^{-\frac{1180}{RT}}$
k_1, hPa^{-1}	$1.16 \times 10^{-7} e^{\frac{25800}{RT}}$	$1.72 \times 10^{-3} e^{\frac{3970}{RT}}$	$1.12 \times 10^{-3} e^{\frac{21500}{RT}}$
k_3, hPa^{-1}	0	0	$6.30 e^{\frac{1010}{RT}}$
k_4, hPa^{-1}	$4.22 \times 10^{-7} e^{\frac{16300}{RT}}$	$1.19 \times 10^{-5} e^{\frac{5070}{RT}}$	$4.28 \times 10^{-6} e^{\frac{3630}{RT}}$
k'_2, hPa^{-1}	$7.28 \times 10^{-2} e^{\frac{3530}{RT}}$	$2.79 \times 10^{-3} e^{\frac{15100}{RT}}$	$4.39 \times 10^3 e^{\frac{449}{RT}}$

k'_3, hPa^{-1}	$1.39 \times 10^{-4} e^{\frac{5800}{RT}}$	$5.10 \times 10^{-5} e^{\frac{3180}{RT}}$	$7.28 \times 10^{-2} e^{\frac{3530}{RT}}$
$\Delta, \%$	28.8	19.6	25.2

From the kinetic equations (2) and (3), it is shown that the reaction followed the Langmuir – Hinshelwood mechanism. The inhibition of raw materials was stronger than that of products. The reaction takes place in the medium coverage area as $\alpha = 0.5$. The order of the apparent rate constant (k) coincides with the order of the adsorption constants of H_2 (k_1) and CO_2 (k'_2): NiMg/Al \ll Ni/Ce $<$ Ni/SBA, indicating that to have a high activity, the catalyst needs a high adsorption affinity with both feed substances. The value of the activation energy (E) is in the opposite order, showing that, by using different carriers, the reaction activation energy can be changed, and that changed the reaction rate.

CONCLUSION

Possessing specific physico-chemical properties NiO catalyst on various supports owned a difference in their catalytic activity and kinetic characteristics. Over three catalysts the general kinetic equation for DRM, following the Langmuir–Hinshelwood mechanism, has been found. In which both CH_4 and CO_2 participate the reaction in form of adsorbed molecules. The adsorption and inhibiting reaction of products is weaker than the raw material. The activation energy of the DRM reaction can be reduced by using new carriers such as CeO_2 and SBA-15, thereby greatly increasing the activity of the NiO catalyst. The highest activity was observed on the catalyst 40 wt.%/SBA-15 thank to its high surface arear, high reductivity and high adsorption ability.

References

- [1] J. Guo, H. Lou, H. Zhao, D. Chai, and X. Zheng, "Dry reforming of methane over nickel catalysts supported on magnesium aluminate spinels," Applied Catalysis A: General, vol. **273**, pp. 75-82, 2004.
- [2] K.-W. J. C. s. f. A. Hyun-Seog Roh, "Carbon dioxide reforming of methane over Ni catalysts supported on Al_2O_3 modified with La_2O_3 , MgO , and CaO ," vol. **12**, pp. 239-252, 2008.
- [3] N. D. Charisiou, G. Siakavelas, K. N. Papageridis, A. Baklavaridis, L. Tzounis, D. G. Avraam, et al., "Syngas production via the biogas dry reforming reaction over

- nickel supported on modified with CeO₂ and/or La₂O₃ alumina catalysts," Journal of Natural Gas Science and Engineering, vol. 31, pp. 164-183, 2016/04/01/ 2016.*
- [4] A. Erdohelyi, J. Cserényi, and F. J. J. o. C. Solymosi, "Activation of CH₄ and its reaction with CO₂ over supported Rh catalysts," vol. 141, pp. 287-299, 1993.
- [5] Y. Li, Y. Wang, X. Zhang, and Z. J. I. J. o. H. E. Mi, "Thermodynamic analysis of autothermal steam and CO₂ reforming of methane," vol. 33, pp. 2507-2514, 2008.
- [6] L. C. Loc, P. H. Phuong, D. Putthea, N. Tri, N. T. T. Van, and H. T. Cuong, "Effect of CeO₂ morphology on performance of NiO/CeO₂ catalyst in combined steam and CO₂ reforming of CH₄," International Journal of Nanotechnology, vol. 15, pp. 968-982, 2018.
- [7] P. H. Phuong, L. C. Loc, H. T. Cuong, and N. Tri, "Effect of NiO Loading and Thermal Treatment Duration on Performance of Ni/SBA-15 Catalyst in Combined Steam and CO₂ Reforming of CH₄," Materials transactions, vol. 59, pp. 1898-1902, 2018.
- [8] H. Setiabudi, K. Lim, N. Ainirazali, S. Chin, and N. J. J. o. M. Kamarudin, "CO₂ reforming of CH₄ over Ni/SBA-15: Influence of Ni loading on the metal-support interaction and catalytic activity," vol. 8, pp. 573-581, 2017.
- [9] S. L. Kiperman, *Basis of kinetics in heterogeneous catalysis.* Chemistry, Moscow (in Russian), 1979.

STUDY AND SYNTHESIS OF Fe₃O₄@POLY(GLYCIDYL METHACRYLATE) NANOCOMPOSITE MATERIALS APPLIED FOR REMOVAL OF Pb (II) IONS FROM AQUEOUS SYSTEMS

NT Hoang^{1,2}, DLM Phuong^{2,5}, NLH Phuong³, LH Phuc¹, LK Vinh¹, NQ Hien¹, NM Tuan⁴

¹ Ho Chi Minh City Institute of Physics, Vietnam Academy of Science and Technology,
1 Mac Dinh Chi Street, Ben Nghe Ward, District 1, Ho Chi Minh City, Vietnam.

² Graduate University of Science and Technology, Vietnam Academy of Science and Technology,
18 Hoang Quoc Viet Street, Cau Giay District, Hanoi City, Vietnam.

³ Tay Do University, 68 Tran Chien Street, Le Binh Ward, Cai Rang District, Can Tho City, Vietnam.

⁴ Institute of Applied Materials Science, Vietnam Academy of Science and Technology, 01A Street TL29,
Thanh Loc Ward, District 12, Ho Chi Minh City, Vietnam.

⁵ Tan Phu Trung Junior High School, 4 Street 77, Cu Chi District, Ho Chi Minh City, Vietnam.

Email: nthoang@hcmip.vast.vn

ABSTRACT

These day, environmental pollution in general and water pollution in particular are becoming more serious than before. Heavy metal ions in wastewater from various industries such as electroplating, tanning, weaving, processing steel and coating... When discharged into the environment and infiltrating into domestic water sources will greatly affect to the living body in general and human health in particular. Lead ion (Pb²⁺) is one of them, their toxicity is not acute, but they are very common in the water and their concentration must be limited. Clinical medicine proves Lead is one of the trace elements that accumulates in brain and bone by the time, which is difficult to be eliminated from the human body. New materials based on magnetic materials for water treatment, which are not only focused on research but also widely apply in practice. In this paper, we will report on the characteristic properties and adsorption capacity lead ions of Fe₃O₄@Poly(glycidyl methacrylate) nanocomposite material. Analytical methods such as XRD, FTIR, SEM ... have been used and the Langmuir adsorption isotherm model has been considered.

Keywords: SPION, hydrogel, nanocomposite, water treatment, Pb(II) ions.

INTRODUCTION

Water is a necessary condition of life, the explosion of human population has led to narrowing of surface water and increasing water pollution. In addition, negative effects from urbanization and industrialization have led to increasingly serious pollution of water, amount of wastewater from factories is not thoroughly treated. Therefore, the content of heavy metals is still abundant, which are metals with a density of > 5 mg/cm³, a group of highly toxic heavy metals such as Mercury (Hg), Chromium (Cr), Lead (Pb), Cadimi (Cd), Arsenic (As), Manganese (Mn), Cobalt (Co)... they are not toxic in free-form elements but very toxic in ionic form. The accumulation of these metal ions in the body will disrupt the synthesis of hemoglobin, vitamin D metabolism, kidney dysfunction, spinal cord destruction and cancer.

Lead ion is a cause of lung cancer, stomach and glioma. Besides, lead poisoning can cause

infertility or miscarriage... The U.S EPA (United States Environmental Protection Agency) set the maximum lead concentration allowed in public drinking water at 15 µg/l. Therefore, the removal of lead ion (Pb²⁺) from water sources living, especially drinking water is an urgent issue to protect health of human.

Using nanocomposite materials with magnetic nanomaterials Fe₃O₄ (for separating and recycling heavy metal ions after adsorption) and background materials are biodegradable polymers (safe for organisms), which is solution we think be reasonable at the present time.

EXPERIMENTAL

1. Materials and characterizations

Materials

Monomer Glycidyl methacrylate (GMA) (2,3 Epoxypropyl), 2,2' Azobis-isobutyronitrile (AIBN), poly-vinyl pyrrolidone (PVP), Iron (III) chloride hexahydrate (FeCl₃. 6H₂O), Iron (II)

chloride tetra hydrate ($\text{FeCl}_2 \cdot 4\text{H}_2\text{O}$), ammonium hydroxide (25%) (NH_4OH), Deionized water and ethanol.

Characterizations

X-ray diffraction (XRD) diagram of patterns were measured by a D8 Advance –Bruker (Germany) diffractometer, using ($\text{Cu K}\alpha$ radiation with $\lambda=1.5406 \text{ \AA}$) in the 2θ range from 20 to 70 degrees at room temperature, due to confirm component phase of materials.

Scanning Electron Microscopy (SEM, JSM-5500) was used to survey the surface morphology of microspheres at voltage of 15 kV . The average size (E_D) and root mean square deviation (C_v) for size distribution were determined by evaluation of the SEM image:

$$D = \frac{\sum n_i d_i}{\sum n_i} \quad ; \quad C_v = \frac{\left(\frac{\sum (d_i - D)^2}{\sum n_i} \right)^{1/2}}{D} \times 100$$

Where d_i was microsphere size; n_i was the number of micro-spheres with size of d_i .

Fourier transform infrared spectroscopy (FTIR) were recorded on a Bruker-Model IFS 28 spectrometer at room temperature. The samples were thoroughly milled with KBr and pressed into pellets.

Magnetic hysteresis loop shows detailed parameters about the magnetic properties of materials by using vibrating sample magnetometry (VSM) (MicroSense USA-Model 029349-A01 6MM) at room temperature.

Pb (II) ions absorption capacity of the material is determined by the atomic absorption spectra (AAS) on Perkin Elmer 3300 system at $\text{pH} \sim 5.5$ and room temperature, maximum adsorption concentration is calculated from the Langmuir isotherm equation:

$$\frac{C_e}{q_e} = \frac{C_e}{q_{max}} + \frac{1}{q_{max} \cdot b}$$

Where q_e is the equilibrium adsorption capacity (mg/g).

C_e is the equilibrium concentration of lead ion in solution (mg/l).

q_{max} (mg/g) is the maximum Langmuir monolayer adsorption capacity.

b is the Langmuir equilibrium constant.

2. Preparation of multifunctional microspheres

Overview diagram of the experimental is shown in *Figure 1*.



Figure 1. Overview diagram of the experimental.

Polymerization of monodisperse poly (glycidyl methacrylate) microspheres (PGMA):

3g PVP, 152.7 (ml) ethanol and 13.5ml H_2O was given into the reaction flask and stir, giving 11.2 ml monomer glycidyl methacrylate (GMA) and 0.24 (g) AIBN were added into the flask. Nitrogen gas (N_2) was bubbled through the solution to remove oxygen from the system during 16 hour at 70°C and then by cooling. Begin stirring, we obtained a colorless solution. After one hour, that solution was transferred to white colour. Then, the sample was washed several times by ethanol and DI water. At the end, the sample was dried, we obtained PGMA sample.

Synthesis and functionalized poly(glycidyl methacrylate) microspheres with super paramagnetic iron oxide nanoparticles (M-PGMA):

dried PGMA was dispersed into DI water and cooled down to 10°C . $\text{FeCl}_3 \cdot 6\text{H}_2\text{O}$ and $\text{FeCl}_2 \cdot 4\text{H}_2\text{O}$ was dissolved in 40 ml of water and cooled down to 10°C - fabricated super paramagnetic iron oxide nanoparticles (SPION), and then mixed with the latex in a rotating container which was rapidly evacuated down to 10 mmHg. After 20 minutes, ammonia solution (25%) was added by suction. The reaction continued for 30 minute at 80°C , the mixture was cooled and the particles were swashed several times with water to remove excessive ammonia. The particles were then dried by lyophilization.

RESULTS AND DISCUSSION

X-ray diffraction (XRD) spectra was used to analyze the crystalline characteristic information of the super paramagnetic nanoparticles Fe_3O_4 . *Figure 2* shows the XRD pattern of samples fabricated under the same experimental conditions- pure Fe_3O_4 nanoparticles and Fe_3O_4 coated with PGMA polymer (M-PGMA). The position of the diffraction peaks at the lattice planes (2 2 0), (3 1 1), (4 0 0) and (4 4 0) on the XRD spectrum is tied to the standard spectrum of pure Fe_3O_4 material.

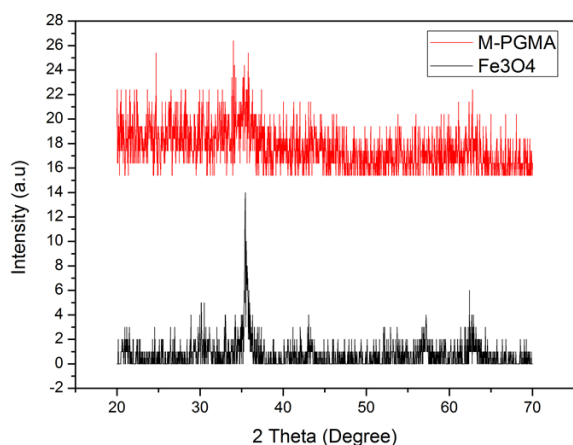


Figure 2. XRD pattern of the Fe_3O_4 nanoparticles and $Fe_3O_4@Poly(glycidyl methacrylate)$.

SEM images of PGMA microspheres (a_1 and a_2) and M-PGMA microspheres (b_1 and b_2) at different scales is shown in Figure 3. It was found that particles of PGMA are spherical and have smooth surface. The beads of M-PGMA are spherical but the surfaces seem not so smooth, because the swollen reagent chloroform changes the morphology of microspheres and some nanoparticle Fe_3O_4 were conglomerated into the surfaces of microspheres.

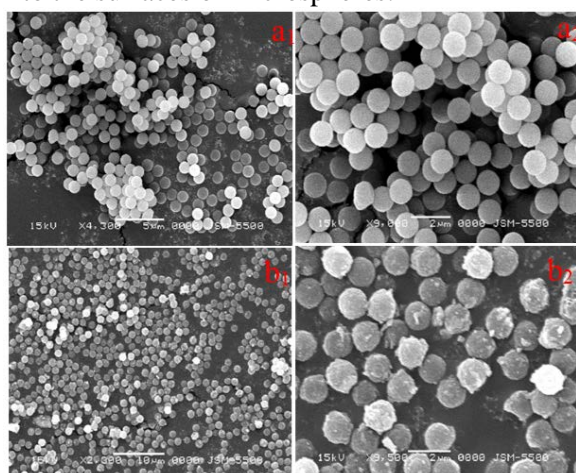


Figure 3. SEM images of (a_1 and a_2) PGMA, (b_1 and b_2) M-PGMA.

The average sizes of microspheres are shown in Table 1

Table 1: The average size and size distribution of microspheres PGMA and M-PGMA

	PGMA	M-PGMA
Size (μm)	1.17	1.39
C_v (%)	0.65	0.71

The FTIR spectra of the two samples, (a).PGMA, (b).M-PGMA are shown in Figure 4.

The absorption peak at nearly identical position such as the band at 3001 cm^{-1} , 2944 cm^{-1} , 2943 cm^{-1} corresponds to C-H bending, absorption peak at wave number 1730 cm^{-1} , 1724 cm^{-1} , 1722 cm^{-1} , 1723 cm^{-1} corresponds to C=O and characteristic of carbonyl group, the band at around 1486 cm^{-1} , 1454 cm^{-1} were assigned to aliphatic O-H stretching. The samples M-PGMA appear a band at 592 cm^{-1} was assigned to the vibration of the Fe-O bond of the iron oxide.

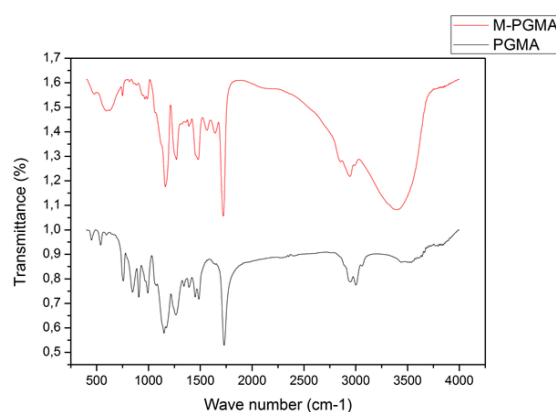


Figure 4. FTIR spectrum of PGMA and M-PGMA.

The magnetic properties of Fe_3O_4 nanoparticles and M-PGMA microspheres was analyzed with VSM as shown in Figure 5.

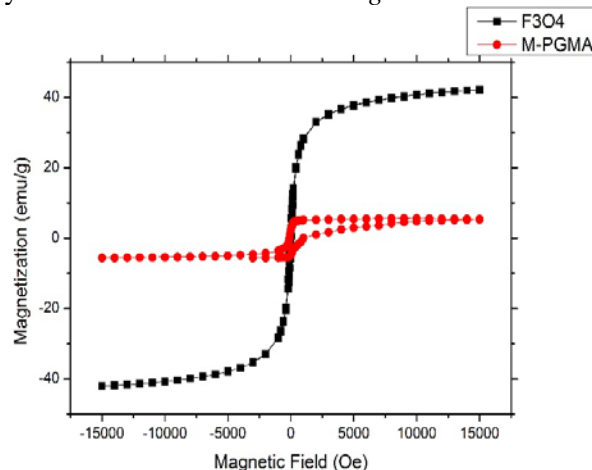


Figure 5. Hysteresis loop of Fe_3O_4 nanoparticles and M-PGMA microspheres.

The saturation magnetization value of superparamagnetic microspheres M-PGMA was 5.6 (emu/g) and Fe_3O_4 nanoparticle was $42,16\text{ (emu/g)}$ at the room temperature. S-like curves, the magnetic hysteresis curve of Fe_3O_4 nanoparticles show which have super paramagnetic properties. The saturation

magnetization of M-PGMA material compared to Fe_3O_4 nanoparticle being significantly reduced, caused by influence of polymer coating on magnetic properties of materials. In addition, the hysteresis loop of M-PGMA material has a small delay, reason is Fe_3O_4 nanoparticles being fixed by the polymer matrix.

Survey results show that the time to reach adsorption equilibrium is about 120 minutes. The maximum adsorption capacity at 30°C. The linear form of the Langmuir equation is shown in Figure 6.

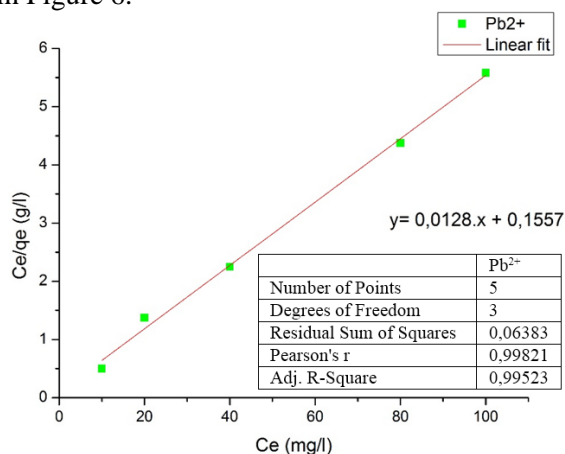


Figure 6. The Langmuir adsorption isotherm linear of M-PGMA for lead ion (Pb^{2+}).

From Figure 6, we can see that the Langmuir isothermal adsorption model describes quite precisely the Pb^{2+} ion adsorption of M-PGMA ($R^2 = 0.99523$). Maximum adsorption capacity q_{max} of M-PGMA for Pb^{2+} ions, it is 78.2 mg/g and the constant $b = 0.0822$ (l/mg).

CONCLUSION

In this paper, we have successfully synthesized $Fe_3O_4@Poly(Glycidyl Methacrylate)$ nano composite material, which is homogeneous dispersion microspheres have 1.39 μm in size with a combination of super paramagnetic properties of super paramagnetic iron oxide nanoparticles Fe_3O_4 (the saturation magnetization value was 5.6 emu/g). Lead ion adsorption capacity in water of the material has been surveyed, applying Langmuir adsorption isotherm model to determine the maximum adsorption capacity q_{max} of $Fe_3O_4@Poly(Glycidyl Methacrylate)$ material is 78.2 mg/g, and Langmuir equilibrium constant b is 0.0822 (l/mg). From the results achieved, we can see that M-PGMA material is capable to removing lead ions (Pb^{2+}) in water treatment applications.

Acknowledgment

This work is completely supported by Ho Chi Minh City institute of Physics - Vietnam Academy Science and Technology (VAST) for basic scientific research at 2019 year.

References

- [1]. Thanh Luu Pham, Kazuya Shimizu, Thanh Son Dao and Utsumi Motoo, *First report on free and covalently bound microcystins in fish and bivalves from vietnam: assessment of risk to human*, SETAC press, vol 9999, No 9999, pp 1-5 (2017).
- [2]. Gutha Yuvaraja, Yixiong Pang, Di-Yun Chen, Ling JunKong, Sajid Mehmood, Munagapati Venkata Subbaiah, Devineni SubbaRao, Chandra Mouli Pavuluri, Jet-ChauWen, Guda Mallikarjuna Reddy, *Modification of chitosan macromolecule and its mechanism for the removal of Pb(II) ions from aqueous environment*, International Journal of Biological Macromolecules (Elsevier), Volume 136, 1 September 2019, Pages 177-188.
- [3]. Shengxiao Zhang, Yuanyuan Zhang Junshen, Liu Qiang, Xu Huaqing, Xiao Xinyu, Wang Hui, Xu Jing Zhou, *Thiol modified $Fe_3O_4@SiO_2$ as a robust, high effective, and recycling magnetic sorbent for mercury removal*, ScienceDirect (Elsivier), (2012).
- [4]. ZhennanShi, ChenXu, PengLuLu, FanYana, LiuYingxi, WangLiLiu, LingLi, *Preparation and the adsorption ability of thiolated magnetic core-shell $Fe_3O_4@SiO_2@C-SH$ for removing Hg^{2+} in water solution*, ScienceDircet, (2018).
- [5]. Débora P. Facchi, André L. Cazetta, Edmilson A. Canesin, Vitor C. Almeida, Elton G. Bonafé, Matt J. Kipper, Alessandro F. Martins, *New magnetic chitosan/alginate/ $Fe_3O_4@SiO_2$ hydrogel composites applied for removal of Pb(II) ions from aqueous systems*, Chemical Engineering Journal (Elsivier) 337 (2018) 595–608.
- [6]. JiahongWang, ShourongZheng, YunShao, JingliangLiu, ZhaoyiXu, DongqiangZhu, *Amino-functionalized $Fe_3O_4@SiO_2$ core-shell magnetic nanomaterial as a novel adsorbent for aqueous heavy metals removal*, ScienceDirect (Elssivier) (2010).

SYNTHESIS OF VARIOUS FUNCTIONAL LUMINESCENT NANOPARTICLES BASED ON ZINC

Thanh Thao Bui¹, Van Khiem Nguyen², Duy Khanh Pham², Ngoc Tinh Cao¹, Thanh Mien Nguyen³, Jin-Woo Oh³, Bich Thi Luong^{2,*}

¹Faculty of Chemical Engineering, Ho Chi Minh City University of Technology, Vietnamese National University - Ho Chi Minh City, Vietnam

²Institute of Applied Materials Science, Viet Nam Academy of Science and Technology, Vietnam

³Department of Nano Fusion Technology, Pusan National University, Busan 46241, Korea

ABSTRACT

ZnSe:X luminescent nanoparticles doped with X such as manganese, copper and silver that emit light were synthesized in aqueous media. Blue and orange emission of as-prepared nanoparticles is a result of doping transition metals. Especially, the various capping agents were applied to control the size of luminescent nanoparticles. In this study, the mercaptopropionic acid (MPA), polyethylene glycol (PEG), Poly vinylalcohol (PVA) and starch were used as capping agents, respectively. Photoluminescence from the obtained nanoparticles was tuned from 450-600 nm by regulating feeding molar ratio [Zn]/[X]. the nanoparticles emit various light with a quantum yield about 35-45%. The sizes of nanoparticles are 20-100 nm and the physical-chemical, structural properties were mentioned.

Keywords: Luminescent nanoparticles, green synthesis, capping agents, aqueous phase synthesis

INTRODUCTION

Colloidal semiconductor nanocrystals (NCs) have attracted great attention in recent years for their unique electrical and optical properties. Interestingly, direct band gap semiconductor NCs are inorganic lumophores that have high quantum efficiencies, color-tunable and narrow emission spectra, and excellent chemical stability [1, 2, 3]. So far, these properties have created many applications for NCs in light-emitting diodes (LEDs), lasers, biological and chemical sensing, and solar cells [4, 5, 6]. Doping with atomic impurities is an efficient way to generate luminescent NCs, due to their strong dopant emission. To date, colloidal NCs have successfully been doped with transition metals (such as Fe, Ni, Mn, Cu) and lanthanides (such as Eu, Er, Tm, Tb) to alter their electronic, optical or magnetic properties [5]. Light emission is independent of the band gap of the host materials and largely immune to the thermal and chemical variations of the surrounding medium [6]. In order for these doped NCs to be luminescent at the colours of the dopant, the excitation energy of the dopant needs to be smaller than the band gap of the host material to enable energy transfer of an exciton in the NC core to the impurity dopant. In this

vein, procedures for doping of high band gap materials, such as zinc selenide or zinc sulfide with manganese (ZnSe:Mn, ZnS:Mn NCs), were developed, which result in visible phosphorescence from the $Mn^{2+} \ ^4T_1 \rightarrow \ ^6A_1$ transition centered at 580 nm[5,10]. Either the various capping agents concentrations can change the PL QYs or the emission colors under UV light (365 nm).

In this paper, we report the synthesis of low toxicity ZnSe:Mn NCs in the aqueous phase is presented using various capping agents such as starch, PVA, PEG AND MPA as a stabilizer at low temperature (80–100 °C).

EXPERIMENTAL

1. Chemicals

Manganese (II) acetate ($Mn(OAc)_2$) ($Mn(CH_3COO)_2 \cdot 4H_2O$, 99.99%), zinc acetate ($Zn(OAc)_2$) ($Zn(CH_3COO)_2 \cdot 2H_2O$, 99.99%) and sodium sulfide (Na_2S), 2-propanol (HPLC grade), 3-mercaptopropionic acid (MPA, 99+%), sodiumborohydride ($NaBH_4$, 96%), selenium powder (99.5%), polyethylene glycol – (PEG 1500), poly vinylalcohol (PVA) and starch. All the chemicals are of analytical grade and purchased from Sigma-Aldrich. Deionized water (DI water) used in all synthesis was high purity grade with a conductivity of 18.2 MΩ cm.

2. Characterization.

Fluorescence measurements were performed using WGY-10 fluorescence spectrophotometer. All optical measurements were carried out at room temperature. The photoluminescence quantum yield (PL QY) of NCs was measured according to the method described in Crosby and Demas [1,2]. PL QYs were determined by comparing the integrated emission of the NCs samples in water with that of fluorescent dye rhodamine 6G (PL QY = 95% in ethanol) with identical optical density (0.05-0.1) at the excitation wavelength. X-ray diffraction measurements were performed on a D/Maxrnt 2000 powder X-ray diffractometer with Cu K α radiation ($\lambda = 1.5418 \text{ \AA}$). The X-ray photoelectron spectra (XPS) were taken on a Thermo Scientific K-alpha electron energy spectrometer using Al K α (1486.6 eV) as the X-ray excitation source (VG Multi-lab ESCA 200 System model). The samples used for XRD, TEM were prepared as follows: the NCs solution was firstly concentrated to one-tenth of the original volume, and then the NCs were precipitated with 2-propanol and collected via centrifugation, finally the colloidal precipitate was dried in a vacuum drying oven. Transmission electron micrographs (TEM) images were acquired using a JEM 2100F transmission microscope with acceleration voltage of 200 kV. TEM samples were prepared by dropping the samples dispersed in water onto carbon coated copper grids with excess solvent evaporated. The average size of NCs was determined using ImageJ software from TEM images.

3. Synthesis

Using Starch, PVA, PEG and MPA, as capping ligand in the preparation of ZnSe or other II-IV semiconductor NCs in the aqueous route due to its preferable binding capacity [1, 2]. NaHSe was produced by reaction between NaBH₄ and Se powder as previous report [2]. An aqueous colloidal ZnSe solution was prepared using the reaction between Zn²⁺ and NaHSe solution following the literature method. The Zn²⁺ precursor solution was prepared by dissolution of 10 ml of zinc acetate 0.1 M in 90 ml of DI water, and 40 ml of capping agents (starch, PVA, PEG, MPA) 0.1 M in three-neck flask, then the pH of this system was adjusted to pH = 6.5 using NaOH 2 M with vigorous stirring. This

three-neck flask was degassed by N₂ bubble in 30 minutes, and the NaHSe solution was injected into the Zn²⁺ precursor solution at room temperature under oxygen-free. The color of the solution changed immediately upon addition of selenide ion solution, indicating the formation ZnSe nanoparticles. The mixture was further stirred to 50-100 °C relating to the capping agent and refluxed for 3 hours for complete ZnSe:Mn crystals growth and age for 24 h followed by filtration. The precipitate was washed several times and dried at room temperature to give a material which readily disperses in water.

RESULTS AND DISCUSSION

1. Photoluminescence (PL)

Fig. 1 shows that the ZnSe:Mn NCs produce light blue-emission at 400–420 nm. Furthermore, Mn²⁺ centered emission at 580–600 nm is increased dramatically from surface passivation as seen in the ZnSe:Mn spectra. The importance of doping Mn in ZnSe shell using different capping agents is that the space effect of agents could affect the size and the amount of Mn²⁺ ions in ZnSe crystals.

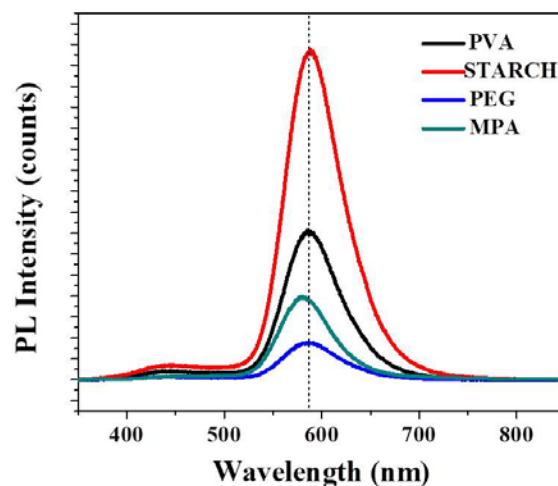


Figure 1. PL spectra of ZnSe:Mn(5%) with various capping agents.

The starch-capped ZnSe:Mn nanoparticles has the highest photoluminescence intensity at 580 nm, the PEG-capped ZnSe:Mn has the lowest PL intensity due to the different capping agents, which prevents the nanoparticles to aggregate and give the various amount Mn²⁺ ions doped into the ZnSe crystals. The higher the doped Mn²⁺ concentration is, the higher the PL intensity is. It is proved that the prevention of aggregation of nanoparticles in the presence of the surfactant is more effective. This capping

agent's molecules bind to the surface of the particle by stabilizing the nuclei and larger nanoparticles against aggregation, hence controlling the growth of nanoparticles. The PEG has the long polymer chains which prevent the entrance of Mn^{2+} ions into the ZnSe crystals. [7-11] The MPA has small molecule, but the nanocrystals may have the high aggregation. So it may cause the low PL intensity. The PLQY of obtained emitting nanoparticles could be 35-45%.

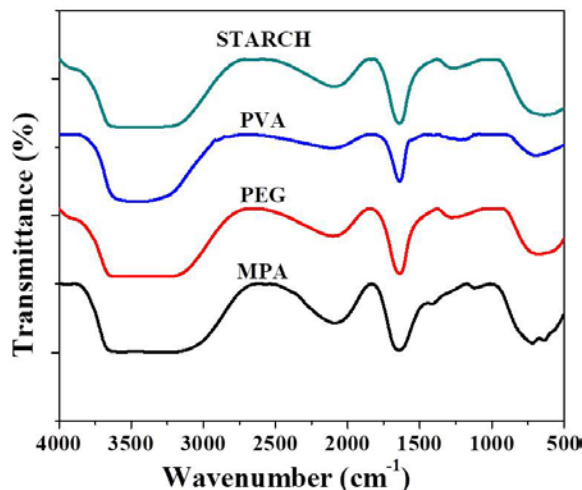


Figure 2. The FT-IR spectra of ZnSe:Mn with various capping agents.

FT-IR spectra confirm the capping of the particles by capping agents (Fig. 2). The strong band at 3298cm^{-1} was attributed to the O-H stretching of starch and it width was ascribed to the formation of inter and intra-molecular hydrogen bond. The band at 2921cm^{-1} was ascribed to the asymmetric stretching of C-H while the band at 1630cm^{-1} was attributed to tightly bound water present in the starch. The two characteristic bands at the fingerprint region of spectra at 1146cm^{-1} and 1075cm^{-1} were attributed to the C-O, C-C stretching and C-O-H bending of starch respectively while the band at 1330 was attributed to the angular deformation of C-H. The prominent band at 992 was attributed to the skeletal mode vibration of α 1-4 glycosidic linkage (C-O-C) while the band at 757 was attributed C-C stretching [8-10].

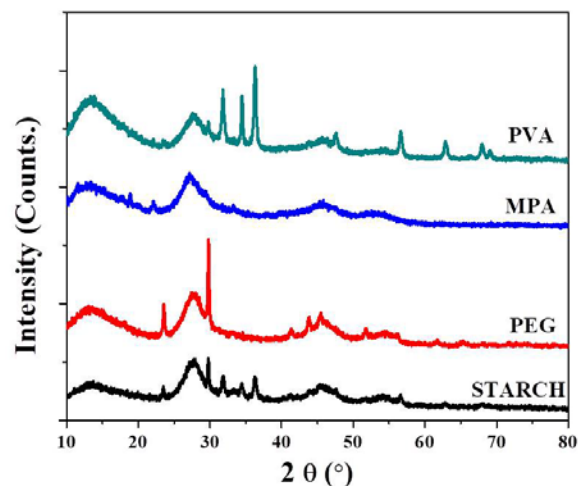


Figure 3. XRD patterns of ZnSe:Mn powders synthesized in various capping agents.

Figure 3 shows the diffraction patterns of ZnSe:Mn synthesized in various capping agents possess zinc-blende crystal structures, due to the display of XRD patterns at the (111), (220) and (311) planes. The MPA-capped ZnSe:Mn nanocrystals has the cubic crystals, while PVA-capped, PEG-capped and starch-capped ZnSe:Mn have wurtzite crystals. This supports the longer polymer chains that ZnSe:Mn can be more easily incorporated in wurtzite ZnSe NCs in cubic crystals [1,2]. In addition, we can conclude that doping Mn^{2+} into the host ZnSe of the shell NCs does not bring about a phase transformation of the crystal structure.

Transmission Electron Microscopy (TEM)

Figure 4 show that the TEM image and particle size distribution of the various capped ZnSe:Mn nanoparticles. This TEM image indicates the monodispersed spherical crystallite. The nanoparticles are clearly well identified and no effective aggregation of bulk particle is formed. The particle range is 20 nm to 100 nm. The MPA-capped ZnSe:Mn and starch-capped ZnSe:Mn nanocrystals have 15-25 nm spheres. However, the PVA-capped, PEG-capped ZnSe:Mn have larger sphere diameters such as 40-100nm. This can be explained according to XRD patterns as well. It could be assessed that the size chains of polymer as a stabilizer causes the number of doped emission ions (Mn^{2+}) and the size of nano crystals [1,9-11].

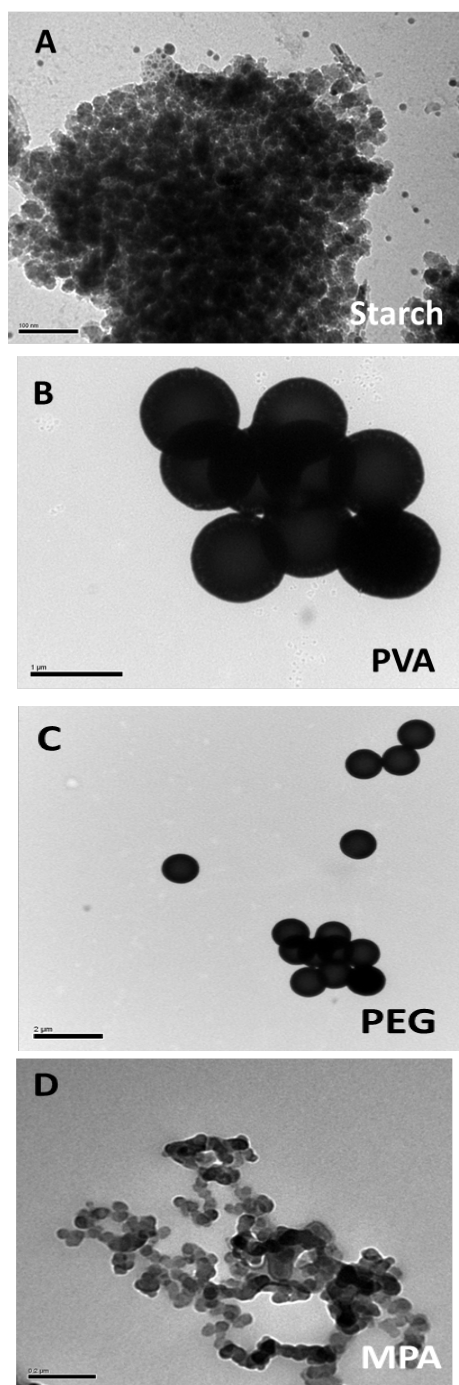


Figure 4. The TEM images of ZnSe:Mn capped with Starch (A), PVA (B), PEG (C) and MPA (D).

CONCLUSION

The present study outlines the synthesis of nanostructured zinc selenide doped Mn²⁺ by hydrothermal method using poly vinylalcohol (PVA), starch, poly ethylene glycol (PEG) and mercaptopropionic acid (MPA) as capping agent. The physico-chemical characterization involved XRD, TEM and PL spectroscopy. The XRD studies showed that the polymer ZnSe

nanoparticles exhibit hexagonal crystal structure. The capping agent modifies the size and the electro-optic properties of ZnSe:Mn the nanoparticles.

The maximum efficiency was observed in the UV light irradiation. This nanoparticles exhibits excellent photo-optonic activity and can be considered as a promising detection for treatment of various bacteria.

Acknowledgment

This research is funded by Vietnam National Foundation for Science and Technology Development (NAFOSTED) under grant number 104.01-2017.6

References

- [1]. Bich. Thi. Luong, Eunsu Hyeong, Sujin Yoon, Jongwan Choi and Nakjoong Kim, Facile synthesis of UV-white light emission ZnSe/ZnS:Mn core/(doped) shell nanocrystals in aqueous phase, RSC Advances, **3** (2013), 23395 – 23401.
- [2]. Bich Thi Luong, Eunsu Hyeong, Seokhwan Ji and Nakjoong Kim, Green synthesis of highly UV-orange emitting ZnSe/ZnS:Mn/ZnS core/shell/shell nanocrystals by a three-step single flask method, RSC Advances, **2** (2012), 12132–12135.
- [3]. Karakoti AS, Shukla R, Shanker R, Singh S. *Surface functionalization of quantum dots for biological applications*. Advances in Colloid and Interface Science, **215** (2015) 28-45.
- [4]. Draaisma GJJ, Reardon D, Schenning APHJ, Meskers SCJ, Bastiaansen CWM, *Ligand exchange as a tool to improve quantum dot miscibility in polymer composite layers used as luminescent downshifting layers for photovoltaic applications*, Journal of Materials Chemistry C, **4** (2016) 5747-5754
- [5]. Yeh P, Yeh N, Lee CH, Ding TJ. *Applications of LEDs in optical sensors and chemical sensing device for detection of biochemicals, heavy metals, and environmental nutrients*. Renewable & Sustainable Energy Reviews, **75** (2017) 461-468.
- [6]. Xuan Truong Mai, Diem Thi Bui, Thanh Thao Bui, Bich Thi Luong, et.al., *Study Of*

Single-Step Synthesis Of Hyperbranched Highly Luminescence Doped ZnSe:Mn, ZnSe:Mn/ZnS Quantum Dots And Their Interactions With Acid Amine, American Journal of Engineering Research (AJER), **7** (2018) 27-32.

- [7]. Ganapaty Alagumuthu, Thangaiya Anantha kumar, *Structural, Optical and Photocatalytic Activity of Polymer Capped Zinc Selenide Nanoparticles*, International Research Journal of Engineering and Technology (IRJET), **3** (2016) 1022 – 2018.
- [8]. K.Senthilkumar, T.Kalaivani, S. Kanagesan, and V.Balasubramanin, *Low temperature method for synthesis of starch-capped ZnSe nanoparticles and its characterization studies*, Journal of Applied Physics, **112** (2012) 114331.
- [9]. Daysi Diaz-Diestra, Juan Beltran-Huarac, Dina P. Bracho-Rincon et.al. *Biocompatible ZnS:Mn quantum dots for reactive oxygen generation and detection in aqueous media*, J. Nanopart Res (2015) 17:461.
- [10]. Abdelhay Aboulaich, Malgorzata Geszke, Lavinia Balan, Jaafar Ghanbaja, Ghouti Medjahdi, Raphaël Schneider, *Water-based route to colloidal Mn-doped ZnSe and core/shell ZnSe/ZnS quantum dots*, Inorg. Chem. **49** (2010) 10940-10948.
- [11]. Sundararajan Parani, Ncediwe Tsolekile, Bambesiwe M.M. May, Kannaiyan Pandian and Oluwatobi S. Oluwafemi, *Mn-Doped ZnSe Quantum Dots as Fluorimetric Mercury Sensor*, Nonmagnetic and Magnetic Quantum Dots (2018) 201-219.

THE EFFECT OF DIFFERENT CONCENTRATIONS OF NITRIC ACID SOLUTION ON THE CHARACTERISTICS OF MWCNTs FUNCTIONALIZED BY A MIXTURE OF HNO₃/ H₂SO₄

Hoa Mai Thi Le, Dam Duy Le, Cuong Kim Thi Phu, Thu Thi Pham and Chien Mau Dang

Institute for Nanotechnology, Vietnam National University-Ho Chi Minh City, Community 6, Linh Trung Ward, Thu Duc District, Ho Chi Minh City, Vietnam;

Email: ltmhoa@vnuhcm.edu.vn

ABSTRACT

In this study, pristine multi-walled carbon nanotubes (p-MWCNTs) are functionalized by wet chemical oxidation methods with a 1:3 mixture of nitric acid and sulfuric acid solutions. The influence of different concentrations of nitric acid solution on the characteristics of MWCNTs are systematical investigated for the first time. Different techniques such as FE-SEM, EDX, Raman and TGA are employed to explore the effect of functionalization on the MWCNTs. The FE-SEM images show that the functionalized MWCNTs are significant improved dispersibility in comparison to p-MWCNTs. EDX measurements indicate that the oxygen content of pristine MWCNTs is 8.27 at%, the percentage increases up to 19.75 at% when MWCNTs is treated with a 1:3 mixture of 4.0M HNO₃/10.0M H₂SO₄ for 20h. Thermal gravimetric analysis demonstrates that the highest weight loss of 30.69% is obtained for the treatment with the 1:3 mixture of 4M HNO₃/ 10M H₂SO₄ for 20h. The oxidation condition of a 1:3 mixture of 4M HNO₃/10M H₂SO₄ demonstrates to be the most effective for functionalization of the MWCNTs with no destruction of the nanotubes

Keywords: Multi-walled carbon nanotubes, wet chemical oxidation, surface functionalization, Raman spectroscopy, thermalgravimetric analysis

INTRODUCTION

Multi-walled carbon nanotubes (MWCNTs) are one of the most promising materials for many applications due to its excellent properties such as unique electrical, mechanical, optical and chemical properties [1,2]. However, dispersion, solubility and processability still limit their applications [3]. To improve dispersion of MWCNTs, wet chemical oxidation is considered as one of the most widely employed methods due to its versatility and efficiency [4,5]. The most common reagents used for oxidation treatment are HNO₃, H₂O₂, H₂SO₄ and KMnO₄ or mixture of them [6,7]. After the oxidation treatment, a variety of functional groups such as carboxylic, carbonyl and hydroxyl groups are formed on the surface of MWCNTs [8].

Oxidation of MWCNTs is considered to be the first step that allows further functionalization by molecular structure or nanoparticles [9]. Therefore, knowledge the influence of the oxidation processes on the nanotubes could allow better controlling the ultimate structure and property of MWCNTs. The main goal of this work is to perform a systematic study of the

influence of different concentrations of nitric acid solution on the properties of multi-walled carbon nanotubes.

EXPERIMENTAL

Materials and chemicals

The pristine multi-walled carbon nanotubes (p-MWCNTs) used in this study have a purity of 95% and outer diameter of 10-40 nm. 65% nitric acid (HNO₃) and 95% sulfuric acid (H₂SO₄) are purchased from Merck, Geman. Distilled water are used as solvent.

Preparation of oxidized MWCNTs

Oxidized MWCNTs (MWCNTs-COOH) is prepared by wet chemical oxidation of p-MWCNTs in a mixture of nitric acid and sulfuric acid solutions. A volume of 20 ml is prepared from a 1:3 mixture of HNO₃ and H₂SO₄. 100 mg of p-MWCNTs is added in the mixture of acids and sonicated at room temperature for 1h, followed by magnetic stirring for 20h at 80°C. The MWCNTs in the acid solution is then repeated several times of dilution with distilled water and filtration until the pH ~ 6. The oxidized MWCNTs are collected and dried at 70°C for

24h. To investigate the effects of different concentrations of nitric acid solution on the nanotubes, we have carried out the functionalization of MWCNTs with different concentrations of 4M, 7M and 14M. The details of these prepared samples and their codes are given in Table 1.

Table 1. Oxidative treatments conducted on the MWCNTs

Samples	Oxidation conditions
S0	No treatment (pristine MWCNTs)
S1	14M HNO ₃ , 80°C, 20h
S-4M	4M HNO ₃ / 10M H ₂ SO ₄ , 80°C, 20h
S-7M	7M HNO ₃ / 10M H ₂ SO ₄ , 80°C, 20h
S-14M	14M HNO ₃ / 10M H ₂ SO ₄ , 80°C, 20h

Characterization techniques.

The surface morphology of nanotubes is observed by Field Emission Scanning Electron Microscope (Hitachi FE-SEM SU8010) using secondary electron and backscattering modes with an accelerating voltage of 10 kV. Energy dispersive X-Ray (EDX) spectrometer attached to the FE-SEM is employed to determine the elemental compositions in the MWCNTs. Thermal Gravimetric Analysis (TGA) is carried out on a TGA/ EVO2G-TG instrument at a heating rate of 10°C/ min in air to determine the contents of functional groups and thermal stability of nanotubes. Raman spectra is recorded by a Jobin Yvon LabRaman Instrument at a He-Ne laser of wavelength at 632.8 nm.

RESULTS AND DISCUSSION

Fig. 1 illustrates the FE-SEM images of the pristine MWCNTs (S0) and functionalized MWCNTs: S1, S-4M, S-7M, S-14M. We use FE-SEM images to compare the dispersion behavior of p-MWCNTs and oxidized MWCNTs. As shown in figure 1(a), the p-MWCNTs tend to agglomerate and are poorly dispersed because of strong interaction between MWCNTs. In addition, the p-MWCNTs contain amorphous carbon. We can see that the sidewall of oxidized MWCNTs (Fig. 1(b-e)) can be observed more clearly due to the removal of the amorphous carbon after acid treatment. As observed in figure 1(b-e), every individual MWCNTs are hollow and tubular in shape and oxidized MWCNTs exhibits the best dispersion. With regard to sample S-14M, there is cutting on the nanotubes

under the oxidation treatment with a 1:3 mixture of 14M HNO₃/10M H₂SO₄ for 20 h.

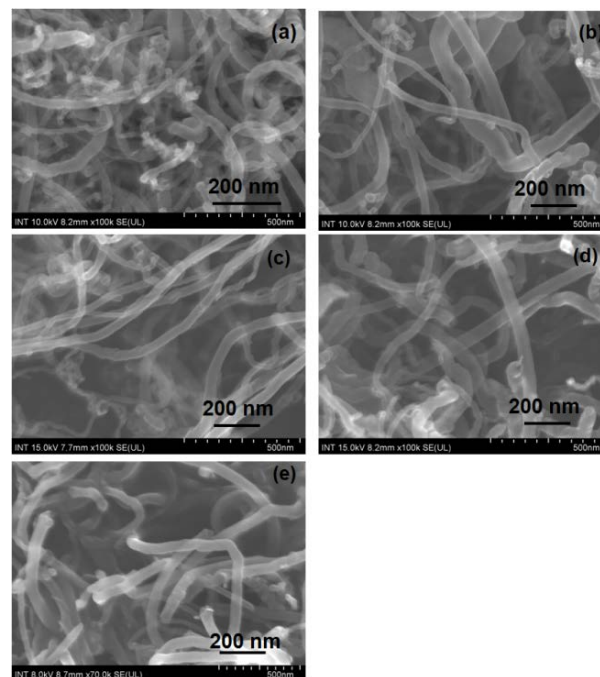


Figure 1. FE-SEM images of (a) pristine MWCNTs (S0) and oxidized MWCNTs: (b) S1, (c) S-4M, (d) S-7M and (e) S-14M.

Energy dispersive X-Ray analysis (EDX) analysis is conducted on several zones of the MWCNTs samples in order to identify the elements present on the surface as shown in figure 2. The elemental composition reported in table 2 shows the atomic percentage (at %). As seen in table 2, the carbon and oxygen are detected in all the samples [7]. EDX analysis also exhibits the presence of a small amount of Al (0.38 at %) in the p-MWCNTs. As seen in figure 2(c, d, e), Al is removed after acid treatment, carbon is the major element, followed by oxygen and with a small content of sulfur [7]. In this work, the oxygen content is of particular interest. According to EDX results in table 2, the oxygen content of S0, S1, S-4M, S-7M and S-14M samples is determined to be 8.27, 12.16, 19.75, 18.23 and 18.85 at%, respectively. It is interesting to notice that the oxygen content increases after chemical oxidation treatment. Particularly, the oxygen contents of the MWCNTs samples treated with a mixture of HNO₃/ H₂SO₄ are much higher in comparison to the samples treated with HNO₃. In addition, the sulfur content in the samples S-4M, S-7M, S-14M is determined to be 0.56, 1.59 and 0.45 at%, respectively.

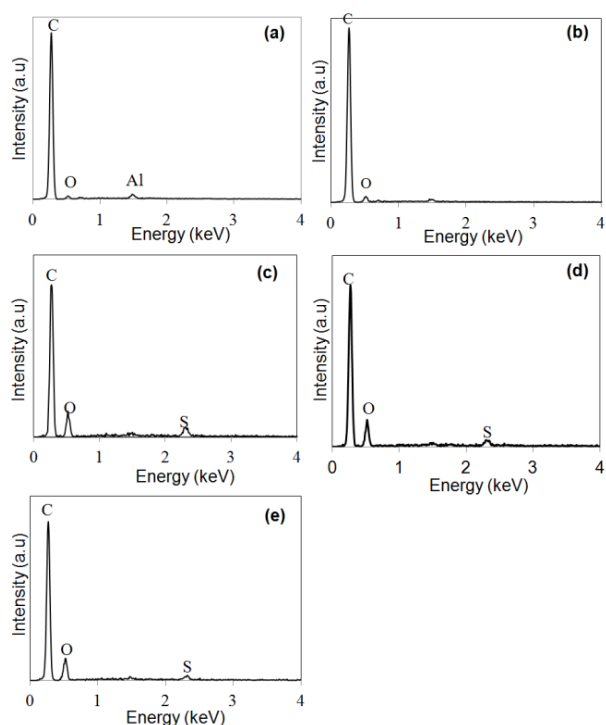


Figure 2. EDX spectra of (a) pristine MWCNTs (S0) and oxidized MWCNTs: (b) S1, (c) S-4M, (d) S-7M and (e) S-14M.

Table 2. Chemical compositions of pristine and oxidized MWCNTs

Samples	Elemental compositions (at%)			
	C	O	Al	S
S0	91.56	8.27	0.18	-
S1	87.83	12.16	-	-
S-4M	79.69	19.75	-	0.56
S-7M	80.18	18.23	-	1.59
S-14M	80.61	18.85	-	0.45

The structure differences between p-MWNTs and oxidized samples are characterized by Raman spectroscopy as indicated in Figure 3. As can be observed in Fig. 3, there are two characteristic peaks in all spectra [5,6,9]. The D band is identified at 1323, 1334, 1338, 1335 and 1341 cm^{-1} for samples S0, S1, S-4M, S-7M and S-14M, respectively. The G band is located at 1579, 1583, 1590, 1587 and 1592 cm^{-1} for samples S0, S1, S-4M, S-7M, S-14M, respectively. It can be seen that the position of the D and G band is shifted to higher wave numbers for oxidized MWCNTs compared to the pristine MWCNT [7-9]. The ratio between the intensity of the D and G bands, noted I_D/I_G , has been calculated for the different samples from the Raman data, and the values are listed in Table 3. The I_D/I_G ratios of the samples S1, S-4M, S-7M

and S-14M corresponding to 1.22, 1.26, 1.24 and 1.37 are slightly increased in comparison to the S0 sample (1.15), indicating the attachment of the carboxylic acid groups [7-9].

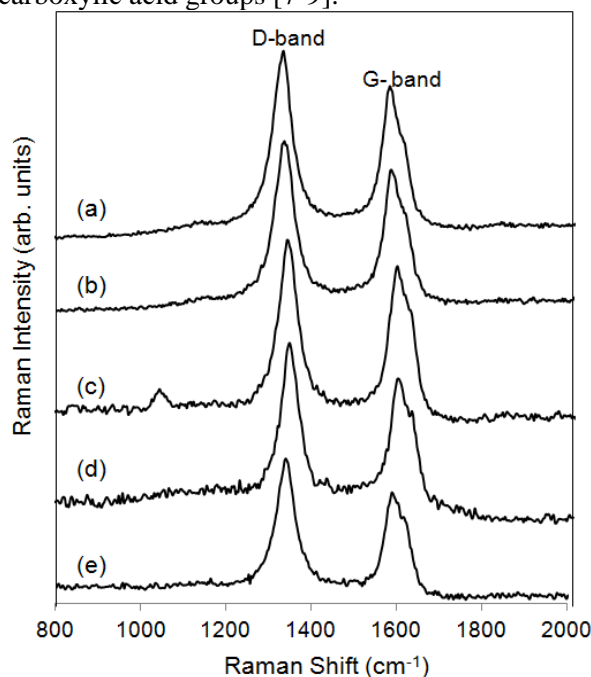


Figure 3. Raman spectra of (a) pristine MWCNT and oxidized MWCNTs: (b) S1, (c) S-4M, (d) S-7M and (e) S-14M.

Table 3. D and G-bands, I_D/I_G ratios for the pristine (S0) and oxidized MWCNTs (S1, S-4M, S-7M and S-14M)

Samples	D band (cm^{-1})	G band (cm^{-1})	I_D/I_G ratios
S0	1323	1579	1.15
S1	1334	1583	1.22
S-4M	1338	1590	1.26
S-7M	1335	1587	1.24
S-14M	1341	1592	1.37

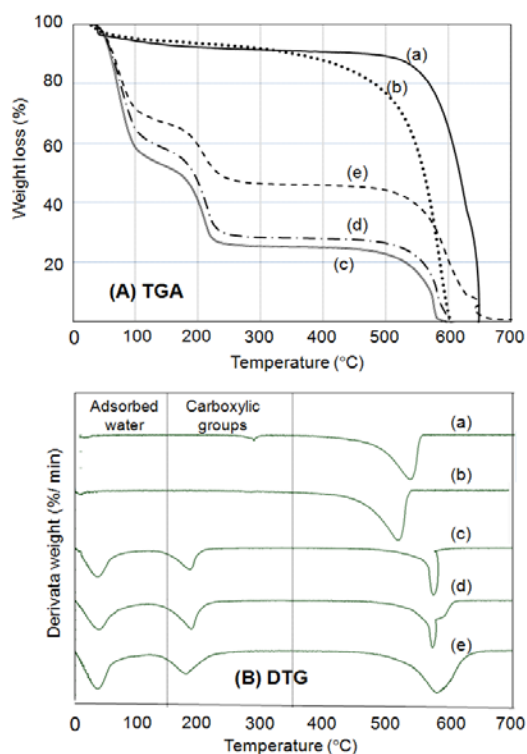


Figure 4. TGA (A) and DTG analysis (B) of the MWCNT samples: (a) S0, (b) S1, (c) S-4M, (d) S-7M and (e) S-14M.

The thermal stability of the surface functional groups of the MWCNTs is investigated by TGA. Fig. 4(A) presents the TGA curves of different MWCNT samples. The derivative weight (DTG) curve associated to the TGA analyses is given in Fig. 4(B). It can be seen in Fig. 4(A) that the thermal degradation of oxidized MWCNTs occurs through a multistep process. The first stage, up to a temperature of 150°C, a weight loss corresponds to the evaporation of adsorbed water [4,7]. In the second stage, the weight loss in a temperature range of 150°C-350°C for oxidized samples S1, S-4M, S-7M, S-14M are measured to be 8.2, 30.6, 27.9 and 21.1 wt%, respectively. It is attributed to the decomposition of the carboxylic groups introduced onto the surface of MWCNTs [4-7]. It can be seen that the weight loss of the sample S1 (~8.20 wt%) is less than that of the other oxidized samples. It should be attributed to the less of carboxylic groups of sample S1 as compared to S-4M, S-7M and S-14M. From the DTG curves in Fig. 4(B), the decomposition of functional groups for the samples S-4M, S-7M and S-14M is found to be at 218, 227 and 228°C, respectively.

CONCLUSION

In this work, the MWCNTs are functionalized using mixtures having different solutions of nitric acid and 10M H₂SO₄. The samples are characterized by FE-SEM, Raman spectroscopy, TGA. After chemical oxidation treatment, the oxygen content increased is confirmed by EDX measurements. The thermal stability of the nanotubes is investigated by TGA decomposition. The oxidation condition of a 1:3 mixture of 4M HNO₃/10M H₂SO₄ promotes an increase in the -COOH groups (~ 30.68 wt%) onto the nanotube surface and demonstrates to be the most effective for functionalization of the MWCNTs with no destruction of the nanotubes.

Acknowledgment

This research is funded by Vietnam National University Ho Chi Minh City (VNU-HCM) under grant number B2019-32-01.

References

- [1] A. Pistone, A. Ferlazzo, M. Lanza, C. Milone, D. Iannazzo, A. Piperno, E. Piperopoulos, S. Galvagno, J. Nanosci. Nanotechnol. **12** (2012) 5054-5060
- [2] F. Aviles, J.V. Cauich-Rodriguez, L. Moo-Tah, A. May-Pat, R. Vargas-Coronado, Carbon **47** (2009) 2970-2975,
- [3] Iosif D. Rosca, F. Watari, M. Uo, T. Akasaka, Carbon **43** (2005) 3124-3131
- [4] Kevin A. Wepasnick, Billy A. Smith, Kaitlin E. Schrote, Hannah K. Wilson, Stephen R. Diegelmann, D. H. Fairbrother, Carbon **49** (2011) 24-36
- [5] Tawfik A. Saleh, Appl. Surf. Sci. **257** (2011) 7746-7775
- [6] A. Pistone, A. Ferlazzo, M. Lanza, C. Milone, D. Iannazzo, A. Piperno, E. Piperopoulos, S. Galvagno, J. Nanosci. Nanotechnol. **12** (2012) 5054-5060,
- [7] Le Thi Mai Hoa, Diamond and Related Materials **89** (2018) 43-51
- [8] B. Scheibe, E. Borowiak-Palen, R. J. Kalenczuk, Mater. Charact. **61** (2010) 185-191
- [9] R. Araujo, M. F. Marques, R. Jonas, I. Grafova, A. Grafov, J. Nanosci. Nanotechnol. **16** (2016) 1174-1180

MORPHOLOGY AND OPTICAL PROPERTIES OF $\text{CePO}_4:\text{Tb}^{3+}$ NANOPARTICLES FABRICATED BY CHEMICAL METHOD

Phuong Hau Thi Pham¹, Chinh Dung Trinh^{1,2}, Dung My Thi Dang¹ and Chien Mau Dang¹

¹ Institute for Nanotechnology, Vietnam National University, Ho Chi Minh City

² The University of Science, Vietnam National University, Ho Chi Minh City

Email: pthphuong@vnuhcm.edu.vn

ABSTRACT

$\text{CePO}_4:\text{Tb}^{3+}$ nanocrystals with monoclinic structures were successfully synthesized by hydrothermal method. The result of X-ray diffractions (XRD) showed that all of the diffraction peaks were well indexed to the monoclinic phase of CePO_4 host (JCPDS, No. 32-0199). Morphology of prepared samples was also studied by Field emission scanning electron microscopy (FE-SEM). All nanorods morphology with $\text{CePO}_4:\text{Tb}^{3+}$ sample synthesized at 120°C for 5 hours with molar ratio of PO_4/Ce at 70 and concentration of Terbium doped at 5% Tb^{3+} and pH controlled at 2. The average length of $\text{CePO}_4:\text{Tb}^{3+}$ nanorods was around 80 - 110 nm. Energy dispersive spectroscopy (EDS) provided a measure for the composition of sample. $\text{CePO}_4:\text{Tb}^{3+}$ nanorods was determined by photoluminescence at 278 nm, showed the high intensity of green emission at 543 nm wavelength which was correspond to ${}^5\text{D}_4\text{-}{}^7\text{F}_5$ transition of Tb^{3+} .

INTRODUCTION

In recent years, much interest has been focused on the synthesis and luminescence of nano-sized rare earth orthophosphates for their potential application in optoelectronic devices and biological fluorescence labeling. $\text{CePO}_4:\text{Tb}^{3+}$ and its solid solutions can be used in luminescent lamps as a highly efficient emitter of green light [1-8]. Also, a few recent studies on the synthesis and properties of 1D cerium orthophosphate nanostructured materials have been reported. Hexagonal $\text{CePO}_4:\text{Tb}^{3+}$ could be easily obtained at low temperature, and the corresponding nanorods/nanowires with a variable size have been hydrothermally synthesized [8–11]. Monoclinic $\text{CePO}_4:\text{Tb}^{3+}$ generally exists as natural monazite, bulk materials of which could be prepared via the solid state reaction and hydrothermal method at high temperature [12, 13]. So far, nano-sized monoclinic $\text{CePO}_4:\text{Tb}^{3+}$ are mainly synthesized in a liquid phase under higher temperature. Nanowires of monoclinic $\text{CePO}_4:\text{Tb}^{3+}$ were synthesized through a hydrothermal reaction at 200°C. Very recently, Haase et al [14] reported

the synthesis of monazite-type $\text{CePO}_4:\text{Tb}^{3+}$ nanoparticles controlled by liquid-phase synthesis in high boiling coordinating solvents at 200°C. Up to now, there is no report about the synthesis of monoclinic $\text{CePO}_4:\text{Tb}^{3+}$ at low temperature. Our purpose is to synthesize $\text{CePO}_4:\text{Tb}^{3+}$ nanorods at small size with high luminescent intensity for use as luminescent substance in security ink. In this paper, we use hydrothermal method to synthesize $\text{CePO}_4:\text{Tb}^{3+}$ nanorods, without using surfactant. The average length of $\text{CePO}_4:\text{Tb}^{3+}$ nanorods was around 80 - 110 nm. $\text{CePO}_4:\text{Tb}^{3+}$ nanorods was determined by photoluminescence at 278 nm, showed the high intensity of green emission at 543 nm wavelength which was correspond to ${}^5\text{D}_4\text{-}{}^7\text{F}_5$ transition of Tb^{3+} .

EXPERIMENT

Materials

$\text{Ce}(\text{NO}_3)_3 \cdot 6\text{H}_2\text{O}$ (99.8%, Aldrich), $\text{Tb}(\text{NO}_3)_3 \cdot 5\text{H}_2\text{O}$ (99.9%, Aldrich), H_3PO_4 (Aldrich) were used as starting materials.

Sodium hydroxide (NaOH, 99%, Aldrich) was used to control pH.

Synthesis of $CePO_4:Tb^{3+}$ nanorods

$CePO_4:Tb^{3+}$ nanorods were synthesized by chemical method. Dissolving 1.5 mmol of $Ce(NO_3)_3 \cdot 6H_2O$ and 0.078 mmol of $Tb(NO_3)_3 \cdot 5H_2O$ (Tb^{3+} doping molar concentration is 5%) with 15 ml DI water in 15 minutes. After that, H_3PO_4 were added into the solution. The pH value of mixture was adjusted to 2 by 5M of NaOH. And then the mixture was poured in Teflon, then sealed tightly. Place the Teflon in Autoclave, and then put it in the oven at $120^\circ C$ in one hour.

Characterization

Particle size and morphology of $CePO_4:Tb^{3+}$ is determined by Field emission scanning electron microscopy (FE-SEM). The crystallite

structure of $CePO_4:Tb^{3+}$ is analyzed by X-ray diffraction spectroscopy. The emission spectra are recorded at room temperature using a Hitachi F-4500 spectrophotometer.

RESULTS AND DISCUSSION

Hydrothermal method is applied in all experiments, however there is difference in different PO_4/Ce molar ratios. The doping concentration of Tb^{3+} was 5 mol% that of Ce^{3+} in $CePO_4$ host, which had been optimized previously by Jinrong *et al*; Yao yao *et al*; Mingyun *et al* [19-21].

In all of the following experiments, molar ratio of Europium ion is fixed at 5% and pH is fixed at 2. The molar ratio of PO_4/Ce is adjusted in turn at: 10; 70; 140 and reaction time for hydrothermal is one hour.

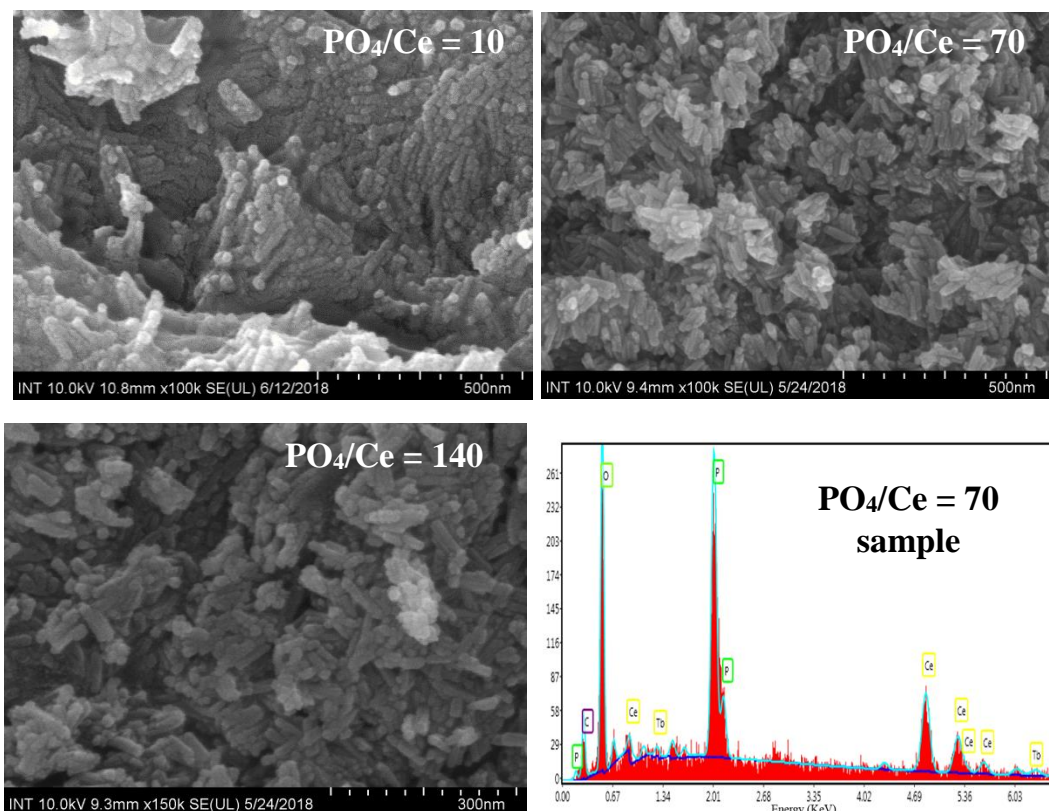


Figure 1. The FE-SEM micrographs of $CePO_4:Tb^{3+}$ nanorods synthesized with different PO_4/Ce molar ratios

Figure. 1 shows the FE-SEM micrographs of $CePO_4:Tb^{3+}$ nanorods synthesized with different

PO_4/Ce molar ratios: 10; 70; 140. According to Figure. 1, the morphology of particles is in

nanorods in all samples. The length distributed from 85 nm to 110 nm with $\text{PO}_4/\text{Ce}=70$ and 140 samples. When the PO_4/Ce ratio is too low, the nanorods morphology of $\text{CePO}_4:\text{Tb}^{3+}$ is not clear with larger length.

The detailed elemental analysis of nanorods is done using energy dispersive X-ray analysis

(EDX), which is shown in Figure 1 (EDX spectrum of sample $\text{PO}_4/\text{Ce}=70$). The EDX study reveals the presence of cerium, terbium, and oxygen, indicating that Tb^{3+} ions were doped into the CePO_4 nanocrystals.

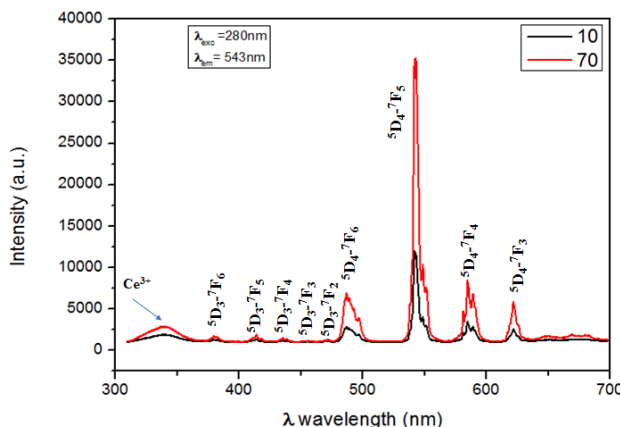


Figure 2. The photoluminescence emission spectrum of $\text{CePO}_4:\text{Tb}^{3+}$ nanorods synthesized with different PO_4/Ce molar ratios

Figure 2 shows the photoluminescence emission spectrum excitation at 280 nm of $\text{CePO}_4:\text{Tb}^{3+}$ nanorods synthesized with different PO_4/Ce molar ratios. All samples reveal the characteristic emission peaks associated with Tb^{3+} ions.

The main emission is at 543 nm based on $^5\text{D}_4-^7\text{F}_5$ with the strongest emissivity

comparatively to the others. The luminescent intensity at 543 nm, green-emitting, which increases by PO_4/Ce molar ratios, shows that the crystal structure of $\text{CePO}_4:\text{Tb}^{3+}$ nanorods becomes better. However have a low emission peak of Ce^{3+} in Figure 2, this is due to incomplete energy transfer from Ce^{3+} to Tb^{3+} .

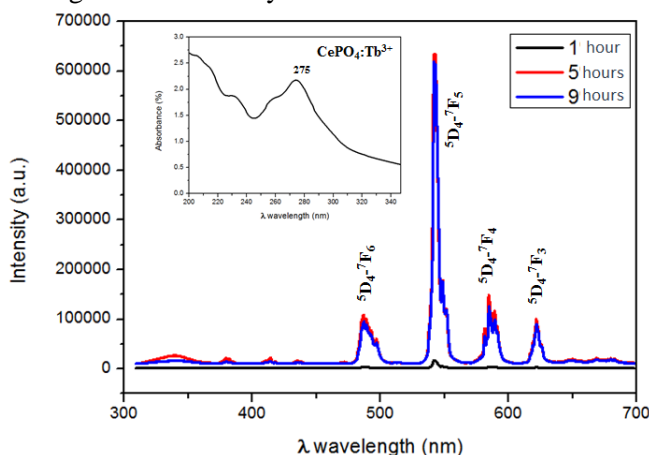


Figure 3. The photoluminescence emission spectrum of $\text{CePO}_4:\text{Tb}^{3+}$ nanorods synthesized with different reaction time of hydrothermal. Inset shows the UV-Vis spectra of $\text{CePO}_4:\text{Tb}^{3+}$ nanorods synthesized with 1h of hydrothermal

In the present investigation, the formation of Tb^{3+} doped $CePO_4$ nanorods is investigated with different hydrothermal reaction time, as follow: 1 hour, 5 hours and 9 hours. With hydrothermal temperature at $120^\circ C$, PO_4/Ce molar ratio is 70 and the other conditions remain unchanged for other samples. Figure 3 shows the emission spectra under excitation at 280 nm of $CePO_4:Tb^{3+}$ nanorods synthesized with different reaction time of hydrothermal. Inset is the UV-Vis spectra of $CePO_4:Tb^{3+}$ nanorods synthesized with 1h of hydrothermal. The optical emission mechanism is the absorption of ultraviolet light

by Ce^{3+} and transfer of energy to Tb^{3+} , which energy is released in the form of fluorescence. Hence, the absorption of Ce^{3+} is displayed in Figure 3 (inset). There is an absorption in the Ce^{3+} related to the peaks at 275 nm of 1 h samples. The 5-hours reaction time synthesized sample has highest peak intensity. The most intense line at ~ 543 nm corresponds to the transition between the 5D_4 and 7F_5 level of the Tb^{3+} ions. We believe that with 9 h reaction time, defect in the crystal appear, leading to a decrease in emission intensity.

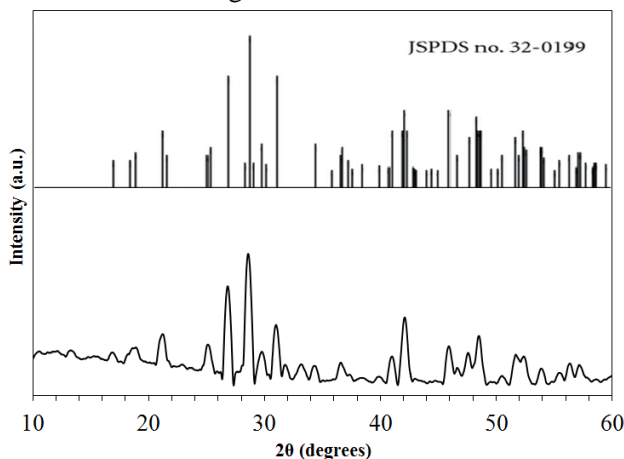


Figure 4. XRD patterns of $CePO_4:Tb^{3+}$ nanorods synthesized at $PO_4/Ce = 70$

Figure 4 shows the XRD patterns of the $CePO_4:Tb^{3+}$ nanorods synthesized at $PO_4/Ce = 70$. $CePO_4$ monoclinic phase (JCPDS, No. 32-0199) attributes in all diffraction peak, indicating the existence of crystalline structure in all nanoparticles [15-20]. The absence of additional peaks for another phases indicated that Tb^{3+} ions have been effectively built into the $CePO_4$ host lattice.

CONCLUSION

The $CePO_4:Tb^{3+}$ nanorods were synthesized by hydrothermal method. All nanorods morphology with $CePO_4:Tb^{3+}$ sample synthesized at $120^\circ C$ for 5 hours with molar ratio of PO_4/Ce at 70 and concentration of Terbium doped at 5% Tb^{3+} and pH controlled at 2. The average length of $CePO_4:Tb^{3+}$ nanorods were around 80 - 110 nm. $CePO_4:Tb^{3+}$ nanorods were well indexed to the

monoclinic phase of $CePO_4$ host (JCPDS, No. 32-0199). $CePO_4:Tb^{3+}$ was determined by photoluminescence at excitation of 278 nm, showed the high intensity of green emission at 543 nm wavelength which was correspond to $^5D_4-^7F_5$ transition of Tb^{3+} .

Acknowledgment

The authors highly appreciate the financial support of the Vietnam National University - Ho Chi Minh City (VNU-HCM)

References

- [1]. K. Hiruma, M. Yazawa, T. Katsuyama, K. Ogawa, K. Haraguchi, M. Kouguchi and H. Kakibayashi, *J. Appl. Phys.*, 1995, **77**, 447.
- [2]. J. Hu, T. W. Odom and C. M. Lieber, *Acc. Chem. Res.*, 1999, **32**, 435.

- [3]. J. D. Justin, K. P. Johnston, R. C. Doty and B. A. Korgel, *Science*, 2000, **287**, 1471.
- [4]. J. Dhanaraj, R. Jagannathan, T. R. N. Kutty and Chung-Hsin. Lu, *J. Phys. Chem. B*, 2001, **105**, 11098.
- [5]. H. Mass, A. Currao and G. Calzaferri, *Angew. Chem., Int. Ed.*, 2002, **41**, 2495.
- [6]. O. Lehmann, H. Meyssamy, K. Kompe, H. Schnablegger and M. Haase, *J. Phys. Chem. B*, 2003, **107**, 7449.
- [7]. H. Meyssamy, K. Riwozki, A. Kornowski, S. Nased and M. Haase, *Adv. Mater.*, 1999, **11**, 840.
- [8]. W. B. Bu, Z. L. Hua, H. R. Chen and J. L. Shi, *J. Phys. Chem. B*, 2005, **109**, 14461.
- [9]. M. H. Cao, C. W. Hu, Q. Y. Wu, C. X. Guo, Y. J. Qi and E. B. Wang, *Nanotechnology*, 2005, **16**, 282.
- [10]. Y. P. Fang, A. W. Xu, R. Q. Song, H. X. Zhang, L. P. You, Jimmy C. Yu and H. Q. Liu, *J. Am. Chem. Soc.*, 2003, **125**, 16025.
- [11]. Y. J. Zhang and H. M. Guan, *J. Cryst. Growth*, 2003, **256**, 156.
- [12]. K. Rajesh, P. Mukundan, P. Krishna, V. R. Nair and K. G. K. Warriar, *Chem. Mater.*, 2004, **16**, 2700.
- [13]. J. W. Anthony, *Am. Mineral.*, 1957, **42**, 904.
- [14]. K. Riwozki, H. Meyssamy, A. Kornowski and M. Haase, *J. Phys. Chem. B*, 2000, **104**, 2824.
- [15]. C. Dong, *J. Appl. Crystallogr.*, 1999, **32**, 838.
- [16]. L. Bo, S. Liya, L. Xiaozhen, Z. Shuiche, Z. Yumeri, W. Tianmain, Y. Sasaki, K. Ishii, Y. Kashiwaya, H. Takahashi and T. Shibayama, *J. Mater. Sci. Lett.*, 2001, **20**, 1071.
- [17]. K. Rajesh, P. Mukundan, P. Krishna Pillai, V. R. Nair and K. G. K. Warriar, *Chem. Mater.*, 2004, **16**, 2700.
- [18]. J. Zhang, L. D. Sun, J. L. Yin, H. L. Su, C. S. Liao and C. H. Yan, *Chem. Mater.*, 2002, **14**, 4172.
- [19]. F. Tao, Z. J. Wang, L. Z. Yao, W. L. Cai and X. G. Li, *Mater. Lett.*, 2007, **61**, 4973.
- [20]. H. B. Li, L. L. Chai, X. Q. Wang, X. Y. Wu, G. C. Xi, Y. K. Liu and Y. T. Qian, *Cryst. Growth Des.*, 2007, **7**, 1918.
- [21]. K. K. Caswell, Christopher M. Bender and Catherine J. J. Murphy, *Nano Lett.*, 2003, **3**, 667

EX-SITU AND IN-SITU SYNTHESIS OF Fe-DOPED TiO₂ NANOROD ARRAYS WITH ENHANCED PHOTOELECTROCHEMICAL ACTIVITY

Pham Thi Minh Huong¹, Ngo Thi Hien Thao¹, Nguyen Thi Minh Thuc¹, Nguyen Tan Lam² and Tran Nam Trung^{1,*}

¹Department of Physics and Materials Science, Faculty of Natural Sciences, Quy Nhon University, Quy Nhon City 59000, Vietnam

²Department of Chemical and Food Engineering, Faculty of Natural Sciences, Quy Nhon University, Quy Nhon City 59000, Vietnam

Email: trannamtrung@qnu.edu.vn

ABSTRACT

Improving the photoresponse of TiO₂ to visible light while maintaining its high photocatalytic activity has been a challenge. Herein, we report our recent efforts to improve the photoelectrochemical (PEC) activity of TiO₂ nanorod arrays by doping with iron (Fe) through two approaches of *ex-situ* and *in-situ* doping processes using a hydrothermal method. The results show that the doping treatments have impacts on the morphology and optical properties of TiO₂ nanorods. Moreover, the effect of *ex-situ* and *in-situ* Fe-doping approaches on the PEC performance of TiO₂ nanorods was investigated. The *in-situ* Fe-doped TiO₂ sample exhibited a significant enhance in the photocurrent density, as high as 2.88 mA/cm² at 0.5 V, which are two times higher than that of the undoped TiO₂ sample. Our results revealed that Fe-doped TiO₂ nanorods can serve as promising photoelectrode materials for PEC applications.

Keywords: Fe-doped TiO₂ nanorods, *ex-situ* doping, *in-situ* doping, hydrothermal, photoelectrochemical

INTRODUCTION

Owing to strong photocatalytic activity, excellent photo- and chemical-stability and cost savings, titanium dioxide (TiO₂) has been emerged as one of the most used materials for solving environmental concerns including air and waste-water purification, sensors and solar energy conversions [1]. In recent years, TiO₂-based photoelectrodes have been considered as superior candidates for photoelectrochemical (PEC) water splitting. However, the performance of pristine TiO₂ semiconductors is restricted due to its wide band gap (~3.0 eV and ~3.2 eV for rutile and anatase phases, respectively) and fast recombination of the photoexcited electron-hole pairs. To address these drawbacks, nanostructuring, surface modification, and impurity ion doping of TiO₂ have been explored to improve its electronic properties, optical sensitivity, and activity [2]. Among these, impurity ion doping of TiO₂ is an effective strategy for improving the photoresponse of TiO₂ to visible light, consequently enhancing the PEC activities. It has been determined that one-dimensional (1D) TiO₂ nanostructures such as nanorods, nanowires, nanotubes, and nanofibers have

better properties than other structures, including large intrinsic specific surface area and creating an offered directional pathway for transporting of electrons. Among their different 1D nanostructures, TiO₂ nanorods have more advantages in the transporting properties because of fewer defects related to barriers blocking the charge carrier transport [3].

In this study, we report our recent efforts to improve the PEC performance of TiO₂ nanorod array photoelectrodes by doping with Fe³⁺ ions through two approaches of *ex-situ* and *in-situ* doping processes. The synthesized TiO₂ nanorod arrays on fluorine-doped tin oxide (FTO) glass substrates have average size and length of ~200 nm and ~3 μm, respectively. The results show that doping treatments have impacts on the morphology and optical properties, which narrowing the optical band gap of TiO₂ nanorods. The *in-situ* Fe-doped TiO₂ sample exhibited the highest photocurrent density in comparison with that of undoped and *ex-situ* Fe-doped TiO₂ samples. These results suggested effective carrier separation and transportation in the Fe-doped TiO₂ nanorods.

EXPERIMENTAL

TiO₂ nanorod arrays were synthesized on FTO glass substrates in a Teflon-lined stainless-steel autoclave by a hydrothermal method. Typically, 0.3 ml of titanium butoxide (C₁₆H₃₆O₄Ti, >97%, Sigma Aldrich) was added to a mixture of 9 ml hydrochloric acid (HCl, 37%, Sigma Aldrich) and 9 ml deionized (DI) water and then was heated at 160 °C for 8 h. After that, the TiO₂ nanorod substrates were rinsed extensively with DI water and dried under N₂ gas. For the *in-situ* doping, 10 mM of iron(III) nitrate nonahydrate (Fe(NO₃)₃·9H₂O, >98%, Sigma Aldrich) was added in the above as-prepared solution and heated at 160 °C for 8 h. For the *ex-situ* doping, the TiO₂ nanorod substrate was immersed in a Teflon-lined autoclave containing 15 ml solution of 10 mM Fe(NO₃)₃·9H₂O and then was heated at 160 °C for 2 h.

The morphologies and structures of the synthesized samples were investigated by using scanning electron microscopy (SEM, Hitachi 4800) and X-ray diffraction (XRD, Siemens D5000). The sample optical property was characterized via an ultraviolet-visible (UV-Vis) spectrophotometer (Jasco V-670). The PEC measurement was performed in 1 M KOH solution using a three-electrode system with an electrochemical analyzer (DY 2300) and a 150 W Xenon solar simulator (Newport 94021A) as a light source. A Pt coil and Ag/AgCl were used as counter and reference electrodes, respectively.

RESULTS AND DISCUSSION

Doping treatments have an impact on the morphology of TiO₂ nanorods. SEM images of undoped TiO₂ nanorods and Fe-doped TiO₂ nanorods with *ex-situ* and *in-situ* doping processes are shown in Figure 1. It can be seen from Figure 1(a) that the nanorod arrays are uniformly formed in high density with a large space between each nanorod. These nanorods appear in tetragonal shapes with a square base. The inset in Figure 1(a) reveal that vertically aligned nanorods were uniformly grown on the FTO substrate. The typical nanorod diameters and lengths about 200 nm and 3 μm, respectively. After doping with Fe via the *ex-situ* doping process, the nanorods were maintained in the same tetragonal shapes in comparison with the undoped sample (Figure 1(b)). However,

there are small nanoparticles formed that cover the surface of the nanorods, as seen in the inset in Figure 1(b). SEM image of the sample synthesized with the *in-situ* doping process shows that there are no obvious changes in morphology by comparing with the SEM image of the undoped sample (Figure 1(c)).

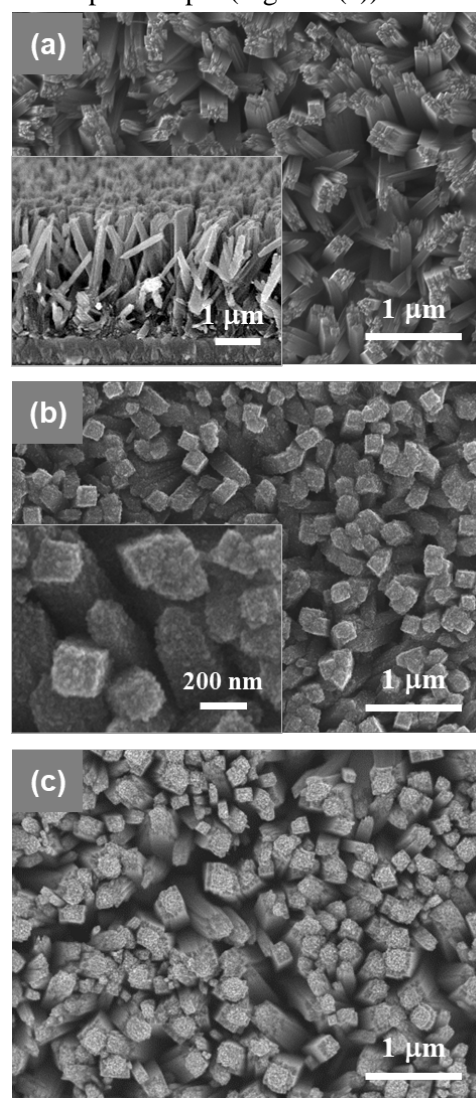


Figure 1. SEM images of (a) undoped TiO₂, (b) *ex-situ* Fe-doped TiO₂ and (c) *in-situ* Fe-doped TiO₂ nanorod arrays on FTO substrates. The insets in (a) and (b) show cross-sectional view and high-resolution SEM images of undoped and *ex-situ* Fe-doped TiO₂ nanorods, respectively.

Figure 2 shows the XRD patterns of undoped and Fe-doped TiO₂ nanorods. All samples possess similar diffraction patterns with strong characteristic peaks at 2θ angles of 36.4° and 63.2°, which can be assigned to (101) and (002) planes of tetragonal rutile TiO₂ structure

(JCPDS No. 88-1175). It is found that Fe doping has no obvious impact on the XRD pattern of TiO₂ nanorods. In addition, it is notable that no iron oxides or metallic iron peaks could be observed in the XRD spectra of both samples using *ex-situ* and *in-situ* Fe doping processes. This can be explained by the so low concentration of Fe doping that under the limit of detection by XRD. On the other hand, due to similar in the ionic radii of Fe³⁺ (0.79 Å) and Ti⁴⁺ (0.75 Å) [4], the Fe³⁺ ions can integrate into the crystal lattice of TiO₂ and can be located at interstices or at some Ti⁴⁺ lattice sites.

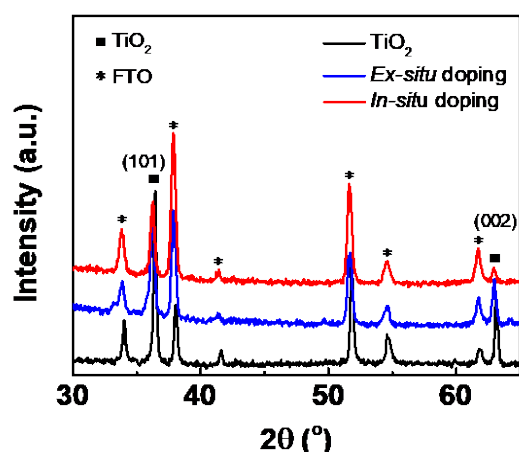


Figure 2. XRD patterns of undoped TiO₂ (black curve), *ex-situ* Fe-doped TiO₂ (blue curve) and *in-situ* Fe-doped TiO₂ (red curve) nanorod arrays on FTO substrates.

Figure 3(a) shows the UV-vis absorption spectra of undoped and Fe-doped TiO₂ nanorods. As can be seen, there is absorption around the wavelength of 410 nm for all samples. This clearly confirms the transitions of electrons from the valence band to the conduction band of TiO₂. It is also found that the absorption intensity of the Fe-doped TiO₂ samples is stronger than that of the undoped TiO₂ sample. In addition, Fe-doped TiO₂ samples have a red-shift in the absorption edge compared with the undoped TiO₂ sample. Therefore, it is suggested that doping Fe³⁺ ions can enhance the absorption intensity in the UV-vis light region and make the red-shift in the band gap transition, which causes the narrowing in the band gap of TiO₂. To evaluate the optical band gap, we use Tauc's equation [5]:

$$(\alpha h\nu) = A(h\nu - E_g)^{1/2} \quad (1)$$

where A is a constant, α is molar extinction coefficient, E_g is the average band gap of the material. The average band gap was estimated from the intercept of the linear portion of the

$(\alpha h\nu)^2$ vs. $h\nu$ plots on $h\nu$ axis as shown in Figure 3(b). The band gap values E_g have been estimated to be 3.06; 3.02 and 2.94 eV for undoped, *ex-situ* Fe-doped and *in-situ* Fe-doped TiO₂ samples, respectively. The narrowing in the band gap of TiO₂ under doping Fe³⁺ ions can be explained by the formation of a dopant energy level within the band gap of TiO₂ [6].

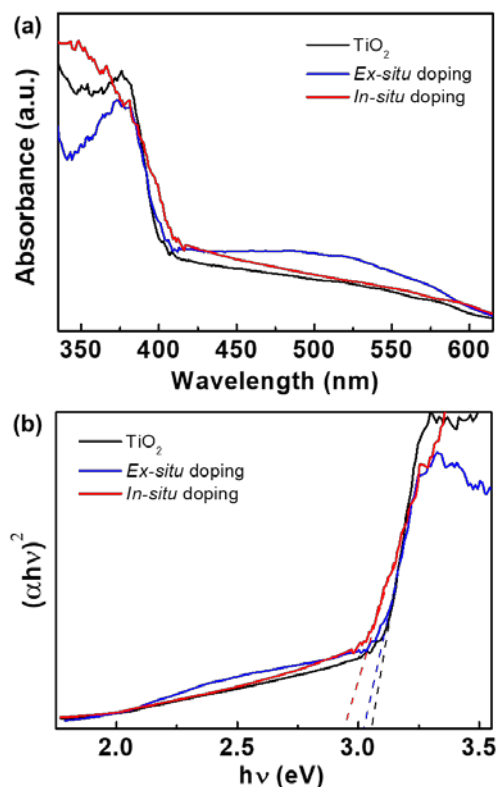


Figure 3. (a) UV-vis spectra and (b) $(\alpha h\nu)^2$ versus $h\nu$ plots of undoped TiO₂ (black curve), *ex-situ* Fe-doped TiO₂ (blue curve) and *in-situ* Fe-doped TiO₂ (red curve) nanorod arrays on FTO substrates.

To evaluate the PEC activity of the synthesized samples, linear sweep voltammetry (LSV) was recorded under illumination of a solar light simulator, as shown in Figure 4(a). Under illumination, the photocurrent density of *ex-situ* Fe-doped TiO₂ sample is 1.48 mA/cm² at 0.5 V, which is the same value of undoped TiO₂ sample. However, the onset potential of *ex-situ* Fe-doped TiO₂ sample (−0.9 V) exhibited a cathodic shift in comparison with undoped TiO₂ sample (−0.6 V). This could be attributed to the built-in potential across the interfaces between TiO₂ nanorods and nanoparticles on its surfaces, as observed in Figure 1(b). The *in-situ* Fe-doped TiO₂ sample exhibited a highest photocurrent density of 2.88 mA/cm² at 0.5 V while

possessing the negative onset potential of -0.6 V, which indicates more electrons are collected from the PEC reaction. This significant increment in the photocurrent density value can be explained through the enhanced absorption due to narrowing the band gap and the energy transfer mechanism from the energy band of Fe^{3+} ions to the conduction band of TiO_2 .

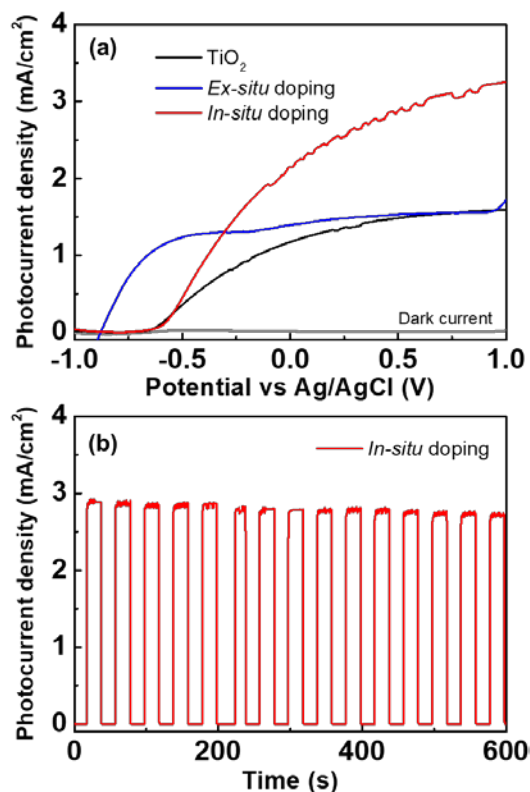


Figure 4. (a) Photocurrent density - potential curves of undoped TiO_2 (black curve), *ex-situ* Fe-doped TiO_2 (blue curve) and *in-situ* Fe-doped TiO_2 (red curve) nanorod arrays on FTO substrates. (b) Photocurrent versus time of *in-situ* Fe-doped TiO_2 nanorods at an applied potential of 0.5 V (vs Ag/AgCl).

The photocurrent of the *in-situ* Fe-doped TiO_2 sample also exhibited outstanding long-term stability of PEC reaction, as seen in Figure 4(b). In addition, the instantaneous increase or decrease in the photocurrent according to the light-on and light-off indicated that the electron-hole pairs immediately generated then separated in the TiO_2 nanorods, respectively. Thus, these results suggested effective carrier separation and transportation and relatively long electron lifetime in the Fe-doped TiO_2 nanorods.

CONCLUSION

In summary, the *ex-situ* and *in-situ* Fe-doped TiO_2 nanorods were synthesized on FTO

substrates via the hydrothermal method. Due to the formation of a dopant energy level within the band gap of TiO_2 , the optical band gap of TiO_2 nanorods was narrowed under doping conditions, which are of 3.02 and 2.94 eV for *ex-situ* and *in-situ* doping approaches, respectively. The *in-situ* Fe-doped TiO_2 sample exhibited a significant enhance in the photocurrent density, as high as 2.88 mA/cm^2 at 0.5 V, which are two times higher than that of the undoped TiO_2 sample. Our results revealed that Fe-doped TiO_2 nanorods can serve as promising photoelectrode materials for PEC applications.

Acknowledgment

This research is funded by Vietnam National Foundation for Science and Technology Development (NAFOSTED) under grant number 103.02-2018.329.

References

- [1]. Mingzheng Ge, Chunyan Cao, Jianying Huang, Shuhui Li, Zhong Chen, Ke-Qin Zhang, S. S. Al-Deyab and Yuekun Lai, *A review of one-dimensional TiO_2 nanostructured materials for environmental and energy applications*, Journal of Materials Chemistry A **4** (2016), 6772–6801.
- [2]. Shaohua Shen, Jie Chen, Meng Wang, Xia Sheng, Xiangyan Chen, Xinjian Feng, Samuel S. Mao, *Titanium Dioxide Nanostructures for Photoelectrochemical Applications*, Progress in Materials Science **98** (2018), 299-385.
- [3]. Jian Tian, Zhenhuan Zhao, Anil Kumar, Robert I. Boughton and Hong Liu, *Recent progress in design, synthesis, and applications of one-dimensional TiO_2 nanostructured surface heterostructures: a review*, Chemical Society Reviews **43** (2014), 6920-6937.
- [4]. B. Santara, P.K. Giri, S. Dhara, k. Imakita, M. Fujii, *Oxygen vacancy-mediated enhanced ferromagnetism in undoped and Fe-doped TiO_2 nanoribbons*, Journal of Physics D: Applied Physics **47** (2014) 235304 – 235318.
- [5]. J. Tauc, A. Menth, *States in the gap*, Journal of Non-Crystalline Solids **8–10** (1972), 569 – 585.
- [6]. K. Nagaveni, M. S. Hegde, Giridhar Madras, *Structure and Photocatalytic Activity of $\text{Ti}_{1-x}\text{M}_x\text{O}_{2+\delta}$ ($M = \text{W}, \text{V}, \text{Ce}, \text{Zr}, \text{Fe}, \text{and Cu}$) Synthesized by Solution Combustion Method*, The Journal of Physical Chemistry B **108** (2004) 20204 - 20212.

COMBUSTION SYNTHESIS AND CHARACTERIZATION OF Eu^{3+} -DOPED GdVO_4 NANOPARTICLE PHOSPHORS

Thai Thi Dieu Hien^{1,2}, Pham Duc Roan¹, Ngo Khac Khong Minh^{2,3,4} and Nguyen Vu^{3,4,*}

¹Faculty of Chemistry, Hanoi National University of Education, Xuan Thuy, Hanoi, Viet Nam

²Nam Can Tho University, Cantho, Viet Nam

³Institute of Materials Sciences, Vietnam Academy of Science and Technology, 18 Hoang Quoc Viet, Hanoi, Viet Nam

⁴Graduate University of Science and Technology, Vietnam Academy of Science and Technology, 18 Hoang Quoc Viet, Hanoi, Viet Nam

ABSTRACT

In this paper, europium-doped gadolinium orthovanadate ($\text{GdVO}_4:\text{Eu}^{3+}$) nanoparticle phosphors were successfully obtained by a straightforward combustion method. The morphologies, crystal structure and optical characteristics were modified by different annealing temperatures (500, 600, 700, 800 and 900°C), and dopant concentration of Eu^{3+} ions (1, 3, 5, 7, 9 mol %). The $\text{GdVO}_4:\text{Eu}^{3+}$ nanoparticle phosphors were characterized by X-ray diffraction (XRD), scanning electron microscopy (SEM), photoluminescence (PL) and lifetime. X-ray patterns show the tetragonal phase and the average particle size was about 30-50 nm. Photoluminescent emission spectra were recorded under excitation wavelength at 312 nm. As a result, the $\text{GdVO}_4:\text{Eu}^{3+}$ nanoparticles show strong characteristics emission of Eu^{3+} ions. Therein, the ${}^5\text{D}_0 \rightarrow {}^7\text{F}_2$ transition was dominated with pure red emission. The best concentration of Eu^{3+} ions was investigated to be 5 mol %.

INTRODUCTION

Orthovanadates activated with rare earth ions have been extensively studied for along time due to their interesting physical and chemical properties. These materials could be applied in optical devices such as solid-state lighting, lasers, cathode ray tubes (CRTs), electroluminescent, field emission and flat panel display devices[1-3]....In $\text{GdVO}_4:\text{RE}^{3+}$ family, GdVO_4 doped with Eu^{3+} ions was an excellent red emitter[4]. Moreover, the VO_4^{3-} groups have a strong absorption of ultraviolet light due to a charge transfer process from O to V in VO_4^{3-} groups. In 1992, Zaguniennyi and co-working introduced GdVO_4 as a host material for RE^{3+} activators which had more desirable properties than YVO_4 [5-6]. In the past, there were many methods to preparation of Eu^{3+} -doped GdVO_4 , such as coprecipitation, solvothermal, molten salt [4,6-9]... In this research, $\text{GdVO}_4:\text{Eu}^{3+}$ nanoparticles were synthesized via a straightforward combustion method because efficient, environmentally friendly and low-cost.

EXPERIMENTAL

All beginning chemicals were analytical grade reagents. Gadolinium (III) oxide (Gd_2O_3 99.9%), Europium(III) oxide (Eu_2O_3 99.99%), NH_4VO_3 (Merck), Urea (Merck) were used as starting materials. Firstly, Gd_2O_3 and Eu_2O_3 were treated by concentrated nitric acid to obtain the rare earth nitrate solutions with a defined concentration. The secondly, the mixture of $\text{Gd}(\text{NO}_3)_3$, $\text{Eu}(\text{NO}_3)_3$ and urea with a defined mole ratio was stirred in 30 min to a transparent solution. Then, add slowly the solution of NH_4VO_3 into the aforementioned solution with strong stirring in 1 hour. After that, the solution was heated until a yellow gel was formed that called precursors. These precursors were dried at 80°C in air for 24 hours, then annealed at 500, 600, 700, 800, 900°C for 2 hours.

The crystalline structure was obtained on an Advance-Bruker D8 x-ray diffractometer using Cu $\text{K}\alpha$ radiation resource ($\lambda=1.5406 \text{ \AA}$) and the scan range was set from 20 to 80 (2θ) with a step of $0,03^\circ\text{s}^{-1}$. The morphology of the final product was examined using a scanning electron microscope (SEM) (HITACHI S-4800). Excitation and

emission spectra were determined by a Cary Eclipse fluorescence spectrophotometer equipped with an 80Hz xenon lamp as the excitation source.

RESULTS AND DISCUSSION

Fig.1 show the XRD pattern of GdVO₄:5%mol Eu³⁺ annealed at 900°C. The phase of this material was identified to tetragonal with lattice constants $a = b = 7.2126\text{\AA}$, $c = 6.3483\text{\AA}$ and it matched well with JCPDS No 17-1260. Beside, no impurity peaks were found. Some characteristic peaks centered at $2\theta = 24.6^\circ, 31.11^\circ, 33.3^\circ, 35.16^\circ, 37.7^\circ, 40.02^\circ, 44.6^\circ, 47.6^\circ, 49.2^\circ, 50.62^\circ,$ and 58.05° corresponding to the (200), (211), (112), (220), (202), (301), (103), (321), (312), (400), and (420) reflection of crystalline GdVO₄:Eu³⁺ [11,12]. These proved that the sample was well crystallized.

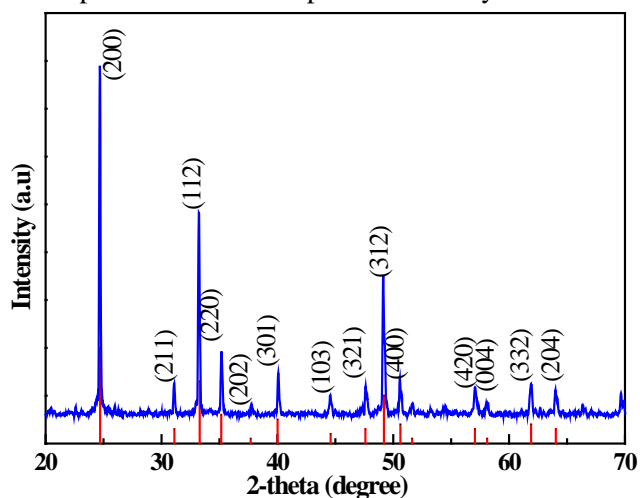


Figure 1. XRD pattern of GdVO₄:5%mol Eu³⁺ annealed at 900°C.

The average size of the phosphors were calculated by Debye-Scherrer equation: $D = \frac{0.89\lambda}{\beta \cos\theta}$. Therein, D is the average crystallite size, λ is the wavelength of the Cu K α radiation, θ is the Bragg angle and β is the full-width at half maximum (FWHM) in radians of the peak at $2\theta = 24.6^\circ$. When the reaction temperature was from 500°C to 900°C, the average crystallite sizes, calculated from the (200) diffraction peak, were 24.76, 27.36, 33.1, 33.24, and 34.1 nm, respectively. It can be observed that the crystallite size increased with increasing annealed temperature.

The surface morphology of GdVO₄:5mol% Eu³⁺ annealed at 900°C nanoparticles was investigated by SEM are provided in Fig. 2. The obtained phosphor powders showed almost similar spherical and consisting of strong agglomerated nanoparticles. The average size of nanoparticle was about 30-40 nm. This result was also consistent with the one of XRD measurement.

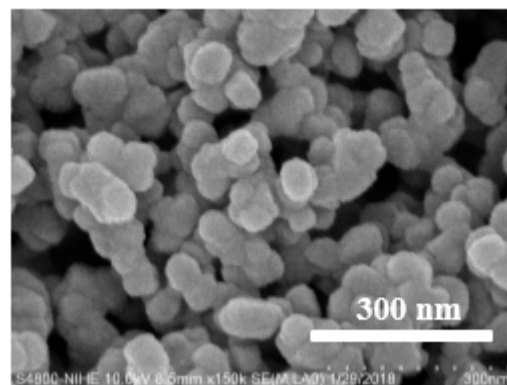


Figure 2. SEM image of GdVO₄:5mol% Eu³⁺ annealed at 900°C phosphor powder.

The photoluminescence excitation (PLE) spectra of GdVO₄:5mol% Eu³⁺ nanoparticles annealed at 900°C was shown in Fig 3. The spectra exhibited a broad absorption band in the range at shorter wavelengths (260-350 nm) and some sharp lines at longer wavelengths (350-500 nm) corresponding to europium 4f transitions. There was a overlapping between both excitation bands. The strong broad band consisted two charge transfer bands. The first broad band around 315 nm attributed to the absorption of VO₄³⁻ vanadate group, namely an electron is transferred from the oxygen 2p orbitals to the vanadium 3d orbitals [6]. The second broad band around 280 nm was the Eu-O charge transfer band. The the f-f transitions of Eu³⁺ ions (4f⁶ electron configuration) in the longer wavelength region can be observed in the spectrum above 350 nm. Several sharp lines centered at 363, 377, 395, 417, and 466 nm correspond to the ⁷F₀→⁵D₄, ⁷F₀→⁵G₄, ⁷F₀→⁵L₆, ⁷F₀→⁵D₃, and ⁷F₀→⁵D₂ transition.

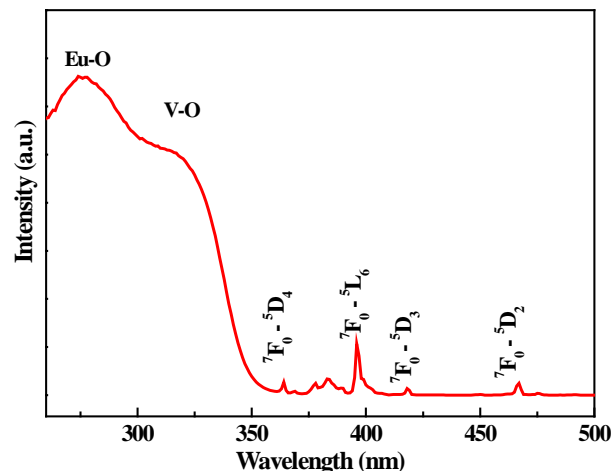


Figure 3. Excitation spectra of $GdVO_4:5 \text{ mol\% } Eu^{3+}$ sample annealed at 900°C .

The red emission spectrum of Eu^{3+} -doped $GdVO_4$ nano-powders annealed at different temperatures was given in Fig.4. The emission spectra of these samples were taken in an identical condition, by exciting the V-O charge transfer band at 313 nm. Generally, all emission spectra had similar shapes and showed the characteristics of the ${}^5D_0 \rightarrow {}^7F_J$ ($J = 1-4$) transition of Eu^{3+} ions such as the peak located at 594 nm can be attributed ${}^5D_0 \rightarrow {}^7F_1$ transition, while the emission peak around 614 - 620 nm correspond to the ${}^5D_0 \rightarrow {}^7F_2$ transition. Besides, two emission lines around 650 nm and 700 nm correspond to the ${}^5D_0 \rightarrow {}^7F_3$ and ${}^5D_0 \rightarrow {}^7F_4$ transition, respectively [6,9,10,12]. However, the ${}^5D_0 \rightarrow {}^7F_0$ transition was completely forbidden by the multipolar and Judd-Ofelt selection rules. The ${}^5D_0 \rightarrow {}^7F_1$ transition is magnetic dipole and its intensity is independent of the host matrix. The ${}^5D_0 \rightarrow {}^7F_2$ transition becomes electric dipole type. It was known as a hypersensitive transition because it is easily affected by the local environment around Eu^{3+} ions. Theoretically, when the Eu^{3+} ions occupied the noncentro symmetric sites, the red emission ${}^5D_0 \rightarrow {}^7F_2$ was dominant [6,13]. The inset of Fig. 4 showed that the intensity of ${}^5D_0 \rightarrow {}^7F_2$ transition increased strongly with increasing annealing temperature from 500 to 900°C . The enhancement of luminescence may be due to the crystal improvement or particle size leading to higher oscillating strengths for the optical transitions.

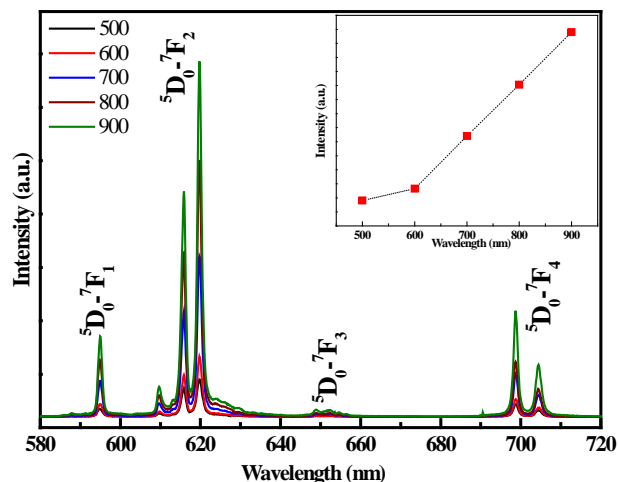


Figure 4. PL emission spectra of $GdVO_4:5 \text{ mol\% } Eu^{3+}$ nanoparticles annealed at different temperatures. Inset: the dependence of the intensity of ${}^5D_0 \rightarrow {}^7F_2$ transition on temperatures.

The dependence of the emission intensity on different Eu^{3+} ions concentrations in $GdVO_4$ samples annealed at 900°C was shown in Fig. 5. The concentration dependence on the optical intensity was observed clearly at the peak centered around 620 nm. It can be observed that the red emission of the ${}^5D_0 \rightarrow {}^7F_2$ transition increased significantly when the concentration of Eu^{3+} increased from 1 mol% and reaching maximum at 5 mol%. Then, the intensity of this transition decreased at 7 mol%. This can be explained as when the concentration of Eu^{3+} ions increased, the number of luminescence centers increased leading to the improvement of fluorescence intensity. However, when the Eu^{3+} concentration was too high, the distance of two inter-nuclear would be decreased. That would cause the probability of non-radiative energy migration between Eu^{3+} ions leading to non-radiative de-excitation, also known as the quenching concentration [14].

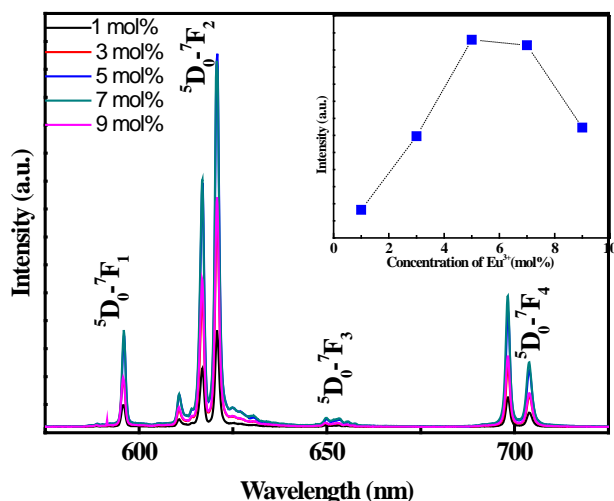


Figure 5. Emission spectra of $GdVO_4: x \text{ mol}\% \text{Eu}^{3+}$ ($x = 1, 3, 5, 7, 9$). Inset: Effects of Eu^{3+} concentration on the intensity of the ${}^5D_0 \rightarrow {}^7F_2$ transition.

The normalized luminescence decay curves of $GdVO_4: x \text{ mol}\% \text{Eu}^{3+}$ were shown in Fig 6. The excitation and emission wavelength were fixed at 313 and 620 nm, respectively. All decay curves could be well fitted into a double-exponential function as in the equation: $I = A_1 \exp(-t/\tau_1) + A_2 \exp(-t/\tau_2)$. Where I is the intensity at time t , A_1 and A_2 are the fitting parameters, τ_1 and τ_2 are the fast and slow components of the luminescence lifetimes [7,13]. The average lifetime τ is calculated as the formula: $\tau = \frac{A_1 \tau_1^2 + A_2 \tau_2^2}{A_1 \tau_1 + A_2 \tau_2}$ and listed in

Table 1.

Table 1. Decay time of $GdVO_4: x \text{ mol}\% \text{Eu}^{3+}$ ($x = 1, 3, 5, 7, 9$) samples

Concentration of Eu^{3+} ions	1 %	3 %	5 %	7 %	9 %
Lifetime (τ) ($\lambda_{\text{ex}}=313\text{nm}$)(ms)	0.96	1.00	1.33	1.02	1.89

As the inset of Fig 6, $GdVO_4: 5 \text{ mol}\% \text{Eu}^{3+}$ had the longest lifetime and decrease when the Eu^{3+} concentration was over 7 mol%. Similar to the result of emission spectra, as the Eu^{3+} ions concentration was too high, the extent of $\text{Eu}^{3+}-\text{Eu}^{3+}$ interaction would be increased. This led to the energy transfer among different Eu^{3+} ions, also known as the non-radiative decay of the excited

state. Thus, these interactions could cause the decrease in the excited state lifetime.

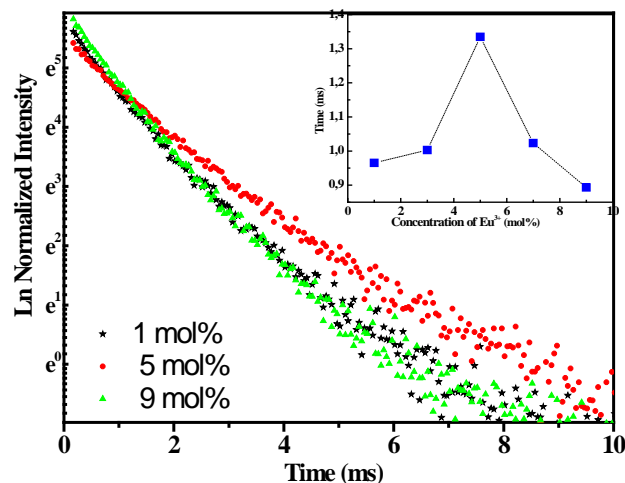


Figure 6. Luminescence decay curves of ${}^5D_0 \rightarrow {}^7F_2$ transition ($\lambda_{em} = 620 \text{ nm}$, $\lambda_{ex} = 313 \text{ nm}$) for $GdVO_4: x \text{ mol}\% \text{Eu}^{3+}$ ($x = 1, 5, 9$). Inset: the decay times with different concentrations of Eu^{3+} .

CONCLUSION

In summary, $GdVO_4$ powders doped Eu^{3+} ions were synthesized successfully via combustion method. XRD result showed that all materials were crystallized with a pure tetragonal phase. The average grain size was about 30-40 nm. The photoluminescence emission increases with annealing temperature. In this study, the optimal temperature for next researches was 900°C . The emission intensity of the ${}^5D_0 \rightarrow {}^7F_2$ was improved clearly with increase in doped concentration of Eu^{3+} from 1 to 5 mol% and then decreased for the higher concentration. Therefore, the quenching concentration was determined as 5 mol%. Moreover, the lifetime of ${}^5D_0 \rightarrow {}^7F_2$ transition increased from 0.96 to 1.33 ms with the increase of Eu^{3+} concentration from 1 to 5 mol% and then decreased gradually. Finally, the best doping concentration of Eu^{3+} in $GdVO_4$ was 5 mol%.

Acknowledgment

This study was supported by Institute of Materials Science, Vietnamese Academy of Science and Technology. A part of the work was done in the National Key Laboratory Electronic Materials and Devices.

References

- [1] Feldmann, C., Jüstel, T., Ronda, C.R. and Schmidt, P.J, *Inorganic Luminescent Materials: 100 Years of Research and Application*, Advanced Functional Materials, **13** (2003), 511-516.
- [2] Henning A. Höpfe, *Recent Developments in the Field of Inorganic Phosphors*, Angew. Chem. Int. Ed **48** (2009) 3572-3582.
- [3] Takuya Orihashi, Toshihiro Nakamura and Sadao Adachi, Resonant energy transfer in (Eu^{3+} , Bi^{3+})-codoped CaZrO_3 red-emitting phosphor, RSC Advances **6** (2016) 66130-66139.
- [4] J. W. Chung, H. K. Yang, B. K. Moon, B. C. Choi, J. H. Jeong, J. S. Bae, K. H. Kim, *The dependence of temperature synthesis of $\text{GdVO}_4:\text{Eu}^{3+}$ nanoparticle phosphors by solvothermal method*, Current Applied Physics **9** (2009) 222–225.
- [5] A. I. Zaguniennyi, V. G. Ostoumov, I. A. Shcherbakov, T. Jensen, J. P. Meyn, and G. Huber, *J. Quantum Electron* **22** (1992) 1071-1072.
- [6] D. J. Jovanovic, Z. Antic, R. M. Krsmanovic, M. Mitric, V. Đorđević, B. Bártová, M. D. Dramicanin, *Annealing effects on the microstructure and photoluminescence of Eu^{3+} -doped GdVO_4 powders*, Optical Materials **35** (2013) 1797–1804.
- [7] Z. Zhiqiang, G. Li, and J. Peiyu, *Molten Salt Synthesis and Luminescent Properties of $\text{GdVO}_4:\text{Eu}^{3+}$ Nanophosphors*, Rare Metal Materials and Engineering **43** (2014) 1588-1593.
- [8] S. Zhou, C. Duan and M. Wang, *Origin of the temperature-induced redshift of the charge transfer band of GdVO_4* , Optics Letters **42** (2017) 4703-4706.
- [9] K. Lenczewska, Y. Gerasymchuk, N. Vu, N.Q. Liem, G. Boulonc and D. Hreniak, *The size effect on the energy transfer in Bi^{3+} - Eu^{3+} co-doped GdVO_4 nanocrystals*, Journal of Materials Chemistry C **5** (2017) 3014-3023.
- [10] K. Park, J. Kim, K.Y. Kim, J.Y. Kim, Y. Kim, S.J. Dhoble, *Photoluminescence enhancement of red-emitting $\text{GdVO}_4:\text{Eu}$ and $\text{YVO}_4:\text{Eu}$ phosphors by adding zinc*, Journal of Rare Earths **31** (2013) 13-17.
- [11] F. Paz-Buclatin, F. Rivera-López, O. González, I. R. Martínez, L. L. Martínez, D. J. Jovanovic', *$\text{GdVO}_4:\text{Er}^{3+}/\text{Yb}^{3+}$ nanocrystalline powder as fluorescence temperature sensor. Application to monitor the temperature of an electrical component*, Sensors and Actuators A: Physical **299** (2019) 111628-11634.
- [12] H. Gu, J. Wang, Z. Wang, M. Zhang, J. Yao, J. Zhang, Z. Du, *Preparation of novel mesoporous $\text{GdVO}_4:\text{Eu}^{3+}$ crystals by CTAB-SDS micellar-assisted hydrothermal method in wide pH range*, Optical Materials **96**(2019) 109254.
- [13] S. Tang, M. Huang, J. Wang, F. Yu, G. Shang, J. Wu, *Hydrothermal synthesis and luminescence properties of $\text{GdVO}_4:\text{Ln}^{3+}$ ($\text{Ln} = \text{Eu}, \text{Sm}, \text{Dy}$) phosphors*, Journal of Alloys and Compounds **513**(2012) 474–480.
- [14] V. Muhr, M. Buchner, T. Hirscha, D. J. Jovanovic', S. D. Dolic', M. D. Dramicanin, O. S. Wolfbeis, *Europium-doped GdVO_4 nanocrystals as a luminescent probe for hydrogen peroxide and for enzymatic sensing of glucose*, Sensors and Actuators B: Chemical **241** (2017) 349-356.

STRUCTURE AND MAGNETIC PROPERTIES OF Nd-Fe-B BASED NANOCOMPOSITE MAGNETS PREPARED BY SPARK PLASMA SINTERING

Duong Dinh Thang¹, **Pham Thi Thanh**^{2,3}, **Nguyen Mau Lam**¹, **Nguyen Hai Yen**^{2,3}, **Pham Van Hao**¹, **Nguyen Huy Ngoc**^{2,3}, **Tran Dang Thanh**^{2,3}, **Nguyen Huy Dan**^{2,3}

¹Hanoi Pedagogical University 2, 32 Nguyen Van Linh, Xuan Hoa, Phuc Yen, Vinh Phuc, Vietnam;

²Institute of Materials Science, Vietnam Academy of Science and Technology, 18 Hoang Quoc Viet, Ha Noi, Vietnam;

³Graduate University of Science and Technology, Vietnam Academy of Science and Technology, 18 Hoang Quoc Viet, Ha Noi, Vietnam.

Email: duongdinhthang@hpu2.edu.vn

ABSTRACT

In this work, we present our results of investigation of nanostructure and magnetic properties of Nd₃Tb₁Fe₇₁Co₅Cu_{0.5}Nb₁B_{18.5} and Nd_{10.5}Fe_{80.5}Nb₃B₆ bulk nanocomposite magnets prepared by spark plasma sintering (SPS). The powder alloys were fabricated by high energy ball milling from melt-spun ribbons of the same composition. The X-ray diffraction (XRD) results manifest the formation of the Nd₂Fe₁₄B and α -Fe magnetic phase. The magnetic properties of the magnets were investigated on pulsed field magnetometer (PFM). The coercivity, H_c, higher than 6 kOe, and maximum energy product, (BH)_{max}, above 10 MGOe, can be obtained for the Nd-Fe-B bulk nanocomposite alloys with appropriate SPS conditions.

Keywords: Hard magnetic materials, Nanocomposite magnets, Exchange-spring magnets, Nd-Fe-B magnets, Spark plasma sintering.

INTRODUCTION

Currently, nanocomposite hard magnetic materials are widely researched by scientists in the world. This kind of material consists of soft and hard magnetic phases in nanometer scales [1]. The exchange-spring interaction between the hard and soft magnetic phases allows to combine both the high coercivity of the hard magnetic phase and the high saturation magnetization of the soft magnetic phase leading to high maximum energy product (BH)_{max} of the materials [2]. These materials use lower content of rare earth than that in the sintered magnets. Therefore, they can increase mechanical and chemical durability and significantly reduce costs [3-6]. Besides, manufacturing technology is also simple and easy to create magnets with a lot of different shapes. However, nanocomposite hard magnetic materials only give (BH)_{max} about 20 MGOe, which is far from the theoretical value (> 100 MGOe), low Curie temperature T_C and unstable manufacturing technology. That sets the goal of research to find out the technology to improve the magnetic properties and stabilize the parameters of the materials. Nowadays, many scientists are trying their best to overcome this

challenge. By using the SPS method we can create exchange-spring magnets with high density from alloy powder [8-9]. A big question is how to improve the magnetic parameters for the materials, increase mechanical and chemical durability, reduce costs, and stabilize technology for manufacturing materials. This paper presents some research results of manufacturing Nd-Fe-B based hard magnetic nanocomposite materials by SPS method.

EXPERIMENTAL

Raw materials of Nd, Tb, Fe, Co, Cu, Nb, Fe-B with high purity were used for manufacturing Nd-Fe-B based alloys. These materials were weighed with the designed nominal compositions, then melted by an arc-melting furnace to create pre-alloys. The pre-alloys were used to fabricate ribbons on a melt-spinning system. Ribbons are crushed by high energy milling ball SPEX 8000D under alcoholic environment. The SPS equipment of Labox-210 - Sinter Land was used for fabricating the Nd-Fe-B based nanocomposite bulk alloys. We used graphite die and punch with diameter of 10 mm for SPS (Fig 1).

Structure of the material was examined by X-ray diffraction (XRD) method. Magnetic properties of the materials were investigated by magnetization measurements on a pulsed field magnetometer (PFM). The demagnetization effect, which depends on shape of measuring specimens, was taken into account in determining $(BH)_{\max}$ of the materials.



Figure 1. Image of graphite die, punch and Nd-Fe-B based bulk samples prepared by SPS method.

RESULTS AND DISCUSSION

In our previous study [10], we showed that the material of $\text{Nd}_3\text{Tb}_1\text{Fe}_{71}\text{Co}_5\text{Cu}_{0.5}\text{Nb}_1\text{B}_{18.5}$ has many advantages such as low content of rare earth, high saturation magnetization M_s and its Curie temperature T_C is higher than other hard magnetic Nd-Fe-B based ones.

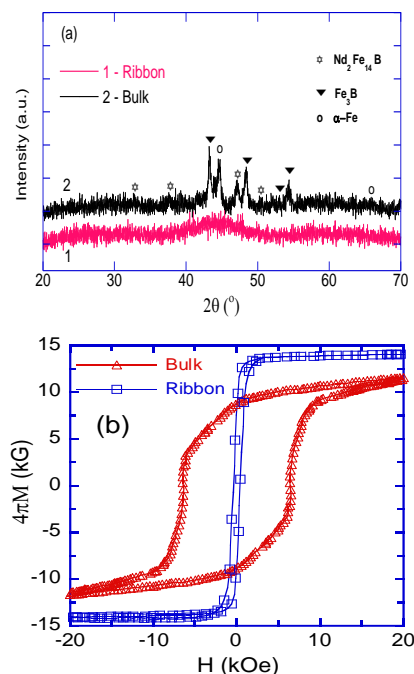


Figure 2. XRD pattern (a) and hysteresis loops (b) of the ribbon and bulk samples of $\text{Nd}_3\text{Tb}_1\text{Fe}_{71}\text{Co}_5\text{Cu}_{0.5}\text{Nb}_1\text{B}_{18.5}$.

In this study, we created alloy powder from $\text{Nd}_3\text{Tb}_1\text{Fe}_{71}\text{Co}_5\text{Cu}_{0.5}\text{Nb}_1\text{B}_{18.5}$ melt-spun ribbons and manufacture bulk alloys by SPS method. Fig. 2a presents XRD pattern of the ribbon (1) with copper wheel velocity of $v = 40 \text{ ms}^{-1}$ and bulk alloy (2) after SPS at 700°C for 5 minutes. In the XRD pattern of the ribbon, we do not see any diffraction peak of the crystalline hard phase of $(\text{Nd,Tb})_2\text{Fe}_{14}\text{B}$, but only see $\alpha\text{-Fe}$ peaks with weak intensity. However, we see that the bulk sample has sharp diffraction peaks. It proves that after SPS, the crystalline phases were formed in the bulk sample. Fig. 2b is hysteresis loop of $\text{Nd}_3\text{Tb}_1\text{Fe}_{71}\text{Co}_5\text{Cu}_{0.5}\text{Nb}_1\text{B}_{18.5}$ samples. The result shows that, the ribbon sample does not show hard magnetic behavior at room temperature. The ribbon sample has coercivity H_c less than 0.5 kOe.

In order to increase the hard magnetic property of the bulk alloy, an SPS process with varying sintering temperature (T_{sps}) and time (t_{sps}) was applied. For the mentioned alloy, the sintering temperature was varied around the crystalline temperature of the $(\text{Nd,Tb})_2\text{Fe}_{14}\text{B}$ hard magnetic phase in the range from 650 to 750°C . The sintering time was chosen as 10 minutes. Hysteresis loop of the sample sintered at 700°C is shown in Fig. 2b. The effects of sintering conditions on the magnetic properties were obviously observed. The hysteresis loop was expanded after sintering. This probably is due to the crystallization of the $(\text{Nd,Tb})_2\text{Fe}_{14}\text{B}$ phase with high magnetocrystalline anisotropy. In addition, the saturation magnetization was not achievable at high external magnetic field, even at about 30 kOe. This is due to highly anisotropic property of the sample. Hard magnetic parameters including H_c , M_r , M_s and $(BH)_{\max}$ were 6.3 kOe, 90 emu/g, 114 emu/g and 10.9 MGOe, respectively. Although H_c was as high as 6.3 kOe the $(BH)_{\max}$ was still low because of low M_r .

One of critical factors reducing the hard magnetic properties of Nd-Fe-B nanocomposites is the existence of crystalline phases of different sizes within the composites because they reduce $(BH)_{\max}$ by reducing the exchange-spring interactions. Some research groups have showed that these effects could be minimized by separation of heterovalent atoms such as Nb, Cr, Zr and V, among which Nb has been emerged to give the highest efficiency [11-12]. In addition, the separation of Nb reduces the formation of Fe-rich phases, induces the formation of domain

wall pinning sites that increases coercivity as well as the squareness of hysteresis loop. Therefore, we investigated the fabrication of nanocomposite $Nd_{10.5}Fe_{80.5}Nb_3B_6$ by SPS method.

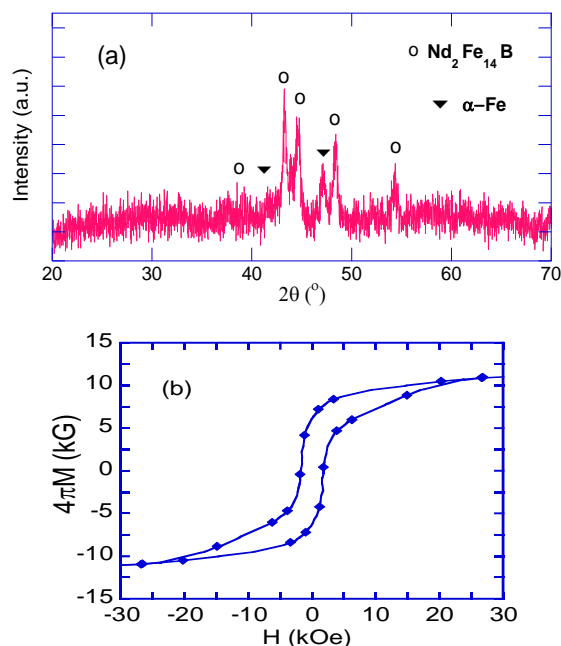


Figure 3. XRD pattern (a) and hysteresis loop (b) of the ribbon sample of $Nd_{10.5}Fe_{80.5}Nb_3B_6$.

XRD pattern of $Nd_{10.5}Fe_{80.5}Nb_3B_6$ (Fig. 3a) indicates the existence of $Nd_2Fe_{14}B$ and $\alpha-Fe$ crystalline phases. From the hysteresis loop shown in Fig. 3b, it is clearly that $Nd_{10.5}Fe_{80.5}Nb_3B_6$ exhibits low hard magnetic properties and multi-magnetic phases. Hard magnetic parameters including H_c , M_r and M_s of $Nd_{10.5}Fe_{80.5}Nb_3B_6$ were quite low to be of 1.34 kOe, 69.2 emu/g and 108.7 emu/g, respectively.

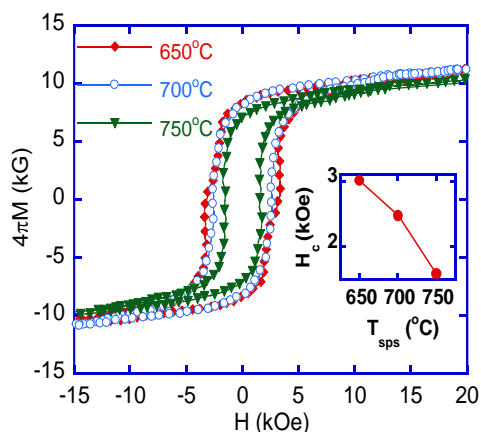


Figure 4. Hysteresis loops of the $Nd_{10.5}Fe_{80.5}Nb_3B_6$ bulk sample after SPS at various temperatures for 5 minutes. The inset shows the SPS temperature (T_{sps}) dependence of coercivity H_c .

In order to stabilize the structure as well as to increase the hard magnetic properties of the materials, we applied SPS method with varying T_{sps} from 600 to 750°C for a t_{sps} of 5 or 10 minutes. Apparently, samples became harder after sintering as shown in Fig. 4 and Fig. 5.

Table 1. H_c , M_r , M_s and $(BH)_{max}$ of the $Nd_{10.5}Fe_{80.5}Nb_3B_6$ bulk sample after SPS at 650, 700 and 750°C for 5 minutes.

T_{sps} (°C)	H_c (kOe)	M_r (emu/g)	M_s (emu/g)	$(BH)_{max}$ (MGOe)
650	3.0	83.3	103.7	9.7
700	2.5	81.4	107.4	7.5
750	1.6	70.3	100.0	4.9

When the sintering time was maintained for 10 minutes, H_c increased from 4.2 to 4.9 kOe as the sintering temperature increased from 600 to 625°C. It could be due to the size of crystalline phase reached more optimal conditions for the hard magnetic properties of materials. However, the hysteresis loop indicates multi-magnetic phase characteristics.

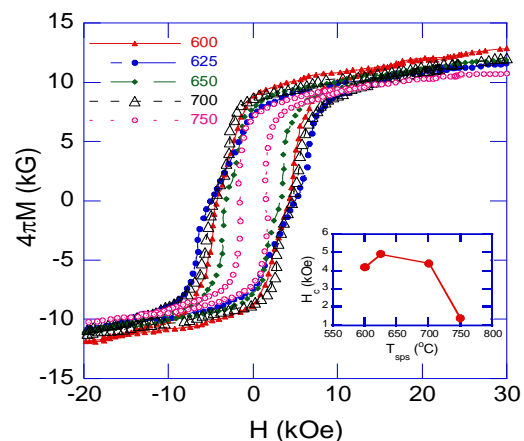


Figure 5. Hysteresis loops of the $Nd_{10.5}Fe_{80.5}Nb_3B_6$ bulk sample after SPS at various temperatures for 10 minutes. The inset shows the SPS temperature (T_{sps}) dependence of coercivity H_c .

Table 2. H_c , M_r , M_s and $(BH)_{max}$ of the $Nd_{10.5}Fe_{80.5}Nb_3B_6$ bulk sample after SPS at various temperatures for 10 minutes.

T_{sps} (°C)	H_c (kOe)	M_r (emu/g)	M_s (emu/g)	$(BH)_{max}$ (MGOe)
600	4.2	87.2	118.6	8.4
625	4.9	73.4	107.4	5.6
650	3.3	77.5	111.7	6.3
700	4.4	88.0	113.2	10.9
750	1.4	71.8	101.4	4.8

The separation of Nb increases the coercivity as well as the squareness of hysteresis loop or $(BH)_{\max}$. Bulk samples exhibited multi-magnetic phases and H_c value that decreased with increasing sintering temperature.

CONCLUSION

Successfully fabricated nanocomposite hard magnetic materials $Nd_3Tb_1Fe_{71}Co_5Cu_{0.5}Nb_1B_{18.5}$ and $Nd_{10.5}Fe_{80.5}Nb_3B_6$ in bulk form by spark plasma sintering (SPS) method. The trends of the influence of SPS process on the magnetic properties of Nd-Fe-B based nanocomposite materials were determined. Both the coercivity H_c and the maximum energy product $(BH)_{\max}$ have greatly changed with varying the SPS conditions. The H_c increases from 0.04 kOe in the ribbons to 6.3 kOe for the bulk sample of $Nd_3Tb_1Fe_{71}Co_5Cu_{0.5}Nb_1B_{18.5}$ by using the SPS conditions of $T_{\text{SPS}} = 700^\circ\text{C}$, $P_{\text{SPS}} = 100$ MPa. The hard magnetic parameters were also improved for the $Nd_{10.5}Fe_{80.5}Nb_3B_6$ alloy by using SPS. The $(BH)_{\max} > 10$ MGOe was achieved for the $Nd_{10.5}Fe_{80.5}Nb_3B_6$ bulk SPS samples. The obtained nanocomposite magnets have high density and mechanical strength, which can meet the requirements of practical applications.

Acknowledgment

This work was supported by Ministry of Education and Training (MOET) and Hanoi Pedagogical University 2 (HPU2) of Viet Nam under grant number of B.2018-SP2-11 and by the collaborative project "Development of permanent magnetic materials" between Korea Institute of Materials Science (KIMS), Korea, and Institute of Materials Science (IMS), Viet Nam.

References

- [1]. R. Coehoorn, D. B. Mooij, J. P. W. B. Duchateau, and K. H. J. Buchow, *Novel permanent magnetic materials made by rapid quenching*, Journal de Physique **49** (1988) 669-670
- [2]. E. F. Kneller, R. Hawig, *The exchange-spring magnet: a new material principle for permanent magnets*, IEEE Trans. Magn. **27** (1991) 3588-3600
- [3]. D. C. Jiles, *Recent advances and future directions in magnetic materials*, J. Acta Materialia **51** (2003) 5907-5939
- [4]. J. Lyubina, O. Gutfleisch, K. H. Müller and L. Schultz, N. M. Dempsey, *Magnetocrystalline anisotropy in L_{10} FePt and exchange coupling in FePt/Fe₃Pt nanocomposites*, J. Appl. Phys. **95** (2005) 0953-8984
- [5]. V. Pop, O. Isnard, I. Chicina, D. Givord, *Magnetic and structural properties of SmCo₅/α-Fe nanocomposites*, J. Magn. Magn. Mater. **310** (2007) 2489-2490
- [6]. Y. Q. Wu, W. Tang, M. K. Miller, I. E. Anderson, R. W. McCallum, K. W. Dennis, & M. J. Kramer, *Microanalytical characterization of multi-rare-earth nanocrystalline magnets by transmission electron microscopy and atom probe tomography*, Journal of Applied Physics, **99** (2006) 08B515
- [7]. R. Skomski R and J. M. D. Coey, *Giant energy product in nanostructured two-phase magnets*, J. Phys. Rev. B **48** (1993)15812
- [8]. W. Q. Liu, Z. Z. Cui, X. F. Yi, M. Yue, Y. B. Jiang, D. T. Zhang, J. X. Zhang and X. B. Liu, *Structure and magnetic properties of magnetically isotropic and anisotropic Nd-Fe-B permanent magnets prepared by spark plasma sintering technology*. J. Appl. Phys. **107** (2010) 09A719-09A719-3
- [9]. Y.L. Huang, Y.Wang, Y.H. Hou, Y.L. Wang, Y.Wu, S.C. Ma, Z.W. Liu, D.C. Zeng, Y. Tian, W.X. Xia, Z.C. Zhong (2016), Journal of Magnetism and Magnetic Materials **399** (2016) 175–178
- [10]. D. D. Thang, P. C. Karmaker, M.O. Rahman, S. M. Hoque, N. V. Thanh, N. M. Lam, N. V. Duong, P. T. Thanh, N. H. Yen, N. T. T. Huyen, L.T. Hung and N. H. Dan, *Influence of Tb and annealing process on magnetic properties of Nd_{4-x}Tb_xFe₇₁Co₅Cu_{0.5}Nb₁B_{18.5} RE-lean hard magnetic nanocomposites*, Proceeding The 7th International Workshop on Advanced Materials Science and Nanotechnology (2014) 144-149
- [11]. T. Miyoshi, H. Kanekiyo and S. Hiroswawa, *Effects of Nb addition on structural and magnetic properties of Fe-B/Nd₂Fe₁₄B - based nanocomposite magnets*, IEEE Trans. Magn. **41** (2005) 3865-3867.
- [12]. C. Zhongmin, Y. Q. Wu, M. J. Kramer, R. S. Benjamin, M. M. Bao and Q. H. Mei, *A study on the role of Nb in melt-spun nanocrystalline Nd-Fe-B magnets*, J. Magn. Magn. Mater. **268** (2004) 105-113.

CARBON SUPPORT MAGNETIC Fe₃O₄, Fe₂MnO₄, Fe₂NiO₄ NANOPARTICLES AS FENTON-LIKE CATALYSTS FOR REMOVAL OF ORGANIC POLLUTANT (METHYL ORANGE) IN WATER

Nguyen Thi Dung, Tran Boi An and Do Manh Huy

Institute of Chemical Technology, Vietnamese Academy of Science and Technology, 01 Mac Dinh Chi,
District 1, Ho Chi Minh, Viet Nam
Email: tranboian@gmail.com

ABSTRACT

A simple method for the preparation of magnetic precursors Fe₃O₄, Fe₂MnO₄, Fe₂NiO₄ immobilized on activated carbon from coconut shell (AC) in the presence of carbon modifying agent HNO₃ followed by calcination at 600°C have been proposed. The samples are characterized by BET, X-ray diffraction (XRD), Scanning electron microscopy (SEM), and vibrating sample magnetometer (VSM). The prepared magnetic materials exhibited high surface areas (about 1000 m²/g) with the average crystallite nano sizes (16 – 20nm). Catalytic activity has been evaluated in Fenton – like oxidation of Methyl Orange (MO). The result showed that the catalytic activity of modifying Fe₃O₄ with the Mn, Ni was higher than Fe₃O₄. After 1 hour of treatment, degradation MO reached 99 %. The leaching test at pH = 3 showed that the magnetic nanoparticles was very stable under low pH condition only very small amount of metals was found in the solution after reaction. Immobilization of magnetic nanoparticles allowed facile separation of the catalyst out of the reaction mixture by external magnetic field and can be reused.

Keywords: Magnetic activated carbon; Fenton reaction; Methyl orange; Heterogeneous catalysts; Degradation.

INTRODUCTION

Advanced oxidation processes (AOPs) based on Fenton and Fenton like catalyst seem to be a promising method for the treatment environmental pollution. However, the application of homogenous Fenton process using ferrous or ferric salts usually have some drawbacks such as: low effective pH range (<3) and the waste sludge after treatment becomes exhausted discharge resulting secondary pollution and need to be removed [1,2]. To overcome this problem, the heterogeneous Fenton- like catalysts immobilized on different supports such as zeolite, clay, activated carbon have been developed and employed [3-16]. Costa et al [17,18] reported that the presence of Co and Mn in magnetite compound to form Fe_{3-x}Co_xO₄ and Fe_{3-x}Mn_xO₄ may strongly promote the oxidation of organic contaminants.

The textile industry produces large volume of wastewater containing many organic pollutants and azo dyes are the most important contaminant found in textile wastewater. Consequently dye need to be removed from wastewater before

discharge into environment. To solve this problem many classical physical method have been developed such as coagulation/flocculation, membrane separation, adsorption [19-21] but the mechanism of this physical processes lead one point pollutant from water to the another point sludge. The organic contamination cannot to be destroyed easily. The effective Fenton-like heterogeneous catalysts are promising material for complete removal of pollutant in water.

The powdered activated carbons (AC) from coconut shell is well used in variety of areas such as support for catalysts, adsorbents in air and pollution control, purifiers in food industries [6]. However powdered AC with small size is very difficult to be separated by the traditional method like filtration because of the blockage of filters. To solve the separation problem, the activated carbon with magnetic particles is favorite material that can be used as Fenton like catalyst to remove pollutant in water and easy to be separated by external magnetic technology.

To immobilize magnetic particles on AC, several methods [18-20,22,23] have been

developed such as reducing impregnation [21], ultrasonic assisted impregnation^[24], chemical coprecipitation [23,25] but these methods usually lead to a significant decrease in the surface area and pore volume compared to pure activated carbon .

In the present work we propose a simple method for the fabrication of magnetic nanoparticles Fe₃O₄, NiFe₂O₄, MnFe₂O₄ based on activated carbons from coconut shell of Vietnam in the presence of acid promoting agent (HNO₃) to obtain high surface area material. The characterization of the materials have been investigated by different method and the catalytic activity was evaluated in Fenton-like oxidation of methyl orange.

EXPERIMENTAL

1. Materials

The commercial activated carbon powder (AC) from coconut shell was provided by Tra Vinh Company of Viet Nam. The salts of MnSO₄, Ni(NO₃)₂ and Fe(NO₃)₃ (Merck) were employed as the magnetic precursors. Nitric acid (HNO₃ 65%), was purchased from Merck. Hydrogen peroxide solution (>30% w/w) (Shanghai Chemical Company). Methyl Orange (MO) from Merck. All chemicals were used directly without purification.

2. Preparation of Carbon supported magnetic Fe₃O₄, NiFe₂O₄, MnFe₂O₄.

The carbon supported magnetic particles (20% mass of MeFe₂O₄/AC with the Me/Fe ratio of 1:2) were prepared using impregnation method as follows: The activated powdered carbon was added into 100 ml of acid solution (HNO₃ – 10%) containing Fe(NO₃)₃·9H₂O (26.12g) or mixture of Fe(NO₃)₃·9H₂O (17.21g) and Ni(NO₃)₂·6H₂O (6.19g) or Fe(NO₃)₃·9H₂O (17.49g) and MnSO₄·H₂O (3.66g). The mixture was heating at 80°C under vigorous magnetic stirring when the water was evaluated. After that the samples were treated at 600°C for 1h in the presence of nitrogen. The materials obtained are denoted as Fe₃O₄/AC, NiFe₂O₄/AC and MnFe₂O₄/AC respectively.

The XRD measurement was carried out on an XRD diffractometer (D8 Advance, Bruker, Germany). The patterns with the Cu-K α radiation ($\lambda = 1.54051 \text{ \AA}$) were recorded in the region of 2θ from 5 to 70°. SEM was carried out by Hitachi S-4800 Scanning Electron Microscope (Hitachi

Co., Japan). BET surface measurement was determined by a surface analyzer (BET-201A, US). The magnetic properties were studied with a VSP (PPMS 6000, US) at room temperature.

3. Catalytic oxidation and analytical method

The heterogeneous Fenton oxidation of MO was carried out in a cylindrical Pyrex vessel with a stirrer at the room temperature with initial pH solution of 4 dosage of solid (1 g/L). A typical run as following: the amount of catalyst was introduced into 200ml Methyl Orange solution with stirring and pH was adjusted to the desired value using HNO₃ or NaOH (0.01M). The mixture was agitated during 15 min to reach equilibrium adsorption of MO, and then desired H₂O₂ concentration (3.2mM/L) was added to the solution. Throughout the reaction, the pH reactant solution was kept constant. Samplings were taken at a given time intervals during the reaction and filtrated through 0.2 mm Millipore membrane filters. The concentration of MO was analyzed immediately using UV-VIS spectrophotometer (UV 1800 Shimadzu, Japan) with absorption band at 465 nm.

The leaching amount of Fe and Ni, Mn in the solution after reaction was determined by AAS method (Spectrometer GBC, Avanta, Australia). The catalytic performance was determined by ratio (C/C₀) concentration of MO at reaction (C) and initial time (C₀).

RESULTS AND DISCUSSION

1. Characterization of samples

The characteristics of the AC, Fe₃O₄/AC, NiFe₂O₄/AC-H and MnFe₂O₄/AC-H are given in Table 1.

Table 1. The characteristic properties of the samples

Sample	Fe ₃ O ₄ (Wt%)	MnFe ₂ O ₄ Mn/Fe (Wt%)	NiFe ₂ O ₄ Ni/Fe (Wt%)	S _{BET} (m ² g ⁻¹)	Average Crystalline size (nm)
AC	-	-	-	1039.7	
Fe ₃ O ₄ /AC	20	-	-	1000.6	19
MnFe ₂ O ₄ /AC		20 1/2	-	906.3	16
NiFe ₂ O ₄ /AC	-	-	20 1/2	964.5	18

XRD patterns for the $\text{Fe}_3\text{O}_4/\text{AC-H}$, $\text{NiFe}_2\text{O}_4/\text{AC-H}$ and $\text{MnFe}_2\text{O}_4/\text{AC-H}$ samples are reported in Fig. 1. By comparison with JCPDS file 251042 for Fe_3O_4 , 100319 for MnFe_2O_4 and 0862267 for NiFe_2O_4 , it was shown that the formation of the ferrite Fe_3O_4 at $2\theta = 18.3^\circ, 30.1^\circ, 35.5^\circ, 37.1^\circ, 43.1^\circ, 53.4^\circ, 56.9^\circ, 62.4^\circ$, Nickel ferrite NiFe_2O_4 at $2\theta = 43.5^\circ, 45^\circ, 51^\circ, 64.1^\circ$, metallic nickel at $2\theta: 43.2^\circ, 51.6^\circ, 76^\circ$ and manganese ferrite Fe_2MnO_4 spinels at $2\theta: 18.1^\circ, 29.8^\circ, 35^\circ, 36.8^\circ, 42.5^\circ, 52.8^\circ, 56.2^\circ, 61.7^\circ$ were observed in the XRD patterns. The average crystalline size calculated according to Debye-Scherrer's equation listed in Table 1 showed the values about 20 nm

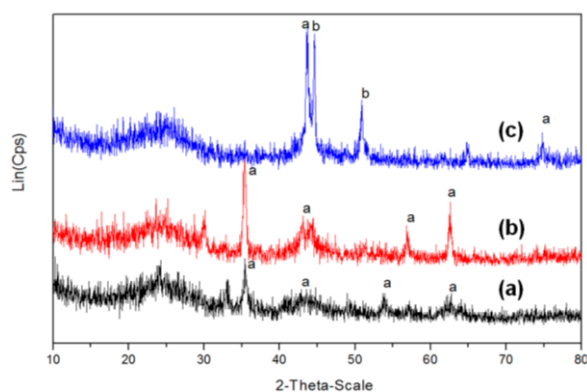


Figure 1. XRD of the samples: $\text{Fe}_3\text{O}_4/\text{AC}$ (a); $\text{MnFe}_2\text{O}_4/\text{AC}$ (b); $\text{NiFe}_2\text{O}_4/\text{AC}$ (c).

The morphologies of the samples was investigated by SEM and shown in Fig.2. Fig.2a shows the views of the pure activated carbon, fig. 2b-d shows the views of the activated carbon with magnetic particles

It can be seen that that the pure activated carbon (a) ferrite particles $\text{Fe}_3\text{O}_4/\text{AC}$ (b), nickel ferrite(c) $\text{NiFe}_2\text{O}_4/\text{AC}$ and Mn ferrite particles $\text{MnFe}_2\text{O}_4/\text{AC}$ (d) (which appear brighter) are deposited mainly on the surface of AC, only the fine particles incorporated in side the pore of AC. Some aggregates of magnetic tended to cover a parts of activated carbon they have own porosity. This observation can explain why the high surface of magnetic composite was obtained

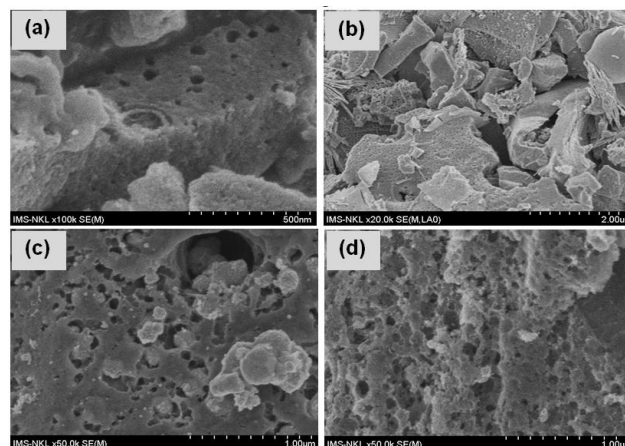


Figure 2. SEM of the AC (a); $\text{Fe}_3\text{O}_4/\text{AC}$ (b); $\text{NiFe}_2\text{O}_4/\text{AC}$ (c); $\text{MnFe}_2\text{O}_4/\text{AC}$ (d)

The typical room-temperature magnetization curve of the $\text{NiFe}_2\text{O}_4/\text{AC}$ is shown in Fig.3 (the other samples are not shown) and the magnetization properties data are listed in Table 2. The saturation magnetization (M_s), coercive field (H_c) and remanent magnetization (M_r) of the samples are lower than those reported for bare Fe_3O_4 nanoparticles ($M_s = 58.94 \text{ emu g}^{-1}$, $H_c = 160.1 \text{ Oe}$, $M_r = 7.4 \text{ emu g}^{-1}$). The low values for both H_c and M_r suggest that the magnetic materials are essentially super paramagnetic. The lower H_c and M_r values implied that they can be separated and re-dispersed easily by an applied magnetic field (Fig. 3). These results show that the magnetic materials and provide a potential advantage for the separation, recovery and reused of catalysts.

Table 2. The magnetic properties of $\text{Fe}_3\text{O}_4/\text{AC}$ and $\text{MnFe}_2\text{O}_4/\text{AC}$, $\text{NiFe}_2\text{O}_4/\text{AC}$ samples

Sample	H_c (Oe)	M_r (emu g^{-1})	M_s (emu g^{-1})
$\text{Fe}_3\text{O}_4/\text{AC}$	108	1.1	6.2
$\text{MnFe}_2\text{O}_4/\text{AC}$	155	1.2	5.8
$\text{NiFe}_2\text{O}_4/\text{AC}$	47	1.0	9.9

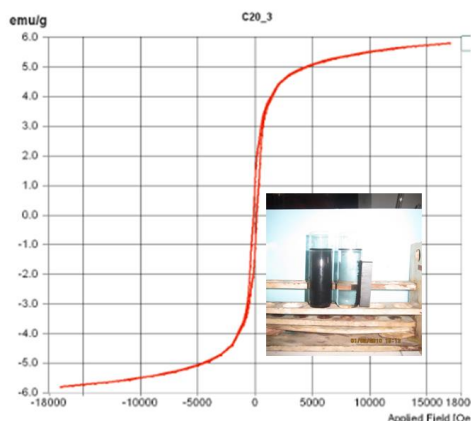


Figure 3. Hysteresis loops of NiFe₂O₄/AC.

2. Degradation of MO by magnetic supported Fenton catalyst MFe₂O₄/AC

The Fenton oxidation behavior of MO was shown in fig. 4. The absorption spectra of MO were scanned in the range 190-700 nm. From fig. 4 we can see that the characteristic absorption band of MO at 465 nm and 270 nm decreased rapidly following reaction time and the former disappeared after 120 min of reaction. This reflects, unequivocally, the breakdown in both the -N=N- bond and the conjugated π* systems.

The catalytic oxidation of MO was carried out on the magnetic materials. The result is shown in fig. 5. It is indicated that MO degradation efficiency for the both modified Fenton MnFe₂O₄/AC and NiFe₂O₄/AC catalysts was higher than Fe₃O₄/AC during reaction time and reached nearly 99 % after 1h, while for the Fe₃O₄/AC it was only about 45%. This result is in agreement with Costa et al [16] who found that the introduction of Ni and Mn into magnetite structure to form Ni_xFe_{3-x}O₄ and Mn_xFe_{3-x}O₄ may strongly promote both the H₂O₂ decomposition and the degradation of organic compounds in aqueous medium.

Comparison the performance activity between nickel and manganese promoter in magnetic material indicated that nickel modifier metal demonstrated more effective than manganese. The reason for the increase in activity of the modifying NiFe₂O₄/AC-H is not clear, but according to Costa et al [17,18] it may be possible cause by electron transfer processes within the MeFe₂O₄/AC-H particles during the reaction. Magnetite is a high conductivity semiconductor with a narrow band gap (0.1eV) and almost metallic character (ca. 10² to 10³ Ω⁻¹cm⁻¹) [26-28] which is also important for electron transport.

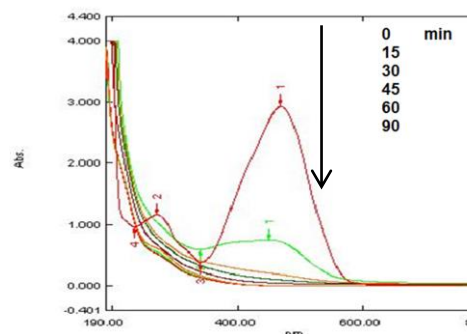


Figure 4. UV-vis spectral changes of MO degradation as a function of time in the presence of 1 g NiFe₂O₄/AC, 3.25 mL⁻¹, pH=4

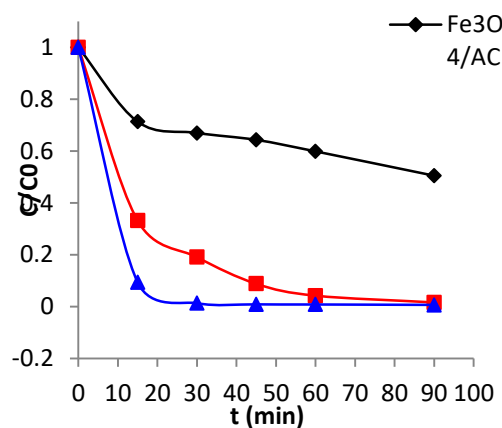


Figure 5. MO removal by adsorption and oxidation on Fe₃O₄/AC, MnFe₂O₄/AC and NiFe₂O₄/AC samples. Experimental conditions: MO 50mgL⁻¹, H₂O₂ 3.2mML⁻¹, catalyst 1gL⁻¹, T=302±1.0K, pH 4.0±0.1

The other fact can be used to explain that beside the magnetic particles, the formation of Ni⁰ metal from Ni⁺² by CO group on the AC at high temperature has been occurred. The presence of Ni⁰ promoted the electron transfer processes from Ni⁰ to Fe⁺³ to obtain Fe⁺²_{surf}



3. Stability of catalyst

After each experiment, the catalyst was separated from the solution by filtration, washed with deionized water and the solution was analyzed for the iron nickel and Mn ions. However the concentrations of leached iron,

nickel and manganese after 2 h of the reaction in our experimental condition were found to be only about 0.47 mg L⁻¹ and 0.30 mg L⁻¹, 0.52 mg L⁻¹ respectively. Therefore the MO degradation is considered as, essentially, a heterogeneous Fenton reaction.

CONCLUSION

Magnetic MFe₂O₄ (M: Ni, Mn) nanoparticles supported on activated carbons from coconut shell) have been prepared in the presence of carbon modifying agent HNO₃ followed by calcinations at 600°C exhibit high surface areas with the super paramagnetic properties. The catalytic activity of the materials in Fenton oxidation of methyl orange showed that for NiFe₂O₄/AC-H and MnFe₂O₄/AC-H the catalytic activity was higher than Fe₃O₄/AC-H. After 2h of treatment, degradation of MO reached 100 %. The leaching test at pH=4 indicated the metals ions were still stay on the AC-H, only very small amount of Fe⁺³, Ni⁺² Mn⁺² was found in the solution. It indicated that the magnetic activated carbon as heterogeneous Fenton catalyst was very stable under studied condition. The magnetic behavior of the samples provided the advantage for the separation, recovery and reuse by external magnetic field.

Acknowledgment

The Authors thank the IWNA 2019 for organizing this conference which is a chance for science discussion and learn more experience in research study.

References

- [1]. Kuznetsova, E.V., Savinov, E.N., Vostrikova, L.A. and Parmon, V.N., *Heterogeneous catalysis in the Fenton-type system FeZSM-5/H₂O₂*, Appl. Catal. B: Environ., **51** (2004) 165-170 .
- [2]. Caudo, S., Centi, G., Genovese, C. and Perathoner, S., *Homogeneous versus heterogeneous catalytic reactions to eliminate organics from waste water using H₂O₂*, Top. Catal., **40** (2006) 207-219.
- [3]. Fajerwerg, K., Castan, T., Foussard, J.N., Perrard, A. and Debellefontaine, H., *Influence de quelques paramètres opératoires sur l'oxydation du phénol par le peroxyde d'hydrogène en présence d'une zéolithe Fe-ZSM-5 dependency on some operating parameters during wet oxidation of phenol by hydrogen peroxide with Fe-ZSM-5 Zeolite*, Environ. Technol., **21**,(2000) 337-344 .
- [4]. Centi, G., Perathoner, S., Torre, T. and Verduna, M.G., *Catalytic wet oxidation with H₂O₂ of carboxylic acids on homogeneous and heterogeneous Fenton-type catalysts*, Catal. Today, **55**, (2000) 61-69.
- [5]. Centi, G., Ciambelli, P., Perathoner, S. and Russo, P., *Environmental catalysis: trends and outlooks*, Catal. Today, **75**, (2002)3-15 .
- [6]. Perathoner, S. and Centi, G., *Wet hydrogen peroxide catalytic oxidation (WHPCO) of organic waste in agro-food and industrial streams*, Top. Catal., **33**, (2005) 207-224 .
- [7]. Tekbas, M., Yatmaz, H. C. and Bektas, N., *Heterogeneous photo-Fenton oxidation of reactive azo dye solutions using iron exchanged zeolite as a catalyst*, Micropor. Mesopor. Mater., **115**, (2008) 594-602 .
- [8]. Kasiri, M.B., Aleboyeh, H. and Aleboyeh, A., *Degradation of Acid Blue 74 using Fe-ZSM5 zeolite as a heterogeneous photo-Fenton catalyst*, Appl. Catal. B: Environ., **84** (2008) 9-15 .
- [9]. Guo, J. and Al-Dahhan, M., *Catalytic wet oxidation of phenol by hydrogen peroxide over pillared clay catalyst*, Ind. Eng. Chem. Res., **42**, (2003) 2450-2460.
- [10]. Feng, J., Hu, X. and Yue, P.L., *Effect of initial solution pH on the degradation of Orange II using clay-based Fe nanocomposites as heterogeneous photo-Fenton catalyst*, Water Res., **40** (2006) 641-646.
- [11]. Chen, J. and Zhu, L., *Heterogeneous UV-Fenton catalytic degradation of dyestuff in water with hydroxyl-Fe pillared bentonite*, Catal. Today, **126** (2007) 463-470.
- [12]. León, M. A. D., Castiglioni, J., Bussi, J. and Sergio, M., *Catalytic activity of an iron-pillared montmorillonitic clay mineral in heterogeneous photo-Fenton process*, Catal. Today, **133-135**,(2008) 600-605 .
- [13]. Chen, Q., Wu, P., Li, Y., Zhu, N. and Dang, Zh., *Heterogeneous photo-Fenton photodegradation of reactive brilliant orange X-GN over iron-pillared montmorillonite under visible irradiation*, J. Hazard. Mater., **168**(2009) 901-908.
- [14]. Jose, J., John, M., Gigimol, M.G. and Mathew, B., *Synthesis characterization*

- and catalytic activity of crosslinked poly(*N*-vinyl-2-pyrrolidone acrylic acid) copolymer-metal complexes, *J. Appl. Polym. Sci.*, **90** (2003) 895-904.
- [15]. Baldrian, P., Cajthaml, T., Merhautová, V., Gabriel, J., Nerud, F., Stopka, P., Hrubý, M. and Beneš, M.J., *Degradation of polycyclic aromatic hydrocarbons by hydrogen peroxide catalyzed by heterogeneous polymeric metal chelates*, *Appl. Catal. B*, **59** (2005) 267-274.
- [16]. Kuznetsova, E.V., Savinov, E.N., Vostrikova, L.A. and Echevskii, G.V., *The catalytic and photocatalytic oxidation of organic substances using heterogeneous Fenton-type catalysts*, *Water Sci. Technol.*, **49** (2004) 109-115 .
- [17]. Costa, R.C.C., Fatima, M., Lelis, F., Oliveira, L.C.A., Fabris, J.D., Ardisson, J.D., Rios, R., Silva, C.N. and Lago, R.M., *Remarkable effect of Co and Mn on the activity of Fe_{3-x}M_xO₄ promoted oxidation of organic contaminants in aqueous medium with H₂O₂*, *Catal. Commun.*, **4**, (2003) 525-529 .
- [18]. Costa, R.C.C., Lelis, M.F.F., Oliveira, L.C.A., Fabris, J.D., Ardisson, J.D., Rios, R., Silva, C.N. and Lago, R.M., *Novel active heterogeneous Fenton system based on Fe_{3-x}M_xO₄ (Fe Co Mn Ni): The role of M²⁺ species on the reactivity towards H₂O₂ reactions*, *J. Hazard. Mater.*, **129** (2006)171-178.
- [19]. Rudge, S.R., Kurtz, T.L., Vessely, C.R., Catterall, L.G. and Williamson, D.L., *Preparation characterization and performance of magnetic iron-carbon composite microparticles for chemotherapy*, *Biomaterials*, **21** (2000) 1411-1420 .
- [20]. Fuertes, A.B. and Tartaj, P., *A facile route for the preparation of superparamagnetic porous carbons*, *Chem. Mater.*, **18**, 1675-1679 (2006).
- [21]. Safarik, I., Nymburska, K. and Safarikova, M., *Adsorption of water-soluble organic dyes on magnetic charcoal*, *J. Chem. Tech. Biotechnol.*, **69**, (1997) 1-4.
- [22]. Oliveira, L.C.A., Rios, R.V.R.A., Fabris, J.D., Garg, V., Sapag, K. and Lago, R.M., *Activated carbon/iron oxide magnetic composites for the adsorption of contaminants in water*, *Carbon*, **40** (2002) 2177-2183.
- [23]. Zhang, G., Qu, J., Liu, H., Cooper, A.T. and Wu, R., *CuFe₂O₄/activated carbon composite: A novel magnetic adsorbent for the removal of acid orange II and catalytic regeneration*, *Chemosphere*, **68** (2007) 1058-1066.
- [24]. Liao, Q., Sun, J. and GAO, L., *Degradation of phenol by heterogeneous Fenton reaction using multi-walled carbon nanotube supported Fe₂O₃ catalysts*, *Colloids Surf. A: Physicochem. Eng. Aspects*, **345** (2009) 95-100.
- [25]. Masala, O. and Seshadri, R., *Magnetic properties of capped soluble MnFe₂O₄ nanoparticles*, *Chem. Phys. Lett*, **402** (2005)160-164.
- [26]. Bard, A.J. and Leland, J.K., *Photochemistry of colloidal semiconducting iron oxide polymorphs*, *J. Phys. Chem.*, **91** (1987) 5076-5083.
- [27]. White, A.F., *Heterogeneous electrochemical reactions associated with oxidation of Ferrous oxide and silicate surfaces*, *Rev. Miner.*, **23** (1990) 467-459.
- [28]. Fan, J., Guo, Y., Wang, J. and Fan, M., *Rapid decolorization of azo dye methyl orange in aqueous solution by nanoscale zerovalent iron particles*, *J. Hazard. Mater.*, **166** (2009) 904-910 .

PREPARATION OF NANOCOMPOSITE PANi@GO-HT VIA DIRECTLY POLYMERIZATION FROM ANILINE

Boi An Tran^{1,3}, **Thanh Thao Phan**^{1,3} and **Xuan Hang To Thi**^{2,3}

¹ Institute of Chemical Technology, Vietnam Academy of Science and Technology,
1 Mac Dinh Chi, Ben Nghe Ward, District 1, Ho Chi Minh City, Vietnam;

² Institute for Tropical Technology, Vietnam Academy of Science and Technology,
18 Hoang Quoc Viet, Cau Giay, Hanoi, Viet Nam

³ Graduate University of Science and Technology,
18 Hoang Quoc Viet, Cau Giay, Hanoi, Viet Nam

Email: tranboian@gmail.com

ABSTRACT

A series of nanocomposite materials of polyaniline on matrix of graphene oxide-hydrothermalite (PANi@GO-HT) was prepared with various mass ratio of monomer aniline and carrier GO-HT. The synthesized PANi@GO-HT nanocomposites were characterized by FTIR, X-ray diffraction (XRD), UV-VIS spectrometer and scanning electrical microscopy (SEM). The results showed that aniline was absorbed on the surface of GO-HT and emeraldine salt of PANi was directly polymerized on the surface of GO via oxidation polymerization method.

Keywords:

INTRODUCTION

In recent years, nano-composite has been the attractive materials for massive applications: environment, medical, corrosion inhibition.... The nano-composite from graphene oxide-hydrothermalite (GO-HT) has been investigated for preparation method as fabrication [1], membrane used as nano-filtration for water desalination [2-3], co-precipitating HT in the presence of GO and used for corrosion inhibitor [4,5,6], gas adsorption [7,8,9], water pollution treatment [10,11,12], catalyst [13,14,15] and energy applications [16,17]. Similarly, nano-composite of PANi@HT is also an attractive materials for widely applications. PANi@HT was used in water treatment due to its high specific area and high stability in various environment, so that PANi@HT can charge the large ion such as Cr⁺, gas sensor, corrosion inhibitor and water treatment [18-23]. For the above advantages of GO, HT and PANI, in this paper, we focus to the matrix from three of GO, HT and PANI for nano-composite. HT was prepared using co-precipitation method in the presence of GO to form GO-HT. Then aniline was immobilized on GO-HT via either adsorption or anion exchange into the interlayer, and the polymerization will perform on the surface of

GO-HT to form nano-composite PANi@GO-HT

EXPERIMENTAL

1. Materials

All chemicals used in this research such as graphite, KMnO₄, Zn(NO₃)₂·6H₂O, Al(NO₃)₃·9H₂O, ammonium persulphate, aniline...were synthesis grade and purchased from MERCK.

2. Preparation of GO-HT

Graphene oxide (GO) was prepared using Hummer method with the announced before [12]. GO-HT was synthesized via co-precipitation of mixture of zinc nitrate and aluminum nitrate with the presence of GO. In details, 6.8 g of Zn(NO₃)₂·6H₂O and 13.6 g of Al(NO₃)₃·9H₂O was dissolved in 50ml de-ionized water. 0.5g of GO was dispersed in 100 ml de-ionized water and the GO solution was sonicated at 400 kHz for about 1 hour and then vigorously magnetic stirred for about 30 minutes. The mixture of zinc-aluminum salt was dropped into the GO solution for co-precipitation. The pH of co-precipitation was controlled at 9.5 - 10 using NaOH 0.2 M. The suspension was centrifuged and

washed with distilled water until neutralized. GO-HT was then vacuum dried at 50°C for 6 hours.

3. Preparation of PANi@GO-HT

50 mg of HT-GO was dispersed in 50ml of ethanol and sonicated for 2 hours, then vigorously magnetic stirred for about 30 minutes in ice bath. Aniline was dissolved in 25ml of 0.5M tartaric acid and APS was dissolved in rest 25ml of 0.5M tartaric. Monomer solution was drop-wise into HT-GO suspension for absorption. Then, APS solution was drop-wised into reaction for polymerization of aniline. The mixture turn from light yellow to blue, and finally turned to dark green solution. The polymerization was keep in ice bath at 2 - 4°C for 12 hours. Then the nano composite was washed with mixture of ethanol: deionized water (50:50). The product was then dried in vacuum at 60°C for 6 hours.

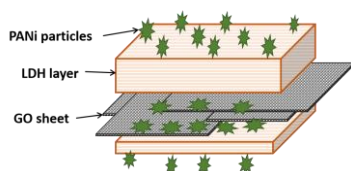


Figure 1. Simulation of nanocomposite PANi@GO-HT.

4. Characterization

Nano-composite PANi@HT-GO was characterized by Fourier transfer IR (KBr, wavelength from 400 - 4000 cm^{-1} , 32 scans, step 8 cm^{-1}), X-ray diffraction, UV-VIS (wavelength from spectrometer and SEM (JEOL).

RESULTS AND DISCUSSION

1. FTIR analysis

Chemical characterization of PANi, GO-HT and PANi@GO-HT are showed in the FT-IR spectra (figure 1). Graphene oxide spectra with strong absorptions at 1716; 1616; 1384; 1053 were presented for -C=O in -COOH group, -C=C- in benzene ring, -C-OH and -C-O-C- respectively. In the FTIR spectra of LDH-GO, there are blue-shifts from 1716 cm^{-1} to 1562 cm^{-1} , 1616 cm^{-1} to 1357 cm^{-1} because of the increase of bond length due to the interactive of GO and LDH. Besides, the bands at 767 and 609 cm^{-1}

referred to the Zn-O and Al-O vibrations which represented the basic lattice of HT.

PANi presented with the strong absorptions at 1558; 1485; 1288; 1130 and 875 cm^{-1} , which were assigned to the C=C in quinonoid and benzenoid ring structure (in-plane and out-of plane bending), C-N in aromatic amine, N=Q=N stretching band, and benzene ring respectively. Through the whole observation, all the above characteristic peaks were appeared in the PANi/GO-HT, indicating that the PANi was successfully attached to the surface of GO-HT. In the other hand, the band at about 3236 cm^{-1} was assigned to the N-H hydrogen bond presented on the GO-HT surface, which also implied the successful composite with PANi.

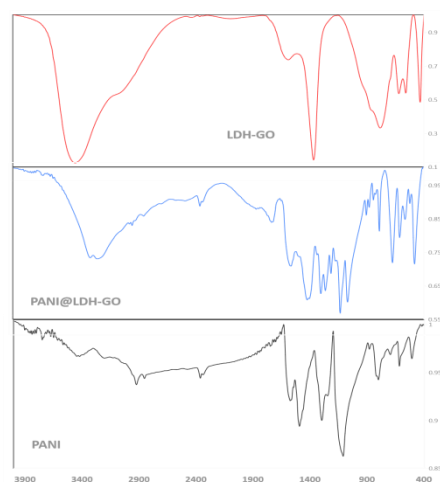


Figure 2. FTIR spectra of (a) GO-HT; (b) PANi@GO-HT and (c) PANI.

2. UV-VIS spectra

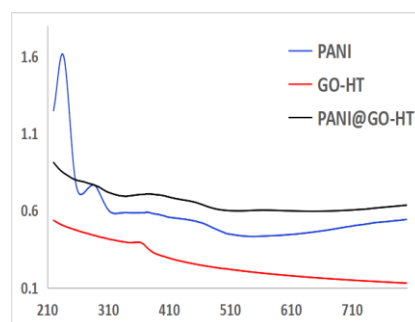


Figure 3. UV-VIS spectra of PANi, GO-HT and PANi@GO-HT.

The UV-VIS spectra showed in Figure 3 has figured out the presence of polyaniline on the carrier GO-HT through the transition of sharpened peak at 280 nm^{-1}

and the broad peak at 380 nm^{-1} finally the shoulder at 495 nm^{-1} . The disappearance of peak at 256 nm^{-1} of PANi on the spectra of PANi@GO-HT can be caused by the linking of PANi with GO-HT make the π - π disappeared.

3. SEM image

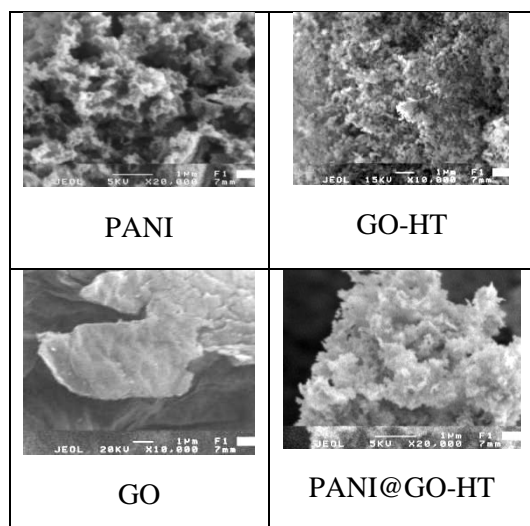


Figure 4. SEM images of (a) polyaniline, (b) Graphene oxide, (c) GO-HT and (d) PANi@GO-HT.

The morphology of materials were observed by SEM images in figure.. In specifically, GO was observed as sheets due to 2D materials structure; PANi was observed as flower flake shape; and LDH-GO was observed as composition of LDH flaky grew under sheet formation trend. The SEM image of PANi@LDH-GO showed the flower flake of PANi cover the structure of LDH-GO as mentioned above.

4. X-ray diffraction

The composition of the material and the structure was determined by the XRD patterns, which were shown in figure 4. As the results, the characteristic diffraction peak of LDH-GO is exactly the same with diffraction peak of LDH [] and appears at 2θ of 11.70° (003), 23.56° (006), 34.58° (012), 39.56° (015), 46.78° (018), 60.26° (110), and 61.64° (113), which is attributed to the formation of nanoplates and the hydroxide layered structure combined with graphene oxide sheets. The spectrum of PANi shows that it has diffraction peak at $2\theta = 14.10^\circ$, 18.38° , 21.06° , 26.84° , and 28.78° , which indicated that tartaric acid doped polyaniline had a certain degree of crystallinity.

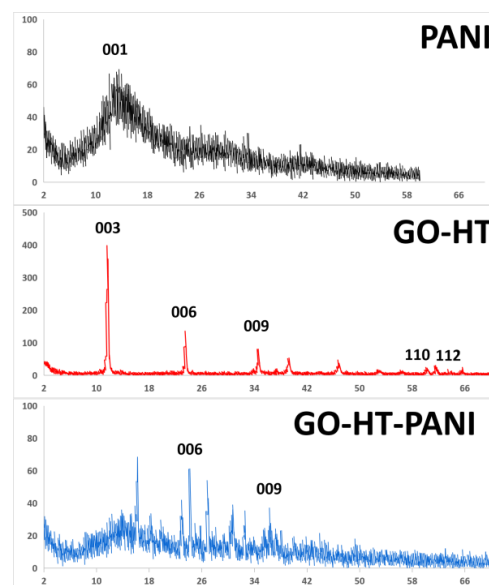


Figure 5: XRD pattern of (a) PANi (b) GO-HT and (c) PANi@GO-HT.

The XRD pattern of PANi@GO-HT had a broad and weak diffraction peaks at about 13.78° and shaped and strong diffraction about 23.04° , 26.84° and 30.42° owing to the PANi chain. In addition, the peak at $2\theta = 63.16^\circ$ could also be obtained, which was due to the (110) reflection corresponding to the GO-HT structure being maintained. The transition of (003) reflection from 11.68° to 16.24° may be accounted by the intercalation of polyaniline into interlayer anions during the synthesis process, and the presence of polyaniline with functional groups in the interlayer give stronger bonds between PANi and GO-HT.

CONCLUSION

In this research, nanocomposite PANi@GO-HT was completely prepared using directed polymerization of polyaniline on GO-HT. The results indicated the layer structure of GO-HT is still maintained and polyaniline grew up on the surface of this carrier with the strong bond between those particles.

Acknowledgment

The Authors thank the IWNA 2019 for organizing this conference which is a chance for science discussion and learn more experience in research study.

References

- [1]. Feifei Wang, Ting Wang, Shiguo Sun, Yongqian Xu, Ruijin Yu, Hongjuan Li, *One-step synthesis of Nickle Iron-layered double hydroxide/reduced graphene oxide/carbon nanofibres composite as electrode materials for asymmetric supercapacitor*, Scientific Reports **8** (2018).
- [2]. Xue Wang, Huixian Wang, Yuanmng Wang, Jian Gao, Jindun Liu, Yatao Zhang, *Hydrotalcite/graphene oxide hybrid nanosheets functionalized nanofiltration membrane fo desalination*, Desalination **451** (2019) 209-218.
- [3]. Yeit Haan Teow, Abdul Wahab Mohammad, *New generation nanomaterials for water desalination: A review*, Desalination **451** (2019) 2-17.
- [4]. Thuy Duong Nguyen, Boi An Tran, Ke Oanh Vu, Anh Son Nguyen, Anh Truc Trinh, Gia Vu Pham, Thi Xuan Hang To, Minh Vuong Phan, Thanh Thao Phan, *Corrosion protection of carbon steel using hydrotalcite/graphen oxide nanohybrid*, Journal of coating technology and research (2018).
- [5]. Thuy Duong Nguyen, Boi An Tran, Thanh Thao Phan, Anh Son Nguyen, Ke Oanh Vu, Anh TRuc Trinh, To Thi Xuan Hang, Marie-Georges Olivie, *Influence of graphene oxide on the corrosion inhibition effect of hydrotalcite loaded with 2 - benzothiazolthio-succinic acid*, Vietnam journal of science and technology **56** NO.3B (2018).
- [6]. Luchun Yan, Meng Zhou, Xiaolu Pang, Kewei Gao. *One-Step in Situ Synthesis of Reduced Graphene Oxide/Zn–Al Layered Double Hydroxide Film for Enhanced Corrosion Protection of Magnesium Alloys*. Langmuir **35** No.19 (2019) 6312-6320.
- [7]. Haslinda Binti Mohd Sidek, Yun Kyung Jo, In Young Kim, and Seong-Ju Hwang. *Stabilization of Layered Double Oxide in Hybrid Matrix of Graphene and Layered Metal Oxide Nanosheets: An Effective Way To Explore Efficient CO2 Adsorbent*. The Journal of Physical Chemistry C **120** No.41 (2016) 23421-23429.
- [8]. Diana Iruetagoiena, Milo S. P. Shaffer, and David Chadwick. *Layered Double Oxides Supported on Graphene Oxide for CO2 Adsorption: Effect of Support and Residual Sodium*, Industrial & Engineering Chemistry Research **54** No.26 (2015) 6781-6792.
- [9]. Ainara Garcia-Gallastegui, Diana Iruetagoiena, Veronica Gouvea, Mohamed Mokhtar, Abdullah M. Asiri, Sulaiman N. Basahel, Shaeel A. Al-Thabaiti, Abdulrahman O. Alyoubi, Milo S. P. Shaffer, *Graphene Oxide as Support for Layered Double Hydroxides: Enhancing the CO2 Adsorption Capacity*, Chemistry of Materials **24** 23 (2012) 4531-4539
- [10]. X.-L. Wu, L. Wang, C.-L. Chen, A.-W. Xu, X.-K. Wang, *Water-dispersible magnetite-graphene-LDH composites for efficient arsenate removal*, J.Mater. Chem., **21** (2011) 204-213
- [11]. X. Yuan, Y. Wang, J. Wang, C. Zhou, Q. Tang, X. Rao, *Calcined graphene/MgAl-layered double hydroxides for enhanced Cr(VI) removal*, Chem. Eng. J., **221** (2013),
- [12]. Tran Boi An, Pham Thi Kim, Nguyen Xuan Dung, Nguyen Thi Dung, Phan Thanh Thao, *Preparation and characterization of nanocomposite layered double hydroxide/graphene oxide and the absorption of methyl orange*, Vietnam Journal of of Chemistry **56** No.3E12 (2018) 123-127
- [13]. M. Kaleesh Kumar, K. C. Swaathini, Niki S. Jha, Shailendra K. Jha, *Facile In-Situ Electrosynthesis and High Electrocatalytic Performance of Interconnected Layered Double Hydroxides/Graphene Hybrids for Dopamine Oxidation: a Comparative Study*, Electroanalysis (2018).
- [14]. Mayra G. Álvarez, Didier Tichit, Francesc Medina, Jordi Llorca. *Role*

- of the synthesis route on the properties of hybrid LDH-graphene as basic catalysts*, Applied Surface Science **396** (2017) 821-831.
- [15].Nesreen S. Ahmed, Robert Menzel, Yifan Wang, Ainara Garcia-Gallastegui, Salem M. Bawaked, Abdullah Y. Obaid, Sulaiman N. Basahel, Mohamed Mokhtar, *Graphene-oxide-supported CuAl and CoAl layered double hydroxides as enhanced catalysts for carbon-carbon coupling via Ullmann reaction*, Journal of Solid State Chemistry **246** (2017) 130-137.
- [16].Long Huang, Bingchuan Liu, Huijie Hou, Longsheng Wu, Xiaolei Zhu, Jingping Hu, Jiakuan Yang, *Facile preparation of flower-like NiMn layered double hydroxide/reduced graphene oxide microsphere composite for high-performance asymmetric supercapacitors*, Journal of Alloys and Compounds **730** (2018) 71-80.
- [17].G. Bishwa Bidita Varadwaj, Vincent O. Nyamori, *Layered double hydroxide- and graphene-based hierarchical nanocomposites: Synthetic strategies and promising applications in energy conversion and conservation*, Nano Research **9** No.12 (2016) 3598-3621.
- [18].Kairou Zhu, Yang Go, Xiaoli Tan and Changlun Chen, *Polyaniline-modified Mg/Al Layered double hydroxide composites and their application in efficient removal of Cr(VI)*, ACS Sustainable Chemistry & Engineering (2016)
- [19].Dong Mei Xu, Mei Yu Guan, Qing Hong Xu, Ying Guo, *Multilayer films of layered double hydroxide/polyaniline and their ammonia sensing behavior*, Journal of Hazardous Materials **262** (2013) 64-70
- [20].D. Sudha and A. Ramasubbu, *Synthesis and characterization of Zn-Al, Mg-Al layered double hydroxides intercalated polymer nanocomposites*, Asian Journal of Chemistry **25** (2013) S120-S124.
- [21].Peng Du, Shihui Qiu, Chengbao Liu, Guangzhou Liu, Haichao Zhao, Liping Wang, *In situ polymerization of sulfonated polyaniline in layered double hydroxide host matrix for corrosion protection*, New Journal of Chemistry (2018)
- [22].Burak Kutlu, Andreas Leuteritz, Regine Boldt, Dieter Jehnichen, Udo Wagenknecht, Gert Heinrich, *PANI-LDH prepared by polymerization-adsorption method and processing to conductive compounds*, Applied Clay Science **72** (2013) 91-95.
- [23].Xiao Zhou Li, Shui Ren Liu, Ying Guo, *Polyaniline-intercalated layered double hydroxide: synthesis and properties for Humidity sensing*, Royal Society of Chemistry Adv. (2016).

FIRST-PRINCIPLE STUDY OF THE ADSORBED HYDROGEN ON THE TWO-DIMENSIONAL CONFINED GERMANENE

Tran Thi Thu Hanh *, Nguyen Minh Phi, Nguyen Van Hoa, Nguyen Hoang Giang, Nguyen Ngoc Thien, Dong Cao Hieu

¹HCM University of Technology, Vietnam National University-Ho Chi Minh City, 268 Ly Thuong Kiet, 14 Ward, 10 District, Ho Chi Minh City, Vietnam

Email: thuhanhsp@gmail.com

ABSTRACT

We investigate the surface reaction of hydrogen atoms on germanene, a two-dimensional hexagonal germanium allotrope [1], using density functional theory. An isolated 2D Ge of a (5×3) unit cell is constructed from MD simulation [2]. The adsorptions of H atom on various sites (top, bridge, center) are investigated using SIESTA calculation. The most stable adsorbed sites are the top sites, and the adsorption energy of that H atom on the 2D germanene is about -1.833 eV.

Keywords: *Hydrogen adsorption; 2D Germanene; Adsorption energy; DFT*

INTRODUCTION

Over the past few years, a series of studies have been carried out for 2D graphene and its ribbon because of its unique properties. The planar honeycomb structure lead to the unusual electronic properties of graphene[1]. It has been shown that the 2D structure of graphene is true stable [2,5,6]. Many scientists predict that the other group IV elements in the periodic table may also have a stable honeycomb structure, so they have conducted studies for these materials [7,8,9].

Among the group IV elements, due to the existence of spin-orbit gap, germanene is a promising material for a quantum-spin Hall effect, unlike graphene [10,11]. Germanene is

formed from a Ge atom layer in the buckled honeycomb lattice. Using first-principle calculations, the stability of germanene is predicted, the interatomic Ge-Ge bond length has been found between 2.310 and 2.443 Å with buckling of 0.737 Å [10,11].

The question is whether the adsorption of hydrogen on this surface will affect this 2D Ge structure? The hydrogen storage capacity of this material is really high to make the coating in gas containers or not? So based on this latest 2D Ge structure, we conduct research on the reaction of hydrogen atoms on the surface of this newly created material.

CALCULATION METHOD

The SIESTA simulation software [16,17] was used to calculate the adsorption of hydrogen on the 2D germanene. The generalized gradient approximation (GGA) to the exchange-correlation function due to Perdew, Burke, and Ernzerhof (PBE) was used in the DFT calculation. The adsorption sites of hydrogen atoms on the 2D Ge are shown in Figure 2. The basic SIESTA calculation parameters were: the DZP (double-zeta polarized) basic set, the mesh-cutoff of 200 Ry, the Fermi Dirac function with the electronic temperature of 300 K for the Brillouin zone integrations. The energy shift for the Ge is 200 meV, which determines the cutoff radius per angular momentum channel. And for the H atoms, the energy shift is 60 meV with the split norm of 0.53 for the second zeta. These

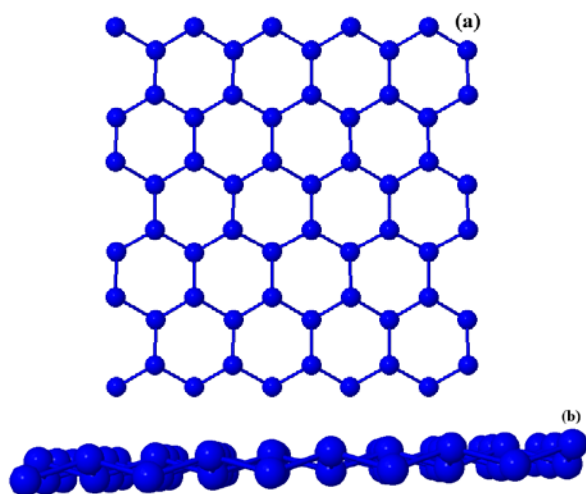


Figure 1. Top view (a) and side view (b) of the buckled Ge model from Ref. [15].

calculation parameters in SIESTA provide reasonable accuracy for previous studies [18,19]. We chose the value of 0.660 Å for the buckling height, of 2.407 Å for the in-plane

nearest-neighbor distance, and of 4.169 Å for the lattice constant, corresponding to the obtained MD data [15] to build the germanene model.

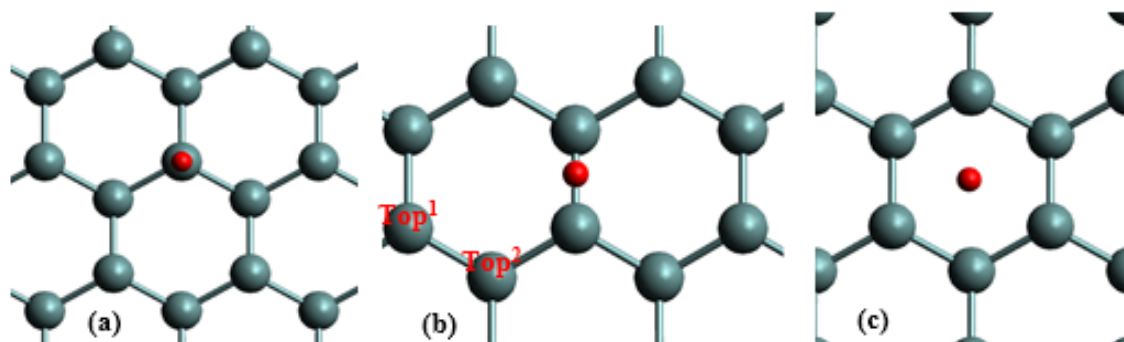


Figure 2: Possible adsorption sites of Ge atom: Top (a), Bridge (b), Center (c).

The calculation of H adsorption on 2D germanene is done through 3 main steps. First, the 2D Ge model is built for finding convergence in the SIESTA calculation with the k-point gradually increases from (4×4×1) to (13×13×1) Monkhorst Pack (MP), or from 11 to 85 k-points. Secondly, after running the SIESTA program and obtaining a relaxing Ge model, we let hydrogen atoms adsorb on different positions on the germanene surface. These locations include top, bridge and center sites (Figure 2).

Table 1. Adsorption energy (eV) of adsorbed hydrogen atom on the 2D germanene when using 5 k-points.

Unit cell	Top ¹	Top ²
(5×3)	-0.183	-1.290

RESULTS AND DISCUSSION

The theory energy calculations showed that the different absorption positions of atoms on the metal surface will give different energy values. Therefore, we calculate the total adsorption energy of system to verify possible adsorption sites of H on the 2D Ge surface. Table 1 shows the adsorption energy of model calculated by the formula:

$$E_{ads} = E_{tot}(N_H) - E_{tot}(0) - \frac{N_H}{2} E_{H_2},$$

where $E_{tot}(N_H)$ is the total energy of the N_H atoms adsorbed on the 2D Ge surface, E_{H_2} is the total energy of the isolated H_2 molecule, and E_{ads} is the adsorption energy of H on Ge.

Eads at the Top¹ is recorded as the lowest value, which means the most stable adsorption site. The hydrogen atoms on the center and on the bridge sites are not stable: the center position moves to the Top² site, and the bridge position moves to the Top¹ site (Fig. 2).

To verify the correctness of the selected parameters in the DFT calculation, the energy convergence is calculated in detail in this study. When the energy value is converged at one point, the selected parameters are highly accurate and can be used as a comparison with experiment. The purpose of examining various number of k-points is to find the value of the calculated parameters at which the energy converges. The calculations is done using (5×3) lateral unit cell with different k-points, on which one H atom is adsorbed on the most stable sites: on the Top¹ and the Top² sites. Figure 3 shows the adsorption energies of hydrogen on 2D germanene with the k-point changed from (3×3×1) to (12×21×1) MP grids.

Based on Figure 3, it can be seen the total energy of the H/Ge system becomes convergence when the number of k-point increases to (9×9×1) MP grids.

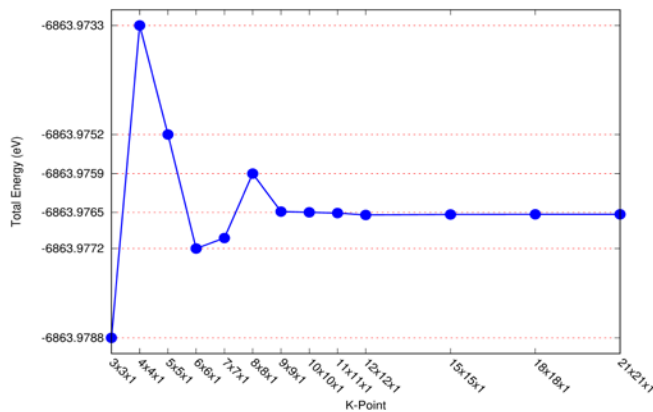


Figure 3: The total energy (eV) of the 2D germanene with different k-points.

CONCLUSION

The adsorption of hydrogen atoms on the two-dimensional confined germanene is studied using the density function theory and generalized gradient approximation. The adsorbed hydrogen is the most stable at the Top1 and Top2 sites. The convergence is observed when using the k-point of (9×9×1) MP grids.

Acknowledgment

This research is funded by Vietnam National University-Ho Chi Minh City (VNU-HCM) under grant number B2018-20-01.

References

- [1]. P. R. Wallace, Phys. Rev. **71** (1947) 622.
- [2]. K.S. Novoselov et al., Nature (London) **438** (2005) 197.
- [3]. Y. Zhang et al., Nature (London) **438** (2005) 201.
- [4]. C. Berger et al., Science **312** (2006) 1191.
- [5]. M. I. Katsnelson et al., Nature Phys. **2** (2006) 620.
- [6]. K. Geim and K. S. Novoselov, Nature Mater. **6** (2007) 183.
- [7]. K. Takeda and K. Shiraishi, Phys. Rev. B **50**, 14916 (1994).
- [8]. E. Durgun, S. Tongay, and S. Ciraci, Phys. Rev. B **72**, 075420 (2005);
- [9]. M. Zhang et al., Chem. Phys. Lett. **379**, 81 (2003).
- [10]. S. Trivedi, A. Srivastava and R. Kurchania, Journal of Computational **11** (2014) 781.

- [11]. L. Seixas, J.E. Padilha and A. Fazzio, Phys. Rev. B **89** (2018) 195403.
- [12]. L. Li, S.Z. Lu, J. Pan, Z. Qin, Y.Q. Wang and Y. Wang, Adv.Mater. **26** (2014) 4820.
- [13]. P. Bampoulis, L. Zhang, A. Safaei, R.V. Gastel and B. Poelsema, J.Appl.Phys. **26** (2014) 1.
- [14]. L. Zhang, P. Bampoulis, A. Houselt and H.J.W. Zandvliet, Appl.Phys.Lett. **107** (2015) 111605.
- [15]. N.H. Giang, T.T.H. Tran, V.V. Hoang, Mater. Res. Express **6** (2019) 086411.
- [16]. J.M. Soler, E. Artacho, J.D. Gale, A. García, J. Junquera, P. Ordejón, D. Sánchez-Portal, J. Phys.: Condens. Matter **14** (2002) 2745.
- [17]. P. Ordejón, E. Artacho, J.M. Soler, Phys. Rev. B **53** (1996) R10441.
- [18]. T.T.T. Hanh, Y. Takimoto, O. Sugino, Surf. Sci. **625** (2014) 104.
- [19]. T.T.T. Hanh, N. T. T. Hang, J. Computational Materials Science **138** (2017) 295.

THE INTERACTION OF HYDROGEN ATOMS ON THE MISSING ROW Pt(110)-(1x2) SURFACE

Tran Thi Thu Hanh*, Nguyen Van Hoa, Nguyen Minh Phi

HCM University of Technology, Vietnam National University-Ho Chi Minh City, 268 Ly Thuong Kiet, 14 Ward, 10 District, Ho Chi Minh City, Vietnam;
Email: thuhanhsp@gmail.com

ABSTRACT

The study of the hydrogen adsorption on the missing row Pt(110)-(1x2) surface in ultrahigh vacuum (UHV) was investigated. The density functional theory (DFT) combined with the approximation oscillation of H on the surface was used. When the H-coverage on the surface $\Theta_{\text{H}}=1\text{ML}$, and taking into account the quantum effect, the bond formed at the edge of the first layer (short bridge) is the most stable site. The quantum effect on adsorption model H/Pt(110)-(1x2) is significant.

Key words: hydrogen adsorption, the missing row Pt(110)-(1x2) surface, the density functional theory DFT.

INTRODUCTION

In recent years, electrochemical surface has been considered as a science that affects many different areas such as microelectronics, catalysts, fuel cells [1, 2]. In particular, the electroadsorption of H on Pt is considered as one of the intensive research models [3-12]. Because Pt has four different types of surface structures Pt(111), Pt(100), Pt(110) and Pt(110)-(1x2), there have been many studies for H adsorption on these surfaces. Gudmundsdóttir et al. and Skúlason et al. performed theoretical calculations to clarify the effects of the faces (111) and (100) [13, 14]. Then, experiment and theory were used to further study the adsorption of H on Pt(110) and Pt(110)-(1x2) surfaces [15 - 20]. Especially for Pt(110)-(1x2) surface, many different research results on the stable adsorption position of H on the surface were given: the most stable trough site was shown in the studies using LEED (low-energy electron diffraction) and vibrational spectroscopy measurements [21 - 23]. Meanwhile, Zhang et al. and Minca et al. used LEED experiment and DFT calculation methods and found the most stable position at short bridge site for small coverage $\sim 0.5\text{ML}$ [17, 18]. Gudmundsdóttir et al. confirmed again the most stable site is short bridge site at low coverage when using TPD (temperature-programmed desorption) and DFT calculation. However, at high coverage, the strongest sites are on the micro-facet or in the trough [24].

The binding position of H on the surface of Pt plays an important role in the electrochemical surface research, but the difference in the binding energy of the stable sites is quite small, so it is necessary to study the phonon effect of H on the surface. In the previous research for H/Pt(111) model, we have succeeded in studying phonon effects on systems based on dft calculations [7]. We have determined that the adsorption energy of H on Pt(111) surface at the top and fcc sites is the same at low H coverage, while at high coverage, the fcc position is more dominant [7]. It is also a motivation for us to continue to study the phonon effect of H on the missing row Pt (110) - (1x2) surface.

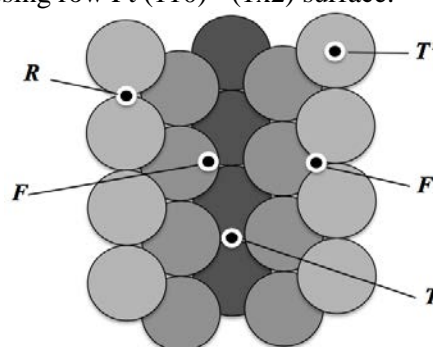


Figure 1. The model of Pt(110)-(1x2) surface onto which H atoms were adsorbed. R is the short bridge on the ridge site, F is the on-top on the micro facet, F' is the hcp hollow site, T' is the on-top on the ridge site, and T is the long bridge site in the trough.

The first goal in this study is to determine the H adsorption energy corresponding to the

position on the surface of Pt (110)-(1×2) surface. Calculations of isothermal adsorption for H/Pt(110)-(1×2) system were done using SIESTA simulation software. With careful inspection of the initial parameters used in the calculation by checking the convergence of layers and k-points, the energy data obtained from our DFT calculation is highly accurate. Then, H was let oscillating on the Pt(110)-(1×2) surface, the phonon study is expressed in two values: the vibrational frequency and the zero point energy (ZPE).

CALCULATION METHOD

This study was applied the DFT calculation method, which similar to that used successfully in the study of H/Pt(111) system [7]. We used SIESTA simulation software [19, 21] to calculate the electronic structures. The generalized gradient approximation (GGA) to the exchange-correlation function due to Perdew, Burke, and Ernzerhof (PBE) was used in the DFT calculation. The adsorption sites of hydrogen on the missing row Pt(110)-(1×2) surface is shown in Figure 1. The basic SIESTA calculation parameters were: the DZP (double-zeta polarized) basic set, the mesh-cutoff of 200 Ry, the Fermi Dirac function with the electronic temperature of 300K for the Brillouin zone integrations. The energy shift for the Pt is 200 meV, which determines the cutoff radius per angular momentum channel. And for the H atoms, the energy shift is 60 meV with the split norm of 0.53 for the second zeta. These calculation parameters in SIESTA provide reasonable accuracy for the results of bare Pt (non-adsorbed H) and adsorption of hydrogen atoms [7]. We also chose the value of 3.9242 Å corresponding to the obtained experimental data [24] to build the platinum model.

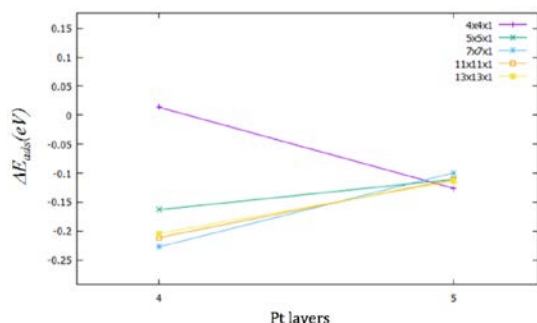


Figure 2. Dependence of Pt layer thickness on the ΔE_{ads} .

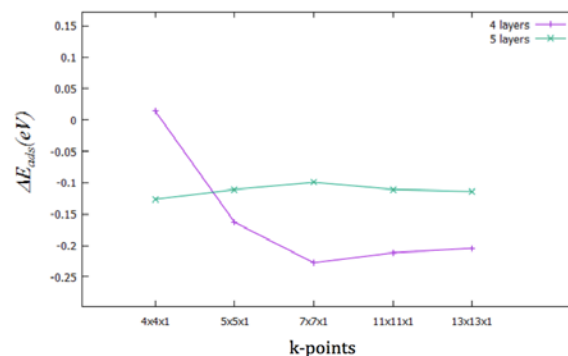


Figure 3. Dependence of Pt layer thickness on the ΔE_{ads} .

The calculation of H adsorption on Pt (110) surface - (1×2) is done through 3 main steps. First, the missing row Pt(110)-(1×2) surface model is built with different atomic layers from 4 to 6 Pt layers. For each case, the k-point in the SIESTA calculation gradually increases from (4×4×1) to (13×13×1) Monkhorst Pack (MP), or from 11 to 85 k-points, for the purpose of finding convergence according to number of layers and k-point. Secondly, after running the SIESTA program and obtaining a relaxing Pt model, we let hydrogen atoms adsorb on different positions on the Pt(110)-(1×2) surface. These locations include fcc (F), hcp(F'), short bridge (R), top (T') and trough (T) sites (Figure 1). Third, to calculate ZPE, the hydrogen atom is let oscillate around the equilibrium position along the z axis by a harmonic oscillation.

RESULT AND DISCUSSION - ENERGY CONVERGENCE

For each type of Pt surface structure, the stable sites of H adsorption on it are also different. Therefore, we begin by calculating the surface adsorption energy to verify possible adsorption sites of H on the Pt(110)-(1×2) surface. Table 1 shows the adsorption energy of model calculated by the formula:

$$E_{ads} = E_{tot}(N_H) - E_{tot}(0) - \frac{N_H}{2} E_{H_2}, \quad (1)$$

where $E_{tot}(NH)$ is the total energy of the NH atoms adsorbed on the Pt(110)-(1×2) surface, E_{H_2} is the total energy of the isolated H_2 molecule, and E_{ads} is the adsorption energy of H on Pt. E_{ads} at the short position (R) are recorded as the lowest value, which means the most stable adsorption site. Therefore, when examining the convergence, we select R site to investigate.

Table 1. Adsorption energy (eV) of H on Pt(110)-(1×2) when using 25 k-points and 1ML of H coverage (Θ H).

Unit cell	Pt layers	T' site	F site	F' site	R site	T site
(1×2)	4	-0.513	-0.535	-0.557	-0.762	-0.602

Table 2. The Pt-H bond length (Å) after optimized H/Pt system.

Pt layers	T' site	F site	F' site	R site	T site
4	1.57	1.82	1.58	1.77	1.77

Table 3. The adsorption energy of the H atom on the missing row Pt(110)-(1×2) surface on the R site and the F site.

Pt layers	(4×4×1) MP		(5×5×1) MP		(7×7×1) MP		(11×11×1) MP		(13×13×1) MP	
	R	F	R	F	R	F	R	F	R	F
4	-0.66	-0.68	-0.75	-0.59	-0.76	-0.53	-0.78	-0.56	-0.77	-0.57
5	-0.57	-0.45	-0.66	-0.52	-0.62	-0.52	-0.66	-0.55	-0.65	-0.54

To verify the correctness of the selected parameters in the DFT calculation, the energy convergence is calculated in detail in this study. When the energy value is converged at one point, the selected parameters are highly accurate and can be used as a comparison with experiment. The purpose of examining various number of layers and k-points is to find the value of the calculated parameters at which the energy converges. The calculations is done using (1×2) lateral unit cell with different Pt layers and k-points, on which one H atom is let adsorb on the most stable sites: on the short bridge (R), and on the fcc (F) sites. Table 3 shows the adsorption energies of hydrogen on Pt(110) surface with the MP grids changed from (4×4×1) to (13×13×1).

Through Figure 2 and Figure 3 we visualize the data of Table 3. Based on Figure 2, it can be seen when the number of layers increases to 5, the value ΔE_{ads} (the adsorption energy on the short bridge relative to that on the fcc) becomes convergence with different k points. This indicates that hydrogen only affects 4 top Pt layers. And Figure 3 shows that the convergence value is approaching when the number of points k increases to (13×13×1) MP.

CONCLUSIONS

Using the density function theory and generalized gradient approximation, the phonon

of hydrogen adsorption on the missing row Pt(110)-(1×2) surface has been studied. Adsorption calculations show that H is the most stable at the short bridge site.

Acknowledgments

This research is funded by Vietnam National Foundation for Science and Technology Development (NAFOSTED) under grant number 103.01-2017.50.

References

- [1]. N.M. Markovic, B.N. Grgur, P.N. Ross, J. Phys. Chem. B **101** (1997) 5405.
- [2]. K. Christmann, G. Ertl, T. Pignet, Surf. Sci. **54** (1976) 365.
- [3]. G. Jerkiewicz, Prog. Surf. Sci. **57** (1998) 137.
- [4]. J.R. Engstrom, W. Tsai, W.H. Weinberg, Chem. Phys. **87** (1987) 3104.
- [5]. A. Lasia, J. Electroanal. Chem. **562** (2004) 23.
- [6]. N.M. Markovic, P.N. Ross, Surf. Sci. Rep. **45** (2002) 117.
- [7]. T.T.T. Hanh, Y. Takimoto, O. Sugino, Surf. Sci. **625** (2014) 104.
- [8]. H. Kita, J. Mol. Catal. A: Chem. **199** (2003) 161.

- [9]. K. Kunimatsu, T. Senzaki, G. Samjeske, M. Tsushima, M. Osawa, *Electrochim. Acta* **52** (2007) 5715.
- [10]. C.R. Henry, *Surf. Sci. Rep.* **31** (1998) 231.
- [11]. S. Dahl, A. Logadóttir, R.C. Egeberg, J.H. Larsen, I. Chorkendorff, E. Törnqvist, J.K. Nørskov, *Phys. Rev. Lett.* **83** (1999) 1814.
- [12]. B. Hvolbaek, T.V.W. Janssens, B.C. Clausen, H. Falsig, C.H. Christensen, J.K. Nørskov, *Nano Today* **2** (2007) 14.
- [13]. S. Gudmundsdóttir, W. Tang, G. Henkelman, H. Jónsson, E. Skúlason, *J. Chem. Phys.* **137** (2012) 164705.
- [14]. E. Skúlason, G.S. Karlberg, J. Rossmeisl, T. Bligaard, J. Greeley, H. Jónsson, J.K. Nørskov, *Phys. Chem. Chem. Phys.* **9** (2007) 3241.
- [15]. G. Anger, H.F. Berger, M. Luger, S. Feistritzer, A. Winkler, K.D. Rendulic, *Surf. Sci.* **219** (1989) L583.
- [16]. C.S. Shern, *Surf. Sci.* **264** (1992) 171.
- [17]. M. Minca, S. Penner, E. Dona, A. Menzel, E. Bertel, V. Brouet, J. Redinger, *New J. Phys.* **9** (2007) 386.
- [18]. Z. Zhang, M. Minca, C. Deisl, T. Loerting, A. Menzel, E. Bertel, *Phys. Rev. B: Condens. Matter Mater. Phys.* **70** (2004) 121401.
- [19]. J.M. Soler, E. Artacho, J.D. Gale, A. García, J. Junquera, P. Ordejón, D. Sánchez-Portal, *J. Phys.: Condens. Matter* **14** (2002) 2745.
- [20]. T.T.T. Hanh, N. T. T. Hang, *J. Computational Materials Science* **138** (2017) 295.
- [21]. P. Ordejón, E. Artacho, J.M. Soler, *Phys. Rev. B* **53** (1996) R10441.
- [22]. J.P. Perdew, K. Burke, M. Ernzerhof, *Phys. Rev. Lett.* **77** (1996) 3865;
- [23]. J.P. Perdew, K. Burke, M. Ernzerhof, *Phys. Rev. Lett.* **78** (1997) 1396.
- [24]. S. Gudmundsdóttir, E. Skúlason, K.J. Weststrate, L. Juurlink, H. Jónsson, *Phys. Chem. Chem. Phys.* **15** (2013) 6323
- [25]. Y. Waseda, K. Hirata, M. Ohtani, *J. High Temp. High Press.* **7** (1975) 221

INVESTIGATION OF NANO-STRUCTURE OF OLIVINE $\text{LiMn}_x\text{Fe}_{1-x}\text{PO}_4$ BY RIETVELD REFINEMENT

Le Thanh Nguyen Huynh^{1,2}, **Viêt Dung Trinh**³, **Van Man Tran**^{1,2}

¹ Department of Physical Chemistry, Faculty of Chemistry, University of Science, Vietnam National University – Ho Chi Minh City

² Applied Physical Chemistry Laboratory, Faculty of Chemistry, University of Science, Vietnam National University – Ho Chi Minh City

³ School of chemical engineering, Hanoi University of Science and Technology
Email: hltnguyen@hcmus.edu.vn

ABSTRACT

In the recent years, olivine LiFePO_4 has been considered as a prospective cathode material for lithium-ion batteries. However, low conductivity is an obstacle to the commercialization of LiFePO_4 ; doping the transition metal such as Mn and Ni is one of solutions for this issue. This work aimed to synthesize the nano-structure Mn-doped olivines $\text{LiMn}_x\text{Fe}_{1-x}\text{PO}_4$ at various content of Mn-doping ($x = 0.1 - 0.5$) via hydrothermal route followed by a carbon coating pyrolyzed. The synthesized olivines were well-crystallized in olivine structure, with larger lattice parameters compared to LiFePO_4 . The XRD patterns were refined by Rietveld refinement confirm the atom sites of olivine as well as evolution of lattice parameters in function of Mn-doping contents.

Keywords: Lithium-ion batteries, Mn-doped olivines, Rietveld refinement

INTRODUCTION

In the last three decades, the world has observed urges for a need of significant breakthroughs in the hi-tech industry. Along with this development, the demand for power storage can provide a large amount of energy with good cycling performance. Lithium-ion batteries (LIBs) have taken those requirements as their advantages. A great deal of researches have delved deeply into the topic of LIBs in order to develop suitable materials to improve the performance of batteries. Cathode materials for LIBs have been an attractive field because they are the determining factor of power density, capacity, lifetime, and cost of the batteries.[1, 2] Besides the popular layered transition metal oxides, olivine materials- LiMPO_4 ($M = \text{Mn, Co, Fe...}$), represented by LiFePO_4 are competitive candidates to the commercialized LiCoO_2 . They are low-cost, easy to synthesize, and non-toxic. High thermal stability and comparable specific capacity (170 mAh/g) to LiCoO_2 (140 mAh/g) is the key to their large-scale application in the future.[3, 4]

Olivine materials are categorized as orthorhombic structure with space group Pnma. The lattice of LiFePO_4 contains $[\text{FeO}_6]$

octahedral sites and $[\text{PO}_4]$ tetrahedral sites sharing vertices and edges. The octahedrons are connected to form tunnel structure, which facilitates the migration of Li^+ ions.[5] The alternate arrangement of $[\text{FeO}_6]$ and $[\text{PO}_4]$ groups, however, leads to low conductivity ($\sim 10^{-9}$ S/cm at room temperature) – the main limitation of LiFePO_4 . [6] In order to solve this issue, many research projects have focused on minimizing the particle size into nano-scale with modern synthetic process. Besides, doping the material with Mn or Ni ($\text{LiMn}_x\text{Fe}_{1-x}\text{PO}_4$ or $\text{LiNi}_x\text{Fe}_{1-x}\text{PO}_4$) is also a promising solution.[7] Nakamura et al reported the Mn^{2+} -substitution in olivine compounds (prepared by solid-state reaction) expended the unit cell along c-axis that facilitated the Li-immigration in doped olivines and the Li^+ diffusions were found out on the order of 10^{-12} cm^2/s [8]. Novikova et al prepared the olivines $\text{LiMn}_x\text{Fe}_{1-x}\text{PO}_4$ ($x = 0 - 0.4$) by sol-gel method and the particles varied in range 400 nm to 4 μm . By Mössbauer spectroscopy, they proved the low content Mn-doping ($x = 0.1, 0.2$) enhanced the discharge capacity to 142 mAh/g (at current density of 55 mA/g) due to the solid solutions formation under gradual changes in the potential of Mn [9].

The objective of this study is to evaluate the influence of Mn-doping on the crystalline structure as well as the electrochemical behaviors of olivine materials $\text{LiMn}_{0.1}\text{Fe}_{0.9}\text{PO}_4$ and $\text{LiMn}_{0.2}\text{Fe}_{0.8}\text{PO}_4$ synthesized by hydrothermal method. Kinetics of Li^+ intercalation was also investigated through diffusion coefficients using cyclic voltammetry.

EXPERIMENTAL

Mn-doped olivine $\text{LiMn}_{0.1}\text{Fe}_{0.9}\text{PO}_4$ (LMFP_19) and $\text{LiMn}_{0.2}\text{Fe}_{0.8}\text{PO}_4$ (LMFP_28) materials were synthesized via hydrothermal method. 150 mL of aqueous solution of $\text{Mn}(\text{CH}_3\text{COO})_2 \cdot 4\text{H}_2\text{O}$ and $\text{Fe}(\text{NO}_3)_3 \cdot 9\text{H}_2\text{O}$ (at the molar ratio of 1:9 or 2:8) with a small amount of N, N-dimethylformamide $\text{C}_3\text{H}_7\text{NO}$ as reducing agent was stirred at 80°C for 1 hour. The solution was then mixed with $\text{LiOH} \cdot \text{H}_2\text{O}$, H_3PO_4 , $\text{C}_6\text{H}_8\text{O}_6$, and HNO_3 and stirred thoroughly at ambient condition for 6 hours using a magnetic stirrer. The mixture was then transferred into a hydrothermal system and annealed at 180°C for 12 hours. The product of this process was separated from the suspension by centrifuge and low-pressure filter, then washed by deionized water and finally dried at 60°C overnight. In order to make a carbon coating, the obtained solid was ground with glucose at the mass ratio of 1:1 and then calcined at 700°C in N_2/Ar atmosphere for 3 hours.

The crystalline structure of as-prepared materials was analyzed by X-ray diffraction by D8-ADVANCED (Bruker) in the 2θ range of 10 - 70° at the scanning rate of $0.020^\circ/\text{step}$ with $\text{CuK}\alpha$ radiation. The morphology and elemental composition evaluation by scanning electron microscopy (SEM) and SEM-EDX, by using a Hitachi FE-SEM S-4800 Scanning Electron Microscope. The proportion of carbon coating on the particles was quantified by thermal analysis from 25°C to 800°C in the air at the scanning rate of $10^\circ\text{C}/\text{min}$ using LABSYS evo TG-DSC 1600 system (Setaram, France).

RESULTS AND DISCUSSION

The X-ray diffraction patterns of two Mn-doped olivines (Figure 1a, b) can be indexed in orthorhombic structure with the space group Pnmb. Results Rietveld refinement, gathered in Table 1 are in good agreement with original olivine structural (JSPDF: 01{083{2092). The Li^+ atoms are located at 4a sites; the Fe, Mn and

P atoms are in 4c sites; the O atoms are in 8a sites. The fraction of Mn:Fe are 0.1:0.9 and 0.2:0.8, approximate matches the EDX results. The X-ray diffraction patterns indicates the presence of a pure and very well crystallized single phase without the impurity phase (e.g. MnO_2 , Li_2O , Fe_2O_3). It is obvious that partially replacing Fe with Mn amplifies the size of the olivines lattice unit, which can be explained by the fact that the ionic radius of Mn^{2+} (80 pm) is superior to that of Fe^{2+} (78 pm). This result agrees with previous reports about Mn-doped olivine [10].

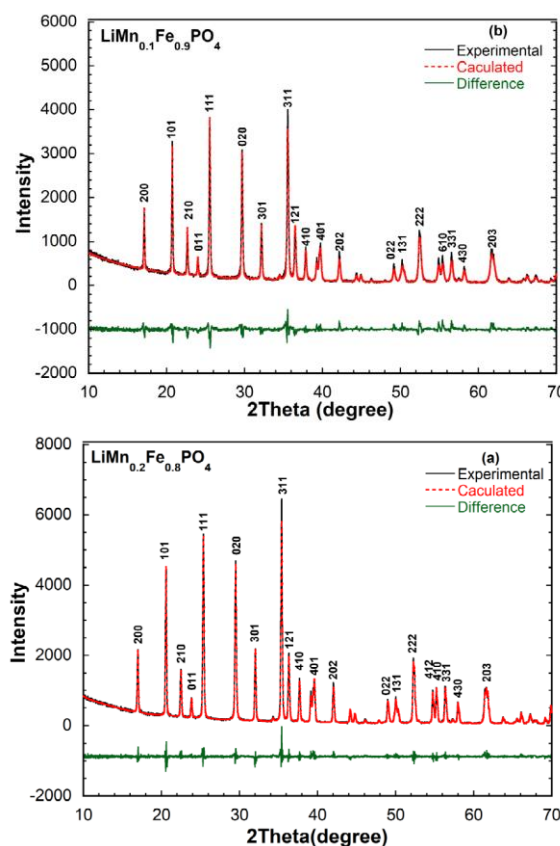


Figure 1. XRD patterns of $\text{LiMn}_{0.1}\text{Fe}_{0.9}\text{PO}_4$ (a) and $\text{LiMn}_{0.2}\text{Fe}_{0.8}\text{PO}_4$ (b)

Table 1 Lattice parameters of $\text{LiMn}_{0.1}\text{Fe}_{0.9}\text{PO}_4$ and $\text{LiMn}_{0.2}\text{Fe}_{0.8}\text{PO}_4$ in comparison with LiFePO_4 .

Sample	a (Å)	b (Å)	c (Å)	V (Å ³)
$\text{LiMn}_{0.1}\text{Fe}_{0.9}\text{PO}_4$	10.346	6.015	4.705	292.8
$\text{LiMn}_{0.2}\text{Fe}_{0.8}\text{PO}_4$	10.384	6.041	4.722	296.2
LiFePO_4	10.334	6.010	4.693	291.5

As-prepared materials morphology was analyzed by scanning electron microscopy. The SEM images (Figure 2) indicate their polyhedral shapes with the sizes varying between 200 and 400 nm. These particles agglomerate into larger secondary particles, and the size varies from 0.5 to 1.0 μm .

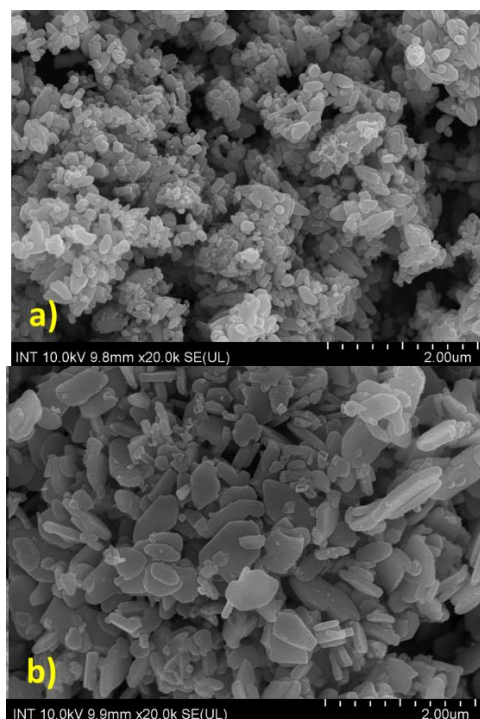


Figure 2 SEM images of $\text{LiMn}_{0.1}\text{Fe}_{0.9}\text{PO}_4$ (a) and $\text{LiMn}_{0.2}\text{Fe}_{0.8}\text{PO}_4$ (b).

The elemental compositions of LMFP_19 and LMFP_28 determined by SEM-EDX are listed in Table 2. The molar ratios of Mn: Fe: P: O of LMFP_19 and LMFP_28 are 0.100: 1.06: 0.94: 3.68 and 0.200: 0.853: 0.950: 3.48 respectively, which are suitable to the theoretical formula.

CONCLUSION

In this study, two olivine-type materials $\text{LiMn}_{0.1}\text{Fe}_{0.9}\text{PO}_4$ and $\text{LiMn}_{0.2}\text{Fe}_{0.8}\text{PO}_4$ were successfully synthesized via hydrothermal method. Both have an orthorhombic structure, and their lattice parameters agreed with the preceding reports.

Acknowledgment

This work is supported by Vietnam National University Ho Chi Minh (VNUHCM) through grant number C2018-18-11.

References

- [1]. Tarascon J-M and Armand M 2001 Issues and challenges facing rechargeable lithium batteries *Nature* **414** 359–67
- [2]. Scrosati B 2000 Recent advances in lithium ion battery materials *Electrochimica Acta* **45** 2461–6
- [3]. Antolini E 2004 LiCoO_2 : formation, structure, lithium and oxygen nonstoichiometry, electrochemical behaviour and transport properties *Solid State Ionics* **170** 159–71
- [4]. Padhi A K, Nanjundaswamy K S and Goodenough J B 1997 Phospho-olivines as Positive-Electrode Materials for Rechargeable Lithium Batteries *Journal of The Electrochemical Society* **144** 1188–94
- [5]. Etacheri V, Marom R, Elazari R, Salitra G and Aurbach D 2011 Challenges in the development of advanced Li-ion batteries: a review *Energy & Environmental Science* **4** 3243–62
- [6]. Choi D and Kumta P N 2007 Surfactant based sol-gel approach to nanostructured LiFePO_4 for high rate Li-ion batteries *Journal of Power Sources* **163** 1064–9
- [7]. Zhengrui X, Gao L, Liu Y and Li L 2016 Review—Recent Developments in the Doped LiFePO_4 Cathode Materials for Power Lithium Ion Batteries vol 163
- [8]. Ding J, Su Z and Tian H 2016 *Synthesis of high rate performance $\text{LiFe}_{1-x}\text{Mn}_x\text{PO}_4/\text{C}$ composites for lithium-ion batteries* vol 42
- [9]. Yu D Y W, Fietzek C, Weydanz W, Donoue K, Inoue T, Kurokawa H and Fujitani S 2007 Study of LiFePO_4 by cyclic voltammetry *Journal of the Electrochemical Society* **154**
- [10]. Dathar G K P, Sheppard D, Stevenson K J and Henkelman G 2011 Calculations of Li-Ion Diffusion in Olivine Phosphates *Chemistry of Materials* **23** 4032–7

HIERARCHICAL STRUCTURES IN GRAFT-TYPE POLYMER ELECTROLYTE MEMBRANES FOR FUEL CELL VEHICLES USING ULTRA SMALL ANGLE X-RAY SCATTERING METHOD

Tran Duy Tap ^{1,*}, La Ly Nguyen ^{1,2,3,*}, Nguyen Nhat Kim Ngan ⁴, Tran Thanh Danh ¹,
Tran Mai Kieu ¹, Dang Van Hoa ¹, Lam Hoang Hao ¹, Huynh Truc Phuong ⁴,
Le Quang Luan ⁵, Tran Thanh Hien ¹, Hoang Thi Lan ⁴, Tran Hoang Long ¹,
Nguyen Thi Hoai My ¹, Phan Thi Quynh Nga ⁴

¹Faculty of Materials Science and Technology, University of Science, Viet Nam National University Ho Chi Minh City, 227 Nguyen Van Cu, District 5, Ho Chi Minh City, Viet Nam.

²Center for Nuclear Techniques, Vietnam Atomic Energy Institute, 217 Nguyen Trai, District 1, Ho Chi Minh City, Viet Nam.

³Institute for Nanotechnology, Viet Nam National University Ho Chi Minh City, Community 6, Linh Trung Ward, Thu Duc District, Ho Chi Minh City, Viet Nam.

⁴Faculty of Physics and Engineering Physics, University of Science, Viet Nam National University Ho Chi Minh City, 227 Nguyen Van Cu, District 5, Ho Chi Minh City, Viet Nam.

⁵Biotechnology Center of Ho Chi Minh City, 2374 Highway 1, District 12, Ho Chi Minh City, Viet Nam.

E-mail: *lalynghuyen279@gmail.com; *tdtap@hcmus.edu.vn

ABSTRACT

Poly(ethylene-*co*-tetrafluoroethylene) (ETFE)-based graft-type polymer electrolyte membranes (ETFE-PEMs) were prepared by a pre-irradiation grafting method, in which polymer substrates are first irradiated using a quantum beam and then immersed in a monomer solution for graft polymerization (grafted-ETFE) and finally sulfonated the grafted films. The hierarchical structures of original ETFE, grafted-ETFE, and ETFE-PEM were investigated by using ultra small-angle X-ray scattering (USAXS). It was founded that the grafted-ETFE and ETFE-PEM films exhibit three scattering peaks, whereas the original ETFE shows only one peaks. A pronounced peak at approximately $q = 0.27 \text{ nm}^{-1}$ ($d = 23 \text{ nm}$), which are observed for all films, was assigned as the scattering from lamellar stacks. A shoulder-like peak at $q_2 = 0.021 \text{ nm}^{-1}$ ($d_2 = 300 \text{ nm}$) was observed. In addition, the SAXS profiles exhibited another shoulder-like peak in q -region at $q_3 = 0.0047 \text{ nm}^{-1}$ ($d_3 = 1340 \text{ nm}$), which is lower than q_2 . One possible explanation of the set of peaks, q_2 and q_3 , should be a set of correlation distances for the short and long periods d_2 and d_3 , perpendicular to the orientated direction originating from oriented crystallite (lamellar grains) structures.

Keywords: ETFE, radiation grafting, fuel cell, hierarchical structure, USAXS

INTRODUCTION

Proton exchange membrane (PEM) fuel cells have attracted many interests in solving the environmental problems since their advantages over other fuel cells in terms of the clean and efficient power generation and lower operating temperature are expected to reduce the fossil fuel consumption, which is believed to be the primary sources causing the climate change. Proton exchange membrane, which consists of super acid groups (i.e., sulfonic acid), has been considered as one of the key components in achieving the high fuel cell performance because of its fuel cell properties such as proton

conductivity, mechanical strength, and thermal and chemical stabilities. Recently, we have reported the synthesis and characterization of poly(styrenesulfonic acid) (PSSA)-grafted ETFE polymer electrolyte membranes (ETFE-PEMs) with a wide range of ion exchange capacity (IEC) at the dry and humidified conditions for fuel cell applications.^{1,2} The ETFE-PEMs showed respectively less dependent proton conductivity on relative humidity (RH) and strong dependence of mechanical strength on the PEM crystallinities. The higher order structures of the ETFE-PEMs were then investigated by using the small- and ultras-small-angle X-ray

scattering (SAXS/USAXS) methods.³ It was founded that, for the ETFE-PEMs with IECs > 2.7 mmol/g, a higher conductivity at 30% RH and compatible tensile strength at 100% RH and 80 °C, in comparison with Nafion-212, were originated respectively from the well-interconnected ion channels around the grains and the remaining lamellar crystals and grains as well. The aim of the present paper is to extend this investigation of SAXS profiles of ETFE-PEMs, especially at ultrasmall-angle X-ray scattering, which has been only a few reports in the filed.

EXPERIMENTAL

Details on the materials and preparation procedures were described in the previous works.^{1,2} The equipments and procedures for the SAXS measurements were also described explicitly in the recent work.³ Principle of SAXS measurement is shown in Figure 1. Briefly, the membranes were prepared by the pre-irradiation grafting method, in which the pristine ETFE films were irradiated by using the ⁶⁰Co γ -rays and then immersed into a styrene solution to give the styrene grafted ETFE (grafted-ETFE). Chemical structures of pristine ETFE film, grafted-ETFE film, and ETFE-PEM are represented in Figure 2. The grafting degree (*GD*) of the grafted-ETFE can be controlled in the range from 4.2 to 117% by changing the styrene concentration and grafting time. The grafted-ETFE films were sulfonated to obtain the poly(styrenesulfonic acid) (PSSA)-grafted ETFE (ETFE-PEM) with an *IEC* range of 0.52–3.1 mmol g⁻¹.

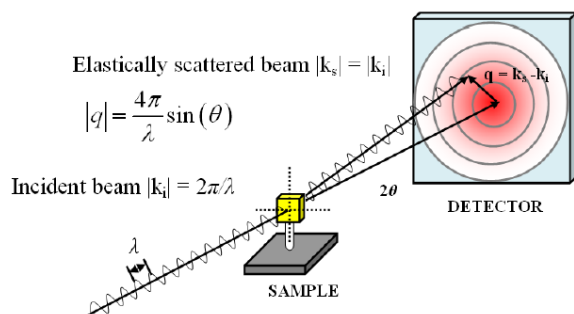


Figure 1. Principle of SAXS measurement is represented, in which *q* is referred to as the modulus of the scattering vector given by $4\pi\sin\theta/\lambda$, where 2θ is the scattering angle and λ is the wavelength of the incident radiation.

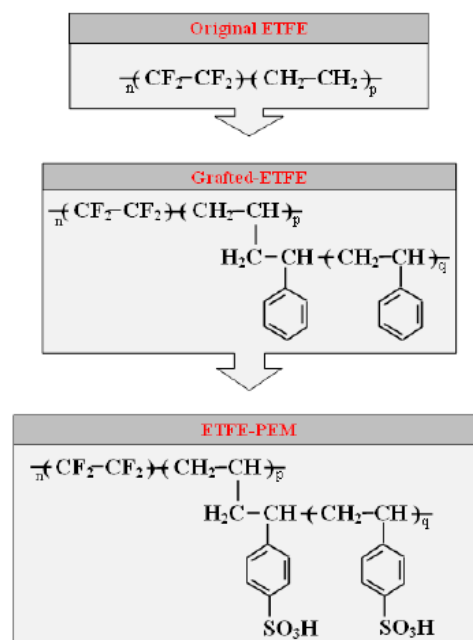


Figure 2. Chemical structures of pristine ETFE film, grafted-ETFE film, and ETFE-PEM.

RESULTS AND DISCUSSION

Figure 3 shows overall USAXS profiles of (1) original ETFE, (2) grafted-ETFE with a grafting degree (*GD*) of 59%, and (3) ETFE-PEM (sulfonated form of the grafted-ETFE) with *IEC* of 2.4 mmol/g in the *q*-ranges = 4×10^{-3} – 3 nm^{-1} (*d*-spacing = 2–1600 nm). In the entire *q*-range, the pristine ETFE possessed only a pronounced peak at approximately $q = 0.27 \text{ nm}^{-1}$ ($d = 23 \text{ nm}$), which was assigned as the scattering from lamellar stacks. In a *q*-region I, grafted-ETFE exhibited a shoulder-like peaks appeared at $q_1 = 0.192 \text{ nm}^{-1}$ ($d_1 = 32.7 \text{ nm}$) being similar to *q*-position in the pristine ETFE indicating that new phases consisting of polystyrene grafts generated under the influences of the lamellar structure of the pristine ETFE. In *q*-region II, a shoulder-like peak at $q_2 = 0.021 \text{ nm}^{-1}$ ($d_2 = 300 \text{ nm}$) was observed. In addition, the SAXS profiles of grafted-ETFE exhibited another shoulder-like peak in *q*-region II at $q_3 = 0.0047 \text{ nm}^{-1}$ ($d_3 = 1340 \text{ nm}$), which is lower than q_2 . In *q*-region II, a shoulder-like peak at $q_2 = 0.021 \text{ nm}^{-1}$ ($d_2 = 300 \text{ nm}$) was observed. In addition, the SAXS profiles of grafted-ETFE exhibited another shoulder-like peak in *q*-region II at $q_3 = 0.0047 \text{ nm}^{-1}$ ($d_3 = 1340 \text{ nm}$), which is lower than q_2 .

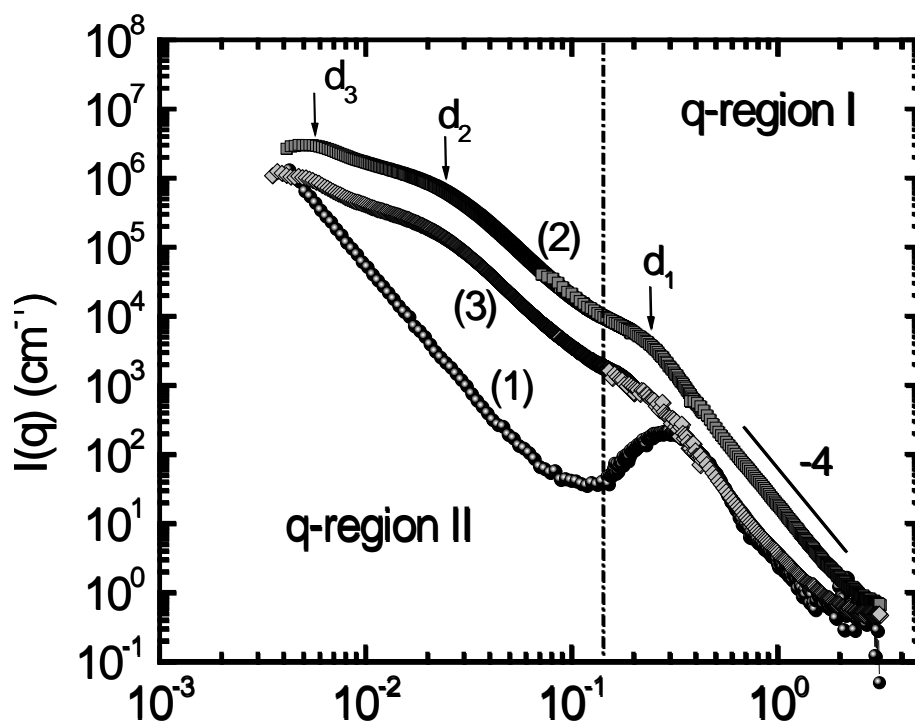


Figure 3. USAXS profiles of (1) original ETFE, (2) grafted-ETFE, and (3) ETFE-PEM with GD of 59%.

One possible explanation of the set of peaks, q_2 and q_3 , should be a set of correlation distances for the short and long periods d_2 and d_3 , perpendicular to the orientated direction originating from orientated crystallite (lamellar grains) structures. SAXS profiles of ETFE-PEMs are similar with those of grafted-ETFE in the entire q -range. By comparing the GD (IEC) dependences of conductivity and mechanical properties of the ETFE-PEMs, the lamellar (d_1) and crystallites (d_2 and d_3) are crucial for former and latter properties, respectively. It should be noted here that the crystalline structures in the lower q -region than $q = 0.021 \text{ nm}^{-1}$ ($d = 300 \text{ nm}$) for the graft-type PEMs have not been reported and the obtained results in this study can contribute the further understanding on the hierarchical structures of the membranes, especially for structures located at ultrasmall-angle X-ray scattering.

CONCLUSION

The hierarchical structures of original ETFE, grafted-ETFE, and ETFE-PEM were investigated by using ultra small-angle X-ray scattering (USAXS). The obtained results indicate that the grafted-ETFE and ETFE-PEM films exhibit three scattering peaks, whereas the original ETFE shows only one peaks. A

pronounced peak at approximately $q = 0.27 \text{ nm}^{-1}$ ($d = 23 \text{ nm}$) relating to the lamellar stacks are observed for all films. A shoulder-like peak at $q_2 = 0.021 \text{ nm}^{-1}$ ($d_2 = 300 \text{ nm}$) was observed. In addition, the SAXS profiles exhibited another shoulder-like peak in q -region at $q_3 = 0.0047 \text{ nm}^{-1}$ ($d_3 = 1340 \text{ nm}$), which is lower than q_2 . One possible explanation of the set of peaks, q_2 and q_3 , should be a set of correlation distances for the short and long periods d_2 and d_3 , perpendicular to the orientated direction originating from orientated crystallite (lamellar grains) structures. The obtained results in this study can contribute the further understanding on the hierarchical structures of the membranes, especially for structures located at ultrasmall-angle X-ray scattering. The relationship between these hierarchical structures and fuel cell properties of ETFE-PEMs will be elucidated in a next paper.

Acknowledgments

This research is funded by Vietnam National University Ho Chi Minh City (VNU-HCM) under grant number C2017-18-19. We thank Dr. Masota Ohnuma for his supports with the SAXS experiments.

References

- [1]. T.D.Tap. S.Sawada. S.Hasegawa. Y.Katsumura. and Y.Maekawa. *Poly(ethylene-co-tetrafluoroethylene) (ETFE)-based graft-type polymer electrolyte membranes with different ion exchange capacities: Relative humidity dependence for fuel cell applications.* Journal of Membrane Science. **447** (2013) 19 – 25.
- [2]. T.D.Tap. D.D.Khiem. L.L.Nguyen. N.Q.Hien. L.Q.Luan. P.B.Thang. S.Sawada. S.Hasegawa. Y.Maekawa. *Humidity and temperature effects on mechanical properties and conductivity of graft-type polymer electrolyte membrane.* Radiation Physics and Chemistry. **151** (2018) 186 – 191.
- [3]. T.D.Tap. S.Sawada. S.Hasegawa. K.Yoshimura. Y.Oba. M. Ohnuma. Y.Katsumura. Y.Maekawa. *Hierarchical structure-property relationships in graft-type fluorinated polymer electrolyte membranes using small- and ultrasmall-angle X-ray scattering analysis.* Macromolecules. **47** (2014) 2373 – 2383.

STUDY ON THE ELECTROCHEMICAL PROPERTIES OF GELLED ELECTROLYTES USING NANO FUMED SILICA IN THE PRESENCE OF SOME OTHER ORGANICS ADDITIVES

Thi Van Anh Nguyen, Thi Thanh Thuy Mai, Thi Xuan Mai and Thi Binh Phan*

Institute of Chemistry, Vietnam Academy of Science and Technology,

18 Hoang Quoc Viet Street, Cau Giay District, Hanoi City, Vietnam;

Email: phanthibinh@ich.vast.vn

ABSTRACT

Gelled electrolyte is made on the basis of liquid glass and sulfuric acid using nano fumed silica in the presence of some other organic additives such as polyacrylamide and polypropylene glycol. Lead-antimony alloy electrodes are prepared to examine the electrochemical properties of manufactured gelled electrolytes through cyclic voltammetric behavior, electrochemical impedance and polarization curves. The results about cyclic voltammetric diagrams showed that the lead solubility increased and the oxygen evolution decreased in the presence of nano fumed silica. Obtained nyquist diagrams all showed that adsorption process occurred, but when nano fumed silica is present, the electrochemical impedance increases. The results of the measurement of the polarization curve showed that when increasing the concentration of nano fumed silica, the excess of oxygen escaping increased sharply, but the escape of hydrogen decreased slightly.

Keywords: Gelled electrolyte, nano fumed silica, cyclic voltammetry, electrochemical impedance spectroscopy, linear polarization.

INTRODUCTION

Sealed lead acid batteries play an increasingly important role in the post and telecommunications industry, especially at telecommunications stations because they do not cause damage to electronic devices around due to restrictions and elimination of exhaust gas during charging. One of the technologies to create sealed lead acid battery is using electrolyte in the gelled form made in many different ways [1,2]. A number of innovations related to the manufacture of this electrolyte have been of interest to scientists, including the addition of organic or inorganic additives [3-6] aimed at achieving a well-structured gelled electrolyte for the easy transfer of gas to contribute to the process of recombination into water. Nano fumed silica (NFS) has also been mentioned in previously published works [7,8], but its use in combination with some organic additives such as polyacrylamide (PAM) and polypropylene glycol (PPG) has been lack of interest.

This paper will present some electro-chemical survey results of antimony lead alloy electrodes in gelled electrolytes made from liquid glass and

sulfuric acid adding NFS in the presence of PAM and PPG.

EXPERIMENTAL

Chemicals

PPG and sulfuric acid are provided by Merck, PAM and NFS by Sigma Aldrich, and liquid glass solution (1.54 g/cm³) from China.

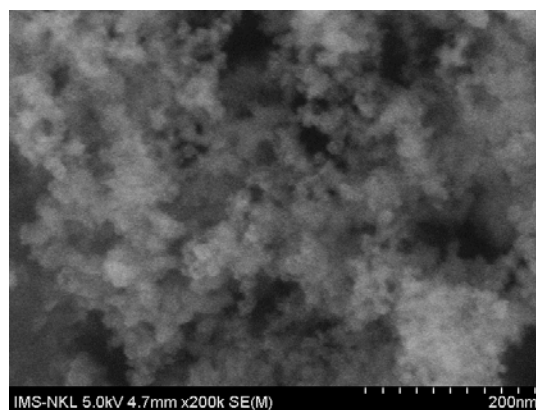


Figure 1. SEM image of NFS.

Preparation of sample

All samples of gelled electrolytes are prepared at the temperature of 2-5°C. The sulfuric acid and liquid glass solutions at density

of 1.37 g/cm³ and 1.54 g/cm³ were used for sample preparation, respectively. NFS is added into distilled water under stirring to create a suspension solution with a concentration of 5%. The weight percent of PAM (0.2 wt%), PPG (0.1 wt%) and NFS (0÷0.8 wt%) was calculated based on the weight ratio to mass of sulfuric acid.

Measuring methods

Cyclic voltammogram (CV), electrochemical impedance spectroscopy (EIS) and polarization curves of PbSb alloy electrodes were measured in gelled electrolyte on the unit IM6 (Zahner-Elektrok, Germany). A three-electrode cell was used, including PbSb alloy electrode (0.6 mm²) as working electrode, platinum plate as counter electrode and a calomel reference electrode.

Scan rate of 100 mV/s and cycle number of 10 were chosen as parameters for CV measurements in the potential area from -0.85 to 2.50 V; an amplitude of 5 mV and frequency from 100 kHz to 10 mHz for EIS study at open current potential (OCP); scan rate for polarization survey in the potential area from -1.5 to 2.7 V was 50 mV/s.

RESULTS AND DISCUSSION

Study on CV diagrams

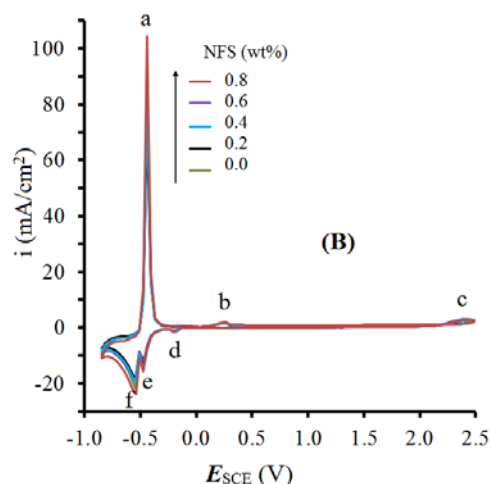
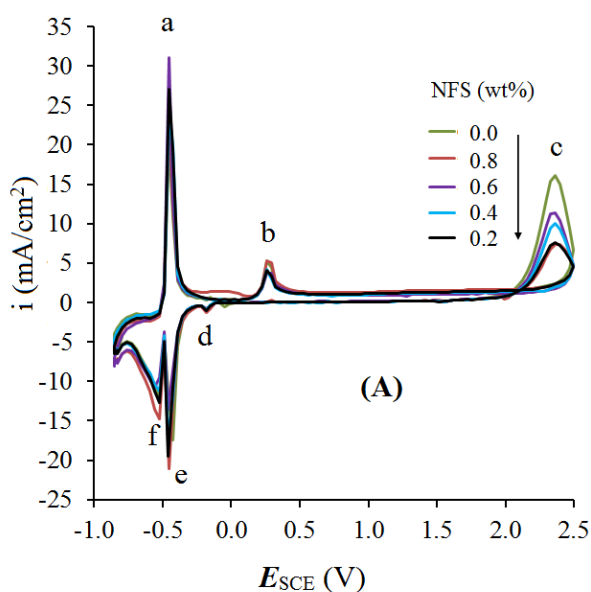


Figure 2. CV diagrams of PbSb alloy electrode in gelled electrolyte using different NFS content in the presence of 0.1 wt% PPG and 0.2 wt% PAM. (A) the first cycle, (B) the 10th cycle.

Research results on CV diagrams in Figure 2 show that there are 3 oxidized peaks (a, b, c) and 3 reducing peaks (d, e, f), in which their peak height is not only dependent on the number of scanning cycle but also on the NFS amount used to make the gelled electrolyte.

Peaks a and b reflect the dissolution of lead to lead (II) and antimony to Sb (III), respectively. Peak c explains the process of oxygen release [9], which decreases sharply in the presence of NFS and when the number of scanning cycle increases.

Peak d shows the reduction process of Sb (III) to Sb, peaks e and f represent the reduction of PbO and PbSO₄ to lead, which were found similar to the published literature [10,11], respectively. The peak of lead solubility (peak a) increased significantly at the 10th cycle (Figure 2B) when NFS content increased, although it did not depend much on the presence of NFS at the first cycle (Figure 2A).

Study on EIS diagrams

Figure 3 shows Nyquist impedance diagrams of the antimony lead alloy electrode measured in gelled electrolytes containing different NFS content (0÷0.8 wt%) in the presence of 0.1 wt% PPG and 0.2 wt% PAM. As we all know, the diameter of Nyquist circle represents the value of charge transfer resistance (R_{ct}) [12], it means this diameter is directly proportional to R_{ct} . In general, the results showed that the R_{ct} increased due to the presence of NFS, in which the highest increase was at the NFS content of 0.2 wt%.

However, it indicated that a rapidly decrease in the case of NFS content increased until 0.6 wt% and then increased again at 0.8 wt% NFS. Therefore, it is not conducive to the charge transfer on the working electrode if using NFS at too little (0.2 wt%) or too high (0.8 wt%) content.

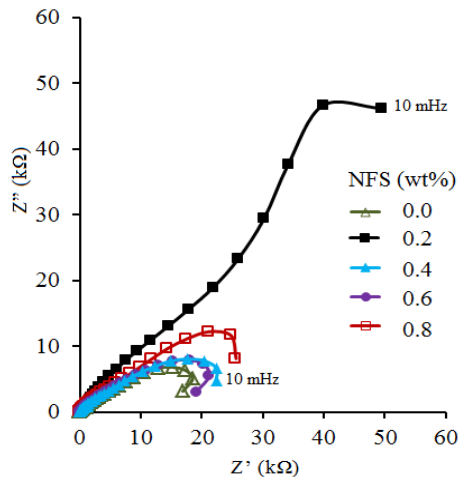


Figure 3. Nyquist diagrams of PbSb alloy electrode in gelled electrolyte using different NFS content in the presence of 0.1 wt% PPG and 0.2 wt% PAM.

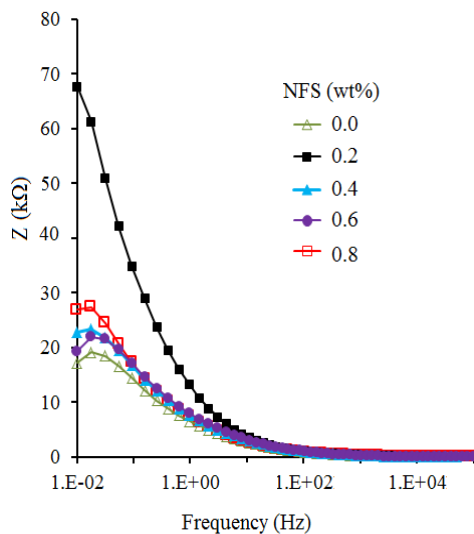


Figure 4. Bode diagrams of PbSb alloy electrode in gelled electrolyte using different NFS content in the presence of 0.1 wt% PPG and 0.2 wt% PAM.

The results given in Figure 4 and Table 1 show that in terms of evaluating the charge transfer process, the limit of using NFS content is 0.6 wt%.

In addition, we also noticed that the appearance of adsorption occurred by observing the impedance spectrum in both Nyquist and

Bode types in the low frequency region gradually approaching 10 mHz.

Table 1. Electrochemical impedance (EI) values at 10 mHz determined from figure 4

NFS (wt%)	EI values (kΩ)
0.0	17.20
0.2	67.67
0.4	22.88
0.6	19.34
0.8	26.90

Study on polarization curves

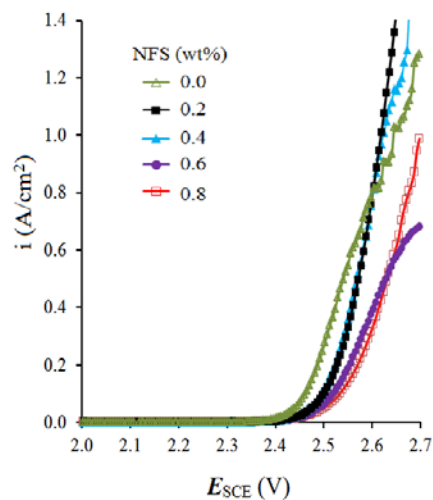


Figure 5. Anodic polarization branch of PbSb alloy electrode in gelled electrolyte using different NFS content in the presence of 0.1 wt% PPG and 0.2 wt% PAM.

The two anode and cathode branches on the polarization curve were investigated because it involved in the process of releasing oxygen and hydrogen from the working electrode.

The polarization segment (Figure 5) in the oxygen drainage region (2.4÷2.7 V) reflects the oxygen overvoltage (OOV). In theory, the more this curve moves toward the positive side, the bigger the OOV is and the oxygen release is inhibited. Observing the curves, we find that when NFS is present, this segment is shifted more positively and the OOV increases with the amount of NFS used.

In contrast, the cathode polarization process (Figure 6) shows that the hydrogen overvoltage (HOV) decreases because the curves are all moved toward less negative ones due to the presence of NFS. However, the HOV as well as the rate of hydrogen escape in gelled electrolyte medium using NFS at 0.4÷0.8 wt% are nearly

the same because these curves are nearly identical.

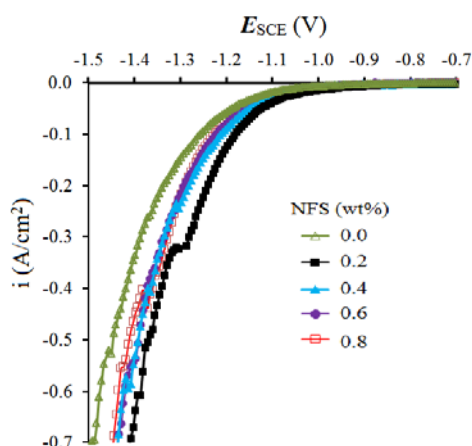


Figure 6. Cathodic polarization branch of PbSb alloy electrode in gelled electrolyte using different NFS content in the presence of 0.1 wt% PPG and 0.2 wt% PAM

CONCLUSION

The presence of NFS besides PPG (0.1 wt%) and PAM (0.2 wt%) significantly contributed to reduce the rate of oxygen escape. Lead dissolution rate was increased not only with number of CV scanning cycle but also with the content of NFS used for the fabrication of gelled electrolyte.

The R_{ct} was increased due to NFS taken part in the formation of gelled electrolyte. The suitable NFS content was 0.6 wt% for use in the manufacture of gelled electrolytes in which R_{ct} varied insignificantly compared to that of gelled electrolyte without NFS.

The presence of NFS improved the oxygen overvoltage very well, but did not improve the hydrogen overvoltage, even reducing HOV. This reduction was not significant at NFS content varied from 0.6 to 0.8 wt%.

Acknowledgment.

This work was supported by the National Foundation for Science and Technology Development of Vietnam (Grant no.: 104.99-2017.345).

References

[1]. D.W.H. Lambert, P.H.J. Greenwood, M.C. Reed. *Advances in gelled-electrolyte technology for valve-regulated lead-acid batteries*. J. Power Sources **107** (2002) 173–179.
 [2]. Valérie Toniazzo. *The key to success: Gelled-electrolyte and optimized separators for stationary lead-acid batteries*. J. Power Sources **158** (2006) 1124–1132.

[3]. Sang Yong An, Euh Duck Jeong, Mi Sook Won, and Yoon Bo Shim. *The optimization of gel electrolytes on performance of valve regulated lead acid batteries*. Bull. Korean Chem. Soc. **29**(5) (2008) 998-1002.
 [4]. Zheng Tang, Jianming Wang,, Xian-xian Mao, Haibo Shao, Quanqi Chen, Zhihua Xu, Jianqing Zhang. *Investigation and application of polysiloxane-based gel electrolyte in valve-regulated lead-acid battery*. J. Power Sources **168** (2007) 49–57.
 [5]. Meiqiong Chen, Wenxian Guo, Min Zhang, Faliang Cheng, Peng Liu, Zhiquan Cai, Yan Zhang. *Effect of polyols on the electrochemical behavior of gel valve-regulated lead-acid batteries*. Electrochimica **164** (2015) 243-252.
 [6]. Metin Gençten, Koray B. Dönmez, Yücel Şahin. *A novel gel electrolyte for valve-regulated lead acid battery*. Anadolu University Journal of Science and Technology A- Applied Sciences and Engineering **18**(1) (2017) 146-160.
 [7]. M.Q. Chena, H.Y. Chen, D. Shu, A.J. Li, D.E. Finlow. *Effects of preparation condition and particle size distribution on fumed silica gel valve-regulated lead-acid batteries performance* J. Power Sources **181** (2008) 161–171.
 [8]. Ke Pan, Guang Shi, Aiju Li, He Li, Ruirui Zhao, FuQian Wang, Wenqing Zhang, Qian Chen, Hongyu Chen, Zhenglin Xiong, David Finlow. *The performance of a silica-based mixed gel electrolyte in lead acid batteries*. J. of Power Sources 209 (2012) 262– 266.
 [9]. T.G. Chang, M.M. Wright and E.M.L. Valeriotte. *The cyclic voltammetry of lead and lead-antimony battery grid alloy in aqueous sulphuric acid*. Report of Project No. 54-80-08), Ottawa-Canada (1977).
 [10]. E.N. Codaro, and F.E. Varela. *A Comparative kinetic study of Pb and Pb-Sb electrodes in sulfuric acid solutions*, J. Braz. Chem. Soc. **8**(2) (1997) 119-123.
 [11]. Phan Thi Binh, Nguyen Thi Van Anh, Mai Thi Thanh Thuy, Mai Thi Xuan, Luong Thi Thanh. *Electrochemical properties of antimony lead electrode in gelled electrolyte prepared by liquid glass and sulfuric acid using polyacrylamide together with polyaniline*. Vietnam J. Chem. **57**(4) (2019) 453-457.
 [12]. M. Sluyters-Rehbach. *Impedances of electrochemical systems: Terminology, nomenclature and representation-Part I: Cells with metal electrodes and liquid solutions (IUPAC Recommendations 1994)*. Pure &Appl. Chem. **66**(9) (1994) 1831-1891.

SENSITIVE ELECTROCHEMICAL MEASUREMENT OF As (III) USING NAFION MODIFIED PLATINUM ELECTRODE VIA ANODE STRIPPING VOLTAMMETRY

Tung Son Vinh Nguyen, Tien Minh Huynh, Linh Duy Nguyen, Tin Chanh Duc Doan, Chien Mau Dang
Institute for Nanotechnology, Vietnam National University-Ho Chi Minh City, Community 6, Linh Trung Ward, Thu Duc District, Ho Chi Minh City, Vietnam;
E-mail: ddctin@vnuhcm.edu.vn

ABSTRACT

Arsenic (As) is considered to be one of the most toxic element in water. Electrochemical techniques for the detection of As(III) have inherent advantages. In this study, a series of electrochemical experiments were performed in order to detect the concentration of Arsenic ion - As (III) concentration in aqueous phase via Anode Stripping Voltammetry (ASV) technique by using Nafion modified on platinum electrodes. The topology of the modified electrodes was characterized with Atomic Force Microscopy (AFM). The electrochemical properties of the modified electrode was performed with ASV method and the optimization parameters were found out: the amplitude of 0.02 V, frequency of 25 Hz, deposition time of 120 s. Under these optimized parameters, the linear response was in range from 0 to 40 ppb with high accuracy ($R^2 = 0.9917$). The responding time was approximately 150 s. The sensitivity of the modified Nafion/Pt electrode was 0.036 $\mu\text{A/ppb}$. The limit of detection was below 10 ppb which is approximately equal with the recommended level of World Health Organization (WHO). The results showed the possibility of using modified Nafion/Pt electrode for detection of As^{3+} in order to test the quality of domestic water.

Keywords: Nafion thin film, Modified electrode, Arsenic, ASV, Anode Stripping Voltammetry.

INTRODUCTION

One of several toxic element that cause a huge concern to human life and environment is As^{3+} . It is responsible for producing numerous types of human's disaster [1]. Arsenic is the 20th most abundant element in the earth's crust, 12th in the human body and 14th in the seawater [2]. It is a poisonous chemical widely distributed around the world and appear in four valence states (-3, 0, 3 and 5) [3]. There have been various research mentioned that As^{3+} is more toxic than inorganic As^{5+} (10 - 70 times) and several hundred times as organic arsenicals [4]. Both of them have contributed significantly to many human health problems such as skin lesions, keratosis, lung cancer and bladder cancer [5]. The World Health Organization's (WHO's) Guideline Value for arsenic in drinking water is 10 $\mu\text{g/L}$ (10 ppb) [6]. Hence, detecting and monitoring As^{3+} concentration in environmental samples have become an extremely important task for researchers all over the world.

Many studies and techniques for detection of Arsenic have been published and developed in the past 10 years. However, most of them are just suitable and workable under laboratory

circumstances such as Atomic Fluorescence Spectrometry (AFS) [7], Atomic Absorption spectrometry (AAS) [8], high performance liquid chromatography-inductively coupled plasma mass spectrometry (HPLC-ICPMS) [9] and Inductive coupled plasma optical emission spectrometry/mass spectrometry (ICP-OES/MS) [10, 11]. These techniques show good limits of detection (LOD), good sensitivity and high accuracy. However, they have some limitations such as complex equipment, high cost, complicated sample preparation and requirement about skilled operators.

In the last decade, electro-analysis has become a promising alternative to qualitatively and quantitatively detect As^{3+} due to its advantages such as low-cost, easy to operate and friendly use [12]. Many electrochemical methods have been used such as Cyclic Voltammetry (CV), Square Wave Anodic Stripping Voltammetry (SWASV), Cathodic Stripping Voltammetry (CSV) and Linear Sweep Anodic Stripping Voltammetry (LSASV) [13, 14]. Recently, Stripping voltammetry has been used. This technique has shown great advantages in sensitivity and selectivity over the voltammetric techniques [15-

17]. In stripping voltammetry of arsenic (III), various electrode materials have been used such as Platinum (Pt), Gold (Au) and variety of carbon electrodes modified with metals (Pt, Au, Ag, Ir). In 1970s, Anodic stripping voltammetry (ASV) of As^{3+} ion solid electrodes was one of the highest attention of scientists [18, 19]. Platinum nanoparticles- modified electrodes have been used in the electrochemical determination of Arsenic [20]. Nafion is a polymeric resin with good cation exchange properties and high mechanical resistances that can be used as an effective protection layer against surfactants and humic substance. Recently, Nafion has been widely used in preparation process of modified electrodes [21, 22]. Nafion coated electrodes have been used for determination of heavy metal cation in natural water [23] and some organic compounds [24].

In this article, we report a Nafion modified platinum electrode which had specific design, low fabrication cost, and could be used as a working electrode for detecting As^{3+} ion at low concentrations. The Anodic Stripping Voltammetry method was performed in various As^{3+} concentrations with the modified Nafion/Pt electrode as working electrode, planar Pt electrode as counter electrode and an external commercial Ag/AgCl electrode as reference electrode. The HCl 0.1 M solution was used as supporting electrolyte. The modified electrode showed high sensitivity and low LOD (approximately 10 ppb). The correlation between magnitude of current and concentration of As^{3+} was also determined.

EXPERIMENTAL

Materials and chemicals

All chemicals and reagents that were used for electrochemical experiments were of analytical grade purchased from Sigma-Aldrich and were used as received without further purification. As(III) standard solutions of $1000 \text{ mg}\cdot\text{L}^{-1}$ were prepared from ultrapure Arsenic trioxide (As_2O_3). Hydrochloric acid (HCl) concentration of 1 M was prepared from HCl 37%. Nafion® 117 solution (5% w/v). These solutions were added to a variety of concentrations that relied on the aim of experiments. Deionized (DI) water with a resistivity of not less than $18.2 \text{ M}\Omega\cdot\text{cm}$ was utilized during the research.

The potentiostat/galvanostat PGSTAT 302N (Metrohm, Autolab, the Netherlands) was used

for all the electro-chemical measurements. An external Ag/AgCl electrode (Basi Inc., US) was used as a reference electrode.

The physical properties of the modified electrode was examined by using Atomic Force Microscope – AFM XE7, Park System, Korea and IR optical microscope system, LUMOS, Brukers Optics, Germany.

Fabrication of the thin film Nafion/Pt electrodes

An electrochemical chip includes one Pt working electrode and one Pt counter electrode (dimension of $1.5 \text{ mm} \times 9 \text{ mm}$) with a distance of 3 mm. Pt layers were sputtered with Univex 350 (Leybold, Germany) and patterned on Si wafer with 700 nm SiO_2 layer by photolithography and lift-off techniques. The fabricated Pt electrodes had a thickness of 250 nm including a layer of titanium as an adhesion layer (**Figure 1**).

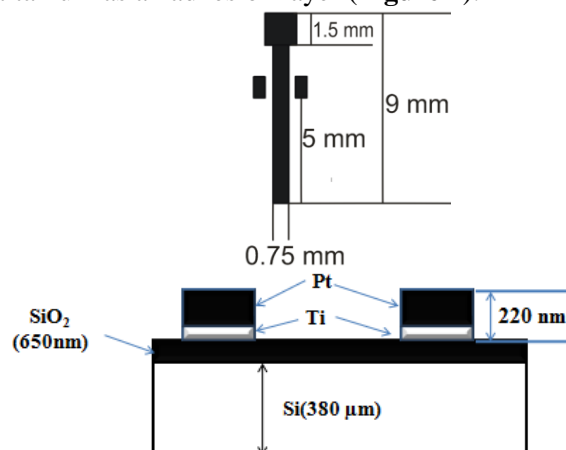


Figure 1. Design of a Pt electrode on an electrochemical chip (top) and cross section of a chip (bottom).

The thickness of the Pt electrodes was measured by a stylus profiler Dektak 6M (Veeco, US). After that, a thin layer of Nafion was formed on the Pt layer by drop-casting method. Finally, the modified electrode was dried under room temperature overnight in order to allow the Nafion thin film stabilized (**Figure 2**).



Figure 2. The photograph of Pt electrode coated with the Nafion layer.

Characterization and measurements

Characterization

Thickness and roughness of the Nafion/Pt electrode was measured by Atomic Force Microscope XE7 (Park System, Korea). The composition of Nafion/Pt film was analyzed by IR optical microscope system, LUMOS (Brukers Optics, Germany).

Electro-chemical measurements

The As^{3+} concentration was diluted in the range of 0 ppb to 40 ppb in HCl 0.1 M acting as the supporting electrolyte. The electrochemical measuring system included one working electrode (Nafion/Pt electrode), one counter electrode (Pt

electrode) and one reference electrode (Ag/AgCl commercial electrode – Basi Inc., USA).

All the electrodes were mounted on three crocodile clips. The modified chip was immersed in the electrolyte solution until the solvent level reach the indication mark (5 mm). The measuring setup is shown in **Figure 3**. Anode Stripping Voltammetry (ASV) was performed with a PGSTAT 302N potentiostat/galvanostat (Metrohm, Autolab, The Netherlands). The step potential was set 2 mV; the frequency for the measurement was 25 Hz, the amplitude was 25 mV and the temperature was about $30^{\circ}\text{C} \pm 1^{\circ}\text{C}$. Each measurement had deposition potential at -0.2 V for 120 s. The anodic stripping was performed from 0.1 V \rightarrow 0.5 V.

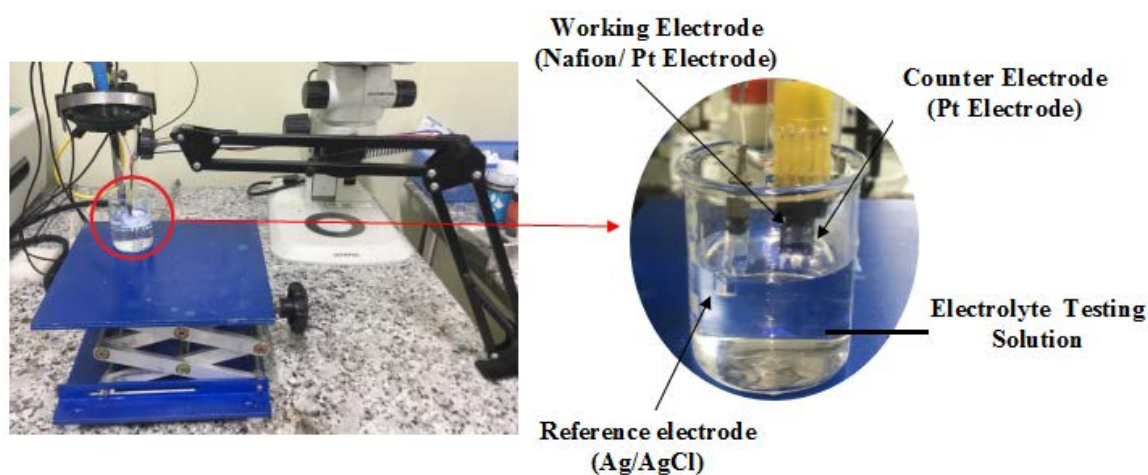


Figure 3. The measuring system set up with the Nafion/Pt electrode and Pt electrode mounted on two crocodile clips and the Ag/AgCl reference electrode.

RESULTS AND DISCUSSION

Characterization analysis of the modified Nafion/Pt electrodes

The modified electrode was observed by Atomic Force Microscope (AFM) to investigate their surface topography and thickness (**Figure 3**). The thickness of Nafion layer was approximately 1139 ± 20 nm. Also, the Nafion layer which was coated on the Pt electrode had a rather smooth surface (**Figure 3**).

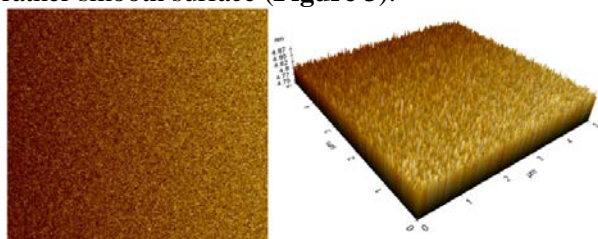


Figure 3. The AFM images and topography spectra of the modified Nafion/Pt electrode.

In addition, a chemical analysis of Nafion layer which was coated on planar Platinum electrode, was performed using energy dispersive IR optical microscope system, LUMOS (Brukers Optics, Germany) with ATR mode, the scanning range from 400 cm^{-1} – 4000 cm^{-1} . **Figure 4** shows the ATR-IR spectra of the Nafion thin film. The transmittance bands at 3456 cm^{-1} and 1642 cm^{-1} are indicated to the stretching vibration and bending vibration of the $-\text{OH}$ functional group. The peaks at 1230 cm^{-1} , 1135 cm^{-1} , 1059 cm^{-1} and 982 cm^{-1} are attributed to the characteristic functional groups of Nafion [25].

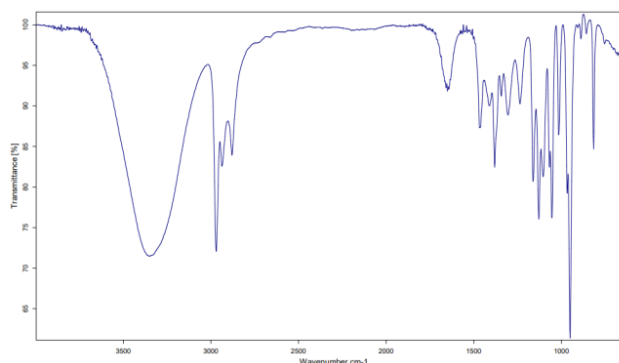


Figure 4. ATR-IR spectra of Nafion layer.

Potential measurements

Arsenic measurements

Figure 5 shows the ASWV plots of the Nafion/Pt electrode in the testing electrolyte which had various As^{3+} concentration range from 0 – 40 ppb. When the concentration of As^{3+} in the electrolyte increases, the magnitude of the current also increases from 1.84 μA to 3.28 μA . The oxidation peak was found at 0.23 V and it corresponded to the oxidation of the As^0 to As^{3+} [26]. The total measuring time was less than 3 minutes. The sensitivity of the modified electrode from 0 – 40 ppb was 0.036 $\mu A/ppb$. It was higher than the sensitivity ($5.07 \cdot 10^{-5}$ $\mu A/ppb$) of E. Mafakheri et al. [27] and 0.005 $\mu A/ppb$ of S. S. Hassan et al. [28].

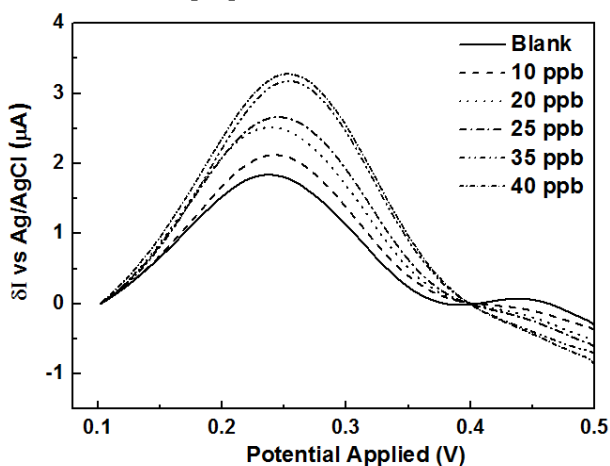


Figure 5. The ASWV plots of the Nafion/Pt electrode in electrolyte solution with various As^{3+} concentration.

The relationship between the magnitude of the current of the cathode peak (0.238 V) and the arsenic concentration was shown in Figure 6. It was linear with high coefficient of determination ($R^2 = 0.9917$).

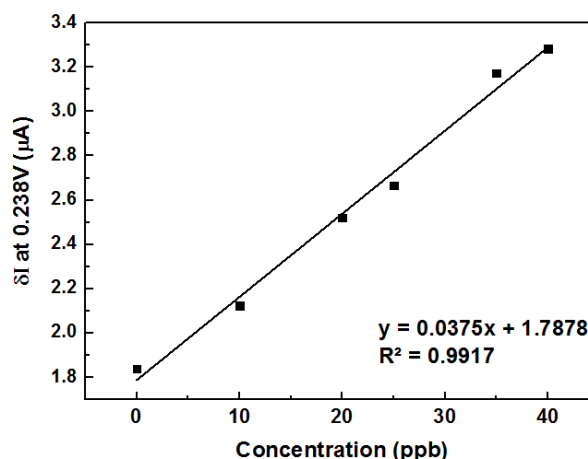


Figure 6. The relationship of the cathode peak current and concentration of As^{3+} in the range of 0 – 40 ppb.

The results shown that the modified Nafion/Pt electrode was able to measure As^{3+} at low concentration (10 ppb) with high accuracy ($R^2 = 0.9917$) and high sensitivity (0.036 $\mu A/ppb$).

Reproducibility of the modified electrode

The reproducibility of the modified electrode was carried out by repeating a measurement of same concentration for 3 times using one electrode (the chosen concentration was 10 ppb). The standard deviation of 3 consecutive measurements was 0.03 and the relative standard deviation (RSD) of the current response was 2.03 %.

CONCLUSION

In this paper, the modified Nafion/Pt electrode was designed and fabricated. A thin layer of Nafion that had the thickness of about $1,139 \pm 20$ nm and had a smooth surface. It was coated on the planar Platinum electrode, acting as a protection layer. Via ASWV method, the modified electrode possessed a good performance to detect arsenic with low LOD (less than 10 ppb), high accuracy ($R^2=0.9917$) and high sensitivity (RSD= 2.03%). Moreover, this modified electrode had more advantages such as fast analysis (less than 3 minutes), ease to use and low cost fabrication.

Acknowledgment

This research is funded by Vietnam National University - Ho Chi Minh City (VNU-HCM) under the grand number TX2019-32-01.

References

- [1] Shah, A.Q., et al., *Hazardous impact of arsenic on tissues of same fish species collected from two ecosystem*. Journal of hazardous materials, 2009. **167**(1-3): p. 511-515.
- [2] Mandal, B.K. and K.T. Suzuki, *Arsenic round the world: a review*. Talanta, 2002. **58**(1): p. 201-35.
- [3] Smedley, P.L. and D.G. Kinniburgh, *A review of the source, behaviour and distribution of arsenic in natural waters*. Applied Geochemistry, 2002. **17**(5): p. 517-568.
- [4] Chen, Y., et al., *Toxic Effect of Inorganic Arsenite [As(III)] on Metabolic Activity of Bacillus subtilis by Combined Methods*. Current microbiology, 2008. **57**: p. 258-63.
- [5] Calderon, W.R.C.C.O.A.R.L., *Arsenic Exposure and Health Effects III*, 1999, San Diego, California: Elsevier Science. 416.
- [6] WHO -Geneva, C., World Health Organization, *Guidelines for drinking-water quality. Vol. 2. Health criteria and other supporting information*. 2nd ed. ed. 1996, Geneva, Switzerland: World Health Organization (WHO).
- [7] Dash, S. and N. Munichandraiah, *Electroanalysis of As(III) at nanodendritic Pd on PEDOT*. Analyst, 2014. **139**(7): p. 1789-1795.
- [8] Aggett, J. and M.R. Kriegman, *The extent of formation of arsenic(III) in sediment interstitial waters and its release to hypolimnetic waters in Lake Ohakuri*. Water Research, 1988. **22**(4): p. 407-411.
- [9] Wang, P., et al., *High-performance liquid chromatography-inductively coupled plasma mass spectrometry based method for the determination of organic arsenic feed additives and speciation of anionic arsenics in animal feed*. J Agric Food Chem, 2010. **58**(9): p. 5263-70.
- [10] Jitmanee, K., M. Oshima, and S. Motomizu, *Speciation of arsenic(III) and arsenic(V) by inductively coupled plasma-atomic emission spectrometry coupled with preconcentration system*. Talanta, 2005. **66**(3): p. 529-533.
- [11] Gil, R., et al., *On-line arsenic co-precipitation on ethyl vinyl acetate turning-packed mini-column followed by hydride generation-ICP OES determination*. Journal of hazardous materials, 2007. **143**: p. 431-6.
- [12] Kopanica, M. and L. Novotný, *Determination of traces of arsenic(III) by anodic stripping voltammetry in solutions, natural waters and biological material*. Analytica Chimica Acta, 1998. **368**(3): p. 211-218.
- [13] Hung, D.Q., O. Nekrassova, and R.G. Compton, *Analytical methods for inorganic arsenic in water: a review*. Talanta, 2004. **64**(2): p. 269-77.
- [14] Luong, J.H.T., E. Lam, and K.B. Male, *Recent advances in electrochemical detection of arsenic in drinking and ground waters*. Analytical Methods, 2014. **6**(16): p. 6157-6169.
- [15] Jagner, D., *Computerised flow potentiometric stripping analysis*. TrAC Trends in Analytical Chemistry, 1983. **2**(3): p. 53-56.
- [16] Hoyer, B. and L. Kryger, *Evaluation of single-point calibration in flow potentiometric stripping analysis*. Talanta, 1986. **33**(11): p. 883-8.
- [17] Cleven, R. and L. Fokkert, *Potentiometric stripping analysis of thallium in natural waters*. Analytica Chimica Acta, 1994. **289**(2): p. 215-221.
- [18] Holak, W., *Determination of arsenic by cathodic stripping voltammetry with a hanging mercury drop electrode*. Analytical Chemistry, 1980. **52**(13): p. 2189-2192.
- [19] Forsberg, G., et al., *Determination of arsenic by anodic stripping voltammetry and differential pulse anodic stripping voltammetry*. Analytical Chemistry, 1975. **47**(9): p. 1586-1592.
- [20] Dai, X. and R.G. Compton, *Detection of As(III) via oxidation to As(V) using platinum nanoparticle modified glassy carbon electrodes: arsenic detection without interference from copper*. Analyst, 2006. **131**(4): p. 516-21.
- [21] Martínez-Huitle, C.A., et al., *Fabrication and application of Nafion®-modified boron-doped diamond electrode as sensor for detecting caffeine*. Diamond and Related Materials, 2010. **19**(10): p. 1188-1193.
- [22] Yan, B., et al., *Glassy carbon electrode modified with G-MoS₂-Nafion acts as an electrochemical biosensor to determine uric acid in human serum*. Molecular medicine reports, 2018. **18**(3): p. 3193-3202.
- [23] Xu, H., et al., *A Nafion-coated bismuth film electrode for the determination of heavy metals in vegetable using differential pulse anodic stripping voltammetry: An alternative to mercury-based electrodes*. Food Chemistry, 2008. **109**: p. 834-839.
- [24] Vreeland, R.F., et al., *Biocompatible PEDOT:Nafion Composite Electrode Coatings for Selective Detection of Neurotransmitters in Vivo*. Analytical Chemistry, 2015. **87**(5): p. 2600-2607.
- [25] Kumari, D., *Vibrational Spectroscopy of Ion exchange Membranes*. 2011.
- [26] Melinte, G., et al., *Electrochemical Fingerprint of Arsenic (III) by Using Hybrid Nanocomposite-Based Platforms*. Sensors (Basel, Switzerland), 2019. **19**(10): p. 2279.
- [27] Mafakheri, E., et al., *Synthesis of Iridium Oxide Nanotubes by Electrodeposition into Polycarbonate Template: Fabrication of Chromium(III) and Arsenic(III) Electrochemical Sensor*. Electroanalysis, 2011. **23**.
- [28] Hassan, S.S., et al., *Nafion stabilized ibuprofen-gold nanostructures modified screen printed electrode as arsenic(III) sensor*. Journal of Electroanalytical Chemistry, 2012. **682**: p. 77-82.

PREPARATION OF SILVER NANOPARTICLES INK FOR INKJET PRINTING TECHNOLOGY

Huong Kim Tran, Ngan Nguyen Le, Dung My Thi Dang and Chien Mau Dang

Institute for Nanotechnology, Vietnam National University-Ho Chi Minh City, Community 6, Linh Trung Ward, Thu Duc District, Ho Chi Minh City, Vietnam;
Email: huongtk@vnuhcm.edu.vn

ABSTRACT

The goal of this paper is to synthesize silver nanoparticles (AgNPs) ink for piezoelectric inkjet printer. Firstly, the colloidal AgNPs are synthesized from silver nitrate (AgNO_3) by wet oxidation method with polyvinyl pyrrolidone (PVP) as capping agent and ethylene glycol (EG) as solvent as well as reducing agent. After that, AgNPs solution is characterized by Ultraviolet-visible spectrophotometry (UV-Vis). Silver nanoparticles inks are prepared from organic solvents to achieve the appropriate physical and chemical parameters for our Dimatix piezoelectric inkjet printers which are particle size less than 50 nm, viscosity in range from 8 to 20 cP and surface tension in range from 22 to 36 mN/m. Additionally, this ink has the stability period more than 7 months which was determined by Ultraviolet-visible spectrophotometry (UV-Vis) and Transmission electron microscopy (TEM). Finally, an antenna was printed by this ink on the paper substrate. A simple conductivity test was performed by LED light bulbs testing. Therefore, this AgNPs ink can be used for inkjet printing technology in future electronic applications.

Keywords: Silver nanoparticles, AgNPs, the conductive ink, inkjet printing technology

INTRODUCTION

Nowadays, the silver nanoparticles have been attracting a lot of research interest all over the world. Many studies have shown that thanks to the rich shape and size of silver nanoparticles lead to the diverse properties such as their mechanical properties, electrical conductivity, thermal conductivity, optical absorption and melting point [1-3]. Their advantages of properties enable them to achieve many potential applications in various fields such as antibacterial activity [4], optical sensor [5], components in composite materials [6], integrated circuits [1] and others [7-10].

In particular, conductive ink based on silver nanoparticles applied to inkjet technology that is increasingly being researched and applied in the manufacture of electronic circuits [7-10]. Therefore, ink is a key problem in this technology. This requires the ink to meet the conditions associated with the inkjet process, including issues such as viscosity, surface tension, and particle size within the device's permissible range. In this paper, the ink has been synthesized with the satisfactory parameters of our inkjet equipment.

To prepare silver nanoparticles ink, firstly, silver nanoparticles should be synthesized. There

are many fabrication methods of silver nanoparticle including chemical reduction [11-12], microwave assisted method [13], irradiation methods [14], etc. In particular, wet chemical method using surfactants (or capping agents) have shown many advantages such as simple process, easy to control the reaction conditions to obtain the desired particle size, and high stability. Generally, there are three main components in chemical method: silver precursors for formation of AgNPs such as AgNO_3 , AgCl , AgClO_4 , etc, reducing agents such as glucose, sodium citrate, ethylene glycol, etc and capping agents such as polyvinylpyrrolidone (PVP), polyvinyl alcohol (PVA), sodium oleate, etc [15-17]. In the paper, Polyvinyl pyrrolidone (PVP) has been used thanks to its' excellent characteristics including stability, controlled particle size, protective capacity of the AgNPs to prevent their agglomeration and oxidation processes and ability to be decomposed after centrifuging and sintering [18].

EXPERIMENTAL

Materials

The chemicals used for the experiments included silver nitrate (AgNO_3 , 99.8% Spain), polyvinyl pyrrolidone (PVP, average molecular

weight of 10,000) purchased from Sigma-Aldrich. The solvents such as ethanol 99%, isopropanol 98%, ethylene glycol 98%, glycerol 98%, ethyl formate 97%, ethyl acetate 99.8%, diethyl oxalate, ethyl glycolate 98%, 2-isopropoxyethanol 99%, 2-methyl-1,3-dioxolane were purchased from Merck, Germany and acetone was purchased from China. All aqueous solutions were prepared using ultrapure water with a resistivity of 18.2 MΩ.cm.

Synthesis of silver nanoparticles and prepare of silver nanoparticles ink

To synthesize the silver nano colloidal solution, first, an appropriate amount of PVP was added in 40 ml EG by an ultrasonic probe (VCX 750, Sonics, USA) and this solution was cooled to room temperature. Next, AgNO₃ was mixed into PVP/EG solution for 3 minutes 30 seconds. This reaction ended when the solution is darker greencolor. The colloid solution was characterized by UV-Vis to make sure silver nanoparticles were formed in the colloid solution. Afterwards, the ultra-centrifuge system (CP80NX, Hitachi, Japan) was used to wash and precipitate AgNPs. After that, the AgNPs powders were dispersed in organic solvents such as 18.2 wt% DI, 18.37 wt% ethanol, 2.22 wt% ethylene glycol, 3.92 wt% isopropanol, 34.36 wt% glycerol, 0.15 wt% 2-isopropoxyethanol, 0.38 wt% ethyl acetate, 0.76 wt% Ethyl formate, 0.18 wt % ethyl glycolate, 0.07 wt% 2-methyl-1,3-dioxolane, 0.09 wt% Diethyloxalate and 1.3 wt% acetone to prepare the 20 ± 2 wt% conductive solution. According to the requirement, the viscosity of ink solution is limited to 8-12cP and the surface tension is about 22-36 mN/m to make sure the ink droplets are well sprayed by Dimatix inkjet printers. Therefore, the ink is synthesized from many types of solvents to adjust accordingly. The viscosity of the ink is then measured by m-VROC Viscometer, RheoSense and surface tension measured by the KSV CAM 101.

Inkjet printing experiments

Dimatix inkjet printer DMP-2800 (Fujifilm Dimatix, USA) was utilized with 16 nozzle cartridges of 10-picoliter drop volume (DMCLCP-11610) for printing antenna on paper substrate by the silver nanoparticle ink. The parameters of the inkjet printing process included substrate temperature set at 32°C, drop spacing of 15 μm and voltage of 25V. These parameters were optimized conditions to obtain good quality

of the printed lines and the ink droplets. After that, simple conductive test was performed to evaluate the quality of antenna by testing LED light bulbs.

RESULTS AND DISCUSSION

The formation of silver nanoparticles

After the AgNPs colloids synthesis, the solution was analyzed by UV-Vis spectrometer and the result was shown in **Figure 1**. **Figure 1** showed the optical absorbance which appeared at a wavelength between 400 nm and 420 nm (the surface plasmon resonance (SPR) peak at 409 nm). Each type of metal nano-particles has a wavelength in UV-Vis range which feature by characteristic oscillation of valence electrons. Wavelength region between 400 nm and 420 nm is attributed to the surface plasmon resonance (SPR) peak of the silver nanoparticles [19-20].

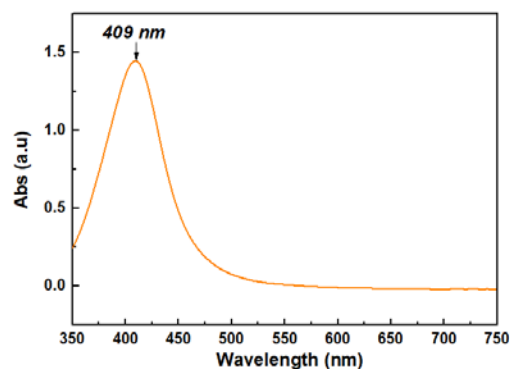


Figure 1. The UV-Vis spectra of the AgNPs with PVP in the EG solution.

3.2. The formation and stability of silver nanoparticles ink

Table 1 showed the viscosity and surface tension of ink in three times. Based on the required viscosity of 8-20 cP and surface tension of 22-36 mN/m, the ink solution was suitable for printing by Dimatix inkjet printer.

Table 1. Surface tension and Viscosity of ink solution

Surface tension (mN/m)	Viscosity (cP)
30.59	9.38
30.68	9.34
30.48	9.32

To investigate the stability of the silver nanoparticle ink, **Figure 2** illustrated the UV-Vis spectra of the AgNPs existence in ink solution. Results of the UV-Vis spectra showed that no oxidation or strong interaction at the surface of the nanoparticles exists. Based on the wavelength

region of the SPR of the silver nanoparticles within 7 months, it showed that the product after 7 months of storage was still stable.

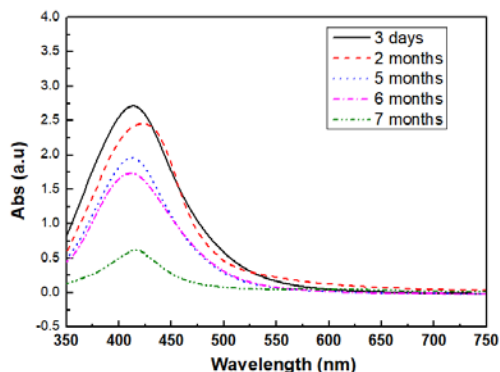


Figure 2. The UV-Vis spectra of the conductive ink based on silver nanoparticles.

Further, the morphology and distribution of AgNPs in the conductive solution was investigated by TEM images. Figure 3 showed that AgNPs ink dispersed well and did not agglomerate within 7 months.

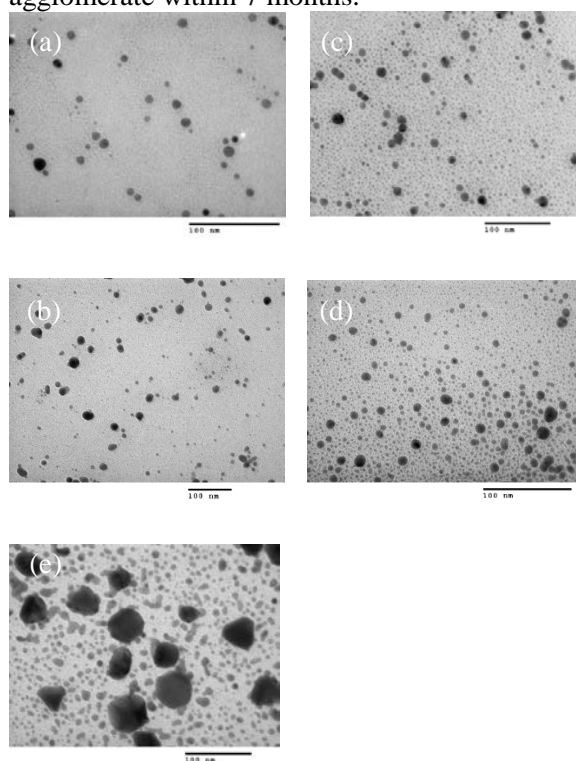


Figure 3. TEM image of synthesized silver nanoparticles ink: (a) 3 days (b) 2 months (c) 5 months (d) 6 months and (e) 7 months.

According to the TEM images after the different times (3 days, 2 months, 5 months, 6 months and 7 months), we computed the diameter region of the AgNPs by ImageJ software. Table 2 showed particle size was less than 50 nm in

during 7 months. It was suitable for printing by Dimatix inkjet printer (the diameter of the printing nozzles was 21.5 μm).

Table 2. AgNPs size in ink solution

Time	3 days	2 months	5 months	6 months	7 months
Size (nm)	8-12	9-15	13-18	10-15	25-35

Inkjet printing experiments

The silver nanoparticles ink was injected into the cartridge of inkjet printer. An antenna design was installed into software of computer. After printing, Figure 4 showed the results of antenna. In this figure, a silver nanoparticle layer had already formed on the paper substrate.



Figure 4. The antenna sample (14 x 6 cm) was printed by the AgNPs ink.

A simple conductivity test was performed by touching an LED to the antenna layer. Figure 5 showed the bulb was lighted, this result was demonstrated that the upper layer can be viewed as an electronic circuit. Therefore, it can be applied to other electronic applications.

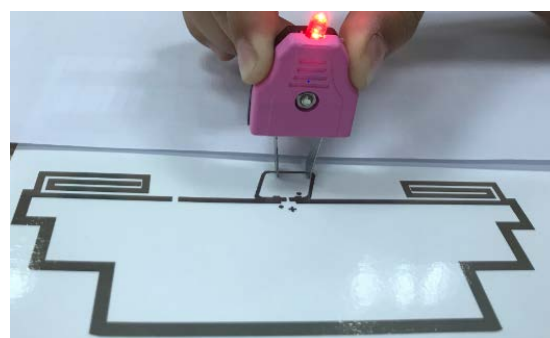


Figure 5. The lighting of LED

CONCLUSION

In this report, the AgNPs ink were prepared from 12 types of solvent as DI, ethanol, ethylene glycol, isopropanol, glycerol, ethyl acetate, 2-isopropoxyethanol, ethyl formate, ethyl glycolate, 2-methyl -1,3-dioxolane,

diethyloxalate and acetone to meet the printer's requirements. The AgNPs existence in ink solution was convinced with the surface plasmon resonance shown in 400-420 nm region of UV-Vis spectrum. The TEM and UV-Vis spectrum observation also confirmed that diameter of particles was smaller than inner diameter of nozzles of the printer and this ink solution had high stability period, more than 7 months. The results showed that our ink can be printed by piezoelectric inkjet printer. After that, simple test proved conductivity of printed pattern by lighting of LED. Therefore, this conductive ink solution can be applied for fabrication of high efficiency electronic circuits by inkjet printing.

Acknowledgment

This research is funded by Vietnam National University – Ho Chi Minh City (VNU-HCM) under the grand number TX2019-32-01.

References

- [1] D. Kim, S. Jeong, S. Lee, B.K. Park, and J. Moon., *Organic thin film transistor using silver electrodes by the ink-jet printing technology*, Thin Solid Films, **515** (2007), 7692-7696
- [2] Sang Hwa Yoon, Jun Ho Lee, Pyoung Chan Lee, and Jae Do Nam, *Sintering and Consolidation of Silver Nanoparticles Printed on Polyimide Substrate Films*, Macromolecular Research, **17** (2009), 568-574
- [3] Vesna V Vodnik, Dusan K. Bozanic, Dusan K. Bozanic, Bibić, N. Jovan M Nedeljković, Jovan M Nedeljković, *Optical Properties of Shaped Silver Nanoparticles*, Journal of Nanoscience and Nanotechnology, **8** (2008), 3511-3516
- [4] VK. Sharma, RA. Yngard, Y. Lin, *Silver nanoparticles: Green synthesis and their antimicrobial activities*, Advanced Colloidal Interface Science. 2009, **145** (2009), 83-96
- [5] Ganesharajah M and Koneswaran M, *Citrate Capped Silver Nanoparticles as Optical Sensor for Ferric Ions*, International Journal of Nanomedicine, **3** (2018), 63-70
- [6] Yingsi Wu, Lun-De Liao, Han-Chi Pan, Leng He, Chin-Teng Lind and Mei Chee Tan, *Fabrication and interfacial characteristics of surface modified Ag nanoparticle based conductive composites*, RSC Advances, **7** (2017) 29702-29712
- [7] Kotthaus S, Gunther B H, Hang R and Schafer H, *Properties of polyacrylic acid-coated silver nanoparticle ink for inkjet printing conductive tracks on paper with high conductivity*, Materials Chemistry and Physics, **147** (2014), 550-556
- [8] Wang F, Mao P, He H, *Dispensing of high concentration Ag nano-particles ink for ultra-low resistivity paper-based writing electronics*, Scientific reports, **6** (2008), 21398
- [9] X.K. Wang, L. Shao, W.L. Guo, J.G. Wang, Y.P. Zhu, C. Wang, *Synthesis of dendritic silver nanostructures by means of ultrasonic irradiation*, Ultrason. Sonochem. **16** (2009), 747-751
- [10] Archana Ghosale et al, *Direct-writing of paper based conductive track using silver nano-ink for electroanalytical application*, Electrochimica Acta, **209** (2016) 511-520
- [11] Cho MS, Choi WH, Kim SG, Kim IH, Lee Y, *A low sintering temperature and electrical performance of nanoparticle copper ink for use in ink-jet printing*, J Nanosci Nanotechnol, **10** (2010), 6888-6891
- [12] Muhammad Akram Raza et al, *Size- and shape-dependent antibacterial studies of silver nanoparticles synthesized by wet chemical routes*, Nanomaterials, **6** (2016), 74, 15 pages
- [13] Yaguo Cai et al, *Large-scale and facile synthesis of silver nanoparticles via a microwave method for a conductive pen*, RSC Adv, **7** (2017), 340041-34048
- [14] M. Tajdidzadeh et al, *Synthesis of silver nanoparticles dispersed in various aqueous media using laser ablation*, The Scientific World Journal, **2014** (2014), 324921, 7 pages
- [15] Pastoriza-Santos I, Liz-Marzán LM, *Formation of PVP-protected metal nanoparticles in DMF*, Langmuir, **18** (2002), 2888-2894
- [16] Qijin Huang et al, *Properties of polyacrylic acid-coated silver nanoparticle ink for inkjet printing conductive tracks on paper with high conductivity*, Materials Chemistry and Physics, **147** (2014), 550-556
- [17] Alaa Fahmy et al, *Ultra-thin films of Poly(acrylic acid)/Silver nanocomposite coatings for antimicrobial applications*, Journal of Spectroscopy, **10** (2016), 11 pages
- [18] B. Ajitha, Y. Ashok Kumar Reddy, P. Sreedhara Reddy, Hwan-Jin Jeon and Chi Won Ahn, *Role of capping agents in controlling silver nanoparticles size, antibacterial activity and potential application as optical hydrogen peroxide sensor*, RSC Advances, **6** (2016), 36171-36179
- [19] D. Paramelle, A. Sadovoy, S. Gorelik, J. Hopley, D.G. Fernig (2014), *A rapid method to estimate the concentration of citrate capped silver nanoparticles from UV - Visible light spectra*, Analyst, **139** (2014), 4855.
- [20] Floriano Cuccureddu, Shane Murphy, Igor V. Shvets, Mauro Porcu and H. W. Zandbergen, *Plasmon Resonance in Silver Nanoparticles Arrays Grown by Atomic Terrace Low-Angle Shadowing*, Nano Letters, **8** (2008), 3248- 3256.

FABRICATION OF GRAPHENE THIN FILMS ON FLAT SUBSTRATE BY SPIN-COATING METHOD COMBINED WITH CORONA PLASMA TREATMENT

Tien Minh Huynh¹, Tung Thanh Viet Nguyen^{1,2}, Chien Mau Dang¹, Tung Thanh Bui¹

¹ Institute for Nanotechnology, Vietnam National University-Ho Chi Minh City, Community 6, Linh Trung Ward, Thu Duc District, Ho Chi Minh City, Vietnam

² University of Technology, Vietnam National University-Ho Chi Minh City, 268 Ly Thuong Kiet St., Ward 15, Dist. 10, Ho Chi Minh City, Vietnam

Email: hmtien@vnuhcm.edu.vn

ABSTRACTS

Graphene is more and more applied in various fields due to its exceptional properties. In this study, graphene was prepared by Modified Hummers method, reduced by thermal/chemical reduction then coated on plane substrate by spin coating. However, graphene cannot stick on the normal substrate thus corona discharge was suggested as a treatment to enhance the adhesion of graphene and substrate. Formed graphene film and the effects of corona treatment were analyzed by some methods such as FE-SEM and elemental analysis of chemical characterization of graphene coated membrane was performed by EDX. The analyzed results shown that corona treatment increased significantly the adhesion between graphene and substrate. Graphene film was formed uniformly with high purity with oxygen weight percentage of 5.63% and carbon weight percentage of 94.37 %. Corona plasma was proved to be an effective and low-cost method for making graphene films to replace thermal CVD or Epitaxy methods.

Keywords: Corona plasma treatment, improved adhesion, surface treatment

INTRODUCTION

Graphene is a 2D material carbon which has attracted tremendous research interest in recent years, owing to its exceptional properties in electronic, mechanical and chemical properties. For example, graphene has high mobility of electrons or holes carrier ($230,000 \text{ cm}^2/\text{Vs}$), transmittance in the visible spectrum is nearly 98%, thermal conductivity is about $3,000 \text{ W/mK}$, surface area is of $2,600 \text{ m}^2/\text{g}$ and many other properties such as Hall effect and magnetism [1-3]. In another side, graphene can be considered as a material that forms different types of graphite derivatives (nanocarbon tubes, fullerene balls) woven with sp^2 carbon atoms. Moreover, graphene has been incorporated as a new building block in composite materials for a wide range of applications taking advantage of its thermal stability and exceptional mechanical properties. The two dimensionality and structural flatness of graphene sheets for thin-film devices and combinations with other semi-conductive materials like silicone have been applied. These

films typically show sheet resistances on the order of several hundred ohm per square at about 80% optical transparency [4-7]. A continuous single-layer graphene film could retain high conductivity at very low (atomic) thickness, and avoid contact resistance that occurs in a carbon nanotube film between interconnected nanotube bundles. Thus, there is another approach to combining the use of graphene and silicon thin film by means of graphene oxide coating on the surface of the plate, then by reducing the graphene, eventually forming a new graphene layer in contact with the silicon film on the glass wafer that was constructed in the CVD process [2, 3, 8]. However, GO is not able to be easily retained on the plate surface. This article considered a new way to increase adhesion to the substrate it is using discharging corona plasma. A corona discharge is a mechanism by which a high-potential electrode current flows into a neutral liquid, normally water, by ionizing the fluid in such a way as to generate a region of plasma around the

electrode. Corona discharge has a number of commercial and industrial applications such as manufacture of ozone, audible noise, changes of chemical composition on the fiber surface, improved color depth considerably of wool fiber and fabric, provided excellent hydrophilic properties, efficient biocidal effect on most bacteria, algae and fungi in water and it is commonly used for surface activation and surface charging application [8-10]. In contrast to traditional plasma technology, which uses a power supply at a radio or a microwave frequency, reduced pressure in some applications involves pump-down and the subsequent repressurization of the parts to be handled, and because of the heating of gas the cooling system is often required. This is the principle for the development of lower power consumption, faster processing time and higher throughput. It therefore leads to a simpler, less complex and more efficient method, which makes it easier to extend the process from the laboratory to a large one. In this paper, plasma corona is added to surface treatment, which improves the wafer's adhesion before deposited graphene layer by spin coating method.

EXPERIMENTAL

Surface treatment using corona plasma method

RCA1 cleaning process [6] was used to remove the contamination on the substrate surface before coating GO. Corona plasma (BD-20V, ELECTRO-TECHNIC PRODUCT, US) was used as a surface treatment method. The samples were exposed to various plasma conditions. The distance between the electrode and the sample surface is unchanged at approximately 1 cm. The plasma time was remain stable at 120s throughout the experiments

Preparation of graphene oxide (GO)

Firstly, Graphite powder (Sigma – Aldrich, Germany) was used to prepared graphene oxide (GO) by the modified Hummers method [11]. Then, the original GO – containing solutions that is diluted with a ratio of 1:100 to spin-coated onto the substrate of glass by spinner (DELTA 6RC, SUSS Microtec, Germany). The coating speed and time were observed throughout the experiments according to the table 1 below.

Table 1. The spin-coating parameters to deposition GO solutions on glass

Symbol	1 st Speed (rpm)	1 st Time (s)	2 st Speed (rpm)	2 st Time (s)
S1	100	5	200	20
S2	100	5	500	20
S3	100	5	1000	20
S4	100	5	1500	20

Finally, the samples were dried with the different thermal reduction about 30 min to convert into the solid thin films on the substrate. All aqueous solutions were prepared with Deionized water (18 MΩ, Purelab, US). Characterization of fabricated graphene layer on glass

Characterization of fabricated graphene layer on the glass substrate

The morphologies of fabricated samples were investigated by Field Emission scanning electron microscope, FE-SEM (SU8000, Hitachi, Japan). Elemental analysis of chemical characterization of graphene coated membrane was performed by EDX (EDAX), Raman spectra of the samples were obtained by LABRAM 300 Instrument (Horiba, France) with a 630.8 nm laser. The Go films thicknesses were characterized by Atom Force Microscope (Park XE7, Korea). The EddyCus® TF map 2525SR (SURAGUS GmbH - Sensors and Instruments, Germany) was used to measure the sheet resistances (up to 10 inches x 10 inches) of graphene films in non-contact mode.

RESULTS AND DISCUSSION

The 120s plasma corona time was used to investigate the effect of rotational speed on the slide surface in accordance with the parameters in Table 1.

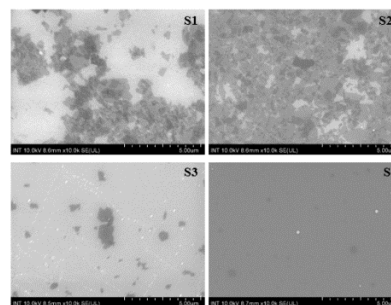


Figure 1. Fe-SEM image with different rotation speeds.

Figure 1 shows the distribution of GO to the substrate with different rotational speeds. As can be seen, the amount of GO sticking to the substrate is relatively large with rotational speeds S1, but there is a phenomenon of agglomeration, uneven distribution forming overlapping films. At rotation speed S2, GO is distributed on the substrate relatively much and evenly. At the speed of S3, only a very small amount of GO is bound to the surface and GO is no longer detected at the speed of S4.

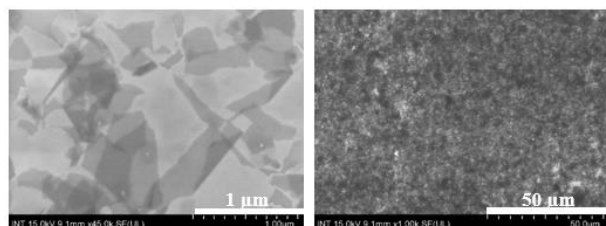


Figure 2. Fe-SEM image with magnification of $\times 45k$ (left) and $\times 1k$ (right) of GO film at rotation speed S2.

From the above results, it can be seen that the S2 rotation speed is optimal for the GO solution to be rotated on the glass substrate, forming a uniform film and covering the substrate surface (Figure 2). At a magnification of 45k (Figure 2) several fragments of the GO membrane can be seen almost transparent, which demonstrates the efficiency of peeling off graphite oxide layers to form monolayer graphene oxide.

The EDX spectra of graphene reduced at 500°C, 600°C, 700°C, 800°C, and 900°C have been carried out in nitrogen. EDX spectrum of graphene shows the presence of signals for carbon and oxygen with carbon weight percentage and oxygen weight percentage as table 2 and figure 3. The results shown that the more the temperature increases, the more the number of oxygen atoms get out of the bond. At 900°C, oxygen is almost completely reduced with oxygen weight percentage of 5.63% and this result is consistent with previous studies [12, 13].

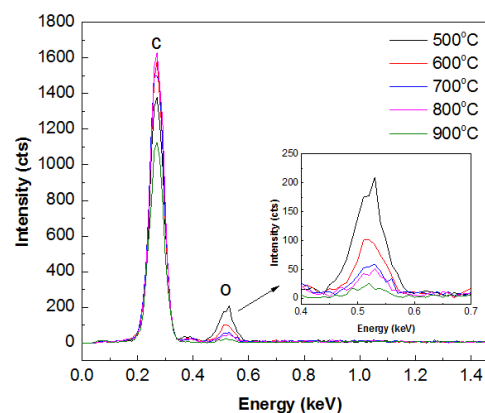


Figure 3. EDX spectrum of graphene films with various thermal reduction from 500°C to 900°C.

Table 2. Atoms weight percentage of fabricated graphene films with different thermal reduction.

Elements	Weight %				
	500°C	600°C	700°C	800°C	900°C
C K	71.89	83.17	90.19	88.55	94.37
O K	28.11	16.83	9.81	11.45	5.63

CONCLUSION

In this study, the GO solutions were well prepared by modified Hummer's method. The substrates were treated with corona plasma at room conditions to improve the surface adhesion. The GO films were well deposited on the substrate with corona plasma treated. The optimal time of plasma process is of 120s. Graphene thin films was formed uniformly with high purity with oxygen weight percentage of 5.63% and carbon weight percentage of 94.37 %. Corona plasma was proved to be an effective and low-cost method for making graphene films to replace thermal CVD.

Acknowledgement

This study is funded by Vietnam National University Ho Chi Minh City (VNUHCM) under the grant number 562-2018-32-02.

Reference

- [1] Nomura, K. and A.H. MacDonald, *Quantum Hall ferromagnetism in graphene*. Physical review letters, 2006. **96**(25): p. 256602.
- [2] Stankovich, S., et al., *Graphene-based composite materials*. nature, 2006. **442**(7100): p. 282.
- [3] Stankovich, S., et al., *Stable aqueous dispersions of graphitic nanoplatelets via the reduction of exfoliated graphite oxide in the presence of poly (sodium 4-styrenesulfonate)*. Journal of Materials Chemistry, 2006. **16**(2): p. 155-158.
- [4] Sutter, P.W., J.-I. Flege, and E.A. Sutter, *Epitaxial graphene on ruthenium*. Nature materials, 2008. **7**(5): p. 406.
- [5] Li, X., et al., *Large-area synthesis of high-quality and uniform graphene films on copper foils*. science, 2009. **324**(5932): p. 1312-1314.
- [6] Dai, B., et al., *High-quality single-layer graphene via reductive reduction of graphene oxide*. Nano Research, 2011. **4**(5): p. 434-439.
- [7] Martinek, T.A. and F. Fülöp, *Peptidic foldamers: ramping up diversity*. Chemical Society Reviews, 2012. **41**(2): p. 687-702.
- [8] Li, X., et al., *Highly conducting graphene sheets and Langmuir–Blodgett films*. Nature nanotechnology, 2008. **3**(9): p. 538.
- [9] Ryu, J., T. Wakida, and T. Takagishi, *Effect of corona discharge on the surface of wool and its application to printing*. Textile Research Journal, 1991. **61**(10): p. 595-601.
- [10] Reina, A., et al., *Large area, few-layer graphene films on arbitrary substrates by chemical vapor deposition*. Nano letters, 2008. **9**(1): p. 30-35.
- [11] Hummers Jr, W.S. and R.E. Offeman, *Preparation of graphitic oxide*. Journal of the american chemical society, 1958. **80**(6): p. 1339-1339.
- [12] Li, X., et al., *Anomalous behaviors of graphene transparent conductors in graphene–silicon heterojunction solar cells*. Advanced Energy Materials, 2013. **3**(8): p. 1029-1034.
- [13] Shi, E., et al., *Colloidal antireflection coating improves graphene–silicon solar cells*. Nano letters, 2013. **13**(4): p. 1776-1781.

SURFACE CHARACTERIZATION OF CORONA PLASMA-TREATED SILICON SURFACE WITH DEPOSITED REDUCED GRAPHENE OXIDE SHEETS FOR SOLAR CELL APPLICATIONS

Tung Thanh Bui¹, Tien Minh Huynh¹, Tung Thanh Viet Nguyen^{1,2} and Chien Mau Dang¹

¹Institute for Nanotechnology, Vietnam National University-Ho Chi Minh City, Community 6, Linh Trung Ward, Thu Duc District, Ho Chi Minh City, Vietnam

²University of Technology, Vietnam National University-Ho Chi Minh City, 268 Ly Thuong Kiet St., Ward 15, Dist. 10, Ho Chi Minh City, Vietnam

Email: bt tung@vnuhcm.edu.vn

ABSTRACTS

Corona discharge has attracted significant interests over decades due to its usefulness and a variety of applications. Adhesion improvement of film surfaces is among the most important applications of plasma treatment. In this study, the adhesive properties of the plasma modified silicon surfaces and reduced graphene oxide (rGO) multilayer films have been investigated. The silicon surfaces were treated by corona plasma treatment before rGO was deposited by spin-coating method. The change in hydrophilicity of modified silicon surface was analyzed by contact angle measurements and surface energy as a function of exposure time. In addition, plasma-treated surfaces have been subjected to an ageing process to determine the durability of the plasma treatment. Changes in morphological and chemical composition of surfaces were observed by Field Emission Scanning Electron Microscopes (FE-SEM) and Atomic force microscopy (AFM). The results show that the roughness of the surface increased due to exposure time of 120s and the average adhesive energy of 5.774 fJ and the plasma-modified silicon substrate rose compared with untreated surface.

Keywords: Corona plasma treatment, improved adhesion, surface treatment

INTRODUCTION

Dye-sensitized solar cells (DSCs) attracted considerable attention due to low cost of manufacturing and respectable efficiency of light-to-electricity conversion [1-3]. Recently, the optimization of DSSC using graphene, graphene oxide and reduced graphene oxide was studied. Like all 2D nanomaterials, they have different characteristics that make them flexible for use in photovoltaic devices, semiconductors, electrodes, among others [4-6]. Reduced graphene oxide is a layer sheet resulting from the chemical reduction of graphene oxide. Reduced graphene oxide has electrical and mechanical properties similar to graphene, making it suitable for a number of applications, including dye-sensitive solar cells. Reasons that have attributed to the increase in the efficiency of the solar cell include an increase in the absorption of dye resulting in an increase in photons absorption [7-10]. Roy-Mayhew et al. dispersed reduced graphene oxide (rGO) by thermal reduction of graphene oxide (GO) in electrolyte poly(ethylene oxide)-poly(propylene oxide)-poly(ethylene oxide) triblock copolymer and polyethylene

oxide, and then prepared rGO as the counter electrode of DSCs by spin coating and subsequent decomposition of polymers. The average photon conversion efficiency was 4.99% [11]. Yen et al. prepared rGO by chemically reducing GO with sodium borohydride (NaBH_4) and by ultrasonic N-methyl-2-pyrrolidone (NMP) dispersing rGO, polyvinylidene fluoride (PVDF) and XC-72. With solvent casting and vacuum drying at 120°C overnight, the rGO films were prepared on FTO glass. For DSCs, they reported a PCE of 2.89% [12].

Nevertheless, rGO sheets can't be easily preserved on the plate surfaces which are chemically inert and nonporous with low surface tensions, such as plastic, glass.... A new method of increasing adhesion on the plate surfaces that are corona plasma discharges. This makes them unable to bond with inks, adhesives, coatings, and other substrates. In general, plasma-enhanced chemical vapor deposition (PECVD) of thin films is carried out by high-frequency or microwave discharges under vacuum conditions ranging from 0.001 to 1 mbar [13]. However these

PECVD process are very costly and particularly when large substrates need to be protected, as a result of the demand for the vacuum system and the space limitations established by the dimensions of the vacuum chamber [14]. Therefore, the improved plasma deposition at atmospheric pressure of thin films without vacuum constraints is an enabling approach to completing in large-scale processes, including polymer foils, metal bands and paper... with low-cost items. Corona discharges are normally carried out under atmospheric pressure. A corona discharge system set-up consists of two electrodes where an insulating layer serving as a dielectric barrier covers at least one electrode. In the gas gap of about 1–10 mm between the electrodes, small localized discharges of very short duration can be observed by applying an alternating high voltage to the electrode system [15, 16]. Gas species in these micro-discharges are partially activated and ionized with ion energies within a range of 1–10 eV corresponding to low-pressure plasma conditions. Corona treatment involves changing the surface energy and binding strength of the substrate by molecular excitation through the use of a corona or electric discharge. Electrical discharge can occur when ambient air is exposed to different voltage potential, which can then cause a collision of neutral molecules, causing the electrically charged molecules to create an ionized air layer. In this study, corona plasma discharge is applied for surface treatment, which improves the adhesion of fabricated rGO thin film on the silicon (Si) substrate. The electrons produced in the corona discharge have a two to three-fold effect on the energy treatment surface required to break molecular bonds on certain plastic (non-metallic) surfaces. The process of corona bonding is difficult to quantify, as treatment is determined by strength setting, the distance from the sample of the handheld electrode, treatment time and sample size. No vacuum pumps are required and any non-conductive surface can be bonded. The synthesis and characterization of corona plasma-treated silicon surface with deposited rGO are reported herein.

EXPERIMENTAL

Prepared of GO and rGO thin films

The synthesis of reduced graphene oxide (rGO) suspension used in the study was done via the chemical reduction of individual graphene oxide (GO) solution were prepared from graphite

powder (< 20 μm , Sigma – Aldrich, Germany) by the modified Hummers method [17, 18]. Then, the GO solutions that is diluted with a ratio of 1:100 to spin-coated onto the substrate of glass by spinner (DELTA 6RC, SUSS Microtec, Germany) with coating speed and time were remained stable throughout the experiments according to the table below.

Table 1. The spin-coating parameters for GO deposition into the glass substrate

1 st Speed (rpm)	1 st Time (s)	2 st Speed (rpm)	2 st Time (s)
100	5	500	20

Before that, substrates were cleaned in an ultrasonic bath with acetone, ethanol, isopropanol for 5 mins for each case, followed by rinsing with DI water and drying with nitrogen blow.

Corona plasma treatment

The corona discharge generator with output voltage is adjustable from 10,000 to 45,000. Output frequency is 4.5 MHz. The input power to the Model BD-20AC is approximately 40 watts. This equipment was supplied by BD-20AC (Electro-Technic Products, US). Plasma treatment was performed with a corona discharge device with a power range of 0–700 W (Figure 1). The substrates were treated with corona plasma at the difference times: 60s, 120s, 180s and 240s.



Figure 1. BD-20AC Laboratory corona treater (Electro-Technic Products, US).

Characterization and properties of rGo thin film on Si substrate

The morphology of fabricated rGO layer was investigated by Field Emission scanning electron microscope, FE-SEM ((SU8000, Hitachi, Japan). The rGO thicknesses and adhesive energy were characterized by Atom Force Microscope (Park XE7, Korea).

RESULTS AND DISCUSSION

As seen in Figure 2, GO thin films begin to appear on silicon surfaces which was treated by corona plasma discharge, the plasma corona time of 120s, it can be found that the film is more uniformly covered than 60s. When corona plasma time increased to 180s, defects appeared on the

substrate and the film clustered. In the other hand, the surfaces were almost burned and easily damaged with formation of some hole and cracks that make surface adhesion reduced at the corona plasma time of 240s.

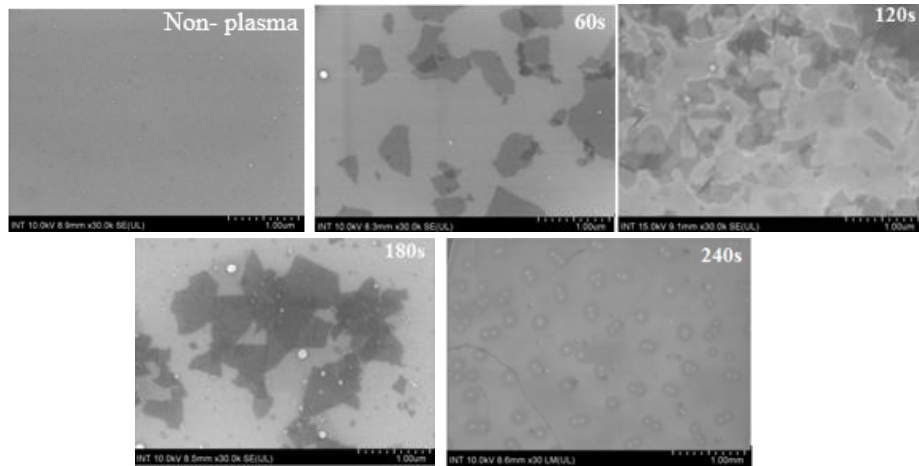


Figure 2. FE-SEM images of fabricated rGO layers with speed S_1 and corona plasma time respectively non-corona plasma, 60s, 120s, 180s and 240s.

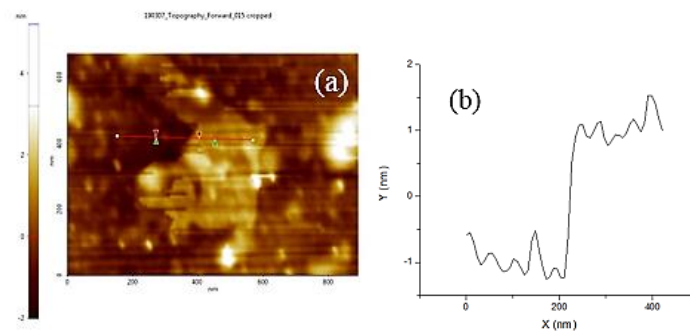


Figure 3. Atomic force microscopy (AFM) analysis of reduced graphene oxide: (a) high-resolution AFM image for height measurement

The reduced graphene oxide was further characterized using Atomic Force Microscopy as displayed in Figure 3. Figure 3a shows a topographical image on Si substrate. Figure 3b shows a two-dimensional line profile recorded along the dashed line of Figure 3a. This height profile of about 2 nm layer thickness, as shown in Figure 3b, supports the presence of a single rGO surface. The result was similar to the previous report [19, 20].

Adhesion at the nano scale is often characterized through simple AFM-based pull-off force measurements in which an AFM tip

(radius of 5 nm) is contacted to a surface and then subsequently retracted. The force is measured via deflection of the compliant AFM cantilever and the pull-off force is defined as the peak attractive force during retraction of the tip from the Si surface. The scans were done under contact mode with a low load ($\sim 3\text{--}5$ nN) to avoid significant deformation of the spike and the image size varied from $1,6 \times 1,6 \mu\text{m}^2$ order to obtain measurements of the detailed features near the apex as well as the overall tip geometry

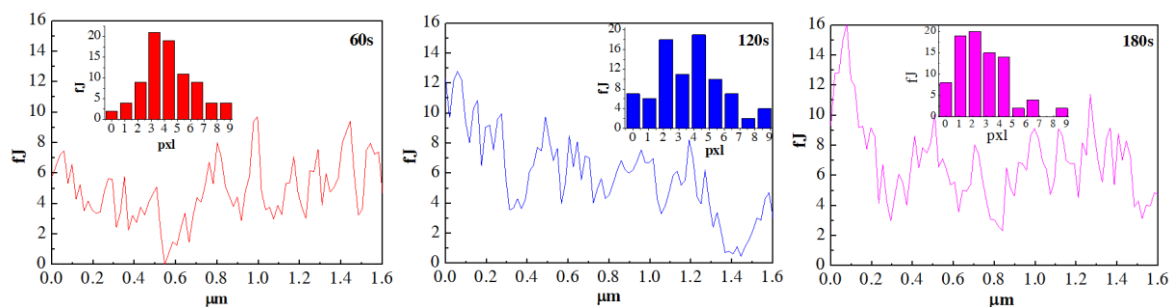


Figure 4. The adhesive energy spectrum and the adhesive energy diagram of fabricated rGO thin film with plasma corona times of 60s, 120s and 180s respectively.

Table 2. The average adhesive energy (fJ) with plasma corona time 60s, 120s and 180s

Time (s)	Adhesive energy (fJ)
60	4.179
120	5.774
180	6.002

Figure 4 and Table 2 shows that the average adhesive energy value (fJ) increases as the plasma corona treatment time increases. On the other hand, the corona time increased from 60s to 120s, the average adhesive energy increased by 1.595 fJ. However, if corona time increased to 180s, the average adhesive energy increased by only 0.228 fJ. The results show that corona plasma time suitable to treated silicon surface is 120s and better results than previous reports [21, 22].

References

- [1] Hagfeldt, A., et al., *Dye-sensitized solar cells*. Chemical reviews, 2010. **110**(11): p. 6595-6663.
- [2] O'regan, B. and M. Grätzel, *A low-cost, high-efficiency solar cell based on dye-sensitized colloidal TiO₂ films*. nature, 1991. **353**(6346): p. 737.
- [3] Wang, Q., et al., *Bessho T and Imai H. J. Phys. Chem. B*, 2006. **2006**: p. 110.
- [4] Fang, X., et al., *Improved properties of dye-sensitized solar cells by incorporation of graphene into the photoelectrodes*. Electrochimica Acta, 2012. **65**: p. 174-178.
- [5] Chong, S., C. Lai, and S. Abd Hamid, *Controllable electrochemical synthesis of reduced graphene oxide thin-film constructed as efficient photoanode in dye-sensitized solar cells*. Materials, 2016. **9**(2): p. 69.
- [6] Yeh, M.H., et al., *Dye-sensitized solar cells with reduced graphene oxide as the*

CONCLUSION

In this study, the substrates were treated with corona plasma discharge at room conditions to improve the surface adhesion. The rGO thin films were well deposited on the substrate with treated corona plasma. The optimal time of corona plasma treatment process is of 120s. In the another hand, formed rGO films had thickness around 2 nm and high adhesive energy of 5.774 fJ.

Acknowledgement

This study is funded by Vietnam National University Ho Chi Minh City (VNUHCM) under the grant number 562-2018-32-02.

counter electrode prepared by a green photothermal reduction process. ChemPhysChem, 2014. **15**(6): p. 1175-1181.

- [7] Gupta, A., T. Sakthivel, and S. Seal, *Recent development in 2D materials beyond graphene*. Progress in Materials Science, 2015. **73**: p. 44-126.
- [8] Koppens, F., et al., *Photodetectors based on graphene, other two-dimensional materials and hybrid systems*. Nature nanotechnology, 2014. **9**(10): p. 780.
- [9] Dubertret, B., T. Heine, and M. Terrones, *The rise of two-dimensional materials*. 2015, ACS Publications.
- [10] Novoselov, K.S., et al., *Electric field effect in atomically thin carbon films*. science, 2004. **306**(5696): p. 666-669.
- [11] Roy-Mayhew, J.D., et al., *Functionalized graphene as a catalytic counter electrode in dye-sensitized solar cells*. ACS nano, 2010. **4**(10): p. 6203-6211.

- [12] Yen, M.-Y., et al., *Platinum nanoparticles/graphene composite catalyst as a novel composite counter electrode for high performance dye-sensitized solar cells*. Journal of materials chemistry, 2011. **21**(34): p. 12880-12888.
- [13] Yasuda, H., et al., *Plasma Polymerization Academic Press Orlando*. Textiltechn./Z. Polymerenforsch., 1985. **27**: p. 599-603.
- [14] Rosocha, L., et al., *Plasma-enhanced combustion of propane using a silent discharge*. Physics of plasmas, 2004. **11**(5): p. 2950-2956.
- [15] Brisset, J., et al., *Chemical reactivity of the gaseous species in a plasma discharge in air: an acid-base study*. Applied Surface Science, 1989. **36**(1-4): p. 530-538.
- [16] Greenwood, O., R. Boyd, and J. Hopkins, *JPS Badyal in: Polymer Surface Modification: Relevance to Adhesion, KL Mittal*. VSP, Utrecht, 1996: p. 17-32.
- [17] Gupta, R., Z. Alahmed, and F. Yakuphanoglu, *Graphene oxide based low cost battery*. Materials Letters, 2013. **112**: p. 75-77.
- [18] Hou, J., Z. Liu, and P. Zhang, *A new method for fabrication of graphene/polyaniline nanocomplex modified microbial fuel cell anodes*. Journal of Power Sources, 2013. **224**: p. 139-144.
- [19] Marcano, D.C., et al., *Improved synthesis of graphene oxide*. ACS nano, 2010. **4**(8): p. 4806-4814.
- [20] Grimm, S., et al., *High-quality reduced graphene oxide by CVD-assisted annealing*. The Journal of Physical Chemistry C, 2016. **120**(5): p. 3036-3041.
- [21] Jiang, T. and Y. Zhu, *Measuring Graphene Adhesion using Atomic Force Microscopy with a Microsphere Tip*. Nanoscale, 2015. **7**.
- [22] Elinski, M.B., et al., *Adhesion and Friction at Graphene/Self-Assembled Monolayer Interfaces Investigated by Atomic Force Microscopy*. The Journal of Physical Chemistry C, 2017. **121**(10): p. 5635-5641.

SILVER NANOPARTICLES-ASSEMBLED GRAPHENE OXIDE SHEETS ON TiO₂ NANOTUBES: SYNTHESIS, CHARACTERIZATION AND PHOTOCATALYTIC ACTIVITY INVESTIGATION

Loan Thuy Thi Pham¹, Khang Duy Vu Nguyen², Anh Phuong Thi Nguyen² and Khoa Dang Nguyen Vo^{1,2}

¹ Graduate University of Science and Technology, Vietnam Academy of Science and Technology, 18 Hoang Quoc Viet Street, Nghia Do Ward, Cau Giay District, Ha Noi, Vietnam

² Institute of Applied Material Science, Vietnam Academy of Science and Technology, 01A Thanh Loc 29 Street, Thanh Loc Ward, District 12, Ho Chi Minh City, Vietnam

Email: yndkhoa@iams.vast.vn

ABSTRACT

In this study, graphene oxide sheets (GO) were first assembled with silver nanoparticles (AgNPs) and then combined with TiO₂ nanotubes (TNTs) by γ -ray irradiation at different doses. Their morphological, physical and chemical properties were investigated using Fourier-transformed infrared (FTIR), UV-Vis, Raman and X-ray diffraction (XRD) spectroscopies, field emission scanning electron (FESEM) and transmission electron (TEM) microscopies. The photocatalytic activity of this composite material was determined by the photodegradation efficiency on rhodamine B (RhB) dye solution and evaluated using a UV-visible spectrophotometer. Results of this work demonstrated that the GO-AgNPs-TNTs materials were successfully synthesized and γ -irradiation dose range affects significantly the material's characteristics. In addition, the formed composites exhibited remarkable photocatalytic activity on RhB degradation, as compared with that of separate GO, AgNPs and TNTs. Consequently, the GO-AgNPs-TNTs nanocomposites possess great potential for photocatalytic applications and can be used to remove environmental contaminants from wastewater.

Keywords: Silver nanoparticles, graphene oxide, TiO₂ nanotubes, photocatalytic activity

INTRODUCTION

Wastewater is increasingly released into the environment, due to direct and/or indirect adverse impacts of overpopulation and industrialization with tons or more of hazardous micro-pollutants such as heavy metals, dyes, fertilizers, pharmaceuticals, pesticides, and other additives [1-2]. Such contaminants present toxicity and thus constitute serious threats to both human and environmental health. It is, therefore, of great significance to design and synthesize efficient and environmental friendly techniques for water purification [3-4]. Titanium dioxide (TiO₂) is among the best photo-catalysts for contamination treatments and solar energy harvesting. Comparing with TiO₂ nanoparticles, TiO₂ nanotubes (TNTs) possess higher specific surface area, with orderly one-dimensional structure, hence their spectacular photocatalytic activity. However, it is not industrially practical for recollecting TiO₂ catalysts in post-treated samples. Zeolite, silica, ceramic and cotton fibres have been used for improving the

separation efficiency [5]. Despite these efforts, TiO₂ recovery remains a problem due to its ease of detaching from the support. Also, the high rate of recombination of photo-generated electron-hole pairs in TiO₂ results in reduced photocatalytic efficiency [6-7].

Among the myriad of nanomaterials currently being selected to synergize with TiO₂, graphene has emerged as the most notable material with a honeycomb structure possessing outstanding mechanical strength, electrical and thermal conductivities, molecules barrier properties and other remarkable abilities [8-9]. Graphene oxide (GO) has a similar structure to graphene, except its several oxygen-containing functional groups such as hydroxyl (-OH), epoxy and alkoxy (C-O-C), carboxylic (-COOH), carbonyl (C=O) groups and so forth [10]. These groups obviously strengthen the bond between GO and TiO₂ and their combination, as a result, is a promising approach to improve the efficiency of photocatalytic

process for decontamination of environmental contaminants.

The scientific interest in silver nanoparticles (AgNPs) has shifted from bare materials to metals-, non-metals, and nanomaterials-combined ones, in order to enhance their very high electrical conductivity, antibacterial activities and excellent catalytic properties. The decoration of silver nanoparticles on GO has been demonstrated an interesting remedy for stabilizing these particles and enhancement of their catalytic activity [11].

γ -Ray irradiation has been used for the synthesis of metals nanoparticles from their corresponding salts, as well as many other hybrid nanomaterials [12-13]. This method shows significant advantages towards others: unnecessary of catalysts or heat treatments and controllable procedures. In this study, γ -ray irradiation was used for the combination of GO, AgNPs and TNTs, with the promise of a spectacular nanocomposite material possessing high photocatalytic activity for wastewater treatments. On the other hands, the effect of dose range on the properties of GO-AgNPs-TNTs nanocomposites was also been investigated.

EXPERIMENTAL

SYNTHESIS OF GO, AgNPs AND TNTs

Graphene oxide sheets (GO) were synthesized using the method published by Marcano et. al. [14], using graphite powder as precursor and potassium permanganate as oxidizer. Silver nanoparticles (AgNPs) were synthesized using the method published by Aherne et. al. [15], with poly(ethylene glycol) (PEG) as the substitute for poly(sodium styrenesulfonate) (PSSS). TiO₂ nanotubes (TNTs) were synthesized based on the method published by Zavala et. al. [16], using TiO₂ anatase nanopowder as titania precursor. Apart from AgNPs, the products were vacuum-dried to obtain dark brown powder for GO and white powder for TNTs.

SYNTHESIS OF GO-AgNPs-TNTs NANOCOMPOSITES BY γ -⁶⁰Co IRRADIATION AND DOSE RANGE'S EFFECT INVESTIGATION

GO and TNTs were dispersed separately in a PEG 0.5 g.L⁻¹ solution by sonication for 30

minutes and then mixed with each other. The mixture was then joined by AgNPs solution and followed by another 30 minutes of sonication. The GO-AgNPs-TNTs mixtures were then irradiated by γ -ray, at the dose range of 5, 10, 15, 20 and 25 kGy. The products were labeled 5, 10, 15, 20 and 25 kGy, respectively.

CHARACTERIZATION OF GO, AgNPs, TNTs AND THEIR NANOCOMPOSITE MATERIALS

For the characterization of GO, AgNPs, TNTs and nanocomposite products, various physicochemical methods were used: Fourier-transformed infrared (FTIR), UV-Vis, Raman and X-ray diffraction (XRD) spectroscopies, field emission scanning electron (FESEM) and transmission electron (TEM) microscopies.

PHOTOCATALYTIC INVESTIGATION

In order to determine the proportion of GO, AgNPs and TNTs in GO-AgNPs-TNTs nanocomposite materials, inductively coupled plasma-mass spectroscopy (ICP-MS) method was used. The nanocomposite materials were dissolved in hot HNO₃ 65 %/HF 10 % solution to convert all components to soluble compounds and they were then evaluated by an ICP-MS spectrometer. The highest proportion values of GO, AgNPs and TNTs were then used for the determination of the essential amount of separate GO, AgNPs and TNTs for photocatalytic experiments.

The proper amount of GO, AgNPs, TNTs, as well as nanocomposite materials, were dispersed in 20 mL of 10-ppm rhodamine B (RhB) solution and sonicated in the dark for 10 minutes so that the absorption equilibrium between the materials and RhB was established. The solutions were then stirred for 60 minutes under natural sunlight irradiation. The photocatalytic reactions were conducted from 11 a.m. to 01 p.m., at which the sunlight's intensity was the most stable. After 60 minutes, the solutions were isolated from the sunlight and filtered to eliminate all remaining catalyst particles to obtain transparent solutions, which were then evaluated by UV-VIS adsorption method.

CHEMICALS AND EQUIPMENT

For the synthesis of GO, AgNPs, TNTs and nanocomposite materials, graphite powder was purchased from ACROS ORGANICS (Germany), silver nitrate, nitric acid 65 % and TiO₂ anatase nanopowder were purchased from MERCK (Germany). All other chemicals were in analytical pure grade and deionized water was used throughout the work. For the photocatalytic activity experiments, RhB dye was purchased from HIMEDIA, India. FTIR spectra was recorded by PerkinElmer Frontier spectrometer, with the wavenumber range of 400-4000 cm⁻¹ as KBr pellets. For the UV-Vis absorption spectra recording and photocatalytic evaluation, the UV-1800 (Shimadzu, Japan) spectrometer was used. Raman spectra was recorded on a Horiba XploraOne spectrometer, with the laser wavelength of 532 nm. For XRD spectra, the Bruker D2 Phaser spectrometer was used, with Cu/Kα as the X-ray source and at scanning speed of 0.5 degree per minute. FESEM images of the materials were taken using FE SEM S-4800 microscope (Hitachi, Japan) and TEM images were taken on a JEOL JEM-1400 (JEOL, USA) microscope. The proportion of GO, AgNPs and TNTs in nanocomposite materials was determined on a PerkinElmer NexION®2000 ICP-MS spectrometer.

RESULTS AND DISCUSSION

MATERIALS CHARACTERIZATION AND DOSE RANGE'S EFFECT INVESTIGATION

After being irradiated by γ-ray with different doses, all nanocomposite solutions were obtained as dark brown solution (Figure 1).

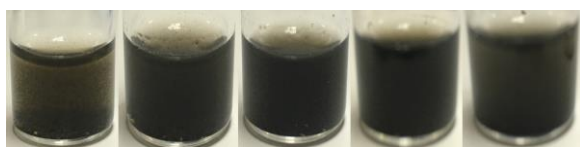


Figure 1. From left to right: the 5, 10, 15, 20 and 25 kGy nanocomposite solutions

The FTIR spectra (Figure 2) indicated the presence of GO's functional groups in nanocomposite materials, at all doses: the hydroxyl -OH (a broad peak at ~3400 cm⁻¹), the carbonyl C=O (a strong peak at ~1600 and ~1700 cm⁻¹) groups, as well as weak signals of C-O single bonds (carboxy, alkoxy and epoxy) and C≡C bonds from 1000 to 1400 cm⁻¹). In addition, signals of AgNPs and TNTs (from 400 to 800

cm⁻¹) were visible in all nanocomposites and weaker than those of separate materials, hence the possibility of bonding between GO, AgNPs and TNTs. The higher the dose was, the stronger the signals of GO's highly-oxidized functional groups and AgNPs were. It can be inferred from this result that GO was highly oxidized and more AgNPs were assembled at the high dose of γ-irradiation.

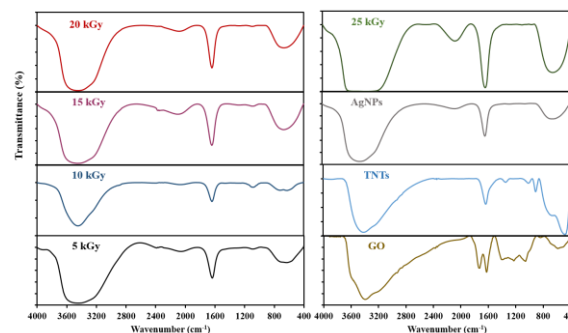


Figure 2. FTIR spectra of GO, AgNPs, TNTs and nanocomposite materials

The UV-Vis adsorption spectra (Figure 3) showed the significant difference between separate materials and nanocomposites. At all doses, the nanocomposites proclaimed the highest similarity with TNTs (the broad peak at ~270 nm) because of the stability of this material under γ-irradiation, compared with GO and AgNPs. The spectra also indicated the presence of a weak adsorption signal of AgNPs (at ~400 nm) in the nanocomposites, of which possible cause is the presence of small amount of unbonded AgNPs in the nanocomposite solutions. As the irradiation dose augmented, this signal diminished because of the degradation of PEG molecules under the high irradiation dose, hence its AgNPs-protective property loss and the release of AgNPs in the solution.

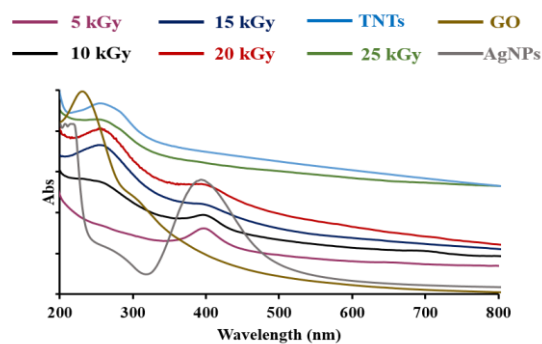


Figure 3. UV-Vis spectra of GO, AgNPs, TNTs and nanocomposite materials

According to the Raman spectra (Figure 4), the D and G peaks of GO (at ~ 1350 and ~ 1600 cm^{-1}) remained unchanged in all nanocomposites, hence the stability of its structure. However, in other Raman shifts, the turbulence of the spectra increased, indicated the possible interaction between GO, AgNPs and TNTs. These results corresponded well with FTIR and UV-Vis spectra.

The XRD spectra (Figure 5) showed the significant signal diminution in both GO, TNTs and AgNPs, compared with separate materials. These results indicated many changes in the structure and crystallization of nanocomposites.

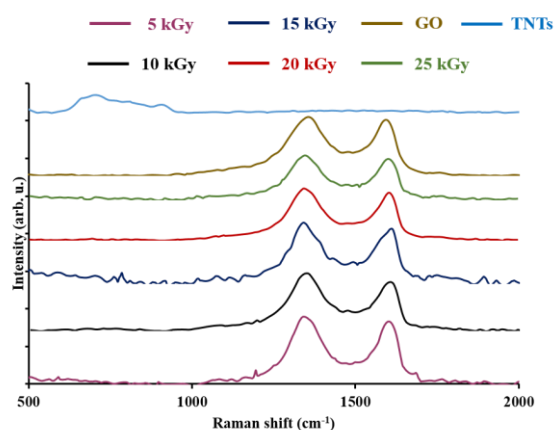


Figure 4. Raman spectra of GO, TNTs and nanocomposite materials

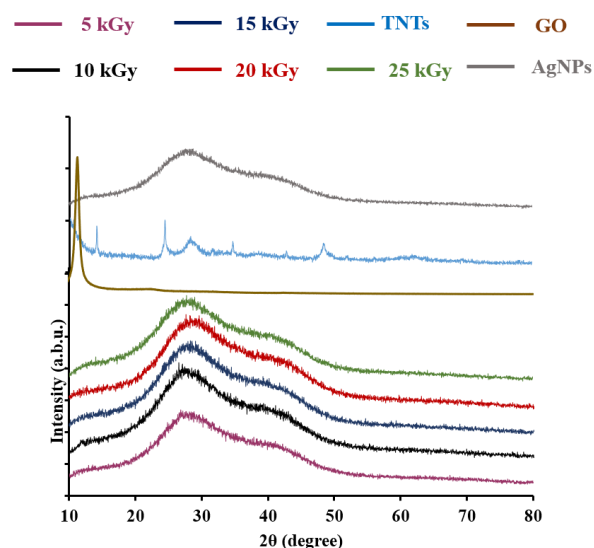


Figure 5. XRD spectra of GO, AgNPs, TNTs and nanocomposite materials

Figure 6 and 7 displays the SEM and TEM images of GO-AgNPs-TNTs nanocomposite

materials. Both SEM and TEM images indicated the significant change in the morphology of nanocomposites under γ -irradiation. The silver nanoparticles were assembled on TiO_2 nanotubes and these were attached on the surface of GO. Some silver nanoparticles were assembled directly on GO's surface. In addition, the higher the dose was, the clearer TiO_2 nanotubes' shape was and the harder it was to observe the silver nanoparticles. It can be inferred from these images that the high dose of γ irradiation promoted the aggregation of silver nanoparticles.

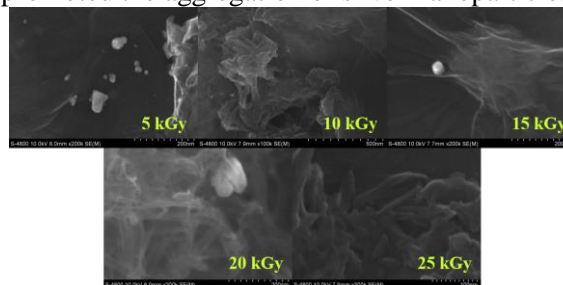


Figure 6. SEM images of GO-AgNPs-TNTs nanocomposites

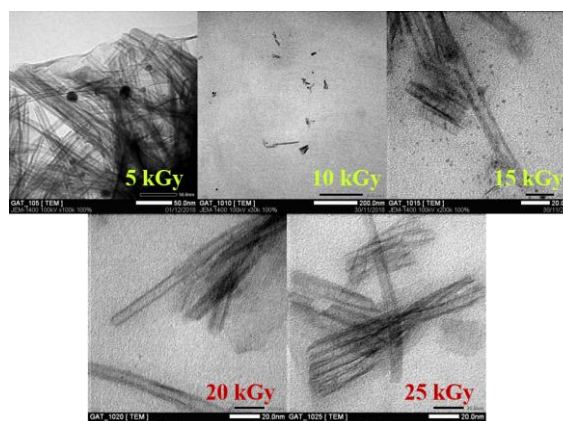


Figure 7. TEM images of GO-AgNPs-TNTs nanocomposites

INVESTIGATION ON THE PHOTOCATALYTIC ACTIVITY OF GO, AgNPs, TNTs AND NANOCOMPOSITES

The proportion of GO, AgNPs and TNTs in nanocomposite materials were shown in Table 1, with bold values being the highest among all samples.

Table 1. GO, AgNPs and TNTs proportion (%) in nanocomposite materials

Sample	GO	AgNPs	TNTs
5 kGy	67.40	0.003E ⁻⁴	32.60
10 kGy	69.12	4.90	25.98
15 kGy	72.31	0.01E ⁻⁴	27.69

20 kGy	64.84	0.01E ⁻⁴	35.16
25 kGy	88.90	0.002E ⁻⁴	11.10

The essential amount of separate GO, AgNPs and TNTs were calculated as follows:

$$\text{Amount (mg)} = (p \times 0.3) / 100$$

Whereas *p* (in %) is the proportion of each material in nanocomposite samples and 0.3 is the amount of nanocomposite samples (in mg) used for the photocatalytic experiments. The amount of GO, AgNPs and TNTs were then calculated as 0.27; 0.02 and 0.10 mg, respectively.

In order to determine the concentration of RhB in post-treated solutions, 10-ppm RhB solution was first evaluated and then its UV-Vis spectra was obtained as in Figure 8.

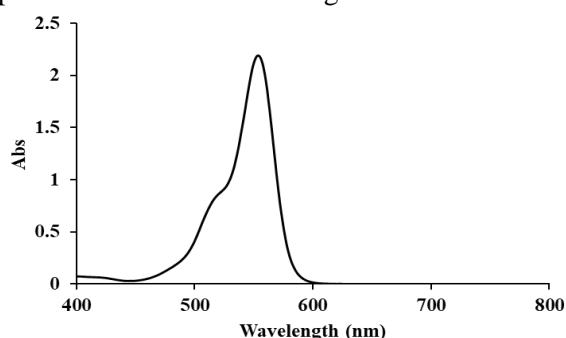


Figure 8. UV-VIS absorption initial 10-ppm Rhodamine B solution

The spectra indicated the maximum UV-Vis adsorption peak of 10-ppm RhB solution was at the wavelength of 553.5 nm. This wavelength was then used to make a standard curve for RhB, with the concentrations of 0, 2, 4, 6, 8 and 10 ppm. The recurrent equation for RhB was determined as $y = 0.2092x + 0.0086$, with R² value as 0.9997.

The decoloration efficiency (DE, %) of all materials was calculated, following the formula:

$$DE (\%) = [1 - (C/C_o)] \times 100$$

Whereas C_o (ppm) is the dye's initial concentration and C (ppm) is the dye's remaining concentration after treated with materials.

The decolouration efficiency of all materials was determined and shown in Table 2.

Table 2. Decoloration efficiency (DE, %) of GO, AgNPs, TNTs and nanocomposites

Material	Abs	C (ppm)	C _o (ppm)	DE (%)
5 kGy	1.438	6.831	10	31.69
10 kGy	0.402	1.879	10	81.21
15 kGy	1.503	7.145	10	28.55

20 kGy	1.329	6.313	10	36.87
25 kGy	0.821	3.881	10	61.18
GO	1.635	7.775	10	22.25
AgNPs	2.069	9.848	10	1.52
TNTs	1.879	8.942	10	10.58

It was obvious in Table 2 that all nanocomposite materials showed higher DE values than those of separate ingredients, among which 10 kGy was the highest. These results also indicated that the high γ -irradiation dose did not always lead to the high photocatalytic activity. It can be explained for these results that at the high irradiation dose, the aggregation of nanoparticles augmented, as well as the possibility of breaking the bonds between GO, AgNPs and TNTs, hence the decrease in photocatalytic activity.

CONCLUSION

In this study, GO-AgNPs-TNTs nanocomposite materials were successfully synthesized under γ -irradiation. The obtained results indicated the way those three ingredients combined: silver nanoparticles were assembled on both TiO₂ nanotubes and GO sheets, and TiO₂ nanotubes were assembled on GO sheets. In addition, the effect of irradiation dose on the nanocomposite materials was investigated and led to our conclusion that the highest dose was not ideal for the synthesis of these nanocomposites, due to the risk of nanoparticles aggregation and bond destruction. The material showed perfect dye-degrading activity under the presence of natural sunlight as the radiation source, compared with bare ingredients. Deeper investigation on the effect of γ -irradiation on material's properties, as well as further studies on antibacterial activity of nanocomposites will be conducted in our further researches.

Acknowledgment

The support of NAFOSTED (National Foundation for Science & Technology Development) code: 104.03-2017.49 and for young scientific of VAST granted of V.N.Đ.K are gratefully acknowledged.

References

- [1] H. Eckert, M. Bobeth, S. Teixeira, K. Kühn, G. Cuniberti, *Modeling of photocatalytic degradation of organic components in water*

- by nanoparticle suspension, Chemical Engineering Journal **261** (2015) 67-75.
- [2] P. M. Martins, C. Ferreira, A. Silva, B. Magalhães, M. M. Alves, L. Pereira, P. Marques, M. Melle-Franco, S. Lanceros-Méndez, *TiO₂/graphene and TiO₂/graphene oxide nanocomposites for photocatalytic applications: A computer modeling and experimental study*, Composites Part B: Engineering **145** (2018) 39-46.
- [3] Y. Luo, W. Guo, H. H. Ngo, L. D. Nghiem, F. I. Hai, J. Zhang, S. Liang, X. C. Wang, *A review on the occurrence of micropollutants in the aquatic environment and their fate and removal during wastewater treatment*, Science of the total environment **473** (2014) 619-641.
- [4] N. Raghavan, S. Thangavel, Y. Sivalingam, G. Venugopal, *Investigation of photocatalytic performances of sulfur based reduced graphene oxide-TiO₂ nanohybrids*, Applied Surface Science **449** (2018) 712-718.
- [5] D. Ghanbari, S. Sharifi, A. Naraghi, G. Nabyouni, *CaFe₂O₄-ZnO magnetic nanostructures: photo-degradation of toxic azo-dyes under UV irradiation*, J. Mater. Sci. Mater. Electron. **27** (2016) 5315.
- [6] Y. Rambabu, U. Kumar, N. Singhal, M. Kaushal, M. Jaiswal, S. S. L. Jain, S. C. Roy, *Photocatalytic reduction of carbon dioxide using graphene oxide wrapped TiO₂ nanotubes*, Applied Surface Science **485** (2019) 48-55.
- [7] Y. Rambabu, M. Jaiswal, S. C. Roy, *Enhanced photoelectrochemical performance of multi-leg TiO₂ nanotubes through efficient light harvesting*, Journal of Physics D: Applied Physics **48(29)** (2015) 295-302.
- [8] A. T. Smith, A. M. LaChance, S. Zeng, B. Liu, L. Sun, *Synthesis, properties, and applications of graphene oxide/reduced graphene oxide and their nanocomposites*, Nano Materials Science **1(1)** (2019) 31-47.
- [9] Y. Cui, S. Kundalwal, S. Kumar, *Gas barrier performance of graphene/polymer nanocomposites*, Carbon **98** (2016) 313-333.
- [10] F. Pendolino, N. Armata, *Graphene oxide in environmental remediation process*, Springer, 2017.
- [11] K. Pichaimuthu, M. Keerthi., S. Chen, T. Chen, C. Su, *Silver Nanoparticles Decorated on Graphene Oxide Sheets for Electrochemical Detection of Ascorbic Acid (AA) in Human Urine Sample*, Int. J. Electrochem. Sci. **13** (2018) 7859-7869.
- [12] C. J. Lee, M. R. Karim, T. Vasudevan, H. J. Kim, K. Raushan, M. J. Jung, D. Y. Kim, M. S. Lee, *A Comparison Method of Silver Nanoparticles Prepared by the Gamma Irradiation and in situ Reduction Methods*, Bull. Korean Chem. Soc. **31(7)** (2010) 1993-1996.
- [13] A. I. El-Batal, M. S. Nagwa, A. A. Ismail, A. A. Rawia, M. F. Rasha, *Impact of Silver and Selenium Nanoparticles Synthesized by Gamma Irradiation and Their Physiological Response on Early Blight Disease of Potato*, Journal of Chemical and Pharmaceutical Research **8(4)** (2016) 934-951.
- [14] D. C. Marcano, D. V. Kosynkin, J. M. Berlin, A. Sinitskii, Z. Sun, A. Slesarev, L. B. Alemany, W. Lu, J. M. Tour, *Improved Synthesis of Graphene Oxide*, ACS Nano **4(8)** (2010) 4806-4814.
- [15] D. Aherne, D. M. Ledwith, M. Gara, J. M. Kelly, *Optical Properties and Growth Aspects of Silver Nanoprisms Produced by a Highly Reproducible and Rapid Synthesis at Room Temperature*, Advanced Functional Materials **18** (2008) 2005-2016.
- [16] M. A. L. Zavala, M. Ávila-Santos, *Synthesis of stable TiO₂ nanotubes: effect of hydrothermal treatment, acid washing and annealing temperature*, Heliyon **3(2017)** (2017) 1-18.

POSTER SESSIONS

***APPLICATIONS OF MICRO-
NANOTECHNOLOGY
(AMN)***

SOLVOTHERMAL SYNTHESIS OF UNDOPED AND Ni-DOPED FeS₂ NANOPARTICLES AND ITS COMPOSITE WITH REDUCED GRAPHENE OXIDE FOR PHOTOCATALYSIS APPLICATION

Ho Dinh Quang¹, Phan Thi Hong Tuyet,¹ Nguyen Hong Quang,¹ Lam Quang Hieu,¹ Duong Ngoc Huyen,² and Nguyen Thi Quynh Hoa^{1*}

¹Vinh University, 182 Le Duan, Vinh city, Vietnam

²Institute of Physics Engineering, Hanoi University of Science and Technology, Vietnam

Email: ntqhoa@vinh.edu.vn

ABSTRACT

The undoped and Ni-doped FeS₂ nanoparticles (NPs) with doping concentration of 4.0 wt.% are successfully synthesized by a facile solvothermal method. The undoped and Ni-doped FeS₂ NPs have a single-crystalline structure of pyrite phase. The photocatalytic activity of the films of undoped and Ni-doped FeS₂ NPs and its composite with reduced graphene oxide (rGO) fabricated by spray pyrolysis method is investigated and evaluated. The smaller size of the NPs is achieved by Ni doping, which seems to be main reason for the improved photocatalytic activity of Ni-doped FeS₂ NPs. In addition, the FeS₂ NPs and rGO composite shows higher the UV and visible light photocatalytic activity compared with both undoped and Ni-doped FeS₂ NPs. The obtained result indicates that the FeS₂ NPs and rGO composite can act as an efficient heterogeneous photocatalyst for degradation of organic contaminant and water treatment.

Keywords: Metamaterials, Visible light, Perfect absorption, Absorber.

INTRODUCTION

Metal sulfides have attracted considerable interest due to their promising properties for electronic, optical and optoelectronic applications [1]. Among them, iron disulfide (FeS₂) is abundant, nontoxic and low-cost material with small band gaps (0.95 eV) and high absorption coefficients, which make it suitable for photovoltaic, lithium ion batteries, hydrogen evolution, photocatalytic degradation of several organic pollutants [2,3]. Up to now, FeS₂ nanoparticles (NPs) have been prepared by several methods, such as hot injection, hydrothermal and solvothermal methods. However, the large scale synthesis of high-dispersive FeS₂ NPs is still challenge for improving their unique properties. Recently, doping with metal ions such as Ni and Co ions is an efficient way to improve the photocatalytic performance of the photocatalysts [4]. Furthermore, the combination of FeS₂ and rGO has been demonstrated to effectively improve the photocatalytic activities in these composite systems [5]. However, most of studies about photocatalytic activity of NPs and NPs and GO composite were implemented in a liquid solution so that it is difficult to get the photocatalyst

recovery process and collect them after use [6].

In this paper, we report the synthesis of undoped and Ni-doped FeS₂ NPs by a facile solvothermal method. The undoped and Ni-doped FeS₂ NPs have a single-crystalline structure of pyrite phase. The photocatalytic activity of undoped and Ni-doped FeS₂ NP and its composite with reduced graphene oxide (rGO) films fabricated by spray pyrolysis method was investigated and evaluated.

EXPERIMENTAL

Synthesis and characterization of Undoped and Ni-doped FeS₂ NPs

The undoped and Ni doped FeS₂ nanoparticles (NPs) were synthesized via a solvothermal method. In a typical synthesis, 7.5 mL of oleylamine was added into a 50 mL teflon-lined stainless steel autoclave containing 0.25 mmol of iron (II) acetylacetonate, 0.25 mmol of 1,2 hexadecandiol, 1.5 mmol of sulfur flakes and 0.0125 mmol of nickel (II) chloride hexahydrate. The reaction mixture was sonicated for an hour to ensure homogenous mixing. The reaction temperature was fixed at 190°C and reaction time was 20 h. The autoclave was then cooled to room temperature naturally and the

precipitate collected via centrifugation. After reaction period, the FeS₂ NPs samples were removed and washed with methanol and toluene, then dried in air before collection for further characterization.

The structure of the FeS₂ and Ni doped FeS₂ NPs were analyzed by X-ray diffraction (XRD) using a D8 Advance Bruker diffractometer using Cu K α radiation with a 0.154 nm wavelength and raman spectra using a LabRAM HR800 (Horiba) with a 632.8 nm excitation laser at a resolution of 1.0 cm⁻¹. The surface morphology was studied in a scanning electron microscope (SEM, JEOL JCM-6000Plus). The optical absorption spectra were obtained from an ultraviolet visible spectroscopy (Agilent, 8453). The Ni doping concentration was determined to be 4 wt.% as analyzed by an inductively coupled plasma mass spectrometry (ICP-MS, Perkin Elmer ELAN 9000).

Synthesis and characterization of GO

GO was synthesized from graphite flakes using the modified Hummers method. The detail synthesis and characterization were carried out as described in our previous study. The GO dispersion was suspended in DI water with concentration of 2 mg/ml.

Preparation of FeS₂ NPs, Ni-doped FeS₂ NPs and FeS₂ NPs and rGO composite films

The films were deposited by spray pyrolysis method onto a 2×2 cm² glass substrate using an airbrush system with the nozzle diameter of 0.2 mm. The inlet pressure is fixed at 3 bar. The distance between the tip of the nozzle and the substrate is kept at 8 cm. The volume of spray solution is 2 ml. The solution of GO, rGO, FeS₂ NPs, and FeS₂ NPs and rGO composite are used to fabrication of the films shown in Figs. 1(a)-(d). The final FeS₂ NPs and FeS₂ NPs and rGO composite (FeS₂ NPs/rGO) films were obtained after spray deposition, which are shown in Figs.1 (e) and (f), respectively.

For the growth of undoped and Ni-doped FeS₂ NPs films: The initial undoped and Ni-FeS₂ NPs solutions (20 mg/ml) were created by diluted undoped and Ni-FeS₂ NPs in cyclohexane. The growth temperature is fixed at 100 °C.

For the growth of the FeS₂ NPs and rGO composite film: The GO dispersion (2 mg/ml) was vigorously mixed with hydrazine monohydrate with a volume ratio of 1:2 for 5 min and then diluted 10 times with DI

water/ethanol/hydrazine monohydrate with a volume ratio of 1:1:2. Sonication was then applied by a sonication bath for one minute in order to obtain stable and homogenous GO-hydrazine dispersion. Finally, the FeS₂ NPs (20 mg/ml) and GO-hydrazine (0.2 mg/ml) solution with a volume ratio of 1:1 was sonicated for 5 min to ensure homogenous mixing. The growth temperature is fixed at 200 °C in order to obtain the rGO [26].

Photocatalytic activity

Photocatalytic activity was studied by measuring the decomposition of methylene blue (MB) in aqueous solution using UV-VIS spectroscopy. In each experiment, the sample was added into 10 mL of MB aqueous solution with concentration of 10⁻⁵M. The white light of a tungsten light bulb (100 W) and UV light of 365 nm (6 W) were used as visible light and UV irradiation sources, respectively.

RESULTS AND DISCUSSION

Fig. 1 shows SEM image of the undoped and Ni-doped FeS₂ NP samples. All the samples exhibit uniform morphology and particle size distribution. The smaller NPs are obtained in the NP sample with Ni doping. The size of undoped and Ni-doped FeS₂ NPs is ~ 100-150 nm and 80-120 nm, respectively.

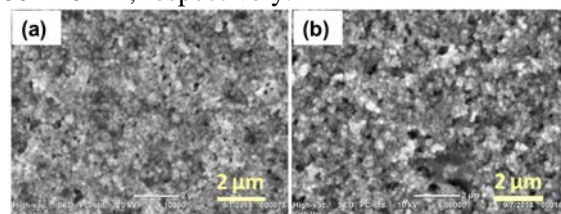


Figure 1. SEM images of the undoped and Ni-doped FeS₂ NPs.

The crystal phases of the undoped and Ni-doped FeS₂ NP samples were investigated using XRD. Fig. 2 shows XRD patterns of these samples. Both undoped and Ni doped FeS₂ NP samples show a similar XRD pattern. The discernible peaks can be indexed as pyrite FeS₂ (JCPDS No. 01-079-0617). No additional peaks corresponding to secondary phases such as metallic nickel and nickel oxide, marcasite, pyrrhotite, troilite or greigite phases are observed. This may either indicates that the concentration of secondary phases formed in the samples is too low to detect by XRD measurement or Ni ions are doped into pyrite FeS₂ matrix. Furthermore, the formation of

a lowered intensity and wider peaks in Ni-doped FeS₂ NP samples corresponds to the decrease the NP size after Ni doping as observed in SEM image (Fig. 1).

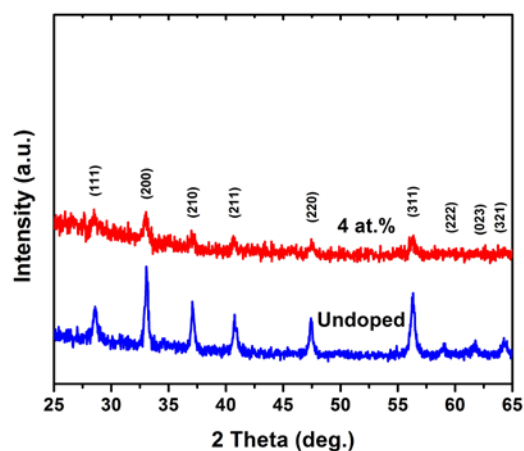


Figure 2. SEM images of the undoped and Ni-doped FeS₂ NPs.

Photocatalytic activity of the undoped NPs, Ni-doped FeS₂ NPs, and FeS₂ NPs and rGO composite samples were evaluated by measuring the decomposition of methylene blue in an aqueous solution. Fig. 3 shows the changes of MB concentration as a function of irradiation time under both UV and visible light. As seen in Fig. 3a, the undoped NPs decompose methylene blue effectively through photocatalytic reaction under visible light irradiation due to its narrow bandgap energy. Compared with the undoped NPs, the Ni-doped FeS₂ NP sample shows much higher photocatalytic activity (Fig. 3a). The Ni doping can be decreased the NP size, resulting in the increase of its specific surface area and improve the visible light photocatalysis. Furthermore, due to the doped of metal ions such as Ni²⁺, the defects were created in FeS₂ matrix that leading to the increase of electron and hole generation. The visible photocatalytic activity is further enhanced by using the FeS₂ NPs and rGO composite. It was reported the composite of FeS₂ NPs and GO composite can improve the visible light photocatalysis compared to pure synthetic FeS₂ NPs. It can be ascribed to the unique properties of GO or rGO such as larger surface area, full surface accessibility, and fast charge transport and the synergistic effects between both components of GO or rGO and NPs. Under UV irradiation, the NPs and rGO composite sample also show much stronger photocatalytic activity than the undoped and Ni-doped FeS₂ NP samples (Fig. 3b).

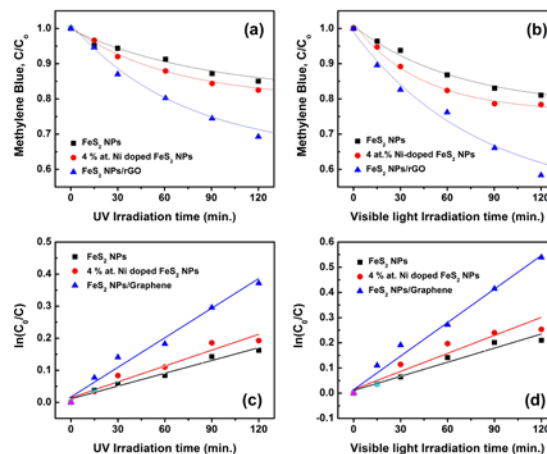


Figure 3. Photocatalytic properties of the undoped NPs sample (solid squares), Ni-doped FeS₂ NPs sample (solid circles) and the FeS₂ NPs and rGO composite under (a) visible light and (b) UV irradiation. The linearized kinetic plots for the degradation o

Moreover, the MB photodegradation clearly obeyed the first-order reaction kinetics. The linearized kinetic plots for the degradation of MB with the presence of the undoped NPs, Ni-doped FeS₂ NPs, and FeS₂ NPs and rGO composite samples under UV and visible light irradiation are shown in Fig. 3 (c) and (d). The apparent rate constants of visible light and UV photocatalytic degradation of MB with the presence of the undoped FeS₂ NPs sample were $1.33 \times 10^{-3} \text{min}^{-1}$ and $1.87 \times 10^{-3} \text{min}^{-1}$, respectively. They increased markedly to $1.65 \times 10^{-3} \text{min}^{-1}$ and $2.17 \times 10^{-3} \text{min}^{-1}$ for Ni-doped FeS₂ NPs sample and $2.95 \times 10^{-3} \text{min}^{-1}$ and $4.3 \times 10^{-3} \text{min}^{-1}$ for the FeS₂ NPs and rGO composite sample, respectively.

CONCLUSION

A facile solvothermal approach was developed to synthesis the undoped and Ni-doped FeS₂ NPs with doping concentration of 4.0 wt.%. The undoped and Ni-doped FeS₂ NPs have a single-crystalline structure of pyrite phase. The photocatalytic activity of the films of the undoped and Ni-doped FeS₂ NPs and FeS₂ NPs and rGO composite fabricated by spray pyrolysis method was investigated. The smaller size of the NPs was achieved by Ni-doping, which seems to be main reason for the improved photocatalytic activity of Ni-doped FeS₂ NPs. Furthermore, the composite of FeS₂ NPs and rGO exhibited higher the UV and visible light photocatalytic compared with both undoped and

Ni-doped FeS₂ NPs. The obtained result revealed that the FeS₂ NPs and rGO composite is a promising candidate for degradation of organic contaminant and water treatment.

Acknowledgment

This research is funded by Vietnam National Foundation for Science and Technology Development (NAFOSTED) under grant number 103.02-2017.367.

References

- [1] C.-H. Lai, M.-Y. Lu and L.-J. Chen, *J. Mater. Chem.* **22**, 19 (2012).
- [2] C. Song, S. Wang, W. Dong, X. Fang, J. Shao, J. Zhu, X. Pan, *Solar Energy* **133**, 429 (2016).
- [3] G. Kaur, B. Singh, P. Singh, M. Kaur, K. K. Buttar, K. Singh, A. Thakur, R. Bala, M. Kumar, A. Kumar, *RSC Adv.* **6**, 99120 (2016).
- [4] F. Long, J. He, M. Zhang, X. Wu, S. Mo, Z. Zou, Y. Zhou, *J. Mater. Sci.* **4**, 1848 (2015).
- [5] W. Liu, L. Xu, X. Li, C. Shen, S. Rashid, Y. Wen, W. Liu and X. Wu, *RSC Adv.* **5**, 2449 (2015).
- [6] N. T. Q. Hoa, Z. Lee, and E. T. Kim, *J. Electrochem. Soc.* **159** K42 (2012).

ENHANCING BIOAVAILABILITY OF SILYMARIN USING REDOX NANOPARTICLE FOR THE TREATMENT OF INFLAMMATION

Nguyen Thi Thu Ha¹, Tran Ngoc Han¹, Mai Huu Phuong¹, Trinh Nhu Thuy², Vong Binh Long^{2*}, Nagasaki Yukio³

¹Faculty of Biology and Biotechnology, University of Science, Vietnam National University, HCMC, Vietnam

²School of Biomedical Engineering, International University, Vietnam National University, HCMC, Vietnam

³Graduate School of Pure and Applied Sciences, University of Tsukuba, Japan

Corresponding email: vblong@hcmiu.edu.vn

ABSTRACT

According to the World Health Organization (WHO), chronic inflammatory disease is one of the biggest threats to health and strongly related to overproduction of reactive oxygen species (ROS). Prolonged inflammation not only causes damage to organs, but also leads to many dangerous diseases such as stroke, autoimmune, cancer, etc. For this reason, anti-inflammatory therapies are gradually becoming an interesting target, which is particularly in the treatment and prevention of cancer. Silymarin is an active compound with the effect of expressing anti-inflammatory activity. However, silymarin has the poor bioavailability due to rapid metabolism and secretion, low permeability on intestinal epithelial cells and low water solubility. In this study, we developed silica-containing redox nanoparticles (siRNP) with 50 – 60 nm in diameter to improve the bioavailability of silymarin through improving its solubility and delivery. Silymarin-loaded siRNP (SM@siRNP) increased significantly antioxidant capacity and anti-inflammatory efficacy in scavenging free radical DPPH, suppressing nitric oxide and producing inflammatory cytokines, as compared to free silymarin, siRNP, and silymarin-encapsulated in si-nRNP, which is the control nanoparticle without ROS scavenging property. In addition, the anti-inflammatory effect of SM@siRNP was also investigated in dextran sodium sulfate-induced colitis mice. The results in this study indicate the potential of SM@siRNP as promising therapy for treatment of inflammatory diseases.

Keywords: inflammation, redox nanoparticles, silymarin.

INTRODUCTION

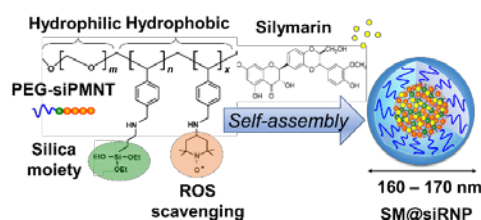
One of the most important scientific discoveries in health research in recent years has shown that inflammation not only plays a role in a few disorders, but also is the origin of many diseases. Inflammatory diseases contribute to the increased mortality in the world. For instance, inflammation involves at least 8 of the top 10 causes of death in the United States today. Accordingly, understanding the mechanisms that affect inflammation in the body, how and when we can intervene to reduce the risk of inflammatory diseases is a top priority for science and the community [11]. It is generally known that reactive oxygen species (ROS) are strong oxidizing molecules, which have a single electron in the outer layer. Therefore, ROS is not stable, it can react with other molecules and tends to receive more electrons for returning to equilibrium. ROS is produced by cells that involved in host immune responses such as neutrophils and played a role in promotion of endothelial dysfunction by oxidizing important

cellular signaling proteins like tyrosine phosphatase [8]. ROS acts as both a signaling molecule and an inflammatory mediator [2].

However, the overproduction of ROS (oxidative stress) is the central progression of many inflammatory diseases. The role of oxidative stress in causing inflammation has been shown in many previous studies [8]. Consequently, antioxidant treatments are a useful measure in controlling and treating inflammation. Milk thistle is an herb that has been used for over 2000 years in the treatment of hepatitis and cirrhosis. Milk thistle extract is a flavonolignan mixture, containing about 70 – 80% silymarin, which has been shown to have antioxidant activity through its ability to scavenge ROS, reduce the formation of proteins carbonyl and reduce peroxidation of lipid [9]. In addition, silymarin also exhibits activities such as regulating intracellular glutathione levels, stabilizing cell membranes and blocking inflammatory pathways through inhibition of triggers. Despite having many potential activities for the treatment of inflammation, the

applicability of silymarin is not appreciated due to poor oral bioavailability. The major limiting factors for bioavailability of silymarin are rapid metabolism and excretion, low permeability on intestinal epithelial cells and low water solubility. One of the methods taken to increase the oral bioavailability of silymarin is using nanotechnology as a drug delivery system [10]. Nano therapy is being studied in developed countries like the US, China, and Japan. To be more precise, nanotechnology has the potential efficacy on improving, and enhancing the effectiveness of hydrophobic drugs. Therefore, the aims of this study are to improve the solubility, enhance antioxidant and anti-inflammatory activities of silymarin for the treatment of inflammation. Nevertheless, one of problems for oral antioxidant is to destroy in the gastrointestinal tract due to the strong oxidative stress. In order to deliver drug intact to blood stream, conventional nanocarrier is not effective.

We have previously confirmed that antioxidant nanoparticle prevents oxidative degradation of antioxidants such as curcumin. Silymarin is another candidate for conventional oral treatment is suitable antioxidant carrier is designed. Formerly, we developed a pH-sensitive-redox-nanoparticle (RNP) with ROS scavenging capacity for colon cancer therapy. However, RNP possess low drug loading capacity and low stability in the gastrointestinal tract after oral administration due to RNP readily disintegrates in acidic pH of the stomach. Consequently, in this study, we developed a silica-containing redox nanoparticle (siRNP) possessing a ROS scavenging moiety of nitroxide radical and a drug absorptive moiety of silica, which can improve the drug loading capacity and stability of the nanoparticle for oral delivery of silymarin. With 50 – 60 nm in diameter, siRNP can improve the bioavailability of silymarin through improving its solubility and evaluate the anti-inflammatory effect *in vitro* and *in vivo* model mice.



Scheme 1: Design of silica-containing redox nanoparticle (siRNP) and silymarin encapsulation [7].

EXPERIMENTAL

Materials and Methods

siRNP was prepared by dialysis of amphiphilic block copolymer PEG-siPMNT, which was synthesized as previously reported (Scheme 1) (cite). Silymarin, MTT agents, DMSO (dimethyl sulfoxide), lipopolysaccharide (LPS), methanol, were purchased from Sigma Aldrich (St. Louis, MO, USA). TEMPOL, DPPH (2,2-diphenyl-1-picrylhydrazyl) were from Tokyo Chemical Industry Co. Ltd.

Cell line and culture

RAW 264.7, a murine monocyte/macrophage cell line, was obtained from ATCC, USA. RAW 264.7 cells were grown in Dulbecco's modified eagle medium (DMEM; Sigma Aldrich, St. Louis, MO) containing 5% fetal bovine serum (Sigma Aldrich, St. Louis, MO), and 1% antibiotics (penicillin/streptomycin/neomycin; Invitrogen, Carlsbad, CA) in a humidified atmosphere of 5% CO₂ at 37 °C.

Characterization of SM@siRNP

Size distribution of siRNP and silymarin@siRNP as measured by dynamic light scattering (DLS, Nanoziser Malvern). Drug loading efficiency and encapsulation efficiency were determined at 326 nm by Ultraviolet-visible (UV-vis). Antioxidant capacity was determined by radical scavenging ability toward DPPH free radical.

Cell viability test

To study the effects of SM@siRNP, silymarin and siRNP on viability of cell, RAW 264.7 was added into 96-well plates (10⁴ cells/well) and incubated for 24 h. Samples were added and incubated for 24 h, followed by adding MTT solution (0.5 mg/mL) to each well and incubated for 4 hr. The formazan crystals were dissolved by addition of DMSO and absorbance was measured at 570 nm.

NO production from RAW 264.7 activated by LPS

Cells were cultured in petri plates (100 mm) with DMEM supplemented with 5% FBS and 1% antibiotics under 5% CO₂ at 37 °C. To study the effects of SM@siRNP, silymarin and siRNP on NO production, cells were plated in 24-well plates (5x10⁴ cells/well). After preincubation for 24 h, samples were added and incubated for 1 h then added LPS (5 µg/mL). To measure the

concentration of NO produced during a 24 h incubation period, a standard Griess reagent (Sigma Aldrich) was using. The medium (50 μ L) and Griess reagent (50 μ L) were mixed in the 96-well plates and left for 10 min at room temperature. Optical density was measured with a microplate reader (Spectra Max, Molecular Devices) at 540 nm.

Determination of anti-inflammatory cytokine

IL-1 β Mouse Uncoated ELISA kit (Invitrogen/Thermo) was used to measure IL-1 β according to manufacture's protocol.

Induction of colitis by DSS and drug administration

The 7-week-old Swiss mice were purchased from Institute of Drug Quality Control Ho Chi Minh city. Colitis in mice was induced by 3% (wt/vol) DSS (5000 daltons; Wako Pure Chemicals, Osaka, Japan) supplemented in the drinking water for 7 days. The experiment included 5 groups: normal control group, DSS-injured group, siRNP, silymarin and SM@siRNP. The equivalent doses of drugs (30 mg/kg/day) were orally administered daily during the 7 days of DSS treatment. Silymarin was suspended in 0.5% (wt/vol) carboxymethyl cellulose.

Statistical analysis

The Student's t test was used to compare the groups. $p < 0.05$ was considered statistically significant.

RESULTS AND DISCUSSION

Characterization of nanoparticles

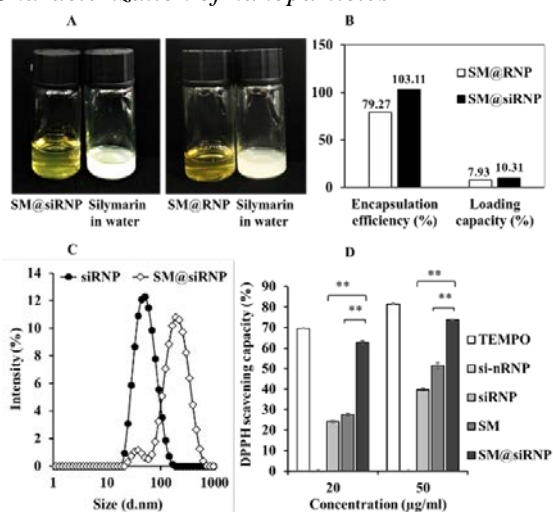


Figure 1. Properties of silica-containing redox nanoparticles. A. Solubility of silymarin in water and after encapsulation into siRNP and RNP. B.

Drug encapsulation efficacy and loading capacity of the nanoparticles. C. Size distribution of nanoparticles was determined using dynamic light scattering (DLS) measurement. D. Antioxidant activity of silymarin@siRNP by DPPH assay.

Silymarin is an anti-inflammatory drug with low solubility (0.04 mg/mL) (Figure 1A). By simply encapsulation into siRNP and RNP, the solubility of silymarin significantly improve which enable silymarin to be able to overcome biological barriers. Especially, they are absorbed easily by intestinal epithelial cells. Both types of redox nanoparticles have increased the bioavailability of silymarin through overcoming the drug's solubility. As shown in Figure 1B, silymarin encapsulation efficiency of siRNP was $\approx 100\%$ and drug loading capacity was $\approx 10\%$ which is significantly higher than that of RNP, indicating that a silica moiety improved the drug loading capacity of siRNP as compared to RNP. In addition, the size of SM@siRNP was 170.9 nm after dialysis, as compared to siRNP (50.7 nm in diameter) (Figure 1C). Silymarin-loaded siRNP (SM@siRNP) increased significantly antioxidant capacity through free radical scavenging activity (Figure 1C) as compared to silymarin and siRNP alone.

The cytotoxicity evaluation

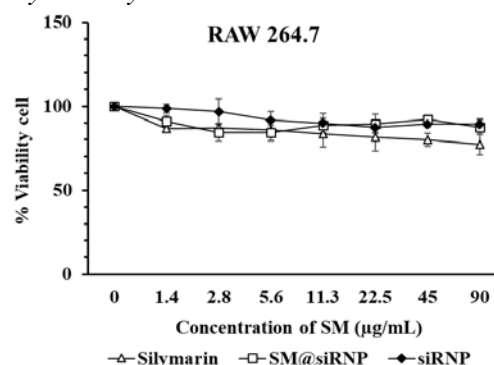


Figure 2. Viability of RAW 264.7 macrophage cell line was measured after 24 h treatment with Silymarin and SM@siRNP and siRNP using MTT assay.

The cytotoxic effects of samples were measured using the MTT assay. As shown in Figure 2, all of samples tested did not demonstrate any significant cytotoxic effects on RAW 264.7 cells. Anti-inflammatory efficacy of SM@siRNP was investigated *in vitro* using lipopolysaccharide (LPS)-induced RAW 264.7 macrophage cell activation. The results showed that SM@siRNP exhibited significantly higher anti-inflammatory efficacy in suppressing nitric oxide (Figure 3), as compared to free silymarin,

siRNP, and silymarin-encapsulated in si-nRNP, the control nanoparticle without ROS scavenging property.

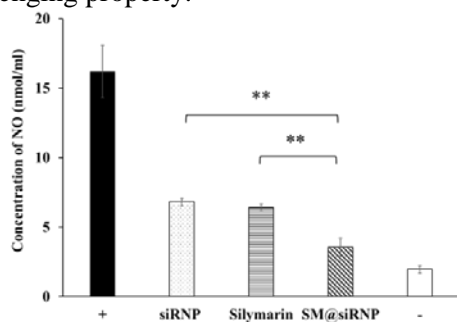


Figure 3. Effects of SM@siRNP as compared to silymarin and siRNP on NO production of LPS-activated RAW 264.7 cells.

IL-1 β is one of the inflammatory markers used to identify inflammatory state accurately. ELISA is a high sensitivity and specificity method that can determine IL-1 β content *in vitro*. IL-1 β values for all groups are presented as concentration (pg/mL). IL-1 β levels were found significantly lower in the SM@siRNP groups compared to that of the SM@si-nRNP group ($p < 0.01$). The results of combining silymarin and siRNP has showed that the ability on reducing the expression level of cytokine IL-1 β was completely effective as compared to the control nanoparticles without antioxidant activity.

Finally, DSS-induced colitis in mice was used to investigate the anti-inflammatory efficacy of SM@siRNP through disease activity index and body weight change. The mice treated with DSS exhibited significantly reduced body weight compared to the healthy mice. SM@siRNP and silymarin-treated mice has a lower loss of body weight than the DSS-treated mice. Especially, the group treated with SM@siRNP restricted the effects of inflammatory process on body weight of mice as compared to other groups. After 7 days of treatment, the severity of colitis was assessed based on disease activity index (DAI). DAI expresses the progressive ability of colitis. The higher its value, the more severe of inflammatory state. The inflammatory state of SM@siRNP-treated mice was less than silymarin and SM@si-nRNP-treated mice.

CONCLUSION

In this study, silymarin was encapsulated in the hydrophobic core of siRNP to improve its

anti-inflammatory activity. Silymarin encapsulation in the siRNP not only improves the solubility, but also increases significantly antioxidant capacity of silymarin. In addition, SM@siRNP exhibited a significantly higher anti-inflammatory efficacy in suppressing nitric oxide and inflammatory cytokine production, as compared to free silymarin, siRNP, and silymarin-encapsulated in si-nRNP, the control nanoparticle without ROS scavenging property. Equally important, the anti-inflammatory investigation on DSS-induced colitis in mice has shown positive results through the assessment of body weight change and disease activity index. From these results, it was demonstrated that the encapsulation of silymarin in siRNP is a promising approach for enhancing its anti-inflammatory activity and potential for treatment of inflammatory diseases.

Acknowledgment

This work was supported by Vietnam National Foundation of Science and Technology Development (NAFOSTED) under Grant number 108.05-2017.327, and Vietnam National University Ho Chi Minh City (VNU-HCM) under grand number C-2019-18-24. This was also partly supported by MEXT Grant-in-Aid for Scientific Research A (18H04160).

References

- [1]. Ahmed Abdal Dayem, et. al, International journal of molecular sciences, 2017, **18** (1), 120.
- [2]. Esra Birben, et. al, World Allergy Organization Journal 2012, **5** (1), 9.
- [3]. Hideyuki Tominaga, et. al, Analytical Communications, 1999, **36** (2), 47-50.
- [4]. Lisa Schmölz, et. al, Journal of immunological methods, 2017, **449**, 68-70.
- [5]. Long Binh Vong, et. al, Advanced healthcare materials, 2017
- [6]. Long Binh Vong, et. al, Gastroenterology, 2012, **143** (4), 1027-1036. e3.
- [7]. Long Binh Vong, et. al, Advanced healthcare materials, 2017, **6** (20), 1700428.
- [8]. Mittal Manish, et. al, Antioxidants & redox signaling, 2014, **20** (7), 1126-1167.
- [9]. Mustafa Cengiz, et. al, Food and Chemical Toxicology 2015, **77**, 93-100.
- [10]. Shamama Javed, et. al, Alternative medicine review, 2011. **16** (3), 239.
- [11] Roma Pahwa, et. al, Chronic inflammation. 2018.

FABRICATION OF PAPER-BASED MICROCHANNEL BY ELECTROHYDRODYNAMIC INKJET PRINTING OF ETHYLENE GLYCOL SOLVENT-BASED INK

Ngan Nguyen Le^{1,2}, Hue Cam Thi Phan¹, Huong Kim Tran¹, Dung My Thi Dang¹ and Chien Mau Dang¹

¹ Institute for Nanotechnology, Vietnam National University-Ho Chi Minh City, Community 6, Linh Trung Ward, Thu Duc District, Ho Chi Minh City, Vietnam;

² University of Science, Vietnam National University-Ho Chi Minh City, 227 Nguyen Van Cu Street, District 5, Ho Chi Minh City, Vietnam

Email: lnngan@vnuhcm.edu.vn

ABSTRACT

Paper-based microchannel is an important component in microfluidic paper-based devices. Paper-based microchannel is usually fabricated by creating hydrophobic patterned lines to bind hydrophilic paper inside. Among many fabrication techniques to make hydrophobic lines, printing method in general and inkjet printing in particular had become more popular due to their advantages of material saving, high accuracy, low-cost, etc. In this paper, electrohydrodynamic (EHD) inkjet printing method, which has been studied and developed in recent years, was utilized for dropping glycol ether solvent-based ink on nitrocellulose paper-like membrane. Results from field emission scanning electron microscope (FE-SEM) showed that this ink could dissolve through membrane and form a transparent hydrophobic layer onto created gap. Moreover, the width of barrier line can be controlled from about 200 μm to 260 μm , which is quite small when comparing with other fabrication methods. Therefore, EHD inkjet printing technology can be applied for fabricating small-scale microfluidic paper-based devices in the future.

Keywords: paper-based microchannel, microfluidic paper-based devices, electrohydrodynamic inkjet printing, glycol ether

INTRODUCTION

Objective of paper-based microchannel is to transfer fluid, reagents, sample, etc. in microfluidic chip; thus, microchannel acts an important role in microfluidic paper-based devices [1-5]. Simple microchannel is made by creating two more hydrophobic lines to compel fluid to flow onto hydrophilic paper line due to capillary action [2-10]. The most important goal of hydrophobic line is to prevent the leakage of fluid out of paper-like microchannel. In order to make good hydrophobic barrier lines, many fabrication methods have been studied recently [5-8, 10-17]. There are four main groups of fabrication method: handcrafting, cutting/shaping, mask usage and printing [11]. Among many fabrication techniques, printing method in general and inkjet printing in particular have become more popular due to their advantages of material saving, high accuracy, low-cost, etc [11,12]. Paper-based microchannel using inkjet printing technology is also divided into two conventional methods:

direct and indirect printing [12]. Different point between them is how the hydrophobic lines are formed during printing step. Direct printing method utilizes hydrophobic inks such as polystyrene, hydrophobic sol-gel, alkyl ketene dimer which had the tendency to transform into solid state by heating [18, 19]. Therefore, the main drawbacks of this method is usage of high viscosity ink, which is quite difficult to be ejected out of nozzle. Indirect printing method presents a two-step procedure. First, paper substrate is coated with a hydrophobic layer on entire surface. Subsequently, low viscosity solvent ink is printed to dissolve hydrophobic layer [12]. Indirect printing method do not need to use high viscosity like direct method. However, paper substrate can be damaged in coating step of hydrophobic layer, leading to unexpected in application steps. Moreover, indirect method wastes more materials than direct method.

In this paper, we use a different way to fabricate hydrophobic lines on nitrocellulose

paper-like substrate. The goal of our inkjet printing step is to dissolve entire depth of nitrocellulose substrate; thus, liquid cannot flow through printed lines. Glycol ether solvent-based ink, which can dissolve nitrocellulose, was used for our printing steps. Moreover, the reaction between ink and nitrocellulose leads to the formation of a transparent hydrophobic film. Therefore, this process uses only one-step procedure to make barrier without damaging other places of paper-like substrate. As a result, this process can be aimed to biological application on paper-based substrate such as microfluidic paper-based analytical devices (μ PADs), which has attracted interest from many researchers in recent years [1-3, 6-12].

EXPERIMENTAL

Materials

Experiments were performed on laminated membrane card (part number: HF135MC100), which were purchased from Merck Millipore. Each card includes three layers, which are nitrocellulose (NC) membrane, polyester and white polystyrene. Di(propylene glycol) methyl ether acetate (DPMA) and nonaethylene glycol monododecyl ether ($C_{12}E_9$) were purchased from Sigma-Aldrich. Borosilicate glass capillary tubes GD-1 purchased from Narishige (Japan) had 1 mm outer diameter, 0.6 mm inner diameter and 90 mm in length.

Experiments with electrohydrodynamic (EHD) inkjet printer

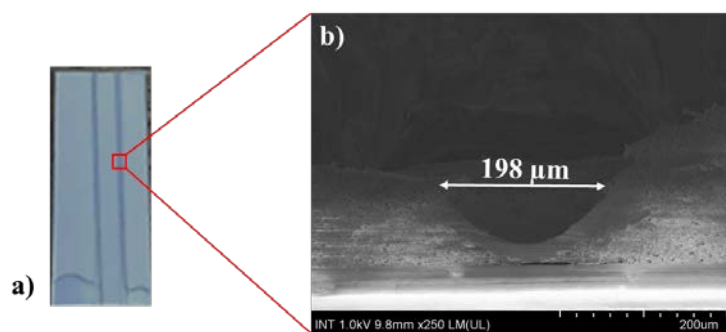
Ethylene glycol solvent-based ink was prepared from di(propylene glycol) methyl ether acetate (DPMA) and nonaethylene glycol monododecyl ether ($C_{12}E_9$) with ratio of 45:55. Dynamic viscosity of this solvent ink was measured by m-VORC viscometer from RheoSense (USA), about 11.5 cP. Simple microchannel including two parallel lines was chosen as design for these experiments. Printing step was carried out on PSJET-300V inkjet

printer. In this work, inner diameter of glass nozzle and vector speed are investigated. Distance between nozzle and substrate was fixed at 400 μ m. Other parameters such as high voltage, pressure of pump were adjusted to assure that a fine jet was ejected out of the nozzle in each experiment. Printed barrier lines were observed by field-emission scanning electron microscope (FE-SEM) Hitachi SU8010. Furthermore, blocking property of printed lines were tested by dipping paper-based microchannel in water.

RESULTS AND DISCUSSION

Relationship between width of barrier line and inner diameter of glass nozzle

There are five glass nozzles were prepared with different inner diameters (35, 40, 45, 50 and 70 μ m). Vector speed were fixed at 0.05 mm/s. After printing step, color of printed lines was changed from white of nitrocellulose membrane to gray of polyester film below (figure 1a). Cross-section images from FE-SEM of these five samples (figure 1b – f) proved that this ethylene glycol solvent-based ink had penetrated porous nitrocellulose membrane and new hydrophobic layer had been formed onto created gap. Another conclusion is that the dense hydrophobic layer, product of reaction between ethylene glycol and nitrocellulose, is transparent. These printed lines have good blocking property based on the results from dipping test. In general, there is an influence of inner diameter of glass nozzle on width of barrier lines. Barrier width was increased from 198 μ m to 467 μ m when inner diameter was increased from 35 μ m to 70 μ m because more solvent-based ink was ejected out of the larger nozzle. The smallest barrier width is 198 μ m by using 35- μ m inner diameter glass nozzle. While inner diameter of glass nozzle is 35 μ m or 40 μ m, the barrier width is not changed so much, about 200 μ m.



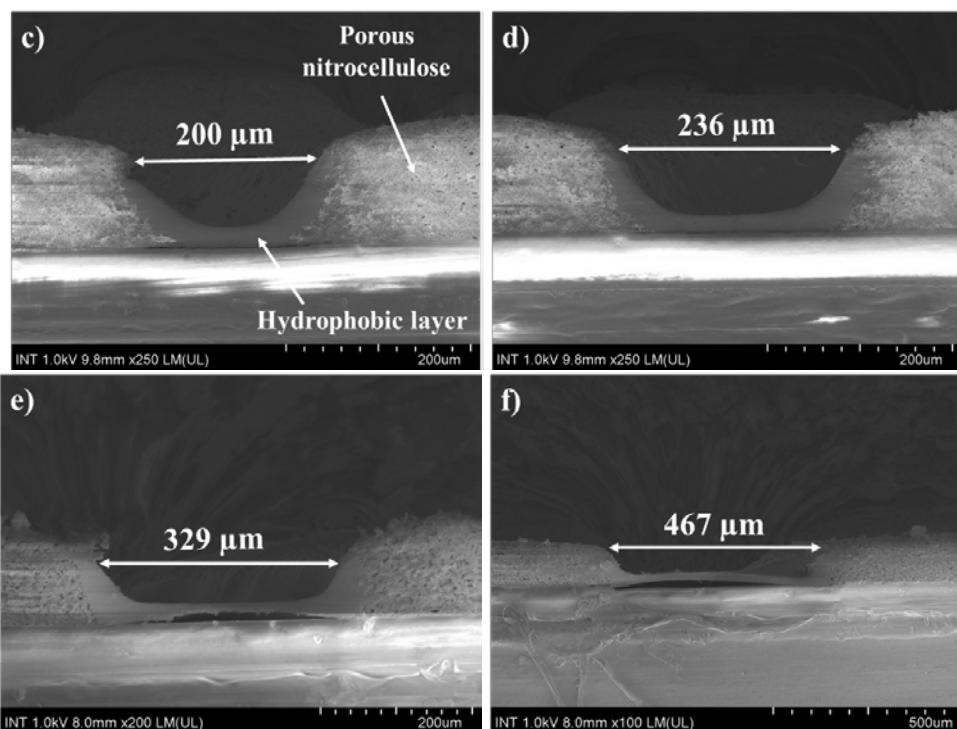
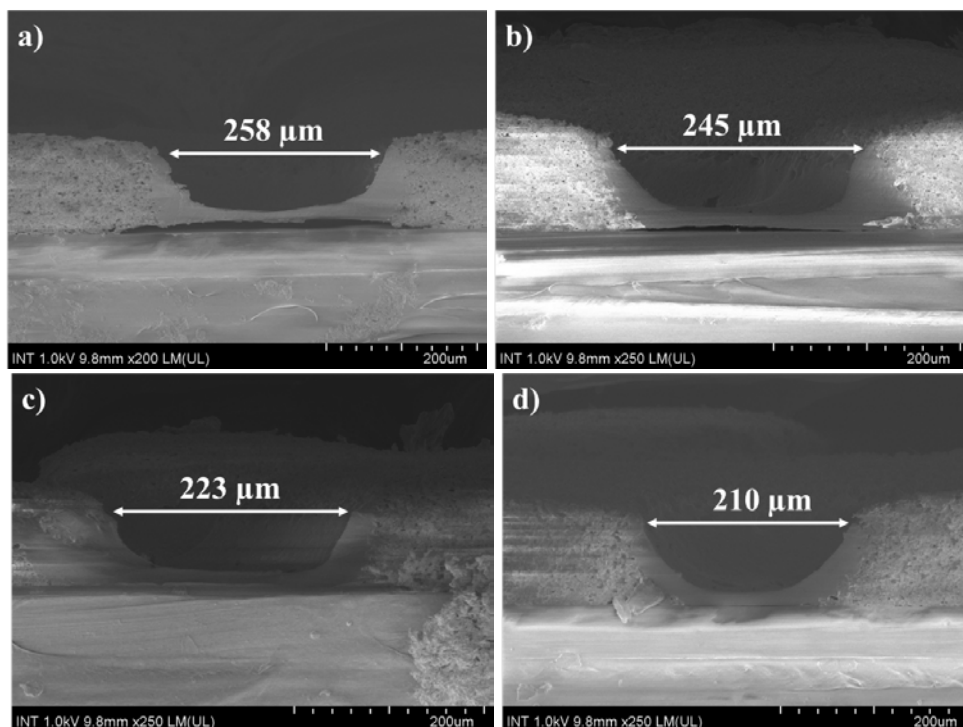


Figure 1. Fabricated paper-based channel (a) and cross-section images from FE-SEM of printed lines when printing with 35-μm (a), 40-μm (b), 45-μm (c), 50-μm (d), and 70-μm (e) inner diameter nozzles

Relationship between width of barrier line and vector speed

Vector speed is implied for the movement speed of stage during printing step. Printed line was printed faster with high vector speed. Cross-section images from FE-SEM of these six

samples corresponding with various vector speed from 0.01 mm/s to 0.06 mm/s have been shown in figure 2. In these samples, only sample which was printed with 0.06 mm/s vector speed did not have good blocking property.



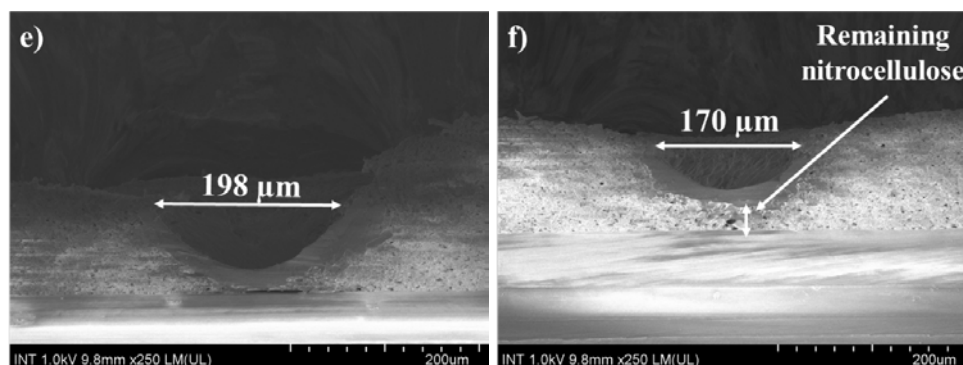


Figure 2. Cross-section images from FE-SEM of printed barrier lines corresponding with various vector speed: 0.01 mm/s (a), 0.02 mm/s (b), 0.03 mm/s (c), 0.04 mm/s (d), 0.05 mm/s (e) and 0.06 mm/s (f)

CONCLUSION

In this report, we was successful in fabricating paper-based micro channel on nitrocellulose paper-like substrate by using electrohydrodynamic inkjet printer to emit ethylene glycol solvent-based ink toward paper substrate. The results proved that this ink could be used to dissolve nitrocellulose and form a new transparent hydrophobic layer onto created gap. Width of barrier could be controlled from about 200 μm to 260 μm by adjusting inner diameter of glass nozzle and vector speed. Moreover, electrohydrodynamic inkjet printing is the promising fabrication process for fabricating microfluidic paper-based analytical devices (μPADs) in next applications.

Acknowledgment

The authors would like to appreciate Ministry of Science and Technology of Vietnam for funding this research under the grant number 03/2019/HĐ-SPĐP.

References

- [1] C. Xu, L. Cai, M. Zhong, S. Zheng, RSC Advances **5** (2015) 4770-4773
- [2] W. Y. Lim, B. T. Goh, S. M. Khor, Journal of Chromatography B **1060** (2017) 424-442
- [3] T. Akyazi, L. Basabe-Desmonts, F. Benito-Lopez, Analytica Chimica Acta **1001** (2018) 1-17
- [4] D. A. Bruzewicz, M. Reches, G. M. Whitesides, Analytical Chemistry **80** (2008) 3387-3392
- [5] Y. Xia, J. Si, Z. Li, Biosensors and Bioelectronics **77** (2016) 774-789
- [6] X. Li, J. Tian, W. Shen, Analytical and Bioanalytical Chemistry **396** (2010) 495-501
- [7] A. W. Martinez, S. T. Phillips, M. J. Butte, G. M. Whitesides, Angewandte Chemie International Edition **46** (2007) 1318-1320
- [8] A. Apilux, Y. Ukita, M. Chikae, O. Chailapakul, Y. Takamura, Lab on a Chip **13** (2013) 126-135
- [9] L. M. Fu, Y. N. Wang, Trends in Analytical Chemistry **107** (2018) 196-211
- [10] C. Liu, F. A. Gomez, Y. Miao, P. Cui, W. Lee, Talanta **194** (2019) 171-176
- [11] D. M. Cate, J. A. Adkins, J. Mettakoonpitak, C. S. Henry, Analytical Chemistry **87** (2015) 19-41
- [12] K. Yamada, T. G. Henares, K. Suzuki, D. Citterio, Angewandte Chemie International Edition **54** (2015) 5294-5310
- [13] P. Lisowski, P. K. Zarzycki, Chromatographia **76** (2013) 1201-1214
- [14] L. Cai, C. Xu, S. Lin, J. Luo, M. Wu, F. Yang, Biomicrofluidics **8** (2014) 056504
- [15] Y. He, W. B. Wu, J. Z. Fu, RSC Advances **5** (2015) 2694-2701
- [16] Y. He, Q. Gao, W. B. Wu, J. Nie, J. Z. Fu, Micromachines **7** (2016) 108
- [17] E. B. Strong, S. A. Schultz, A. W. Martinez, N. W. Martinez, Scientific Reports **9** (2019) 7
- [18] K. Abe, K. Suzuki, D. Citterio, Analytical Chemistry **80** (2008) 6928-6934
- [19] X. Li, J. Tian, G. Garnier, W. Shen, Colloids and Surfaces B: Biointerfaces **76** (2010) 564-570

STUDY ON THE ANTIFUNGAL EFFICIENCY AGAINST *Rhizoctonia solani* CAUSE COLLAR ROOT ROT DISEASE ON *Brassica integrifolia* OF LDH NANOPARTICLES IMMOBILIZED ORGANIC SALICYLATE

Nguyen Xuan Tuan¹, Tran Duc Trong¹, Tran Le Truc Ha², Duong Hoa Xo¹, Le Quang Luan¹

¹ Biotechnology Center of Ho Chi Minh City, 374, Highway 1, Quarter 2, Trung My Tay Ward, District 12, Ho Chi Minh City, Vietnam.

² Nguyen Tat Thanh University, 300A Nguyen Tat Thanh Street, Ward 13, District 4, Ho Chi Minh City, Vietnam;

Email: lequangluan@gmail.com

ABSTRACT

In this study, natural salicylate was immobilized into Al-Mg-LDH nanoparticles (SA-LDH-NPs) for evaluating the *in vitro* inhibited efficiency on the growth of *R. solani* at various concentrations. In PGA medium, the fungicidal efficiency SA-LDH-NPs against *R. solani* was increased by the increase of supplemented product concentration. Particularly, at the treatment of 12 mg/mL, its fungicidal efficiency was found at 45.5% and the growth of *R. solani* was completely inhibited by the addition of 20 mg/mL SA-LDH-NPs after cultivation of 40 hrs. In addition, *in vivo* effectiveness of this product for preventing and treating the collar root rot disease (Rhizoctonia disease) caused by *R. solani* fungus on *Brassica integrifolia* was also investigated. The results showed that the treatment of 5 mg/mL of SA-LDH-NPs reduced the disease incidence into 4.4% compared to 46.7% of the untreated control and at the treatment of 10 mg/mL, all plants were not infested after 12 days of infection. For the *in vivo* elimination test, treatment of 10 mg/mL SA-LDH-NPs reduced the disease incidence into 6.7% from 80% after 12 treating days and almost the infested plants were recovered by the treatment of 15 mg/mL SA-LDH-NPs. Thus, the SA-LDH-NPs has the potential to develop natural biological fungicide, safe for farmer and high efficiency in prevention and elimination of fungal diseases in vegetable.

Keywords: *Brassica integrifolia*, prevention, Rhizoctonia disease, SA-LDH-NPs, treatment

INTRODUCTION

According to General Statistics Office of Vietnam, in the early 6 months of 2019, the total vegetable area was estimated about 663,700 hectares, increased to 1.7% compared to same period of 2018. In Ho Chi Minh City, the vegetable area was about 10,863 hectares, accounted for 1.65% of the total national vegetable area and 16.4% of the total agricultural area of the City. Although, the vegetable area was small but the vegetable production of Ho Chi Minh City reached to 304,707 tons and served 33.3% of the vegetable demand [1]. However, the vegetable growers are now facing many difficulties due to the outspread of many diseases by microorganisms, among them, the collar root rot disease caused by *Rhizoctonia solani* is now severely affecting vegetable growth and yield. The disease usually occurs in monoculture with a high humidity, causing a “damping off” symptom [2]. Nowadays, growers often use many chemical

products that cause environmental pollution and negative impact to vegetable quality.

Salicylic acid (SA) is well known as the naturally antifungal product, this product is environmental- friendly and nontoxic to human and animal as well. It has a wide range of antifungal activity. However, SA needs a carrier for protection against disadvantageous conditions such as UV light, high temperature and high pH.

Layered double hydroxide (LDH) nanoparticles also known as hydrotalcites or anionic clays are a group of clay minerals that have shown the prospects as the carrier for both inorganic and organic materials. LDHs have a general formula of $[M^{II}_{1-x} M^{III}_x(OH)_2]_x(A^{n-})_{x/n} \cdot yH_2O$ where M^{2+} and M^{3+} are divalent and trivalent metal cations, respectively; A is the anions, and x is the ratio $M^{3+} / (M^{2+} + M^{3+})$ [3]. The anions between the layers are diverse such as: polymers, organic dyes, surfactants, organic acids and so on [4]. Al-Mg-LDHs have

demonstrated to be one type of important and green carrier due to the excellent biocompatibility, nontoxicity or low toxicity. So that, this research aims to immobilize the natural organic salicylate into Al-Mg-LDHs nanoparticles and uses as naturally fungicide for preventing and treating the collar root rot disease (Rhizoctonia disease) caused by *R. solani* fungus on *Brassica integrifolia*.

EXPERIMENTAL

A. Materials

SA-LDHs-NPs was synthesised by co-precipitation method [5]. The plant pathogenic fungi used in this study were *R. solani* (caused collar root rot disease) isolated from infected *Brassica integrifolia* in Ho Chi Minh City area. The PGA (Potato Glucose Agar) media was used for *in vitro* test and *B. integrifolia* NV1 was provided by Nam Viet Seed Co. was used for *in vivo* test.

B. *In vitro* antifungal activities of SA-LDHs-NPs

The antifungal activity of added SA-LDHs-NPs was performed on PGA medium treated with different concentrations (0 - 20 mg/mL) of SA-LDHs-NPs. *R. solani* (6 mm in diameter) were put at the center of a petri dish containing supplemented medium and incubated at room temperature. The antifungal effect was evaluated when mycelial growth in the control plate reached the edge of the petri dish and calculated by the following equation: $D (\%) = (R_0 - R) \times 100/R_0$, where R_0 and R are mycelial diameters of the control and treated samples, respectively [6].

C. *In vivo* Fungicidal Effect of SA-LDHs-NPs against *R. solani* on *B. integrifolia*.

In prevention test, the nine-day-old and free disease *B. integrifolia* was sprayed 3 times every 2 days with 100 mg/mL of SA-LDHs-NPs solution containing 2.5 - 10 mg/mL. After that, these lower stems (15 plants/treatment) were wounded before inoculating with 100 mL of *R. solani* solution. The possive control were foliar sprayed with the same volume of distilled water and the cheking was treated with only natural SA at concentration of 7.5 mg/mL.

For elimination test, lower stems of nine-day-old *B. integrifolia* (disease free) (15 plants for each treatment) were wounded and inoculated with 100 mL of *R. solani* solution.

Afer 8 days of innoculating and 50% the tested plants were infected in all treatments; the tested plants were foliar sprayed with 100 mL SA-LDHs-NPs solution with concentrations of 0, 5, 10, 15 and 20 mg/mL every 2 days up to 3 times. The possive control were foliar sprayed with the same volume of distilled water and the cheking was treated with only 15 mg/mL of the native SA.

The disease severity and disease incidence of each treatment were determined every 3 days until the negative control (innoculated by pathogeneuos fugus and sprayed with only distilled water) were dead or completely recovery and caculated based on QCVN 01-169: 2014 [7]. All experiments were repeated three times. Data were statistically analyzed using the ANOVA.

RESULTS AND DISCUSSION

A. *In vitro* antifungal activities of SA-LDHs-NPs

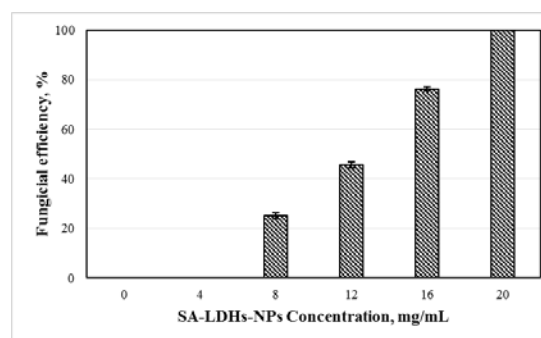


Figure 1. The antifungal effect against *R. solani* of SA-LDHs-NPs at various concentration after 40 hours incubation

The results in Figure 1 and 2 indicated that the fungal colonies developed full of the petri dish after only 40 hours incubation in control. In contrast, SA-LDHs-NPs inhibited the growth of *R. solani* and the fungicidal efficiency was inversely proportional to the SA-LDHs-NPs concentration. At the low concentration of SA-LDHs-NPs (< 8 mg/mL) the fungicidal efficiency was low, achieved 23.25%. At the high SA-LDHs-NPs concentration (12 mg/mL), the fungicidal efficiency increased speedily, the fungicidal efficiency was 45.5 and 76.1% at concentration of 12 and 16 mg/mL, the pathogeneuos fungus was completely inhibited by the addition of 20 mg/mL. Other previous reports show that SA has ability to inhibit the growth of several pathogeneuos fuguses such as: *Colletotrichum capsici* [8], *Botrytis cinerea*, *Rhizoctonia solani*,

Otrytis cinerea, *Fusarium oxysporum*, *Penicillium expansum* and *Rhizopus stolonifer* [9]. In our previous study indicated that the

antifungal activity was due to SA and LDHs only played the protective role [5].

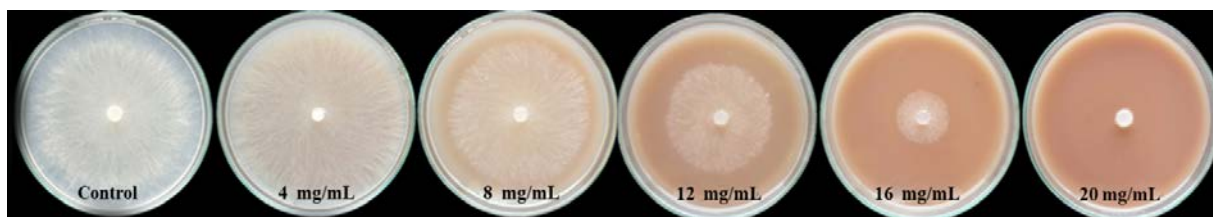


Figure 2. The growth of *R. solani* colonies after 40 hours incubated on media supplemented with various of SA-LDHs-NPs concentrations

**B. In vivo Fungicidal Effect of SA-LDHs-NPs against *R. solani* on *B. integrifolia*.
The prevention effect of SA-LDHs-NPs on fungal pathogen**

Table 1. The effect of SA- LDHs-NPs concentration on pathogen defense response of *B. integrifolia*

SA concentration, mg/mL	Disease incidence, %				Disease severity, %			
	3 days ^a	6 days	9 days	12 days	3 days	6 days	9 days	12 days
Control (+)	0.0 ^e ± 0.0	0.0 ^d ± 0.0	0.0 ^d ± 0.0	0.0 ^d ± 0.3	11.1 ^e ± 0.0	11.1 ^e ± 0.0	11.1 ^f ± 0.0	11.1 ^d ± 0.0
Checking	68.9 ^b ± 3.9	55.6 ^b ± 3.9	51.1 ^b ± 3.9	46.7 ^b ± 3.9	40.3 ^b ± 0.9	38.3 ^b ± 1.7	35.8 ^b ± 0.9	28.9 ^b ± 1.5
0 (Control -)	100 ^a ± 0.0	91.1 ^a ± 3.9	86.7 ^a ± 0.0	80.0 ^a ± 0.0	61.0 ^a ± 2.3	71.9 ^a ± 1.5	77.3 ^a ± 0.9	82.2 ^a ± 0.0
2.5	51.1 ^c ± 3.9	33.3 ^c ± 0.0	22.2 ^c ± 3.9	11.1 ^c ± 3.9	33.3 ^c ± 0.0	27.9 ^c ± 0.9	22.0 ^c ± 0.9	15.1 ^c ± 0.9
5	48.9 ^c ± 3.9	31.1 ^c ± 3.9	20.0 ^c ± 0.0	4.4 ^{cd} ± 3.9	31.9 ^c ± 2.57	25.4 ^c ± 0.9	19.0 ^d ± 0.9	12.6 ^{cd} ± 1.5
7.5	42.2 ^{cd} ± 3.9	28.9 ^c ± 3.85	17.8 ^c ± 3.9	4.4 ^{cd} ± 3.9	27.4 ^d ± 1.5	22.0 ^d ± 0.9	17.5 ^{de} ± 0.9	12.1 ^{cd} ± 0.9
10	35.6 ^d ± 3.9	26.7 ^c ± 0.0	15.6 ^c ± 3.9	0.0 ^d ± 0.0	24.9 ^d ± 1.7	19.51 ^d ± 0.86	16.5 ^e ± 0.9	11.1 ^d ± 0.0

In a column, means followed the same letter are not significantly different with $p < 0.05$. The duration was observed after *B. integrifolia* infected with *R. solani*. Positive control: none-innoculated, negative control: inoculated and untreated, checking: treated with 7.5 mg/mL native SA



Figure 3. The growth of *B. integrifolia* after 12 days of infection in prevention test. Positive control: none-innoculated, negative control: inoculated and untreated, checking: treated with 7.5 mg/mL natural SA.

There were several papers reported the *in vitro* antifungal effect of SA, but the result for *in vivo* studies on plants is still limited. In addition, *R. solani* is the causative fungus of collar root rot disease and all the diseases on vegetable plant may suffer from, that caused by the *R. solani* is the most devastating. In this study the role of SA-LDHs-NPs on antifungal effect against *R. solani* was investigated.

The results in Table 1 and Figure 3 showed that in negative control the disease incidence was 100% and disease severity was 61%. The lower stems of these *B. integrifolia* were rotten and appeared white mycelia in the wound, the rotten area was more than 50% of the lower stem area.

After 12 days of infection, the disease severity increased to 82%, almost infected plants were died. Meanwhile, in the treated plants, the disease incidence and disease severity

significantly decreased by increasing its concentration. In particular, the treatment with 2.5, 5 and 7.5 mg/mL SA-LDHs-NPs the disease incidence decreased from 50% to 11.1, 4.4 and 4.4%, the disease severity decreased from about 30% to 15.1, 12.6 and 11.1%. Especially, the plants treated with of 10 mg/mL were completely recovered, the disease incidence was 0% and the disease severity was 11.1% after 12 days of infection. While in the checking the disease incidence and disease severity were 2 folds higher than that of 7.5 mg/mL SA-LDHs-NPs.

The elimination effect of SA-LDHs-NPs on fungal pathogen

The results in Table 2 and Figure 4 showed that disease incidence and disease severity decreased by the increased SA-LDHs-NPs concentration. After 12 days of inoculation, the disease incidence was 6.7, 4.4 and 2.2%, the disease severity was 12.6, 12.1 and 11.6% almost the same as the positive control. Meanwhile, in checking treatment (treated with 15 mg/mL native SA) the disease incidence were about 42% and the disease severity was 3 folds higher than the same concentration of SA-LDHs-NPs. In addition, in checking, the infected plants appeared toxic symptoms such as curly leaves. The results also indicate that the LDHs not only maintains the fungicidal activity of SA against fungus but also reduced the toxicity of the native SA.

Table 2. The eliminate effect of SA- LDHs-NPs concentration on infected *B. integrifolia*

SA concentration, mg/mL	Disease incidence, %				Disease severity, %			
	3 days	6 days	9 days	12 days	3 days	6 days	9 days	12 days
Control (+)	0.0 ^e ± 0.00	0.0 ^e ± 0.0	0.0 ^e ± 0.0	0.0 ^d ± 0.0	11.1 ^d ± 0.0	11.1 ^e ± 0.0	11.1 ^f ± 0.0	11.1 ^d ± 0.0
Checking	86.7 ^c ± 0.0	75.6 ^b ± 3.9	55.6 ^b ± 3.9	42.2 ^b ± 3.9	52.6 ^b ± 1.5	41.2 ^d ± 0.9	41.3 ^b ± 0.9	38.3 ^b ± 0.9
Control (-)	100 ^a ± 0.0	95.6 ^a ± 3.9	88.9 ^a ± 3.9	80.0 ^a ± 0.0	61.0 ^a ± 2.3	66.4 ^a ± 1.7	75.8 ^a ± 0.9	82.2 ^a ± 0.0
5	95.6 ^{ab} ± 3.9	84.4 ^{ab} ± 3.9	44.4 ^c ± 3.9	20.0 ^e ± 6.7	58.5 ^a ± 2.6	46.7 ^b ± 1.5	27.9 ^c ± 0.9	16.5 ^e ± 0.9
10	93.3 ^{abc} ± 0.0	80.0 ^b ± 6.7	35.6 ^{cd} ± 3.9	6.7 ^d ± 6.7	53.6 ^b ± 0.9	45.2 ^{bc} ± 1.5	21.5 ^d ± 1.5	12.6 ^d ± 1.5
15	91.1 ^{bc} ± 3.9	77.8 ^b ± 3.9	33.3 ^d ± 0.0	0.0 ^d ± 0.0	50.1 ^{bc} ± 0.9	43.2 ^{cd} ± 0.9	20.0 ^{de} ± 0.0	11.1 ^d ± 0.0
20	88.9 ^{bc} ± 3.9	75.6 ^b ± 3.9	28.9 ^d ± 3.9	0.0 ^d ± 0.0	47.7 ^c ± 2.3	41.7 ^d ± 0.9	19.0 ^e ± 0.9	11.1 ^d ± 0.0

In a column, means followed the same letter are not significantly different with $p < 0.05$. The duration was observed after *B. integrifolia* treated with SA- LDHs-NPs. Positive control: without inoculated, negative control: inoculated and untreated, checking: treated with 15 mg/mL native SA.



Figure 4. The growth of *Brassica integrifolia* after 12 days of infection in treatment test. Positive control: un inoculated, negative control: inoculated and untreated, checking: treated with 15 mg/mL native SA.

CONCLUSION

SA-LDHs-NPs is a naturally and high tech product with a great potential for using as a biofungicide for the prevention and elimination of fungal diseases in vegetable. This is suitable for production of safety agro-products with a low cost and sustainable.

References

[1] Sở Nông nghiệp và PTNT thành phố Hồ Chí Minh, Báo cáo kết quả thực hiện công tác chỉ đạo, điều hành, tình hình sản xuất nông nghiệp và phát triển nông thôn tháng 7 và 7 tháng đầu năm 2019, Hồ Chí Minh, 2019.

- [2] Đỗ Tân Dũng, *Nghiên cứu bệnh lở cổ rễ (R. solani Kuhn) gây hại một số cây trồng cạn vùng Hà Nội, năm 2011-2012*. Tạp chí Khoa học và Phát triển **11**(4) (2013) 459-465.
- [3] Q.H. Hu, Z.P. Xu, S.Z. Qiao, F. Haghseresht, M. Wilson, G.Q. Lu, *A novel color removal adsorbent from heterocoagulation of cationic and anionic clays*, Journal of Colloid and Interface Science **308**(1) (2007) 191-199.
- [4] R. Roto, F. Nindiyasari, I. Tahir, *Removal of hexacyanoferrate (II) using Zn-Al-OA hydrotalcite as an anion exchanger*, Journal of Physical Science **20** (2009) 73-84.
- [5] L. Q. Luan, N. T. N. Anh, N. X. Tuan, D. H. Xo. *Study on preparation of LDH nanoparticles immobilize organic salicylate with a potential as a naturally safety fungicide for plants*. Proc. IWNA 2017, Phan Thiet-2017, 217-222.
- [6] S. W. Kim, J. H. Jung, K. Lamsal, Y. S. Kim, J. S. Min, Y. S. Lee, *Antifungal effects of silver nanoparticles (AgNPs) against various plant pathogenic fungi*, Mycobiology **40** (2012) 53-58.
- [7] Bộ Nông Nghiệp và Phát Triển Nông Thôn, *Quy Chuẩn Kỹ Thuật Quốc Gia Về Phương Pháp Điều Tra Phát Hiện Dịch Hại Cây Rau Họ Hoa Thập Tự*, Hà Nội, 2014.
- [8] B. Prithiviraj, U. P. Singh, M. Manickam, A. B. Ray, *Antifungal activity of anacardic acid, a naturally occurring derivative of salicylic acid*, Canadian Journal of Botany **75**(1) (1997) 207-211.
- [9] A. Wodnicka, E. Huzar, M. Krawczyk, H. Kwiecień, *Synthesis and antifungal activity of new salicylic acid derivatives*, Polish Journal of Chemical Technology **19**(1) (2017) 143-148.

HIGH EFFECTIVE ADSORPTION OF URANIUM FROM AQUEOUS SOLUTION BY REDUCED GRAPHENE OXIDE - ZINC/NICKEL FERRITE - POROUS POLYANILINE NANOCOMPOSITE

Tran Quang Dat¹, Nguyen Vu Tung¹, Nguyen Tran Ha¹ and Pham Van Thin¹

¹Le Quy Don Technical University, 236 Hoang Quoc Viet, Hanoi

Email: dattqmta@gmail.com

ABSTRACT

It is very essential and difficult to extract and separate uranium from waste solutions. In this work, the efficient adsorbent composites consisting of reduced graphene oxide, $Zn_{0.5}Ni_{0.5}Fe_2O_4$ nanoparticles and porous polyaniline were successfully synthesized by different techniques, namely, exfoliation, reduction, hydrothermal and polymerization in brine solution. Scanning electron microscopy (SEM), X-ray diffraction (XRD), Fourier transform infrared spectroscopy (FTIR), and vibrating sample magnetometer (VSM) were used to determine the microstructure and magnetic characteristics of composite materials. To study the efficiency of uranium adsorption from solution, the batch experiments were performed. The adsorption kinetics reached equilibrium in 90 min and were distinguished with pseudo second - order - model. The adsorption isotherm coincided well with Langmuir model and the capacity of the composites for uranium was calculated to be 2680 mg/g at pH = 6. In addition, the excellent regeneration ability of adsorbents indicates that this ternary nanocomposite can be used as a promising adsorbent for aquatic uranium treatment.

Keywords: porous, polyaniline, ferrite, reduced graphene oxide, uranium.

INTRODUCTION

Consumption of coal, oil and other sources of fossil fuel energy has contributed to a growing number of environmental problems. It has become a common goal for the world to grow clean energy and achieve economic and environmental sustainability. As the most important material of the nuclear power industry, uranium has been receiving increasing attention. With huge ocean reserves (a thousand times the amount of soil on the land) if the uranium in the seawater is effectively harvested, a significant and sustainable supplement of nuclear power plant materials will be produced. [1] Now, solvent extraction, precipitation, ion exchange and adsorption are the main methods of uranium extraction from water. Due to its simple operation, high economic performance, high extraction capability and minimal contamination, adsorption is considered to be one of the most promising technologies for uranium extraction from seawater [2].

Due to their low cost, low toxicity and fast separation from the solution, magnetic

nanomaterials have attracted a lot of attention in recent years [3-8].

Nano carbon materials such as carbon nanotube, graphene and graphene oxide were commonly used adsorbents because they have advanced properties: high surface area per unit of weight and more active working sites [9].

Polyaniline (PANI) was used to adsorb heavy metal ions and radionuclides from aqueous solution because of its large quantities of primary and secondary amino groups. Furthermore, porous structures with a large surface area may increase the adsorption of uranium [6-9].

Herein, we developed the ternary composites and used the adsorbents prepared to adsorb uranium from aqueous solution. The composites composed of reduced graphene oxide (RGO), $Zn_{0.5}Ni_{0.5}Fe_2O_4$ ferrite (ZNF) and porous polyaniline (RGO-ZNF-PANI) was synthesized by Hummers method, hydrothermal and polymerization in brine solution.

EXPERIMENTAL

All chemicals were used in this work is analytical grade. The solutions were prepared with deionized water (DI). RGO was synthesized from graphite powder by a modified Hummers method [6-8]. RGO - Zn_{0.5}Ni_{0.5}Fe₂O₄ composite was prepared by the hydrothermal method [3-6]. Next, the brine solution (50 mL of 25% NaCl) was prepared from anhydrous NaCl and DI water [15] for synthesis the RGO-ZNF-porous PANI composite. Then, a mixture of 0.5 mmol aniline and 4.5 mL HCl solution was added to the brine solution slowly. To achieve good uniformity, the mixture was stirred for 1 h. After that, a mount of RGO-ZNF composite was slowly added into the mixture. Then a watery solution containing 1.14 g ammonium persulfate was added drop-wise to the prepared mixture. The polymerization reaction continued at room temperature with vigorous mechanical stirring for 8 h. After the reaction, the reluctant was collected and repeatedly washed with acetone and water. At last, the composite material was dried in a vacuum oven at 50 °C for 12 h.

The composite's morphology and crystal structure were observed using scanning electron microscopy (SEM – S4800), X-ray diffraction (XRD, Bruker D5 with Cu K α 1 radiation $\lambda = 1.54056 \text{ \AA}$), and Fourier transform infrared spectroscopy (FTIR, Perkin Spectrum Two). The vibrating sample magnetometer (VSM, DMS 880) was used to measure magnetic properties of the composite.

The adsorption experiments of uranium were conducted by bath method. We mixed RGO-ZNF-PANI adsorbent with 200 mL of uranium solution in a conical flask and kept the temperature at 25 °C in all of the adsorption experiments. The internal magnetic field was used to separate the adsorbent from the uranium solution after the adsorption had reached the equilibrium. The concentration of residual uranium in the solution was measured by inductively coupled plasma mass spectrometry (ICP-MS).

The adsorption capacity of uranium ions (Q_e , mg/g) was calculated by the following equation:

$$Q_e = \frac{C_o - C_e}{m} V \quad (1)$$

Where C_o and C_e (mg/L) are the concentrations of the uranium at initial and equilibrium states, respectively, m is the weight

of adsorbent (g), and V is the volume of the solution (L).

The optimized adsorption conditions included the adsorbent mass, pH and adsorption time. The solution's initial pH has been modified by adding 0.1 mol/L HNO₃ and 0.1 mol/L NaOH solutions. The uranium laden on RGO-ZNF-PANI was desorbed by using 0.1 mol/L HNO₃ solution. The recovered adsorbent was washed several times with water, ethanol and dried at 50 °C.

RESULTS AND DISCUSSION

Characterization of materials

Fig. 1(a) shows that the thin RGO sheets were exfoliated from graphite, but tend to deform and wrinkle strongly. The ultra-thin nanosheets is clear and distinct with several nanometers in thickness. In the Fig. 1(b), the ZNF nanoparticles have covered almost completely the whole surface of the RGO leaves. In this figure, it can be seen that the particle sizes range from 15 to 25 nm in diameter. The surface morphology of the RGO-ZNF-PANI composite is shown in Fig. 1(c). The PANI fibers have connected together randomly and with the surfaces of RGO-ZNF. Additionally, it is clear to observe the pore channels from porous PANI. The porous PANI fibers could enhance the surface area distinctly which offers many advantages for efficient adsorbent.

In the XRD pattern of composite (Fig. 2), there are several weak peak corresponding to porous PANI structure at about 14.53 °, 19.96 ° and 24.85 °. The few characteristic peaks for planes such as (220), (311), (400), (422), (511) and (440) were observed in the XRD pattern. The XRD data indicated that the ZNF particles in RGO-ZNF-PANI composite have face-centered cubic trevorite structure. The value of crystallite size of the ZNF nanoparticles was evaluated using the Scherrer formula $d = k\lambda/\beta\cos\theta$, where k is equal 0.94, λ is the X-ray wavelength, β is the peak full width half maxima (FWHM) and θ is the diffraction peak position. Results obtained by calculation with the (311) peak display that the crystallite size of ZNF is 20 nm. This data is in great correspondence with the previous analysis of the SEM image.

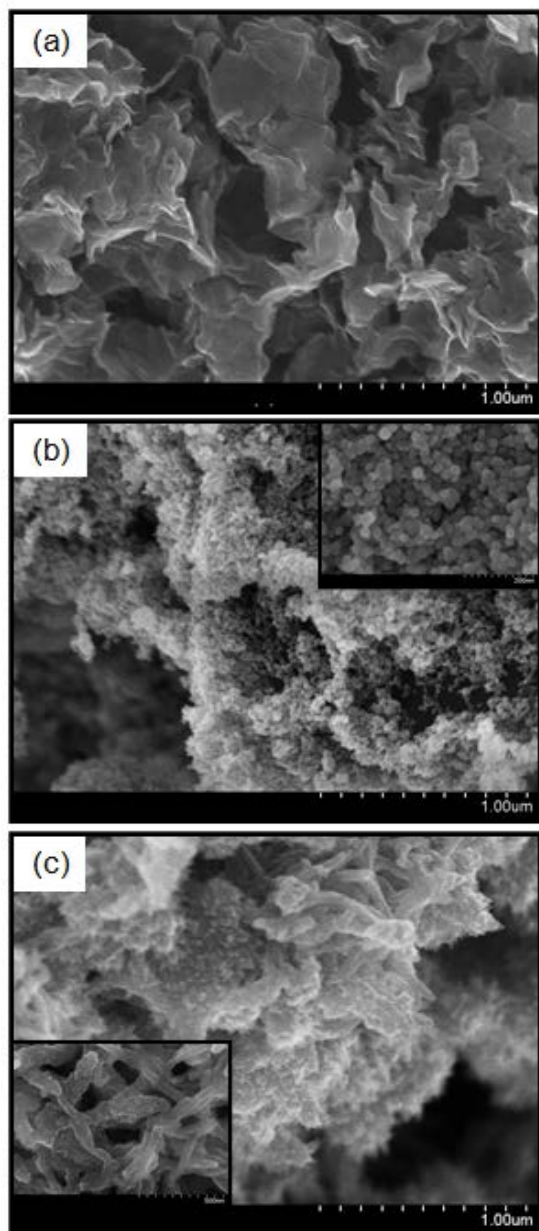


Figure 1. SEM images of RGO (a), RGO-ZNF (b) and RGO-ZNF-porous PANI (c).

FTIR spectra of RGO-ZNF-PANI is shown in Fig. 3. The peaks at 1590 and 1497 cm^{-1} could be attributed to the vibration of C=C stretching of quinonoid and benzenoid rings. The stretching vibrations of C-N located at 1293 and 1244 cm^{-1} . The peak at 1047 cm^{-1} corresponds to the vibrations of C-O bonds. The peak at 797 cm^{-1} is related to vibrations of C-H bonds. The absorption peak at 571 cm^{-1} corresponds to the vibration of Fe-O bond [15-16]. The XRD pattern and FTIR spectra demonstrate that RGO, ZNF, and PANI exist in this composite. The composite was successfully prepared.

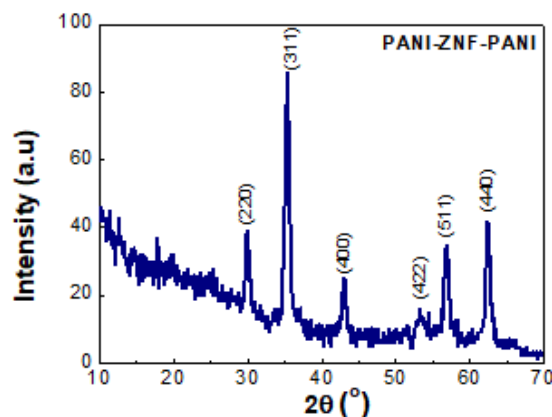


Figure 2. XRD pattern of RGO-ZNF-PANI.

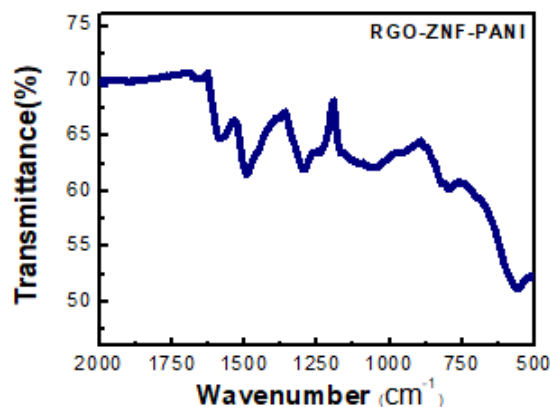


Figure 3. FTIR spectra of RGO-ZNF-PANI.

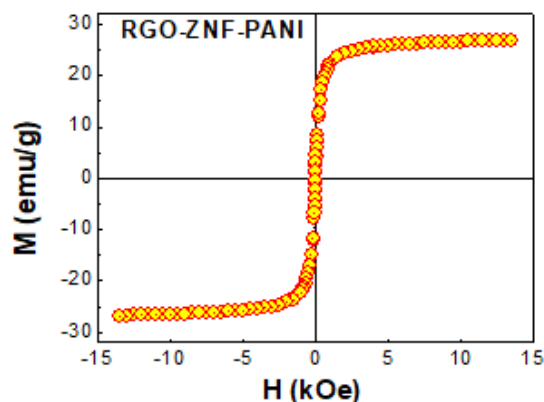


Figure 4. RGO-ZNF-PANI magnetic hysteresis loop at room temperature.

The RGO-ZNF-PANI magnetic hysteresis loop at room temperature is shown in Fig. 4. The result displays that the remanence and coercive force are near zero. This data indicated that obtained composite was typically superparamagnetic-like. The maximum value of magnetization of RGO-ZNF-PANI composite is about 27 emu/g. A high saturation magnetization

makes this adsorbent easy to isolate from the solution by applying an inner magnetic field.

Adsorption studies

Fig. 5 displays the impact of the adsorbed amount on the adsorption capacity of uranium. With the increase in adsorbent mass, the percentage of uranium adsorption significantly increases. When the mass of adsorbent over 10 mg per 200 mL solution, the uranium adsorption capacity remains almost constant. Therefore, from an economic perspective, the 10 mg adsorbent dose was selected as the optimal dose.

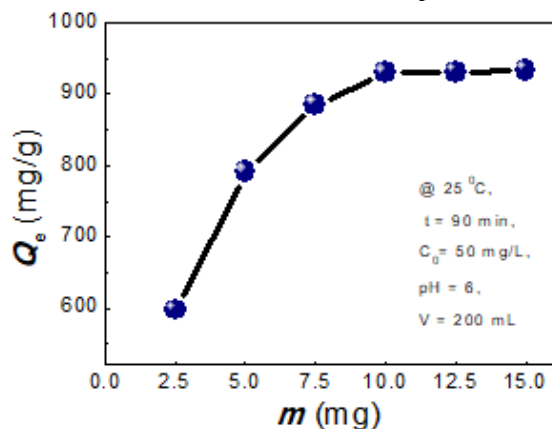


Figure 5. Effect of the adsorbent dose on the uranium adsorption.

The effect of initial pH on the uranium adsorption of RGO-ZNF-PANI is shown in Fig. 6. The capacity adsorption of uranium increases sharply when the pH increases from 4 to 6. As the pH value was increased continually from 6 to 10, the adsorption ability decreases. This result indicates that the sorption ability of RGO-ZNF-PANI for uranium ions is strongest at $pH = 6$. Uranium ions hydrolysis and protonation-deprotonation of RGO-ZNF-PANI adsorbent in solution was predicted that affects pH -dependent uranium adsorption on composite [10]. When the pH is below 6, uranium occurs primarily in the form of UO_2^+ species and the amino groups of the adsorbent, on the other hand, are predominantly occupied by H^+ . The repulsion between uranium ions and surface-positive adsorbent led to a fall in the adsorption of uranium ions. With the increase in pH , protons are released from the surface of the composite with the increase in pH , leaving more binding uranium adsorption sites. Hence, the amount of adsorbed uranium on the composite surfaces is increased. On the contrary, uranium is present in solution as anionic species when pH is over 6.

And the surface of RGO-ZNF-PANI composite changed to negative charge. It would inhibit the adsorption of uranium ions on this adsorbent.

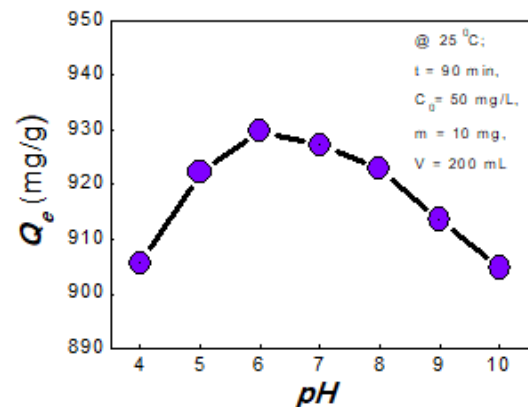


Figure 6. Effect of pH on uranium adsorption.

The contact time effect of uranium adsorption is displayed in Fig. 7. As the observation of this figure, the amount of uranium adsorption on the composite increases and retains at high value after 90 min. It indicates that the adsorption process was established the equilibrium state. Two common kinetic models were used to treat the experimental data, namely pseudo-first-order and pseudo-second-order to determine kinetic parameters [6-8]. The results are shown in Fig. 8. The pseudo-second-order equation fits well with the experimental data, and the correlation coefficient obtained for pseudo-second-order equation is higher than that of pseudo-first-order. Furthermore, the sorption capacities calculated by the pseudo-second-order model are very close to the experimental values. These results suggest that a pseudo-second-order sorption is the predominant mechanism.

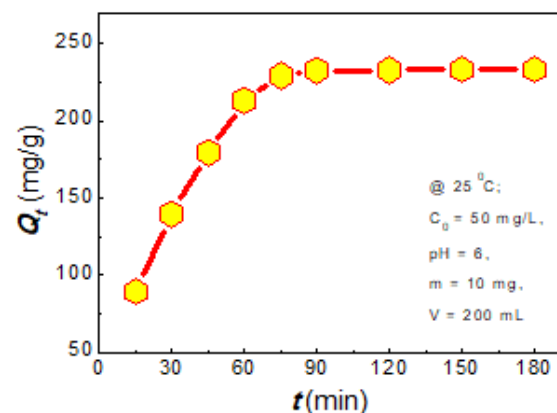


Figure 7. Effect of contact time on the uranium adsorption.

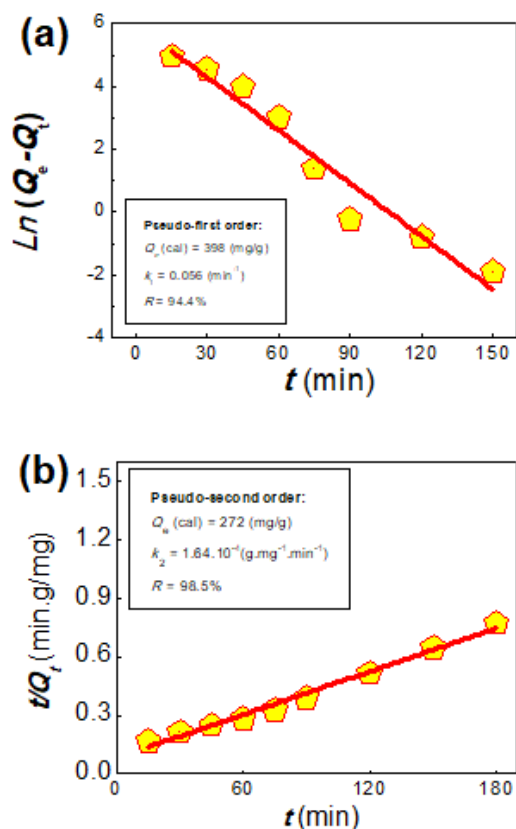


Figure 8. Pseudo-first-order (a), pseudo-second-order (b) plot for the adsorption.

The adsorption isotherm of uranium on RGO-ZNF-PANI composite at room temperature is displayed in Fig. 9. The data showed that the uranium adsorption amount increased as the increasing of equilibrium concentration and did not approach the saturated state in this experiment. The maximum adsorbed uranium quantity of RGO-ZNF-porous PANI in our experimental condition is 1743 mg/g.

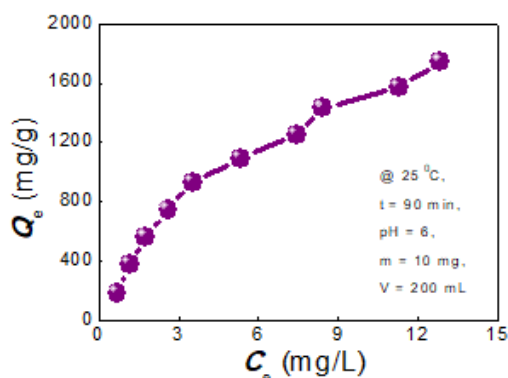


Figure 9. Effect of equilibrium concentration on the adsorption.

In order to determine the uranium adsorption properties of this composite, the adsorption data

have been estimated by using typical isotherm models, such as the Langmuir and the Freundlich models [11]. Fig. 10 displays the result of the fitting of two isotherm models. Because of higher correlation coefficient and having good matching with the experimental data, it is reasonable to choose Langmuir isotherm to characterize the uranium adsorption behavior of RGO-ZNF-PANI composite. According the Langmuir model, the adsorbent surface is monolayer and homogeneous and no interaction between the active sites occurs. The maximum of uranium adsorption capacity which was calculated from Langmuir model is about 2680 mg/g. The adsorption of uranium in the presence of this adsorbent can be allocated to the interaction between the active surfaces of RGO-ZNF-PANI and uranium species in the solution. There are some kind of sites, centers adsorption onto surface of this composite such as functional surface groups imine, amine, protonated amine, carboxyl, active center owing to nano sized ferrite particles [6-9]. Additionally, with porous structure of PANI, the area of active surface is enhanced so the uranium adsorption could be significantly improved [17].

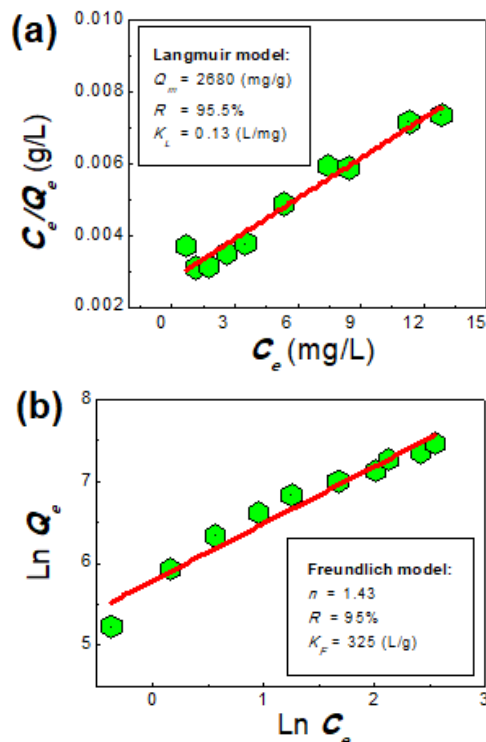


Figure 10. The uranium adsorption isotherms: Langmuir model (a), Freundlich model (b).

The amount of uranium adsorbed on the RGO-ZNF-PANI composite as a function of

cycle number is shown in Fig. 11. When the uranyl ion permeated into inner RGO-ZNF-PANI composite, it is possible to form the stable complex and could be difficult to desorb. Hence, there is a slight reduction of adsorption capacity after six cycles from 232 mg/g to 226 mg/g. This data showed that RGO-ZNF-PANI adsorbent has acceptable chemical stability in adsorption - desorption process of uranium from aqueous solution.

The adsorption capacity of RGO-ZNF-PANI is higher than that of other adsorbents [4-14]. The higher specific adsorption capacity is directly correlated to the high surface area of this composite. Due to the specific area of RGO, the porous structure of PANI and the nanometer size of ZNF particles, the specific surface area of RGO-ZNF-PANI composite is improved expressively. In addition, with numerous pores in small fiber of PANI, the active complex groups are increased which exhibit good affinity for uranium ions. Compared with RGO-ZNF-PANI adsorbent ($Q_m = 1885$ mg/g) [6], RGO-ZNF-porous PANI material has an adsorption capacity is higher than 1.42 times. Despite the fact that it is not easy to compare adsorbents, the RGO-ZNF-PANI composite has a very good adsorption performance of adsorption capacity and kinetic characteristics.

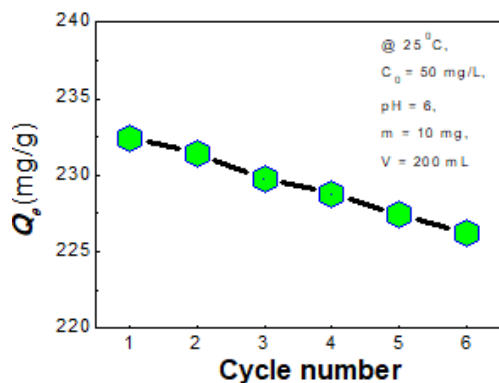


Figure 11: Effect of uranium adsorption - desorption cycles on the adsorption capacity.

CONCLUSION

The RGO-ZNF-PANI nanocomposite has been successfully synthesized and used as an active adsorbent for adsorption of uranium from the aqueous solution. The adsorption process was well suitable with pseudo-second-order and Langmuir isotherm models. The maximum uranium adsorption capacity of RGO-ZNF-PANI composite was estimated to be 2680 mg/g at $pH = 6$ and 25 °C. The high adsorption

capacity of this adsorbent was related to the high specific area of surface, more functional groups. Spent RGO-ZNF-PANI can be effectively recovered by using magnetic separation and efficiently regenerated. The RGO/CF/PANI composite is considered as suitable material for the collection and preconcentration of uranium from seawater and nuclear waste.

Acknowledgment

This paper was supported by Le Quy Don Technical University, Vietnam.

References

- [1] D. Li, S. Egodawatte, D.I. Kaplan, S.C. Larsen, S.M. Serkiz, J.C. Seaman, K.G. Scheckel, J. Lin, Y. Pan, *Sequestration of $U(VI)$ from acidic, alkaline, and high ionic-strength aqueous media by functionalized magnetic mesoporous silica nanoparticles: capacity and binding mechanisms*, Environmental Science and Technology **51** (2017) 14330-14341.
- [2] P. D. Bhalara, D. Punetha and K. Balasubramanian, *A review of potential remediation techniques for uranium (VI) ion retrieval from contaminated aqueous environment*, Journal of Environmental Chemical Engineering **2** (2014) 1621-1634.
- [3] T.Q. Dat, L.D. Vi, D. Q. Hung, *Uranium removal activity of $Cu_{0.5}Ni_{0.5}Fe_2O_4$ superparamagnetic nanoparticles prepared by large scale method*, Vietnam Journal of Science and Technology **52** (3A) (2014) 66-73 (in Vietnamese).
- [4] T.Q. Dat, N.V. Toan, P.V. Thin, D.Q. Hung, *Adsorption of uranium from aqueous solution by $Cu_{0.5}Ni_{0.5}Fe_2O_4$ - reduced graphene oxide*, Vietnam Journal of Science and Technology **54** (5A) (2016) 9-19.
- [5] T.Q. Dat, V.D. Thao, P.T. Hung, D.Q. Hung, *Aqueous uranium activity removal by $CoFe_2O_4$ nanoparticles*, Malaysian Journal of Chemistry **19** (1) (2017) 59-66.
- [6] T.Q. Dat, P.T. Hung, D.Q. Hung, *Efficient removal of uranium from aqueous solution by reduced graphene oxide- $Zn_{0.5}Ni_{0.5}Fe_2O_4$ ferrite-polyaniline nanocomposite*, Journal of Electronic Materials, **46** (6) (2017) 3273-3278.
- [7] T.Q. Dat, N.V. Tung, P.V. Thin, D.Q. Hung, *RGO/CNF/PANI as an effective adsorbent for the adsorption of uranium from*

- aqueous solution, Vietnam Journal of Science and Technology **56** (1) (2018) 25-32.
- [8] T.Q. Dat, N.T. Ha, P.V. Thin, D.Q. Hung, *Synthesis of RGO/CF/PANI magnetic composites for effective adsorption of uranium*, IEEE Transactions on Magnetics **54** (6) (2018).
- [9] D. Shao, G. Hou, J. Li, T. Wen, X. Ren, and X. Wang, *PANI/GO as a super adsorbent for the selective adsorption of uranium (VI)*, Chemical Engineering Journal **255** (2014) 604-612.
- [10] S. Duan, X. Xu, X. Liu, Y. Wang, T. Hayat, A. Alsaedi, Y. Meng, J. Li, *Highly enhanced adsorption performance of U(VI) by non-thermal plasma modified magnetic Fe₃O₄ nanoparticles*, Journal of Colloid and Interface Science **513** (2018) 92-103.
- [11] J. Wei, X. Zhang, Q. Liu, Z. Li, L. Liu, J. Wang, *Magnetic separation of uranium by CoFe₂O₄ hollow spheres*, Chemical Engineering Journal **241** (2014) 228-234.
- [12] L. Chen, S. Feng, D. Zhao, S. Chen, F. Li and C. Chen, *Efficient sorption and reduction of U(VI) on zero-valent iron-polyaniline-graphene aerogel ternary composite*, J. Coll. Inter. Sci. **490** (2017) 197-206.
- [13] L. Tan, Q. Liu, D. Song, X. Jing, J. Liu, R. Li, S. Hu, L. Liu and J. Wang, *Uranium extraction using a magnetic CoFe₂O₄-graphene nanocomposite: kinetics and thermodynamics studies*, New J. Chem. **39** (2015) 2832-2838.
- [14] M.T. Aljarrah, M.S. Al-Harshsh, M. Mayyas, M. Alrebaki, *In situ synthesis of quaternary ammonium on silica-coated magnetic nanoparticles and its application for the removal of uranium (VI) from aqueous media*, Journal of Environmental Chemical Engineering **6** (5) (2018) 5662-5669.
- [15] A.C. Anbalagan, S.N. Sawant, *Brine solution-driven synthesis of porous polyaniline for supercapacitor electrode application*, Polymer **87** (2016) 129-137.
- [16] D. Donescu, R.C. Fierascu, M. Ghiurea, D.M. Maximean, C.A. Nicolae, R. Somoghi, C.I. Spataru, N. Stanica, V. Raditoiu, R. Vasile, *Synthesis and magnetic properties of inverted core-shell polyaniline-ferrite composite*, Applied Surface Science **414** (2017) 8-17.
- [17] C. Duan, J. Zheng, *Porous coralloid Polyaniline/SnO₂ -based enzyme-free sensor for sensitive and selective detection of nitrite*, Colloids and Surfaces A **567** (2019) 271-277.

ANTIFUNGAL ACTIVITY OF SILVER NANOPARTICLES AGAINST *Neoscytalidium dimidiatum* CAUSES BLACK ROT ON DRAGON FRUIT TREE *Hylocereus undatus*

Anh Van Thi Le , Dung My Thi Dang and Chien Mau Dang

Institute for Nanotechnology, Vietnam National University-Ho Chi Minh City, Community 6, Linh Trung
Ward, Thu Duc District, Ho Chi Minh City, Vietnam;

Email: ltvanh@vnuhcm.edu.vn

ABSTRACT

Silver nanoparticles (SNPs) form has high antimicrobial activity, is therefore widely used for various sterilization purpose. There have been relatively a lot of studies on the applicability of silver nanoparticles in order to control plant diseases. This material were tested in the modern study to examine the antifungal activity on *Neoscytalidium dimidiatum*, the plant – pathogenic fungi, causes black rot on dragon fruit tree (*Hylocereus undatus*). In vitro petri dish assays indicated that SNPs had effect on control the *N. dimidiatum* development. Silver nanoparticles were found effective at 5ppm inhibited 80% the mycelial growth of *N. dimidiatum* when added it into cultures. At the 25ppm concentration, silver nanoparticles showed of 85% inhibitor rate of spore germination after 24 hours treatment. For the treated dragon fruit trees before they were infected with *N. dimidiatum*, the SNPs at 25ppm, showed high effective to inhibit the expression of symptoms of black rot disease, incidence rate in the treatment was 27% compare with 90% in the control.

Keywords: Antifungal, Silver Nanoparticles, *Hylocereus undatus*, *Neoscytalidium dimidiatum*

INTRODUCTION

SNPs is a kind of material with a lot of applications, such as sensors, catalysts, anticancer agents and antimicrobial agents. SNPs have exhibited activity against bacteria, fungi and viruses [1]. Silver is known to attack a broad range of biological processes in microorganisms including the alteration of cell membrane structure and functions. Silver also inhibits the expression of proteins associated with ATP production [2, 3]. Beside all of the characteristic of silver, SNPs has small size (1 – 100nm) can interact with cell surfaces (plasma membranes, plant cellulose walls, bacterial and fungal cell walls, and membranes). SNPs can penetrate and pass through the organism's external envelopes. The plasma membrane's permeability for small-sized SNPs allows for accumulation of them in internal compartments of cells[4].

In recent years, SNPs is used as common antimicrobial agents to have potential applications of it to manage of plant diseases. SNP presents multiple modes of inhibitory action against harmful microorganisms.

Therefore, it may be used for control of various important plant-pathogenic fungi [5-7]. Ouda et al researched the ability to inhibit mycelial growth of *Alternaria alternata* and *Botrytis cinerea*. The application of 15ppm concentration of silver nanoparticles produced maximum inhibition of the growth of fungal hyphae, 59.3 and 52.9% inhibition percentage with *A. alternata* and *B. cinerea*, respectively [8]. Kim and co-workers demonstrated that SNPs were very effective against 18 plant phytopathogenic fungi species as *Alternaria sp.*, *Fusarium sp.*, *Botrytis cinerea*, *Clasdosporium cucumerium*,... on *in vitro* petri dish when they compared inhibitor rate of radial growth of fungal mycelium on the potato dextrose agar (PDA) plate treated with different concentrations SNPs and control plate [9].

In this study, we was used SNPs, which were produced by Institute for Nanotechnology have nanoparticle size is smaller than 20nm in deionized water with Polyvinylpyrrolidone (PVP) and Etylen glycol in the composition as stabilizers.

Objectives of the present study were determined the inhibitory properties of SNPs against *Neoscytalidium dimidiatum*, a plant-pathogenic fungi, which causes black rot on dragon fruit tree. And to evaluate the efficacy of SNPs for suppression of plant pathogenic fungi *in vitro* by assessing radial growth of fungal mycelium to calculate radial inhibition, inhibitor rate of spore germination. In greenhouse study, we examined incidence rate of dragon fruit tree which were infected the fungal and treated with SNPs.

MATERIALS AND METHODS

Materials

SNPs at initial concentration of 200 ppm and different working concentrations of SNPs were prepared by diluting the original stock solution with distilled water.

N. dimidiatum was isolated from black rot spot diseases of dragon fruit branch and confirmed by Koch's postulates. The fungi were grown on potato glucose agar (PGA) for this experimentation. Fungal mycelium was obtained by cutting square agar plugs (5x5mm) at the edge of the fungal colonies that were incubated 24 hr at 28 ± 2°C. Fungal spores were accepted by incubating the fungi petri dish 5 days at 28 ± 2°C until the spores appear, using a clean cotton swab and salt water 0.9% to collect the spores.

Dragon fruit branches were planted in plastic pots in greenhouses for creating young shoots. Used them to conduct experiments when their length was from 5 – 10 cm.

Methods

Inhibitory properties of SNPs against the mycelial growth

Experiment was performed on PGA growth medium treated with different concentrations (0-negative control; 0,5; 1; 2; 3; 4; 5 ppm) of SNPs. 5 mL of SNPs having different concentrations was poured into potato glucose agar (PGA) prior to plating in a petri dish (90 × 15 mm) so that the SNPs reached the experimental concentration. Media containing SNPs was incubated at room temperature (25°C). After 24 hr of incubation, agar plugs of uniform size (5x5mm) containing fungi were inoculated simultaneously at the center of each petri dish containing silver nanoparticles, followed by incubation at 28 ± 2°C for 7 days. Radial growth

of fungal mycelium was recorded every day. Radial inhibition was calculated when growth of mycelia in the control plate reached the edge of the petri dish. The following formula was used for calculation of the inhibition rate (%).

$$\text{Inhibitor rate (\%)} = \frac{R-r}{R} \quad (1)$$

With:

- R is the radial growth of fungal mycelia on the control plate.
- r is the radial growth of fungal mycelia on the plate treated with AgNPs.

Inhibition rates were determined based on five replicates of each experiment, inhibition rate of control = 0%.

Inhibitory properties of SNPs against the spore germination

SNPs solution was mixed in saline 0.9% in test tube, and added solution of fungal spore suspension to obtain 5 mL solution of fungal spore concentration of 10⁵ spore/ml. 10 different SNPs concentrations (0 – negative control, 1; 5; 10; 15; 20; 25; 50; 75; 100 ppm), incubation at 28 ± 2°C. Counted the germination of spores at time before treatment, 3, 6, 24 and 48 hours after incubation by 40X eyepiece optical microscope with erythrocyte counting chamber, determined the number of germinated spores in a total of 100 spores. A spore is confirmed to germinate when the germ's length is longer than itself. Radial inhibition of germination was calculated by the fomula (1) with:

- R is the radial germination of fungi on the control tube.
- r is the radial germination of fungi on the tubes treated with SNPs.

Inhibition rates were determined based on 3 replicates of each experiment, inhibition rate of control = 0%.

Inhibitory properties of SNPs against black rot pathogenic on dragon fruit tree in greenhouse

Experiment was performed on two types of time of processing with experiment design in table 1, T1 and T2 were treated SNPs 3 times by wet spraying the branches.

T1: 1st treatment before infected fungi 10 days, 2nd, 3rd treatment after infected fungi 10 days and 20 days.

T2: 1st, 2nd, and 3rd treatment after infected fungi 10 days, 20 days and 30 days.

The fungal spores suspension had concentration of 10⁵ spore/ml was scanned on the branches of dragon fruit with a brush in the afternoon. Recorded number of infected branches after 7, 17, 27 and 37 days fungal infection. The infected branch is branch with at least one pathogenic spot. The following formula was used for calculation of incidence rate (%)

$$\text{Incidence rate (\%)} = \frac{A}{B}$$

Incidence rates were determined based on 20 replicates (branches) of each experiment, inhibition rate of control = 0%.

With:

- A is the number of infected braches.
- B is the total branches in experiment.

Table 1. Experimental design

Treatment	Content
Control (PC)	Infected <i>N. dimidiatum</i> for trees, treating with distilled water
T1-SNPs	Infected <i>N. dimidiatum</i> for trees, treating with SNPs 25ppm. Beganed 1 st SNPs treatment before fungal injection
T2-SNPs	Infected <i>N. dimidiatum</i> for trees, treating with SNPs 25ppm. The fungi was injected before treated 1 st SNPs

Statistical analysis: Data were analyzed by T-test, Minitab 16 software, with t= 95%.

RESULTS AND DISCUSSION

Inhibitory properties of SNPs against the mycelial growth

The fungi showed growth inhibition with the increase of incubation time. In control treatment, after 2 days incubation, growth of mycelia in the control plate reached the edge of the petri dish. High ability inhibition was observed on PGA medium against *N. dimidiatum* in the treatment with 3 ppm or more, 4 ppm concentration resulted in greater than 80% inhibition on PGA against the fungi. In the treatments, *N.*

dimidiatum mycelia did not grow on PGA agar containing SNPs, they only grew around agar plugs. Therefore, the results suggested that maximum inhibition was obtained on PGA treated with the 4 ppm concentration of SNPs. Data on inhibition effects of *N. dimidiatum* mycelia are shown in fig 1.

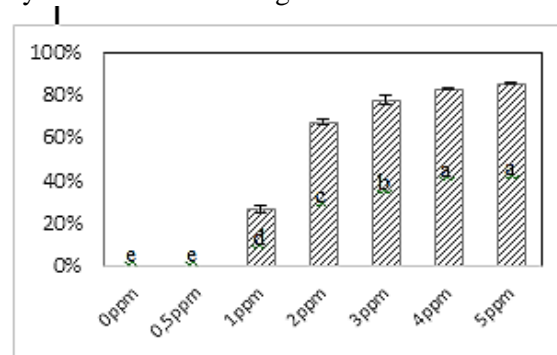


Figure 1. Radial inhibition of *N. dimidiatum* mycelia after 3 days treated by SNPs

Inhibitory properties of SNPs against the spore germination

After 24 hr incubation, the SNPs treatments all had properties that inhibited the germination of *N. dimidiatum* spores (fig.1). At the 48 hours, this rate did not change significantly. The radial germination of fungi on the tubes was treated with SNPs having a concentration of 25ppm reduced 80% less than the control, the germs in this treatment did not grow and long as well as in the control. At the 50, 75 and 100 ppm concentration, SNPs inhibited almost completely the fungal spores germination, respectively 92; 94 and 97% compared with the control.

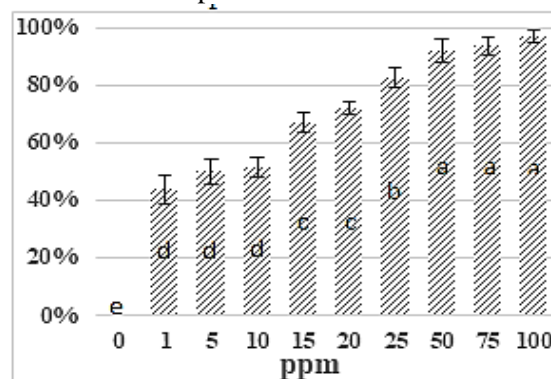


Figure 2. Radial inhibition of *N. dimidiatum* spores germination after 24 hours treated by SNPs

Inhibitory properties of SNPs against black rot pathogenic on dragon fruit tree in greenhouse

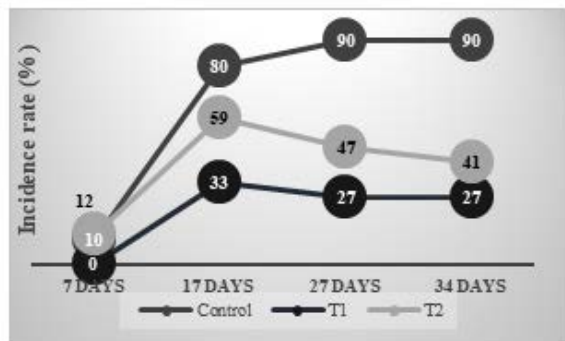


Figure 3. Incidence rate of *N. dimidiatum* to dragon fruit branches treated by SNPs

SNPs had the ability to reduce incidence rate the treated treatment. When handling SNPs before fungal infection (T1), experimental treatment efficiency was higher than spraying nanoparticles after fungal infection (T2). In T1 treatment, incidence rate was 27%, compared to 90% in the control after 27 days infected the fungi. Spraying SNPs before fungal infection helped to increase the prevention effect of dragon fruit.

CONCLUSION

Findings from the current investigation demonstrated that SNPs bioactive inhibited development of *N. dimidiatum* mycelia and spore. When treated in dragon fruit tree, SNPs reduced black rot disease symptoms on the branches caused by fungal pathogens *N. dimidiatum*. This study was the first to demonstrate that the inhibitory effect of SNPs against *Neoscytalidium dimidiatum*. It is also the basis for conducting experiments on a larger scale

Acknowledgments

This research is funded by Vietnam National University – Ho Chi Minh City (VNU-HCM) under the grand number TX2019-32-01

References

- [1] Mallmann, E.J.J., et al., *Antifungal activity of silver nanoparticles obtained by green synthesis*. Revista do Instituto de Medicina Tropical de Sao Paulo, 2015. **57**(2): p. 165-167.
- [2] Jo, Y.-K., B.H. Kim, and G. Jung, *Antifungal Activity of Silver Ions and*

- Nanoparticles on Phytopathogenic Fungi*. Plant Disease, 2009. **93**(10): p. 1037-1043.
- [3]. Yamanaka, M., K. Hara, and J. Kudo, *Bactericidal actions of a silver ion solution on Escherichia coli, studied by energy-filtering transmission electron microscopy and proteomic analysis*. Appl Environ Microbiol, 2005. **71**(11): p. 7589-93.
- [4]. Skonieczna, M. and D. Hudy, *Biological Activity of Silver Nanoparticles and Their Applications in Anticancer Therapy*, in *Silver Nanoparticles - Fabrication, Characterization and Applications*. 2018.
- [5]. Jung, J.-H., et al., *The Effect of Nano-Silver Liquid against the White Rot of the Green Onion Caused by Sclerotium cepivorum*. Mycobiology, 2010. **38**(1): p. 39-45.
- [6]. Kim, S.W., et al., *Antifungal Effects of Silver Nanoparticles (AgNPs) against Various Plant Pathogenic Fungi*. Mycobiology, 2012. **40**(1): p. 53-8.
- [7]. Lamsal, K., et al., *Inhibition Effects of Silver Nanoparticles against Powdery Mildews on Cucumber and Pumpkin*. Mycobiology, 2011. **39**(1): p. 26-32.
- [8]. Ouda, S.M., *Antifungal Activity of Silver and Copper Nanoparticles on Two Plant Pathogens, Alternaria alternata and Botrytis cinerea*. Research Journal of Microbiology, 2014. **9**(1): p. 9.
- [9]. Kim, S.W., et al., *Antifungal Effects of Silver Nanoparticles (AgNPs) against Various Plant Pathogenic Fungi*. Mycobiology, 2012. **40**(1): p. 53-58.

SURFACE ENHANCED RAMAN SCATTERING OF METHYLENCE BLUE ADSORBED ON GOLD NANOPARTICLES

Thi Ha Tran^{1,2}, Thi Huyen Trang Nguyen¹, Thanh Cong Bach², Nguyen Hai Pham², Cong Doanh Sai², Quang Hoa Nguyen², Trong Tam Nguyen³, Khac Hieu Ho⁴, Viet Tuyen Nguyen^{2*}

¹Department of Physics, Faculty of Basic Science, Hanoi University of Mining and Geology, Duc Thang, Tu Liem, Hanoi

²Vietnam National University, University of Science, 334 Nguyen Trai, Thanh Xuan, Hanoi

³Department of Physics, Faculty of Basic –Fundamental Sciences, Vietnam Maritime University, 484 Lach Tray – Le Chan - Hai Phong

⁴Institute of Research and Development, Duy Tan University, 03 Quang Trung, Danang, Vietnam
Email: nguyenviettuyen@hus.edu.vn

ABSTRACT

Gold nanoparticles are well-known for surface plasmon resonant related applications such as: surface enhanced Raman scattering, photovoltaics. In these applications, particle size is extremely important due to its effect on surface plasmon resonant peak position. In this report, thin films of gold were first fabricated by sputtering methods. Gold nanoparticles were developed by annealing the as prepared gold thin films at 300°C. The as-prepared nanoparticles was characterized with scanning electron microscopy, absorption spectroscopy while Raman spectroscopy was used to study the surface enhanced Raman scattering. The as-prepared arrays of gold nanoparticles show excellent SERS activity with organic dye methylene blue as probe. Particle size shows clear effect on enhancement of Raman signal methylene blue.

Keywords: Gold nanoparticles; sputtering; thermal annealing; surface plasmon.

INTRODUCTION

Since its discovery, surface enhanced Raman scattering (SERS) is expected to provide a sensitive tool for chemical and biomedical sensing and imaging [1–3]. In this technique, preparation of noble metals nanoparticles is extremely important because they serve as the platform for Raman enhancement. Self assembled monolayer of gold or silver nanoparticles developed from solution phase is reported to provide good enhancement of Raman signal [4–6]. However, one main limitation of this method is the randomness of the aggregation of nanoparticles during synthesis, which often leads to poor repeatability of the prepared SERS substrates. This in turn prevents the capability of using these substrates for quantitative study. Hence, development of SERS substrates based on evenly distributed array of noble metal is of great interest.

In this research, we report of using gold nanoparticles array on sodalime glass to effectively enhanced Raman scattering. The 2D arrays of gold nanoparticles were fabricated by sputtering and annealing method. Morphology

and surface plasmon resonance property of the samples were then characterized with scanning electron microscope and absorption spectroscopy, respectively. Surface enhanced Raman scattering on the as prepared gold nanoparticle array was also studied.

EXPERIMENTAL

Thin films of gold were prepared on sodalime glass substrates. Ultrasonic bath was applied to clean the substrates. The substrates were cleaned with double distilled water, ethanol and acetone in 10 min each cycle several times to clean the surface. The samples were then dried before being transferred into vacuum chamber for sputtering process. DC sputtering system integrated in Scanning electron microscope was utilized to prepare gold thin films. Heat treatment was not applied during sputtering process. Base pressure in vacuum chamber is maintained at 6 Pa. A gold disk (purity of 99.99%) of 2.5 inches was used as target. The current for sputtering was fixed at 30 mA while sputtering time was from 10s to 50s. The thickness of obtained films was estimated

by the correlation between sputtering time and thickness given by the manufacture of sputtering system.

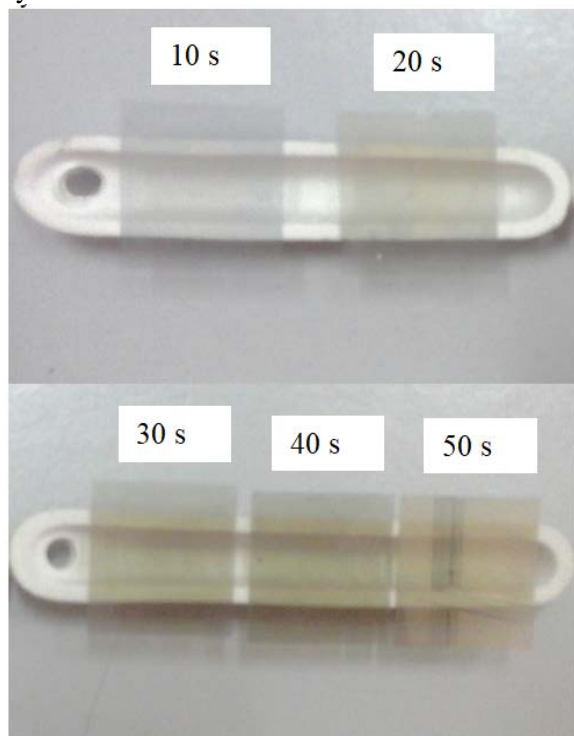


Figure 1. Image of gold nanoparticles array prepared by sputtering and thermal annealing method. The sputtering time is 10s, 20s, 30s, 40s and 50s.

In the next step, the as-prepared thin films were annealed at 300°C in 2h. The heat treatment helps to form array of gold nanoparticle distributed quite evenly on the substrates.

The samples were then studied with scanning electron microscope and absorption spectroscopy. Raman spectrometer Lamram HR 800 was used to investigate surface enhanced Raman scattering of the as-fabricated substrates with Methylene blue as Raman probe. Laser power was estimated as 0.2 mW at the surface sample. Raman signal was collected with a 50x long working distance lens.

RESULTS AND DISCUSSION

Figure 2 presents SEM images of array of gold nanoparticles formed by annealing gold thin films sputtered in 10 s and 40s. As can be seen from the figure that the nanoparticles have uniform size and quasi spherical shape.

It is noted that particles size increases with increasing sputtering time. Average particles size of gold nanoparticles developed from thin

films sputtered in 10s is about 30nm while that of the sample sputtered in 40s is over 100nm with a broad size distribution.

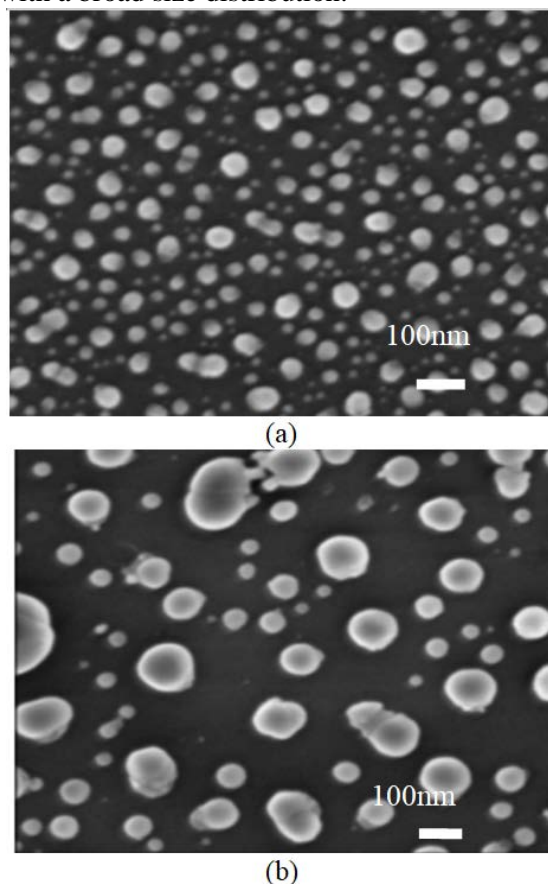


Figure 2. SEM images of gold nanoparticles obtained by annealing gold thin films sputtered in 10 s (a) and 40s (b).

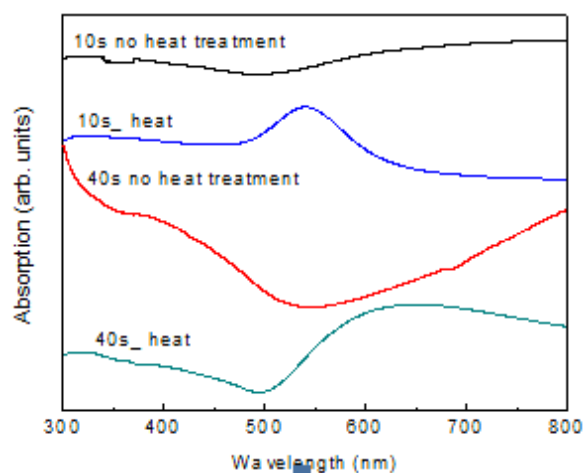


Figure 3. Absorption spectra of gold thin films with and without heat treatment.

Figure 3 shows absorption spectra of the sputtered gold thin films before and after annealing at 300°C in 2h. The absence of plasmon peak in the absorption spectra before

annealing process implies that gold was formed as a continuous thin layer on substrates.

After heat treatment, clear plasmon peaks of gold in the absorption spectra demonstrate that gold layers were transformed into nanoparticles due to the shrinkage induced by heat treatment. Absorption data show agreement with SEM images where broader plasmon peaks and red shift of plasmon peak correspond to growth of particle size as well as size distribution.

SEM images and absorption data show that gold nanoparticles of different size, and tunable surface plasmon resonance were obtained by controlling sputtering time. Surface enhanced Raman scattering of methylene blue adsorbed on these gold nanoparticle was studied to demonstrate the application of surface plasmon resonance in biomedical field. Figure 4 shows Raman spectra of methylene blue adsorbed on gold nanoparticles array prepared from thin films of 40s sputtering.

Raman spectra clearly illustrate characteristic Raman peaks of methylene blue at 1299, 1393, 1497, 1621 cm^{-1} . Table 1 summarizes the corresponding vibration modes of methylene blue. The Raman peaks in our study agree well with those reported previously for this material.

Raman data shows that the asprepared gold nanoparticles are good SERS substrates of high sensitivity, which allow detecting methylene blue at very low concentration of 10^{-10} M.

Estimated enhancement factor of the asprepared SERS substrates based on gold nanoparticles was 3.8×10^7 . The result is promising and show that SERS substrate based on gold nanoparticles has some advantages such as simple processing, high purity.

Table 1. Raman peak position and assignment of the corresponding vibration mode

Observed Raman peak	Raman vibration mode [1,7]
1299	(CH); (C-N) ring
1393	(C9-N10); (C3-N2); (C-N) ring; (CH)
1497	(CH ₂)twist ; (CH)
1621	(C-C)/(C-N)

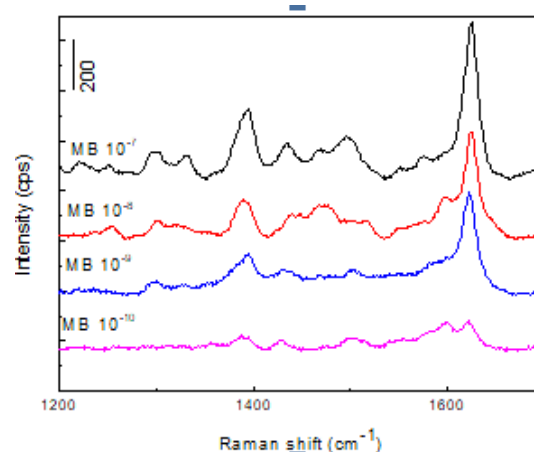


Figure 4. Raman spectra of methylene blue adsorbed on gold nanoparticles prepared from gold thin films sputtered in 40s.

CONCLUSION

Uniform gold nanoparticles were prepared on sodalime glass by combining sputtering and thermal annealing method. Surface plasmon peak position of gold nanoparticle is dependent upon particle size, which can be tuned conveniently by controlling sputtering time. The as-prepared gold nanoparticle array can serve as good surface enhanced Raman scattering platform and can be applied in biomedical analyzing. Further optimization of enhancement factor is being conducted.

Acknowledgment

This research is funded by Vietnam National Foundation for Science and Technology Development (NAFOSTED) under grant number 103.02-2017.351. One of the author, Phd student Thi Ha Tran, would like to thank the Domestic Master/ PhD Scholarship Programme of Vingroup Innovation Foundation for supporting tuition fee.

References

- [1] S. Dutta Roy, M. Ghosh, J. Chowdhury, *Adsorptive parameters and influence of hot geometries on the SER(R) S spectra of methylene blue molecules adsorbed on gold nanocolloidal particles*, *J. Raman Spectrosc.* **46** (2015) 451–461. doi:10.1002/jrs.4675.
- [2] Y. Li, J. Dykes, T. Gilliam, N. Chopra, *A new heterostructured SERS substrate: Free-standing silicon nanowires decorated with graphene-encapsulated gold*

- nanoparticles*, *Nanoscale*. **9** (2017) 5263–5272. doi:10.1039/c6nr09896g.
- [3] P.G. Yin, L. Jiang, T.T. You, W. Zhou, L. Li, L. Guo, S. Yang, *Surface-enhanced Raman spectroscopy with self-assembled cobalt nanoparticle chains: Comparison of theory and experiment*, *Phys. Chem. Chem. Phys.* **12** (2010) 10781–10785. doi:10.1039/c002662j.
- [4] A. Vincenzo, P. Roberto, F. Marco, M.M. Onofrio, I. Maria Antonia, *Surface plasmon resonance in gold nanoparticles: a review*, *J. Phys. Condens. Matter*. **29** (2017) 203002. <http://stacks.iop.org/0953-8984/29/i=20/a=203002>.
- [5] B.S. Lee, D.Z. Lin, T.J. Yen, *A low-cost, highly-stable surface enhanced raman scattering substrate by si nanowire arrays decorated with au nanoparticles and Au backplate*, *Sci. Rep.* **7** (2017) 1–7. doi:10.1038/s41598-017-04062-4.
- [6] W.R. Premasiri, J.C. Lee, A. Sauer-Budge, R. Théberge, C.E. Costello, L.D. Ziegler, *The biochemical origins of the surface-enhanced Raman spectra of bacteria: a metabolomics profiling by SERS*, *Anal. Bioanal. Chem.* **408** (2016) 4631–4647. doi:10.1007/s00216-016-9540-x.
- [7] G.N. Xiao, S.Q. Man, *Surface-enhanced Raman scattering of methylene blue adsorbed on cap-shaped silver nanoparticles*, *Chem. Phys. Lett.* **447** (2007) 305–309. doi:10.1016/j.cplett.2007.09.045.

HIGH PACKAGING EFFICIENCY AND COLOR PERFORMANCE OF WHITE LEDS BY HEMISPHERE DOME OF YELLOW PHOSPHOR PACKAGING

Quang-Khoi Nguyen^{1,2}, Shih-Kang Lin¹, Mai Van Tan², Vu Thi Ngoc Nuong², Vo Tran Khoa Nguyen², Trinh Thi Ngoc Huyen², Ton Nu Quynh Trang², Nguyen Van Hieu², Lam Quang Vinh², Vu Thi Hanh Thu², and Ching-Cherng Sun¹

¹Department of Optics and Photonics, National Central University, Taoyuan City, Taiwan;

²Faculty of Physics and Physics Engineering, VNUHCM-University of Science, Hochiminh City, Vietnam.

Email: quangkhoigialai@gmail.com; vtthu@hcmus.edu.vn; ccsun@dop.ncu.edu.tw

ABSTRACT

The yellow phosphor material of yttrium aluminum garnet (YAG) is used in packaging of white light phosphor-converted based on blue LED chip with using the structure of hemisphere dome of yellow phosphor. At the correlated color temperature (CCT) 5500 K, the white LEDs showed a high packaging of 60% and color rendering of 63. These results are meaningful in the context of energy-saving and improvement of the white LEDs efficiency. In addition, the effect of the injected current on the blue LED chip and CCT of white LEDs were also investigated. The injected current induced a small drift of CCT with increasing of injected current. Therefore, it is important to keep the injected current constant in operating process to maintain the color efficiency of white LEDs.

Keywords: White LEDs, packaging efficiency, color performance, YAG, hemisphere dome.

INTRODUCTION

Solid-state lighting (SSL) has been gradually replacing the incandescent light bulbs owing to its advantages, including high energy efficiency, fast response, acceptable color rendering, long-lifetime and low cost. There are many ways to generate white light such as dichromatic, trichromatic and tetrachromatic approaches [1-3]. Based on the dichromatic approach, the white light is created by the combination of a blue LED die and yellow phosphor. The quality of pcWLEDs depends on many factors such as blue LEDs die, type of yellow phosphor, packaging technology, thermal management, encapsulant material. In packaging technology, there are several main factors that affect the properties of pcWLEDs are phosphor loss, geometry loss, Stoke loss, packaging structure. Since type of blue LED die and phosphor material are usually fixed by the manufacturer, so the Stoke loss can be doing minimum by choosing the suitable kind of LED and yellow phosphor. The different weight concentration of yellow phosphor can cause different effects on the output power due to the backward scattering problem. Packaging structure can affect to the optical path length of the photon that will effect the color performance

of pcWLEDs. A problem that usually occurs in the process of making white light is backward scattering when blue light emitted from LED die hit to the phosphor. This is extremally serious as using a high weight concentration of phosphor.

With the motivation of fabrication a pcWLEDs have high packaging efficiency and color performance, based on our best knowledge on the packaging technology, we conducted the study of the packaging of white light phosphor-converted based on blue LED chip with using the structure of hemisphere dome of yellow phosphor. In this study, based on the principle of the dichromatic approach, the yellow phosphor material of yttrium aluminum garnet (YAG) and blue LED die were used. Using a hemisphere packaging structure of low weight concentration of yellow phosphor of 7.5%, the optical properties of pc-WLEDs were investigated including CCT, packaging efficiency and CRI. Besides, the effect of different injected current on the optical properties (CCT, CRI) and thermal characteristics of pcWLEDs were also studied.

EXPERIMENT

Blue die type of CREE EZ 700 made by the CREE company. The emission spectrum of blue

die showed a peak emission is at the wavelength of 449 nm. Chip was bonded on the sub-mount of Aluminum Nitride (AlN). Silver glue was used to attach the LED die on the sub-mount. By using the die bonding machine, blue LED die is attached on the sub-mount by silver glue. The wire bonding process was conducted as follows: gold wire with a diameter of 50 nm used to do the wire bonding between an electrode on the LED die and the sub-mount. Next, the packaging process of pc-WLEDs with hemisphere dome of yellow phosphor was conducted as follows: Mixing of silicone gel A, B, and phosphor powder was prepared, then stirred uniform. The air in the mixture was pushed out by the vacuum pump. The weight concentration of phosphor in the mixture used in this study is 7.5 %. Next, this mixture is poured into the metal molding with hemisphere shape. Then it was put in the vacuum pump again. Finally, chip on sub-mount was put on this molding and adjusted for an accurate position. After doing solid at temperature 130 °C in 5 minutes, we will get the sample of pc-WLEDs with hemisphere dome of yellow phosphor .

RESULTS AND DISCUSSION

The EL spectrum of bare blue LED.

Figure 1 showed the EL spectrum of bare blue LED die that used in the packaging of pc-WLEDs. Spectrum of bare blue LED showed a narrow band with wavelength from 400 to 500 nm, the peak of blue emission band is at the wavelength of 449 nm. At the value of injected current and forward voltage of 50 mA and 2.945 V, respectively, the radiated power of bare blue light is 54.4 mW.

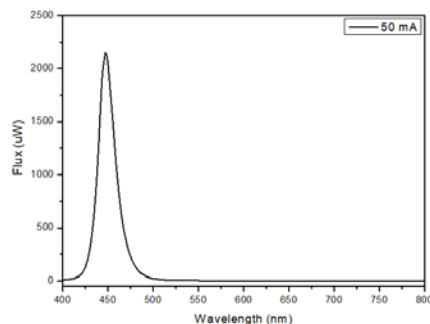


Figure 1. EL spectrum of bare blue LED die.

Packaging the phosphor converted white LEDs with using hemisphere of yellow phosphor dome.

Structure of phosphor converted white LEDs with using hemisphere of yellow phosphor dome

Figure 2 was the schematic illustration of the structure of pc-WLEDs using hemisphere of yellow phosphor dome. In this structure of packaging, Blue die was bonded on the sub-mount of aluminum nitride (AlN). The interconnection between electrode on Blue die and integrated circuit in the AlN was conducted by the gold wire through the wire bonding process and using wire bonding machine. The hemisphere of yellow phosphor dome was obtained from the mixing of silicone gel and yellow phosphor YAG. Finally, after a curing process at a temperature of 130 degrees Celsius for 10 minutes by using the molding with hemisphere shape, we will obtain the sample of phosphor-converted white LEDs having the packaging structure of hemisphere of yellow phosphor dome. The radius of dome is 2.5 mm.

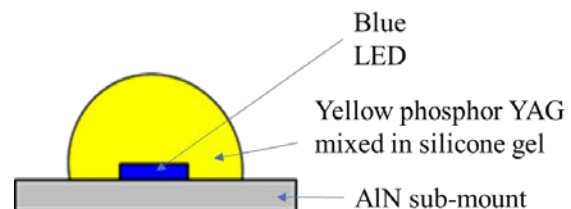


Figure 2. Schematic illustration of the structure of pc-WLEDs using hemisphere of yellow phosphor dome

EL spectrum of the sample of pc-WLEDs with hemisphere dome of yellow phosphor.

Figure 3 showed the EL spectrum of the sample of pc-WLEDs with hemisphere dome of yellow phosphor. White light spectrum include two main region of blue band and broad yellow band. The way of generating white light by a combination between blue light and yellow light is a simple, effective and low cost way in field of Solid State Lighting.

In this study, the used concentration of phosphor was 7.5%, the property of the pc-WLEDs with hemisphere dome of yellow phosphor that were investigated include of correlated color temperature (CCT), packaging efficiency and color rendering index (CRI). Under given current of 350 mA, the value of CCT value was 5508K. This value of CCT indicated the white light is belong the type of cool white light. The color coordinate (x,y) in the chromaticity coordinate was (0.3325,0.3882). The location of the pc-WLEDs in the chromaticity was shown in the Figure 3.

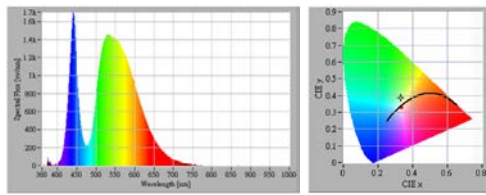


Figure 3. The EL spectrum of the sample of pc-WLEDs with hemisphere dome of yellow phosphor (left) and its location in chromatic diagram (right).

To evaluate the performance of packaging process in the generation of white light, the packaging was calculated. Packaging efficiency is the ratio between the power of generated white light to the power of bare blue light that excited to the yellow phosphor. Due to the extraction efficiency in the hemisphere packaging structure, if we want to have a correct value of packaging efficiency then a corrected factor need to be used. Under driven current 350 mA, the power of generated white light and power of blue light emitted from bare blue LED die were 0.232 W and 0.3 W, respectively. Applied the correct factor of 1.288 in calculation of packaging efficiency [4], we obtained the corrected value of packaging efficiency was 60 %. Compare to other reported result of other study used different type of packaging structure, this value of packaging efficiency is high. It indicated the high efficiency of packaging technology that used in this study.

The ability of color rendering of pc-WLEDs evaluated through the value of color rendering index (CRI). Under the driven current of 350 mA, the general colorendering index was 63. This value is lower as compare to to the CRI of white light source based on the trichromatic (CRI>80) and tetrachromatic (CRI>90) approaches [1]. Figure 4 showed the value of each special color rendering index from R1 to R8. The color of R1, R2, R3, R4, R5, R6, R7, and R8 is light grayish red, dark grayish yellow, strong yellow-green, moderate yellowish green, light bluish green, light blue, light violet and light reddish purple. The corresponding value of special value are 57.7, 69.2, 82.3, 66.2, 59.2, 55.4, 71.8 and 45.6. These values showed the light source is very good in redering color of sample R2, R3,R4 and R7.

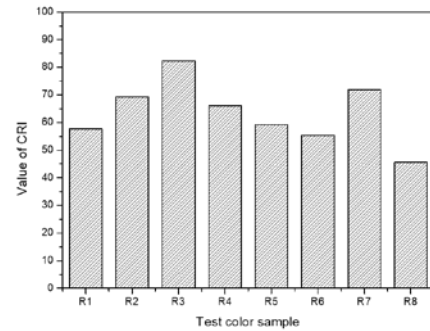


Figure 4. The value of each special color rendering index from R1 to R8

Effect of driven current on the CCT and general CRI of pcWLEDs.

To have a more comprehensive evaluation of the quality of the packaging technology in our work. We conducted the investigation with changing the injected current, then evaluate the property of pc-WLEDs with hemisphere dome of yellow phosphor in the aspect of CCT, CRI, and generated temperature. Different values of driving current used in the investigation are 50, 100, 150, 200, 250, 300 and 350 mA. After the handling data, the effect of driving current on the CCT, CRI, and generated temperature will be evaluated.

Figure 5 showed the CCT values at different injected currents. There was a variation of CCT with changing of injected current. Changing of CCT may come from the effect injected current on the power of generated blue light. Different power of blue light excited to the phosphor can leads to the different power of yellow light be generated. The changing of the ratio of blue light power and the generated yellow light will cause the variation of CCT as the injected current changed. However, as the inject current change from 50 mA to 350 mA, the maximum deviation of CCT is 154 K. This CCT deviation is not significant.

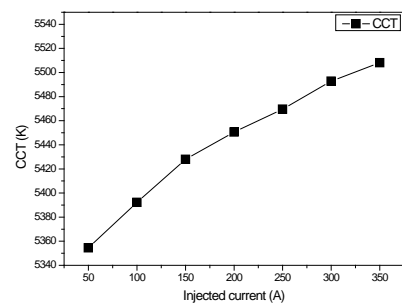


Figure 5. The CCT values at different injected currents.

While the injected current showed a light variation of CCT, the general CRI was not to be affected as changing the injected current. This was shown in Figure 6, at different injected current, the value of general CRI was still had the same value of 63.

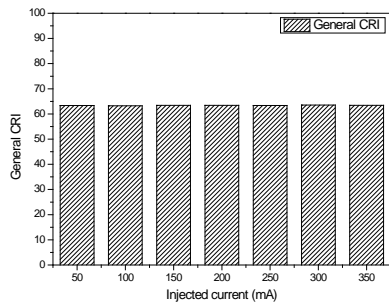


Figure 6. The CRI values at different injected currents.

The thermal property of pcWLED was investigated. The thermocouple is put at the backside of the sub-mount where was the path of the generated heat. Figure 7 showed the generated temperature is a function of injected current. The higher the value of the injected current was, the higher the value of the generated temperature. Since the injected current showed a big impact on the temperature of pcWLEDs, it is necessary to apply a suitable way to dissipate the generated heat. This will help the pcWLED to avoid some risks such as CCT drift, the problem of blue light leakage or degradation of yellow phosphor in luminescence efficiency.

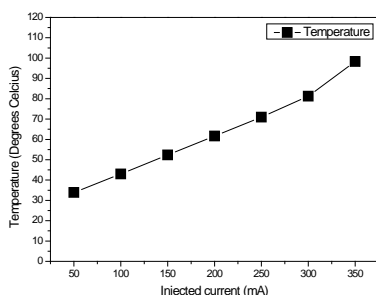


Figure 7. The generated temperature at different injected current.

CONCLUSION

Based on the dichromatic method of creating white light, we have used the yellow phosphor material YAG in the creation of white light through combination with blue light emitted from the blue die. A packaging structure of the

hemisphere yellow phosphor dome was conducted in the packaging of pcWLEDs. A cool white light with CCT 5500K was fabricated that showed a high packaging efficiency of 60 % and an acceptable value of general CRI of 63. Besides, the investigation of the optical property includes CCT, packaging efficiency and CRI, the effect of different injected current on the CCT, CRI and temperature were also studied. According to that, to the inject current change from 50 mA to 350 mA, the maximum deviation of CCT is 154 K. Although, CCT value showed a small variation, the general CRI was not be affected as changing injected current and the value of general CRI still remain value of 63. However, the generated temperature is a function of the injected current. Thus, it is necessary to keep the injected current constant in operating process to maintain high performance for pcWLEDs.

Acknowledgement

This research is funded by Vietnam National University HoChiMinh City (VNU-HCM) under grant number VL2019-18-01.

References

- [1] E.Fred Schubert, *Light-Emitting Diodes*, Cambridge University Press. New York, 2006.
- [2] Zukauskas A, Shur M, Gaska R, *Introduction to Solid State Lighting*, New York: John Wiley & Sons (2002).
- [3] Schubert EF, Kim JK, *Solid-state light sources getting smart*, Science, **308** (5726), 1274–1278 (2005).
- [4] C-C Sun, et al, *Packaging efficiency in phosphor-converted white LEDs and its impact to the limit of luminous efficacy*, Journal of Solid State Lighting **1:19** (2014).

REDUCING THE INFLUENCE OF BACKWARD SCATTERING IN WHITE LEDS PACKAGING WITH USING REMOTE YELLOW PHOSPHOR STRUCTURE

Quang-Khoi Nguyen^{1,2}, Shih-Kang Lin¹, Mai Van Tan², Vu Thi Ngoc Nuong², Vo Tran Khoa Nguyen², Trinh Thi Ngoc Huyen², Ton Nu Quynh Trang², Nguyen Van Hieu², Lam Quang Vinh², Vu Thi Hanh Thu², and Ching-Cherng Sun¹

¹Department of Optics and Photonics, National Central University, Taoyuan City, Taiwan;

²Faculty of Physics and Physics Engineering, VNUHCM-University of Science, Hochiminh City, Vietnam.

E-mail: quangkhoigialai@gmail.com, ccsun@dop.ncu.edu.tw

ABSTRACT

The combination of a blue LED die and the yellow phosphor is a useful method to generate white light. In white light packaging technology, the backward scattering is one of the main factors that affect the optical property of phosphor-converted white light-emitting diodes (pc-WLEDs). This problem can be solved by using a low weight concentration of yellow phosphor in the packaging process. With this motivation, we conducted the experiment to package the pc-WLEDs by using yellow phosphor weight concentration of 7.5% to investigate the properties of pc-WLEDs. These remote yellow phosphor structures corresponding to the thickness of yellow phosphor plate of 0.6 mm, 1.2 mm 1.5 mm and 2.0 mm were fabricated. The optical properties of pc-WLEDs including correlated color temperature (CCT), packaging efficiency and color rendering index (CRI) were investigated. The correlated color temperature (CCT) is 7449 K, 6020 K, 4883 K, and 4468 K. The packaging efficiency is 63.7, 63.9, 55.7 and 52.8, respectively. The values of CRI are 70.5, 65.9, 57.7 and 50, respectively. These results showed that at the low concentration of 7.5%, the value of CCT can be modified by changing the thickness of the phosphor plate. The high value of packaging efficiency indicated that the energy loss was reduced. This is meaningful in term of energy saving in white LEDs packaging technology. We can reduce the effect of backward scattering and enhance the packaging efficiency.

Keywords: pc-WLEDs, high packaging efficiency, remote yellow phosphor structure and backward scattering.

INTRODUCTION

Solid-state lighting (SSL) has been gradually replacing the incandescent light bulbs owing to its advantages, including high energy efficiency, fast response, acceptable color rendering, long-lifetime and low cost [1-3]. A simple and useful method to generate white light is the combination of a blue LED die and yellow phosphor.

However, a problem that can't to avoid in process for making white light is backwards scattering when blue light emitted from LED die hit to the phosphor. This problem becomes serious when using a high weight concentration of phosphor. Consequence of this is reducing the power of output white light. In another way, an amount of optical power is loosed in case of high backward scattering happened. Therefore, reducing the optical loss is a requirement that

need to be solved in pc-WLEDs packaging technology. This will contribute to a higher power of output white light. Based on the scattering behavior of yellow phosphor, the backward scattering can be reduced by using a low weight concentration of yellow phosphor. In this paper we proposed an idea of using low weight concentration of yellow phosphor of 7.5% to reduce the effect of the backward scattering problem in pc-WLEDs packaging process. Besides that, a simple and effective technique was used to make the pc-WLEDs. The optical properties of pc-WLEDs were investigated including CCT, packaging efficiency and CRI. Results of packaging efficiency showed that the backward scattering can be reduced with using low weight concentration of phosphor while still show a high packaging efficiency.

EXPERIMENT

Packaging structure of pc-WLEDs include three main components: a blue chip was bonded on a MCPCB (metal core printed circuit board), a reflector cup and phosphor plate that made from mixture of silicone gel A, B and yellow phosphor by molding method. LED chip is CREE EZ1000 with emission peak at 449 nm. The LED dies were bonded on sub-mount by die bonding machine, then attached on the MCPCB. The inject current was 50 mA to avoid thermal effect. Phosphor plates made from a mixture of silicone gel A, B and yellow phosphor material (YAG phosphor CN-YY550L). The weight concentration of yellow phosphor that used is 7.5%. For making phosphor plate, this mixture will be cured in the molding which has different thickness. Finally, after curing process at temperature of 140 degrees of Celsius, plates were taken out of the molding. In our study, the thickness of different phosphor plate includes 0.6 mm, 1.0 mm, 1.2 mm, 1.5 mm and 2.0 mm were made. The components of LED die on MCPCB, reflector cup and yellow phosphor plate were connected to obtain a complete packaging structure of pc-WLEDs. The cross-section of packaging structure of pc-WLEDs is illustrated in Figure 1a.

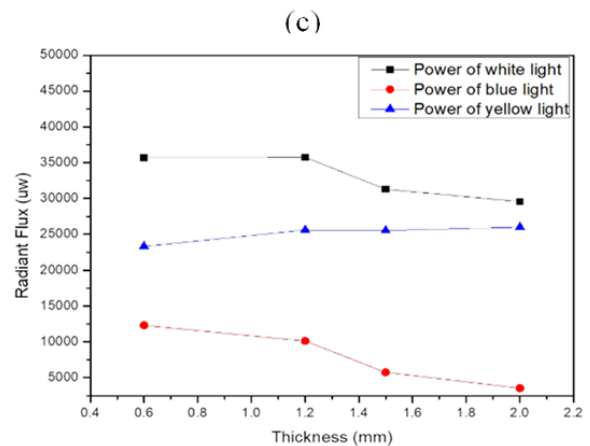
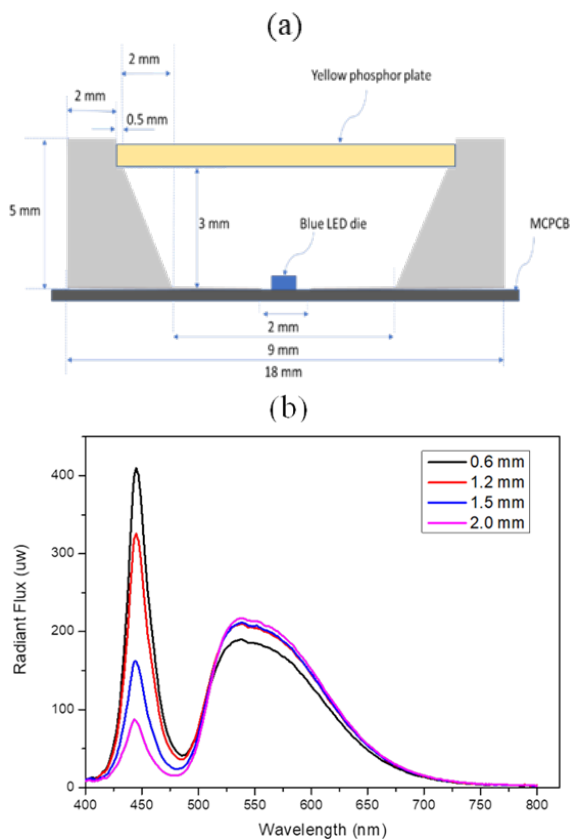


Figure 1. a) The cross-section of packaging structure of pc-WLEDs, b) EL spectra of samples and c) Corresponded emitted power of samples.

RESULTS AND DISCUSSION

Figure 1b and 1c showed the emission spectrum of pc-WLEDs and emitted power of samples that used different thickness of phosphor plates 0.6 mm, 1.2 mm, 1.5 mm and 2.0 mm, respectively. There are two clear bands in the emission spectra of pc-WLEDs including blue band and yellow band. The blue band is narrow with the wavelength range from 400 nm to 500 nm. While the yellow band is broad with the wavelength range from 500 nm to 800 nm. The shape of spectra shows that according the thicker phosphor plate, the intensity of blue light is decreased while the intensity of yellow band was increased. This showed clearly in the changing of area of blue band as well as the area of yellow band. Figure 2a showed the correlated color temperature of pc-WLEDs with phosphor plate at different thickness. Corresponding to the thickness 0.6 mm, 1.2 mm, 1.5 mm and 2.0 mm, the corresponded value of CCT are 7449 K, 6020 K, 4883 K and 4468 K, respectively. The value of CCT depends on the ratio of blue light power to yellow light power. The larger value of this ratio, the higher value of CCT. Consider the pc-WLEDs where the phosphor thickness from 0.6 mm to 2.0 mm. The thicker phosphor plate, power of blue light decreased while the power of yellow light is increased. Therefore, the ratio of blue light power to yellow light power is decreased. This leads the value of CCT be decreased. The changing of CCT value versus the thickness of phosphor plates showed that at a fixed weight concentration 7.5% of yellow phosphor, the value of CCT can be modified by changing the thickness of phosphor plate.

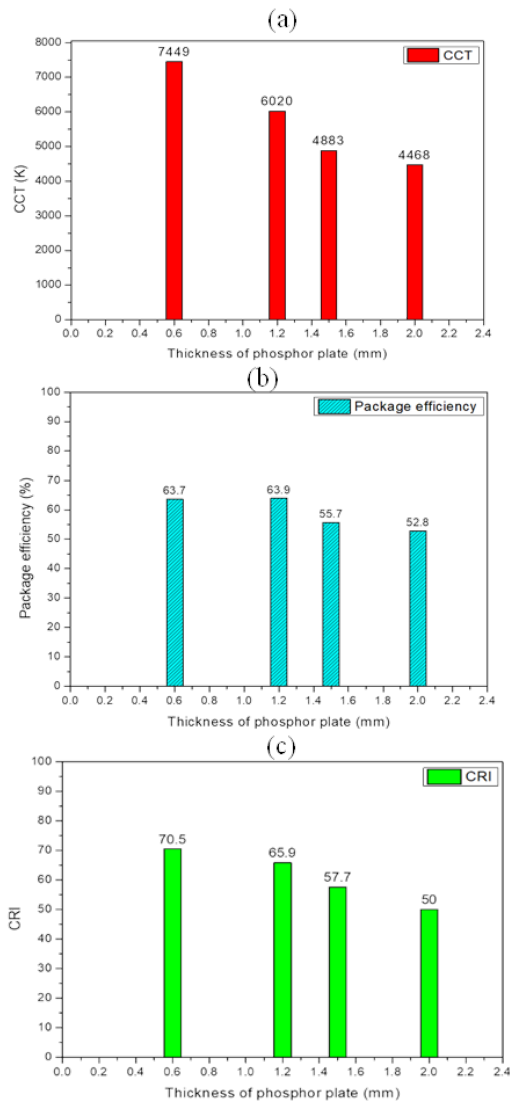


Figure 2. The results of a) correlated color temperature, b) Packaging efficiency and c) color rendering index.

Packaging efficiency is defined by the ratio of power of white light to the power of bare blue light. The packaging efficiency has important meaning such as showing the how good of packaging technology in control the optical loss, saving the energy when loss optical power be transferred to the useful light. Therefore, packaging efficiency is an important factor to evaluate the quality of pc-WLEDs packaging technology. Figure 2b showed the packaging efficiency of sample corresponding to the phosphor thickness 0.6 mm, 1.0 mm, 1.5 mm and 2.0 mm, respectively. Their packaging efficiency are 63.7 % (at CCT of 7449K), 63.9% (at CCT of 6020K), 55.7 % (at CCT of 4883 K) and 52.8 % (at CCT of 4468 K). It is noticeable the sample 1.2 mm which the package efficiency is 63.9% (at CCT of 6020K). Usually, when

using more yellow phosphor to get a lower value of CCT, it is often to face the problem of backward scattering that makes the packaging efficiency lower. However, the value of packaging efficiency of 63.9% is still higher the above value of 63% (at CCT 6500K). Therefore, the value of packaging efficiency in our study can considered as high values. Using this technique of packaging, the package can get high value. Figure 2c showed the average color rendering index of pc-WLEDs using phosphor plate 0.6 mm, 1.2 mm, 1.5 mm and 2.0 mm, respectively. The corresponded average CRI values are 70.5, 65.9, 57.7 and 50, respectively. These values are belonging to two main group of good and poor CRI. The CRI values of 70.5, and 65.9 are evaluated well while CRI values of 57.7 and 50 are poor. Corresponding to the decreasing of CCT, the value of average CRI is decreased correspondingly. The CRI is still needed to study more to get a higher value such as 80, 90 or 95 for application that high CRI is required.

CONCLUSION

The effect of backward scattering in the packaging process was reduced by using a weight concentration of yellow phosphor of 7.5%. We can reduce the concentration of phosphor while still reach high packaging efficiency of 63.9 at CCT of 6020 K. This technology of packaging is simple when it doesn't need to use a complex technique to dispense the phosphor material. The achieved results showed that this technique can be considered a good solution for pc-WLEDs package technology in term of simple fabrication, low cost and energy efficiency.

Acknowledgement

This research is funded by Vietnam National University HoChiMinh City (VNU-HCM) under grant number VL2019-18-01.

References

- [1] E.Fred Schubert, *Light-Emitting Diodes*, Cambridge University Press., New York, 2006.
- [2] Zukauskas A, Shur M, Gaska R, *Introduction to Solid State Lighting*, New York: John Wiley & Sons (2002).
- [3] Schubert EF, Kim JK, *Solid-state light sources getting smart*, Science, **308** (5726), 1274–1278 (2005).

EFFECTS OF SILVER NANOPARTICLES TO THE GROWTH OF WHITE LEG SHRIMP (*LITOPENAEUS VANNAMEI*)

Thanh Chi Nguyen¹, Thinh Huu Nguyen², Phuong Hong Lam¹, Mai Thi Le¹, Dung My Thi Dang¹, Tin Chanh Duc Doan¹, Chien Mau Dang¹

¹Institute for Nanotechnology (INT), Vietnam National University-Ho Chi Minh City (VNUHCM) Community 6, Linh Trung Ward, Thu Duc District, Ho Chi Minh City, Vietnam.

²Faculty of Fisheries, Nong Lam University, HCM City, Vietnam (NLUHCM).

E-mail: ddctin@vnuhcm.edu.vn

ABSTRACT

One of the new solutions to limit disease that is to use silver nanoparticles (AgNPs) as a biocide in combination with conventional culture procedures. The purpose is to minimize the density of *Vibrio* spp. which is causing disease in water and preventing epidemic outbreaks. Although it has been used for a long time in the aquaculture field, research on the effect of AgNPs on aquatic animal health is still limited, especially in white leg shrimp. Therefore, this study was conducted to assess the impact of AgNPs on shrimp health at different concentrations. In the treatment that using AgNPs with a concentration of 0.05 ppm, the growth indicators of shrimp are the best compared to the remaining treatments. In particular, the specific growth rate (length and weigh) are $SGR_L = 3.13 \pm 0.02$ (% / day), $SGR_W = 8.01 \pm 0.71$ (% / day). In particular, the addition of AgNPs at the concentration of 0.05 ppm has brought effective control of *Vibrio* spp. without affecting the aerobic bacteria population in the water environment.

Keywords: AgNPs, *Vibrio* spp., *Litopenaeus vannamei*

INTRODUCTION

Some studies had been demonstrated the antibacterial effect of AgNPs against common pathogenic bacteria infecting species of aquaculture interest. For example, the antibacterial effect of AgNPs that synthesized using *Prosopis chilensis* extract has been tested in *Penaeus monodon* infected with *Vibrio cholerae*, *V. harveyi*, and *V. parahaemolyticus* (Kandasamy et al., 2013) [1]. Moreover, the effect of AgNPs synthesized using green tea extract was tested in *Fenneropenaeus indicus* infected with *V. harveyi* (Vaseeharan et al., 2010) [2]. Recently, Juárez-Moreno et al. (2017) demonstrated the antiviral properties of AgNPs against white spot syndrome virus infecting juvenile *Litopenaeus vannamei* [3]. Therefore, the use of nanoparticles against pathogens is a promising field in aquaculture.

The mechanisms on the biocidal action of AgNPs are mainly related to the sulfhydryl groups of enzymes and proteins like glucose-6-phosphate dehydrogenase and glutathione reductase, by interfering with the protein normal functions. AgNPs also inhibits DNA replication,

and in bacteria it induces oxidative stress in the cell wall, where important cellular functions occur, affecting the maintenance of the internal ion balance. In this way, bacteria exposed to AgNPs showed growth inhibition, massive loss of potassium, and suppresses the chemical transportation from the cell wall (Hwang et al., 2007; Luoma, 2008) [4]. Although the effective antimicrobial activity of AgNPs has been proven, there have been very few experiments conducted on aquatic organisms. Thus, the objective of this study is determining the antibacterial effects of AgNPs to the growth in the Pacific white shrimp, *Litopenaeus vannamei*.

EXPERIMENT

2.1. Material

Post larvae (Litopenaeus vannamei)

White leg shrimp (*Litopenaeus vannamei*) is purchased from Grobest Ben Tre Company. Shrimp microbiological analysis experiments are conducted at Institute for Nanotechnology (INT). In some 60 liters volume composite tanks, the water that is used in this experiment is natural seawater filtered through a membrane

follow by chlorine treatment. Shrimp are raised in order to meet the testing requirements such as healthy, lively, fresh color and uniform size.

AgNPs Solution

AgNPs solution with high antibacterial properties is produced by INT – VNU with the average particles size is of 2-5 nm, high purity, high activity, good stability (in 6 months) and high repeatability. All testing solutions are used in this experiment are made from the original 200 ppm Ag NPs solution.

2.2 Experimental design

The experiment was conducted for 45 days with AgNPs to assess the effect of AgNPs on shrimp health.

Table 1. Concentration of AgNPs solution used in the experimental treatments

Experimental	Concentration of AgNPs
Exp I	0,05 ppm
Exp II	0,1 ppm
Exp III	0,2 ppm
Control	0 ppm

The seedlings are firstly stocked in a 500 liters tank to be familiar with the experimental conditions for 5 days. They are then divided into some other small tanks to do the test. The post shrimp are prepared in 14 small tanks (65 liters per tank), which contains 5 liters of water that have salinity 15 ‰ salinity. The stocking density is 30 shrimps / tank. Post shrimps have an average weight of 0.03 ± 0.001 mg and an average length of 1.10 ± 0.02 mm. Every day, shrimp were fed 3 times (at 7h, 12h, and 17h) with industrial feed, which is the size and amount of feed changed to suit shrimp growth during the experiment. The replacement water source was used to clean water supplemented with AgNPs in the correct concentration with the treatments that were prepared at the beginning of the experiment. After 45th day, all the shrimp were weighed to record the final weight, which were compared to the initial weight that have taken on the first day. The survival rates of the shrimp were also estimated by enumerating the individuals in each aquarium. The weight gain in grams (WG), specific growth rate (SGR), feed conversion ratio (FCR) were calculated as follows:

Daily weight gain (DWG) = $(W2 - W1) / (T)$
 Specific growth rate

$$(SGR) = ((\ln W2 - \ln W1)/T).100$$

Where

W1 = initial weight,

W2 = final weight

T = the number of days in the feeding period.

Feed conversion ratio (FCR) = feed intake (kg)/weight gain (kg)

Survival rate (%) = (final numbers / initial numbers).100

Total Vibrio monitoring

Presumptive analyses of *Vibrio* spp. were performed at the beginning and end of the trial, by water sampling. The preparation of sample dilutions and bacteriological assays were performed by using the method described by APHA (2005). Water samples were serially diluted (10⁻¹ to 10⁻⁵) in sterile saline solution (2.5% NaCl). Aliquots of 0.1 mL from dilutions were applied using the spread-plate method on thiosulphate–citrate–bile sucrose (TCBS) agar and incubated at 30°C for 24 h. Colony forming units (CFU) were counted on plates containing between 25 and 250 colonies and recorded as CFU/mL.

2.3. Method of data processing

The statistical analysis of empirical data was performed using Excel 7.0 software and Minitab 16 software to process the data collected during the study.

RESULTS AND DISCUSSION

3.1. Result of *Vibrio* spp. in the treatments

In the beginning, all treatments were free of *Vibrio* spp. because the water has been thoroughly disinfected with Chlorine However, in the 4th week, *Vibrio* spp. in the treatments showed signs of rapid increase, due to the accumulation of feces, leftovers in water and algae growth. At week 5, the density of *Vibrio* spp. in the control treatment started to increase sharply ($1.01.10^3$ CFU/mL) and exceeded the safe threshold for shrimps. In the two treatments A1 (0.05 ppm) and A2 (0.1 ppm) began to increase with a density of $0.18.10^3$ CFU/ml; $0.13.10^3$ CFU/mL and significant difference compared to the control treatment ($p < 0.05$). Especially, in treatment A3 (0.2 ppm), there was remarkable effectiveness in controlling *Vibrio* spp., particularly at the end of the experiment; the bacterial density was only 0.09×10^3 CFU / mL.

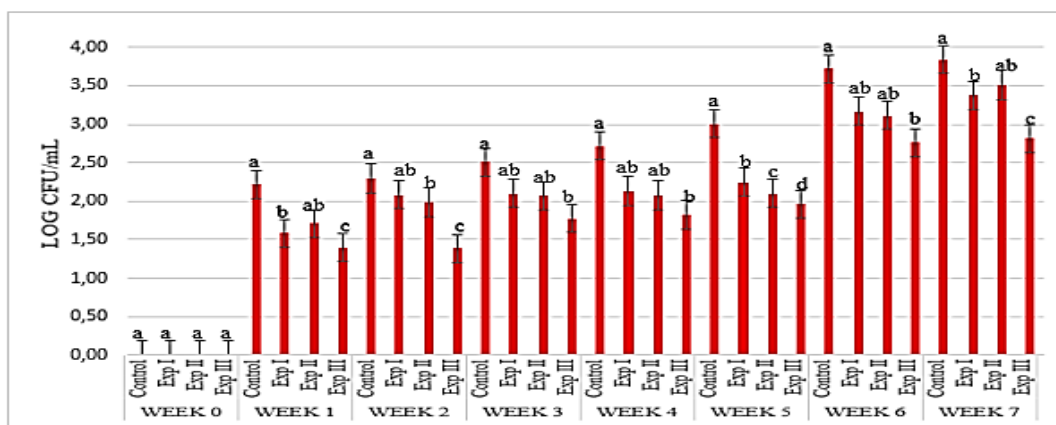


Figure 1. Changes of *Vibrio* spp. in pond water. Values (mean ± SD) with different letters are statistically significant from each other (*t*-test; *P*<0.05)

The density of *Vibrio* spp. maintenance of less than 10³ CFU / mL and a percentage of blue colonies (typical colonies of *V. parahaemolyticus* and *V. vulnificus* on TCBS selective medium) less than 100 CFU/ml are considered to be within the safe range [5]. Besides, AgNPs products of the INT are recognized by the Pasteur Institute in Ho Chi Minh City to kill bacteria on fruits and shrimp disease bacteria. Testing results of AgNPs also confirmed that AgNPs are capable of killing cyanobacteria and types of bacteria: *Escherichia coli*, *Vibrio anguillarum*, *Vibrio harveyi*, *V.*

Fluviialis, *V. Parahaemolyticus* [6]. Thus, when AgNPs is added to water as a bactericide, it can effectively control the density of *Vibrio* spp. In particular, at the concentration of 0.05 ppm, AgNPs have a control effect *Vibrio* spp. In water at the early stage of stocking, it is effective to reduce a part of pathogenic bacteria when these bacteria increase.

3.2 Results of evaluating the growth of shrimps in all treatments after 45 days.

Table 2. Growth rate of shrimp in experimental treatments.

Experimental duration	Experimental			
	Control	Exp I (0.05 ppm)	Exp II (0.1 ppm)	Exp III (0.2 ppm)
Survival (%)	86,7±3,33 ^{ab}	87,8±1,92 ^a	87,8±1,92 ^a	83,3±3,33 ^b
Final weight(g)	0,74 ± 0,10 ^b	1,14 ± 0,39 ^a	0,86 ± 0,08 ^b	0,77 ± 0,08 ^b
Final length(cm)	3,83 ± 0,06 ^c	4,50 ± 0,03 ^a	4,36 ± 0,06 ^b	4,25 ± 0,15 ^{bc}
DLG (mm/day)	0,06 ± 0,00 ^c	0,08±0,00 ^a	0,07±0,00 ^b	0,07±0,00 ^b
SGR _L (%/day)	2,77 ± 0,04 ^c	3,13±0,02 ^a	3,06±0,03 ^b	3,00±0,08 ^b
Weight gain (g/ day)	0,02±0,01 ^a	0,02±0,00 ^a	0,02±0,00 ^a	0,02±0,00 ^a
SGR _w (%/day)	7,12±0,30 ^c	8,01±0,71 ^a	7,45±0,21 ^b	7,19±0,24 ^b
FCR	1,11±0,18 ^c	1,09±0,30 ^c	1,25±0,03 ^b	1,56±0,12 ^a

The widespread applications of different AgNPs are present in aquaculture. Recently, several research groups focused their efforts on the knowledge of toxicological effects of metal and metal oxides nanoparticles in marine organisms. Despite this growth in the field and with the remarkable antiviral and/or immunostimulant activity observed for AgNPs in other organisms. After 45 days of experiment, body weight was about 0.74 - 1.14 g / head and body length was about 3.83 - 4.5 cm / head. The value of SGRL and SRGW of shrimp were

respectively 2.77 - 3.13% / day and 7.12 - 8.01% / day. . This confirms that the results of this study are completely consistent. In addition, the growth targets of the control treatments were statistically different from the treatments supplemented with AgNPs. In particular, in the treatment using AgNPs at the concentration of 0.05 ppm, there was a clear difference compared to the remaining treatments, specifically, the average body weight and length of shrimp were 1.14 g / head and 4.50 cm / head. In particular, the growth rate of shrimp weight in the

treatment using AgNPs with 0.05 ppm had SGRL and SGRW values of 3.13% / day and 8.01% / day, the highest among all the experiments. In addition, in treatments using AgNPs with concentrations of 0.1 ppm and 0.2 ppm, there was no significant difference compared to control treatments ($p < 0.05$).

The FCR value of shrimp after 45 days of experiment was about 1.09 -1.56 of which, in the treatment using AgNPs at 0.05 ppm had the lowest FCR, significant difference compared to the statistics. With the remaining treatments and control treatments ($p < 0.05$). AgNPs treatment in WSSV-infected *Penaeus vannamei* had an immunostimulant effect, using non-toxic concentrations, by the induction of shrimp innate immune response. Our results have shown that AgNPs promotes the expression increase of LGBP, a key component in the innate immune system of arthropods [7]. We suggest that these occur through the recognition of metallic silver of AgNPs or by their interaction with the WSSV viral envelope to trigger the PAMPs recognition proteins activation. Both suggested processes, acting independently or concomitantly, decrease mortality of infected shrimps.

CONCLUSION

In experiments, the results showed that the addition of AgNPs at appropriate concentration has the effect of killing *Vibrio* spp. without affecting the microbial ecosystem in the culture water. In the treatment using AgNPs with a concentration of 0.05 ppm, the growth indicators of shrimp were superior to the remaining treatments. In particular, the relative growth rate in terms of length and volume are $SGRL = 3.13 \pm 0.02$ (% / day), $SGRW = 8.01 \pm 0.71$ (% / day) and FCR reach 1.09 ± 0.30 . Based on the research results, we recommend using AgNPs at a concentration of 0.05 ppm for 45 days to control *Vibrio* spp. aims to limit the disease.

Acknowledgement

The authors highly appreciate the financial support of the Institute for Nanotechnology (INT), Vietnam National University - Ho Chi Minh City (VNUHCM). This research is funded by the Mekong Delta program office under project No: 02/2017/HĐ-KHCN-TNB.ĐT/14-19/C04.

References

- [1] Kandasamy, K., N.M. Alikunhi, G. Manickaswami, A. Nabikhan & G. Ayyavu. 2013. *Synthesis of silver nanoparticles by coastal plant Prosopis chilensis (L.) and their efficacy in controlling vibriosis in shrimp Penaeus monodon*. Appl. Nanosci., **3**: 65-73.
- [2] Vaseeharan, B., P. Ramasamy & J.C. Chen. 2010. *Antibacterial activity of silver nanoparticles (AgNps) synthesized by tea leaf extracts against pathogenic Vibrio harveyi and its protective efficacy on juvenile Fenneropenaeus indicus*. Lett. Appl. Microbiol., **50**: 352-356.
- [3] Juarez-Moreno K., Mejía-Ruiz C. H., Díaz F., Reyna-Verdugo H., Re A. D., Vazquez-Felix E. F., Bogdanchikova N., 2017. *Effect of silver nanoparticles on the metabolic rate, hematological response, and survival of juvenile white shrimp Litopenaeus vannamei*. Chemosphere, **169**, 716 – 724.
- [4] Hwang J., Yoon K. Y., Byeon J. H., Park and J. H., (2007). *Susceptibility constants of Escherichia coli and Bacillus subtilis to silver and copper nanoparticles*. Sc. Total Environ. **373**, 572 – 575.
- [5] Tinh Huu Nguyen, Truc Thi Thanh Luu, 2014. *Practicing disease diagnosis on aquatic animals*, Faculty of Fisheries, Nong Lam University, HCM City, Vietnam.
- [6] Dinh Sang, April 15, 2015. *Application of Nano Silver in treating shrimp ponds*. <URL:http://nanobacdietkhuan.com/2015/04/ung-dung-nano-bac-trong-xu-ly-aonuoitom.html>.
- [7] Ochoa-Mez A. R., Álvarez-Sánchez A. R., Romo-Quiñonez C. R., Barraza A., Magallón-Barajas F. J., Chávez-Sánchez A., Mejía-Ruiz C. H., 2018. *Silver nanoparticles enhance survival of white spot syndrome virus infected Penaeus vannamei shrimps by activation of its immunological system*. Fish & Shellfish Immunology.

EFFICIENT ANTITUMOR EFFECT OF SORAFENIB-LOADED SILICA CONTAINING REDOX NANOPARTICLE

Tran Ngoc Han¹, Nguyen Trinh Quynh Nhu¹, Vong Binh Long^{2*}, Nagasaki Yukio³

¹Faculty of Biology and Biotechnology, University of Science, Vietnam National University HCM, Vietnam

²School of Biomedical Engineering, International University, Vietnam National University HCM, Vietnam

³Graduate School of Pure and Applied Sciences, University of Tsukuba, Japan

*Corresponding email: yblong@hcmiu.edu.vn

ABSTRACT

Currently, cancer is a leading cause of death worldwide. Although chemotherapy is a common method to kill cancer cells, many side effects exist due to non-specific distribution of antitumor drugs. For example, sorafenib is an oral multikinase inhibitor that can suppress tumor cell proliferation, angiogenesis and induce cancer cell apoptosis; however, sorafenib is a hydrophobic antitumor drug with low bioavailability and severe side effects which greatly restricted its clinical application. To overcome these issues, in this study, we developed a silica containing redox nanoparticle (siRNP) to improve bioavailability of sorafenib and suppress its unwanted side effect. siRNP was designed from PEG-siPMNT, an amphiphilic block copolymer possessing high drug absorption characteristics of silica moieties in addition to antioxidant properties of nitroxide radical to scavenge reactive oxygen species. Our result showed that siRNP was successfully prepared with 50-60 nm in diameter and siRNP significantly improved the solubility of sorafenib after encapsulation. Using MTT assay, we confirmed that sorafenib-loaded siRNP significantly improved the antiproliferative effect of sorafenib against colon cancer cell and liver cancer cell lines. Interestingly, sorafenib-loaded siRNP significantly decreased toxicity of free sorafenib in normal endothelial cell. In tumor bearing mice model, we also confirmed that the anticancer activity of sorafenib-loaded siRNP was remarkably improved as compared to free sorafenib. In summary, the siRNP exhibits a promising potential as hydrophobic drug nano-carrier for cancer treatment.

Keywords: Cancer, Redox Nanoparticle, Reactive Oxygen Species, Sorafenib, Adverse Effect

INTRODUCTION

At present, cancer is one of the leading causes of death. Although chemotherapy is a common method to kill cancer cells, many side effects exist due to non-specific distribution of antitumor drugs, causing serious damages on healthy tissues and organs. Since most of conventional anticancer drugs are hydrophobic, it is not easy to solubilize in aqueous media, which reduces their therapeutic efficiency. For example, sorafenib is an oral multikinase inhibitor that can suppress tumor cell proliferation, angiogenesis and induce cancer cell apoptosis; however, sorafenib is a hydrophobic antitumor drug with low bioavailability and severe side effects which greatly restricted its clinical application [4]. On the other hand, oxidative stress is defined as an imbalance between production of reactive oxygen species (ROS) and antioxidant defenses and overproduced ROS cause the damage of important biomolecules and cells lead to the

increase tumor progression and metastasis [3]. Therefore, it is important to suppress overproduced ROS in tumor environment. It has been reported that combination treatments of antitumor drug and antioxidant were reported to improve antitumor efficiency [3,5]. However, low molecular weight antioxidants are not always effective to scavenge ROS at the tumor environment since they spread entire body and rapidly metabolizes after administration. To improve bioavailability of sorafenib and suppress the ROS-induced toxicity, we have been developing antioxidant nanoparticles (siRNP) to solubilize the sorafenib by encapsulation into siRNP (sorafenib@siRNP). siRN was prepared by self-assembling PEG-siPMNT, an amphiphilic block copolymer possessing high drug absorption characteristics of silica moieties in addition to antioxidant properties of nitroxide radical to scavenge ROS [6]. In this study, we investigated the nanoparticle properties before and after loading sorafenib as well as the anticancer

activity of sorafenib@siRNP *in vitro* and *in vivo* as compared to free sorafenib. Our results showed that sorafenib@siRNP exhibited significantly higher therapeutic treatment against cancer cell lines and suppressed tumor growth in tumor bearing mice without any noticeable toxicity.

EXPERIMENTAL

Materials

siRNP was prepared by dialysis of amphiphilic block copolymer PEG-siPMNT, which was synthesized as previously reported [2]. Sorafenib (LC Laboratorises), DMSO (dimethyl sulfoxide) (Xilong Chemical Industry Incorporated Co. Ltd), DPPH (2,2-diphenyl picrylhydrazyl), Dimethylformamide (DMF, FUJIFILM-Wako – Japan), 4-amino-2,2,6,6-tetramethylpiperidine-1-oxyl (amino-TEMPO, Tokyo Chemical Industry, Tokyo, Japan), 2,2-Diphenyl-1-(2,4,6 trinitrophenyl) hydrazyl (DPPH) Sigma-Aldrich (St. Louis, MO, USA), 2,5-diphenyl-2H-tetrazolium bromide (MTT) Sigma-Aldrich (St. Louis, MO, USA).

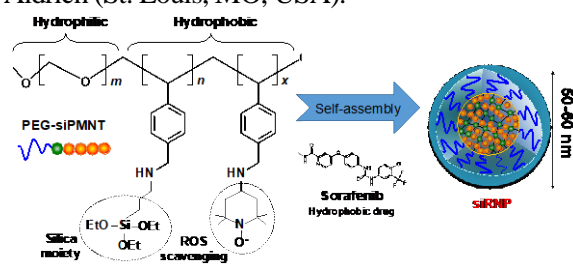


Figure 1. Molecular structure of PEG-siPMNT and schematic illustration of the sorafenib encapsulated silica containing redox nanoparticle (siRNP) [2].

Preparation of siRNP and sorafenib@siRNP

The siRNP was prepared from PEG-siPMNT by the dialysis method (Fig. 1). PEG-siPMNT was dissolved in DMF, and the polymer solution was transferred into a membrane tube (Spectra/Por, molecular-weight cutoff size 3500; Spectrum Laboratories, Inc., Rancho Dominguez, CA) and then dialyzed for 24 h against 2 L of water, which was changed after 2, 5, 8 and 20 h. After 24 h, the solution was used as siRNP.

For preparation of sorafenib@siRNP, suitable ratios of PEG-siPMNT and sorafenib were dissolved in DMF and the resulting solution was transferred into the membrane tube and dialyzed against 2 L of water for 24 h similar to the preparation of siRNP to obtain sorafenib@siRNP.

Characterization of siRNP

The sizes of siRNP and sorafenib@siRNP were evaluated by DLS (dynamic light scattering) using a Zetasizer Nano ZS (Malvern Instruments, Ltd., Malvern, UK). The DLS measurements were carried out at 25 °C at a detection angle of 173°. The antioxidant activity of nanoparticle was measured by DPPH antioxidant assay. Reaction were wrapped in aluminum foil and kept at 30 °C for 30 min in dark. All measurements were done under dim light and measurements were done at 517 nm.

Cell line and culture

Human liver carcinoma cell (Hep-G2), colon cancer cell (C-26) and bovine aortic endothelial cell (BAEC) were obtained from Riken BioResource Center (Riken Tsukuba Institute, Ibaraki, Japan). Cell lines were cultured by Dulbecco's Modified Eagle Medium (DMEM, Sigma-Aldrich, St. Louis, MO) containing 5% fetal bovine serum (Sigma-Aldrich, St. Louis, MO), and 1% antibiotics (penicillin/streptomycin/neomycin, Invitrogen, Carlsbad, CA) in a humidified atmosphere of 5% CO₂ at 37 °C.

Animals

All experiments were performed using 7-week-old male Balb/c mice (22-25 g) purchased from Charles River Japan, Inc. (Kanagawa, Japan). Mice were maintained in the experimental animal facilities at the University of Tsukuba. All experiments were performed according to the Guide for the Care and Use of Laboratory Animals at the University of Tsukuba (Application #18-193).

Cell uptake

Cellular uptake of siRNP *in vitro* was observed in colon cancer C-26 cell by Rhodamin-labeled siRNP using a fluorescent microscope.

Cell viability assay

The anticancer activity and toxicity of sorafenib@siRNP was evaluated by cell viability using MTT test. Cell lines (HepG2, C-26 and BAEC) were seeded into 96-well plate (10⁴ cells/well) and incubated for 24 h at 37 °C, 5% CO₂. Samples including free sorafenib and sorafenib@siRNP were added and kept for 24 h at 37 °C, 5% CO₂. MTT solution (0.5 mg/mL) was added to each well and incubated for 4 h at 37 °C, 5% CO₂. The formazan crystals were dissolved by addition of DMSO and absorbance was measured at 570 nm.

Murine model of colon cancer

Preparation of murine model of colon cancer was conducted by injecting colon cancer cells. C-26 cells (10^6 cells/mouse) were transplanted subcutaneously into the mice's right leg. The mice was intraperitoneally injected with sorafenib or sorafenib@siRNP for 12 d after tumor inoculation. Tumor volumes were measured and calculated as $1/2 \times \text{length} \times \text{width}^2$.

RESULTS AND DISCUSSION

Characterization of siRNP

Sorafenib, is a hydrophobic drug, was encapsulated into siRNP by self-assembling using dialysis method. After encapsulation in siRNP, sorafenib solubility was significantly improved as shown in Figure 2A. The prepared nanoparticles were analyzed by transmission electron microscopy (TEM) after drying up, which showed spherical shape (Fig. 2C) with the hydrodynamic size of nanoparticle was about 44 nm, which was further confirmed by DLS measurement (Fig. 2B). the size of siRNP slightly increases after sorafenib encapsulation (Fig. 2B). Antioxidant activity of siRNP was lower than nitroxide radical TEMPOL, which can be explained due to the confinement of nitroxide radical into the core of siRNP (Fig. 2D).

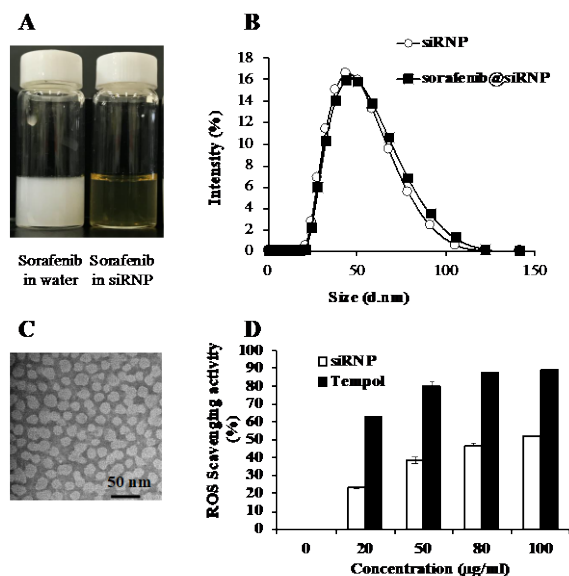


Figure 2. The characterizations of siRNP and effect of sorafenib@siRNP, A. Solubility of sorafenib, B. The size of siRNP, C. The TEM image of siRNP, D. Antioxidant activity activity of siRNP.

Cell uptake

The internalization of nanoparticle into cancer cell plays important role in cancer therapeutics. As shown in Figure 3, using Rhodamine-labeled siRNP

(red signal), it is confirmed that siRNP rapidly internalizes into colon cancer cell within 1 h and localized in cytosol, which suggesting the potential drug delivery of siRNP into cancer cells.

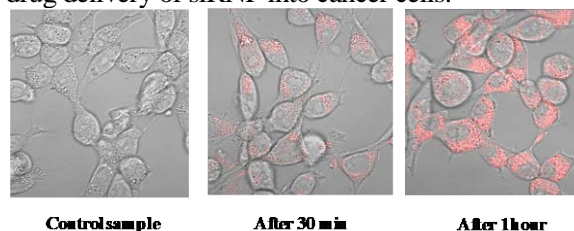


Figure 3. Cellular uptake of Rhodamin-labeled siRNP in colon cancer cell using fluorescent microscope.

Cell viability in vitro

The anticancer activity was evaluated using liver cancer cell (Hep-G2) and colon cancer cell (C-26). As shown in Fig. 4A and B, the anticancer activity of sorafenib@siRNP was significantly improved as compared to free sorafenib. It is interesting to note that sorafenib@siRNP remarkably decreased its toxicity against normal cell line (BAEC) (Fig. 4C). On the basis of these *in vitro* assessments, it is anticipated that the encapsulation of sorafenib in siRNP has potential high activity in cancer treatment.

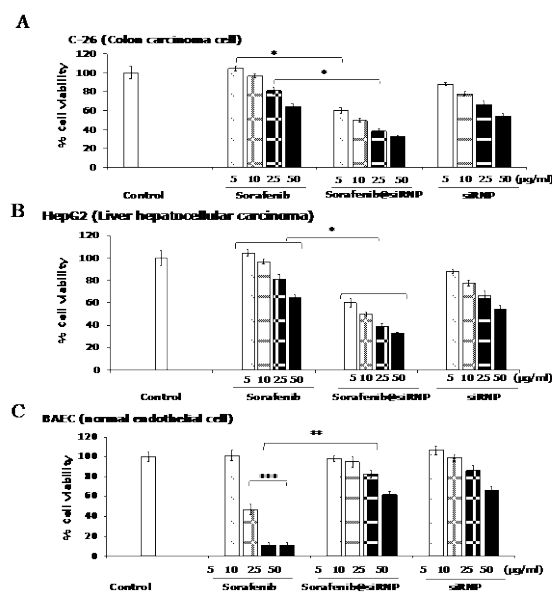


Figure 4. Effect of sorafenib@siRNP on cell viability, A. Cytotoxicity capacity of sorafenib@siRNP against colon cancer cell C-26, B. Cytotoxicity capacity of sorafenib@siRNP against liver hepatocellular carcinoma, C. Cytotoxicity capacity of sorafenib@siRNP against normal cell BAEC

Antitumor activity in vivo

Finally, *in vivo* experiment using colon cancer bearing mice, the treatment of sorafenib@siRNP exhibited significantly higher anticancer efficacy to suppress tumor growth as compared to free sorafenib and sorafenib-loaded control nanoparticle (without ROS scavenging property). This result indicates that siRNP not only improved the bioavailability of sorafenib, but also enhanced anticancer treatment by ROS scavenging effect.

CONCLUSION

Using silica containing redox nanoparticle (siRNP) to encapsulated sorafenib was able to enhance solubility of hydrophobic drug improving its bioavailability. Moreover, sorafenib@siRNP with antioxidant activity exhibited the higher antiproliferative effect against cancer cells and decreased toxicity in normal cells. Sorafenib@siRNP also exhibited higher anticancer efficacy in tumor bearing mice model as compared to free sorafenib without noticeable adverse effect. The results in this study indicate potential applications of siRNP as drug nano-carrier in cancer treatment.

Acknowledgment

This work was supported by Vietnam National Foundation for Science and Technology Development (NAFOSTED under Grant number 108.05-2017.327) and Vietnam National University Ho Chi Minh City (VNU-HCM) under grant number C2019-18-24. This was also partly supported by MEXT Grant-in-Aid for Scientific Research A (18H04160).

References

- [1] Hossain, Md Amran, et al. "Silica-installed redox nanoparticles for novel oral nanotherapeutics—improvement in intestinal delivery with anti-inflammatory effects." *Journal of drug targeting* 22.7 (2014): 638-647
- [2] Long Binh Vong, Shinya Kimura, and Yukio Nagasaki. "Newly Designed Silica-Containing Redox Nanoparticles for Oral Delivery of Novel TOP2 Catalytic Inhibitor for Treating Colon Cancer." *Advanced healthcare materials* 6.20 (2017): 1700428
- [3] Reuter, Simone, et al. "Oxidative stress, inflammation, and cancer: how are they linked?." *Free radical biology and medicine* 49.11 (2010): 1603-1616.
- [4] Sun, Tianmeng, et al. "Engineered nanoparticles for drug delivery in cancer therapy." *Angewandte Chemie International Edition* 53.46 (2014): 12320-12364. *Gastroenterology* 143.4 (2012): 1027-1036.
- [5] Thangavel, Sindhu, et al. "Redox nanoparticles inhibit curcumin oxidative degradation and enhance its therapeutic effect on prostate cancer." *Journal of Controlled Release* 209 (2015): 110-119.
- [6] Vong, L. B., Tomita, T., Yoshitomi, T., Matsui, H., & Nagasaki, Y. (2012). "An orally administered redox nanoparticle that accumulates in the colonic mucosa and reduces colitis in mice". *Gastroenterology*, 143(4), 1027-1036.

NIKEL NANOPARTICLES LOADED ON CERIA OXIDE SPHERES AS CATALYST FOR DRY REFORMING OF METHANE

Diep Ngoc Le, Phuc Hoan Tu, Dung Trung Dao, Tin Chanh Duc Doan*, Chien Mau Dang
Institute for Nanotechnology, Vietnam National University-Ho Chi Minh City, Community 6, Linh Trung Ward, Thu Duc District, Ho Chi Minh City, Vietnam;
Email: ddctin@vnuhcm.edu.vn

ABSTRACT

In this paper, Nickel particles were loaded on ceria oxide flowers dispersed on framework of inorganic fibers as catalyst for dry reforming methane. The tests of dry reforming of methane were performed at 700-800°C. With the Ni/Ce flowers, at 700°C, 750°C and 800°C initial CH₄ conversion and after 100 h were 85-63%, 93-88%, 96-87%, respectively. Without the dispersion of ceria oxide flowers, these were 96-70% at 800°C. The samples after 100 hours of reforming at 800°C were reactivated and then reforming the reaction again for another 100 hours. The conversion of CH₄ after hydrogen reactivation was higher and more stable than the original catalyst by a few %.

Keywords: dry reforming, ceria oxide flower, reactivation

INTRODUCTION

CO₂ and CH₄ are the major greenhouse gases generated by human activities such as transportation, electricity, industry, etc. and fermentation of organic waste [1]. To suppress global warming, it is necessary to promote usage of CH₄ and CO₂ mixture as energy resources. In rural areas, organic wastes derived from agriculture activities have to be utilized as renewable resources. For power generation, these are digested under anaerobic condition (methane fermentation) to produce biogas (60% CH₄-40% CO₂) [2].

Dry reforming is a method to produce syngas (mixture of hydrogen and carbon monoxide) from the reaction of methane and carbon dioxide follow the reaction: CH₄ + CO₂ ↔ 2 CO + 2 H₂ [3]. With the syngas product (hydrogen and carbon monoxide), dry reforming can be applied directly to solid oxide fuel cell. The side reactions which lead to the formation of coke (carbon) are the main reason for the reduction of the methane conversion by time. The catalysts frequently used for dry reforming reaction are transition metals (Cu, Co, Ni...) or noble metal catalysts (Pt, Ru, Rh...) supported on oxide-based materials [4].

Ceria (CeO₂) has attracted much attention to be used as the promoters for three-way catalysts, catalyst supports, electrolytes for solid oxide fuel cells, oxygen sensors. Besides, CeO₂ can be processed and formed in various structures

and morphologies including nanowires, nanorods, nanotubes, and mesoporous structures via various synthesis routes using different techniques such as sol-gel method, hydrothermal method and template-assisted method [5].

In this paper, the flower-like ceria microspheres were prepared by hydrothermal synthesis method and used as a catalyst support to load transition metal Ni for dry reforming of methane. The porous structured catalyst (PSC) samples were fabricated from the obtained flower-catalyst, alumina-silica fiber and was used as a catalyst for methane reforming. The dry reforming characterization was performed at 700-800°C and the methane conversion of the samples was calculated basing on the concentrations of the gases by gas chromatography (GC).

EXPERIMENTAL

Preparation of Flowerlike-CeO₂ Powder (Ce(F))

To obtain Ce(F), 15 mL Ce(NO₃)₃ solution of 0.05M (0.0075 mol) and 75mL glucose solution of 0.02M (0.015 mol) under magnetic stirring followed by adding acrylic acid (2.05 mL – 0.03 mol) to form a translucent solution. After that, 6.6 mL ammonia solution (25 wt %) was diluted in 20 mL deionized, and the diluted ammonia solution was supplied dropwise to the above mixture. The solution was

stirred at 30°C for 5 h to form a deep brown solution and transferred into a Teflon-lined autoclave (150 mL), sealed and kept at 180°C for 72 h, and naturally cooled down to room temperature. The resulting orange suspension was washed with water and alcohol for several times, and then dried at 80°C overnight. The flowerlike-Ce(OH)CO₃ microspheres were finally obtained. By the subsequent calcination at 600°C for 6 h in air, the flowerlike-CeO₂ (Ce(F)) microspheres were obtained.

Preparation of NiO/Ce(F) Catalyst Powder

The NiO/Ce(F) catalyst powder was prepared by the impregnation method. 2 g of Ce(F) was added into 4 mL of 0.5 M Ni(NO₃)₂ solution with polyvinylpyrrolidone (5 wt%), and kept for 5 h, then dried at 80 °C for 8 h. The green powder was calcined at 550 °C for 6 h to obtain NiO/Ce(F) powder.

Preparation of PSC samples

Ni/Ce(F)-PSC. 1.21 g of ceramic fiber (Al₂O₃: 48 wt%, SiO₂: 52 wt%) and 0.012 g of cotton fiber were mixed in 100 mL of DI water. After adding 2.42 g of NiO/Ce(F) and 0.6 mL of 2 wt% cationic polymer solution (polydiallyldimethylammonium chloride), the suspension underwent ultrasonic treatment for 15 min followed by magnetic stirring for 1 h. Then, 0.6 mL of 2 wt% anionic polymer solution (acrylamide-co-acrylic acid) was added with continuous magnetic stirring for 15 minutes. After 1 h stabilization, the suspension was mixed again just before filtration to obtain a wet-state sheet with a diameter of 6.6 cm, which was pressed and dried at 80°C overnight. Finally, 3-3.5 wt% Ni-loaded Ce(F)-dispersed PSC (Ni/Ce(F)-PSC) was obtained by heat treatment at 600°C for 5 h with subsequent reduction treatment.

Ni/PSC. The Ni/PSC was prepared with the same process of the Ni/Ce(F)-PSC but without the NiO/Ce(F) powder. After obtaining pure ceramic paper (including ceramic fiber only after heat treatment at 600°C for 5 h), the Ni/PSC was prepared by the impregnation method: 4 mL of 0.5 M Ni(NO₃)₂ solution was added into the pure ceramic paper, kept overnight and dried at 80°C in 8 h. The green paper was calcined at 600°C for 6 h to obtain the Ni/PSC have 8-10 wt% Ni-loaded PSC (Ni-PSC).

Dry Reforming Tests with PSCs

Dry reforming of CH₄ was performed in a reactor and follow the procedure of Shiratori et. Al. [6], as shown in **Figure 1**. Three PSCs with a thickness of 1.5 mm for each PSC were installed in an porcelain tube with 20mm of inner diameter, the temperature was increased to reaction temperature within under N₂ atmosphere for 1 h and applied 150 mL min⁻¹ of H₂ to reduce NiO to Ni catalyst. To start the 100-h dry reforming test, the mixed gas of CH₄ and CO₂ (20 mL min⁻¹ for each gas) was applied with a gas hourly space velocity (GHSV) of ~2300 h⁻¹. The mixed gases after reforming reaction were analyzed every 1 h in the first 40-h and 2 h in the next 60-h by automatic gas chromatography (GC-20B; Shimadzu Corp., Japan).

The conversion of CH₄ and GHSV were calculated as follows:

Methane conversion (%):

$$X_{CH_4} (\%) = \left(1 - \frac{\%CH_4 \text{ out}}{\%CH_4 \text{ in}}\right) * 100$$

$$GHSV = \frac{\text{total reaction flow rate (mL h}^{-1}\text{)}}{\text{total catalytic volume (cm}^3\text{)}}$$

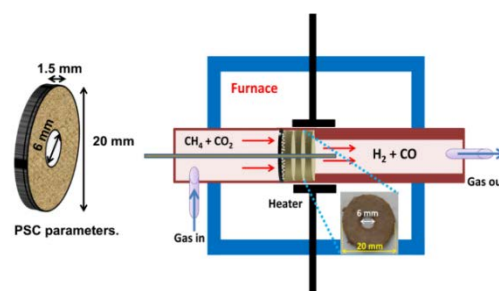


Figure 1. Schematic illustration of the setup for the test of DRM using PSCs

Reactivation of PSC

The PSC after 100 h of dry reforming reaction was reactivated by gas supply of 100 mL.min⁻¹ CO₂ for 1 h at the previous reaction temperature. Then the 100-h dry reforming was started for the next test, the mixed gas of CH₄ and CO₂ (20 mL min⁻¹ for each gas) was applied.

Characterizations

The microstructures of Ce(F), NiO/Ce(F), Ni-PSC, Ni/Ce(F)-PSC were observed by a field emission scanning electron microscope (FE-SEM-SU8000, Hitachi, Japan). The percentage of nickel loading was determined by inductively coupled plasma (ICP) spectrometer (Shimadzu ICPE-9000, Japan). Raman spectroscopic analysis of coke/ carbon deposited on the PSC samples after reforming tests was carried out

using a Raman microscope Labram 300, Horiba Jobin Yvon, France.

RESULTS AND DISCUSSION

Characterization of PSCs

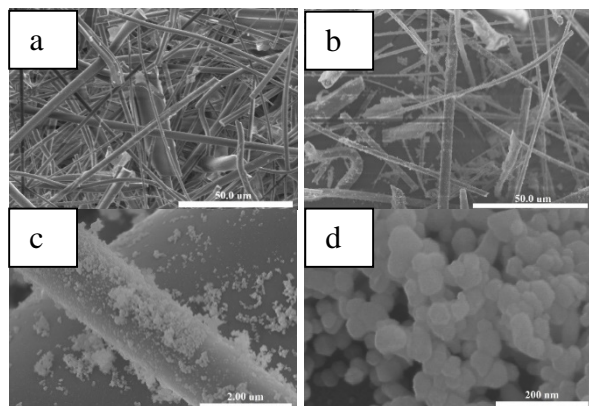


Figure 2. Structure of PSC blank (a), Ni-PSC (b, c, d).

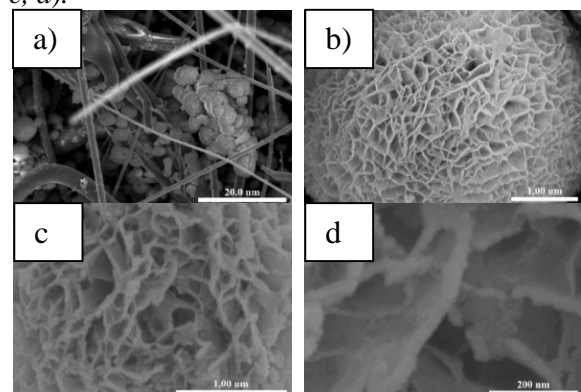


Figure 3. Structure of Ni/Ce(F)-PSC (a), Ce(F) (b), Ni/Ce(F) (c, d).

Figure 2a shows the fiber network of PSC blank. Figure 2b, c, d show the fiber network of Ni/PSC including NiO nanoparticles formed on the fiber surface. Particle size was about 20-50 nm. Figure 3a shows the structure of the Ni/Ce(F)-PSC in which, Ni/Ce(F) flowerlike microspheres on the ceramic fiber. Figure 3b describes the structure of Ce(F). Figure 3c, d show the distribution of Ni particles on the Ce(F) surface, where the Ni particles are evenly distributed across the petals of the Ce(F). The NiO nanoparticles were formed on the porous flowerlike CeO₂ with the diameter of about 30-50 nm. Ni loading in theory and Ni loading measured by ICP of PSCs are summarized in Table 1.

Table 1. Ni loading PSCs

Sample	%Ni theory	% Ni ICP
Ni-PSC	8-10	7.3

Ni/Ce(F)-PSC	3-3.4	3.0
--------------	-------	-----

Dry reforming tests with the PSCs

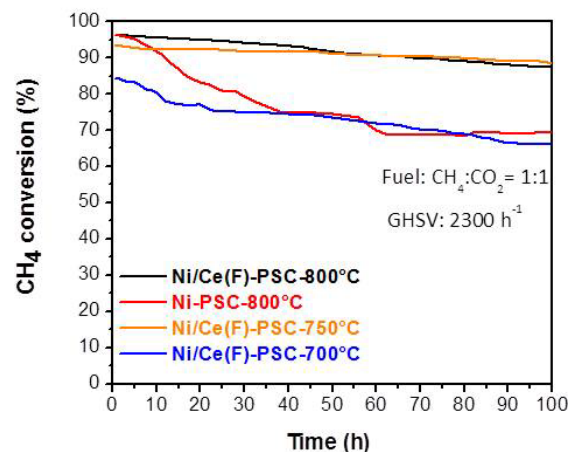


Figure 4. CH₄ conversion measured during 100 h DRM test.

Figure 4 shows the CH₄ conversion measured during 100 h DRM test at 700, 750 and 800°C.

At 700°C, with the Ni/Ce(F)-PSC, the initial CH₄ conversion was 84%, conversion decreases by more than 20% after 100 hours application. At 750 and 800°C, the conversion rate decreases by about 5-7% after 100 h. For Ni-PSC, when the reaction at 800°C the conversion efficiency decreases rapidly after more than 30%. The Ni/Ce(F)-PSC and Ni-PSC after 100 hours of reforming at 800°C were reactivated by catalyzing CO₂ through the catalyst and then reforming the reaction again for another 100 hours. The results are shown in Figure 5. It can be seen that after reactivating the reforming reaction of Ni/Ce(F)-PSC and Ni-PSC, the conversion of CH₄ to hydrogen was higher and more stable than the original catalyst by a few %.

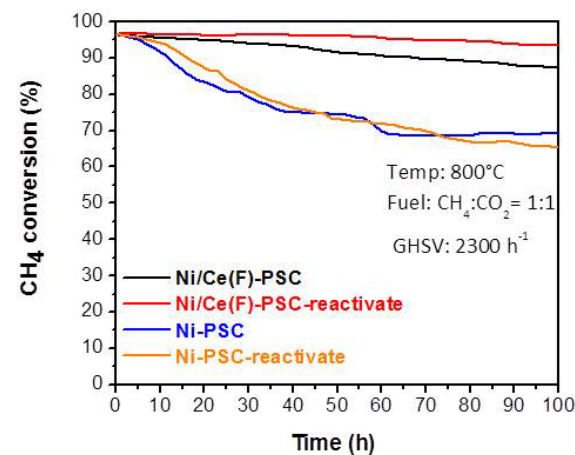


Figure 5. CH_4 conversion measured during 15 h DRM test at $750^\circ C$.

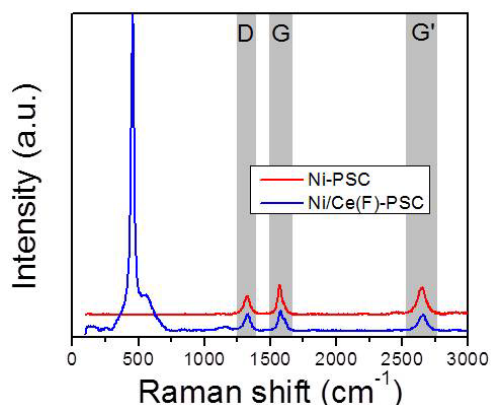


Figure 6. Raman spectra of the PSCs after 100 hours of reactivation.

From the carbon raman result (Figure 6) of the PSCs after 100 hours of reactivation, it can be seen that the amount of carbon in Ni-PSC was higher than the Ni/Ce(F)-PSC. Their FESEM results (Figure 7) show that the carbon deposited on the PSC was carbon nanotubes.

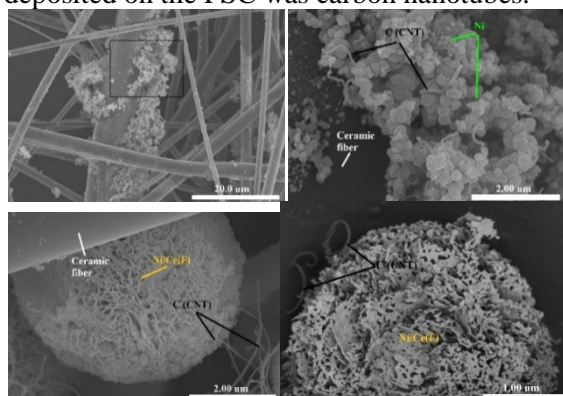


Figure 7. Structure of Ni-PSC (a, b), Ni/Ce(F)-PSC (c, d) after 100 hours of reactivation.

CONCLUSION

In this study, the flower-like ceria microspheres with Ni nano particles were embedded on the PSC as a catalyst support for dry reforming of methane. With the amount of Ni in Ni-PSC higher Ni/Ce(F)-PSC, the methane conversion was lower and no more stable after 100 h at $800^\circ C$. Moreover, the coke amount formed on the catalyst was significantly reduced in the presence of the CeO_2 flowers whereas the methane conversion efficiency was maintained.

Acknowledgment

This research is funded by Vietnam National University - Ho Chi Minh City (VNUHCM) under grant number B2017-32-01. We

appreciate Science and Technology Research Partnership for Sustainable Development (SATREPS), Japan International Cooperation Agency (JICA) for equipment support.

References

- [1] G. Zhang, J. Liu, Y. Xu and Y. Sun, A review of CH_4CO_2 reforming to synthesis gas over Ni-based catalysts in recent years (2010–2017), *Int. J. Hydrog. Energy*, **43**(32), 15030 (2018).
- [2] K. Hagos, J. Zong, D. Li, C. Liu, and X. Lu. *Anaerobic co-digestion process for biogas production: Progress, challenges and perspectives*, *Renew. Sust. Energ. Rev.*, **76**, 1485 (2017).
- [3] Leimert, J. M., Karl, J. and Dillig, M. *Dry reforming of methane using a nickel membrane reactor*, *Processes*, **5** 82, (2017).
- [4] Mohamedali, M., Henni, A. and Ibrahim, H. *Recent advances in supported metal catalysts for syngas production from methane*, *Chem. Eng. J.* **2** 9, (2018).
- [5] H. Li, G. Lu, Q. Dai, Y. Quang, Y. Guo and Y. Guo, *Hierarchical organization and catalytic activity of high-surface-area mesoporous ceria microspheres prepared via hydrothermal routes*. *ACS Appl Mater Interfaces* Vol.2: 838-846, (2010).
- [6] Nguyen, T., Tran, D., Sakamoto, M., Uchida, T., Sasaki, K., To, T., Doan, D., Dang, M. and Shiratori, Y. *Ni-loaded (Ce, Zr) O_2 - δ -dispersed paper-structured catalyst for dry reforming of methane*. *Int. J. Hydrogen Energy* **43** 4951, (2018).